ELSEVIER

FUEL CELLS:

TECHNOLOGIES FOR FUEL PROCESSING

EDITED BY

D. SHEKHAWAT, J.J. SPIVEY, AND D.A. BERRY

FUEL CELLS: TECHNOLOGIES FOR FUEL PROCESSING

Edited by

DUSHYANT SHEKHAWAT

JAMES J. SPIVEY

DAVID A. BERRY

ELSEVIER

AMSTERDAM • BOSTON • HEIDELBERG • LONDON
NEW YORK • OXFORD • PARIS • SAN DIEGO
SAN FRANCISCO • SINGAPORE • SYDNEY • TOKYO

Elsevier
The Boulevard, Langford Lane, Kidlington, Oxford, OX5 1GB, UK
Radarweg 29, PO Box 211, 1000 AE Amsterdam, The Netherlands

Library of Congress Cataloging-in-Publication Data
A catalog record for this book is available from the Library of Congress

British Library Cataloguing in Publication Data
A catalogue record for this book is available from the British Library

ISBN: 978-0-444-53563-4

Printed and bound in Spain

11 12 13 14 10 9 8 7 6 5 4 3 2 1

Preface

FUEL CELLS: TECHNOLOGIES FOR FUEL PROCESSING

Fuel cells are rapidly approaching commercial viability. Fuel cells are clean and efficient energy sources for transportation, stationary, and distributed power. Private industry, academia, as well as government agencies (particularly in developed countries) are actively engaged in developing cost effective fuel cell technology. The fuel processor is a critical component of a fuel cell power system and must be able to provide a clean H_2 or H_2-rich synthesis gas to the fuel cell stack for long-term operation. In spite of the increasing technical and commercial importance of fuel cells, there are few books in which fuel processing technology is treated comprehensively. The majority of books over the years about fuel cells address fuel processing technologies only briefly; e.g., in a single section in a chapter.

Fuel Cells: Technologies for Fuel Processing provides an overview of the most important aspects of fuel reforming to the generally interested reader, researcher, technologist, teacher, student, or engineer. The topics covered include all aspects of fuel reforming: fundamental chemistry, different modes of reforming, catalysts, catalyst deactivation, fuel desulfurization, reaction engineering, novel reforming concepts, thermodynamics, heat and mass transfer issues, system design, and recent research and development.

By focusing on the fundamentals, this book is intended to be a source of information now and in the future. By avoiding time-sensitive information/analysis (e.g., economics) this book will serve as a single source of information for scientists and engineers in fuel processing technology. The material is presented in such a way that this book will serve as a reference for graduate level courses, fuel cell developers, and fuel cell researchers.

No attempt is made to describe the fuel cell itself—e.g., there is no in-depth discussion of the various electrolytes in proton exchange membrane (PEM) or solid oxide fuel cells (SOFCs). Rather, a sufficient description of the fuel cell is included to show how it affects the fuel reformer—e.g., CO removal from the reformate is required by PEMs, but not SOFCs. Also, no attempt was made to include the hydrogen production from non-carbon sources such as water electrolysis, borohydrides, etc.

It is a pleasure to thank those who have made this project possible. First of all, we would like to thank all our coauthors. We are very grateful they were able to dedicate their valuable time to this project. It has been our pleasure to work with all the contributors involved in this book. Their effort in combining their own research with recent literature in the field of fuel processing is highly appreciated. This effort would not have been possible without their willingness to share their valuable knowledge, insight, and experience. Moreover, we express our gratitude

for their responsiveness to deadlines and review comments.

We also want to express our sincere gratitude to all reviewers who provided their thoughtful and timely comments. We would like to thank Debra Benson (Performance Results Corporation, Morgantown, WV) for her skillful assistance in modifying and redrawing several figures for this book. We would like to thank Stacy Kief (U.S. Department of Energy, Morgantown, WV) for authentication of the text. We gratefully acknowledge Mark W Smith (URS Corporation, Morgantown, WV) for his kind suggestions throughout this project. Thanks to Mike Bergen (URS Corporation) for his support during this book. Also, thanks to Anita Koch (development editor) and Poulouse Joseph (project manager) from Elsevier for their help in coordinating the publication process. Our appreciation also extends to the senior Acquisition Editor for Chemistry and Chemical Engineering books Kostas Marinakis for his support of this project. We would also to thank Elsevier for their commitment to this book.

Dushyant Shekhawat
James J. Spivey
David A. Berry

Editors Biography

Dushyant Shekhawat

Dushyant Shekhawat is a researcher at National Energy Technology Laboratory (U.S. Department of Energy), Morgantown, WV, USA. He received his BS in Chemical Engineering from the University of Minnesota in Twin Cities and his PhD in Chemical Engineering from the Michigan State University in East Lansing. His research interests include: fuel processing for fuel cell applications, reaction engineering, surface chemistry, heterogeneous catalysis, energy, fuel cell, plasma and radio frequency- assisted fuel reforming, and plasma chemistry. He has served as a guest-editor for the special issues of Catalysis Today (Reforming of Liquid Hydrocarbon Fuels for Fuel Cell Application) and the journal of Fuel (Advanced Fossil Energy Utilization). Shekhawat is a registered Professional Engineer (PE) in West Virginia and also serves on the NCEES's PE Chemical Engineering Exam Committee, which produces the Professional Engineer Examination for chemical engineers. He is a member of the American Chemical Society and American Institute of Chemical Engineers.

David A. Berry

David A. Berry is Director of the Separations and Fuel Processing Division at the Department of Energy's National Energy Technology Laboratory (NETL). He has 24 years of extensive experience in energy-related research & development programs involving coal, oil, and natural gas. His research career has spanned fundamental through system-level development most specifically related to fuel cell, turbine and gasification technologies. His current focus is on CO_2 capture research and development of catalytic oxidation and syngas conversion processes. He has served on the Editorial Board for Catalysis Today.

James J. Spivey

James J. Spivey is the Shivers Professor of Chemical Engineering at Louisiana State University (LSU). He received his BS and MS at North Carolina State University, and his PhD from LSU. He currently serves as Director of the Center for Atomic-level Catalyst Design, a U.S. Dept. of Energy-funded Center focusing on developing new computational, synthesis, and characterization tools for heterogeneous catalysts. His research career has been directed toward the application of fundamental catalysis to problems such as clean energy, conversion of syngas to higher value products, environmental catalysis, and activation of CO_2 and methane. He is the Editor-in-Chief of Catalysis Today, and Editor of the Catalysis book series published by the Royal Society of Chemistry (Cambridge, UK), and is also a Fellow of the Royal Society of Chemistry.

Contributors

Ahmet K. Avci Department of Chemical Engineering, Boğaziçi University, Bebek 34342, Istanbul, Turkey, Phone: +90-212-3597785, Email: avciahme@boun.edu.tr

David A. Berry National Energy Technology Laboratory, U. S. Department of Energy, 3610 Collins Ferry Rd, Morgantown, WV 26507, USA, Phone: +1-304-285-4430, Email: david.berry@netl.doe.gov

Robert A. Dagle Pacific Northwest National Laboratory, P.O. Box 999, Richland, WA 99352, USA, Phone: +1-509-375-6264, Email: robert.dagle@pnl.gov

Alexander Fridman A.J. Drexel Plasma Institute, Drexel University, 3141 Chestnut Street, Philadelphia, PA 19104, USA, Phone: +1-215-895-1542, Email: af55@drexel.edu

Michael J. Gallagher URS Corporation, National Energy Technology Laboratory, 3610 Collins Ferry Rd, Morgantown, WV 26507, USA, Phone: +1-304-285-4835, Email: michael.gallagher@ur.netl.doe.gov

Santosh K Gangwal Southern Research Institute - North Carolina, Advanced Energy and Transportation Technologies, 5201 International Drive, Durham, NC 27712, USA, Phone: +1-919-282-1053, Email: gangwal@southernresearch.org

Jing Gao Institute of Catalysis, Department of Chemistry, Zhejiang University, Hangzhou, 310028, China, Phone: +86-571-88273283, Email: pinkjinggao@163.com

John B. Hansen Haldor Topsøe A/S, Nymøllevej 55, DK-2800 Kgs. Lyngby, Denmark, Phone: +45-4527-2459, Email: jbh@topsoe.dk

Daniel J. Haynes National Energy Technology Laboratory, U. S. Department of Energy, 3610 Collins Ferry Rd, Morgantown, WV 26507, USA, Phone: +1-304-285-1355, Email: daniel.haynes@netl.doe.gov

Zhaoyin Hou Institute of Catalysis, Department of Chemistry, Zhejiang University, Hangzhou, 310028, China, Phone: +86-571-885103987, Email: zyhou@zju.edu.cn

Ayman M. Karim Pacific Northwest National Laboratory, P.O. Box 999, Richland, WA 99352, USA, Phone: +1-509 375-4186, Email: ayman.karim@pnl.gov

David L. King Pacific Northwest National Laboratory, P.O. Box 999, Richland, WA 99352, USA, Phone: +1-509-375-3908, Email: david.king@pnl.gov

Guosheng Li Pacific Northwest National Laboratory, P.O. Box 999, Richland, WA 99352, USA, Phone: +1-509-371-6520, Email: guosheng.li@pnl.gov

Hui Lou Institute of Catalysis, Department of Chemistry, Zhejiang University, Hangzhou, 310028, China, Phone: +86-571-88273283, Email: louhui@tom.com

Rich Mastanduno Precision Combustion, Inc., 410 Sackett Point Road, North Haven, CT 06473, USA, Phone: +1-203-287-3700 x264, Email: rmastanduno@precision-combustion.com

Jens R. Rostrup-Nielsen Haldor Topsøe A/S, Nymøllevej 55, DK-2800 Kgs. Lyngby, Denmark, Phone: +45-4527-2397, Email: jrn@topsoe.dk

Z. Ilsen Önsan Department of Chemical Engineering, Boğaziçi University, Bebek 34342, Istanbul, Turkey, Phone: +90-212-3596412, Email: onsan@boun.edu.tr

Subir Roychoudhury Precision Combustion, Inc., 410 Sackett Point Road, North Haven, CT 06473, USA, Phone: +1-203-287-3700 x267, Email: sroychoudhury@precision-combustion.com

Dushyant Shekhawat National Energy Technology Laboratory, U. S. Department of Energy, 3610 Collins Ferry Rd, Morgantown, WV 26507, USA, Phone: +1-304-285-4634, Email: dushyant.shekhawat@netl.doe.gov

Mark W. Smith URS Corporation, National Energy Technology Laboratory, 3610 Collins Ferry Rd, Morgantown, WV 26507, USA, Phone: +1-304-285-4126, Email: mark.smith@netl.doe.gov

James G. Speight CD & W Inc., 2476 Overland Rd, Laramie, WY 82070, USA, Email: jamessp8@aol.com

James J. (Jerry) Spivey Gordon A. and Mary Cain Department of Chemical Engineering, Louisiana State University, S. Stadium Drive, Baton Rouge, LA 70803, USA, Phone: +1-225-578-3690, Email: jjspivey@lsu.edu

Yu Su Pacific Northwest National Laboratory, P.O. Box 999, Richland, WA 99352, USA

Mark C. Williams URS Corporation, National Energy Technology Laboratory, 3610 Collins Ferry Rd, Morgantown, WV 26507, USA, Phone: +1-304-285-4344, Email: mark.williams@ur.netl.doe.gov

Xiaoming Zheng Institute of Catalysis, Department of Chemistry, Zhejiang University, Hangzhou, 310028, China, Phone: +86-571-88273283, Email: xmzheng@dial.zju.edu.cn

CHAPTER

1

Introduction to Fuel Processing

Dushyant Shekhawat [*], *David A. Berry* [*], *James J. Spivey* [†]

[*] National Energy Technology Laboratory, U.S. Department of Energy, 3610 Collins Ferry Road, Morgantown, WV 26507-0880, USA and [†] Department of Chemical Engineering, Stadium Drive, Louisiana State University, Baton Rouge, LA 70803, USA

OUTLINE

1.1. CLEAN ENERGY

One of the most critical challenges facing the world is the development of clean, reliable, and efficient energy conversion processes. Because the standard of living of virtually all nations is directly related to per capita energy consumption [1,2], the demand for energy will inevitably increase. At the same time, it is widely accepted that this increasing demand for energy must not compromise the environment.

Advanced technologies designed to meet this challenge include processes as different as wind, solar, hydroelectric, photovoltaic, and others. Among the most promising near-term technologies are those based on fuel cells, which convert chemical energy into electrical energy with higher efficiencies and far fewer environmental effects than other options. Several studies have recently reported on the technical viability and economics of fuel cell systems for various applications [3–14]. Fuel cells are being developed for use in transportation as well as for stationary and distributed power systems.

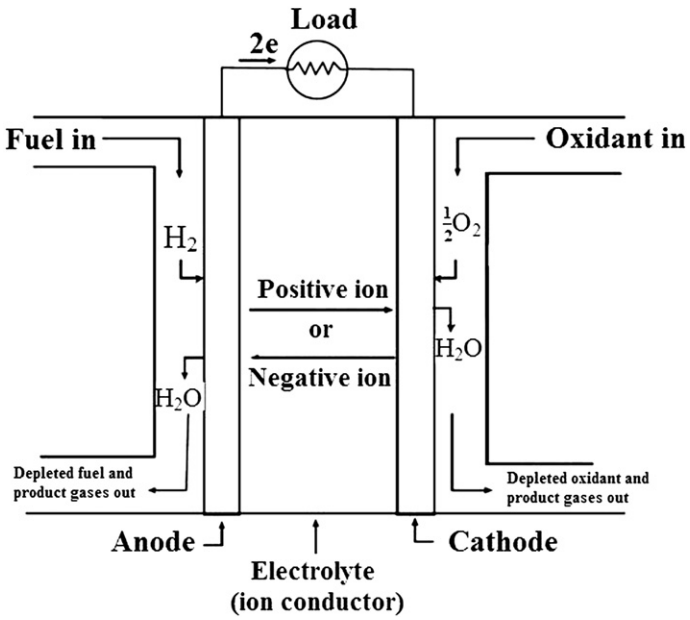

FIGURE 1.1 Schematic representation of an individual fuel cell [15].

1.2. FUEL CELLS

Fuel cells are essentially continuously operating batteries, which generate electricity from a fuel, such as hydrogen, and an oxidant, such as air. A schematic representation of a fuel cell with the product/reactant gases and the ion conduction flow directions through the cell is shown in Fig. 1.1.

Each type of fuel cell is designed to meet a different application. For example, the proton exchange membrane (PEM) fuel cell is being pursued by a number of companies because of its low operating temperature, response to transients [16], and compact size, which make it desirable for a number of residential [17–20], commercial, and military [21] applications. Solid oxide fuel cells (SOFCs) are being developed for small-scale stationary power applications, auxiliary power units (APUs) for vehicles [8,22–24], mobile generators for civilian as well as military applications [25]. See Chapter 2 for a detailed discussion of various fuel cells and their specific applications.

1.3. FUEL PROCESSORS

The purpose of a fuel processor is to convert a commonly available fuel, such as gasoline, diesel, or natural gas, into a gas stream containing primarily, or only, the compound(s) required by the fuel cell. A representative process diagram for a fuel processor designed to convert a liquid fuel (with added water to maximize H_2 yield and prevent catalysts

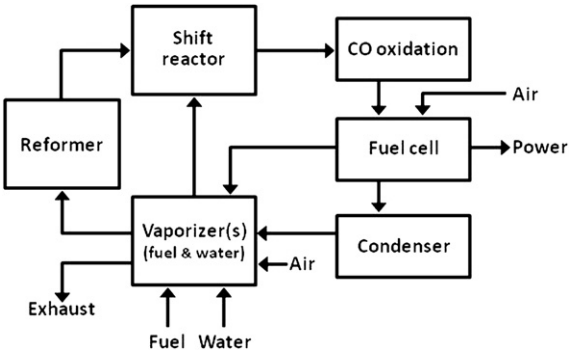

FIGURE 1.2 Generic fuel processor.

deactivation) into a CO-free gas stream containing essentially only H_2 and CO_2 is shown in Fig. 1.2. The fuel processor may consist of three steps, depending on the type of fuel cell (high or low temperature) it is coupled with: reforming of the liquid fuel into syngas, water gas shift (WGS), and preferential oxidation of CO.[1]

The fuel to power the fuel cells can, in principle, be a wide range of oxidizable compounds, such as hydrogen, CO, CH_4, and methanol. Regardless of the type of fuel cell, the fuel processor must produce a hydrogen-rich gas stream. Because a widely available hydrogen infrastructure does not exist, the hydrogen-rich gas can most readily be derived from the reforming of hydrocarbon fuels, which can take advantage of a well-developed existing infrastructure. Depending on the application, there are a wide range of conventional fuels, such as natural gas (methane) [26,27], methanol [28,29], ethanol [30,31], dimethyl ether [32,33], propane [34,35], butane [36,37], gasoline [38,39], kerosene [40,41], jet fuels [24,42], diesel [43,44], and biodiesel [45,46], which can be reformed to produce the hydrogen-rich reformate needed to power the fuel cell. Alcohol-based fuels are also widely studied for the production of H_2 for fuel cells because they can be reformed at relatively low temperatures and are free of sulfur compounds. Fischer–Tropsch fuels, which contain virtually no sulfur, aromatics, metals, or other toxics [47], are also being considered for reforming applications.

Because each type of fuel cell requires a different fuel, the fuel processor must be designed to match the fuel cell. For example, low-temperature fuel cells like PEMs require relatively pure hydrogen and cannot operate in the presence of CO concentrations greater than 10–20 ppm for any significant time. However, high-temperature fuel cells like SOFCs can utilize CO as well as hydrogen, so the shift reactor and CO oxidation step would not be needed, and reformate could be fed directly to the fuel cell.

1.4. REFORMING MODES

There are three predominant modes of catalytic reforming: partial oxidation (POX), steam reforming (SR), and oxidative steam reforming (OSR).[2] All three involve oxidation of the hydrocarbon fuel to produce a hydrogen-rich synthesis gas. These three reactions are shown below[3]:

$$\text{POX}: \ C_nH_m + \frac{n}{2}O_2 \rightarrow nCO + \frac{m}{2}H_2 \qquad (1.1)$$

$$\text{SR}: \ C_nH_m + nH_2O \rightarrow nCO + \left(n + \frac{m}{2}\right)H_2 \qquad (1.2)$$

[1] In this configuration, water is added to maximize H_2 yield and to minimize catalyst deactivation. Water is not essential, but illustrates one design option. Also note that the fuel cell exhaust, consisting primarily of steam and CO_2, is condensed and (at least partially) recycled in this example. This can help maximize overall thermodynamic efficiency. A separate gas cleanup step, which would typically be located just downstream of the reformer, is not shown, but may be needed in some applications.

[2] Autothermal reforming (ATR) is a special case of OSR, in which the ratio of oxygen and steam is such that the net heat of reaction is zero at the reformer temperature.

[3] These reactions show only CO and H_2 as the products. CO_2 and H_2O are inevitably present in the product gas as well, but are not shown here for the sake of simplicity since CO and H_2 are the oxidizable products of the reforming reactions, and hence the fuels of interest for fuel cell applications. Note that the stoichiometry of the OSR reaction is not unique - there is no unique set of stoichiometric coefficients that balance the equation. See note 2 – ATR corresponds to one set of coefficients that both balances the equation and results in a net heat of reaction of zero at the reformer temperature.

$$\text{OSR}: \ C_nH_m + H_2O + O_2 \rightarrow CO + H_2 \quad (1.3)$$

The mode of operation has a significant impact on overall efficiency and operating characteristics of a fuel cell system. In principle, the reactions within the fuel processor can be either non-catalytic (thermal) or catalytic. Depending on the fuel, mode of reforming, and catalyst type, temperatures for catalytic systems typically range from 600 °C to 1000 °C [48,49]. The higher temperatures required for non-catalytic reforming can lead to formation of unwanted oxides of nitrogen. Non-catalytic reformers also require more costly materials of construction, and result in lower system efficiency due to the larger temperature difference between the fuel cell and reformer. For these reasons, they are not widely used, and are not considered further here.

Each of these modes is covered in a separate chapter (SR – Chapter 4, POX – Chapter 5, and OSR – Chapter 6). Additional modes of reforming such as CO_2 (dry) reforming (Chapter 7) and plasma reforming (Chapter 8) are also discussed in detail in this book.

1.5. THERMAL INTEGRATION OF THE FUEL PROCESSOR AND FUEL CELL

Thermal integration is an important aspect of the fuel processor. Fig. 1.3a depicts a fuel cell coupled to a catalytic POX reformer. This type of reformer operates at temperatures very close to the ~800 °C operating temperature of modern SOFCs. However, both the reformer and the fuel cell involve exothermic oxidation reactions, and heat is produced in both. This does not allow for a high degree of thermal integration and limits overall system efficiency.

Catalytic SR represents the other end of the reforming spectrum (Fig. 1.3b). Fuel is mixed with steam instead of O_2 in the reformer, to produce a very hydrogen-rich synthesis gas. The reaction is highly endothermic, and therefore requires an external source of heat to maintain the reactor temperature. The amount of energy required is generally on the order of 22% of the lower heat of combustion of a liquid fuel [48].

OSR is actually a hybrid of POX and SR (Fig. 1.3c), and is arguably the most thermally efficient means of producing a hydrogen-rich gas stream from liquid fuels [50]. In this type of reactor, fuel, air, and steam are mixed and reacted in a thermally neutral manner such that the endothermic SR reaction is thermally balanced by the exothermic POX reactions (i.e., no net heat gain/loss).

1.6. CHALLENGES FOR FUEL CELLS AND FUEL PROCESSORS

1.6.1. Fuel Flexibility

Although fuel cells provide a clean, efficient alternative to conventional energy conversion processes, widespread use of fuel cells requires a production and distribution network for the hydrogen-rich gas stream that these systems require. As fuel cell technology becomes more economically practical, an adequate gaseous fuel supply must be provided to meet the large-scale demand. This will likely require that fuel processors be designed to generate a relatively uniform hydrogen-rich gas stream from the wide range of fuels that are available at different locations – natural gas, ethanol, gasoline, diesel, etc. These fuels contain widely varying classes of compounds – methane, aromatics, etc. – as well as varying levels of contaminants that must be removed, such as sulfur. This requires different types of catalysts and post-reformer treatment process, such as sulfur removal and water gas shift steps.

For example, consider the most widely available fuels – gasoline and diesel. Despite their logistical appeal as feedstocks for H_2 production,

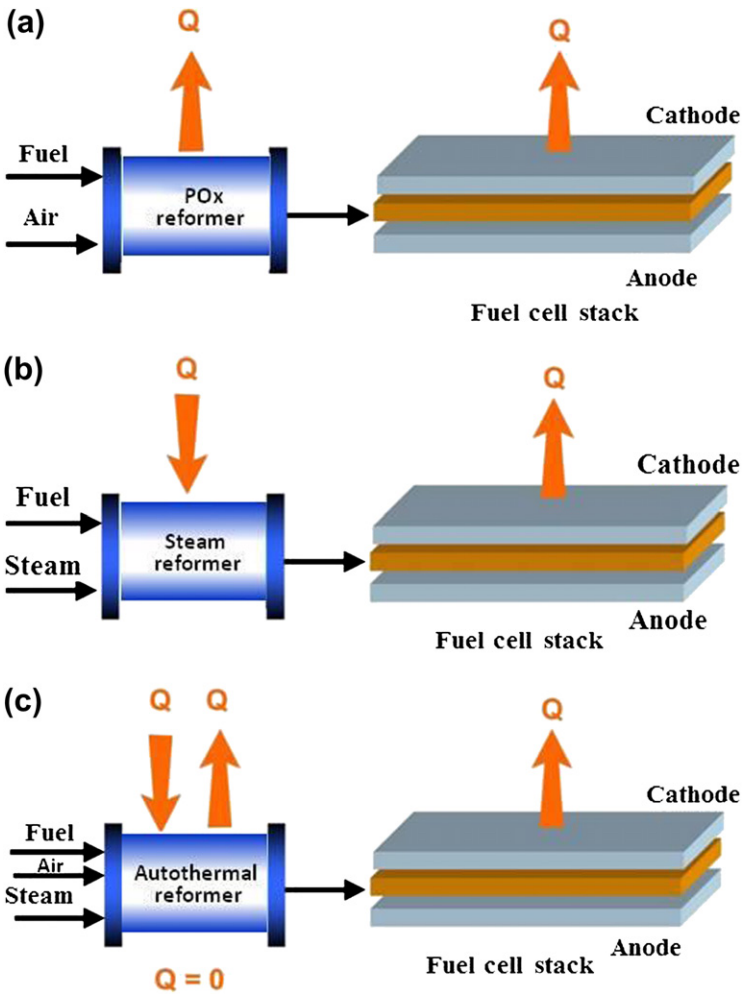

FIGURE 1.3 Thermal integration of reformer with fuel cell system: (a) partial oxidation (POX) reformer, (b) steam reformer, and (c) autothermal reformer.

these fuels are relatively difficult to reform for a variety of reasons related to both catalyst and reactor design. These fuels are complex variable mixtures of hundreds of hydrocarbon compounds containing mainly olefins, alkanes, naphthenes, and aromatics. The differing boiling points of these components can make fuel vaporization and mixing in fuel processors difficult. Pyrolytic and carbon-forming tendencies of some hydrocarbon species at the elevated temperature required to vaporize all components may lead to carbon deposition on the catalyst.

1.6.2. Catalyst

The reformer catalyst is perhaps the most critical element of the fuel processor. The catalyst must be active and selective for the fuel of choice; and stable and resistant to poisoning and sintering while subjected to transients in flow, temperature, and pressure [51,52]. For successful operation at commercial scale, the reforming process must be able to achieve high conversion of the hydrocarbon feedstock at high space velocities, as well as at high H_2 and CO selectivities.

Some fuel components may have detrimental effects on the catalysts as well as on the reaction rates [53]. For example, aromatics present in diesel decrease the rate of reforming of the paraffins because the aromatics are strongly adsorbed on the active metal sites. Aromatics in liquid fuels can also contribute significantly to the carbon formation, as compared to the paraffins and cycloparaffins. Increasing reaction temperatures to reform these difficult compounds can trigger excessive sintering of the catalyst or vaporization of the active metal itself, leading to rapid deactivation. In some applications (e.g., remote locations or portable power systems), water cannot be easily added to the feed stream, even though it would reduce undesirable carbon formation. Sulfur is present in most hydrocarbon fuels, and represents a poison to these metal-based catalytic processes.

Even the interpretation of laboratory research can be an issue. In a fixed bed laboratory reactors at reforming temperatures (800−1000 °C), the following sequence of reactions is thought to take place [54]. Very near the reactor inlet, O_2 is quickly consumed to produce primarily CO_2 and H_2O. Next, steam and CO_2 reforming[4] and WGS take place, making it difficult to study these reactions independently because of the experimental complexity of measuring the reactants and products at various points in the reactor. This problem was recognized even in the earliest work on the POX of methane [55]. This complexity, often coupled with significant rates of deactivation, makes the task even more complicated. Moreover, the highly exothermic nature of the complete oxidation reaction must also be taken into account, because it leads to hot spots at the reactor inlet. The net result of these experimental difficulties is that there are unavoidable temperature and concentration gradients in the reactor that are almost certainly laboratory specific. This may account for the sometimes conflicting results in the literature for studies carried out at nominally similar conditions.

1.7. SCOPE OF THIS BOOK

The book provides a thorough analysis of the important aspects of fuel-processing technology to the generally interested reader, researcher, technologist, or industrial practitioner. The book includes all aspects of fuel reforming: fundamental chemistry, different modes of reforming, catalysts, catalyst deactivation, fuel desulfurization, reaction engineering, novel reforming concepts, thermodynamics, heat and mass transfer issues, system design, and recent research and development.

1.7.1. Fundamental Focus

By focusing on the fundamentals, the book is intended to be as useful in the future, as it hopefully is at present. Time-sensitive information/analysis (e.g., economics) is intentionally avoided. Instead, our intent is that the book will serve as a source of information for scientists or engineers in fuel-processing technology. This book provides information not currently available from a single literature source, and is organized to serve as a reference book for graduate-level courses, fuel cell developers, and fuel cell researchers.

1.7.2. Fuel Cell Details

No attempt is made to describe the fuel cell itself − for example, there is no in-depth discussion of the various electrolytes in PEM or SOFCs. The reader is referred to numerous recent references on fuel cells [15,56−59]. Rather, we include only a sufficient description of the fuel cell (Chapter 2) to show how it

[4] CO_2 reforming, also known as dry reforming, is the following reaction: $C_nH_m + nCO_2 \rightarrow 2nCO + 2\left(n + \frac{m}{2}\right)H_2$.

affects the fuel processor – for example, CO removal from the reformate is required by PEMs, but not SOFCs. Also, no attempt is made to include the hydrogen production from non-carbon sources such as water electrolysis, borohydrides, etc.

References

[1] Sheffield J. World population growth and the role of annual energy use per capita. Technological Forecasting and Social Change 1998;59(1):55–87.

[2] Joyeux R, Ripple RD. Household energy consumption versus income and relative standard of living: a panel approach. Energy Policy 2007;35(1):50–60.

[3] Erdmann G. Future economics of the fuel cell housing market. Int J Hydrogen Energy 2003;28 (7):685–94.

[4] Agnolucci P. Economics and market prospects of portable fuel cells. Int J Hydrogen Energy 2007; 32(17):4319–28.

[5] Bompard E, Napoli R, Wan B, Orsello G. Economics evaluation of a 5 kW SOFC power system for residential use. Int J Hydrogen Energy 2008;33(12): 3243–7.

[6] El-Sharkh MY, Tanrioven M, Rahman A, Alam MS. Economics of hydrogen production and utilization strategies for the optimal operation of a grid-parallel PEM fuel cell power plant. Int J Hydrogen Energy 2010;35(16):8804–14.

[7] Granovskii M, Dincer I, Rosen MA. Economic and environmental comparison of conventional, hybrid, electric and hydrogen fuel cell vehicles. J Power Sources 2006;159(2):1186–93.

[8] Jain S, Chen H-Y, Schwank J. Techno-economic analysis of fuel cell auxiliary power units as alternative to idling. J Power Sources 2006;160(1):474–84.

[9] Lipman TE, Edwards JL, Kammen DM. Fuel cell system economics: comparing the costs of generating power with stationary and motor vehicle PEM fuel cell systems. Energy Policy 2004;32 (1):101–25.

[10] Frenette G, Forthoffer D. Economic & commercial viability of hydrogen fuel cell vehicles from an automotive manufacturer perspective. Int J Hydrogen Energy 2009;34(9):3578–88.

[11] Millette J, Dostie M, Morneau JF. Impact of residential fuel cell system parameters on its economic assessment. J Fuel Cell Sci Technol 2008;5(3).

[12] Barreto L, Makihira A, Riahi K. The hydrogen economy in the 21st century: a sustainable development scenario. Int J Hydrogen Energy 2002;28(3):267–84.

[13] Bernay C, Marchand M, Cassir M. Prospects of different fuel cell technologies for vehicle applications. J Power Sources 2002;108(1–2):139–52.

[14] Teagan WP, Bentley J, Barnett B. Cost reductions of fuel cells for transport applications: fuel processing options. J Power Sources 1998;71(1,2):80–5.

[15] Fuel cell handbook. 7th ed. Morgantown, WV: U.S. Department of Energy; 2004.

[16] El-Sharkh MY, Rahman A, Alam MS, Byrne PC, Sakla AA, Thomas T. A dynamic model for a stand-alone PEM fuel cell power plant for residential applications. J Power Sources 2004;138(1–2):199–204.

[17] Gencoglu MT, Ural Z. Design of a PEM fuel cell system for residential application. Int J Hydrogen Energy 2009;34(12):5242–8.

[18] Hamada Y, Nakamura M, Kubota H, Ochifuji K, Murase M, Goto R. Field performance of a polymer electrolyte fuel cell for a residential energy system. Renewable and Sustain Energy Rev 2005; 9(4):345–62.

[19] Kazempoor P, Dorer V, Ommi F. Evaluation of hydrogen and methane-fuelled solid oxide fuel cell systems for residential applications: system design alternative and parameter study. Int J Hydrogen Energy 2009;34(20):8630–44.

[20] Sammes NM, Boersma R. Small-scale fuel cells for residential applications. J Power Sources 2000;86 (1–2):98–110.

[21] Patil AS, Dubois TG, Sifer N, Bostic E, Gardner K, Quah M, et al. Portable fuel cell systems for America's army: technology transition to the field. J Power Sources 2004;136(2):220–5.

[22] Baratto F, Diwekar UM, Manca D. Impacts assessment and trade-offs of fuel cell-based auxiliary power units: Part I: System performance and cost modeling. J Power Sources 2005;139(1–2):205–13.

[23] Lawrence J, Boltze M. Auxiliary power unit based on a solid oxide fuel cell and fuelled with diesel. J Power Sources 2006;154(2):479–88.

[24] Shi L, Bayless DJ. Analysis of jet fuel reforming for solid oxide fuel cell applications in auxiliary power units. Int J Hydrogen Energy 2008;33(3): 1067–75.

[25] Singhal SC. Solid oxide fuel cells for stationary, mobile, and military applications. Solid State Ionics 2002;152–153:405–10.

[26] Heinzel A, Vogel B, Hübner P. Reforming of natural gas – hydrogen generation for small scale stationary fuel cell systems. J Power Sources 2002;105 (2):202–7.

[27] Enger CB, Lødeng R, Holmen A. A review of catalytic partial oxidation of methane to synthesis gas with emphasis on reaction mechanisms over transition

metal catalysts. Appl Catal A: Gen 2008;346(1–2): 1–27.
[28] Sá S, Silva H, Brandão L, Sousa JM, Mendes A. Catalysts for methanol steam reforming – A review. Appl Catal B: Env 2010;99(1–2):43–57.
[29] Breen JP, Ross JRH. Methanol reforming for fuel-cell applications: development of zirconia-containing Cu-Zn-Al catalysts. Catal Today 1999;51(3–4):521–33.
[30] Rabenstein G, Hacker V. Hydrogen for fuel cells from ethanol by steam-reforming, partial-oxidation and combined auto-thermal reforming: a thermodynamic analysis. J Power Sources 2008;185(2):1293–304.
[31] Vaidya PD, Rodrigues AE. Insight into steam reforming of ethanol to produce hydrogen for fuel cells. Chem Eng J 2006;117(1):39–49.
[32] Faungnawakij K, Shimoda N, Viriya-empikul N, Kikuchi R, Eguchi K. Limiting mechanisms in catalytic steam reforming of dimethyl ether. Appl Cat B: Env 2010;97(1–2):21–7.
[33] Semelsberger TA, Borup RL. Thermodynamic equilibrium calculations of hydrogen production from the combined processes of dimethyl ether steam reforming and partial oxidation. J Power Sources 2006;155 (2):340–52.
[34] Liu Z, Mao Z, Xu J, Hess-Mohr N, Schmidt VM. Operation conditions optimization of hydrogen production by propane autothermal reforming for PEMFC application. Chin J Chem Eng 2006;14(2): 259–65.
[35] Zeng G, Tian Y, Li Y. Thermodynamic analysis of hydrogen production for fuel cell via oxidative steam reforming of propane. Int J Hydrogen Energy 2010; 35(13):6726–37.
[36] Biesheuvel PM, Geerlings JJC. Thermodynamic analysis of direct internal reforming of methane and butane in proton and oxygen conducting fuel cells. J Power Sources 2008;185(2):1162–7.
[37] Ferrandon M, Kropf AJ, Krause T. Bimetallic Ni-Rh catalysts with low amounts of Rh for the steam and autothermal reforming of n-butane for fuel cell applications. Appl Cat A: Gen 2010;379(1–2):121–8.
[38] Ferrandon M, Mawdsley J, Krause T. Effect of temperature, steam-to-carbon ratio, and alkali metal additives on improving the sulfur tolerance of a Rh/ La-Al_2O_3 catalyst reforming gasoline for fuel cell applications. Appl Cat A: Gen 2008;342(1–2):69–77.
[39] Qi A, Wang S, Fu G, Wu D. Integrated fuel processor built on autothermal reforming of gasoline: a proof-of-principle study. J Power Sources 2006;162(2): 1254–64.
[40] Yoon S, Bae J, Kim S, Yoo Y-S. Self-sustained operation of a kWe-class kerosene-reforming processor for solid oxide fuel cells. J Power Sources 2009;192(2):360–6.
[41] Kobori Y, Matsumoto T, Anzai I, Ueno S, Oishi Y. Kerosene reforming catalyst for fuel cell application – Kinetic and modeling analysis of steam reforming. In: Anpo M, Onaka M, Yamashita H, editors. Stud Surf Sci Catal. Elsevier; 2003;145:477–8.
[42] Roychoudhury S, Lyubovsky M, Walsh D, Chu D, Kallio E. Design and development of a diesel and JP-8 logistic fuel processor. J Power Sources 2006; 160(1):510–3.
[43] Kang I, Bae J. Autothermal reforming study of diesel for fuel cell application. J Power Sources 2006;159(2): 1283–90.
[44] Thormann J, Pfeifer P, Schubert K, Kunz U. Reforming of diesel fuel in a micro reactor for APU systems. Chem Eng J 2008;135(Suppl. 1):S74–81.
[45] Nahar GA. Hydrogen rich gas production by the autothermal reforming of biodiesel (FAME) for utilization in the solid-oxide fuel cells: a thermodynamic analysis. Int J Hydrogen Energy 2010;35(17): 8891–911.
[46] Slinn M, Kendall K, Mallon C, Andrews J. Steam reforming of biodiesel by-product to make renewable hydrogen. Bioresour Technol 2008;99(13): 5851–8.
[47] Ahmed S, Kopasz JP, Russell BJ, Tomlinson HL. Gas-to-liquids synthetic fuels for use in fuel cells: reformability, energy density, and infrastructure compatibility, In: Third International Fuel cell Conference; Nagoya, Japan; 1999. Nov. 30–Dec. 3.
[48] Jamal Y, Wyszynski ML. On-board generation of hydrogen-rich gaseous fuels. A review. Int J Hydrogen Energy 1994;19(7):557–72.
[49] Naidja A, Krishna CR, Butcher T, Mahajan D. Cool flame partial oxidation and its role in combustion and reforming of fuels for fuel cell systems. Prog Energy Combust Sci. 2003;29(2):155–91.
[50] Ahmed S, Krumpelt M. Hydrogen from hydrocarbon fuels for fuel cells. Int J Hydrogen Energy 2001;26(4): 291–301.
[51] Pettersson LJ, Westerholm R. State of the art of multi-fuel reformers for fuel cell vehicles: problem identification and research needs. Int J Hydrogen Energy 2001;26(3):243–64.
[52] Ghenciu AF. Review of fuel processing catalysts for hydrogen production in PEM fuel cell systems. Current Opinion Solid State Mater Sci 2002;6(5): 389–99.
[53] Shekhawat D, Berry DA, Haynes DJ, Spivey JJ. Fuel constituent effects on fuel reforming properties for fuel cell applications. Fuel 2009;88(5): 817–25.
[54] O'Connor AM, Ross JRH. The effect of O_2 addition on the carbon dioxide reforming of methane

over Pt/ZrO_2 catalysts. Catal Today 1998;46(2–3): 203–10.
[55] Prettre M, Eichner C, Perrin M. The catalytic oxidation of methane to carbon monoxide and hydrogen. Trans Faraday Soc 1946;43:335–40.
[56] Hoogers G, editor. Fuel cell technology handbook. Boca Raton, FL: CRC Press; 2003.
[57] Larminie J, Dicks A. Fuel cell systems explained. 2nd ed. Chichester, UK: Wiley & Sons Ltd.; 2003.
[58] Basu S. Recent trends in fuel cell science and technology. New York: Springer; 2007.
[59] Srinivasan S. Fuel cells: from fundamentals to applications. New York: Springer; 2006.

CHAPTER

2

Fuel Cells

Mark C. Williams

National Energy Technology Laboratory, 3610 Collins Ferry Road, Morgantown, WV 26507-0880, USA

OUTLINE

2.1. INTRODUCTION

This chapter provides a brief overview of fuel cell technology. First, it briefly discusses the basic principle of fuel cells. Then, an overview of the major fuel cell types and their characteristics is provided. It is not the intent of the chapter to discuss the details of fuel cell technologies. The reader is therefore referred elsewhere for detailed discussions of fuel cells and their components [1–5].

Fuel cells are electrochemical devices that convert the chemical energy of a chemical reaction directly into electrical energy and heat. Electrochemical reactions are the most efficient means to convert chemical energy to electrical energy. On earth, there is chemical energy generated from the sun, available either via stored energy from coal and petroleum or from biomass residues and human wastes. Fuel cells are energy conversion systems that efficiently generate electricity for stationary or transportation applications from these fuels.

In principle, a fuel cell operates like a battery, but does not run down or require recharging like a battery as long as fuel and oxidant are supplied. In an application where all the fuel and/or oxidant must be deployed with the

fuel cell during a mission, the fuel cell is in effect a battery. Unlike the typical battery, its energy density is not constant but approaches that of the fuel used as the duration of the mission increases. Fuel cells as batteries are most interesting for longer duration missions. Hence, in transportation applications, the fuel cell on hydrogen has a much longer distance between refueling or recharging than current batteries.

The basic physical structure or building block of most fuel cells consists of an electrolyte layer in contact with porous anode and cathode electrodes on either side. In the dual chamber fuel cell, a fuel enters the anode and an oxidant enters the cathode. These are separated by a selectively conductive electrolyte. Conduction through the electrolyte can occur in either direction − anode to cathode or cathode to anode − depending on the fuel cell. The fuel cell can be designed so that select species conduct. These charge carriers include H^+, $CO_3{}^{2-}$, O^{2-}, OH^-, etc. If a particular fuel cell which has been designed to allow conduction of a particular species is used, then either the oxidant or the fuel must be transformed at the cathode or anode, respectively, into that charge carrier species. Enzymatic and biological fuel cells have been developed using organic fuels and various charge carriers. Table 2.1 shows the types and associated electrochemical reactions that occur in the common fuel cells.

In a typical proton-conducting fuel cell, gaseous fuels are fed continuously to the anode (negative electrode) section and an oxidant (e.g., O_2 from air) is fed continuously to the cathode (positive electrode) section. With the help of a catalyst, the hydrogen atom oxidizes into a proton (H^+) and an electron (e^-) that takes different paths to the cathode. The proton passes through the electrolyte. The electrons generate a current that can be utilized before they return to the cathode to form O^{2-}. The oxygen ion then reunites with the proton to form a molecule of water.

Fig. 2.1 is a simplified diagram that demonstrates how a typical solid oxide fuel cell (SOFC) works. The solid state SOFC is an oxygen ion conductor. The oxygen anion is conducted from cathode across the electrolyte to the anode where it electrochemically reacts with a fuel, typically either H_2 or CO, to produce H_2O and CO_2, respectively.

Practically speaking, direct oxidation of the fuel is the most efficient approach to conversion

TABLE 2.1 Electrochemical Reactions and Charge Carriers in Fuel Cells

Fuel cell	Charge carrier through electrolyte	Anode reaction	Cathode reaction
Direct carbon (DCFC − SOFC-based)	O^{2-}	$C + O^{2-} \rightarrow CO_2 + 2e^-$	$½O_2 + 2e^- \rightarrow O^{2-}$
Polymer electrolyte (PEFC or PEM)	H^+	$H_2 \rightarrow 2H^+ + 2e^-$	$½O_2 + 2H^+ + 2e^- \rightarrow H_2O$
Phosphoric acid (PAFC)	H^+	$H_2 \rightarrow 2H^+ + 2e^-$	$½O_2 + 2H^+ + 2e^- \rightarrow H_2O$
Alkaline (AFC)	OH^-	$H_2 + 2OH^- \rightarrow 2H_2O + 2e^-$	$½O_2 + H_2O + 2e^- \rightarrow 2OH^-$
Molten carbonate (MCFC)	$CO_3{}^{2-}$	$H_2 + CO_3{}^{2-} \rightarrow H_2O + CO_2 + 2e^-$ $CO + CO_3{}^{2-} \rightarrow 2CO_2 + 2e^-$	$½O_2 + CO_2 + 2e^- \rightarrow CO_3{}^{2-}$
Solid oxide (SOFC)	O^{2-}	$H_2 + O^{2-} \rightarrow H_2O + 2e^-$ $CO + O^{2-} \rightarrow CO_2 + 2e^-$ $CH_4 + 4O^{2-} \rightarrow 2H_2O + CO_2 + 8e^-$	$½O_2 + 2e^- \rightarrow O^{2-}$

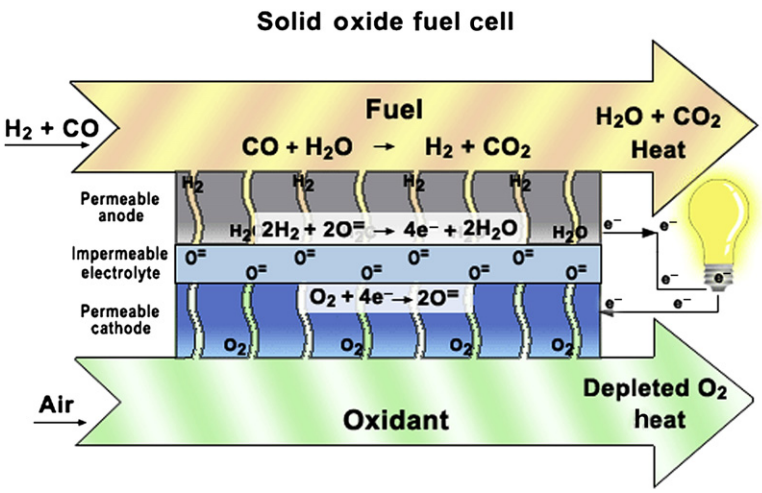

FIGURE 2.1 SOFC design and operation (NETL).

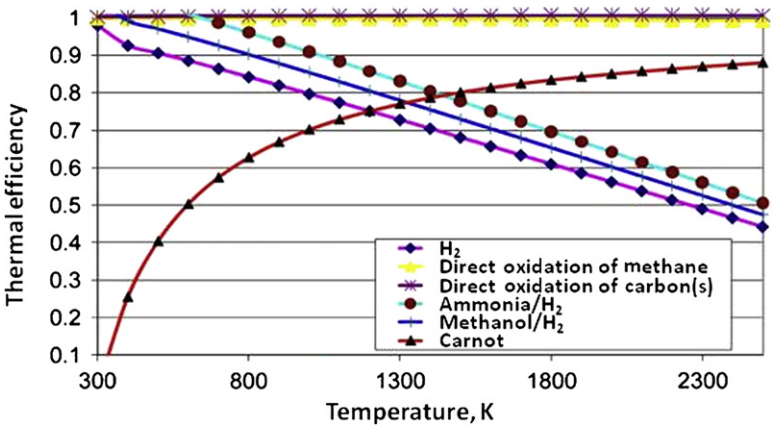

FIGURE 2.2 Fuel cell intrinsic thermal efficiency for various fuels and oxygen at various temperatures.

as it avoids intermediary steps of fuel reforming with its associated thermal losses. Fig. 2.2 shows the fuel cell intrinsic thermal efficiency for five anodic reactions — hydrogen oxidation, ammonia oxidation, methanol oxidation, direct oxidation of methane, and direct oxidation of solid carbon (graphite). The ammonia and methanol reactions are actually endothermic with large negative $\Delta^r G$. However, above 400 K, methanol and water are mostly reformed in an endothermic reaction to hydrogen, so the $\Delta^r G$ for hydrogen was used and the $\Delta^r H$ for the combined reactions (methanol reforming and hydrogen oxidation) was used in calculating thermal efficiency. In the case of ammonia, it decomposes by 600 K to hydrogen so the $\Delta^r G$ for hydrogen and the $\Delta^r H$ for the combined reactions — ammonia disassociation and hydrogen oxidation — were used.

From Fig. 2.2 alone one would conclude that there is great theoretical efficiency potential for direct carbon fuel cell (DCFC), polymer electrolyte fuel cell (PEFC), direct oxidation of methane, and intermediate temperature SOFC. One would also conclude that ammonia and methanol are better than hydrogen. High

efficiency is very desirable, but real fuel cells have irreversibilities. However, their inefficiencies, in some cases, can be made up for through hybridization with the Carnot engine. Hybrids are combinations of energy conversion devices. Many combinations of energy conversion devices are possible, but the combination of the high-temperature fuel cell with the gas turbine is a very high efficiency one [6,7]. In the direct fuel cell turbine hybrid concept, the fuel cell replaces the turbine combustor. The turbine expands the high-temperature fuel cell exhaust. The system efficiency is raised through the production of addition electric power.

The direct oxidation of H_2, CO, NH_3, CH_4, CH_3OH, and C with oxygen has been demonstrated in various basic fuel cell configurations. However, in many cases, the fuel must be reformed into a fuel species which can be directly oxidized in the fuel cell, such as H_2. In this sense, the anodic reaction is coupled to reforming reactions. On or before the anode, methane, for example, reacts with water to form hydrogen which is the direct oxidation species. The same thing can occur on the cathode. In the molten carbonate fuel cell (MCFC), oxygen is reacted with CO_2 into CO_3^{2-} which is the charge carrier.

A fuel cell system that includes a fuel reformer can utilize the resultant H_2 from any hydrocarbon fuel (e.g., natural gas, gasoline, and diesel fuel) or oxygenated hydrocarbon fuel (e.g., methanol, ethanol, and biodiesel). The most common oxidant is gaseous O_2, which is readily available from air for the majority of applications, and again easily stored in a closed environment. Emissions from a fuel cell system are much smaller than emissions from the cleanest fuel combustion processes.

Integration of a fuel cell with reforming varies with the fuel. Reforming of methane generally occurs at 600–700 °C. Hydrogen, the more readily oxidized fuel, is produced by CH_4 and CO reacting with H_2O through the steam reforming ($CH_4 + H_2O \rightarrow 3H_2 + CO$) and water gas shift ($CO + H_2O \rightarrow H_2 + CO_2$) reactions, respectively. Fuel cells which can operate at this temperature and which integrate best with reformers with minimum loss of efficiency are the SOFC and MCFC. The SOFC is the most versatile fuel cell because of its wide operating temperatures. These two fuel cell types are anion charge carriers; every molecule of fuel does not have to be broken down to a proton charge carrier. Instead, anion charge carriers are transported to the anode where a variety of anodic and reforming reactions can take place. This results in great fuel flexibility.

Sometimes when endothermic reforming reactions are coupled to the anodic reaction, the available waste heat is used to support the overall reaction. Similarly, available mass may be coupled to the anodic and/or cathodic reaction through a coupled reaction. Coupling of reactions at the anode and cathode is sometimes referred to as chemical or electrochemical looping if there is a generation–regeneration cycle outside the fuel cell.

2.2. FUEL CELL FUNDAMENTALS

To understand and quantify fuel cell performance, one must begin with the thermodynamic description of the fuel cell. A fuel cell continuously produces electrical work and waste heat. The fuel cell is not allowed to run down since it is an open system. The fuel cell is operated continuously for a given time period, Δt, during which reactants (fuel and oxidant) are added and products removed to maintain an electrical potential. If current is allowed to flow, a difference in electrical potential (also known as electrochemical overpotential) is maintained at the electrode interface through which charge transfer can occur. Charge carriers migrate across the cell when there is non-equilibrium between the electrical and chemical potentials across the cell. The

movement occurs from a higher to lower potential energy. Thus, the chemical affinity or change in Gibbs free energy of reaction drives an electric current. The change in Gibbs free energy of reaction is available at any instant to perform electrical work.

The Gibbs free energy, G, is defined to be [8]:

$$G = E + PV - TS \tag{2.1}$$

where P = pressure, V = volume, T = temperature, E = energy, and S = entropy.

At constant pressure and temperature (usual conditions of an electrochemical reaction), the change in the Gibbs free energy for a reaction, $\Delta^{r}G$ (J/mole) is:

$$\Delta^{r}G = \Delta E + P\Delta V - T\Delta^{r}S \tag{2.2}$$

From the first law of thermodynamics, assuming the fuel cell is operated reversibly,

$$\Delta E = q + w = q + w_{\text{electrical}} - P\Delta V \tag{2.3}$$

where, q = heat and w = work (J/mole).

Thus, equating terms and simplifying,

$$\Delta^{r}G = q + w_{\text{electrical}} - T\Delta^{r}S \tag{2.4}$$

Again, assuming reversible operation of the fuel cell,

$$q = q_{\text{reversible}} = T\Delta^{r}S \tag{2.5}$$

Thus,

$$\Delta^{r}G = w_{\text{electrical}} \tag{2.6}$$

The change in Gibbs free energy of reaction (J/mole) is referenced to the amount of fuel. The electrical work (J) in an open system operated continuously over a given time period, Δt, where reactants (moles/second) are added and products removed to maintain the electrical potential is given for hydrogen–oxygen reaction by

$$m_{H_2}\Delta^{r}G\Delta t = m_{H_2}w_{\text{electrical}}\Delta t = W_{\text{electrical}} \tag{2.7}$$

m_{H_2} = flow rate of hydrogen for the H_2/O_2 reaction (moles/sec),

Δt = operation time (sec).

The average rate of work generation during the time interval, Δt, is the power (J/sec).

One can mathematically demonstrate that for any direct anodic oxidation reaction for any fuel cell or hybrid system containing any fuel cell at any operating temperature and any pressure, the reversible work, $w_{\text{electrical}}$, (J/mole) is equal to the change in Gibbs free energy of reaction at the standard state (STP), $\Delta^{r}G^{o}$ [9–11]. This reversible work is regarded as the maximum work. For the case of direct oxidation of hydrogen, one has

$$W_{\text{rev}} = m_{H_2\text{inlet}}\ w_{\text{rev}} = m_{H_2\text{inlet}}\ \Delta^{r}G^{o}\Delta t \tag{2.8}$$

where $m_{H_2\text{inlet}}$ = flow rate of hydrogen fuel into system

In practice, inerts and/or water are added to or are present in a reformate with the hydrogen entering the system. These are heated and compressed at the inlet and expanded and cooled at the outlet. The addition of water will alter the equilibrium concentration of H_2 and O_2 and affect the Nernst Voltage through $\Delta^{r}G$ which is a function of temperature, pressure, and concentrations. In addition, not all of the fuel may be utilized in the fuel cell. However, the W_{rev} is independent of the state of the fuel cell [11].

It is important to understand how well a fuel cell performs on a fuel. Exergy is a measure of heat quality or capability to do work. Exergetic efficiency, ζ, is the ratio of actual electrical work and the reversible work:

$$\zeta = \frac{W_{\text{electrical}}}{W_{\text{rev}}} \tag{2.9}$$

Using Eq. (2.7), the actual or observed electrical work for direct oxidation of hydrogen a fuel cell is given by

$$m_{H_2\text{utilized}}\Delta^{r}G_{\text{act}}\Delta t = W_{\text{electrical}} \tag{2.10}$$

where

$\Delta^r G_{act}$ = actual change in Gibbs free energy of reaction associated with the electrical work, J/mole,

$m_{H_2utilized}$ = flow rate of hydrogen utilized by fuel cell (moles/sec)($m_{H_2utilized}$ equals the amount in the fuel cell anode inlet, $m_{H_2anode\ inlet}$, minus the amount in the anode outlet, $m_{H_2anode\ outlet}$)

For reforming done prior to the system, $m_{H_2inlet} = m_{H_2anode\ inlet}$. Thus, from Eqs (2.8), (2.9), and (2.10)

$$\zeta = \frac{m_{H_2utilized}\Delta^r G_{act}\Delta t}{m_{H_2inlet}\Delta^r G^o \Delta t} = \mu_F \frac{\Delta^r G_{act}}{\Delta^r G^o} \tag{2.11}$$

where fuel utilization (μ_F) is

$$\mu_F = \frac{m_{H_2utilized}}{m_{H_2inlet}} \tag{2.12}$$

Using Eq. (2.8) for the reversible work, one can calculate the maximum thermal efficiency (maximum work for given energy input) of a fuel cell or fuel cell hybrid (fuel cell and heat engine) system for the H_2 oxidation reaction, where $\Delta^r H^o$ is the reaction enthalpy for hydrogen direct oxidation (J/mole) at STP and where the inlet hydrogen is completely utilized in the fuel cell:

$$\eta_{th\ max} = \frac{\Delta^r G^o}{\Delta^r H^o} \tag{2.13}$$

For the H_2 oxidation reaction, $\eta_{th\ max}$ equals 0.83 (HHV) and 0.945 (LHV). One can also define a fuel cell intrinsic thermal efficiency at any temperature $\eta_{int}(T)$ by $\Delta^r G_{th}(T)/\Delta^r H^o$ (see Fig. 2.2). One can also define for the fuel cell an intrinsic exergetic efficiency at any temperature [9,10,12]:

$$\zeta_{int}(T) = \frac{\Delta^r G_{th}(T)}{\Delta^r G^o} \tag{2.14}$$

$\Delta^r G_{th}(T)$ is defined as the free energy of the reaction, here the H_2 oxidation reaction, at temperature, T, for unit concentrations of products and reactants. $\Delta^r G_{th}(T)$ is associated with $E^o(T)$. $\Delta^r G^o$ at STP with unit species concentrations is associated with E^o.

The actual thermal efficiency of the fuel cell is defined as the ratio of the work output to energy input, so we have:

$$\eta = \frac{m_{H_2utilized}\ \Delta^r G_{act}\Delta t}{m_{H_2inlet}\ \Delta^r H^o \Delta t} = \mu_F \frac{\Delta^r G_{act}}{\Delta^r H^o} \tag{2.15}$$

It can be shown from Eqs (2.11), (2.13), (2.14), and (2.15) that

$$\eta = \frac{\mu_F \Delta^r G_{act}}{\Delta^r H^o} = \frac{\zeta}{\zeta_{int}(T)}\eta_{int}(T) = \zeta \eta_{th\ max} \tag{2.16}$$

If one knows the reversible work which is a function of fuel, system components, and system structure, one can separate thermal efficiency into an exergetic component and a fuel component. Exergetic efficiency and the fuel are equally important.

From Eq. (2.16), we see thermal efficiency performance is exergetically limited. For any direct oxidation reaction, it is the product of a constant, the maximum thermal efficiency possible, $\eta_{th\ max}$, times the exergetic efficiency, ζ. It is important to understand the maximum possible thermal efficiency a fuel cell system is capable of obtaining on a fuel, $\eta_{th\ max}$, and then what of this efficiency it actually achieves, ζ.

Exergetic performance is determined by fuel cell performance which ultimately means fuel cell voltage. The link between the macroscopic thermodynamic parameters and fuel cell voltage can be developed as follows.

The $W_{\text{electrical}}$ is also defined electrically as:

$$W_{\text{electrical}} = -nFE \tag{2.17}$$

where
n = mole,
F = Faraday's constant (J/mole/volt),
E = fuel cell voltage (volt).
In general, from Eqs (2.7), (2.10), and (2.17):

$$m_{H_2}\Delta^{r}G\Delta t = W_{\text{electrical}} = -nFE \tag{2.18}$$

Since for the H_2 direct oxidation reaction,

$$2m_{H_2}\Delta t = n \tag{2.19}$$

Then, in general:

$$\Delta^{r}G = -2FE \tag{2.20}$$

Specifically, using Eq. (2.20),

$$\Delta^{r}G_{\text{act}} = -2FE \tag{2.21}$$

and

$$\Delta^{r}G^{o} = -2FE^{o} \tag{2.22}$$

so

$$\begin{aligned}\zeta &= \frac{m_{H_2\text{utilized}}}{m_{H_2\text{inlet}}}\frac{\Delta^{r}G_{\text{act}}}{\Delta^{r}G^{o}}\frac{\Delta t}{\Delta t} \\ &= \mu_F\frac{-2FE}{-2FE^{o}}\frac{\Delta t}{\Delta t} = \frac{\mu_F E}{E^{o}}\end{aligned} \tag{2.23}$$

One of the central, steady-state fuel cell performance equations is thus given by:

$$\zeta = \frac{\mu_F E}{E^{o}} \tag{2.24}$$

and combining with Eq. (2.16), one has

$$\eta = \zeta\eta_{\text{th max}} = \frac{\mu_F E}{E^{o}}\eta_{\text{th max}} \tag{2.25}$$

Exergetic efficiency and thermal efficiency are actually time-dependent functions describing the performance of the fuel cell at any time t. These can be written as:

$$\zeta(t) = \frac{\mu_F(t)E(t)}{E^{o}} \tag{2.26}$$

and

$$\eta(t) = \zeta(t)\eta_{\text{th max}} = \frac{\mu_F(t)E(t)}{E^{o}}\eta_{\text{th max}} \tag{2.27}$$

2.3. FUEL CELL DEGRADATION

DR_ζ (t), the exergetic efficiency rate of change, is a natural and instantaneous measure of the change in fuel cell performance occurring at any time t:

$$\frac{\partial}{\partial t}(\zeta(t)) = DR_\zeta(t) \tag{2.28}$$

It can be seen from Eqs (2.26) and (2.27) that the rate of change in exergetic efficiency and rate of change of thermal efficiency are directly proportional.

Equation (2.28) is the second central equation for fuel cell performance since it is an equation that can be used in the assessment of degradation [13], generally defined as the change of area-specific resistance (ASR) with time.

Degradation primarily from corrosion limits the practical operating life of fuel cells. Components must meet certain general requirements in order to be useful. No components may exhibit any significant changes in volume between room temperature and the fabrication temperature. The fuel cell components must be chemically stable in order to limit chemical interactions with other fuel cell components. They must have similar thermal expansion in order to minimize thermal stresses that may cause delamination and cracking during thermal cycling or fabrication. It is also desirable that fuel cell components have high strength and durability, are easy to fabricate, and are

relatively inexpensive. The assessment of degradation needs to include phenomena such as electronic shorting.

2.4. FUEL CELL OPERATION

Fuel cells can be operated in a variety of modes, including constant fuel utilization, constant fuel flow rate, constant voltage, constant current, etc. For the case of constant μ_F and constant E, from Eq. (2.28), $DR_\xi(t) = 0$, in which case the fuel cell is operating at constant exergetic efficiency. This mode of operation is achieved by lowering the current by lowering the hydrogen flow rate as the fuel cell degrades. As can be seen from Eqs (2.26) and (2.27), to operate at constant exergetic efficiency is to operate at constant thermal efficiency. However, efficiency is not the only important performance measure. As the current is lowered at constant voltage operation, the fuel cell power density is decreasing. Below a certain level of power or power density, given by

$$P(t) = E(t)J(t) \tag{2.29}$$

It is no longer economical to operate a fuel cell or fuel cell system. Power is the third central equation for fuel cell performance. General expressions can be derived for fuel cell performance involving the variables E, J, μ_F, pressure, and fuel flow rate to explore the full envelope of fuel cell operation.

The actual fuel cell potential is decreased from its full potential, the Nernst potential, because of irreversible losses. Multiple phenomena contribute to irreversible losses in an actual fuel cell. For the hydrogen oxidation reaction, the functionality of fuel cell voltage, E, is typically given by [14–16]:

$$E(T) = E_N(T) - \frac{LJ}{A\sigma} - R_{ohmic}\,J - \eta^a_{act} - \eta^c_{act} - \eta^a_{conc} - \eta^c_{conc} \tag{2.30}$$

$$E_N(T) = E^o_{H_2/O_2rxn}(T) + \frac{RT}{2F}\ln\left[\frac{P_{H_2(a)}P^{1/2}_{O_2(c)}}{p_{H_2O(a)}}\right] = \text{Nernst voltage} \tag{2.31}$$

where

F = Faraday's constant,

J = appropriate current (amperes/cm^2),

σ = electrolyte charge carrier conductivity (S/cm),

L = electrolyte thickness (cm),

A = fuel cell active area (cm^2),

η^a_{act} = activation polarization for the anode,

η^c_{act}= activation polarization for the cathode,

η^a_{conc} = concentration polarization for the anode,

η^c_{conc}= concentration polarization for the anode,

R_{ohmic} = series ohmic resistance of all non-electrolyte fuel cell components including interconnect, interlayers, and contact layers,

$E^o_{H_2/O_2rxn}(T)$ = voltage at unit concentrations for H_2/O_2 reaction at temperature T.

The six negative terms on the RHS of Eq. (2.30) are the usual definition of ASR. The comprehensive functionality of E and the more general definition of ASR have recently been developed for solid-state fuel cells with dense, mixed, ionic-electronic conducting electrolytes using the Wagner mass transfer model (MTM) [13,17–19]:

$$E = E_{MTM}\left[1 - \frac{(J_{O^=} - J_{ext})}{J_{O^=}}\right] - L\frac{J_{O^=}}{A\sigma_{O^=}} - R_{ohmic}\,J - \eta^a_{act} - \eta^a_{act} - \eta^a_{conc} - \eta^a_{conc} - \eta_{leakage} \tag{2.32}$$

where

R_{ohmic} = series ohmic resistance of all non-electrolyte fuel cell components, including

interconnect, interlayers, and contact layers, which is multiplied by the appropriate current, J, for each type

$J_{O^=}$, J_e, and J_{ext} are the current terms from the Wagner MTM,

$(J_{O^=} - J_{ext})/J_{O^=}$ = the shorting ratio,

$\eta_{leakage}$= fuel leakage polarization,

E_{MTM} (anode–electrolyte interface to cathode–electrolyte interface) is the reversible voltage in the Wagner MTM model.

The comprehensive model for solid-state fuel cells incorporates not only the typical definition of ASR, but also electronic shorting, leakage, and other current loss mechanisms. The first term on the RHS of Eq. (2.32) is not an ASR term.

A general ASR definition for solid-state fuel cells can be defined as follows:

$$\mathrm{ASR} = R_{\mathrm{ionic}} + R_{\mathrm{ohmic}} + \{\eta^{a}_{act} + \eta^{c}_{act} + \eta^{a}_{conc} + \eta^{c}_{conc}\}/J_{O^=} + R_{\mathrm{leakage}} \tag{2.33}$$

where $R_{ionic} = L/A\sigma_o$ = ionic resistance of electrolyte and $R_{leakage} = \eta_{leakage}/J_{leakage}$ = resistance attributed to fuel leakage.

This definition of ASR is very general and reduces to the usual ASR definition for J_e approaching zero. Even when generalized, ASR and rate of change of ASR are not broad enough concepts to incorporate all the phenomena affecting fuel cell performance, such as electronic shorting. The exergetic efficiency concept must be used with the comprehensive definition of E. As has been mentioned elsewhere [15], J_e can never be zero due to the requirements of local equilibrium. $J_{O^=}$ is used in the denominator since this is the ionic current the electrolyte and cathode actually see. It is also used in the anodic overpotentials since that is the current that must flow to react with the oxygen at the anode–electrolyte interface.

The goal of fuel cell developers should be to maximize exergetic or thermal efficiency and to minimize degradation while producing as much power as possible. These three goals involve elaborate tradeoffs. These tradeoffs are achieved by modifications to fuel cell design (more conductive electrolyte, better electrocatalysts, improvement in electrode structures, thinner cell components, etc.) [1]. For a certain fuel cell design, it is possible to improve the cell performance by adjusting the operating conditions (e.g., higher temperature, higher gas pressure, and change in gas composition to lower the contaminant concentration). However, for any fuel cell, compromises exist between attaining higher performance by operating at higher temperature or pressure and the problems associated with the stability and/or durability of cell components encountered at the more severe conditions.

As shown in Fig. 2.3, the activation polarization (reaction rate loss) is significant at lower current densities [1]. At this point, electronic barriers must be overcome prior to ion and current flow. Ohmic polarization (resistance loss) changes directly with current, increasing over the entire range of current because cell resistance remains essentially constant. Concentration polarization (gas transport loss) occurs over the entire range of current density, but they become significant at high limiting currents where it becomes difficult to provide enough reactant flow to the cell reaction sites.

Changing the cell operating parameters (pressure and temperature) can have an advantageous or a disadvantageous impact on fuel cell performance and on the performance of other system components [1]. There are innumerable tradeoffs. Changes in operating conditions may decrease the cost of the cell, but increase the cost of the system. Therefore, compromises in the operating parameters are essential to meet the application requirements – lower system cost and acceptable cell life. Operating conditions are based on defining specific system requirements, such as power level, voltage, or system weight. It is a matter of selecting a cell operating point (cell voltage and related current density) until the design

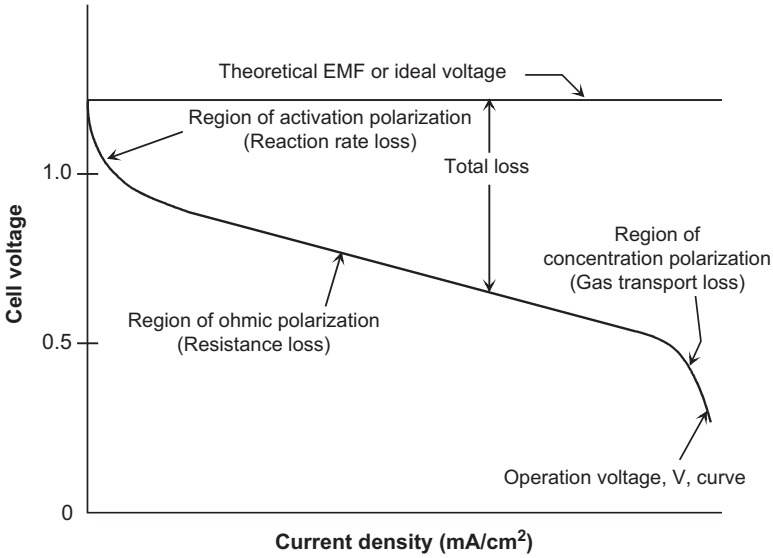

FIGURE 2.3 Typical current voltage performance [1].

requirements are satisfied (such as lowest cost, smallest unit, and highest power density). For example, a design point at high current density will allow a smaller cell size at lower capital cost to be used for the stack, but the result is a lower system efficiency (because of the lower cell voltage) and higher operating cost. This type of operating point would be typified by a vehicle application, where light weight and small volume are important drivers for cost-effectiveness. Operating at a lower current density, but higher voltage (higher efficiency and lower operating cost) would be more suitable for stationary power plant operation. It is evident that the selection of the cell design point interacts with the application objectives.

In summary, there are three central performance measures for fuel cells. The first is exergetic efficiency, which is measured by thermal efficiency. It permits the direct comparison of the performance of all fuel cell types operating on the same fuel, if desired. The second is exergetic efficiency rate of change which is useful in degradation and which is a broader, more inclusive concept than the rate of change of ASR. The third is power or power density, which can be related to the economic viability of the fuel cell or fuel cell system. Fuel cell system design and operation is ultimately the resolution of the tradeoffs among them.

2.5. FUEL CELL TYPES

Fuel cells can be designed in various ways — single chamber, dual chamber, etc. — including many geometries, planar, tubular, radial, etc., and using many fuels and electrolyte charge carriers. Distinction of fuel cell types begins with the type of electrolyte used in the cells, the charge carrier, and the operating temperature. Low-temperature fuel cells (PEFC, AFC, and PAFC) require noble metal electrocatalysts to achieve practical reaction rates at the anode and cathode, and H_2 is the only acceptable fuel for the PEFC. With high-temperature fuel cells (MCFC and SOFC), the requirements for catalysis are relaxed, and the number of potential fuels expands. (Other types of fuel cells are not addressed here, such as biological and

enzymatic fuel cells.) For example, carbon monoxide "poisons" a noble metal anode catalyst such as platinum in low-temperature fuel cells, but it competes with H_2 as a reactant in high-temperature fuel cells where non-noble metal catalysts such as nickel can be used. Table 2.2 shows the materials used for the various fuel cells.

The operating temperature and required useful life of a fuel cell dictate the physicochemical and thermomechanical properties of materials used in the cell components (e.g., electrolyte, electrodes, and interconnect) [1]. Aqueous electrolytes are limited to temperatures of >200 °C because of their high water vapor pressure and/or rapid degradation at higher temperatures. The operating temperature also determines the type of fuel that can be used in a fuel cell. The low-temperature fuel cells with aqueous electrolytes are, in most practical applications, restricted to H_2 as a fuel. In high-temperature fuel cells, CO and even CH_4 can be used because of the inherently rapid electrode kinetics and the lesser need for high catalytic activity at high temperature.

2.5.1. Direct Carbon Fuel Cell (DCFC)

The DCFC has been under development for many years. It was researched as early as 1896 [20], but an intense research and development is necessary to realize its potential. MCFC, SOFC, or AFC technologies can be used as the basis for the DCFC technology.

Nanoparticles of carbon if produced could be highly reactive. These hold great promise for subsequent development. LLNL [21,22] has examined the relationship between the nanostructure of carbons and their electrochemical reactivity in molten salts by correlating significant differences in the 3D atomic structure of carbon fuels with their electrochemical reactivities. The more disordered the carbon atoms, the more easily they yield electrons. DCFC performance depends on disorder more than on carbon purity or even aggregate surface area. Extremely fine (10−1000 μm) carbon particles with a high degree of structural disorder on the 30−100 nm scale work well. Fine carbon particles, when mixed with molten carbonate to form a dense paste or slurry, operate like rigid electrodes when the melt is brought into contact with an inert metallic screen or graphite current collector.

The major development required is for the anode and anode chamber, for all the modes of the DCFC. The reactor strategy − batch or flow − depends on the purity of the solid graphite particles. In the SOFC-mode case, special anode materials − tungsten carbide, vanadium carbide, zirconia carbide, titanium

TABLE 2.2 Basic Fuel Cell Materials

	SOFC	Molten carbonate	Phosphoric acid	Alkaline	Polymer membrane
Electrolyte	Y_2O_3 - stabilized ZrO_2 (YSZ)	Li_2CO_3 K_2CO_3	H_3PO_4	KOH	Perfluorosulfonic acid
Cathode	Sr-doped $LaMnO_3$	Li-doped NiO	Pt on C	Pt-Au	Pt on C
Anode	Ni/YSZ	Ni	Pt on C	Pt-Pd	Pt on C
Temperature	800−1000 °C	650 °C	200 °C	100 °C	90 °C
Fuel	H_2, CO	H_2, CO	H_2	H_2	H_2

carbide, nickel metal, and carbon – have been researched [23]. Several transition metal carbides were investigated as anodes. Observed values of open circuit voltage (OCV) of carbide anode SOFCs were found to be in the same order as the oxygen potentials calculated for the respective metal carbide/metal oxide equilibrium. All the carbide anodes showed better performance than graphite anode. No CO_2 was detected even at high oxygen potentials due to its reduction. The vanadium carbide was able to best activate the carbon solids. Redox reactions of anodes play an important role in activating carbon. Oxidation of the anodes themselves hinders the electrochemical reactions. The CO evolution was not proportional to the current density due to consumption of oxygen for the oxidation of TiC.

For the molten carbonate type DCFC [24], Selman has identified the following research needs, primarily dealing with the anode chamber: (1) Wetting characteristics of various types of carbon, in melts of variable basicity (cation composition, and OH-added) and temperature; (2) Spectroscopic characterization of molten carbonate in reducing medium, in contact with carbon, to establish identity of stable and semi-stable species; (3) Molecular dynamics calculations to establish the relative stability of carbon–carbonate–CO–CO_2 configurations in the melt; and (4) Monte-Carlo (stochastic) modeling of assemblies consisting of cells representing carbon particles, gas bubbles (CO_2, CO), and carbonate melt. Buoyant forces, interfacial forces, and electrochemical reactions need to be accounted for, cell to cell.

Cell and stack area and height scale up, heat removal, performance degradation as a result of electrolyte contamination, and electrolyte purification and reinjection processes are also critical issues which need to be addressed for all DCFC technologies. Other special R&D requirements vary with the developer's technology and system development schemes.

2.5.2. Polymer Electrolyte Fuel Cell (PEFC)

Because of the intrinsic nature of the materials used, the polymer electrolyte fuel cell, also commonly referred to as proton exchange membrane (PEM) fuel cell, operates at temperatures less than 100 °C, typically in the 60–80 °C range. The PEFC's OCV (1.23 V) is the highest OCV for any fuel cell, but it has never been realized during practical operation – the reason given is the electrodes are not at equilibrium. The maximum often observed is 1.1 V. The practical operating voltage is much lower to avoid competing corrosion reactions involving carbon.

When compared to other fuel cells, PEFC technology has been capable of very high current densities [1]. While most technologies can operate up to approximately 1 A/cm^2, the polymer membrane cell has operated at up to 4 A/cm^2 [25]. This ability is due primarily to the membrane used. Other desirable attributes include fast start capability and rapid response times to load changes. Because of the high power density capability, smaller and lighter-weight stacks are possible. Other beneficial attributes of the cell include no corrosive fluid hazard and lower sensitivity to orientation. As a result, the PEFC is particularly suited for vehicular power application. Near term the fuel of choice is hydrogen with storage on-board in the form of a pressurized gas. The PEFC is also being considered widely for portable and other applications using hydrogen. The typical embodiment of direct methanol oxidation fuel cell is a variation of the PEFC.

The low operating temperature of a PEFC has both advantages and disadvantages. Low temperature operation is advantageous because the cell can start from ambient conditions quickly, especially when pure hydrogen fuel is available. It is a disadvantage in that carbon monoxide-containing fuel streams from reformed methane or other hydrocarbons, because carbon will attack or poison the platinum

catalyst sites, masking the catalytic activity and reducing cell performance. The effect is reversible by flowing a CO-free gas over the electrode. To minimize the CO poisoning, operating temperatures must be greater than 120 °C, at which point there is a reduction in chemisorption and electro-oxidation. Due to CO affecting the anode, only a few ppm of CO can be tolerated at 80 °C. Because reformed and shifted hydrocarbons contain about 1% of CO, a mechanism to eliminate CO in the fuel gas is needed. This can be accomplished after reforming with preferential oxidation (PrOx) that selectively oxidizes CO relative to over H_2 using a precious metal catalyst. The low operating temperature also means that little, if any, heat is available from the fuel cell for endothermic reforming [26]. Poor integration with hydrocarbon fuels is expected with the PEFC since reforming temperatures are much higher than PEFC operating temperatures resulting in low system efficiencies from heating and cooling gas streams. The fuel of choice for the PEFCs preferably would be contaminant-free hydrogen fuel which could be produced by other means than reforming, such as electrolysis or hydrogen from solar.

The standard electrolyte material in PEFCs belongs to the fully fluorinated Teflon®-based family similar to that produced by E.I. DuPont de Nemours for space application in the mid-1960s. The membrane is characterized by its equivalent weight (inversely proportional to the ion exchange capacity). A typical equivalent weight range is 800−1100 milliequivalents per dry gram of polymer. Nafion membranes have exhibited long life in selected operating conditions and electrochemical applications. In selected fuel cell tests and water electrolysis systems, lifetimes of over 50,000 h have been reported.

Due to Nafion's present expense and other engineering issues, new alternative membranes are being developed by a number of companies. Recent PEFC development has focused on operation in the 160 °C range using new ion exchange membranes. The higher operating temperature eliminates CO poisoning by eliminating CO occlusion of the platinum sites. Both temperature and pressure have a significant influence on cell performance. Present cells operate at 80 °C over a pressure range of 0.0010−1.0 MPa. Nominally, 0.285 MPa is used for some transportation applications. Using appropriate current collectors and supporting structure, PCFCs and electrolysis cells should be capable of operating at pressures of up to 200 MPa and differential pressures of up to 3.5 MPa.

2.5.3. Alkaline Fuel Cell (AFC)

The alkaline fuel cell was one of the first modern fuel cells to be developed, beginning in 1960. The application at that time was to provide on-board electric power for the Apollo space vehicle. Desirable attributes of the AFC include excellent performance compared to other candidate fuel cells due to its active O_2 electrode kinetics and flexibility to use a wide range of electrocatalysts. The AFC continues to be used: it now provides on-board power for the Space Shuttle Orbiter with cells manufactured by UTC Fuel Cells. These AFCs operate at relatively high temperature and pressure to meet the requirements for space applications. More recently, a major focus of the technology is for terrestrial applications in which low-cost components operating at near-ambient temperature and pressure with air as the oxidant are desirable.

The unusual economics for remote power applications (i.e., space, undersea, and military applications) result in the cell itself not being strongly constrained by cost. The consumer and industrial markets, however, require the development of low-cost components if the AFC is to successfully compete with alternative technologies. Much of the recent interest in AFCs for mobile and stationary terrestrial

applications has addressed the development of low-cost cell components. In this regard, carbon-based porous electrodes play a prominent role. It remains to be demonstrated whether alkaline cells will prove commercially viable for the mass-market transportation sector [27]. AFCs are susceptible to electrolyte poisoning by CO_2 which must be removed.

2.5.4. Phosphoric Acid Fuel Cell (PAFC)

The phosphoric acid fuel cell was the first fuel cell technology to approach commercialization. There have been only minor changes in cell design in recent years. The major US manufacturer, UTC Fuel Cells, has concentrated on improving cell stability and life, and in improving the reliability of system components at reduced cost. Nevertheless, further increases in power density and reduced cost are needed to achieve economic competitiveness with other energy technologies.

A major breakthrough in PAFC technology that occurred in the late 1960s was the development of carbon black and graphite for cell construction materials [28,29]. Carbon black and graphite were sufficiently stable to replace the more expensive gold-plated tantalum cell hardware used at the time. The use of high-surface-area graphite to support platinum permitted a dramatic reduction in Pt loading without sacrificing electrode performance. However, carbon corrosion and Pt dissolution become an issue at cell voltages above ~0.8 V.

In the mid-1960s, the conventional porous electrodes were polytetrafluoroethylene (PTFE)-bonded Pt black, and the loadings were about 9 mg Pt/cm^2. During the past two decades, Pt supported on carbon black has replaced Pt black in porous PTFE-bonded electrode structures such as the electrocatalyst. A dramatic reduction in Pt loading has also occurred; the loadings are currently about 0.10 mg Pt/cm^2 in the anode and about 0.50 mg Pt/cm^2 in the cathode.

The operating temperatures and acid concentrations of PAFCs have been increased to achieve higher cell performance. Temperatures of about 200 °C (392 °F) and acid concentrations of 100% H_3PO_4 were commonly used. Today, UTC has elevated the temperature to 204 °C (400 °F) in a new commercial embodiment, which should improve its integrability with hydrocarbon reformers.

2.5.5. Molten Carbonate Fuel Cell (MCFC)

The MCFC operates at ~650 °C (1200 °F). The operating temperature range is very narrow. The high operating temperature is needed to achieve sufficient conductivity of its carbonate electrolyte yet allow the use of low-cost metal cell components. An effect associated with this high temperature is that noble metal catalysts are not required for the cell electrochemical oxidation and reduction processes. The higher operating temperature of MCFCs provides the opportunity for achieving higher overall system efficiencies (potential for heat rates below 7500 Btu/kWh) and greater flexibility in the use of available fuels. On the other hand, the higher operating temperature places severe demands on the corrosion stability and life of cell components, particularly in the aggressive environment of the molten carbonate electrolyte.

The temperature and catalyst of state-of-the-art MCFCs provide the proper environment for the water gas shift reaction to produce H_2 and CO_2 from CO and H_2O. An MCFC that reacts only H_2 and CO is known as an external reforming (ER) MCFC. An internal reforming (IR) MCFC has a reforming catalyst placed in proximity to the anode to promote the reforming reaction to produce H_2 and CO_2 from CH_4 and H_2O. The direct oxidation of CO and CH_4 in a high-temperature SOFC is feasible without or with catalyst.

In the mid-1960s, electrode materials were, in many cases, precious metals, but the technology

soon evolved to the use of Ni-based alloys at the anode and oxides at the cathode. Since the mid-1970s, the materials for the electrodes and electrolyte structure (molten carbonate/$LiAlO_2$) have remained essentially unchanged. A major development in the 1980s was the evolution in the technology for fabrication of electrolyte structures [30,31]. Over the past 28 years, the performance of single cells has improved from about 10 mW/cm^2 to >150 mW/cm^2. During the 1980s, both the performance and endurance of MCFC stacks showed dramatic improvements. Several MCFC stack developers have produced cell stacks with cell areas up to 1 m^2 cells. Tall, full-scale stacks fabricated to date include several FuelCell Energy (FCE) 300 plus cell stacks with ~9000 cm^2 cell area producing >1 MW. Today, FCE has demonstrated hundreds of plants worldwide and extended life to over 30,000 h.

2.5.6. Solid Oxide Fuel Cell (SOFC)

The SOFC is viable for generating electricity from hydrocarbon fuels and being efficiently integrated with reformers. The higher operating temperature, from 700 °C to 1000 °C, allows internal reforming and promotes rapid kinetics with non-precious materials. The high temperature of the SOFC, however, places stringent requirements on its materials. The development of suitable low-cost materials and low-cost fabrication of ceramic structures has been a focus of research. The SOFC integrates well with large coal gasification plants that are able to take advantage of synergies to produce high efficiency, 99% CO_2 capture, and low water consumption [32].

Two different design configurations are being developed for SOFCs motivated by (1) considerations of how to seal the anode and cathode compartments, (2) ease of manufacturing, and (3) minimizing losses due to electric resistance. The two principal types are tubular and planar as shown in Fig. 2.4. Operating between 900 °C and 1000 °C, the tubes have relatively high electrical resistance but are simple to seal. Some tubular designs eliminate the need for seals and allow for thermal expansion. Several tubular units are presently operating in the field, with tens of thousands of hours of demonstrated operation. In the tubular configuration, bundles of tubes that are closed at one end are arranged in parallel. Air is introduced to the inside of each tube while fuel flows over the outside of the cells. Oxygen ions migrate through the electrolyte to react with fuel; the flow of ions produces electricity.

The planar SOFC is composed of flat, thin ceramic plates. The planar SOFC operates at 800 °C or even less. Ultra-thin electrode/electrolyte sheets have low electrical resistance in order to achieve high power density and efficiency. Operation at temperatures lower than the tubular SOFC enables less exotic materials

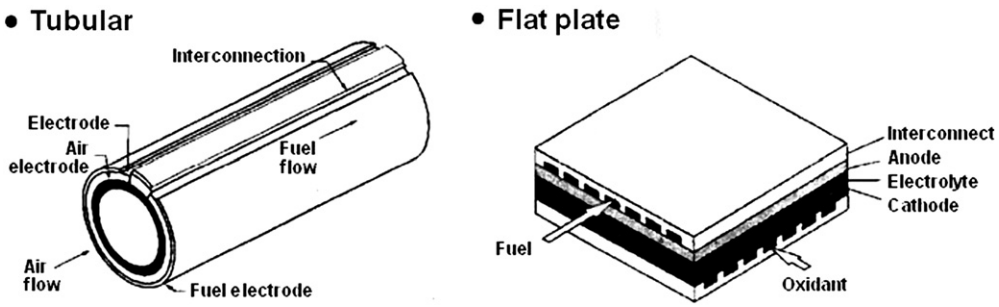

FIGURE 2.4 Tubular and planar cell configurations [1].

of construction, thus saving on cost. In the planar configuration, the anode, electrolyte, and cathode form thin, flat layers that are sintered together, and then separated by bipolar plates similar to the design of other types of fuel cells. The plates can be rectangular, square, circular, or segmented in series and can be manifolded externally or internally. Many of the planar SOFCs use metallic bipolar plates and are operated at a lower temperature than the all-ceramic tubular design. With currently hundreds of stack tests having been run by Versa and Delphi and record-breaking electrochemical performance, the planar SOFC has emerged as the low-cost potential, high-performance SOFC. Since 2000, DOE's Solid-State Energy Conversion Alliance has made an order of magnitude improvement in SOFCs increasing power density and lowering the projected costs [32]. The typical embodiment of direct methane oxidation fuel cell is a variation of the SOFC.

References

[1] National Energy Technology Laboratory Fuel cell handbook. 7th ed. Morgantown, WV: U.S. Department of energy; 2004.

[2] Hoogers G, editor. Fuel cell technology handbook. Boca Raton, FL: CRC Press; 2003.

[3] Larminie J, Dicks A. Fuel cell systems explained. 2nd ed. Chichester: Wiley & Sons Ltd; 2003.

[4] Basu S. Recent trends in fuel cell science and technology. New York: Springer; 2007.

[5] Srinivasan S. Fuel cells: from fundamentals to applications. New York: Springer; 2006.

[6] Williams MC. U.S. DOE stationary fuel cell program. Palm Springs, CA: Fuel cell seminar extended abstracts; 2005.

[7] Williams MC. NETL overview. Pittsburgh, PA: Presentation at U.S. DOE DCFC symposium; 2003.

[8] Wark K. Applied thermodynamics for engineers. New York: McGraw-Hill; 1977.

[9] Williams MC, Yamaji K, Yokokawa H. Fundamental thermodynamic studies of fuel cells using MALT2. J Fuel Cell Sci Technol 2009;6:97–102.

[10] Williams MC, Yamaji K, Yokokawa H. Fundamental thermodynamic studies of fuel cells and hybrids. J Fuel Cell Sci Technol 2009;6:113–6.

[11] Winkler W. Thermodynamics. In: Singhal SC, Kendall K, editors. High temperature solid oxide fuel cells: fundamentals, design, and applications. Oxford, UK: Elsevier; 2003. p. 53–82.

[12] Winkler W. SOFC-integrated power plants for natural gas. Proceedings of first European solid oxide fuel cell forum. Lucerne, Switzerland: Oct 3–7, 1994. p. 821–48.

[13] Williams M, Yamaji K, Horita T, Sakai N, Yokokawa H. Exergetic studies of intermediate-temperature, solid oxide fuel cell electrolytes. J Electrochem Soc 2009;156(4):B546–51.

[14] Virkar A, Williams MC, Singhal SC. In: Williams M, Krist K, editors. ECS Transactions. Concepts for ultra-high power density solid oxide fuel cells 2007; 5(1):401–22.

[15] Virkar AV. Theoretical analysis of the role of interfaces in transport through oxygen ion and electron conducting membranes. J Power Sources 2005;147 (1–2):8–31.

[16] Zhao, Virkar AV. Dependence of polarization in anode-supported solid oxide fuel cells on various cell parameters. J Power Sources 2005;141(1): 79–95.

[17] Yokokawa H, Sakai N, Horita T, Yamaji K, Brito ME. Electrolytes for solid-oxide fuel cells. MRS Bull 2005;30(8):591–5.

[18] Kawada T, Yokokawa H. Materials and characterization of solid oxide fuel cell. Key Eng Mater 1997;125–126:187–248.

[19] Choudhury NS, Patterson JW. Steady-state chemical potential profiles in solid electrolytes. J Electrochem Soc. 1970;117(11):1384–8.

[20] Zecevic S, Patton EM, Parhami P. Electrochemistry of direct carbon fuel cell based on metal hydroxide electrolyte. Presentation at U.S. DOE DCFC Symposium. Pittsburgh, PA: July 2003.

[21] Cherepy NJ, Krueger R, Fiet KJ, Jankowski AF, Cooper JF. Direct conversion of carbon fuels in a carbonate fuel cell. J Electrochem Soc. 2005;152 (1):A80–7.

[22] Cooper JF. Turning carbon directly into electricity. Livermore, CA: Science and Technology Review; June 2001. p. 4–12.

[23] Horita T, Sakai N, Kawada T, Yokokawa H, Dokiya M. An investigation of anodes for direct-oxidation of carbon in solid oxide fuel cells. J Electrochem Soc. 1995;142(8):2621–4.

[24] Selman R. DCFC research needs. Presentation at US DOE DCFC symposium. Pittsburgh, PA: 2003.

[25] Watkins DS. Proceedings of 33rd International Power Sources Symposium. Cherry Hill, NJ: Electrochemical Society; June 13–16, 1988. p.782–91.

[26] Krumpelt M, Kumar R, Miller J, Christianson C. Fuel cell seminar. Tucson, AZ; Nov 29-Dec 2, 1992. p. 35.
[27] McLean GF, Niet T, Prince-Richard S, Djilali N. An assessment of fuel cell technology. Int J Hydrogen Energy 2002;27(5):507–26.
[28] Appleby AJ. In: Sarangapani S, Akridge JR, Schumm B, editors. Proceedings of the workshop on the electrochemistry of carbon. Pennington, NJ: The Electrochemical Society, Inc; 1984. p. 251.
[29] Kordesch KV. Survey of carbon and its role in phosphoric acid fuel cells, BNL 51418. Prepared for Brookhaven National Laboratory, Dec 1979.
[30] Maru HC, Paetsch L, Pigeaud A. In: Selman RJ, Claar TD, editors. Proceedings of the symposium on molten carbonate fuel cell technology. Pennington, NJ: The Electrochemical Society, Inc; 1984. p. 20.
[31] Petri RJ, Benjamin TG. Proceedings of the 21st intersociety energy conversion engineering conference, vol. 2. Washington, DC: American Chemical Society; 1986. 1156.
[32] Surdoval WA. U.S. DOE's stationary fuel cell program: energy production in a carbon challenged world. Palm Springs, CA: Extended Abstracts of Fuel Cell Seminar; Nov 2009.

CHAPTER

3

Fuels for Fuel Cells

James G. Speight

CD & W Inc, 2476 Overland Road, Laramie, WY 82070-4808, USA

OUTLINE

3.1. INTRODUCTION

For the past one hundred years, liquid hydrocarbon fuels have been a major driving force behind industrialized countries [1,2]. Product demand has increased at a phenomenal rate, and we have reached the point where the demand to the liquid hydrocarbon fuels culture is approaching and other fuel sources are being sought. At the same time, traditional markets such as North America and Europe are experiencing moderate increase in demand, whereas emerging Asian markets such as India and China are witnessing a rapid surge. This has resulted in a squeeze on existing refineries, prompting a fresh technological approach to optimize efficiency and throughput. Major oil companies and technology suppliers/licensors are investing heavily to revamp their refining technologies in an effort to cater to the growing needs of customers.

As other sources and types of fuels are being sought, it is considered useful to include information on the various types of liquid fuels and

the relevant chemical and physical properties of these fuels as a means of comparison to the fuels of the future.

Just as a regular fuel generates energy by combustion, a fuel cell (the subject matter of this book) is a device that generates electricity by a chemical reaction. In fact, a fuel cell is an electrochemical cell that produces electricity through the reaction, triggered in the presence of an electrolyte, between the fuel (on the anode side) and an oxidant (on the cathode side). The reactants flow into the cell and the reaction products flow out of it, while the electrolyte remains within it and the reactions that produce electricity take place at the electrodes. Hydrogen or hydrogen-rich synthesis gas is the basic fuel for fuel cells. Unfortunately, the lack of widely available alternative sources of hydrogen dictates that the hydrogen (or hydrogen-rich synthesis gas) be derived from hydrocarbon fuels. Depending on the application (stationary, central power, remote, auxiliary, transportation, military, etc.), there are a wide range of conventional fuels, such as natural gas, liquefied petroleum gas (LPG), light distillates, methanol, ethanol, dimethyl ether, naphtha, gasoline, kerosene, jet fuels, diesel, and biodiesel, that could be used in reforming processes to produce hydrogen (or hydrogen-rich synthesis gas) to power fuel cells.

Hydrocarbon fuels behave differently and in order to place fuel cells in the proper perspective, this chapter is an overview, with some degree of detail, of the manufacture and properties of the common fuels as well as a description of various biofuels. This would not be an exhaustive treatment of all fuel properties, but only of those relevant to fuel processing for the purpose of providing hydrogen (or hydrogen-rich synthesis gas) for fuel cells, e.g., aromatic content (which affects coking), olefin content, contaminant levels, additives, and boiling point range (which affects vaporization of the fuels in the fuel processor), all of which may affect the catalysts used for fuel processing.

3.2. FOSSIL FUELS

Fossil fuels (petroleum, natural gas, tar sand bitumen coal, and oil shale) [3] are fuels formed by the anaerobic decomposition of buried organic matter usually over a period of millions of years.

Over geological time, the organic matter, mixed with mud, was buried under heavy layers of sediment. The resulting heat and pressure brought about chemical changes to the organic matter, eventually leading to a variety of gaseous, liquid, and solid fuels and fuel sources.

Fossil fuels range from volatile compounds with a high hydrogen/carbon atomic ratio (e.g., methane) to nonvolatile materials such as tar, sand, bitumen, and coal – both of which contain lower proportions of hydrogen and higher amounts of carbon.

A fuel mixture usually contains a wide range of organic compounds (usually hydrocarbons). The specific mixture of hydrocarbons gives a fuel its characteristic properties, such as boiling point, melting point, density, viscosity, as well as a host of other properties.

3.2.1. Gaseous Fuels

Gaseous fuels are those fuels which exist in the gaseous form and can be isolated from natural sources or by manufacture from other sources. The types and properties of the gaseous fuels are varied (Table 3.1), but the common gaseous fuels are natural gas as well as propane and butane [4].

3.2.1.1. Natural Gas

Natural gas, which is predominantly methane (also called marsh gas and swamp gas in older texts and more recently landfill gas), is a naturally occurring gaseous fossil fuel that is found in oil reservoirs, natural gas reservoirs, and coal beds.

For clarification, natural gas is not the same as town gas, which is manufactured from coal, and the terms coal gas, manufactured gas,

TABLE 3.1 General Properties and Description of Gaseous Hydrocarbons

	Molecular weight	Boiling point (°C)	Ignition temperature (°C)	LHV (kJ/mole)	HHV (kJ/mole)	Flammability limits in air (% v/v)
Methane	16.0	−161.5	482−632	799.7	889.3	5.0−15.0
Ethane	30.1	−88.6	515	1429.4	1561.6	3.0−12.5
Ethylene	28.0	−103.7	490	1320.3	1408.2	2.8−28.6
Propane	44.1	−42.1	450	2044.4	2219.7	2.1−10.1
Propylene	42.1	−47.7	458	1927.0	2060.9	2.00−11.1
n-Butane	58.1	0.5	405	2658.8	2875.8	1.86−8.41
iso-Butane	58.1	−11.7	462	2657.0	2872.8	1.80−8.44
n-Butene	56.1	−6.0	443	2542.0	2718.1	1.98−9.65
iso-Butene	56.1	−6.9	465	2485.0	2706.2	1.8−9.0

producer gas, and synthetic natural gas (SNG) are also used for gas produced from coal [3]. Depending on the production process, gas from coal is a mixture of hydrogen, carbon monoxide, methane, and volatile hydrocarbons in varying amounts with small amounts of carbon dioxide and nitrogen as impurities.

The principal constituent of natural gas is methane (Table 3.2). Other constituents are alkanes such as ethane, propane, and the butanes. Many natural gases contain nitrogen as well as carbon dioxide and hydrogen sulfide. Trace quantities of argon, hydrogen, and helium may also be present. Generally, the hydrocarbons having a higher molecular weight than methane, carbon dioxide, and hydrogen sulfide are removed from natural gas prior to its use as a fuel. Gases produced in a refinery contain methane, ethane, ethylene, propylene, hydrogen, carbon monoxide, carbon dioxide, and nitrogen, with low concentrations of water vapor, oxygen, and other gases.

The composition of natural gas, manufactured gas, and mixed gas can vary so widely, and no single set of specifications could cover all situations. The requirements are usually based on performances in burners and equipment, on minimum heat content, and on maximum sulfur content [5]. Gas utilities in most states come under the supervision of state commissions or regulatory bodies, and the utilities must provide a gas that is acceptable to all

TABLE 3.2 General Properties of Natural Gas

Relative molar mass	16−20
Carbon content (wt%)	73−75
Hydrogen content (wt%)	27−25
Oxygen content (wt%)	0−0.4
Hydrogen-to-carbon atomic ratio	3.5−4.0
Density relative to air @15 °C	0.6−1.5
Boiling temperature (°C)	−162
Autoignition temperature (°C)	540−560
Vapor flammability limits (vol%)	5−15
Flammability limits	0.7−2.1
Lower heating/calorific value (kJ/mole)	950
Methane concentration (vol%)	80−100
Ethane concentration (vol%)	0−5
Nitrogen concentration (vol%)	0−15
Carbon dioxide concentration (vol%)	0−5
Sulfur concentration (ppmw)	0−5

types of consumers and that will give satisfactory performance in all kinds of consuming equipment. However, there are specifications for LPG (ASTM D1835) which depend upon the required volatility.

The different methods for natural gas analysis include absorption, distillation, combustion, mass spectroscopy, infrared spectroscopy, and gas chromatography (ASTM D2163, ASTM D2650, and ASTM D4424). The methods chosen depend upon the composition of the natural gas and the amount of sulfur compounds that need to be removed.

Absorption methods involve absorbing individual constituents one at a time in suitable solvents and recording of contraction in volume measured. Distillation methods depend on the separation of constituents by fractional distillation and measurement of the volumes distilled. In combustion methods, certain combustible elements are caused to burn to carbon dioxide and water, and the volume changes are used to calculate composition. Infrared spectroscopy is useful in particular applications. For the most accurate analyses, mass spectroscopy and gas chromatography are the preferred methods.

The specific gravity of product gases, including LPG, may be determined conveniently by a number of methods and a variety of instruments (ASTM D1070).

The heat value of gases is generally determined at constant pressure in a flow calorimeter in which the heat released by the combustion of a definite quantity of gas is absorbed by a measured quantity of water or air. A continuous recording calorimeter is available for measuring heat values of natural gases (ASTM D1826).

Although not a petroleum-derived gas, gas from coal (coal gas) is a flammable gaseous fuel supplied to the user via a piped distribution system. The more general term town gas refers to manufactured gaseous fuels produced from coal for sale to consumers and municipalities. In the first half of the twentieth century, it was also known as illumination gas.

In the simplest sense, coal gas was manufactured by the destructive distillation of coal, a process which yielded a product that was chemically and physically distinct from that of the range of gaseous fuels such as manufactured gas, synthesis gas (syngas), and producer gas, which are made by partial combustion of feedstock in a specific mixture of air or oxygen or steam [3]. However, this distinction about the production process is immaterial to the product itself or to its naming at any rate in modern usage.

3.2.1.2. *Liquefied Petroleum Gas*

Liquefied petroleum gas (LPG) is the term applied to certain specific hydrocarbons and their mixtures, which exist in the gaseous state under ambient conditions but can be converted to the liquid state under conditions of moderate pressure at ambient temperature. These are the low-boiling hydrocarbons fraction of the alkane series, derived from refinery processes, crude oil stabilization plants, and natural gas processing plants comprising propane, butane, *iso*-butane, and to a lesser extent propylene or butylene.

The most common commercial products are propane, butane, or some mixture of the two (Table 3.1) and are generally extracted from natural gas or crude petroleum. Propylene and butylenes result from cracking other hydrocarbons in a petroleum refinery and are two important chemical feedstocks.

Mixed gas is a gas prepared by adding natural gas or LPG to a manufactured gas, giving a product of better utility and higher heat content or Btu value.

3.2.2. Gasoline

Gasoline, also called gas (United States and Canada), or petrol (Great Britain) or benzine (Europe) is one of several liquid fuels produced from petroleum (Table 3.3) and is a mixture of volatile, flammable liquid hydrocarbons derived from petroleum and used as fuel for internal-combustion engines [2]. Gasoline was

TABLE 3.3 General Properties of Liquid Products from Petroleum

	Chemical formula	Mol. wt	Composition (wt%)		Specific gravity	Boiling point (°C)	Autoignition temperature (°C)	Flash point (°C)	Heating values (kJ/kg)		Flammability limits (vol%)
			C	H					LHV	HHV	
Gasoline	C4–C12	113	85–88	12–15	0.720	35–225	257	−43	43,500	46,500	1.4–7.6
Kerosene	C10–C16	170	85	15	0.800	150–300	210	37–72	43,100	46,200	0.7–5.0
JP-4	C6–C11	119	86	14	0.751–0.802	45–280	246	−23 - 1	42,800	45,800	1.3–8.0
JP-7	C10–C16	166	87	13	0.779–0.806	60–300	241	43–66	43,500	46,800	0.6–4.6
Diesel fuel	C8–C25	200	87	13	0.850	180–340	315	60–80	42,800	45,800	1.0–6.0
Fuel oil #1	C9–C16	200	87	13	0.875	150–300	210	37–72			0.7–5.0
Fuel oil #2	C11–C20				0.920		256	52–96			
Fuel oil #4		198			0.959		263	61–115			
Fuel oil #5					0.960			69–169			
Fuel oil #6					0.960	175–345		66			

TABLE 3.4 Properties of Hydrocarbons Generally Found in Liquid Products from Petroleum

	Molecular weight	Specific gravity	Boiling point (°C)	Ignition temperature (°C)	Flash point (°C)	Flammability limits in air (% v/v)
n-Pentene	70.1	0.641	30	260	−49	1.6–7.7
iso-Pentane	72.1	0.621	28	420	−51	1.3–9.2
Neopentane	72.1		10	449	−61	1.4–7.1
n-Pentane	72.1	0.626	36	260	−40	1.4–7.8
Benzene	78.1	0.879	80	560	−11	1.3–6.7
Neohexane	86.2	0.649	50	425	−48	1.2–7.6
n-Hexane	86.2	0.659	69	225	−22	1.2–7.0
Toluene	92.1	0.867	161	533	4	1.2–6.8
n-Heptane	100.2	0.668	215	215	−4	1.0–6.0
Xylene	106.2	0.861	138	464	17	1.0–6.0
iso-Octane	114.2	0.702	118	447	−12	0.8–5.9
n-Octane	114.2	0.707	126	220	13	0.9–3.2
Naphthalene	128.2	1.162	218	525	79	0.9–5.9
t-butylbenzene	134.2	0.867	169	450	44	0.7–5.7
trans-Decalin	138.2	0.870	187	250	57	0.7–4.9
cis-Decalin	138.2	0.896	193	250	57	0.7–4.9
n-Decane	142.2	0.735	174	210	46	0.8–5.4
1-methylnaphthalene	142.2	1.025	242	529	82	0.7–6.5
n-Dodecane	170.3	0.753	216	203	71	0.6–[a]
n-Tetradecane	198.4	0.767	250	200	99	0.5–[a]
n-Hexadecane (*n*-cetane)	226.4	0.773	287	201	135	
iso-Cetane	226.4	0.793	240		102	

[a]*No data available for upper flammability limit (UFL)*

originally a by-product of the petroleum industry (kerosene being the principal product) and became the preferred automobile fuel because of its high energy of combustion and capacity to mix readily with air in a carburetor of the internal combustion engine.

Gasoline is a mixture of hydrocarbons that usually boil below 180 °C (356 °F) or, at most, below 200 °C (392 °F). The hydrocarbon constituents in this boiling range are those that have 4–12 carbon atoms in their molecular structure and fall into three general types: alkanes (including the cycloalkanes and branched materials), alkenes, and aromatics (Table 3.4).

Gasoline is manufactured to meet specifications (ASTM D4814) and regulations and not to achieve a specific distribution of hydrocarbons by class and size. However, chemical composition often defines properties. For example, volatility is defined by the individual

hydrocarbon constituents, and the lowest boiling constituent(s) defines the volatile as determined by certain test methods.

Gasoline was at first produced by distillation, simply separating the volatile, more valuable fractions of crude petroleum [2]. Later processes, designed to raise the yield of gasoline from crude oil, thermally decomposed (cracked) higher molecular weight constituents into lower molecular weight products.

Thermal cracking, employing heat and high pressures, was introduced in 1913 but was replaced after 1937 by catalytic cracking, the application of catalysts that facilitate chemical reactions producing more gasoline. Other methods used to improve the quality of gasoline and increase its supply include polymerization, alkylation, isomerization, and reforming. In a modern refinery, the product of each of these processes is a blending stock for the production of sales gasoline.

Polymerization is the conversion of gaseous alkenes, such as propylene and butylene, into larger molecules in the gasoline range. Alkylation is a process combining an alkene and alkane such as *iso*-butane. Isomerization is the conversion of straight-chain hydrocarbons to branched-chain hydrocarbons. Reforming is the use of either heat or a catalyst to rearrange the molecular structure.

3.2.2.1. *Automotive Gasoline*

Automotive gasoline typically contains about almost 200 (if not several hundred) hydrocarbon compounds and the relative concentrations of the compounds vary considerably depending on the source of crude oil, refinery process, and product specifications. Typical hydrocarbon chain lengths range from C_4 through C_{12} with a general hydrocarbon distribution consisting of alkanes (4–8%), alkenes (2–5%), *iso*-alkanes (25–40%), cycloalkanes (3–7%), cycloalkenes (l–4%), and aromatics (20–50%). However, these proportions vary greatly. Highly branched alkanes, which are particularly valuable constituents of gasoline(s), are not usually the principal alkane constituents of straight-run gasoline. The more predominant alkane constituents of straight-run gasoline are usually the normal (straight-chain) isomers, which may dominate the branched isomer(s) by a factor of 2 or more. This is presumed to indicate the tendency to produce long uninterrupted carbon chains during petroleum maturation rather than those in which branching occurs. However, this trend is somewhat different for the cyclic constituents of gasoline, i.e., cycloalkanes (naphthenes) and aromatics. In these cases, the preference appears to be for several short side chains rather than one long substituent.

Trace amounts of sulfur compounds also occur in gasoline. On January 1, 2006, the sulfur content for gasoline produced at most refineries was lowered to a per-gallon maximum of 80 parts per million (ppm), with an overall maximum annual average of 30 ppm. The per-gallon sulfur limit for some gasoline in the Rocky Mountain area was lowered to 80 ppm on January 1, 2007; this standard does not apply to all gasoline, because there are different regulations for some gasoline in the Rocky Mountain area and small refiners.

3.2.2.2. *Aviation Gasoline*

Aviation gasoline is a form of automotive gasoline that has been especially prepared for use for aviation piston engines. It has an octane number suited to the engine, a freezing point of −60°C (−76 °F), and a distillation range usually within the limits of 30–180°C (86–356 °F) compared to −1–200 °C (30–390 °F) for automotive gasoline. The narrower boiling range ensures better distribution of the vaporized fuel through the more complicated induction systems of aircraft engines. Aircraft operates at altitudes at which the prevailing pressure is less than the pressure at the surface of the earth (pressure at 5300 m is 0.05 MPa compared to 0.1 MPa at the surface of the earth). Thus, the vapor pressure of aviation gasoline must be limited to reduce boiling in the tanks, fuel lines,

and carburetors. As a consequence, aviation gasoline does not usually contain the gaseous hydrocarbons (butanes) that give automobile gasoline the higher vapor pressures for starting at cold temperatures.

Aviation gasoline is composed of alkanes and *iso*-alkanes (50−60%), moderate amounts of cycloalkanes (20−30%), small amounts of aromatics (10%), and usually no alkenes, whereas motor gasoline may contain up to 30% alkenes and up to 40% aromatics.

The manufacture of aviation gasoline is dependent on the availability and selection of fractions containing suitable hydrocarbons. The lower boiling hydrocarbons are usually found in straight-run naphtha from certain crude petroleum. These fractions have high contents of *iso*-pentanes and *iso*-hexane and provide needed volatility, as well as high octane number components. Higher boiling *iso*-alkanes are provided by aviation alkylate, which consists mostly of branched octanes. Aromatics, such as benzene, toluene, and xylene, are obtained from catalytic reforming or a similar source.

3.2.2.3. *Gasohol*

In the late twentieth century, the rising price of petroleum (and hence of gasoline) led to the increasing use of gasohol, which is a mixture of 90% unleaded gasoline and 10% ethanol (ethyl alcohol). Gasohol burns well in gasoline engines and is a desirable alternative fuel for certain applications because of the availability of ethanol, which can be produced from grains, potatoes, and certain other plant matter. Methanol and a number of other alcohols and ethers are considered high-octane enhancers of gasoline [6]. They can be produced from various hydrocarbon sources other than petroleum and may also offer environmental advantages insofar as the use of oxygenates would presumably suppress the release of vehicle pollutants into the air.

3.2.2.4. *Octane Rating*

Gasoline performance and hence quality of an automotive gasoline are determined by its resistance to knock, for example, detonation or ping during service. The antiknock quality of the fuel limits the power and economy that an engine using that fuel can produce: the higher the antiknock quality of the fuel, the more the power and efficiency of the engine.

In 1922, tetraethyl lead was discovered to be an excellent antiknock material when added in small quantities to gasoline, and gasoline containing tetraethyl lead became widely available. However, the problem of how to increase the antiknock characteristics of cracked gasoline became acute in the 1930s. One feature of the problem concerned the need to measure the antiknock characteristics of gasoline accurately. This was solved in 1933 by the general use of a single-cylinder test engine, which allowed comparisons of the antiknock characteristics of gasoline to be made in terms of octane numbers. The octane numbers formed a scale ranging from 0 to 100: the higher the number, the greater the antiknock characteristics. In 1939, a second and less severe test procedure using the same test engine was developed, and results obtained by this test were also expressed in octane numbers.

Octane numbers are obtained by the two test procedures: those obtained by the first method are called *motor octane numbers* (indicative of high-speed performance) (ASTM D2700 and ASTM D2723) and those obtained by the second method are called *research octane numbers* (indicative of normal road performance) (ASTM D2699 and ASTM D2722). Octane numbers quoted are usually, unless stated otherwise, research octane numbers.

In the test methods used to determine the antiknock properties of gasoline, comparisons are made with blends of two pure hydrocarbons, *n*-heptane and *iso*-octane (2,2,4-trimethylpentane). *Iso*-octane has an octane number of 100 and is high in its resistance to knocking;

n-heptane is quite low (with an octane number of 0) in its resistance to knocking.

n-Alkanes have the least desirable knocking characteristics, and these become progressively worse as the molecular weight increases. *Iso*-alkanes have higher octane numbers than the corresponding normal isomers, and the octane number increases as the degree of branching of the chain is increased. Alkenes have markedly higher octane numbers than the related alkanes; naphthenes are usually better than the corresponding *n*-alkanes but rarely have very high octane numbers; aromatics usually have quite high octane numbers.

3.2.2.5. Additives in Gasoline

Additives are gasoline-soluble chemicals that are mixed with gasoline to enhance certain performance characteristics or to provide characteristics not inherent in the gasoline. Additives are generally derived from petroleum-based materials, and their function and chemistry are highly specialized. They produce the desired effect at the parts-per-million (ppm) concentration range.

3.2.2.5.1. ANTIOXIDANTS

Oxidation inhibitors (antioxidants) are aromatic amines and hindered phenols that prevent gasoline components (particularly alkenes) from reacting with oxygen in the air to form peroxides or gums. Peroxides can degrade antiknock quality, cause fuel pump wear, and attack plastic or elastomeric fuel system parts, soluble gums can lead to engine deposits, and insoluble gums can plug fuel filters. Inhibiting oxidation is particularly important for fuels used in modern fuel-injected vehicles, as their fuel recirculation design may subject the fuel to more temperature and oxygen-exposure stress.

3.2.2.5.2. CORROSION INHIBITORS

Corrosion inhibitors are carboxylic acids and carboxylates that prevent free water in the gasoline from rusting or corroding pipelines and storage tanks. Corrosion inhibitors are less important once the gasoline is in the vehicle. The metal parts in the fuel systems of today's vehicles are made of corrosion-resistant alloys or of steel coated with corrosion-resistant coatings. More plastic parts are replacing metals in the fuel systems and, in addition, service station systems and operations are designed to prevent free water from being delivered to a vehicle's fuel tank.

3.2.2.5.3. DEMULSIFIERS

Demulsifiers are polyglycol derivatives that improve the water-separating characteristics of gasoline by preventing the formation of stable emulsions.

3.2.2.5.4. ANTI-ICING

Anti-icing additives are surfactants, alcohols, and glycols that prevent ice formation in the carburetor and fuel system. The need for this additive is being reduced as older-model vehicles with carburetors are replaced by vehicles with fuel injection systems.

3.2.2.5.5. DYES AND MARKERS

Dyes are oil-soluble solids and liquids used to visually distinguish batches, grades, or applications of gasoline products. For example, gasoline for general aviation, which is manufactured to different and more exacting requirements, is dyed blue to distinguish it from motor gasoline for safety reasons.

Markers are a means of distinguishing specific batches of gasoline without providing an obvious visual clue. A refiner may add a marker to its gasoline so it can be identified as it moves through the distribution system.

3.2.2.5.6. DRAG REDUCERS

Drag reducers are high-molecular-weight polymers that improve the fluid flow characteristics of low-viscosity petroleum products. Drag

reducers lower pumping costs by reducing friction between the flowing gasoline and the walls of the pipe.

3.2.2.5.7. OXYGENATES (FUEL ADDITIVES)

Oxygenates are carbon-, hydrogen-, and oxygen-containing combustible liquids that are added to gasoline to improve performance. The addition of oxygenates gasoline is not new since ethanol (ethyl alcohol or grain alcohol) has been added to gasoline for decades. Thus, oxygenated gasoline is a mixture of conventional hydrocarbon-based gasoline and one or more oxygenates. The current oxygenates belong to one of two classes of organic molecules: alcohols and ethers. The most widely used oxygenates in the United States are ethanol, methyl tertiary-butyl ether (MTBE), and tertiary-amyl methyl ether (TAME). Ethyl tertiary-butyl ether (ETBE) is another ether that could be used. Oxygenates may be used in areas of the United States where they are not required as long as concentration limits (as refined by environmental regulations) are observed.

Of all the oxygenates, MTBE is attractive for a variety of technical reasons. It has a low vapor pressure, can be blended with other fuels without phase separation, and has the desirable octane characteristics. If oxygenates achieve recognition as vehicle fuels, the biggest contributor will probably be methanol, the production of which is mostly from synthesis gas derived from methane.

The higher alcohols also offer some potential as motor fuels. These alcohols can be produced at temperatures below 300 °C (572 °F) using copper oxide−zinc oxide−alumina catalysts promoted with potassium. *Iso*-butyl alcohol is of particular interest because of its high octane rating, which makes it desirable as a gasoline-blending agent. This alcohol can be reacted with methanol in the presence of a catalyst to produce MTBE. Although it is currently cheaper to make *iso*-butyl alcohol from *iso*-butylene, it can be synthesized from syngas with alkali-promoted zinc oxide catalysts at temperatures above 400 °C (752 °F) [7].

3.2.2.6. Adulteration

Adulteration differs from contamination insofar as unacceptable materials deliberately are added to gasoline for a variety of reasons not to be discussed here. Such activities may not only lower the octane number but will also adversely affect volatility, which in turn also affects performance. In some countries, dyes and markers are used to detect adulteration (e.g., ASTM D86 distillation testing and/or ASTM D2699/ASTM D2700 octane number testing may be required to detect adulteration).

3.2.3. Kerosene

Kerosene (kerosine), also called alkane or alkane oil, is a flammable pale-yellow or colorless oily liquid with a characteristic odor. It is obtained from petroleum and used for burning in lamps and domestic heaters or furnaces, as a fuel or fuel component for jet engines, and as a solvent for greases and insecticides.

Kerosene is intermediate in volatility between gasoline and gas/diesel oil. It is a medium oil distilling between 150 and 300 °C (302−572°F). Kerosene has a flash point at about 25 °C (77 °F) and is suitable for use as an illuminant when burned in a wide lamp. However, like gasoline, the properties of kerosene can vary (Table 3.3) depending upon the boiling point range isolated from petroleum.

The term kerosene is also too often incorrectly applied to various fuel oils, but a fuel oil is actually any liquid or liquid petroleum product that produces heat when burned in a suitable container or that produces power when burned in an engine.

Kerosene was the major refinery product before the onset of the automobile age, but now kerosene can be termed one of several secondary petroleum products after the primary refinery product − gasoline. Kerosene originated

as a straight-run petroleum fraction (naturally occurring and distilled directly from petroleum) that boiled between approximately 205 and 260 °C (401−500 °F) [2]. Some crude oils, for example, those from the Pennsylvania oil fields, contain kerosene fractions of very high quality, but other crude oils, such as those having an asphalt base, must be thoroughly refined to remove the majority of aromatics (although some still exist in kerosene) and sulfur compounds before a satisfactory kerosene fraction can be obtained.

Chemically, kerosene is a mixture of hydrocarbons; the chemical composition depends on its source, but it usually consists of a variety of hydrocarbons, each containing from 10 to 16 carbon atoms per molecule; the constituents include *n*-dodecane, alkyl benzenes, and naphthalene and its derivatives.

Kerosene, because of its use as burning oil, must be free of aromatic and unsaturated hydrocarbons, as well as free of the more obnoxious sulfur compounds. The desirable constituents of kerosene are saturated hydrocarbons, and it is for this reason that kerosene is manufactured as a straight-run fraction and not by a cracking process.

Although the kerosene constituents are predominantly saturated materials, there is evidence for the presence of substituted tetrahydronaphthalene (Table 3.4). Dicycloalkanes also occur in substantial amounts in kerosene. Other hydrocarbons with both aromatic and cycloalkane rings in the same molecule, such as substituted indan, also occur in kerosene. The predominant structure of the binuclear aromatics appears to be that in which the aromatic rings are condensed, such as naphthalene, whereas the isolated two-ring compounds, such as biphenyl, are only present in traces, if at all.

Kerosene was first manufactured in the 1850s from coal tar; hence the name coal oil is often applied to kerosene, but petroleum became the major source after 1859. From that time, the kerosene fraction is and has remained a distillation fraction of petroleum. However, the quantity and quality vary with the type of crude oil, and although some crude oils yield excellent kerosene quite simply, others produce kerosene that requires substantial refining.

Kerosene is a very stable product, and additives are not required to improve the quality. Apart from the removal of excessive quantities of aromatics by the Edeleanu process, kerosene fractions may need only a lye wash or a doctor treatment if hydrogen sulfide is present to remove mercaptans [2].

Kerosene is by nature a fraction distilled from petroleum that has been used as a fuel oil from the beginning of the petroleum-refining industry. As such, low proportions of aromatic and unsaturated hydrocarbons are desirable to maintain the lowest possible level of smoke during burning. Although some aromatics may occur within the boiling range assigned to kerosene, excessive amounts can be removed by extraction; that kerosene is not usually prepared from cracked products almost certainly excludes the presence of unsaturated hydrocarbons.

The essential properties of kerosene are flash point, fire point, distillation range, burning, sulfur content, color, and cloud point. In the case of the flash point (ASTM D56), the minimum flash temperature is generally placed above the prevailing ambient temperature; the fire point (ASTM D92) determines the fire hazard associated with its handling and use.

The boiling range (ASTM D86) is of less importance for kerosene than for gasoline, but it can be taken as an indication of the viscosity of the product, for which there is no requirement for kerosene. The ability of kerosene to burn steadily and cleanly over an extended period (ASTM D187) is an important property and gives some indication of the purity or composition of the product.

The significance of the total sulfur content of a fuel oil varies greatly with the type of oil and the use to which it is put. Sulfur content is of great importance when the oil to be burned

produces sulfur oxides that contaminate the surroundings. The color of kerosene is of little significance, but a product darker than usual may have resulted from contamination or aging, and in fact a color darker than specified (ASTM Dl56) may be considered by some users as unsatisfactory.

Finally, the cloud point of kerosene (ASTM D2500) gives an indication of the temperature at which the wick may become coated with wax particles, thus lowering the burning qualities of the oil [2].

Jet fuels are sometimes classified as kerosene or naphtha-type [2]. Kerosene-type fuels include Jet A, Jet A-1, JP-5, and JP-8. Naphtha-type jet fuels, sometimes referred to as wide-cut jet fuel, include Jet B and JP-4.

Military organizations around the world use a different classification system of JP numbers. Some are almost identical to their civilian counterparts and differ only by the amounts of a few additives; Jet A-1 is similar to JP-8 and Jet B is similar to JP-4. Other military fuels are highly specialized products and are developed for very specific applications. JP-5 fuel is fairly common and was introduced to reduce the risk of fire on aircraft carriers (has a higher flash point − a minimum of 60 °C).

3.2.4. Diesel Fuel

Diesel fuel oil is essentially the same as furnace fuel oil, but the proportion of cracked gas oil is usually less since the high aromatic content of the cracked gas oil reduces the cetane value of the diesel fuel.

The allowable sulfur content for ultra-low sulfur kerosene and ultra-low sulfur diesel (15 ppm) is much lower than the previous US on-highway standard for low sulfur diesel (500 ppm), which not only reduces emissions of sulfur compounds (a cause of acid rain) but also allows advanced emission control systems to be fitted that would otherwise be poisoned by these compounds. These systems can greatly reduce emissions of oxides of nitrogen and particulate matter.

Diesel fuels were originally straight-run products obtained from the distillation of crude oil. However, with the use of various cracking processes to produce diesel constituents, diesel fuels also may contain varying amounts of selected cracked distillates to increase the volume available for meeting the growing demand. Care is taken to select the cracked stocks in such a manner that specifications are met.

Under the broad definition and properties of diesel fuel (Table 3.3), many possible combinations of characteristics (such as volatility, ignition quality, viscosity, gravity, stability, and other properties) exist. To characterize diesel fuels and thereby establish a framework of definition and reference, various classifications are used in different countries.

An example is ASTM D975 in the United States in which grades No. l-D and 2-D are distillate fuels, the types most commonly used in high-speed engines of the mobile type, in medium speed stationary engines, and in railroad engines. Grade 4-D covers the class of more viscous distillates and, at times, blends of these distillates with residual fuel oils. No. 4-D fuels are applicable for use in low and medium speed engines employed in services involving sustained load and predominantly constant speed.

Cetane number is a measure of the tendency of a diesel fuel to knock in a diesel engine. The scale is based upon the ignition characteristics of two hydrocarbons *n*-hexadecane (cetane) and 2,3,4,5,6,7,8-heptamethylnonane (isocetane). Cetane has a short delay period during ignition and is assigned a cetane number of 100; isocetane has a long delay period and has been assigned a cetane number of 15. Just as the octane number is meaningful for automobile fuels, the cetane number is a means of determining the ignition quality of diesel fuels and is equivalent to the percentage by volume of cetane in the blend

with isocetane, which matches the ignition quality of the test fuel (ASTM D613).

The manufacture of fuel oils at one time largely involved using what was left after removing desired products from crude petroleum. Now fuel oil manufacture is a complex matter of selecting and blending various petroleum fractions to meet definite specifications, and the production of a homogeneous, stable fuel oil requires experience backed by laboratory control.

Like gasoline, additives are also available for diesel fuel. Diesel fuel additives have two main functions. The first of diesel fuel additive is to maintain injector cleanliness. A clean injector will spray a perfect "fox tail" pattern mist of diesel fuel allowing for efficient combustion. Dirty injectors produce a fuel spray that is not a uniformly fine mist which will affect fuel mileage, power output, and idle quality, among other things. The second role of diesel fuel additives is to prevent gelling in cold weather. Without the proper additive diesel engines will not start when the temperature gets below a certain point.

3.2.5. Jet Fuels

Jet fuel is a light petroleum distillate (often boiling in the gasoline and kerosene boiling ranges) that is available in several forms suitable for use in various types of jet engines (Table 3.3). Jet fuel comprises both gasoline- and kerosene-type jet fuels meeting specifications for use in aviation turbine power units and is often referred to as gasoline-type jet fuel and kerosene-type jet fuel.

Gasoline-type jet fuel includes all light hydrocarbon oils for use in aviation turbine power units that distill between 100 and 250 °C (212−482 °F). It is obtained by blending kerosene and gasoline or naphtha in such a way that the aromatic content does not exceed 25% in volume. Additives can be included to improve fuel stability and combustibility.

Kerosene-type jet fuel is a medium distillate product that is used for aviation turbine power units. It has the same distillation characteristics and flash point as kerosene (between 150 and 300 °C, 302 and 572 °F, but not generally above 250 °C and 482 °F). In addition, it has particular specifications (such as freezing point), which are established by the International Air Transport Association (IATA).

ASTM D1655 specifications allow for certain additives to be added to jet fuel: (1) antioxidants to prevent gumming, usually based on alkylated phenols; (2) antistatic agents to dissipate static electricity and prevent sparking; (3) corrosion inhibitors used for civilian and military fuels; (4) a fuel system icing inhibitor is often mixed at the point-of-sale so that users with heated fuel lines do not have to pay the extra expense; and (5) biocides to remediate microbial (i.e., bacterial and fungal) growth present in aircraft fuel systems.

3.2.6. Fuel Oil

Fuel oil (Table 3.3) is classified in several ways but generally may be divided into two main types: distillate fuel oil and residual fuel oil. Distillate fuel oil is vaporized and condensed during a distillation process and thus has a definite boiling range and does not contain high-boiling constituents. A fuel oil that contains any amount of the residue from crude distillation of thermal cracking is a residual fuel oil. The terms distillate fuel oil and residual fuel oil are losing their significance, since fuel oil is now made for specific uses and may be either distillates or residuals or mixtures of the two. The terms domestic fuel oil, diesel fuel oil, and heavy fuel oil are more indicative of the uses of fuel oils.

Domestic fuel oil is fuel oil that is used primarily in the home. This category of fuel oil includes kerosene, stove oil, and furnace fuel oil; they are distillate fuel oils.

Diesel fuel oil is also a distillate fuel oil that distils between 180 and 380 °C (356−716 °F).

Several grades are available depending on uses: diesel oil for diesel compression ignition (cars, trucks, and marine engines) and light heating oil for industrial and commercial uses.

Heavy fuel oil comprises all residual fuel oils (including those obtained by blending). Heavy fuel oil constituents range from distillable constituents to residual (non-distillable) constituents that must be heated to 260 °C (500 °F) or more before they can be used. The flash point is always above 50 °C (122 °F), and the density is always higher than 0.900. In general, heavy fuel oil usually contains cracked residual, reduced crude, or cracking coil heavy product, which is mixed (cut back) to a specified viscosity with cracked gas oils and fractionator bottoms. For some industrial purposes in which flames or flue gases contact the product (ceramics, glass, heat treating, and open hearth furnaces), fuel oils must be blended to contain minimum sulfur contents, and hence low-sulfur residues are preferable for these fuels.

No. 1 fuel oil is a petroleum distillate that is one of the most widely used of the fuel oil types. It is used in atomizing burners that spray fuel into a combustion chamber where the tiny droplets bum while in suspension. It is also used as a carrier for pesticides, as a weed killer, as a mold release agent in the ceramic and pottery industry, and in the cleaning industry. It is found in asphalt coatings, enamels, paints, thinners, and varnishes. No. 1 fuel oil is a light petroleum distillate (straight-run kerosene) consisting primarily of hydrocarbons in the range C_9−C_{16}. Fuel oil No. l is very similar in composition to diesel fuel; the primary difference is in the additives.

No. 2 fuel oil is a petroleum distillate that may be referred to as domestic or industrial. The domestic fuel oil is usually lower boiling and a straight-run product. It is used primarily for home heating. Industrial distillate is a cracked product or a blend of both. It is used in smelting furnaces, ceramic kilns, and packaged boilers. No. 2 fuel oil is characterized by hydrocarbon chain lengths in the C_{11}−C_{20} range. The composition consists of aliphatic hydrocarbons (straight chain alkanes and cycloalkanes) (64%), unsaturated hydrocarbons (alkenes) (1−2%), and aromatic hydrocarbons (including alkyl benzenes and 2-ring, 3-ring aromatics) (35%) but contains only low amounts of the polycyclic aromatic hydrocarbons (<5%) [2].

No. 6 fuel oil (also called Bunker C oil or residual fuel oil) is the residuum from crude oil after naphtha-gasoline, No. 1 fuel oil, and No. 2 fuel oil have been removed. No. 6 fuel oil can be blended directly to heavy fuel oil or made into asphalt. Residual fuel oil is more complex in composition and impurities than distillate fuels. Limited data are available on the composition of No. 6 fuel oil. Polycyclic aromatic hydrocarbons (including the alkylated derivatives) and metal-containing constituents are components of No. 6 fuel oil.

Stove oil, like kerosene, is always a straight-run fraction from suitable crude oils, whereas other fuel oils are usually blends of two or more fractions, one of which is usually cracked gas oil. The straight-run fractions available for blending into fuel oils are heavy naphtha, light and heavy gas oils, reduced crude, and pitch. Cracked fractions, such as light and heavy gas oils from catalytic cracking, cracking coil tar, and fractionator bottoms from catalytic cracking, may also be used as blends to meet the specifications of the different fuel oils.

Since the boiling ranges, sulfur contents, and other properties of even the same fraction vary from crude oil to crude oil and with the way the crude oil is processed, it is difficult to specify which fractions are blended to produce specific fuel oils. In general, however, furnace fuel oil is a blend of straight-run gas oil and cracked gas oil to produce a product boiling in the 175−345 °C (347−653 °F) range.

The manufacture of fuel oils at one time largely involved using what was left after removing desired products from crude petroleum. Now fuel oil manufacture is a complex

matter of selecting and blending various petroleum fractions to meet definite specifications, and the production of a homogeneous, stable fuel oil requires experience backed by laboratory control.

3.3. OXYGENATED FUELS

Although fossil fuels have been the dominant energy resource throughout the twentieth century, oxygenated fuels such as alcohols ($C_nH_{2n+1}OH$) have seen considerable historical use. For example, methanol and ethanol can be synthesized biologically, and they have characteristics which allow them to be used in current engines.

When obtained from biological sources, alcohols are known as bioalcohols (e.g., bioethanol). There is no chemical or physical difference between biologically produced alcohols and those obtained from other sources.

3.3.1. Methanol

Historically, methanol (wood alcohol) (Table 3.5) was first produced by destructive distillation (pyrolysis) of wood. Biomethanol may be produced by gasification of organic materials to synthesis gas followed by conventional methanol synthesis.

The destructive distillation of wood to produce wood alcohol has been the major source of methanol from the early 1800s, but this relatively inefficient method of methanol production was replaced in the late 1920s by processes based on the conversion of synthesis gas (mixtures of carbon monoxide and hydrogen) to methanol [3,8].

$$CO + 2H_2 \rightarrow CH_3OH$$

In the early 1970s, the process was modified by the development of low-pressure processes that replaced the more expenses high-pressure methods [8]. Currently, the majority of methanol production is based on low-pressure processes and uses feedstocks such as natural gas (especially in those countries with an abundance of low-cost natural gas) [3 and references cited therein, 8].

Synthesis gas (a mixture of CO and H_2) is first produced in a reformer in which a mixture of the hydrocarbon feedstock and steam is passed through a heated tubular reformer. The ratio of hydrogen and carbon in the syngas may need to be adjusted. The syngas is cooled and then compressed before being fed to the methanol converter. The methanol synthesis takes place in the presence of copper-based catalysts at 250–260 °C (482–500 °F). The crude methanol is recovered and purified by distillation [2,3,8,9].

Methanol, like ethanol, burns at lower temperatures than gasoline. Using methanol as a fuel in spark ignition engines can offer an increased thermal efficiency and increased power output (as compared to gasoline) due to its high octane rating (114) and high heat of vaporization.

Methanol, just like ethanol, contains soluble and insoluble contaminants. These soluble contaminants, halide ions such as chloride ions, have a large effect on the corrosivity of alcohol fuels. Halide ions increase corrosion in two ways: they chemically attack passivating oxide films on several metals causing pitting corrosion, and they increase the conductivity of the fuel. Increased electrical conductivity promotes electric, galvanic, and ordinary corrosion in the fuel system. Soluble contaminants, such as aluminum hydroxide, itself a product of corrosion by halide ions, clog the fuel system over time [10].

Methanol is hygroscopic and absorbs water vapor directly from the atmosphere, which may cause phase separation of methanol–gasoline blends. Since methanol vapor is heavier than air, it will linger close to the ground, and if the concentration of methanol is above 6.7% in air, it can be lit by a spark and will explode above 12 °C (54 °F) [11,12].

TABLE 3.5 General Properties of Oxygenated Fuels

	Chemical formula	Mol. wt.	Composition (wt%)			Specific gravity	Boiling point (°C)	Autoignition temperature (°C)	Flash point (°C)	Heating values (kJ/kg)		Flammability limits (vol%)
			C	H	O					LHV	HHV	
Methanol	CH_3OH	32.04	37.5	12.6	49.9	0.796	65	464	11	20,100	22,900	7.3–36.0
Ethanol	C_2H_5OH	46.07	52.2	13.1	34.7	0.794	78	423	13	27,000	29,800	4.3–19.0
Dimethyl ether	$(CH_3)_2O$	46.07	52.2	13.1	34.7	0.610	−24	350		28,900	31,700	
Biodiesel	C12–C22	292	77	12	11	0.880	315–350		100–170	37,500	40,200	

3.3.2. Ethanol

Ethanol (C_2H_5OH; ethyl alcohol, alcohol, grain-spirit, grain alcohol, drinking alcohol) is a volatile, flammable, and colorless liquid (Table 3.5). It is a psychoactive drug, best known as the type of alcohol found in alcoholic beverages and in thermometers. In common usage, it is often referred to simply as alcohol.

Ethanol can be used as a transport fuel, mainly as a biofuel additive for gasoline, and is widely used in United States and Brazil. Modern automobiles in the United States use blends of up to 10% ethanol, and the use of this fuel blend is actually mandated in many states and cities. In Brazil, the government has mandated that a blend of 25% ethanol and 75% gasoline (E25 blend) will be used as a vehicle fuel [3,13].

Ethanol fuel is a gasoline alternative that is manufactured from the conversion of carbon-based feed stocks such as sugar cane, sugar beets, switch grass, corn, and barley. In the dry milling process (production of bioethanol), the corn kernel or other starchy grain is ground into flour (*meal*) and processed without separating out the various component parts of the grain. The meal is mixed with water to form a slurry (*mash*) to which enzymes are added to convert the starch to dextrose; ammonia is added for pH control and as a nutrient to the yeast [3,14].

The mash is heated to reduce bacteria levels ahead of fermentation after which the mash is cooled and transferred to fermenters, where yeast is added to convert sugar(s) to ethanol and carbon dioxide. During process, the mash is agitated and cooled to facilitate the activity of the yeast. After fermentation, the product is transferred to distillation columns, where the ethanol is separated from the remaining stillage. The ethanol is concentrated using conventional distillation and then dehydrated using a molecular sieve system [14].

In the wet milling process [15,16], the grain is soaked in water (steeped) and dilute sulfurous acid for 24–48 h, which facilitates separation of the grain into its component parts. The slurry is then processed through a series of grinders to separate the corn germ after which corn oil is extracted from the germ either (1) on-site or (2) sold to crushers who extract the corn oil. The remaining fiber, gluten, and starch components are further segregated using centrifuges, screens, and hydrocyclone separators [15,16].

The steeping liquor is concentrated in an evaporator. This concentrated product, heavy steep water, is co-dried with the fiber component and is then sold as corn gluten feed to the livestock industry. The gluten component (protein) is filtered and dried to produce the corn gluten meal co-product. The starch and any remaining water from the mash can then be processed in one of three ways: fermented into ethanol, dried and sold as dried or modified corn starch, or processed into corn syrup [15,16].

3.3.3. Dimethyl Ether

Dimethyl ether (CH_3OCH_3) is an organic compound and is the simplest ether (Table 3.5). It is a colorless gas that is a useful precursor to other organic compounds and an aerosol propellant as well as a clean-burning liquid fuel.

Dimethyl ether is primarily produced by converting natural gas (and to a lesser extent by the gasification of coal) to synthesis gas (which can also be produced from biomass) that is then converted into methanol in the presence of catalyst (usually copper-based) [3], with subsequent methanol dehydration in the presence of a different catalyst (e.g., silica-alumina) resulting in the production of dimethyl ether (methanol dehydration):

$$2CH_4 + O_2 \rightarrow 2CO + 4H_2$$

$$CO + 2H_2 \rightarrow CH_3OH$$

$$2CH_3OH \rightarrow CH_3OCH_3 + H_2O$$

Alternatively, dimethyl ether can be produced through direct synthesis, using a dual catalyst system that permits both methanol synthesis

and dehydration in the same process unit with no methanol isolation and purification. Both the one-step and two-step processes are commercially available. Currently, there is more widespread application of the two-step process, since it is relatively simple and start-up costs are relatively low [3].

Biodiesel is made through a chemical process (transesterification) — the process leaves behind two products: (1) alkyl esters (the chemical name for biodiesel) and (2) glycerin (used in soaps and other products) [3]:

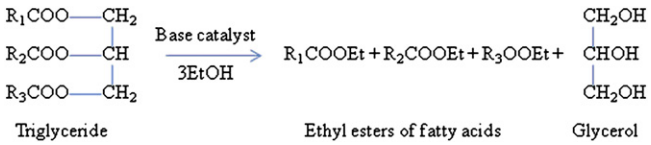

Dimethyl ether is a promising fuel in gasoline engines, diesel engines. Some engine modifications are necessary to convert a diesel engine to burn dimethyl ether. During combustion of dimethyl ether, there are very low emissions of particulate matter, carbon monoxide, and nitrogen oxides, and there are no sulfur emissions.

3.3.4. Biodiesel

Biodiesel (Table 3.5) is a fuel produced from biological source [17] and is the generic name for fuels obtained by esterification of vegetable oil. The esterification can be done either by methanol or by ethanol. Biodiesel can be used in a diesel engine without modification and is a clean burning alternative fuel produced from domestic, renewable resources [3]. The fuel is a mixture of fatty acid alkyl esters made from vegetable oils, animal fats, or recycled greases [3].

Biodiesel is produced through a process in which organically derived oils are combined with alcohol (ethanol or methanol) in the presence of a catalyst to form ethyl or methyl ester. Biodiesel can be made from any vegetable oil, animal fats, waste vegetable oils, or microalgae oils. Soybeans and Canola (rapeseed) oils are the most common vegetable oils used for biodiesel production [3].

The oil is extracted by the use of a press and then mixed in specific proportions with other agents that cause a chemical reaction. The results of this reaction are two products, biodiesel and soap. After a final filtration, the biodiesel is ready for use. After curing, the glycerin soap that is produced as a by-product can be used as is or can have scented oils added before use.

The transesterification reaction is affected by alcohol type, molar ratio of glycerides to alcohol, type and amount of catalyst, reaction temperature, reaction time, and free fatty acids and water content of vegetable oils or animal fats [3]. Generally, the reaction temperature is held near the boiling point of the alcohol, and the reactions take place at low temperatures (approximately 65 °C) and at modest pressures (0.2 MPa). Biodiesel is further purified by washing and evaporation to remove any remaining methanol.

Transesterification reactions can be catalyzed by *alkalis* or *enzymes*. Usually, industrial processes use sodium or potassium hydroxide or sodium or potassium methoxide as catalyst [3]. Enzyme-catalyzed procedures, using lipase as catalyst, do not produce side reactions, but the lipases are very expensive for industrial scale production and a three-step process was required to achieve a 95% conversion. The acid-catalyzed process is useful when a high amount of free acids are present in the vegetable oil, but the reaction time is very long (48—96 h), even at the boiling point of the alcohol, and

a high molar ratio of alcohol was needed (20:1 wt/wt to the oil).

Biodiesel is a liquid which varies in color between golden and dark brown depending on the feedstock from which it is produced. It is practically immiscible with water and has a high-boiling point and low vapor pressure (ASTM D6751). Typical methyl ester biodiesel has a flash point of approximately 150 °C (302 °F), making it rather non-flammable. Biodiesel has a density of approximately 0.88 g/cm^3 less than that of water. Biodiesel uncontaminated with starting material can be regarded as non-toxic.

Biodiesel has a viscosity similar to diesel produced from petroleum (petrodiesel). It can be used as an additive in formulations of diesel to increase the lubricity of pure ultra-low sulfur diesel (ULSD) fuel, which is advantageous because it has virtually no sulfur content [3]. Much of the countries that use biodiesel use the B factor to state the amount of biodiesel in any fuel mix. For example, fuel containing 20% biodiesel is labeled B20 and pure biodiesel is B100. Blends of 20% biodiesel with 80% petroleum diesel (B20) can generally be used in unmodified diesel engines, but when used in the pure form (B100), biodiesel (B100) may require engine modifications to optimal performance. Biodiesel has about 5−8% less energy density than petrodiesel but better lubricity and more complete combustion than petrodiesel [18].

Pure, non-blended biodiesel can be poured straight into the tank of any diesel vehicle. As with normal diesel, low-temperature biodiesel is sold during winter months to prevent viscosity problems. Some older diesel engines still have natural rubber parts which will be affected by biodiesel.

The extra lubrication provided by biodiesel fuel helps improve the longevity of your engine, as well as boosting engine performance, and also helps eliminate engine knocks and noise. In addition, biodiesel fuel can be stored in any type of tank and has a much higher flash point (approximately 300 °C) compared to petrodiesel approximately (150 °C).

Biodiesel production is a very modern and technological area for researchers due to the relevance that it is winning everyday because of the increase in the petroleum price and the environmental advantages [19]. The successful introduction and commercialization of biodiesel in many countries around the world has been accompanied by the development of standards to ensure high product quality and user confidence [20]. In general, biodiesel compares well to petroleum-based diesel [21,22].

References

[1] Guthrie VB. Petroleum products handbook. 1st ed. New York, NY: McGraw-Hill; 1960.

[2] Speight JG. The chemistry and technology of petroleum. 4th ed. Boca Raton, FL: CRC Press/Taylor & Francis Group; 2007.

[3] Speight JG. Synthetic fuels handbook: properties, processes, and performance. New York, NY: McGraw-Hill; 2008.

[4] Mokhatab S, Poe WA, Speight JG. Handbook of natural gas transmission and processing. Amsterdam, Netherlands: Elsevier; 2006.

[5] Speight JG. Handbook of petroleum product analysis. Hoboken, NJ: John Wiley & Sons Inc.; 2002.

[6] Mills GA, Ecklund EE. Alcohols as components of transportation fuels. Annu Rev Energy 1987;12: 47−80.

[7] Speight JG. Chemical process and design handbook. New York, NY: McGraw-Hill; 2002.

[8] Cheng WH, Kung HH. Methanol production and use. New York, NY: Marcel Dekker Inc.; 1994.

[9] Speight JG. The chemistry and technology of coal. 2nd ed. New York, NY: Marcel Dekker Inc.; 1994.

[10] Brinkman N, Halsall R, Jorgensen SW, Kirwan JE. The development of improved fuel specifications for methanol (M85) and ethanol (Ed85). SAE Technical Paper 940764; 1994.

[11] Speight JG. Lange's handbook of chemistry. 16th ed. New York, NY: McGraw-Hill; 2005.

[12] Lied DR. Handbook of chemistry and physics. 84th ed. Boca Raton, FL: CRC Press; 2003.

[13] Ethanol fact book. Clean Fuels Development Coalition 2007, Bethesda, MD, USA.

[14] Dale RT, Tyner WE. Economic and technical analysis of ethanol dry milling: Model description. Purdue

University; 2006. Staff Paper # 06-04, Available from: http://www.ecn.purdue.edu/~lorre/16/Midwest%20Consortium/DM%20DescManual%2042006-1.pdf; 2010 [accessed 16.07.10].
[15] Corn Refiners Association Inc. The corn refining process (2002), Available from: http://www.corn.org/theprocess.htm; 2010 [accessed 16.07.10].
[16] Corn Products International Inc., The corn wet milling process (2007), Available from: http://www.cornproducts.com/overview/contactus/index.php; 2010 [accessed 16.07.10].
[17] Lee S, Speight JG, Loyola SK. Handbook of alternative fuel technologies. Boca Raton, FL: CRC-Taylor & Francis Group; 2007.
[18] Kinas JA. Production of biodiesels from multiple feedstock's and properties of biodiesels and biodiesel/diesel blends, U.S. DOE Report NREL/SR-510−31460; 2003.
[19] Machete JM, Miguel VU, Erase AF. Possible methods for biodiesel production. Renewable Sustain Energy Rev 2007;11(6):1300−11.
[20] Knothe G. Dependence of biodiesel fuel properties on the structure of fatty acid alkyl esters. Fuel Proc Tech 2005;86(10):1059−70.
[21] Loreto E, Goodwin Jr JG, Bruce DA, Suwannakarn K, Liu Y, Lopez DE. The catalysis of biodiesel synthesis. In: Spivey JJ, Dooley KM, editors. Catalysis. Cambridge, UK: The Royal Society of Chemistry; 2006. p. 41−83.
[22] Pinto AC, Guarieiro LLN, Rezende MJC, Ribeiro NM, Torres EA, Lopes WA, et al. Biodiesel: an overview. J Braz Chem Soc 2005;16(6B):1313−30.

CHAPTER

4

Steam Reforming for Fuel Cells

J.R. Rostrup-Nielsen, J. Bøgild Hansen

Haldor Topsøe A/S, Lyngby, Denmark

OUTLINE

Fuel Cells **DOI: 10.1016/B978-0-444-53563-4.10004-5**

4.1. ROUTES TO HYDROGEN

Steam reforming of hydrocarbons is a well-established process for the petrochemical industry and for refineries [1–3]. Traditionally, a major part of the hydrogen consumption in refineries was produced as a by-product from other refinery processes, mainly catalytic reforming ("platforming"). However, there is a fastgrowing need for increased hydrogen production capacity in refineries due to the need for deep desulfurization of fuels and for hydrocracking of heavy oil fractions [4]. This need is being met mainly by installation of steam reforming-based hydrogen plants. The conversion of oil sands in Canada has also resulted in large hydrogen plants based on steam reforming of natural gas [5].

The total hydrogen consumption can be estimated to about 250×10^9 Nm^3/year with refinery industry accounting for the majority (>90%). About the same amount is used as mixtures of hydrogen and nitrogen for the ammonia synthesis and mixtures of hydrogen and carbon oxides (synthesis gas) for synthesis of methanol. With this and other uses in the chemical industry, the total hydrogen consumption amounted to about 50 MMt/year (630×10^9 Nm^3/year) in 2002 [4,6].

Hydrogen may play a future role in the energy sector, for example, for fuel cells [6–8]. Plants supplying hydrogen for the buildup of a future hydrogen infrastructure are faced with a dilemma when based on fossil fuels [6]. Centralized large-scale hydrogen production is penalized by significant costs for compression and transportation. Therefore, decentralized production at gas stations appears the optimum solution, but CO_2 sequestration appears feasible only with large-scale production. Without CO_2 sequestration, it may be better to use natural gas directly in the car.

Hydrogen (and synthesis gas) can be produced from almost any carbon source ranging from natural gas and oil products to coal and biomass [9]. Today, natural gas and other hydrocarbons are the dominant feedstocks for the production of hydrogen, because the investments are about one-third of that for a coal-based plant. Steam reforming of natural gas is the preferred route.

4.2. STEAM REFORMING OF NATURAL GAS

4.2.1. Thermodynamics

The steam reforming reactions are listed in Table 4.1, which also shows values for heats of reactions and equilibrium constants.

The reaction between steam and methane is strongly endothermic and is driven by the positive entropy resulting from the formation of more molecules. Thermodynamically, methane conversion is favored by high temperature, low pressure, and high steam to methane ratio. Typical conversion plots are shown in Fig. 4.1.

Using actual conversions as a measure of the extent of this reaction is not convenient, since the conversion must be compared to equilibrium. Instead, the so-called temperature approach [1] to equilibrium is used, which is defined by

$$\begin{aligned} \Delta T_{\text{app,ref}} &= T_{\text{exit}} - T_{\text{eq}} \\ \Delta T_{\text{app,shf}} &= T_{\text{eq}} - T_{\text{exit}} \end{aligned} \tag{4.1}$$

T_{eq} is the temperature on the equilibrium curve having the same conversion as the actual outlet gas, T_{exit}. By this definition, the temperature approach will always be positive, provided the reaction path is below the equilibrium curves.

The steam reforming of higher hydrocarbons can be considered irreversible at the industrial reforming conditions [1].

4.2.2. Tubular Reformer

Industrial steam reforming is carried out in a fired reactor, the tubular reformer [1,10], in

TABLE 4.1 Reforming Reactions

		$\ln K_p = a + b/T$[$]	
Steam reforming	$-\Delta H^o_{298}$; **kJ mol^{-1}**	**a**	**b**
1. $CH_4 + H_2O = CO + 3H_2$	−206	30.446	−27106
2. $CO + H_2O = CO_2 + H_2$	41	−3.798	4160
3. $CH_4 + CO_2 = 2CO + 2H_2$	−247	34.244	−31266
4. $C_nH_m + nH_2O = nCO + (n + \frac{m}{2})H_2$			
Ethane	−347	60.42	−45256
n-heptane	−1107	21.053	−141717
5. $CH_4 = C + 2H_2$	−75	12.69[%]	−10779[%]
6. $2CO = C + CO_2$	172	−21.09	20486
7. $CO + H_2 = C + H_2O$	131	−17.29	16326

[$] *Standard state: 25 °C, 0.1 MPa, linear regression 500–900 °C.*
[%] *Whisker carbon.*

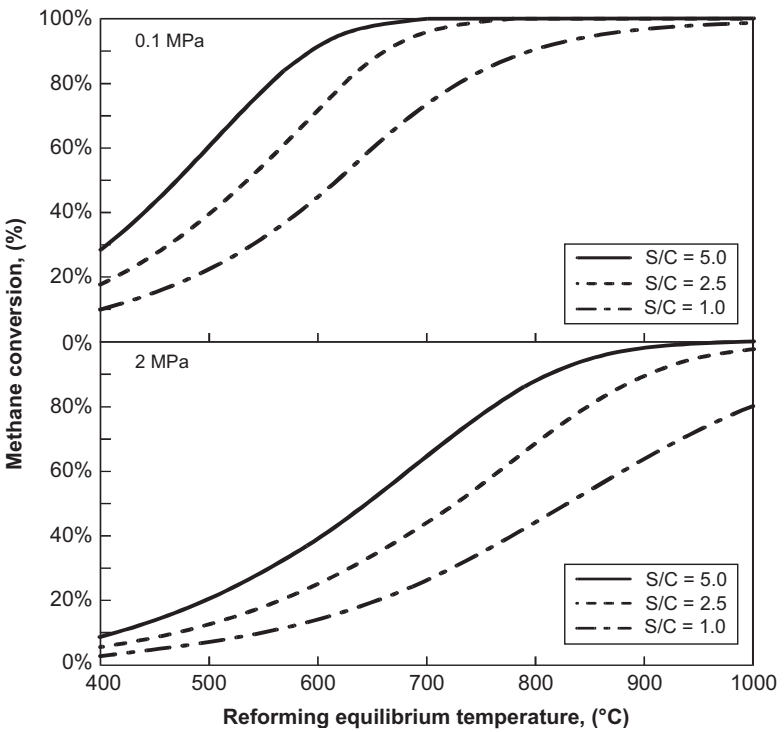

FIGURE 4.1 Steam reforming and methane conversion; *Reprinted from Rostrup-Nielsen et al. [11], Copyright (2002), with permission from Elsevier.*

which catalyst tubes are placed in a fired furnace supplying the required for the desired conversion. The catalyst tubes have a typical diameter of 10 cm and a length of about 10 m. They are made of high alloy steel to withstand the high tube wall temperatures (typically close to 1000 °C) and the high thermal stresses caused by the high heat fluxes amounting to average fluxes of 0.1 MW/m^2. The industrial breakthrough for the process 50 years ago was a result of design for operation at high pressure (2–4 MPa), thereby reducing the energy consumption for compression of the large volume of the syngas product. Today, hydrogen plants are built for hydrogen production of about 200,000 Nm^3/h with 400–500 reformer tubes. A hydrogen plant reformer is shown in Fig. 4.2.

The product gas leaves the reformer tubes close to thermodynamic equilibrium. This makes it easy to predict the operation and to calculate the need for heat supply from a simple enthalpy balance [1,10].

FIGURE 4.2 Tubular reformer in hydrogen plant.

4.2.3. Nickel-Based Catalysts

Steam reforming catalysts are typically based on nickel. With these catalysts, the gas composition in the reformer tube quickly approaches equilibrium [1,11,12], so that the driving force for the reforming reaction is the slope of the temperature profile as the methane content at equilibrium decreases with increasing temperature. In commercial reactors, there is a large surplus of catalyst activity in a tubular reformer, because the tube dimensions and the number of tubes are determined by the maximum allowable heat flux and other mechanical considerations, leaving the catalyst volume as a dependent variable [1,8]. Still, there is a need for high catalyst activity because high activity means that the heat transfer for a given conversion can take place at a lower tube wall temperature [10].

The catalyst must ensure equal distribution of flow between the tubes in a tubular reformer and across the catalyst bed in an adiabatic reformer. Maldistribution may cause local overheating or channeling and hence shorter life of the reformer tubes. The catalyst should be mechanically stable under all process conditions as well as conditions during start-up and shutdown of the reformer. In particular, resistance to conditions during upsets may become critical. Breakdown of catalyst pellets may cause partial or total blockage of some tubes resulting in severe temperature gradients within or between tubes [1,10]. The formation of carbon may result in the same problems.

4.2.3.1. Support

The support must show high mechanical stability because of exposure to high temperatures well above 800 °C and steam partial pressures close to 3 MPa [1,12], involving steam

partial pressures and temperatures without losing strength. Furthermore, it should not contain volatile components. High area supports such as γ-alumina, chromia, etc., can be used for catalysts for low-temperature adiabatic reforming, but these supports suffer from substantial sintering and weakening at temperatures above 500 °C. The deterioration is strongly accelerated by the high steam partial pressure and stability tests at atmospheric pressure can therefore be misleading. Because silica is volatile ($Si(OH)_4$) at high temperatures in high pressure steam, it is now excluded from catalysts for steam reforming [1,12], unless it is combined with alkali. Silica would be slowly removed from the catalyst (or brickwork) and deposited in boilers, heat exchangers, and catalytic reactors downstream of the reformer.

4.2.3.2. *Promoters/Alloys*

Alkali metals are used as promoters to eliminate carbon formation, but are slowly volatilized from the catalyst. The alkali loss is enhanced by high temperature, but may to some extent be controlled by the addition of acidic components (silica). The volatilized alkali may deposit in colder parts of the plant where the resulting hydroxyl ions will strongly promote stress corrosion in stainless steel. Moreover, alkali may react with some catalyst support materials such as alumina forming the weak β-alumina, resulting in a decrease of the mechanical strength. While resistant to high temperature, catalysts based on magnesia are sensitive to steaming at low temperatures because of the risk of hydration. The reaction may result in breakdown of the catalyst because it involves an expansion of the molecular volume.

Alloying nickel with groups 1B metals (Cu, Ag) may cause a drastic decrease of the activity [18] although small amounts (1 wt%) of copper may cause the activity to increase.

At steaming conditions at high temperature, formation of the nickel aluminum spinel may start at temperatures above about 700 °C [1,10], but a less well-defined interaction between nickel oxide and η- or γ-alumina is apparent already at lower temperatures. It is possible to form a "surface spinel" below 600 °C, which may hardly be identified by X-ray methods alone. A similar trend is observed for the reaction between nickel and magnesium oxide [1,10].

4.2.3.3. *Catalyst Particles*

The shape of the catalyst pellet should be optimized to achieve maximum activity with minimum pressure drop. The pressure drop depends strongly on the void fraction of the packed bed and decreases with increasing particle size. Similarly, the effective catalyst activity per volume is roughly proportional to the surface to volume ratio of the catalyst pellet due to the low catalyst effectiveness factor at conditions of practical interest (typically below 0.1 for a tubular reformer) [1,10].

In order to fulfill the above-mentioned requirements to the catalyst, the particles are usually made of ceramic material of cylindrical shape with one or more internal holes. Solutions based on the use of ceramic foam as catalyst support have also been considered [13] together with other shapes such as monoliths and even catalyzed hardware [14,15]. The use of such catalyst formulations are often developed together with new reactor concepts taking advantage of the surplus catalyst activity in conventional steam reformers.

4.2.3.4. *Activation*

The catalyst in industrial plants can be activated by various reducing agents such as hydrogen, ammonia, methanol, and hydrocarbons added to steam [1]. The reaction with hydrogen is nearly thermoneutral and accordingly, the equilibrium constant, $K_p = p_{H_2O}/p_{H_2}$ varies little with temperature. Metallic nickel will be stable with approximately 0.3 and 0.6 vol% hydrogen in steam at 400 °C and 800 °C,

respectively. In practice, K_p may be lower, as the free energy of nickel oxide decreases due to interaction with the support material. The reduction of pure nickel oxide by hydrogen starts at temperatures 200–250 °C depending on the calcination temperature. Supported catalysts require higher temperatures to show a reasonable reduction rate. This may be ascribed to interaction with the support. When the formation of nickel aluminum spinel has taken place, temperatures above 800 °C [10] may be required for complete reduction.

4.2.3.5. Nickel Dispersion

The activity of a nickel catalyst is related to the nickel surface area. It is important to refer reaction rates to unit surface area in terms of the specific activity or turnover frequency (TOF) in order to compare catalysts and to analyze catalytic phenomena. Sintering of the nickel crystals results in no significant change in TOF. However, for small nickel particles ($d_{Ni} < 10$ nm), there is a significant increase of TOF with increased dispersion [19].

The most widely used method for measurements of the nickel surface area is chemisorption (of hydrogen [16] or hydrogen sulfide [10]). The average nickel particle size (d_{Ni}; in nm) and the nickel dispersion (Disp; in %) can be estimated from the nickel surface area:

$d_{Ni} = 6.8 \times$ (Ni content (wt%))/(Ni area (m^2/g))

$Disp = 101/d_{Ni}$

The TOF (molecules/site/s) may be calculated from:

TOF = 10.9 × (rate (mol/g/h))/(Ni area (m^2/g))

The nickel surface area is generally increased with higher nickel contents in the catalyst [10], but the dispersion or utilization of the nickel tends to decrease with increasing nickel content. Accordingly, many commercial catalysts are optimized at nickel contents around 15 wt%. Through special preparation methods, it is possible to obtain high dispersions even at high nickel contents, but because of sintering effects at high nickel loadings practice often shows an optimum in nickel area depending on the nickel content.

4.2.3.6. Sintering

Most tubular reformers operate above the Tammann temperature of nickel ($T_{Tammann} = {}^1/_2\ T_{melt} = 581$°C), at which nickel is prone to sintering, which is the growth of the nickel particles and a decrease of nickel surface area and of activity. However, the sintering phenomenon is more complex and may take place below the Tammann temperature [17] as well.

Sintering is influenced by many parameters, including temperature, chemical environment, catalyst composition and structure, and support morphology. The most important parameters are the temperature and the atmosphere in contact with the catalyst. The presence of water greatly accelerates sintering.

One mechanism considers particle migration and coalescence, where particles move over the support and collide, forming larger crystals with a loss of overall metal surface area. This mechanism dominates at low temperatures. At high temperatures, particle coarsening proceeds via transport of metal atoms or small agglomerates over the carrier and between metal particles (atom migration and Ostwald ripening). The time dependencies of crystal growth are $t^{1/7}$ and $t^{1/3}$ for particle migration and coalescence and atom migration, respectively. The transition temperature between particle migration and Ostwald ripening depends on process conditions (H_2O/H_2, etc.) and the catalyst composition [1,17].

4.2.4. Non-Nickel Catalysts

The group VIII metals are active for the steam reforming reaction [20,21]. The TOF is typically 2–5 s^{-1} at 500 °C for steam reforming of methane on nickel ($H_2O/CH_4 = 4$. $H_2O/H_2 = 10$, 0.1 MPa [10]). Most of the group VIII noble

metals have higher Tammann temperatures than nickel and should be more resistant to sintering. All group VIII metals show a significant decrease in TOF when the catalyst contains alkali [1,22]. It means that even traces of alkali metal may blur TOF measurements if not recognized. The deactivation depends strongly on the type of support, the effect being less on acidic supports that bind alkali more strongly. This all hints that alkali works on nickel via the gas phase. All group VIII metal catalysts are sensitive to sulfur poisoning (refer Section 4.2.7).

Cobalt shows a lower activity than nickel [10] – probably attributable to the process conditions, with the H_2O/H_2 value being close to levels that cause oxidation of the metal. Iron is active for steam reforming, but only at strongly reducing conditions. Rhodium and ruthenium are the most active and nickel the most preferred because of its cost. Rhodium and ruthenium show TOF values about ten times higher than nickel, platinum, or palladium. Most studies [10,19,20] find a sequence of activity (TOF); Ru, Rh > Ni, Ir > Pt, Pd. This sequence has also been confirmed by DFT calculations [19].

4.2.5. Non-Metal Catalysts

Difficulties in desulfurizing heavy feedstocks have led to attempts to use non-metallic catalyst for steam reforming. However, these non-metal catalysts have far less activity.

4.2.5.1. Ceria

Ceria has an activity almost two orders of magnitude less than that of nickel [23,24]. However, the low activity might be sufficient for the reforming process [25] in a high-temperature fuel cell operating at 800 °C, where the balance between the rate of reforming and the rate of the electrochemical reaction is critical [22]. With an activation energy of 105 kJ/mol, the ratio of rates at 800 °C and 500 °C is about 96.

4.2.5.2. Carbides

Molybdenum carbide and tungsten carbide are catalysts for steam and CO_2 reforming and catalytic partial oxidation (CPOX) [26,27]. However, in synthesis gas, the carbides are stable only at elevated pressures (approximately 0.9 MPa) and they are transformed into the oxides at ambient pressure. Molybdenum carbide will hardly be stable in a plug flow reactor [26], because the carbide will be oxidized at the inlet.

4.2.5.3. Non-Catalytic Reforming

Non-catalytic steam reforming requires high temperatures. Methane cracks above 1000 °C into radicals leading to the formation of ethylene, acetylene, and coke [28]. These radicals may react with steam radicals, but temperatures above 1500 °C are necessary for significant conversion [29]. One approach to improve rates is the use of plasma technology (see Chapter 8 for more details) [8], the key issue being the power consumption. As thermal plasma reforming is not sensitive to sulfur poisoning, it may represent a solution for steam reforming of logistic fuels (jet fuel and diesel) [30].

The thermal cracking of higher alkanes becomes significant above 650 °C [31,32] with the formation of alkenes, aromatics, and coke. This is applied in steam crackers in ethylene plants where steam is added as a diluent and for minimizing coke formation. There have been attempts to improve the steam cracking process by installing a catalyst (K/ZrO_2) in the cracking tubes [1,32]. This resulted in co-production of syngas and light alkenes from heavy gas oil and naphtha.

4.2.6. Mechanism and Kinetics

The mechanism of steam reforming of methane is well described by recent fundamental studies [19,33]. DFT calculations [34,35], adsorption studies [11,34], and observations by in situ high-resolution transmission electron

microscopy (HRTEM) [36] have shown that step sites play a key role in methane activation. This is illustrated by the energy diagram for the individual reaction steps [34] shown in Fig. 4.3 on the dense Ni(111) surface and the stepped Ni (211) surface.

Methane may be activated on any single surface atom [19,35], but stabilizes on high coordination sites at steps having a lower barrier for the further dissociation of methane. The activation of water does not depend strongly on the coordination number of the surface metal atom [35].

For both surfaces, the highest barrier is the surface reaction to carbon monoxide which may indicate a two-step mechanism involving both the CH_4 activation as well as the CO desorption [10,11,19]:

$$\begin{aligned} CH_4 + {}^* &\rightarrow CH_x{}^* + {}^1/_2(4-x)H_2 \\ CH_x{}^* + OH^* &\rightarrow CO + {}^1/_2(x+1)H_2 + 2^* \\ H_2O + {}^* &= OH^* + {}^1/_2H_2 \end{aligned} \qquad (4.2)$$

This was supported by an expanded analysis [19] by using the free energy (and not the total energy (enthalpy) as used in Fig. 4.3). It was shown for nickel that the barrier for formation decreases with temperature indicating that a one-step mechanism may dominate at high temperatures. This trend is reflected by kinetic studies.

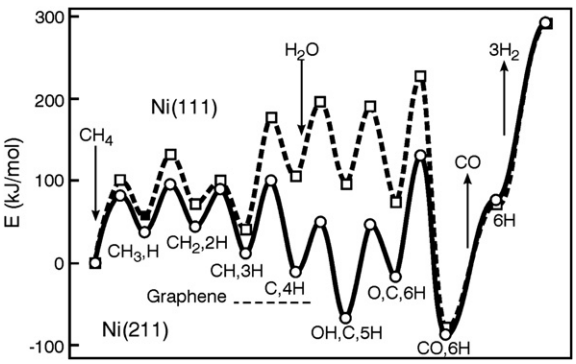

FIGURE 4.3 Energy diagram for steam reforming of methane. DFT calculations; *Reprinted from Bengaard et al. [34], Copyright (2002), with permission from Elsevier.*

In general, the kinetics of the steam reforming reaction is found to be first order with respect to methane partial pressure [1,11,37–39] with an activation energy in the range of 100–120 kJ/mol.

However, at lower temperatures (<550 °C), a denominator term may result in an overall zero dependency of total pressure [11]. One example [38] is a complex Langmuir–Hinshelwood expression, using a classical approach for the steam reforming reaction:

$$R_{\text{int},1} = \frac{k_{\text{int},1}}{p_{H_2}^{2.5} \cdot Z^2} \cdot \left(p_{CH_4} \cdot p_{H_2O} - \frac{p_{H_2}^3 \cdot p_{CO}}{K_{\text{eq},1}} \right) \qquad (4.3)$$

in which,

$$Z = 1 + K_{a,CO} \cdot p_{CO} + K_{a,H_2} \cdot p_{H_2} + K_{a,CH_4} \cdot p_{CH_4} + K_{a,H_2O} \cdot \frac{p_{H_2O}}{p_{H_2}}$$

It has been shown that the denominator term depends on the composition of the catalyst [10]. The presence of alkali results in a large adsorption term for steam [10]. Alkali also results in a significant decrease of the TOF, probably because alkali atoms block the step sites [11].

There is a general agreement that CO_2 reforming on nickel can be described by the same kinetics as steam reforming [36,39–43]. The change in mechanism with carbon dioxide instead of steam would have little practical impact on reforming, because steam will be present not far from the inlet, but also in the center of the catalyst particle as a consequence of the low effectiveness factors of catalysts in industrial reformers. CO_2 reforming results in lower atomic ratio of H/C, which means a higher risk of carbon formation (refer Section 4.2.8). CO_2 reforming is of less interest for the manufacture of hydrogen, but it may be applied when converting biogas (CO_2 and CH_4) for fuel cells.

4.2.7. Sulfur Poisoning

The group VIII metals are subject to sulfur poisoning with nickel being most sensitive [2]. The H_2S/Ni system is well described in terms of a two-dimensional sulfide [2]. The sulfur coverage can be estimated from the expression [10,44]:

$$\theta_s = 1.45 - 9.53 \cdot 10^{-5} \cdot T + 4.17 \cdot 10^{-5} \cdot T \ln\left(\frac{p_{H_2S}}{p_{H_2}}\right) \qquad (4.4)$$

As an example, a sulfur coverage of 0.5 at 500 °C corresponds to $H_2S/H_2 = 1.6 \times 10^{-12}$. In practice, this means that all sulfur is retained at this temperature. At 850 °C, a ratio $H_2S/H_2 = 1 \times 10^{-6}$ corresponds to a coverage of 0.7. The sulfur coverage is independent of the H_2O/H_2 ratio [10]. The chemisorption process is reversible, but normally the driving force for desorption is low [10]. This means that the catalyst life is dependent on the efficiency of the desulfurization of the feedstock.

Catalytic partial oxidation (CPOX) over noble metals is less sensitive to sulfur poisoning [45]. In the presence of oxygen, sulfur is oxidized to SO_2 which is not adsorbed on the catalyst. Nickel will be oxidized in the presence of oxygen, but rhodium, a typical catalyst for CPOX, will not. This means that rhodium stays active as long as oxygen is present. After depletion of oxygen, SO_2 will be reduced to H_2S, which will be chemisorbed on the catalyst as well as on downstream catalysts and anodes.

Removal of hydrogen sulfide and lower mercaptans is easily accomplished over zinc oxide, whereas more heavy sulfur components require hydrodesulfurization (HDS) over CoMo catalysts. The most difficult sulfur components are dibenzylthiophenes [46] as illustrated in Fig. 4.4.

It is evident that even after deep desulfurization, the dibenzylthiophene remains almost untouched. The amount of this component increases strongly with the final boiling point of the feedstock, which corresponds to a significant difference between difficulty of desulfurization of kerosene and various diesel fuels. Special CoMo catalysts and high hydrogen partial pressure are required to obtain desulfurization below 1 ppm sulfur [46].

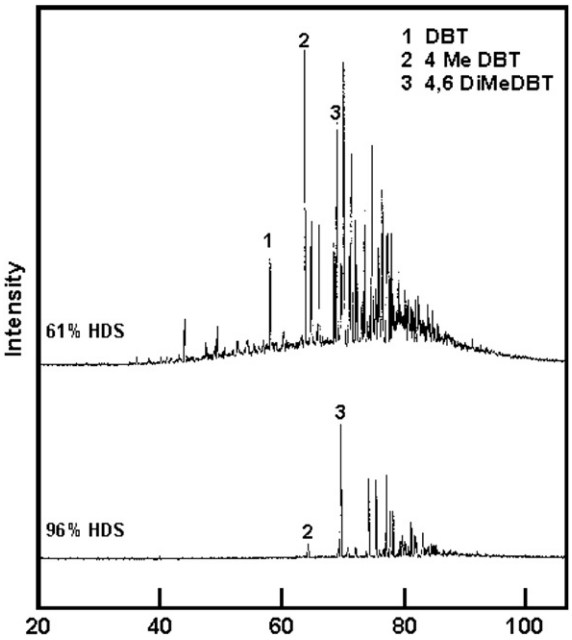

FIGURE 4.4 HDS of diesel. Gas chromatogram of desulfurized product; *Reprinted from Cooper and Knudsen [46], Copyright (2006), with permission from Springer.*

4.2.8. Carbon Formation

Carbon formation may take place by different routes [1,10]:

- whisker carbon
- gum formation
- pyrolytic coke

Whisker carbon is formed on nickel as fibers from carbon monoxide, methane, and higher hydrocarbons. They grow from a nickel crystal with a diameter close to that of the nickel crystal [1,36] as illustrated in Fig. 4.5.

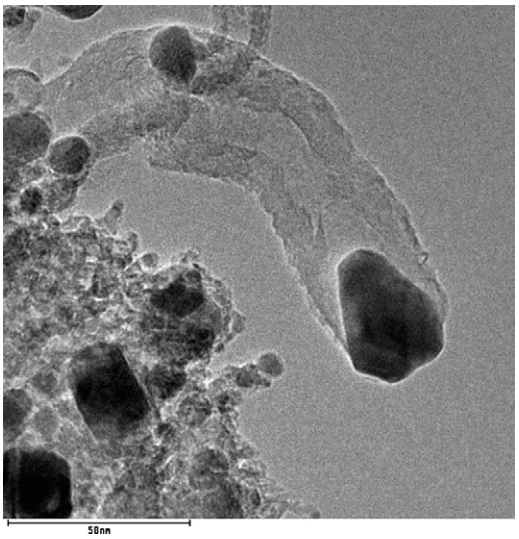

FIGURE 4.5 Whisker carbon on nickel catalyst.

The fibers are strong and may result in a breakdown of the catalyst pellet. This may have a serious impact on the operation of the tubular reactor as the carbon and the broken catalyst pellets may result in maldistribution of feed and overheating of the reformer tubes [1,10]. As shown in Fig. 4.3, adsorbed carbon atoms are most stable on the Ni(211) surface [39,47]. This was confirmed by HRTEM studies [36] showing that the nucleation of carbon takes place at step sites. The nickel particle size has an impact on the nucleation of carbon. The smaller the crystals, the more difficult is the initiation of carbon formation. The carbon formation depends on the kinetic balance between the surface reaction of the adsorbed hydrocarbon with oxygen species and the further dissociation of the hydrocarbon into adsorbed carbon atoms, which can nucleate into solid carbon. The rate of carbon formation is far less on noble metals than on nickel [42]. The whisker growth mechanism is also blocked by sulfur poisoning of the nickel surface [48].

For the reversible decomposition of carbon monoxide and methane, the potential for carbon can be assessed by the "principle of equilibrated gas" [1,10] as a simple guideline using simple thermodynamic calculations.

Principle of equilibrated gas: Carbon formation is to be expected on a nickel catalyst if the gas composition corresponds to one with a thermodynamic driving force for carbon after the establishment of the methane reforming and the shift equilibrium. This implies that the composition used to calculate the equilibrium corresponds to the composition after accounting for the reforming and shift equilibrium.

The thermodynamic properties used to calculate the driving force for carbon should be for the whisker carbon and not graphite. This implies smaller equilibrium constants for the two decomposition reactions (Reactions 5 and 6 in Table 4.1).

When using the decomposition of methane (Reaction 5 in Table 4.1) this means:

$$-\Delta G = RT \cdot \ln\left(Kp \cdot \left(p_{CH4}/p_{H_2}{}^2\right)_{eq}\right) \qquad (4.5)$$

in which Kp is the equilibrium constant for methane decomposition and $(p_{CH4}/p_{H_2}{}^2)$eq are the partial pressures after equilibration of the reforming and shift reactions.

Carbon is predicted for $-\Delta G > 0$. As the surface energy of the whisker carbon increases with smaller whisker diameter and because this is related to the diameter of the nickel crystal, the equilibrium constants for the carbon forming reactions depend on the nickel crystal size.

The carbon limit is often expressed as temperatures above which or below which there is a thermodynamic potential for carbon formation. The carbon limits are a function of the atomic ratios O/C, H/C, and inert/C, and of total pressure. The equilibrium calculations result in no simple upper or lower carbon limits. There may be upper and lower carbon limits for certain conditions [1]. In general, however, there is a tendency for higher carbon limits from steam reforming and lower carbon limits for CO_2 reforming.

One way of representing areas for potential for carbon formation is demonstrated in

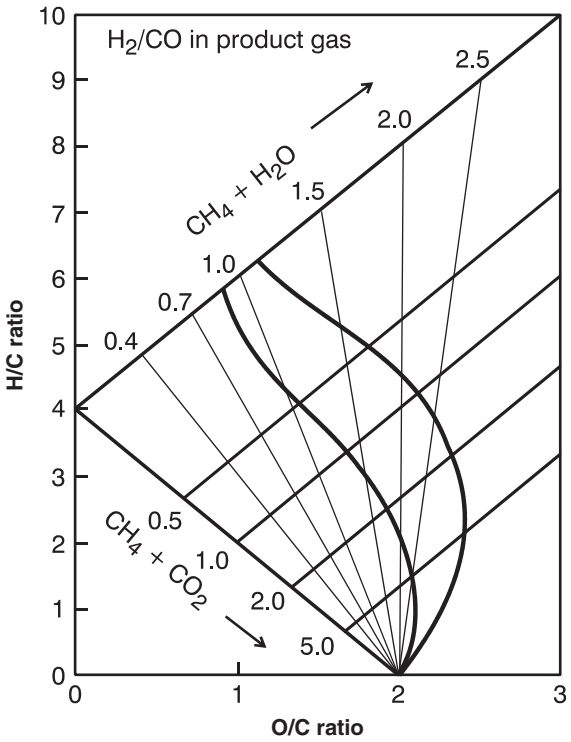

FIGURE 4.6 Carbon diagram (principle of equilibrated gas); carbon is formed for conditions to the left of the curve. Curves 1 and 2 represent graphite data and whisker carbon, respectively *(Adapted from [49])*.

Fig. 4.6 [1,49]. The diagram illustrates that CO_2 reforming is more critical than steam reforming. For steam to carbon ratios applied in hydrogen plants ($H_2O/CH_4 > 1.5$), there is no risk of carbon formation. The carbon limit curve can be moved to the left when using noble metal catalysts, because the noble metals show significantly smaller equilibrium constants for decomposition of methane and carbon monoxide.

The principle of equilibrated gas is not a "law of nature," but an empirical guideline. It is possible to exceed what may appear to be the thermodynamic limit. This can be done by sulfur-passivated catalyst as practiced in the SPARG process [49]. The principle of equilibrated gas predicts conditions where carbon formation is expected (except for noble metals and SPARG). It does not guarantee that carbon is not formed if the principle predicts no potential in the equilibrated gas. Methane may decompose to carbon instead of reacting with steam to form the required syngas even when there is no potential for carbon in the equilibrated gas. This is of course not possible in a closed system, but in an open system carbon may be stable at steady state and the accumulation of carbon may continue [1,10]. This is the situation for steam reforming of higher hydrocarbons.

4.3. STEAM REFORMING OF OTHER FEEDSTOCKS

4.3.1. Liquid Hydrocarbons

Higher hydrocarbons are converted successively by terminal C—C bond cleavage (on nickel) into adsorbed C_1 species [10,50,51]:

$$C_nH_m + {}^* = C_nH_{m-y}{}^* = C_{(n-1)}H_z{}^* + CH_x{}^* \quad (4.6)$$

$$C_{(n-1)}H_z{}^* = C_{(n-2)}H_z{}^* + CH_x{}^*$$

without desorption of the higher hydrocarbon species.

Except for aromatic molecules, higher hydrocarbons are more reactive (per carbon atom) than methane. Benzene has reactivity comparable to that of methane [10]. The kinetic order with respect to the hydrocarbon decreases with the size of the hydrocarbon, which means that liquid hydrocarbons in principle can be easily converted by steam reforming. However, in practice, this is limited by the higher risk of sulfur poisoning and by the potential for carbon formation.

4.3.1.1 Carbon Formation

Higher hydrocarbons may lead to carbon formation by all three mechanisms listed in Sec 4.2.8 (whisker carbon, gum, and pyrolytic

coke). Thermodynamics predicts carbon formation as long as the higher hydrocarbons are present. Carbon may be stable in a steady state in spite of the principle of equilibrated gas as defined above. The risk of carbon formation may be assessed by the critical steam to hydrocarbon (S/C) ratio [10,52]. This decreases with temperature and depends on the type of hydrocarbon and the type of catalyst. Olefins and aromatics form carbon more easily than paraffins [10]. Even traces of ethylene originating from thermal cracking in preheaters, dehydration of ethanol, or oxidative coupling of methane may be critical. Carbon formation is to be expected if the actual S/C ratio is lower than the critical ratio.

Pyrolytic coke is a high-temperature phenomenon resulting from thermal cracking of higher hydrocarbons [1,10]. Hence, the risk depends on the residence time/temperature exposure of the hydrocarbon in the equipment (the kinetic severity factor [32]). Pyrolytic coke may deposit on tube walls or encapsulate catalyst particles.

4.3.1.2. *Effect of Promoters on Carbon Formation*

The kinetic balance can be influenced by catalyst promoters [1] by enhancing the adsorption of steam or by blocking the step sites where carbon formation takes place. For example, steam adsorption is enhanced by potassium [10,52] as reflected by a negative reaction order with respect to water. The presence of alkali results in a significant decrease of the activity reflected by a lower pre-exponential factor. This is not the case with active magnesia, which shows the promoting effect of enhanced steam adsorption (although smaller than that for alkali promotion), but without the loss of activity [1,10]. As a result, a Ni/MgO catalyst is able to process liquid hydrocarbons, even kerosene and diesel if properly desulfurized [50]. Similar promoter effects have been reported for La_2O_3 and Ce_2O_3 for CO_2 and steam reforming [43,53].

Another approach for inhibition of carbon formation is to retard the full dissociation of the hydrocarbon into adsorbed carbon atoms [1]. This was the explanation in a series of studies of the impact of a number of oxides such as La, Ce, Ti, Mo, and W [41,54,55]. Blockage of sites for nucleation of carbon was reported for the addition of Bi [56] or B [57] to nickel and for bimetallic catalysts such as Ni/Au [58], Pt/Re [59], Pt/Sn [60], and Ni/Sn [61,62]. Ensemble control by means of sulfur passivation [48,49] will not work in a tubular reformer in the presence of higher hydrocarbons which will crack during heat up over the completely deactivated catalyst in the cold part of the tube.

4.3.1.3. *Temperature Effects*

Naphtha can be processed directly in the tubular reformer when using promoted catalysts [50,51,63], as practiced in many industrial units, but the control of the preheat temperature and heat flux profile may be critical [51]. This is a severe constraint as the heat required in the tubular reformer (and hence the reformer costs) may be reduced by increasing preheat temperature. However, the preheater may then work as a "steam cracker" producing olefins from higher hydrocarbons in the feed [32]. The olefins easily form carbon in the reformer. Apart from the pressure, the conditions in the tubular steam reformer and in the preheater are not far from that of a steam cracker in an ethylene plant.

These constraints are removed when using an adiabatic pre-reformer [11,64] operating in the temperature range 350–550 °C. All higher hydrocarbons are converted to C1 components and hydrogen in the pre-reformer and the reforming and shift reactions are brought into equilibrium. Downstream of the pre-reformer it is possible to heat the gas to around 650 °C, thus reducing the size of the tubular reformer. The pre-reforming catalyst is typically a highly active nickel catalyst. This catalyst also works

as an effective sulfur guard for the tubular reformer and downstream catalysts, by removing any traces of sulfur still left after the desulfurization section.

However, the low-temperature operation may result in catalyst deactivation because of coke formation [65,66]. The adsorbed hydrocarbon species may slowly polymerize in competition with the C−C bond cleavage. If so, the nickel particles may slowly be encapsulated in a polymer film, deactivating the catalyst. The data in Fig. 4.7 show results from low-temperature steam reforming of heavy feedstock at adiabatic conditions [10,67]. The deactivation results in a change of the axial temperature profile. The deactivation is more pronounced with aromatic feed and may be depressed by hydrogen. In practice, coke formation is overlapped by sulfur poisoning. If so, the catalyst life is related to the sulfur capacity of the pre-reforming catalyst.

With jet fuel (kerosene), the catalyst is gradually poisoned by sulfur, resulting in a movement of the temperature profile. When operating on diesel, sulfur poisoning is accompanied by formation of a polymer film (gum), causing a larger movement of the temperature profile. Steam reforming of the sulfur-free and paraffinic diesel from the Fischer−Tropsch synthesis does not result in this type of deactivation.

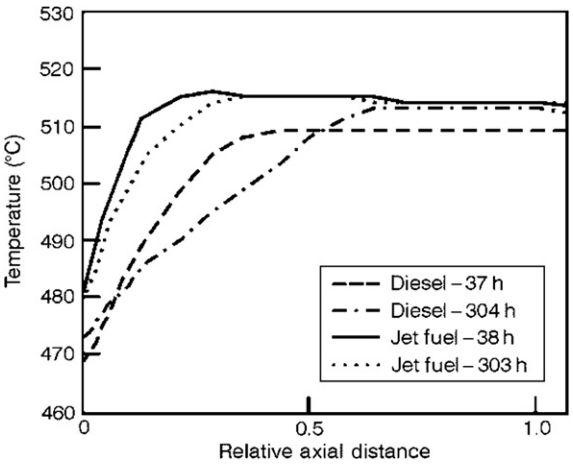

FIGURE 4.7 Adiabatic pre-reforming of "logistic fuels." Temperature profiles from Topsoe RKNGR catalyst [67] *(Reproduced with permission of the authors).*

4.3.2. Alcohols

4.3.2.1. Methanol

The thermodynamic constraints described for steam reforming disappear when methanol is used as feed [68]. The reaction takes place over a copper catalyst above 200 °C. This catalyst is not active for the methanation reaction. This means that a methane-free gas can be produced at low temperatures and at high pressures and that full conversion to CO_2 (and CO) and hydrogen is achieved. The heat of reaction is less than for steam reforming of hydrocarbons. In contrast, the use of nickel catalysts results in methane-rich gases [69,70] and an overall exothermic process.

Methanol reforming (decomposition) over Cu/Zn/Al catalysts [68,71,72] is a well-established technology [73], and is mainly used for small hydrogen plants (less than 1000 Nm^3/h). Since the amount of heat required per mole of hydrogen is far less than for steam reforming of natural gas, the equipment becomes much cheaper than the tubular reformer. On the other hand, the heat of evaporation on a mass basis of methanol is about four times higher than that of naphtha. The optimum choice of operating conditions [73] is around a steam to methanol ratio of 1.5 and a temperature in the range 250−300 °C. The pressure does not influence the reaction rate, but very high pressures limit the equilibrium conversion, which otherwise is above 99%. Like methanol, dimethyl ether (DME) is easily converted over Cu/Zn/Al catalysts [74,75] with little change in the layout of the plant [76].

The interest in fuel cells for automotive applications has resulted in a large number of investigations of reforming of methanol [72,77] for onboard reforming or for distributed units for

hydrogen production. Compact units have been studied using microchannel reformer or plate for reformers [78,79] or a combination with selective hydrogen membranes [80]. Because copper catalysts are sensitive to air during shutdown and start-up of onboard reformers, there has been an interest in palladium catalysts for the methanol reforming process [81].

4.3.2.2. *Ethanol*

Ethanol has attracted interest as a feedstock for syngas production [82], thereby coupling biotechnology to classical catalysis. However, steam reforming of ethanol is not as simple as the conversion of methanol, because ethanol is easily dehydrated to ethylene, which is a coke precursor. Moreover, the reaction involves the breakage of a carbon−carbon bond. This means that copper catalysts are not suitable, as they are poor catalysts for hydrogenolysis. On the other hand, group VIII metals like nickel being active for hydrogenolysis are also active for carbon formation. Therefore, there are many attempts to identify catalysts with stable performance [82]. It appears that noble metal catalysts (Ru,Rh) [83,84], promoted Co catalysts [25,85], or bi-metallic catalysts such as Ni,Cu catalyst [86] look promising.

4.3.3. Other Oxygenates

Glycerol being a by-product from the manufacture of biodiesel has been considered as a source for hydrogen by reforming [87]. Aqueous phase reforming (APR) [88] is a promising route for converting oxygenated hydrocarbons, such as simple alcohols, ethylene glycol, glycerol and sugars (sorbital glucose, etc.), into hydrogen and carbon dioxide. The reaction is carried out at temperatures in the range 150−265 °C over a platinum catalyst or bimetallic catalysts [88] including a non-noble metal catalyst, Ni,Sn [61].

4.4. HYDROGEN PRODUCTION

4.4.1. Industrial Hydrogen Manufacture by Steam Reforming

The supply pressure of industrial hydrogen plants in refineries is typically 2−3 MPa [4,9]. Thermodynamics would then predict favorable operation at high S/C ratios. However, modern hydrogen plants are typically designed for low S/C ratios [4,9]. This reduces the mass flow through the plant and thus the size of the equipment, so that less gas is heated in the reformer, with a resulting lower number of tubes as illustrated in Table 4.2.

A low S/C ratio increases the amount of unconverted methane from the reformer, but this is partly compensated by increasing the exit temperature. The non-converted methane is recovered in a unit for pressure swing adsorption (PSA) for cleaning the hydrogen to a purity of 99.999% H_2 [4]. The off-gas from the PSA unit is then used as fuel for the reformer as illustrated in the flow diagram in Fig. 4.8.

Figure 4.8 shows the installation of a low-temperature adiabatic pre-reformer upstream of the tubular reformer [4,11]. This eliminates the risk of thermal cracking of the higher hydrocarbons into olefins in the preheater, which allows the use of a high preheat temperature to the tubular reformer. It may be increased from the conventional 500 °C to above 600 °C,

TABLE 4.2 Typical Conditions for Hydrogen Plants Using Steam Reforming of Methane (100,000 Nm^3 H_2/h) [9]

Design	H_2O/CH_4	PMPa	T_{inlet}°C	T_{exit}°C	H_2	CO	CO_2	CH_4	Process duty MW
Previous	4.5	3	500	850	75.2	11.1	10.5	3.2	97.8
Modern	1.8	3	650	920	71.1	17.6	4.6	6.8	85.4

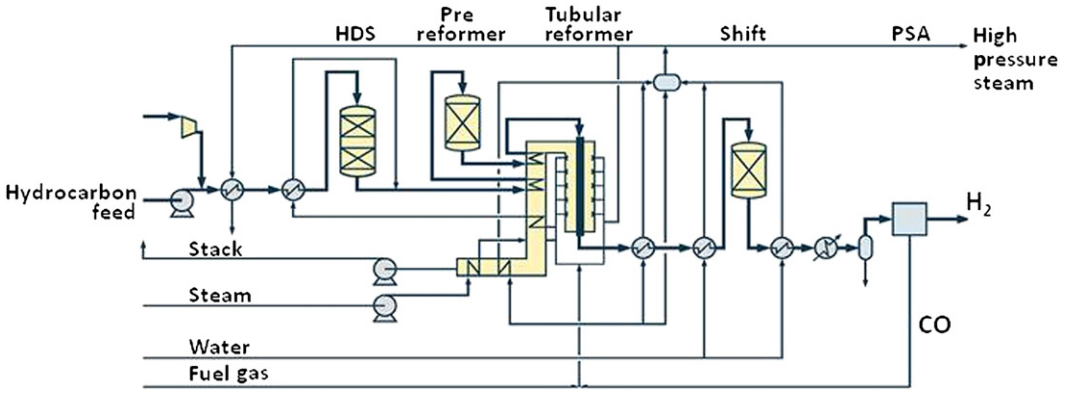

FIGURE 4.8 The SMR-based hydrogen plant layout and key operating parameters (low S/C (≤2.0) and high reformer outlet temperature (>900 °C)).

which means that less heat has to be transferred through the tubes in the reformer or that more gas can be processed in a given reformer. The pre-reformer is also applied when the feedstock is naphtha or heavier liquids (Fig. 4.7). The pre-reformer operating a low temperature also works as an effective sulfur guard for the tubular reformer and the downstream shift catalyst by removing any traces of sulfur.

4.4.2. Heat Recovery

A modern hydrogen plant as shown in Fig. 4.8 is highly efficient as the energy consumed in a methane-based plant (approximately 12.6 GJ/1000 Nm^3 H_2) is very close to the theoretical minimum (11.8 GJ/1000 Nm^3 H_2) [4]. However, most hydrogen plants suffer from a surplus of steam production which may not always be exported. Only about 50% of the heat fired in the tubular reformer is recovered, mainly as high pressure steam [1,4]. In ammonia plants the steam is used to drive the syngas compressor, but in hydrogen plants there is little need for steam.

It is possible to completely eliminate the steam export by replacing the tubular reformer with a convective reformer in which the flue gas as well as the product gas is cooled by heat exchange with the process gas flowing through the catalyst bed such that all gas streams are leaving the reformer at about 600 °C [1,89]. In this way, the amount of waste heat is reduced from 50% to 20% of the fired heat. Convective reformers are industrially proven [89] but are not feasible for large units because the heat transfer is mainly by convection, which in general leads to lower heat fluxes (and larger equipment). However, convective reforming can minimize the steam export from a large tubular reformer (and hence improve the productivity) [90] by utilizing the heat in the hot product gas for supplementary heat input to the process instead of raising steam. This chemical recuperation of heat may take place by the installation of a parallel convective reformer heated by the hot product gas from the tubular reformer. In this way, it is possible to increase the capacity of a hydrogen plant by 30% with the same reformer or to reduce the steam export by 40% [90].

4.4.3. Steam Reforming for Fuel Cell Plants

Hydrogen manufacture for fuel cells differs from large-scale industrial hydrogen manufacture in a number of ways such as size, pressure,

product quality, and system integration [68,91]. The size is smaller, which allows for more compact designs, eliminating the constraints of the tubular reformer and the need for a surplus of catalyst. Microchannel reformers may take advantage of utilizing the catalyst more efficiently either by catalyzed hardware on heat transfer surfaces [15,92,93] or by splitting the heat transfer and reaction in a series of adiabatic reactors and heat exchangers [94]. The catalyst beds may be monoliths with low pressure drop and the heat exchangers of compact microchannel design [9].

The microchannel reformers show high heat transfer rates [93]. This means fast heating of the feed stream (within milliseconds); hence the possibility of avoiding coke from thermal cracking in preheaters and over deactivated catalyst [2]. This also means that sulfur-passivated reforming [49] (blockage of sites for nucleation of carbon by sulfur) might be applied. The microchannel design achieves a high productivity per volume [93]. However, there is little economy of scale and the feasibility is limited to small- to medium-sized capacities.

The low pressure makes pressure drop constraints more critical, often resulting in the risk of maldistribution of flow. Low pressure makes desulfurization of heavy feedstocks difficult because hydrodesulfurization (HDS) requires hydrogen at high pressure. This may result in selection of the less sulfur-sensitive CPOX for the fuel processing, then leaving the sulfur removal problem to cleaning of the CPOX product gas for H_2S.

Low pressure means that PSA is not directly applicable for purification of hydrogen. Instead, a series of catalytic steps should be used depending on the requirements to purity of the hydrogen product [68,95]. This includes low temperature shift and methanation as used in conventional hydrogen plants or preferential oxidation (PROX) of carbon monoxide.

4.4.3.1. Process Configuration for Fuel Cell Applications: SOFC

The layout of the fuel processing system depends on the type of fuel cell. Two typical system applications can be used to illustrate the differences between low- and high-temperature fuel cell applications [95]. The feedstock in both cases is natural gas. In the SOFC system (Fig. 4.9), natural gas is preheated and desulfurized. The feed is then mixed with recycled anode off-gas to provide steam and heat to an adiabatic pre-reformer operating with an inlet temperature around 450−500 °C. All heavier hydrocarbons are quantitatively steam reformed, preventing carbon formation in the preheater and anode. The fuel gas and air temperatures are increased to around 650 °C in the feed/effluent preheaters. On the cathode side, the air used to cool the stack is compressed in a blower. Part of the off-gas is sent to a catalytic burner. The burner exhaust gases are used for steam generation during the start-up phase, fuel preheating and heating. The fuel utilization of the stack is set to 85%. Total fuel utilization is somewhat higher, thanks to the anode recycling. The design cell voltage is 0.75 V. Other efficiencies are typically air compressor = 72%, anode recycle blower = 55%, and DC/AC inverter = 95%.

4.4.3.2. Process Configuration for Fuel Cell Applications: PEMFC

In the PEMFC system, shown in Fig. 4.10, the feedstock is preheated and desulphurized before steam is added. Steam reforming is carried out in a heat-exchange reformer, where heat is supplied to the reforming catalyst bed both from hot flue gas and the exit gas from the reforming catalyst bed. The CO content in the gas is first lowered to a few thousand ppm in a shift section and finally brought down below 50 ppm in a PROX step, where CO is selectively oxidized to CO_2 using air. The exit gas from the PROX is cooled down, delivering

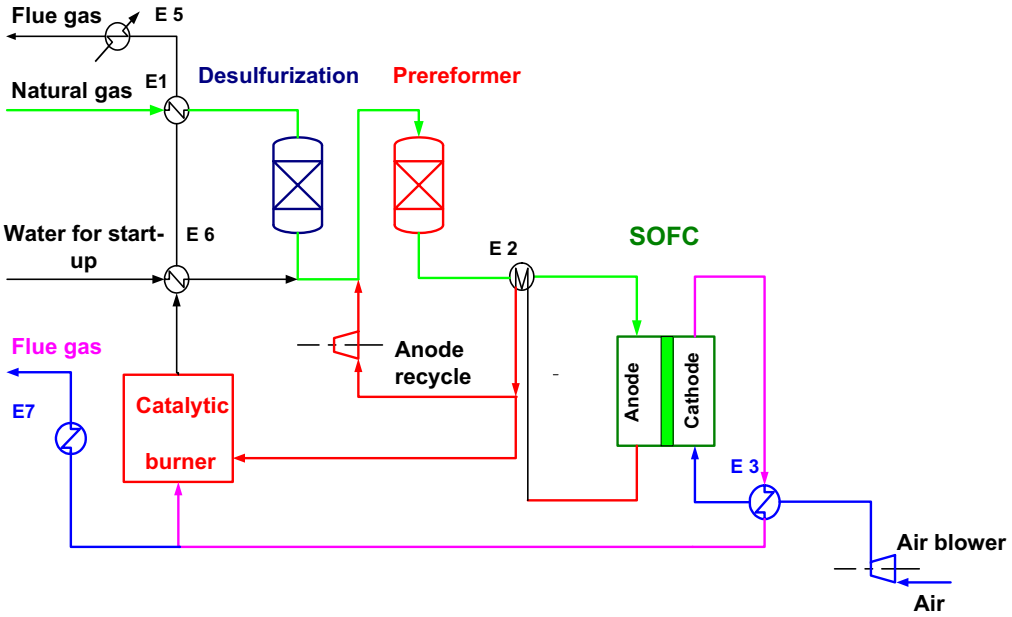

FIGURE 4.9 Basic layout of a 250-kW_e SOFC-based CHP system; *Reprinted from Fontell et al. [95], Copyright (2004), with permission from Elsevier.*

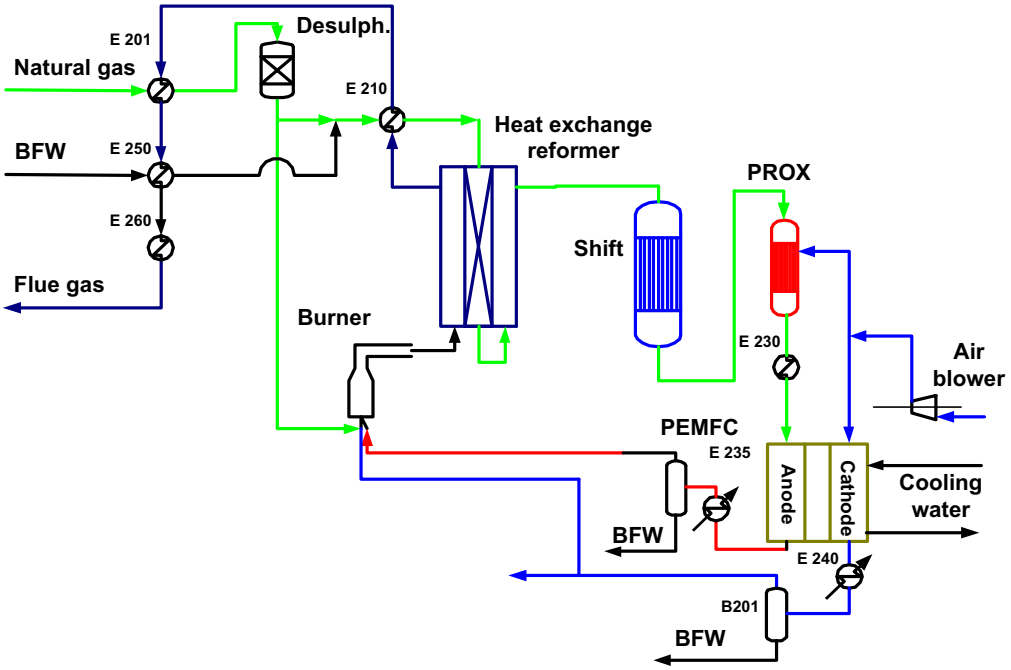

FIGURE 4.10 Basic layout of a 250-kW_e PEMFC system [96].

heat to a HVAC system, before entering the anode. The PEMFC is cooled by water, which also delivers heat to the HVAC system. The hot flue gas from the burner, which may be of catalytic or thermal type, delivers heat directly to the heat-exchange reformer and provides reformer feed preheat, natural gas preheat, and steam generation before excess is delivered for heating. The assumptions concerning efficiencies used in the PEMFC study are the same as in the SOFC case.

4.4.3.3. *Comparison of SOFC and PEMFC processes*

When comparing the two systems it is instructive to consider the energy flows of the SOFC in the Sankey diagram in Fig. 4.11, showing the energy contents of the streams. In the energy balance, it is necessary to take into account the enthalpy flow of the oxygen passing through the electrolyte. It can be seen that the cathode air in/out heat exchanger is a major piece of equipment. Only part of the enthalpy from the electrochemical reaction is available to do useful external work (exergy). The rest is dissipated in the fuel cell as heat and mainly removed with the cathode air. This heat transfer is the main source of exergy losses in the plant.

It is calculated that approximately half of the waste heat from the oxidation reaction is used to drive the internal reforming reaction in the anode chamber. This reaction not only reduces the size of the in/out exchanger and reduces the parasitic loss for air compression, but also "upgrades" waste heat to chemical energy. This is a major reason for the higher electrical efficiency of the SOFC system compared to the PEMFC system as shown in Table 4.3, where the exergetic efficiencies are also given.

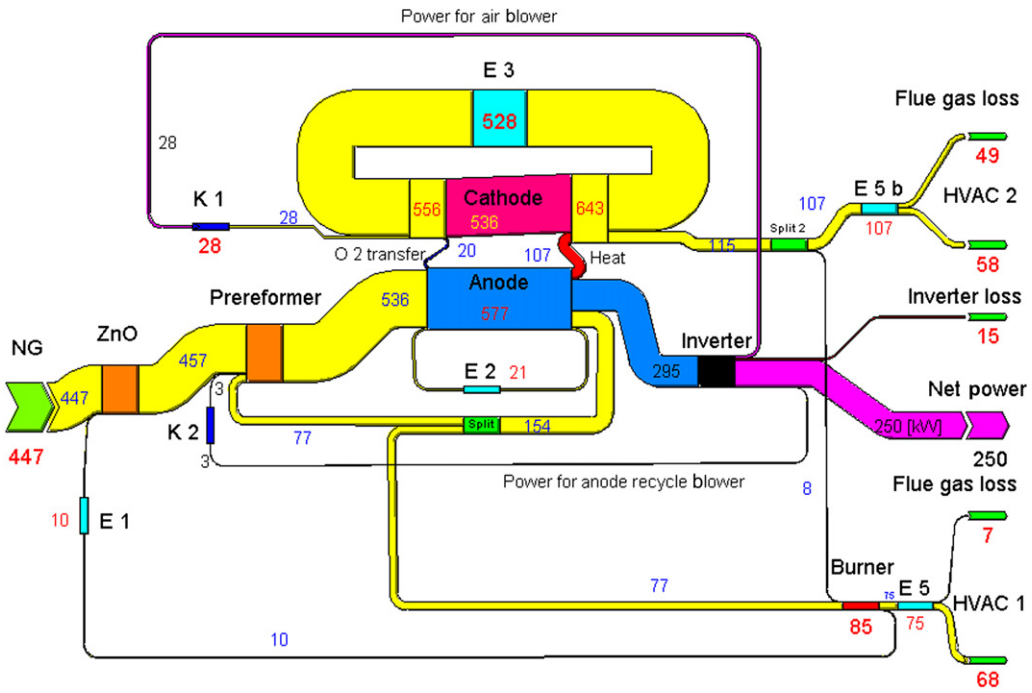

FIGURE 4.11 Energy flows in a 250-kW SOFC CHP system in kJ/s [96].

TABLE 4.3 Efficiencies of Fuel Cell Systems [96]

Efficiency %	SOFC	PEMFC
$\eta_{electrical}$	55.9	36.7
$\eta_{thermal}$ flue gas at 70 °C	32.3	45.7
η_{total}	88.2	82.4
η_{exergy}	56.6	39.2

Table 4.3 illustrates the advantages of SOFC versus PEMFC, as the price of electricity is normally more than the double of that of heat. The exergy efficiencies further emphasize this conclusion. The calculated efficiencies for the PEMFC system correspond well to the number reported for a 250-kW demonstration unit [97]. A breakdown of the exergy losses arising in the PEMFC and SOFC systems is shown in Fig. 4.12.

The major culprit in the PEMFC system is the stack, because waste heat is not recuperated by internal reforming and is degraded directly to the 60 °C level of the cooling water. Secondly, the need for extensive methane reforming (low methane leakage) dictates a high exit temperature of above 800 °C from the heat-exchange reformer. This fact, together with the extra heating duty for the reformer compared with the adiabatic pre-reformer in the SOFC case, makes the use of additional fuel necessary. The exergy loss in the burner unit system is thus significant. The heat exchange occurring in the reformer, shift, and PROX also contributes. The contribution of the shift and PROX subsystems to the total exergy loss is approximately 3%, so even if CO tolerant anodes for PEMFC were developed, they would not change the efficiencies significantly.

A HT PEMFC system would, however, be simpler and cheaper. It could also more easily handle transient operation. The exergy losses in the heat exchangers in the SOFC system is, however, higher than in the PEMFC system, mainly due to the cathode air in/out exchanger. If the high-temperature heat, available in the SOFC system, were used in a heat engine, for example, a gas turbine, the advantages of the SOFC would be even more pronounced.

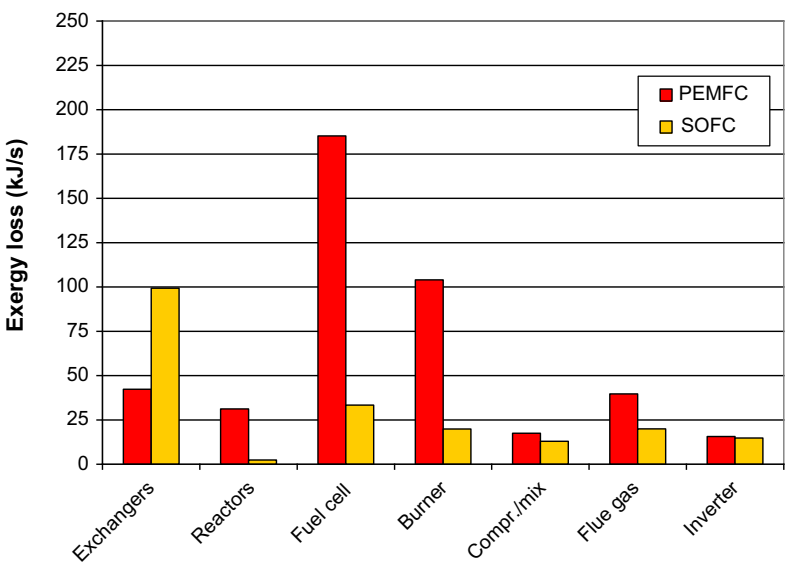

FIGURE 4.12 Exergy losses in PEMFC and SOFC 250-kW CHP systems [96].

4.5. CONCLUSIONS

The steam reforming of hydrocarbons, particularly methane, is well established in industry. The mechanism is understood at the atomic scale on basis of recent fundamental studies including DFT calculations. This is true also for the mechanism of carbon formation, which is an important secondary phenomenon. At normal conditions, for the manufacture of hydrogen, carbon formation is rarely a problem when the right catalyst promoters are used.

It is possible to steam-reform heavy distillates, provided they have been desulfurized. If not, sulfur will accumulate on the pre-reformer catalyst and the sulfur capacity of the catalyst determines the life of the catalyst. Proper desulfurization of heavy feeds represents a problem for fuel cell plants because of the low operating pressure, which means that CPOX (which is less sensitive to sulfur poisoning) may become the preferred technology inspite of a lower electric system efficiency.

Methanol and DME are easily converted by steam reforming, whereas it remains a challenge to find a stable catalyst for conversion of ethanol.

The development of multichannel reformers has resulted in a significant process intensification contributing to low system costs.

References

[1] Rostrup-Nielsen JR, Christiansen LJ. Concepts in syngas preparation (Catalytic science series). London: Imperial College Press; 2011.

[2] Rostrup-Nielsen JR. Steam reforming. Chapter 13.11. In: Ertl G, Knözinger H, Schüth F, Weitkamp J, editors. Handbook of heterogeneous catalysis, vol. 6. Weinheim: Wiley-VCH Verlag; 2008. p. 2882–905.

[3] Brightling J, Farnell P, Foster C, Beyer F. Steam reforming – 50 years of development and the challenges for the next 50 years. AIChE 50th Annual safety in ammonia plants and related facilities. 2005;46: p. 190–201.

[4] Rostrup-Nielsen JR, Rostrup-Nielsen T. Large-scale hydrogen production. Cattech 2002;4:150–9.

[5] Ratan S, Baade W, Wolfson D. The large hydrogen plant challenge. Hydrocarbon Eng 2005;10(7):37–40.

[6] Gielen D, Simbolotti G, editors. Prospects for hydrogen and fuel cells. Paris: Int Energy Agency; 2005.

[7] Rostrup-Nielsen JR. Fuels and energy for the future: the role of catalysis. Catal Rev Sci Eng 2004; 46:247–70.

[8] Holladay JD, Hu J, King DL, Wang Y. An overview of hydrogen production technologies. Catal Today 2009;139:244–60.

[9] Rostrup-Nielsen J. Reforming and gasification – fossil energy carriers. In: Stolten D, editor. Hydrogen and fuel cells: fundamentals, technologies and applications. Weinheim: Wiley-VCH; 2010. p. 291–306.

[10] Rostrup-Nielsen JR. Steam reforming. Chapter 1. In: Anderson JR, Boudart M, editors. Catalysis, science and technology, vol. 5. Berlin: Springer-Verlag; 1984. p. 1–117.

[11] Rostrup-Nielsen JR, Sehested J, Nørskov JK. Hydrogen and synthesis gas by steam- and CO_2 reforming. Adv Catal 2002;47:65–139.

[12] Ridler DE, Twigg MV. Steam reforming. Chapter 5. In: Twigg MV, editor. Catalyst handbook. London: Wolfe Publishing Ltd; 1989. p. 225–82.

[13] Richardson JT, Twigg MV. Preparation and properties of ceramic foam catalyst support. Stud Surf Sci Catal 1995;91:345–59.

[14] Rostrup-Nielsen JR. Production of synthesis gas. Catal Today 1993;18:305–24.

[15] Farrauto RJ, Lui Y, Ruettinger W, Ilinich Q, Shore L, Giroux T. Precious metal catalysts supported on ceramic and metal monolithic structures for the hydrogen economy. Catal Rev Eng Sci 2007;49: 141–96.

[16] Bartholomew CH, Pannell RB. The stoichiometry of hydrogen and carbon monoxide chemisorption on alumina- and silica-supported nickel. J Catal 1980;65:390–401.

[17] Sehested J. Four challenges for nickel steam-reforming catalysis. Catal Today 2006;111:103–10.

[18] Bernardo CA, Alstrup I, Rostrup-Nielsen JR. Carbon deposition and methane steam reforming on silica-supported Ni-Cu catalysts. J Catal 1985;96:517–34.

[19] Jones G, Jakobsen JG, Shim SS, Keis J, Anderson MP, Rossmeisl J, et al. First principles calculations and experimental insight into methane steam reforming over transition metal catalysts. J Catal 2008;259: 147–60.

[20] Kikuchi E, Tanoka S, Yamazaki Y, Morita Y. Steam reforming of hydrocarbons on noble metal catalysts – 1. The catalytic activity in methane-steam reaction. Bull Jpn Pet Inst 1974;16:95–8.

[21] Wei J, Iglesia E. Mechanism and site requirements for activation and chemical conversion of methane on supported Pt clusters and turnover rate comparisons among noble metals. J Phys Chem B 2004;108: 4094–103.
[22] Rostrup-Nielsen JR, Christiansen LJ. Internal steam reforming in fuel cells and alkali poisoning. Appl Catal A: Gen 1995;126:381–90.
[23] Mogensen M, Lybye D, Kammer K, Bonanos N. Ceria revisited: electrolyte or electrode material? 2005. In: Singhal SC, Mizusaki J, editors. Proceedings – Electrochem Soc; 2005. p. 1068–74.
[24] Mosqueda B, Toyir J, Kaddouri A, Gélin P. Steam reforming of methane under water deficient conditions over gadolinium-doped ceria. Appl Catal B: Env 2009;88:361–7.
[25] Lin SS-Y, Kim DH, Ha SY. Metallic phases of cobalt-based catalysts in ethanol steam reforming: the effect of cerium oxide. Appl Catal A: Gen 2009;355: 69–77.
[26] Clarigde JB, York APE, Brungs AJ, Marquez-Alvarez C, Sloan J, Tsang SC, et al. New catalysts for the conversion of methane to synthesis gas: molybdenum and tungsten carbide. J Catal 1998;180:85–100.
[27] Sehested J, Jacobsen CJH, Rokni S, Rostrup-Nielsen JR. Activity and stability of molybdenum carbide as a catalyst for CO_2 reforming. J Catal 2001;201:206–12.
[28] Back MH, Back RA. Thermal decomposition and reactions of methane. In: Albright LF, Crynes BL, Corcoran WH, editors. Pyrolysis, theory and industrial practice, Chapter 1. New York: Academic Press; 1983. p. 1–24.
[29] Karim GA, Metwally M. A kinetic investigation of the reforming of natural gas for the production of hydrogen. Int J Hydrogen Energy 1979;5:293–304.
[30] Frost L, Hartvigsen J, Elangovan S. Co-electrolysis of steam and carbon dioxide as feed to a methanation reaction. Proc Annual AIChE Meeting 2007;8.
[31] Ross LL. Pyrolysis furnace design: conventional and novel pyrolysis. In: Albright LF, Crynes BL, Corcoran WH, editors. Theory and industrial practice, Chapter 1. New York: Academic Press; 1983. p. 327–64.
[32] Zdonik SB, Green EJ, Haller LP. How cracking proceeds in the ethylene-pyrolysis reaction. Oil Gas J 1967;65(26):96–101.
[33] van Santen RA. Complementary structure sensitive and insensitive catalytic relationships. Acc Chem Res 2009;42:57–66.
[34] Bengaard HS, Nørskov JK, Sehested JS, Clausen BS, Nielsen LP, Molenbroek AM, et al. Steam reforming and graphite formation on Ni catalysts. J Catal 2002;209:365–84.
[35] van Grootel PW, Hensen EJM, van Santen RA. DFT study on H_2O activation by stepped and planar Rh surfaces. Surf Sci 2009;603:3275–81.
[36] Helveg S, López-Cartes C, Sehested J, Hansen PL, Clausen BS, Rostrup-Nielsen JR, et al. Atomic-scale imaging of carbon nanofibre growth. Nature 2004;427:426–9.
[37] Wei J, Iglesia E. Isotopic and kinetic assessment of the mechanism of reactions of CH_4 with CO_2 or H_2O to form synthesis gas and carbon on nickel catalysts. J Catal 2004;224:370–83.
[38] Xu J, Froment GF. Methane steam reforming, methanation and water-gas shift: I. Intrinsic kinetics. AIChE J 1989;35:88–96.
[39] Avetisov AK, Rostrup-Nielsen JR, Kuchaev VL, Bak Hansen J-H, Zyskin AG, Shapatina EN. Steady-state kinetics and mechanism of methane reforming with steam and carbon dioxide over Ni catalyst. J Mol Catal A: Chem 2010;315:155–62.
[40] Bodrov IM, Apel'baum LO. Reaction kinetics of methane and carbon dioxide on a nickel surface. Kinet Katal 1967;8:379–82.
[41] Bradford MCJ, Vannice MA. CO_2 reforming of CH_4 over supported Pt catalysts. J Catal 1998;173:157–71.
[42] Rostrup-Nielsen JR, Bak Hansen J-H. CO_2-reforming of methane over transition metals. J Catal 1993;144:38–49.
[43] Zhang Z, Verykios XE. Mechanistic aspects of carbon dioxide reforming of methane to synthesis gas over Ni catalysts. Catal Lett 1996;38:175–9.
[44] Alstrup I, Rostrup-Nielsen JR, Røen S. High temperature hydrogen sulfide chemisorption on nickel catalysts. Appl Catal 1981;1:303–14.
[45] Rostrup-Nielsen JR. Methane conversion for fuel cells: the role of sulphur. Stud Surf Sci Catal 2007; 167:153–8.
[46] Cooper BH, Knudsen KG. Ultra deep desulfurization of diesel: how an understanding of the underlying kinetics can reduce investment costs. In: Hsu CS, Robinson PR, editors. Practical advances in petroleum processing, vol. 1, Chapter 10. New York: Springer Science; 2006. p. 297–316.
[47] Abild-Pedersen F, Nørskov JK, Rostrup-Nielsen JR, Sehested J, Helveg S. Mechanisms for catalytic carbon nanofiber growth studied by ab initio density functional theory calculations. Phys Rev B 2006;73(11). Article Number 115419.
[48] Rostrup-Nielsen JR. Sulfur-passivated nickel catalysts for carbon-free steam reforming of methane. J Catal 1984;85:31–43.
[49] Dibbern HC, Olesen P, Rostrup-Nielsen JR, Tøttrup PB, Udengaard N. Make low H_2/CO syngas using sulfur passivated reforming. Hydrocarb Proc 1986;65(1):71–4.

[50] Rostrup-Nielsen JR, Christensen T, Dybkjær I. Steam reforming of liquid hydrocarbons. Stud Surf Sci Catal 1998;113:91–5.
[51] Rostrup-Nielsen JR. Hydrogen via steam reforming of naphtha. Chem Eng Prog 1977;73(9):87–92.
[52] Andrew SPS. Catalysts and catalytic processes in the steam reforming of naphtha. Ind Eng Chem Prod Res Develop 1969;8:321–4.
[53] Natesakhawat S, Watson RB, Wang X, Ozkan US. Deactivation characteristics of lanthanide-promoted sol–gel Ni/Al_2O_3 catalysts in propane steam reforming. J Catal 2005;234:496–508.
[54] Borowiecki T, Golebiowski A, Stasinska B. Effects of small MoO_3 additions on the properties of nickel catalysts for the steam reforming of hydrocarbons. Appl Catal A: Gen 1997;153:141–56.
[55] Cheng Z, Wu Q, Li J, Zhu Q. Effects of promoters and preparation procedures on reforming of methane with carbon dioxide over Ni/Al_2O_3 catalyst. Catal Today 1996;30:147–55.
[56] Trimm DL. Coke formation and minimisation during steam reforming reactions. Catal Today 1997;37: 233–8.
[57] Xu J, Chen L, Tan KF, Borgna A, Saeys M. Effect of boron on the stability of Ni catalysts during steam methane reforming. J Catal 2009;261:158–65.
[58] Besenbacher F, Chorkendorff I, Clausen BS, Hammer B, Molenbroek AM, Nørskov JK, et al. Design of a surface alloy catalyst for steam reforming. Science 1998;279:1913–5.
[59] Richardson JT, Hung J-K, Zhao J. CO_2–CH_4 reforming with Pt-Re/γ-Al_2O_3 catalysts. Stud Surf Sci Catal 2001;136:203–7.
[60] Stagg SM, Resasco DE. Effects of promoters and supports on coke formation on Pt catalysts during CH_4 reforming with CO_2. Stud Surf Sci Catal 1997; 111:543–50.
[61] Shabaker JW, Huber GW, Dumesic JA. Aqueous-phase reforming of oxygenated hydrocarbons over Sn-modified Ni catalysts. J Catal 2004;222: 180–91.
[62] Saadi S, Hinnemann B, Helveg S, Appel CC, Abild-Pedersen F, Nørskov JK. First-principles investigations of the Ni3Sn alloy at steam reforming conditions. Surf Sci 2009;603:762–70.
[63] Bridger GW, Chinchen GC. Hydrocarbon reforming catalysts. In: Catalyst handbook. London: Wolfe Scientific Books; 1970. p. 64–96.
[64] Rostrup-Nielsen J. Syngas for C1-chemistry. limits of the steam reforming process. Stud Surf Sci Catal 1988;36:73–8.
[65] Jackson SD, Thomson SJ, Webb G. Carbonaceous deposition associated with the catalytic steam-reforming of hydrocarbons over nickel alumina catalysts. J Catal 1981;70:249–63.
[66] Christensen TS. Adiabatic prereforming of hydrocarbons – an important step in syngas production. Appl Catal A: Gen 1996;138:285–309.
[67] Piwetz MM, Larsen JS, Christensen TS. Hydrodesulfurization and pre-reforming of logistic fuels for use in fuel cell applications. Proc 1996 Fuel Cell Seminar. Orlando, FL: 1996. p. 780–93.
[68] Rostrup-Nielsen JR. Conversion of hydrocarbons and alcohols for fuel cells. Phys Chem Chem Phys 2001;3:283–8.
[69] Rostrup-Nielsen JR, Skov A, Christiansen LJ. Deactivation in pseudo-adiabatic reactors. Appl Catal 1986;22:71–83.
[70] Cockerham RG, Percival G. Experiments on the production of peak-load gas from methanol and light petroleum distillates. Trans Inst Gas Eng 1957–58;107: 390–433.
[71] Jiang CJ, Trimm DL, Wainwright MS, Cant NW. Kinetic mechanism for the reaction between methanol and water over a Cu-ZnO-Al_2O_3 catalyst. Appl Catal A: Gen 1993;93:145–58.
[72] Kundu A, Shul YG, Kim DH. Methanol reforming processes. Chapter 7. In: Zhao TS, Kreuer K-D, Nguyen TV, editors. Advances in fuel cells, vol. 1; 2007. p. 419–72.
[73] Bøgild Hansen J. In: Vielstich W, Lamm A, Gasteiger HA, editors. Handbook of fuel cells: fundamentals, technology, and applications, vol. 3 (1). New York: John Wiley & Sons Ltd., p. 141-8
[74] Tanaka Y, Kikuchi R, Takeguchi T, Eguchi K. Steam reforming of dimethyl ether over composite catalysts of γ-Al_2O_3 and Cu-based spinel. Appl Catal B: Env 2005;57:211–22.
[75] Feng D, Wang Y, Wang D, Wang J. Steam reforming of dimethyl ether over CuO–ZnO–Al_2O_3–ZrO_2 + ZSM-5: a kinetic study. Chem Eng J 2009;146:477–85.
[76] Bøgild Hansen J, Pålsson J. Oxygenates and ammonia as SOFC fuels. Proc 1st European Fuel Cell Technol Appl Conf 2005:49.
[77] Trimm DL, Önsan ZI. On board fuel conversion for hydrogen fuel cell driven vehicles. Catal Rev Sci Eng 2001;43:31–84.
[78] Cao C, Palo DR, Tonkovich AY, Wang Y. Catalyst screening and kinetic studies using microchannel reactors. Catal Today 2007;125:29–33.
[79] Pan L, Wang S. Methanol steam reforming in a compact plate-fin reformer for fuel-cell systems. Int J Hydrogen Energy 2005;30:973–9.
[80] Basile A, Gallucci F, Paturzo L. A dense Pd/Ag membrane reactor for methanol steam reforming: experimental study. Catal Today 2005;104:244–50.

[81] Chin YH, Dagle R, Hu J, Dohnalkova AC, Wang Y. Steam reforming of methanol over highly active Pd/ZnO catalyst. Catal Today 2002;77:79–88.
[82] Haryanto A, Fernando S, Murali N, Adhikari S. Current status of hydrogen production techniques by steam reforming of ethanol: a review. Energy Fuels 2005;19:2098–106.
[83] Rass-Hansen J, Christensen CH, Sehested J, Helveg S, Rostrup-Nielsen JR, Dahl S. Renewable hydrogen: carbon formation on Ni and Ru catalysts during ethanol steam-reforming. Green Chem 2007;9:1016–21.
[84] Liguras DK, Kondarides DI, Verykios XE. Production of hydrogen for fuel cells by steam reforming of ethanol over supported noble metal catalysts. Appl Catal B: Env 2003;43:345–54.
[85] Llorca J, Homs N, Sales J, de la Piscina PR. Efficient production of hydrogen over supported cobalt catalysts from ethanol steam reforming. J Catal 2002;209:306–17.
[86] Zhang L, Liu J, Li W, Guo C, Zhang J. Ethanol steam reforming over Ni-Cu/Al_2O_3-M $_y$O $_z$ (M = Si, La, Mg, and Zn) catalysts. J Nat Gas Chem 2009;18:55–65.
[87] Adhikari S, Fernando S, Haryanto A. Production of hydrogen by steam reforming of glycerin over alumina-supported metal catalysts. Catal Today 2007;129:355–64.
[88] Cortright RD, Davda RR, Dumesic JA. Hydrogen from catalytic reforming of biomass-derived hydrocarbons in liquid water. Nature 2002;418:964–7.
[89] Dybkjær I, Winter-Madsen S. Advanced reforming technologies for hydrogen production. Hydrocarbon Eng 1998;3(1):56.
[90] Rostrup-Nielsen JR, Winter-Madsen S. Large scale manufacture of hydrogen from hydrocarbons. Prepr Pap Am Chem Soc Div Pet Chem 2008;53(1):82–4.
[91] Kolb G, editor. Fuel processing for fuel cells. Weinheim: Wiley-VHC; 2008.
[92] Tonkovich ALY, Yang B, Perry ST, Fitzgerald SP, Wang Y. From seconds to milliseconds to microseconds through tailored microchannel reactor design of a steam methane reforme. Catal Today 2007;120:21–9.
[93] Lerou J, Tonkovich AL, Silva L, Perry S, McDonald J. Microchannel reactor architecture enables greener processes. Chem Eng Sci 2010;65:380–5.
[94] Seris ELC, Abramowitz G, Johnston AM, Haynes BS. Demonstration plant for distributed production of hydrogen from steam reforming of methane. Chem Eng Res Des 2005;83(A6):619–25.
[95] Fontell E, Kivisaari T, Christiansen N, Bøgild Hansen J, Pålsson J. Conceptual study of a 250 kW planar SOFC system for CHP application. J Power Sources 2004;131:49–56.
[96] Palsson J, Hanseb JB, Christiansen N, Nielsen JU, Kristensen S. Solid oxide fuel cells – assessment of the technology from an industrial perspective. Denmark: Presentation at Risø National Laboratory International Energy Conference. May 19–21, 2003.
[97] Barisic Z. Alstom Ballard PEM fuel cell power plants – European field trial program. Brussels: Proceedings of the Business of Fuel Cells for Stationary Applications in Europe. Nov, 2001.

CHAPTER

5

Catalytic Partial Oxidation

Mark W. Smith, Dushyant Shekhawat

National Energy Technology Laboratory, U.S. Department of Energy, 3610 Collins Ferry Road, Morgantown, WV 26507-0880, USA

OUTLINE

5.1. INTRODUCTION

Catalytic partial oxidation (CPOX) is an attractive option to produce H_2 and CO from hydrocarbon fuels for fuel cell applications. In particular, CPOX is suitable for compact or mobile fuel-processing systems integrated with solid oxide fuel cells (SOFCs) due to similarity of operating conditions and the utilization of currently available infrastructure fuels. CPOX can also be followed by the water gas shift (WGS) reaction to produce a pure H_2 stream for use in polymer electrolyte membrane (PEM) fuel cells.

CPOX has the advantage of inherently rapid reforming kinetics with quick light-off characteristics and response to transients. Since there is no need to feed water, as in steam reforming (SR) and oxidative-steam reforming (OSR), CPOX reactors are smaller and more easily integrated into transportation-based, onboard fuel reforming systems, as well as remote and distributed power applications. Additionally, the exothermic nature of this process reduces the heat needed to be supplied to the system, making it ideal for integration with high-temperature fuel cells. Challenges for the CPOX of hydrocarbons include catalyst deactivation from high-temperature sintering, metal vaporization, support degradation, coke formation, and poisoning from sulfur and other contaminants.

The reactions occurring in the CPOX of hydrocarbons are complex. The overall CPOX reaction can be described by Eq. (5.1). However, several side reactions can occur and are presented in Table 5.1 using methane as the hydrocarbon species. The most significant side reactions are the WGS (5.4), SR (5.5), and CO_2 reforming (5.6), which help determine the final synthesis gas composition. This composition will vary based on the hydrocarbon fuel used and the reaction conditions selected.

$$C_nH_mO_p + q(O_2 + 3.76N_2) \rightarrow wCO + xCO_2 + yH_2 + zH_2O + (3.76q)N_2 \quad (5.1)$$

Typical operating conditions provided are the temperature range of 700−1000 °C, atmospheric pressure, oxygen-to-carbon (O/C) ratio = 1.2, and the gas hourly space velocity (GHSV) range from several thousands to several hundred thousands scc g_{cat}^{-1} h^{-1}. Enger et al. [1] provided a very useful set of tables that summarize all the different methane CPOX catalysts

TABLE 5.1 Side Reactions[a] in the Hydrocarbon Partial Oxidation System (Adapted from [1])

$CH_4 + 2O_2 \rightarrow CO_2 + 2H_2O$	Combustion	(5.2)
$CH_4 + O_2 \rightarrow CO_2 + 2H_2$		(5.3)
$CO + H_2O \leftrightarrow CO_2 + H_2$	Water gas shift	(5.4)
$CH_4 + H_2O \leftrightarrow CO + 3H_2$	Steam reforming	(5.5)
$CH_4 + CO_2 \leftrightarrow 2CO + 2H_2$	CO_2 reforming	(5.6)
$CO + H_2 \leftrightarrow C + H_2O$		(5.7)
$CH_4 \leftrightarrow C + 2H_2$	Methane decomposition	(5.8)
$2CO \leftrightarrow CO_2 + C$	Boudouard	(5.9)
$CO + 0.5O_2 \rightarrow CO_2$		(5.10)
$H_2 + 0.5O_2 \rightarrow H_2O$		(5.11)

[a] *All reactions involving O_2 are thermodynamically irreversible.*

found in the authors' review of literature, their promoters, supports, and references.

In this chapter, the CPOX of various hydrocarbon fuels is discussed for a variety of catalysts and operating conditions. The fuels discussed include light (gaseous) and heavy (liquid) hydrocarbons, as well as oxygenated hydrocarbons (alcohols, dimethyl ether (DME), and biodiesel). The catalysts used in the CPOX process are typically noble metals (Pt, Ru, Pd, or Rh), and transition metals such as Ni and Co dispersed onto an appropriate support. However, substituting these metals into thermally stable oxide structures is believed to provide additional thermal stability and some resistance to deactivation.

Section 5.2 discusses an examination of the thermodynamic equilibrium compositions at atmospheric pressure for the hydrocarbon fuels at different O/C ratios and temperatures. Section 5.3 is an analysis of the reaction mechanisms and kinetics that have been proposed in literature for CPOX.

Sections 5.4–5.6 cover the CPOX of different fuel types (gaseous, liquid, and oxygenated hydrocarbons). Specifically, these sections look at a variety of factors that affect the CPOX of these fuels, including reaction conditions, catalyst, and the specific fuel being reformed. The catalyst properties that are examined include activity of transition and noble metals, metal loading or substitution, surface properties, and resistance to deactivation. Further, the effect of the catalyst support properties, such as morphology, composition, and ionic conductivity, is discussed. Finally, the factors related to the fuel type include the presence of unsaturated and/or aromatic hydrocarbon species, sulfur-containing species, and oxygenated compounds.

Several reviews on the CPOX of hydrocarbons have been published in recent years. The largest amount of research reported and reviewed has been related to the CPOX of methane [1–6], while fewer studies have been reviewed related to the CPOX of higher hydrocarbons [7,8]. These references are recommended for a broad examination of work that has been conducted in this field. Major points of discussion provided in these reviews are briefly summarized in the appropriate sections of this chapter for background. However, this chapter is not intended to be another review. Instead, the most important issues and factors identified by the authors with regard to the current state of research on the CPOX of hydrocarbons and oxygenated hydrocarbons are identified and analyzed in detail. Further, this analysis is used to suggest recommendations for future research in Section 5.7.

Although beyond the scope of this chapter, it is worth mentioning that a great deal of research has been reported on CPOX with other oxygen-containing gas species fed along with oxygen to promote secondary reforming reactions [9–30]. In particular, CO_2 and/or steam have been added to reduce CO_2 emissions and reduce carbon deposition on the catalyst. In any system that utilizes a recycle stream, these studies are very important.

5.2. THERMODYNAMICS

Thermodynamic calculations have been conducted for the POX (Eq. (5.1)) of the various fuel types discussed in this chapter. The effects of temperature and O/C ratios are examined in this section. O/C ratio is defined as the atomic ratio of oxygen fed by air to the carbon number of the fuel species. The ratio does not consider oxygen contained in the fuel (i.e., alcohols, biodiesel; see Eq. (5.1)). Equilibrium product distributions and carbon formation characteristics for several representative fuels are examined over the temperature range of 300–1000 °C and over an O/C ratio of 0.9–1.5. All calculations were conducted at atmospheric pressure; therefore, the effect of pressure on these systems is not addressed. For an

TABLE 5.2 Enthalpy of POX Reaction for Various Hydrocarbon Fuels: O/C = 1.2, 900 °C (Calculations Using HSC Chemistry 5.0 [31])

Hydrocarbon	Δ*H* (kJ/kmol)	Δ*H* (kJ/kmol C)
CH_4	55.90	55.90
C_2H_6	20.70	10.35
C_3H_8	−5.59	−1.86
C_4H_{10}	−28.70	−7.18
C_6H_{14}	−78.70	−13.12
C_8H_{18}	−129.00	−16.13
$C_{10}H_{22}$	−178.00	−17.80
$C_{12}H_{26}$	−228.00	−19.00
$C_{14}H_{30}$	−278.00	−19.86
$C_{16}H_{34}$	−328.00	−20.50
$C_{18}H_{38}$	−378.00	−21.00

examination of pressure effects on the POX of methane, the reader is referred to Enger et al. [1].

5.2.1. Heat of Reaction

Table 5.2 shows enthalpy values for selected C_1−C_{18} hydrocarbons. The enthalpies of reaction for all alkanes decrease with increasing carbon number; however, the enthalpy for each hydrocarbon per carbon atom approaches a near-constant value for a given set of conditions. These values are the enthalpy for each hydrocarbon divided by the number of carbon atoms per mole.

The enthalpy values for the POX of methane, isooctane, and *n*-tetradecane (TD), according to Eq. (5.1), at an O/C = 1.2 from 300 °C to 1000 °C, are presented in Fig. 5.1. Isooctane was selected as a model compound for gasoline; TD was selected as a model compound for diesel fuel. At temperatures above 700 °C, the enthalpy becomes slightly positive for methane, indicating that the endothermic reactions (SR and CO_2 reforming) dominate. At these higher temperatures, the steam and CO_2 produced from an increase in combustion reaction increase the extent of these reactions.

5.2.2. Effect of Temperature

Figure 5.2 shows the effect of temperature on methane POX over a temperature range of 300−1000 °C at an O/C ratio of 1.2 and atmospheric pressure. H_2 and CO levels increase up to ~750 °C, after which they remain essentially constant. The CO_2 level increases slightly up to ~550 °C, at which point it begins to be consumed by reforming of the remaining

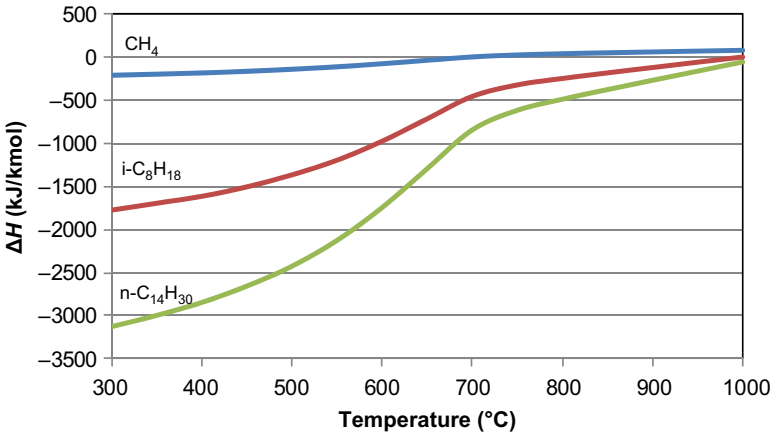

FIGURE 5.1 Enthalpy of reaction for POX of methane, i-octane, and TD at different temperatures: O/C = 1.2, 0.10 MPa (calculations using HSC Chemistry 5.0 [31]).

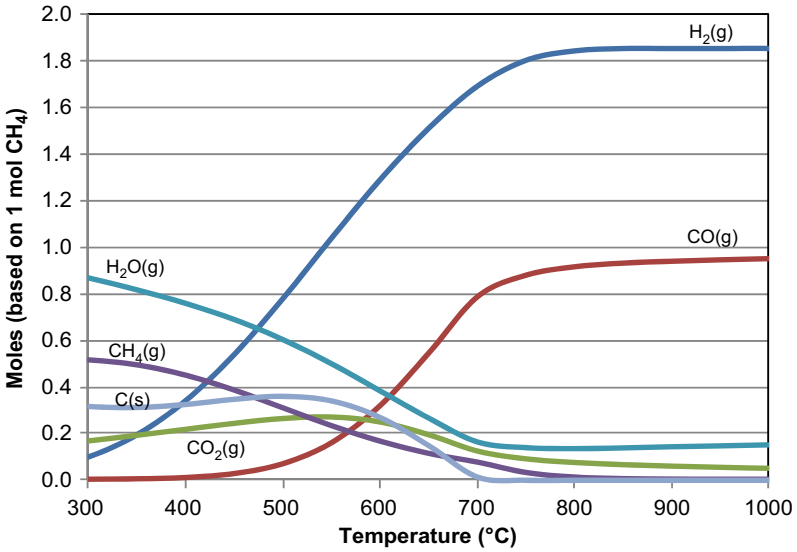

FIGURE 5.2 Equilibrium product distribution for the POX of methane for different temperatures: O/C = 1.2, P = 0.10 MPa (calculations using HSC Chemistry 5.0 [31]).

methane (Eq. (5.6)). H_2O and C decrease up to ~700 °C, beyond which carbon is thermodynamically unfavorable. Complete conversion of methane is accomplished at ~800 °C. Above 800 °C, there is a slight and gradual increase in CO and H_2O, along with a decrease in CO_2, indicating that the reverse WGS reaction is occurring.

Figure 5.3 shows the effect of temperature on TD POX over a temperature range of 300–1000 °C at an O/C ratio of 1.2 and atmospheric pressure. Unlike methane, the H_2 produced does not level off, but reaches a maximum at ~750 °C before gradually declining due to formation of water. The CO continues to increase through this temperature range from

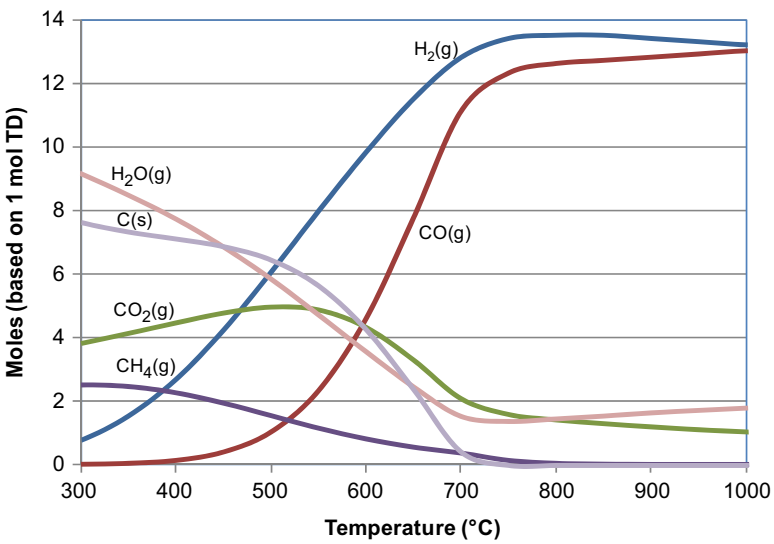

FIGURE 5.3 Equilibrium product distribution for the POX of TD for different temperatures: O/C = 1.2, 0.10 MPa (calculations using HSC Chemistry 5.0 [31]).

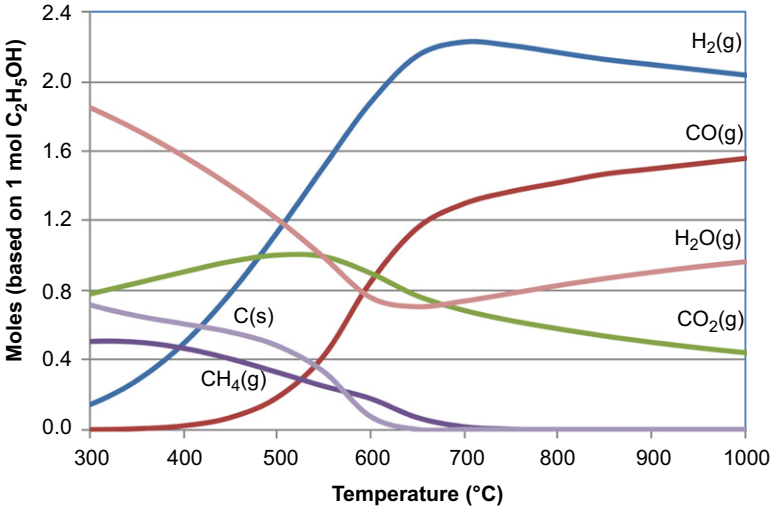

FIGURE 5.4 Equilibrium product distribution for the POX of ethanol for different temperatures: O/C = 1.2, 0.10 MPa (calculations using HSC Chemistry 5.0 [31]).

the reverse WGS. Complete hydrocarbon conversion is achieved at ~800 °C; carbon formation goes to zero at ~710 °C.

Figure 5.4 shows the effect of temperature on ethanol POX over a temperature range of 300–1000 °C at an O/C ratio of 1.2 and atmospheric pressure. The decrease in H_2 at high temperatures is more pronounced than with the hydrocarbon fuels. Also, the increase in H_2O at high temperatures is more significant. Complete ethanol conversion occurs at ~720 °C, and the carbon produced goes to zero at ~610 °C.

5.2.3. Effect of O/C Ratio

The effect of the O/C ratio on the product distributions for methane POX at 900 °C is shown in Fig. 5.5. Conversion of methane is

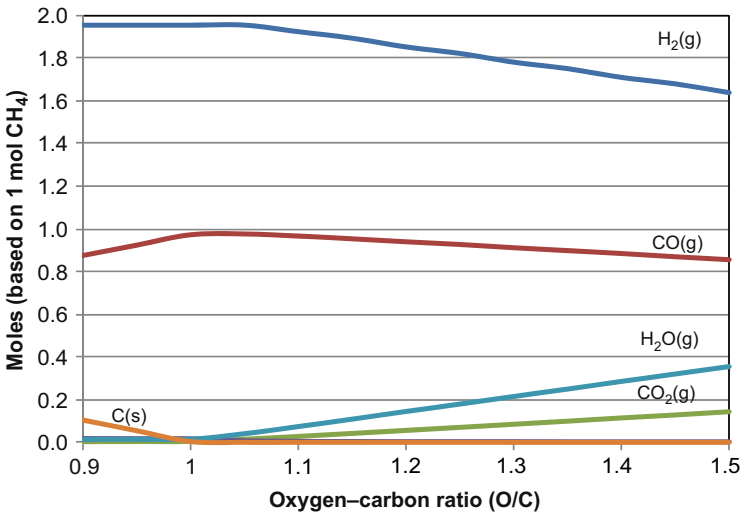

FIGURE 5.5 Equilibrium product distribution for the POX of methane for different O/C ratios: 900 °C, 0.10 MPa (calculations using HSC Chemistry 5.0 [31]).

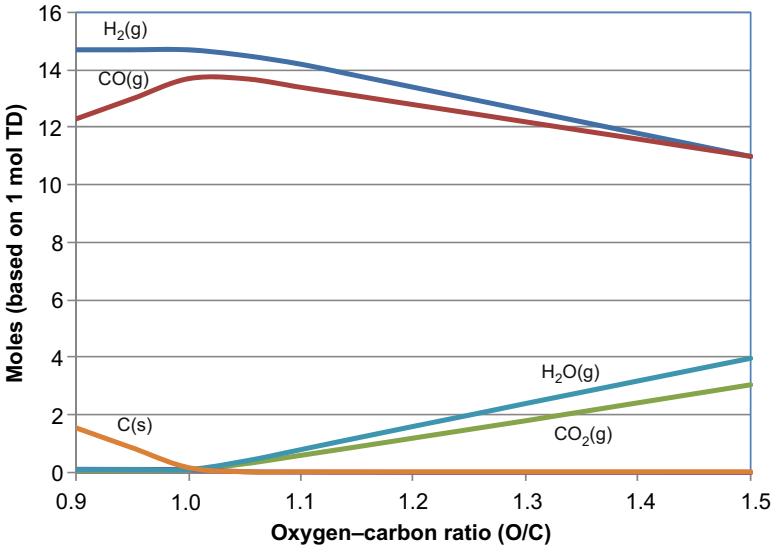

FIGURE 5.6 Equilibrium product distribution for the POX of TD for different O/C ratios: 900 °C, 0.10 MPa (calculations using HSC Chemistry 5.0 [31]).

complete over the range of O/C ratios studied. Thermodynamically, carbon formation goes to zero at O/C ratios greater than 1.0, with the highest H_2 and CO yields near this ratio. The levels of combustion products, CO_2 and H_2O, increase with a corresponding decline in H_2 and CO levels above an O/C of 1.0.

The effect of the O/C ratio on the product distributions for TD POX at 900 °C is shown in Fig. 5.6. The trends for this hydrocarbon are qualitatively identical to those for methane.

A comparison of oxygenated hydrocarbons to alkanes is presented in Table 5.3. Here, the temperature for each fuel above which carbon formation is thermodynamically unfavorable is presented for an O/C ratio of 1.2. This temperature for methane and ethane is more than 100 °C higher than for the alcohols. It should be noted that the oxygen in the alcohols is not calculated into the O/C ratio. This indicates that operating conditions for POX of alcohols can be significantly lower than alkanes. Another example is $C_{19}H_{36}O_2$, a model compound for biodiesel, which has a "zero carbon" temperature 29 °C lower than $C_{14}H_{30}$ and $C_{18}H_{38}$, model compounds for ordinary diesel. Table 5.3 also shows that the temperature at which the enthalpy equals zero for oxygenated hydrocarbons is consistently higher than alkanes with the same carbon number.

Based on the above results, the effect of the O/C ratio on the product distributions for ethanol POX was calculated at 600 °C, rather than 900 °C, and is presented in Fig. 5.7. Under

TABLE 5.3 Comparison of Thermodynamic Properties for Oxygenated Hydrocarbons to Alkanes: O/C = 1.2 (Calculations Using HSC Chemistry 5.0 [31])

Fuel	$T_{C=0}$ (°C)	$T_{\Delta H=0}$ (°C)
CH_4	706	699
C_2H_6	711	840
$C_{14}H_{30}$	713	1031
$C_{18}H_{38}$	713	1039
CH_3OH	512	1202
C_2H_5OH	612	1111
C_2H_6O	612	1253
$C_{19}H_{36}O_2$	684	1167

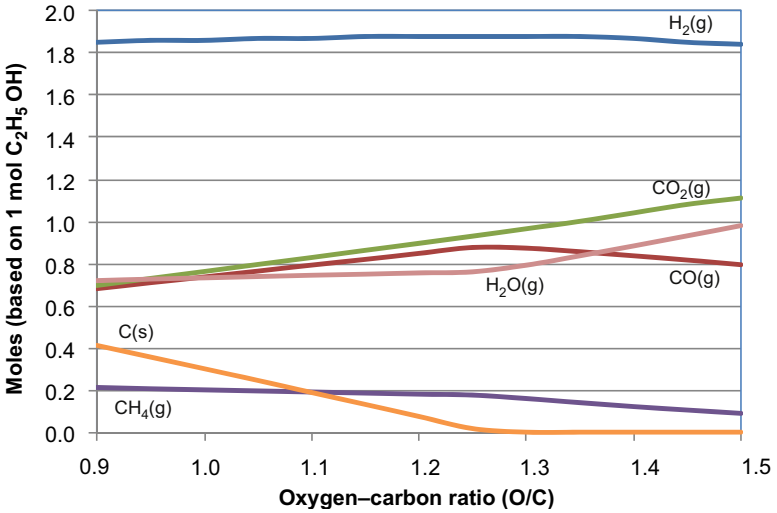

FIGURE 5.7 Equilibrium product distribution for the POX of ethanol for different O/C ratios: 600 °C, 0.10 MPa (calculations using HSC Chemistry 5.0 [31]).

these conditions, complete conversion of hydrocarbons (CH_4) is not accomplished. Further, an O/C ratio of 1.25 is required to eliminate carbon formation.

5.3. REACTION MECHANISMS AND KINETICS

5.3.1. Reaction Mechanisms

The reaction mechanisms for the CPOX of hydrocarbons are extremely complex. This discussion focuses on the CPOX of methane for simplicity and is generalized for any catalyst. Additional discussions of mechanism related to specific catalytic metals are given in Section 5.4. The mechanisms for higher hydrocarbons are much more complex with a significantly greater number of possible side reactions and intermediate steps. Additionally, cracking reactions become significant for higher hydrocarbons, making the mechanism even more difficult to predict.

There are several challenges to determining a reaction mechanism for the CPOX of methane. First, it is likely that more than one mechanism is occurring for a given reaction system. Second, the nature of the catalyst, which may change over time, can affect which mechanism dominates. Further, the interaction of the active metal with the support may play a role. Third, the reaction mechanism can change under different operating conditions (O/C ratio, temperature, space velocity, etc.). These factors and their potential effects on the reaction mechanisms for the CPOX of methane are discussed in depth in the following paragraphs.

Two main mechanisms for the CPOX of methane have been proposed and reviewed in literature: direct and indirect [6]. In the direct mechanism, methane is decomposed to elemental carbon and hydrogen. Next, the elemental carbon on the surface of the catalyst reacts with oxygen on the surface to form CO. Finally, H_2 and CO gas desorb from the surface to yield synthesis gas.

In the indirect mechanism, sometimes referred to as combustion and reforming reactions (CRRs), the formation of the products takes place in two separate regions, or zones, of the reactor. First, a portion of the methane reacts with oxygen to form combustion products (H_2O and CO_2). This is followed by SR and CO_2 reforming reactions with the remaining

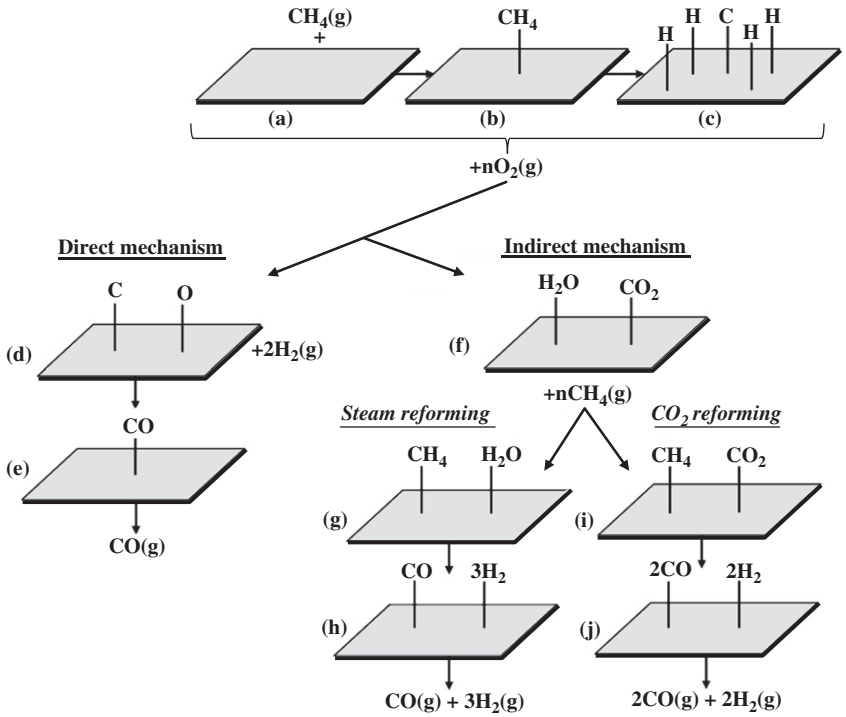

FIGURE 5.8 Diagram comparing the direct and indirect mechanism for the CPOX of methane.

methane in the second region of the bed. Additionally, a mixture of the direct and indirect mechanisms has been proposed.

Figure 5.8 shows a simplified comparison of the direct and indirect mechanism for the CPOX of methane on a catalyst surface. The first three steps are the adsorption and decomposition of methane to carbon and hydrogen species on the surface, present in both mechanisms, represented in Fig. 5.8a–c. The dissociation of methane to each CH_x species is not presented. For the direct mechanism, the dissociative adsorption of oxygen follows, which oxidizes the surface carbon to CO (Fig. 5.8d and e). This is then desorbed into the bulk gas.

For the indirect mechanism, the combustion products CO_2 and H_2O are formed from the adsorbed oxygen (Fig. 5.8f). This can occur if the rate of oxidation of the CO species is faster than the rate of CO desorption and if the OH species (not shown) formed from the reaction of oxygen with surface hydrogen are very stable, also leading to deep oxidation. The indirect mechanism then can take two parallel pathways to convert the remaining methane via SR (Fig. 5.8g and h) and CO_2 reforming (Fig. 5.8i and j). These reactions are both highly endothermic and dominate once all the oxygen fed with the methane is consumed in the first part of the bed. Other possible side reactions not shown are the WGS and methanation reactions.

Table 5.4 provides a summary of the studies reviewed by York et al. [6] for the direct and indirect mechanisms for methane CPOX. They correlate the mechanism to reduced versus oxidized catalyst surfaces, where reduced sites promote the direct mechanism and oxidized sites promote the indirect mechanism. In some studies, both oxidized and reduced species are

TABLE 5.4 Summary of Methane CPOX Mechanisms Provided by York et al. [6]

Direct mechanism			Indirect mechanism		
Author(s)	**Metal(s)**	**Support(s)**	**Author(s)**	**Metal(s)**	**Support(s)**
Peters et al. [36]	N/A	N/A	Dissanayake et al. [37]	Ni	Alumina
Au et al. [38–39]	Ni	Silica, alumina	Vermeiren et al. [40]	Ni	Alumina, silica, zirconia, zeolites
Hu and Ruckenstein [41–42]	Ni	La_2O_3	Heitnes et al. [43–44]	Ni, Pt, Pd	Alumina, cordierite
Mallens et al. [45]	Pt	N/A	Passos et al. [46]	Pt	Alumina, zirconia, Ceria
Passos et al. [46]	Pt	Yttria	Hochmuth [47]	Pt/Pd	Ceria/alumina
Hickmann and Schmidt [32–35,48]	Pt, Pt-Rh	Alumina	Oh et al. [49]	Pt, Pd, Rh w/ and w/o Ce	Alumina
Baerns et al. [50–52]	Rh	Alumina	Heitnes et al. [53]	Pt-wire gauze	N/A
Qin et al. [54]	Ru	MgO	Horn et al. [55]	Rh	Alumina
Wang et al. [56]	Rh	Alumina	Boucouvalas et al. [57]	Rh	Alumina
			Wang et al. [56]	Rh	Alumina

present. It is given that the indirect mechanism is expected for the catalyst exotherm studies reported. Further, it is concluded that the direct mechanism proposed by Hickmann and Schmidt [32–35] is reasonable at low surface coverage; however, the indirect mechanism is more strongly supported for "working catalysts."

5.3.1.1. Direct Mechanism

A complete set of steps for the direct mechanism for the CPOX of methane is much more complex than shown in Fig. 5.8. One such set of reaction steps is provided by Wang et al. [56]. Their mechanism studies were conducted with Rh/Al_2O_3 through the use of temporal analysis of products (TAPs). This method used a pulse reactor under vacuum with residence times for each pulse that are less than the reaction, adsorption, and/or desorption times. The results of this study yielded a mechanism consisting of 24 steps divided into five categories: (1) adsorption and dissociation of methane, (2) surface reactions, (3) desorption, (4) events on Al_2O_3 sites, and (5) inverse spillover from the support to the metal surface. These steps are listed in Table 5.5.

Step 1 in Table 5.5 shows the dissociative adsorption of oxygen, which was not shown in Fig. 5.8. Steps 2–6 provide a more detailed step-by-step look at the adsorption and dissociation of methane represented previously in Fig. 5.8a–c. Step 8 is the formation of CO from the reaction of surface oxygen and carbon, while Steps 7, 9, 10, and 13 show the formation of hydroxyl groups and their role in oxidizing surface carbon species to CO through the formation of –COH. Weak Me–O (Me: metal) bonds help produce CO as primary product.

Steps 11, 12, 16, and 17 show the formation of combustion products, CO_2 and H_2O. As

TABLE 5.5 CPOX Reaction Mechanism by Wang et al. [56]

Adsorption steps and dissociation of methane

$O_2 + 2^* \leftrightarrow 2O^*$ (1)
$CH_4 + ^* \leftrightarrow CH_4^*$ (2)
$CH_4^* + ^* \leftrightarrow CH_3^* + H^*$ (3)
$CH_3^* + ^* \leftrightarrow CH_2^* + H^*$ (4)
$CH_2^* + ^* \leftrightarrow CH^* + H^*$ (5)
$CH^* + ^* \leftrightarrow C^* + H^*$ (6)

Surface reaction steps

$O^* + H^* \leftrightarrow OH^* + ^*$ (7)
$C^* + O^* \leftrightarrow CO^* + ^*$ (8)
$C^* + OH^* \leftrightarrow COH^* + ^*$ (9)
$COH^* + ^* \leftrightarrow CO^* + H^*$ (10)
$CO^* + O^* \leftrightarrow CO_2^* + ^*$ (11)
$CO^* + OH^* \leftrightarrow CO_2^* + H^*$ (12)
$CH_x^* + OH^* \leftrightarrow CH_{x+1}O^* + ^*$ (13)
$CH_x^* + O^* \leftrightarrow CH_xO^* + ^*$ (14)
$CH_xO^* + ^* \leftrightarrow CO^* + xH^*$ (15)
$OH^* + H^* \leftrightarrow H_2O^* + ^*$ (16)
$2OH^* \leftrightarrow H_2O^* + O^*$ (17)

Desorption steps

$CO^* \leftrightarrow CO + ^*$ (18)
$2H^* \leftrightarrow H_2 + 2^*$ (19)
$CO_2^* \leftrightarrow CO_2 + ^*$ (20)
$H_2O^* \leftrightarrow H_2O + ^*$ (21)

Events on Al_2O_3 sites

$H_2O + \#O\# \leftrightarrow OH\# + H{-}O\#$ (22)
$OH\# + H{-}O\# \leftrightarrow O\# + H_2O\#$ (23)

Inverse spillover from the support to the metal surface

$H_2O\# + ^* \leftrightarrow H_2O^* + \#$ (24)

**Metal sites and # Al_2O_3 sites.*

mentioned earlier, the stability of the adsorbed CO and OH surface species will control the extent of the formation of these products. Although this is discussed as a direct mechanism, it does not exclude the formation of these over-oxidized species. However, this is not considered as an indirect mechanism since it does not include steps for the reaction of methane with adsorbed water or CO_2.

Steps 22–24 show how the nature of the support can play a role in the formation of hydroxyl and the combination of these hydroxyl groups to form water on the support surface. This demonstrates how the nature of the support can affect the steps in the CPOX of methane.

In the direct mechanism, reaction conditions require reduced, highly active metals and low methane conversion, which suggest low temperatures and/or high space velocities. The increased space velocity can cause reduction in methane conversion from either shorter residence time or decreased catalyst surface temperatures. Longer residence time of adsorbed species on the catalyst surface increases the formation of combustion products, leading to the indirect mechanism. Differences between the bulk gas and surface temperatures have been shown to be as high as 300 °C [37]; therefore, lower temperatures can suppress the combustion reactions, again leading to the direct mechanism.

The dissociation of methane has been reported as the rate-limiting step for CPOX. The oxidation state of the active metal and the role of oxygen in methane dissociation are subjects of debate. Au and Wang [58] studied Rh and RhO catalysts for the CPOX of methane. They reported that reduced Rh metal was the active site for the reaction and that RhO reduces quickly to a metallic site. At high Rh surface coverages, the dispersion was low, and it was determined that the larger metal sites could completely dissociate methane. At low coverages and high dispersion, it was determined that lattice oxygen could play a role in the dissociation of methane.

TABLE 5.6 Comparison of Methane Dissociation With and Without Oxygen Participation [58]

Elementary reaction	E_a(kJ/mole)	Surface oxygen adsorbed	E_a (kJ/mole)		
			On-top	Bridge	Hollow
$CH_4 \rightarrow CH_3 + H$	61	$CH_4 + O \rightarrow CH_3 + OH$	0	56	77
$CH_3 \rightarrow CH_2 + H$	103	$CH_3 + O \rightarrow CH_2 + OH$	31	95	116
$CH_2 \rightarrow CH + H$	100	$CH_2 + O \rightarrow CH + OH$	25	89	111
$CH \rightarrow C + H$	21	$CH + O \rightarrow C + OH$	0	33	61

Oxygen adsorbed on the metal has been reported to promote dehydrogenation, while oxygen adsorbed on bridge or hollow sites does not. Some studies report that methane is activated by lattice oxygen of the support, while others suggest its dissociation takes place on the active metal site with no interaction with oxygen. Au and Wang [58] used the bond-order conservation Morse-potential approach [59] to evaluate the activation of methane with and without the interaction of chemisorbed oxygen. A comparison of the activation energies for these two scenarios is given in Table 5.6. It was determined that oxygen can play a role in the dissociation of methane, but that it occurs with oxygen species at the on-top sites and not with the bridge or hollow sites.

5.3.1.2. *Indirect Mechanism*

The indirect mechanism along a typical catalyst bed can be represented by Fig. 5.9. At the top of the bed, all oxygen is consumed by the exothermic reaction with a portion of the methane in the feed. This region can be on the order of 10% of the total bed and is controlled by the O/C ratio and temperature. A temperature spike as well as localized hot spots promote the formation of combustion products. The remaining methane is converted in the bottom portion of the catalyst bed through endothermic secondary reforming reactions with the methane and water produced in the first region.

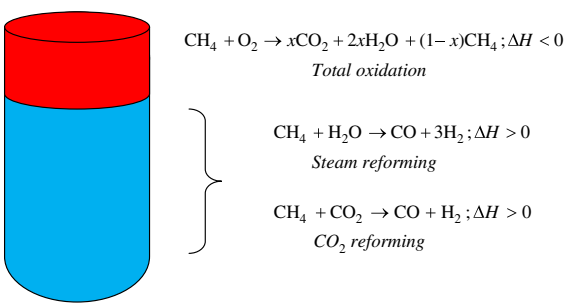

FIGURE 5.9 Schematic diagram of CPOX reactor with indirect mechanism.

Horn et al. [55,60,61] present results supporting the indirect mechanism for the CPOX of methane over Rh catalysts. Although their studies included autothermal conditions, the mechanism proposed is analogous. In their investigations, spatially resolved measurements of temperature and gas compositions down the length of the catalyst bed were made through the use of a quartz capillary tube. These experiments, accompanied by numerical simulations, studied CPOX of methane over a range of O/C ratios and flow rates. Some of their results are presented in Fig. 5.10. Their results support the indirect mechanism and found that oxygen conversion is complete within the first 2 mm of the catalyst bed, where some H_2 and CO are formed. Carbon dioxide was also formed in the oxidation zone, but additional amounts were formed in some cases downstream from the WGS reaction. Additionally, the results suggested that CO_2 reforming did not occur and was therefore not considered part of their mechanism. Instead, unconverted methane

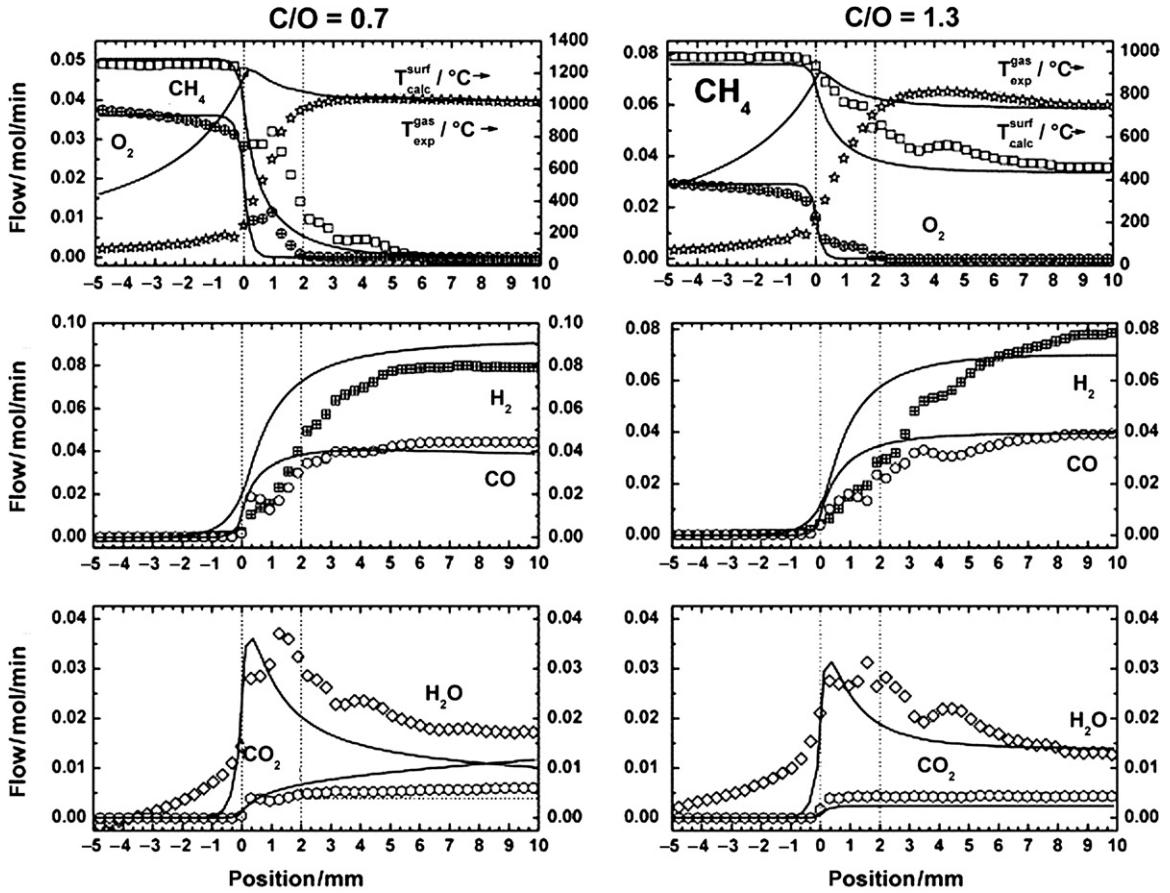

FIGURE 5.10 Species and temperature profiles for CPOX of methane at different C/O ratios. *Reprinted from Horn et al. [55], Copyright (2006), with permission from Elsevier.*

reacted with steam in the feed and steam formed in the oxidation region at the inlet. Figure 5.10 from one of these investigations [55] provides the composition and temperature profiles for one of the conditions reported.

5.3.1.3. Effect of Space Velocity

Typically, increasing space velocity reduces conversion since the residence time decreases. In an exothermic reaction, like the oxidation of methane, increasing the space velocity should therefore decrease the amount of heat generated and consequently reduce the temperature spike at the front of the catalyst bed (Fig. 5.11). Further, an increase in the flow of a lower temperature feed should decrease the temperature spike, especially in cases with heavy dilution. As stated earlier, the difference in gas feed temperature could have a significant effect on the catalyst surface temperature. However, there appears to be some inconsistencies surrounding these trends in the literature.

It has been reported that increasing the space velocity increases the conversion of methane under partial oxidation conditions and also increases the temperature spike at the front of the catalyst bed. For example, Fig. 5.12 shows the measured gas phase temperature of a study

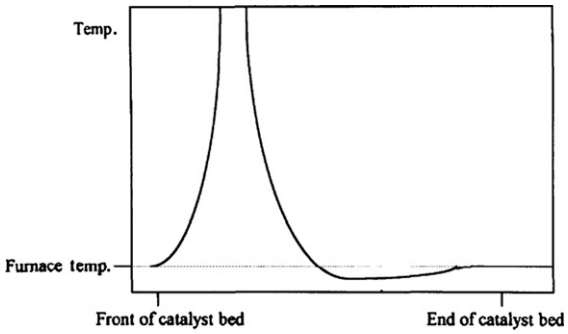

FIGURE 5.11 Schematic representation of the temperature found in CPOX catlayst beds. *Reprinted from Tsang et al. [3], Copyright (1995), with permission from Elsevier.*

conducted by Enger et al. [63] using a Ni-based catalyst. It is clear that the increased space velocity resulted in a higher temperature spike at the front of the reactor bed. The temperature spike occurring before the beginning of the bed was explained by the potential presence of catalyst fine particles in the "inert" portion of the bed, which likely occurred during loading of the reactor.

This phenomenon is also reported by Tsang et al. [3]. Here, the catalyst was Ni/MgO, and

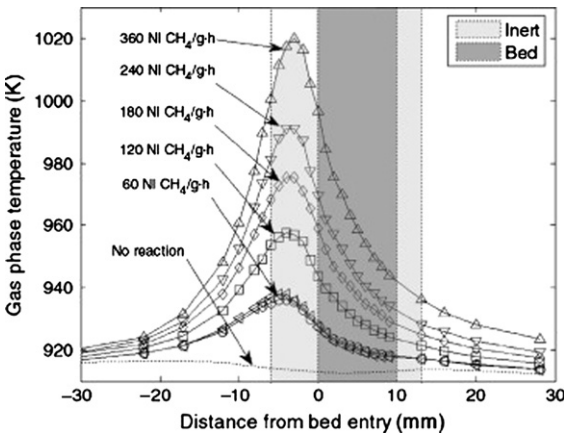

FIGURE 5.12 Position of temperature spike in reactor bed for CPOX of CH_4 on Ni/α-Al_2O_3. *Reprinted from Enger et al. [63], Copyright (2009), with permission from Elsevier.*

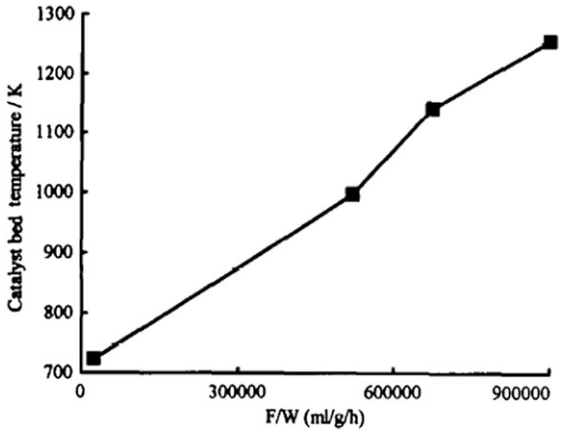

FIGURE 5.13 Effect of flow rate on catalyst-bed temperature using Ni/MgO (Ni/Mg = 3) catalysts. Furnace temperature = 723 K, O/C = 1.0. *Reprinted from Tsang et al. [3], Copyright (1995), with permission from Elsevier.*

the space velocity is reported up to 900,000 ml $g^{-1}h^{-1}$ (Fig. 5.13). The furnace around the reactor was set at 973 K, and the highest measured temperature in the catalyst bed approached 1300 K at the highest space velocity tested.

It should be considered that the expectation of a decreased conversion with higher space velocity may be assuming a specific mechanism, which if not representative of what is actually taking place, may alter the response of the system to different conditions. It must also assume that the starting gas velocities are already beyond the flow regime where mass and heat transfer limitations are not issues. It is possible, therefore, that reports of increasing conversion with increasing space velocity indicate that the initial flows were not high enough to overcome diffusion and heat transfer resistance. It may also indicate the presence of two zones in the catalyst bed where different reactions dominate, as in the indirect mechanism. In this case, an increase in flow may result in a decrease in the initial conversion of methane at the front of the bed but increased heat transfer at the end of the bed where secondary reforming reactions occur, leading to an overall increase in methane conversion from steam and CO_2 reforming.

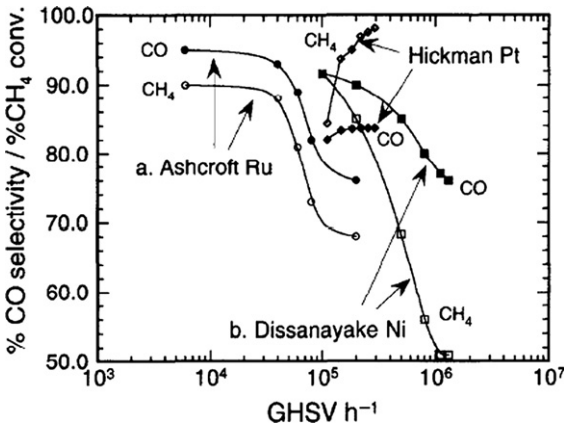

FIGURE 5.14 Plot of the effect of GHSV on CO selectivity and CH_4 conversion. (a) Vernon et al. [64] (Ashcroft Ru), (b) Dissanayake et al. [37], and (c) Hickman and Schmidt [32]. *Reprinted from Bharadwaj and Schmidt [2], Copyright (1995), with permission from Elsevier.*

As discussed in Section 5.3.1, the catalyst used will determine which mechanism dominates and, as a result, can potentially yield apparently contradictory results under similar conditions. Figure 5.14 provides an example of how this can occur. In their review of CPOX literature, Bharadwaj and Schmidt [2] generated this figure from three different studies for comparison. Three different catalysts are represented: Ni, Ru, and Pt. For the Ni and Ru catalysts, the trend expected for increasing space velocity is observed − methane conversion decreases. This figure also shows that CO selectivity decreases with increasing space velocity for these catalysts. However, for the Pt catalyst reported by Hickman and Schmidt [32], there is a steady increase in methane conversion and an increase followed by a leveling off of CO selectivity as space velocity increases. It should be noted that the range of space velocity studied for the Pt catalyst is relatively narrow. It may be expected that, if the Pt catalyst were to be tested at higher space velocities, it too would begin to yield a decrease in methane conversion and a concomitant drop in CO selectivity.

It would be impossible to draw any conclusions from the data in Fig. 5.14 without closely examining the operating conditions associated with each study. For example, the studies conducted on the Ru and Ni catalyst had an O/C ratio in the feed of 1.0 and 1.12, respectively, while the study conducted with the Pt catalyst had an O/C ratio of 2.22. This alone may explain the observed difference. Further, the Ni and Ru catalyst studies were conducted at similar temperatures, 800 °C and 777 °C, respectively. The Pt catalyst was tested at 1227 °C. Therefore, even at lower temperatures, the excess oxygen present for the Ni and Ru catalysts will result in a higher yield of combustion products (CO_2 and H_2O) corresponding to lower CO selectivity. For the Pt catalyst, the inlet oxygen concentration is sub-stoichiometric, which produces less combustion products even as the methane conversion increases. Also, at the higher temperatures, the exothermic WGS reaction will be suppressed.

5.3.1.4. *Effect of Catalyst Oxidation State*

When conducting mechanistic studies for the CPOX of methane, many factors can produce apparently contradicting results. However, the feed conditions, the metal type, and the nature of the catalyst surface, as well as the catalyst−surface interactions, should be carefully considered. It is likely under typical operating conditions both mechanisms may be present, at least for some period of time. While the catalyst may initially produce syngas via the direct mechanism, as the catalyst changes over time, the indirect mechanism may emerge. Indeed, it is not a question of which mechanism is at work, but which mechanism dominates, and for how long.

Boucouvalas et al. [65] reported a direct mechanism for a Ru catalyst supported on titanium oxide, Ru/TiO_2. This catalyst was compared to Ni, Rh, Pd, Ir, and Ru catalysts supported on alumina. Low methane conversions (oxygen conversion $< 100\%$) produced a

minimal rate of reforming reactions due to oxidized or partially oxidized metal surfaces and produced synthesis gas primarily by the direct mechanism. It was found that, as methane conversion increased, the formation of H_2O and CO_2 increased, leading to an increase in reforming reactions. The alumina-supported catalysts produced syngas via the indirect mechanism due to the oxidation of the metal surfaces. However, the Ru/TiO_2 catalyst maintained high CO selectivity even at lower methane conversions, suggesting that the direct mechanism could still dominate. The ability of Ru/TiO_2 to maintain a reduced surface under oxidizing conditions was determined to promote the direct mechanism. Isotopic labeling experiments estimated that the total CO produced by steam and CO_2 reforming (indirect mechanism) was less than 8% of the total CO produced. The interaction of the Ru with the TiO_2 support was believed to produce a different type of surface state, which was not able to be fully characterized.

Another example of the effect of metal oxidation state can be found in a study by Rabe et al. [66]. This work also examined Ru catalyst and used pulses of CH_4/O_2 and measured the products. The results of this study are presented in Fig. 5.15 and indicate that, for the partially oxidized surface, CO_2 was the primary product and that, as the Ru became more reduced with the higher number of pulses, CO became the primary product. This supports again that an oxidized catalyst promotes the indirect mechanism.

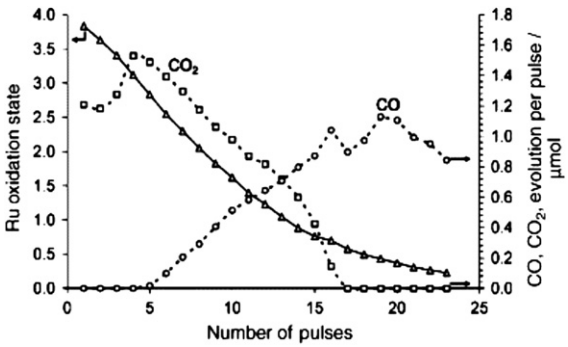

FIGURE 5.15 Effect of metal oxidation state on reaction mechanism. *Reprinted from Rabe et al. [66], Copyright (2007), with permission from the Royal Society of Chemistry.*

5.3.1.5. *Mechanism for Methanol*

A complete discussion of the reaction mechanisms for oxygenated hydrocarbons would be too complex for the scope of this chapter. Although all oxygenates adsorb on a catalyst through the oxygen lone pair electrons, they contain such a broad range of functional groups that a general discussion of the reaction mechanism is not practical. Therefore, a brief discussion of the mechanism for the CPOX of methanol will suffice as an illustration, and some more detailed discussion for other oxygenates are provided in Section 5.6.

The CPOX of methanol can be said to proceed similar to the indirect mechanism of methane. However, the first step after adsorption is the formation of a methoxy species, followed by the formation of formate species, and ultimately surface C, H, and O. These surface species then combine to form synthesis gas. The product distribution will depend heavily on the reaction conditions (i.e., O/C ratio, temperature, space velocity, etc.). One proposed mechanism for methanol CPOX is given by Eq. (5.12) [68].

$$\begin{aligned} CH_3O^* \rightarrow CH_2O^* + H^* \rightarrow CHO^* + 2H^* \\ \rightarrow CO^* + 3H^* \end{aligned} \tag{5.12}$$

5.3.2. Kinetic Studies

Kinetic studies for the CPOX of methane are very difficult for many of the same reasons as mechanism studies. First, an appropriate mechanism must be selected. Because the reactions occur very rapidly, mass transfer limitations may dominate. These limitations can make kinetic measurements inaccurate. Further, erroneous results can be obtained from the presence of hot spots, heat transfer limitations, surface

coverage, and oxidation state of the active surface. Factors that contribute most to hot spots include contact time, solid dilution, gas dilution, and metal loading. Different approaches to overcome these challenges include the use of high space velocities, dilute feed streams, and dilute or low-coverage catalysts, all of which have undesired consequences for industrial applications.

Kinetic studies have been conducted with the goal of analyzing both direct and indirect reaction mechanisms. Boucouvalas et al. [65] examined the direct reaction mechanism with Ru/TiO_2 catalyst. The effects of heat and mass transfer limitations were first studied over Rh catalysts since Rh is most active for methane CPOX. An additional concern identified in this study was the difference in temperature between the catalyst surface and the temperature measured in the gas stream. This difference was reported to be as high as 300 °C [37].

Boucouvalas et al. [65] also discussed the challenges encountered by increasing the space velocity in the reactor. While high space velocities can be used to overcome mass transfer limitations, they can contribute to an increase in the temperature spike at the front of the catalyst bed. To avoid this, both the reactant mixture and catalyst bed were diluted to operate in the kinetic regime.

Hu and Ruckenstein [42] conducted transient kinetic studies for methane CPOX over Ni/La_2O_3 catalyst. As shown in Table 5.4, their results supported the direct mechanism. The kinetic studies were conducted at low temperatures (450−700 °C) and atmospheric pressure, using pulse-transient analysis. The rate-controlling step was found to be the reaction between surface carbon species and surface oxygen species. This was supported by the fact that the formation of these species and the desorption of CO were much faster than the formation of CO. Theoretical values for the activation energy for methane decomposition and oxidation of carbon on a Ni (111) surface also confirmed this as the limiting step. Further, it was shown that as the number of pulses increased, the CO selectivity decreased due to the oxidation of the catalyst. Overall, the methane conversion is dependent on its rate of dissociation, and CO selectivity was dependent on the binding strength of the oxygen species to the metal surface (i.e., strong binding produced higher CO selectivities).

TABLE 5.7 Reaction Mechanism Steps for Kinetic Study [69]

Reaction	Reaction rate	Step
$CH_4 + {}^*_1 \rightarrow$ intermediate 1 $\rightarrow$ C-$^*_1$ + 4H-$^*_1$	RDS	1
$O_2 + {}^*_2 \rightarrow O_2 - {}^*_2$	Equilibrium	2
O_2-$^*_2 + {}^*_2 \rightarrow$ 2O- $^*_2$	Fast	3
C- $^*_1$ + O-$^*_2 \rightarrow$ CO-$^*_1 + {}^*_2$	RDS	4
CO-$^*_1$ + O-$^*_2 \rightarrow CO_2 + {}^*_1 + {}^*_2$	Fast	5
H-$^*_1$ + O-$^*_2 \rightarrow$ OH-$^*_1 + {}^*_2$	Very fast	6
OH-$^*_1$ + H-$^*_1 \rightarrow H_2O + 2{}^*_1$	Very fast	7

A kinetic study over Ni/La_2O_3 catalyst was conducted by Tsipouriari and Verykios [69]. Their findings suggested the indirect mechanism, although they did concede that CO could be formed by the direct mechanism at low oxygen concentration, depending on the oxidation state of the Ni crystallites. Both the decomposition of methane and reaction of adsorbed C and O to form CO were identified as the rate determining steps. A mechanism is provided for the formation of CO_2 from adsorbed CO, which is assumed to precede later reforming reactions. Table 5.7 presents the mechanism proposed in this study.

In their experiments, methane and oxygen conversions were less than 10%. The main conclusions of this study were that the oxygen partial pressure strongly affected the rate of reaction, while the partial pressure of methane did not. Also, it was determined that direct

TABLE 5.8 Partial Oxidation of Methane Reaction Scheme over Supported Pt Adapted from the Proposition of de Smet et al. [71] to Account for the Reversible Oxygen Adsorption, Carbon Species Oxidation, and CO_2 Formation; *Reprinted from Gubanova et al. [70], Copyright (2009), with permission from Elsevier.*

Reaction	A or S^0 ($Pa^{-1}\,S^{-1}$ or S^{-1})	E_{act} (kJ mol^{-1})	Rate equation	Step
$O_{2(g)} + 2^* \rightarrow 2O^*$	0.11	0	$k_{1a}P_{O_2}\theta^*$	1a
$2O^* \rightarrow O_{2(g)} + 2^*$	1.7×10^{13}	200	$k_{1b}\theta_O^2$	1b
$CH_{4(g)} + 2O^* \rightarrow C^* + 2H_2O_{(g)} + {}^*$	2.4×10^5	48.2	$k_2 P_{CH_4}\theta_O^2$	2
$C^* + O^* \rightarrow CO^* + {}^*$	1.0×10^{13}	62.8	$k_{3a}\theta_C\theta_O$	3a
$CO^* + {}^* \rightarrow C^* + O^*$	1.0×10^{11}	184	$k_{3b}\theta_{CO}\theta^*$	3b
$CO^* + O^* \rightarrow CO_{2(g)} + 2^*$	1.9×10^9	30	$k_{4a}\theta_{CO}\theta_O$	4a
$CO_{2(g)} + 2^* \rightarrow CO^* + O^*$	6.3×10^2	28	$k_{4b}P_{CO_2}\theta^{2*}$	4b
$CO^* \rightarrow CO_{(g)} + {}^*$	1.0×10^{13}	126	$k_{5a}\theta_{CO}$	5a
$CO_{(g)} + {}^* \rightarrow CO^*$	0.84	0	$K_{5b}P_{CO}\theta^*$	5b

* *Denotes a Pt active site or a site located on the ceria* k_x *denotes the term* $A_x \exp(-E_{act,x}/RT)$ *or* $S^0_x \exp(-E_{act,x}/RT)$, *respectively.*

oxidation occurs at low oxygen partial pressures under specific conditions. However, under typical oxygen partial pressures, the Ni catalyst will be oxidized, which is active for combustion of methane to CO_2. Based on this mechanism, the following rate expression was developed:

$$R = \frac{k_1 K_2 k_3 P_{CH_4} P_{O_2}}{(k_1 K_2 P_{CH_4} P_{O_2} + k_1 P_{CH_4} + K_2 k_3 P_{O_2})} \quad (5.13)$$

This kinetic model predicted well the kinetics for the indirect mechanism and was in good agreement with the experimental data.

Another kinetic study was conducted using a 1.4-wt% $Pt/Pr_{0.3}Ce_{0.35}Zr_{0.35}O_x/\alpha\text{-}Al_2O_3$ catalyst by Gubanova et al. [70]. The mechanism was a sequence initially used in similar studies by de Smet et al. [71] and includes steps for reversible oxygen adsorption, carbon species oxidation, and CO_2 formation. Table 5.8 provides the modified reaction sequence used to compare to experimental data. The kinetic model developed matched the experimental results for H_2 formation well; however, the mechanism for H_2 formation was not clear. Instead of being produced by methane decomposition, reforming reactions, or WGS, it appeared to be formed by the dissociation of water. This mechanism for H_2 formation is not typically associated with CPOX.

Table 5.9 presents a reaction scheme and rate expressions for the same study [70]. It incorporates the formation of H_2 by the coupling of surface hydrogen species (Step 6a) from the dissociation of methane (Step 2). This scheme also presents the step for H_2 formation from the dissociation of water (Step 7b). The model demonstrated good agreement with experimental data. The most significant conclusion of this paper had to do with the role of the ceria support in the kinetic rates. The kinetic model considers CO_2 reforming, since ceria catalyzes CO_2 dissociation, and suggests this as a parallel reaction pathway not present in other data presented in literature for a Pt gauze catalyst.

One final example of kinetic model development is by de Groote and Froment [72]. This study examined methane CPOX over a Ni catalyst. It compared a varying degree of reduction (VDR) model to a bivalent (BV) catalyst model and included the effects of co-feeding

TABLE 5.9 POM Reaction Scheme over Supported Pt Proposed in this Study Accounting for H_2 Production. *Reprinted from Gubanova et al. [70], Copyright (2009), with permission from Elsevier.*

Reaction	A or S ($Pa^{-1}\,S^{-1}$ or S^{-1})	E_{act} (kJ mol^{-1})	Rate equation	Step
$O_{2(g)} + 2^* \rightarrow 2O^*$	0.68	0	$k_{1a}P_{O_2}\theta^{2*}$	1a
$2O^* \rightarrow O_{2(g)} + 2^*$	1.0×10^{14}	200	$k_{1b}\theta^2_O$	1b
$CH_{4(g)} + 5^* \rightarrow C^* + 4H^*$	9.35×10^3	125.2	$k_2 P_{CH_4}\theta^5_O$	2
$C^* + O^* \rightarrow CO^* + ^*$	1.0×10^{13}	62.8	$k_{3a}\theta_C\theta_O$	3a
$CO^* + ^* \rightarrow C^* + O^*$	1.0×10^{11}	184	$k_{3b}\theta_{CO}\theta^*$	3b
$CO^* + O^* \rightarrow CO_{2(g)} + 2^*$	3.2×10^{13}	37.4	$k_{4a}\theta_{CO}\theta_O$	4a
$CO_{2(g)} + 2^* \rightarrow CO^* + O^*$	9.9×10^3	10	$k_{4b}P_{CO_2}\theta^*_2$	4b
$CO^* \rightarrow CO_{(g)} + ^*$	1.0×10^{13}	126	$k_{5a}\theta_{CO}$	5a
$CO_{(g)} + ^* \rightarrow CO^*$	0.71	0	$k_{5b}P_{CO}\theta^*$	5b
$2H^* \rightarrow H_{2(g)} + 2^*$	1.0×10^{14}	159.7	$k_{6a}\theta^2_H$	6a
$H_{2(g)} + 2^* \rightarrow 2H^*$	0.02	0	$k_{6b}P_{H_2}\theta^{2*}$	6b
$2H* + O^* \rightarrow H_2O_{2(g)} + 3^*$	1.0×10^{13}	20	$k_{7a}\theta^2_H\theta_O$	7a
$H_2O_{(g)} + 3^* \rightarrow 2H^* + O^*$	1.0×10^6	69	$k_{7b}P_{H_2O}\theta^{3*}$	7b

* *Denotes a Pt active site or a site located on the ceria; k_x denotes the term A_x exp ($-E_{act,x}/RT$) or $S^0{}_x$ exp ($-E_{act,x}/RT$), respectively.*

CO_2 and steam. The indirect mechanism was assumed, and the reaction steps are provided in Table 5.10. The methane SR and CO_2 reforming reactions are shown in Steps 2 and 5, respectively.

TABLE 5.10 Indirect Reaction Mechanism Steps for Kinetic Study by de Groote and Froment [72]

Reaction	Step
$CH_4 + 2O_2 \rightleftarrows CO_2 + 2H_2O$	1
$CH_4 + H_2O \rightleftarrows CO + 3H_2$	2
$CH_4 + 2H_2O \rightleftarrows CO_2 + 4H_2$	3
$CO + H_2O \rightleftarrows CO_2 + H_2$	4
$CH_4 + CO_2 \rightleftarrows 2CO + 2H_2$	5
$2CO \rightleftarrows C + CO_2$	6
$CH_4 \rightleftarrows C + 2H_2$	7
$C + H_2O \rightleftarrows CO + H_2$	8

The kinetic equations for these steps are provided in Table 5.11. The model was used to compare two states of the Ni catalyst. The first was the VDR model, and the second was the BV-model catalyst. The results of these simulations were compared to typical values in an industrial autothermal reformer, and both models were found to be in good agreement with observed data. It was concluded, therefore, that the calculated equilibrium values were accurate. The significant difference between the two models was identified as their predicted temperatures, which was higher for the VDR model. The significance of this finding is the effect of temperature on the Ni catalyst sites.

5.3.3. Summary for Mechanisms and Kinetics

Two mechanisms for the CPOX of methane were discussed and contrasted: direct and

TABLE 5.11 Kinetic Equations for Study by de Groote and Froment *Reprinted from de Groote and Froment [72], Copyright (1996), with permission from Elsevier.*

Kinetic equation	Step
$r_1 = \frac{k_1[CH_4][O_2]}{((1+K_1)[CH_4]+K_2[O_2])^2} + \frac{k_2[CH_4][O_2]^{0.5}}{1+K_1[CH_4]+K_2[O_2]}$	1
$r_2 = \frac{k_3/p_{H_2}^{2.5}(p_{CH_4}p_{H_2O} - p_{H_2}^3 p_{CO}/K_3)}{(1+K_{CO}P_{CO}+K_{H_2}P_{H_2}+K_{CH_4}P_{CH_4}+K_{H_2O}P_{H_2O}/P_{H_2})^2}$	2
$r_3 = \frac{\frac{k_3}{p_{H_2}^{3.5}}(p_{CH_4}p_{H_2O}^2 - p_{H_2}^4 p_{CO_2}/K_5)}{(1+K_{CO}P_{CO}+K_{H_2}P_{H_2}+K_{CH_4}P_{CH_4}+K_{H_2O}P_{H_2O}/P_{H_2})^2}$	3
$r_4 = \frac{\frac{k_4}{P_{H_2}\left(P_{CO}P_{H_2O} - \frac{P_{H_2}P_{CO_2}}{K_4}\right)}}{\left(1+K_{CO}P_{CO}+K_{H_2}P_{H_2}+K_{CH_4}P_{CH_4}+\frac{K_{H_2O}P_{H_2O}}{P_{H_2}}\right)^2}$	4
$r_5 = \frac{k_6P_{CO} - k_7P_{CO_2}/P_{CO}}{1+K_OP_{CO_2}/P_{CO}}$	5
$r_6 = \frac{\frac{k_8P_{CH_4}}{P_{H_2}^{1.5}} - k_9p_{H_2}^{0.5}}{(1+K_{H_2}P_{H_2})^2}$	6
$r_7 = \frac{k_{10}P_{H_2O}/P_{H_2}}{(1+K_{H_2}P_{H_2}+K_wP_{H_2O}/P_{H_2})^2}$	7
$r_8 = f(P_{O_2})$	8

indirect. Several factors that impact the reaction mechanism were analyzed, including the effect of temperature, O/C ratio, space velocity, and nature of the catalyst. Higher hydrocarbons generally exhibit the indirect mechanism, but the details of their mechanisms were not addressed due to the extreme complexity of reactions. A brief discussion of the reaction mechanism for oxygenates was also provided.

Several kinetic studies were also examined for methane. A comprehensive review of kinetic studies reported in literature was not given. Instead, examples were selected to demonstrate some of the approaches that have been taken and to highlight a few issues that must be considered when developing a mechanistic and kinetic model. There are few kinetic studies reported for higher hydrocarbons. One excellent example that is recommended for review, but was not discussed is the work by Rabe et al. [67].

5.4. LIGHT HYDROCARBONS

5.4.1. Methane

The CPOX of methane (natural gas) will be discussed initially and separately from other

lower hydrocarbons (C_2–C_4). There is enough difference in the properties and behavior of methane to justify this. For example, methane is much more stable, and its light-off temperature is much higher than its autoignition temperature. These properties can impact the operating conditions as well as the reaction mechanism discussed in the previous section.

A thorough review of the CPOX of methane was presented by Enger et al. [1], with a focus on reaction mechanisms over different metal catalysts. A summary of catalyst development and research conducted using cobalt and nickel catalysts is provided, as well as the effects of different promoting metals. For noble metal catalysts, only brief reviews of research conducted using iridium, palladium, and platinum were provided. More extensive discussion was given for rhodium and ruthenium catalysts, with emphasis on the effects of the catalyst supports. Because the mechanism is catalyst dependent, "methane dissociation, binding site preferences, the stability of OH surface species, surface residence times of active species and contributions from lattice oxygen atoms and support species" all contribute to observed results [1].

5.4.1.1. Base Metal Catalysts

The base metals that have been examined most for the CPOX of methane are Ni, Co, and Fe, and to a much lesser degree Cu. Supported Ni has been used for decades in industrial methane SR. These metal catalysts are attractive since they are significantly cheaper than noble metals; however, they have much lower activity and are more quickly deactivated by carbon formation, sulfur poisoning, and oxidation.

5.4.1.1.1. MODIFIED ALUMINA SUPPORTS

These metal catalysts are often supported on high surface area alumina supports to provide high levels of dispersion. Under the high temperature, highly oxidizing conditions of methane CPOX catalytic activity can be lost by the vaporization of the active metal, agglomeration of metal sites into larger clusters, which reduces dispersion, and encapsulation of the metals in collapsed pores from support sintering. Additionally, the formation of inactive spinel crystal structures may occur ($NiAl_2O_4$, $CoAl_2O_4$, and $FeAl_2O_4$). One approach to mitigate this issue is the addition of other metals to the surface of the alumina support to reduce sintering. For example, Ba and La have been added to alumina supports to retard the conversion of higher surface area γ-alumina to low surface area α-alumina. La has been shown to also slow down the incorporation of the Ni, Co, and Fe metals into the alumina support to form the spinel structure.

Table 5.12 provides the results of the temperature programmed reduction (TPR) study conducted by Slagtern et al. [73] for Ni, Co, and Fe catalysts on alumina with La. The reduction

TABLE 5.12 Results of TPR Studies and CO Selectivity Data for Ni, Co, and Fe Catalysts over La-Promoted Alumina Supports [73]

Catalyst	Temperature of peak maxima (°C)	Extent of reduction from H_2 consumption (%)	Temperature for total oxidation (°C)	CO selectivity (%)
Ni/Al_2O_3	770	117[a]	600	2
$Ni/La/Al_2O_3$	400, 995	100[a]	750	45
$Fe/La/Al_2O_3$	320, 505, 790, 930	53[b]	750–850	35–45
$Co/La/Al_2O_3$	950	10[c]	750	25

[a]*Assuming Ni(II);* [b]*Assuming Fe(III);* [c]*Assuming Co(II).*

TABLE 5.13 H_2/CO Ratios for Ni, Co, and Fe Catalysts over La-Promoted Alumina Supports. *Reprinted from Slagtern et al. [73], Copyright (1998), with permission from Elsevier.*

Temperature (°C)	Equilibrium	Ni/Al_2O_3	$Ni/La/Al_2O_3$	$Co/La/Al_2O_3$	$Fe/La/Al_2O_3$
600	2.7	0	0	*	0
700	2.1	0.2	0	1.8	0
800	2.0	1.0	0	2.0	0
900	2.0	1.9	1.0	2.0	1.9

* *Not possible to estimate*

peak for Ni decreases from 770 °C to 400 °C when La is added; the peak at 995 °C corresponds to reduction of the support. This result indicates that the Ni metal is more easily reduced when La is present, which would result in higher activity. The $Fe/La/Al_2O_3$ yielded four reduction peaks at 320, 505, 790, and 930°C, but was only 53% reducible. $Co/La/Al_2O_3$ yielded a single peak at 950 °C, and only 10% was reducible. Table 5.12 also shows that $Ni/La/Al_2O_3$ had improved CO selectivity over Ni/Al_2O_3, while the greatest CO selectivity was achieved by $Co/La/Al_2O_3$ at 45%; however, this does not necessarily suggest overall better performance, since the overall conversion is not presented.

Slagtern et al. [73] also compared the H_2/CO ratios obtained by these catalysts presented in Table 5.13. These results demonstrate that the $Co/La/Al_2O_3$ catalyst produced near-equilibrium values as low as 700 °C, while the $Ni/La/Al_2O_3$ and $Fe/La/Al_2O_3$ catalyst produced no H_2 until 900 °C. The Ni/Al_2O_3 catalyst showed some activity at 700 °C and yielded near-equilibrium values at 900 °C. These results seem to be in conflict with the results from the TPR data, suggesting that reducibility is not a main indicator of performance for this catalyst system.

5.4.1.1.2. BASIC SUPPORTS

The effect of the catalyst support has been studied extensively for the CPOX of methane for all types of metal catalysts. For this discussion, Ni-based catalysts will be used as an illustration, although support effects are seen with all catalysts. Indeed, the proper selection of a catalyst support is as significant as the active metal. The support can provide the desired metal dispersion. It can also be susceptible to degradation under extreme reaction conditions. Further, as discussed in Section 5.3, the support can even play a role in the reaction mechanism by lowering the activation energy of adsorbed species (i.e., methane) and can enhance the participation of adsorbed surface or lattice oxygen in the overall mechanism.

To demonstrate this point, the effect of several oxide supports on Ni catalysts for the CPOX of methane will be examined. A study presented by Tang et al. [74] compares Ni metal supported on MgO, CeO_2, and CaO. Figure 5.16 presents the results of temperature programmed oxidation (TPO) experiments on the Ni catalysts supported by the three different supports after (a) methane decomposition and (b) CO disproportionation. The Ni/MgO catalyst produced the least amount of CO_2 during the TPO, indicating that it had the smallest amount of surface carbon species. The Ni/CeO_2 catalyst demonstrated the highest level of methane decomposition indicated by the highest amount of CO_2 evolution. This catalyst also produced two different CO_2 peaks, suggesting that carbon was present on two different

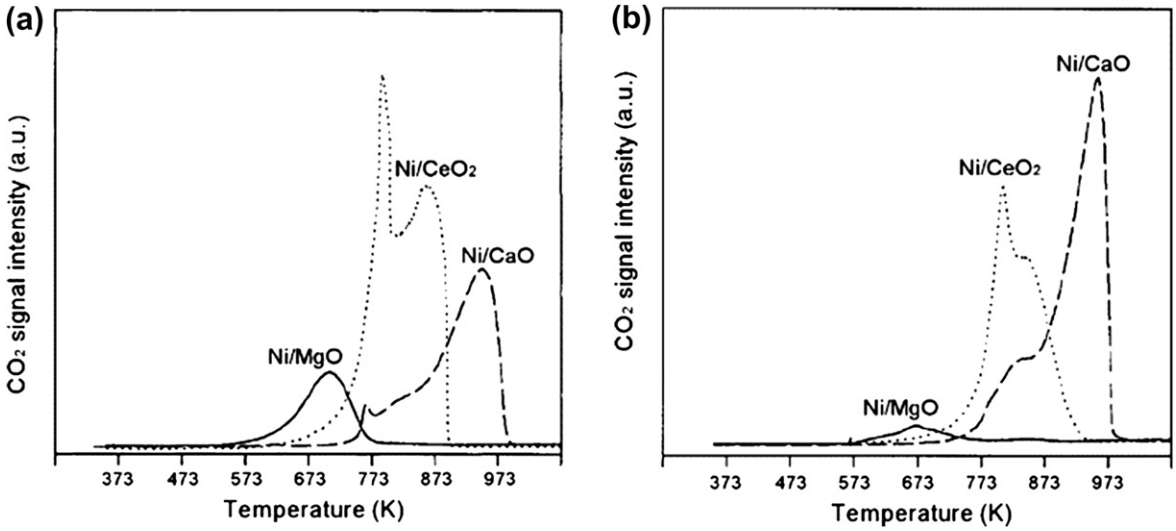

FIGURE 5.16 Effect of support on Ni reforming catalysts in TPO experiments after (a) methane decomposition and (b) CO disproportionation. *Reprinted from Tang et al. [74], Copyright (1998), with permission from Springer.*

types of surface sites. The first peak at ~773 K is attributed to carbon adsorbed to the Ni sites. It is likely that methane decomposition also occurred on the CeO_2 support, which produced the higher temperature peak. The Ni/CaO produced a very small peak at ~773 K, but a larger peak above 900 K also from carbon adsorbed on the support.

5.4.1.1.3. BASIC PROMOTERS

The addition of promoter metals can directly alter the nature of the active metal site. This approach includes the addition of alkali earth metals to increase the basic nature of the catalyst surface. This approach can affect the bonding strength of carbon to the active site to mitigate coke formation by making them less acidic. This may extend the life of the catalyst; however, it is usually at the sacrifice of initial activity due to the covering of active sites.

An excellent example of the use of basic promoters is found in a study by Ma et al. [75]. Ni catalysts supported onto γ-alumina supports were promoted with rare earths and other basic metals. The nature of the Ni sites was altered as evidenced by the H_2-TPR data presented in Fig. 5.17. The Ni metal without a promoter had a reduction peak around 650

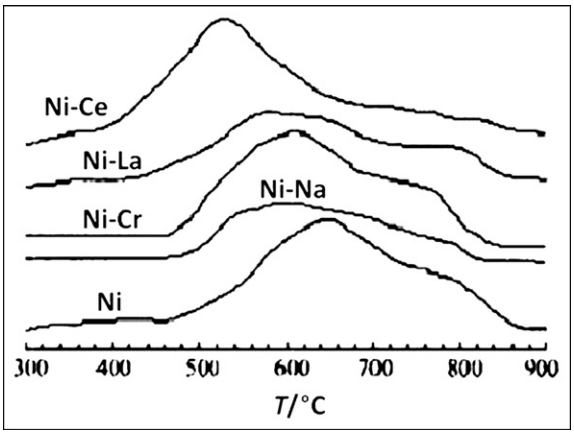

FIGURE 5.17 H_2-TPR spectra of promoted Ni catalysts. *Reprinted from Ma et al. [75], Copyright (2006), with permission from Elsevier.*

TABLE 5.14 Effect of Basic Promoters on CPOX of Methane with Ni/γ-Al_2O_3 Catalysts [75]

Promoter	X_{CH_4} (%)	S_{H_2} (%)	S_{CO} (%)	POX (%)	Comb. (%)	Reaction 5.3 (%)
–	80.2	92.6	89.2	89.2	7.4	3.4
Na	89.2	97.4	90.3	90.3	2.6	7.1
Sr	91.8	98.1	91.9	91.9	1.9	6.2
La	93.9	100	93.7	93.7	0	6.3
Ce	92.1	100	92.8	92.8	0	7.2

°C. Promotion with Na, Cr, La, and Ce shifted the reduction peak to a lower temperature in all cases, with Ce giving the lowest temperature peak near 500 °C. The lower reduction temperature also indicates a reduction in the interaction of the Ni sites to the support.

The performance data of the promoted Ni catalysts presented by Ma et al. [75] is summarized in Table 5.14. It is clear that the presence of the promoter improved conversion and H_2 selectivity in all cases with only moderate improvement in CO selectivity. Also, the rate of the combustion reaction decreases significantly and is zero for the La- and Ce-promoted Ni catalysts. The increase in H_2 selectivity can be attributed to the increase in Reaction 5.3 ($CH_4 + O_2 = CO_2 + 2H_2$). The effect of the promoters can be attributed to a reduction in the interaction of the Ni sites to the alumina support, evidenced by the TPR results. This may be explained further by a reduction in the role of lattice oxygen from the support, which reduces the chance for over-oxidation, leading to combustion products. It must also be considered that the promoters reduced the bond strength of the adsorbed H_2 and CO species, allowing them to desorb more rapidly, thus preventing oxidation to combustion products.

It is worth mentioning that, while in the case of alumina, a reduction in the metal-support interaction can produce a benefit for CPOX of methane, there are catalysts and reaction conditions that see a benefit in the interaction that could be lost by the presence of certain promoters. It would, therefore, be undesirable to combine these approaches. One specific example is oxygen-conducting supports, which is discussed in the following section.

5.4.1.1.4. OXYGEN-CONDUCTING SUPPORTS

Another type of support that has been studied a great deal for the CPOX of methane is an oxygen-conducting support. The use of a support with enhanced oxygen transport can improve the rate of oxidation of adsorbed carbon species to CO and CO_2 by providing more rapid delivery of oxygen to the active metal site. It is also beneficial when lattice oxygen plays a role in the activation of the methane. Here, Ni catalysts supported on ceria-based materials will be examined in detail as an example of how oxygen-conducting supports can help minimize carbon deposition. Figure 5.18 provides a potential mechanism for the transport of oxygen to adsorbed carbon species.

A series of doped ceria materials were examined for total ionic conductivity by Salazar et al. [76], and the results are presented Fig. 5.19. High ionic conductivity has been shown to correlate to high levels of oxygen vacancies, which produce oxygen-ion conductivity. Gadolinium-doped ceria (GDC), lanthanum-doped ceria (LDC), and zirconia-doped ceria (ZDC) all yielded much higher ionic conductivity over pure ceria at 800 °C.

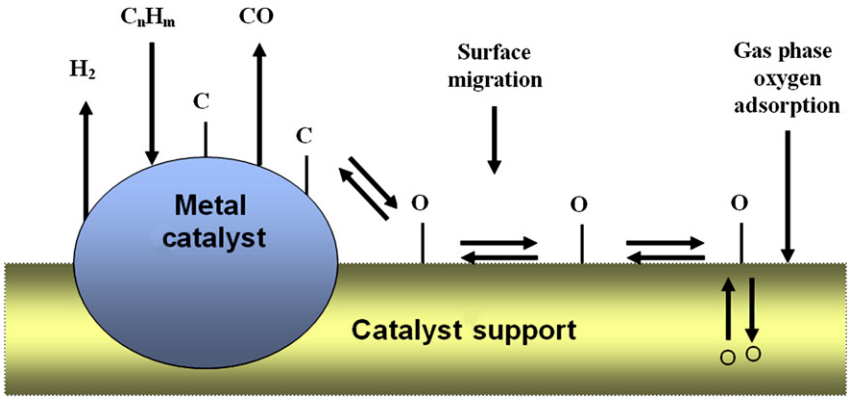

FIGURE 5.18 Proposed mechanism for the transport of gas phase oxygen with a supported catalyst.

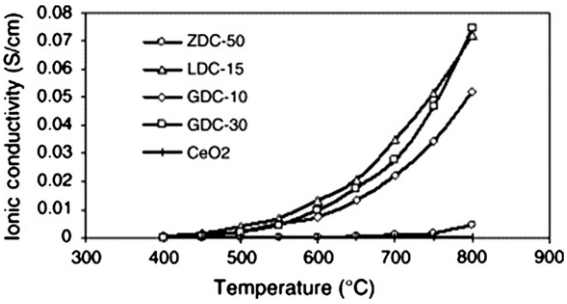

FIGURE 5.19 Ionic conductivity of several doped ceria support materials (ZDC-50: $(Ce_{0.56}Zr_{0.44})O_{2-x}$, GDC-10: $(Ce_{0.91}Gd_{0.09})O_{2-x}$, GDC-30: $(Ce_{0.71}Gd_{0.29})O_{2-x}$, and LDC-15: $(Ce_{0.88}La_{0.12})O_{2-x}$). *Reprinted from Salazar et al. [76], Copyright (2006), with permission from International Association for Hydrogen and Energy.*

The presence of additional oxygen mobility in the catalyst support produced a significant reduction in deactivating carbon formation. One example of this was presented by Dajiang et al. [77]. Ni was supported onto Al_2O_3, ZDC, and ZDC + Al_2O_3. The composition and average carbon formation of these materials under CPOX of methane are presented in Table 5.15. Clearly, the presence of ZDC decreased the amount of carbon formed on the Ni catalysts over the pure Al_2O_3.

Temperature programmed reaction results for the catalysts studied by Dajiang et al. [77] are presented in Fig. 5.20. Methane conversion and CO selectivity indicate that the Ni catalyst supported by ZDC + Al_2O_3 gave the highest CH_4 conversion and CO selectivity. Somewhat surprising is the result that Ni/Al_2O_3 yielded better conversion and selectivity than the Ni/ZDC. However, the CPOX studies conducted for 24 h in Fig. 5.21 show that conversion drops off sharply after 20 h on stream for the Ni/Al_2O_3, while the Ni/ZDC conversion, initially lower, remains stable.

TABLE 5.15 Characterization Data of Ni Catalysts with Alumina and Zirconia-Doped Ceria Supports [77].

Catalyst	Ni loading (wt%)	Surface area (m^2/g)	Ratio ($Ce_{0.6}Zr_{0.4}O_2$:Al_2O_3)	Average coking rate ($g/g_{cat}/h$)
Ni/CeO_2-ZrO_2	8	25.8	3:0	0.008
Ni/CeO_2-ZrO_2-Al_2O_3	8	165.3	1:2	0.004
Ni/Al_2O_3	8	156.3	0:3	0.027

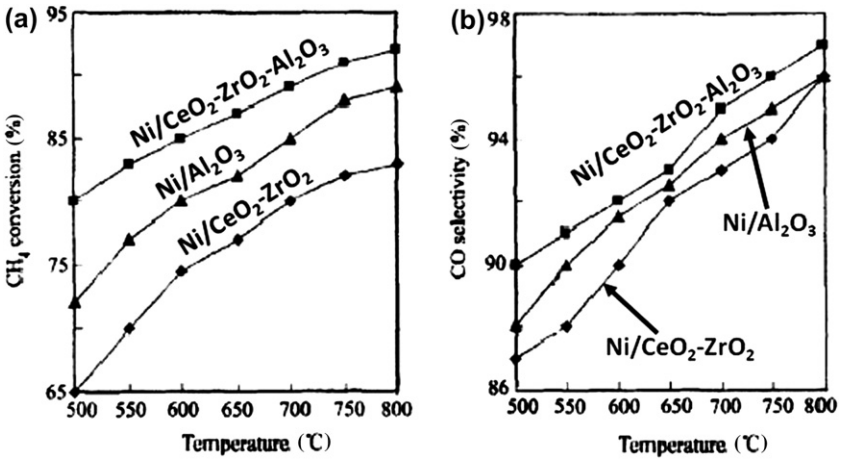

FIGURE 5.20 Methane conversion and CO selectivity at different temperatures for CPOX with Ni catalysts on alumina and oxygen-conducting supports. *Reprinted from Dajiang et al. [77], Copyright (2007), with permission from Elsevier.*

Surface area measurement of the materials presented in Fig. 5.20 is also given in Table 5.15 and shows that the ZDC-supported catalyst possessed a much lower BET surface area than the other materials. This is significant since a lower surface area will produce a lower dispersion. It is likely that the Ni deposits on the ZDC catalyst were much larger clusters since the metal loading was the same for all three catalysts at 8 wt%. Even though the GHSV was the same, what could be called the "effective space velocity" based on the total number of available metal sites would be much higher for the Ni/ZDC catalyst, which could account for the lower methane conversion. Although different preparation methods may be able to produce a ZDC support of higher surface area, it is not likely that it would retain the same level of ionic conductivity.

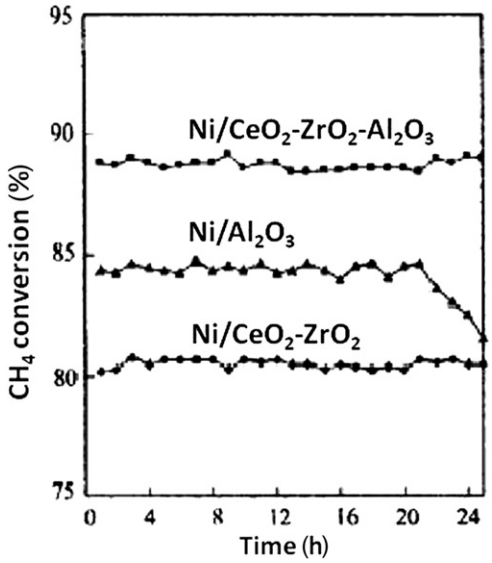

FIGURE 5.21 Methane conversion over time for CPOX with catalysts on alumina and oxygen-conducting supports. *Reprinted from Dajiang et al. [77], Copyright (2007), with permission from Elsevier.*

Another series of doped ceria-supported Ni catalyst were studied by Salazar-Villalpando and Reyes [78] for the CPOX of methane. These were prepared using the supports presented in Fig. 5.19. The TPR profiles for these materials are presented in Fig. 5.22. The reducibility of ceria is significantly increased by the presence of the dopants. This increase in reducibility can improve the performance of the catalyst under reaction conditions.

5.4.1.2. Noble Metal Catalysts

Noble metals are attractive for the CPOX of methane because they posses inherently much higher activity and selectivity than base metal catalysts. One major reason for their superior

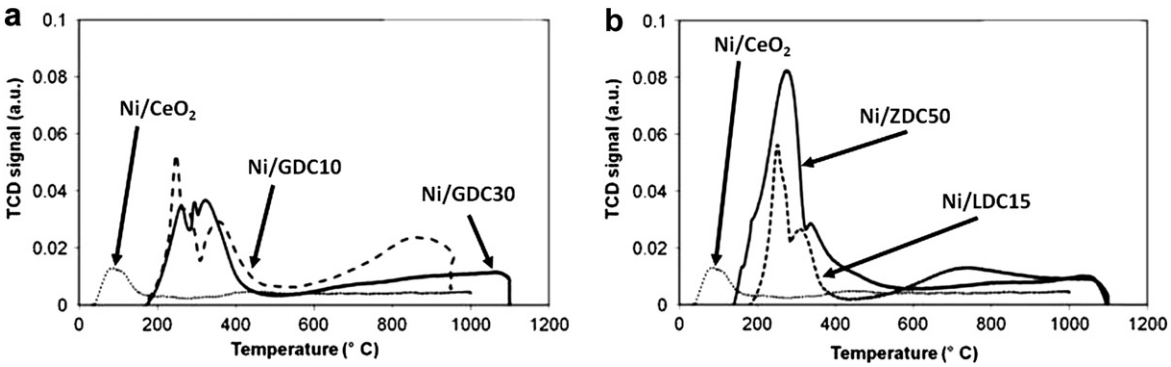

FIGURE 5.22 TPR profiles for Ni catalysts on several doped-ceria supports (ZDC-50: $(Ce_{0.56}Zr_{0.44})O_{2-x}$, GDC-10: $(Ce_{0.91}Gd_{0.09})O_{2-x}$, GDC-30: $(Ce_{0.71}Gd_{0.29})O_{2-x}$, and LDC-15: $(Ce_{0.88}La_{0.12})O_{2-x}$). *Reprinted from Salazar-Villalpando and Reyes [78], Copyright (2009), with permission from Elsevier.*

performance is their ability to remain in a reduced state even under highly oxidizing conditions. They are also more resistant to carbon formation and sulfur poisoning. However, they are significantly more expensive than other metal catalysts, making them less favorable for large-scale use.

5.4.1.2.1. RHODIUM AND PLATINUM CATALYSTS

The majority of research for the CPOX of methane with noble metals has been conducted using Pt and Rh catalysts. Both the direct and indirect mechanisms have been reported for these metals (see Table 5.4). Under similar conditions, the properties of Pt and Rh are different such that different steps in the mechanism are more favorable for one than the other. For example, Freni et al. [4] produced the diagram shown in Fig. 5.23 from studies conducted by Schmidt's group [32,33,35,79] to compare the results they observed for these two metals. As shown in Fig. 5.23, Pt catalysts promote the formation of surface hydroxyls more easily than Rh, which will result in higher yields of steam. This is because the activation energy for this step over Pt (10.5 kJ/mol) was much lower than for Rh (83.7 kJ/mol). This would clearly favor the indirect mechanism, since SR reactions would be faster. In contrast, Rh catalysts are more active for the dissociation of methane to CH_x species, which can be oxidized to form CO as the primary product. This supports the reports of Rh catalysts operating under the direct mechanism. Other factors not represented in this diagram are the strength of the bonds of the carbon species formed from methane dissociation with the active metal site. Strongly adsorbed carbon will remain on the catalyst for longer periods of time, which will increase the potential for full oxidation to

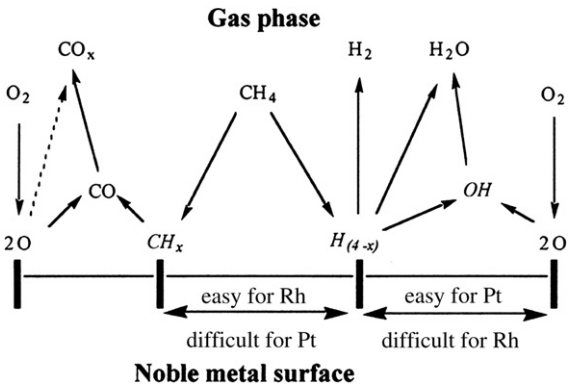

FIGURE 5.23 Diagram comparing surface reactions on Pt and Rh catalysts. *Reprinted from Freni et al. [4], Copyright (2000), with permission from Elsevier.*

CO_2. Also important is the desorption rate of surface adsorbed CO, which if high enough will result in it being the primary product.

Another study with Rh and Pt was reported by Hickman and Schmidt [48]. They presented potential energy diagrams (not shown) for Pt and Rh for each step in their proposed mechanism for comparison to demonstrate how different the surface reactions for these metals can be. One major difference is that it takes twice as much energy for Pt (43.1 kJ/mol) for the combined adsorption and dissociation of methane and oxygen gas to the monatomic surface species of each element than for Rh (20.9 kJ/mol). This is consistent with the result that Rh catalyzes the direct mechanism. It would be valuable to conduct the same comparison for the reaction mechanisms for SR, CO_2 reforming, and WGS to determine which catalyst is better for promoting secondary reforming reactions for operating conditions where that mechanism dominates. The authors are not aware of such comparisons for these two metals.

5.4.1.2.2. STRUCTURED SUPPORTS

As with base metal catalysts, the support used for the CPOX of methane can have a significant effect on the performance and mechanism. The results presented in many similar studies of Pt and Rh over various aluminas and doped ceria supports yielded qualitatively the same effects as the base metals (see Section 5.4.1.1). However, a number of studies have been conducted on Pt and Rh catalysts on various support structures such as monoliths, foams, and wire gauze. Often, these supports are ceramics, since they can withstand the high operating temperatures of CPOX and since many are chemically inert.

Changing the structure of the support will affect the catalyst performance differently than changing its composition, surface properties, or crystal phase. In the previous sections, the properties of the supports impacted performance by altering rates of adsorption, binding energies, surface reactions, and product selectivities. The structure of the support will have greater impact on heat and mass transport properties. These are especially important for CPOX of hydrocarbons because of the presence of both exo- and endothermic reactions. Further, when selecting a support structure, sufficient gas mixing and velocities are required to prevent hot spots from oxygen-rich zones and soot formation from fuel-rich zones.

Researchers from the University of Minnesota [32,34–35,60,80–82] conducted several studies on methane CPOX using different support structures. One example to illustrate the importance of support structure is a study using Pt and Rh catalysts on metal gauze, α-Al_2O_3 foams, and extruded cordierite monoliths [32]. Figure 5.24 shows the methane conversion, CO and H_2 selectivities for several different catalysts. For methane conversion, the Pt/Rh catalysts supported on the alumina foam performed the best, while the Pt on Rh gauze performed the worst. The Pt/Rh foam also yielded the highest methane conversion of all catalysts tested. However, the Pt on Rh gauze yielded the highest CO selectivity. Overall, the Pt supported on the extruded cordierite consistently produced the lowest conversion and selectivities.

Improving the transport properties of a catalyst-support system can require novel support structure designs. An example of one such design is a short channel length, high cell density substrate called a Microlith® developed by Lyubovsky et al. [83]. This substrate is coated with a high surface area ceramic, which is impregnated with noble metal catalysts. The studies conducted on CPOX of methane with the Microlith® have supported the claims that the substrates avoid boundary layer buildup and improve overall heat and mass transport. The enhanced transport allowed for complete conversion of methane, even under fuel-rich conditions. Figure 5.25 is an image comparing the Microlith® to a typical monolith support.

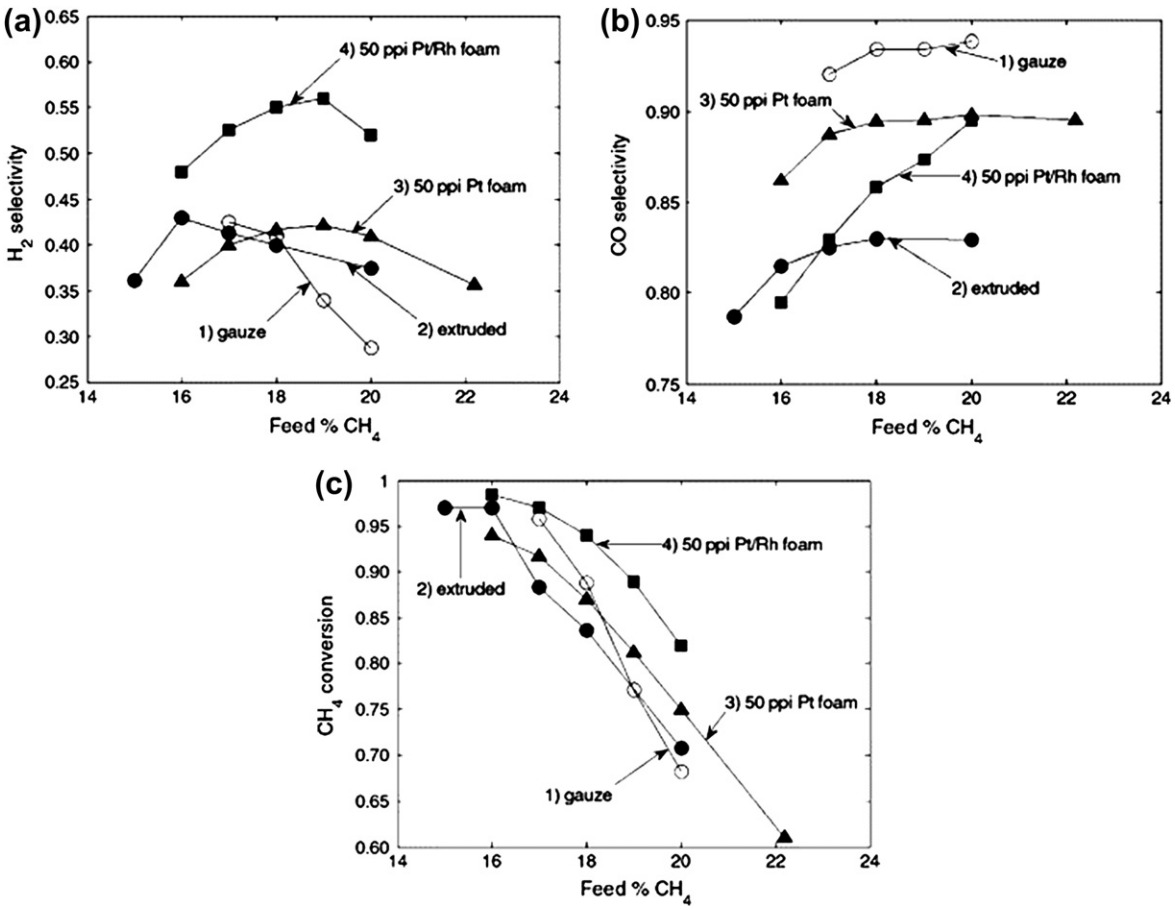

FIGURE 5.24 Methane conversion and selectivities for CPOX with Pt and Rh catalysts on various structured supports. *Reprinted from Hickmann and Schmidt [32], Copyright (1992), with permission from Elsevier.*

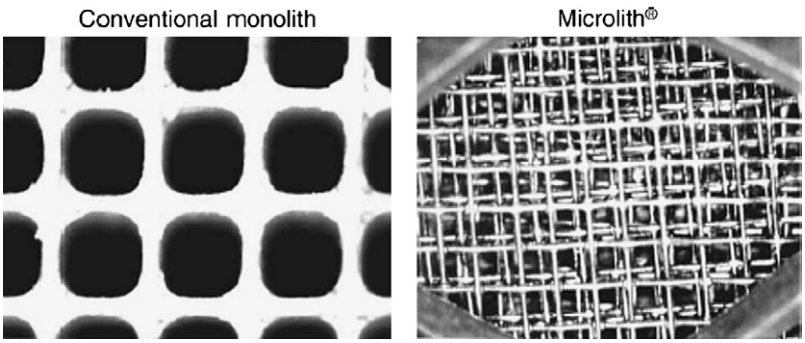

FIGURE 5.25 Comparison of a conventional monolith to the Microlith® substrate. *Reprinted from Lyubovsky et al. [83], Copyright (2003), with permission from Elsevier.*

TABLE 5.16 Properties of Conventional Monolith and Novel Microlith® Substrate. *Reprinted from Lyubovsky et al. [83], Copyright (2003), with permission from Elsevier.*

Property	Monolith	Microlith®
Cells/cm^2	60	400
Geometric surface area (m^2/l)	2.4	6.3
Channel length (cm)	7–10	0.007
Channel length to diameter ratio (L/d)	70–12	0.3

Table 5.16 compares some properties of the two supports. The number of cells and surface area per volume of reactor allow for much higher catalyst loading density for the Microlith®. Further, the significant difference in the L/d ratio (channel length to diameter ratio) explains why the Microlith® has such improved transport and mixing properties.

5.4.1.2.3. OTHER SUPPORT SYSTEMS

Ru catalysts have been studied over various supports. One study examined the use of $Pr_2Ru_2O_7$ pyrochlore catalyst [84]. It was determined, however, that the active species was reduced Ru metal on a PrO_2 support. The significance of this difference is discussed in more detail in Section 5.5, when higher hydrocarbon CPOX is examined using substituted oxide catalysts where the active species may remain partially in the oxide structure.

Boucouvalas et al. [65] conducted a study with Ru catalyst supported on titanium oxide, Ru/TiO_2. This catalyst was compared to Ni, Rh, Pd, Ir, and Ru catalysts supported on alumina. To minimize hot spots and overcome mass and heat transfer limitations, high space velocities, dilute reactants, and dilute catalyst beds were employed. The alumina-supported catalysts produced syngas via the indirect mechanism due to the oxidation of the metal surfaces. The ability of Ru/TiO_2 to maintain a reduced surface under oxidizing conditions led to CH_4 conversion via the direct mechanism. Isotopic labeling experiments showed the total CO produced by steam and CO_2 reforming (indirect mechanism) was less than 8% of the total CO produced. The interaction of the Ru with the TiO_2 support was believed to produce a different type of surface state, which was not fully characterized. Some of the data from this study are presented in Fig. 5.26. These results demonstrate a marked improvement in performance for Ru supported on titania over alumina.

One final group of supports that should be mentioned is mixed oxides with high thermal stability (i.e., perovskites, pyrochlores, and hexaaluminates). These supports have been considered for CPOX of methane specifically because of the high operating temperatures, temperature spikes, and potential for hot spots, all of which will eventually cause the support pores to collapse and deactivate the catalysts. A significant amount of work has been done using these supports for methane combustion [85–91], but recent work has been done on methane CPOX as well. Some considerations when using thermally stable oxide supports are that there is a trade-off in surface area compared to traditional alumina supports. While the support may not sinter as rapidly, the catalyst dispersion is limited, which can reduce performance. Further, the Me–O (Me: metal) interaction with these supports is much stronger, which may reduce desired lattice oxygen mobility for oxidation steps in the CPOX mechanism. To overcome this, the catalyst may require promotion with an oxygen-conducting material.

One example of the use of this type of support is a study by Xiao et al. [92], which examined a Co/W carbide catalyst supported by an Mn-substituted hexaaluminate combustion catalyst. The hexaaluminate support was shown to stabilize the carbide catalyst and

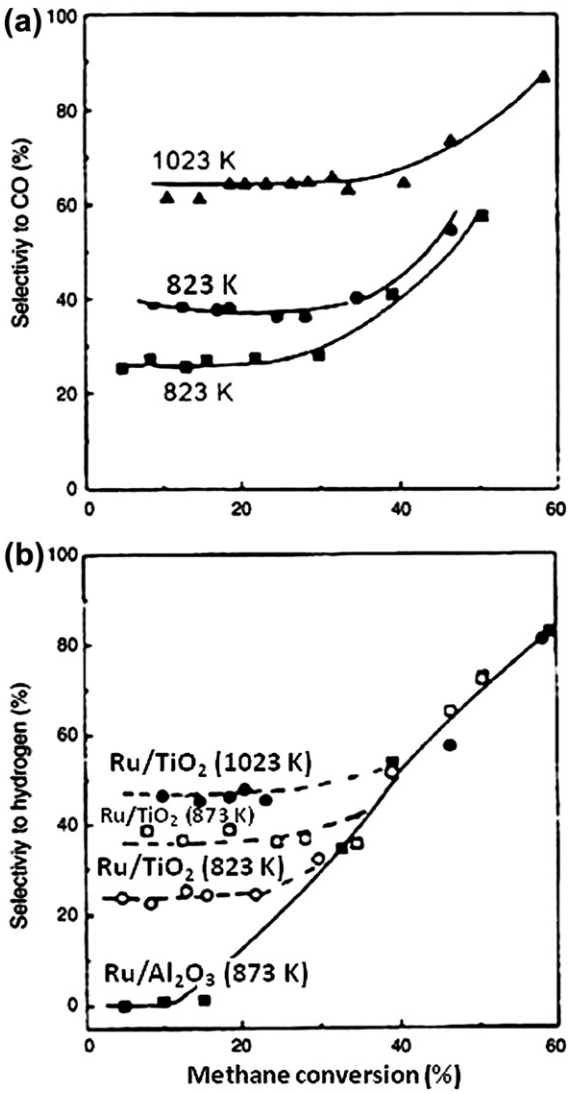

FIGURE 5.26 CO selectivity (a) and H_2 selectivity (b) for CPOX with Ru catalysts on alumina and titania supports as a function methane conversion. *Reprinted from Boucouvalas et al. [65], Copyright (1996), with permission from SpringerLink.*

enhance the combustion zone of the reactor. The additional heat from this zone was used to drive reforming reactions. Further, the carbide catalyst showed resistance to deactivation by oxidation.

5.4.1.3. Bimetallic Catalysts

The use of bimetallic catalyst systems is another approach to improve performance for CPOX. This approach differs from promoted catalysts in that bimetallic catalysts are comprised of two metals that are separately active for the reaction, but at different ratios can display a synergistic effect. This may be the result of the metals being more active for different steps in a reaction mechanism. This can be very useful for complex mechanisms like CPOX.

The separate activity of each metal does not imply that there is not an interaction between them or that their properties and not modified. This was demonstrated by Basile et al. [93], who identified a synergistic effect with a Ni-Rh catalyst in hydrotalcite materials for the CPOX of methane. This was evidenced by the superior performance of the catalysts containing both metals over the catalysts containing one or the other, and it was concluded that the presence of the Rh helped the Ni metal to remain in a reduced state even in the presence of oxygen-rich conditions. Ru-Ni and Ir-Ni catalysts were also studied, but the initial tests in which these were included produced indistinguishable performance between the catalysts since they all operated near-equilibrium conditions. Only the Rh and Ni catalysts were tested under conditions where oxygen conversion was incomplete.

Basile et al. [93] also used the CO_2 reforming of methane to characterize the resistance of the catalysts to carbon formation. The catalyst with both Rh and Ni contained 0.67 g of carbon after reaction, while the Rh and Ni catalysts separately contained 0.71 and 3.05 g of carbon, respectively. This was explained by the Ni being more active for the conversion of CO_2 and Rh being more active for the conversion of methane.

Another bimetallic catalyst system that was studied for the conversion of methane was a Ni-Sn catalyst examined by Nikolla et al. [94].

Although the study was for SR, this approach, which reduced carbon formation, is applicable to CPOX as well. This work used DFT calculations to predict that alloying Sn with a Ni catalyst will preferentially oxidize surface C atoms rather than form C−C bonds. It was also suggested that the catalysts would have a lower thermodynamic driving force for carbon nucleation. Ultimately, reactor studies confirmed the model predictions, and the Sn-Ni catalysts produced less carbon than the Ni catalysts for the reforming of methane, propane, and isooctane.

Other examples of bimetallic catalysts are studies of modified Ni catalysts [63] and modified Co catalysts by Enger et al. [95]. These studies are included in this section since many of the bimetallic systems were comprised of two metals that are independently active for CPOX of methane, and for purposes of this discussion are not considered to be merely promoters. The Ni and Co catalysts were combined with very small amounts of a number of different metals. All catalysts were supported on alumina.

Ni was modified with Co, Fe, Cr, Mn, W, and Mo (Me/Ni = 1/15 molar), and with Re, Cu, Pt, Rh, and Pd (Me/Ni = 1/100). The most interesting results for the Me/Ni catalysts were that the addition of metals that are difficult to reduce (W, Fe, and Mn) decreased the amount of combustion at the front of the catalyst bed, while the addition of easily reducible metals (Mo, Pt, Pd, and Rh) increased the combustion activity, resulting in larger temperature gradients.

Co was modified with Ni, Fe, Cr, Re, Mn, W, Mo, V, and Ta (Me/Co = 1/15). For these catalysts, Mo, Fe, W, V, and Ta all demonstrated detrimental effects on CPOX performance. Similar to the Me/Ni catalysts, this was attributed to their tendency to be easily oxidized.

5.4.2. Ethane, Propane, and Butane

The use of light hydrocarbons other than methane for CPOX has been investigated and reported in literature, although to a much lesser degree. For the most part, the catalysts are the same, but there are differences in the operating conditions and mechanisms. The most significant difference is due to the much higher stability of methane, which requires higher light-off temperatures. Further, the difference in the rate of methane decomposition on the catalyst surface compared to other gaseous hydrocarbons can affect the overall reaction mechanism. The additional step of breaking the C−C bond in C_2−C_4 hydrocarbons has implications for which catalyst is appropriate.

The CPOX of methane over Rh-coated monoliths and ethane over Pt-coated monoliths was studied by Witt and Schmidt [96]. This study focused on the effect of gas flow rate. The main findings were that methane conversion and selectivity dropped more significantly than ethane at high space velocities. This is certainly due to the higher activation energy of methane.

Ni and Pt catalysts were studied by Corbo and Migliardini [97] to compare the partial oxidation of methane to that of propane for H_2 production. The catalysts were Ni/Al_2O_3 and Pt/CeO_2. Table 5.17 presents a summary of the data for all three catalysts for the CPOX of methane and propane. For both methane and propane, the H_2 yield and selectivity with Pt/CeO_2 was consistently lower than with the Ni-based catalysts. The CO + CO_2 yield was also lowest with the Pt/CeO_2 catalyst in all cases. However, the overall conversion, represented by turnover frequency (TOF), was the highest with the Pt/CeO_2 catalyst for methane and the second highest for propane. This indicates that while the Ni catalysts were more selective, their overall conversion was lower.

Another interesting point of this study is that, for propane, all performance results were better with all three catalysts than for methane. Therefore, these catalysts were determined to be better for CPOX of propane than for methane. The main conclusion of the study was that a combined Ni-Pt/CeO_2 catalyst may produce

TABLE 5.17 Performance of Ni and Pt Catalysts for CPOX of Methane and Propane at Maximum Performance Temperature [97]

	Methane				Propane			
Catalyst	**H_2 yield (%)**	**CO + CO_2 yield (%)**	**H_2 selectivity (%)**	**TOF (s^{-1})**	**H_2 yield (%)**	**CO + CO_2 yield (%)**	**H_2 selectivity (%)**	**TOF (s^{-1})**
NiO 14 wt% CaO 13 wt%	64	75	85	0.74	88	92	95	0.80
NiO 14 wt% K_2O 6 wt%	53	63	80	0.56	86	93	92	0.62
Pt 1 wt% − CeO_2	44	60	75	0.84	58	72	75	0.73

Space velocity = 620 l g_{cat}^{-1} h^{-1}, $O_2/C = 0.53$.

even better performance from a potential synergistic effect. Further work with this approach was recommended.

A study that examined the CPOX of methane, ethane, propane, and butane was conducted by Huff et al. [98]. The catalysts were Ni, Ir, Pd, Pt, and Rh. Table 5.18 provides a summary of their thorough analysis. The most important trend to notice is the increase in formation of ethylene and other cracking products at higher carbon numbers with Pt catalysts. The heat supplied from the exothermic combustion drives the cracking reactions, which then leads to dehydrogenation reactions on the catalyst surface. This is also a result of the tendency of Pt to form hydroxyls, evidenced even with methane and ethane by the high water formation (and low H_2 selectivity). Further, the formation of propyl and butyl groups from propane and butane, respectively, can lead to dehydrogenation products since both can adsorb at a primary or secondary carbon. Adsorption at a secondary

TABLE 5.18 Summary of Analysis of CPOX of C_1−C_4 Hydrocarbons by Huff et al. [98]

Catalyst	**Methane**	**Ethane**	**Propane**	***n*-Butane**
Ni	High conversion Highest H_2 selectivity Lowest CO selectivity	–	–	–
Ir	Low conversion Low H_2 selectivity Low CO selectivity	–	–	–
Pt	Lowest conversion Lowest H_2 selectivity Moderate CO selectivity	Primary products ethylene and water from OH formation	Ethylene and water; cracking products present due to heat from comb	High level of cracking products leading to dehydrogenation
Pd	Rapid deactivation from carbon formation	Initial performance similar to Pt; deactivation from carbon formation	Similar to Pt, but with rapid deactivation, as with methane and ethane	–
Rh	Highest conversion High H_2 selectivity Highest CO selectivity	Primary products syngas; high conversion and selectivity	Primary products syngas; less likely to form cracking products	Primary products syngas; high conversion and selectivity

carbon leads to olefin formation, and ultimately to deactivating carbon formation. Overall, the Rh catalyst was identified as the best for conversion and high selectivity to syngas for all four fuels.

5.4.3. Summary for Light Hydrocarbons

The CPOX of light hydrocarbons (C_1–C_4) was discussed for many catalyst and support systems. Base metal and noble metal catalysts were examined for hydrocarbon conversion and selectivity to H_2 and CO (syngas). The effects of several support systems were analyzed, and the effect of different promoters was evaluated. The role of the support structure on enhancing catalytic performance was investigated, and the bimetallic catalyst approach was considered.

5.5. HIGHER HYDROCARBONS

CPOX of liquid hydrocarbon fuels is an attractive option for H_2 and CO production for compact or mobile fuel-processing systems. Two major issues that distinguish the CPOX of liquid hydrocarbons and lower hydrocarbons are the propensity to coke the catalyst from unsaturated and/or aromatic compounds found in conventional liquid fuels and the presence of residual organic sulfur compounds, such as dibenzothiophene (DBT), that are not easily removed through hydrodesulfurization. The reactions occurring in the CPOX of liquid hydrocarbons are extremely complex. High temperatures from the combustion zone at the front of the catalyst bed result in the fragmentation of the heavier molecular weight hydrocarbons. To avoid excessive fragmentation of the feed, which could result in the formation of unsaturated hydrocarbons and carbon deposits on the catalyst, feed preheat temperatures for liquid fuels range from ambient to just above their boiling point. Reaction temperatures are typically in the range of 700–900 °C. If organic sulfur is present in the feed, then the reactor is typically operated at higher temperatures, where metal sulfides are less stable. The O_2 in the feed initially converts organic sulfur compounds in the feed into SO_2; however, SO_2 may later be converted into H_2S.

5.5.1. Base Metal Catalysts

Studies on base metal catalysts on a variety of supports for the CPOX of liquid hydrocarbons are presented extensively in literature. These catalysts are desirable because of their relatively low cost compared with noble metals. However, they are less active and more prone to deactivation from coke and sulfur poisoning.

5.5.1.1. Promoters

Ni-based catalysts are typically modified with various promoters to limit coke formation, often by neutralizing acid sites thought to be responsible for coking. *n*-Heptane CPOX was studied over NiLiLa/γ-alumina by Ran et al. [99]. The catalyst was tested over the temperature range of 700–850 °C at an O/C = 1 and a GHSV of 38,000 $cm^3\ g^{-1}\ h^{-1}$. The LiLa promoter was added to both disperse the Ni over the surface of the catalyst and to titrate active Lewis acid sites on the catalyst surface. This catalyst converted 100% of the *n*-C_7 in the feed with 93% H_2 selectivity over a period of 4 h. Similar results were obtained from *n*-C_7 CPOX when the catalyst LiLaNiO/γ-Al_2O_3 was combined with a dense oxygen permeation membrane $Ba_{0.5}Sr_{0.5}Co_{0.8}Fe_{0.2}O_3$ that can supply pure O_2 for the reaction [100]. The H_2 selectivity of Ni/γ-alumina, also tested in the study, dropped to 30% after 4 h [99].

5.5.1.2. Substituted Oxides and Oxygen-Conducting Supports

Another approach to limit catalyst deactivation is to incorporate the active metal into a thermally stable oxide structure. CPOX of

n-tetradecane, a diesel surrogate fuel, was studied over a series of hexaaluminate catalysts with the general formula $ANi_xAl_{12-x}O_{19}$ (A = La, Ba, Sr) by Gardner et al. [101–102]. Carbon formation and sulfur poisoning resistance were achieved by substituting the Ni into the hexaaluminate structure. The TPR profile of $LaNiAl_{11}O_{19}$ in H_2 exhibited a single broad reduction peak for Ni^{2+} to Ni^0 centered at 996 °C, indicating that the substitution of Ni into the hexaaluminate structure imparted a high degree of reduction stability. This catalyst was tested isothermally at 850 °C, O/C = 1.2, and a GHSV = 10,000 $cm^3\ g^{-1}\ h^{-1}$. The average H_2 selectivity obtained over 24 h was 66.2%, and CO was 60%. The H_2/CO ratio remained unchanged over this time period at 1.18.

Figures 5.27 and 5.28 present results of CPOX activity tests on *n*-tetradecane over Ni-substituted La- and Sr-hexaaluminates, respectively [102]. The La-hexaaluminate catalyst exhibited a continual decline in H_2 production, with no recovery once the sulfur species was removed, while the Sr-hexaaluminate suffered an initial decrease in H_2 production but remained more stable over the time period it was exposed to sulfur in the feed. The total carbon deposited in the catalyst bed, determined after reaction by TPO, was less for the Sr-hexaaluminate than the La-hexaaluminate. These results suggested that the Sr-hexaaluminate catalyst was more resistant to deactivation from carbon formation in the presence of sulfur, and this was attributed to a reduction in surface acidity since Sr is more basic than La.

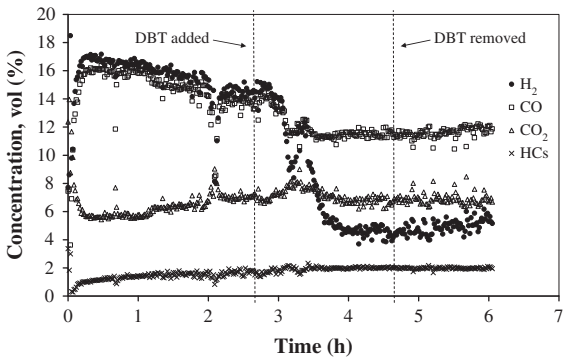

FIGURE 5.27 Step function response to the introduction of 50 ppmw sulfur as DBT during the partial oxidation of *n*-tetradecane over $LaNi_{0.4}Al_{11.6}O_{19-\delta}$. Test conditions were GHSV = 50,000 $cm^3\ g^{-1}\ h^{-1}$, O/C = 1.2, 850 °C, and 0.2 MPa. *Reprinted from Gardner et al. [102], Copyright (2007), with permission from Elsevier.*

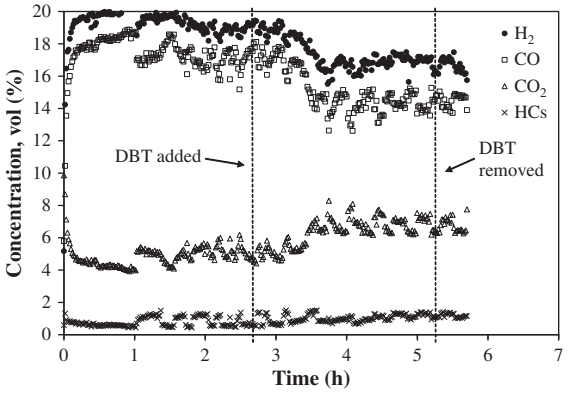

FIGURE 5.28 Step function response to the introduction of 50 ppmw sulfur as DBT during the partial oxidation of *n*-tetradecane over $SrNi_{0.4}Al_{11.6}O_{19-\delta}$. Test conditions were GHSV = 50,000 $cm^3\ g^{-1}\ h^{-1}$, O/C = 1.2, 850 °C, and 0.2 MPa. *Reprinted from Gardner et al. [102], Copyright (2007), with permission from Elsevier.*

A comparison of three Ni-based catalysts (3 wt% Ni/alumina, 3 wt% Ni/GDC, and bulk 3 wt% Ni-substituted Ba-hexaalumina, BNHA) for the CPOX of *n*-tetradecane (TD) was presented by Smith et al. [103]. The results are shown in Fig. 5.29. The 3 wt% Ni/alumina produced the highest H_2 and CO yields. The 3% Ni/GDC demonstrated very low H_2 and CO production, even on pure TD. The poor performance of this material may be explained by the low surface area of the support, which produces fewer and larger metal sites that are more likely to deactivate under these conditions. The lower yields of H_2 and CO may also be an indication that the oxygen-conducting support inhibits the activity of the Ni sites by preventing them from fully reducing to a metallic state.

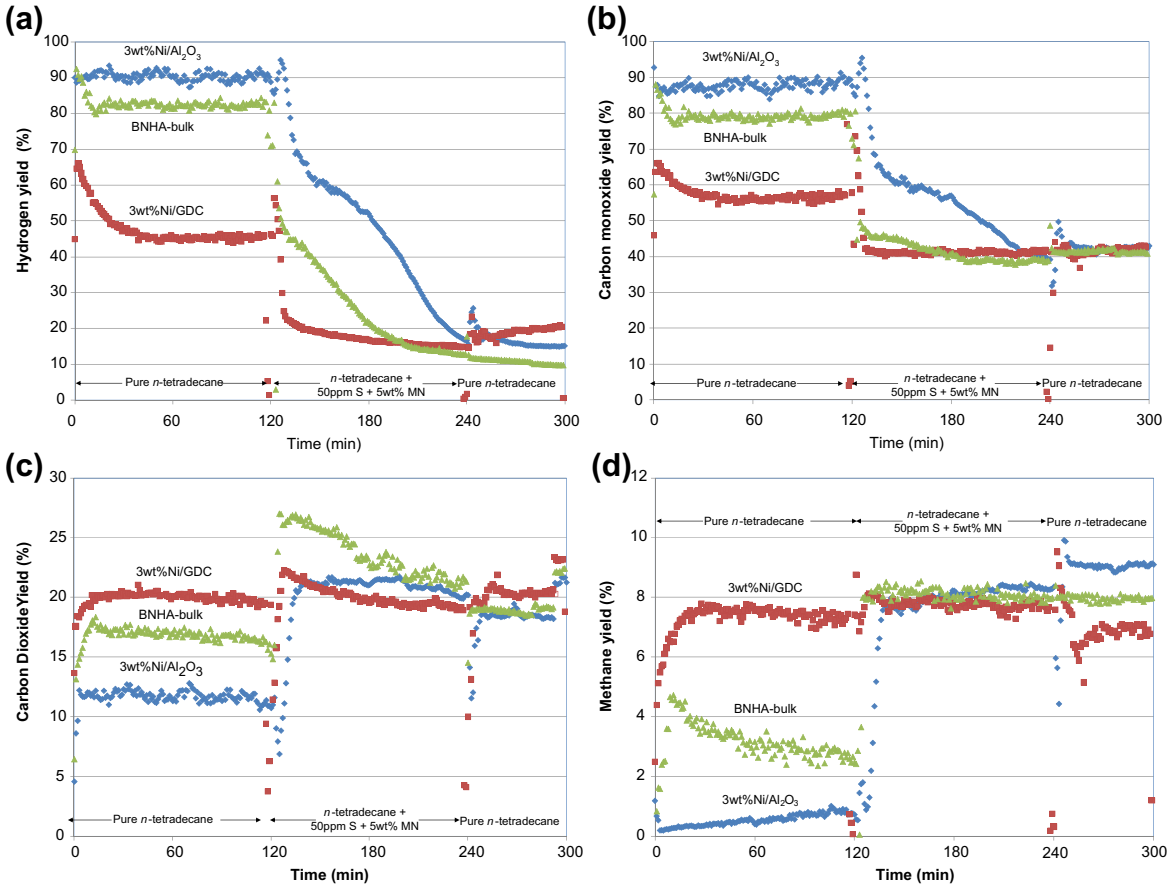

FIGURE 5.29 Effect of oxygen-conducting supports and metal substitution into an oxide structure on CPOX of *n*-tetradecane: GHSV = 50,000 $cm^3 g_{cat}^{-1} h^{-1}$, O/C = 1.2, 900 °C, and 0.23 MPa. *Reprinted from Smith et al. [103], Copyright (2010), with permission from Elsevier.*

For the bulk BNHA, relatively few of the metal sites in the hexaaluminate material are available for participation in the reaction [102]. This may explain the slightly lower initial activity before the DBT and MN are introduced into the feed as well as the relatively rapid deactivation in the presence of these contaminants. All three catalysts deactivated completely within 2 h of exposure to the contaminants, with the H_2 and CO yields reaching those of a reactor filled only with quartz material [104]. A corresponding increase in carbon dioxide and unconverted hydrocarbon (represented as methane) yields occurs after exposure to contaminants, also indicative of catalyst site deactivation. None of the materials recovered activity when the feed was switched back to pure TD.

The type of oxide structure that the active metal is substituted into also has an effect on the performance of the CPOX catalyst. This is demonstrated well in a study by Haynes et al. [105], where the Ni-substituted hexaalumina in the previous study is compared to a Ni-substituted pyrochlore with the general formula $La_{2-x}Sr_xZr_{2-y}Ni_yO_{7-\delta}$, where the value of y produces an equivalent 3 wt% Ni-substitution level. The results of this study are presented in Fig. 5.30.

The results show that the presence of MN and DBT produces an immediate drop in synthesis gas yields from the equilibrium values for each catalyst. Active Ni sites in the BNHA are easily deactivated, indicating that reducing the critical ensemble number of Ni atoms did not prevent deactivation by MN and DBT. The LSZN catalyst is distinguished by the behavior of its H_2 and CO yields in the presence of the contaminants. Ni substituted into the pyrochlore structure is not continuously deactivated by the MN and DBT, but rather is able to remain active and selective toward H_2 and CO, albeit at lower than pre-contaminant levels.

A noticeable difference is also seen in the behavior of the olefins produced by the LSZN catalyst. The olefin formation rate increases sharply after the first hour in the presence of MN and DBT, but only continues to increase slightly after the initial spike. Together, these results coupled with the behavior of the synthesis gas yields show that the sites involved in the eventual formation of H_2 and CO do not become completely deactivated by the contaminants. Instead, the data would appear to suggest that the adsorption of MN and DBT only decreases the turnover frequency of the active sites, limiting the approach to equilibrium, rather than continuously accumulating on the surface and leading to eventual deactivation. The Ni in the pyrochlore structure is believed to be able to retain catalytic properties in the presence of the contaminants through improved oxygen-ion conductivity that occurs as a result of Sr substitution. Improving this property provides a localized oxygen source from the pyrochlore lattice to react with the strongly adsorbed carbon-forming precursors. Deactivation of the Ni is then prevented during the timescale of this study because the accumulation of refractory surface carbon species is limited. Instead, most surface carbon is gasified into CO/CO_2, and active sites become freed for further reactions.

After the contaminants were removed from the feed, activity does not return for the BNHA catalysts. Evaluating the gaseous product yields during the recovery period to those produced in the absence of a catalyst showed comparable product selectivity. High selectivity to olefins is observed, and H_2 and CO yields are produced at an H_2/CO ratio of much less than 1. This indicates the catalyst has been irreversibly deactivated by the contaminants. Meanwhile, the LSZN is able to recover a portion of its initial activity, showing that most of the effects of the MN and DBT are reversible. H_2 and CO yields both increase, while olefin products return to pre-contaminant levels, and CO_2 and CH_4 yields both decrease. The ability to recover activity suggests that the contaminants act, for the most part, as kinetic inhibitors to the H_2 and CO producing sites.

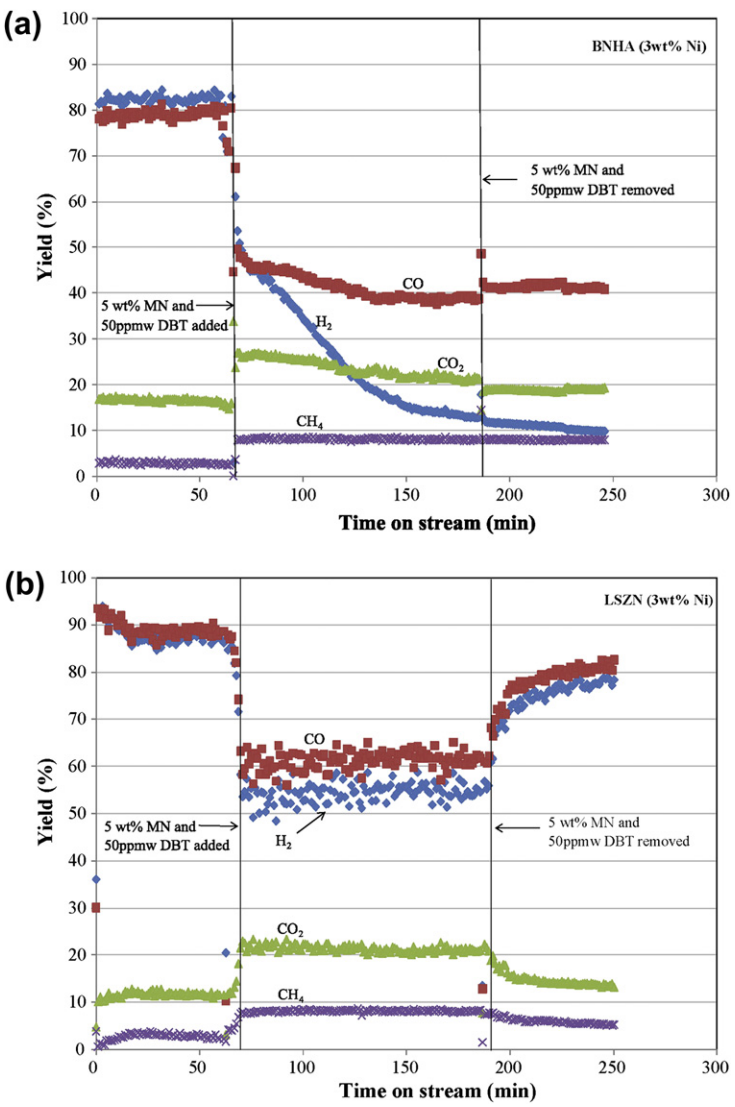

FIGURE 5.30 Dry gas yields for (a) BNHA and (b) LSZN catalyst during 4 h CPOX of *n*-tetradecane with 5 wt% MN and 50 ppmw DBT: GHSV = 50,000 $cm^3 g_{cat}^{-1} h^{-1}$, O/C = 1.2, 900 °C, and 0.23 MPa. *Reprinted from Haynes et al. [105], Copyright (2010), with permission from Elsevier.*

However, total initial activity is not recovered, signifying some activity loss was irreversible.

One final aspect in comparing these two catalysts is the amount of carbon measured in the reactor after each test by TPO. For BNHA the total carbon was 2.4 g/g_{cat}, while for LSZN the total carbon was 0.4 g/g_{cat}. This suggests that the carbon formation is related to the catalyst deactivation.

5.5.1.3. *Substituted Oxides on Oxygen-Conducting Supports*

The use of oxygen-conducting supports to enhance catalyst performance can also be

applied to metal-substituted oxide catalysts. Smith et al. [106] examined the combined approach to catalyst design of substituting Ni into an oxide structure and supporting it onto an oxygen-conducting material. These studies were conducted on *n*-tetradecane (TD) with sulfur and aromatic species. The purpose of the study was to compare catalysts with Ni substituted into a barium-hexaaluminate structure (BNHA) to systems comprised of BNHA layers over GDC, an oxygen-conducting support. The BNHA catalyst layer was supported onto the GDC.

The results of this study are presented in Fig. 5.31. It was demonstrated that the stability provided by the oxide phase limited the sintering of Ni sites seen in pure Ni metal catalysts. Further, the presence of the oxygen conduction of GDC from the gas phase, through the support to the active sites, promoted the oxidation of deposited coke precursors and reduced carbon formation.

Another study by the same group demonstrated that the method for depositing the BNHA catalyst onto GDC for the same set of experiments had a significant effect on the benefit provided by the oxygen-conducting support [103]. Catalysts were prepared using two different methods: (1) conventional incipient wetness impregnation (IWI), in which a non-porous GDC support was impregnated in the conventional manner with aqueous precursors, then dried and calcined to form a supported hexaaluminate; and (2) solid-state mixing (SSM), in which solid hexaaluminate and GDC particles were mechanically ground together and thermally treated to produce a final catalyst.

Figure 5.32 presents the data from this study. Both of the GDC-supported BNHA materials demonstrated greatly reduced deactivation, with significantly reduced carbon formation compared to bulk BNHA. This was attributed to the oxygen-conducting property of the GDC, which reduced the rate of deactivation of the reaction sites by sulfur and aromatic species. The material prepared by IWI demonstrated more stable H_2 and CO yield than the material prepared by SSM. Although both catalysts deactivated in the presence of the contaminants, the activity of the catalyst prepared by IWI recovered more quickly after they were removed. This material also maintained >50% of its initial H_2 production for more than 4 h

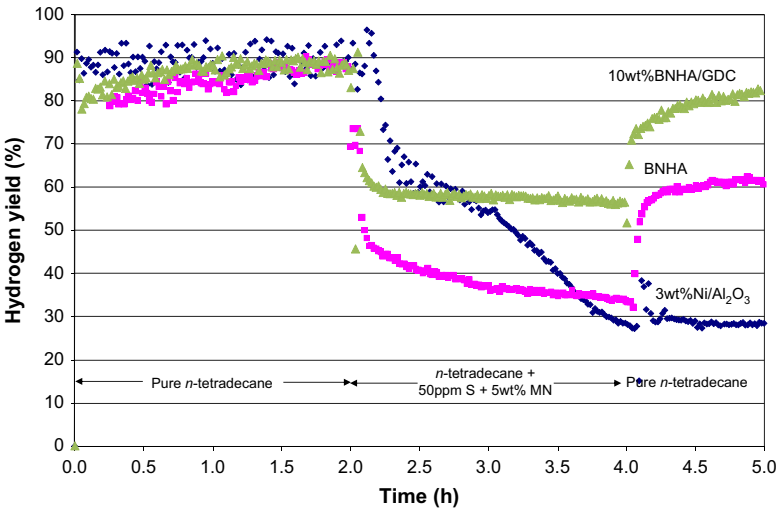

FIGURE 5.31 Effect of oxygen-conducting support on Ni-substituted hexaaluminate catalysts for the CPOX of *n*-tetradecane in the presence of MN and DBT [106].

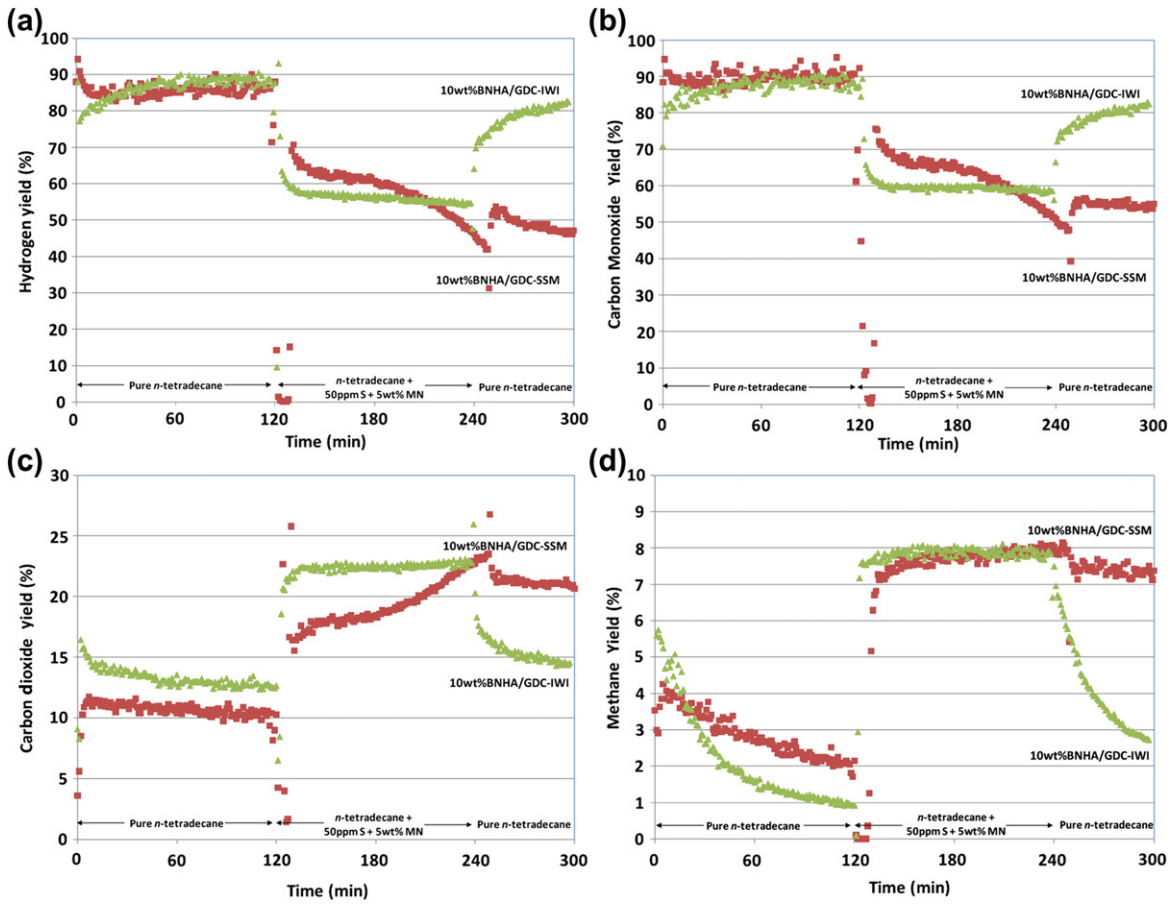

FIGURE 5.32 Performance of 10 wt% BNHA/GDC-SSM and 10 wt% BNHA/GDC-IWI in the partial oxidation of *n*-tetradecane: GHSV = 50,000 $cm^3 g_{cat}^{-1} h^{-1}$, O/C = 1.2, 900 °C, and 0.23 MPa: (a) H_2 yield, (b) CO yield, (c) CO_2 yield, and (d) methane yield. *Reprinted from Smith et al. [103], Copyright (2010), with permission from Elsevier.*

TABLE 5.19 Total Bed Carbon (TBC) Formed During CPOX Tests. *Reprinted from Smith et al. [103], Copyright (2010), with permission from Elsevier.*

Catalyst	TBC (g)
Blank reactor	0.29
GDC	0.26
Bulk BNHA	0.87
10 wt% BNHA/GDC-SSM	0.62
10 wt% BNHA/GDC-IWI	0.60

after exposure to the contaminants, while the H_2 for the material prepared by SSM dropped to this same level within 2 h.

Table 5.19 compares the total carbon formed on un-catalyzed GDC, bulk BNHA, and the two GDC-supported BNHA catalysts. The total carbon formed in a reactor filled only with the quartz material is also provided. The total carbon formed on the quartz and on the GDC was quantitatively similar, indicating that carbon formation occurs on the reactor packing material and/or reactor wall, even in the absence of reaction. This was expected since the TD conversion in the presence of GDC was equal to the conversion in the presence of quartz only.

TPO results in Fig. 5.33 show similar profiles for the two GDC-supported catalysts. Further, the TPO peak temperature and shape of the curves for the quartz and the GDC alone show qualitatively similar carbon deposition as for these catalysts. Comparing the bulk BNHA with the two GDC-supported BNHA materials shows a clear reduction in the total carbon deposition, consistent with the hypothesis that the oxygen-conducting GDC reduces carbon formation. The GDC support also appears to prevent the formation of the most refractory carbon, as evidenced by the higher TPO temperature required to oxidize the carbon on the bulk BNHA.

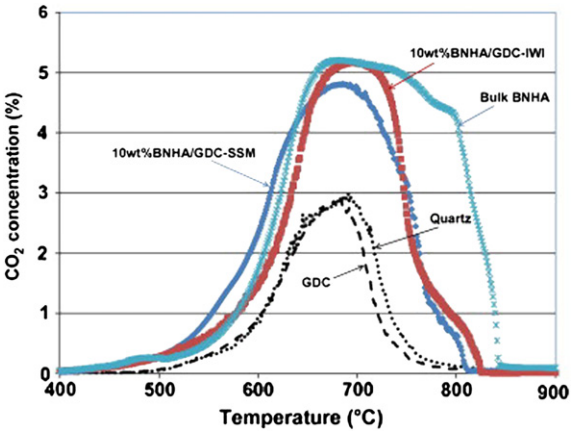

FIGURE 5.33 TPO plots for reactor beds after partial oxidation tests. *Reprinted from Smith et al. [103], Copyright (2010), with permission from Elsevier.*

5.5.2. Noble Metal Catalysts

The use of noble metal catalysts for CPOX of liquid hydrocarbons has been widely reported in literature. These metals have higher activity and resistance to deactivation than transition metal catalysts, resulting in shorter reaction times, smaller bed sizes, and longer stability. However, these catalysts are much more expensive than other metal catalysts.

Earlier in this section, the issue of sulfur poisoning was identified as a more significant challenge with liquid hydrocarbons than for lighter fuels. Figure 5.34 provides the Gibbs free energy for the sulfides of several metals typically used in CPOX [31]. Pt is the least likely to form a sulfide at typical operating conditions, while Ni is the most likely.

5.5.2.1. Promoters

Tanaka et al. [107] reported that gasoline CPOX over Rh, Pt, and Pt-Rh is promoted by alkali (Li) and alkaline earth metals (Ba, Ca, K) supported on magnesium aluminate spinel. The catalysts were tested isothermally at 800 °C at an air-to-fuel ratio of 5.1 and GHSV 50,000 h^{-1}. Li, Mg and MgLi promoters were

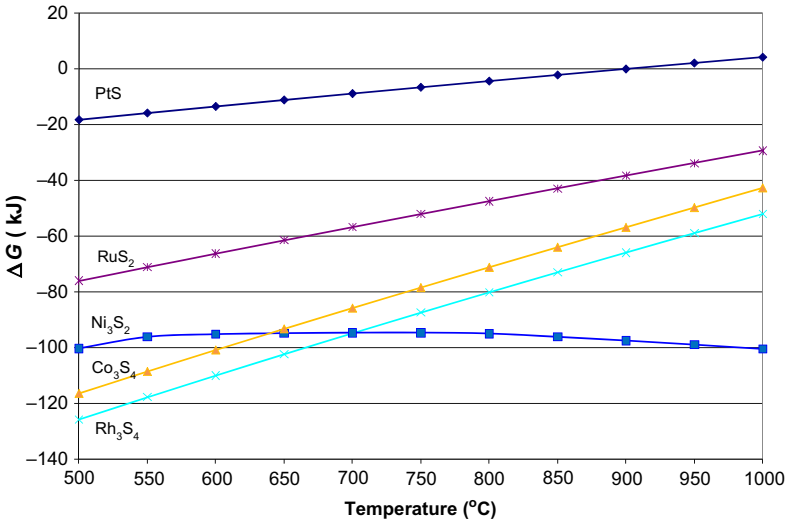

FIGURE 5.34 Gibbs free energy for sulfides of common metals used in CPOX.

added to Pt supported on $MgAl_2O_4$ spinel. All catalysts produced similar H_2 and CO concentrations of 23 and 25 vol%, respectively. There was a discernible difference in the carbon deposition. The unpromoted Pt catalyst showed carbon levels of 0.02 wt% carbon, where the alkali and alkaline earth promoted Pt catalysts had carbon levels of 0.01 wt%.

In another study by the same group [107], K, Ca, and CaK promoters were added to Rh supported on $MgAl_2O_4$ spinel. Both modified and unmodified catalysts produced similar H_2 and CO concentrations of 23 and 25 vol%, respectively. The different modifiers did affect carbon production on the catalysts. The unpromoted Rh catalyst showed carbon levels of 0.03 wt% carbon, where the RhK catalyst had 0.02 wt% carbon, the RhCa 0.015 wt%, and the RhCaK only 0.01 wt%. Bimetallic PtRh with Li, Ba, and LiBa modifiers supported on $MgAl_2O_4$ spinel was also examined for H_2 and CO yields and carbon formation resistance, with similar results to previous work for the yields. The unpromoted PtRh catalyst showed carbon levels of 0.01 wt% carbon, where the promoted PtRh catalysts all showed reduced coking levels of 0.005 wt%.

5.5.2.2. Supports

The catalyst support is as critical as the active catalyst for the CPOX of higher hydrocarbons. The catalyst may be deposited as a metal onto the support or as a mixed oxide. The support can provide the desired level of metal dispersion and morphology to optimize the catalyst performance by enhancing mass and heat transfer properties. Further, as discussed in Section 5.3, the support often plays a role in the surface reaction mechanism. Therefore, the properties of the support surface are as critical as the catalyst itself.

Shekhawat et al. [108] conducted CPOX studies on *n*-tetradecane (TD) containing sulfur and polynuclear aromatics over supported Rh and Pt catalysts. The tests were designed to examine the effect of the support on the metal catalyst. The supports used were alumina and ZDC, an oxygen-conducting support. The studies were conducted in three steps: (1) CPOX of pure TD for 1 h to establish a baseline, (2) TD + contaminant for 2 h, and (3) pure TD for 2 h to examine recovery of activity. The sulfur contaminant species was DBT and was added at a level of 1000 ppmw. The aromatic

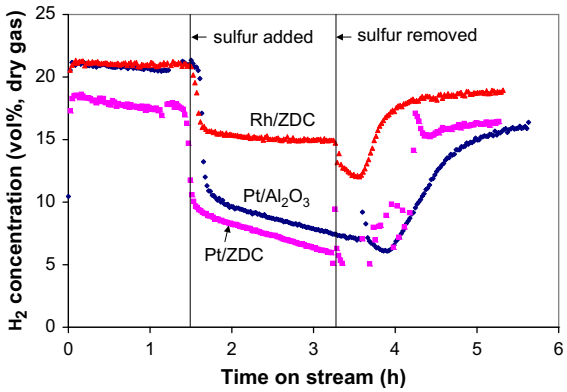

FIGURE 5.35 CPOX step response plot for H_2 production (concentration, dry gas vol%) from TD with 1000 ppmw sulfur. *Reprinted from Shekhawat et al. [108], Copyright (2006), with permission from Elsevier.*

contaminant species was 1-methylnapthalene (MN) and was added to a level of 5 wt%.

The H_2 production for each catalyst under the two different conditions is shown in Figs 5.35 and 5.36. The Rh/ZDC catalyst produced the best performance in the presence of both DBT and MN. This was attributed to both the better activity of Rh over Pt, as well as the effect of the oxygen-conductivity of the ZDC. The latter was not verified in this study, since no testing was reported for Rh/alumina. Indeed, the data

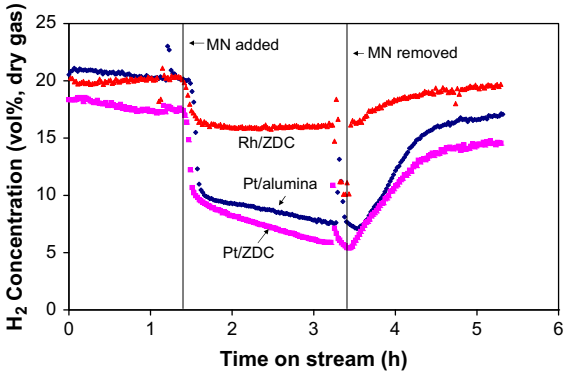

FIGURE 5.36 CPOX step response plot for H_2 production (concentration, dry gas vol%) from TD with 5 wt% 1-methylnaphthalene. *Reprinted from Shekhawat et al. [108], Copyright (2006), with permission from Elsevier.*

presented for Pt indicated that the alumina support was better. However, as discussed in Section 5.4.1.1.4, the surface area of the support is important since it can effect the dispersion. In this study, the alumina support had a surface area of 198 m^2/g compared to 70 m^2/g. Therefore, it is possible that under these conditions that the benefit of the high surface area was greater than the benefit of the oxygen conductivity of the support.

Rh-based catalysts have also been investigated on various support structures, resulting in different H_2 and CO yields. Gasoline and naphtha CPOX over a supported Rh catalyst were reported by Fujitani and Muraki [109]. For γ-alumina-supported Rh catalyst, maximum yields of 96% of both H_2 and CO were reported with 0.2 wt% Rh loading at 700 °C, an air equivalence ratio of 0.41. A 0.05 wt% Rh supported on zirconia yielded 98% H_2 and 85% CO at 725 °C, an equivalence ratio of 0.41. However, 0.1 wt% Rh loaded on a honeycomb structure of α-alumina-magnesia gave the highest yield of H_2 and CO (both 98%) at 820 °C, air equivalence ratio of 0.41. Furthermore, carbon deposition was not observed with these supported Rh catalysts.

The CPOX reaction has also been studied using reactors with very short contact times. Cyclohexane, *n*-C_6, *n*-C_8, *n*-C_{10}, *n*-C_{16}, *i*-C_8, toluene, naphthalene, and gasoline CPOX have been studied over Rh-based monolithic catalysts at millisecond contact times [110–113]. Several factors affect the conversion and selectivity of these fuels. The mean cell density, typically defined as pores per inch (ppi) for foam materials (e.g., 40 ppi corresponds to a mean cell diameter of ~0.6 mm), significantly affected the syngas selectivities, but the gas space velocity did not.

Krummenacher et al. [114] have reported syngas selectivities greater than 80% with greater than 99% conversion of hydrocarbons from the catalytic CPOX of *n*-C_{10} and *n*-C_{16} over a Rh-coated monolith at 5–25 ms contact times. CPOX of a high-grade diesel fuel

(10 ppm sulfur, 8% aromatics, and 90% alkanes) produced syngas at greater than 98% fuel conversion. Maximum selectivities of H_2 and CO observed were 70% and 80%, respectively, at an O/C ratio of 1.4 and 25 ms contact time.

5.5.2.3. *Substitution into Oxide Structures*

One of the challenges for the hexaaluminate structure is the limitation to which metals can be substituted into the lattice. No reports of substituting larger metals like Rh into the hexaaluminate structure were found. However, Rh and Ru have been successfully substituted into oxides such as perovskites and pyrochlores. Haynes et al. [104,115,116] reported CPOX testing on *n*-tetradecane for Rh- and Ru-substituted pyrochlores with a great deal of success. These catalysts demonstrated high performance and stability in the presence of sulfur and aromatics.

Figures 5.37 and 5.38 show the performance for the CPOX of *n*-tetradecane of a Ru- and a Rh-substituted pyrochlore, respectively [104,116]. Both catalysts successfully reform the fuel into H_2 and CO, even in the presence of sulfur and aromatic species. Further, the Rh-substituted pyrochlore exhibits stable performance even in the presence of a much higher sulfur concentration of 1000 ppmw, compared to 50 ppmw for Ru.

5.5.3. Summary of Higher Hydrocarbons

The CPOX of higher hydrocarbons presents additional challenges to catalyst performance due to the presence of high sulfur and aromatic contaminant species. These components can quickly deactivate traditional catalysts from sulfur poisoning and coke formation. As a result, different approaches to catalyst design must be taken. The approaches discussed in this section included the use of oxygen-conducting supports and/or substitution into thermally stable oxides. Even with these types of materials, noble metals will likely need to be used, even if simply added in small quantities to base metal catalysts.

5.6. OXYGENATED HYDROCARBONS

5.6.1. Alcohols

Alcohols are an attractive fuel type for transportation applications mainly because they are liquids and are easily prepared from synthesis

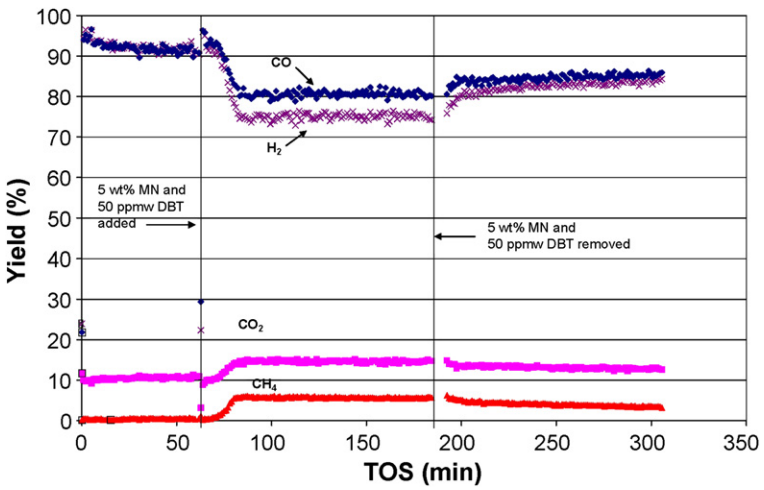

FIGURE 5.37 Yields for LSRuZ during 5 h CPOX experiment: GHSV = 50,000 $cm^3\ g_{cat}^{-1}\ h^{-1}$, O/C = 1.2, 900 °C, and 0.23 MPa. *Reprinted from Haynes et al. [116], Copyright (2010), with permission from Elsevier.*

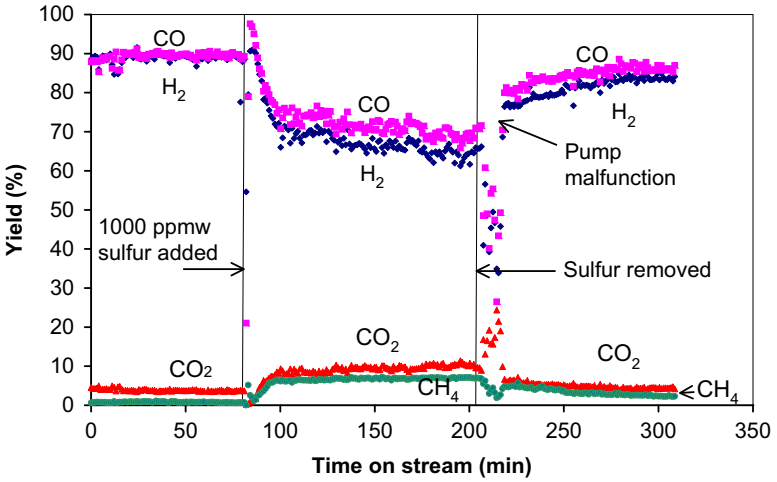

FIGURE 5.38 Yields for LSRhZ during 5 h CPOX experiment: GHSV = 50,000 $cm^3\ g_{cat}^{-1}\ h^{-1}$, O/C = 1.2, 900 °C, and 0.23 MPa. *Reprinted from Haynes et al. [104], Copyright (2009), with permission from Elsevier.*

gas. Typically, the CPOX of alcohols can be run at lower temperatures than the CPOX of alkanes since they are more easily activated. Ni, Pt, and Rh [68,117–120] have been shown to be good catalysts for CPOX of alcohols, although Cu, Zn, Pd, and Au can be more common [121–126], especially for methanol and ethanol. The purpose of this section will be to provide some basic insight into the conversion of different alcohols and product distributions, rather than a comparison or detailed analysis of the various catalysts used.

Cao and Hohn [68] examined the CPOX of methanol over Pt/Al_2O_3. These studies were conducted from 500 °C to 700 °C and at an O/C ratio of 0.5–2.0. Formate was identified as an important intermediate species and is formed from surface methoxy groups, which come from the dissociative adsorption of methanol at the oxygen site by splitting the O–H bond. Indirect formate decomposition was identified to be dominant for CO_2 production at high temperatures. Important trends in the data were that CO_2 production increased as temperature decreased. This is likely due to an increase in the rate of CO desorption preventing it from being oxidized on the surface. Overall, both H_2 and CO selectivities were higher at higher temperatures. Also, higher oxygen concentrations favored H_2 and HCOOH formation; CO_2 also increased with increasing oxygen.

The CPOX of ethanol was studied by Liguras et al. [118]. Ni/La_2O_3 catalysts were supported on cordierite monoliths, ceramic foams, and γ-alumina pellets. The catalyst prepared by wash-coating on cordierite monoliths was determined to be excellent for H_2 production from ethanol. Although this catalyst had significant coke formation, it did not appear to affect the activity or selectivity. The catalyst supported on zirconia–alumina foam gave slightly better performance. The same group examined the use of Ru catalysts for the CPOX of ethanol [117]. These materials also utilized cordierite monoliths, ceramic foams, and γ-alumina pellets. In contrast to the study on Ni catalysts, the Ru catalyst on the ceramic foams gave the best performance. This was attributed to the smaller pore sizes and higher tortuosity.

Other noble metal catalysts supported on alumina foams were studied for the CPOX of ethanol by Salge et al. [119]. The catalysts were Rh, Rh-Ce, Pt, Pd, and Rh-Ru. Ethanol was found to adsorb dissociatively as an ethoxide

species. To produce syngas, these species then decompose to carbon, oxygen, and hydrogen species. H_2 and CO are formed by surface reaction of these species. The Rh catalysts produced syngas by this mechanism, and the Rh-Ce catalyst was found to give the highest selectivity and stability. This was partially attributed to the red-ox properties of Ce. In contrast, it was demonstrated that the ethoxides formed on the surfaces of Pt and Pd leads to dehydrogenation and acetaldehyde formation, yielding little syngas production.

A major contribution to the study of the CPOX of alcohols is the work by Wanat et al. [120], who examined methanol, ethanol, 1-propanol, and 2-propanol. A significant amount of data was provided in this effort. One set of results selected for this discussion are presented in Fig. 5.39, which compares the reaction of all four alcohols over one catalyst

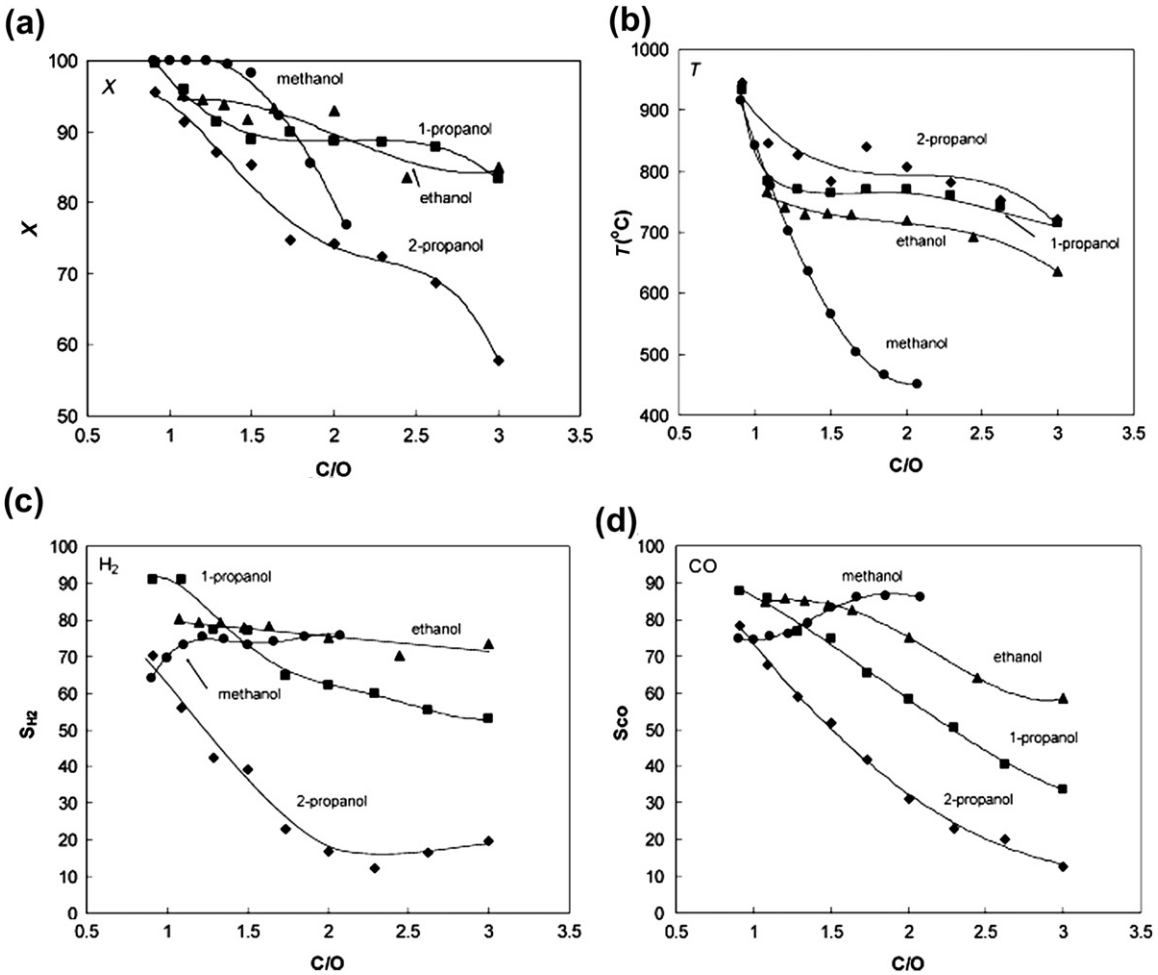

FIGURE 5.39 CPOX of different alcohols at varied C/O ratio with Rh-Ce catalyst on a foam monolith. *Reprinted from Wanat et al. [120], Copyright (2005), with permission from Elsevier.*

(Rh-Ce on a foam monolith). Methanol conversion was nearly complete until very carbon-rich conditions were reached. Ethanol and 1-propanol had much higher conversions than 2-propanol. The temperature trends were similar for all alcohols, decreasing with lower oxygen concentrations, although for methanol the temperature drop is more drastic. Both H_2 and CO selectivities increased for methanol at higher oxygen concentrations, which can be correlated to the much lower reactor temperatures. Overall, 2-propanol had the lowest conversion, as well as the lowest H_2 and CO selectivities.

Some of the major conclusions for the entire study, which examined other catalysts and reaction conditions, state that Rh-Ce catalyst was the best for H_2 and CO with little formation of higher products. Rh and Rh-Co catalysts produced less H_2 and CO with more higher products. The trends were similar for all alcohols, except for methanol, which produced no higher products. Methanol and ethanol produced mostly H_2 and CO; however, higher alcohols have the potential to produce larger products. The size and structure of the alcohol will influence product distributions significantly. The difference in performance between 1-propanol and 2-propanol is an excellent example of how the structure can change the overall conversion and selectivity.

5.6.2. Dimethyl Ether (DME)

The CPOX of DME, CH_3OCH_3, for H_2 and CO production has several advantages. First, it has a high H/C ratio and energy density. DME is inert, non-carcinogenic, non-mutagenic, non-corrosive, and non-toxic [127–128]. Further, its production from syngas is more economical and thermodynamically favorable than methanol. DME would also require less costly infrastructure for transport and storage since it possesses similar physical properties as LPGs.

Zhang et al. [129-130] studied the CPOX of DME over Rh-, Pt-, and Ni-based catalysts at ambient pressure and 600–750 °C with yields greater than 90% and little methane production. The reaction mechanism is analogous to the indirect mechanism for methane CPOX. In fact, promoting initial combustion is critical to prevent DME decomposition to CH_4, CO, and H_2, which yields low H_2 and CO production. Therefore, it was demonstrated that a catalyst that suppresses DME decomposition and is active for reforming will promote high H_2 and CO yields. Different alkaline metal promoters were added to Rh and Pt catalysts and the optimal performance was obtained with Na-Rh/Al_2O_3. 6 wt%Ni/Al_2O_3 was used as the reforming catalyst.

Wang et al. [131] examined catalysts on a variety of supports including alumina, silica, magnesium oxide, yttrium-stabilized zirconia, samarium-doped ceria, and a LaGa-perovskite. The activities for the CPOX of DME with the catalysts supported on Al_2O_3 were found to be ranked as follows: Ni > Rh > Co >> Ru > Fe > Pt >> Ag. The catalyst that was most active and selective for conversion of DME to syngas was $Ni/LaGaO_3$.

5.6.3. Biodiesel

Bio-derived fuels have received increasing interest over the past few years in efforts to reduce net carbon emissions from energy usage. Since liquid fuels will remain the primary transportation energy source for the foreseeable future, biodiesel is an attractive fuel option. Biodiesel is prepared by the trans-esterification of vegetable oils or animal fat by reaction with an alcohol. The resulting product is a mono-alkyl ester with a long hydrocarbon chain often containing one or more unsaturated bonds. For more details on this fuel type, see Chapter 3.

Like other liquid hydrocarbons, biodiesel can be vaporized and reformed to produce H_2 and

CO. Reforming of biodiesel does not possess the same challenges as conventional petro-diesel since it does not contain sulfur or aromatic species. Further, there is a reduction in coke formation due to the presence of oxygen in the fuel itself.

There are very few studies in literature that report on the CPOX of biodiesel. One study by Nguyen and Leclerc [132] examined the CPOX of methyl acetate as a model fuel for biodiesel. These experiments were conducted on Rh and Rh-Ce catalysts. The most important findings of this study include that the primary products from the oxidation of methyl acetate are CO and H_2O, rather than CO_2 and H_2O. Further, methyl acetate produced less syngas than biodiesel reported in another study, which used a soy oil-derived fuel [133]. This was suggested to be related to the likelihood that biodiesel will have longer carbon chains attached to the methyl ester functional group, which may be more reactive than a single methyl group. Nevertheless, since the methyl ester group in biodiesel will limit H_2 yield, the authors stated the need to develop catalysts that target the decomposition of methyl esters.

5.6.4. Summary of Oxygenated Hydrocarbons

The CPOX of different oxygenated hydrocarbons were discussed with a number of base and noble metal catalyst. The differences in mechanism, product distribution, and operating conditions for different alcohols were identified. The use of DME for syngas production was evaluated. The potential for the CPOX of biodiesel fuels was also considered.

5.7. FUTURE DEVELOPMENT AND APPLICATIONS

5.7.1. Substituted Oxides on Oxygen-Conducting Supports

The development of hydrocarbon POX catalysts by National Energy Technology Laboratory research group [76,101–105,108,115,116,134–139], discussed in detail in Sections 5.4 and 5.5, is summarized well by Fig. 5.40. Starting with a traditional supported metal catalyst, the three major modes of deactivation (thermal

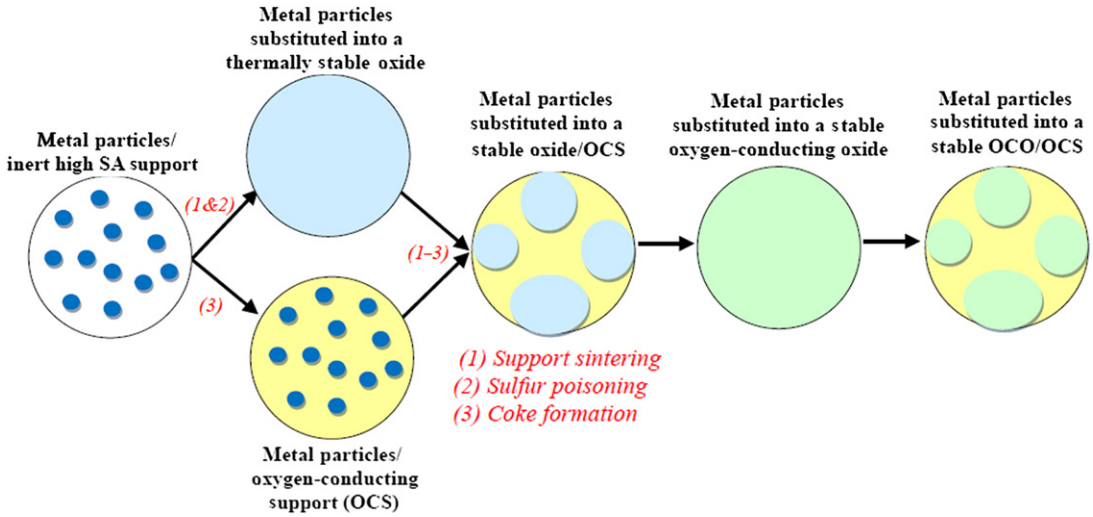

FIGURE 5.40 Development of POX catalyst for reforming hydrocarbons.

sintering, sulfur poisoning, and coke formation) were addressed initially by two separate approaches. The first was substituting the metal into a thermally stable oxide structure, which helped reduce both the thermal sintering and sulfur poisoning. Separately, supporting the active metal onto an oxygen-conducting support helped mitigate carbon formation. Combining these approaches produced the greatest level of success. Ultimately, the best catalyst design consisted of substituted oxides containing a certain level of oxygen conductivity (i.e., pyrochlores) deposited onto an oxygen-conducting support.

However, a very important aspect of this catalyst design approach remains to be conducted. While superior performance was attained with this catalyst system [134,138–139], the interaction of the active phase and the support needs to be fully characterized. Specifically, the nature of the active phase and the manner in which it is deposited onto the support can affect its interaction with the support and overall performance. Further, the optimal size of the active phase deposits and their overall ratio to the support will be different for various combinations of materials that can be selected for specific fuels and reaction conditions. Therefore, a method for designing such a catalyst system is needed that can incorporate at a minimum the catalytic activity, morphology, and oxygen-conductivity of an active and support phase.

5.7.2. Multistaged Reactor

The use of a staged reactor system operates on the assumption of an indirect mechanism for the CPOX of hydrocarbons (see Section 5.3.1). This approach could take one of two forms to produce a desired product distribution: multiple oxygen feed locations, or multiple catalyst formulations.

5.7.3.1. Multiple Oxygen Feed Locations

The approach of feeding a portion of the oxygen supplied to different locations along the length of the reactor could be used to reduce or eliminate the exotherm at the leading edge of the catalyst bed [140–141]. This could promote an increase in the extent of reaction from the direct mechanism. It may also allow control of product distribution in the syngas, specifically the CO/CO_2 ratio. Minimizing the temperature spike and the presence of hot spots may also allow the use of less-expensive reactor materials, reduction in catalyst loss from vaporization, and support sintering.

5.7.3.2. Multiple Catalyst Formulations

The approach of using multiple catalyst compositions at different positions in a reactor for the CPOX of methane has been presented in several recent studies [140–144]. Figure 5.41 is a diagram of the justification for such an approach. In considering reactor design, it may be advantageous to enhance the reactions occurring in a region where the rate-limiting steps occur. Further, like the staged oxygen feed approach, the temperature spike may be reduced through the use of a less-oxidizing catalyst in the front part of the bed. Of greatest interest may be the

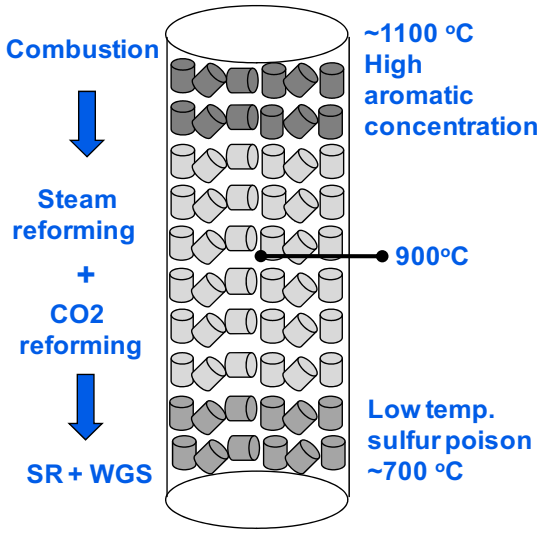

FIGURE 5.41 Graded catalyst bed design.

ability to reduce cost by decreasing the amount of expensive noble metal catalyst needed. This may be accomplished by the use of less-expensive catalysts like Ni or Ru in the regions of the reactor where conditions are less conducive to deactivation of these metals. The studies previously cited that examined gas composition with respect to reactor position would be most helpful for this design approach [55,60,61].

The graded catalyst bed approach may prove to be most helpful for the CPOX of higher hydrocarbons because these fuels often contain organic sulfur and aromatic species. Therefore, the form these species take at different positions of the reactor may be more or less likely to deactivate non-noble metal catalyst, again possibly providing an opportunity to reduce cost by their use in these sections. The front section of the catalyst bed may deactivate rapidly due to higher temperatures and contaminant concentrations. Further, the end portion of the catalyst bed may also cause significant deactivation for catalysts susceptible to sulfur poisoning due to the lower temperatures resulting from the endothermic reforming reactions. Therefore, it may be necessary only to use noble metal catalysts in one or both of these sections and a less-expensive alternative may be used in the remaining parts of the reactor.

5.7.3. Field-assisted CPOX

The application of different electromagnetic fields to heterogeneous catalyst systems has received increasing attention in the last 10 years. For example, radio frequency (RF) and plasma fields applied to a CPOX system have the potential to improve the overall performance by reducing the amount of carbon formation in the reactor and on the catalyst surface by supplying energy to hydrocarbon species that are difficult to convert and can lead to the formation of coke precursors. This approach could allow for the use of less-expensive catalyst materials, as well as drastically extending the life of the catalyst. The combination of a catalyst with a plasma system for the partial oxidation of methane [145] and liquid hydrocarbon fuels [146] has been reported. Due to the higher levels of aromatic and unsaturated hydrocarbons, the application of plasma may be most beneficial for the CPOX of liquid hydrocarbons. Sobacchi et al. [146] showed a significant improvement in H_2 production from gasoline with the plasma-assisted system over catalyst alone at relatively low temperatures. While exact mechanisms are unknown, the data presented in these studies is compelling and suggests a tremendous opportunity for additional research. A much more detailed discussion of the application of a plasma field to the reforming of hydrocarbon fuels can be found in Chapter 8.

Another field of interest is the application of microwaves to catalytic systems. Two reviews are available that examine the application of microwaves to a variety of reaction systems, which utilize heterogeneous catalysis [147–148]. These reactions include oxidative coupling of methane, selective oxidation of aliphatic and aromatic hydrocarbons, and reforming of methane with carbon dioxide.

5.7.4. CPOX with Recycle

The presence of steam in the reactant gas of a catalytic fuel reformer decreases the formation of carbon, minimizing catalyst deactivation. However, the operation of the reformer without supplemental water reduces the size, weight, cost, and overall complexity of the system. Shekhawat et al. [135] examined two options for adding steam to the reformer inlet: (1) recycle of a simulated fuel cell anode exit gas (comprised of mainly CO_2, H_2O, and N_2 and some H_2 and CO) and (2) recycle of the reformate from the reformer exit back to the reformer inlet (mainly comprised of H_2, CO, and N_2 and some H_2O and CO_2). The anode gas recycle reduced the carbon formation and increased the H_2 concentration in the reformate. However,

reformer recycle was not as effective due principally to the lower water content in the reformate compared to the anode gas. In fact, the reformate recycle showed slightly increased carbon formation compared to no recycle. In an attempt to understand the effects of individual gases in these recycle streams (H_2, CO, CO_2, N_2, and H_2O), individual gas species were independently introduced to the reformer feed.

The main conclusions of this study were as follows: (1) Recycle of a simulated anode offgas increased CO and H_2 yields and greatly reduced carbon deposition compared to recycle of a simulated reformer product gas. (2) The total quantity of carbon formed decreased monotonically with anode gas recycle ratio, due to the higher levels of carbon dioxide and steam that oxidize the carbon. (3) The separate effects of five individual components of the recycle gas (H_2, CO, CO_2, H_2O, and N_2) show that carbon dioxide and water decrease carbon formation, while H_2 has the same effect as the presumably unreactive nitrogen; CO increases carbon formation compared to nitrogen; the decrease in carbon formation due to carbon dioxide is believed to be due to the Boudouard reaction while steam in the recycle stream gasifies carbon to CO + H_2. The results of this study suggest that additional research and optimization of a recycle stream would be beneficial for a reformer-solid oxide fuel cell system.

References

[1] Enger BC, Lødeng R, Holmen A. A review of catalytic partial oxidation of methane to synthesis gas with emphasis on reaction mechanisms over transition metal catalysts. Appl Catal A: Gen 2008;346 (1–2):1–27.

[2] Bharadwaj SS, Schmidt LD. Catalytic partial oxidation of natural gas to syngas. Fuel Proc Technol 1995;42(2–3):109–27.

[3] Tsang SC, Claridge JB, Green MLH. Recent advances in the conversion of methane to synthesis gas. Catal Today 1995;23(1):3–15.

[4] Freni S, Calogero G, Cavallaro S. Hydrogen production from methane through catalytic partial oxidation reactions. J Power Sources 2000;87(1–2): 28–38.

[5] York APE, Xiao T, Green MLH. Brief overview of the partial oxidation of methane to synthesis gas. Topics Catal 2003;22(3–4):345–58.

[6] York APE, Xiao T, Green MLH, Claridge JB. Methane oxyforming for synthesis gas production. Catal Rev 2007;49(4):511–60.

[7] Shekhawat D, Berry DA, Gardner TH, Spivey JJ. Catalytic reforming of liquid hydrocarbon fuels for fuel cell applications. In: Spivey JJ, Dooley KM, editors. Catalysis. Cambridge: The Royal Society of Chemistry; 2006;19:184–253.

[8] Krumpelt M, Krause TR, Carter JD, Kopasz JP, Ahmed S. Fuel processing for fuel cell systems in transportation and portable power applications. Catal Today 2002;77(1–2):3–16.

[9] Michael BC, Donazzi A, Schmidt LD. Effects of H_2O and CO_2 addition in catalytic partial oxidation of methane on Rh. J Catal 2009;265(1):117–29.

[10] Jing QS, Zheng XM. Combined catalytic partial oxidation and CO_2 reforming of methane over ZrO_2-modified Ni/SiO_2 catalysts using fluidized-bed reactor. Energy 2006;31(12):2184–92.

[11] Schneider A, Mantzaras J, Jansohn P. Experimental and numerical investigation of the catalytic partial oxidation of CH_4/O_2 mixtures diluted with H_2O and CO_2 in a short contact time reactor. Chem Eng Sci 2006;61(14):4634–49.

[12] Cellier C, Blangy B, Mateos-Pedrero C, Ruiz P. Modification of catalytic performances due to the co-feeding of hydrogen or carbon dioxide in the partial oxidation of methane over a NiO/γ-Al_2O_3 catalyst. Catal Today 2006;112(1–4):112–6.

[13] Burke NR, Trimm DL. The relative importance of CO_2 reforming during the catalytic partial oxidation of CH_4-CO_2 mixtures. In: Xinhe B, Yide X, editors. Stud Surf Sci Catal. Elsevier; 2004 ;147:299–34.

[14] He S, Jing Q, Yu W, Mo L, Lou H, Zheng X. Combination of CO_2 reforming and partial oxidation of methane to produce syngas over Ni/SiO_2 prepared with nickel citrate precursor. Catal Today 2009;148(1–2):130–3.

[15] He S, Wu H, Yu W, Mo L, Lou H, Zheng X. Combination of CO_2 reforming and partial oxidation of methane to produce syngas over Ni/SiO_2 and Ni-Al_2O_3/SiO_2 catalysts with different precursors. Int J Hydrogen Energy 2009;34(2):839–43.

[16] Choudhary VR, Mondal KC. CO_2 reforming of methane combined with steam reforming or partial oxidation of methane to syngas over $NdCoO_3$ perovskite-type mixed metal-oxide catalyst. Appl Energy 2006;83(9):1024–32.

[17] Choudhary VR, Mondal KC, Choudhary TV. Partial oxidation of methane to syngas with or without simultaneous steam or CO_2 reforming over a high-temperature stable-NiCoMgCeO$_x$ supported on zirconia-hafnia catalyst. Appl Catal A: Gen 2006;306:45–50.

[18] Cellier C, Clef DL, Mateos-Pedrero C, Ruiz P. Influence of the co-feeding of CO, H_2, CO_2 or H_2O in the partial oxidation of methane over Ni and Rh supported catalysts. Catal Today 2005;106(1–4):47–51.

[19] Puolakka KJ, Juutilainen S, Krause AOI. Combined CO_2 reforming and partial oxidation of n-heptane on noble metal zirconia catalysts. Catal Today 2006;115 (1–4):217–21.

[20] Jing Q, Lou H, Mo L, Fei J, Zheng X. Combination of CO_2 reforming and partial oxidation of methane over Ni/BaO-SiO_2 catalysts to produce low H_2/CO ratio syngas using a fluidized bed reactor. J Mol Catal A: Chem 2004;212(1–2):211–7.

[21] Souza MMVM, Schmal M. Combination of carbon dioxide reforming and partial oxidation of methane over supported platinum catalysts. Appl Catal A: Gen 2003;255(1):83–92.

[22] Tsyganok AI, Inaba M, Tsunoda T, Suzuki K, Takehira K, Hayakawa T. Combined partial oxidation and dry reforming of methane to synthesis gas over noble metals supported on Mg-Al mixed oxide. Appl Catal A: Gen 2004;275(1–2):149–55.

[23] Wang W, Stagg-Williams SM, Noronha FB, Mattos LV, Passos FB. Partial oxidation and combined reforming of methane on Ce-promoted catalysts. Catal Today 2004;98(4):553–63.

[24] Larentis AL, de Resende NS, Salim VMM, Pinto JC. Modeling and optimization of the combined carbon dioxide reforming and partial oxidation of natural gas. Appl Catal A: Gen 2001;215(1–2):211–24.

[25] Liu S, Xiong G, Dong H, Yang W. Effect of carbon dioxide on the reaction performance of partial oxidation of methane over a LiLaNiO/γ-Al_2O_3 catalyst. Appl Catal A: Gen 2000;202(1):141–6.

[26] Choudhary VR, Uphade BS, Mamman AS. Partial oxidation of methane to syngas with or without simultaneous CO_2 and steam reforming reactions over Ni/$AlPO_4$. Micro Meso Mater 1998;23(1–2):61–6.

[27] Claridge JB, Green MLH, Tsang SC. Methane conversion to synthesis gas by partial oxidation and dry reforming over rhenium catalysts. Catal Today 1994;21(2–3):455–60.

[28] Uchijima T, Nakamura J, Sato K, Aikawa K, Kubushiro K, Kunimori K. Production of synthesis gas by partial oxidation of methane and reforming of methane with carbon dioxide. In: Curry-Hyde HE, Howe RF, editors. Stud Surf Sci Catal. Elsevier; 1994; 81: 325–7.

[29] Hutchings GJ, Scurrell MS, Woodhouse JR. Direct partial oxidation of methane: effect of the oxidant on the reaction. Appl Catal 1988;38(1):157–65.

[30] Vernon PDF, Green MLH, Cheetham AK, Ashcroft AT. Partial oxidation of methane to synthesis gas, and carbon dioxide as an oxidising agent for methane conversion. Catal Today 1992;13(2–3):417–26.

[31] Roin A. HSC Chemistry Ver. 5.0. Outokumpu Research; 2002. Oy, Finland.

[32] Hickmann DA, Schmidt LD. Synthesis gas formation by direct oxidation of methane over Pt monoliths. J Catal 1992;138(1):267–82.

[33] Hickmann DA, Schmidt LD. Production of syngas by direct catalytic oxidation of methane. Science 1993;259:343.

[34] Hickmann DA, Schmidt LD. Synthesis gas formation by direct oxidation of methane over monoliths. Washington, D.C.: American Chemical Society Meeting; 1993.

[35] Hickmann DA, Schmidt LD. Synthesis gas formation by direct oxidation of methane over rhodium monoliths. Catal Lett 1993;17:223.

[36] Peters K, Rudolf M, Voetter H. Brennstoff-Chem 1955;36:257.

[37] Dissanayake D, Rosynek MP, Kharas KCC, Lunsford JH. Partial oxidation of methane to carbon monoxide and hydrogen over a Ni/Al_2O_3 catalyst. J Catal 1991;132(1):117–27.

[38] Au CT, Hu YH, Wan HL. Pulse studies of CH_4 interaction with NiO/Al_2O_3 catalysts. Catal Lett 1994;27(1–2):199–206.

[39] Au CT, Wang HY, Wan HL. Mechanistic studies of CH_4/O_2 conversion over SiO_2-supported nickel and copper catalysts. J Catal 1996;158(1):343–8.

[40] Vermeiren WJM, Blomsma E, Jacobs PA. Catalytic and thermodynamic approach of the oxyreforming reaction of methane. Catal Today 1992;13(2–3):427–36.

[41] Hu YH, Ruckenstein E. Pulse-MS study of the partial oxidation of methane over Ni/La_2O_3 catalyst. Catal Lett 1995;34(1(2)):41–50.

[42] Hu YH, Ruckenstein E. Transient kinetic studies of partial oxidation of CH_4. J Catal 1996;158(1):260–6.

[43] Heitnes K, Lindberg S, Rokstad OA, Holmen A. Catalytic partial oxidation of methane to synthesis gas. Catal Today 1995;24(3):211–6.

[44] Heitnes K, Lindberg S, Rokstad OA, Holmen A. Catalytic partial oxidation of methane to synthesis gas using monolithic reactors. Catal Today 1994; 21(2–3):471–80.

[45] Mallens EPJ, Hoebink JHBJ, Marin GB. An investigation on the reaction mechanism for the partial oxidation of methane to synthesis gas over platinum. Catal Lett 1995;33(3,4):291–304.

[46] Passos FB, Oliveira ER, Mattos LV, Noronha FB. Effect of the support on the mechanism of partial oxidation of methane on platinum catalysts. Catal Lett 2006;110(1–2):161–7.
[47] Hochmuth JK. Catalytic partial oxidation of methane over a monolith supported catalyst. Appl Catal B: Env 1992;1(2):89–100.
[48] Hickmann DA, Schmidt LD. Steps in methane oxidation on platinum and rhodium surfaces. High-temperature reactor simulations. AIChE J 1993;39:1164.
[49] Oh SH, Mitchell PJ, Siewert RM. Methane oxidation over alumina-supported noble metal catalysts with and without cerium additives. J Catal 1991;132(2):287–301.
[50] Walter K, Buyevskaya OV, Wolf D, Baerns M. Rhodium-catalyzed partial oxidation of methane to CO and H_2. In situ DRIFTS studies on surface intermediates. Catal Lett 1994;29(1,2):26170.
[51] Buyevskaya OV, Walter K, Wolf D, Baerns M. Primary reaction steps and active surfaces sites in the rhodium-catalyzed partial oxidation of methane to CO and H_2. Catal Lett 1996;38(1,2):81–8.
[52] Buyevskaya OV, Wolf D, Baerns M. Rhodium-catalyzed partial oxidation of methane to CO and H_2. Transient studies on its mechanism. Catal Lett 1994; 29(12):249–60.
[53] Heitnes K, Rokstad OA, Holmen A. Partial oxidation of methane over platinum metal gauze. Catal Lett 1996;36:25–30.
[54] Qin D, Lapszewicz J, Jiang X. Comparison of partial oxidation and steam-CO_2 mixed reforming of CH_4 to syngas on MgO-supported metals. J Catal 1996;159 (1):140–9.
[55] Horn R, Williams KA, Degenstein NJ, Schmidt LD. Syngas by catalytic partial oxidation of methane on rhodium: mechanistic conclusions from spatially resolved measurements and numerical simulations. J Catal 2006;242(1):92–102.
[56] Wang D, Dewaele O, de Groote AM, Froment GF. Reaction mechanism and role of the support in the partial oxidation of methane on Rh/Al_2O_3. J Catal 1996;159(2):418–26.
[57] Boucouvalas Y, Zhang Z, Verykios XE. Heat transport limitations and reaction scheme of partial oxidation of methane to synthesis gas over supported rhodium catalysts. Catal Lett 1994;27:131–42.
[58] Au CT, Wang HY. Mechanistic studies of methane partial oxidation to syngas over SiO_2-supported rhodium catalysts. J Catal 1997;167(2):337–45.
[59] Shustorovich E. The bond-order conservation approach to chemisorption and heterogeneous catalysis: applications and implications. In: DD Eley HP, Paul BW, editors. Adv Catal: Academic Press; 1990. p. 101–63.
[60] Horn R, Williams KA, Degenstein NJ, Bitsch-Larsen A, Dalle Nogare D, Tupy SA, et al. Methane catalytic partial oxidation on autothermal Rh and Pt foam catalysts: oxidation and reforming zones, transport effects, and approach to thermodynamic equilibrium. J Catal 2007;249(2):380–93.
[61] Horn R, Williams KA, Degenstein NJ, Schmidt LD. Mechanism of H_2 and CO formation in the catalytic partial oxidation of CH_4 on Rh probed by steady-state spatial profiles and spatially resolved transients. Chem Eng Sci 2007;62(5):1298–307.
[62] Prettre M, Eichner C, Perrin M. The catalytic oxidation of methane to carbon monoxide and hydrogen. Trans Faraday Soc 1946;43:335–40.
[63] Enger BC, Lødeng R, Holmen A. Evaluation of reactor and catalyst performance in methane partial oxidation over modified nickel catalysts. Appl Catal A: Gen 2009;364(1–2):15–26.
[64] Vernon PDF, Green MLH, Cheetham AK, Ashcroft AT. Partial oxidation of methane to synthesis gas. Catal Lett 1990;6:181–6.
[65] Boucouvalas Y, Zhang Z, Verykios XE. Partial oxidation of methane to synthesis gas via the direct reaction scheme over Ru/TiO_2 catalyst. Catal Lett 1996;40(3(4)):189–95.
[66] Rabe S, Nachtegaal M, Vogel F. Catalytic partial oxidation of methane to synthesis gas over a ruthenium catalyst: the role of the oxidation state. Phy Chem Chem Phys 2007;9:1461–8.
[67] Rabe S, Vogel F, Truong T-B, Shimazu T, Wakasugi T, Aoki H, et al. Catalytic reforming of gasoline to hydrogen: kinetic investigation of deactivation processes. Int J Hydrogen Energy 2009;34(19):8023–33.
[68] Cao C, Hohn KL. Study of reaction intermediates of methanol decomposition and catalytic partial oxidation on Pt/Al_2O_3. Appl Catal A: Gen 2009;354 (1–2):26–32.
[69] Tsipouriari VA, Verykios XE. Kinetic study of the catalytic partial oxidation of methane to synthesis gas over Ni/La_2O_3 catalyst. In: Parmaliana A, Sanfilippo D, Frusteri F, Vaccari A, Arena F, editors. Stud Surf Sci Catal; 1998; 119: 795–800.
[70] Gubanova EL, Schuurman Y, Sadykov VA, Mirodatos C, van Veen AC. Evaluation of kinetic models for the partial oxidation of methane to synthesis gas over a $Pt/PrCeZrO_x$ catalyst coated on a triangular monolith. Chem Eng J 2009;154(1–3):174–84.
[71] De Smet CRH, de Croon MHJM, Berger RJ, Marin GB, Schouten JC. An experimental reactor to study the intrinsic kinetics of catalytic partial oxidation of methane in the presence of heat-transport limitations. Appl Catal A: Gen 1999;187 (1):33–48.

[72] de Groote AM, Froment GF. Simulation of the catalytic partial oxidation of methane to synthesis gas. Appl Catal A: Gen 1996;138(2):245–64.
[73] Slagtern A, Swaan HM, Olsbye U, Dahl IM, Mirodatos C. Catalytic partial oxidation of methane over Ni-, Co- and Fe-based catalysts. Catal Today 1998;46(2–3):107–15.
[74] Tang S, Lin J, Tan KL. Partial oxidation of metane to syngas over Ni/MgO, Ni/CaO and Ni/CeO_2. Catal Lett 1998;51:169–75.
[75] Ma D, Mei D, Li X, Gong M, Chen Y. Partial oxidation of methane to syngas over monolithic Ni/γ-Al_2O_3 catalyst – effects of rare earths and other basic promoters. J Rare Earths 2006;24(4):451–5.
[76] Salazar M, Berry DA, Gardner TH, Shekhawat D, Floyd D. Catalytic partial oxidation of methane over Pt/ceria-doped catalysts: effect of ionic conductivity. Appl Catal A: Gen 2006;310:54–60.
[77] Dajiang M, Yaoqiang C, Junbo Z, Zhenling W, Di M, Maochu G. Catalytic partial oxidation of methane over Ni/CeO_2-ZrO_2-Al_2O_3. J Rare Earths 2007;25(3): 311–5.
[78] Salazar-Villalpando MD, Reyes B. Hydrogen production over Ni/ceria-supported catalysts by partial oxidation of methane. Int J Hydrogen Energy 2009;34(24):9723–9.
[79] Bharadwaj SS, Schmidt LD. Synthesis gas formation by catalytic oxidation of methane in fluidized bed reactors. J Catal 1994;146(1):11–21.
[80] Bodke AS, Bharadwaj SS, Schmidt LD. The effect of ceramic supports on partial oxidation of hydrocarbons over noble metal coated monoliths. J Catal 1998;179(1):138–49.
[81] Hohn KL, Schmidt LD. Partial oxidation of methane to syngas at high space velocities over Rh-coated spheres. Appl Catal A: Gen 2001;211(1):53–68.
[82] Donazzi A, Michael BC, Schmidt LD. Chemical and geometric effects of Ce and washcoat addition on catalytic partial oxidation of CH_4 on Rh probed by spatially resolved measurements. J Catal 2008;260 (2):270–5.
[83] Lyubovsky M, Karim H, Menacherry P, Boorse S, LaPierre R, Pfefferle WC, et al. Complete and partial catalytic oxidation of methane over substrates with enhanced transport properties. Catal Today 2003; 83(1–4):183–97.
[84] Poirier MG, Jean G, Poirier MP. Partial oxidation of methane over a praseodymium/ruthenium pyrochlore catalyst. In: Kevin JS, Emerson CS, editors. Stud Surf Sci Catal. Elsevier; 1992;73:359–66.
[85] Klvana D, Vaillancourt J, Kirchnerova J, Chaouki J. Combustion of methane over $La_{0.66}Sr_{0.34}Ni_{0.3}Co_{0.7}O_3$ and $La_{0.4}Sr_{0.6}Fe_{0.4}Co_{0.6}O_3$ prepared by freeze-drying. Appl Catal A: Gen 1994;109(2):181–93.
[86] Jang BWL, Nelson RM, Spivey JJ, Ocal M, Oukaci R, Marcelin G. Catalytic oxidation of methane over hexaaluminates and hexaaluminate-supported Pd catalysts. Catal Today 1999;47(1–4):103–13.
[87] McCarty JG, Wise H. Perovskite catalysts for methane combustion. Catal Today 1990;8(2):231–48.
[88] Arai H, Yamada T, Eguchi K, Seiyama T. Catalytic combustion of methane over various perovskite-type oxides. Appl Catal 1986;26:265–76.
[89] Machida M, Eguchi K, Arai H. Catalytic properties of $BaMAl_{11}O_{19-\alpha}$ (M = Cr, Mn, Fe, Co, and Ni) for high-temperature catalytic combustion. J Catal 1989;120(2):377–86.
[90] Machida M, Eguchi K, Arai H. Effect of structural modification on the catalytic property of Mn-substituted hexaaluminates. J Catal 1990;123(2): 477–85.
[91] Machida M, Eguchi K, Arai H. Effect of additives on the surface area of oxide supports for catalytic combustion. J Catal 1987;103(2):385–93.
[92] Xiao T-C, Hanif A, York APE, Green MLH. Methane partial oxidation to synthesis gas over bimetallic cobalt/tungsten carbide catalysts and integration with a Mn substituted hexaaluminate combustion catalyst. Catal Today 2009;147(3–4):196–202.
[93] Basile F, Fornasari G, Trifirò F, Vaccari A. Rh-Ni synergy in the catalytic partial oxidation of methane: surface phenomena and catalyst stability. Catal Today 2002;77(3):215–23.
[94] Nikolla E, Schwank J, Linic S. Promotion of the long-term stability of reforming Ni catalysts by surface alloying. J Catal 2007;250(1):85–93.
[95] Enger BC, Lødeng R, Holmen A. Modified cobalt catalysts in the partial oxidation of methane at moderate temperatures. J Catal 2009;262 (2):188–98.
[96] Witt PM, Schmidt LD. Effect of flow rate on the partial oxidation of methane and ethane. J Catal 1996;163(2):465–75.
[97] Corbo P, Migliardini F. Hydrogen production by catalytic partial oxidation of methane and propane on Ni and Pt catalysts. Int J Hydrogen Energy 2007;32(1):55–66.
[98] Huff M, Torniainen PM, Schmidt LD. Partial oxidation of alkanes over noble metal coated monoliths. Catal Today 1994;21(1):113–28.
[99] Ran R, Xiong G, Sheng S, Yang W, Stroh N, Brunner H. Catalytic partial oxidation of n-heptane for hydrogen production. Catal Lett 2003;88 (1–2):55–9.

[100] Zhu W, Xiong G, Han W, Yang W. Catalytic partial oxidation of gasoline to syngas in a dense membrane reactor. Catal Today 2004;93–95:257–61.
[101] Gardner TH, Shekhawat D, Berry DA. Partial oxidation of n-tetradecane over lanthanum Ni-hexaaluminate. In: AIChE Fall Meeting. Austin: TX; 2004.
[102] Gardner TH, Shekhawat D, Berry DA, Smith MW, Salazar M, Kugler EL. Effect of nickel hexaaluminate mirror cation on structure-sensitive reactions during n-tetradecane partial oxidation. Appl Catal A: Gen 2007;323:1–8.
[103] Smith MW, Berry DA, Shekhawat D, Haynes DJ, Spivey JJ. Partial oxidation of liquid hydrocarbons in the presence of oxygen-conducting supports: effect of catalyst layer deposition. Fuel 2010;89: 1193–201.
[104] Haynes DJ, Berry DA, Shekhawat D, Spivey JJ. Catalytic partial oxidation of n-tetradecane using Rh and Sr substituted pyrochlores: effects of sulfur. Catal Today 2009;145(1–2):121–6.
[105] Haynes DJ, Campos A, Smith MW, Berry DA, Shekhawat D, Spivey JJ. Reducing the deactivation of Ni-metal during the catalytic partial oxidation of a surrogate diesel fuel mixture. Catal Today 2010; 154(3–4):210–6.
[106] Smith MW, Berry DA, Shekhawat D, Haynes DJ, Spivey JJ. Effect of oxide catalysts and oxygen-conducting supports on partial oxidation of liquid hydrocarbons. In: American Chemical Society 237th National Meeting and Exposition, 2009, Salt Lake City, UT.
[107] Tanaka M, Takemura M, Ito N. Catalysts for reforming hydrocarbon fuels. United States Patent No. 4088608, to Nippon Soken, Inc., Japan, 1978.
[108] Shekhawat D, Gardner TH, Berry DA, Salazar M, Haynes DJ, Spivey JJ. Catalytic partial oxidation of n-tetradecane in the presence of sulfur or polynuclear aromatics: Effects of support and metal. Appl Catal A: Gen 2006;311:8–16.
[109] Fuhitani Y, Muraki H. Process for partially oxidizing hydrocarbons. United States Patent No. 4087259, to Kabushiki Kaisha Toyota Chuo Kenkyusho, Japan, 1978.
[110] O'Connor RP, Schmidt LD. Catalytic partial oxidation of cyclohexane in a single-gauze reactor. J Catal 2000;191(1):245–56.
[111] Schmidt LD, Klein EJ, Leclerc CA, Krummenacher J, West KN. Syngas in millisecond reactors: higher alkanes and fast lightoff. Chem Eng Sci;8(3-6):1037–41.
[112] O'Connor RP, Klein EJ, Henning D, Schmidt LD. Tuning millisecond chemical reactors for the catalytic partial oxidation of cyclohexane. Appl Catal A: Gen 2003;238(1):29–40.
[113] Subramanian R, Panuccio GJ, Krummenacher JJ, Lee IC, Schmidt LD. Catalytic partial oxidation of higher hydrocarbons: reactivities and selectivities of mixtures. Chem Eng Sci 2004;59(22–23):5501–7.
[114] Krummenacher JJ, West KN, Schmidt LD. Catalytic partial oxidation of higher hydrocarbons at millisecond contact times: decane, hexadecane, and diesel fuel. J Catal 2003;215(2):332–43.
[115] Haynes DJ, Berry DA, Shekhawat D, Spivey JJ. Catalytic partial oxidation of n-tetradecane using pyrochlores: effect of Rh and Sr substitution. Catal Today 2008;136(3–4):206–13.
[116] Haynes DJ, Campos A, Berry DA, Shekhawat D, Roy A, Spivey JJ. Catalytic partial oxidation of a diesel surrogate fuel using an Ru-substituted pyrochlore. Catal Today 2010;155:84–91.
[117] Liguras DK, Goundani K, Verykios XE. Production of hydrogen for fuel cells by catalytic partial oxidation of ethanol over structured Ru catalysts. Int J Hydrogen Energy 2004;29(4):419–27.
[118] Liguras DK, Goundani K, Verykios XE. Production of hydrogen for fuel cells by catalytic partial oxidation of ethanol over structured Ni catalysts. J Power Sources 2004;130(1–2):30–7.
[119] Salge JR, Deluga GA, Schmidt LD. Catalytic partial oxidation of ethanol over noble metal catalysts. J Catal 2005;235(1):69–78.
[120] Wanat EC, Suman B, Schmidt LD. Partial oxidation of alcohols to produce hydrogen and chemicals in millisecond-contact time reactors. J Catal 2005;235 (1):18–27.
[121] Fixman EM, Abello MC, Gorriz OF, Arrúa LA. Preparation of Cu/SiO_2 catalysts with and without tartaric acid as template via a sol-gel process: characterization and evaluation in the methanol partial oxidation. Appl Catal A: Gen 2007;319:111–8.
[122] Schuyten S, Guerrero S, Miller JT, Shibata T, Wolf EE. Characterization and oxidation states of Cu and Pd in $Pd\text{-}CuO/ZnO/ZrO_2$ catalysts for hydrogen production by methanol partial oxidation. Appl Catal A: Gen 2009;352(1–2):133–44.
[123] Chang F-W, Ou T-C, Roselin LS, Chen W-S, Lai S-C, Wu H- M. Production of hydrogen by partial oxidation of methanol over bimetallic $Au\text{-}Cu/TiO_2\text{-}Fe_2O_3$ catalysts. J Mol Catal A: Chem 2009;313 (1–2):55–64.
[124] Ou T-C, Chang F-W, Roselin LS. Production of hydrogen via partial oxidation of methanol over bimetallic $Au\text{-}Cu/TiO_2$ catalysts. J Mol Catal A: Chem 2008;293(1–2):8–16.

[125] Chang F-W, Lai S-C, Roselin LS. Hydrogen production by partial oxidation of methanol over ZnO-promoted Au/Al_2O_3 catalysts. J Mol Catal A: Chem 2008;282(1−2):129−35.

[126] Rabe S, Vogel F. A thermogravimetric study of the partial oxidation of methanol for hydrogen production over a $Cu/ZnO/Al_2O_3$ catalyst. Appl Catal B: Env 2008;84(3−4):827−34.

[127] Faungnawakij K, Shimoda N, Fukunaga T, Kikuchi R, Eguchi K. Cu-based spinel catalysts CuB_2O_4 (B = Fe, Mn, Cr, Ga, $Al_{0.75}Mn_{0.25}$) for steam reforming of dimethyl ether. Appl Catal A: Gen 2008;341(1−2):139−45.

[128] Nilsson M, Jozsa P, Pettersson LJ. Evaluation of Pd-based catalysts and the influence of operating conditions for autothermal reforming of dimethyl ether. Appl Catal B: Env 2007;76(1−2):42−50.

[129] Zhang Q, Du F, He X, Liu Z-T, Liu Z-W, Zhou Y. Hydrogen production via partial oxidation and reforming of dimethyl ether. Catal Today 2009;146 (1−2):50−6.

[130] Zhang Q, Li X, Fujimoto K, Asami K. Hydrogen production by partial oxidation and reforming of DME. Appl Catal A: Gen 2005;288(1−2):169−74.

[131] Wang S, Ishihara T, Takita Y. Partial oxidation of dimethyl ether over various supported metal catalysts. Appl Catal A: Gen 2002;228(1−2):167−76.

[132] Nguyen BNT, Leclerc CA. Catalytic partial oxidation of methyl acetate as a model to investigate the conversion of methyl esters to hydrogen. Int J Hydrogen Energy 2008;33(4):1295−303.

[133] Subramanian R, Schmidt LD. Renewable olefins from biodiesel by autothermal reforming. Angewandte Chemie International Edition 2005;44:302−5.

[134] Haynes DJ, Berry DA, Shekhawat D, Smith MW, Spivey JJ. Long term reforming of commercial diesel fuel using a layered pyrochlore catalyst. In: Spring National Meeting. San Francisco, CA: American Chemical Society; 2010.

[135] Shekhawat D, Berry DA, Gardner TH, Haynes DJ, Spivey JJ. Effects of fuel cell anode recycle on catalytic fuel reforming. J Power Sources 2007;168(2):477−83.

[136] Shekhawat D, Berry DA, Haynes DJ, Spivey JJ. Fuel constituent effects on fuel reforming properties for fuel cell applications. Fuel 2009;88(5):817−25.

[137] Shekhawat D, Berry DA, Spivey JJ. Reforming of liquid hydrocarbon fuels for fuel cell applications. Catal Today 2008;136(3−4). 189.

[138] Smith MW, Berry DA, Shekhawat D, Haynes DJ, Spivey JJ. Catalytic material development for a SOFC reforming system: application of an oxidative steam reforming catalyst to a monolithic reactor. In: 8th International Fuel Cell Science, Engineering and Technology Conference. Brooklyn, NY: American Society of Mechanical Engineers; 2010.

[139] Smith MW, Berry DA, Shekhawat D, Haynes DJ, Spivey JJ. Ni-substituted oxide catalysts with oxygen ion conductivity for hydrocarbon reforming. In: 2010 Spring National Meeting. San Antonio, TX: American Institute of Chemical Engineers; 2010.

[140] Xu J, Wei W, Tian A, Fan Y, Bao X, Yu C. Temperature profile in a two-stage fixed bed reactor for catalytic partial oxidation of methane to syngas. Catal Today 2010;149(1−2):191−5.

[141] Shen S, Pan Z, Dong C, Jiang Q, Zhang Z, Yu C, et al. A novel two-stage reactor process for catalytic oxidation of methane to synthesis gas. In: Iglesia E, Spivey JJ, Fleisch TH, editors. Stud Surf Sci Catal. Elsevier; 2001;136:99−104.

[142] Zhu J, Rahuman MSMM, van Ommen JG, Lefferts L. Dual catalyst bed concept for catalytic partial oxidation of methane to synthesis gas. Appl Catal A: Gen 2004;259(1):95−100.

[143] Tong GCM, Flynn J, Leclerc CA. A dual catalyst bed for the autothermal partial oxidation of methane to synthesis gas. Catal Lett 2005;102:131−7.

[144] Zhu H, Kee RJ, Engel JR, Wickham DT. Catalytic partial oxidation of methane using RhSr- and Ni-substituted hexaaluminates. Proc Combustion Institute 2007;31(2):1965−72.

[145] Bromberg L, Cohn DR, Rabinovich A, Alexeev N. Plasma catalytic reforming of methane. Int J Hydrogen Energy 1999;24(12):1131−7.

[146] Sobacchi MG, Saveliev AV, Fridman AA, Kennedy LA, Ahmed S, Krause T. Experimental assessment of a combined plasma/catalytic system for hydrogen production via partial oxidation of hydrocarbon fuels. Int J Hydrogen Energy 2002; 27(6):635−42.

[147] Will H, Scholz P, Ondruschka B. Microwave-assisted heterogeneous gas-phase catalysis. Chem Eng Tech 2004;27(2):113−22.

[148] Zhang X, Hayward DO. Applications of microwave dielectric heating in environment-related heterogeneous gas-phase catalytic systems. Inorganica Chimica Acta 2006;359(11):3421−33.

CHAPTER

6

Oxidative Steam Reforming

Daniel J. Haynes, Dushyant Shekhawat

National Energy Technology Laboratory, U.S. Department of Energy, 3610 Collins Ferry Rd, Morgantown, WV 26507, USA

OUTLINE

6.1. INTRODUCTION

Applications for fuel cells are numerous, and as such, the desired power demands will vary depending on the intended use. To meet these needs, the hydrocarbon fuel must be converted into a synthesis gas stream with a sufficient concentration of H_2 (and CO for high-temperature cells).

The choice of the proper reforming chemistry is one of the fundamental considerations in the overall design process of a reforming system. Each available option has implications that affect various important design features, including thermal energy management of the system, as well as the capability to produce the amount of H_2 required for the desired energy load of the fuel cell.

The previous two chapters have explored process parameters, mechanism, kinetics, and catalysts for reforming using either steam (steam reforming) or oxygen (partial oxidation). Another reforming option exists in which both steam and oxygen are fed together as oxidants to reform the hydrocarbon fuel into a H_2-rich fuel stream suitable for fuel cells. This reforming method is commonly referred to as oxidative steam reforming (OSR), and can be expressed by the following general Eq. (6.1):

$$C_nH_mO_p + aO_2 + bH_2O \rightarrow cH_2 + dCO + eCO_2 + fCH_4 \tag{6.1}$$

As seen from Eq. (6.1), OSR generally can be considered a combination of partial oxidation and steam reforming. Feeding air and steam together utilizes the heat generated from exothermic oxidation of the fuel to promote the endothermic steam-reforming reactions. In fact, a unique operating condition exists for all fuels in which the heat from the oxidation reactions thermally balances the endothermic steam-reforming reactions, rendering the overall reaction thermoneutral. This is called autothermal reforming (ATR), which is a special case of OSR. Fuel-reforming processes using both air and steam outside thermoneutral conditions are commonly referred to as ATR, but will be considered as OSR in this chapter.

Despite the obvious advantages of the ability to conduct a reaction with minimal need for heat transfer, autothermal operation is difficult to achieve due to heat losses from the system. Heat losses are typically compensated for by running at higher oxygen-to-carbon (O/C) ratios. Feed compositions are generally selected based on the overall carbon number as well as the structure of the fuel (e.g., paraffin, aromatics). Optimal operating conditions for OSR have been determined to be O/C ratio = 0.7−1.0, steam-to-carbon ratio (S/C) = 1.5−2.0, and temperatures roughly around 700−800 °C [1,2]. In the absence of a catalyst, the reaction kinetics for OSR are too slow for equilibrium to be attained in the gas phase. Therefore, the reactions must be catalyzed. Group VIII metals (Rh, Ru, and Pt) and Ni are known to be active and selective catalysts for the OSR of hydrocarbons to form synthesis gas.

OSR has been an established technology for H_2 generation since the late 1950s [3]. It is capable of producing H_2 efficiently at high throughputs, which generally makes it the preferred method for industrial use in petrochemical production [3]. However, using OSR for such applications requires a separation plant to remove N_2 from air to reduce process gas volumes. Oxygen separation is very capital intensive (almost 40% of total cost) and generally precludes the use of OSR for large-scale applications.

H_2 requirements for fuel cell uses are considerably lower than those produced at industrial scale [4], and for these purposes OSR still has benefits over SR and partial oxidation (POX) systems. The work from Argonne National Laboratory [4−6] has shown that OSR makes practical sense for transportation applications. Much like POX, having O_2 as a reactant allows

for fast kinetics, which results in rapid start-up times and responsiveness to transients. However, a reformate with higher a H_2/CO ratio can be produced compared with POX alone due to the presence of steam. Compared to a SR process for the same application, less thermal integration is required in the reactor design; therefore, the complexity of the reactor and the overall reactor weight are reduced. SR processes are heat transfer limited, and hence the reactors tend to be heavier due to the amount of metal needed to allow for sufficient heat exchange. Lighter reactor components also have a direct benefit on fuel consumption during start up, as it has been found that, for a given reactor mass, the energy required to heat a reformer to its operating temperature is directly proportional to its operating temperature [6]. Unlike POX, however, the steam present in OSR reduces the overall heat of reaction. This permits a wider selection of materials which can be used for reactor components, because the operating temperatures seen in the reactor are lower in comparison to POX.

Like any process however, OSR does have some disadvantages. Using steam requires a water storage and supply system, which adds weight, complexity, and cost to the process. Also, as with any system that uses water, appropriate insulation is needed for applications in colder climates, and added space would be required for a reservoir in an already confined area (assuming for transportation use). Attempts to mitigate storage problems have looked into recycling the fuel cell exhaust to provide the necessary water requirements to maintain reforming capabilities under OSR conditions [7]. Progress on a fuel processor linked to a fuel cell is still in development stages, and it is unclear what solution will be used in a commercial OSR unit at this time.

This chapter will explore aspects of OSR chemistry that are important in a fuel-reforming process. Reaction thermodynamics, mechanism, kinetics, and catalysts active for OSR will be discussed in detail to provide insight into designing a fuel-processing system based on this reaction.

6.2. THERMODYNAMICS

Evaluating thermodynamics of the OSR reaction will provide insight into the effects of temperature, feed composition, and pressure on product distribution, and ultimately H_2 content. Understanding these effects can in turn provide a foundation for system design by helping establish optimal operating conditions, areas for thermal integration, and catalyst evaluation. Numerous studies have analyzed the functional dependence of these variables on the OSR thermodynamic equilibrium of specific fuels. Representative studies are presented in Table 6.1.

6.2.1. Contributing Reactions

The OSR reaction is not as direct and simple as Eq. (6.1) appears. The reaction sequence actually consists of a complex series of sub-reactions which have their own intrinsic kinetic dependence on temperature, and local species concentration in the reactor. OSR is the net sum of all these reactions occurring between the various

TABLE 6.1 Thermodynamic Studies on Common Hydrocarbon Feedstocks

Fuel	Reference
Methane/Natural gas	[4,8–15]
Propane/LPG	[16]
Methanol	[11,17–19]
Ethanol	[11,12,19–21]
Glycerol	[22]
Isooctane/Gasoline	[11,23–25]
Diesel/Jet fuel	[25–30]

chemical species that results in a product composition that is rich in H_2 and CO. The key reactions responsible for the eventual production of synthesis gas are presented below:

Complete oxidation

$$C_nH_mO_p + O_2 \rightarrow H_2O + CO_2 \quad (6.2)$$

Incomplete oxidation

$$C_nH_mO_p + O_2 \rightarrow H_2O + CO \quad (6.3)$$

$$C_nH_mO_p + O_2 \rightarrow H_2 + CO_2 \quad (6.4)$$

Partial oxidation

$$C_nH_mO_p + \frac{n}{2}O_2 \rightarrow H_2 + CO \quad (6.5)$$

Steam reforming

$$C_nH_mO_p + H_2O \rightarrow H_2 + CO \quad (6.6)$$

Dry reforming

$$C_nH_mO_p + CO_2 \rightarrow H_2 + CO \quad (6.7)$$

Water-gas shift

$$CO + H_2O \leftrightarrow H_2 + CO_2 \quad (6.8)$$

Some major undesirable side reactions that occur, which reduce selectivity to H_2 are:

Hydrogen oxidation

$$H_2 + O_2 \leftrightarrow H_2O \quad (6.9)$$

Carbon monoxide oxidation

$$CO + \frac{1}{2}O_2 \leftrightarrow CO_2 \quad (6.10)$$

Methanation

$$C + 2H_2 \leftrightarrow CH_4 \quad (6.11)$$

$$CO + 3H_2 \leftrightarrow CH_4 + H_2O \quad (6.12)$$

$$CO_2 + 4H_2 \leftrightarrow CH_4 + 2H_2O \quad (6.13)$$

Reverse water-gas shift

$$CO_2 + H_2 \leftrightarrow H_2O + CO \quad (6.14)$$

Reaction conditions for OSR can also promote the formation of carbon, which is another undesirable reaction product. Carbon accumulation can lead to uneven heat transfer, blocked or constrained flow through the reactor, as well as catalyst deactivation. Listed below are several routes for carbon formation:

Decomposition

$$C_nH_m \leftrightarrow nC + \frac{m}{2}H_2 \quad (6.15)$$

Boudouard

$$2CO \leftrightarrow C + CO_2 \quad (6.16)$$

CO and CO_2 Hydrogenation

$$CO + H_2 \leftrightarrow H_2O + C \quad (6.17)$$

$$CO + 2H_2 \leftrightarrow 2H_2O + C \quad (6.18)$$

6.2.2. Effect of Temperature

The equilibrium composition of a reformate produced in the OSR of CH_4 (O/C = 0.7, S/C = 1.5) is shown in Fig. 6.1. Under these conditions, the conversion of CH_4 becomes noticeable at about 400 °C as endothermic steam-reforming reaction (Eq. (6.6)) becomes more favorable, and reaches completion (>99%) at 700 °C. The maximum concentration of H_2 is obtained at about 750 °C. Beyond this temperature, the ratio of H_2/CO begins to decrease, because energetics for the reverse water-gas shift reaction (Eq. (6.14)) then becomes favorable. Carbon formation (designated as solid elemental carbon) is not predicted above 150 °C.

Figures 6.2 and 6.3 show the equilibrium reformate gas composition for the OSR (O/C = 0.7, S/C = 1.5) of two additional fuels: a surrogate diesel mixture (comprising 40 wt% *n*-tetradecane, 40 wt% decalin, and 20 wt% 1-methylnaphthalene), and C_2H_5OH. Conversion of these larger fuels is nearly complete at 100 °C, and no other hydrocarbon compounds besides CH_4

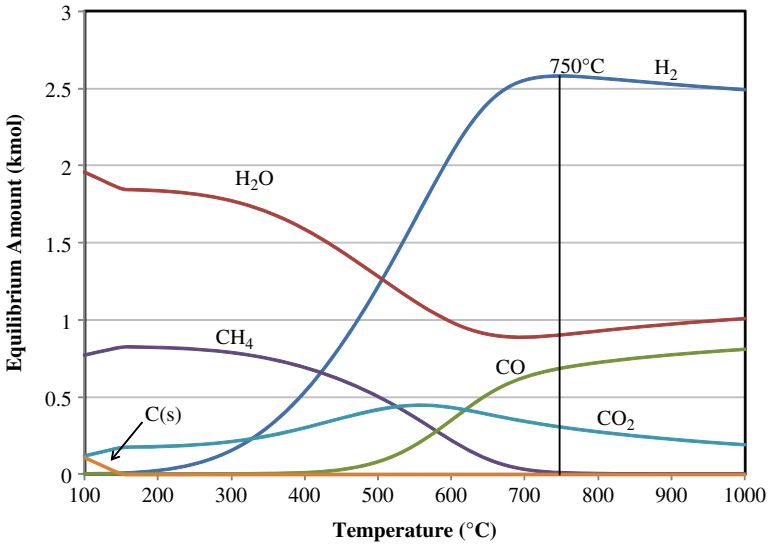

FIGURE 6.1 Effect of operating temperature on reformate compositions for OSR of 1 kmol CH_4 at an O/C = 0.7, S/C = 1.5, and 0.1 MPa. All products are gases except C(s). (Calculations by HSC Chemistry v6.12 [31].)

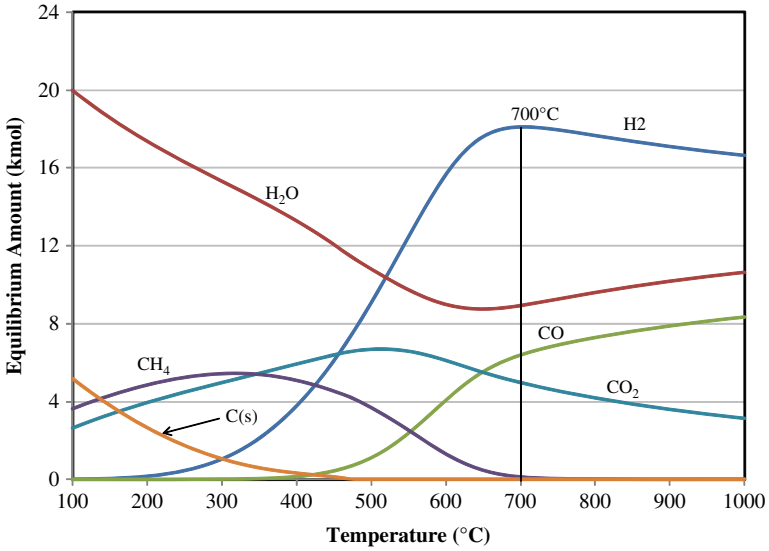

FIGURE 6.2 Effect of operating temperature on reformate compositions for OSR of 1 kmol surrogate diesel mixture (40 wt% *n*-tetradecane, 40 wt% decalin, and 20 wt% 1-methylnaphthalene) at an O/C = 0.7, S/C = 1.5, and 0.1 MPa. Average molecular formula for mixture is $C_{11.5}H_{20.7}$. All products are gases except C(s). (Calculations by HSC Chemistry v6.12 [31].)

are predicted in significant concentrations (>0.1 mol% of gas composition). Comparing the temperatures at which maximum H_2 concentrations are obtained for these fuels to that of CH_4 shows this value is dependent on the fuel used, and also the size of hydrocarbon molecule. Oxygenated compounds, in this case C_2H_5OH, require slightly lower processing temperatures (685 °C for C_2H_5OH) to achieve maximum H_2 yields than non-oxygenated compounds (700 °C for surrogate diesel, and 750 °C for CH_4). Effect of size of hydrocarbon molecule on maximum H_2 concentration is illustrated by comparing Figs 6.1 and 6.2, in which the maximum H_2

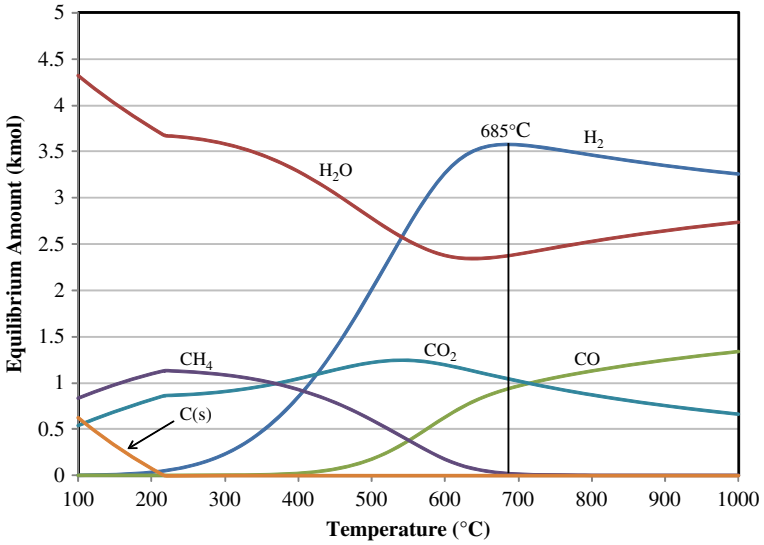

FIGURE 6.3 Effect of operating temperature on reformate compositions for OSR of 1 kmol C_2H_5OH at an O/C = 0.7 (O/C ratio does not take into account O contained in C_2H_5OH), S/C = 1.5, and 0.1 MPa. All products are gases except C(s). (Calculations by HSC Chemistry v6.12 [31].)

level for the surrogate diesel fuel is obtained at a temperature 45 °C lower than that required for CH_4. These equilibrium results also show the carbon formation boundary is extended to higher temperatures for larger fuels, independent of class (i.e., oxygenated, aliphatic, or aromatic). The temperature at which carbon formation becomes thermodynamically unfavorable for C_2H_5OH is 210 °C (65 °C greater than that for CH_4), and 480 °C for the surrogate diesel (330 °C greater than that for CH_4). However, it should be noted that carbon formation is not predicted at temperatures in which reforming of these fuels normally takes place, which is usually 400–500 °C for ethanol, and 700–900 °C for CH_4 and diesel.

6.2.3. Effect of Oxidant to Fuel ratio – O/C and S/C

6.2.3.1. Increasing O/C Ratio

Figure 6.4 illustrates the effects of O/C ratio on the equilibrium gas composition for the OSR of CH_4 at 800 °C and 1 atm. The trends observed as the O/C ratio is increased show a decline in the selectivity toward H_2 and CO. As more O_2 is introduced, Eqs. (6.3), (6.4), and (6.9) become progressively more favorable, and therefore the selectivity changes as sufficient O_2 is present to oxidize more H- and C-species into H_2O and CO_2. Continually increasing the O/C ratio will ultimately lead to conditions for stoichiometric combustion (Eq. (6.2)), at which only H_2O and CO_2 are present at equilibrium. It should be noted that the trends seen in Fig. 6.4 for increasing O/C ratio are similar for both heavier hydrocarbon fuels (C_{16}) [29], as well as oxygenates (CH_3OH) [17].

6.2.3.2. Increasing S/C ratio

Also shown in Fig. 6.4 are the effects of increasing the S/C ratio during the OSR of CH_4 at 800 °C and 1 atm. Trends for increasing S/C ratio show an increase in H_2 formation and a decrease in CO concentrations at any given O/C ratio. Adding more steam increases the amount of steam reforming occurring in the system (Eq. (6.8)), thus resulting in more H_2 at equilibrium. Increasing steam concentrations also promotes the water-gas shift reaction

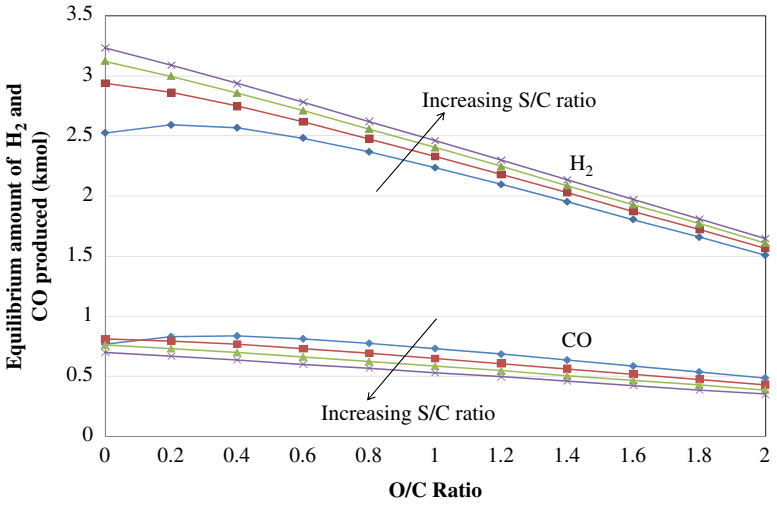

FIGURE 6.4 Effect of O/C and S/C ratios on H_2 and CO products (dry basis) from the OSR of 1 kmol of CH_4 at 800 °C and 0.1 MPa. (◆) S/C = 1; (■) S/C = 1.5; (▲) S/C = 2.0; (x) S/C = 2.5 (Equilibrium calculations performed by HSC Chemistry v6.12 [31].)

(Eq. (6.8)) which further increases H_2 concentrations and decreases CO concentration. As with the O/C ratio, trends seen in Fig. 6.4 for increasing S/C ratio are also similar for both heavier hydrocarbon fuels (C_{16}) [29], and oxygenates (CH_3OH) [17].

6.2.3.3. *Autothermal Operation*

Autothermal operation is the point at which the energy requirements of the steam-reforming reactions occurring in the bed are thermally balanced in situ by oxidation reactions. The following method developed by Ahmed and Krumpelt [4] can be used to estimate the O/C and S/C ratios for ATR operation. As stated earlier, the generalized stoichiometry for the OSR reaction can be represented by Eq. (6.1).

The maximum amount of H_2 can be obtained from this reaction if it is assumed that a stoichiometric amount of steam is present to convert all carbon-containing species to CO_2 as shown by the following expression [4,19,29]:

$$\begin{aligned} &C_nH_mO_p + \alpha O_2 + (2n - 2\alpha - p)H_2O \\ &\quad \rightarrow \left(2n - 2\alpha - p + \frac{m}{2}\right)H_2 + nCO_2 \end{aligned} \tag{6.19}$$

Based on reaction stoichiometry, the maximum amount of H_2 formed is $(2n - 2\alpha - p + m/2)$. The reaction enthalpy corresponding to the stoichiometric reaction shown by Eq. (6.19) is then

$$\begin{aligned} \Delta H_r = {} & n\Delta H_{f,CO_2} - (2n - 2\alpha - p) \\ & \Delta H_{f,H_2O} - \Delta H_{f,fuel} \end{aligned} \tag{6.20}$$

At the ATR point, $\Delta H_r = 0$. Rearranging Eq. (6.20) to obtain the thermoneutral stoichiometric O_2 coefficient, α, gives

$$\alpha_0 = n - \frac{p}{2} + \frac{1}{2}\left[\frac{\Delta H_{f,fuel} - n\Delta H_{f,CO_2}}{\Delta H_{f,H_2O}}\right] \tag{6.21}$$

Values of α_0 for various hydrocarbon fuels have been determined by Ahmed and Krumpelt [4] using the method shown here. These values are shown in Table 6.2.

6.2.3.4. *Reaction Enthalpy*

Oxidant feed compositions not only affect H_2 and CO yields, but also the energy requirements of the reaction. One can observe the general effects of varying oxidant levels on the reaction enthalpy by adjusting the value of α shown in Eq. (6.19). For various values of α, the energy required or produced by the reaction can be

TABLE 6.2 Calculated Thermoneutral O_2 Stoichiometrtic Coefficient for Commonly Used Hydrocarbon Fuels [4]

Hydrocarbon fuel $C_nH_mO_p$	ΔHf, fuel (kJ/mol)	Thermoneutral O_2 stoichiometric coefficient (α_0)
Methanol, $CH_3OH(l)$	−238.9	0.23
Methane, $CH_4(g)$	−74.9	0.44
Acetic acid, $C_2H_4O_2(l)$	−487.0	0.47
Ethane, $C_2H_6(g)$	−84.5	0.77
Ethylene glycol, $C_2H_6OH(l)$	−454.4	0.41
Ethanol, $C_2H_6O(l)$	−277.0	0.61
Pentene, $C_5H_{10}(g)$	−20.9	1.59
Pentane, $C_5H_{12}(g)$	−146.4	1.87
Cyclohexane, $C_6H_{12}(l)$	−156.1	2.14
Benzene, $C_6H_6(l)$	48.9	1.78
Toluene, $C_7H_8(l)$	12.1	2.16
Iso-octane, $C_8H_{18}(l)$	−259.4	2.93
Gasoline, $C_{7.3}H_{14.8}O_{0.1}(l)$	−221.7	2.61
n-Tetradecane*, $C_{14}H_{30}(l)$	−403.7	5.07
n-Hexadecane*, $C_{16}H_{34}(l)$	−456.9	5.78
Diesel [32] *, $C_{16.2}H_{30.6}(l)$	−426.3	5.79

** Values were not provided in reference [4], but were determined using the same method (Eq. (6.21)).*

controlled. Eq. (6.22) shows the different modes of operation that can be achieved for increasing values of α.

$$\alpha = \begin{cases} 0 & \text{Steam reforming} \\ n - \dfrac{p}{2} + \dfrac{1}{2}\left(\dfrac{\Delta H_{f,fuel} - \Delta H_{f,CO_2}}{\Delta H_{f,H_2O}}\right) & \text{Thermoneutral} \\ n - \dfrac{p}{2} & \text{Partial oxidation} \\ n + \dfrac{m}{4} - \dfrac{p}{2} & \text{Combustion} \end{cases} \tag{6.22}$$

Eq. (6.19) is plotted in Fig. 6.5 for several hydrocarbon fuels to further show the reaction enthalpy change as a function of α, in terms of O/C ratio, for the idealized stoichiometric expression in Eq. (6.19). Figure 6.5 shows that the carbon number of the hydrocarbon fuel has an impact on the magnitude of the reaction enthalpy (either positive or negative). Specifically, this can be seen as the absolute value of

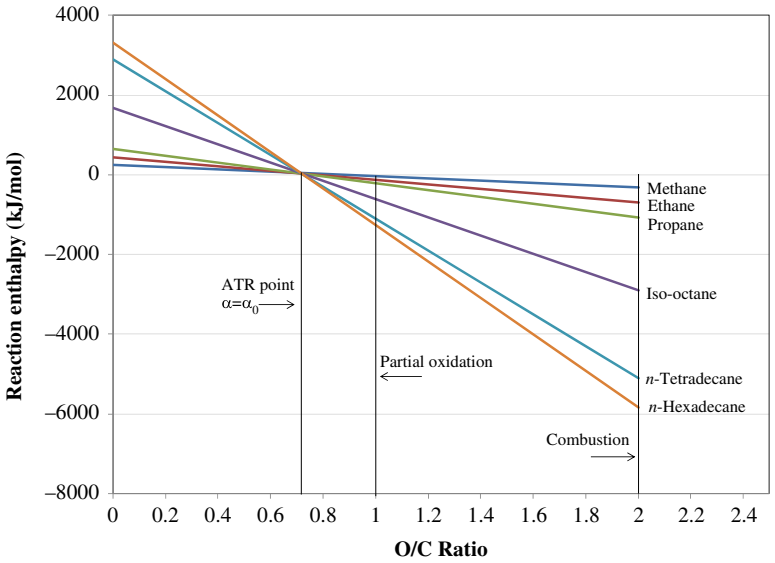

FIGURE 6.5 Enthalpy change (assuming product water as liquid [4]) as a function of O/C ratio for the ATR of various hydrocarbon fuels.

the slope of the plots increases with increasing carbon number of the fuel. Although the stoichiometric coefficient for oxygen increases as a function of carbon number in Table 6.2, the corresponding O/C ratio at which the ATR condition is reached is roughly the same for each fuel, as determined by the method shown in Section 6.2.3.3.

From Fig. 6.5 it can be seen that for each fuel, the reaction enthalpy is the most energy intensive at the steam reforming condition ($\alpha = 0$). Although this condition corresponds to the highest hydrogen concentration (i.e., produces the most H_2, as shown in Fig. 6.4), external heat must be provided. The required heat may be supplied by combustion of a portion of the fuel, or possibly from recycled exhaust of the fuel cell—assuming the reformer is used in conjunction with a high-temperature fuel cell. Increasing the O/C ratio from the SR decreases the external energy requirements of the reaction, until the ATR point is reached, at which the reaction is thermoneutral. The ATR operation condition is considered the most energy efficient because the maximum H_2 yield is obtained with no net heat required. At O/C ratios above the ATR point, the reaction enthalpy becomes exothermic. Once the O/C ratio is increased beyond the partial oxidation condition ($\alpha = n - p/2$), excess oxygen is present to oxidize H_2 into H_2O [4]. Finally, at sufficiently high O/C ratios, conditions for complete combustion are reached, and all H and C species undergo complete oxidation to H_2O and CO_2. An operating spectrum is shown in Fig. 6.6 to qualitatively illustrate the operating conditions of an oxidative steam reformer.

6.2.4. Effect of Pressure

The effect of pressure on reformate composition is shown in Fig. 6.7 for the OSR of 1 kmol of CH_4 at 800 °C, O/C = 0.7, and S/C = 1.5. The conversion of reactants to products during the OSR reaction is accompanied by a volume expansion (product moles > reactant moles), and therefore lower pressures are favored thermodynamically. H_2 concentrations decline over the observed pressure range due to the increasing pressure inhibiting the CH_4 steam-reforming reaction. O_2 however is still

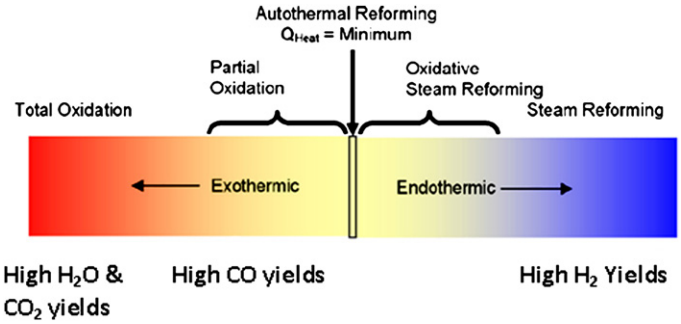

FIGURE 6.6 Illustration depicting the range of operating conditions for the reforming of ethanol; *Reprinted from Rabenstein and Hacker [20], Copyright (2008), with permission from International Association for Hydrogen Energy.*

completely consumed over the entire pressure range at these conditions. Carbon formation (elemental carbon) remains thermodynamically unfavorable over said pressure range.

Operating a fuel processor above ambient pressure also does not offer practical advantages from a system design perspective. The reactor components must be designed to withstand elevated pressures, which are usually heavier and therefore require more heat to bring the system to its operating temperature. In addition, the feed air must be compressed to the pressure of the operating stream, which also lowers the process efficiency.

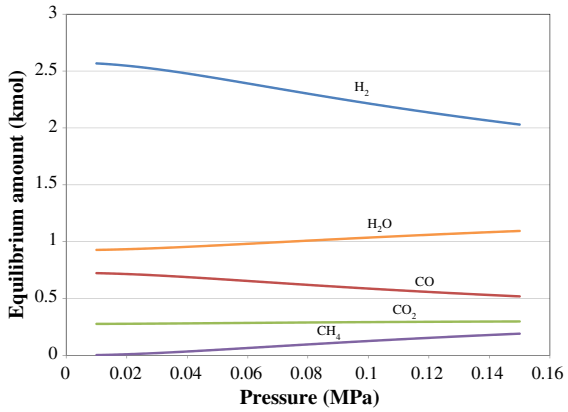

FIGURE 6.7 Equilibrium product distribution as a function of pressure for the OSR of 1 kmol CH_4 (O/C = 0.7, S/C = 1.5, and 800 °C). (Calculation performed using HSC Chemistry v6.12 [31].)

6.3. MECHANISM

There is no generally accepted mechanism describing the conversion of all hydrocarbons or oxygenated hydrocarbons under OSR conditions. The reaction mechanism is dependent on the catalyst, the fuel type, and the reaction conditions applied. The OSR reaction involving either or both aliphatic and aromatic hydrocarbons has been mainly described by two different reaction mechanisms: (1) combustion-reforming mechanism and (2) pyrolysis-oxidation mechanism. The conversion of oxygenated compounds is believed to proceed through decomposition followed by reforming reactions. These three mechanisms are discussed in detail in the following sections.

6.3.1. Combustion-Reforming Mechanism

This proposed mechanism is similar to the indirect reaction pathway described for catalytic partial oxidation (CPOX) [33–35]. It is speculated that under OSR conditions, the hydrocarbon conversion takes place in two consecutive steps [36–40]. First, part of the fuel undergoes combustion with all available oxygen at the top portion of the catalyst bed, forming mainly H_2O and CO_2 as products. A very small section of the catalyst bed is utilized during this step, due to the fast kinetics of combustion. If the reaction takes place according to the stoichiometry, 25% of the fuel is

converted during this process by the oxygen. The remaining unconverted fuel fragments are then converted into synthesis gas primarily through endothermic steam- and CO_2-reforming reactions down the rest of the catalyst bed. Though the endothermic reactions dominate after the initial combustion zone, the equilibrium of the WGS/RWGS also takes place in this region, and plays a role in synthesis gas selectivity. A representation of the overall combustion-reforming mechanism is depicted in Fig. 6.8.

The mechanism in Fig. 6.8 has been supported by several studies in which temperature profiles were measured at multiple points down the length of the catalyst bed [40–44]. Higher temperatures were observed in the top part of the catalyst bed, followed by lower temperatures in the remainder of the catalyst bed. The IR image shown in Fig. 6.9 [40] reflects the reaction profile of the OSR of CH_4 occurring over a commercial Rh/Al_2O_3. Although temperature is an aggregate measurement, the observed temperatures are consistent with the combustion-reforming mechanism.

It has also been found that the type of catalytic metal will influence the shape and magnitude of the peaks in the observed temperature profile [36,40,42]. For first row transition metals, like

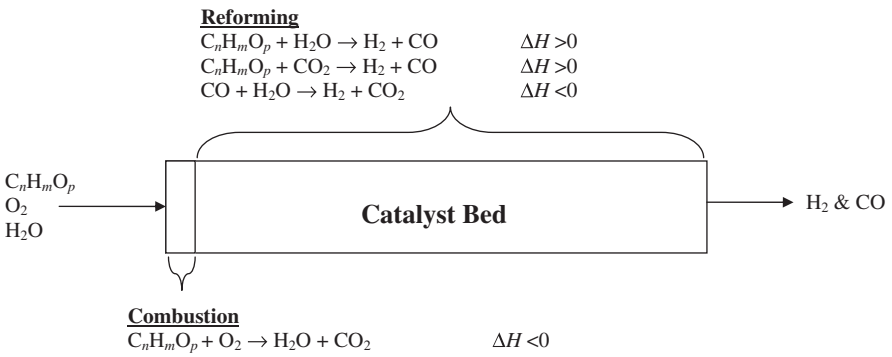

Step 1: $2CH_4 + O_2 + H_2O = 0.5CO_2 + 2.0H_2O + 1.5CH_4$

Step 2: $1.5CH_4 + 2.0H_2O$ or $0.5CO_2 = CO + H_2$

FIGURE 6.8 Reaction scheme describing the combustion-reforming mechanism for the OSR of a fuel.

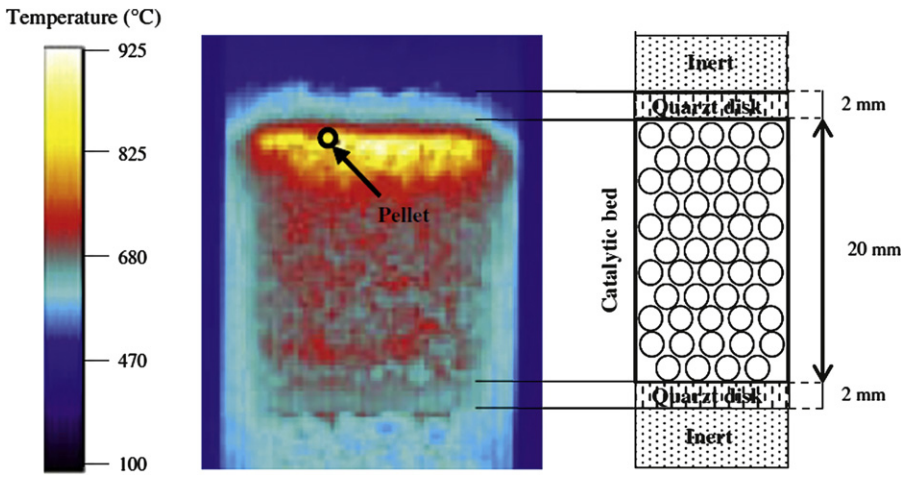

FIGURE 6.9 Thermographic image of catalyst bed (Rh/Al_2O_3) during the OSR of CH_4; *Reprinted from Simeone et al. [44], Copyright (2008), with permission from International Association for Hydrogen Energy.*

Ni, temperature profile results suggest that the reforming zones are almost distinctly separate [42]. Measurements along the Ni catalyst bed show noticeable high-temperature readings at the front, which then decrease as the flow progresses down the length of the reactor.

Under oxidizing atmospheres, Ni^0 has a strong thermodynamic tendency to be converted into Ni^{2+} [36,45]. It has been found that this oxidized form of Ni is known to be active for combustion reaction, but not for reforming reactions [36,41,42,46]. Therefore, it is speculated that the Ni at the bed inlet is readily oxidized by the feed gas to NiO, which promotes the combustion reaction, and consequently produces a significant temperature rise in that region [41]. In the remainder of the reactor (oxygen-depleted zone), reforming reactions (mainly SR and CO_2) occur over reduced Ni.

Noble metals such as Pt are not easily oxidized and are more stable in metallic form even in a highly oxidizing environment [42,47]. Consequently the combustion and reforming zones overlap more for these metals because both sets of reactions can take place on the same catalyst surface [42]. Peak temperatures are therefore reduced due to the overlap between reaction zones, and the resulting temperature profiles are less severe compared with those for Ni-based catalysts [36,42,48,49].

A study by Li et al. [36] found the overlapping effects between catalyst zones to be in the order Rh > Pt >> Pd for Group VII metals, with the latter, Pd, showing minimal overlap. It is speculated that because Rh is a much more active reforming catalyst than oxidation catalyst (compared with other noble metals such as Pt and Pd) a lower temperature gradient was seen during OSR reaction and Rh was therefore reported to be a better OSR catalyst than Pt and Pd [36,44]. The difference in temperature profiling for metals like Ni (zones do not overlap) and noble catalysts (zones overlap) can be shown schematically in Fig. 6.10.

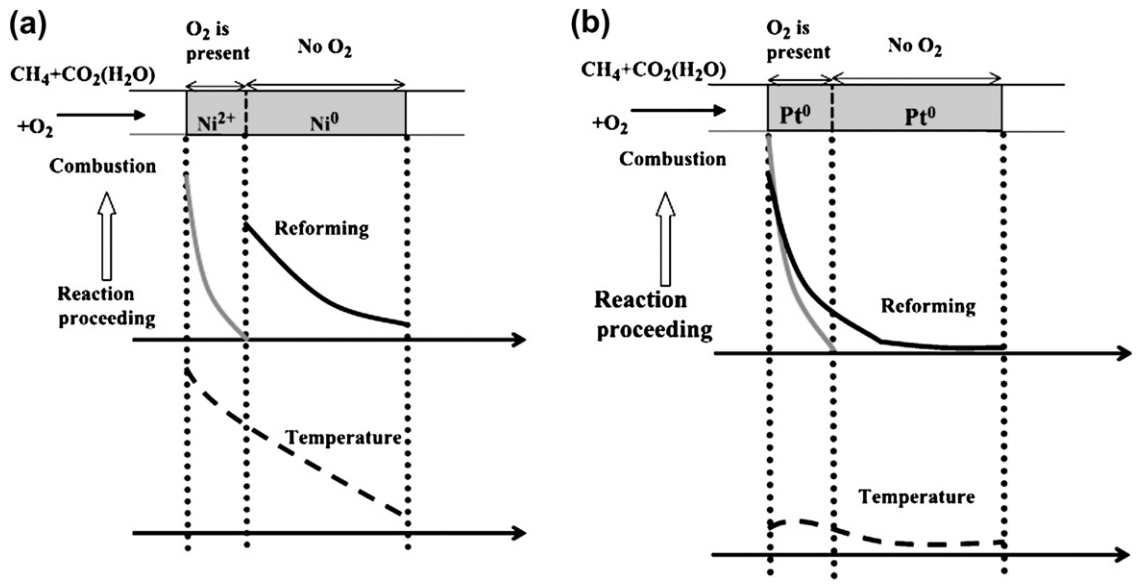

FIGURE 6.10 Model scheme of the effect of oxygen addition to steam and dry reforming of methane on the temperature profile of the catalyst bed. (a) Ni catalysts, (b) Pt catalyst; *Reprinted from Tomishige et al. [42], Copyright (2004), with permission from Elsevier.*

The combustion-reforming mechanism describing the OSR reaction process has also been studied by varying the contact time [37,50]. While running at short contact times (0.15 ms), Sato et al. [50] saw high selectivity to CO_2 and low fuel conversion (~20%) during the OSR of n-C_4H_{10} (O/C = 1.0, S/C = 1.0, and 450 °C) using a Ni/MgO catalyst. Increasing the contact time from 0.15 to 1 ms resulted in a decrease in CO_2 selectivity, while improving the selectivities of both H_2 and CO, and also conversion (~95%). Collectively these results suggest that the first step in OSR is a highly exothermic combustion reaction, which is then followed by reforming reactions to produce synthesis gas. At the shorter contact times, the high CO_2 selectivities indicated that combustion was the main reaction. Meanwhile, the endothermic reactions forming synthesis gas are kinetically restricted at the higher gas velocities because of their much slower reaction rates. However, the observed increase in synthesis gas production and corresponding decrease in CO_2 selectivity begins to occur as the gas velocities become more suitable for the reforming reactions, suggesting the reactions producing H_2 and CO occur after the combustion reaction is complete. Also, CO selectivity decreased by increasing the contact time (to 10 ms) likely due to water-gas shift and methanation reactions.

Researchers [33,51–55] at the University of Minnesota found that spatially resolved concentration profiles coupled with temperature profiling can be used to help understand the reaction chemistries occurring during OSR and POX. Results from the spatially resolved species and temperature profiles measured during the catalytic partial oxidation (CPOX) of methane (CPOX results are shown here because of more clarity in H_2O and CO_2 profiles compared with OSR results) over a Rh/Al_2O_3 catalyst (Fig. 6.11) also confirms that the reaction proceeds through two zones in series, which were designated as exo- and endothermic reforming zones. Their results confirm that oxygen was consumed early

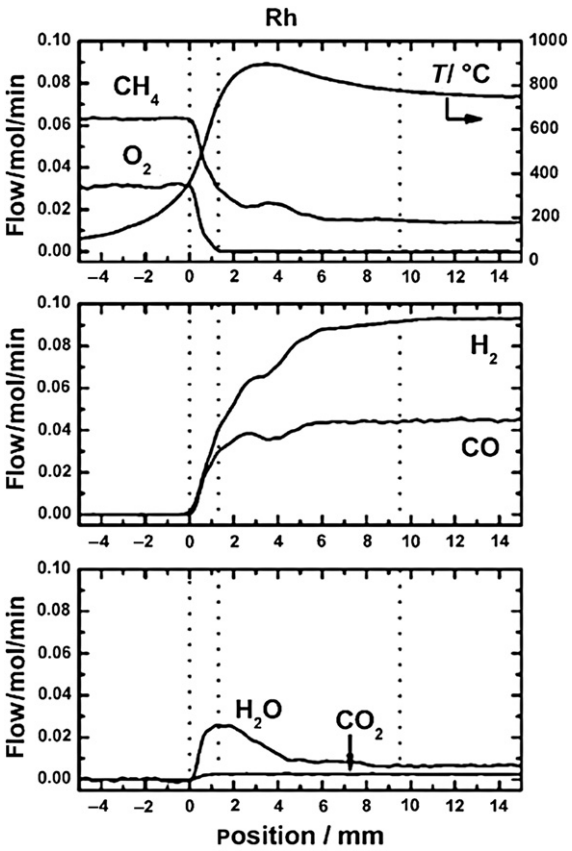

FIGURE 6.11 Schematic of mechanism: zone length depend on the type of catalyst; *Reprinted from Horn et al. [53], Copyright (2007), with permission from Elsevier.*

and rapidly over a short portion of the bed, roughly 1.3 mm for the Rh catalyst. This length is dependent on the catalyst metal used. Under the same conditions, the length of the oxidation zone was 2.3 mm for a Pt catalyst [53].

However, the observed trends in gas compositions down the length of the bed from the spatial profile suggest the overall reforming chemistry differed slightly than that commonly hypothesized for the combustion reforming mechanism. Their results found the formation, and role of CO_2 reforming to be minimal. The major products formed through the conversion of CH_4 with O_2 were H_2, CO, and H_2O. With

the oxygen levels depleted, steam was found to be the clear co-reactant with CH_4, not CO_2. The steam concentration reached a maximum at the end of the oxidation zone, but began to disappear, along with CH_4, as H_2 and CO formation increased down the length of the bed.

6.3.1.1. *Effect of O/C and H_2O/C Ratios*

Increasing the O/C carbon ratio above >1.0 at a constant S/C ratio in OSR begins to selectively produce combustion products. The oxidation of H_2 appears to be more favorable than that of CO, likely because the smaller H_2 molecule faces fewer diffusional resistances in the boundary layer. The result of H_2 oxidation is a lower H_2/CO ratio in the reformate. The increase in the reactor temperature accompanying the oxidation also facilitates the reverse WGS reaction, which further reduces the H_2/CO ratio.

Increasing the S/C ratio at a constant O/C ratio will increase the H_2/CO ratio for two reasons: (1) higher H_2O concentrations favor the WGS reaction and (2) excess H_2O will increase the IR absorptivity of the gas, thereby lowering the reactor temperature, which is favorable for WGS. Interestingly, increasing either O/C or S/C does not affect the peak temperature location, but rather the peak temperature and the outlet bed temperature [33,40,44]. The water addition increases cooling in the endothermic reforming zone, and it behaves as a diluent in the combustion zone. Therefore, the peak temperature location is not affected by the steam addition, but the outlet temperature of the reactor bed decreases as S/C ratio increases. Steam addition also does not affect the O_2 conversion in the combustion zone. The combustion zone length and overall CH_4 conversion were observed to be independent of steam to carbon ratio for methane OSR [33].

6.3.2. Pyrolysis-reforming Mechanism

In this mechanism [56,57], CO and H_2 are believed to be produced by direct partial oxidation of hydrocarbon without the production of CO_2 and H_2O as assumed in the combustion-reforming mechanism. In the pyrolysis-reforming mechanism, the hydrocarbon dissociatively adsorbs onto the catalyst surface, followed by successive α-scission of the C−C bond. The resulting C1 species react with adsorbed O_2 or steam to form H_2 and CO. The suggested mechanism is as follows (adapted from [58]):

$$O_2(g) + 2^* \leftrightarrow 2O^* \tag{6.23}$$

$$CH_4(g) + {}^* \leftrightarrow CH_4{}^* \tag{6.24}$$

$$CH_4{}^* + {}^* \leftrightarrow CH_3{}^* + H^* \tag{6.25}$$

$$CH_3{}^* + {}^* \leftrightarrow CH_2{}^* + H^* \tag{6.26}$$

$$CH_2{}^* + {}^* \leftrightarrow CH^* + H^* \tag{6.27}$$

$$CH^* + {}^* \leftrightarrow C^* + H^* \tag{6.28}$$

$$C^* + O^* \leftrightarrow CO^* + {}^* \quad \text{(Rate-determining step)} \tag{6.29}$$

$$CO^* \leftrightarrow CO(g) + {}^* \tag{6.30}$$

$$CO^* + O^* \leftrightarrow CO_2^* + {}^* \tag{6.31}$$

$$CO_2{}^* \leftrightarrow CO_2 + {}^* \tag{6.32}$$

$$H^* + H^* \leftrightarrow H_2{}^* \tag{6.33}$$

$$O^* + 2H^* \leftrightarrow H_2O^* \tag{6.34}$$

Using transient analysis of methane/O_2 pulses over a catalytic system, researchers observed a delay in CO_2 generation compared with CO [58−60]; suggesting CO is a direct product of methane oxidation whereas CO_2 is subsequently produced from CO through the WGS reaction. Fig. 6.12 [60] shows the delay between CO and CO_2 production, which suggests the direct formation of CO and H_2 over a Pt-based catalyst.

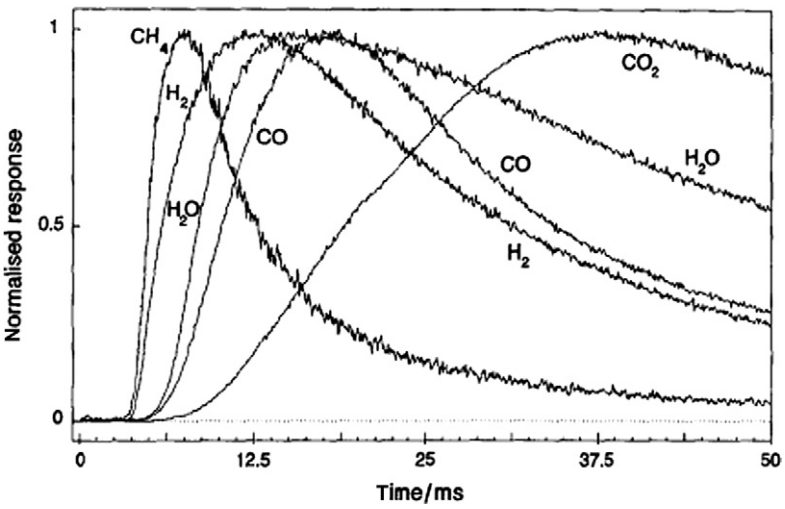

FIGURE 6.12 Normalized responses of CH_4, CO, CO_2, H_2, and H_2O as a function of time. CH_4 pulse experiment at 750 °C, 10 min after the O_2 treatment; *Reprinted from Mallens et al. [60], Copyright (1995), with permission from Springer.*

Mallens et al. [60] reported three different oxygen species during partial oxidation of methane: platinum oxide, chemisorbed oxygen, and gas-phase (bulk) oxygen. It was concluded that the platinum oxide and chemisorbed oxygen are responsible for the direct formation of CO, while the gas-phase oxygen oxidized the recently formed CO and H_2 into combustion products. They suggested a reaction mechanism, very similar to the Eqs. (6.23)−(6.34), in which methane is first dissociated on the catalyst surface into CH_x, which then reacts with chemisorbed oxygen or metal oxide to produce CO. H_2 is produced from the associative desorption of chemisorbed hydrogen atoms.

6.3.3. Decomposition and Reforming Mechanism for Oxygenates

Oxygenated hydrocarbons include a wide range of functional groups such as alcohols, ethers, aldehydes, and esters, and therefore discussing a detailed mechanism for each type of functional groups is not within the scope of this chapter. However, all oxygenated hydrocarbons basically follow a similar mechanism in which they preferably adsorb on the catalyst through lone pair electrons on the oxygen and, therefore, the sticking coefficient for oxygenates on metal catalysts is significantly higher than hydrocarbons (e.g., the sticking coefficient for methanol on Rh is 0.294 while it is only 0.229 for methane) [61]. This strong adsorption on the catalytic surface and subsequent cleavage of O−H, C−H, C−O, and C−C bonds produces adsorbed species such as H, C, O, or CO which react to form H_2 and CO [62].

For example, Mhadeshwar et al. [61] provided the following mechanism for methanol reforming.

$$CH_3OH(g) + {}^* \leftrightarrow CH_3OH^* \tag{6.35}$$

$$CH_3OH^* + {}^* \leftrightarrow CH_2OH^* + H^* \tag{6.36}$$

$$CH_2OH^* + {}^* \leftrightarrow CH_2O^* + H^* \tag{6.37}$$

$$CH_2O^* + {}^* \leftrightarrow CHO^* + H^* \tag{6.38}$$

$$CHO^* + {}^* \leftrightarrow CO^* + H^* \tag{6.39}$$

$$CO^* \leftrightarrow CO(g) + {}^* \tag{6.40}$$

$$2H^* \leftrightarrow H_2(g) + 2^* \tag{6.41}$$

In this mechanism, the adsorbed methanol goes through several C−H bond scissions,

producing a formyl group and eventually synthesis gas [61–64]. Dauenhauer et al. [62] believed that the methanol decomposition begins with O–H bond cleavage, producing a methoxy group, which proceeds to formaldehyde by C–H bond cleavage. However, Mhadeshwar et al. [61] reported that the activation energy for producing a methoxy group from the adsorbed methanol is significantly higher than for a hydroxymethyl group (83.7 vs. 38.9 kJ/mole); suggesting that methanol decomposition initiates with C–H bond cleavage to form a hydroxymethyl group which then converts to formaldehyde by O–H bond cleavage.

OSR of dimethyl ether proceeds with similar mechanism to methanol reforming except the first step is hydrolysis of DME to methanol [63] followed by methanol reforming as discussed above.

6.4. KINETICS

A fundamental understanding of the reaction kinetics is essential in process development, scale-up, and design. Determination of detailed reaction kinetics for OSR is very challenging, particularly for liquid hydrocarbons since liquid hydrocarbons are complex mixtures of hundreds of components, and each one undergoes several different reactions. In addition to the reactions associated with reforming, other reactions may take place: water-gas shift, carbon formation, methanation, hydrocracking, dehydrocyclization, dehydrogenation, ring opening, hydrogenation, etc. Also, the activity of the catalyst changes rapidly during the reaction and the kinetics vary with catalyst, fuel composition, and operating conditions. It would be desirable to develop predictive models to account for variations in these parameters.

6.4.1. Hydrocarbons

The kinetics of OSR of hydrocarbons are mainly described by two approaches: (1) Combination of individual reactions and (2) Fundamental. These two approaches are discussed in the following sections.

6.4.1.1. Combination of Individual Reactions Approach

In OSR, a series of reactions (Eqs. 6.2–6.14) are likely to take place depending on the reaction conditions. However, some reactions such as Boudouard reaction, methanation reaction, decomposition reaction, partial combustion reaction, and CO_2 reforming are generally ignored in the kinetic modeling of OSR of hydrocarbons for simplification. Only reactions such as steam reforming, total combustion, and water-gas shift reaction that significantly affect the kinetics of OSR of hydrocarbons are considered. In this approach, researchers adopt the reaction kinetics for these significant reactions from published literature to develop a kinetic model for OSR of hydrocarbons. A number of models can be found for total combustion, steam reforming, and water-gas shift reaction. Researchers use different combinations of rate expressions for these individual reactions. They make some modification in the original form of rate expressions to reflect their reaction conditions or catalysts. For example, kinetic models for steam reforming and water-gas shift from Xu and Froment [65] over Ni-based catalyst are widely used by researchers for SR and WGS steps in the OSR of methane, while the steam reforming model from Tottrup [66] is widely used for higher hydrocarbons.

The combination of individual reactions used by various researchers and the corresponding rate expressions for these individual reactions are summarized in Table 6.3. The approach is also explained by an example below from Pacheco et al. [67].

Pacheco et al. [67] developed and validated a pseudo-homogeneous mathematical model for OSR of isooctane and subsequent water-gas shift. They assumed two-step mechanism for OSR of isooctane: combustion of isooctane

TABLE 6.3 Summary of the Combination of Individual Reaction Approach

Research group (fuel)	Individual reactions considered	Kinetic rate equations adopted from
Halabi et al. [68]; Hoang et al. [69–70] (methane)	$CH_4 + 2O_2 = CO_2 + 2H_2O$	Ma et al. [71]; Trimm and Lam [72]
	$CH_4 + H_2O = CO + 3H_2$	Xu and Froment [65]
	$CO + H_2O = CO_2 + H_2$	Xu and Froment [65]
	$CH_4 + 2H_2O = CO_2 + 4H_2$	Xu and Froment [65]
Nah and Palanki [73] (heptane)	$C_7H_{16} + 7H_2O = 7CO + 15H_2$	Tottrup [66]
	$CH_4 + H_2O = CO + 3H_2$	Xu and Froment [65]
	$CO + H_2O = CO_2 + H_2$	Xu and Froment [65]
	$CH_4 + 2H_2O = CO_2 + 4H_2$	Xu and Froment [65]
Rabe et al. [10] (gasoline)	$C_mH_n + mH_2O = mCO + (m + n/2)H_2$	Tottrup [66]
	$CH_4 + H_2O = CO + 3H_2$	
	$CO + H_2O = CO_2 + H_2$	
	$CO_2 + 4H_2 = CH_4 + 2H_2O$	
Papadias et al. [74] (gasoline)	$C_mH_n + (m + n)/2O_2 = mCO_2 + (n/2)H_2$	Power law rate expression
	$C_mH_n + mH_2O = mCO + (m + n/2)H_2$	Dubien et al. [75]
	$CO + H_2O = CO_2 + H_2$	Wheeler et al. [76]

followed by steam and CO_2 reforming, and water-gas shift reaction. Their model uses Langmuir–Hinshelwood–Hougen–Watson (LHHW) kinetics in which the expressions were obtained from literature for combustion, steam reforming, CO_2 reforming, and WGS to determine the kinetic parameters from isooctane OSR experimental data over Pt on ceria. Table 6.4 shows the rate expression used by Pacheco et al. [67] in the reformer modeling. The parameters of these rate expressions are summarized in Table 6.5.

Shigarov et al. [78] modeled OSR of diesel assuming that two reactions (combustion of hydrocarbons and steam reforming of hydrocarbons) occur simultaneously in the reactor, but the reaction rate is controlled by the external

TABLE 6.4 Rate Equations Used in the Reforming Model by Pacheco et al. [67]; *Reprinted from Pacheco et al. [67], Copyright (2003), with permission from Elsevier.*

Reaction	Expression for r_i	T (°C)	Catalyst	Reference
$C_8H_{18} + 16O_2 \Rightarrow 8CO_2 + 9H_2O$	$r_1 = k_1 P_{iC8} P_{O_2}$	800–900	Ni/Al_2O_3	[77]
$C_8H_{18} + 8H_2O \Rightarrow 8CO + 17H_2$	$r_2 = \frac{k_2}{P_{H_2}^{2.5}}\left(\frac{P_{iC8}P_{H_2O} - P_{H_2}^3 P_{CO}/K_1}{(1 + K_{CO}P_{CO} + K_{H_2}P_{H_2} + K_{iC8}P_{iC8} + K_{H_2O}P_{H_2O}/P_{H_2})^2}\right)$	500–750	$Ni/MgAl_2O_3$	[65]
$C_8H_{18} + 8CO_2 \Rightarrow 16CO + 9H_2$	$r_3 = k_3 P_{iC8} P_{CO_2}\left(1 - \frac{P_{CO}^2 P_{H_2}^2}{K_3 P_{iC8} P_{CO_2}}\right)$	800–900	Ni/Al_2O_3	[77]
$C_8H_{18} + 16H_2O \Rightarrow 8CO_2 + 25H_2$	$r_4 = \frac{k_4}{P_{H_2}^{3.5}}\left(\frac{P_{iC8}P_{H_2O}^2 - P_{H_2}^4 P_{CO_2}/K_4}{(1 + K_{CO}P_{CO} + K_{H_2}P_{H_2} + K_{iC8}P_{iC8} + K_{H_2O}P_{H_2O}/P_{H_2})^2}\right)$	500–750	$Ni/MgAl_2O_3$	[65]
$CO + H_2O \Rightarrow CO_2 + H_2$	$r_5 = \frac{k_5}{P_{H_2}}\left(\frac{P_{CO}P_{H_2O} - P_{H_2}P_{CO_2}/K_5}{(1 + K_{CO}P_{CO} + K_{H_2}P_{H_2} + K_{iC8}P_{iC8} + K_{H_2O}P_{H_2O}/P_{H_2})^2}\right)$	500–750	$Ni/MgAl_2O_3$	[65]

TABLE 6.5 Results of the Kinetic Parameter Regression for the Rate Equations Used in Table 6.4; *Reprinted from Pacheco et al. [67], Copyright (2003), with permission from Elsevier.*

Parameter	Pre-exponential factor	Activation energy (kJ/mol)
k_1 (mol/(g_{cat} s bar^2))	2.58E + 08	166.0
k_2 (mol $bar^{0.5}$/g_{cat} s))	2.61E + 09	240.1
k_3 (mol/g_{cat} s bar^2))	2.78E − 05	23.7
k_4 (mol $bar^{0.5}$/(g_{cat} s))	1.52E + 07	243.9
k_5 (mol/(g_{cat} s bar))	1.55E + 01	67.1
K_{H_2O} (dimensionless)	1.57E + 04	88.7*

* *Heat of adsorption of water (ΔH_{H_2O}).*

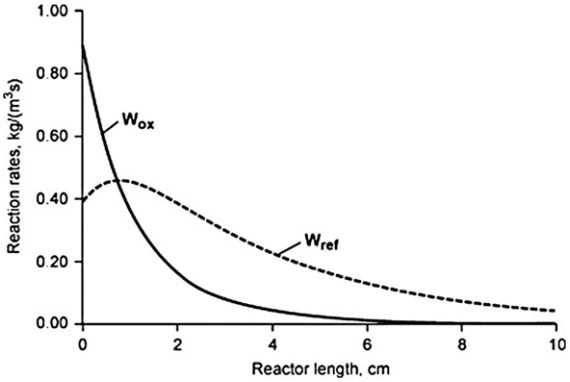

FIGURE 6.13 Distribution of apparent reaction rates along the catalyst bed during OSR of diesel (O/C = 1.0, S/C = 1.67, and inlet temperature = 346 °C); *Reprinted from Shigarov et al. [78], Copyright (2009), with permission from Elsevier.*

mass transfer of hydrocarbons. However, the kinetic model ignored other side reactions (carbon formation, methanation, etc.) that may be occurring during OSR of diesel. The surface concentration of hydrocarbons participating in each competing reaction (combustion and SR) was determined by the ratio of kinetic rates of both reactions. They also estimated that hydrocarbon bulk-surface flux (or mass transfer) determines the overall reaction rate, not the oxygen concentrations. Their reaction model is similar to the two-step reaction mechanism for OSR. Interestingly, the model predicts that steam-reforming reaction initiates even at the top of the catalyst bed, but is dominated by the combustion reaction (see Fig. 6.13). The high reaction rate of steam-reforming reaction at the inlet of the reactor bed may extend the catalyst life because it helps minimize hot spots, which can be detrimental to the catalyst.

Models that treat the kinetics to the major reactions independently fail to capture the effects of one reaction on others. For example, highly exothermic combustion reactions at the initial stage of the catalyst bed not only generate temperature gradient across the catalyst bed, but also produce highly active intermediate species. Both the temperature gradient and highly active intermediate species affect other reactions, whether they occur in parallel or sequentially. Also, these kinetic models assume that the kinetics for the SR of hydrocarbons dictate the reaction in most of the reactor. Therefore, there is a need for a kinetic model to describe the OSR reaction process that is not based on individual reactions.

6.4.1.2. *Fundamental Approach*

Dorazio and Castaldi [79] extended the *n*-heptane homogeneous reaction mechanism (which is readily available) to larger hydrocarbons by including *n*-tetradecane decomposition reactions such as partial oxidation, steam reforming, and cracking reactions. A simplified transition state theory approach was used to calculate the kinetic parameters which were not available in open literature. A sensitivity analysis was also performed to identify the dominating reaction paths during the reforming reaction of *n*-tetradecane. This was done by omitting reactions sequentially and then observing the effects on conversion and product species concentrations. If the conversion or product species concentrations are greatly affected by omitting

a reaction, then it means that the reaction represents an important step in the mechanism of reforming of *n*-tetradecane. The model agrees with the experimental values at a range of temperatures and space velocities. From sensitivity analysis, it was observed that cracking of tetradecane, oxidation reactions of resulting hydrocarbons, and water-gas shift reaction are dominant reaction pathways. Steam reforming of *n*-tetradecane, and the hydrocarbons resulting from cracking reactions, does not significantly contribute to the reaction mechanism.

Parmar et al. [80] developed two LHHW-type models for OSR of tetradecane on Pt/Al_2O_3. For the first model, they used the reaction mechanism proposed by Rostrup-Nielsen [81] in which it is assumed that the hydrocarbon chemisorbs on a dual catalytic site, followed by irreversible successive α-scission of the C−C bond. For the second model, they used the mechanism proposed by Zaera [82] in which it is assumed that the hydrocarbon chemisorbs on the catalyst with the C−H bond scission. The chemisorbed alkyl species could undergo a number of subsequent reactions. The model affirms the two step mechanism for OSR and that the combustion reaction dominates at the initial 15−20% of the catalyst bed for high space velocities and at 5% of the catalyst bed at low space velocities.

6.4.2. Methanol

There is little in open literature on the OSR kinetics of oxygenated hydrocarbons. Power law-type rate expressions have been reported for methanol. Reitz et al. [83] conducted experiments over $Cu/ZnO/Al_2O_3$ at low conversions of methanol and O_2, 3 and 20% respectively, and a temperature range of 180−225 °C to develop a power law-type rate expression for the OSR kinetics of methanol. The rate depends positively on methanol and O_2 concentrations and is hindered by water. The activation energy (E_a) for the reaction was reported to be 115 ± 6 kJ/mol and the pre-exponential factor (A_0) was $6 \pm 0.2 \times 10^8$ mol/(min.g_{cat}.$kPa^{0.22}$) Interestingly, the activation energy for the reaction was reported to vary significantly with water partial pressures, ranging from 134 to 106 kJ/mol at partial pressures of 8.2 and 27 kPa, respectively, while it was almost independent of methanol and O_2 partial pressures.

Mizsey et al. [84] used the combination of individual reaction approach for the OSR kinetics of methanol over a commercial copper catalyst. The individual reactions used in their kinetic model were dimethyl ether formation, methanol decomposition, WGS reaction, and steam reforming. The activation energies estimated for these individual reactions were 117 kJ/mol (DME formation), 81 kJ/mol (methanol decomposition), 76 kJ/mol (steam reforming), and 50 kJ/mol (WGS).

6.5. CATALYTIC OSR OF HYDROCARBONS

The key requirements for catalytic materials designed for the OSR of hydrocarbons into synthesis gas are generally the same as those for SR and POX.

1. Having both O_2 and H_2O as reactants requires the catalyst to be active and selective for major reactions involved in both the SR and the POX reaction sequences.
2. Physically (or thermally) robust. Reforming temperatures can be upward of about 800 °C to obtain maximum H_2 yields and avoid carbon formation. Operating at these temperatures for extended periods of time can cause loss of active surface area through sintering/agglomeration of catalytic metal. Temperature cycling also takes a physical toll on the catalyst material which can cause degradation. It has been speculated that the reforming catalysts will have to operate at gas hourly space velocities (GHSV) of 200,000 h^{-1} (based on volumetric flow of feed at 25 °C and

0.1 MPa) while maintaining >90% fuel conversion, and H_2 selectivity >80% for roughly 5000 h [6].

3. Chemically robust. The catalyst must maintain structural integrity in both oxidizing and reducing conditions while operating at high fuel conversion and synthesis gas selectivity for extended lengths of time. The catalyst must also be resistant toward carbon formation and sulfur poisoning. Both are pervasive problems in reforming processes, as carbon and sulfur can irreversibly adsorb on active sites, reducing turnover frequency and eventually deactivating the catalyst.

The effects of thermal deactivation by sintering and chemical deactivation by carbon formation and sulfur poisoning are strongly interconnected with each other as illustrated by Fig. 6.14. The cluster size of a metal has been shown to influence both its activity and resistance to deactivation. Metal clusters of smaller sizes are believed to contain a higher number of defects, i.e. more kink and edge sites, which are believed to be the active sites [85]. Translating this into activity, Wei and Iglesia [85] observed commonly used reforming metals like Pt, Ru, and Rh to have greater CH_4 turnover rates with smaller clusters. Ensemble effects due to the cluster size of the active metal have also been shown to alter the deactivation mechanism by carbon and sulfur [86–88]. Larger metal clusters are prone to have a much stronger interaction with carbon and sulfur as they have a much higher electron density than smaller particles [87]. This allows them to form strong, and oftentimes irreversible covalent bonds with the pi-electrons in the p-orbital of sulfur and carbon.

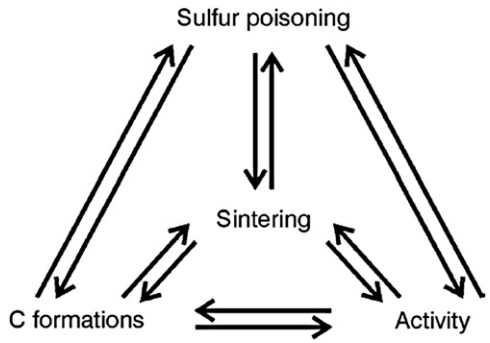

FIGURE 6.14 Relationship between each deactivation phenomena and catalyst activity; *Reprinted from Sehested [89], Copyright (2006), with permission from Elsevier.*

Transition metals are known to exhibit activity for the OSR of hydrocarbon fuels into synthesis gas. These catalytic metals can be broadly categorized as non-precious or precious metals. Most metals that are active for SR and POX individually are also active for OSR. The following sections will discuss issues with using these catalysts used for producing a H_2-rich synthesis gas from the reforming of major hydrocarbon fuels.

6.5.1. Natural Gas/Methane

Natural gas is a well-known source of hydrogen. Current uses of natural gas for domestic heating and power generation have promoted the development of a vast and complex distribution network to ensure a cheap and reliable fuel supply. With such availability, synthesis gas derived from natural gas may be an ideal fuel for stationary fuel cells.

Methane is the primary component of natural gas. Despite a favorable H/C atomic ratio (4/1) compared with other fuels, such as coal (~1.1/1), reforming of methane is challenging due to the inherent refractory nature and symmetry of the molecule. The energy required to dissociate the initial C–H bond to activate the methane molecule is high, requiring 435 kJ/mol [90], thus necessitating elevated reaction temperatures (700–900 °C) to achieve high conversion levels. These temperatures may be sufficiently high so that the product of the initial C–H bond scission is more reactive than the methane itself [91]. The challenges facing the development of catalysts for the OSR of CH_4 include overcoming the geometric

resistance (symmetry) to activate the methane molecule and producing stable, long-term H_2-rich synthesis gas yields.

6.5.1.1. Non-Precious Metals

6.5.1.1.1. NICKEL

Intrinsic activities of metals for OSR of CH_4 have been found to correlate with those observed for steam reforming: Rh, Ru > Ni > Pt > Pd > Co [92]. Although nickel may not be the most active, the study and development of nickel-based catalysts for the OSR of methane has been the focus of many studies because of the favorable commercial aspects of Ni: inexpensive, widely available, and appreciable activity. Under OSR conditions, Ni catalysts can reach synthesis gas yields and conversion levels of methane which are close to equilibrium (see Fig. 6.15). The high activity of Ni may be due to the dissociation of CH_4 being highly thermodynamically favorable over Ni surfaces [93].

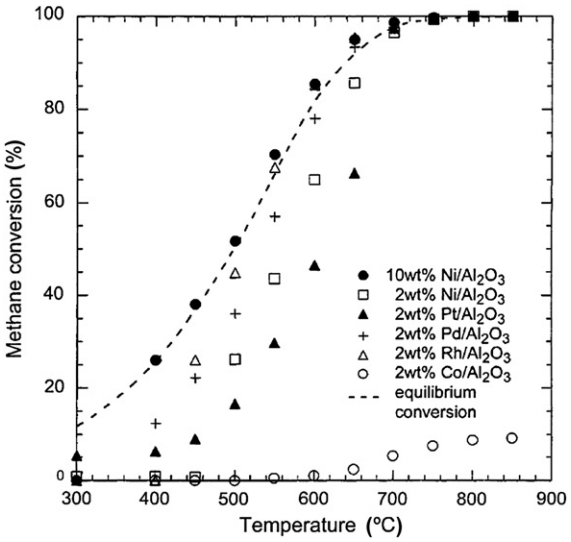

FIGURE 6.15 Temperature dependence of conversion over various supported metals catalysts during OSR of CH_4 (O/C = 0.2, S/C = 2.5, SV = 7200 h^{-1}); *Reprinted from Ayabe et al. [13], Copyright (2003), with permission from Elsevier.*

Despite the relatively high activity of Ni, the specific weight loadings of Ni are usually higher compared with noble metals (lower turnover frequency) to obtain sufficient activity to reach equilibrium. This is also illustrated in Fig. 6.15.

While higher metal loadings of Ni can be afforded due its low cost, sintering rates and carbon formation are also more pronounced compared with more expensive noble metal catalysts. The sintering temperature of Ni (i.e., $T_{Tam} = 0.5 \times T_{melt}(K)$) is 590 °C [94], which is well below the normal operating temperatures for OSR (750–900 °C).

Carbon formation over Ni has also been well characterized in the literature [89,94,95]. During reforming, the morphology of the carbon species formed on Ni catalysts can have three main forms: encapsulating, pyrolytic, and/or filamentous. Scanning Electron Microscopy (SEM) images of each type of carbon formed over a $Ni/MgAl_2O_4$ catalyst are shown in Fig. 6.16. Filament or whisker carbon is the most detrimental form to the dispersion of Ni. This type of carbon is also unique to Ni and other non-precious metals like Co [96,97] because the carbon atoms are soluble in the metal lattice [94]. The growth of carbon filaments is believed to occur as adsorbed carbon atoms diffuse through large Ni crystallites (>7 nm [98]) and condense at the base, thus lifting the Ni particle off the surface, forming the whisker [89,94,95].

Nickel and other non-precious metals also have a strong thermodynamic tendency to be oxidized by gas-phase oxygen (see Fig. 6.17). As stated earlier in Section 6.3.1, oxidized Ni promotes the combustion of CH_4, which leads not only to lower H_2 and CO yields, but also to severe hot spots and temperature gradients in the bed.

For supported Ni-based catalysts to be used for extended periods of time, they need to be modified to limit the extent of the chemical and thermal deactivation to which they are susceptible. In other words, it is necessary to maintain small, stable crystallites under reaction

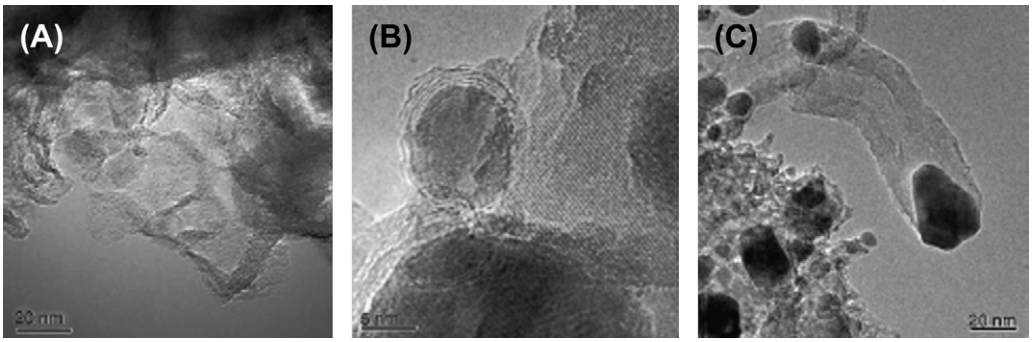

FIGURE 6.16 SEM images illustrating the different carbon morphologies which form over a $Ni/MgAl_2O_4$ catalyst: (A) Pyrolytic, (B) Encapsulating, and (C) Filamentous; *Reprinted from Sehested [89], Copyright (2006), with permission from Elsevier.*

conditions. This can be done through specific synthesis routes, addition of promoting metal, and/or the choice of support. Each of these is discussed below.

EFFECT OF PRECURSOR The synthesis method is instrumental in producing uniform converge of the support with small Ni crystallites. The easiest technique to obtain a well-dispersed supported catalyst is wet impregnation. In its simplest form, this method only requires contacting the high surface area (HSA) support with aqueous-metal solution of desired weight loading, drying, and calcination. The choice of water-soluble metal salts, either acetate, nitrate, sulfide, or chloride, has shown to influence the Ni particle size. The interaction between the precursor and the support is important because it ultimately defines the extent of the interaction between the metal and the support. Larger metal particles have a smaller interface with the support and therefore the interaction between the two will be much weaker.

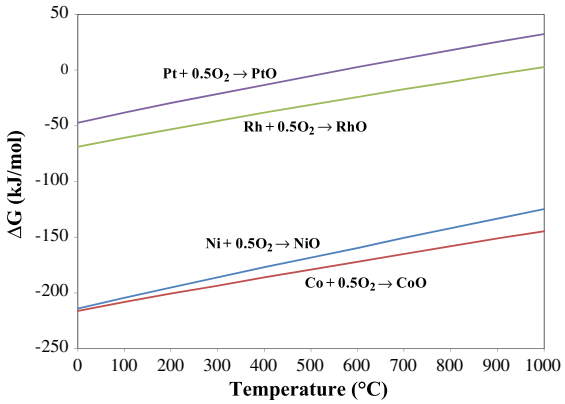

FIGURE 6.17 Change in Gibb's Free energy for the oxidation of several catalyst metals as a function of temperature. Calculations by HSC Chemistry v 6.12 [31].

Table 6.6 from a study by Li et al. [99] shows the effect of three different precursors on the particle size of a series of $Ni/\gamma\text{-}Al_2O_3$ catalysts. It can be seen that the chloride precursor has a greater impact on particle size, while those for the nitrate and acetate are similar. In terms of OSR activity, shown in terms of CH_4 conversion in Table 6.6 [99], it can be seen that the catalysts with larger particle sizes, prepared from the chloride precursor, are consistently less active than those prepared from nitrate or acetate precursors.

PROMOTERS

Noble metals The high thermodynamic potential for Ni to undergo oxidation under reaction conditions is disadvantageous for OSR because Ni metal becomes oxidized at the front of the bed and loses reforming activity. Severe hot spots occur in this region as NiO promotes combustion of the fuel. Hot spot

TABLE 6.6 Effect of Precursor on Catalyst Properties and Activity of Ni during OSR of CH_4 (O/C = 1.0, S/C = 0.75, and 800 °C) (equilibrium values: >99% CH_4 conversion and H_2/CO = 2.8); *Reprinted from Li et al. [99], Copyright (2005), with permission from Elsevier.*

			Particle size of Ni (nm)				
Precursor	**Ni (wt%)**	**H/Ni$_{total}$ (%)***	**Adsorption†**	**XRD‡**	**Ni^0/Ni$_{total}$ (%)§**	**CH_4 conversion (%)**	**H_2/CO**
$Ni(NO_3)_2$	0.4	10.9	9	–	101	97	2.7
	0.9	8.0	12	–	102	97	2.8
	2.6	5.8	17	19	100	98	2.6
$Ni(CH_3COO)_2$	0.4	11.2	9	–	105	96	2.8
	0.9	9.3	10	–	102	97	2.7
	2.6	5.7	17	19	102	98	2.6
$NiCl_2$	0.4	2.6	38	34	103	92	2.8
	0.9	1.6	59	62	102	94	2.8
	2.6	1.2	82	77	98	93	2.8

* *Total (reversible and irreversible) H_2 chemisorption at 25 °C.*
† *Average particle size (average volume–area) based on H_2 adsorption amount.*
‡ *Calculated from Scherrer equation, using the half-width at half-height of the strong intensity metal peak. Sample was pretreated at H_2 flow, 850 °C and 0.5 h.*
§ *Reduction degree; determined by H_2-TPR profiles.*

formation results in poor heat transfer to the lower part of the bed as well as degradation of the catalyst. It has been determined that the addition of a small amount of noble metals (<1 wt%) to Ni suppresses the undesirable oxidation, while maintaining equilibrium conversion of CH_4 to H_2 and CO [100]. Table 6.7 shows that the highest observed bed temperature is reduced by the addition of noble metals, compared with the unmodified nickel catalyst. With the exception of Pd, it can also be seen that the noble metal which produced the lowest bed temperature had the highest effect on hot spot suppression when combined with Ni.

The higher CH_4 conversion has shown to be a result of enrichment at the surface by the noble metal, forming what is known as a near surface alloy (NSA). An NSA can be defined as an alloy in which the solute metal is present near the surface in concentrations that are different from the bulk [101]. The formation of such an alloy influences adsorption/desorption energies of species as well as other catalytic properties of the host material [102].

To form an NSA it is desirable for there to be a fairly weak interaction between the Ni host and noble metal [100]. This allows for a sufficiently negative segregation energy, E_{seg}, between Ni and noble metal (E_{seg} is defined as the energy required to move the solute atom from the bulk to the surface of the host atom [101]), and promotes segregation to lower the surface energy between the metals, resulting in the formation of small noble metal clusters at the Ni surface. As a result, the noble metal is able to retain its metallic character while interacting with Ni at the surface. With such small loadings, an interaction that is too strong will result in a positive E_{seg}, causing the benefits of the noble metal to be lost as it will be too soluble in the Ni lattice [100].

The presence of a noble metal at the surface lowers the oxygen affinity and improves reducibility of the Ni particle because H_2 dissociation

TABLE 6.7 OSR of CH_4 (O/C = 1.0, S/C = 0.75, and 850 °C) Over Group VIII Promoted Ni/Al_2O_3 Catalysts; *Reprinted from Yoshida et al. [100], Copyright (2009), with permission from Elsevier.*

Catalyst (wt%)	W/F (g h/mol)	CH_4 conversion (%)	H_2/CO	CO selectivity (%)	Highest bed temperature (°C)
Ni(10.6)	0.04	>99	2.8	81	1076
Pd(0.07)	0.23	64	1.9	91	1036
Pd(0.07) + Ni(10.6)	0.04	>99	2.8	81	972
Pd(0.2) + Ni(10.6)	0.04	>99	2.9	81	986
Pt(0.14)	0.04	96	2.3	83	903
Pt(0.14)) + Ni(10.6)	0.04	>99	2.9	81	1026
Pt(0.4)) + Ni(10.6)	0.04	>99	2.9	81	1004
Au(0.14)	0.04	<1	–	–	–
Au(0.14)) + Ni(10.6)	0.04	>99	2.8	80	1004
Au(0.4)) + Ni(10.6)	0.04	>99	2.8	81	1015
Ir(0.14)	0.04	93	2.4	82	935
Ir(0.14)) + Ni(10.6)	0.04	>99	2.9	80	1035
Ir(0.4)) + Ni(10.6)	0.04	>99	2.8	80	1013
Rh(0.07)	0.04	>99	2.8	81	887
Rh(0.07) + Ni(10.6)	0.04	>99	2.9	79	1004
Rh(0.2) + Ni(10.6)	0.04	>99	2.8	82	985
Ru(0.07)	0.04	>99	2.7	81	905
Ru(0.07) + Ni(10.6)	0.04	>99	2.9	81	1024
Ru(0.2) + Ni(10.6)	0.04	>99	2.9	81	995
Equilibrium		>99	2.9	81	

can be catalyzed at a lower temperature over noble metal clusters and transferred to the NiO by a hydrogen spillover mechanism [103]. Studies have speculated that improving the reducibility of Ni, allows the endothermic reforming reactions to take place in the bed inlet, in addition to combustion [49,100,104,105]. The more intimate contact between exothermic and endothermic reforming reactions improves heat transfer and reduces the intensity of the temperature gradients. However, the reduced metal may alter the mechanism in the presence of oxygen. Temperature resolved XANES by Parizotto et al. [103] suggested the presence of Pt (0.05 wt%) in 15 wt% Ni/Al_2O_3 promotes the activation of CH_4 through decomposition ($CH_4 \rightarrow CH_3 + H$). The conversion of CH_4 could proceed through decomposition, avoiding the formation of CO_2 and the energy release associated with its formation.

The synthesis method has been shown to influence the surface concentration of the noble metals. Studies have found both sequential and co-impregnation methods to be effective in

producing noble metal enriched surfaces. While some results are conflicting, the choice of method appears to be dependent on Ni loading. For low loadings of Ni, both Li et al. [49] and Mukainakano et al. [105] found sequential addition to be more effective for NSA formation with 0.1 wt% Pt-promoted 2.6 wt% Ni/Al_2O_3, and 0.05, 0.1 wt% Pd- or Rh-promoted 0.9 or 2.6 wt% Ni/Al_2O_3, respectively. In two different studies Yoshida et al. [100,104] found the co-impregnation method to be more effective for NSA formation with the same metals, Pt, Pd, and Rh and Ni/Al_2O_3 containing higher loadings of Ni (10.6 wt% Ni). Consistent with these results, Dantras et al. noted a 10 wt% $Ni/CeZrO_2$ promoted with either Ag, Fe, Pt, or Pd (0.1 wt%) prepared by co-impregnation was more active due to a higher Brunauer-Emmett-Teller (BET) surface area, and therefore higher dispersion, compared with the counterparts prepared by the successive impregnation method [106].

In addition to mitigating hot spots, noble metals can be added to Ni to lower the temperatures for the conversion of CH_4 into synthesis gas. The activity benefits of the addition of a small amount of Pd or Pt to 13 wt% Ni/Al_2O_3, shown in terms of conversion and H_2 production, are illustrated in Fig. 6.18.

Non-noble metals Other metals are also effective in promoting the activity of Ni by improving stability and resistance to carbon formation. A few have shown success (see Table 6.8) directly in the OSR of CH_4, and others in directly relevant reforming reactions which occur in the OSR process. These include Co, Au, Sn, Ag, and Ce. The effects of each metal are different, and the level of dopant depends

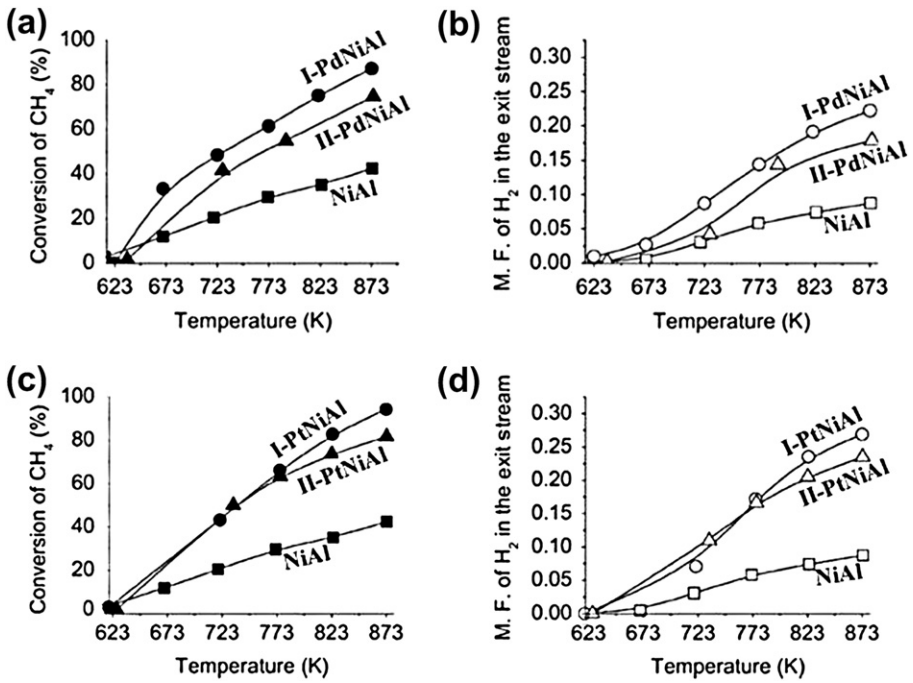

FIGURE 6.18 Conversion of CH_4 and mole fraction (M.F.) of H_2 in the exit stream from the OSR of CH_4 (S/C = 4, O/C = 1); I-PdNiAl (0.10 wt% Pd), II-PdNiAl (0.24 wt% Pd), I-PtNiAl (0.05 wt% Pt); II-PtNiAl (0.27 wt% Pt). Nickel content is 13 wt% in all catalysts; *Reprinted from Dias and Assaf [107], Copyright (2004), with permission from Elsevier.*

TABLE 6.8 Promoting Metals Which Improve Activity and Stability Ni-Based Catalysts for Reforming of Methane

Promoting Metal	Amount (wt%)*	Reaction	Reference
Ag	≤2.3	OSR	[106,110]
Au	1–2	SR	[111]
Co	30–57	POX, CO_2 reforming	[112–115]
Sn	1–3	SR	[108,116,117]
Ce	19–70	OSR	[118]

** Metal basis (i.e., calculated based on promoter wt relative to promoter + Ni).*

on the solubility of the solute metal in the Ni host, among other factors. For example, only a small amount of Sn (1–3 wt% metal basis) was found to improve the carbon resistance of Ni/YSZ (15–20 wt% Ni) during SR of CH_4 by forming an NSA much like the noble metals. The Sn was proposed to displace/occupy the highly active undercoordinated sites (e.g. kinks or edge sites) at the surface which may serve as nucleation sites for carbon formation [108]. Meanwhile, metals like Ni and Co form a homogenous alloy [109] and can be combined in larger amounts to improve activity and resistance to carbon formation compared with monometallic Ni.

Omata et al. [119] utilized an artificial neural network (ANN) to survey elements in the periodic table to determine the optimum promoting metal for a 10 wt% Ni/α-Al_2O_3 catalyst. Seventeen physiochemical properties and experimentally measured performance data (taken in hot spot-free conditions) for nine additives (0.05 molar ratio promoter to Ni) were used to train the ANN. The trained ANN was then used to predict conversion, and H_2 and CO selectivity for 54 additives. Of those tested, La, Nd, Pr, Ti, and Sc were predicted to give performance better than the unpromoted Ni catalyst. H_2 selectivity versus conversion is shown in Fig. 6.19 for each of these metals determined during validation testing (650 °C; O/C = 0.96; S/C = 0.93). These results indicated the accuracy of the ANN predictions for the additives, and either Nd or Sc are effective promoters beyond the traditionally known Ce and La.

Basic elements from the alkali and alkaline series are probably the most common promoters for Ni-based catalysts. Their presence improves the rate of carbon gasification and also reduces the methanation reaction present during steam reforming [120]. The effects of these metals are still debatable, but studies have pointed to a possible combination of certain benefits, which include improving steam–carbon reaction, neutralizing acid sites on the support, binding to active step sites, suppressing polymerization and cracking reactions, which form carbon, and controlling ensemble effects [109,121,122]. Because of their successful use in steam reforming applications, both Groups I and II base metals can be used in applications with high steam concentrations. However, alkali promoters are volatile in high-temperature environments [120] and would probably be limited with feeds having higher O/C ratios.

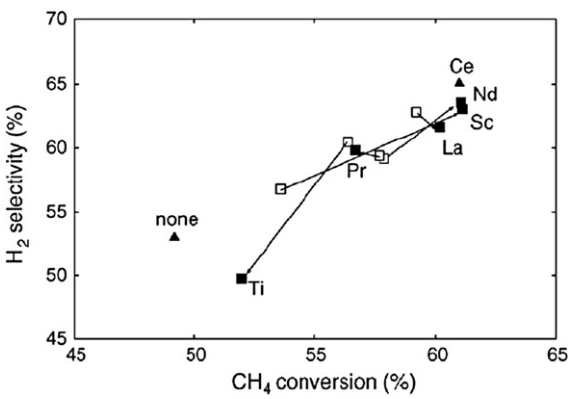

FIGURE 6.19 Comparison of ANN-predicted and experimentally validated activity for OSR of CH_4 for 10 wt% Ni/α-Al_2O_3 (650 °C; O/C = 0.96; S/C = 0.93). Shaded: predicted by ANN and unshaded: experimental; *Reprinted from Omata et al. [119], Copyright (2008), with permission from Elsevier.*

SUPPORTS A wide variety of metal oxide materials have been studied as supports for not only Ni, but all reforming catalysts. The types of oxides can be categorized as reducible or irreducible [123,124]. Oxides known to be reducible are those used for semiconductor applications, and include mainly CeO_2, GdO_2, Nb_2O_5, Ta_2O_5, TiO_2, and ZrO_2. Irreducible oxides include Al_2O_3, MgO, and La_2O_3, which are the more traditional support materials known for their high thermal stability. When selecting a support material, tradeoffs are often made between cost and activity. For this reason, the irreducible oxides have been widely used in industrial applications, and continue to be commonly studied. However, as will be discussed later, it has been recently discovered that although they are more expensive, some reducible oxides are desirable because of their ability for their lattice oxygen to participate in the reaction, and also reduce the rate of carbon accumulation.

Supports are critical for catalyst activity as they serve as a substrate for the dispersion of the catalytic metal. They also can impart thermal stability through interaction with the metal. Beyond this, there is conflicting evidence whether supports actually play a role in the reforming reactions. It has been argued that intrinsic activity of the metal is independent of support type [125,126] and is only dependent on dispersion [127,128]. Meanwhile, others have found turnover frequency to be affected by the nature of the support, and deactivation is also linked to support [124,129,130]. Because the history of a material, its preparation method, pretreatment, and testing environment vary between studies, direct comparison of results regarding the role of the support is difficult.

Although functionality of the support carrier remains up for debate, it has been found that an acidic support promotes carbon formation. The acidic sites promote dehydrogenation and cracking reactions, which form carbon precursors. Hence materials with basic properties are often used as supports or basic oxide materials are added to the more acidic supports (e.g., $MgAl_2O_4$) [131] to neutralize the acid sites. Commonly used support materials ranked in order of their decreasing acidity are $Al_2O_3 > ZrO_2 > TiO_2 > ZnO > SiO_2 > La_2O_3 > MgO$ [132,133]. The particle size of the metal may also be dependent on the acidity of the support. With directly comparable metal loadings, supports with higher acid character produced smaller metal particles sizes which improve ensemble control and resistance to carbon formation [134].

Alumina γ-Alumina is used as a support for Ni-based catalyst in industrial steam reforming applications and is therefore widely used in OSR studies. It is suitable as a support due to the favorable trade-offs between high surface area (HSA), pore structure, mechanical stability, cost, and availability. However, γ-Al_2O_3 supported Ni catalysts eventually deactivate through pore collapse and loss of surface area as operating temperatures are near the phase transition region where γ-Al_2O_3 is converted into α-Al_2O_3. In addition, loss of metallic surface area occurs as Ni migrates into the alumina support, forming $NiAl_2O_4$ spinel phase, which is difficult to reduce and readily forms carbon [135]. To improve structural stability and maintain HSA, textural promoters are added into the alumina structure [120,128,136]. Structural promoters can also be added to improve resistance to carbon formation and sulfur poisoning [120,128,136].

Commonly used promoters include La, Y, Ce, Pr, Zr, Mg, Ca, Sr, or Ba [128,136–138]. The partial replacement of Al with any one or combination of these elements can improve thermal stability of the γ-Al_2O_3. Added performance benefits of the promoters may include improved surface alkalinity (carbon resistance), reduced Ni migration, and improved lattice oxygen mobility (from Ce or Pr), which helps to reduce carbon. Table 6.9 exemplifies the improved activity benefits from the addition of textural promoter Zr, structural promoter Ce,

TABLE 6.9 Product Yields Illustrating Improvement of Activity after the Addition of Zr, Ce, or both to 10 wt% Ni/Al_2O_3 (O/C = 1.0, S/C = 1.25, 750 °C, GHSV = 4800 h^{-1}); *Reprinted from Cai et al. [138], Copyright (2008), with permission from Elsevier.*

Catalyst	CH_4 Conversion (%)	CO Selectivity (%)	H_2/CO ratio	H_2/CO_x ratio
Ni/Al_2O_3	73	40.3	2.7	1.7
Ni/ZrO_2-Al_2O_3	92	73.9	2.3	2.1
$Ni/CeO_2/Al_2O_3$	93	100	2.3	2.3
Ni/ZrO_2-CeO_2-Al_2O_3	93	67.4	3.3	2.5

and the combination of the two to 10 wt% Ni/Al_2O_3 for the OSR of CH_4 at 750 °C (O/C = 1.0; S/C = 2.5). Both CH_4 conversion and CO selectivity are greatly improved by the addition of the promoters compared with Ni/Al_2O_3. The addition of both Ce and Zr together appeared to greatly improve WGS activity as the H_2/CO ratio is much higher compared with those with only Zr, Ce, or no promoter.

Basic supports Chaudhary et al. [139–141] have investigated alkaline metals as supports for Ni catalysts for various reforming reactions. The basic nature of these materials makes them appealing as supports because of their ability to prevent carbon formation. The studies have found Ni-Mg and Ni-Ca to possess activity for reforming, while Ni supported on Sr or Ba are much less active. In particular, it has been observed that Ni forms complete solid solution with Mg at high calcination temperatures, but not with the other metals. The formation of this solid has been found to be advantageous because, unlike the $NiAl_2O_4$ solid which forms while using Al_2O_3, the Ni-MgO was found to maintain high activity as well as resistance to carbon formation [139,142]. The solid solution prevents the clustering of Ni metal, which promotes carbon growth, by maintaining small well-dispersed Ni particles which are active and accessible to the reactant gases.

Oxygen-conducting supports Other than traditional support materials, researchers have recently investigated some reducible oxide materials with oxygen ion-conducting properties (also known as lattice oxygen mobility) to reduce the carbon deposition. These materials are characterized by their ability to have lattice oxygen ions participate in the reaction, which provides a localized oxygen supply at the surface to improve gasification rates of adsorbed carbon, and limit its accumulation on/near the active meal. Oxygen vacancies formed in the solid during this process may be replenished by the incorporation of oxygen from steam or O_2 in the feed.

The well-characterized ability to store and release oxygen, and redox properties, has led several studies to select CeO_2 as a support material to reduce carbon formation [143,144]. However surface redox cycles for pure CeO_2 are limited to 350–400 °C. Above these temperatures, reducing atmospheres will destroy the morphology of the Ce particles causing pore filling and subsequent surface area reduction [144]. The addition of Zr as a structural promoter has shown to stabilize Ce in the cubic fluorite phase and improve OSC and redox potential of the material at elevated temperatures [145,146]. An optimal ratio exists in terms of OSC and thermal stability depending on the amount of dopant/promoter, and for CeO_2–ZrO_2 mixtures – a 1:1 molar ratio has been identified to be the optimal [146,147].

The effect of oxygen-conducting support on carbon formation for Ni catalysts can be seen in Fig. 6.20. Five catalysts including Ni/Al_2O_3,

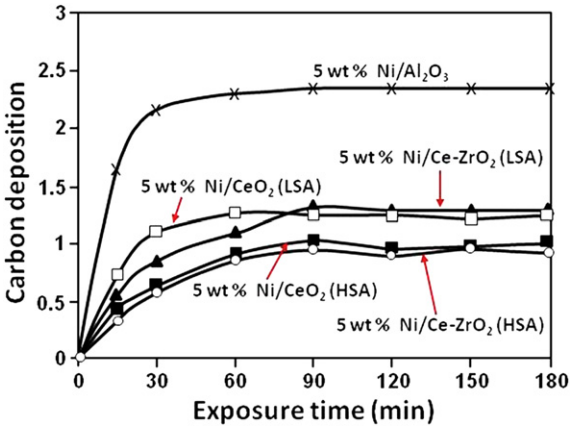

FIGURE 6.20 Effect of support on carbon deposition (mmol g_{cat}^{-1}) after decomposition of 5% CH_4 in H_2 at 900 °C; *Reprinted from Laosiripojana et al. [145], Copyright (2008), with permission from Elsevier.*

low surface area (LSA) Ni/CeO_2 and $Ni/Ce\text{-}ZrO_2$, and HSA Ni/CeO_2 and $Ni/Ce\text{-}ZrO_2$ were exposed to 5% CH_4 in He for increasing amounts of time at 900 °C. The catalysts then underwent a temperature-programmed oxidation to determine the amount (mmol carbon/g_{cat}) of carbon formed [145]. From the plot, two trends are observable. First, all four Ce-containing supports have less carbon at each exposure time compared with the Al_2O_3-supported catalysts, thus illustrating that oxygen conductivity reduces carbon formation. Secondly, surface area has a slight effect on carbon formation probably due to the larger available interface between adsorbed C and oxygen from the support.

6.5.1.1.2. OTHER NON-PRECIOUS METALS

COBALT Studies investigating cobalt-based catalysts for reforming are fewer than Ni. This is likely because Co exhibits a lower turnover frequency for OSR than Ni (see Fig. 6.15) and has a much greater tendency for carbide formation, which is the precursor for whisker carbon [131,148]. Activity loss through oxidation is also much more difficult to overcome using Co as a catalyst because of its higher thermodynamic tendency for oxidation than Ni (see Fig. 6.17). Despite such drawbacks, Co catalysts have been shown to produce high yields of synthesis gas for POX and SR reactions individually. With high yields achievable for these reactions, an active form of cobalt is possible for OSR with the use of the proper support and/or promoters.

One notable support is MgO. MgO-supported Co forms a solid solution under oxidizing conditions, much like Ni, and has been shown to produce CH_4 conversions >90% and H_2 and CO selectivities >94% under CPOX conditions ($O/C = 1$; $T = 850$ °C) for over 100 h [149]. A catalyst with similar composition (24 wt% Co/MgO) would likely be effective under OSR conditions, especially at high oxygen concentrations (near CPOX). The addition of small amounts of noble metals like Pt, Pd, Rh [150], and also Ni, Fe, and Zn [47] have shown improved activity and stability of Co particles over traditional supports like γ-Al_2O_3 or SiO_2 for both SR and CPOX, which would otherwise form an inactive solid solution or be deactivated by oxidation and/or carbon.

IRON AND COPPER Iron and copper are also known to possess reforming activity, but neither is likely to be considered a viable catalyst for the OSR of CH_4. Studies have shown these metals to have much lower activity and selectivity compared with formulations containing directly comparable weight loadings of Ni and Co for either SR [151] or CPOX [152]. The limitations of Fe are likely because of its much greater oxidation potential than the other metals, which makes it difficult to maintain the reduced form in the presence of O_2 and steam during the OSR of CH_4. This is probably the reason Fe favors combustion products over reforming [152]. Carbide formation is also strongly favored and much higher over Fe than Ni and Co [148].

The poor activity of Cu can probably be related to its low activity for CH_4 activation

[93]. Thermal stability is also an issue for Cu particles. The melting point of Cu is roughly 400 °C lower than the other three metals; therefore, its sintering potential is much greater.

6.5.1.2. Noble Metals

Noble metals are often studied as catalysts because of their high intrinsic activity for reforming, and greater resistance toward sintering (high T_{Tam}). They also have a lower susceptibility to form carbon compared with non-noble metal catalysts [153]. An obvious advantage of these metals is their tolerance toward the formation of the destructive whisker carbon that plagues Ni- and Co-based catalysts. Price and availability are, however, limiting factors when using noble metals, and should be considered during catalyst development. The weight loadings required to obtain the desired activity and selectivity are much lower compared with non-noble metals, which may make economics of using noble metals less restrictive, assuming issues with deactivation (mainly carbon) are addressed.

6.5.1.2.1. RHODIUM

Rhodium has been identified as the most active catalyst for the OSR of CH_4 (see Fig. 6.15) and is therefore often considered to be the benchmark case in terms of performance. As Rh is more active for SR than almost all metals in terms of rate and extent of reaction [92,154], its use is advantageous for OSR as reactions involving SR consume a large portion of the catalytic bed, assuming the reaction takes place through the two-step combustion-reforming mechanism mentioned in Section 6.3.1. The high selectivity of Rh to synthesis gas may be correlated to its slightly higher oxygen affinity compared with other noble metals. It is believed this reduces the reaction between surface oxygen and dissociated hydrogen atoms on the surface into hydroxyl radicals, which eventually form water [155], because the activation energy barrier is higher for OH formation over Rh (83.7 kJ/mol) than metals which are more easily reduced, like Pt (10.5 kJ/mol) [131].

The effect of support on activity and selectivity of Rh has been investigated for CPOX [123] and CO_2 reforming [124]. It was found that, in general, Rh had lower conversion and yields of H_2 and CO on reducible oxides like CeO_2, Nb_2O_5, and Ta_2O_5 compared with irreducible oxides Al_2O_3, MgO, and La_2O_3 [123,124]. The lower activity of Rh was speculated to be a result of a partial coverage of Rh particles by the reducible oxides, which promoted the combustion reaction. Meanwhile, Rh has been shown to have a strong interaction with the irreducible oxides surfaces, forming highly active, small, and well-dispersed crystallites [156]. Although the reaction conditions used in these studies may not be directly comparable to OSR, the material properties which affect the catalytic activity of Rh are likely the same for OSR.

The oxygen-conducting materials (OCM), while supports themselves, are often applied to the surface of nonconducting oxides, usually alumina, to help mitigate carbon formation and take advantage of HSA, thermal stability, strong interaction between active metal and support layer. Other components are often added in addition to the OCM that have some promoting benefit, usually to help further improve basicity of the surface to limit carbon formation.

Yuan et al. [147] observed the effects of the sequential addition of 20 wt% $Ce_{0.5}Zr_{0.5}O_2$ alone, and $Ce_{0.5}Zr_{0.5}O_2$ + 2.5 wt% MgO on the activity of a 0.15 wt% Rh/α-Al_2O_3 catalyst during OSR of CH_4 at 800 °C, O/C = 0.92, S/C = 2.0. A direct improvement in both conversion (not shown) and selectivity (see Fig. 6.21) was seen from the addition of each additional component. The increase in catalytic activity and selectivity was likely a result of the intimate contact between Rh and the OCM, which apparently improved its WGS activity, and also the gasification of carbonaceous species

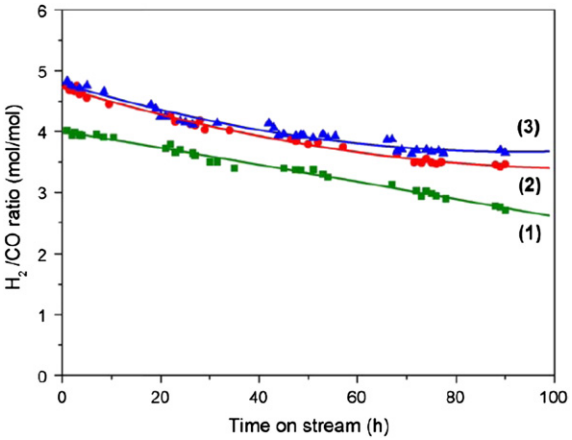

FIGURE 6.21 H_2/CO ratio produced over (1) 0.15 wt% $Rh/\alpha\text{-}Al_2O_3$, (2) 0.15 wt% Rh/20 wt% $Ce_{0.5}Zr_{0.5}O_2/\alpha\text{-}Al_2O_3$, (3) 0.15 wt% Rh/2.5 wt% MgO/20 wt% $Ce_{0.5}Zr_{0.5}O_2/\alpha\text{-}Al_2O_3$ during OSR of CH_4 at 800 °C, O/C = 0.92, S/C = 2.0; *Reprinted from Yuan et al. [147], Copyright (2009), with permission from Elsevier.*

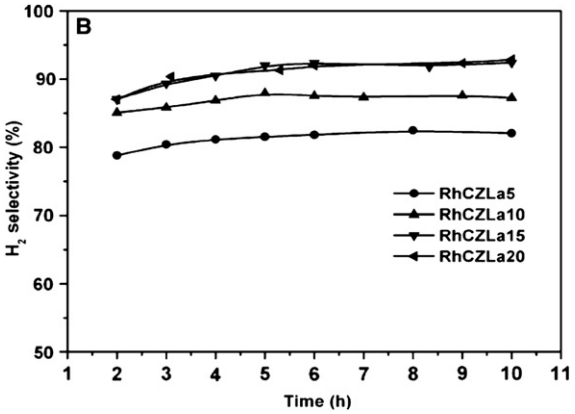

FIGURE 6.22 Effect of La substitution (RhCZLa20; 20 mol% La) on H_2 selectivity for a 0.1 wt% $Rh/Ce_{0.5}Zr_{0.5}O_2$ catalyst during the OSR of CH_4 (O/C = 0.92; S/C = 2.0; 850 °C); *Reprinted from Cao et al. [158], Copyright (2009), with permission from Springer.*

around the active Rh particles. Although not mentioned, deactivation with time on stream for the $Rh/\alpha\text{-}Al_2O_3$ may have been linked to the incorporation of Rh atoms into the spinel structure of the $\alpha\text{-}Al_2O_3$ [157]. The presence of the OCM and MgO may then have also helped maintain activity by stabilizing the Rh particles on the surface. Through further catalyst optimization they found a 0.33 wt% Rh/2.52 wt% MgO/43.2 wt% $Ce_{0.5}Zr_{0.5}O_2$/54.0% cordierite honeycomb catalyst to be continuously active and selective for over 2000 h on pure CH_4, and 500 h on simulated natural gas at 800 °C, O/C = 0.92, S/C = 2.0.

The activity of Rh on reducible supports may be improved through the addition of trivalent rare earth (RE) elements into the structure of the support. Cao et al. [158] tested a series of La-doped (5–15 mol%) 0.1 wt% $Rh/Ce_2Zr_2O_2$ for the OSR of CH_4 (O/C = 0.92; S/C = 2.0; T = 850 °C) and found the presence of La to increased both conversion (from 49 to 60%) and H_2 selectivity (see Fig. 6.22). There appears to be a limit to the benefit of La however, as further addition of La (20 mol%) led to slightly lower conversions and H_2 selectivity. Both Ce and Zr levels were decreased in the support to compensate for La substitution to maintain a molar ratio of 1:1, because this was identified to be the optimal ratio for oxygen storage capacity (OSC) and textural properties. The presence of La is believed to enhance the interaction of Rh with the support surface through the formation of La–Rh interfacial species.

The use of Rh metal in conditions where excess water is needed to promote the WGS shift reaction may be limiting. Rh is known to have lower WGS activity compared with other metals like Pt or Pd [159]. Shown in Fig. 6.23, Rh/MgO is shown to produce higher amounts of CO during CPOX compared with a nominally identical Pt catalyst [160]. However, when steam was introduced into the feed, the amount of CO produced over Rh remained roughly the same as for CPOX conditions, while the amount of CO decreased for Pt due to its higher shift activity. One way to improve WGS activity of Rh is to use a support with high OSC, as noted by Yuan et al. [147] in Fig. 6.21. In a study evaluating a series of trivalent RE-doped

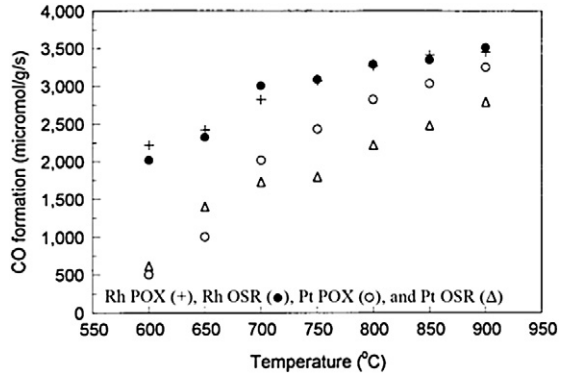

FIGURE 6.23 CO formation rate for 0.5 wt% Rh/MgO and 0.5 wt% Pt/MgO during CPOX (O/C = 1) and OSR conditions (O/C = 0.84, S/C = 0.16, and 550,000 h^{-1}); *Reprinted from Qin et al. [160], Copyright (1996), with permission from Elsevier.*

$Ce_{0.45}Zr_{0.45}RE_{0.1}$ supports for Rh (0.1 wt%), Cao et al. [161] found a correlation between maximum OSC of the support material and highest H_2/CO ratio. La-substituted oxide exhibited both maximum OSC, and H_2/CO ratio.

6.5.1.2.2. OTHER NOBLE METALS

PLATINUM Studies have found Pt-based catalysts to be active and selective for the conversion of CH_4 through OSR into synthesis gas [39,162,163]. Ruiz et al. [39] evaluated the influence of several supports on the CH_4 conversion (selectivity not shown) over 1.5 wt % Pt at 800 °C, O/C = 1.0, and S/C = 0.2 (see Fig. 6.24). As the conditions resembled those for CPOX (i.e., low S/C ratio), deactivation over time on stream was linked to the formation of carbon. The $Ce_{0.75}Zr_{0.25}O_2$ material calcined at either 800 or 1000 °C was able to provide the most stable conversion for Pt likely because of its higher OSC properties, which prevented carbon accumulation. The deactivation of $Ce_{0.5}Zr_{0.5}O_2$ material conflicts with data postulated by Cao et al. [146] earlier. Differences are likely attributed to the synthesis method used to prepare the supports (Cao et al. [146] used urea combustion method, while Ruiz et al. [39] utilized a co-precipitation method), which affects the distribution of the Ce and Zr in the oxide system and also morphological features of the material which influence the OSC.

When Al_2O_3 is the desired support for Pt, either the addition of Ce or Zr has been shown to improve activity and selectivity of Pt/Al_2O_3 to synthesis gas for the OSR of CH_4. During the time shown in Fig. 6.24, deactivation of the

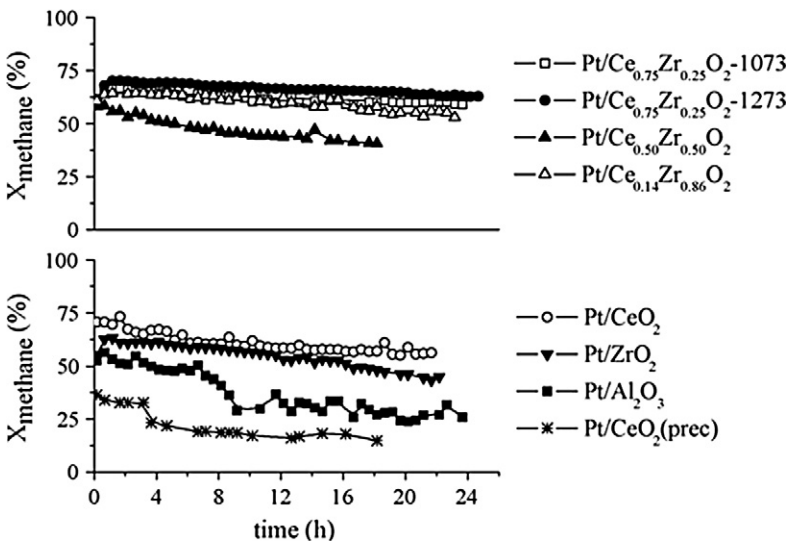

FIGURE 6.24 Comparison of different supports on the activity of 1.5 wt% Pt (S/C = 0.2, O/C = 1.0, WHSV = 260 h^{-1}, and 800 °C); *Reprinted from Ruiz et al. [39], Copyright (2008), with permission from Elsevier.*

catalyst was likely accelerated by the degradation of Al_2O_3 support and sintering of Pt particles. The addition of 12 wt% Ce to the alumina structure hinders the accumulation of carbon on the Pt particles, and promotes stability of the Al_2O_3 support [162]. Also, the interaction of Ce and Pt suppresses the formation of volatile and mobile PtO_2 by improving the reducibility of the metal [162]. Meanwhile the addition of 10 wt% Zr to the surface of Al_2O_3 improves resistance to carbon formation through the interaction of Pt-Zr at the metal support interface [163].

Despite the fact that Pt has the highest rate of CH_4 activation compared with other metals like Rh, Ru, and Ir over similar particle sizes and supports, its selectivity to synthesis gas is often lower than Rh during OSR [164]. This can be attributed to the combined effects of its high selectivity to H_2O and CO_2, a reflection of its high combustion activity [165–167], in the oxidation zone [55,154] and marginal steam reforming activity [92]. The formation of H_2O is suspected to be favored over Pt compared with Rh, because of its lower energy barrier for hydroxyl group formation (10.5 kJ/mol for Pt and 83.7 kJ/mol over Rh).

RUTHENIUM Ru catalysts have shown intrinsic activity equally as high, if not higher than Rh, for both SR [92] and CPOX reactions [160]. Interestingly, however, there is little research on Ru as a catalyst for OSR of CH_4. With its high activity for these reactions, Ru would make an excellent catalyst for the OSR of CH_4 at prices substantially lower than Rh.

Rabe et al. [168] investigated a series of noble metal catalysts for the low-temperature OSR of CH_4 into synthesis gas concentrations that are suitable for gas to liquid (GTL) applications. Lower reaction temperatures provide the advantages of using cheaper materials and reduced operating costs of the GTL process. Reforming studies were performed at 550 and 650 °C (see Table 6.10) over supported Pt, Rh, and Ru catalysts. The weight loading of active metals and support materials was not held constant, which prevents a direct comparison of activity between metals. In general, however,

TABLE 6.10 Comparison of Conversion, Yields and M Factors Produced over Pt, Rh, and Ru Catalysts During the Low Temperature OSR of CH_4 (O/C = 0.85, S/C = 2.9, and 650 °C) [168]

Catalyst	T_{out}* (°C)	X_{CH_4} (%)	Y_{CO}† (%)	Y_{CO_2}†(%)	Y_{H_2}‡(%)	M§
0.3 wt% Pt/Al_2O_3	635	60.9	15.8	44.6	42.0	1.35
1 wt% Pt/Al_2O_3	n.d.¶	62.2	18.6	43.7	43.9	1.41
5 wt% Ru/Al_2O_3	643	84.5	25.6	59.0	74.0	1.92
5 wt% Ru/5 wt% $Ce\text{-}Al_2O_3$	638	79.0	23.2	56.2	62.9	1.67
1 wt% Rh/5 wt% $Ce\text{-}ZrO_2$	639	83.8	22.5	56.3	71.0	2.00
Equilibrium	639	85.6	27.5	58.5	77.2	2.01

* *T_{out} measured at exit of bed.*

†*Yield CO or CO_2;* $Yco_x = \dfrac{CO_x out}{CH_4 in}$

‡*Yield H_2;* $Y_{H_2} = \dfrac{H_2 out}{2CH_4 in}$

§M *factor;* $M = \dfrac{(H_2 - CO_2)}{(CO - CO_2)}$; *Ideally 2.1 for Fischer–Tropsch synthesis.*

¶*n.d. not detected.*

Ru catalysts were found to be acceptable for GTL applications, along with the Rh catalysts, when reaction temperature was 650 °C. Both produced yields close to that predicted by equilibrium, which resulted in an M factor ($M = (H_2 - CO_2)/(CO - CO_2)$) nearly suitable for GTL applications (2.1). On the other hand, the Pt catalysts were found to have lower conversions, and were more active and selective for combustion products, which is consistent with results mentioned earlier.

Another study by the same group [169] evaluated the effects of synthesis method (sol-gel vs. impregnation) on activity and sulfur tolerance of the 5 wt% Ru/γ-Al_2O_3, and 1 wt% Rh/5 wt% Ce-doped ZrO_2 (5Ce-ZrO_2) catalysts during the low-temperature OSR of CH_4 (550 °C; O/C = 1.0; S/C = 2.0) with and without sulfur (as thiophene) in the feed. Again, given the different active metal weight loadings and support materials used, a direct comparison between metals is complicated. Little effect of synthesis method was observed in the absence of sulfur, as all catalysts proved to be highly active and selective to synthesis gas at the low reaction temperatures for over 50 h time on stream (see Table 6.11). During sulfur studies, the Rh-based catalysts were rapidly deactivated by both low (10 ppm) and high (400 ppm) levels of sulfur regardless of synthesis method. Interestingly, the sulfur (either low or high amounts) was found to poison the activity of Rh, not through the formation of irreversible sulfides, but by increasing its potential to be oxidized into the less-active Rh_2O_3. Ru catalysts, meanwhile, proved to be more sulfur tolerant in general than Rh at the lower levels of sulfur. The best catalyst produced by the modified sol-gel method had a 3% drop in conversion and an 8% drop in H_2 yield. The results appear to suggest highly active Ru sites undergo a passivation, but there is no irreversible accumulation which deactivates activity. Increasing the sulfur content to 400 ppm resulted in complete deactivation for all Ru catalyst through the formation of irreversible Ru sulfides.

It should be noted that the effects of sulfur on catalytic activity are generally more pronounced

TABLE 6.11 Conversions and Yields During Low Temperature OSR of CH_4 (O/C = 1.0, S/C = 2.0, and 550 °C) With and Without Sulfur for 5 wt% Ru/γ-Al_2O_3, and 1 wt% Rh/5 wt% Ce doped ZrO_2 Synthesized by Wetness Impregnation (w.i.) and sol-gel (s.g.) methods. Data Points are Taken after 50 h TOS for Sulfur Free and 10 ppm Sulfur Experiments and at 30 h TOS for 400 ppm Experiments [169]

Catalyst	Thiophene (ppm)	CH_4 Conversion (%)	H_2O Conversion (%)	O_2 Conversion (%)	H_2 Yield	CO Yield	CO_2 Yield
Equilibrium		76.2	17.7	100.0	0.62	0.18	0.57
5 wt%	0	59.4	9.3	100.0	0.39	0.10	0.48
Ru/Al_2O_3	10	51.5	−4.0	100.0	0.26	0.11	0.39
w.i.	400	2.6	−16.7	2.1	0.0	0.0	0.04
5 wt%	0	63.4	10.8	100.0	0.42	0.11	0.50
Ru/Al_2O_3	10	60.3	6.0	100.0	0.39	0.10	0.48
s.g.	400	17.1	−9.0	100.0	0.05	0.02	0.18
1 wt%	0	57.1	8.4	100.0	0.31	0.08	0.44
Rh/5 wt%	10	33.9	−7.9	100.0	0.09	0.01	0.33
Ce-ZrO_2 w.i.	400	27.2	−9.0	100.0	0.06	0.01	0.31
1 wt%	0	57.5	9.2	100.0	0.34	0.09	0.47
Rh/5 wt%	10	28.9	−8.2	100.0	0.07	0.01	0.31
Ce-ZrO_2 s.g.	400	22.8	−9.0	100.0	0.04	0.01	0.23

at lower temperatures because Gibbs free energy for metal-sulfide formation is highly favorable [29]. Should a reformate stream be desired from a low sulfur-containing fuel, the study by Requies et al. [169] shows Ru-based catalysts offer sulfur tolerance at lower temperatures. However, in general sulfur poisoning can be reduced by increasing the reaction temperature to around 800 °C, so that irreversible metal-sulfide formation becomes less thermodynamically favorable.

6.5.2. C_2–C_6 Hydrocarbons

6.5.2.1. Catalysts

Liquefied petroleum gas (LPG) and other heating fuels are also viable sources of H_2. These fuels have a higher caloric value than natural gas, and can be liquefied at ambient temperature which allows for convenient storage and transportation. Relative to components in NG, these fuels are more reactive due to the larger carbon number. However, for their conversion into synthesis gas, scission of multiple C–C bonds is required. During this process highly reactive carbon radicals are formed, which increases the propensity for carbon formation.

Other than carbon formation, the catalytic reforming of fuels C_2–C_6 presents no new challenges compared with CH_4 reforming. The main active catalysts for the conversion of these fuels are similar (Ni, Rh, Pt, and Pd), as are the strategies for improving activity and resistance to carbon formation with supports, promoters, and/or other active components (see Table 6.12). Therefore, the discussion regarding the conversion of these fuels into synthesis gas will be brief.

6.5.2.1.1. HYDROTALCITES

In addition to the catalysts listed in Table 6.12, researchers have also applied hydrotalcite-type mixed oxides as catalyst for the OSR of propane, as well as other fuels like CH_4. Hydrotalcites (HT) have the general formula $[Mg^{2+}_{1-x}Al^{3+}_{x}(OH)_2]^{x+}(CO_3)\cdot mH_2O$ [177]. The HT structure can be visualized as net positive sheets of Mg-Al-OH brucite layers stacked between an interlayer containing the CO_3^{2-} anions and water. Upon calcination of the HT

TABLE 6.12 Catalysts From Literature Studies Which were Used for OSR of Lighter Gaseous Hydrocarbons Besides CH_4

Catalyst	Weight% active metal	Fuel	Reference
$Ni/LaAlO_3$ $Ni\text{-}Ce/LaAlO_3$	15.0	Propane	[170]
Ni/MgO Co/MgO Cu/MgO Fe/MgO	20.0	Butane	[50]
Rh/Al_2O_3	0.01	Propane	[171]
Rh/Al_2O_3/Fecralloy	n.g.*	Propane	[172]
$Ru/La_{0.75}Sr_{0.25}Cr_{0.5}Mn_{0.5}O_{3-\delta}$	5.0	Propane	[173]
$Pd/CeO_2/Al_2O_3$	1.0	Propane	[174]
Pt/CeO_2	1.0	Propane	[175]
Pt/CeO_2	1.13	Propane	[176]

* *n.g. = not given*

precursor, a homogeneous mixed oxide structure is obtained. The temperature treatment by calcination is reversible, as the oxide materials show a unique ability to reconstruct the original HT structure when rehydrated [177].

Chemical and morphological features, including HSA and basic surface properties, have attracted researchers to use HT-derived oxide materials as catalysts for reforming [178]. Catalysts are prepared from these HT precursors by substitution, either partial or total, of Mg and/or Al by both active metals and other non-active promoting metals. The lattice of the mixed oxide structure provides a framework for the homogenous dispersion of the catalytic metal, which leads to small, stabilized, and highly active metal particles.

The advantages of dispersion and sintering control with HTs at reaction temperatures have provided an alternative to supported Ni-based catalysts, which are known to readily sinter and form carbon. Figure 6.25 illustrates the activity benefits of dispersing Ni (15 wt%) into the MgAl-HT-derived compound versus a similar amount supported on γ-Al_2O_3 for the OSR of propane (O/C = 1.35; S/C = 3.0) [178]. It was observed that the smaller and more dispersed Ni crystals in the Ni/MgAl compound have a much higher activity, as conversion of propane reaches 100% at a temperature 200 °C lower than the γ-Al_2O_3 supported catalyst. The Ni/MgAl is also more selective toward H_2 over the temperature range tested 400−700 °C (not shown). Improvements in activity were attributed to the improved thermal stability of the dispersed Ni and also lower amount of deposited carbon.

Activity of Ni substituted into the HT structure is not completely resistant to deactivation, and has still been shown to be oxidized and have its activity reduced by carbon under reaction conditions [178,179]. Much like the supported Ni catalyst, small amounts of noble metals (Pt, Pd, or Ru) can be doped into the structure with Ni, and have been shown to improve activity and reduce carbon formation [178,180]. Noble metals themselves can also be substituted as the active form, as HT-derived mixed oxides can accommodate a wide variety of substitutions [181].

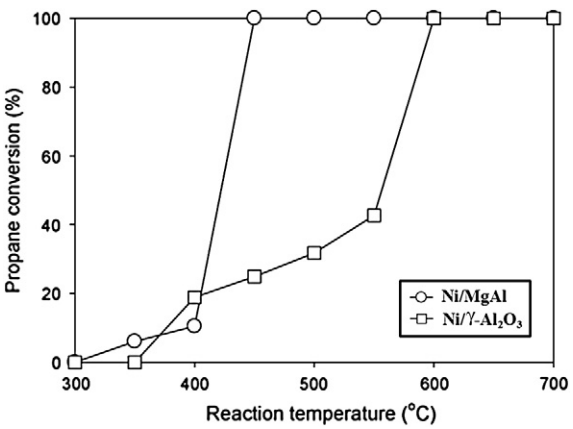

FIGURE 6.25 Comparison of activity for OSR of propane (O/C = 1.35, S/C = 3.0, 9600 ml (STP) g_{cat}^{-1} h^{-1}) for Ni/MgAl-hydrotalcite like oxide and traditional Ni/γ-Al_2O_3; *Reprinted from Lee et al. [178], Copyright (2009), with permission from Elsevier.*

6.5.3. Transportation Fuels

Heavier liquid hydrocarbon fuels, like gasoline and diesel, have higher gravimetric and volumetric H_2 densities compared with lighter gaseous hydrocarbon fuels in a convenient, transportable form. OSR of these fuels is therefore desirable in transportation applications where H_2 storage is currently limited and cannot adequately meet the demands of the fuel cell load. Compared to lighter molecular weight hydrocarbons, gasoline and diesel are more challenging to reform. Rates of carbon formation are much higher since longer chain alkanes will undergo pyrolysis upon vaporization. The carbon chains linked to the C-radicals formed during the reaction will readily deposit onto the catalyst surface and easily polymerize into graphitic carbon. The presence of aromatics and

polyaromatic compounds, which are not found in other fuels, further contributes to carbon formation as they are not only less reactive, but also chemically similar to graphitic carbon.

Sulfur compounds are also commonly found in these fuels at higher levels than other fuels. Levels of sulfur can reach up to 3000 ppmw for military fuels, however, most fuels like pump gasoline and diesel will have substantially less (9–15 ppmw). For fuels containing sulfur, reforming temperatures must be kept high to reduce the irreversible formation of metal sulfides. At the expense of obtaining maximum H_2 yields, which occurs around 700 °C (see Fig. 6.2), temperatures for reforming are usually maintained above 800 °C to minimize sulfur poisoning, although higher operating temperatures also reduces carbon formation. Researchers from Argonne National Lab (ANL) [182] show the performance benefits, in terms of reforming efficiency (likely defined by HHV of H_2/HHV fuel, but not mentioned), for increasing reaction temperature for OSR of dodecane (O/C = 1.0; S/C = 1.0) from 700 to 800 °C (Fig. 6.26). Catalyst tests were performed over a Ru-substituted perovskite catalyst. Figure 6.26 shows three sequential steps in their catalyst test: (1) establish baseline activity of OSR of *n*-dodecane, (2) examine effect of adding 50 ppmw sulfur for an extended time, and (3) remove sulfur to establish recovery to baseline. It can be seen that the efficiency of the catalyst in each part of the test was higher at 800 °C, especially in the presence of sulfur. The recovery was also greater indicating the effects of sulfur were reduced at the elevated temperature.

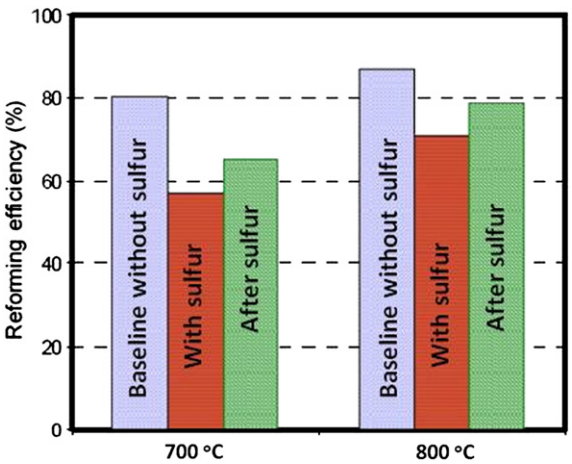

FIGURE 6.26 Effect of increasing operating temperature on reforming efficiency of a Ru-substituted perovskite ($LaCr_{0.95}Ru_{0.05}O_3$) in the presence of sulfur (O/C = 1.0, S/C = 1.0, and 100,000 h^{-1}). *Reprinted from Liu et al. [182], Copyright (2004), with permission from authors.*

6.5.3.1. *Nickel-Based Catalysts*

6.5.3.1.1. ALUMINA

Ni-based catalysts studied for the OSR of transportation fuels primarily consist of a variation of Ni/Al_2O_3, which is used for commercial CH_4 SR applications. These are considered benchmark catalysts for reforming due to their widespread use and well-characterized physical and chemical properties, as well as their low cost.

When used as a catalyst for OSR of larger MW hydrocarbon fuels, the Ni-based SR catalysts suffer rapid deactivation from carbon formation, sulfur poisoning, and thermal degradation. Deactivation of these catalysts is likely due to the large clusters of Ni on the surface. Despite the presence of promoters, these clusters can be easily poisoned by carbon and sulfur. Moon et al. [183] performed an initial screening study on a commercial Ni-based catalyst ($Ni\text{-}SiO_2\text{-}MgAl_2O_4$) to determine the effects of gasoline constituents (either aromatics or sulfur) on carbon formation. Based on the catalyst used, it was established that the accumulation of carbon could be reduced at temperatures >640 °C. Meanwhile, the presence of sulfur was found to not only promote carbon formation, but also deactivate the catalyst through irreversible sulfur poisoning. Consistent with the work by Liu et al. [182], it was recommended that an elevated operating temperature (>770 °C) was needed to minimize the effects of sulfur.

Continuing their work on the development of carbon and sulfur tolerant Ni-based catalysts, Moon and coworkers [184,185] evaluated numerous supported transition metal catalyst formulations for the OSR of isooctane with and without sulfur. The addition of small amounts of either Fe, Co, or Mo (2.94 wt%) to Ni (11.76 wt%)/MgO/Al_2O_3 improved H_2 yields compared with a 14.7 wt% $Ni/MgO/Al_2O_3$ catalyst, possibly by enhancing the WGS reaction [184]. Promoted catalysts also showed tolerance to small levels of sulfur in the feed. The $Ni/Fe/MgO/Al_2O_3$ catalyst produced near-equilibrium amounts of H_2 for over 700 h during OSR of isooctane (700 °C; O/C = 1; S/C = 3) with less than 5 ppmw sulfur [184]. In the presence of higher levels of sulfur (100 ppmw), the Fe-promoted Ni catalyst had a slower rate of deactivation compared with the commercial catalyst ($Ni-SiO_2-MgAl_2O_4$) when tested at the same conditions (700 °C; O/C = 1; S/C = 3) for 25 h (see Fig. 6.27)

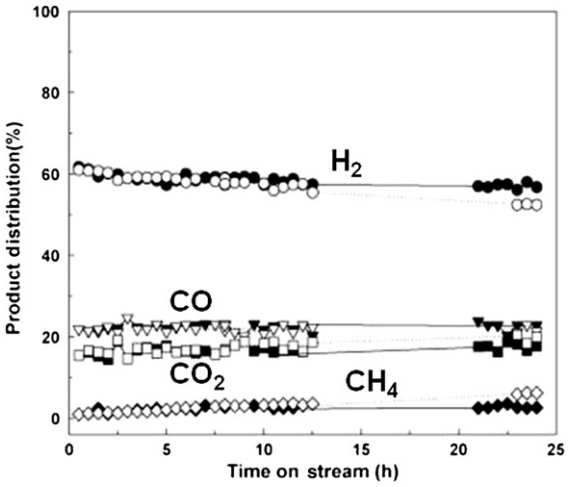

FIGURE 6.27 Activity test of commercial CH_4-reforming catalyst and 2.94 wt% Fe/11.76 wt% $Ni/MgO/Al_2O_3$ catalyst for OSR of isooctane containing 100 ppmw S (O/C = 1, S/C = 3, 700 °C and 8776 h^{-1}); shaded symbols: Fe-promoted catalyst and open symbols: commercial catalyst; *Reprinted from Kim et al. [184], Copyright (2008), with permission from Elsevier.*

[183,184]. Activity loss could likely be attributed to morphological changes on the catalysts which were more pronounced for the commercial catalyst. Increasing levels of sulfur were found to accelerate the BET surface area loss, as well as active metal surface area reduction, even in the Fe-promoted Ni metal catalysts. High levels of sulfur promoted severe carbon formation on each catalyst. Despite showing more stable activity, the Fe-promoted Ni catalyst had 20 wt% carbon formed after the 25-h time on stream [183,184]. While this value was lower than the commercial catalyst, the amount is still limiting, and given sufficient time would eventually deactivate the catalyst completely.

6.5.3.1.2. OXYGEN-CONDUCTING SUPPORTS

Krumpelt et al. [6] from ANL developed a series of new reforming catalysts using concepts of material properties from solid oxide fuel cell-based technologies for supports. Commonly used transition metals were supported on oxygen-conducting substrates such as Ce, Zr, or $LaGaO_3$ doped with small amounts of non-reducible oxides (Gd, Sm, or Ze) for the OSR of i-C_8 (O/C = 0.46 and S/C = 1.14). Although specific weight loadings for each metal were not provided, the supported non-precious metals were shown to have comparably activity, in terms of conversion, to noble metals at temperatures above 700 °C. However, for most catalysts, the selectivity to synthesis gas was much lower than the precious metals, which generally precludes their use for reforming. Their results, shown in Fig. 6.28, confirm Ni to be the most active and selective non-precious metal. Co also shows favorable activity and selectivity, but is again lower than Ni at all conditions tested. Activity improvements are believed to be a result of an interaction between the metal and oxygen vacancies in the support, which provide an oxygen supply to the metal-reducing carbon formation around the active metal.

Schwank's group from the University of Michigan have investigated the interaction

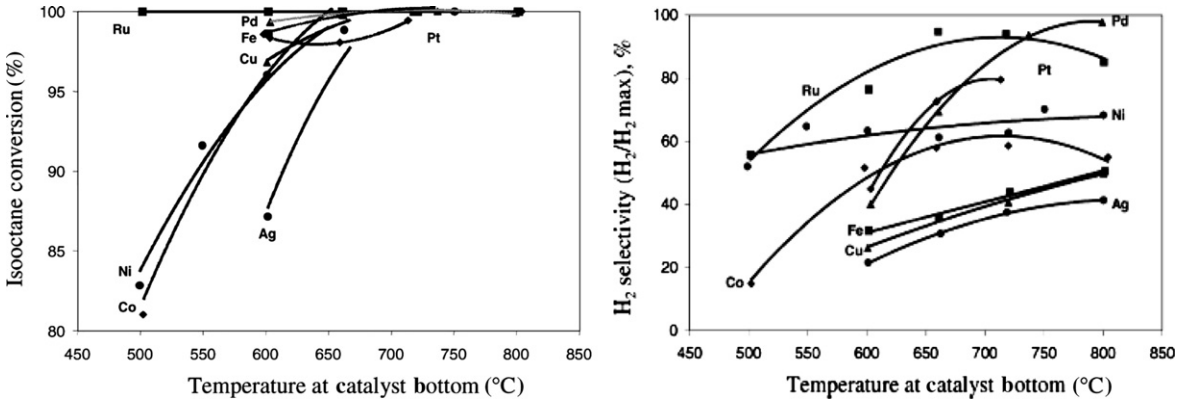

FIGURE 6.28 Conversion and H_2 selectivity as a function of temperature for the OSR of i-C_8 (O/C = 0.46, S/C = 1.14, and 3000 h^{-1}) over various transition metals supported on Sm-Gd-doped ceria; *Reprinted from Krumpelt et al. [6], Copyright (2002), with permission from Elsevier.*

between Ni and $Ce_{0.75}Zr_{0.25}O_2$ (CZO) on activity and carbon formation for the OSR of gasoline and diesel surrogates. High conversions and selectivities to reforming products have been observed over various forms (either powder or foam) and weight loadings of Ni [186,187]. Despite the oxygen-conducting properties of the support, carbon formation, especially variations of that with a filament nature, was still observed to be a major hindrance for Ni during reaction, even at weight loadings as low as 5 wt % [98,188,189]. OSR experiments on engineered foam catalysts (23 wt% CZO/cordierite) containing Ni loadings between 1 and 16 wt% suggest a weight loading of 2 wt% was a compromise between optimal synthesis gas yields and carbon formation [98,186]. The formation of filament carbon was found to require a critical particle size for growth and a minimum number of Ni atoms per unit support area [189]. They determined that by maintaining Ni particles below 26 nm during reaction, carbon formation over Ni/CZO could be minimized [98].

PEROVSKITES To avoid the thermal degradation (sintering) and corresponding deactivation by carbon and sulfur of supported metals, researchers have employed mixed-metal oxides containing Ni or Co to improve size control of active metal particles during the OSR of heavier hydrocarbons [190–194]. Perovskite-type materials have been widely studied as anode and cathode materials for solid oxide fuel cells, and the same properties utilized for these applications are advantageous for reforming: thermal stability, OSC, and oxygen-ion mobility. Perovskites have the general formula ABO_3 where A is a trivalent lanthanide series element, and B is a trivalent transition metal. In general, the element in the A-site provides thermal stability and B-site is responsible for catalytic activity.

Both the A-site and the B-site in the perovskite structure can be doped with other elements to improve catalyst stability and performance giving the general formula $A_{1-x}A'_xB_{1-y}B'_yO_{3-z}$. The partial substitution of the A-site element with one of a different valence has been shown to create structural defects in the lattice, which may improve oxygen mobility, and help reduce carbon formation. The acid-base nature of the dopant in the A-site may also play a role in limiting carbon formation. Alkaline earth metals are often used as A-site dopants for perovskites, as they provide improved Lewis basicity, a property linked to suppression of carbon [193,195], and oxygen vacancies due to their lower valence.

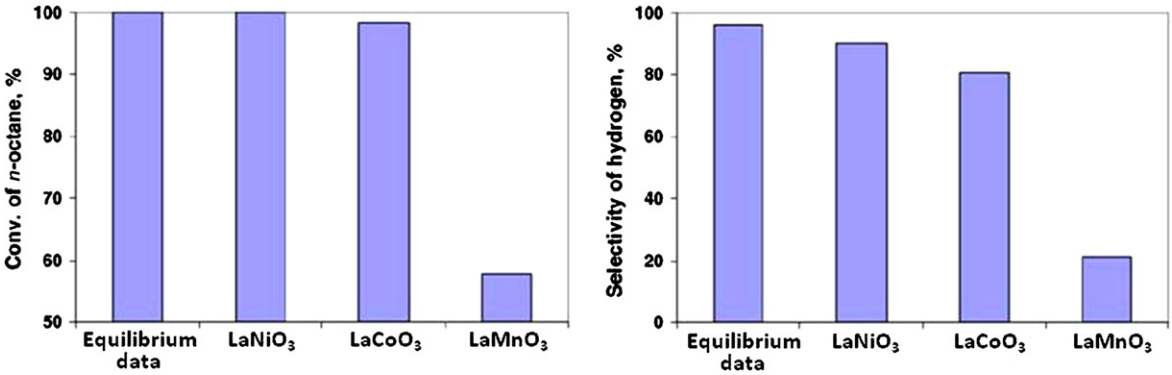

FIGURE 6.29 Isooctane conversion and H_2 selectivity of undoped perovskite materials (O/C = 0.76, S/C = 2.0, 650 °C, and 8000 h^{-1}); *Reprinted from Qi et al. [194], Copyright (2005), with permission from Elsevier.*

As shown in Fig. 6.29, undoped $LaNiO_3$ and $LaCoO_3$ perovskites were found to produce near-equilibrium conversion and selectivity of H_2 during OSR of i-C_8 at 650 °C [194]. However, these materials were not structurally stable in the OSR atmospheres and both catalysts were reduced under the reaction conditions and decomposed into Ni/NiO or Co/CoO and La_2O_3, which are essentially supported metal catalysts [191,193]. While high yields of H_2 were produced over these catalysts, the benefits of dispersion of the perovskites diminished and the metal particles were susceptible to carbon formation and sulfur poisoning.

Mawdsley et al. [193] found that the structural stability of perovskite materials could be improved by the substitution of a majority of Ni or Co with less active, but more stable metals (Fe, Cr, and Mn) with minimal decrease in H_2 yield for OSR of i-C_8 at 700 °C. Cr was shown to be the best in terms of H_2 yield and conversion. However, when these catalysts ($LaM_{0.9}Ni_{0.1}O_3$) were then further substituted with Sr in the A-site and tested for activity in the OSR of i-C_8 with various levels of sulfur, all were

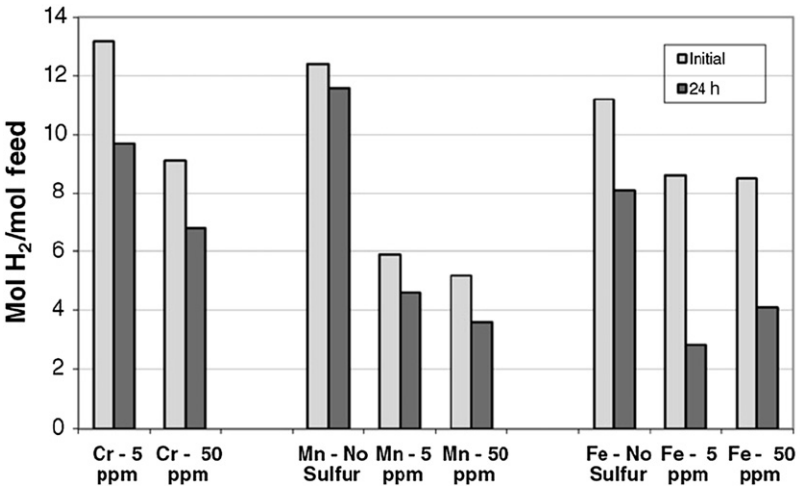

FIGURE 6.30 The effect of sulfur (5 and 50 ppmw) on the OSR of i-C8 gasoline surrogate fuel. ($La_{0.8}Sr_{0.2}Cr_{0.9}Ni_{0.1}O_3$, $La_{0.8}Sr_{0.2}Mn_{0.9}Ni_{0.1}O_3$, and $La_{0.8}Sr_{0.2}Fe_{0.9}Ni_{0.1}O_3$); (O/C = 0.9, S/C = 1.6, 700 °C, and 25,000 h^{-1}); *Reprinted from Mawdsley et al. [193], Copyright (2008), with permission from Elsevier.*

shown to have a low tolerance to sulfur, even levels as low as ~5ppmw. Of their compositions tested the $La_{0.8}Sr_{0.2}Cr_{0.9}Ni_{0.1}O_3$ had the highest sulfur tolerance (Fig. 6.30). SEM images showed existence of whisker carbon on the surface of both $La_{0.8}Sr_{0.2}Fe_{0.9}Ni_{0.1}O_3$ and $La_{0.8}Sr_{0.2}Cr_{0.9}Ni_{0.1}O_3$ catalysts, suggesting that Ni metal still enriched the surface and formed clusters large enough to promote this type of carbon. In light of these results, it is likely that deactivation is due to the combination of both sulfur poisoning and carbon formation.

The addition of Ce into the A-site of the perovskite structure has been shown to improve catalyst activity. Ce is believed to promote localized oxygen transfer from the bulk to the active metal and help reduce the rate of carbon formation. Despite improved oxygen mobility, Ce was found to have limited solubility in the perovskite lattice. According to Qi et al. [194] when the Ce substitution level for a $La_{1-x}Ce_xMeO_3$ catalyst (Me = Ni, Co, Fe, etc.) exceeds $x > 0.05$, segregation of both Ce and Me will occur. They found yields of H_2 and CO to increase up to Ce substitution level of $x = 0.2$, but decreased upon further addition. At substitution level of $x = 0.5$ no perovskite phase was observed at all and yields were lowest (see Table 6.13). Erri et al. [190] found that while some Ce segregation was observed, its substitution significantly improved carbon resistance compared with perovskites without Ce during the OSR of a JP-8 surrogate fuel (Table 6.14). Although the Ce-substituted perovskite may have greater carbon resistance, little benefit in terms of sulfur tolerance is obtained. Qi et al. [194] found sulfur concentrations higher than 5 ppmw would severely deactivate the Ce-containing perovskite catalysts.

To improve sulfur tolerance of perovskites, Dinka and Mukasyan [196] investigated the substitution of 2 wt% non-noble metal (Me = K, Na, Li, Cs, Co, Mo) or noble metal (Me = Pt, Pd, Ru, Re) dopant into the structure of a $La_{0.6}Ce_{0.4}$ $Fe_{0.8-z}Ni_{0.2}Me_zO_3$ perovskite. All dopants led to an increase in conversion and H_2 content compared with the catalyst with no additive for OSR of a JP-8 surrogate containing 50 ppmw sulfur (800 °C; O/C = 0.7, S/C = 3, and GHSV = 130,000 h^{-1}). Interestingly, almost all non-noble metals had undetectable levels of carbon during this reaction. However, the noble metals showed considerable carbon formation, with the exception of Ru.

Sulfur and carbon tolerance of alkali metals may be explained by a modification of the electronic properties of the metal by improving surface basicity and electron donor properties [197], which may hinder adsorption of electron-rich C and S molecules through steric effects.

TABLE 6.13 Effect of Partial Substitution of La with Ce on Perovskite ($La_{1-x}Ce_xNiO_3$) Activity (O/C = 0.76, S/C = 2.0, 800 °C, and 8000 h^{-1}) [194]

	Yield of (CO + H_2), mol/mol C		*n*-Octane conv. (%)	
x	Initial	8 h	Initial	8 h
0	2.34	2.20	100	98
0.1	2.30	2.30	100	100
0.2	2.36	2.36	100	100
0.5	2.12	2.12	98	98

TABLE 6.14 Effect of Ce Addition on Carbon Formation on Perovskite Catalysts after OSR of JP-8 Surrogate (O/C = 0.75, S/C = 3.0, 650 °C, WHSV = 130,000 h^{-1}) [190]

Catalyst	Carbon (wt%)
$LaFe_{0.8}Ni_{0.2}O_3$	0.6
$LaFe_{0.6}Ni_{0.4}O_3$	0.5
$LaFe_{0.4}Ni_{0.6}O_3$	1.8
$La_{0.6}Ce_{0.4}Fe_{0.8}Ni_{0.2}O_3$	0.1
$La_{0.6}Ce_{0.4}Fe_{0.6}Ni_{0.4}O_3$	0.2
$La_{0.6}Ce_{0.4}Fe_{0.4}Ni_{0.6}O_3$	0.1

Large amounts of carbon formation on noble metals Pt, Pd, and Re may be a result of their segregation to the surface and forming metal clusters, which are active for the decomposition of hydrocarbons but also large enough to easily accumulate carbon and be deactivated by sulfur. Without further characterization it is not clear why Ru has higher resistance to carbon formation. However, Ru may remain well dispersed at the surface in clusters small enough to not be deactivated by carbon and sulfur. The presence of Ru may also improve the stability of the perovskite by hindering the diffusion of oxygen from the lattice while under reducing atmospheres [191]. Further testing of perovskite $La_{0.6}Ce_{0.4}Fe_{0.8-z}Ni_{0.2}Me_zO_3$ catalysts with optimized Ni loading doped with Ru (1 wt%) or K (2 wt%) has shown these materials to exhibit tolerance of sulfur levels up to 220 ppmw during OSR of a JP-8 surrogate fuel as shown in Fig. 6.31.

6.5.3.2. *Noble Metals*

6.5.3.2.1. RHODIUM

Catalyst development efforts at ANL determined Rh metal to be the most active and selective catalyst for the OSR of higher hydrocarbons [198,199]. A Rh catalyst supported onto an oxygen-conducting oxide, gadolinium-doped ceria (GDC), was found to be more active than corresponding Ni or Pt catalyst on the same support, and had product yields close to equilibrium (see Fig. 6.32) [198]. Their results are consistent with those obtained by Ayabe et al. [13] shown in Fig. 6.15, suggesting the activity of metals for OSR of higher hydrocarbons may also follow similar trends which were observed for OSR of CH_4 and steam reforming.

When selecting a substrate carrier for a Rh catalyst, dispersion and reducibility of the metal must be considered. Ferrandon et al. [133] evaluated five supports, Gd-CeO_2, Y-ZrO_2, γ-Al_2O_3, La-Al_2O_3, and $CaAl_{12}O_{19}$ each containing 2 wt% Rh, for the OSR of isobutane. Isobutane was selected as a surrogate to represent the C_4 compounds formed during the cracking of isooctane at the bed entrance. It was found that the order of activity, dispersion, and reducibility all followed the ranking Rh/La-Al_2O_3 > Rh/Y-ZrO_2 > Rh/Gd-CeO_2 > Rh/γ-Al_2O_3 > Rh/$CaAl_{12}O_{19}$ suggesting these properties may be useful for evaluating a support material. Their

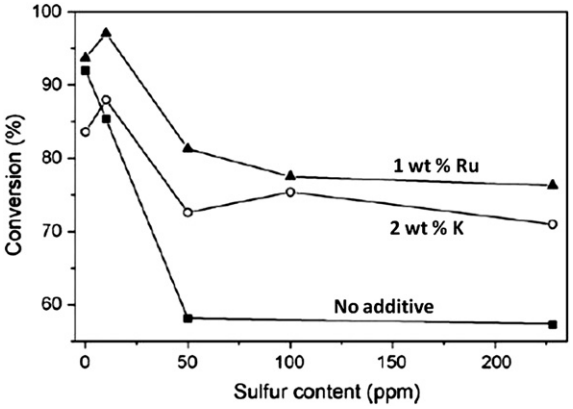

FIGURE 6.31 Sulfur tolerance of modified perovskite catalysts during OSR of JP-8 surrogate fuel. Catalyst is $La_{0.6}Ce_{0.4}Fe_{0.8}Ni_{0.2}O_3$ modified with either 2 wt% K or 1 wt % Ru (O/C = 0.7, S/C = 3.0, 800 °C, and 130,000 h^{-1}); *Reprinted from Dinka and Mukasyan [196], Copyright (2007), with permission from Elsevier.*

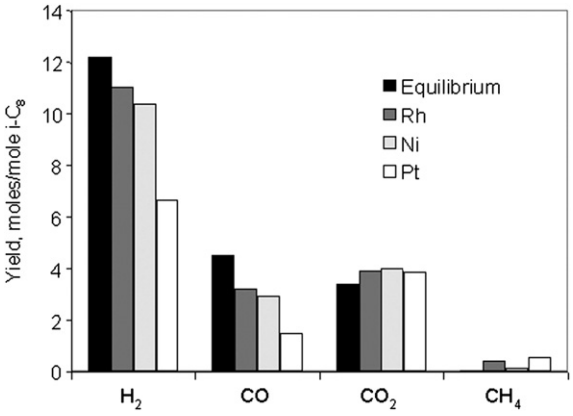

FIGURE 6.32 Yields of H_2, CO, CO_2, and CH_4 produced over Rh-, Pt-, or Ni-CGO supported on a cordierite monolith during OSR of i-C_8 (O/C = 1.0, S/C = 1.2, 700 °C, and 11,000 h^{-1}); *Reprinted from Krause et al. [198], Copyright (2002), with permission from ANL.*

results also concluded that the supports only served to disperse the Rh and did not play a role in the reaction.

Rh on a calcium-impregnated alumina support (0.5 wt% Rh on 15 wt% calcium, balance alumina) was also found to limit carbon formation from OSR of No. 2 fuel oil at a low O/C ratio of 0.72 [200,201]. Therefore, pyrolytic carbon formation, which occurs at high temperatures, can therefore also be minimized. Greater than 98% conversion of No. 2 fuel oil was obtained at an O/C ratio of 0.72.

Wieland et al. [202] observed that a small amount of Pt metal present in the Rh-based catalyst could significantly improve the catalyst activity for OSR of gasoline range fuels. They claimed that the role of Pt is to enhance oxidation activity, whereas Rh provides high SR activity. The Rh-Pt/alumina catalyst used in the study was supported on monolithic honeycombs and had a Rh:Pt ratio of 3:10 by weight. The geometry (metal monolith, ceramic monolith, or ceramic foam) of the support did not affect the product composition [203].

The differences in reactions at different reactor position was studied by Springmann et al. [204], who reported product compositions for OSR of model compounds as a function of reactor length in a metal monolith coated with a proprietary noble metal containing Rh. As expected, the oxidation reactions take place at the reactor inlet, followed by the SR, shift, and methanation reactions. Figure 6.33 shows the product concentration profiles for a 1-hexene feed, which are typical results for all the fuels tested. These results show that steam, formed from the oxidation reactions, reaches a maximum shortly after the reactor inlet, after which it is consumed in shift and reforming reactions. This corresponds to the combustion-reforming mechanism described in Section 6.3.1. H_2, CO and CO_2 concentrations increase with reactor length and temperature. In this reactor, shift equilibrium is not reached, and the increase in CO with distance from the inlet is the net result of the shift and SR reactions.

The use of Rh supported onto washcoated alumina monoliths has attracted interest for OSR of higher hydrocarbons [205,206]. Reyes

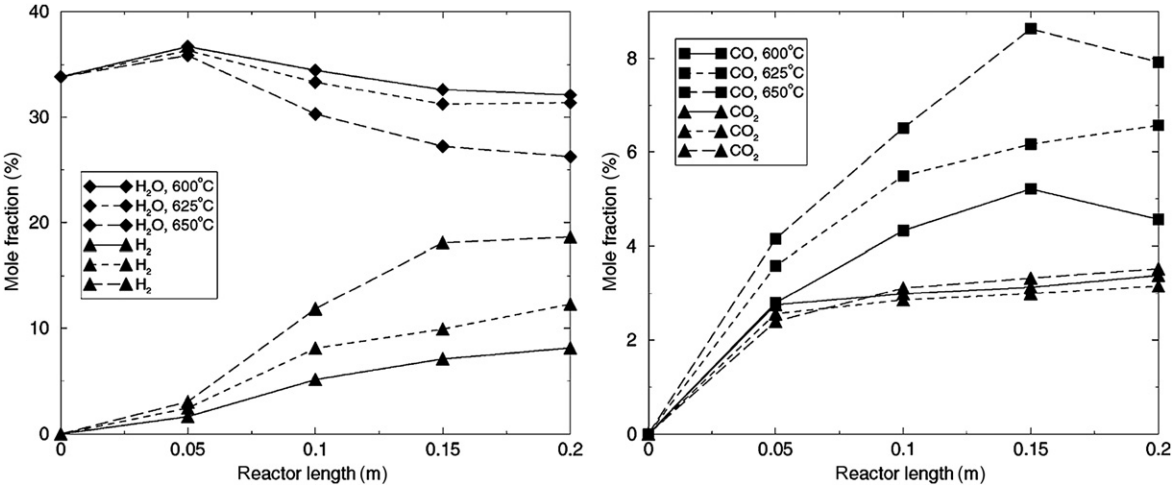

FIGURE 6.33 Product profiles for 1-hexene OSR as a function of reactor length (S/C = 2.3, 0.3 MPa, 600−650 °C, and $(n_{air}/n_{fuel})_{actual}/(n_{air}/n_{fuel})_{stoichiometric} = \lambda = 0.32$); *Reprinted from Springmann et al. [204], Copyright (2002), with permission from Elsevier.*

et al. [206] carried out OSR of *n*-C_6 in monolithic catalysts containing Rh as an active component. A maximum H_2 selectivity of 170% (due to H_2 from water) was obtained from the reforming of *n*-C_6 at an O/C ratio of 1, a S/C of 1, preheat temperature of 700 °C, and GHSV of 68,000 h^{-1}. Brandmair et al. [205] also carried out OSR of *n*-C_6 over Rh supported onto ceramic monoliths at similar conditions, and reported that the Rh catalyst provided better performance over time.

6.5.3.2.2. OTHER NOBLE METALS

A comparison of Al_2O_3-supported Pd and Pt showed that their activity is comparable to or greater than Ni catalysts up to 600 °C, but they were less active at higher temperatures [207]. Interestingly, bimetallic Ni-Pd catalyst had much greater activity than either the Pd/Al_2O_3 or Ni/Al_2O_3 (Fig. 6.34a), though the difference in reaction conditions among the studies does not allow a direct comparison of the results. Moreover, the metal loadings of the catalysts were not provided. However, this result is in agreement with Zhang et al. [208,209] who studied a Ni-Pd bimetallic catalyst and compared it to a Ni catalyst on an identical alumina support. They observed a similar improvement in activity and stability for the Ni-Pd catalyst, but the difference was not as dramatic as shown in Fig. 6.34a. As expected, selectivity to CO + H_2 depended on the O/C and S/C ratios, but was independent of temperature (Fig. 6.34b). However, the Ni-Pd bimetallic catalyst showed a better performance than the Ni-Pt or individual metals over 500 h on stream for OSR of *n*-C_8 [208,209].

A direct comparison of Al_2O_3-supported Pt, Pd, and Ru suggests that Ru is the most active metal for diesel OSR, at least on this support. Berry et al. [210] studied diesel OSR at a temperature range of 750–850 °C and GHSVs of 25,000–200,000 h^{-1}. Activity increased in the order: Pd < Pt < Ru. Complete conversion of diesel was obtained at 850 °C and space velocity of 50,000 h^{-1} from the OSR of diesel over the γ-alumina-supported Ru catalyst.

Encouraging results have been reported on other noble metal-based bimetallic catalysts. Researchers at Engelhard Corporation [211–213] reported reforming of a No. 2 fuel oil containing 1200 ppm sulfur in a dual-bed autothermal process. A preheated stream of steam, air, and No. 2 fuel oil (S/C = 2.57 and O/C = 0.82) was introduced into the first catalytic oxidation zone, which comprised Pt group metal (PGM) catalysts (Pt/Pd in equal portions by weight) dispersed on

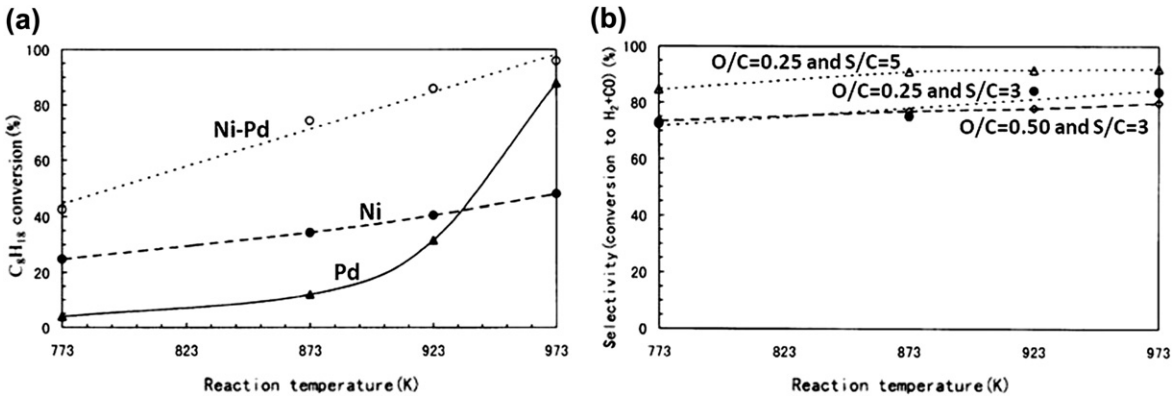

FIGURE 6.34 OSR of *n*-C_8 (a) Activity comparison of reforming catalysts (note: Ni-Pd catalysts tested under "non-reduction" conditions; Ni and Pd under "reduction" conditions) and (b) Selectivity of Ni-Pd catalysts; *Reprinted from Yanhui and Diyong [207], Copyright (2001), with permission from International Association for Hydrogen Energy.*

a lanthana-baria stabilized alumina washcoat. The conversion of O_2 was complete, giving a temperature high enough for SR. The first-stage effluent was then introduced into a second catalyst zone which contained a PGM SR catalyst (Pt-Rh/Al_2O_3). The hydrocarbon conversion was greater than 96% with a maximum H_2 composition of 63% (N_2-free basis) in the product gas stream. Over the same catalyst bed configuration, a JP-4 hydrocarbon produced a H_2 composition of 62% (N_2 free basis) with a complete conversion of the fuel [214].

Similar improvement in Pt-based catalyst activity by the addition of a second metal has been shown for Pd-Pt/alumina and Ni-Pt/ceria [215,216]. High H_2 yields from OSR of diesel, compared with monometallic catalysts, were shown at S/C = 3, O/C = 1, preheat temperature = 400 °C, and space velocity = 17,000 h^{-1} (Fig. 6.35). Based on TPR and XPS studies, they attributed this superior performance of bimetallic catalysts to synergistic effects from strong metal–metal interaction in the bimetallic sample. The order of impregnation had no affect on the performance of Pt-Pd catalysts (Fig. 6.35a), but interestingly, the impregnation order in a Pt-Ni bimetallic catalyst significantly affected H_2 selectivity (Fig. 6.35b). Higher H_2 yields were always observed when the Pt was impregnated second. Also, the Pt-Ni/ceria catalyst showed better sulfur resistance capabilities over 50 h in the presence of a sulfur-laden JP-8 fuel.

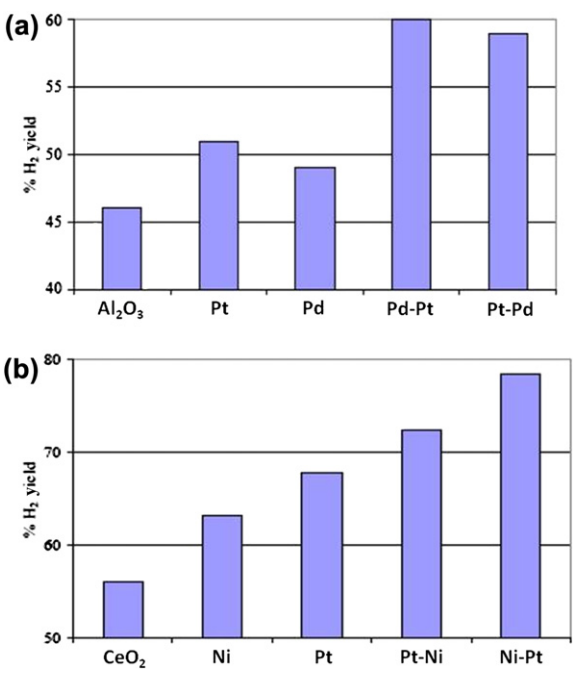

FIGURE 6.35 H_2 yields from OSR of diesel (a) over alumina-supported Pd and/or Pt catalysts (b) over ceria supported Pt and/or Ni catalysts (O/C = 1.0, S/C = 3.0, preheat temperature = 400 °C, 17,000 h^{-1}); *Reprinted from Cheekatamarla and Lane [216], Copyright (2005), with permission from International Association for Hydrogen Energy.*

6.5.3.3. Mixed Metal Oxides (substituted oxides)

6.5.3.3.1. PEROVSKITES

In the effort to develop catalysts with comparable activity and selectivity to benchmark Rh catalysts, researchers at ANL have investigated perovskite-type oxides substituted with other noble metals as cheaper alternatives. Liu and Krumpelt [217] observed Ru-doped lanthanum chromite and lanthanum aluminate catalysts to produce high yields of synthesis gas during OSR of *n*-dodecane (O/C = 1.0, S/C = 1.5, 800 °C, and 50,000 h^{-1}). As shown in Table 6.15, H_2 yields were greater for the Ru catalysts than Rh- and Ni-substituted oxides. Further testing of the Ru-substituted perovskite, $LaCr_{0.95}Ru_{0.05}O_3$, for the OSR of dodecane containing 50 ppmw sulfur (as dibenzothiophene) showed the catalyst to have a high sulfur tolerance, with >75% reforming efficiency (calculation not given, but likely HHV H_2 formed/HHV fuel) and COx selectivity (>95%) for 100 h. Characterization of the material suggested Ru enrichment at the surface during reaction conditions, permitting a greater amount of Ru to be exposed to the reactant gases, as opposed to residing in the bulk. However, Ru still remained atomically dispersed

TABLE 6.15 H_2 yield (mol H_2/mol fuel) and CO_x selectivity of produced over doped perovskites during OSR of dodecane (O/C = 1.0, S/C=1.5, 800°C, and 50,000 h^{-1}) [217].

Catalyst	H_2 yield (mol H_2/mol fuel)	COx selectivity
$La_{0.8}Sr_{0.2}Cr_{0.95}Ru_{0.05}O_3$	16	>90
$LaCr_{0.95}Ru_{0.05}O_3$	22	>95
$La_{0.8}Sr_{0.2}Cr_{0.95}Rh_{0.05}O_3$	19	>85
$La_{0.8}Sr_{0.2}Al_{0.95}Ru_{0.05}O_3$	20	>90
$LaAl_{0.95}Ru_{0.05}O_3$	21	>95
$La_{0.8}Sr_{0.2}CrO_3$	9	>65
$La_{0.8}Sr_{0.2}Cr_{0.9}Ni_{0.1}O_3$	8	>65

in the B-site, avoiding large crystallite sizes, which are deactivated by sulfur and carbon.

6.5.3.3.2. PYROCHLORES

Researchers at the National Energy Technology Laboratory (NETL) have found pyrochlore materials to be viable catalysts for the reforming of logistic fuels into synthesis gas [218–221]. A pyrochlore has a general formula $A_2B_2O_7$, which differs slightly from the perovskite. High thermal and chemical stability makes pyrochlores attractive for high-temperature and redox atmospheres. Pyrochlores can also be partially substituted with multiple cations in both A- and B-sites to tailor their catalytic properties for high activity and resistance to deactivation by carbon and sulfur.

A lanthanum zirconate ($La_2Zr_2O_7$) pyrochlore catalyst modified with Sr in A-site, and either Ni, Ru, or Rh in the B-site was observed to be less susceptible to deactivation by sulfur and carbon during CPOX of 5 wt% 1-methlynaphthalene (MN) and 50 ppmw sulfur in *n*-tetradecane compared with the same metals supported on γ-Al_2O_3 [218–221]. Resistance to deactivation was believed to be a result of not only stabilization of the metal particles in the pyrochlore structure, but also oxygen-ion mobility which occurs after the replacement of La^{3+} with Sr^{2+}. Much like perovskites, alkaline properties of Sr probably also assisted with carbon gasification and prevention of sulfur accumulation.

The sulfur and carbon resistance of the pyrochlores has promoted the continued development of the pyrochlore formulation and synthesis at NETL. Through systematic testing

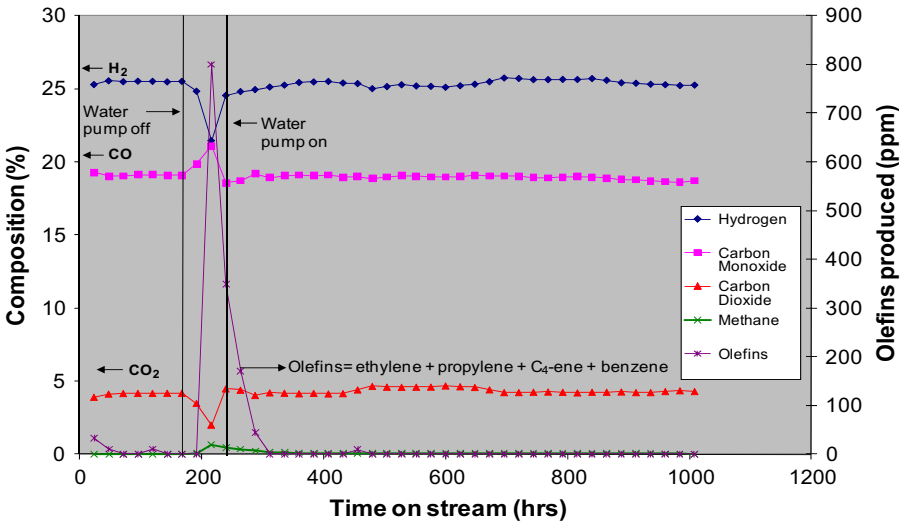

FIGURE 6.36 OSR of commercial diesel fuel (9 ppmw S) using NETL developed pyrochlore (O/C = 1.0, S/C = 0.5, 900 °C, and 25,000 h^{-1}) [222].

and characterization, a pyrochlore formulation was developed to be capable of long-term OSR operation [222]. Figure 6.36 shows that a pyrochlore formulation produced roughly equilibrium yields of synthesis gas for over 1000 h during OSR of a commercial diesel (9 ppmw sulfur; O/C = 1.0, S/C = 0.5, T = 900 °C, and 25,000 h^{-1}). The catalyst was a modified version of those tested for the CPOX studies mentioned in Chapter 5.

6.5.4. Oxygenated Compounds

Oxygenated compounds are another class of fuels which can also be considered to be major H_2 resources along with NG, and petroleum-based resources. Increased interest in these fuels has emerged for the sustainable production of H_2, because they are generally derived from renewable biomass resources. The physical properties of these fuels make them attractive for reforming. These include low boiling point, low processing temperature, and minimal amounts of contaminants.

6.5.4.1. Methanol

OSR of methanol (OSRM) has been suggested for hydrogen production as an alternative to energy intensive steam reforming. The reaction can be expressed by the following equation [223].

$$CH_3OH + \alpha O_2 + (1 - 2\alpha)H_2O \rightarrow (3 - 2\alpha)H_2 + CO_2 \quad (6.42)$$

6.5.4.1.1. COPPER-BASED CATALYSTS

Variations of Cu-based catalysts are the most commonly reported for the OSRM, especially derivates of $CuO/ZnO/Al_2O_3$ systems which originated as a catalyst for commercial low-temperature WGS and methanol synthesis processes. It is highly desirable for Cu-based catalysts to have high dispersion and metal surface area, since its reforming activity depends greatly on these properties. The reducibility of Cu is also an important factor in determining the efficiency of the Cu catalysts in OSRM when redox properties of the catalyst play a part in the mechanism for H_2 formation [224].

PROMOTERS FOR COPPER Promoters are added to Cu to improve its dispersion and reducibility. Zn is the most common promoter for commercial Cu-based catalysts. The role of Zn, and other promoting metals, may also lead to improved adsorption of methanol [223,225]. It has also been suggested that the promoters may lead to spillover effects of hydrogen (from Cu to promoter) and oxygen (from promoter to Cu), which may affect the reaction mechanism [225].

Alumina is commonly used as a structural modifier to improve mechanical strength and dispersion of a Cu catalyst. However high loadings of Al_2O_3 promote a strong interaction between Cu and Al_2O_3 (>10 wt% in the case for Chang et al. [223]), which can lead to increased reduction temperature, lower Cu surface area, and lower conversions.

Other promoters added to Cu-Al solid solutions include Cr, Zn, Zr, Ce [226,227], and their combinations [223,228]. The promotional effect of some of these components when added to a Cu-Al system can be exemplified by the study by Lindstrom et al. [229], which evaluated a series of $Cu/M/Al_2O_3$ catalysts (M = Cr, Zn, and Zr) with various weight loadings of Cu (3–12 wt%) and (Cu/M weight ratios; 4–0.25) for the OSRM (O/C = 0.15 and S/C = 1.3). Over all Cu : M loadings tested for activity, Zn-promoted catalysts had the highest conversions, H_2 production rate (mmol/kg_{cat}/s), and turnover frequency than the Cr and Zr catalysts (see Table 6.16). Characterization techniques showed Zn-promoted catalysts had consistently higher Cu metal surface area, lower reduction peak maxima, and more reducible Cu. No strong trends in performance are observed with Cu/Zn ratio in Table 6.16, which is consistent with the literature. Values between 4 and 0.7 have been reported to be optimal for activity and H_2 production from methanol reforming [230–233].

TABLE 6.16 Effect of Promoting Metal on H_2 Production Rate, Conversion and TOF for Cu Catalysts during OSRM at (O/C = 0.15, S/C = 1.3 and 300 °C; O/C and S/C do not include O from fuel) [229]

Catalyst*	H_2 production rate (mmol/kg_{cat}/s)	Conversion (%)	TOF (10^3 s^{-1})†
Cu_{15}	135	73.0	154
Zn_{15}	15	8.2	0
Cr_{15}	14	7.4	0
Zr_{15}	16	8.6	0
Cu_9/Zn_6	133	72.0	114
Cu_6Zn_9	161	87.0	153
Cu_9Cr_6	81	44.0	71
Cu_6Cr_9	109	59.0	138
Cu_9Zr_6	76	41.0	86
Cu_6Zr_9	91	49.0	136

** Subscript of catalyst is weight percent.*
†TOF is defined as methanol molecules converted per surface copper atom per second.

EFFECT OF SYNTHESIS METHOD Since the activity of Cu for OSRM is known to be sensitive to its physicochemical properties (i.e., dispersion, surface area, and particle size), the method used to synthesize the catalyst greatly influences reforming activity. Many studies have focused on the effect of preparation method to produce an active and selective Cu-based catalyst for the OSRM. While the best synthesis method for a desired composition may not be obvious, generally one can be guided based on which components (mainly alumina) are present in the catalyst.

The co-precipitation (CP) method appears to be suitable for producing highly active and selective Cu-based catalysts containing alumina [223,227,228,231]. The catalysts synthesized by this method have adequate BET SA, Cu SA, and low reducibility for high methanol conversions and H_2 selectivities. Shen and Song [231] investigated several synthesis methods for a Cu/Zn/Al catalyst (33/43/24 by weight), including hydrotalcite-type, impregnation, and CP on activity for steam reforming and OSRM at 230 °C. The catalyst produced by CP was found to have the highest conversion and yields of H_2 for both reactions compared with the catalysts synthesized by the other methods.

In cases where Cu-Zr or Cu-Ce solid solutions are used, other methods have been shown to be more effective for synthesis. This is likely due to the fact that CP may not provide adequate mixing to form a uniform solid solution, and/or the required SA to obtain high Cu dispersion, small particle sizes, and lower reducibility. A study by Shan et al. [234] investigated three synthesis methods (deposition-precipitation (DP), CP, and complexation-combustion (CC)) on activity for OSRM of a $Ce_{0.9}Cu_{0.1}O_y$ catalyst (O/C = 0.6, S/C = 1.3). The catalyst produced by combustion-complexation was found to have the highest methanol conversions and selectivities to H_2 (see Fig. 6.37) over all temperature ranges. The catalysts synthesized by the CP and DP methods were found to have a poor interaction between Cu and CeO_2, and produced a greater amount of CuO dispersed on CeO_2. The catalyst produced by the CC method had more uniformly distributed Cu^{2+} within the CeO_2 structure, which therefore led to more lattice defects. The resulting solid solution was found to have lower Cu reduction temperatures, and better redox properties due to a synergistic function between Cu^{2+}/Cu^{+} and Ce^{4+}/Ce^{3+}, which was attributed to its higher activity. Some alternate synthesis methods are summarized in Table 6.17, along with important properties of the resulting Cu-based catalysts.

6.5.4.2. *Ethanol*

Ethanol reforming has been gaining attention as a source of H_2 for fuel cells. It is considered to be a promising renewable fuel supply, because significant amounts can be

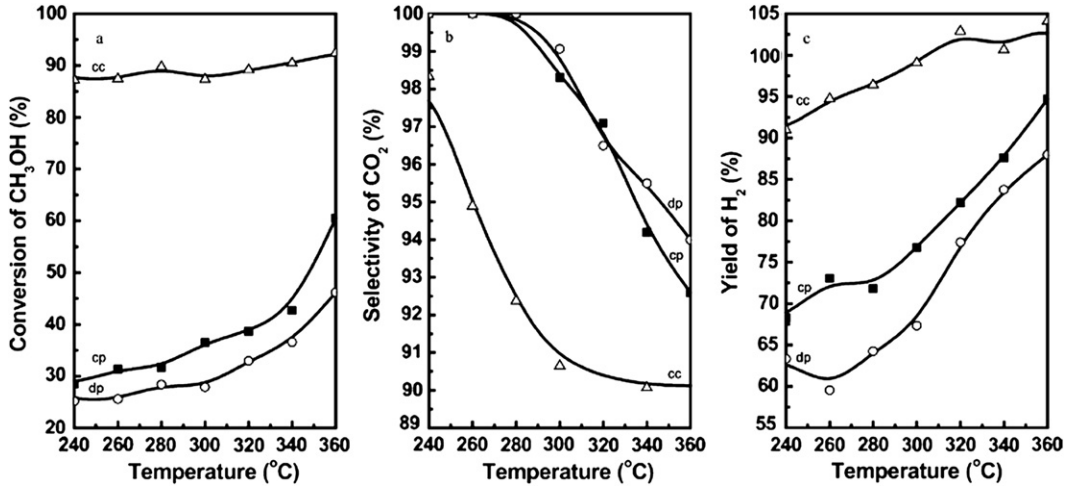

FIGURE 6.37 Effect of synthesis method [deposition-precipitation (DP), coprecipitation (CP) and complexation-combustion (CC)] on methanol conversion, CO_2 selectivity and H_2 selectivity for a $Ce_{0.9}Cu_{0.1}O_y$ during OSRM (O/C = 0.6, S/C = 1.3); *Reprinted from Shan et al. [234], Copyright (2004), with permission from Elsevier.*

produced from the fermentation of a wide variety of abundant starch-rich materials (i.e., sugar cane, corn, potatoes, etc.). Also, ethanol is less toxic than methanol and other liquid hydrocarbons.

The oxidative steam reforming of ethanol (OSRE) and higher alcohols is different than methanol reforming since a cleavage of at least one C−C bond is involved. Therefore, reactions require comparatively higher temperatures than methanol, typically between 450−600 °C, and use metals like Ni, Rh, Ru, Pt, and Ir which are known to be active for the scission of C−C bonds.

Using Ni (20 wt%), Youn et al. [239] evaluated the effect of support for the OSRE at

TABLE 6.17 Additional Synthesis Methods and the Physicochemical Properties of Cu-based Catalysts

Catalyst	Cu (wt%)	Preparation Method*	BET SA (m^2/g)	Cu SA (m^2/g)	Cu dispersion (%)	X_{MeOH} (%)	Conditions
Cu-ZrO_2 [235]	4.5	Sol-gel	131	24.4	85	72	T = 400 °C O/C = 0.12 S/C = 1.1
Cu-ZrO_2 [236]	75	GCOP	72	18.4	–	100	T = 260 °C S/C = 1.3
Cu-ZrO_2 [237]	50	SRGOA-N	45	14.8	–	71	T = 240 °C S/C = 1.3
Cu-Zn-Cr [238]	2.5	UNC	68	–	–	>85	T = 250 °C O/C = 0.32 S/C = 1.2

** Abbreviations: GCOP-coprecipitated oxalate precursor method; SASG-Surfactant assisted sol-gel; SRGOA-N- soft reactive grinding of oxalic acid with nitrate precursors; UNC-urea-nitrate combustion method.*

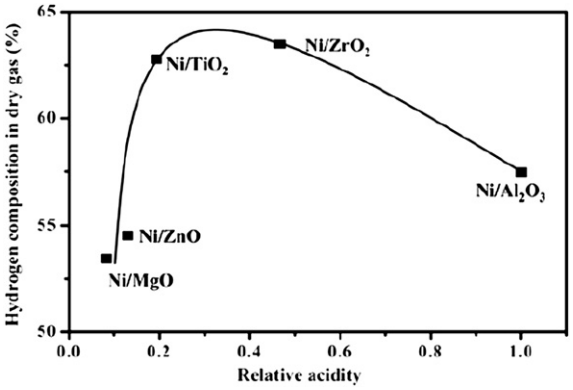

FIGURE 6.38 Comparison of support in terms of H_2 composition vs. relative support activity for 20 wt% Ni after 3 h TOS for OSRE (O/C = 0.5, S/C = 1.5, and 500 °C). Oxygen from ethanol not included in O/C or S/C ratios; *Reprinted from Youn et al. [239], Copyright (2008), with permission from Springer.*

500 °C (O/C = 0.5; S/C = 1.5). After 3 h time on stream, their results, (see Fig. 6.38) shown in terms of H_2 composition as a function of support acidity, suggest that TiO_2 and ZrO_2 supports with more moderate acidity produce higher amounts of hydrogen. The relative acidity is defined as the ratio of support acidity/acidity Ni/Al_2O_3. TiO_2 and ZrO_2 are also known to have some redox capabilities, which helps prevent carbon formation during reaction. More basic supports, MgO and ZnO, were determined to be less active because of the formation of a solid solution which limited the amount of exposed active Ni particles. The highly acidic alumina was found to promote undesirable side reactions, likely due to the formation of carbon, which caused the rapid deactivation of the Ni.

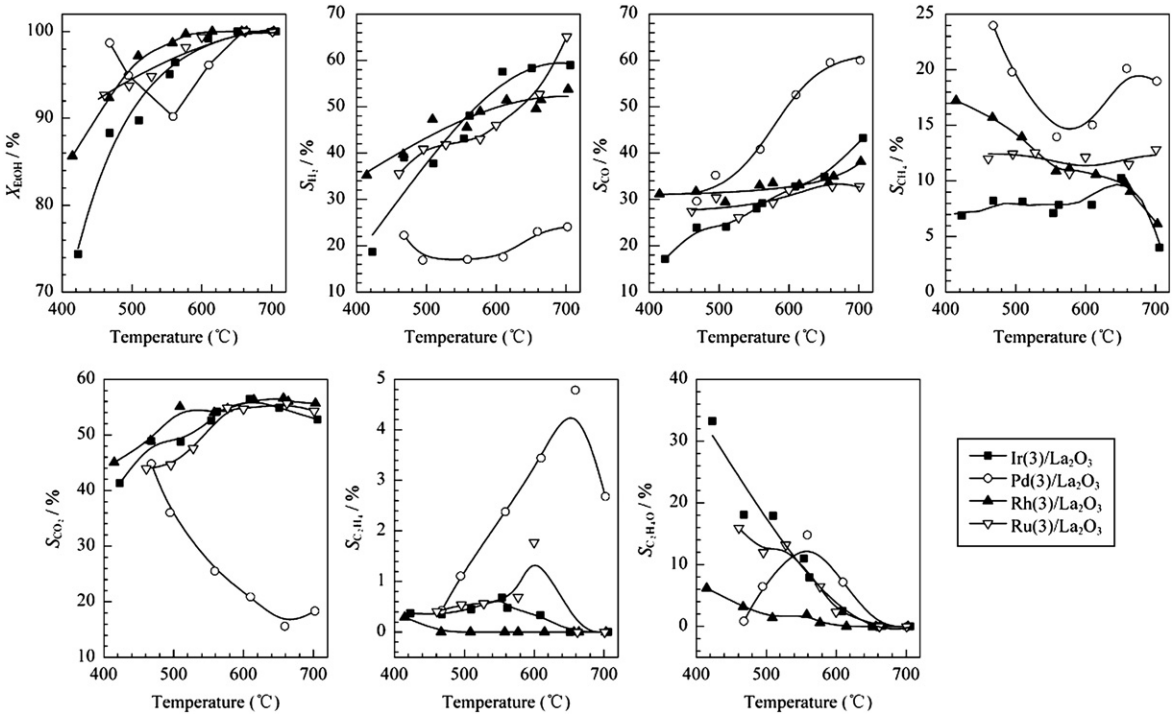

FIGURE 6.39 Comparison of conversion and product selectivities for 3 wt%M/La_2O_3 (M = Ir, Pd, Rh, or Ru) for OSRM (O/C = 0.83 and S/C = 1.3) at different temperatures. Oxygen from ethanol not included in O/C or S/C ratios; *Reprinted from Chen et al. [240], Copyright (2009), with permission from Elsevier.*

Chen et al. [240] performed an extensive study of OSRE using noble metals (3 wt% Ir, Pd, Rh, or Ru) supported over various oxides (γ-Al_2O_3, CeO_2, ZrO_2, and La_2O_3). For all metal catalysts, La_2O_3 was found to be the best functional support, because of its considerable activity and selectivity for the OSRE (650 °C; O/C = 1; S/C = 2) in the absence of a catalytic metal. Conversions and product selectivities for the different metals supported over La_2O_3 are shown in Fig. 6.39. All metals reached conversion near 100% around 600 °C. Pd was recognized to have the lowest selectivity to H_2 and highest selectivity to CH_4 and other carbon by-products. Consistent with the literature, Rh was observed to be the most active and selective to H_2 [241], especially at temperatures <500 °C. Rh also had the lowest selectivity to acetaldehyde and ethylene compared with the other metals. Ir and Ru proved to be cheaper alternatives to Rh, as they produced similar selectivities to H_2 and CO_2. It is worth mentioning that the Ir catalyst had the lowest selectivity to CH_4 over all temperatures. This correlates to the activation and conversion of CH_4 not being a major pathway over Ir for H_2 production, which is especially advantageous at lower temperatures where such a process is limited by its energetics.

6.5.4.3. *Biodiesel*

Biodiesel is mainly produced through the transesterification of vegetable oil or animal fats into long-chain methyl esters. While biodiesel fuels are currently synthesized to supplant diesel for transportation purposes, they can also be reformulated into large quantities of H_2 and CO through OSR for fuel cells. Structurally they are similar to the *n*-paraffin compounds contained in traditional diesel, yet they are much cleaner and easier to reform catalytically because they do not contain aromatic and sulfur compounds.

Despite recent interest in biodiesel synthesis, studies involving the reforming of biodiesel are not yet commonly reported.

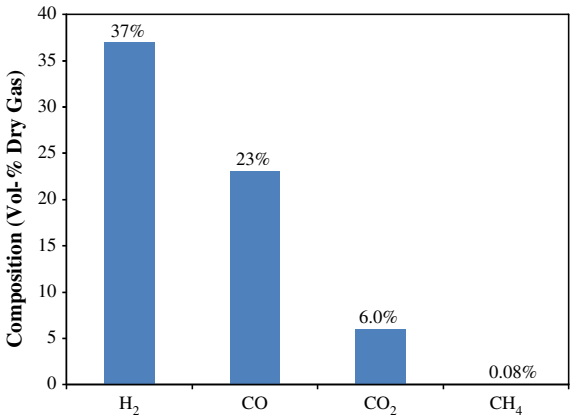

FIGURE 6.40 Synthesis gas composition produced during the OSR of biodiesel using layered Rh-based pyrochlore monolith after 100 h TOS (O/C = 0.5, S/C = 0.5, 900 °C, and 25,000 h^{-1}) [242].

From the available literature, a study by researchers at the NETL [242] found biodiesel to be highly reactive and easily converted into H_2 and CO. Using a structured monolith consisting of Rh-based pyrochlore/zirconia-doped ceria/Al_2O_3, a reforming unit was run on biodiesel (O/C = 0.6, S/C = 0.5, 900 °C and 25,000 h^{-1}) for over 100 h. The average dry gas composition from the run is shown in Fig. 6.40. Based on these results, it can be surmised from this work that catalysts active for biodiesel reforming are similar to those used for commercial diesel reforming.

6.6. FUTURE WORK

6.6.1. Staged Reactor Configuration

In the discussion provided in the "Catalytic Partial Oxidation (CPOX)" chapter (Chapter 5), future work was recommended on developing a staged reactor approach to converting hydrocarbons to syngas (Section 5.7.2). This is motivated by the two-zone, or indirect, reaction mechanism discussed in both the CPOX and OSR chapters. Two approaches were

recommended: multiple oxygen feed locations, and multiple catalyst formulations. Although multiple catalyst formulations could also potentially benefit OSR, the justifications for future work are similar to those for CPOX. Furthermore, the significant presence of SR throughout the reactor may minimize the benefit seen in a graded catalyst bed approach. Therefore, additional discussion of this approach is not needed.

However, multiple feed locations of oxygen to the reactor may provide additional benefits for OSR and deserves further emphasis. Differences in the kinetic rates between the oxidation and reforming reactions have been shown to result in the formation of severe temperature gradients in the bed when the O_2 and steam are co-fed. Their formation is not advantageous to reforming efficiency ($\eta_{ref} = \frac{HHV_{H_2} + HHV_{CO}}{HHV_{fuel}}$; for high-temperature fuel cell), as they signify heat losses and transfer resistances. Catalyst materials in the hot spot region also degrade quickly, and require special modification.

Typically, structured or engineered monoliths have been employed to mitigate heat transfer concerns, as they permit better temperature distribution as well as a more uniform gas flow, which minimizes diffusion resistances. The effective transfer of heat, however, has still been observed to be an issue, even for monoliths, because of the uneven rate of heat generated at the catalyst surface and that transferred to the incoming gases in the front portion of the bed [53].

An effective alternative may rely on reactor design. By developing a process to uniformly distribute oxygen concentrations down the length of the catalyst bed, the rapid and localized oxidation of the fuel, and its associated temperature rise, at the bed entrance would be avoided. The distribution of the oxidation reactions down the length of the bed would likely result in more uniform bed temperatures, and provide effective heat transfer between oxidation and reforming reactions, which would in this case occur more intimately.

6.6.2. Bimetallic Substituted Oxides

A number of studies have been presented here which applied multiple metal additions to a supported catalyst for OSR. In some cases the additional metal was used as a promoter to modify the activity and/or deactivation resistance of the catalytic metal(s). Other metal addition was used to modify the support properties and/or its interaction with the active metal(s). Building on the successes achieved in the OSR of Transportation Fuels (Section 6.5.3) through the use of substituted oxides (i.e., perovskites and pyrochlores), a potentially significant area for development of these catalysts exists in combining a bimetallic catalyst approach with a substituted oxide.

This approach differs from the use of promoting metal substitution, as done in the A- and/or B-sites of these materials, which are used to modify properties like surface acid-base character, morphology, ion conductivity, and carbon formation. Instead, this approach would examine the substitution of two different catalytic metals (i.e., Ni and Rh) that are active independently for OSR, and are substituted at a sufficient level in which both participate in the reaction.

In essence, this would be accomplished by selecting metals that are highly active and selective for different steps in the reaction mechanism. However, the approach will not simply provide a benefit from direct alloy formation between the metals, which may alter their electronic properties in favorable ways, but may also provide a synergistic effect through the simultaneous participation in the overall reaction. For example, the substitution of both Ni and Rh together may reduce the formation of destructive filament carbon due to the high activity and carbon resistance of the Rh metal, which would be in proximity to the Ni atoms at the surface, but not in alloy form.

References

[1] Qi A, Wang S, Fu G, Wu D. Autothermal reforming of n-octane on Ru-based catalysts. Appl Catal A: Gen 2005;293:71–82.

[2] Borup RL, Inbody MA, Semelsberger TA, Tafoya JI, Guidry DR. Fuel composition effects on transportation fuel cell reforming. Catal Today 2005;99(3–4):263–70.

[3] Ferreira-Aparicio P, Benito MJ. New trends in reforming technologies: from hydrogen industrial plants to multifuel mircroreformers. Catal Rev Sci Eng 2005;47:491–8.

[4] Ahmed S, Krumpelt M. Hydrogen from hydrocarbon fuels for fuel cells. Int J Hydrogen Energy 2001;26(4):291–301.

[5] Danial DE, Kumar R, Ahluwalia RK, Krumpelt M. Fuel processors for automotive fuel cell systems: a parametric analysis. J Power Sources 2001;102(1–2):1–15.

[6] Krumpelt M, Krause TR, Carter JD, Kopasz JP, Ahmed S. Fuel processing for fuel cell systems in transportation and portable power applications. Catal Today 2002;77(1–2):3–16.

[7] Shekhawat D, Berry DA, Gardner TH, Haynes DJ, Spivey JJ. Effects of fuel cell anode recycle on catalytic fuel reforming. J Power Sources 2007;168 (2):477–83.

[8] Huang C, T-Raissi A. Thermodynamic analyses of hydrogen production from sub-quality natural gas: Part II: steam reforming and autothermal steam reforming. J Power Sources 2007;163(2):637–44.

[9] Huang C, T-Raissi A. Thermodynamic analyses of hydrogen production from sub-quality natural gas: Part I: pyrolysis and autothermal pyrolysis. J Power Sources 2007;163(2):645–52.

[10] Chan SH, Wang HM. Thermodynamic analysis of natural-gas fuel processing for fuel cell applications. Int J Hydrogen Energy 2000;25(5):441–9.

[11] Semelsberger TA, Brown LF, Borup RL, Inbody MA. Equilibrium products from autothermal processes for generating hydrogen-rich fuel-cell feeds. Int J Hydrogen Energy 2004;29(10):1047–64.

[12] Liu S, Zhang K, Fang L, Li Y. Thermodynamic analysis of hydrogen production from oxidative steam reforming of ethanol. Energy Fuels 2008;22:1365–70.

[13] Ayabe S, Omoto H, Utaka T, Kikuchi R, Sasaki K, Teraoka Y, et al. Catalytic autothermal reforming of methane and propane over supported metal catalysts. Appl Catal A: Gen 2003;241(1–2):261–9.

[14] Seo YS, Shirley A, Kolaczkowski ST. Evaluation of thermodynamically favourable operating conditions for production of hydrogen in three different reforming technologies. J Power Sources 2002;108 (1–2):213–25.

[15] Dalle ND, Baggio P, Tomasi C, Mutri L, Canu P. A thermodynamic analysis of natural gas reforming processes for fuel cell application. *Chem Eng Sci* 2007;62(18–20):5418–24.

[16] Zeng G, Tian Y, Li Y. Thermodynamic analysis of hydrogen production for fuel cell via oxidative steam reforming of propane. Int J Hydrogen Energy 2010;35(13):6726–37.

[17] Wang S, Wang S. Thermodynamic equilibrium composition analysis of methanol autothermal reforming for proton exchanger membrane fuel cell based on FLUENT Software. J Power Sources 2008; 185(1):451–8.

[18] Chan SH, Wang HM. Thermodynamic and kinetic modelling of an autothermal methanol reformer. J Power Sources 2004;126(1–2):8–15.

[19] Hagh BF. Stoichiometric analysis of autothermal fuel processing. J Power Sources 2004;130(1–2): 85–94.

[20] Rabenstein G, Hacker V. Hydrogen for fuel cells from ethanol by steam-reforming, partial-oxidation and combined auto-thermal reforming: a thermodynamic analysis. J Power Sources 2008;185(2):1293–304.

[21] Benito M, Padilla R, Sanz JL, Daza L. Thermodynamic analysis and performance of a 1 kW bioethanol processor for a PEMFC operation. J Power Sources 2007;169(1):123–30.

[22] Wang H, Wang X, Li M, Li S, Wang S, Ma X. Thermodynamic analysis of hydrogen production from glycerol autothermal reforming. Int J Hydrogen Energy 2009;34(14):5683–90.

[23] Villegas L, Guilhaume N, Provendier H, Daniel C, Masset F, Mirodatos C. A combined thermodynamic/experimental study for the optimisation of hydrogen production by catalytic reforming of isooctane. Appl Catal A: Gen 2005;281(1–2):75–83.

[24] Docter A, Lamm A. Gasoline fuel cell systems. J Power Sources 1999;84(2):194–200.

[25] Ersoz A, Olgun H, Ozdogan S, Gungor C, Akgun F, TirIs M. Autothermal reforming as a hydrocarbon fuel processing option for PEM fuel cell. J Power Sources 2003;118(1–2):384–92.

[26] Parmar RD, Kundu A, Karan K. Thermodynamic analysis of diesel reforming process: mapping of carbon formation boundary and representative independent reactions. J Power Sources 2009;194 (2):1007–20.

[27] Kang I, Bae J. Autothermal reforming study of diesel for fuel cell application. J Power Sources 2006;159 (2):1283–90.

[28] Kaila RK, Krause AOI. Autothermal reforming of simulated gasoline and diesel fuels. Int J Hydrogen Energy 2006;31(13):1934–41.

[29] Shekhawat D, Berry DA, Gardner TH, Spivey JJ. Catalytic reforming of liquid hydrocarbon fuels for fuel cell applications. In: Spivey JJ, Dooley KM, editors. Catalysis, vol. 27. Cambridge, UK: The Royal Society of Chemistry; 2006. p. 184–253.

[30] Ibarreta AF, Sung C-J. Optimization of Jet-A fuel reforming for aerospace applications. Int J Hydrogen Energy 2006;31(8):1066–78.

[31] Roine A, Lamberg P, Mansikka-aho J, Bjorklund P, Kentala J-P, Talonen T. HSC Chemistry v6.12. Outotec Research Oy; 2007.

[32] Lindermeir A, Kah S, Kavurucu S, Mühlner M. On-board diesel fuel processing for an SOFC-APU–Technical challenges for catalysis and reactor design. Appl Catal B: Env 2007;70(1–4):488–97.

[33] Michael BC, Donazzi A, Schmidt LD. Effects of H_2O and CO_2 addition in catalytic partial oxidation of methane on Rh. J Catal 2009;265(1):117–29.

[34] York APE, Xiao T, Green MLH. Brief overview of the partial oxidation of methane to synthesis gas. Top Catal 2003;22:345–58.

[35] Au CT, Wang HY. Mechanistic studies of methane partial oxidation to syngas over sio_2-supported rhodium catalysts. J Catal 1997;167(2):337–45.

[36] Li B, Maruyama K, Nurunnabi M, Kunimori K, Tomishige K. Temperature profiles of alumina-supported noble metal catalysts in autothermal reforming of methane. Appl Catal A: Gen 2004;275(1–2):157–72.

[37] Pino L, Vita A, Cipitì F, Laganà M, Recupero V. Performance of Pt/CeO_2 catalyst for propane oxidative steam reforming. Appl Catal A: Gen 2006;306:68–77.

[38] Prettre M, Eichner CH, Perrin M. Catalytic oxidation of methane to carbon monoxide and hydrogen. Trans Faraday Soc 1946;43:335–40.

[39] Ruiz JAC, Passos FB, Bueno JMC, Souza-Aguiar EF, Mattos LV, Noronha FB. Syngas production by autothermal reforming of methane on supported platinum catalysts. Appl Catal A: Gen 2008;334(1–2):259–67.

[40] Simeone M, Salemme L, Scognamiglio D, Allouis C, Volpicelli G. Effect of water addition and stoichiometry variations on temperature profiles in an autothermal methane reforming reactor with Ni catalyst. Int J Hydrogen Energy 2008;33(4):1252–61.

[41] Mukainakano Y, Yoshida K, Okumura K, Kunimori K, Tomishige K. Catalytic performance and QXAFS analysis of Ni catalysts modified with Pd for oxidative steam reforming of methane. Catal Today 2008;132(1–4):101–8.

[42] Tomishige K, Nurunnabi M, Maruyama K, Kunimori K. Effect of oxygen addition to steam and dry reforming of methane on bed temperature profile over Pt and Ni catalysts. Fuel Process Technol 2004;85(8–10):1103–20.

[43] Simeone M, Menna L, Salemme L, Allouis C. Temperature evolution on Rh/Al_2O_3 catalyst during partial oxidation of methane in a reverse flow reactor. Exp Therm Fluid Sci 2010;34(3):381–6.

[44] Simeone M, Salemme L, Allouis C. Reactor temperature profile during autothermal methane reforming on Rh/Al_2O_3 catalyst by IR imaging. Int J Hydrogen Energy 2008;33(18):4798–5808.

[45] Dissanayake D, Rosynek MP, Kharas KCC, Lunsford JH. Partial oxidation of methane to carbon monoxide and hydrogen over a Ni/Al_2O_3 catalyst. J Catal 1991;132(1):117–27.

[46] Yamazaki O, Tomishige K, Fujimoto K. Development of highly stable nickel catalyst for methane-steam reaction under low steam to carbon ratio. Appl Catal A: Gen 1996;136(1):49–56.

[47] Enger BC, Lødeng R, Holmen A. Modified cobalt catalysts in the partial oxidation of methane at moderate temperatures. J Catal 2009;262(2):188–98.

[48] Li B, Kado S, Mukainakano Y, Miyazawa T, Miyao T, Naito S, et al. Surface modification of Ni catalysts with trace Pt for oxidative steam reforming of methane. J Catal 2007;245(1):144–55.

[49] Li B, Kado S, Mukainakano Y, Nurunnabi M, Miyao T, Naito S, et al. Temperature profile of catalyst bed during oxidative steam reforming of methane over Pt-Ni bimetallic catalysts. Appl Catal A: Gen 2006;304:62–71.

[50] Sato K, Nagaoka K, Nishiguchi H, Takita Y. n-C_4H_{10} autothermal reforming over MgO-supported base metal catalysts. Int J Hydrogen Energy 2009;34(1):333–42.

[51] Bitsch-Larsen A, Horn R, Schmidt LD. Catalytic partial oxidation of methane on rhodium and platinum: spatial profiles at elevated pressure. Appl Catal A: Gen 2008;348(2):165–72.

[52] Dalle ND, Degenstein NJ, Horn R, Canu P, Schmidt LD. Modeling spatially resolved profiles of methane partial oxidation on a Rh foam catalyst with detailed chemistry. J Catal 2008;258(1):131–42.

[53] Horn R, Williams KA, Degenstein NJ, Bitsch-Larsen A, Dalle ND, Tupy SA, et al. Methane catalytic partial oxidation on autothermal Rh and Pt foam catalysts: oxidation and reforming zones, transport effects, and approach to thermodynamic equilibrium. J Catal 2007;249(2):380–93.

[54] Horn R, Williams KA, Degenstein NJ, Schmidt LD. Syngas by catalytic partial oxidation of methane on rhodium: mechanistic conclusions from spatially resolved measurements and numerical simulations. J Catal 2006;242(1):92–102.

[55] Horn R, Williams KA, Degenstein NJ, Schmidt LD. Mechanism of H_2 and CO formation in the catalytic partial oxidation of CH_4 on Rh probed by steady-state spatial profiles and spatially resolved transients. Chem Eng Sci 2007;62(5):1298–307.

[56] Hickman DA, Schmidt LD. Synthesis gas formation by direct oxidation of methane over Pt monoliths. J Catal 1992;138(1):267–82.

[57] Hickman DA, Schmidt LD. Steps in CH_4 oxidation on Pt and Rh surfaces – high temperature reactor simulations. AIChE J 1993;39(7):1164–77.

[58] Hu YH, Ruckenstein E. Transient kinetic studies of partial oxidation of CH_4. J Catal 1996;158(1):260–6.

[59] Mallens EPJ, Hoebink JHBJ, Marin GB. The reaction mechanism of the partial oxidation of methane to synthesis gas: a transient kinetic study over rhodium and a comparison with platinum. J Catal 1997;167 (1):43–56.

[60] Mallens EPJ, Hoebink JHBJ, Marin GB. An investigation on the reaction-mechanism for the partial oxidation of methane to synthesis gas over platinum. Catal Lett 1995;33(3–4):291–304.

[61] Mhadeshwar AB, Vlachos DG. Hierarchical multiscale mechanism development for methane partial oxidation and reforming and for thermal decomposition of oxygenates on Rh. J Phys Chem B 2005; 109(35):16819–35.

[62] Dauenhauer PJ, Salge JR, Schmidt LD. Renewable hydrogen by autothermal steam reforming of volatile carbohydrates. J Catal 2006;244(2):238–47.

[63] Semelsberger TA, Ott KC, Borup RL, Greene HL. Generating hydrogen-rich fuel-cell feeds from dimethyl ether (DME) using Cu/Zn supported on various solid-acid substrates. Appl Catal A: Gen 2006;309(2):210–23.

[64] Shishido T, Yamamoto Y, Morioka H, Takehira K. Production of hydrogen from methanol over Cu/ZnO and $Cu/ZnO/Al_2O_3$ catalysts prepared by homogeneous precipitation: steam reforming and oxidative steam reforming. J Mol Catal A: Chem 2007;268(1–2):185–94.

[65] Xu J, Froment GF. Methane steam reforming, methanation and water-gas shift: I. Intrinsic kinetics. AIChE J 1989;35(1):88–96.

[66] Tøttrup PB. Evaluation of intrinsic steam reforming kinetic parameters from rate measurements on full particle size. Appl Catal 1982;4(4):377–89.

[67] Pacheco M, Sira J, Kopasz J. Reaction kinetics and reactor modeling for fuel processing of liquid hydrocarbons to produce hydrogen: isooctane reforming. Appl Catal A: Gen 2003;250(1):161–75.

[68] Halabi MH, de Croon MHJM, van der Schaaf J, Cobden PD, Schouten JC. Modeling and analysis of autothermal reforming of methane to hydrogen in a fixed bed reformer. Chem Eng J 2008;137(3):568–78.

[69] Hoang DL, Chan SH. Modeling of a catalytic autothermal methane reformer for fuel cell applications. Appl Catal A: Gen 2004;268(1–2):207–16.

[70] Hoang DL, Chan SH, Ding OL. Hydrogen production for fuel cells by autothermal reforming of methane over sulfide nickel catalyst on a gamma alumina support. J Power Sources 2006;159(2):1248–57.

[71] Ma L, Trimm DL, Jiang C. The design and testing of an autothermal reactor for the conversion of light hydrocarbons to hydrogen. I. The kinetics of the catalytic oxidation of light hydrocarbons. Appl Catal A: Gen 1996;138(2):275–83.

[72] Trimm DL, Lam C- W. The combustion of methane on platinum–alumina fibre catalysts–I: kinetics and mechanism. Chem Eng Sci 1980;35(6):1405–13.

[73] Nah CY, Palanki S. Analysis of heptane autothermal reformer to generate hydrogen for fuel cell applications. Int J Hydrogen Energy 2009;34(20): 8566–73.

[74] Papadias D, Lee SHD, Chmielewski DJ. Autothermal reforming of gasoline for fuel cell applications: a transient reactor model. Ind Eng Chem Res 2006; 45(17):5841–58.

[75] Dubien C, Schweich D, Mabilon G, Martin B, Prigent M. Three-way catalytic converter modelling: fast- and slow-oxidizing hydrocarbons, inhibiting species, and steam-reforming reaction. Chem Eng Sci 1998;53(3):471–81.

[76] Wheeler C, Jhalani A, Klein EJ, Tummala S, Schmidt LD. The water-gas-shift reaction at short contact times. J Catal 2004;223(1):191–9.

[77] Jin W, Gu X, Li S, Huang P, Xu N, Shi J. Experimental and simulation study on a catalyst packed tubular dense membrane reactor for partial oxidation of methane to syngas. Chem Eng Sci 2000;55(14):2617–25.

[78] Shigarov AB, Kireenkov VV, Kuzmin VA, Kuzin NA, Kirillov VA. Autothermal reforming of diesel fuel in a structured porous metal catalyst: both kinetically and transport controlled reaction. Catal Today 2009;144(3–4):341–9.

[79] Dorazio L, Castaldi MJ. Autothermal reforming of tetradecane ($C_{14}H_{30}$): a mechanistic approach. Catal Today 2008;136(3–4):273–80.

[80] Parmar RD, Kundu A, Thurgood C, Peppley BA, Karan K. Kinetic studies of the autothermal reforming of tetradecane over Pt/Al_2O_3 catalyst in a fixed-bed reactor. Fuel 2010;89(6):1212–20.

[81] Rostrup-Nielsen J. In: Anderson JR, Boudard M, editors. Catalytic steam reforming. Catalysis Science and Technology, vol. 5. Berlin: Springer-Verlag; 1984. p. 1–118.

[82] Zaera F. Selectivity in hydrocarbon catalytic reforming: a surface chemistry perspective. Appl Catal A: Gen 2002;229(1−2):75−91.
[83] Reitz TL, Ahmed S, Krumpelt M, Kumar R, Kung HH. Characterization of CuO/ZnO under oxidizing conditions for the oxidative methanol reforming reaction. J Mol Catal A: Chem 2000;162(1−2):275−85.
[84] Mizsey P, Newson E, Truong T-b, Hottinger P. The kinetics of methanol decomposition: a part of autothermal partial oxidation to produce hydrogen for fuel cells. Appl Catal A: Gen 2001;213(2):233−7.
[85] Wei J, Iglesia E. Mechanism and site requirements for activation and chemical conversion of methane on supported Pt clusters and turnover rate comparisons among noble metals. J Phys Chem B 2004;108:4094−103.
[86] Barbier J, Corro G, Marecot P, Bournonville JP, Franck JP. Structure sensitivity and coke formation on Pt/Al_2O_3 catalysts. React Kinet Catal Lett 1985;28 (2):245−50.
[87] Barbier J, Corro G, Zhang Y, Bournonville JP, Franck JP. Coke formation on platinum-alumina catalyst of wide varying dispersion. Appl Catal 1985;13(2):245−55.
[88] Barbier J, Marecot P. Effect of presulfurization on the formation of coke on supported metal catalysts. J Catal 1986;102(1):21−8.
[89] Sehested J. Four challenges for nickel steam-reforming catalysts. Catal Today 2006;111(1−2):103−10.
[90] Choudhary TV, Goodman DW. Methane activation on Ni and Ru model catalysts. J Mol Catal A: Chem 2000;163(1−2):9−18.
[91] Schuurman Y, Mirodatos C. Uses of transient kinetics for methane activation studies. Appl Catal A: Gen 1997;151(1):305−31.
[92] Jones G, Jakobsen JG, Shim SS, Kleis J, Andersson MP, Rossmeisl J, et al. First principles calculations and experimental insight into methane steam reforming over transition metal catalysts. J Catal 2008;259(1):147−60.
[93] Liao M-S, Zhang Q-E. Dissociation of methane on different transition metals. J Mol Catal A: Chem 1998;136(2):185−94.
[94] Trimm DL. Catalysts for the control of coking during steam reforming. Catal Today 1999;49(1−3):3−10.
[95] Bartholomew CH. Mechanisms of catalyst deactivation. Appl Catal A: Gen 2001;212(1−2):17−60.
[96] Wang H, Liu Y, Wang L, Qin YN. Study on the carbon deposition in steam reforming of ethanol over Co/CeO2 catalyst. Chem Eng J 2008;145(1):25−31.
[97] Wang HY, Ruckenstein E. Formation of filamentous carbon during methane decomposition over Co-MgO catalysts. Carbon 2002;40(11):1911−7.
[98] Gould BD, Chen X, Schwank JW. n-Dodecane reforming over nickel-based monolith catalysts: deactivation and carbon deposition. Appl Catal A: Gen 2008;334(1−2):277−90.
[99] Li B, Watanabe R, Maruyama K, Kunimori K, Tomishige K. Thermographical observation of catalyst bed temperature in oxidative steam reforming of methane over Ni supported on [alpha]-alumina granules: effect of Ni precursors. Catal Today 2005; 104(1):7−17.
[100] Yoshida K, Begum N, Ito S-i, Tomishige K. Oxidative steam reforming of methane over $Ni/[alpha]\text{-}Al_2O_3$ modified with trace noble metals. Appl Catal A: Gen 2009;358(2):186−92.
[101] Greenly J, Mavrikakis M. Alloy catalysts designed from first principles. Nat Mater 2004;3:810−5.
[102] Bozzolo G, Noebe RD, Khalil J, Morse J. Atomistic analysis of surface segregation in Ni-Pd alloys. Appl Surf Sci 2003;219(1−2):149−57.
[103] Parizotto NV, Zanchet D, Rocha KO, Marques CMP, Bueno JMC. The effects of Pt promotion on the oxi-reduction properties of alumina supported nickel catalysts for oxidative steam-reforming of methane: temperature-resolved XAFS analysis. Appl Catal A: Gen 2009;366(1): 122−9.
[104] Yoshida K, Okumura K, Miyao T, Naito S, Ito S-i, Kunimori K, et al. Oxidative steam reforming of methane over $Ni/[alpha]\text{-}Al_2O_3$ modified with trace Pd. Appl Catal A: Gen 2008;351(2):217−25.
[105] Mukainakano Y, Li B, Kado S, Miyazawa T, Okumura K, Miyao T, et al. Surface modification of Ni catalysts with trace Pd and Rh for oxidative steam reforming of methane. Appl Catal A: Gen 2007;318: 252−64.
[106] Dantas SC, Escritori JC, Soares RR, Hori CE. Effect of different promoters on $Ni/CeZrO_2$ catalyst for autothermal reforming and partial oxidation of methane. Chem Eng J 2010;156(2): 380−7.
[107] Dias JAC, Assaf JM. Autothermal reforming of methane over $Ni/[gamma]\text{-}Al_2O_3$ catalysts: the enhancement effect of small quantities of noble metals. J Power Sources 2004;130(1−2):106−10.
[108] Nikolla E, Schwank J, Linic S. Comparative study of the kinetics of methane steam reforming on supported Ni and Sn/Ni alloy catalysts: the impact of the formation of Ni alloy on chemistry. J Catal 2009; 263(2):220−7.
[109] Takanabe K, Nagaoka K, Nariai K, Aika K-i. Titania-supported cobalt and nickel bimetallic catalysts for carbon dioxide reforming of methane. J Catal 2005; 232(2):268−75.

[110] Parizotto NV, Fernandez RF, Marques CMP, Bueno JMC. Promoter effect of Ag and La on stability of Ni/Al_2O_3 catalysts in reforming of methane processes. In: 8th natural gas conversion symposium. Brazil: 2007.

[111] Chin Y-H, King DL, Roh H-S, Wang Y, Heald SM. Structure and reactivity investigations on supported bimetallic AuNi catalysts used for hydrocarbon steam reforming. J Catal 2006;244(2):153–62.

[112] San-José-Alonso D, Juan-Juan J, Illán-Gómez MJ, Román-Martínez MC. Ni, Co and bimetallic Ni-Co catalysts for the dry reforming of methane. Appl Catal A: Gen 2009;371(1–2):54–9.

[113] Zhang J, Wang H, Dalai AK. Development of stable bimetallic catalysts for carbon dioxide reforming of methane. J Catal 2007;249(2):300–10.

[114] Koh ACW, Chen L, Kee Leong W, Johnson BFG, Khimyak T, Lin J. Hydrogen or synthesis gas production via the partial oxidation of methane over supported nickel-cobalt catalysts. Int J Hydrogen Energy 2007;32(6):725–30.

[115] Xu J, Zhou W, Li Z, Wang J, Ma J. Biogas reforming for hydrogen production over nickel and cobalt bimetallic catalysts. Int J Hydrogen Energy 2009; 34(16):6646–54.

[116] Nikolla E, Schwank J, Linic S. Promotion of the long-term stability of reforming Ni catalysts by surface alloying. J Catal 2007;250(1):85–93.

[117] Nikolla E, Schwank JW, Linic S. Hydrocarbon steam reforming on Ni alloys at solid oxide fuel cell operating conditions. Catal Today 2008;136(3–4):243–8.

[118] Lee WS, Kim TY, Woo SI. High-throughput screening for the promoters of alumina supported Ni catalysts in autothermal reforming of methane. Top Catal 2010;53:123–8.

[119] Omata K, Endo Y, Ishii H, Masuda A, Yamada M. Effective additives of Ni/-Al_2O_3 catalyst at low methane conversion of oxidative reforming for syngas formation. Appl Catal A: Gen 2008;351(1):54–8.

[120] Ghenciu AF. Review of fuel processing catalysts for hydrogen production in PEM fuel cell systems. Curr Opin Solid State Mater Sci 2002;6(5):389–99.

[121] Lisboa JDS, Santos DCRM, Passos FB, Noronha FB. Influence of the addition of promoters to steam reforming catalysts. Catal Today 2005;101(1):15–21.

[122] Twigg MV. Catalyst handbook. 2nd ed. London: Manson Publishing; 1996.

[123] Ruckenstein E, Hang Hu Y. Methane partial oxidation over NiO/MgO solid solution catalysts. Appl Catal A: Gen 1999;183(1):85–92.

[124] Wang HY, Ruckenstein E. Carbon dioxide reforming of methane to synthesis gas over supported rhodium catalysts: the effect of support. Appl Catal A: Gen 2000;204(1):143–52.

[125] Erdohelyi A, Cserenyi J, Solymosi F. Activation of CH_4 and its reaction with CO_2 over supported Rh catalysts. J Catal 1993;141(1):287–99.

[126] Mark MF, Maier WF. CO_2-reforming of methane on supported Rh and Ir catalysts. J Catal 1996;164 (1):122–30.

[127] Wei J, Iglesia E. Structural requirements and reaction pathways in methane activation and chemical conversion catalyzed by rhodium. J Catal 2004;225 (1):116–27.

[128] Alvarez-Galvan MC, Navarro RM, Rosa F, Briceño Y, Gordillo Alvarez F, Fierro JLG. . Performance of La, Ce-modified alumina-supported Pt and Ni catalysts for the oxidative reforming of diesel hydrocarbons. Int J Hydrogen Energy 2008;33(2):652–63.

[129] Zhang ZL, Tsipouriari VA, Efstathiou AM, Verykios XE. Reforming of methane with carbon dioxide to synthesis gas over supported rhodium catalysts: I. Effects of support and metal cystallite size on reaction activity and deactivation characteristics. J Catal 1996;158(1):51–63.

[130] Nakamura J, Aikawa K, Sato K, Uchijima T. Role of support in reforming of CH_4 with CO_2 over Rh Catalysts. Catal Lett 1994;25(3–4):265–70.

[131] Freni S, Calogero G, Cavallaro S. Hydrogen production from methane through catalytic partial oxidation reactions. J Power Sources 2000;87(1–2): 28–38.

[132] Youn MH, Seo JG, Lee H, Bang Y, Chung JS, Song IK. Hydrogen production by auto-thermal reforming of ethanol over nickel catalysts supported on metal oxides: effect of support acidity. Appl Catal B: Env 2010;98(1–2):57–64.

[133] Ferrandon M, Krause T. Role of the oxide support on the performance of Rh catalysts for the autothermal reforming of gasoline and gasoline surrogates to hydrogen. Appl Catal A: Gen 2006;311: 135–45.

[134] Råberg LB, Jensen MB, Olsbye U, Daniel C, Haag S, Mirodatos C, et al. Propane dry reforming to synthesis gas over Ni-based catalysts: influence of support and operating parameters on catalyst activity and stability. J Catal 2007;249(2):250–60.

[135] Christian Enger B, Lødeng R, Holmen A. A review of catalytic partial oxidation of methane to synthesis gas with emphasis on reaction mechanisms over transition metal catalysts. Appl Catal A: Gen 2008;346(1–2):1–27.

[136] Alvarez-Galvan MC, Navarro RM, Rosa F, Briceño Y, Ridao MA, Fierro JLG. Hydrogen production for fuel cell by oxidative reforming of diesel surrogate: influence of ceria and/or lanthana over the activity of Pt/Al_2O_3 catalysts. Fuel 2008;87(12):2502–11.

[137] Santos DCRM, Madeira L, Passos FB. The effect of the addition of Y_2O_3 to Ni/[alpha]-Al_2O_3 catalysts on the autothermal reforming of methane. Catal Today 2010;149(3−4):401−6.

[138] Cai X, Cai Y, Lin W. Autothermal reforming of methane over Ni catalysts supported over ZrO_2-CeO_2-Al_2O_3. J Nat Gas Chem 2008;17:201−7.

[139] Choudhary VR, Mamman AS. Energy efficient conversion of methane to synthesis gas over NiO-MgO solid solution. Appl Energy 2000;66: 161−75.

[140] Choudhary VR, Rajput AM, Mamman AS. NiO-alkaline earth oxide catalysts for oxidative methane-to-syngas conversion: influence of alkaline earth oxide on the surface properties and temperature-programmed reduction/reaction by H_2 and methane. J Catal 1998;178(2):576−85.

[141] Choudhary VR, Uphade BS, Mamman AS. Oxidative conversion of methane to syngas over nickel supported on commercial low surface area porous catalyst carriers precoated with alkaline and rare earth oxides. J Catal 1997;172(2):281−93.

[142] Wang S, Lu GQM. CO_2 reforming of methane on Ni catalysts: effects of the support phase and preparation technique. Appl Catal B: Env 1998;16 (3):269−77.

[143] Vlaic G, Di Monte R, Fornasiero P, Fonda E, Kaspar J, Graziani M. Redox property-local structure relationships in the Rh-loaded CeO_2-ZrO_2 mixed oxides. J Catal 1999;182(2):378−89.

[144] Fornasiero P, Balducci G, Di Monte R, Kaspar J, Sergo V, Gubitosa G, et al. Modification of the Redox Behaviour of CeO_2 Induced by Structural Doping with ZrO_2. J Catal 1996;164(1): 173−83.

[145] Laosiripojana N, Chadwick D, Assabumrungrat S. Effect of high surface area CeO_2 and Ce-ZrO_2 supports over Ni catalyst on CH_4 reforming with H_2O in the presence of O_2, H_2, and CO_2. Chem Eng J 2008;138(1−3):264−73.

[146] Cao L, Pan L, Ni C, Yuan Z, Wang S. Autothermal reforming of methane over Rh/$Ce_{0.5}Zr_{0.5}O_2$ catalyst: effects of the crystal structure of the supports. Fuel Process Technol 2010;91(3):306−12.

[147] Yuan Z, Ni C, Zhang C, Gao D, Wang S, Xie Y, et al. Rh/MgO/$Ce_{0.5}Zr_{0.5}O_2$ supported catalyst for autothermal reforming of methane: the effects of ceria-zirconia doping. Catal Today 2009;146(1−2): 124−31.

[148] Sacco A, Geurts FWAH, Jablonski GA, Lee S, Gately RA. Carbon deposition and filament growth on Fe, Co, and Ni foils using CH_4−H_2−H_2O−CO−CO_2 gas mixtures. J Catal 1989;119(2):322−41.

[149] Wang HY, Ruckenstein E. Partial oxidation of methane to synthesis gas over alkaline earth metal oxide supported cobalt catalysts. J Catal 2001;199(2): 309−17.

[150] Profeti LPR, Ticianelli EA, Assaf EM. Co/Al_2O_3 catalysts promoted with noble metals for production of hydrogen by methane steam reforming. Fuel 2008;87(10−11):2076−81.

[151] Hu X, Lu G. Comparative study of alumina-supported transition metal catalysts for hydrogen generation by steam reforming of acetic acid. Appl Catal B: Env 2010;99(1−2):289−97.

[152] Slagtern Å, Swaan HM, Olsbye U, Dahl IM, Mirodatos C. Catalytic partial oxidation of methane over Ni-, Co- and Fe-based catalysts. Catal Today 1998;46(2−3):107−15.

[153] Valdes-Perez RE, Fishtik I, Zeigarnik AV. Predictions of activity patterns for methane reforming based on combinatorial pathway generation and energetic. In: American Chemical Society, Division of Fuel Chemistry; 1999. p. 541−4.

[154] Panuccio GJ, Schmidt LD. Species and temperature profiles in a differential sphere bed reactor for the catalytic partial oxidation of n-octane. Appl Catal A: Gen 2007;332(2):171−82.

[155] Krummenacher JJ, Schmidt LD. High yields of olefins and hydrogen from decane in short contact time reactors: rhodium versus platinum. J Catal 2004;222(2):429−38.

[156] Wang R, Liu X, Chen Y, Li W, Xu H. Effect of metal-support interaction on coking resistance of Rh-based catalysts in CH_4/CO_2 reforming. Chin J Catal 2007;28(10):865−9.

[157] Burch R, Loader PK, Cruise NA. An investigation of the deactivation of Rh/alumina catalysts under strong oxidising conditions. Appl Catal A: Gen 1996;147(2):375−94.

[158] Cao L, Ni C, Yuan Z, Wang S. Autothermal reforming of methane over CeO_2-ZrO_2-La_2O_3 supported Rh catalyst. Catal Lett 2009;131:474−9.

[159] Bunluesin T, Gorte RJ, Graham GW. Studies of the water-gas-shift reaction on ceria-supported Pt, Pd, and Rh: implications for oxygen-storage properties. Appl Catal B: Env 1998;15(1−2):107−14.

[160] Qin D, Lapszewicz J, Jiang X. Comparison of partial oxidation and steam-CO_2 mixed reforming of CH_4 to syngas on MgO-supported metals. J Catal 1996; 159(1):140−9.

[161] Cao L, Ni C, Yuan Z, Wang S. Correlation between catalytic selectivity and oxygen storage capacity in autothermal reforming of methane over Rh/$Ce_{0.45}Zr_{0.45}RE_{0.1}$ catalysts (RE = La, Pr, Nd, Sm, Eu, Gd, Tb). Catal Comm 2009;10(8):1192−5.

[162] Ferreira AP, Zanchet D, Araújo JCS, Liberatori JWC, Souza-Aguiar EF, Noronha FB, et al. The effects of CeO_2 on the activity and stability of Pt supported catalysts for methane reforming, as addressed by in situ temperature resolved XAFS and TEM analysis. J Catal 2009;263(2):335–44.

[163] Souza MMVM, Schmal M. Autothermal reforming of methane over $Pt/ZrO_2/Al_2O_3$ catalysts. Appl Catal A: Gen 2005;281(1–2):19–24.

[164] Cronauer DC, Krause T, Salinas J, Wagner A, Wagner J. Comparison of Rh, Pt, and Rh-Pt supported on an oxide-ion conducting substrate as catalysts for autothermal reforming of methane. American Chemical Society, Divisions of Fuel Chemistry; 2006. p. 297–9.

[165] Bozo C, Guilhaume N, Garbowski E, Primet M. Combustion of methane on CeO_2-ZrO_2 based catalysts. Catal Today 2000;59(1–2):33–45.

[166] Gélin P, Primet M. Complete oxidation of methane at low temperature over noble metal based catalysts: a review. Appl Catal B: Env 2002;39(1):1–37.

[167] Lyubovsky M, Smith LL, Castaldi M, Karim H, Nentwick B, Etemad S, et al. Catalytic combustion over platinum group catalysts: fuel-lean versus fuel-rich operation. Catal Today 2003;83(1–4):71–84.

[168] Rabe S, Truong T-B, Vogel F. Low temperature catalytic partial oxidation of methane for gas-to-liquids applications. Appl Catal A: Gen 2005;292:177–88.

[169] Requies J, Rabe S, Vogel F, Truong TB, Filonova K, Barrio VL, et al. Reforming of methane over noble metal catalysts: catalyst deactivation induced by thiophene. Catal Today 2009;143(1–2):9–16.

[170] Lim S-S, Lee H-J, Moon D-J, Kim J-H, Park N-C, Shin J-S, et al. Autothermal reforming of propane over Ce modified $Ni/LaAlO_3$ perovskite-type catalysts. Chem Eng J 2009;152(1):220–6.

[171] Silberova B, Venvik HJ, Walmsley JC, Holmen A. Small-scale hydrogen production from propane. Catal Today 2005;100(3–4):457–62.

[172] Aartun I, Venvik HJ, Holmen A, Pfeifer P, Görke O, Schubert K. Temperature profiles and residence time effects during catalytic partial oxidation and oxidative steam reforming of propane in metallic microchannel reactors. Catal Today 2005;110(1–2):98–107.

[173] Barison S, Fabrizio M, Mortalò C, Antonucci P, Modafferi V, Gerbasi R. Novel $Ru/La_{0.75}Sr_{0.25}Cr_{0.5}Mn_{0.5}O_{3-[delta]}$ catalysts for propane reforming in IT-SOFCs. Solid State Ionics 2010; 181(5–7):285–91.

[174] Faria WLS, Dieguez LC, Schmal M. Autothermal reforming of propane for hydrogen production over $Pd/CeO_2/Al_2O_3$ catalysts. Appl Catal B: Env 2008; 85(1–2):77–85.

[175] Recupero V, Pino L, Vita A, CipitI F, Cordaro M, Laganà M. Development of a LPG fuel processor for PEFC systems: laboratory scale evaluation of autothermal reforming and preferential oxidation subunits. Int J Hydrogen Energy 2005;30(9): 963–71.

[176] Vita A, Pino L, Cipitì F, Laganà M, Recupero V. Structured reactors as alternative to pellets catalyst for propane oxidative steam reforming. Int J Hydrogen Energy 2010;35(18):9810–7.

[177] Takehira K. "Intelligent" reforming catalysts: trace noble metal-doped Ni/Mg(Al)O derived from hydrotalcites. J Nat Gas Chem 2009;18(3):237–59.

[178] Lee H-J, Lim Y-S, Park N-C, Kim Y- C. Catalytic autothermal reforming of propane over the noble metal-doped hydrotalcite-type catalysts. Chem Eng J 2009;146(2):295–301.

[179] Miyata T, Li D, Shiraga M, Shishido T, Oumi Y, Sano T, et al. Promoting effect of Rh, Pd and Pt noble metals to the Ni/Mg(Al)O catalysts for the DSS-like operation in CH_4 steam reforming. Appl Catal A: Gen 2006;310:97–104.

[180] Li D, Nishida K, Zhan Y, Shishido T, Oumi Y, Sano T, et al. Sustainable Ru-doped Ni catalyst derived from hydrotalcite in propane reforming. Appl. Clay Sci 2009;43(1):49–56.

[181] Nagaoka K, Jentys A, Lercher JA. Methane autothermal reforming with and without ethane over mono- and bimetal catalysts prepared from hydrotalcite precursors. J Catal 2005;229(1):185–96.

[182] Liu D-J, Krumpelt M, Chien H-T, Sheen SH. Catalysts and fuel mixing for diesel reformer in fuel cell auxiliary power unit. In: Fuel Cell Seminar. San Antonio, TX: 2004.

[183] Moon DJ, Ryu JW, Lee SD, Ahn BS. Partial oxidation (POX) reforming of gasoline for fuel-cell powered vehicles applications. Korean J Chem Eng 2002; 19(6):921–7.

[184] Kim DH, Ryu JW, Choi EH, Gong GT, Lee H, Lee BG, et al. Production of synthesis gas by autothermal reforming of iso-octane and toluene over metal modified Ni-based catalyst. Catal Today 2008;136 (3–4):266–72.

[185] Moon DJ, Ryu JW, Lee SD, Lee BG, Ahn BS. Ni-based catalyst for partial oxidation reforming of iso-octane. Appl Catal A: Gen 2004;272(1–2):53–60.

[186] Gould BD, Chen X, Schwank JW. Dodecane reforming over nickel-based monolith catalysts. J Catal 2007;250(2):209–21.

[187] Gould BD, Tadd AR, Schwank JW. Nickel-catalyzed autothermal reforming of jet fuel surrogates: n-Dodecane, tetralin, and their mixture. J Power Sources 2007;164(1):344–50.

[188] Chen X, Gould BD, Schwank JW. n-Dodecane reforming over monolith-based Ni catalysts: SEM study of axial carbon distribution profile. Appl Catal A: Gen 2009;356(2):137–47.

[189] Chen X, Tadd AR, Schwank JW. Carbon deposited on Ni/CeZrO isooctane autothermal reforming catalysts. J Catal 2007;251(2):374–87.

[190] Erri P, Dinka P, Varma A. Novel perovskite-based catalysts for autothermal JP-8 fuel reforming. Chem Eng Sci 2006;61(16):5328–33.

[191] Navarro RM, Alvarez-Galvan MC, Villoria JA, González-Jiménez ID, Rosa F, Fierro JLG. Effect of Ru on $LaCoO_3$ perovskite-derived catalyst properties tested in oxidative reforming of diesel. Appl Catal B: Env 2007;73(3–4):247–58.

[192] Villoria JA, Alvarez-Galvan MC, Navarro RM, Briceño Y, Gordillo Alvarez F, Rosa F, et al. Zirconia-supported $LaCoO_3$ catalysts for hydrogen production by oxidative reforming of diesel: optimization of preparation conditions. Catal Today 2008;138 (3–4):135–40.

[193] Mawdsley JR, Krause TR. Rare earth-first-row transition metal perovskites as catalysts for the autothermal reforming of hydrocarbon fuels to generate hydrogen. Appl Catal A: Gen 2008;334(1–2):311–20.

[194] Qi A, Wang S, Fu G, Ni C, Wu D. La-Ce-Ni-O monolithic perovskite catalysts potential for gasoline autothermal reforming system. Appl Catal A: Gen 2005;281(1–2):233–46.

[195] Horiuchi T, Sakuma K, Fukui T, Kubo Y, Osaki T, Mori T. Suppression of carbon deposition in the CO_2-reforming of CH_4 by adding basic metal oxides to a Ni/Al_2O_3 catalyst. Appl Catal A: Gen 1996;144 (1–2):111–20.

[196] Dinka P, Mukasyan AS. Perovskite catalysts for the auto-reforming of sulfur containing fuels. J Power Sources 2007;167(2):472–81.

[197] Díaz A, Odriozola JA, Montes M. Influence of alkali additives on activity and toxicity of H_2S and thiophene over a Ni/SiO_2 catalyst. Appl Catal A: Gen 1998;166(1):163–72.

[198] Krause T, Mawdsley J, Rossignol C, Kopasz J, Applegate D, Ferrandon M, et al. DOE progress report for hydrogen, fuel cells, and infrastructures technologies program 2002:332–6.

[199] Mawdsley J, Ferrandon M, Rossignol C, Ralph J, Miller L, Kopasz J, et al. DOE progress report for hydrogen, fuel cells, and infrastructures technologies program- catalysts for autothermal reforming 2003:1–5.

[200] Houghtby WE, Buswell RF, Bett JAS, Lesieur RR, Meyer AP, Preston JL, et al. Development of the adiabatic reformer to process No. 2 fuel oil and coal-derived liquid fuels. Electric Power Research Institute; Feb. 1981.

[201] Setzer HJ, Lesieur RR, Karavolis S, Wnuck WG. Autothermal reforming catalyst and process. U.S. Patent No. 4473543 to USA: United Technologies Corp; 1984.

[202] Wieland S, Baumann F, Ahlborn R. Process for the autothermal catalytic steam reforming of hydrocarbons. U.S.A: 2002.

[203] Wieland S, Baumann F, Starz K-A. New catalysts for autothermal reforming of gasoline and water gas shift reaction. In: Fuel cell seminar. Portland, OR: 2000.

[204] Springmann S, Friedrich G, Himmen M, Sommer M, Eigenberger G. Isothermal kinetic measurements for hydrogen production from hydrocarbon fuels using a novel kinetic reactor concept. Appl Catal A: Gen 2002;235(1–2):101–11.

[205] Brandmair M, Apfel H, Find J, Cremers C, Stimming U, Lercher J. Kilowatt-scale autothermal gasoline reformer for mobile applications. In: Fuel cell seminar. Miami, FL: 2003.

[206] Reyes SC, Sinfelt JH, Feeley JS. Evolution of processes for synthesis gas production: recent developments in an old technology. Ind Eng Chem Res 2003;42(8):1588–97.

[207] Yanhui W, Diyong W. The experimental research for production of hydrogen from n-octane through partially oxidizing and steam reforming method. Int J Hydrogen Energy 2001;26(8):795–800.

[208] Zhang J, Wang Y, Ma R, Wu D. Characterization of alumina-supported Ni and Ni-Pd catalysts for partial oxidation and steam reforming of hydrocarbons. Appl Catal A: Gen 2003;243(2):251–9.

[209] Zhang J, Wang Y, Ma R, Wu D. Investigation of alumina-supported Ni and Ni-Pd catalysts for partial oxidation and steam reforming of n-octane. Korean J Chem Eng 2003;20(2):288–92.

[210] Berry DA, Shekhawat D, Gardner TH, Rogers W. Fuel processing of diesel fuel for auxiliary power units. In U.S. DOE Progress Report for Hydrogen, Fuel Cells, and Infrastructure Technologies Program; 2002. p. 337–41.

[211] Ham DO, Lewis PF, Lord GW, Yarrington RM, Hwang HS. Hydrocarbon auththermal reforming program Corp. E, Editor. Feb. 1982.

[212] Heck RM, Flanagan P. Catalytic partial oxidation process. USA: Engelhard Corp; 1989.

[213] Hwang HS, Heck RM, Yarrington RM. Fuel cell electric power production. U.S. Patent No. 4522894, to USA: Engelhard Corp; 1985.

[214] Dunn S. Hydrogen futures: toward a sustainable energy system. Int J Hydrogen Energy 2002;27(3): 235–64.

[215] Cheekatamarla PK, Lane AM. Efficient bimetallic catalysts for the hydrogen production from diesel fuel. Prepr Symp − Am Chem Soc Div Fuel Chem 2004;49(1):139−41.

[216] Cheekatamarla PK, Lane AM. Efficient bimetallic catalysts for hydrogen generation from diesel fuel. Int J Hydrogen Energy 2005;30(11):1277−85.

[217] Liu D-J, Krumpelt M. Activity and structure of perovskites as diesel-reforming catalysts for solid oxide fuel cells. Int J Appl Ceram Technol 2005;2: 301−7.

[218] Haynes DJ, Berry DA, Shekhawat D, Spivey JJ. Catalytic partial oxidation of n-tetradecane using pyrochlores: effect of Rh and Sr substitution. Catal Today 2008;136(3−4):206−13.

[219] Haynes DJ, Berry DA, Shekhawat D, Spivey JJ. Catalytic partial oxidation of n-tetradecane using Rh and Sr substituted pyrochlores: effects of sulfur. Catal Today 2009;145(1−2):121−6.

[220] Haynes DJ, Campos A, Berry DA, Shekhawat D, Roy A, Spivey JJ. Catalytic partial oxidation of a diesel surrogate fuel using an Ru-substituted pyrochlore. Catal Today 2010;155(1−2):84−91.

[221] Haynes DJ, Campos A, Smith MW, Berry DA, Shekhawat D, Spivey JJ. Reducing the deactivation of Ni-metal during the catalytic partial oxidation of a surrogate diesel fuel mixture. Catal Today 2010; 154(3−4):210−6.

[222] Haynes DJ, Smith MW, Shekhawat D, Berry DA, Spivey JJ. Long term reforming of commercial diesel fuel using a layered pyrochlore catalyst. In: ACS Spring National Meeting. San Francisco, CA: 2010.

[223] Chang C-C, Chang C-T, Chiang S-J, Liaw B-J, Chen Y.- Z. Oxidative steam reforming of methanol over $CuO/ZnO/CeO_2/ZrO_2/Al_2O_3$ catalysts. Int J Hydrogen Energy 2010;35(15):7675−83.

[224] Agrell J, Birgersson H, Boutonnet M, Melián-Cabrera I, Navarro RM, Fierro JLG. Production of hydrogen from methanol over Cu/ZnO catalysts promoted by ZrO2 and Al2O3. J Catal 2003;219(2):389−403.

[225] Matter PH, Ozkan US. Effect of pretreatment conditions on Cu/Zn/Zr-based catalysts for the steam reforming of methanol to H_2. J Catal 2005; 234(2):463−75.

[226] Turco M, Cammarano C, Bagnasco G, Moretti E, Storaro L, Talon A, et al. Oxidative methanol steam reforming on a highly dispersed $CuO/CeO_2/Al_2O_3$ catalyst prepared by a single-step method. Appl Catal B: Env 2009;91(1−2):101−7.

[227] Patel S, Pant KK. Hydrogen production by oxidative steam reforming of methanol using ceria promoted copper-alumina catalysts. Fuel Process Technol 2007; 88(8):825−32.

[228] Patel S, Pant KK. Kinetic modeling of oxidative steam reforming of methanol over $Cu/ZnO/CeO_2/Al_2O_3$ catalyst. Appl Catal A: Gen 2009;356(2): 189−200.

[229] Lindström B, Pettersson LJ, Govind Menon P. Activity and characterization of Cu/Zn, Cu/Cr and Cu/Zr on [gamma]-alumina for methanol reforming for fuel cell vehicles. Appl Catal A: Gen 2002;234 (1−2):111−25.

[230] Breen JP, Ross JRH. Methanol reforming for fuel-cell applications: development of zirconia-containing Cu-Zn-Al catalysts. Catal Today 1999;51(3−4): 521−33.

[231] Shen J-P, Song C. Influence of preparation method on performance of Cu/Zn-based catalysts for low-temperature steam reforming and oxidative steam reforming of methanol for H_2 production for fuel cells. Catal Today 2002;77(1−2):89−98.

[232] Günter MM, Ressler T, Jentoft RE, Bems B. Redox behavior of copper oxide/zincoxide catalysts in the steam reforming of methanol studied by in situ x-ray diffraction and absorption spectroscopy. J Catal 2001;203(1):133−49.

[233] Durga Kumari V, Subrahmanyam M, Ratnamala A, Venugopal D, Srinivas B, Phanikrishna Sharma MV, et al. Correlation of activity and stability of $CuO/ZnO/Al_2O_3$ methanol steam reforming catalysts with Cu/Zn composition obtained by SEM-EDAX analysis. Catal Comm 2002;3(9):417−24.

[234] Shan W, Feng Z, Li Z, Zhang J, Shen W, Li C. Oxidative steam reforming of methanol on $Ce_{0.9}Cu_{0.1}O_Y$ catalysts prepared by deposition-precipitation, coprecipitation, and complexation-combustion methods. J Catal 2004;228(1):206−17.

[235] Esposito S, Turco M, Bagnasco G, Cammarano C, Pernice P, Aronne A. Highly dispersed sol-gel synthesized $Cu-ZrO_2$ materials as catalysts for oxidative steam reforming of methanol. Appl Catal A: Gen 2010;372(1):48−57.

[236] Yao C-Z, Wang L-C, Liu Y-M, Wu G-S, Cao Y, Dai W-L, et al. Effect of preparation method on the hydrogen production from methanol steam reforming over binary Cu/ZrO_2 catalysts. Appl Catal A: Gen 2006;297(2):151−8.

[237] Wang L-C, Liu Y-M, Chen M, Cao Y, He H-Y, Wu G-S, et al. Production of hydrogen by steam reforming of methanol over Cu/ZnO catalysts prepared via a practical soft reactive grinding route based on dry oxalate-precursor synthesis. J Catal 2007;246(1):193−204.

[238] Hong X, Ren S. Selective hydrogen production from methanol oxidative steam reforming over Zn-Cr catalysts with or without Cu loading. Int J Hydrogen Energy 2008;33(2):700−8.

[239] Youn MH, Seo JG, Cho MK, Jung JC, Kim H, La KW, et al. Effect of support on hydrogen production by auto-thermal reforming of ethanol over supported nickel catalyst. Korean J Chem Eng 2008;25:236–8.

[240] Chen H, Yu H, Tang Y, Pan M, Yang G, Peng F, et al. Hydrogen production via autothermal reforming of ethanol over noble metal catalysts supported on oxides. J Nat Gas Chem 2009;18(2):191–8.

[241] Salge JR, Deluga GA, Schmidt LD. Catalytic partial oxidation of ethanol over noble metal catalysts. J Catal 2005;235(1):69–78.

[242] Siefert N, Shekhawat D, Gemmen R, Berry DA, Robey E, Bergen R, et al. Operation of a solid oxide fuel cell on biodiesel with a partial oxidation reformer. Fuel Cell 2010–33326. Brooklyn, NY: ASME; 2010.

CHAPTER

7

Dry (CO_2) Reforming

Jing Gao, Zhaoyin Hou, Hui Lou, Xiaoming Zheng

Department of Chemistry, Zhejiang University, Hangzhou, China

OUTLINE

7.1. INTRODUCTION

Hydrogen is forecasted to be a major source of eco-friendly clean fuel and energy carriers in future. It can be efficiently converted to electricity in fuel cells with lower emission of greenhouse gases. The development of new methods that can produce hydrogen increased quickly because of the rapid progress and demand in fuel cell technology. Until now, hydrocarbon reforming with steam, particularly steam reforming of CH_4, is generally the largest and most economic way to produce hydrogen.

Since 1993, production of hydrogen via dry (CO_2) reforming of methane and propane (Eqs (7.1) and (7.2)) and followed water-gas shift reaction (Eq. 7.3) have received much attention because of the utilization of greenhouse gases (both hydrocarbons and CO_2).

$$\begin{aligned} CH_4(g) + CO_2(g) &= 2CO(g) + 2H_2(g) \\ \Delta H^{o}_{298K} &= 247.2\ \text{kJ/mol} \end{aligned} \tag{7.1}$$

$$\begin{aligned} C_3H_8(g) + 3CO_2(g) &= 6CO(g) + 4H_2(g) \\ \Delta H^{o}_{298K} &= 644.8\ \text{kJ/mol} \end{aligned} \tag{7.2}$$

$$\begin{aligned} CO(g) + H_2O(g) &= CO_2(g) + H_2(g) \\ \Delta H^{o}_{298K} &= -42.1\ \text{kJ/mol} \end{aligned} \tag{7.3}$$

And more recently, reforming of biomass and biomass-derived oxygenates (such as ethanol, dimethyl ether, and glycerol) to H_2-rich synthesis gas is also a hot research topic.

Among the published papers, dry reforming of methane is the largest and the most economical way to produce hydrogen. More than 1800 papers have been published until April 2010, and most of these contributions were well summarized by Bradford and Vannice [1], Hu and Ruckenstein [2,3], Rostrup-Nielsen et al. [4], York et al. [5], and P. Ferreira-Aparicio et al. [6].

In this chapter, we want to introduce the recent progress in production of H_2-rich synthesis gas via dry reforming of hydrocarbons (methane, ethane, propane, and *n*-octane) and oxygenates mainly on the basis of papers published after 2004. In general, this process is attractive from the environmental and economical view point because of the potential utilization of greenhouse gases as resources, but dry reforming of hydrocarbons is highly energy consuming and catalyst deactivation.

7.2. THERMODYNAMICS

7.2.1. Heat of Reaction

Table 7.1 summarizes the thermodynamics parameters of dry reforming of methane, ethane, propane, *n*-butane, *n*-pentane, and *n*-hexane. It is found that all these reforming reactions are endothermic, and the calculated enthalpy (ΔH) increases with the number of carbon atom in hydrocarbons. At the same time, the calculated Gibbs free energies decrease with the increasing temperature, indicating that dry reforming proceeds more easily at higher temperature. It is also worth noting that the spontaneous occurring temperature of dry reforming reaction (at which ΔG reaches 0 kJ/mol) decreases with increasing carbon atoms.

7.2.2. Equilibrium Conversion

7.2.2.1. Effect of CO_2/Fuel Ratio

The stoichiometric molar ratio of CO_2/CH_4 is 1 in dry reforming of CH_4 (Eq. 7.1). Excess amount of CO_2 in feed could increase the conversion of methane. Figure 7.1 shows the plot of CO_2/CH_4 feed ratio versus equilibrium amount of product species at 750 °C and 900 °C. Both CO and H_2 are major products in a wide range of CO_2/CH_4 ratios at elevated temperatures; feeding CO_2/CH_4 at a ratio of 1.0 mainly yields CO and H_2. Higher CO yield could be

TABLE 7.1 Thermodynamic Properties of Dry Reforming of Hydrocarbons

Reaction	T/°C	ΔH (kJ/mol)	ΔG (kJ/mol)
$CH_4(g) + CO_2(g) = 2CO(g) + 2H_2(g)$	300	256.0	96.6
	400	257.8	68.6
	500	258.9	40.4
	600	259.6	12.4
	700	259.9	−16.3
	800	259.9	−44.7
	900	259.5	−73.0
	1000	258.8	−101.4
$C_2H_6(g) + 2CO_2(g) = 4CO(g) + 3H_2(g)$	700	446.8	−103.4
$C_3H_8(g) + 3CO_2(g) = 6CO(g) + 4H_2(g)$	700	641.1	−182.5
$C_4H_{10}(g) + 4CO_2(g) = 8CO(g) + 5H_2(g)$	700	838.1	−258.2
$C_5H_{12}(g) + 5CO_2(g) = 10CO(g) + 6H_2(g)$	700	1032.8	−337.2
$C_6H_{14}(g) + 6CO_2(g) = 12CO(g) + 7H_2(g)$	700	1229.9	−416.4

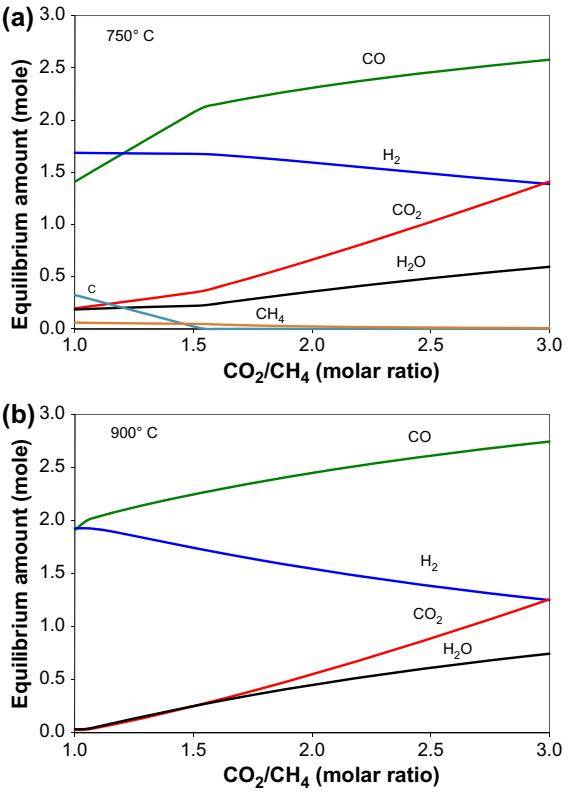

FIGURE 7.1 Effect of CO_2/CH_4 ratio on dry reforming of methane; equilibrium amount of product species from 1 mole of methane at 750 °C (a) and 900 °C (b), 0.1 MPa (The amount of carbon (C) and CH_4 formed are not shown for 900 °C (b) since their concentrations in the reaction product are low).

achieved with rising CO_2/CH_4 ratio, but the yield of H_2 decreases as the formation of byproduct H_2O via the reverse water-gas shift reaction (Eq. 7.4).

$$CO_2(g) + H_2(g) = CO(g) + H_2O(g)$$
$$\Delta H^{o}_{298K} = 42.1 \text{ kJ/mol} \qquad (7.4)$$

7.2.2.2. *Effect of Temperature and Pressure*

Figure 7.2 illustrates the effect of temperature on a stoichiometric mixture of methane and CO_2 at a constant pressure (0.1 MPa) with an O/C=1 in feed. It is quite clear that methane is the most stable molecular structure during dry reforming reaction. There is no significant conversion of methane and CO_2 below 500 °C, and the calculated equilibrium conversion of methane is 95.6% at 800 °C. The final H_2/CO ratio in product gas reaches 1.08 in dry reforming of methane. Higher conversion and higher selectivity to H_2 and CO are obtained with increasing temperatures.

Pressure also plays an important role in the equilibrium composition in dry reforming. Because all dry reforming reactions are volume expansion processes, increasing pressure is unfavorable. As shown in Fig. 7.3, the conversions of methane and CO_2 and the yield of H_2 and CO decrease quickly with increasing pressure.

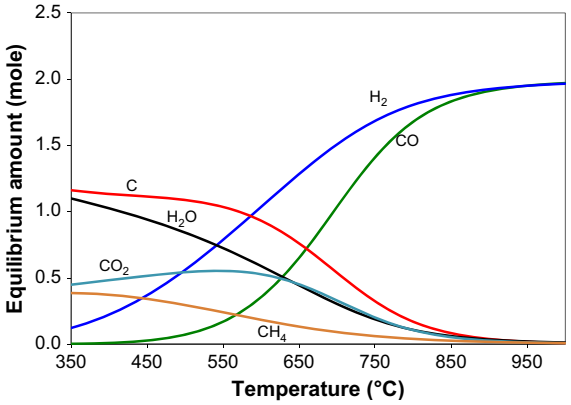

FIGURE 7.2 Effect of temperature on dry reforming of methane; equilibrium amount of product species from 1 mole of methane at 0.1 MPa and O/C = 1.

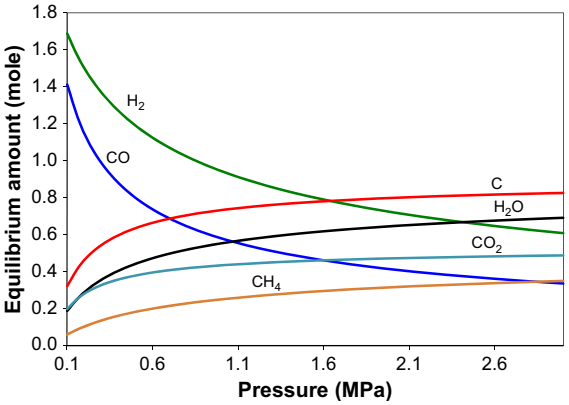

FIGURE 7.3 Effect of pressure on dry reforming of methane; equilibrium amount of product species from 1 mole of methane at 750 °C and O/C = 1.0.

7.3. CATALYSTS FOR DRY REFORMING OF METHANE

Until now, more than 10 kinds of single metals and a large number of alloys have been reported for the dry reforming reactions. Among them, Ni, Co, Rh, and Pt were the most reported catalysts. These catalysts are summarized in Table 7.2.

7.3.1. Ni-Based Catalysts

Due to its higher reactivity, availability, and lower price compared with that of noble metals, nickel is the most frequently reported metal in dry reforming of methane. However, Ni-based catalysts deactivate easily due to carbon deposition and/or metal sintering. Therefore, much efforts have focused on improving the activity and stability of Ni in the following aspects: changing the nature of the support, selecting the support and catalyst preparation method, and the addition of promoters.

Al_2O_3 and SiO_2 supported Ni catalysts have been widely investigated for the dry reforming of methane. Ni/Al_2O_3 and Ni/SiO_2 prepared by impregnation had high initial conversions but deactivated with time due to carbon deposition or sintering [13,39,45,47]. Many modification methods have been studied to improve the performance of Ni/Al_2O_3 and Ni/SiO_2 catalysts, which includes different preparation methods, pretreatments and precursors, or adding metal or oxide promoters to influence the acidity–basicity, the dispersion of Ni, and/or the metal–support interaction.

7.3.1.1. Preparation Methods and Ni Particle Size

Ni-alumina aerogel catalysts showed higher activity and stability with remarkably low coking rate than conventional NiO/Al_2O_3 catalysts prepared via impregnation due to its highly dispersed Ni particles [9,25]. $Ni\text{-}Al_2O_3$ catalyst prepared by sol-gel method also exhibited its effectiveness in the dry reforming reaction of methane with low carbon deposition and stable catalytic activity for 30 h at 750 °C and 0.1 MPa [8].

Ni/SiO_2 catalysts prepared by depositing nickel hydroxides in a sol-gel-derived wet silica gel that possessed high Ni dispersion and high thermal stability also exhibited high and stable

TABLE 7.2 Recently Reported Catalysts for Dry Reforming of Methane

Metal	Support	References
Ni-Only Catalyst		
Ni	Al_2O_3	[7–27]
Ni	Na_2O-Al_2O_3	[28]
Ni	K_2O-Al_2O_3	[28]
Ni	MgO-Al_2O_3	[20,28,29]
Ni	CaO-Al_2O_3	[19,20,28–30]
Ni	MnOx/$MnAl_2O_4$,MnO/γ-Al_2O_3	[31,32]
Ni	La_2O_3-Al_2O_3	[20,29,33–36]
Ni	CeO_2-Al_2O_3	[20,34,37,38]
Ni	ZrO_2-Al_2O_3	[14,38–40]
Ni	CeO_2-ZrO_2-Al_2O_3	[38]
Ni	SiO_2	[10,12,13,24,41–49]
Ni	CaO-MgO-SiO_2	[12]
Ni	MgO	[10,24,46,50–58]
Ni	$MgAl_2O_4$	[59]
Ni	MgO-$MgAl_2O_4$	[60]
Ni	CaO	[19,61,62]
Ni	SrO	[61]
Ni	BaO	[61]
Ni	$BaTiO_3$	[63]
Ni	La_2O_3	[18,19,24,43,64]
Ni	CeO_2	[24,65]
Ni	Yttria-doped ceria	[66]
Ni	CeO_2–La_2O_3	[67]
Ni	Sm_2O_3	[62]
Ni	Sm_2O_3–CaO	[62]
Ni	ZrO_2	[14,68–72]
Ni	CeO_2-ZrO_2	[34,68,73]
Ni	La_2O_3-ZrO_2	[68]
Ni	K_2O-ZrO_2	[68,74]
Ni	TiO_2	[13,46,75]
Ni	SiC	[76,77]
Ni	Alumina-aluminum phosphate	[78]
Ni	USY-zeolite	[79]
Ni	Zeolite A, X, Y, and ZSM-5	[80]
Ni	Zeolite HY	[81,82]
Ni	Zeolite β	[82]
Ni	Mesoporous titania/silica	[83]
Ni	Clinoptilolite	[84]
Ni	Al-pillared montmorillonites	[85]
Ni	Nickel-containing smectite clay	[86]
Ni	Mesoporous Ni/Mg/Al	[87]
Ni	Hydroxyapatite, fluoroapatite	[88]
Promoted Ni catalysts		
Ni-K	Al_2O_3	[8,11,89]
Ni-K	CeO_2-Al_2O_3	[37,90,91]
Ni-K	MnO-Al_2O_3	[37]
Ni-Sn	Al_2O_3	[8]
Ni-Mn	Al_2O_3	[8]
Ni-Ca	Al_2O_3	[8]
Ni-Ca	Ce-ZrO_2	[70]
Ni-Co	Al_2O_3	[7]
Ni-Co	Al-Mg-O	[92]

(*Continued*)

TABLE 7.2 Recently Reported Catalysts for Dry Reforming of Methane (*cont'd*)

Metal	Support	References
Ni-Co	Single-walled carbon nanotubes	[93]
Ni-Ce	Al_2O_3	[7]
Ni-Cu	Al_2O_3	[7]
Ni-Fe	Al_2O_3	[7]
NiCoMg	Zirconia–hafnia	[94]
Ni-Cu	SiO_2	[44]
Rh-Ni	Boron nitride	[95]
Rh-Ni	Al_2O_3	[95–98]
Rh-Ni	SiO_2	[99]
Rh-Ni	MgO	[100]
Rh-Ni	La_2O_3	[101]
Rh-Ni	ZrO_2	[102]
Pt-Ni	MgO	[100]
Pt-Ni	HY	[82]
Pt-Ni	Zeolite β	[82]
Pd-Ni	MgO	[100]
Ni-Me	Me = (Co, Fe, Cu, or Mn) Al–Mg–O	[103]
Ni-Ca	ZrO_2	[104]
Ni-Ce	Mixed oxide	[105]
Perovskite-type catalysts		
	$LaNiO_3$, La_2NiO_4	[67,106–110]
	$LaNi_{1-x}Co_xO_3$	[111]
	$LaNi_{1-y}B_yO_{3-d}$ (B = Mg, Co)	[112]
	$La_{1-x}Sr_xNiO_3$	[113]
	$Ln_{1-x}Ca_xRu_{0.8}Ni_{0.2}O_3$ (Ln = La, Sm, Nd)	[114]
	$M_xLa_{1-x}Ni_{0.3}Al_{0.7}O_{3-d}$ (M = Li, Na, K)	[115]
	$LaNi_{1-x}Rh_xO_3$	[116]
	$La_{1-x}Ce_xNiO_3$	[117]
$LaNiO_x$	ZSM-5	[118,119]
La_2NiO_4	MCM-41	[119]
La_2NiO_4	γ-Al_2O_3	[119]
Co-based catalysts		
Co	Al_2O_3	[120–124]
Co	SiO_2	[120,125]
Co	MgO	[120,126]
Co	CaO	[120]
Co	SrO	[120]
Co	BaO	[120]
Co	TiO_2	[127,128]
Co	Macroporous silica-alumina	[129,130]
Co	MgO-SiO_2	[125]
Noble metal catalysts		
Rh	Al_2O_3	[15,131–140]
Rh	CeO_2/Al_2O_3	[136]
Rh	SiO_2	[141,142]
Rh	La_2O_3-SiO_2	[141,143]
Rh	La_2O_3	[141,144]
Rh	ZrO_2	[138]
Rh	Yttria-stabilized zirconia (YSZ)	[139]
Rh	Nb_2O_5	[131]
Rh	TiO_2	[131]
Rh	Ceramic foam	[145]
Rh	NaY zeolite	[131,146]
Rh	Al-pillared montmorillonites	[85]
Pt	Al_2O_3	[15,147–152]

TABLE 7.2 Recently Reported Catalysts for Dry Reforming of Methane (*cont'd*)

Metal	Support	References
Pt	La_2O_3/Al_2O_3	[153]
Pt	ZrO_2-Al_2O_3	[152]
Pt	Na−Al_2O_3	[149]
Pt	K−Al_2O_3	[149]
Pt	SiO_2,	[154]
Pt	ZrO_2/SiO_2	[153]
Pt	MgO	[155]
Pt	ZrO_2	[138,147−152, 154,156,157]
Pt	Ce-ZrO_2	[147,158]
Pt	TiO_2	[150,151,154]
Pt	$SrTiO_3$	[159]
Pt	Cr_2O_3,	[154]
Pt	Zeolite HY	[82]
Pt	Zeolite β	[82]
Pt-Sn	SiO_2	[32]
Pt-Sn	ZrO_2	[32]
Pt-Re	Ceramic foam	[145]
Ir	Al_2O_3	[15,133,160,161]
Ir	SiO_2	[160]
Ir	La_2O_3	[160]
Ir	TiO_2	[160]
Ir	ZrO_2	[160]
Ir	Y_2O_3	[160]
Ir	MgO	[160]
Ir	$Ce_{0.9}Gd_{0.1}O_{2-x}$	[162]
Pd	Al_2O_3	[15,163]
Pd	CeO_x/γ-Al_2O_3	[163]
Ru	Al_2O_3	[15,164,165]
Ru	SiO_2	[165]
Ru	La_2O_3	[164,166]
Ru	ZrO_2	[164]
Ru	Y_2O_3	[164]
Other catalysts		
Mo_2C		[167−172]
Mo_2C	Al_2O_3	[173−175]
Mo_2C	ZrO_2	[170,174−176]
Mo_2C	MgO	[175]
Co_6W_6C		[177]
MoS_2		[178]
WS_2		[178]
Coal char		[179]
Carbon		[180]
$Ce_xZr_{1-x}O_2$		[181]
CeO_2		[182]

activity under high space-time velocity and high temperature [42].

Recently, it was reported that the coke resistance ability of the Ni/SiO_2 catalysts was improved greatly by plasma treatment [45]. This improvement in performance was attributed to that the interaction between the Ni particles and the silica was strengthened, and the Ni dispersion on the surface of SiO_2 was improved after the plasma treatment. Smaller-sized and more homogeneous Ni particles were formed in the plasma-treated Ni/SiO_2 catalyst [45].

In published papers, the dependence between the catalytic activity of Ni catalysts and its preparation method is concluded in that the highly dispersed Ni is more active. In order to disclose the relation between Ni particles and its activity in the activation of methane, the author of this chapter had prepared a series of different-sized Ni catalysts on the surface of

SiO_2 via direct impregnation of Ni-complex precursors [183]. It was disclosed that methane decomposition performs quickly on small-sized Ni. The calculated turnover frequency of methane was 9.8 s^{-1} on 45.0 nm sized Ni catalyst and increased to 12.6 s^{-1} when the Ni particle size decreased to 4.5 nm. The decomposition of methane could be accelerated by the CO_2 and O_2 in feed. The turnover frequency of CH_4 reached 20.6 s^{-1} on 4.5 nm sized Ni catalyst and remained stable during the first 5 pulse in a CH_4-CO_2 atmosphere. But the initial turnover frequency of methane was 15.6 s^{-1} on 45.0 nm sized Ni catalyst, and it decreased continuously with the pulse number. The turnover frequency of methane further increased to 22.5 and 16.4 s^{-1} over 4.5 and 45.0 nm sized Ni catalysts, respectively, when oxygen was added in feed. Also, the calculated methane decomposition rate decreased with the pulse number only on 45.0 nm sized Ni catalyst. These results disclosed that small-sized Ni catalysts were more effective and stable for methane decomposition, and CO_2 and O_2 can promote the conversion of methane; these data are summarized in Table 7.3.

7.3.1.2. Basic Promoters and Supports

As carbon formation occurs easily during dry reforming process, it was suggested that increase in adsorption and activation of CO_2 would accelerate the gasification of the surface carbons and retard the formation of inactive carbon. In order to increase the alkalinity of the catalyst, a lot of basic materials were selected to support Ni catalysts. At the same time, alkali-, alkaline-, and rare-earth metals promoted Ni catalysts were also reported extensively.

Juan-Juan et al. [11] found that K-modified Ni/γ-Al_2O_3 catalysts prepared by impregnation reduced the accumulation of carbon on the catalyst surface, but caused a decrease in the catalytic activity. K-modified Ni-Al_2O_3 catalyst prepared by a sol-gel method also exhibited lower carbon deposition rate and higher stability at the detected 30 h, but a slightly less activity than Ni-Al_2O_3. The higher stability of K-modified Ni-Al_2O_3 catalyst was contributed to that the reducibility of nickel species was increased by the added potassium, as potassium modified the interaction between metal and its support materials. At the same time, some potassium would migrate from the support to the Ni surface, which made a fraction of the active sites neutralized [8]. However, the addition of Ca, Mn, and Sn to Ni-Al_2O_3 caused a dramatic reduction of catalytic activity due to the formation of inactive graphite forms of carbon [8].

Certain amount of alkaline-earth metal oxide MgO and CaO could improve the catalytic

TABLE 7.3 Methane Conversion on Different-Sized Ni and Different Environment at 700 °C

	CH_4 decomposition (TOF (s^{-1}))		CH_4-CO_2 (TOF (s^{-1}))		CH_4-O_2 (TOF (s^{-1}))	
Pulse No.	**45.0 nm**	**4.5 nm**	**45.0 nm**	**4.5 nm**	**45.0 nm**	**4.5 nm**
1	9.8	12.6	15.6	20.6	16.4	22.5
2	7.6	9.6	15.2	20.3	15.8	22.4
3	7.0	9.5	12.1	21.2	15.4	23.0
4	6.8	8.8	11.3	20.7	15.4	22.4
5	6.3	7.4	11.4	21.3	12.0	22.4

Reprinted with permission from Hou et al. [183], copyright (2007) Elsevier.

performance of Ni/Al_2O_3 and Ni/SiO_2 because the strong interaction between Ni and supports and the basic property of metal oxide could depress carbon formation in the dry reforming process [12,29]. The presence of CeO_2 and La_2O_3 led to the increase in Ni reducibility in Ni/CeO_2-Al_2O_3 and Ni/La_2O_3-Al_2O_3, which was an important indicator of high activity and stability of these Ni catalysts relative to Al_2O_3 [34]. The addition of ZrO_2 improved the stability of Ni/Al_2O_3 in the dry reforming of methane, as it enhanced the dissociation of CO_2, which led to the formation of reactive oxygen intermediates at the boundary between ZrO_2 and nickel [39].

A series of basic oxides such as MgO and rare earth metal oxides La_2O_3 supported Ni catalysts were developed and investigated in detail by research groups of Ruckenstein [53,54,58, 61,64], Tomishige [56,57], and Verykios [18,19].

Hu and Ruckenstein [53] found that NiO/MgO catalyst prepared by impregnation formed the entire NiO-MgO solid solution, and had very high CO yield and stability in dry reforming of methane. In NiO/MgO, the increased binding between the two oxides prevented the sintering of the solid solution and the clustering of Ni. $Ni_{0.03}Mg_{0.97}O$ solid solution showed higher carbon resistance ability than supported Ni/MgO and NiO-Al_2O_3 because CO_2 activated easily at the boundary between nickel particles and MgO in $Ni_{0.03}Mg_{0.97}O$ [57]. Xu et al. [52] demonstrated that a kind of $Ni_xMg_{1-x}O$ (x = 0.02−0.15) solid solution with Ni particles of size 3−20 nm had a strong interaction with the support and was extremely stable in dry reforming of methane. At 750 °C and 0.1 MPa, with $CH_4/CO_2 = 1.0$ in feed, $Ni_{0.015}/Ni_{0.050}Mg_{0.950}O$ catalyst is stable during 50 h on stream even with a rather high gas hourly space velocity (GHSV, 2.4×10^5 ml g^{-1} h^{-1}). The observed conversion of CH_4 decreased from 84% (equilibrium conversion of methane at 750 °C, 86%) to 29% when the use of GHSV increased from 1.6 $\times$ 10^4 to 2.4 $\times$ 10^5 ml g^{-1} h^{-1}.

Verykios' group [18,19] reported that Ni/La_2O_3 catalyst was remarkably stable in dry reforming of methane compared to Ni/γ-Al_2O_3, Ni/CaO/γ-Al_2O_3, and Ni/CaO due to the formation of $La_2O_2CO_3$. Further, $La_2O_2CO_3$ decomposed to CO and oxygen species successively; these active oxygen species would react with carbon accumulated on Ni crystallites during CH_4 cracking, producing CO that leads to the special stability characteristics.

7.3.1.3. *Perovskite-Type Catalysts*

Batiot-Dupeyrat et al. [109] reported that perovskite $LaNiO_3$ could be used as a catalyst precursor for dry reforming of methane without pretreatment, and this catalyst was stable for more than 100 h. The reported conversions of CH_4 and CO_2 reached to 90 and 87%, respectively and the H_2/CO molar ratio in product gas was 1. The higher stability can be attributed to that nickel particles obtained by the reduction of the highly dispersed $LaNiO_3$ precursor. The reduced La_2NiO_4 also presented higher activity without carbon deposition than Ni/La_2O_3 due to the smaller nickel particles (7 nm) [106]. But the fresh La_2NiO_4 catalyst without reductive pretreatment led to the formation of multiwall carbon nanotubes derived from methane decomposition [110].

Mg-substituted $LaNi_{1-x}Mg_xO_{3-\delta}$ further increased catalytic activity of $LaNiO_3$, but cobalt (in $LaNi_{1-x}Co_xO_{3-\delta}$) decreased the catalytic activity of $LaNiO_3$, which may be attributed to the formation of Co-Ni alloy [112].

The introduction of alkali metals (Li, Na, K) into $M_xLa_{1-x}Ni_{0.3}Al_{0.7}O_{3-d}$ (x = 0, 0.2, 0.5, 0.8, and 1.0) mixed-oxide perovskites as catalysts for the dry reforming of methane to produce syngas was also investigated. Among them, $Li_{0.2}La_{0.8}Ni_{0.3}Al_{0.7}O_{2.8}$ showed less carbon formation; $Na_{0.5}La_{0.5}Ni_{0.3}Al_{0.7}O_{2.5}$ exhibited high yield; and $K_{0.5}La_{0.5}Ni_{0.3}Al_{0.7}O_{2.5}$ produced an H_2/CO ratio close to 1 over a wide

temperature range [115]. When a small amount of rhodium was added to the Ni-based perovskites ($LaNi_{0.95}Rh_{0.05}O_3$), it modified the catalyst surface and also improved the reduction and dispersion of nickel. These improved characteristics enhanced the catalytic performance [116]. The supported cylindrical $LaNiO_x$/ZSM-5 catalyst (φ = 3 mm, length = 10 to 15 mm) also had high activity (97% CH_4 conversion and 94% CO_2 conversion at 850 °C, GHSV=1.3 × 10^3 h^{-1}) and almost remained a constant in the range of 100 h [119].

7.3.1.4. Nanocomposite Supports

The properties and particle size of supports have a strong effect on the catalytic activity and stability of nickel catalysts. Ni/CeO_2 catalysts prepared by a hybrid polymeric precursor had highly dispersed Ni nanoparticles (4 nm sized particles) that embedded within the ceria matrix, showed good stability, and had higher carbon resistance in dry reforming of CH_4 [65]. Nanocomposite Ni/ZrO_2 catalysts (Fig. 7.4) showed extremely stable performance compared to larger zirconia particles (>25 nm) supported Ni catalysts [72]. The nickel catalyst supported on nanocrystalline zirconia prepared by the surfactant-assisted route showed higher activity and stability than zirconia prepared by sucrose as a chelating agent, which was related to the high thermal stability of the support prepared by surfactant-assisted route during the reaction [69]. ZrO_2 with high-surface area and completely single tetragonal crystalline phase supported nickel catalysts are also extremely active and stable for methane dry reforming. At 700 °C, GHSV = 1.5 × 10^4 ml g^{-1} h^{-1}, methane conversion decreased only slightly during 50 h on stream. The addition of basic promoters (such as CeO_2, La_2O_3, and K_2O) changed the interaction between metal and its support materials and improved the basicity of catalysts. These characteristics further increased activity and stability of the catalysts [68].

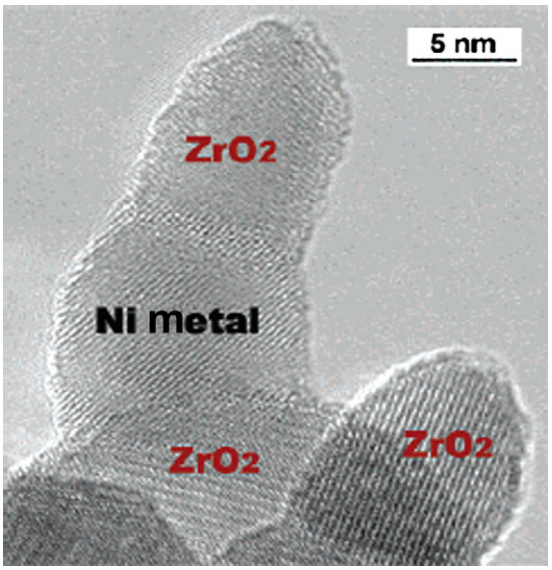

FIGURE 7.4 High-resolution TEM microgram of the reduced Ni/ZrO_2-AS catalyst *(reprinted with permission from Xu et al. [72], copyright (2003) American Chemical Society.*

In addition, catalysts with well-developed porosity are also highly active in dry reforming of methane. The author of this chapter found that Ni/Mg/Al catalysts that possessed mesoporous structure and large surface area exhibited higher methane conversion and lower coke formation rate. This higher activity and stability was attributed to Ni dispersed highly on the supports because of its larger mesopore surface areas, and the higher accessibility of CH_4 and CO_2 to active Ni sites because of the larger pore channels in the mesoporous supports [87].

Mesoporous smectite-type clays containing Ni [86] prepared in different conditions can produce different-sized Ni crystallites and those having smaller Ni crystallites showed higher activity. It was found that 8 wt% Ni/clinoptilolite [84] exhibited not only high activity and selectivity but also remarkable stability.

7.3.2. Co-Based Catalysts

Ruckenstein and Wang [120] compared the activities of MgO, CaO, SrO, BaO, γ-Al_2O_3, and SiO_2 supported Co catalysts for the dry reforming of CH_4. It was found that the yield of CO and H_2 reached 93% and 90%, respectively, on Co/MgO catalyst at 60,000 ml g^{-1} h^{-1} and remained stable for 50 h. This higher activity and stability was possible because the solid solution of CoO and MgO formed easily, and this solid solution enhanced the interactions between Mg and Co and prevented metal sintering and coking. But the stability of Co on γ-Al_2O_3 support changed with the loading amount of Co and its calcination temperature. Carbon deposition and oxidation of Co would be responsible for the deactivation of Co/γ-Al_2O_3 [121]. Hou and Yashima [122] found that the surface species of Co in Co/α-Al_2O_3 catalysts, reforming activity, and coke formation rate depended strongly on its calcination temperature and reduction conditions. Bouarab et al. [125] reported that the addition of MgO to SiO_2 increased the activity of Co/SiO_2 because the basic function of the support increased the H-abstraction of methane and CO_2 adsorption and decreased the carbon deposition.

It was also reported that pure CoO_x-MgO is catalytically inactive for methane reforming with CO_2. But the activity and H_2 selectivity (>94%) of a commercial low surface-area macroporous silica-alumina (SA-5205, M/S Norton Co., USA) supported CoO_x-MgO were improved obviously [129]. The catalytic performance of the metal oxide used for precoating the support followed the order: MgO > ZrO_2 > CeO_2 > Y_2O_3 > ThO_2 [129]. When anatase TiO_2 supported Co catalyst was reduced below 850 °C, it became inactive due to significant carbon deposition. But the catalyst could keep its activity in the first 24 h, and the amounts of deposited coke were insignificant when the reduction temperature increased to 850 °C and above. The deactivation of Co/TiO_2 was attributed to the oxidation of the metallic cobalt. Small amount of ruthenium (Ru/Co = 0.05) added in Co/TiO_2 could inhibit the oxidation of the cobalt and could also inhibit the carbon deposition on the active sites [127].

7.3.3. Noble Metal Catalysts

Besides Ni and Co, noble metal (Rh, Pt, Ir, Pd, and Ru) catalysts were also investigated widely in dry reforming of methane due to their excellent carbon resistance ability.

Rh catalyst. Mark and Maier [133] suggested that CH_4 conversion increased only with increasing metal surface area and was independent of the nature of the support (γ-Al_2O_3, α-Al_2O_3, TiO_2, ZrO_2, SiO_2, TiO_2-SiO_2, Al_2O_3-SiO_2, ZrO_2-SiO_2). There was no detectable effect of the pore structure or nature of the support on the reaction rate. But Wang and Ruckenstein [132] compared the catalytic performance of Rh on a series of reducible oxides (CeO_2, Nb_2O_5, Ta_2O_5, TiO_2, and ZrO_2) and irreducible oxides (γ-Al_2O_3, La_2O_3, MgO, SiO_2, and Y_2O_3); they found that the yields to CO and H_2 were lower when Rh were supported on reducible oxides. The yields of CO and H_2 reached 83–85% and 76–79%, respectively, on Rh/MgO and Rh/γ-Al_2O_3 at a high space velocity of 60,000 ml $g^{-1}h^{-1}$. Hou et al. [15] also found that a mesoporous Al_2O_3 supported Rh catalyst was highly active and stable for the dry reforming of methane, and only intermediate catalytically active carbons formed on the mesoporous Al_2O_3 supported Ni catalysts. CeO_2 could further improve the activity and coke resistance ability of Rh/Al_2O_3 [136] because the coexistence of Ce^{4+}/Ce^{3+} and $Rh^0/Rh^{\delta+}$ redox couples can accelerate the activation of CH_4 and CO_2.

Pt catalysts. Bradford and Vannice [154] found that TiO_2 and ZrO_2 were the promising supports for Pt catalysts among TiO_2, ZrO_2, Cr_2O_3, and SiO_2 in dry reforming of methane, due to the presence of the metal–support

interactions and mobile TiOx species in the Pt/TiO_2 catalyst preventing carbon deposition. It was found that 1 wt% Pt/ZrO_2 was an excellent catalyst for 500 h without significant deactivation, and the catalytic activity was determined by the accessibility of Pt on the Pt-ZrO_2 perimeter [138,157]. And the addition of ZrO_2 improved the stability of Pt/Al_2O_3 due to strong Pt−Zr^{n+} interactions, which promoted CO_2 dissociation in dry reforming [152]. ZrO_2 on the surface of SiO_2 (SZrOs) and La_2O_3 on the surface of Al_2O_3 (SLaOs) are also good supports for Pt catalysts compared with Pt/Al_2O_3 and Pt/SiO_2 attributed to the activation of CO_2 adsorbed on the basic sites of surface-phased ZrOs and surface-phased LaOs [153]. Pt/$Ce_{0.5}Zr_{0.5}O_2$ showed a good catalytic performance due to the enhanced reducibility and oxygen exchange capacity of $Ce_{0.5}Zr_{0.5}O_2$ [158].

But the deactivation of Pt was disclosed by Bitter et al. [150]. They found that the deactivation of Pt catalysts depended strongly on the support and the metal particle size, and carbon formation rate decreased in the order of Pt/γ-Al_2O_3 >> Pt/TiO_2 > Pt/ZrO_2. Larger-sized Pt catalysts (with Pt particles >1 nm) deactivated easily compared to catalysts with smaller Pt particles. Characterizations disclosed that carbon deposition rather than metal sintering was the main reason for its deactivation. Small amounts of Na or K (0.3 wt%), especially Na, enhanced the stability of Pt/Al_2O_3 because of the increasing basic sites [149].

Ir catalysts. Nakagawa et al. [160] found that the activity order of supported iridium catalysts in the dry reforming of methane was as follows: TiO_2 > ZrO_2 > Y_2O_3 > La_2O_3 > MgO > Al_2O_3 > SiO_2. At 600 °C and 36,000 ml g^{-1} h^{-1}, the conversion of CH_4 and CO_2 over 5 wt% Ir/TiO_2 catalyst was 27.6% and 37.9%, and the yield of H_2 and CO was 22.4% and 32.7%, respectively. Ir/$Ce_{0.9}Gd_{0.1}O_{2-x}$ catalyst [162] was found fairly stable for 20 h, which appeared as a good candidate for anode material in view of the direct conversion of biogas in solid oxide fuel cells (SOFCs) applications.

Pd catalysts. Pd/α-Al_2O_3 catalyst with an average particle size of 5 nm exhibited an initial activity comparable to that of Pt/ZrO_2 catalysts and a high and constant selectivity to H_2 with $CO/H_2 \approx 1$ [163]. However, the catalytic activity decreased by 50% after 24 h, mainly due to carbon formation and metal sintering. The addition of Ce in Pd-CeO_x/α-Al_2O_3 can suppress the formation of carbon deposition and reduce metal sintering.

Ru catalysts. Ru/La_2O_3 catalyst was stable for 80 h at 550−630 °C at a P_{CO_2}/P_{CH_4} ratio of 1 in feed. However, when the amount of CO_2 increased to $P_{CO2}/P_{CH4} > 1$, Ru/La_2O_3 deactivated quickly at 550 °C because of the partial oxidation of Ru in excess CO_2 atmosphere [166].

7.3.4. Noble-Metal Promoted Ni Catalysts

Several works have demonstrated that dry reforming of methane proceeds easily with Rh, Ir, Ru, and Pt catalysts. However, the application of noble metals at industrial scale is difficult because of the limited resource and high price. In 1993, Rostrup-Nielsen and Hansen [184] compared the activity of Ni and a series of noble metal catalysts for dry reforming of methane; it was confirmed that Ni possessed similar activity as noble metals, but coke formation on Ni catalyst was a major drawback.

Hou and Yashima [98] found that small amounts of Rh-promoted Ni/Al_2O_3 catalysts could combine the advantages of both Ni and Rh and exhibited excellent performance, with higher activity and lower carbon formation rate during the dry reforming of methane. Temperature programmed desorption (TPD) studies disclosed that the activation of CO_2 performed easily on small amounts of Rh-promoted Ni/Al_2O_3 catalysts as that of pure Rh/Al_2O_3 and the active surface oxygen derived

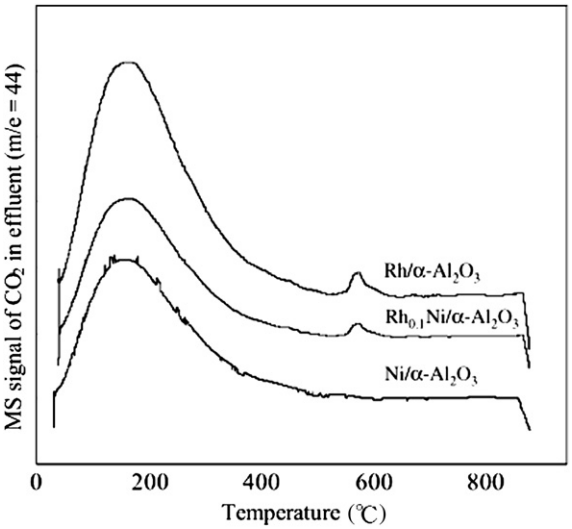

FIGURE 7.5 CO_2-TPD profile of Ni/Al_2O_3, $Rh_{0.1}$Ni/Al_2O_3, and Rh/Al_2O_3 *(reprinted with permission from Hou and Yashima [98], copyright (2003) Springer).*

from CO_2 decomposition improved the gasification of surface carbon (see Fig. 7.5).

More recently, Wu and Chou [95] also found that Rh improved the activity and stability of Ni for dry reforming. The optimum ratio of Rh/Ni loading on boron nitride was 0.01. The ratio of H_2 and CO as the products was near 0.7. The maximum conversions of CH_4 and CO_2 reached 72% and 81%, respectively, at 700 °C, while only slight deactivation was observed during 6 h of reaction time.

Irusta et al. [102] also reported that Ni-Rh bimetallic exhibited the highest activity at 550 °C, but only the monometallic Rh on ZrO_2 support was stable. When Rh was added, Ni-Rh formed on the surface of catalyst; carbonaceous deposition on this alloy is negligible. At the same time, Ni-Rh alloys formation would reduce the strong interaction between Rh and ZrO_2.

7.3.5. Metal Carbide Catalysts

Claridge et al. [167] found that molybdenum and tungsten carbide materials with large surface area could be prepared via the temperature programming reduction of the relevant metal oxide with methane/hydrogen. And these catalysts are effective for methane steam reforming, methane dry reforming, and methane partial oxidation to synthesis gas. But the activities and stabilities of the carbide catalysts are dependent strongly on the reaction pressure. At atmospheric pressure, it has higher initial activity (more than 90% methane and CO_2 conversions, at GHSV $= 2.9 \times 10^3$ h^{-1} and 847 °C), but are deactivated quickly because of the oxidation of Mo_2C to MoO_2. When operated at higher pressure (0.83 MPa), the conversion of methane decreased to about 62% (at GHSV $= 2.9 \times 10^3$ h^{-1} and 847 °C), but the stability was enhanced remarkably, and no catalyst deactivation was detected during the catalytic reaction of 72 h. The activity of β-Mo_2C (91 m^2 g^{-1}) was comparable with those of 5 wt% Ir/Al_2O_3 and 5 wt% Rh/Al_2O_3, which had good catalytic performance for methane dry reforming. However, the activity of α-WC (39 m^2 g^{-1}) was low.

Since then, much attention has been paid to molybdenum carbide and tungsten carbide catalysts because of their easy preparation method and higher activity compared to some noble metal catalysts, and the most important aspects are because this kind of catalyst is stable at elevated pressure and carbon-free. LaMont and Thomson [172] investigated the effect of mass transfer on the stability of Mo_2C for methane dry reforming. They found that stability of Mo_2C at higher pressures could be attributed to the decreased mass transfer rates by increased pressure ensuring adequate reductive product gases within the boundary layer of catalyst to prohibit the oxidation of Mo_2C to MoO_2, neither attributed to increasing the inherent activity of Mo_2C, nor attributed to higher pressures enhancing the carburization process against the oxidation of Mo_2C. Therefore, in order to prohibit deactivation, the reforming reaction should manipulate at low mass flow rates. The packed bed reactors with

low ratio of height to diameter would be required at higher space velocities or introduction of reductive product gases to the top of the bed reactor would be desirable.

For improving the stability of Mo_2C against oxidation, a series of Al_2O_3, ZrO_2, and MgO supported Mo_2C were also reported by Darujati and Thomson [175] and Tsuji et al. [176]. It was found that Al_2O_3 supported Mo_2C catalyst showed much higher activity than a bulk Mo_2C catalyst because of the high surface area and high thermal stability of Al_2O_3 [175].

Thermodynamic calculations showed that Mo_2C only exhibits stable performance at high product concentrations [168], and the carbon formed on Mo_2C is lower than that on nickel-based catalysts. The calculated Gibbs-free energy of carbon formation on a Mo_2C catalyst is 4.5 kJ/mol higher than that on Ni catalyst with up to 250 nm nickel particles at 700 °C.

In conclusion, the greatest advantage of Mo_2C is its excellent carbon resistance ability compared to Ni catalyst, but the stability of this catalyst is lower. However, Sehested et al. [168] disclosed that Mo_2C catalyst was more than two orders of magnitude less active than 1.8% $Ru/MgAl_2O_4$ catalyst on the basis of weight.

7.4. REACTION MECHANISM AND KINETICS OF DRY REFORMING OF METHANE

7.4.1. Ni-Only Catalyst

The reaction mechanism for methane dry reforming over a Ni foil was first proposed by Bodrov and Apel'baum [185]. They suggested that CH_4 is first adsorbed at an active site to yield CH_2 species, which is a rate-determining step. CO_2 is converted to CO by the reverse water-gas shift reaction ($CO_2 + H_2 \rightarrow CO + H_2O$), H_2 and CO was also produced via reaction of H_2O with CH_x species.

But this mechanism was modified subsequently and several possible reaction mechanisms have been reported.

On Ni-based catalysts, it is widely accepted that the reforming reaction begins via CH_4 dissociated adsorption on the surface of active sites.

$$CH_4 + (5-x)^* \rightarrow CH_x^* + (4-x)\ H^* \quad (7.5)$$

$$CO_2 + H^* \rightarrow CO + OH^* \quad (7.6)$$

$$CH_x^* + OH^* \rightarrow CH_xO^* + H^* \quad (7.7)$$

$$CH_xO^* \rightarrow CO^* + x/2\ H_2 \quad (7.8)$$

$$CO^* \rightarrow CO + ^* \quad (7.9)$$

$$2H^* \rightarrow H_2 + 2^* \quad (7.10)$$

Where adsorbed hydrogen derived from methane decomposition (Eq. (7.5)) on active sites (H*) is essential for the adsorption and activation of CO_2 on Ni/SiO_2 because it was confirmed that CO_2 cannot be dissociated on Ni-only surface [186]. On Ni/SiO_2 catalyst, the main argument is that which reaction is the rate-determining step. Pulsed surface reaction analysis was used to probe the mechanism of methane dry reforming on Ni/SiO_2, Ni/MgO, Ni/Al_2O_3, and Ni/TiO_2 by Osaki et al. [187]. They suggested that two steps that are responsible for H_2 production (CH_4 adsorbed and dissociated to form CH_x species (Eq. (7.5)) and the subsequent surface reaction of CH_x and CO_2 (or O) (Eq. (7.7)) are the rate-determining steps.

On the other hand, Hu and Ruckenstein [49] suggested that NiO/SiO_2 had no activity for methane dry reforming reaction and the surface reaction between C and O species constitutes the rate-determining step of the reforming

reaction over Ni/SiO_2 and Ni/MgO. In this case, the mechanism could be described as:

$$CH_4 + {}^* \rightarrow CH_3^* \rightarrow CH_2^* \rightarrow CH^* \rightarrow C^* \quad (7.11)$$

$$CO_2 + {}^* \rightarrow O^* + CO \quad (7.12)$$

$$CH_x^* + O^* \rightarrow CO + x/2\ H_2 + 2^* \quad (7.13)$$

$$H_2O + {}^* \rightarrow O^* + H_2 \quad (7.14)$$

$$CO + 2^* \rightarrow C^* + O^* \quad (7.15)$$

More recently, researchers at Zhejiang University found that the consumption of CO_2 and the formation of H_2 and CO followed the consumption of CH_4 on Ni/SiO_2 in CH_4 pulse-injected surface reactions in a $10\%CO_2/Ar$ flow (Fig. 7.6) [188]. This result indicates that methane decomposition and CO_2 gasification of CH_x species derived from methane decomposition took place consecutively on Ni/SiO_2, and gasification of carbonaceous species might be the rate-determining step.

All these suggested mechanisms are adaptive in their reaction conditions. The difference among these mechanisms would originate from the nature of the catalysts (such as the particle size of Ni) and the reaction conditions they used (the second mechanism was proposed at a high reaction temperature of 800–950 °C).

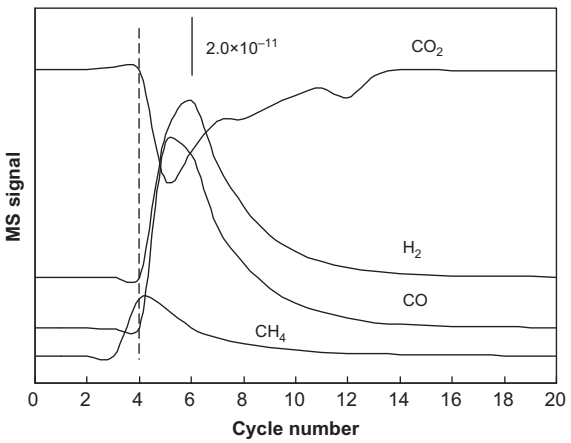

FIGURE 7.6 MS profile of CH_4 pulse reaction in 10% CO_2/Ar on Ni/SiO_2 *(reprinted with permission from Guo et al. [188], copyright (2009) International Association for Hydrogen Energy).*

7.4.2. Rare Earth Metals Supported Ni Catalyst

Verykios' group [18,19] contributed significantly to the dry reforming of methane over the Ni/La_2O_3 catalyst, and found that methane activation is the rate-determining step, while the reaction between surface carbon species (CH_x, $x = 0–3$) and the oxidant (including CO_2 activation) is the rate-determining step on the $Ni/\gamma\text{-}Al_2O_3$ catalyst. The CH_4 activation over the Ni/La_2O_3 catalyst may be a slow step due to the detection of reversibly adsorbed CH_4 under reaction conditions. Compared to CH_4 activation, the dissociation of the CO_2 molecule over Ni/La_2O_3 catalyst is a fast step. The reaction mechanism over rare earth oxides and alkaline oxides supported Ni is expressed as follows.

A strong interaction between CO_2 and Rn_2O_3 would accelerate formation of surface $Rn_2O_2CO_3$ species (Eq. (7.16)) (where Rn refers to rare earth metals such as La [18] and Gd [188]).

$$CO_2 + Rn_2O_3 \rightarrow Rn_2O_2CO_3 \quad (7.16)$$

$$CH_4 + (5-x)^* \rightarrow CH_x^* + (4-x)H^* \quad (7.5a)$$

$$Rn_2O_2CO_3 + CH_x^* \rightarrow 2CO^* + Rn_2O_3 + x/2\ H_2 \quad (7.17)$$

$$Rn_2O_2CO_3 + C \rightarrow 2CO + Rn_2O_3 \quad (7.18)$$

The surface $Rn_2O_2CO_3$ species react with CH_x species produced from CH_4 dissociation (Eq. (7.5)) quickly, and more active sites (*) are

recovered after the gasification of CH_x*, where the adsorption and decomposition of methane in gas phase were further enhanced (Eq. (7.5)). Therefore, the interfacial area between Ni and oxycarbonate particles should be the most active sites of the catalyst.

$Rn_2O_2CO_3$ species might react with H* species derived from CH_4 dissociation to produce CO and OH* as shown in Eq. (7.19).

$$Rn_2O_2CO_3 + H^* \rightarrow Rn_2O_3 + CO + OH^* \quad (7.19)$$

In this mechanism, the activation of CO_2 was enhanced greatly via formation of carbonate species ($Rn_2O_2CO_3$), and this enhanced CO_2 activation ability further improved decomposition of CH_4, and methane activation was the rate-determining step.

Besides the experimental data reported by Verykios group [18,19], it was found that H_2 and CO were produced immediately when CH_4 was pulse injected in a 10%CO_2/Ar flow on $NiGd_{0.45}/SiO_2$ [188] (Fig. 7.7). This result means that the decomposition of methane and the gasification of carbonaceous species would occur simultaneously. Consequently, the formation of $Gd_2O_2CO_3$ on the surface of $NiGd_{0.45}/SiO_2$ in CO_2 flow would accelerate the decomposition of CH_4.

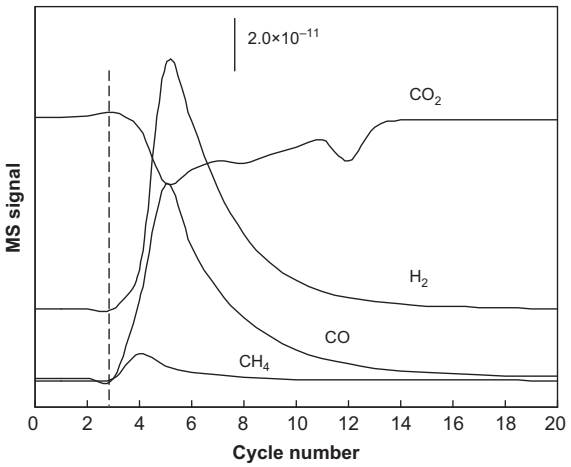

FIGURE 7.7 MS profile of CH_4 pulse reaction in 10% CO_2/Ar on $NiGd_{0.45}/SiO_2$ *(reprinted with permission from Guo et al. [188], copyright (2009) International Association for Hydrogen Energy).*

7.4.3. Kinetics

Wang and Lu [17] suggested that dry reforming reaction could be described in a Langmuir–Hinshelwood mechanism with intermediate CH_x species and dissociated adsorption of CO_2. On the surface of Ni/Al_2O_3 catalyst, they found that the rate of dry reforming of methane could be described in:

$$r = \frac{k_1 P_{CH_4} P_{CO_2}}{(1 + K_1 P_{CH_4})(1 + K_2 P_{CO_2})} \quad (7.20)$$

At a definite partial pressure of CH_4, if P_{CO_2} is higher (in a case of higher CO_2/CH_4 ratio in feed), that is $K_2 P_{CO_2} >> 1$, Eq. (7.20) is approximated by:

$$r = \frac{k_1' P_{CH_4}}{1 + K_1 P_{CH_4}}, \text{where } k_1' = \frac{k_1}{K_2} \quad (7.21)$$

which indicates that the reaction order is the zeroth-order with reference to CO_2 partial pressure.

If P_{CO_2} is lower, that is, $K_2 P_{CO_2} << 1$, Eq. (7.20) will be approximated as:

$$r = \frac{k_1 P_{CH_4} P_{CO_2}}{1 + K_1 P_{CH_4}} \quad (7.22)$$

This reaction is of the first-order with respect to CO_2 partial pressure. Similarly, at definite pressure of CO_2, if $K_1 P_{CH_4} << 1$, Eq. (7.20) is simplified to:

$$r = \frac{k_1 P_{CH_4} P_{CO_2}}{1 + K_2 P_{CO_2}} \quad (7.23)$$

The kinetic parameters for the model of the reaction rate in Eq. (7.20) were also calculated and summarized by Wang and Lu (Table 7.4) [17].

Recently, the reaction kinetics of dry reforming of methane over 0.5%$Pt/SrTiO_3$ catalyst

was studied in detail by Topalidis et al. [159]. They found that in the temperature range 540–620 °C and partial pressure range $0.083 < P_{CH_4}, P_{CO_2} < 0.667$, this reaction could be explained by using Langmuir–Hinshelwood kinetics with the reactants adsorbed on different active sites of the catalysts, namely the methane is weakly adsorbed on the metallic phase and CO_2 is strongly adsorbed on the oxide phase of the catalyst. The rate of methane conversion by fitting the experimental data is:

$$R_{CH_4} = k_1 P_{CH_4} \tag{7.24}$$

The apparent activation energy for methane dry reforming was calculated to be ~123 kJ/mol.

The rate of CO_2 conversion could be described as a similar empirical equation:

$$R_{CO_2} = k_2 (P_{CH_4})^m (P_{CO_2})^n \tag{7.25}$$

But the calculated results illustrate that the rate of CO_2 is dependent on both variable reaction orders, namely, m increases from 0.0 to 0.30 and n increases from 0.3 to 0.6 in the temperature range of 540–620 °C. The variable reaction order is presumably because of the reverse water-gas shift reaction which may also occur simultaneously during the dry reforming reaction [159].

On the surface of Ni/La_2O_3 catalyst, the rate expression of r_{CH_4} is [107]:

$$r_{CH_4} = \frac{K_1 k_2 K_3 k_4 [CH_4][CO_2]}{K_3 k_4 [CO_2] + K_1 K_3 k_4 [CH_4][CO_2] + K_1 k_2 [CH_4] + K_1 k_2 K_3 [CO_2]} \tag{7.26}$$

where K_1 is the equilibrium constant for methane adsorption, k_2 is the rate constant of the dissociation of methane on the Ni surface, K_3 is the equilibrium constant of the reaction between CO_2 and La_2O_3 to form the oxycarbonate, and k_4 is the rate constant of the reaction between the oxycarbonate species and the carbon deposited on the surface of Ni clusters. To calculate the kinetic constants individually, the value of K_1k_2 is defined as: $K_1k_2 = 2.61 \times 10^{-3}\exp(-4300/T)$ (mol g^{-1} s^{-1}). And the values of K_1, k_2, K_3, and k_4 can be found in reference [107].

TABLE 7.4 The Kinetic Parameters for the Model of the Reaction Rate in Eq. (7.20)

Temp (°C)	$k_1/(\mu mol/g_{cat}\cdot s\cdot kPa^2)$	$K_1/(kPa^{-1})$	$K_2/(kPa^{-1})$
500	0.20	0.00082	4.3
550	0.29	0.015	2.3
600	0.24	0.023	0.80
650	0.25	0.020	0.50
700	0.32	0.035	0.43

Reprinted with permission from Wang and Lu [17], copyright (1999) American Chemical Society.

7.5. DRY REFORMING OF ETHANE

As ethane and propane are present in natural gas and in the product gas of biomass gasification, dry reforming of ethane and propane has been investigated recently [189–191]. Thermodynamic calculations indicate that dry reforming of ethane and propane is more favorable than that of methane reforming (see Table 7.1).

$$C_2H_6(g) + 2CO_2(g) = 4CO(g) + 3H_2(g)$$
$$\Delta H^o_{298K} = 429.5\ kJ/mol \tag{7.27}$$

Solymosi et al. [192] studied the effects of different amounts of C_2H_6 in the dry reforming of methane reaction over Rh/ZSM-5 at 500 °C. It was found that carbon deposition and the deactivation of the catalyst occurred heavily when the added amount of ethane in a reacting gas mixture increased to 4–5%. They further

found that the dry reforming of C_2H_6 occurred rapidly above 427 °C, and mainly H_2 and CO formed in the product gas with a ratio of 0.3–0.6 on Rh/ZSM-5 [189]. On the same catalyst, more significant deactivation of the catalyst was detected in dry reforming of ethane with the stoichiometric CO_2/C_2H_6 ratio compared to the dry reforming of CH_4, which could be attributed to the lower reactivity of hydrocarbon fragments produced by the dissociation of ethane than those formed from CH_4 dissociation. However, the catalyst deactivation can be reduced or almost inhibited by adding a large amount of CO_2.

7.6. DRY REFORMING OF PROPANE

7.6.1. Catalysts

Dry reforming of propane has attracted much attention for the lower reforming temperature and lower vapor pressure of propane compared with methane at ambient temperature, which makes it more favorable for fuel cell cars with internal reforming [193].

$$C_3H_8(g) + 3CO_2(g) = 6CO(g) + 4H_2(g)$$
$$\Delta H^{o}_{298K} = 644.8\ \text{kJ/mol} \qquad (7.28)$$

Sutton et al. [194] compared the activities of Ni/Al co-precipitated, 1 wt% Ru/Al_2O_3, and 1 wt% Pt/ZrO_2 for the CO_2 reforming of hydrocarbons in a model gas stream (42 mol% H_2, 15.5 mol% CO, 5.1 mol% CH_4, 19.0 mol% CO_2, and 18.3 mol% C_3H_8) produced in biomass gasification. Above 600 °C, dry reforming reaction became increasingly favorable and resulted in a continual increase in the H_2 and CO content and a reduction in the CO_2, CH_4, and C_3H_8 content. However, at 800 °C, CO_2 was consumed completely and carbon deposition formed via the cracking of the hydrocarbons.

Al_2O_3 supported Rh, Ru, Ir, Pt, Pd [195], and Re [196] were investigated thoroughly for dry reforming of C_3H_8 by Solymosi's group. It was found that the specific activities decrease in the sequence of Ru > Ph > Pd > Pt = Ir (Table 7.5). The activity of Re/Al_2O_3 depended strongly on the reduction temperature and C_3H_8/CO_2 ratio. At $C_3H_8/CO_2 = 1{:}3$, the initial conversion of propane was only 53%. A higher conversion of C_3H_8 (~90%) was achieved at $C_3H_8/CO_2 = 1{:}6$ [196]. The adsorption, decomposition, and reaction of propane with CO_2 were further studied over Rh supported on Al_2O_3, SiO_2, TiO_2, and MgO catalysts [197]. The conversion of C_3H_8 decreased in the order of Al_2O_3, TiO_2, MgO, and SiO_2. The ratio of H_2/CO was the highest (0.53–0.64) on Rh/TiO_2, which was explained by the extended dissociation of CO_2 due to the electronic interaction between Rh and TiO_2.

Ni/Mg(Al)O hydrotalcite-derived catalyst was exceptionally stable for 34 days for the dry reforming of propane to synthesis gas at 600 °C and 0.1 MPa [198]. In propane dry reforming, it was observed that the intrinsic activity of the Ni catalyst on different supports (SiO_2, Al_2O_3, Mg(Al)O, MgO, CaO) depends mainly on the size of Ni particles in the range of 4.5–11 nm [193]. There was a volcano-type correlation between intrinsic activity of catalyst and basicity of support. Ni/Mg(Al)O with the

TABLE 7.5 CO_2 Reforming of Propane over Alumina-Supported Pt Metals at 650 °C

Metals	Dispersion (%)	Conversion of propane (%)	H_2/CO ratio	N_{H_2} (s^{-1})	N_{CO} (s^{-1})
Rh	31.0	63.5	0.54	0.849	1.592
Ru	4.5	45.3	0.62	6.67	10.76
Ir	87.0	7.6	0.50	0.076	0.153
Pt	48.0	5.4	0.25	0.047	0.187
Pd	16.0	4.3	0.53	0.117	0.219

Data were taken at 110 min on stream.
Reproduced with permission from Solymosi and Tolmacsov [195], copyright (2002) Springer.

highest dispersed Ni particles exhibited the best catalytic performance.

7.6.2. Reaction Mechanism and Kinetics

Sutton et al. [190] investigated the kinetic of CO_2 reforming of propane over Ru/Al_2O_3 and found that the reaction order with respect to C_3H_8 was of zeroth-order and the order with respect to CO_2 was 0.3. The activation energy of the C_3H_8 conversion was calculated as 86 kJ mol^{-1}.

Kinetic data showed good correlation coefficients not only for Langmuir–Hinshelwood mechanism but also for Mars–van Krevelen. According to the Langmuir–Hinshelwood mechanism, it may be tentatively proposed that the mechanism follows the generalized reaction sequence below:

$$C_3H_8 + (9-x)^* \rightarrow C_3H_x^* + (8-x)H^* \quad (7.29)$$

$$CO_2 + ^* \rightarrow CO_2^* \quad (7.30)$$

$$C_3H_x^* \rightarrow 3C^* + xH^* \quad (7.31)$$

$$CO_2^* + H^* \rightarrow CO^* + OH^* \quad (7.32)$$

$$C^* + OH^* \rightarrow CO + H^* \quad (7.33)$$

$$2H^* \rightarrow H_2 + ^* \quad (7.34)$$

$$OH^* + H^* \rightarrow H_2O + 2^* \quad (7.35)$$

$$CH_x^* + OH^* \rightarrow CH_xO^* + H^* \quad (7.36)$$

$$CH_xO^* \rightarrow CO^* + x/2H_2 \quad (7.37)$$

$$CO^* \rightarrow CO + ^* \quad (7.38)$$

According to Mars–van Krevelen, the possible reaction sequence is shown below:

$$C_3H_8(g) \rightarrow C_yH_x(Ru^*) \quad (7.39)$$

$$C_yH_x(Ru^*) \rightarrow yC_{(Ru^*)} + xH_{(Ru^*)} \quad (7.40)$$

$$C_{(Ru^*)} + O_{(Al_2O^*x)} \rightarrow CO_{(Al_2O^*x)} \quad (7.41)$$

$$CO_2(g) + (Al_2O^*x) \rightarrow CO_{(Al_2O^*x)} + O_{(Al_2O^*x)} \quad (7.42)$$

$$2H_{(Ru^*)} \rightarrow H_2(g) \quad (7.43)$$

Surface carbon reacts with the lattice oxygen of the alumina, located close to the $Ru-Al_2O_3$ interface, to form adsorbed CO (Eq. (7.41)). The lattice oxygen is then replaced with oxygen from CO_2 in the gas phase to form carbon monoxide (Eq. (7.42)).

Solymosi et al. [195–197] found that CO_2 was involved in the rate-determining step of the dry reforming of propane over supported Rh [197] and Re/Al_2O_3 [196]. A possible mechanism for the dry reforming of propane on Re catalysts was proposed as follows:

$$CO_2(g) + 2^* = CO^* + O^* \quad (7.44)$$

$$C_3H_8^* + O^* = C_3H_7^* + OH^* \quad (7.45)$$

$$C_3H_7^* = C_3H_6(g) + (1/2)H_2 \quad (7.46)$$

$$C_3H_7^* \rightarrow 3C(s) + (7/2)H_2(g) + ^* \quad (7.47)$$

$$C_3H_6^* + O^* = C_3H_5^* + OH^* \quad (7.48)$$

$$C_3H_5^* = C_3H_4^* + (1/2)H_2(g) \quad (7.49)$$

$$C_3H_4^* + O^* = C_2H_4^* + CO(g) \quad (7.50)$$

$$C_3H_5^* = 3C(s) + (5/2)H_2(g) + ^* \quad (7.51)$$

$$C_xH_y^* + CO_2(g) \rightarrow CO(g) + H_2(g) \quad (7.52)$$

$$C(s) + O^* = CO(g) \quad (7.53)$$

$$C(s) + OH^* = CO(g) + (1/2)H_2 + ^* \quad (7.54)$$

C_xH_y fragments derived from the decomposition of C_3H_8 could improve the dissociation of

CO_2 (Eq. (7.52)), and adsorbed O produced in the decomposition of CO_2 further facilitates the dissociation of C_3H_8 [197].

The order of the reaction was also zeroth in C_3H_8, and it was 0.6 with respect to CO_2 on Re/Al_2O_3 [196]. The activation energy of the dry reforming of propane was 84 kJ mol^{-1}, indicating that the process was limited by the diffusion.

7.7. REFORMING OF HIGHER HYDROCARBONS

Hydrocarbons such as transportation gasoline are possible raw materials for the production of hydrogen or syngas [199,200]. However, few works on CO_2 reforming of higher hydrocarbons were published.

$$C_7H_{16}(g) + 7CO_2(g) \rightarrow 8H_2(g) + 14CO(g) \quad \Delta H^{o}_{298K} = +1395 \text{ kJ/mol} \tag{7.55}$$

Puolakka and Krause [199] studied CO_2 reforming of *n*-heptane on a 15 wt% Ni/Al_2O_3 catalyst as the model compound of gasoline (Eq. (7.55)). At 900 °C the conversions of *n*-heptane and CO_2 reached 100% and 42%, respectively. The molar ratio of H_2 to CO (0.32) was less than the stoichiometric ratio (0.57), indicating the occurrence of the reverse water-gas shift reaction and the reverse Boudouard reaction. The activity of the catalyst decreased obviously during the 6.5 h experiment. Combining CO_2 reforming with partial oxidation can decrease both the energy requirement and the catalyst deactivation by coke formation. Puolakka et al. [200] also studied the combined CO_2 reforming and partial oxidation of *n*-heptane over zirconia supported various noble metal catalysts between 700 and 900 °C. The activity of the detected metals decreased in the order of Rh, Pd, Ir, and Pt. The activity and selectivity over the 0.25 wt% Rh/ZrO_2 catalyst were comparable with those over a commercial 15 wt% NiO/Al_2O_3 catalyst. The conversions and product compositions approximated were compared to the calculated thermodynamic equilibrium.

7.8. DRY REFORMING OF OXYGENATED HYDROCARBONS

Currently, production of hydrogen is an energy-intensive processing, mainly from nonrenewable hydrocarbons, such as steam reforming of natural gas. The full environmental benefits of using hydrogen as a fuel could be realized when using renewable resources. In this respect, reforming of oxygenated hydrocarbons derived from biomass, such as ethanol, dimethyl ether, and glycerol attracted much attention in the last few years.

7.8.1. Ethanol

Ethanol could be produced from various biomass sources, such as energy crops, residues from agriculture or forestry, and parts of municipal solid waste. Recently, ethanol is being considered as an economically attractive alternative fuel and as a fuel additive and hydrogen source with low pollutant emissions. Thermodynamic calculations indicate that hydrogen production via ethanol reforming is more favorable than the reforming of hydrocarbons and can proceed at temperatures typically below 500 °C (see Fig. 7.8). This higher reactivity at lower temperature is important to improve the heat integration for vehicles equipped with fuel cells. At the same time, ethanol is free of sulfur, which is considered to be a catalyst poison in the reforming of hydrocarbons.

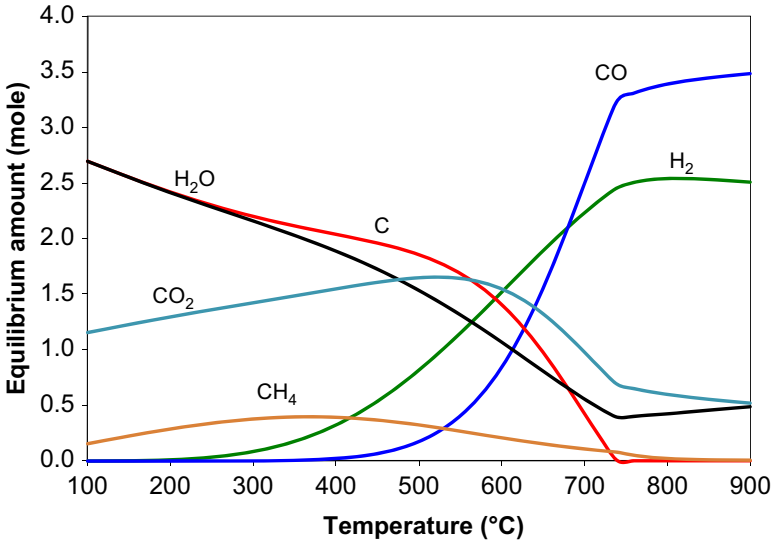

FIGURE 7.8 Effect of temperature on dry reforming of ethanol; equilibrium amount of product species from 1 mole of ethanol at 0.1 MPa and O/C = 1.

$$C_2H_5OH(g) + CO_2(g) = 3CO(g) + 3H_2(g)$$
$$\Delta H^{o}_{298K} = 296.8 \text{ kJ/mol} \tag{7.56}$$

Jankhah et al. [201] found that carbon steel was an active catalyst precursor for ethanol cracking to hydrogen and carbon nanofilaments (CNFs) at 550 °C, but thermal cracking and thermal reforming of ethanol were not beneficial under the same operating conditions. It was found that space velocity had an important influence on the reactivity for dry reforming of ethanol. At a flow rate of 25 ml/min, no significant cracking or reforming activity was observed, while some products were detected at a flow rate of 3 ml/min (according to the reactor's volume, the calculated GHSV was 750 and 90 h^{-1}, respectively) (see Fig. 7.9) [202]. And

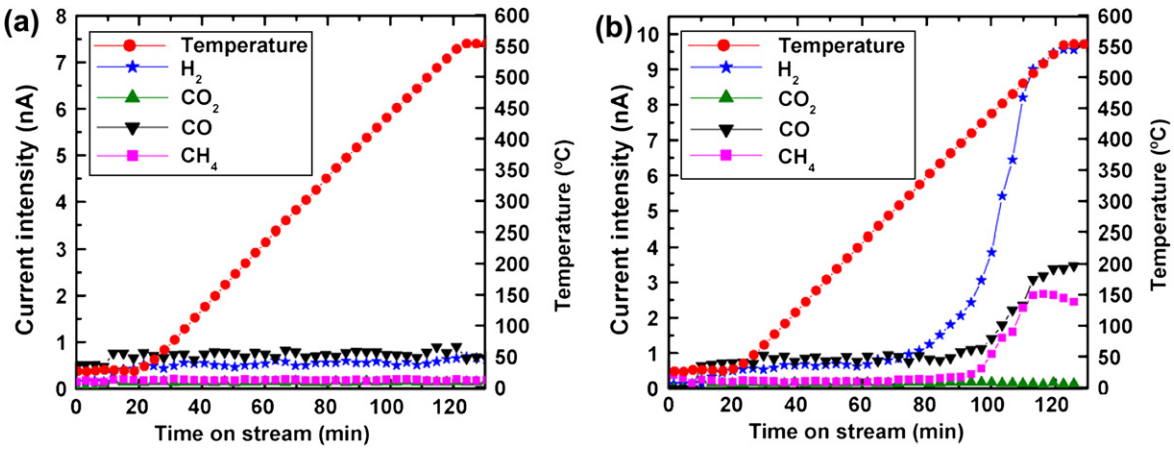

FIGURE 7.9 Product gas of dry reforming of ethanol at 550 °C with fresh steel as catalyst (a) at a flow rate of 25 ml/min, and (b) at a flow rate of 3 ml/min *(reprinted with permission from Blanchard et al. [202], copyright (2008) Elsevier).*

a CO_2/EtOH ratio of 1 favors the production of hydrogen and CNFs in catalytic reforming of ethanol.

Recently, Hu and Lu [203] found that CO_2 reforming of ethanol proceeded efficiently above 700 °C over Ni/Al_2O_3 catalyst, and the CO/H_2 ratio in produced syngas is close to 1. These results were attributed to the competitive reaction of ethanol decomposition with dry reforming at lower temperatures (see Fig. 7.10). Carbon formation is significant at lower temperature and lower CO_2/ethanol ratio. Higher reaction temperature and higher CO_2/ethanol ratio in feed can reduce the coke deposition significantly.

In summary, a biomass-derived ethanol can be utilized as a source of hydrogen via dry reforming with CO_2; this process is more favorable compared with dry reforming of hydrocarbons, and a CO/H_2=1 product gas is formed over Fe_3C and Ni/Al_2O_3 catalyst. But the research works in reaction mechanism and technology are scarce since dry reforming of ethanol has just been initiated.

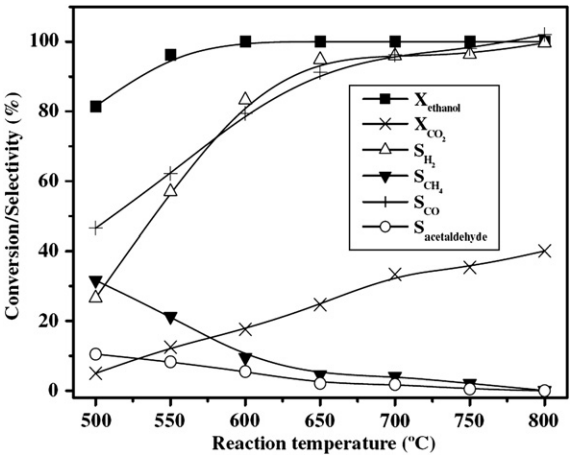

FIGURE 7.10 Feedstocks conversion and product distribution versus temperature: LHSV (liquid hourly space velocity) 5.2 h^{-1}; CO_2/ethanol 3; 0.1 MPa *(Reprinted with permission from Hu and Lu [203], copyright (2009) Elsevier).*

7.8.2. Dimethyl Ether

Biomass-derived dimethyl ether (DME) is also considered a promising hydrogen manufacturing carrier.

$$CH_3OCH_3(g) + CO_2(g) = 3CO(g) + 3H_2(g)$$
$$\Delta H^{o}_{298K} = 245.9\ \text{kJ/mol} \tag{7.57}$$

Thermodynamic calculations indicate that DME reforming is more favorable than that of ethanol in its lower energy input and lower temperature (thermodynamic product distribution is very similar to ethanol; see Fig. 7.8). There are several advantages for operating at lower reforming temperature: (i) reformate with lower CO concentrations was obtained; (ii) reformate with lower CO concentration was suitable for high-temperature polymer electrolyte fuel cells; (iii) downstream CO cleanup steps of the reformer was reduced; and (vi) a low temperature water-gas shift unit was sufficient [204].

Nilsson et al. [204] investigated the autothermal reforming (also known as oxidative stream reforming) of DME on the surface of Pd supported on ZnO, Al_2O_3, and $ZnAl_2O_4$ catalyst. High DME conversion and high H_2 selectivity were found in the temperature range of 350–450 °C (at O_2:DME = 0.7, H_2O:DME = 2.5, and GHSV = 15,000 h^{-1}). Pd/ZA (1000) + γ-Al_2O_3 showed the best catalytic performance, and a 100% conversion of the DME and a 100% selectivity of hydrogen were achieved at 450 °C. For all catalysts, at 450 °C, the concentration of CO, CH_4, and CH_3OH in the product gas was less than 5%, 2%, and 0.5%, respectively. Considering the combination of a water-gas shift unit and a DME-fueled autothermal reformer, the obtained CO concentrations can be reduced to 0.5–1%. The product gas, therefore, could be used as feed for the high-temperature polymer electrolyte fuel cells without further purifying. Zhang et al. [205] also found that the yield of H_2 was more than

90% over Pt/Al_2O_3 and Ni-MgO combined catalysts during the partial oxidation of DME at 700 °C, 0.1 MPa, $DME/O_2/Ar = 30/32/128$ ml/min. The hybrid catalyst exhibited higher activity and stability than the dual-bed ones. High temperature and low space velocity were favorable to increase H_2 yield due to the increased rate of the reaction, and the reforming reaction was a low rate reaction.

In summary, biomass-derived DME is a source of hydrogen via steam reforming and partial oxidation. This process is thermodynamically favorable than dry reforming of hydrocarbons and ethanol. But no report on the dry reforming of DME was published until now.

7.8.3. Glycerol

Glycerol, also called glycerin, is a sugar alcohol, which is a colorless, odorless, viscous, sweet-tasting, low toxicity, water-soluble liquid. Glycerol is a by-product of biodiesel-manufacture. The biodiesel production for 2008 in EU27 and USA was over 7.7 and 2.3 million metric tons, respectively. That is, more than 1.0 million metric tons of glycerol was produced as a by-product. Currently disposal of surplus glycerol is done by incineration. This has resulted in a market surplus of crude glycerol typically containing 20% water and esterification catalyst residues. The crude glycerol, however, can be purified and refined. Recently, much effort has been made to convert glycerol to value-added molecules, such as conversion to propylene glycol, acrolein, ethanol, and epichlorhydrin. In addition, it could be used to produce hydrogen gas.

Thermal cracking of glycerol to CO and H_2 can be performed easily, while this cracking is an endothermic process that needs a huge energy input. In order to decrease the amount of energy input, partial oxidation of glycerol to hydrogen should be more favorable.

$$\begin{aligned} C_3H_8O_3 &= 3CO(g) + 4H_2(g) \\ \Delta H^o_{298K} &= 342.1\ \text{kJ/mol} \end{aligned} \tag{7.58}$$

$$\begin{aligned} C_3H_8O_3 + 1/2O_2(g) &= 2CO(g) + CO_2(g) + 4H_2(g) \\ \Delta H^o_{298K} &= 59.1\,\text{kJ/mol} \end{aligned} \tag{7.59}$$

$$\begin{aligned} C_3H_8O_3 + O_2(g) &= CO(g) + 2CO_2(g) + 4H_2(g) \\ \Delta H^o_{298K} &= -233.8\ \text{kJ/mol} \end{aligned} \tag{7.60}$$

$$\begin{aligned} C_3H_8O_3 + 3/2O_2(g) &= 3CO_2(g) + 4H_2(g) \\ \Delta H^o_{298K} &= -506.8\ \text{kJ/mol} \end{aligned} \tag{7.61}$$

Kunkes et al. [206] reported in their study on the transformation of aqueous glycerol solutions (30 and 80 wt%) over Pt/C, Re/C, and Pt-Re/C catalysts. They found that the turnover frequencies of H_2, CO, CO_2, and light alkanes (methane, ethane, and propane) increased with the addition of Re to Pt/C catalysts at 275 °C and atmospheric pressure. The H_2/CO ratio increased with the addition of Re, demonstrating that Re improved the rate of water-gas shift reaction. Over Pt-Re/C catalyst with an atomic ratio equal to 1, increasing pressure or decreasing temperature caused the increasing of alkanes and light oxygenated hydrocarbons (ethanol, methanol, propanediols, and acetone) at the cost of CO and CO_2.

To our best knowledge, there are no papers on dry reforming of glycerol or partial oxidation of glycerol to synthesis gas reported in the literature.

7.9. SUMMARY

Dry (CO_2) reforming of hydrocarbons, ethanol, and DME is a promising way in the

production of H_2-rich synthesis gas. Among the published works, dry reforming of methane was investigated thoroughly due to the abundant resource of methane in nature gas. At the same time, activation of methane, the most stable molecular structure (C−H bond energy, 435 kJ/mol), also attracted the attention of researchers all over the world. Several research papers on dry reforming of methane have been published and great achievements are in progress. But there are still two main drawbacks that hinder the commercialization and application in large scale. One is that all these reforming reactions are endothermic, and the calculated enthalpy (ΔH) increases with the number of carbon atoms in hydrocarbons. Another is that the carbon deposition occurs easily even on the surface of noble metals, and the deposited carbon would cause deactivation. And yet many commercial operations include CO_2 in the feed to their reformers to adjust syngas composition.

In the past 20 years, most of the published work focused on improving the stability of the catalysts via decreasing the carbon deposition rate. These studies include in changing the nature of the support, the addition of promoters, optimizing the preparation method of support and catalyst, and increasing the dispersion of metals. Sufficient progresses in decreasing the carbon deposition rate were achieved on different types of catalysts, such as alkaline oxide (MgO) and rare earth metal (La_2O_3) supported Ni catalysts, nano-sized ZrO_2 supported Ni, Pt catalysts, and highly dispersed Ni catalysts prepared via a hydrotalcite-type precursors.

But the first drawback (endothermic reactions that require large energy input) does not get enough attention until now. Autothermal reforming (combined partial oxidation and dry reforming) technology and solar energy utilization plus dry reforming technology were recommended.

References

[1] Bradford MCJ, Vannice MA. CO_2 reforming of CH_4. Catal Rev 1999;41(1):1−42.

[2] Hu YH, Ruckenstein E. Binary MgO-based solid solution catalysts for methane conversion to syngas. Catal Rev 2002;44(3):423−53.

[3] Hu YH, Ruckenstein E. Catalytic conversion of methane to synthesis gas by partial oxidation and CO_2 reforming. Adv Catal 2004;48:297−345.

[4] Rostrup-Nielsen JR, Sehested J, Norskov JK. Hydrogen and synthesis gas by steam- and CO_2 reforming. Adv Catal 2002;47:65−139.

[5] York APE, Xiao TC, Green MLH, Claridge JB. Methane oxyforming for synthesis gas production. Catal Rev 2007;49:511−60.

[6] Ferreira-Aparicio P, Benito MJ, Sanz JL. New trends in reforming technologies: from hydrogen industrial plants to multifuel microreformers. Catal Rev 2005;47:491−588.

[7] Halliche D, Bouarab R, Cherifi O, Bettahar MM. Carbon dioxide reforming of methane on modified Ni/alpha-Al_2O_3 catalysts. Catal Today 1996;29: 373−7.

[8] Luna AEC, Iriarte ME. Carbon dioxide reforming of methane over a metal modified Ni-Al_2O_3 catalyst. Appl Catal A: Gen 2008;343:10−5.

[9] Osaki T, Horiuchi T, Sugiyama T, Suzuki K, Mori T. Catalysis of NiO-Al_2O_3 aerogels for the CO_2-reforming of CH_4. Catal Lett 1998;52:171−80.

[10] Wang SB, Lu GQM. CO_2 reforming of methane on Ni catalysts: effects of the support phase and preparation technique. Appl Catal B: Env 1998;16:269−77.

[11] Juan-Juan J, Roman-Martınez MC. Effect of potassium content in the activity of K-promoted Ni/Al_2O_3 catalysts for the dry reforming of methane. Appl Catal A: Gen 2006;301:9−15.

[12] Tang SB, Qiu FL, Lu SJ. Effect of supports on the carbon deposition of nickel-catalysts for methane reforming with CO_2. Catal Today 1995;24:253−5.

[13] Ruckenstein E, Hu YH. Role of support in CO_2 reforming of CH_4 to syngas over Ni catalysts. J Catal 1996;162:230−8.

[14] Pompeo F, Nichio NN, Souza MMVM, Cesar DV, Ferretti OA, Schmal M. Study of Ni and Pt catalysts supported on alpha-Al_2O_3 and ZrO_2 applied in methane reforming with CO_2. Appl Catal A: Gen 2007;316:175−83.

[15] Hou ZY, Chen P, Fang HL, Zheng XM. Yashima T. Production of synthesis gas via methane reforming with CO_2 on noble metals and small amount of noble-(Rh-) promoted Ni catalysts. Int J Hydrogen Energy 2006;31:555−61.

[16] Juan-Juan J, Roman-Martınez MC, Illan-Gomez MJ. Nickel catalyst activation in the carbon dioxide reforming of methane effect of pretreatments. Appl Catal A: Gen 2009;355:27–32.

[17] Wang SB, Lu GQ. A comprehensive study on carbon dioxide reforming of methane over Ni/gamma-Al_2O_3 catalysts. Ind Eng Chem Res 1999;38:2615–25 (Max).

[18] Tsipouriari VA, Verykios XE. Carbon and oxygen reaction pathways of CO_2 reforming of methane over Ni/La_2O_3 and Ni/Al_2O_3 catalysts studied by isotopic tracing techniques. J Catal 1999;187: 85–94.

[19] Zhang ZL, Verykios XE, MacDonald SM, Affrossman S. Comparative study of carbon dioxide reforming of methane to synthesis gas over Ni/La_2O_3 and conventional nickel-based catalysts. J Phys Chem 1996;100:744–54.

[20] Cheng ZX, Wu QL, Li JL, Zhu QM. Effects of promoters and preparation procedures on reforming of methane with carbon dioxide over Ni/Al_2O_3 catalyst. Catal Today 1996;30:147–55.

[21] Cui YH, Zhang HD, Xu HY, Li WZ. Kinetic study of the catalytic reforming of CH_4 with CO_2 to syngas over Ni/alpha-Al_2O_3 catalyst: the effect of temperature on the reforming mechanism. Appl Catal A: Gen 2007;318:79–88.

[22] Cui YH, Xu HY, Ge QJ, Li WZ. Kinetic study on the CH_4/CO_2 reforming reaction: Ni-H in Ni/alpha-Al_2O_3 catalysts greatly improves the initial activity. J Mol Catal A: Chem 2006;243:226–32.

[23] Chen P, Hou ZY, Zheng XM, Yashima T. Carbon deposition on meso-porous Al_2O_3 supported Ni catalysts in methane reforming with CO_2. React Kinet Catal Lett 2005;86:51–8.

[24] Wang SB (Max), Lu GQ. Catalytic activities and coking characteristics of oxides-supported Ni catalysts for CH_4 reforming with carbon dioxide. Energy Fuels 1998;12:248–56.

[25] Kim JH, Suh DJ, Park TJ, Kim KL. Effect of metal particle size on coking during CO_2 reforming of CH_4 over Ni-alumina aerogel catalysts. Appl Catal A: Gen 2000;197:191–200.

[26] Fajardo HV, Martins AO, de Almeida RM, Noda LK, Probst LFD, Carreno NLV, et al. Synthesis of meso-porous Al_2O_3 macrospheres using the biopolymer chitosan as a template: a novel active catalyst system for CO_2 reforming of methane. Mate Lett 2005;59: 3963–7.

[27] Wang SB, Lu GQ. Reforming of methane with carbon dioxide over Ni/Al_2O_3 catalysts: effect of nickel precursor. Appl Catal A: Gen 1998;169: 271–80.

[28] Horiuchi T, Sakuma K, Fukui T, Kubo Y, Osaki T, Mori T. Suppression of carbon deposition in the CO_2-reforming of CH_4 by adding basic metal oxides to a Ni/Al_2O_3 catalyst. Appl Catal A: Gen 1996;144: 111–20.

[29] Roh HS, Jun KW. Carbon dioxide reforming of methane over Ni catalysts supported on Al_2O_3 modified with La_2O_3, MgO, and CaO. Catal Surv Asia 2008;12:239–52.

[30] Goula MA, Lemonidou AA, Efstathiouy AM. Characterization of carbonaceous species formed during reforming of CH_4 with CO_2 over Ni/CaO-Al_2O_3 catalysts studied by various transient techniques. J Catal 1996;161:626–40.

[31] Seok SH, Choi SH, Park ED, Han SH, Lee JS. Mn-promoted Ni/Al_2O_3 catalysts for stable carbon dioxide reforming of methane. J Catal 2002;209:6–15.

[32] Stagg SM, Romeo E, Padro C, Resasco DE. Effect of promotion with Sn on supported Pt catalysts for CO_2 reforming of CH_4. J Catal 1998;178:137–45.

[33] Slagtern A, Olsbye U, Blom R, Dahl IM, Fjellvag H. Characterization of Ni on La modified Al_2O_3 catalysts during CO_2 reforming of methane. Appl Catal A: Gen 1997;165:379–90.

[34] Kumar P, Sun YP, Idem RO. Comparative study of Ni-based mixed oxide catalyst for carbon dioxide reforming of methane. Energy Fuels 2008;22: 3575–82.

[35] Olsbye U, Wurzel T, Mleczko L. Kinetics and reaction engineering studies of dry reforming of methane over a Ni/La/Al_2O_3 catalyst. Ind Eng Chem Res 1997;36:5180–8.

[36] Cui YH, Zhang HD, Xu HY, Li WZ. The CO_2 reforming of CH_4 over Ni/La_2O_3/α-Al_2O_3 catalysts: the effect of La_2O_3 contents on the kinetic performance. Appl Catal A: Gen 2007;331:60–9.

[37] Pechimuthu NA, Pant KK, Dhingra SC, Bhalla R. Characterization and activity of K, CeO_2, and Mn promoted Ni/Al_2O_3 catalysts for carbon dioxide reforming of methane. Ind Eng Chem Res 2006;45:7435–43.

[38] Pompeo F, Gazzoli D, Nichio NN. Stability improvements of Ni/alpha-Al_2O_3 catalysts to obtain hydrogen from methane reforming. Int J Hydrogen Energy 2009;34:2260–8.

[39] Therdthianwong S, Siangchin C. Improvement of coke resistance of Ni/Al_2O_3 catalyst in CH_4/CO_2 reforming by ZrO_2 addition. Fuel Proc Tech 2008;89: 160–8.

[40] Therdthianwong S, Therdthianwong A, Siangchin C, Yongprapat S. Synthesis gas production from dry reforming of methane over Ni/Al_2O_3 stabilized by ZrO_2. Int J Hydrogen Energy 2008;33:991–9.

[41] Gamman JJ, Millar GJ, Rosea G, Drennanb J. Characterisation of SiO_2-supported nickel catalysts for carbon dioxide reforming of methane. J Chem Soc, Faraday Trans 1998;94(5):701–10.

[42] Takahashi R, Sato S, Sodesawa T, Tomiyama S. CO_2-reforming of methane over Ni/SiO_2 catalyst prepared by homogeneous precipitation in sol-gel-derived silica gel. Appl Catal A: Gen 2005;286: 142–7.

[43] Gronchi P, Centola E, Rosso RD. Dry reforming of CH_4 with Ni and Rh metal catalysts supported on SiO_2 and La_2O_3. Appl Catal A: Gen 1997;152:83–92.

[44] Michalkiewicz B, Srenscek-Nazzal J, Ziebro J. Optimization of synthesis gas formation in methane reforming with carbon dioxide. Catal Lett 2009;129:142–8.

[45] Pan YX, Liu CJ, Shi P. Preparation and characterization of coke resistant Ni/SiO_2 catalyst for carbon dioxide reforming of methane. J Power Sources 2008;176:46–53.

[46] Bradford MCJ, Vannice MA. Catalytic reforming of methane with carbon dioxide over nickel catalysts .2. Reaction. Appl Catal A: Gen 1996;142:97–122.

[47] Kroll VCH, Swaan HM, Mirodatos C. Methane reforming reaction with carbon dioxide over Ni/SiO_2 catalyst .1. Deactivation studies. J Catal 1996;161:409–22.

[48] Kroll VCH, Swaan HM, Lacombe S, Mirodatos C. Methane reforming reaction with carbon dioxide over Ni/SiO_2 catalyst: II. A mechanistic study. J Catal 1997;164:387–98.

[49] Hu YH, Ruckenstein E. Transient response analysis via a broadened pulse combined with a step change or an isotopic pulse. Application to CO_2 reforming of methane over NiO/SiO_2. J Phys Chem B 1997;101: 7563–5.

[50] Djaidja A, Libs S, Kiennemann A, Barama A. Characterization and activity in dry reforming of methane on NiMg/Al and Ni/MgO catalysts. Catal Today 2006;113:194–200.

[51] Chen P, Zhang HB, Lin GD, Tsai KR. Development of coking-resistant Ni-based catalyst for partial oxidation and CO_2-reforming of methane to syngas. Appl Catal A: Gen 1998;166:343–50.

[52] Wang YH, Liu HM, Xu BQ. Durable Ni/MgO catalysts for CO_2 reforming of methane: activity and metal-support interaction. J Mol Catal A: Chem 2009;299:44–52.

[53] Hu YH, Ruckenstein E. The characterization of a highly effective NiO/MgO solid solution catalyst in the CO_2 reforming of CH_4. Catal Lett 1997;43:71–7.

[54] Ruckenstein E, Hu YH. The effect of precursor and preparation conditions of MgO on the CO_2 reforming of CH_4 over NiO/MgO catalysts. Appl Catal A: Gen 1997;154:185–205.

[55] Shamsi A. Carbon formation on Ni-MgO catalyst during reaction of methane in the presence of CO_2 and CO. Appl Catal A: Gen 2004;277:23–30.

[56] Chen YG, Tomishige K, Fujirnoto K. Formation and characteristic properties of carbonaceous species on nickel-magnesia solid solution catalysts during CH_4-CO_2 reforming reaction. Appl Catal A: Gen 1997;161:Ll1–7.

[57] Tomishige K, Chen YG, Fujimoto K. Studies on carbon deposition in CO_2 reforming of CH_4 over nickel-magnesia solid solution catalysts. J Catal 1999; 181:91–103.

[58] Ruckenstein E, Hu YH. Role of lattice oxygen during CO_2 reforming of methane over NiO/MgO solid solutions. Catal Lett 1998;51:183–5.

[59] Guo JJ, Lou H, Zheng XM. The deposition of coke from methane on a $Ni/MgAl_2O_4$ catalyst. Carbon 2007;45:1314–21.

[60] Aparicio LM. Transient isotopic studies and microkinetic modeling of methane reforming over nickel catalysts. J Catal 1997;165:262–74.

[61] Ruckenstein E, Hu YH. Carbon dioxide reforming of methane over nickel alkaline earth metal oxide catalysts. Appl Catal A: Gen 1995;133:149–61.

[62] Zhang WD, Liu BS, Tian YL. CO_2 reforming of methane over Ni/SM_2O_3-CaO catalyst prepared by a sol-gel technique. Catal Comm 2007;8:661–7.

[63] Li XC, Hu QH, Yang YF, Chen JR, Lai ZH. Effects of sol-gel method and lanthanum addition on catalytic performances of nickel-based catalysts for methane reforming with carbon dioxide. J Rare Earths 2008; 26:864–8.

[64] Ruckenstein E, Hu YH. Interactions between Ni and La_2O_3 in Ni/La_2O_3 catalysts prepared using different Ni precursors. J Catal 1996;161:55–61.

[65] Valentini A, Carreno NLV, Probst LFD, Barison A, Ferreira AG, Leite ER, et al. Ni:CeO_2 nanocomposite catalysts prepared by polymeric precursor method. Appl Catal A: Gen 2006;310:174–82.

[66] Wang JB, Wu YS, Huang TJ. Effects of carbon deposition and de-coking treatments on the activation of CH_4 and CO_2 in CO_2 reforming of CH_4 over Ni/yttria-doped ceria catalysts. Appl Catal A: Gen 2004;272:289–98.

[67] Li L, Liu BS, Leung JWH, Au CT, Cheung ASC. CH_4/CO_2 reforming over La_2NiO_4 and 10%NiO/CeO_2-La_2O_3 catalysts under the condition of supersonic jet expansion via cavity ring-down spectroscopic analysis. Catal Today 2008;131:533–40.

[68] Rezaei M, Alavi SM, Sahebdelfar S, Bai P, Liu XM, Yan ZF. CO_2 reforming of CH_4 over nanocrystalline zirconia-supported nickel catalysts. Appl Catal B: Env 2008;77:346–54.

[69] Rezaei M, Alavi SM. Nanocrystalline zirconia as support for nickel catalyst in methane reforming with CO_2. Energy Fuels 2006;20:923–9.
[70] Chang JS, Hong DY, Li XS, Park SE. Thermogravimetric analyses and catalytic behaviors of zirconia-supported nickel catalysts for carbon dioxide reforming of methane. Catal Today 2006;115:186–90.
[71] Zhang QH, Li Y, Xu BQ. Reforming of methane and coalbed methane over nanocomposite Ni/ZrO_2 catalyst. Catal Today 2004;98:601–5.
[72] Xu BQ, Wei JM, Yu YT, Li Y, Li JL, Zhu QM. Size limit of support particles in an oxide-supported metal catalyst: Nanocomposite Ni/ZrO_2 for utilization of natural gas. J Phys Chem B 2003;107:5203–7.
[73] Chen JX, Wu QY, Zhang JX, Zhang JY. Effect of preparation methods on structure and performance of $Ni/Ce_{0.75}Zr_{0.25}O_2$ catalysts for CH_4-CO_2 reforming. Fuel 2008;87:2901–7.
[74] Rezaei M, Alavi SM, Sahebdelfar S, Yan ZF. Effects of K_2O promoter on the activity and stability of nickel catalysts supported on mesoporous nanocrystalline zirconia in CH_4 reforming with CO_2. Energy Fuels 2008;22:2195–202.
[75] Osaki T. Effect of reduction temperature on the CO_2-reforming of methane over TiO_2-supported Ni catalyst. J Chem Soc Faraday Trans 1997;93(4): 643–7.
[76] Liu HT, Li SQ, Zhang SB, Chen L, Zhou GJ, Wang JM, et al. Catalytic performance of monolithic foam Ni/SiC catalyst in carbon dioxide reforming of methane to synthesis gas. Catal Lett 2008;120:111–5.
[77] Nguyen DL, Leroi P, Ledoux MJ, Pham-Huu C. Influence of the oxygen pretreatment on the CO_2 reforming of methane on Ni/beta-SiC catalyst. Catal Today 2009;141:393–6.
[78] Pelletier L, Liu DDS. Stable nickel catalysts with alumina-aluminum phosphate supports for partial oxidation and carbon dioxide reforming of methane. Appl Catal A: Gen 2007;317:293–8.
[79] Ginsburg JM, Pina J, Solh TEl, de Lasa HI. Coke formation over a nickel catalyst under methane dry reforming conditions: thermodynamic and kinetic models. Ind Eng Chem Res 2005;44:4846–54.
[80] Luengnaruemitchai A, Kaengsilalai A. Activity of different zeolite-supported Ni catalysts for methane reforming with carbon dioxide. Chem Eng J 2008; 144:96–102.
[81] Jeong H, Kim KI, Kim D, Song IK. Effect of promoters in the methane reforming with carbon dioxide to synthesis gas over Ni/HY catalysts. J Mol Catal A: Chem 2006;246:43–8.
[82] Pinheiro AN, Valentini A, Sasaki JM, Oliveira AC. Highly stable dealuminated zeolite support for the production of hydrogen by dry reforming of methane. Appl Catal A: Gen 2009;355:156–68.
[83] Zhang SB, Wang JK, Liu HT, Wang XL. One-pot synthesis of Ni-nanoparticle-embedded mesoporous titania/silica catalyst and its application for CO_2-reforming of methane. Catal Comm 2008;9: 995–1000.
[84] Nimwattanakul W, Luengnaruemitchai A, Jitkarnka S. Potential of Ni supported on clinoptilolite catalysts for carbon dioxide reforming of methane. Int J Hydrogen Energy 2006;31:93–100.
[85] Barama S, Dupeyrat-Batiot C, Capron M, Bordes-Richard E, Bakhti-Mohammedi O. Catalytic properties of Rh, Ni, Pd and Ce supported on Al-pillared montmorillonites in dry reforming of methane. Catal Today 2009;141:385–92.
[86] Iwasa N, Takizawa M, Arai M. Preparation and application of nickel-containing smectite-type clay materials for methane reforming with carbon dioxide. Appl Catal A: Gen 2006;314:32–9.
[87] Hou ZY, Yashima T. Meso-porous Ni/Mg/Al catalysts for methane reforming with CO_2. Appl Catal A: Gen 2004;261:205–9.
[88] Boukha Z, Kacimi M, Pereira MFR, Faria JL, Figueiredo JL, Ziyad M. Methane dry reforming on Ni loaded hydroxyapatite and fluoroapatite. Appl Catal A: Gen 2007;317:299–309.
[89] Osaki T, Mori T. Role of potassium in carbon-free CO_2 reforming of methane on K-promoted Ni/Al_2O_3 catalysts. J Catal 2001;204:89–97.
[90] Pechimuthu NA, Pant KK, Dhingra SC. Deactivation studies over Ni-K/CeO_2-Al_2O_3 catalyst for dry reforming of methane. Ind Eng Chem Res 2007;46: 1731–6.
[91] Nandini A, Pant KK, Dhingra SC. Kinetic study of the catalytic carbon dioxide reforming of methane to synthesis gas over Ni-K/CeO_2-Al_2O_3 catalyst. Appl Catal A: Gen 2006;308:119–27.
[92] Zhang JG, Wang H, Dalai AK. Kinetic studies of carbon dioxide reforming of methane over Ni-Co/Al-Mg-O bimetallic catalyst. Ind Eng Chem Res 2009;48:677–84.
[93] Qu YQ, Sutherland AM, Guo T. Carbon dioxide reforming of methane by Ni/Co nanoparticle catalysts immobilized on single-walled carbon nanotubes. Energy Fuels 2008;22:2183–7.
[94] Choudhary VR, Mondal KC, Choudhary TV. Methane reforming over a high temperature stable-NiCoMgOx supported on zirconia-hafnia catalyst. Chem Eng J 2006;121:73–7.
[95] Wu JCS, Chou HC. Bimetallic Rh-Ni/BN catalyst for methane reforming with CO_2. Chem Eng J 2009;148: 539–45.

[96] Nowosielska M, Jozwiak WK, Rynkowski J. Physicochemical characterization of Al_2O_3 supported Ni-Rh systems and their catalytic performance in CH_4/CO_2 reforming. Catal Lett 2009;128:83–93.

[97] Quiroga MMB, Luna AEC. Kinetic analysis of rate data for dry reforming of methane. Ind Eng Chem Res 2007;46:5265–70.

[98] Hou ZY, Yashima T. Small amounts of Rh-promoted Ni catalysts for methane reforming with CO_2. Catal Lett 2003;89:193–7.

[99] Jozwiak WK, Nowosielska M, Rynkowski J. Reforming of methane with carbon dioxide over supported bimetallic catalysts containing Ni and noble metal – I. Characterization and activity of SiO2 supported Ni-Rh catalysts. Appl Catal A: Gen 2005;280:233–44.

[100] Chen YG, Tomishige K, Yokoyama K, Fujimoto K. Promoting effect of Pt, Pd and Rh noble metals to the $Ni_{0.03}Mg_{0.97}O$ solid solution catalysts for the reforming of CH_4 with CO_2. Appl Catal A: Gen 1997;165:335–47.

[101] Irusta S, Cornaglia LM, Lombardo EA. Hydrogen production using Ni-Rh on La_2O_3 as potential low-temperature catalysts for membrane reactors. J Catal 2002;210:7–16.

[102] Irusta S, Cornaglia LM, Lombardo EA. Hydrogen production using Ni-Rh on ZrO_2 as potential low-temperature catalysts for membrane reactors. J Catal 2002;210:263–72.

[103] Zhang JG, Wang H, Dalai AK. Development of stable bimetallic catalysts for carbon dioxide reforming of methane. J Catal 2007;249:300–10.

[104] Liu SG, Guan LX, Li JP, Zhao N, Wei W, Sun YH. CO_2 reforming of CH_4 over stabilized mesoporous Ni-CaO-ZrO_2 composites. Fuel 2008;87:2477–81.

[105] Kim DK, Stowe K, Müller F, Maier WF, Kim DK. Mechanistic study of the unusual catalytic properties of a new Ni-Ce mixed oxide for the CO_2 reforming of methane. J Catal 2007;247:101–11.

[106] Gallego GS, Mondragon F, Barrault J, Tatibouet JM, Batiot-Dupeyrat C. CO_2 reforming of CH_4 over La-Ni based perovskite precursors. Appl Catal A: Gen 2006;311:164–71.

[107] Gallego GS, Batiot-Dupeyrat C, Barrault J, Mondragon F. Dual active-site mechanism for dry methane reforming over Ni/La_2O_3 produced from $LaNiO_3$ perovskite. Ind Eng Chem Res 2008;47:9272–8.

[108] Slagtern A, Olsbye U, Blom R, Dahl IM, Fjellvag H. In situ XRD characterization of La-Ni-Al-O model catalysts for CO_2 reforming of methane. Appl Catal A: Gen 1996;145:375–88.

[109] Batiot-Dupeyrat C, Gallego GAS, Mondragon F, Barrault J, Tatibouet JM. CO_2 reforming of methane over $LaNiO_3$ as precursor material. Catal Today 2005;107–108:474–80.

[110] Gallego GS, Mondragon F, Tatibouet JM, Barrault J, Batiot-Dupeyrat C. Carbon dioxide reforming of methane over La_2NiO_4 as catalyst precursor – Characterization of carbon deposition. Catal Today 2008;133–135:200–9.

[111] Valderrama G, Kiennemann A, Goldwasser MR. Dry reforming of CH_4 over solid solutions of $LaN_{1-x}Co_xO_3$. Catal Today 2008;133–135:142–8.

[112] Gallego GS, Batiot-Dupeyrat C, Barrault J, Florez E, Mondragon F. Dry reforming of methane over $LaNi_{1-x}B_yO_{3-\delta}$ (B=Mg, Co) perovskites used as catalyst precursor. Appl Catal A: Gen 2008;334:251–8.

[113] Valderrama G, Goldwasser MR, de Navarro CU, Tatibouet JM, Barrault J, Batiot-Dupeyrat C, Martınez F. Dry reforming of methane over Ni perovskite type oxides. Catal Today 2005;107–108:785–91.

[114] Goldwasser MR, Rivas ME, Pietri E, Pérez-Zurita MJ, Cubeiro ML, Gingembre L, et al. Perovskites as catalysts precursors: CO_2 reforming of CH_4 on $Ln_{1-x}Ca_xRu_{0.8}Ni_{0.2}O_3$ (Ln = La, Sm, Nd). Appl Catal A: Gen 2003;255:45–57.

[115] Khalesi A, Arandiyan HR, Parvari M. Production of syngas by CO_2 reforming on $M_xLa_{1-x}Ni_{0.3}Al_{0.7}O_{3-d}$ (M = Li, Na, K) catalysts. Ind Eng Chem Res 2008;47:5892–8.

[116] Rivas ME, Fierro JLG, Goldwasser MR, Pietri E, Perez-Zurita MJ, Griboval-Constant A, et al. Structural features and performance of $LaNi_{1-x}Rh_xO_3$ system for the dry reforming of methane. Appl Catal A: Gen 2008;344:10–9.

[117] Lima SM, Assaf JM, Pena MA, Fierro JLG. Structural features of $La_{1-x}Ce_xNiO_3$ mixed oxides and performance for the dry reforming of methane. Appl Catal A: Gen 2006;311:94–104.

[118] Zhang WD, Liu BS, Zhu C, Tian YL. Preparation of La_2NiO_4/ZSM-5 catalyst and catalytic performance in CO_2/CH_4 reforming to syngas. Appl Catal A: Gen 2005;292:138–43.

[119] Tian L, Zhao XH, Liu BS, Zhang WD. Preparation of an industrial Ni-based catalyst and investigation on CH_4/CO_2 reforming to syngas. Energy Fuels 2009;23:607–12.

[120] Ruckenstein E, Wang HY. Carbon dioxide reforming of methane to synthesis gas over supported cobalt catalysts. Appl Catal A: Gen 2000;204:257–63.

[121] Ruckenstein E, Wang HY. Carbon deposition and catalytic deactivation during CO_2 reforming of CH_4 over Co/gamma-Al_2O_3 catalysts. J Catal 2002;205:289–93.

[122] Hou ZY, Yashima T. Supported Co catalysts for methane reforming with CO_2. React Kinet Catal Lett 2004;81(1):153–9.

[123] Hao ZG, Zhu QS, Jiang Z, Li HZ. Fluidization characteristics of aerogel Co/Al_2O_3 catalyst in a magnetic fluidized bed and its application to CH_4-CO_2 reforming. Power Tech 2008;183:46–52.

[124] Ji L, Tang S, Zeng HC, Lin J, Tan KL. CO_2 reforming of methane to synthesis gas over sol-gel-made Co/gamma-Al_2O_3 catalysts from organometallic precursors. Appl Catal A: Gen 2001;207:247–55.

[125] Bouarab R, Cherifi O, Auroux A. Reforming of methane by CO_2 in presence of cobalt-based catalysts. Green Chem 2003;5:209–12.

[126] Wang HY, Ruckenstein E. CO_2 reforming of CH_4 over Co/MgO solid solution catalysts-effect of calcination temperature and Co loading. Appl Catal A: Gen 2001;209:207–15.

[127] Nagaoka K, Takanabe K, Aika K. Influence of the reduction temperature on catalytic activity of Co/TiO_2 (anatase-type) for high pressure dry reforming of methane. Appl Catal A: Gen 2003;255:13–21.

[128] Nagaoka K, Takanabe K, Aika K. Influence of the phase composition of titania on catalytic behavior of Co/TiO_2 for the dry reforming of methane. Chem Commun 2002:1006–7.

[129] Mondal KC, Choudhary VR, Joshi UA. CO_2 reforming of methane to syngas over highly active and stable supported CoO_x (accompanied with MgO, ZrO_2 or CeO_2) catalysts. Appl Catal A: Gen 2007;316:47–52.

[130] Choudhary VR, Mondal KC, Choudhary TV. CO_2 reforming of methane to syngas over CoO_x/MgO supported on low surface area macroporous catalyst carrier: influence of Co loading and process conditions. Ind Eng Chem Res 2006;45:4597–602.

[131] Portugal UL, Santos ACSF, Damyanova S, Marques CMP, Bueno JMC. CO_2 reforming of CH_4 over Rh-containing catalysts. J Mol Catal A: Chem 2002;184:311–22.

[132] Wang HY, Ruckenstein E. Carbon dioxide reforming of methane to synthesis gas over supported rhodium catalysts: the effect of support. Appl Catal A: Gen 2000;204:143–52.

[133] Mark MF, Maier WF. CO_2-reforming of methane on supported Rh and Ir catalysts. J Catal 1996;164:122–30.

[134] Stevens RW, Chuang SSC. In situ IR study of transient CO_2 reforming of CH_4 over Rh/Al_2O_3. J. Phys Chem B 2004;108:696–703.

[135] Verykios XE. Mechanistic aspects of the reaction of CO_2 reforming of methane over Rh/Al_2O_3 catalyst. Appl Catal A: Gen 2003;255:101–11.

[136] Wang R, Xu HY, Liu XB, Ge QJ, Li WZ. Role of redox couples of $Rh^0/Rh^{\delta+}$ and Ce^{4+}/Ce^{3+} in CH_4/CO_2 reforming over Rh-CeO_2/Al_2O_3 catalyst. Appl Catal A: Gen 2006;305:204–10.

[137] Yokota S, Okumura K, Niwa M. Strong inhibition effect of sulfur impurities in alumina supports on the catalytic activity of Rh in the CH_4-CO_2 reforming reaction. Appl Catal A: Gen 2006;310:122–6.

[138] Bitter JH, Seshan K, Lercher JA. Mono and bifunctional pathways of CO_2/CH_4 reforming over Pt and Rh based catalysts. J Catal 1998;176:93–101.

[139] Efstathiou AM, Kladi A, Tsipouriari VA, Verykios XE. Reforming of methane with carbon dioxide to synthesis gas over supported rhodium catalysts. 2. A steady-state tracing analysis: Mechanistic aspects of the carbon and oxygen reaction pathways to form CO. J Catal 1996;158:64–75.

[140] Tsipouriari VA, Efstathiou AM, Verykios XE. Transient kinetic study of the oxidation and hydrogenation of carbon species formed during CH_4/He, CO_2/He, and CH_4/CO_2 reactions over Rh/Al_2O_3 catalyst. J Catal 1996;161:31–42.

[141] Gronchi P, Mazzocchia C, Rosso RD. Carbon-dioxide reaction with methane on La_2O_3 supported Rh catalysts. Energy Conver Mgmt 1995;36(6–9):605–8.

[142] Wang HY, Au CT. Carbon dioxide reforming of methane to syngas over SiO_2-supported rhodium catalysts. Appl Catal A: Gen 1997;155:239–52.

[143] Munera JF, Cornaglia LM, Cesar DV, Schmal M, Lombardo EA. Kinetic studies of the dry reforming of methane over the Rh/La_2O_3-SiO_2 catalyst. Ind Eng Chem Res 2007;46:7543–9.

[144] Munera JF, Irusta S, Cornaglia LM, Lombardo EA, Cesar DV, Schmal M. Kinetics and reaction pathway of the CO_2 reforming of methane on Rh supported on lanthanum-based solid. J Catal 2007;245:25–34.

[145] Richardson JT, Garrait M, Hung JK. Carbon dioxide reforming with Rh and Pt-Re catalysts dispersed on ceramic foam supports. Appl Catal A: Gen 2003;255:69–82.

[146] Bhat RN, Sachtler WMH. Potential of zeolite supported rhodium catalysts for the CO_2 reforming of CH_4. Appl Catal A: Gen 1997;150:279–96.

[147] Mattos LV, Rodino E, Resasco DE, Passos FB, Noronha FB. Partial oxidation and CO_2 reforming of methane on Pt/Al_2O_3, Pt/ZrO_2, and Pt/Ce-ZrO_2 catalysts. Fuel Proc Tech 2003;83:147–61.

[148] O'Connor AM, Schuurman Y, Ross JRH, Mirodatos C. Transient studies of carbon dioxide reforming of methane over Pt/ZrO_2 and Pt/Al_2O_3. Catal Today 2006;115:191–8.

[149] Ballarini AD, de Miguel SR, Jablonski EL, Scelza OA, Castro AA. Reforming of CH_4 with CO_2 on Pt-supported catalysts – effect of the support on the catalytic behaviour. Catal Today 2005;107–108:481–6.

[150] Bitter JH, Seshan K, Lercher JA. Deactivation and coke accumulation during CO_2/CH_4 reforming over Pt catalysts. J Catal 1999;183:336–43.
[151] Bitter JH, Hally W, Seshan K, van Ommen JG, Lercher JA. The role of the oxidic support on the deactivation of Pt catalysts during the CO_2 reforming of methane. Catal Today 1996;29:349–53.
[152] Souza MMVM, Aranda DAG, Schmal M. Coke formation on $Pt/ZrO_2/Al_2O_3$ catalysts during CH_4 reforming with CO_2. Ind Eng Chem Res 2002;41:4681–5.
[153] Chen YZ, Liaw BJ, Lai WH. ZrO_2/SiO_2- and La_2O_3/Al_2O_3-supported platinum catalysts for CH_4/CO_2 reforming. Appl Catal A: Gen 2002;230:73–83.
[154] Bradford MCJ, Vannice MA. CO_2 reforming of CH_4 over supported Pt catalysts. J Catal 1998;173:157–71.
[155] Yang M, Papp H. CO_2 reforming of methane to syngas over highly active and stable Pt/MgO catalysts. Catal Today 2006;115:199–204.
[156] van Keulen ANJ, Seshan K, Hoebink JHBJ, Ross JRH. TAP investigations of the CO_2 reforming of CH_4 over Pt/ZrO_2. J Catal 1997;166:306–14.
[157] Bitter JH, Seshan K, Lercher JA. The state of zirconia supported platinum catalysts for CO_2/CH_4 reforming. J Catal 1997;171:279–86.
[158] Noronha FB, Fendley EC, Soares RR, Alvarez WE, Resasco DE. Correlation between catalytic activity and support reducibility in the CO_2 reforming of methane over $Pt/Ce_xZr_{1-x}O_2$ catalysts. Chem Eng J 2001;82:21–31.
[159] Topalidis A, Petrakis DE, Ladavos A, Loukatzikou L, Pomonis PJ. A kinetic study of methane and carbon dioxide interconversion over $0.5\%Pt/SrTiO_3$ catalysts. Catal Today 2007;127:238–45.
[160] Nakagawa K, Anzai K, Matsui N, Ikenaga N, Suzuki T, Teng YH, et al. Effect of support on the conversion of methane to synthesis gas over supported iridium catalysts. Catal Lett 1998;51:163–7.
[161] Mark MF, Mark F, Maier WF. Reaction kinetics of the CO_2 reforming of methane. Chem Eng Technol 1997;20:361–70.
[162] Wisniewski M, Boreave A, Gelin P. Catalytic CO_2 reforming of methane over $Ir/Ce_{0.9}Gd_{0.1}O_{2-x}$. Catal Comm 2005;6:596–600.
[163] Schulz PG, Gonzalez MG, Quincoces CE, Gigola CE. Methane reforming with carbon dioxide. The behavior of Pd/alpha-Al_2O_3 and Pd-CeO_x/alpha-Al_2O_3 catalysts. Ind Eng Chem Res 2005;44:9020–9.
[164] Matsui N, Anzai K, Akamatsu N, Nakagawa K, Ikenaga N, Suzuki T. Reaction mechanisms of carbon dioxide reforming of methane with Ru-loaded lanthanum oxide catalyst. Appl Catal A: Gen 1999;179:247–56.
[165] Ferreira-Aparicio P, Rodrıguez-Ramos I, Anderson JA, Guerrero-Ruiz A. Mechanistic aspects of the dry reforming of methane over ruthenium catalysts. Appl Catal A: Gen 2000;202:183–96.
[166] Carrara C, Munera J, Lombardo EA, Cornaglia LM. Kinetic and stability studies of Ru/La_2O_3 used in the dry reforming of methane. Top Catal 2008;51:98–106.
[167] Claridge JB, York APE, Brungs AJ, Marquez-Alvarez C, Sloan J, Tsang SC, et al. New catalysts for the conversion of methane to synthesis gas: molybdenum and tungsten carbide. J Catal 1998;180:85–100.
[168] Sehested J, Jacobsen CJH, Rokni S, Rostrup-Nielsen JR. Activity and stability of molybdenum carbide as a catalyst for CO_2 reforming. J Catal 2001;201:206–12.
[169] LaMont DC, Thomson WJ. Dry reforming kinetics over a bulk molybdenum carbide catalyst. Chem Eng Sci 2005;60:3553–9.
[170] Naito S, Tsuji M, Miyao T. Mechanistic difference of the CO_2 reforming of CH_4 over unsupported and zirconia supported molybdenum carbide catalysts. Catal Today 2002;77:161–5.
[171] LaMont DC, Gilligan AJ, Darujati ARS, Chellappa AS, Thomson WJ. The effect of Mo_2C synthesis and pretreatment on catalytic stability in oxidative reforming environments. Appl Catal A: Gen 2003;255:239–53.
[172] LaMont DC, Thomson WJ. The influence of mass transfer conditions on the stability of molybdenum carbide for dry methane reforming. Appl Catal A: Gen 2004;274:173–8.
[173] Darujati ARS, Thomson WJ. Kinetic study of a ceria-promoted Mo_2C/gamma-Al_2O_3 catalyst in dry-methane reforming. Chem Eng Sci 2006;61:4309–15.
[174] Naito S, Takada A, Tokizawa S, Miyao T. Mechanistic study on the methane activation over various supported molybdenum carbide catalysts with isotopic tracer methods. Appl Catal A: Gen 2005;289:22–7.
[175] Darujati ARS, Thomson WJ. Stability of supported and promoted-molybdenum carbide catalysts in dry-methane reforming. Appl Catal A: Gen 2005;296:139–47.
[176] Tsuji M, Miyao T, Naito S. Remarkable support effect of ZrO_2 upon the CO_2 reforming of CH_4 over supported molybdenum carbide catalysts. Catal Lett 2000;69:195–8.
[177] Shao HF, Kugler EL, Ma WP, Dadyburjor DB. Effect of temperature on structure and performance of in-house cobalt-tungsten carbide catalyst for dry reforming of methane. Ind Eng Chem Res 2005;44:4914–21.

[178] Osaki T, Horiuchi T, Suzuki K, Moil T. Catalyst performance of MoS_2 and WS_2 for the CO_2-reforming of CH_4 - Suppression of carbon deposition. Appl Catal A: Gen 1997;155:229–38.

[179] Haghighi M, Sun ZQ, Wu JH, Bromly J, Wee HL, Ng E, et al. On the reaction mechanism of CO_2 reforming of methane over a bed of coal char. Proc Comb Inst 2007;31:1983–90.

[180] Song QL, Xiao R, Li YB, Shen LH. Catalytic carbon dioxide reforming of methane to synthesis gas over activated carbon catalyst. Ind Eng Chem Res 2008;47:4349–57.

[181] Wu QY, Chen JX, Zhang JY. Effect of yttrium and praseodymium on properties of $Ce_{0.75}Zr_{0.25}O_2$ solid solution for CH_4-CO_2 reforming. Fuel Proc Tech 2008;89:993–9.

[182] Laosiripojana N, Assabumrungrat S. Catalytic dry reforming of methane over high surface area ceria. Appl Catal B: Env 2005;60:107–16.

[183] Hou ZY, Gao J, Guo JZ, Liang D, Lou H, Zheng XM. Deactivation of Ni catalysts during methane autothermal reforming with CO_2 and O_2 in a fluidized bed reactor. J Catal 2007;250(2):331–41.

[184] Rostrup-Nielsen JR, Hansen JHB. CO_2-reforming of methane over transition-metals. J Catal 1993;44 (1):38–49.

[185] Bodrov IM, Apel'baum LO. Reaction kinetics of methane and carbon dioxide on a nickel surface. Kinet Catal 1967;8:326.

[186] Guo JZ, Hou ZY, Gao J, Zheng XM. DRIFTS study on adsorption and activation of CH_4 and CO_2 on Ni/SiO_2 catalyst with various Ni particle sizes. Chin J Catal 2007;28(1):22–6.

[187] Osaki T, Masuda H, Mori T. Intermediate hydrocarbon species for the CO_2-CH_4 reaction on supported Ni catalysts. Catal Lett 1994;29:33–7.

[188] Guo JZ, Gao J, Chen BH, Hou ZY, Fei JH, Lou H, et al. Catalytic conversion of CH_4 and CO_2 to synthesis gas on Ni/SiO_2 catalysts containing Gd_2O_3 promoter. Int J Hydrogen Energy 2009;34:8905–11.

[189] Solymosi F, Szoke A, Ovari L. Decomposition of ethane and its reaction with CO_2 over Rh/ZSM-5 catalyst. J Catal 1999;186:269–78.

[190] Sutton D, Moisan JF, Ross JRH. Kinetic study of CO_2 reforming of propane over Ru/Al_2O_3. Catal Lett 2001;75(3–4):175–81.

[191] Olafsen A, Daniel C, Schuurman Y, Raberg LB, Olsbye U, Mirodatos C. Light alkanes CO_2 reforming to synthesis gas over Ni based catalysts. Catal Today 2006;115:179–85.

[192] Solymosi F, Szoke A, Egri L. Decomposition of methane and its reaction with CO_2 over Rh/ZSM-5 catalyst. Top Catal 1999;8:249–57.

[193] Raberg LB, Jensen MB, Olsbye U, Daniel C, Haag S, Mirodatos C, et al. Propane dry reforming to synthesis gas over Ni-based catalysts: influence of support and operating parameters on catalyst activity and stability. J Catal 2007;249(2):250–60.

[194] Sutton D, Parle SM, Ross JRH. The CO_2 reforming of the hydrocarbons present in a model gas stream over selected catalysts. Fuel Proc Tech 2002;75: 45–53.

[195] Solymosi F, Tolmacsov P. Decomposition of propane and its reactions with CO_2 over alumina-supported Pt metals. Catal Lett 2002;83(3–4):183–6.

[196] Solymosi F, Tolmacsov P, Zakar TS. Dry reforming of propane over supported Re catalyst. J Catal 2005;233: 51–9.

[197] Solymosi F, Tolmacsov P, Kedves K. CO_2 reforming of propane over supported Rh. J Catal 2003;216: 377–85.

[198] Olafsen A, Slagtern A, Dahl IM, Olsbye U, Schuurman Y, Mirodatos C. Mechanistic features for propane reforming by carbon dioxide over a Ni/Mg (Al)O hydrotalcite-derived catalyst. J Catal 2005;229: 163–75.

[199] Puolakka KJ, Krause AOI. CO_2 reforming of n-heptane on a Ni/Al_2O_3 catalyst. Stud Surf Sci Catal 2004;153:137–40.

[200] Puolakka KJ, Juutilainen S, Krause AOI. Combined CO_2 reforming and partial oxidation of *n*-heptane on noble metal zirconia catalysts. Catal Today 2006;115: 217–21.

[201] Jankhah S, Abatzoglou N, Gitzhofer F. Thermal and catalytic dry reforming and cracking of ethanol for hydrogen and carbon nanofilaments' production. Int J Hydrogen Energy 2008;33:4769–79.

[202] Blanchard J, Oudghiri-Hassani H, Abatzoglou N, Jankhah S, Gitzhofer F. Synthesis of nanocarbons via ethanol dry reforming over a carbon steel catalyst. Chem Eng J 2008;143:186–94.

[203] Hu X, Lu GX. Syngas production by CO_2 reforming of ethanol over Ni/Al_2O_3 catalyst. Catal Comm 2009; 10:1633–7.

[204] Nilsson M, Jansson K, Jozsa P, Pettersson LJ. Catalytic properties of Pd supported on ZnO/$ZnAl_2O_4$/Al_2O_3 mixtures in dimethyl ether autothermal reforming. Appl Catal B: Env 2009;86:18–26.

[205] Zhang QJ, Li XH, Fujimoto K, Asami K. Hydrogen production by partial oxidation and reforming of DME. Appl Catal A: Gen 2005;288:169–74.

[206] Kunkes EL, Simonetti DA, Dumesic JA, Pyrz WD, Murillo LE, Chen JG. The role of rhenium in the conversion of glycerol to synthesis gas over carbon supported platinum-rhenium catalysts. J Catal 2008; 260:164–77.

CHAPTER

8

Plasma Reforming for H_2-Rich Synthesis Gas

Michael J. Gallagher, Jr. [1], *Alexander Fridman* [2]

[1] **National Energy Technology Laboratory, U.S. Department of Energy, 3610 Collins Ferry Rd., Morgantown, WV 26507, USA**

[2] **A.J. Drexel Plasma Institute, Drexel University, 3141 Chestnut Street, Philadelphia, PA 19104, USA**

OUTLINE

Fuel Cells **DOI: 10.1016/B978-0-444-53563-4.10008-2**

8.1. INTRODUCTION

In the search for cleaner, more efficient energy-producing technologies, the fuel cell stands out as one that has the potential to revolutionize how energy is produced throughout the world. As research and development of fuel cell technology continue to grow, so does the portfolio of fuel processing technologies that can deliver the hydrogen and synthesis gas (syngas) required to power them. Currently, most conventional syngas production technologies rely on the conversion of hydrocarbons through chemical processes of steam reforming (SR), oxidative steam reforming (OSR), and partial oxidation (POX). Many of these hydrocarbon conversion systems are operated with assistance from metal catalysts, such as nickel, platinum, and rhodium, in order to accelerate the fuel conversion reactions and lower the required reaction temperatures. Catalytic assistance during reforming can improve efficiency and ultimately lower the energy cost to produce syngas.

Electrically driven ionized gases, such as plasmas, have been involved in fuel conversion and combustion systems over a century and were originally used as a convenient thermal energy source to ignite/initiate combustion reactions. Recently, plasmas have been investigated for their potential to exhibit catalytic effects primarily because of complex interactions of their excited species (electrons, ions, radicals) in fuel conversion reactions [1]. Some evidence has been found for the plasma catalysis effect in lowering the required ignition temperatures for combustion systems [2]; however, more work is needed to elucidate the catalytic effects in fuel-rich syngas production systems. Plasma-assisted fuel conversion is therefore the topic of this chapter and further examination will be made of the types of plasmas used in fuel conversion, evidence of the plasma catalysis effect, and the future challenges to the plasma community in order to demonstrate the effectiveness of this technology.

8.1.1. What Is Plasma?

Plasma is often described as the fourth state of matter, and this refers to the chemical, thermal, or electrical breakdown of a gas, often forming a luminous ionized state comprised of a mix of particles: positive and negative ions, electrons, radicals, and neutral gas atoms and molecules [3]. The act of ionization, when an electron is separated from an atom or molecule leaving a positive ion behind (or attached, thereby creating a negative ion), can be created by means of chemical and/or thermal energy or the electro-dynamic forces from an electric field. A flame is a well-known type of weakly ionized, low-temperature plasma, consisting primarily of a heated pool of radicals and molecules and small amounts of electrons and ions created from chemical and thermal ionization processes [2]. Other types of man-made and some naturally occurring plasmas are created by a strong electric field generated by high potential from the accumulation of charge (e.g., lightning in clouds) or a high voltage source. The electrons within the background gas near the electric field absorb energy from the field, ionize, and then establish a flow of current within channels of the electrically conductive ions and electrons.

Plasmas are categorized as thermal or non-thermal, with the primary difference being how energy is deposited into the plasma gas stream. In thermal plasmas, energy is spent to heat the entire gas stream, and temperatures often range from 10,000 to 100,000 K (10–100 electron volts (eV)). The joule heating effect is responsible for high gas temperatures in thermal plasmas where power is initially transferred from the electric field to electrons and then to the background neutral gas species by way of a large number of electron–neutral collisions [4]. Thermal plasmas are generally considered as expensive heat sources because of the large amount of electrical power needed to generate them, but they are useful in certain industrial applications when extremely high temperatures are needed. For example, thermal arc plasmas are used in metallurgical applications where high temperatures are used to separate aluminum metal from the naturally occurring mineral bauxite (aluminum oxide). In thermal plasmas, the temperatures of all of the plasma components approach thermal equilibrium, which is why these plasmas are often referred to as *equilibrium* plasmas. Alternatively, in non-thermal plasmas, also referred to as *non-equilibrium* plasmas, the temperatures of the plasma components are not the same and electrons often have much greater temperatures than the other gas components. The background gas molecules in non-thermal plasmas are relatively cold (near room temperature), but they can absorb and store energy from the plasma in their thermodynamic energy modes (rotational, vibrational, and electronic). Non-thermal plasmas can influence processes such as molecular dissociation, which lead to the formation of active chemical species that act as aggressive oxidizing and reducing agents. Radicals, such as atomic oxygen (O), hydroxyl (OH), and electronically excited oxygen, are among the many species that are known to influence the kinetics of fuel conversion reactions. Non-thermal plasma-generated radicals and ions behave very much like catalysts, as they can participate in chain reactions that promote or accelerate reaction pathways. Non-thermal plasmas are quite useful in many chemical processing applications, such as chemical etching during microchip manufacturing, because their low gas temperatures and active species can provide control over the chemical selectivity of a process [5].

8.2. TYPES OF PLASMAS USED IN FUEL PROCESSING APPLICATIONS

Both thermal and non-thermal plasmas have many commercial and industrial applications,

but not all types of plasmas are beneficial for fuel processing applications. For example, thermal arc plasmas, while effective at satisfying the thermodynamic energy requirements for fuel conversion reactions because of their high gas temperatures, have low overall energy efficiency because the high energy cost to create the plasma is often comparable to, if not greater than, the heating value of the obtained products. In addition, excessively high temperatures created by plasma arcs can promote pyrolysis reactions and lead to undesirable fuel cracking and/or the formation of olefin byproducts, such as ethylene and acetylene. Certain types of non-thermal plasmas are not desirable for fuel conversion systems because they are weakly ionized and cannot produce a high enough concentration of active species to effectively stimulate conversion. The most effective plasma discharges used in fuel conversion applications have the ability to simultaneously provide high electron temperature and density with a high degree of non-equilibrium to support selective chemical processes [6]. Such plasma discharges include gliding arc plasmas (transitional arcs) and microwave plasmas. In the section that follows, a brief introduction of each type of discharge will be presented to highlight its characteristics and demonstrate the benefits for fuel conversion applications.

8.2.1. Arc Plasmas

Thermal arc plasmas have been used in many industrial and commercial applications throughout history including metallurgy, waste disposal, lighting applications, and ignition systems in vehicles. Arc plasmas are high-current (30 A to 30 kA), low-voltage (10−100 V) discharges that attain very high gas temperatures (10,000−100,000 K or 10−100 eV) due to the high degree of joule heating from the discharge current. Their high gas temperature sustains high current flow by influencing the mechanism by which electrons are supplied to the discharge, namely the thermionic field emission mechanism. Essentially, the thermionic mechanism relies on the synergistic combination of high metal electrode temperature and help from the external electric field that allows a large number of electrons to escape the electrode metal surface thus providing a high flux of current into the discharge [3]. The high temperatures of thermal plasmas can lead to problems such as evaporation and erosion of electrodes that can only be prevented by employing complex electrode cooling systems. Thermal arc plasmas are favorable for certain fuel conversion applications involving solid fuels like coal or biomass, because they can provide the high temperatures needed for gasification. But they have the significant drawback of high electrical energy cost to operate them and therefore have limited applications in syngas and hydrogen production systems.

8.2.2. Non-Thermal Gliding Arc Plasmas

An alternative to high power thermal arc systems is a type of transitional non-thermal plasma called gliding arc. Gliding arc is an auto-oscillating discharge that begins as a thermal arc plasma, and through the force of convective air flow or a magnetic field, it is elongated and cooled until it transitions into a non-thermal plasma. As the arc elongates and extends beyond a certain critical length, heat losses from the arc column exceed power provided by the power supply, and it is not possible to sustain the plasma in a state of thermodynamic equilibrium [6]. At this point, the arc begins to rapidly cool ($T \sim$ 2000 K); current decreases yet power remains constant, therefore voltage increases as does the reduced electric field strength. Increases in the reduced electric field provide for a change in the ionization mechanism that provides for a non-equilibrium distribution of energy (mostly-goes to electrons) and thus the arc transitions into a non-thermal plasma. A non-equilibrium temperature distribution among the other

degrees of freedom was experimentally demonstrated [7], where vibrational temperatures of approximately 3700 K and average electron energies in the range of 0.8−1.1 eV were measured [8]. Gliding arc plasmas are sometimes referred to as *warm* plasmas because they have translational gas temperatures in the range of 2200−2500 K, which are in between the gas temperatures of cold plasmas (300 K) and thermal plasmas (≥10,000 K) [1]. Figure 8.1(a) shows a schematic of a planar gliding arc discharge configuration, where the initial breakdown occurs in the smallest gap between the two electrodes. Figure 8.1 (b) depicts an image of several arcs at various lengths between two diverging electrodes with the non-thermal regime near the top of the image, where the arc lengths are longest.

The 2D planar (flat) geometry of the gliding arc discharge is somewhat effective in fuel conversion systems but is limited because the reactant gas steam can easily flow around the arc and avoid making contact with the discharge. The best arrangement for gliding arc plasma systems is to rotate the arc in a vortex chamber (3D cylindrical geometry) as shown in Fig. 8.2. Vortex-based gliding arc reformers have the advantage of providing good mixing and contact of reactants with the plasma discharge. Gliding arc plasmas have shown some of the best reforming results for conversion of a wide range of hydrocarbons with low electrical energy cost for syngas production [9].

8.2.3. Microwave and Radio Frequency Plasma Discharges

Plasma discharges that are sustained with high-frequency electromagnetic fields have been employed in various syngas production systems [1]. Radio frequency (RF) and microwave discharges are the two types used for this purpose, and they have the unique advantage that the plasma does not need to be in direct contact with the electrodes. Electrode-less operation is often preferred for extremely high temperature reforming applications because it can eliminate the need for complicated electrode cooling. Initiating high-frequency plasmas is more challenging than DC plasmas because they require complex and somewhat more

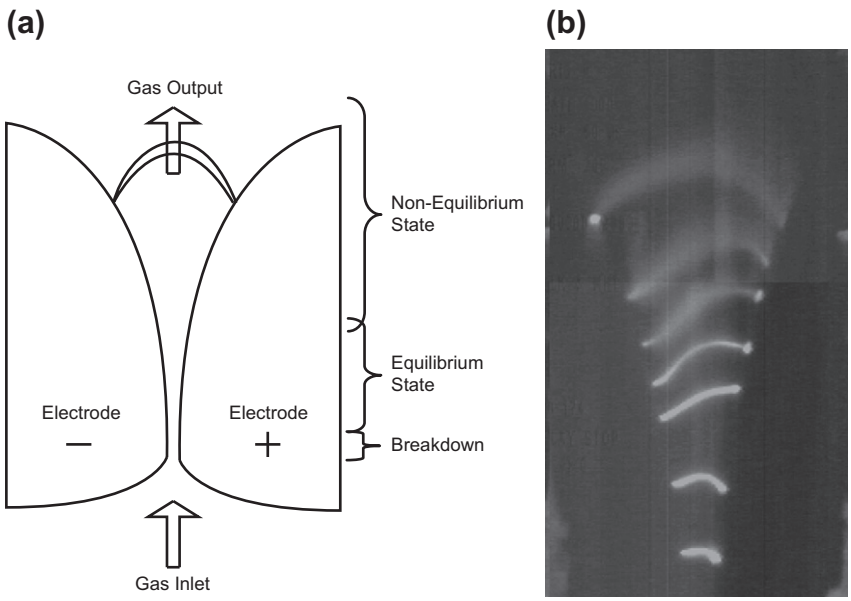

FIGURE 8.1 (a) Schematic of the planar gliding arc showing how the discharge is pushed and elongated by gas flow, causing a transition from equilibrium to non-equilibrium state. (b) An image of several snapshots of the discharge at various lengths along the diverging electrodes *(Reprinted from Fridman [1] Copyright (2008), with permission from Cambridge University Press).*

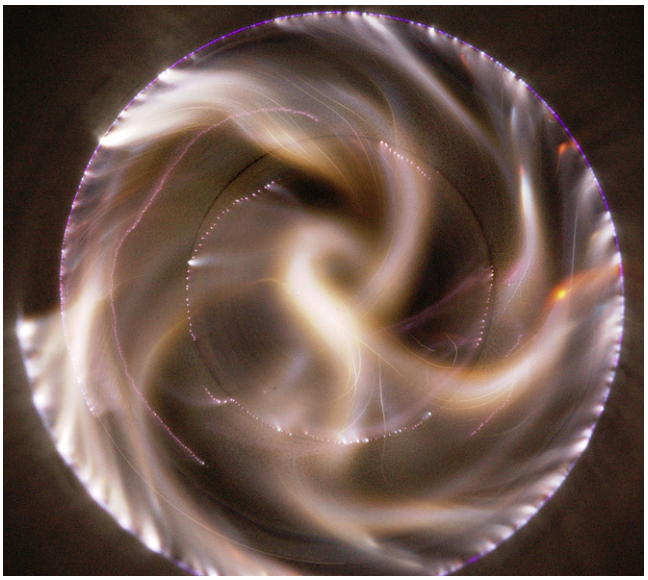

FIGURE 8.2 Photograph of a gliding arc plasma discharge in reverse vortex flow configuration in top view.

expensive power supplies that include a high-frequency generator. More importantly, the plasma must be coupled and matched as a load in the power circuit. In RF plasmas, the electromagnetic fields generated by the power supply interact with the plasma through processes known as inductive or capacitive coupling, with the former used to generate thermal discharges and the latter primarily used for generating non-thermal plasmas. The idea of coupling the electromagnetic field to the plasma discharge is very important because the plasma is sustained by the energy absorbed by the field, and poor coupling means that the efficiency of the power supply and the overall circuit is low. The frequencies used to generate RF plasmas are typically in the range between 0.1 and 100 MHz.

In microwave plasmas, the wavelengths are very small, on the order of centimeters, and approach the dimensions of the reactor itself. Often, waveguides are used to collect and concentrate the electromagnetic waves within the reactor. Not all of the wave power is dissipated in the discharge, however; typically about half is absorbed, a quarter of it is transmitted through the discharge, and another quarter is reflected. The benefit of using complex discharges, such as microwave plasmas, is that the high degree of coupling between the electromagnetic field and the discharge creates conditions that are strongly non-equilibrium with a high degree of ionization. This is much better than the other non-thermal plasmas, where energy density is low and ionization is weak, with only a small fraction of high energy electrons created. In microwave plasmas, increased energy input is used very efficiently in producing a larger fraction of high energy electrons along with higher amounts of vibrationally excited species as compared to other non-thermal plasmas. High power microwave discharges with 95% efficiency have been developed [10], and the increased amount of energetic species can boost the plasma catalysis effect, although the cost of such improvements is a more complex design and more expensive power generation equipment. Microwave

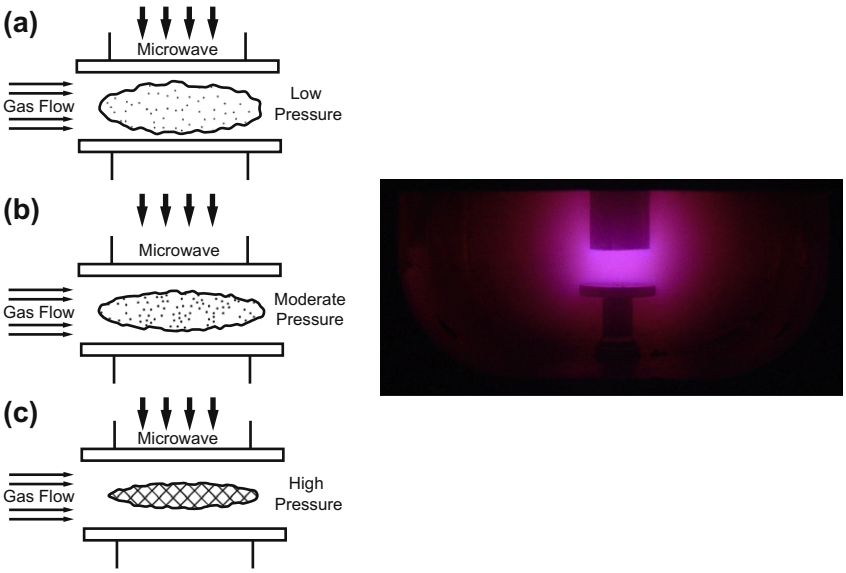

FIGURE 8.3 Microwave plasma configurations in: (a) low pressure provide for a more diffuse and uniform discharge, (b) moderate pressure, and (c) high pressure where the discharge can contract and attain properties similar to a thermal plasma *(Reprinted from Fridman [1] Copyright (2008), with permission from Cambridge University Press). Photograph (right) shows a low-pressure microwave discharge (Photo courtesy of S.K. Remillard [11], Hope College, Holland, MI, USA).*

plasmas can be operated in a wide range of pressures from milliTorr to near atmospheric; however, at higher pressures, the discharge tends to contract and behave similar to a thermal plasma. Figure 8.3 shows various configurations of microwave plasmas [1] and a photo of a low-pressure microwave discharge [11].

8.2.4. Dielectric Barrier Discharge

The dielectric barrier discharge (DBD) is a well known commonly used non-thermal plasma discharge that is employed in many industrial processes related to surface treatments of materials such as polymers and textiles [12,13], ozone generation [14,15], and air sterilization in heating, ventilation, and air conditioning (HVAC) systems [16]. DBD plasmas have a layered electrode structure in which two metal electrodes are separated by a thin layer of dielectric material, often made from ceramic, quartz, or glass (Fig. 8.4). The dielectric barrier acts to limit current flow once the plasma discharge is ignited and prevents the discharge from transitioning into a plasma spark, which can result in much higher gas temperatures, shock waves, and noise. DBD plasmas typically operate with either an AC frequency (0.5–500 kHz) or in a pulsed DC mode and most often have a non-uniform, filamentary structure consisting of a series of microdischarges. DBD plasmas are often used in basic research studies because they are weakly ionized,

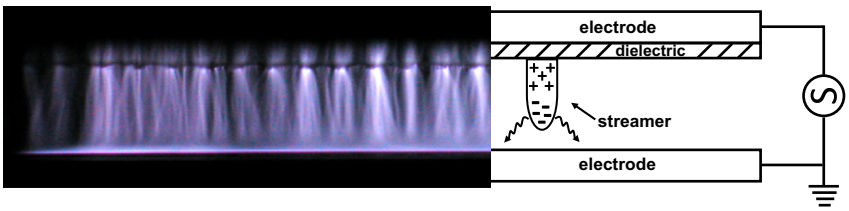

FIGURE 8.4 Dielectric barrier discharge plasma in a planar configuration.

yet strongly non-equilibrium, and are relatively easy to construct.

DBD plasmas have had limited success in fuel conversion systems mainly because of their low power density due to their limited current and low gas temperatures. Since POX and SR reactions require an elevated initial temperature to proceed (800–1100 K), non-thermal DBD systems usually require additional energy to be spent for reactant pre-heating in order to be effective. In addition, the irregular structure of DBD plasmas is not ideal for uniform gas treatment within fuel conversion systems.

8.2.5. Continuous and Pulsed Corona

The corona discharge is another type of strongly non-equilibrium, yet weakly ionized plasma that can be found in nature during electrical storms near sharp edges, points, or thin wires (i.e., near regions of high electric field strength). A corona discharge can be created with a strong, continuous DC electric field and often requires only one electrode. The space surrounding the high-voltage electrode can itself function as a sink for charged particles, thus completing the circuit. Man-made corona discharges are typically arranged with a point-to-plane geometry or as a concentric annulus (thin wire inside of a tube). The strong non-uniformity of the electric field between the two electrodes is the driving force that initiates the corona discharge. As a rule of thumb, the characteristic size of the high voltage electrode should be much less than the distance between electrodes. The corona discharge can become unstable if additional voltage or current is applied causing breakdown between electrodes and forming a strong plasma channel, known as a spark. Spark formation should be avoided because it causes local overheating of the gas as well as non-uniformity of treatment, which is undesirable for many applications. Continuous coronas are then limited in terms of power input; however, one way to increase the power of corona discharges while avoiding spark formation is to use a pulsed power supply to deliver a high amplitude voltage (steep wave front) with short rise times. Pulsed-periodic voltage delivers fast and effective power transfer into the discharge but stops short of spark formation as long as the pulse width is shorter than the transition time (on the order of 100–300 nanoseconds with electrode distances at 1–3 cm) [4]. Corona discharges are attractive for fundamental studies of the plasma catalysis effect in combustion and fuel conversion due to their strongly non-equilibrium nature and good spatial uniformity. Researchers in this area have had success integrating pulsed-corona discharges in shock tubes to study the effect of plasma active species on ignition delay times [17]. However, in practical large-scale commercial and industrial fuel conversion systems, corona plasmas have not been proven to be very effective at stimulating conversion with high efficiency. Figure 8.5 shows a 10 kW pulsed corona discharge used

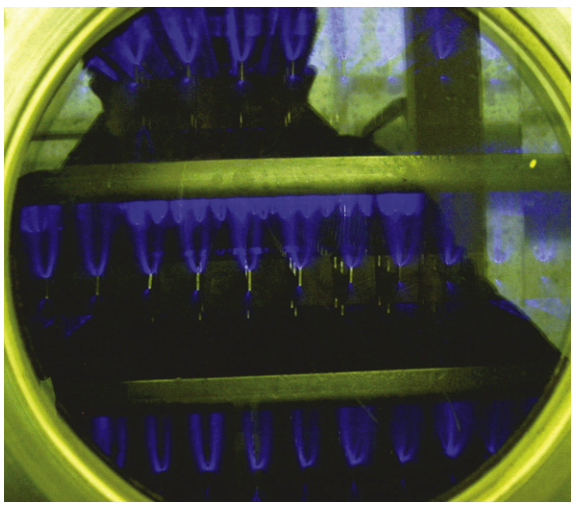

FIGURE 8.5 10 kW pulsed corona discharge used for cleaning volatile organic compounds from paper mills *(Reprinted from Fridman [1] Copyright (2008), with permission from Cambridge University Press).*

for cleaning flue gases from paper mills and wood plants [18].

8.3. PLASMA AS AN ALTERNATIVE TO TRADITIONAL CATALYSTS IN FUEL REFORMING

The kinetic limitations of fuel conversion processes often require higher reaction temperatures than what is necessary to produce the same results when the system is at thermodynamic equilibrium. Lower reaction temperatures are desired not only from the obvious viewpoint of improving energy efficiency, but because higher temperatures can open reaction pathways that may ultimately lead to undesirable coking and soot formation in hydrocarbon reforming systems. Therefore, many modern fuel conversion systems incorporate a catalyst of some kind in order to lower activation energy barriers and thus lower the required reaction temperatures and avoid unwanted by-product formation.

Researchers that incorporate plasma into fuel reforming systems claim that plasma behaves like a catalyst [1]. The effect of *plasma catalysis*, in essence, is caused by the interaction of charged and excited particles generated by plasma that allows for the reduction or removal of activation energy barriers in fuel conversion reactions. It was demonstrated long ago that most exothermic ion−molecule reactions have no activation energy requirement and therefore proceed without barrier [19]. This is because the charge−dipole attraction in plasma-induced ion−molecular reactions is stronger than the quantum-mechanical repulsion between molecules, and thus overcomes most barriers for exothermic reactions to proceed [4].

The major drawback of using plasma for its catalytic properties is that it requires a constant (electrical) energy source in order to sustain it. Some plasma active species have long lifetimes once they are generated, for example, nitrogen oxide (NO) and ozone (O_3) can survive for several minutes and travel long distances from the plasma source. But most of the highly reactive plasma species have very short lifetimes, and recombination occurs in short distances within the plasma itself or near the plasma boundaries and reactor walls. One could even describe plasma as a catalyst that needs constant regeneration from the continuous loss of electrons, ions, and radicals through recombination processes. The need for constant energy input to sustain the plasma raises questions about the economics and the energy cost of using plasma in fuel conversion systems. The cost of using plasma as a catalyst in fuel conversion systems is dependent on how well its active species, particularly ions, participate in fuel conversion reactions. The energy cost to create one ion is high, around 10−30 eV, and therefore the ion should participate in multiple chain reactions to be cost-effective. It is possible to organize such chain reactions in fuel conversion systems; however, many of the kinetic mechanisms involving plasma active species in fuel-rich hydrocarbon conversion reactions are still unknown. Much of the plasma fuel conversion and syngas production research over the past decade has been focused on the design of engineering systems that are capable of producing more syngas at higher conversion rates while operating with lower plasma energy cost. In order to maximize the catalytic effect of plasma, more focus is needed to identify the key reaction mechanisms and pathways for product formation in plasma-assisted fuel conversion processes.

Alternatively, there has been a greater emphasis on identifying plasma mechanisms for the enhancement of ignition and combustion, where reaction mechanisms involving plasma active species and fuels, such as hydrogen and methane, have been identified [20−22]. In the field of plasma-assisted combustion, researchers have discovered that plasma-induced gas excitation can significantly reduce ignition temperature by as much as 600 K and increase a flame's

blow off velocity with very high energy efficiency (less than 1% of burner power is input as plasma power) [2]. Such breakthroughs were made possible through support from the aerospace industry and large contributions from government military research institutions for projects related to jet engine ignition at high altitudes. In addition, plasma combustion researchers have investigated the effects of non-thermal plasma on ignition and stabilization of flames (see Fig. 8.6) [23,24], combustion in supersonic flows [25,26], moderate pressures, and lean mixtures [27].

Plasma combustion researchers have employed experimental installations, such as shock tubes with advanced diagnostics, to specifically isolate and prove the plasma effect for ignition enhancement. The plasma-assisted fuel conversion community is beginning to follow the example of the plasma combustion/aerospace industry in order to answer the most important questions related to the plasma influenced mechanisms of syngas production and the overall significance of plasma for fuel conversion.

8.3.1. Thermal versus Non-thermal Mechanisms of Plasma Catalysis

As stated in the previous section, most of what is known about the plasma catalysis effect is related to mechanisms for *fuel-lean* (or *oxygen-rich*) ignition/combustion of hydrocarbons. These mechanisms, however, overlap *fuel-rich* conversion processes such as POX, since POX is known to begin with a short combustion phase where nearly all oxidizers are consumed to form a small amount of combustion products (H_2O, CO_2) and higher temperatures [28]. In this section, we discuss the specific mechanisms of plasma catalysis related to ignition/combustion and review the postulated mechanisms related to plasma-assisted fuel reforming processes such as POX and steam and dry (CO_2) reforming.

Plasma-assisted ignition and combustion systems are driven by two types of kinetic mechanisms, thermal and non-thermal. The thermal mechanism, in which plasma's contribution is through gas heating alone, results in a local temperature increase, exponential acceleration of elementary combustion reactions, chain propagation of fuel oxidation, and ultimately stable combustion [1]. This mechanism is well known and one of its earliest applications was the spark ignition in internal combustion engines [29]. The thermal ignition mechanism is not very relevant for applications because, although it is the easiest to organize, it has a high energy cost since electrical energy from the plasma is spent non-selectively and is distributed into many degrees of freedom

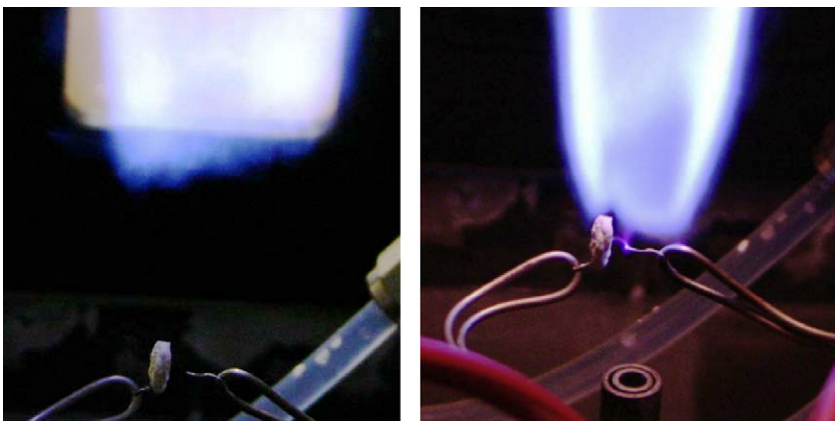

FIGURE 8.6 An illustration of plasma discharge enhanced flame stabilization. The flame is lifted off from the burner without plasma (left) and is attached to the region of plasma discharge (right) *(Reprinted from Kim et al. [24] Copyright (2006), with permission from the Institute of Electronics and Electrical Engineers).*

that are irrelevant for ignition and combustion (i.e., heating of inert nitrogen). Alternatively, non-thermal plasma mechanisms for ignition and combustion have been shown to induce oxidation reactions as a result of interactions between active species, such as excited particles and ions. Often, significant fractions of neutral chemical species acquire and store energy internally (through vibrational or electronic excitation) resulting from collisions between ions and electrons in plasma. This stored energy may be used to overcome activation energy barriers for reactants otherwise in their ground states [30]. Additionally, the non-thermal ignition mechanism allows plasma energy to be used selectively in the creation of these useful active species.

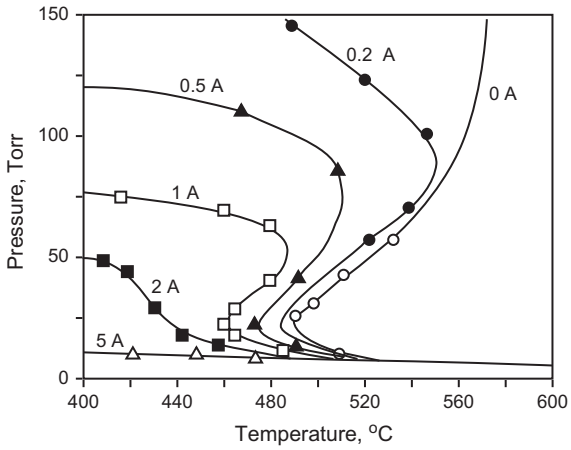

FIGURE 8.7 Demonstration of the effect of plasma in lowering the autoignition temperature of a H_2—O_2 mixture, thereby changing the explosion limit for each increment change in applied current [29]. The "0A" curve corresponds to the conventional autoignition limit when no plasma discharge is present *(Reprinted from Fridman [1] Copyright (2008), with permission from Cambridge University Press).*

8.3.2. Non-thermal Plasma-Induced Mechanisms of Ignition and Stabilization of Flames

There are several known reaction pathways in which the various active particles generated by non-equilibrium plasmas can participate in the stimulation of ignition and combustion of hydrocarbon fuels [1]. Among these options, there are three primary groups of important plasma species, namely excited species, radicals, and ions. The effect generated by the plasma active species in ignition systems is related to shifting the ignition limit, where chain-branching and terminating reactions are balanced. The classical results demonstrating the effect of electrical discharges on the explosion limits for a simple H_2—O_2 mixture [29,31,32] are shown in Fig. 8.7. The effect of increasing plasma current is shown, including the case of "0A" (i.e., no current), which is the conventional H_2—O_2 explosion limit (typically referred to as the S-shaped curve). In the area to the right of the curves, corresponding to higher temperatures, the chain-branching reactions dominate, and this is known as the explosive region. As demonstrated from Fig. 8.7, plasma lowers the threshold temperature required for autoignition, an effect otherwise known as subthreshold ignition. In essence, plasma active species are able to accelerate chain-branching reactions faster than chain terminating reactions at temperatures below the predicted autoignition temperature, where traditional chemical kinetics predict that ignition is impossible. The effect of plasma species on the hydrogen—oxygen ignition reaction has been well studied and is presented in the following sections as a means to explain some of the known effects of plasma catalysis as it relates to ignition and combustion systems.

8.3.2.1. Effect of Excited Species on Subthreshold Ignition in H_2—O_2 Mixtures

Chain-branching and terminating reactions for H_2—O_2 mixtures can be controlled by suppressing the formation of the relatively stable chain-terminating hydroperoxy radical (HO_2) or by accelerating chain-branching radical

formation (H, OH). The most important chain-propagating reactions are described below:

$$H + O_2 \rightarrow OH + O \quad (8.1)$$

$$O + H_2 \rightarrow H + OH \quad (8.2)$$

$$H + O_2 + M \rightarrow HO_2 + M \quad (8.3)$$

Stimulation of chain-branching reactions can occur by means of employing vibrationally or electronically excited particles to destroy the metastable HO_2* complex, thereby recovering the chain-branching radicals O and OH:

$$H + O_2 \rightarrow HO_2^* \quad (8.4)$$

$$HO_2^* + P^* \rightarrow OH + O + P \quad (8.5)$$

where P* represents an excited plasma particle [33]. An additional mechanism to avoid the formation of the HO_2 radical involving vibrationally excited nitrogen (N_2*) is accomplished through the reaction [34]:

$$H + O_2 + N_2^* \rightarrow OH + O + N_2 \quad (8.6)$$

In addition to suppressing formation of the HO_2 radical, it is possible to stimulate the dissociation of HO_2 through vibrational excitation in the following plasma-induced mechanism:

$$HO_2 + N_2^* \rightarrow OH + O + N_2 \quad (8.7)$$

It should be noted that vibrationally excited nitrogen is included in the above mechanisms because it is considered as one of the most stable of the vibrational species produced by plasma.

8.3.2.2. *Effect of Ions on Subthreshold Ignition in H_2–O_2 Mixtures*

The role of plasma-generated ions in fuel conversion and combustion reactions was previously discussed and relates to charge attractive forces that can overcome quantum-mechanical reaction barriers resulting in the plasma-catalysis effect. Kosarev and Starikovskii [35] proposed a low-temperature hydrogen oxidation mechanism involving negative ions from plasma:

$$e + O_2 + M \rightarrow O_2^- + M \quad (8.8)$$

$$O_2^- + H_2 \rightarrow OH^- + OH \quad (8.9)$$

$$OH + H_2 \rightarrow H_2O + H \quad (8.10)$$

$$H + O_2 + M \rightarrow HO_2 + M \quad (8.11)$$

$$OH^- + H \rightarrow H_2O + e \quad (8.12)$$

$$OH^- + HO_2 \rightarrow H_2O + O_2 + e \quad (8.13)$$

The effectiveness of this mechanism is limited by competition between electron detachment and the fast recombination processes of reactions (8.12) and (8.13) [1]. Other ionic mechanisms similar to this one may be responsible for the effects related to subthreshold ignition and can be applied to ignition and combustion of hydrocarbons. More investigation is needed in this area to further understand the effects of ions and to apply these principles to fuel conversion and hydrogen production systems.

8.3.2.3. *Effect of Radicals and Other Long-Lived Species on Subthreshold Ignition*

Plasma-generated oxidizing radicals, such as atomic oxygen (O), ozone (O_3), nitrogen oxide (NO), and other hydrocarbon radicals like CH, CH_2, CH_3 have been investigated to provide insight into their influence on the kinetic pathways of ignition and combustion [27,36]. Starikovskaia [20] performed an efficiency analysis of the effects of atomic oxygen on ignition of H_2–O_2 mixtures at various initial temperatures and found that, at lower temperatures, the main effect of ignition acceleration was caused by fast local gas heating upon recombination of atomic oxygen to O_2. Following on this concept, a plasma-related variant of the thermal ignition mechanism known as the radical-thermal bootstrap mechanism was developed to explain some of the subthreshold ignition

results. Again, the idea is that instantaneous thermalization of plasma energy caused by heating upon recombination and relaxation of plasma radicals can boost temperatures from subthreshold to above-threshold conditions. The radical-thermal bootstrap mechanism is considered a thermal mechanism for ignition; however, it is possible to accelerate the bootstrap effect by using non-thermal plasmas through short oxidation chains below the autoignition limit, thereby increasing the energy efficiency over the thermal ignition mechanism alone [1].

An additional mechanism involving the long-lived NO radical has also been shown to improve subthreshold ignition by suppressing chain-terminating processes through the following mechanism:

$$NO + HO_2 \rightarrow NO_2 + OH \quad (8.14)$$

$$H + NO_2 \rightarrow NO + OH \quad (8.15)$$

The above mechanism can be effective for stimulating ignition, not only because NO has a long lifetime, but also because it is produced with relatively high concentrations in combustion systems.

Additional mechanisms that describe observed reductions in ignition delay time and ignition temperature that involve plasma-generated oxygen atoms have been investigated in systems with higher hydrocarbon species including methane and ethylene [37,38].

8.3.3. Effect of Plasma Active Species on Hydrogen-Rich Syngas Production Systems

All of the previously described mechanisms explained the effect of some of the plasma active species on ignition and combustion of mostly hydrogen–oxygen systems. Less is known about the effect of plasma active species on conversion of hydrocarbon fuels to hydrogen-rich synthesis gas (H_2, CO); however, there are a few research groups that are making progress in identifying plasma's role in these reactions [39,40]. Many investigations have focused on methane conversion in plasma-assisted processes such as direct decomposition (pyrolysis) [41–46]; methane oxidative conversion using air and pure O_2 [47–50], H_2O and CO_2 [51]; and OSR [52–54]. The following sections provide an overview of the mechanisms of plasma catalysis as they relate to these syngas production processes.

8.3.4. Some Plasma Catalysis Mechanisms for Methane Conversion

8.3.4.1. Direct Decomposition (Pyrolysis)

Direct non-oxidative conversion of methane with the plasma-catalysis effect can occur with the production of hydrogen and carbon:

$$CH_4 \rightarrow C(s) + 2H_2 \quad (8.16)$$

This process has the potential to produce CO_2-free hydrogen, although it is endothermic and requires thermal energy input ($\triangle H = 0.7$ eV/mol) to sustain the process. Experimental work using non-thermal plasmas for pyrolysis was performed by Givotov et al. [55] using microwave plasmas with some preheating of reactants. It was found that the addition of plasma energy caused a decrease in the reaction temperature, and it is believed that a fraction of the input plasma energy (<20%) is spent in catalytic stimulation of reaction (8.16). Givotov et al. [55] postulated several possible mechanisms of plasma-stimulated pyrolysis including process stimulation from non-uniform temperature distributions in the discharge, effect of plasma radicals and excited species, CH_4 decomposition on the surface of carbon clusters, and the ion-Winchester mechanism. The methyl ion radical CH_3^+ was found to provide the most

effective chain stimulation for the production of hydrogen and multiple carbon cluster growth to sizes up to C_{20}. The ion-Winchester mechanism is thought to have the strongest effect in CH_4 decomposition, and it begins with dissociative ionization by electron impact:

$$e + CH_4 \rightarrow CH_3^+ + H + e + e \quad (8.17)$$

Carbon cluster formation with hydrogen production then proceeds through the following:

$$CH_3^+ + CH_4 \rightarrow C_2H_5^+ + H_2 \quad (8.18)$$

Increasing growth of carbon clusters occurs through the attachment of CH_2 groups, with additional hydrogen production occurring through two pathways:

$$C_nH_{2n+1}^+ + CH_4 \rightarrow C_{n+1}H_{2n+3}^+ + H_2 (\text{for } n > 1) \quad (8.19)$$

$$C_nH_{2n+1}^+ + CH_4 \rightarrow [C_{n+1}H_{2n+5}^+]^* \quad (8.20)$$

Chain termination of this process occurs due to recombination of charged particles:

$$e + C_{n+1}H_{2n+3}^+ \rightarrow C_{n+1}H_{2n+2}^+ + H \quad (8.21)$$

$$e + CH_3^+ \rightarrow CH_2 + H \quad (8.22)$$

The experimental results of plasma-assisted pyrolysis are described in Section 8.4.4.

8.3.4.2. *Partial Oxidation*

There have been fewer studies on the mechanisms of the plasma catalysis effect for the POX of methane and other hydrocarbon fuels as compared to pyrolysis and ignition/combustion studies. This may be due to the fact that several of the reaction mechanisms for plasma stimulation of pyrolysis (non-oxidative) and ignition/combustion (highly oxidative) overlap within the POX (moderately oxidative) processes. POX begins with a rapid-oxidation phase in which nearly all free oxygen is consumed to form the combustion products H_2O and CO_2 [28,56]. Because of this rapid combustion phase, regions of fuel-rich mixtures are created in which almost no oxidizers are present, and pyrolysis reactions can occur almost simultaneously. Nair et al. [54] suggested that the mechanisms of plasma-stimulated POX of methane begin with the following four reactions:

$$e + CH_4 \rightarrow CH_3 + H + e \quad (8.23)$$

$$e + CH_4 \rightarrow CH_2 + H_2 + e \quad (8.24)$$

$$e + CH_4 \rightarrow CH + 3H + e \quad (8.25)$$

$$e + O_2 \rightarrow 2O + e \quad (8.26)$$

In this mechanism, electrons from the plasma are postulated to play an important role in non-oxidative CH_4 decomposition, while free oxygen is converted into aggressive oxygen radicals.

Nair et al. [54] combined experimental investigation of methane POX in a DBD plasma at low temperatures (<200 °C) with a kinetic model, which included over 180 reactions with 29 species. Their investigation showed that at low temperatures, C_1 oxygenated species (such as CH_2O and CH_3O) are formed as intermediate products and are then further oxidized to syngas products CO and H_2. They also noted that the greatest limitation of plasma-assisted POX is low selectivity toward H_2 because of the plasma's affinity to oxidize H_2 to H_2O; however, this may be improved by moving to a combined steam-oxidative reforming process.

Rusanov et al. [57] described a short-chain mechanism for the non-thermal plasma conversion of methane that includes intermediate products acetylene and ethylene. This process is described in the framework of several conversion zones within a plasma reformer: the zone ahead of the combustion wave front, the high temperature zone immediately behind the combustion front, and the zone beyond (far behind) the combustion front. The zone beyond

the combustion front includes some amount of combustion products from the rapid oxidation phase (CO_2, H_2O), some POX products (CO, H_2), and some amount of pyrolysis products (C_2H_2, C_2H_4). The process also includes a short chain mechanism that describes the creation and destruction of the intermediate residual hydrocarbons by the following:

$$H_2O + H \rightarrow OH + H_2^* \quad (8.27)$$

$$2C_2H_2 + 2OH \rightarrow 2CO + 2CH_3 \quad (8.28)$$

$$2CH_3 \rightarrow C_2H_4 + H_2 \quad (8.29)$$

$$C_2H_4 + M \rightarrow C_2H_3 + H + M \quad (8.30)$$

$$C_2H_3 + M \rightarrow C_2H_2 + H + M \quad (8.31)$$

This process can also be used to describe acetylene conversion to syngas.

Researchers are currently continuing efforts to identify and understand the underlying mechanisms related to plasma-assisted POX, steam, and CO_2 reforming. Greater knowledge of these mechanisms will ultimately help scientists and engineers to optimize future plasma-assisted reforming systems. In the meantime, the existing experimental plasma reforming systems can provide valuable information about the effects such as temperature, plasma energy input, and other factors, which are known to have a direct impact on the efficiency of plasma reformers.

8.3.5. Advantages of Plasma Catalysis in Fuel Reforming Systems

There are several other important factors that contribute to the advantages of using plasma for fuel cell-based conversion systems over traditional catalytic systems. These factors are particularly important for transportation applications where plasma reformers may be combined with fuel cells to power electric motors onboard vehicles. The following sections highlight these important factors.

8.3.5.1. Rapid Start-Up

Traditional thermal catalytic systems require long preheating times in order to reach the required activation temperatures for the metal catalysts to become effective. These temperatures are in the range of 900−1300 K [58], and given the typical high density of packed-bed and monolith-structured catalyst systems, this can require preheating times on the order of tens of minutes to hours in duration. The principle advantage of plasma reformer systems is that the plasma has a near-instantaneous response and requires no preheating to initiate fuel conversion reactions. This is especially important for onboard reformers for vehicles where plasma reformers could be used to generate hydrogen or hydrogen-rich syngas for fuel cells.

8.3.5.2. Sulfur Tolerant Process

Most metal-based catalyst systems suffer from deactivation problems due to impurities in the fuel feedstock stream which can bind with active sites on the catalyst surface [59]. Deactivation by sulfur, which is commonly found in liquid hydrocarbon fuels such as Diesel and JP-8, is often irreversible and can render the catalyst useless. Catalyst deactivation can also occur from coke and carbonaceous deposits on catalyst surfaces that can occur during reforming reactions; however, it is possible to regenerate by increasing oxygen and temperature and burning off the coke/soot [60]. Plasma-based fuel conversion systems do not suffer from these limitations because it is a gaseous-phase, volumetric catalyst with no surfaces with which these compounds can bind.

8.3.5.3. Reduced Carbon By-Product Formation

Many researchers report observations of little or no soot formation in rich and ultra-rich plasma-assisted fuel conversion systems [47,61,62]. One explanation of this observed

effect is that plasma is strongly oxidative and can provide fast oxidation of soot precursors. The strong oxidative effect is due in part to the acidic nature of air-driven plasmas. The acidic nature of plasma begins with the ionization of air (21% O_2–79% N_2) and leads to a large production of N_2^+ ions, which can then easily react with water through the following:

$$N_2^+ + H_2O \rightarrow N_2 + H_2O^+ \qquad (8.32)$$

Although water is only present in small quantities in air, the presence of water ions leads to interactions with neutral water molecules forming hydronium ions and hydroxyl radicals:

$$H_2O^+ + H_2O \rightarrow H_3O^+ + OH \qquad (8.33)$$

The efficiency of production of H_3O^+ and OH from these reaction mechanisms determines the level of acidity of air plasmas and defines plasma's overall oxidative nature.

As previously mentioned, the surfaces of metal catalysts can induce soot formation because they can act as deposition sites where carbon products and soot prefer to condense. Some researchers have combined plasma and metal catalysts in so-called plasma-catalytic reformers, in order to eliminate soot formation while still realizing the benefits of catalyst reforming. In this way, plasma acts as an initiator of reforming reactions, preventing soot formation on the catalyst surface, while the catalyst itself acts to improve heat transfer in the post-plasma region and complete the reforming reactions. Combined plasma-catalytic reforming is described in more detail in Section 8.6.

8.3.5.4. *Small and Compact Systems*

The characteristic size of atmospheric pressure plasma reformers for syngas production can be quite small and compact. An example of such a reformer is the Gliding-Arc Plasmatron device from Drexel University [62], which has a total volume of less than 1 l and is capable of producing up to 20 kW of syngas from heavy hydrocarbons such as diesel (Fig. 8.8) [63]. Such a compact design is again important for vehicular-based onboard reforming systems and portable auxiliary power units.

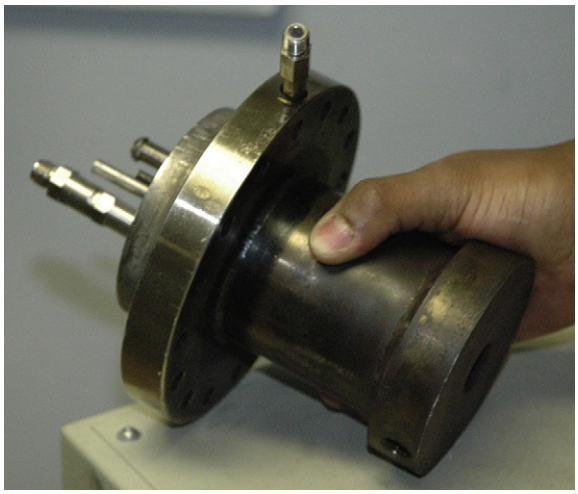

FIGURE 8.8 Photograph of a portable Gliding Arc Plasmatron Device from Drexel University [63].

8.3.5.5. *Possibility of Combining Desulfurization and Reforming*

Another advantage of the plasma catalytic effect in fuel conversion systems is the possibility of combining syngas production and desulfurization together in one process. When sulfur-containing fuels are reformed into syngas, the sulfur is typically converted into hydrogen sulfide gas, which can then react with active sites on metal catalyst surfaces causing solid sulfur to bind with the catalyst and deactivate it. Non-thermal plasma has the capability to dissociate H_2S with low energy input (1.2 eV/mol) and create solid sulfur and H_2 as products [64,65]. In addition, some researchers have investigated the effectiveness of non-thermal plasma in converting

H_2S within syngas streams with varying degrees of success [66].

8.4. PLASMA REFORMING OF METHANE

Plasma-assisted conversion of light, gaseous hydrocarbons has been widely investigated, and the research areas have focused on pyrolysis, steam or CO_2 (dry) reforming, and POX to synthesis gas. Conversion of methane has drawn the most attention due to its high content within abundant natural gas resources and also the large database of kinetic information that describes the details of methane combustion and POX reactions, which some researchers have utilized for modeling and simulation of plasma-assisted conversion [67,68]. In this section, the most relevant results related to plasma-assisted conversion will be presented. The focus will be on results which provide the lowest plasma energy cost with good conversion, such as those from microwave and gliding arc plasma systems.

The primary issue with plasma-assisted conversion is reducing the electrical energy cost of plasma to produce syngas. While it is true that researchers have shown success at reforming various hydrocarbons into syngas with high power thermal plasma systems, the energy cost in these systems is too high and amounts to tens of percent of the heating value of the fuel [9]. Plasma should only be used to stimulate the process, as a catalyst does, and efforts should be made to avoid using plasma as an expensive electrical power source to provide gas heating. Many researchers have therefore focused their efforts to use non-thermal plasmas for fuel conversion because they have relatively cold gas temperatures and can produce a high degree of reactive radicals, vibrationally excited species, and high energy electrons that can stimulate energy efficient chain reactions. The most widely used parameter to measure energy input from plasma-assisted reformers is the specific energy cost of plasma to produce syngas. The specific energy cost is often described in terms of electron volts per molecule of hydrogen produced (eV/mol H_2), but others use more familiar units such as kWh/m^3 and kJ/mol (for reference: 1 eV/molecule $\approx$ 1.2 kWh/m^3 and 100 kJ/mol). Since the specific energy cost to produce syngas is dependent on the amount of syngas produced, it is inherently tied to the physical conversion for each set of conditions for each system. In other words, if the specific energy cost for a particular system is high, the system may have had poor physical conversion of fuel to syngas, and therefore the energy input into the system per mole of syngas produced is high. The specific energy cost can be used as a baseline parameter to compare the electrical cost of plasma to the required reaction enthalpy and externally supplied thermal energy. The specific energy cost can also be used to compare the costs of plasma with other technologies such as catalytic reformers.

8.4.1. Plasma-Assisted Partial Oxidation

Many non-thermal atmospheric pressure plasmas have been used to investigate methane POX, such as microwave discharges [57,69,70], pulsed corona [71,72], and gliding arc [47,49,61]. Gliding arc plasmas are ideal for conversion of hydrocarbons because of their proven non-equilibrium effects [6] and relatively high power density, which is desirable for high-productivity industrial systems. In addition, gliding arc plasmas have demonstrated some of the highest yields and energy efficiencies of all plasma fuel conversion systems thus far [9]. Kalra et al. [61] investigated methane conversion using a gliding arc in tornado (GAT) system where a rotating gliding arc discharge was elongated to a fixed length between two ring electrodes inside a vortex chamber. This configuration included an

internal heat exchanger to provide heat recuperation and allowed for preheating of reactants to temperatures around 700 K. Experimental results for conversion efficiency are shown in Fig. 8.9, where approximately 85% conversion of methane was observed at an O/C ratio of 1.3. A kinetic model was developed to simulate the expected methane conversions with and without plasma, which are shown as the solid and dotted lines, respectively in Fig. 8.9. The experimental results of plasma-assisted conversion matched reasonably well with model predictions and were higher than the predicted conversion by thermal energy alone.

The electrical energy cost to produce syngas was approximately 0.09 kWh/m^3, which is a small fraction (3%) of the total chemical power of the system. In addition, there was no soot formation observed in the range of O/C ratios investigated when the plasma discharge was present; however, soot formation was observed in trials without the presence of the plasma.

Additional work on methane POX using microwave plasma discharges was performed by Babaritskii et al. [69] with the goal of separating the effect of thermal heating from the plasma energy input for stimulating methane conversion. In these trials, a continuous, atmospheric-pressure microwave discharge (2.45 GHz, power: 0.5–3 kW) was used to generate the non-equilibrium plasma, and thermal energy was varied by controlling the preheat temperatures of the fuel/air mixture and the O/C ratio. The results in Fig. 8.10 show that when plasma power (E_{disch}) is kept constant at 1.7 J/cm^3 (curve 1) and 3 J/cm^3 (curve 2), there is an increase in conversion (α^*) with increasing thermal energy input (reflected in increasing ε_{tot}). However, a larger rate of conversion occurs when thermal energy is kept constant at 1.7 J/cm^3 and plasma power is varied, which is apparent by the steeper slope of curve 3.

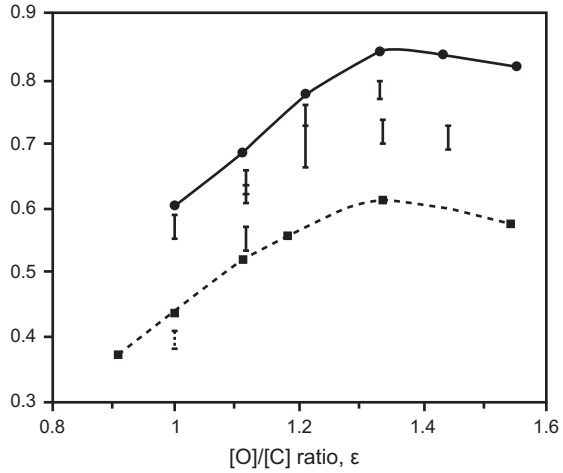

FIGURE 8.9 Methane conversion as a function of the O/C ratio for the GAT system. Kinetic simulation results with plasma effect are shown with solid line with dots; plasma experimental results are shown with solid bars; kinetic simulation results without plasma are shown as dotted line; and experimental results without plasma are shown as dotted bar *(Reprinted from Fridman [1] Copyright (2008), with permission from Cambridge University Press).*

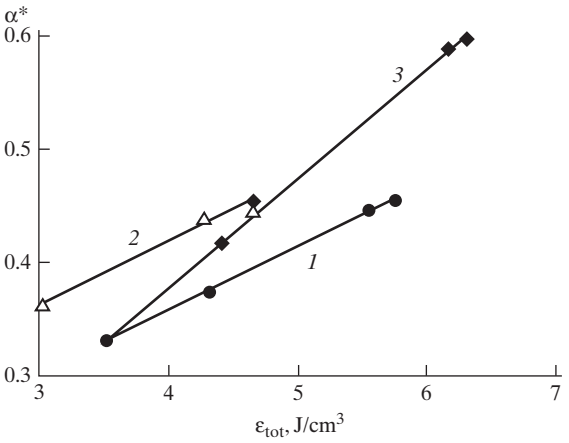

FIGURE 8.10 Relative conversion of methane into synthesis gas as a function of the total specific energy input in a coaxial microwave plasmatron. Variation in thermal energy input at (1) E_{disch} = 1.7 J/cm^3 = const, (2) E_{disch} = 3 J/cm^3 = const, and (3) change in the discharge energy input at E_T = 1.7 J/cm^3 = const *(Reprinted from Babaritskii et al. [69] Copyright (2004), with permission from Pleiades Publishing, Inc.).*

These results demonstrate that the effect of non-thermal plasma in stimulating POX processes is greater than the effect of adding the equivalent amount of thermal energy alone. The reported conversion in these results is low (~60%) compared to results obtained in gliding arc systems (~85%); however, this experiment highlights that the plasma catalytic effect is not necessarily a result of plasma-induced thermal deposition of energy into the reaction. Better reforming results using microwave plasmas were obtained by Rusanov et al. [73] who demonstrated methane conversions of 70% and 100% at plasma energy consumptions of 0.25 and 0.5 eV/molecule, respectively. They attributed these results to plasma-induced initiation of chain processes. Further investigations are needed to elucidate the detailed mechanisms of the plasma catalytic effect in plasma-assisted POX systems.

8.4.2. Plasma-Assisted Steam-Reforming

Plasma-assisted conversion of hydrocarbons with water vapor is a method that holds great promise because it can be organized effectively and has the potential to produce very high hydrogen selectivity and yields [51]. The methane steam-reforming process is endothermic, and it requires thermal energy input of approximately 2.2 eV/molecule to produce syngas at a ratio of H_2:CO of 3:1 under thermodynamic equilibrium conditions [1]. Givotov et al. [55] described results of methane SR using a pulsed microwave plasma (9 GHz frequency, up to 100 kW power per pulse, pulse frequency of 1 kHz, and pulse duration 0.3–1 μs) with reactant preheating from 500 to 570 °C and CH_4:H_2O ratios of 1:1 and 1:2. With plasma energy input of approximately 5% of the total thermal energy of the process, methane conversion increased from 10% to 16%. Results showing the increase in conversion with and without plasma are shown in Fig. 8.11. Total conversion in this case was low (only 16% H_2 in exhaust), but the presence of plasma boosts conversion and decreases energy costs by 30–60%, corresponding to a specific energy cost of approximately 2.1 eV/molecule H_2 produced [1].

Sekine et al. [74] investigated steam-methane reforming at a steam/carbon ratio of 1 using a pulsed spark discharge (30 kV, 0–10 mA, pulse frequency 0–300 Hz). The experiments were performed at low reaction temperatures of 393 K, which are significantly lower than typical catalytic reforming systems (800 K). The results indicated that the maximum methane conversion achieved was only 55%; however, selectivity to hydrogen was high (85%) and a high H_2/CO ratio of 4 was observed. There were some small amounts of C_2 hydrocarbons present, with acetylene predominant, but it was discovered that the selectivity to compounds other than hydrogen can be controlled by changing the partial pressure of steam. The energy cost to produce hydrogen

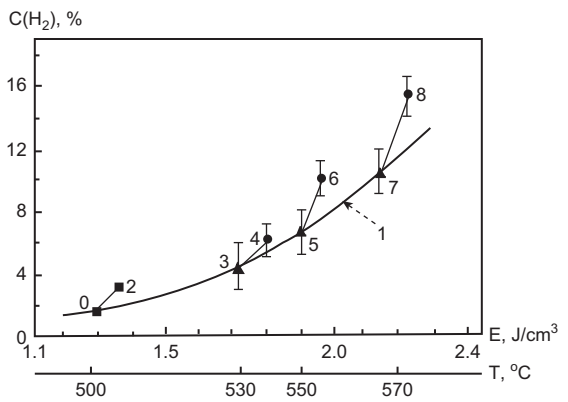

FIGURE 8.11 Hydrogen concentration (%) as a function of specific energy input (J/cm^3) for microwave plasma-assisted methane-steam reforming. Curve 1 represents reforming with thermal energy input only (no plasma); Points 2, 4, 6, and 8 represent experimental results with microwave plasma discharge *(Reprinted from Fridman [1] Copyright (2008), with permission from Cambridge University Press).*

was reported to be 2.7–3 eV/molecule at the highest conversion levels.

8.4.3. Plasma-Assisted Carbon Dioxide (Dry) Reforming

The process of methane conversion to syngas using carbon dioxide can provide the possibility of utilizing a major greenhouse gas pollutant and provide for better carbon resource management. This is especially desirable if the syngas produced by CO_2 is not burned but used for chemical synthesis processes. Similar to SR, CO_2 (dry) reforming of methane is an endothermic process that requires a slightly higher energy input of 2.6 eV/molecule. Many types of non-thermal plasmas have been investigated using this process: DBD [75–78], pulsed corona [79], and gliding arc [80–82]. The plasma catalysis effect for this process was best demonstrated by Mutaf-Yardimci et al. [79] when they investigated the effect of preheating on conversion both with and without a pulsed corona discharge. Hydrogen generation nearly doubled when the discharge was switched on (from 3.8% to 7.2% in exhaust), and power consumption of the discharge was less than 5% of the required reaction enthalpy. These results are attributed to a plasma-induced chain mechanism involving methanol and formaldehyde thermal decomposition for methane–carbon dioxide mixtures.

8.4.4. Plasma-Assisted Pyrolysis

Pyrolysis is an important fuel conversion scheme for acetylene production and is involved in the process of methane decomposition into hydrogen and solid carbon (see Eq. (8.16)). Thermal arc plasmas have been used in the industrial production of acetylene, ethylene, and hydrogen for more than 50 years in a process also termed electric cracking, and the mechanisms by which this occurs are well known. The thermal plasma arcs used in pyrolysis can have power levels as high as 10 MW with arc lengths reaching as long as 1 m [1]. Givotov et al. [55] investigated microwave plasma-assisted pyrolysis of ethane to hydrogen gas and solid carbon (soot) with zero CO_2 emissions. The pulsed microwave discharge was operated at a frequency of 9 GHz with average power of 30–100 W, pulse duration 0.3–1 μs, pulse frequency of 1 kHz, and power per pulse near 100 kW. It was found that the addition of plasma energy caused a decrease in the reaction temperature, and it is believed that a fraction of the input plasma energy (<20%) is spent in catalytic stimulation of the reaction.

8.5. PLASMA REFORMING OF LIQUID HYDROCARBONS

Non-thermal plasmas have been used in a variety of transportation applications related to the conversion of refined liquid hydrocarbon fuels, such as gasoline, diesel, and JP-8. There are four major applications where plasma systems have been specifically developed for use onboard vehicles, including development of vehicular auxiliary power units that convert fuel-to-electricity using plasma reformers combined with fuel cells [83,84], hydrogen-enriched combustion for improved engine performance and reduced toxic emissions [85,86], plasma after-treatment and reduction of exhaust pollutants such as nitrogen oxides (NO_X) and solid particulates [87–90], and regeneration of NO_X adsorbers and diesel particulate filters [91–93]. Plasma reformers, in general, have several advantages over catalytic systems that make then attractive for the automotive industry including near instantaneous start-up time, no preheating requirements, and small and compact design.

Plasma researchers face several challenges when reforming liquid hydrocarbon fuels such as diesel, because they contain a mixture of variable-length hydrocarbon chains and include

some fractions of polycyclic aromatic compounds. Reforming aromatic compounds can be difficult due to the multiple kinetic pathways that can lead to solid carbon and soot formation. Many plasma researchers, however, have reported no soot or solid carbon formation even in regimes in which it is thermodynamically favorable [47,62]. It is hypothesized that plasma is acting to oxidize carbon-forming precursor molecules, and thus soot and coke formation can be avoided.

Another challenge for the plasma reforming community is to find ways to improve hydrogen selectivity when reforming liquid hydrocarbon fuels. Many of the plasma reforming results presented in the literature show good conversion of fuel to syngas products, but hydrogen selectivity is lower than equilibrium predictions because a portion of the hydrogen is either oxidized to H_2O or preserved in the form of light hydrocarbons (LHCs). Oxidation of H_2 is inevitable even in fuel-rich conditions, such as POX, because of the oxidative nature of plasma, which is due in part to the multiple oxidative radicals that it produces and the fast rate of the H_2-O_2 reaction. When hydrogen selectivity is decreased because of the production of LHCs, this may be the result of some amount of fuel pyrolysis that occurred in the vicinity of the plasma discharge − an effect which is more prevalent in higher temperature plasmas, such as gliding arc. The fact that the LHCs are preserved in the exhaust also points to incomplete reforming that is most likely caused by heat losses in the post-plasma treatment zone or insufficient residence time to allow the reactions to complete. Such problems are related to system optimization and can be avoided. The LHCs preserved in the product stream are mostly comprised of methane in the range of a few percent of the absolute volume concentration, with smaller amounts of ethylene, acetylene, and ethane (usually less than 1−2%). Although the concentrations of the LHCs are typically low, in some cases they can account for as much as 40% of the heating value of the syngas product stream [62]. Nevertheless, the presence of the LHCs may not a pose a problem when the syngas stream is being fed to solid oxide fuel cells (SOFCs), especially when methane is the major component. SOFCs can reform methane internally even at high concentrations (up to 25% of the molar concentration) [94]. Additionally, methane in the syngas product stream was also shown to be beneficial to the thermal management characteristics of a SOFC because it can be endothermically reformed in the high temperatures of the anode side of the fuel cell, where abundant H_2O is present.

A large amount of research on liquid hydrocarbon reforming has been performed using gliding arc and microwave plasmas, which have demonstrated the best results thus far. Therefore, the focus of this section will be to describe the major results from plasma-assisted conversion from these discharges.

8.5.1. Plasma-Assisted Partial Oxidation of Diesel Fuel and Its Surrogates into Synthesis Gas

Some of the best conversion results for POX of diesel fuel to syngas using plasma have been obtained with vortex-based gliding arc plasma reformers. Bromberg et al. [95] achieved good conversion of atomized liquid diesel in a vortex-based gliding arc plasmatron at high flow rates (fuel flow rates up to 2 g/s) without the use of a metal-based catalyst (Fig. 8.12).

Atomized fuel was injected into the reactor in the axial direction with a curtain of air that flowed along the walls to prevent the fuel droplets from making contact, thus preventing conditions for pyrolysis. A series of vortex nozzles generated a swirling flow that pushed and elongated the gliding arc discharge and provided good mixing of the reactants with the discharge. The plasmatron reformer has the capability to operate in a wide dynamic

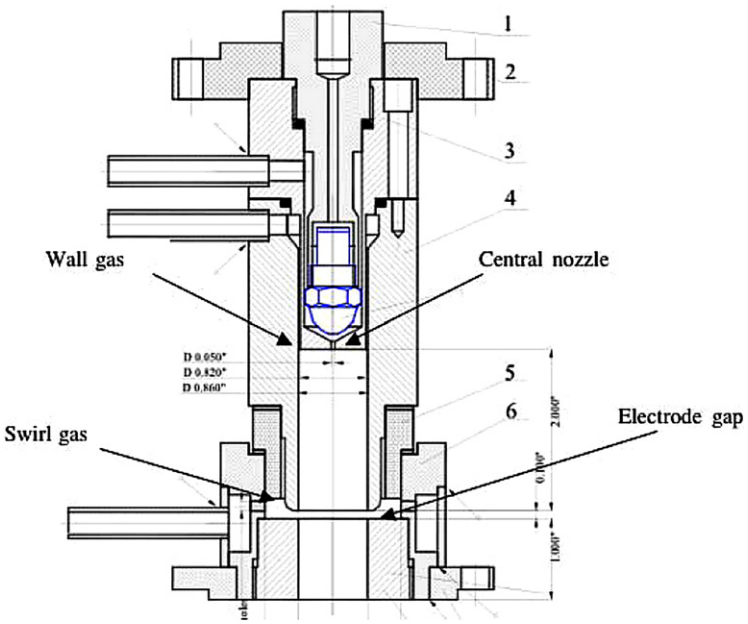

FIGURE 8.12 Schematic of the Gen 3 Plasmatron gliding arc plasma diesel reformer *(Reprinted from Bromberg et al. [95] Copyright (2006), with permission from the Massachusetts Institute of Technology).*

range while using limited electrical power. At an O/C ratio of 1.1, diesel fuel flow rate of 0.8 g/s, and plasma power of 250 W, the energy conversion efficiency was approximately 70%. The gas composition of the exhaust from this experiment is shown in Table 8.1. An opacity meter was also used to detect the presence of solid carbon products, and none were observed under these conditions. However, some LHCs were produced and included equal parts of CH_4 and C_2H_4.

Similar results were found by Gallagher et al. [62] during reforming of *n*-tetradecane ($C_{14}H_{30}$) using gliding arc plasma. n-Tetradecane was used as a surrogate of diesel fuel due to its general paraffin-like structure, although it does not contain aromatic compounds. The system utilized a reverse vortex plasma reformer (Fig. 8.13), which provides good mixing and contact of reactants with the plasma discharge. The reverse vortex flow (RVF) scheme has an outer swirling rotation along with a low-pressure area at its center with some component of axial flow, which makes the flow behave very similar to a natural tornado. The exhaust diaphragm is much smaller than the internal diameter of the vessel cylinder, and this causes the vortex flow to reverse direction and initially flow upwards into the vessel. The RVF scheme was used because it has greater thermal

TABLE 8.1 Exhaust Gas Composition from the Gliding Arc Plasmatron for Partial Oxidation of Diesel Fuel from [95]

Concentration (volume %)	
H_2	8.2
O_2	1.4
N_2	68.7
CH_4	2.6
CO	14.3
CO_2	4.7
C_2H_4	2.4
C_2H_2	0.0

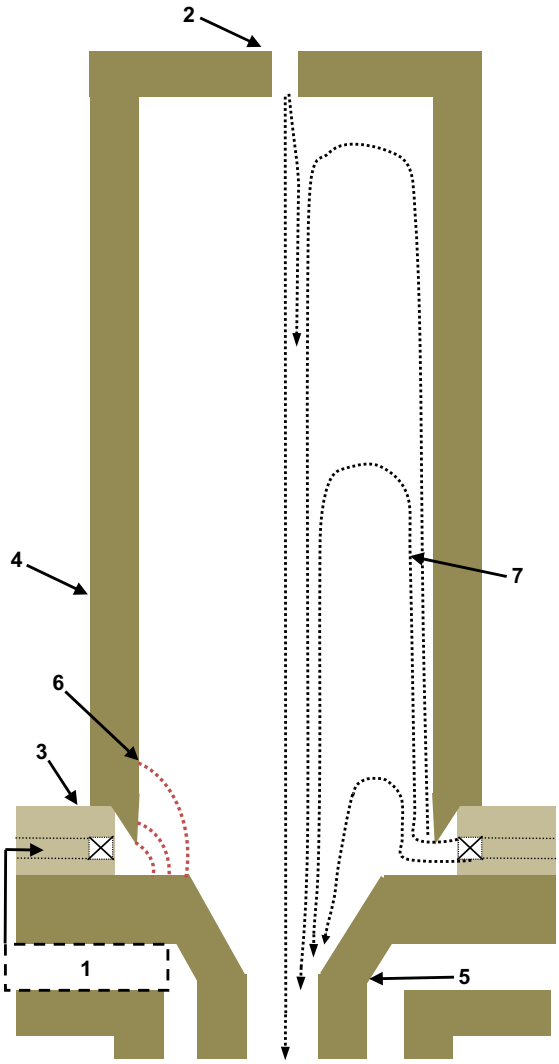

FIGURE 8.13 Cross-sectional drawing of the RVF-GA reactor. (1) Fuel and air premixing chamber, (2) additional air input port (optional), (3) ceramic dielectric ring, (4) high voltage electrode, (5) exhaust nozzle, (6) plasma discharge, and (7) streamlines of flow indicating flow recirculation that occurs as a result of the reverse vortex configuration *(Reprinted from Gallagher et al. [62] Copyright (2010), with permission from Elsevier).*

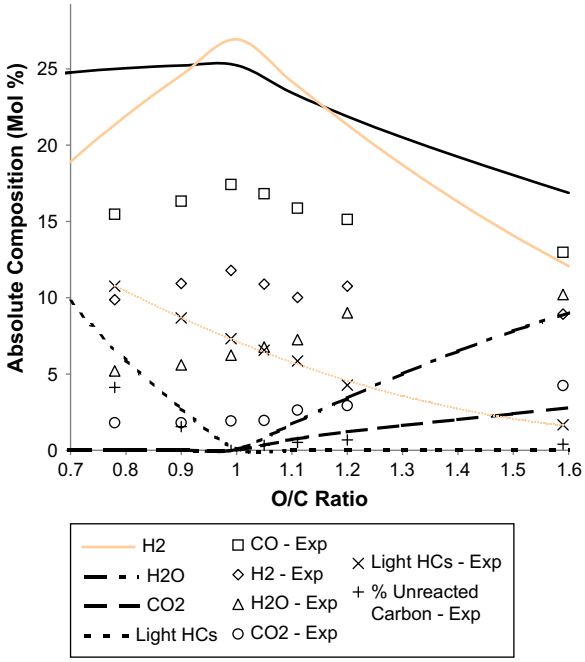

FIGURE 8.14 Example of absolute composition of product stream versus the O/C ratio from a gliding arc reformer operating under partial oxidation conditions *(Reprinted from Gallagher et al. [62] Copyright (2010), with permission from Elsevier).*

efficiency as compared with conventional forward vortex flow (FVF).

The absolute composition of products as a function of O/C ratio is shown in Fig. 8.14 for two similar vortex-based gliding arc plasma reformers. The solid and dashed lines in Fig. 8.14 show the expected concentration of major products: H_2, CO, H_2O, CO_2, and LHCs, which are included as a lumped category and were comprised of mostly methane. Experimental H_2O concentration was estimated through atomic balances, and the results show that 5% was present even at low O/C ratios (0.8), where not enough oxygen is available for stoichiometric POX.

These results point to the two-stage kinetic mechanism of POX in which an initial rapid oxidation begins and all free oxygen reacts

with fuel to produce mostly CO_2, H_2O, and reaction heat, leaving a large amount of unreacted fuel remaining. A second, much slower endothermic reforming phase follows, in which the residual fuel reacts with CO_2 and H_2O to further produce syngas. A short pyrolysis stage may occur in parallel, in which heavy hydrocarbon molecules are broken apart into smaller LHC fragments (CH_4, C_2H_4) without producing coke/soot. Conversion in this case can be optimized with longer contact of the fuel and oxidizers with the discharge or with improved heat insulation in the post-plasma reaction zone, where heat losses can contribute to incomplete conversion. Energy conversion efficiency reached as high as 83% and the plasma power was kept constant near 250 W, which is approximately 3.5% of the total chemical power of the system (at fuel flow rate of 0.15 g/s).

8.5.2. Plasma-Assisted Reforming of Ethanol

The POX of ethanol using non-thermal plasmas has been investigated, although the there are a limited number of publications that can be found in the literature in this area. Hadidi et al. [96] used an atmospheric pressure gliding arc discharge combined with a nickel catalyst to reform ethanol to hydrogen-rich synthesis gas. Hydrogen yields as high as 80% were achieved at O/C ratios 1.5−1.7 with very little carbon formation (opacity meter reading: 0.1). The O/C ratios used in their experiments included the oxygen bound within the fuel (at an O/C ratio of 0.5). Hadidi et al. [96] noted that oxygen bound to ethanol does not change the required amount of oxygen from air needed to reform the fuel. Petitpas et al. showed through a comparison of thermodynamic modeling and a summary of the results from previous catalytic studies that an ideal O/C ratio of 1.1 (also including oxygen bound within ethanol) is expected for the POX of ethanol; however, their own experimental observations demonstrated that O/C ratios near 1.6 were needed for adequate reforming using non-thermal plasma [97]. The disparity is related to the temperatures employed in plasma experiments versus metal-catalyst-based experiments (and assumed in thermodynamic modeling). Bromberg used no preheating for reactants and Petitpas kept preheat temperatures below 500 K, whereas metal catalyst-based POX systems typically employ temperatures 900−1200 K. Petitpas et al. [97] suggested the following plasma mechanism for ethanol decomposition which involves several steps of hydrogen abstraction:

$$CH_3CH_2OH \rightarrow CH_3CH_2O + 1/2\ H_2 \quad (8.34)$$

$$CH_3CH_2O \rightarrow CH_3CHO + 1/2\ H_2 \quad (8.35)$$

$$CH_3CHO + O \rightarrow CH_3COO + 1/2\ H_2 \quad (8.36)$$

$$CH_3CH_2O \rightarrow CH_4 + CO + +1/2\ H_2 \quad (8.37)$$

$$OH + CH_3COO \rightarrow CH_4 + CO + O \quad (8.38)$$

8.5.3. Plasma-Assisted Oxidative Steam Reforming of Various Liquid Hydrocarbon Fuels

In OSR, also known as auto-thermal reforming, both POX and SR processes are combined and air and H_2O are used together as fuel oxidizers. The advantage of OSR is found in the energy balance of the process, where it is possible to achieve thermo-neutral conditions with a zero net enthalpy change ($\triangle H = 0$) in the process due to equal contributions between exothermic and endothermic reactions. It is also possible to achieve increased hydrogen yields and improved hydrogen selectivity under OSR conditions because syngas can be derived from the oxidizers themselves (i.e., H_2 from H_2O).

Paulmier and Fulcheri [84] used an OSR scheme to convert gasoline into syngas with

a flat gliding arc reformer that contained two sets of electrodes that could provide two independent plasma discharges. This system was also capable of operating at elevated pressures (up to 300 kPa) and at temperatures up to 773 K. Experiments were performed near autothermal reforming conditions: H_2O/C ratio: 2.5 and variable air ratio: 0.1−0.4. The results showed a maximum output composition of syngas at atmospheric pressure of H_2: 7% and CO: 4% with an additional large amount of CH_4: 9%. Reforming improved at higher pressures (250 kPa) where a maximum efficiency of 27% was achieved at an air ratio of 0.4, H_2O/C ratio of 2.5, inlet temperature of 773 K, and fuel power of 10 kW. It should be noted that while increasing pressure caused an increase in conversion, it also lengthened the delay between extinction/ignition cycles of the gliding arc discharge. Gliding arc discharges are auto-oscillating, and they normally extinguish and re-ignite periodically; higher pressures make breakdown more difficult and can increase the delay between breakdowns making large gaps where there is no discharge. The low conversion efficiency observed in these experiments was most likely a result of both the increased discharge extinction time and the flat geometry of the discharge, which is known to have poor mixing with reactants.

Researchers from Drexel University, Ceramatec, Inc., and Auburn University combined a gliding arc plasma reformer with a SOFC to create a *non-thermal plasma auxiliary power unit* for military tanks (under funding from the U.S. Army through TARDEC) [63]. As stated earlier, non-thermal plasma reforming technology is well suited for vehicular onboard reforming because the systems are typically compact, are capable of working with high-sulfur fuels (JP8 can have up to 3000 ppm), and have a near instantaneous start-up time. In this system, a gliding arc Plasmatron reformer, similar to the one described in [62], was used to generate syngas using an OSR scheme by recycling a portion of the high temperature SOFC anode tail gas exhaust back into the reactant stream. The flow diagram in Fig. 8.15 shows the components of the system along with the compositions of the reactant and product streams. The system is designed to support a 10 kWe SOFC and contains two plasma reformers that can process up to 16 kW_{th} of fuel each (approximately 32 kW_{th} total). The SOFC anode tail gas was created in the laboratory for initial trials and was preheated to temperatures near 1123 K (similar to the operating temperature of most SOFCs). The simulated anode tail gas mixture, which was comparable in composition to a real SOFC

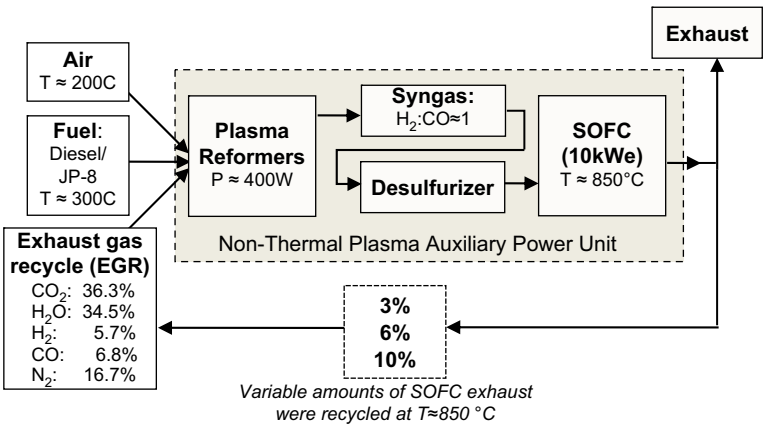

FIGURE 8.15 A scheme of the major components of a non-thermal plasma auxiliary power unit. This system was operated in OSR mode, and a variable portion of the SOFC exhaust was recycled back into the reformer to provide H_2O and CO_2.

exhaust, contained a mixture of the following components: 36.3% CO_2, 34.5% H_2O, 5.7% H_2, 6.8% CO, and 16.7% N_2. In addition, some amount of air was also used during reforming and was preheated to temperatures less than 473 K. Reforming experiments using both diesel fuel and JP-8 were performed, and the fuels were vaporized using a custom-made wall-heated coiled-tube vaporizer.

The recycled SOFC exhaust gas recycle (EGR) was varied between 3%, 6%, and 10%. The fuel flow rates were kept constant for each trial at 0.3 g/s for 3% and 6% EGR; however, lower fuel flow rates of 0.15 and 0.1 g/s were used during the 10% EGR trials. The results presented in the following paragraphs show reforming results using one plasma reformer; because all reactant flow rates were split between the two reformers, it is assumed that the behavior of the second reformer will be identical.

Thermodynamic equilibrium simulations of the system were initially performed using HSC Chemistry, version 6.0, and the anticipated energy conversion efficiencies were found for two cases: production of syngas only (H_2 and CO), and syngas plus LHCs, which are mostly comprised of methane. Figures 8.16 and 8.17 show the equilibrium energy conversion efficiencies for syngas plus LHCs (H_2, CO, and LHCs) and syngas only (H_2 and CO) as a function of increasing air-to-fuel oxygen to carbon (O/C) ratio, respectively. These figures also include increasing amounts of SOFC EGR in increments of 0, 3, 6, and 10%, where 0% EGR is analogous to the POX case. As evidenced by Figs 8.16 and 8.17, the peaks of maximum energy conversion efficiency increase with the amount of SOFC EGR. This is intuitive because as EGR increases, the concentration of H_2O and CO_2 reactants increases, replacing air as the primary oxidizer required for conversion. But if this trend were to continue with ever-increasing amounts of EGR, the system would shift away from the thermo-neutral point ($\triangle H = 0$) to the endothermic SR regime ($\triangle H > 0$). Attaining good conversion in the endothermic reforming regime is not feasible in this system given the limited amount of heat available. The solid black dots on Figs 8.16 and 8.17 mark the region where solid carbon formation is predicted to occur. The

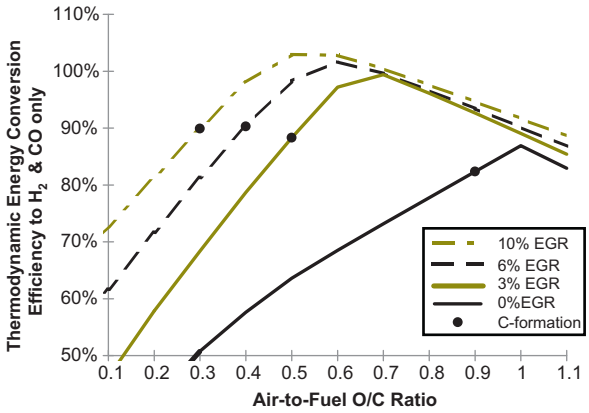

FIGURE 8.16 Thermodynamic equilibrium energy conversion efficiency versus the air-to-fuel O/C ratio for production of H_2, CO, plus light hydrocarbons (primarily CH_4) using various amounts of SOFC exhaust gas recycle. The black dots represent the predicted onset of carbon formation with decreasing O/C ratio.

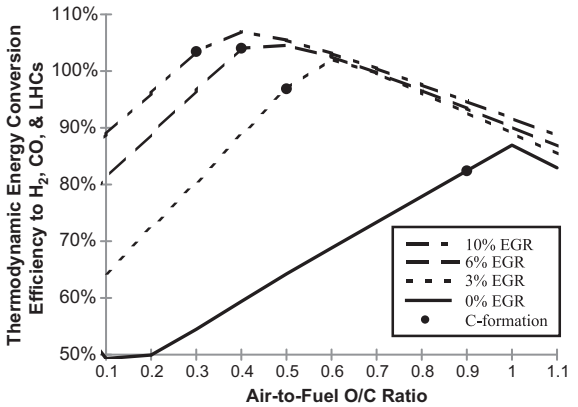

FIGURE 8.17 Thermodynamic equilibrium energy conversion efficiency versus the air-to-fuel O/C ratio for production of H_2 and CO only using various amounts of SOFC exhaust gas recycle. The black dots represent the predicted onset of carbon formation with decreasing O/C ratio.

carbon-forming region is located to the left of the maximum of the conversion efficiency peaks and spans leftward with decreasing air-to-fuel O/C ratios.

The experimental energy conversion efficiency was measured based on a series of trials using commercial-grade low-sulfur diesel fuel. The standard energy conversion efficiency definition is slightly modified here to account for the additional amount of H_2 and CO coming from the EGR stream of the SOFC:

$$\text{Modified energy conversion efficiency \%} = \frac{\text{LHV}_{\text{products}} \times 100}{\text{LHV}_{\text{fuel}} + (\text{LHV}_{\text{H}_2} + \text{LHV}_{\text{CO}})_{\text{EGR}}} \tag{8.39}$$

The experimental modified energy conversion efficiency as a function of the air-to-fuel O/C ratio is shown in Fig. 8.18. The solid and dashed lines in Fig. 8.18 show the predicted thermodynamic equilibrium efficiencies for different EGR amounts. The points show experimental data from gliding arc assisted reforming of diesel fuel at a fuel flow rate of 0.3 g/s. Also included are several cases of increasing EGR from a SOFC. It is evident that higher amounts of EGR introduced into the system lead to lower energy conversion efficiency. This contradicts the thermodynamic equilibrium predictions and is most likely a result of kinetic limitations within the system. As the EGR increases, so do the volumetric flow rates of reactants within the system. As a consequence, the residence time of treatment also decreases, and the slower endothermic fuel reforming reactions may not have enough time to reach completion. In addition, there could also be heat losses in the post-plasma reaction zone which could act to quench the reforming reactions prematurely. Trials with longer residence time, which were achieved by scaling back all reactant flow rates by 50% (m_{fuel} = 0.15 g/s) and 70% (m_{fuel} = 0.15 g/s), showed improvement in the energy conversion efficiency and H_2O consumption, which is demonstrated in Fig. 8.19.

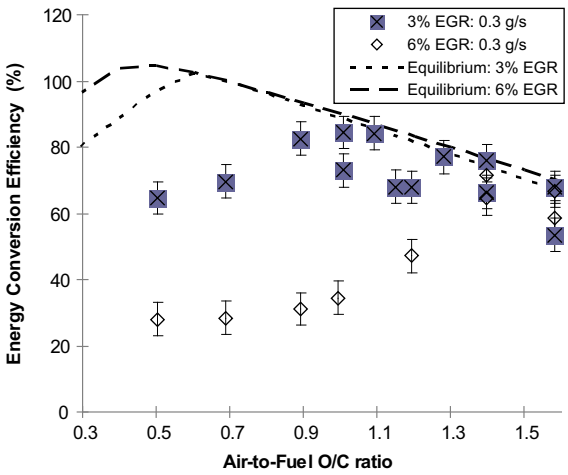

FIGURE 8.18 Comparison of the experimental and predicted energy conversion efficiency versus the air-to-fuel O/C ratio for the cases of 3% and 6% SOFC exhaust gas recycle.

Figure 8.20 shows the equilibrium H_2O consumption compared to the experimental consumption with respect to increasing air-to-fuel oxygen to carbon (O/C) ratio. Several cases of variable SOFC EGR were investigated using diesel fuel. For the case of 10% EGR shown here, the flow rates of all reactants were reduced by 50% thereby increasing the residence time of treatment. The experimental points follow a similar trend to the predicted H_2O consumption at thermodynamic equilibrium, which is represented by the solid and dashed lines. Negative consumption is analogous to production of H_2O, and this occurs at increasing O/C ratios as expected. CO_2 consumption (not shown) was almost negligible, and this result is expected given that H_2O consumption was low and the endothermic H_2O reforming reaction requires 0.5 eV/mol less energy than conversion with CO_2.

The results presented in Figs 8.18–8.20 describe an advanced auxiliary power unit that incorporated a gliding arc plasma reformer with a SOFC. Variable amounts of exhaust gases from the SOFC were recycled back into the

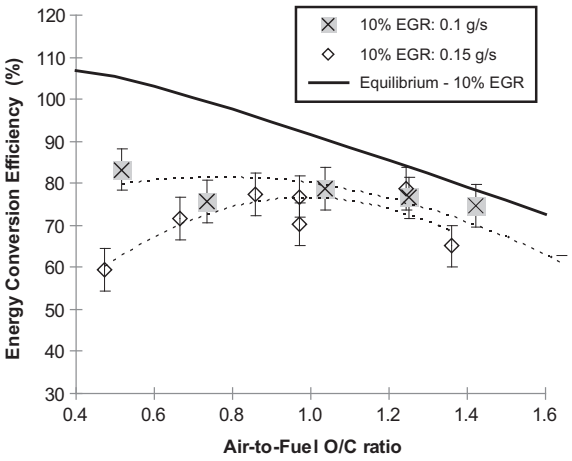

FIGURE 8.19 Comparison of experimental and predicted energy conversion efficiency versus the air-to-fuel O/C ratio for the case of 10% SOFC exhaust gas recycle. Note: experimental values using lower fuel flow rates are shown.

plasma reformer in an effort to reach autothermal reforming conditions in which the net enthalpy of the process is nearly zero. The presence of SOFC exhaust gases improved energy conversion efficiency; however, ever-increasing amounts of EGR caused a reduction in conversion. This result was attributed to a kinetic limitation in the system in which higher recycle gas flow reduced residence time for reaction completion. Upon scaling back flow rates of all reactants, thus increasing residence time, the energy conversion efficiency improved further, reaching as high as 80%.

Integration of plasma fuel reformers within auxiliary power units for vehicles is in an early stage of development, and the results look promising. Before the syngas reformate from plasma reformers can be integrated with an actual SOFC, some improvement is needed to reduce C_2 hydrocarbons that have been reported in the product streams. The concentrations of these LHCs are low (1−2% in absolute concentration), but compounds, such as acetylene and ethylene, are known to cause degradation in the performance of the SOFC. Future efforts to optimize plasma fuel conversion systems may reduce unconverted hydrocarbons and improve syngas yields, thereby eliminating this problem.

The experimental results of plasma-assisted liquid hydrocarbon conversion show that high levels of conversion are possible with good

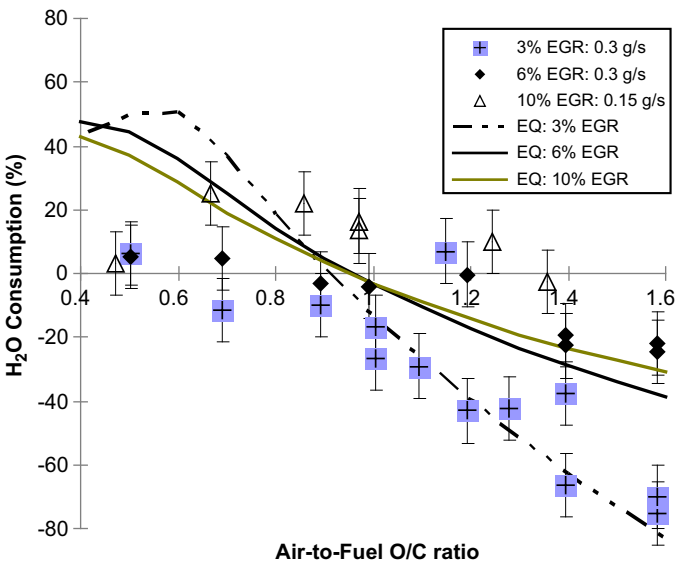

FIGURE 8.20 Comparison of the experimental and predicted H_2O consumption versus the air-to-fuel O/C ratio for various amounts of SOFC exhaust gas recycle.

energy conversion efficiency. This is especially true in cases where transitional (warm) non-equilibrium plasma discharges like gliding arc [9] are employed. One possible reason for the improved reforming with gliding arc plasmas, compared to DBDs or corona discharges, is because the higher translational gas temperatures accelerate the kinetics of the reforming reactions while the plasma radicals act simultaneously to reduce energy barriers and prevent unwanted by-product (coke) formation. This hypothesis has not been proven however, and some researchers believe that low-current transitional arcs like gliding arc contribute energy through gas heating alone with no catalytic effects from plasma active species [67]. Further work is needed to elucidate the plasma catalysis effect in plasma-assisted reforming systems and understand the underlying mechanisms so that future fuel conversion systems may be improved and optimized.

8.6. COMBINED PLASMA-CATALYTIC REFORMING OF HYDROCARBON FUELS INTO HYDROGEN-RICH SYNTHESIS GAS

There is a distinction between reforming hydrocarbon fuels using plasma independently for its own catalytic properties, which is referred to as *plasma catalysis*, and reforming using the *plasma-catalytic* approach that combines plasma with traditional metal catalysts. Investigations involving the plasma-catalytic approach have grown significantly over the past decade, and the results have demonstrated a positive synergistic effect, with improved reforming results that are often better than the results produced by either technology alone. Researchers have applied the plasma-catalytic approach for hydrocarbon reforming using various schemes that include CO_2 (dry) reforming [98,99], SR [100,101], POX reforming [102–105], and non-oxidative reforming [42,106]. Both plasma and traditional catalyst technologies have their own drawbacks with regard to hydrocarbon conversion, namely energy spent on gas heating in plasmas can be expensive and energy inefficient, and catalysts have flow restrictions due to their high density and deactivation problems from sulfur and soot formation that can occur on their surfaces. However, combining these technologies into plasma-catalytic hybrid reactors can work to eliminate the weaknesses of both technologies by providing increased conversion at lower reaction temperatures, avoiding soot and unwanted byproduct formation, and improving energy costs and efficiency.

Plasma-catalytic reforming systems are most commonly arranged in either a single-stage and two-stage configuration [107]. In the single stage configuration, the plasma and catalyst regions can completely or partially overlap and the plasma discharge is ignited within the catalyst bed or on electrodes that are coated with catalyst material. The single stage configuration is somewhat more complex because the overlapping catalyst and plasma discharge are known to have strong interactions which can affect the properties of both. For instance, the electrical conductivity and the sharp edges of pelletized metal catalyst material can affect the reduced electric field of the plasma thereby altering the types and concentrations of the active species it produces [107]. In addition, the behavior of the catalyst can be influenced by plasma-induced surface heating [103] and possibly by other unknown effects caused by current flowing across the catalyst surface. The plasma and catalyst regions are separated in the two-stage configuration, with plasma placed upstream from the catalyst bed to provide pre-processing or downstream for post-processing of the catalyst-treated effluent. Pre-processing of reactants is more commonly used and has also yielded the best results [107] in terms of conversion because it is believed that the plasma can excite hydrocarbon molecules in such a way that they are more easily

converted by the catalyst material. Regardless of their differences, researchers have shown that both the single-stage and two-stage plasma-catalytic systems are capable of providing improved reforming with greater results compared to either plasma or catalyst alone.

8.6.1. Plasma-Catalytic Two-Stage Configuration for Hydrocarbon Reforming

Sobacchi et al. [105] used a two-stage plasma-catalytic reformer to compare the effects of pre-processing and post-processing for the oxidative steam reforming of isooctane into synthesis gas. In this system, a pulsed corona discharge was developed using a wire-into-cylinder coaxial electrode configuration and combined with a separate catalyst bed reformer in such a way that it could be placed either upstream (pre-processing) or downstream (post-processing) from the catalyst. The plasma-catalytic system was placed inside a tube furnace in order to control the catalyst bed temperature, which was varied from 900 to 1073 K. Figure 8.21 shows a schematic of the system.

The catalyst used in these trials was specially developed by Argonne National Laboratory, and the details of its composition were not provided in [105]. The system was operated using a simulated air mixture of 50% O_2−50% N_2, which was held constant at an air-to-fuel O/C ratio of approximately 1. Steam was introduced at an H_2O/C ratio of 1.1, and the fuel flow rate was low (0.04 ml/min) with a heating value of 22 W. Figure 8.22 shows a comparison of hydrogen yields between pre-processing, post-processing, and the pure catalyst case. It is clear that at low temperatures (near 910 K), hydrogen yields increased nearly 2.5 times for both the plasma pre- and post-processed cases compared to the pure catalyst case. Despite the increase in yield, the plasma-catalytic system cannot obtain maximum hydrogen yields (denoted by the straight dashed line in Fig. 8.22) at these low temperatures; however, the authors noted that a significant fraction of isooctane remains unconverted in this regime. In addition, some heavy organic acids produced by POX were detected in the exhaust. The maximum H_2 yield occurred at higher reaction temperatures, near 1073 K, where the synergistic effect between plasma and catalyst seems to wane and become indistinguishable from the pure catalyst case. Figure 8.22 also shows that the pre-processed reactant stream had slightly

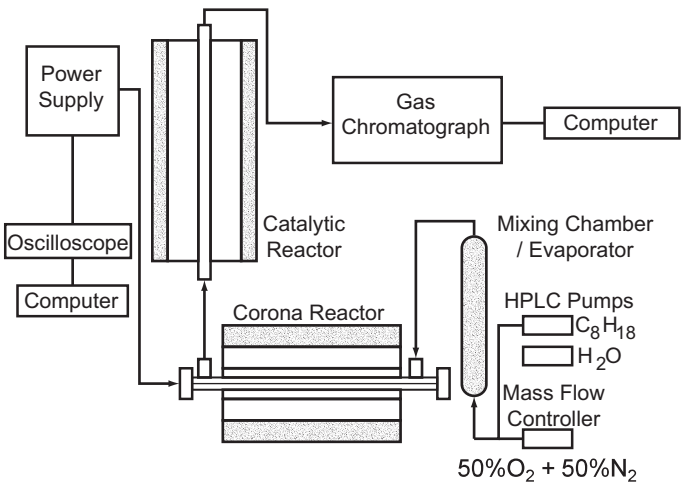

FIGURE 8.21 Schematic of the plasma-catalytic two-stage pulsed corona reformer *(Reprinted from Sobacchi et al. [105] Copyright (2002), with permission from International Association for Hydrogen Energy).*

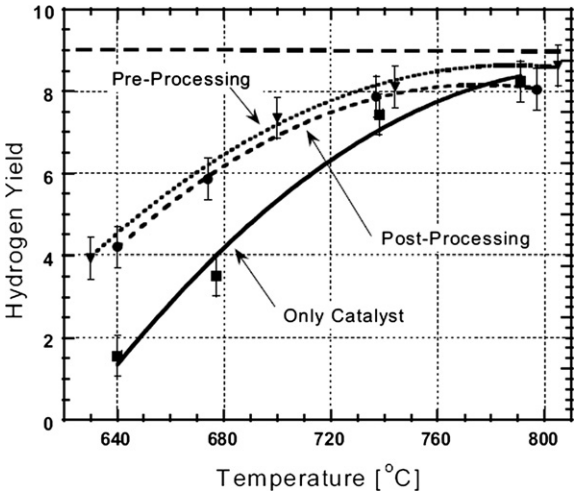

FIGURE 8.22 Hydrogen yield as a function of temperature for system configurations that include: plasma pre-processing, post-processing, and catalyst only. The maximum possible H_2 yield from isooctane is represented by the straight dashed line *(Reprinted from Sobacchi et al. [105] Copyright (2002), with permission from International Association for Hydrogen Energy).*

better conversion and product yields over the post-processed stream. The authors observed slight changes in power input to the corona discharge between the pre- and post-processed cases, which can occur because of the dissimilar reactant compositions, and a slight pressure increase located upstream of the catalyst bed caused by the dense packing of the catalyst material. The authors attribute the improved reforming in the plasma pre-processed case to plasma stimulation of the kinetically suppressed and slower initial stages of isooctane oxidation which allows the catalyst to act more effectively on the intermediate oxidized components and ultimately move the reforming reaction along further. The plasma power was kept below 8 W in all trials and was varied slightly to examine its effect on hydrogen yield. It was found that increasing plasma power had little positive effect on conversion of isooctane to hydrogen and eventually caused a decrease in hydrogen yield. Experiments were performed intermittently for more than 100 h, and the catalyst showed stable performance throughout with no signs of deactivation or plugging. The results presented here show that low power non-thermal plasma combined with metal catalyst has a positive synergistic effect that promotes greater fuel conversion and higher hydrogen yields at low overall reaction temperatures.

8.6.2. Plasma-Catalytic Single-Stage Configuration for Hydrocarbon Reforming

A single stage setup using a DBD plasma-catalytic hybrid reactor for methane steam-reforming was demonstrated by Nozaki et al. [108]. A strong synergistic effect between plasma and catalyst was observed in the temperature range between 400 and 600 °C, with almost no effect observed below 200 °C. Figure 8.23 shows the methane conversion curve as a function of temperature for three

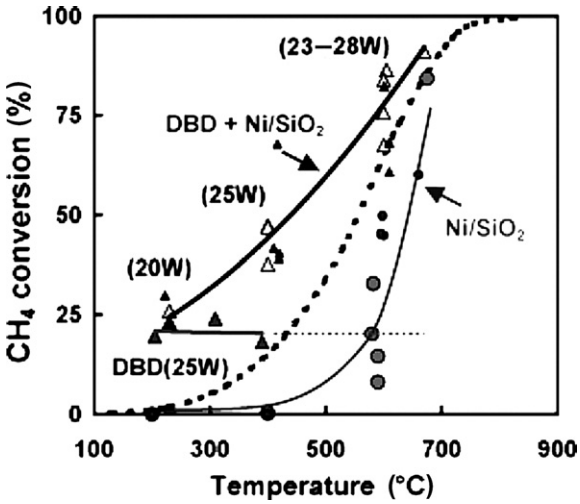

FIGURE 8.23 Methane conversion versus temperature is shown for four separate cases: DBD plasma only, Ni/SiO_2 catalyst only, combined DBD + Ni/SO_2, and equilibrium methane conversion (dashed line) *(Reprinted from Nozaki et al. [108] Copyright (2004), with permission from American Chemical Society).*

cases: DBD only, Ni/SiO_2 catalyst only, and DBD + Ni/SiO_2. The results show that the methane conversion curve is shifted 200 °C towards the low-temperature region for the case of DBD + Ni/SiO_2, which exceeds the expected conversion at equilibrium (dashed line). At higher reaction temperatures (approaching 700 °C), the plasma-catalytic effect seems to diminish and conversion approaches the equilibrium and catalyst-only case. Energy cost and energy efficiency were reported to be 134 MJ/kg H_2 and 69%, respectively. The authors noted that while conversion was higher than equilibrium in the low-temperature case, product selectivity mainly followed the equilibrium predictions. The authors suggest that the reason for higher than predicted conversion of methane may be the result of plasma-induced electron impact excitation, which can further induce vibrational excitation of methane. Vibrationally excited methane is known to have a sticking probability of one to two orders of magnitude higher than ground state methane, thus promoting dissociative chemisorptions on catalyst surfaces [109].

The plasma-catalytic synergistic effect has shown promise in its ability to promote greater conversion and product yields than stand-alone plasma or catalyst technologies. Two-stage systems have demonstrated better reforming results thus far, but determining which configuration is best for reforming is not possible at this time. Studies of plasma-catalytic systems are still in progress, and a comprehensive comparison between single-stage or two-stage systems is not yet available. In general, the consensus among researchers seems to be that plasma is effective at increasing the internal energy of reactants and specifically stimulating vibrational excitation which can be effectively utilized in thermal catalysis reactions. Further research in this area is needed to identify the roles of plasma and catalysts in combined systems and to investigate the detailed kinetic mechanisms responsible for the synergy that provides improved conversion and product selectivity.

8.7. CONCLUSIONS AND FUTURE TRENDS

Plasma has been used in fuel conversion and combustion systems for over a century; however, only in the recent decades has non-thermal plasma and the idea of a plasma catalysis effect been investigated as a possible means to enhance or replace traditional thermal or catalytic reforming systems. At this time, the detailed mechanisms by which the plasma active species participate in fuel reforming reactions, such as POX and oxidative steam reforming, are still largely unknown. There is an ongoing effort to identify and understand the plasma catalysis effect for fuel-lean combustion and ignition systems. The researchers working in this area have taken a careful approach to gain a fundamental understanding of the complex interaction of plasma in fuel ignition processes, flames, and combustion reactions. They have employed scientific research installations, such as shock tubes, coupled with advanced diagnostics to elucidate the kinetic roles of plasma active species. Plasma fuel conversion researchers are beginning to adopt such an approach in order to gain knowledge about the important fundamental mechanisms that plasma has to offer. Such knowledge will help future scientists and engineers to develop more efficient fuel conversion and syngas production systems.

Regardless of the gaps in the fundamental knowledge of the plasma-induced mechanisms in fuel conversion reactions, many researchers have designed, built, and tested experimental installations using various types of plasmas to convert hydrocarbons into syngas with varying degrees of success. The plasma reformer systems that have demonstrated the best results thus far employ vortex-stabilized gliding arc or microwave plasmas. The former discharge is much

easier to implement due to the simple and inexpensive DC power supplies; however, one potential limitation of gliding arc systems is the possibility of operating in the energetically costly thermal plasma arc mode. Microwave plasmas are an even better choice for fuel conversion systems because they are strongly non-equilibrium and have high power density – two of the most important requirements that are needed for the plasma catalysis effect. On the other hand, microwave plasma systems require sophisticated (and expensive) power supplies along with complex power coupling requirements, which makes their implementation into engineering systems potentially troublesome. Advances in electronics manufacturing may reduce the cost of implementing microwave plasmas within fuel conversion systems in the future, but until that time, gliding arc plasmas should be considered as a better option.

There are several interesting research areas being explored within the realm of plasma-assisted fuel conversion that may hold great promise in the near future. Researchers working with the plasma-catalytic approach, where plasma is combined with traditional metal catalysts, have found that it is possible to produce higher amounts of syngas at lower temperatures than thermodynamic equilibrium predictions. In addition, combining plasma and surface catalyst technologies may reduce the drawbacks of each technology. For example, plasma pretreating of reactants may prevent coke formation and eliminate sulfur compounds, thereby protecting metal catalysts from poisoning problems. Also, the enhanced activity of the catalyst downstream from the plasma can help to boost syngas yields and eliminate residual LHCs, thus improving energy conversion efficiency and reducing plasma's specific energy cost to produce syngas. The plasma-catalytic approach for fuel reforming has exciting future prospects, and the synergistic effects of combining these technologies could play an essential role in the future of fuel cell technology.

References

[1] Fridman A. Plasma chemistry. New York: Cambridge University Press; 2008.

[2] Starikovskii AY. Plasma supported combustion. Proc Combus Inst 2005;30(2):2405–17.

[3] Raizer YP. In: Allen JE, editor. Gas discharge physics. Berlin: Springer-Verlag; 1991.

[4] Fridman A, Kennedy LA. In: Plasma physics and engineering. New York: Taylor and Francis; 2004.

[5] Graves DB. Plasma processing. IEEE Trans Plasma Sci 1994;22(1):31–42.

[6] Fridman A, Nester S, Kennedy LA, Saveliev A, Mutaf-Yardimci O. Gliding arc gas discharge. Prog Energy Combust Sci 1999;25:211–31.

[7] Kuznetsova IV, Kalashnikov NY, Gutsol AF, Fridman AA, Kennedy LA. Effect of "overshooting" in the transitional regimes of the low-current gliding arc discharge. J Appl Phys 2002;92(8):4231–7.

[8] Gangoli S, Gutsol AF, Fridman AA. A non-equilibrium plasma source: magnetically stabilized gliding arc discharge: 1. Design and diagnostics. Plasma Sources Sci Technol 2010;19(6).

[9] Petitpas G, Rollier JD, Darmon A, Gonzalez-Aguilar J, Metkemeijer R, Fulcheri L. A comparative study of non-thermal plasma assisted reforming technologies. Int J Hydrogen Energy 2007;32(14):2848–67.

[10] Givotov VK, Rusanov VD, Fridman A. In: Diagnostics of non-equilibrium chemically active plasma. Moscow: Atomizdat Publishing House; 1985.

[11] Remillard SK. *Resonator Plasma_2-792631.jpg*. 4 June 2009. Hope College, Holland, MI, USA. <http://www.hope.edu/academic/physics/research/uploaded_images/resonator_plasma_2-792631.JPG>; website accessed on Nov 29, 2010.

[12] Hocker H. Plasma treatment of textile polymers. Pure Appl Chem 2002;74(3):423–7.

[13] Gilman AB. Interaction of chemically active plasma with surfaces of synthetic materials. In: Fortov VE, editor. Encyclopedia of low-temperature plasma. Moscow: Pleiades Publishing; 2000. vol. 4, p. 393.

[14] Kogelschatz U. Dielectric-barrier discharges: their history, discharge physics, and industrial applications. Plasma Chem Plasma Process 2003;23(1):1–46.

[15] Vezzo G, Lopez JL, Freilich A, Becker KH. Optimization of large-scale ozone generators. IEEE Trans Plasma Sci 2009;37:890–6.

[16] Gallagher MJ, Vaze N, Gangoli S, Vasilets V, Gutsol A, Milovanova TN, et al. Rapid inactivation of airborne bacteria using atmospheric pressure dielectric barrier grating discharge. IEEE Trans Plasma Sci 2007;35(5):1501–10.

[17] Kosarev IN, Starikovskaia SM, Starikovskii AY. Shock tube study of artificial ignition of N_2O:

O_2:H_2:Ar mixtures. In: Hannemann H, Seiler F, editors. Shock waves. Berlin-Heidelberg: Springer; 2009. p. 769–74.

[18] Sobacchi MG, Saveliev AV, Kennedy LA, Lock E, Fridman A, Gutsol A, et al. Pulsed corona plasma technology for treating VOC emissions from pulp mills. In TAPPI Paper Summit, Spring Technical and International Environmental Conference. Atlanta, GA, USA: 2004.

[19] Talrose VL, Ph.D., Dissertation. Moscow: N.N. Semenov Institute of Chemical Physics; 1952.

[20] Starikovskaia SM. Plasma assisted ignition and combustion. J Phys D: Appl Phys 2006;39:265–99.

[21] Lou G, Bao A, Nishihara M, Keshav S, Utkin YG, et al. Ignition of premixed hydrocarbon-air flows by repetitively pulsed, nanosecond pulse duration plasma. Proc Combust Inst 2007;31(2):3327–34.

[22] Anikin NB, Starikovskaia SM, Starikovskii AYu. Study of the oxidation of alkanes in their mixtures with oxygen and air under the action of pulsed volume nanosecond discharge. Plasma Phys Rep 2004;30:1028–42.

[23] Ombrello T, Qin X, Ju Y, Gutsol A, Fridman A, Carter C. Combustion enhancement via stabilized piecewise nonequilibrium gliding arc plasma discharge. AIAA J 2006;44:142–50.

[24] Kim W, Do H, Godfrey-Mungal M, Cappelli MA. Plasma-discharge stabilization of jet diffusion flames. IEEE Trans Plasma Sci 2006;34(6):2545–51.

[25] Leonov SB, Yarantsev DA. Plasma-induced ignition and plasma-assisted combustion in high-speed flow. Plasma Sources Sci Technol 2007;16:132–8.

[26] Macheret SO, Shneider MN, Miles RB. Energy efficiency of plasma-assisted combustion in ram/scramjet engines. In 36th AIAA Plasma Dynamics and Lasers Conference. Toronto, Canada: 2005.

[27] Chintala N, Bao A, Lou G, Adamovich IV. Measurements of combustion efficiency in nonequilibrium RF plasma-ignited flows. Combust Flame 2006;144(4):744–56.

[28] Rostrup-Nielsen JR. Syngas in perspective. Catal Today 2002;17:243–7.

[29] Gorchakov G, Lavrov F. Influence of electric discharge on the region of spontaneous ignition in the mixture $2H_2$-O_2. Acta Physicochim. URSS 1934:139–44.

[30] Plasma Science Committee and Committee on Atomic, Molecular, and Optical Sciences. Database needs for modeling and simulation of plasma processing. Washington, DC: National Research Council; 1996.

[31] Nalbandjan A. Acta Physicochimica URSS 1934;1:305.

[32] Dubovitsky F. Acta Physicochimica URSS 1935;2:361.

[33] Haas FM. Plausibility analysis of branching radical reclamation from HO_2 in plasma-stimulated ignition below the autoignition temperature threshold. Thesis, Drexel University; 2006.

[34] Bozhenkov S, Starikovskaia SM, Starikovskii AYu. Nanosecond gas discharge ignition of H_2 and CH_4 containing mixtures. Combust Flame 2003;133:133–46.

[35] Kosarev IN, Starikovskii AYu. Mechanism for electric breakdown in a chemically nonequilibrium system and the influence of the chain oxidation reaction in a H_2-air mixture on the breakdown threshold. Plasma Phys Rep 2000;26(8):701–9.

[36] Campbell CS, Egolfopoulos FN. Kinetics paths to radical-induced ignition of methane/air mixtures. Combustion Sci Technol 2005;177:2275–98.

[37] Aleksandrov NL, Kindysheva SV, Kukaev EN, Starikovskaya SM, Starikovskii AYu. Simulation of the ignition of a methane-air mixture by a high-voltage nanosecond discharge. Plasma Phys Rep 2009;35(10):867–82.

[38] Adamovich IV, Choi I, Jiang N, Kim J-H, Keshav S, Lempert WR, et al. Plasma assisted ignition and high-speed flow control: non-thermal and thermal effects. Plasma Sources Sci Technol 2009;18(3).

[39] Nozaki T, Muto N, Kado S, Okazaki K. Dissociation of vibrationally excited methane on Ni catalyst Part 1. Application to methane steam reforming. Catal Today 2004;89:57–65.

[40] Nair SA, Nozaki T, Okazaki K. In situ Fourier Transform Infrared (FTIR) study of nonthermal plasma-assisted methane oxidative conversion. Ind Eng Chem Res 2007;46:3486–96.

[41] Kovacs T, Deam RT. Methane reformation using plasma: an initial study. J Phys D: Appl Phys 2006;39:2391–400.

[42] Mlotek M, Sentek J, Krawczyk K, Schmidt-Szalowki K. The hydbrid plasma-catalytic process for non-oxidative methane coupling to ethylene and ethane. Appl Catal A: Gen 2009;366:232–41.

[43] Yang Y. Direct non-oxidative methane conversion by non-thermal plasma: modeling study. Plasma Chem Plasma Proces 2003;23(2):327–46.

[44] Slovetskii DI. Plasma chemical processes in petroleum chemistry (review). Pet Chem 2006;46 (5):323–32.

[45] Yao S, Nakayama A, Suzuki E. Methane conversion using a high frequency pulsed plasma: important factors. Am Inst Chem Eng J 2001;47(2):413–8.

[46] Rykalin NN, Tsvetkov Yu. V, Petrunichev VA, Glushko IK. In: Physics, engineering, and application of low-temperature plasma, Nauka (Science). Kazakhstan: Alma-Ata; 1970. p. 602.

[47] Bromberg L, Cohn DR, Rabinovich A, Alexeev N. Plasma catalytic reforming of methane. Int J Hydrogen Energy 1999;24:1131–7.
[48] Luche J, Aubry O, Khacef A, Cormier JM. Syngas production from methane oxidation using non-thermal plasma: experiments and kinetic modeling. Chem Eng J 2009;149:35–41.
[49] Czernichowski A, Czernichowski M, Czernichowski P, Cooley T. Reforming of methane into syngas in a plasma-assisted reactor. Fuel Chem Div Preprints 2002;47(1):280.
[50] Lee DH, Kim KT, Cha MS, Song YH. Optimization scheme of a rotating gliding arc reactor for partial oxidation of methane. Proc Combust Inst 2007;31:3343–51.
[51] Pushkarev AI, Zhu AM, Li XS, Sazonov RV. Methane conversion in low-temperature plasma. High Energy Chem 2009;43(3):156–62.
[52] Cormier JM, Rusu I. Syngas production via methane steam reforming with oxygen: plasma reactors versus chemical reactors. J Phys D: Appl Phys 2001;34:2798–803.
[53] Ouni F, Khacef A, Cormier JM. Effect of oxygen on methane steam reforming in a sliding discharge reactor. Chem Eng Technol 2005;29(5):604–9.
[54] Nair SA, Nozaki T, Okazaki K. Methane oxidative conversion pathways in a dielectric barrier discharge reactor – Investigation of gas phase mechanism. Chem Eng J 2007;132:85–95.
[55] Givotov VK, Potapkin BV, Rusanov VD. Low-temperature plasma chemistry. In: Lebedev YA, Plate NA, Fortov VE, editors. Encyclopedia of low-temperature plasma. Moscow: Pleiades Publishing; 2005. Vol. 8.1, p. 4.
[56] Zhu J, Zhang D, King KD. Reforming of CH_4 by partial oxidation: thermodynamic and kinetic analysis. Fuel 2001;80:899–905.
[57] Rusanov VD, Babaritskii AI, Baranov IE, Bibikov MB, Deminskii MA, Demkin SA, et al. Nonequilibrium effect of atmospheric-pressure microwave-discharge plasma on methane and kerosene conversion into synthesis gas. Doklady Chem 2004;395(2):82–5.
[58] Shekhawat D, Berry DA, Gardner TH, Spivey JJ. Catalytic reforming of liquid hydrocarbon fuels for fuel cell applications. In: Spivey JJ, Dooley KM, editors. Catalysis. Cambridge, UK: The Royal Society of Chemistry; 2006. p. 184–253.
[59] Shawal-Nasri N, Jones JM, Dupont VA, Williams A. A comparative study of sulfur poisoning and regeneration of precious-metal catalysts. Energy Fuels 1998;12:1130–4.
[60] Moulijn JA, van Diepen AE, Kapteijn F. Catalyst deactivation: is it predictable? What to do? Appl Catal A: Gen 2001;212:3–16.
[61] Kalra CS, Gutsol AF, Fridman A. Gliding arc discharges as a source of intermediate plasma for methane partial oxidation. IEEE Trans Plasma Sci 2005;33(1):32.
[62] Gallagher MJ, Geiger R, Polevich A, Rabinovich A, Gutsol A, et al. On-board plasma-assisted conversion of heavy hydrocarbons into synthesis gas. Fuel 2010;89(6):1187–92.
[63] Gallagher MJ, Geiger R, Rabinovich A, Fridman A. Partial oxidation of heavy hydrocarbon fuels for auxiliary power units using non-thermal plasma. Tampa, FL: American Institute of Chemical Engineers Spring National Meeting; 2009.
[64] Nunnally T, Gutsol K, Rabinovich A, Fridman A, Starikovsky A, Gutsol A, et al. Dissociation of H_2S in non-equilibrium gliding arc "tornado" discharge. Int J Hydrogen Energy 2009;34(18):7618–25.
[65] Asisov RI, Vakar AK, Gutsol AF, Givotov VK, Krasheninnikov EG, Krotov MF, et al. Plasmachemical methods of energy carrier production. Int J Hydrogen Energy 1985;10(7/8):475–7.
[66] Harkness JBL, Doctor RD. Plasma-chemical treatment of hydrogen sulfide in natural gas processing. Chicago, IL: Argonne National Laboratory, Gas Research Institute; 1993.
[67] Benilov MS, Naidis GV. Modeling of hydrogen-rich gas production by plasma reforming of hydrocarbon fuels. Int J Hydrogen Energy 2006;31:769–74.
[68] Indarto A, Choi JW, Lee H, Song HK. Kinetic modeling of plasma methane conversion using gliding arc. J Natural Gas Chem 2005;14:13–21.
[69] Babaritskii AI, Baranov IE, Bibikov MB, Demkin SA, Zhivotov VK, Konovalov GM, et al. Partial hydrocarbon oxidation processes induced by atmospheric pressure microwave-discharge plasma. High Energy Chem 2004;38(6):407–10.
[70] Deminsky M, Jivotov V, Potapkin B, Rusanov V. Plasma-assisted production of hydrogen from hydrocarbons. Pure Appl Chem 2002;74(3):413–8.
[71] Okumoto M, Kim HH, Takashima K, Katsura S, Mizuno A. Reactivity of methane in nonthermal plasma in the presence of oxygen and inert gases at atmospheric pressure. IEEE Trans Ind Appl 2001;37 (6):1618–24.
[72] Supat K, Chavadej S, Lobban LL, Mallinson RG. Combined steam reforming and partial oxidation of methane to synthesis gas under electrical discharge. Ind Eng Chem Res 2003;42:1654.
[73] Rusanov VD, Babaritskii AI, Gerasimov EN, Deminskii MA, Demkin SA, Zhivotov VK, et al. Stimulation of the Partial Oxidation of Methane in a Microwave Discharge. Doklady Akademii Nauk (Doklady Physical Chemistry) 2003;389(3):324–7.

[74] Sekine Y, Urasaki K, Kado S, Matsukata M, Kikuchi E. Nonequilibrium pulsed discharge: A novel method for steam reforming of hydrocarbons or alcohols. Energy Fuels 2004;18:455–9.

[75] Kogelschatz U, Zhou LM, Xue B, Eliasson B. In: Eliasson B, Riemer PWF, Wokaun A, editors. Greenhouse gas control technologies, Oxford: Pergamon (Elsevier); 1999.

[76] Gesser HD, Hunter NR, Probawono D. The CO_2 reforming of natural gas in a silent discharge reactor. Plasma Chem Plasma Process 1998;18:241–5.

[77] Song HK, Lee H, Choi JW, Na B. Effect of electrical pulse forms on the CO_2 reforming of methane using atmospheric dielectric barrier discharge. Plasma Chem Plasma Process 2004;24(1):57.

[78] Larkin DW, Caldwell TA, Lobban LL, Mallinson RG. Oxygen pathways and carbon dioxide utilization in methane partial oxidation in ambient temperature electric discharges. Energy Fuels 1998;12:740–4.

[79] Mutaf-Yardimci O, Saveliev AV, Fridman AA, Kennedy LA. Employing plasma as a catalyst in hydrogen production. Int J Hydrogen Energy 1998;23(12):1109–11.

[80] Indarto A. Kinetic of CO_2 reduction by gliding arc plasma. Asian J Water Environ Pollut 2006;4 (1):191–4.

[81] Lesueur H, Czernichowski A, Chapelle J. Electrically assisted partial oxidation of methane. Int J Hydrogen Energy 1994;19:139–44.

[82] Indarto A, Yang DR, Choi JW, Lee H, Song HK. Gliding arc plasma processing of CO_2 conversion. J Hazardous Mater 2006;146(1/2):309–15.

[83] Czernichowski A, Czernichowski P, Wesolowska K. Plasma-assisted reforming of some liquid fuels into synthesis gas. In 6th European SOFC forum. Lucerne, Switzerland; 2004.

[84] Paulmier T, Fulcheri L. Use of non-thermal plasma for hydrocarbon reforming. Chem Eng J 2005;106:59–71.

[85] Cohn DR, Rabinovich A, Titus CH, Bromberg L. Near-term possibilities for extremely low emission vehicles using onboard plasmatron generation of hydrogen. Int J Hydrogen Energy 1997;22(7):715–23.

[86] Horng RF, Wen CS, Liauh CT, Chao Y, Huang CT. Driving characteristics of a motorcycle fuelled with hydrogen-rich gas produced by an onboard plasma reformer. Int J Hydrogen Energy 2008;33:7619–29.

[87] Bromberg L, Cohn DR, Heywood J, Rabinovich A. Onboard plasmatron generation of hydrogen rich gas for diesel engine exhaust aftertreatment and other applications. Massachusetts Institute of Technology, Plasma Science and Fusion Center, JA-02-30; 2002.

[88] Penetrante BM, Hsiao MC, Merritt BT, Vogtlin GE. Fundamental limits on NOx reduction by plasma. In Dearborn, MI: SAE meeting & Expo; 1997.

[89] Tonkyn RG, Barlow SE, Hoard JW. Reduction of NOX in synthetic diesel exhaust via two-step plasma-catalysis treatment. Appl Catal B: Env 2003;40(3):207–17.

[90] Mok YS, Koh DJ, Shin DN, Kim KT. Reduction of nitrogen oxides from simulated exhaust gas by using plasma-catalytic process. Fuels Process Technol 2004;86(3):303–17.

[91] Bromberg L, Crane S, Rabinovich A, Kong Y, Cohn DR, Heywood J, et al. Hydrogen generation from plasmatron reformers: a promising technology for NOx adsorber regeneration and other automotive applications. Massachusetts Institute of Technology, Plasma Science and Fusion Center, JA-03-27; 2003.

[92] Bromberg L, Cohn DR, Wong V. Regeneration of diesel particulate filters with hydrogen rich gas. Massachusetts Institute of Technology, Plasma Science and Fusion Center, RR-05-2; 2005.

[93] Yoshida K, Rajanikanth BS, Okubo M. NO_X reduction and desorption studies under electric discharge plasma using a simulated gas mixture: a case study on the effect of corona electrodes. Plasma Sci Technol 2009;11:327–33.

[94] EG&G Technical Services. Fuel cell handbook. Morgantown, WV: U.S. Department of Energy; 2004. p. 8–64.

[95] Bromberg L, Cohn DR, Rabinovich A, Alexeev N, Samokhin A, Hadidi K, et al. Onboard plasmatron hydrogen production for improved vehicles. Massachusetts Institute of Technology, Plasma Science and Fusion Center, JA-06-3; 2006.

[96] Hadidi K, Bromberg L, Cohn DR, Rabinovich A, Alexeev N, Samokhin A. Plasma catalytic reforming of biofuels. Massachusetts Institute of Technology, Plasma Science and Fusion Center, JA-03-28; 2003.

[97] Petitpas G, Gonzalez-Aguilar J, Darmon A, Fulcheri L. Ethanol and E85 reforming assisted by a non-thermal arc discharge. Energy Fuels 2010;24:2607–13.

[98] Long H, Shang S, Tao X, Yin Y, Dai X. CO_2 reforming of CH4 by combination of cold plasma jet and Ni/g-Al_2O_3 catalyst. Int J Hydrogen Energy 2008;33:5510–5.

[99] Kraus M, Eliasson B, Kogelschatz U, Wokaun A. CO_2 reforming of methane by the combination of dielectric-barrier discharges and catalysis. Phys Chem Chem Phys 2001;3:294–300.

[100] Nozaki T, Tsukijihara H, Fukui W, Okazaki K. Kinetic analysis of the catalyst and nonthermal plasma hybrid reaction for methane steam reforming. Energy Fuels 2007;21:2525–30.

[101] Sekine Y, Haraguchi M, Tomioka M, Matsukata M, Kikuchi E. Low-temperature hydrogen production by highly efficient catalytic system assisted by electric field. J Phys Chem: A 2010;114(11):3824–33.
[102] Pietruszka B, Anklam K, Heintze M. Plasma-assisted partial oxidation of methane to synthesis gas in a dielectric barrier discharge. Appl Catal A: Gen 2004;261:19–24.
[103] Heintze M, Pietruszka B. Plasma catalytic conversion of methane into syngas: the combined effect of discharge activation and catalysis. Catal Today 2004;89:21–5.
[104] Horng RF, Huang CT, Lai MP, Wen CS, Chiu WC. Characteristics of hydrogen production by a plasma-catalyst hybrid converter with energy saving schemes under atmospheric pressure. Int J Hydrogen Energy 2008;33:3719–27.
[105] Sobacchi MG, Saveliev AV, Fridman AA, Kennedy L, Ahmed S, Krause T. Experimental assessment of a combined plasma/catalytic system for hydrogen production via partial oxidation of hydrocarbon fuels. Int J Hydrogen Energy 2002;27:635–42.
[106] Liu C, Marafee A, Mallinson R, Lobban L. Methane conversion to higher hydrocarbons in a corona discharge over metal oxide catalysts with OH groups. Appl Catal A: Gen 1997;164:21–33.
[107] Chen HL, Lee HM, Chen SH, Chao Y, Chang MB. Review of plasma catalysis on hydrogen reforming for hydrogen production – interaction, integration, and prospects. Appl Catal B: Env 2008;85:1–9.
[108] Nozaki T, Muto N, Kado S, Okazaki K. Minimum energy requirement for methane steam reforming in plasma-catalyst reactor. Am Chem Soc Div Fuel Chem 2004;49(1):179.
[109] Nozaki T, Muto N, Kado S, Okazaki K. Dissociation of vibrationally excited methane on Ni catalyst Part 2. Process diagnostics by emission spectroscopy. Catal Today 2004;89:67–74.

CHAPTER

9

Nonconventional Reforming Methods

Dushyant Shekhawat

National Energy Technology Laboratory, U.S. Department of Energy, 3610 Collins Ferry Road, Morgantown, WV 26507-0880, USA

OUTLINE

9.1. SCOPE OF THE CHAPTER

Several methods for reforming of hydrocarbons or oxygenated hydrocarbons to syngas have been presented in this book (Chapter 4: Steam Reforming, Chapter 5: Partial Oxidation, Chapter 6: Oxidative Steam Reforming, Chapter 7: CO_2 (Dry) Reforming; Chapter 8: Plasma Reforming). However, there are some existing approaches and new developments that merit discussion but do not fall neatly into any of the previous chapters. Therefore, these approaches and developments will be briefly discussed in this chapter.

This chapter contains information on Decomposition of hydrocarbons (Section 9.2), supercritical reforming (Section 9.3), non-catalytic thermal reforming in porous media (Section 9.4), radio frequency (RF)-assisted reforming (Section 9.5), and pre-reforming (Section 9.6).

Fuel Cells **DOI: 10.1016/B978-0-444-53563-4.10009-4**

9.2. DECOMPOSITION OF HYDROCARBONS

Decomposition of hydrocarbon fuels by pyrolysis or cracking has been studied as a reforming process to produce H_2 from hydrocarbon fuels in a single step [1,2]. In this process, heat is added at appropriate temperatures to dissociate the fuels. The decomposition reaction of hydrocarbon fuels can be represented by Reaction (9.1).

$$C_nH_m = nC(s) + m/2H_2(g); \Delta H_{298K} > 0 \quad (9.1)$$

The hydrocarbon fuel decomposes solely as a result of thermal energy; no oxidant (O_2, air, or water) is needed. Thus, the decomposition process produces hydrogen as only gaseous product along with solid carbon without any carbon oxide (CO or CO_2) production. Therefore, this eliminates all downstream gas processing to produce H_2, such as water gas shift, preferential oxidation, or carbon capture to remove carbon oxides. The overall process is particularly suitable for the low-temperature fuel cells, which require a CO-free gas as a fuel, such as PEM fuel cells. Also, it is easier to separate, handle, transport, and store the solid carbon compared to gaseous CO_2, which makes the decomposition reaction favorable for the carbon sequestration [2]. Consequently, the decomposition of hydrocarbons can be an economically viable option for H_2 production if the associated costs of carbon capture and sequestration are factored in the economics. However, the energy value associated with the solid carbon product could also further improve the economic viability of the decomposition process. The solid carbon formed is a valuable product and can be sold as carbon blacks, carbon nanotubes (CNTs), or carbon nanofibers (CNFs).

The decomposition reaction is endothermic and requires high temperatures (>1200°C), but can occur at relatively low temperatures in the presence of an appropriate catalyst. The catalyst deactivation due to carbon formation is a challenge since solid carbon is a product of the process. Resulting carbon formation on the catalyst makes this process rather complicated for use with onboard fuel-cell applications. However, the catalyst can be regenerated by passing air or steam through the reactor to burn off or gasify carbon in a cyclic process.

Most literature on decomposition is limited to methane since methane decomposition gives higher amount of H_2 per mole of carbon produced. Industrially, methane decomposition is mainly used to produce carbon black, whereas H_2 produced is used as a fuel for the process [1].

9.2.1. Thermodynamics

The effect of temperature and pressure on methane decomposition is given in Figs 9.1 and 9.2, respectively. Methane decomposition initiates at 400 °C and needs at least 900 °C for the complete conversion. Also, methane decomposition is not favorable at elevated pressures; the methane conversion at 900 °C decreases from 96% at 0.1 MPa to 60% at 2 MPa. Decomposition of higher hydrocarbons (not shown here) is qualitatively similar to methane decomposition; however, results in lower H_2/C ratio in the product compared to methane.

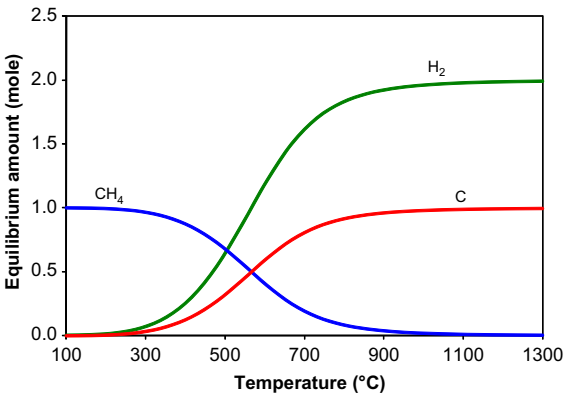

FIGURE 9.1 Effect of temperature on methane decomposition; products from 1 mole of methane at 0.1 MPa. *(Calculations using HSC Chemistry 6.12 [3])*

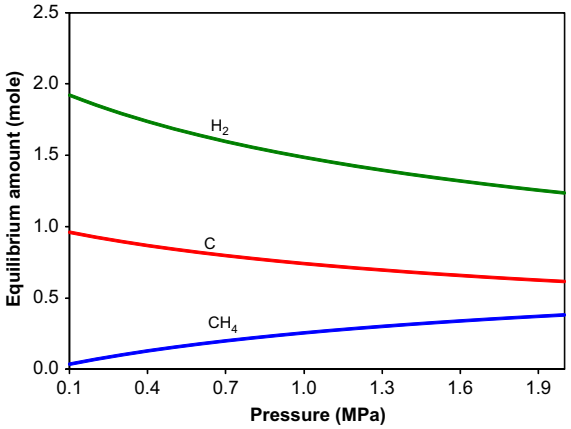

FIGURE 9.2 Effect of pressure on methane decomposition; products from 1 mole of methane at 900 °C. *(Calculations using HSC Chemistry 6.12 [3])*

9.2.2. Mechanism

The decomposition initiates with dissociative adsorption of the hydrocarbon molecule on the metal active sites, followed by stepwise dissociation of adsorbed species until the elemental carbon and hydrogen are formed [4,5]. The mechanism of methane decomposition on the metal catalyst can be depicted as follows (adapted from [5]).

$$CH_{4,g} = CH_{3,a} + H_a \quad (9.2)$$

$$CH_{(3-x),a} = CH_{(2-x),a} + H_a \quad (9.3)$$

$$nC_a = C_{n,c}(\text{carbon crystalline growth}) \quad (9.4)$$

$$2H_a = H_{2,g} \quad (9.5)$$

(subscripts: $0 \leq x \leq 2$; g − gaseous; a − adsorbed on the catalyst surface; c − carbon crystalline growth).

Although the reaction mechanism of decomposition over the carbon-based catalysts is not fully understood, it is believed that this follows a similar pattern as for metal catalysts [5].

9.2.3. Catalysts

The type of catalysts used for hydrocarbon decomposition is generally dictated by the reaction temperature as well as the type of carbon by-product to be produced. Decomposition catalysts can be classified into two categories: metal-based and carbon-based catalysts. Within the metal-based catalysts, Ni-based catalysts are widely reported in the open literature for decomposition reactions (see Table 9.1). However, the Ni-based catalysts are active and stable only at low temperatures (500−700 °C) where the decomposition reactions are not thermodynamically favorable and, consequently, higher concentration hydrogen effluent (H_2 >60%) cannot be obtained at these temperatures. The activity and stability of the Ni-based catalysts depend primarily on the Ni loading and the support material. The carbon formed from the Ni-based catalysts is valuable carbon products such as carbon black, CNFs, and CNTs. Other transition metal catalysts reported in the literature are Cu, Fe, Co, Pd, Pt, and Ru.

However, the bimetallic catalysts have shown higher catalyst activity toward the hydrocarbon cracking reactions compared to monometallic catalysts. Non-nickel metal-based catalysts can be used at elevated temperatures (700−1000 °C) but the catalyst deactivation occurs very rapidly. Noble metals can be used at temperatures up to 1000 °C and produce graphitic carbon.

Carbon-based catalysts (e.g., activated carbons, carbon blacks, carbon fibers, and carbon nanotubes) are generally used at ~900 °C and produce turbostratic carbon (disordered graphite). Thermal cracking requires elevated temperatures (~1300°C) and produces amorphous carbon. Figure 9.3 summarizes the temperature range and type of carbon formed from various catalysts reported in the literature for methane decomposition [6]. These catalysts are summarized in Table 9.1.

The most commonly used support material for the metal catalysts is Al_2O_3; but other support materials like SiO_2 and TiO_2 are also reported (see Table 9.1). Noble metals (Pd, Pt, and Rh) have been reported as promoters to enhance the stability of transitional metal

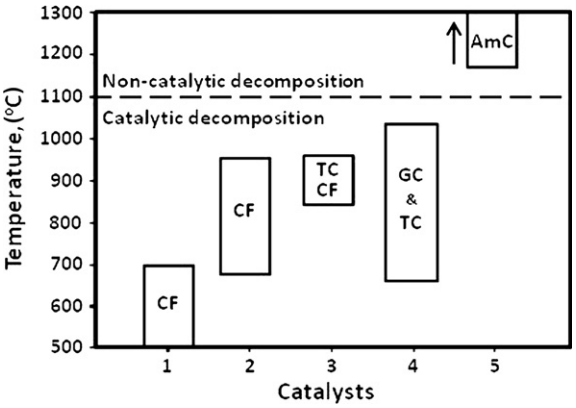

FIGURE 9.3 Summary of the temperature range and type of carbon formed from various catalysts reported in the literature. Catalysts: Ni-based (1); Fe-based (2); carbon-based (3); other metals and bimetallic catalysts (4); and noncatalytic (5). Carbon products: carbon filaments (CF); turbostratic carbon (TC); graphite carbon (GC); and amorphous carbon (AmC). *Reprinted from Muradov and Veziroglu [6], Copyright (2005), with permission from International Association for Hydrogen Energy.*

catalysts at elevated temperatures as well as their carbon accumulation capability [7]. Generally, the carbon formation on the catalyst occurs on the metal sites. However, the encapsulation of metallic particles by non-reactive graphitic carbon can cause rapid catalyst deactivation.

Recently, carbon-based catalysts are receiving attention for H_2 production from decomposition reactions. They have several advantages over supported metal catalysts, because there is no need for carbon separation or catalyst regeneration from the catalyst surface. However, carbon-catalyzed decomposition reactions are generally slower than the metal-catalyzed reactions; the activation energy of carbon-catalyzed methane decomposition lies between the activation energies for non-catalytic (thermal) and metal-catalyzed reactions [5]. The carbon produced from the reaction can serve as a catalyst; however, some carbon is needed in the reactor at start-up. The carbon produced can be sold as a valuable product. A variety of carbon-based catalyst materials have been reported in the literature: carbon black, carbon nanotube, fullerene, glassy carbon, synthetic diamond powders, graphite, and activated carbon. It is believed that the rate of hydrocarbon decomposition increases with increasing surface area of carbon material used [1,5,8]. Also, the cost of carbon-based catalysts is less than metal-based catalysts. These materials are also resistant to sulfur or additives that may be present in the liquid hydrocarbon fuels. It has been also reported that small amounts of ZnO and CaO mixed with carbon catalysts used for the sulfur-laden fuels such as diesel fuel can minimize deactivation by sulfur poisoning [2]. Also, carbon-based catalysts can be used at elevated temperatures (>900 °C) where the decomposition reaction is thermodynamically favorable. The carbon buildup on the surface of the original catalyst can be continuously removed from the reactor, for example, using steam or air in a fluidized bed reactor [9].

9.2.4. Reactor Design

Heat input, catalyst replacement, catalyst generation, and carbon separation are some of the issues that must be addressed during the reactor design for thermal decomposition. Generally, fixed bed, tubular, spouted, and fluidized bed reactors are reported in the literature for methane decomposition (see Table 9.1).

Higher temperatures are required for a complete hydrocarbon conversion and maximum hydrogen yields. Generally, the heat required for the decomposition reaction is provided by partially burning the feed. The biggest challenge is to remove the carbon solid from the catalyst. At the same time, the catalyst is also deactivated by carbon deposits so that the catalyst should be regenerated or replaced continuously to maintain the same level of activity all the time. For commercial application, both reactions — decomposition and regeneration — need to be carried out continuously. For continuous production of hydrogen from cracking of hydrocarbon, a dual fixed-bed

TABLE 9.1 Summary of Various Catalysts Reported in the Literature (Fixed-bed Reactor System and Methane as a Fuel Unless Noted)

Catalyst	Reaction conditions; significant conclusion(s)	Reference
Fe_3O_4	800–900 °C; no deactivation for 75 h	[10]
NiO	500 °C, 90,000 cc g_{cat}^{-1} h^{-1}; Ni catalyst with size of ~11 nm gave the highest H_2 yields; larger sizes resulted in lower H_2 yields	[11]
Raney type alloys (Ni, Co, Fe, Cu–Fe, Ni–Cu,)	400–900 °C; bimetallic catalysts performed better in terms of catalyst stability and activity	[4,12–14]
15% Ni/SiO_2	650 °C, 30,000 h^{-1}; no catalyst degradation over 10 cycles of cracking-regeneration cycles	[15]
Ni/SiO_2	450–650 °C, 18,000 cc g_{cat}^{-1} h^{-1}; optimum C_2H_6 conversion and H_2 production at 500 °C	[16]
Ni/SiO_2, Ni/TiO_2, Ni/Al_2O_3, Pd–Ni/SiO_2	550–650 °C; Pd–Ni catalyst was the best for repetitive cracking-generation cycles at high temperatures	[17]
Ni/SiO_2	550 °C; CH_4, C_2H_6, C_3H_8, C_4H_{10}, C_6H_{14}, and C_8H_{18}; H_2 selectivity increases with carbon number	[18]
Ni/SiO_2 Fe/SiO_2	550°C; 2 wt% silicate in Ni/SiO_2 deactivates the catalyst fast 700°C; silicate can either inhibit or promote carbon formation depending on its concentration in Fe/SiO_2	[19]
Ni/HZSM5, Ni/MgO, Ni/MoO_3, Ni/SiO_2, Ni/HY, Ni/ZrO_2	450–550 °C; Ni/ZrO_2 produced the highest levels of H_2	[20,21]
Ni/Nb_2O_5, Ni-Cu/Nb_2O_5	500–600 °C, 24,000 cc g_{cat}^{-1} h^{-1}; bimetallic catalyst performed the best	[22]
$NiCu/Al_2O_3$	500–740 °C; composition of the metal particle depends on the reaction temperature and the catalyst induction scheme	[23,24]
Pd–M/Al_2O_3, (M = Pd, Fe, Co, Ni, Ag, Cu, Rh)	700–850 °C; Pd–Co catalysts showed the highest activity and stability at high temperatures	[25]
Cu/Al_2O_3	800–1000 °C; fluidized-bed; Cu–Al spinel active phase	[7]
Co/MgO, Co/SiO_2, Co/Al_2O_3	475–600 °C; Co/Al_2O_3 provided best performance in terms of carbon formation	[26]
Ni/activated carbon	550–750 °C; deactivated catalyst have a larger Ni crystal size than the fresh one; Ni_3C formed during decomposition	[27]
Ni/carbon fibers	530 °C; CH_4, C_2H_4, 1-C_4H_8, n-C_8H_{18}; ~20 nm Ni crystallites are most active for the reaction	[28]
Activated carbon	750–950 °C; catalyst activity does not directly depend on the catalyst surface area	[8]
Activated carbon	750–900 °C; several activated carbons tested – no significant difference in activity observed	[29]
Activated carbon	750–950 °C; microporous carbons with high content of oxygenated surface groups showed highest initial conversion	[30]

(*Continued*)

TABLE 9.1 Summary of Various Catalysts Reported in the Literature (Fixed-bed Reactor System and Methane as a Fuel Unless Noted)—cont'd

Catalyst	Reaction conditions; significant conclusion(s)	Reference
Activated carbon	750–950 °C; catalytic reaction occurs in the micropores	[31]
Activated carbon	850 °C; fluidized bed; activity similar to fixed-bed reactor systems	[9]
Activated carbon	850–950 °C; TGA; optimum long-term catalyst activity obtained at the reaction temperature of 950 °C and regeneration temperature of 1000 °C	[32]
Activated carbon	CH_4 (850 °C), *n*-C_6H_{14} (650 °C), gasoline (750 °C), diesel (750 °C); addition of small amount of unsaturated hydrocarbons to methane increases H_2 production	[33]
Activated carbon	C_3H_8 (920 °C) and gasoline (880 °C); carbon produced in the process also are catalytically active for H_2 production	[34]
Carbon black	750–1050 °C; fluidized bed; catalyst activity maintained over time despite of changes in catalyst surface properties during the reaction	[35]
Carbon black	850–950 °C; fluidized bed; CH_4 and C_3H_8; stable performance over time	[1]
Carbon black	900 °C; C_3H_8; produced H_2-rich gas with >70% of H_2 concentrations	[34]
Carbon nanotube, fullerene, graphite, glassy carbon, synthetic diamond powder	850 °C; discuss the mechanism of carbon-catalyzed decomposition and the nature of active sites on the carbon surface	[5,36]

reactor system (alternating beds for the reaction and regeneration) or fluidized bed coupled with a regenerator has to be employed. Regeneration is generally carried out by flowing air (combustion) or steam (gasification) over the deactivated catalysts. The heat produced from the combustion of gas or gasified carbon can be used for the decomposition reaction. However, a better catalyst that can remain active even after significant carbon is deposited could provide larger catalyst residence time in the reaction zone.

9.3. SUPERCRITICAL REFORMING

A supercritical water oxidation technique for H_2 production is gaining a great attention because of unique properties of supercritical water that may change the fuel reactivity, thermodynamic equilibrium, and the reaction pathway. The properties of supercritical water such as solubility, density, and viscosity are significantly different than liquid or vaporized water. The supercritical properties of water and other chemicals of interest are listed in Table 9.2.

The higher solubility of hydrocarbons in supercritical water makes it behave like a super organic solvent that can solubilize large hydrocarbons easily. Its higher diffusivity and lower viscosity and density greatly reduce the heat and mass transfer resistances. In a heterogeneous catalytic system, supercritical water due to its super solubility can extract carbonaceous species from catalyst pores in situ during a reaction. This in situ extraction may result in increased pore accessibility, enhanced catalyst

TABLE 9.2 Critical Point Properties of Chemicals of Interest [37]

	T_{boil} (°C)	T_c (°C)	P_c (MPa)	ρ_c (mol/l)
Water	100	374	22.1	17.9
Methane	−162	−83	4.6	10.1
Methanol	65	240	8.1	8.5
Ethanol	78	241	6.3	6.0
Isooctane	100	271	2.6	2.1
n-Octane	96	297	2.5	2.0
1-Methylnaphthalene	242	499	3.6	–
Isocetane	240	419	1.6	–
n-Hexadecane (Cetane)	281	449	1.4	1.0

resistance to coking and sulfur poisoning, and better product selectivity. The high-pressure product stream available from a supercritical reformer may provide a significant advantage in downstream processing such as H_2 separation using metal membranes or H_2 storage since compressing a liquid feed is more economically favorable than the gaseous compression [38].

The higher pressures used in supercritical reforming increase the capital costs (high pressure equipment) as well as operating costs (feed compression) and thus may limit the viability of supercritical reforming to certain fuels. The gaseous fuels such as natural gas and LPG may not be suitable to be reformed at the supercritical conditions due to high costs associated with compressing gaseous feed. Supercritical reforming of liquid hydrocarbon fuels (e.g., diesel and gasoline) may be beneficial, but have not been widely used. Oxygenated liquid fuels (methanol, ethanol, etc.) are the most viable fuels for supercritical reforming. They are highly miscible with water; therefore, feed preparation is not challenging. Also, fuels like ethanol are mainly produced from biomass and contain up to 10 mol of water/mole of ethanol. Therefore, supercritical reforming of ethanol for the H_2 production eliminates need for costly azeotropic separation to remove water from the ethanol–water mixtures. But a disadvantage of this process is corrosion in the presence of oxidizing environment. However, the production of H_2 during supercritical reforming as well as relatively lower residence times may alleviate the potential corrosion [39]. Furthermore, ammonia formation, if air is also used as an oxidant, may significantly curtail H_2 yield and consequently the overall performance of the system.

A schematic of a typical configuration for continuous supercritical reforming process is shown in Fig. 9.4. Fuel and water are generally fed separately to avoid any reactions during preheating. After preheating, two feed streams are mixed just before the reactor inlet. The reformer effluent is cooled down quickly and depressurized. After depressurization, the effluent is separated into liquid and gaseous streams in a phase separator.

9.3.1. Thermodynamics and Mechanism

Supercritical reforming of methanol is shown as an example to illustrate the effects of temperature, pressure, and methanol concentrations on

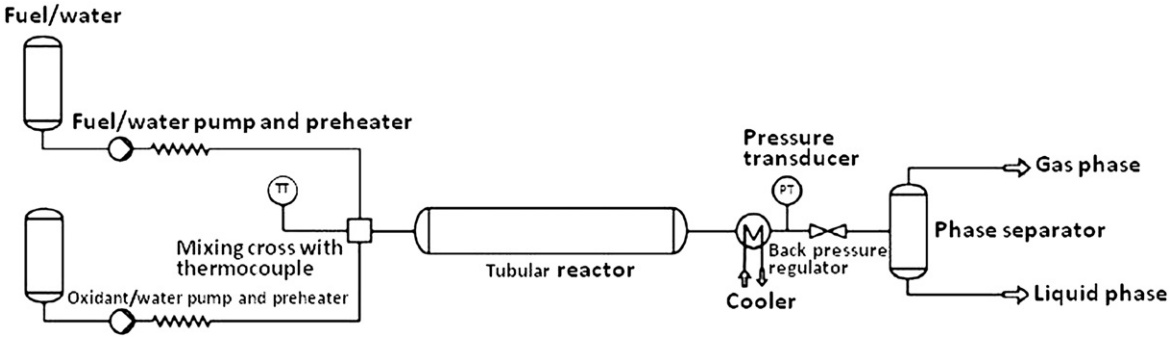

FIGURE 9.4 Schematic of a typical configuration for continuous supercritical reforming process. *Reprinted from Vogel et al. [40], Copyright (2005), with permission from Elsevier.*

the supercritical reforming thermodynamics. The major reactions involved during methanol reforming are:

$$CH_3OH(g) + H_2O(g) = CO_2(g) + 3H_2(g); \quad \Delta H_{298K} = +49.3\ kJ \tag{9.6}$$

$$CH_3OH(g) = CO(g) + 2H_2(g); \quad \Delta H_{298K} = +90.5\ kJ \tag{9.7}$$

$$CO(g) + H_2O(g) = CO_2(g) + H_2(g); \quad \Delta H_{298K} = -41.1\ kJ \tag{9.8}$$

$$CO(g) + 3H_2(g) = CH_4(g) + H_2O(g); \quad \Delta H_{298K} = -205.9\ kJ \tag{9.9}$$

$$CO_2(g) + 4H_2(g) = CH_4(g) + 2H_2O(g); \quad \Delta H_{298K} = -205.9\ kJ \tag{9.10}$$

$$2CO(g) = C + CO_2(g); \ \Delta H_{298K} = -172.4\ kJ \tag{9.11}$$

$$C + H_2O(g) = CO(g) + H_2(g); \quad \Delta H_{298K} = +131.3\ kJ \tag{9.12}$$

$$CH_4(g) = C + 2H_2(g); \ \Delta H_{298K} = +74.6\ kJ \tag{9.13}$$

Reactions (9.6)–(9.8), (9.12), and (9.13) are desired for maximum reformer efficiencies while Reactions (9.9)–(9.11) are not desired. Higher reaction temperatures favor all the desired reactions (endothermic reactions) except Reaction (9.8) and do not favor any of the undesired reactions. Higher pressures do not favor any of the desired reactions, and instead favor the undesired reactions during supercritical reforming.

Figure 9.5 shows the effect of pressure on the equilibrium product distribution from the supercritical reforming of methanol at an S/C of 7 and 700 °C. At those conditions, thermodynamic carbon formation is not expected while methanol conversion is almost complete at all pressures.

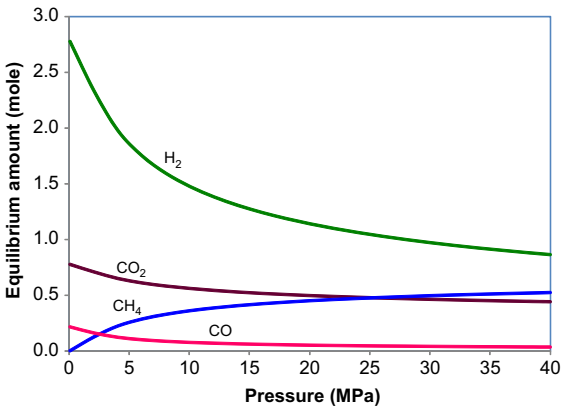

FIGURE 9.5 Effect of pressure on methanol reforming: products from 1 mole of methanol at an S/C ratio of 7 (~20 wt% methanol) and 700 °C. *(Calculations using HSC Chemistry 6.12 [3])*

However, hydrogen production decreases while methane production significantly increases with increasing pressures because the methanation reaction (Reactions (9.9) and (9.10)) is favorable at higher pressures; but there is little impact of the pressures on the product distribution beyond the critical pressure of water (22.1 MPa), which is also observed experimentally [41]. At this pressure, 50% of methanol is converted into methane, which is not desired in the feed for low-temperature fuel cells such as PEM. However, the efficiency of a high-temperature fuel cell such as SOFC is increased significantly if the feed contains around 25% of methane due to better thermal integration. Also, high-pressure operation increases the SOFC efficiency [42]. The methane yields can be minimized by performing the reforming at elevated temperatures (Fig. 9.6) or by using higher steam to methanol ratios (Fig. 9.7).

Higher temperature operation will significantly affect the capital cost as well as the operating costs. However, higher steam to carbon ratios can be economically favorable particularly for the feed like ethanol produced from fermentation of the biomass, which contains up to 90% water and can be reformed without

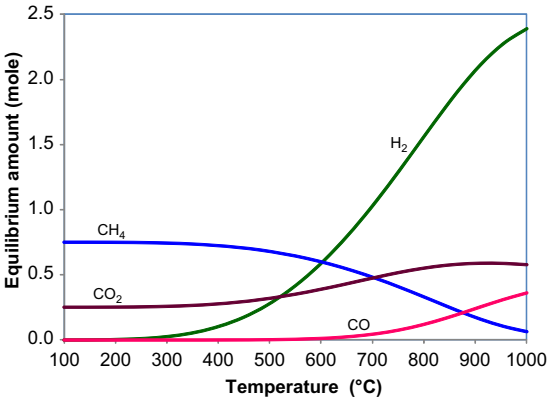

FIGURE 9.6 Effect of temperature on methanol reforming: products from 1 mol of methanol at an S/C ratio of 7 (~20 wt% methanol) and 26.0 MPa. *(calculations using HSC Chemistry 6.12 [3])*

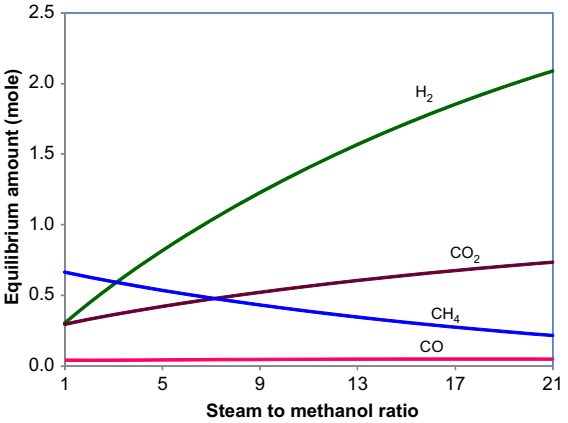

FIGURE 9.7 Effect of steam-to-methanol ratio on methanol reforming: products from 1 mol of methanol at 26.0 MPa and 700 °C. *(calculations using HSC Chemistry 6.12 [3])*

further purification. Methane formation is thermodynamically favored at the supercritical conditions; however, it is not kinetically favored at those conditions. Therefore, lowering the residence times can also decrease the methane formation by not allowing the species to reach the equilibrium [38].

It is believed that supercritical reforming of alcohols (methanol and ethanol) in water proceeds through formation of aldehydes, which then decompose into CO and lower hydrocarbons or H_2; while additional hydrogen is formed via water gas shift reaction [40,41].

$$\mathrm{RCH_2OH} = \mathrm{RCHO} + \mathrm{H_2} (\mathrm{R} = \mathrm{CH_3} \text{ for ethanol and } \mathrm{R} = \mathrm{H} \text{ for methanol}) \tag{9.14}$$

$$\mathrm{RCHO} = \mathrm{CO} + \mathrm{RH} \tag{9.15}$$

$$\mathrm{CO} + \mathrm{H_2O} = \mathrm{CO_2} + \mathrm{H_2} \tag{9.16}$$

Watanabe et al. [43] also suggested a similar mechanism for supercritical reforming of *n*-hexadecane (a model compound of diesel fuel) in the presence of air. Reforming of hydrocarbons in supercritical media proceeds through formation

of aldehyde and/or ketone, which then decomposes into CO and lower hydrocarbons. This decomposition reaction is followed by the water gas shift reaction.

There have been several studies to investigate the kinetic modeling of methanol [44–47] and ethanol [41] reforming at the supercritical conditions. However, there has been significant discrepancy among those models due to inconsistency in the experimental configurations and conditions [40]. It is not the intent of this chapter to discuss the details of kinetic modeling. The reader is therefore referred elsewhere for detailed discussions of kinetic modeling of supercritical reforming [40]. Important points regarding supercritical reforming kinetics are summarized here.

- Lower mass transfer limitation due to low viscosity and high diffusivity of the supercritical media results in higher apparent reaction rates.
- The formation of OH radical from the reaction of H_2O with HO_2 radical is a rate-limiting step for the alcohol reforming (methanol and ethanol) particularly at lower alcohol concentrations in the supercritical media [46,48].
- The gas phase combustion chemistry can be applied to describe the chemistry occurring during supercritical reforming (non-catalytic) within the same temperature range [46].
- The reaction induction time decreases with increasing reaction temperature [46].
- The mechanisms and kinetics of the reforming reaction in the presence of catalyst have yet to be established [49]. More work is needed to understand the role of the catalyst particularly for the metal wall reactors used for supercritical reforming.
- The kinetics literature is limited to methanol and ethanol studies. No such study has been found for the supercritical reforming of liquid hydrocarbon fuels such as diesel.

9.3.2. Metal Reactor Wall as a Catalyst

Many of the supercritical water reforming studies use a metal reactor in which the reactor walls catalyze the reforming reaction [49–52]. The reactor vessel used for the supercritical reforming has to be constructed from the alloys such as Inconel® and Hastelloy® to withstand the supercritical conditions for an extended period. Inconel® (Inconel® 625: 58 wt% nickel, 20–23% chromium, 8–10% molybdenum, 5% iron, 3–4% niobium, and 3% other metals) and Hastelloy® (Hastelloy® C-22: 56 wt% nickel, 22% chromium, 13% molybdenum, 3% iron, 3% tungsten, and 3% other metals) contain significant amount of nickel, chromium, and molybdenum, which are generally contained in catalysts used for steam reforming process. Although the wall reactor provides relatively small surface area for the catalyst embedded in it compared to the supported catalysts, the kinetics and mechanism of the wall-catalyzed reforming process are not fully established yet.

Boukis et al. [49] treated the inner surface of the wall reactor with 3 wt% H_2O_2 in water at 600 °C and 25 MPa for 50 h to maximize the Ni-content on the wall surface. They reported that the surface was completely covered with a thick layer of nickel oxides after the treatment and observed almost complete conversion with high H_2 yield from methanol reforming at 400–600 °C and 25–45 MPa. The better performance of the pre-treated wall reactor was attributed to the enhanced methanol decomposition and the water gas shift reaction in the presence of high Ni content on the surface. Surprisingly, lower methane yields were observed most likely due to shorter residence times used in this study, despite the fact that Ni is an active methanation catalyst. They also conducted a pilot plant study with a methanol flow rate of 1000 kg/h in which the treated reactor successfully mimicked the laboratory scale results [50].

Interestingly, Taylor et al. [51] evaluated an Inconel® 625 tubular reactor for reforming

methanol and diesel at 550–700 °C, 27.6 MPa, and S/C = 2–10. Methanol reforming with the Inconel® reactor yielded near-equilibrium compositions; however, diesel reforming led to large amounts of black residue (probably coke) in the reactor. It was claimed that the black residue resulted from incomplete mixing of the diesel and water.

9.3.3. Catalysts

The catalysts used in supercritical reforming are different from those used in conventional steam reforming process mainly because of high pressure operation. Generally, alkali (e.g., NaOH, KOH, K_2CO_3), metal (e.g., Ru, Ni, Pt, Pd), or metal oxide (ZrO_2) catalysts are used in supercritical reforming [53]. The main function of the catalyst is to (a) catalyze the desirable reactions such as hydrogen abstraction from the fuel molecule to initiate the reaction or (b) water gas shift reaction to minimize the CO conversion to methane via methanation reactions. At the same time, the catalyst should not be favorable for the undesired reactions such as methanation reaction. Gadhe and Gupta [38] eliminated the methane formation by adding alkali catalysts (0.83 wt% KOH or 0.68 wt% K_2CO_3) to the 10 wt% aqueous methanol feed in an Inconel® 600 reactor. It is believed that the methanation capability of nickel catalysts can be reduced significantly if the nickel catalyst is promoted by alkalis [54].

Byrd et al. [41] employed a Ru-supported alumina catalyst (5 wt% Ru/Al_2O_3), an active WGS catalyst, to selectively promote the WGS reaction over the methanation reaction. The hydrogen yields were significantly higher with the catalyst compared to a blank reactor (4.5 vs 3 mole of H_2/mole of ethanol feed). Also, the methane formation was decreased by conducting the reforming reaction at low residence time, lower ethanol concentrations, and high temperatures.

Gadhe and Gupta [39] used an interesting scheme to catalyze the methanol reforming in a supercritical medium by in situ-generated copper nanoparticles. The copper nanoparticles were generated by feeding aqueous solution of copper acetate along with methanol in supercritical water. A H_2 yield of 1.25 per mole of methanol was observed with the catalyst while it was less than 0.5 mol of H_2/mole of methanol without the catalyst. The presence of metallic copper, cuprous oxide, and cupric oxide was confirmed with the X-ray diffraction. This scheme continuously supplies the new catalyst while simultaneously removing the used catalyst and, therefore, this may be very beneficial for the feed containing sulfur, which may deactivate the catalyst if not removed.

Methanol and ethanol are the widely studied fuels for supercritical reforming to produce H_2. There are few studies using liquid hydrocarbon fuels. Among them, Watanabe et al. [55] conducted reforming of *n*-hexadecane (a diesel surrogate) to investigate base catalysts (ZrO_2 and NaOH) in supercritical water (400 °C and 40.5 MPa). Interestingly, the hexadecane conversion was not affected in the presence of catalysts but the hydrogen yields were significantly increased; yields of H_2 were four times higher with NaOH, and 1.5 times higher with ZrO_2, compared to reaction without a catalyst. They attributed the higher hydrogen yields to the enhanced decomposition of intermediate species (i.e., aldehydes and ketones) to CO, and WGS reaction in the presence of base catalysts. Pinkwart et al. [56] used four commercial SR catalysts with varying Ni content to reform diesel fuel in supercritical water. Highest yields of H_2 were obtained from *n*-decane reforming with higher Ni-content catalysts at 550 °C, 25.3 MPa, an S/C of 9.6, and a residence time of 40 s. No carbon formation was observed.

Supercritical reforming looks promising due to benefits arising from the supercritical fluid properties. However, it is still at the academic

level and further exploration of H_2 production for fuel cell applications is needed. The supercritical reforming mechanism in the presence of catalyst needs to be explained clearly to understand the role of the catalyst in the reaction. Further understanding of the role of the catalyst would certainly help in designing an optimal catalyst for each fuel to be reformed. There is a need to establish the stability and durability of the catalyst in a harsh environment like in supercritical reforming to be considered for commercialization.

9.4. NON-CATALYTIC THERMAL REFORMING IN POROUS MEDIA

Recently, non-catalytic thermal reforming using porous media combustion is gaining momentum for H_2 production from hydrocarbon reforming [57–67]. This non-catalytic approach involves combustion of a hydrocarbon fuel in a catalytically inert porous media at fuel-rich conditions. The basic principle is the internal heat transfer from the product gases to the entering feed through solid conduction and solid-to-solid radiation (from the post-flame zone to the pre-flame zone) characteristics of the porous media [68]. Consequently, the combustion temperature increases more than the adiabatic flame temperature predicted by thermodynamics, producing superadiabatic temperature conditions in the upstream of the system. Typical solid and gas temperature, and heat release at the interface of the two zones of porous media are shown in Fig. 9.8. Combustion in porous media increases the flame stability as well as flammability at increased inlet flow rates and equivalence ratios. This superadiabatic temperature makes it possible to burn the fuel at ultra-rich fuel conditions that may not be possible at combustion in the absence of the porous media. Syngas can be generated from hydrocarbons in porous media combustion typically at an equivalence ratio of 2.0–3.5; however, syngas from oxygenated hydrocarbons is generated at richer equivalence ratios (up to 9.3 for methanol [57]).

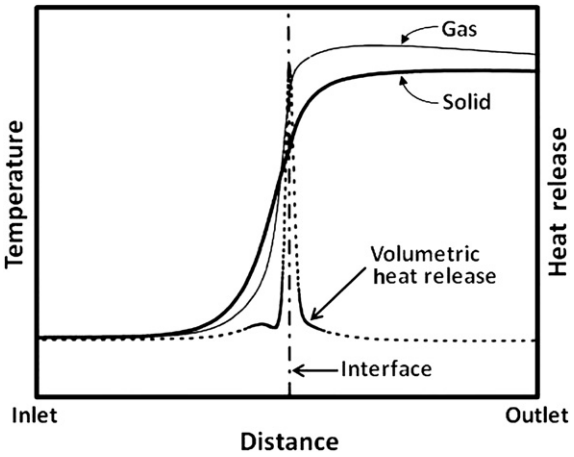

FIGURE 9.8 Typical solid and gas temperature and heat release at the interface of the two zones of porous media. *Adapted from Barra et al. [68], Copyright (2003), with permission from Elsevier.*

9.4.1. Types and Reaction Mechanism

The porous combustion reforming systems can be classified according to the mechanics of the flame in the porous media: stationary and transient (non-stationary). In the stationary system, the flame is stabilized within the porous media. The flame stabilization generally occurs at the interface of a two-section reactor in which the porous media with smaller pores is used in the first section (upstream) and the porous matrix with larger pores is used in the second section [57]. The smaller pores generally prevent the flame to propagate upstream because of the shorter optical thickness and the higher heat losses compared to the large pores. In the transient system, the unsteady state flame freely propagates in either the upstream or downstream direction within the porous media and is also known as filtration combustion.

Similar to conventional catalytic partial oxidation, reforming in porous media is also believed

to occur in two stages [58]. The partial oxidation of hydrocarbons initiates at the upstream the porous bed through complete oxidation of the fuel, producing H_2O and CO_2 that then react via steam reforming and CO_2 reforming, respectively, with unconverted hydrocarbons down the remainder of the porous bed to produce H_2-rich syngas [58,66,69]. Dhamrat and Ellzey [59] also showed computationally that the initial partial oxidation phase is exothermic, while the downstream of the bed is endothermic in a porous media reactor.

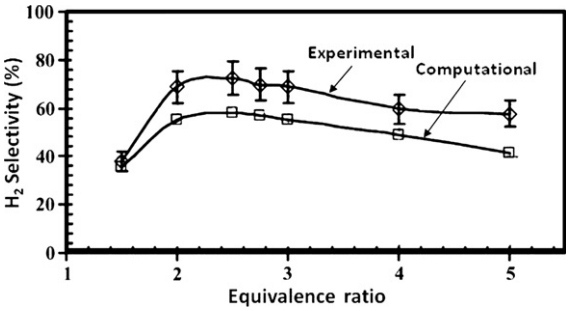

FIGURE 9.9 Effect of equivalence ratio on H_2 selectivity (moles of H_2 produced $\times$ 100/moles of CH_4 converted) from methane reforming in porous media comprised of yttria-stabilized zirconia with inlet velocity of 55 cm/s. *Reprinted from Dhamrat and Ellzey [59], Copyright (2006), with permission from Elsevier.*

9.4.2. Important Parameters in Non-catalytic Thermal Reforming

The important parameters that affect this reforming process are equivalence ratio, inlet feed velocity, reactor pressure, porosity, and the heat transfer properties of the porous media such as its thermal conductivity and specific heat. Changing any of these parameters would mainly affect combustion wave velocity and/or peak combustion temperatures inside the porous media reactor. The combustion wave velocity determines the extent of the steam reforming zone if it is assumed that the porous media reforming occurs in two zones (combustion first and SR and CO_2 reforming in downstream); e.g., smaller wave velocity would result in a shorter steam reforming zone, which results in lower hydrocarbon conversion as well as lower H_2 yield. On the other hand, higher peak combustion temperatures result in higher conversion and therefore higher H_2 yield. Hence, the overall performance of the reactor is due to the combined effect of the combustion wave velocity and peak temperature. Also, the main parameter in porous media reforming is the heat transfer properties of the porous material. The dependence of the porous media reforming properties on the equivalence ratio is distinctive. The increase in equivalence ratio enhances the hydrocarbon conversion to hydrogen up to a point; then the temperature starts decreasing with further increase in the equivalence ratio due to ultra-rich conditions and thus decreasing the hydrocarbon conversion sharply (Fig. 9.9). The summary on the effects of various parameters on the reforming properties of porous media is given in Table 9.3.

9.4.3. Porous Media Bed Materials

The porosity of the porous material is an important parameter, which dictates the superadiabatic temperature within the porous medium and hence determines the extent of reforming occurring in the porous media. Packed beds (porosity ~40%) or ceramic foams (porosity ~ 85%) are generally used as porous media in the reactor in order to produce H_2-rich synthesis gas [60]. High surface area inert porous materials such as alumina, zirconia, or silica pellets (spheres or cylinders) can be used in a packed bed reactor design, which is generally considered a very robust design for periodic thermal cycles expected in filtration combustion. Yttria-stabilized zirconia (YSZ) and cordierite have been reported as a material for ceramic foam reactor beds.

Fay et al. [60] examined YSZ foam (3.9 pores/cm) and alumina pellets (3 mm spheres) theoretically as well as experimentally for methane

TABLE 9.3 Effect of Increasing the Value of Various Parameters on the Reforming Properties of Porous Media

Parameter	Wave velocity	Peak temperatures	Hydrocarbon conversion to H_2
Equivalence ratio	Increase	Slight decrease	Increase
Inlet velocity	Increase	Increase	Increase
Preheat temperature	Increase	Increase	Increase
Pressure	Decrease	Increase	Decrease
Thermoconductivity	Slight decrease	Decrease	Decrease
Specific heat	Significantly decrease	Not changed	Decrease
Particle diameter	Decrease	Decrease	Decrease
Porosity	Increase	Increase	Increase

reforming and observed that the ceramic foam design provided significantly higher methane conversion to hydrogen compared to packed bed design. They attributed the higher H_2 production from YSZ to its higher porosity. Higher porosities of ceramic foams result in elevated superadiabatic temperatures in the porous media, which can consequently result in higher conversion of hydrocarbons as well as hydrogen production. Contrary to these results, Pedersen-Mjaanes et al. [57] observed higher conversion (66%) of methane to syngas with a packed bed reactor comprised of alumina beads compared to 56% conversion inside the alumina foam burner. However, it was not explained why the packed-bed design outperformed the theoretically favored ceramic foam design. Furthermore, the alumina beads were used for more than 100 h of testing without any degradation while the cordierite foams lasted only 20 h.

9.4.4. Reactor Design for Reforming in Porous Media

Several types of reactor designs have been reported in the literature for the porous media reforming for hydrogen production. The research group at the University of Illinois at Chicago [58,61,62] used a reciprocal flow burner (Fig. 9.10) in which the feed flow direction was reversed in a porous media reactor at a certain level. This periodic reversal in the flow direction allowed preheating the reactants with the energy

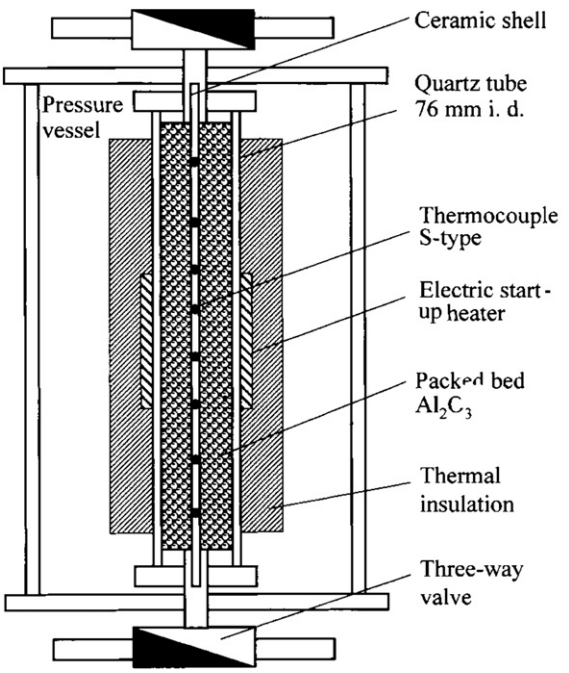

FIGURE 9.10 Schematic of reverse flow burner. *Reprinted from Drayton et al. [58], Copyright (1998), with permission from Elsevier.*

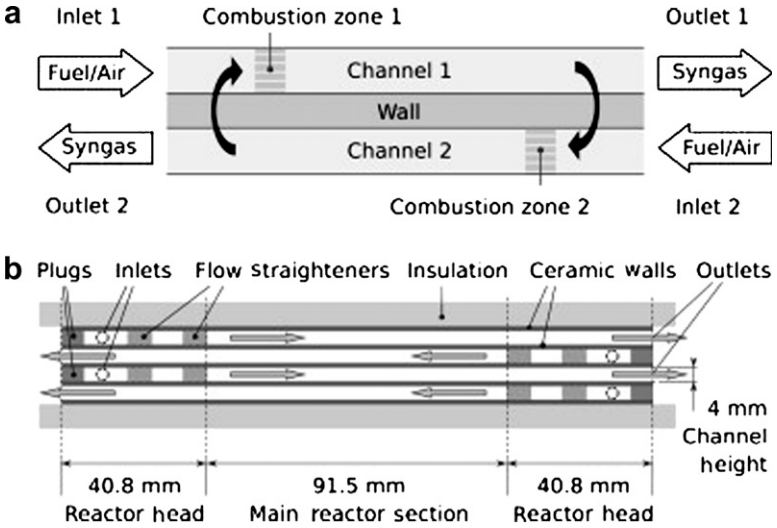

FIGURE 9.11 Porous media reforming in a reactor consisted of channels with opposing flow paths. *Reprinted from Schoegl and Ellzey [63], Copyright (2009), with permission from Elsevier.*

stored in the porous medium. Consequently, superadiabatic conditions are created and, in turn, extend the flammability limits as well as the flame stability, which are essential for the porous media reforming to occur. They used a packed bed reactor design with alumina as an inert media.

Schoegl et al. [63,64] used a reactor comprised of four parallel channels (Fig. 9.11) with alternating flow paths to convert methane and propane into H_2-rich synthesis gas. Alternating flow paths provides heat exchange across the channel walls between the reactants and products to obtain a certain temperature level where the stabilized flame front is achieved. The reactor setup with stabilized combustion front provides a continuous operation of the reformer, whereas the combustion front has to be reinitiated once it reaches at the end of the reactor in the transient system making it less viable for the H_2 production systems.

Pedersen-Mjaanes et al. [57] used a two-section reactor design for porous media reforming of various fuels in fuel-rich flames stabilized within the porous media. This design is fundamentally different from reactors used for filtration combustion, which consist of a single section of porous media. They used a fine porous media in the first section, while a coarse porous media in the second section of the reactor. A stabilized flame was observed at the interface of the two sections.

Weinberg et al. [65] used a spouted bed combustor containing 1.5-mm spheres of firebrick or quartz as a porous media to produce hydrogen-rich syngas from methane. They observed higher methane conversion (92% from quartz and 82% from firebrick) as well as higher syngas production (55% H_2 and 26% CO from quartz and 50% H_2 and 23% CO from firebrick) at similar reaction conditions with the quartz bed material. The better performance of the quartz as a bed material was attributed to better heat recirculation in the quartz material.

The addition of steam during reforming in porous media should theoretically enhance the hydrogen yields significantly as well as provide an efficient thermal integration. Recently, however, Dobrego et al. [70] numerically showed that the H_2 yields as well as fuel (methane) conversions can be effectively increased by adding small amounts of steam into the system. However, the addition of water to the system may complicate the design of the

system. Higher preheating temperatures will be required to avoid any water condensation in porous media. Also, heat losses around the system have to be minimized to sustain the endothermic steam reforming reactions. There are no experimental studies reported yet in the literature using water in the porous media to enhance the H_2 production.

9.4.5. Reforming of Various Fuels in Porous Media

Research in porous media reforming has been mainly limited to methane or gaseous fuels, but recently some studies have been reported on liquid fuel reforming using porous media. Pedersen-Mjaanes et al. [57] conducted porous media reforming of methanol and gasoline in addition to methane in fuel-rich flames stabilized within the porous media. Both gasoline and methanol have very similar trends to methane. However, the flame propagation into the foam was significantly slower with gasoline as a fuel compared to methane and methanol. Also, significant carbon formation was observed on the foam as well as reactor hardware, particularly in the reactor downstream. The gasoline conversion to syngas was only 36% with a high selectivity to lower hydrocarbons.

Dixon et al. [66] also reported reforming of liquid heptane to syngas in a filtration wave propagating through a packed bed of alumina pellets. They observed maximum syngas production at an equivalence ratio of 2.8 and inlet feed velocities <60 cm/s. The heptane conversion was almost complete; but lower hydrocarbons, predominantly methane with trace amount of C_2-C_3 olefins, were observed. Carbon formation was observed in the reactor downstream on pellets as well as on the reactor wall, particularly at partial oxidation conditions (higher equivalence ratios, i.e., >2.5).

Pastore and Mastorakos performed *n*-heptane and diesel reforming in two-layer porous media at relatively fuel-lean conditions (equivalence ratio of 2) [67]. *n*-Heptane reforming produced H_2 and CO with a concentration of about 13% and 15%, respectively. Diesel reforming in porous media produced H_2 and CO with a concentration of about 15% and 19%, respectively.

References [69,71] give kinetics of H_2 production in porous media, which is beyond the scope of this book.

9.5. RADIO FREQUENCY (RF)-ASSISTED REFORMING

Catalyst deactivation due to carbon formation on the catalytic sites is a major challenge, particularly in higher hydrocarbon (e.g., diesel, jet fuels) reforming for H_2 production. A number of novel approaches or concepts have been evaluated to reduce the carbon formation. One approach is radio frequency (RF)-induced catalytic fuel reforming, which has been shown to be effective in enhancing the performance of reforming catalysts by reducing carbon formation [72,73]. The observed effects of RF-fields on catalysis are increased catalyst activity and selectivity, reduced carbon formation, and reduced reactor heating. However, it is not known yet what mechanism (improved heating, excited surface states, or other mechanism) causes the improved catalyst performance.

Dieckmann [72] has demonstrated that the performance of a Ni-based catalyst for diesel reforming can be significantly enhanced by applying an RF electromagnetic field. Figure 9.12 shows the effect of RF field (50 kHz at 92 V/cm and 350 kHz at 98 V/cm) on the olefin formation on the Ni-based catalyst during reforming of a 50 ppmw sulfur diesel fuel. It is believed that olefins are precursors to the carbon formation [74]. They reported that the RF field reduced carbon formation by a factor of $\sim$4. The carbon formation was also inversely proportional to the applied RF field strength.

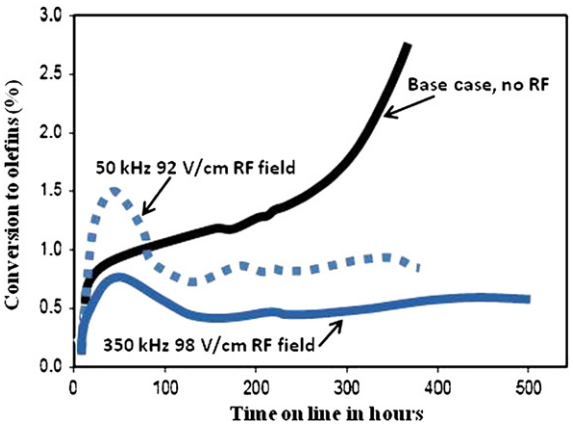

FIGURE 9.12 Effect of RF field on a Ni-based catalyst for diesel reforming. *Adapted from [72].*

However, the carbon formation was not a function of the frequency of the applied field over a range of 50−460 kHz. Interestingly, the olefin production first increases and then decreases for the RF runs (Fig. 9.12). This catalyst activation over time was attributed to the reaction of surface Ni or NiO with the support to produce a catalyst Ni^{3+} in an octahedral site in the support structure [72].

Although, application of RF field to heterogeneous catalytic systems has shown promise [72,73,75,76], the fundamentals of the technology need to be explored to learn more about the mechanism and its applicability to fuel reforming.

9.6. PRE-REFORMING

Conventional liquid fuels contain widely differing levels of complex organic compounds, which are difficult to reform and require higher temperatures and lower space velocities. For example, aromatics are more prone to coking during reforming; their presence can lower the yields of syngas over time due to catalyst deactivation. Furthermore, aromatics may hinder the overall reforming rate by occupying catalytic active sites for a longer time, due to a π-complexation between the d-electrons of the metal and π-electrons of the aromatics. Complex sulfur compounds, particularly in diesel and jet fuels, may poison the catalyst and fuel cell electrodes. However, conversion of such complex hydrocarbons into a light gas mixture before the reformer can minimize the effects of these compounds.

Additionally, pre-reforming can be used to convert higher gaseous hydrocarbons (>C1) into smaller molecules (CO, H_2, CH_4, etc.) for fuel cells with internal reforming capabilities such as SOFC. Gaseous fuels such as natural gas can be reformed internally on the SOFC anode. However, higher hydrocarbons present in natural gas can deactivate particularly a nickel-based anode if higher steam-to-carbon ratio is not used. Higher steam-to-carbon ratio results in lower temperatures at the reaction site due to endothermic steam reforming reaction. This not only lowers the reaction rate and hence the operating cost, but also provides favorable conditions for carbon deposition on the anode. Therefore, steam-to-carbon ratio can be reduced significantly by using a pre-reforming process prior to SOFC instead of using a steam reforming process.

Typically, the pre-reforming process is performed in a fixed-bed reactor upstream of the main reformer [77]. A schematic diagram showing the potential integration of a typical pre-reformer with a reformer (for liquid hydrocarbon fuels) or SOFC (for natural gas) is given in Fig. 9.13. In the pre-reformer, higher hydrocarbons are converted into a mixture of CO, CO_2, H_2, CH_4, and light hydrocarbons through a series of reactions:

Steam reforming:

$$C_nH_m + H_2O \rightarrow CO + H_2 + CH_4 + C_{n'}H_{m'},\ \Delta H_{298} > 0 \quad (9.17)$$

Methanation reaction:

$$CO + 3H_2 \leftrightarrow CH_4 + H_2O,\ \Delta H_{298K} = -205.9\ \text{kJ/mol} \quad (9.18)$$

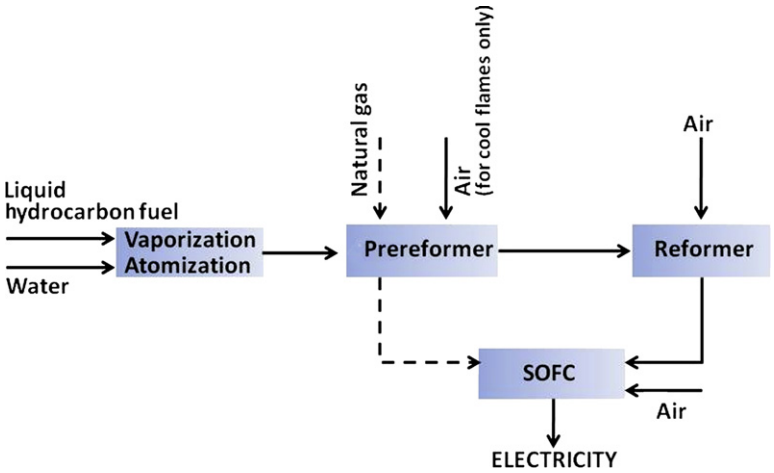

FIGURE 9.13 Schematic diagram showing the potential integration of a typical pre-reformer with a reformer (for liquid hydrocarbon fuels) or SOFC (for natural gas) (For cool flames: air is used as on oxidant instead of water).

Water gas shift reaction:

$$CO + H_2O \leftrightarrow CO_2 + H_2,\ \Delta H_{298K} = -41.2\ \text{kJ/mol} \quad (9.19)$$

Irreversible and endothermic SR (Reaction (9.17)) is followed by two equilibrium-driven exothermic reactions: methanation (Reaction (9.18)) and WGS (Reaction (9.19)). The pre-reforming is carried out at a relatively low temperature range, i.e., 400–550 °C, with the overall reaction being close to autothermal, depending on the steam/oxygen content of the feed. Pre-reforming provides the following advantages [77–79]:

- Traces of sulfur can be eliminated prior to entering the main reformer or fuel cell, due to the lower operating temperatures of the pre-reformer, which favors the deposition of sulfur on the Ni-based pre-reforming catalyst. Therefore, there would not be any need of a desulfurization unit in the downstream of a reformer. Also, the lifetime of the reformer, as well as downstream shift catalysts, is extended due to the complete sulfur removal in the pre-reformer.
- The probability of carbon formation on the reformer or fuel cell catalyst is significantly decreased since no higher hydrocarbons are present in the feed to the reformer itself.
- The main reformer can be operated at a lower S/C ratio without any catalyst deactivation, thereby reducing its size and heat duty.
- The pre-reformer provides a feed flexibility because it would convert any hydrocarbon feedstock (e.g., diesel, jet fuels, gasoline) into lower hydrocarbons and carbon oxides. Therefore, the carbon-containing feed to the main reformer would be always lower hydrocarbons and carbon oxides irrespective of the hydrocarbons in the initial feedstock.
- The pre-reformer allows for greater feed temperatures to the main reformer, thereby reducing the size of the latter.
- Liquid hydrocarbons are generally preheated to make sure that they are vaporized and well mixed before entering into the main reformer. However, they may undergo homogenous gas phase cracking reaction at the preheating temperatures, producing olefins, which are known coke precursors and deactivate the reforming catalyst. Pre-reforming those liquid hydrocarbons can eliminate the homogeneous cracking reactions and thus olefin production.

A wide variety of fuels such as diesel [77,80,81], jet fuel [77,82,83], and NATO F-76 [79] have been reformed in an adiabatic pre-reformer. However, fuels such as natural gas [84], propane [85], and butane [86,87] were also subject of pre-reforming for direct reforming fuel cell applications. In those gaseous fuels, higher hydrocarbons are converted to methane and carbon oxides, which can be directly used in SOFCs without carbon formation on the anode.

9.6.1. Catalyst and Reactor Configurations

Typically, a Ni-based steam reforming catalyst is used in the pre-reforming process [79]. The catalyst must be highly active, since the reaction occurs at low temperatures. Therefore, higher Ni-content (up to 25%) steam reforming catalyst is preferred for pre-reforming. Alkali promoters, such as those used in an SR catalyst, are also used to reduce carbon formation.

Christensen [77] used a high surface area Ni catalyst supported on magnesium oxide for adiabatic pre-reforming of diesel and jet fuels. The pre-reforming was conducted at 480 °C, 2.5 MPa, and an S/C ratio of 2.4 for an extended period (diesel for 1020 h and jet fuel for 495 h). Catalyst deactivation during diesel fuel reforming was significantly higher than that of jet fuel reforming, due to both coke formation and sulfur poisoning, whereas jet fuel reforming suffered only from sulfur poisoning. Larger concentrations of less volatile components such as polyaromatics found in diesel are probably responsible for coke formation during diesel reforming.

Chen et al. [88] added lanthana in the Ni-based catalyst (50% NiO/18% La_2O_3/alumina) to improve its carbon resistance as well as catalytic activity for pre-reforming of gasoline for an autothermal reformer. The gasoline conversion to lower hydrocarbons over the lanthana-modified catalyst was 100% at 480 °C, 0.5 MPa, S/C = 2.7, and GHSV = 40,000 h^{-1}. Arena et al. [89] conducted pre-reforming of *n*-hexane over 19% Ni/MgO (450 °C, S/C =1.5−3.5, H_2/C = 1) in the presence of hydrogen in the feed to reduce the catalyst deactivation due to encapsulation carbon. It was believed that the carbon deposited on the catalyst surface readily reacts with the adsorbed hydrogen atoms, facilitating methanation reaction and reducing the carbon accumulation on the surface.

Precious metal catalysts can also be used in pre-reforming. Pfefferle [82] carried out pre-reforming of JP-4 fuel in the presence of H_2 with Pt and Rh supported on alumina containing 6% silica at a temperature below 700 °C. The presence of H_2 in the feed allows pre-reforming to occur at low temperatures and, subsequently, an S/C ratio as low as 1 can be used without substantial catalyst deactivation. More than 90% hydrocarbon conversion to methane, H_2, CO, and CO_2 was observed in pre-reformer without any catalyst deactivation. Chen et al. [90] used 1 wt% Pt supported on gadolinium-doped ceria (GDC) to pre-reform propane gas for direct utilization of the resulting reformate in an SOFC. A complete conversion of propane into CH_4, H_2, CO, and CO_2 without any carbon formation was observed at 650 °C and an S/C of 0.5. Zheng et al. [83] used 2-wt% $Rh/CeO_2-Al_2O_3$ catalyst for pre-reforming of jet fuels at 512 °C and an S/C of 3.

Pre-reformers with multiple catalyst bed configurations can also be used. Minet et al. [80,81] used a combination of calcium aluminate that contained a high loading of calcium (a silica and Ni-free SR catalyst) at the front-end, and a Ni-based CaO−alumina catalyst at the back-end of the reactor for pre-reforming of No. 2 fuel oil. High S/C ratios (3.9−6.7), as well as high temperatures (940−1000 °C) were utilized in this study. The effluent from the pre-reformer was fed to an autothermal reformer containing a Ni-based CaO−alumina catalyst. Up to 60% of hydrocarbons were

converted into CO and CO_2 in the pre-reformer without any catalyst deactivation due to carbon formation.

Catalytic cracking as a pre-reforming step was utilized by Campbell et al. [91] for JP-8 fuel. Two different types of catalysts were studied in a packed reactor: Mn supported on γ-Al_2O_3, and mixed MFI and BEA acidic zeolites. Both catalysts gave similar conversion levels over a range of temperatures and space velocities. The primary compounds formed from the JP-8 fuel catalyst cracking were determined to be H_2, CH_4, C_2H_4, C_3H_6, and benzene. Each type of catalyst gave greater than 80% cracking conversion at liquid hour space velocity (LHSV) of 5.5 h^{-1} and <250 °C, while a temperature greater than 520 °C was required for LHSV of 44 h^{-1}. The light sulfur species present in the cracked gas product stream can be removed by adsorption in the pre-reformer itself. Non-volatiles and higher aromatics − which are difficult to convert into lighter hydrocarbons in the catalytic cracking process − can be removed by gas/liquid separation. Thus, the light product gas stream can be steam reformed into H_2-rich gas without any catalyst deactivation due to sulfur or coke precursors.

Recently, cool flame partial oxidation (POX) has gained attention for use in atomization and vaporization in reforming liquid fuels (see Fig. 9.13) [92–96]. At temperatures as low as 120 °C, fuel–air mixtures can react chemically and produce very weak flames called "cool flames." Unlike conventional flames, cool flames generate very little heat, CO, formaldehyde, and other oxygenated compounds. This technique is limited to catalytic POX and consists of two isolated and thermally independent reaction chambers. In the first reactor, processing of the complex fuels via a cool flame leads to reaction products comprised of small molecules, such as lower molecular weight alkenes and oxygenated compounds, including aldehydes, ketones, and alcohols. These small molecules are sent to the second reactor for reforming to produce syngas. Oxygenated compounds formed in the first reactor are more easily reformed in the second reactor, and are thought to form less carbon in the reformer than the corresponding hydrocarbons (e.g., ethanol would form less carbon in the reformer than ethane).

References

[1] Muradov N. Hydrogen via methane decomposition: an application for decarbonization of fossil fuels. Int J Hydrogen Energy 2001;26(11):1165–75.

[2] Ahmed S, Aitani A, Rahman F, Al-Dawood A, Al-Muhaish F. Decomposition of hydrocarbons to hydrogen and carbon. Appl Catal A: Gen 2009;359(1–2):1–24.

[3] Roine A. HSC chemistry. Outotec Research Oy; 2008.

[4] Cunha AF, Órfão JJM, Figueiredo JL. Catalytic decomposition of methane on Raney-type catalysts. Appl Catal A: Gen 2008;348(1):103–12.

[5] Muradov N, Smith F, T-Raissi A. Catalytic activity of carbons for methane decomposition reaction. Catal Today 2005;102–3:225–33.

[6] Muradov NZ, Veziroglu TN. From hydrocarbon to hydrogen-carbon to hydrogen economy. Int J Hydrogen Energy 2005;30(3):225–37.

[7] Ammendola P, Chirone R, Lisi L, Ruoppolo G, Russo G. Copper catalysts for H_2 production via CH_4 decomposition. J Mol Catal A: Chem 2007;266(1–2):31–9.

[8] Krzyzynski S, Kozlowski M. Activated carbons as catalysts for hydrogen production via methane decomposition. Int J Hydrogen Energy 2008;33(21):6172–7.

[9] Lee KK, Han GY, Yoon KJ, Lee BK. Thermocatalytic hydrogen production from the methane in a fluidized bed with activated carbon catalyst. Catal Today 2004;93–95:81–6.

[10] Konieczny A, Mondal K, Wiltowski T, Dydo P. Catalyst development for thermocatalytic decomposition of methane to hydrogen. Int J Hydrogen Energy 2008;33(1):264–72.

[11] Li Y, Zhang B, Xie X, Liu J, Xu Y, Shen W. Novel Ni catalysts for methane decomposition to hydrogen and carbon nanofibers. J Catal 2006;238(2):412–24.

[12] Cunha AF, Órfão JJM, Figueiredo JL. Methane decomposition on Fe-Cu Raney-type catalysts. Fuel Process Technol 2009;90(10):1234–40.

[13] Cunha AF, Órfão JJM, Figueiredo JL. Methane decomposition on Ni-Cu alloyed Raney-type catalysts. Int J Hydrogen Energy 2009;34(11):4763–72.

[14] Cunha AF, Mahata N, Orfao JJM, Figueiredo JL. Methane decomposition on La_2O_3-promoted Raney-Type Fe catalysts. Energy Fuels 2009;23(8):4047–50.
[15] Aiello R, Fiscus JE, zur Loye H-C, Amiridis MD. Hydrogen production via the direct cracking of methane over Ni/SiO_2: catalyst deactivation and regeneration. Appl Catal A: Gen 2000;192(2):227–34.
[16] Chin SY, Chin Y-H, Amiridis MD. Hydrogen production via the catalytic cracking of ethane over Ni/SiO_2 catalysts. Appl Catal A: Gen 2006;300(1):8–13.
[17] Otsuka K, Takenaka S, Ohtsuki H. Production of pure hydrogen by cyclic decomposition of methane and oxidative elimination of carbon nanofibers on supported-Ni-based catalysts. Appl Catal A: Gen 2004;273(1–2):113–24.
[18] Otsuka K, Shigeta Y, Takenaka S. Production of hydrogen from gasoline range alkanes with reduced CO_2 emission. Int J Hydrogen Energy 2002;27(1):11–8.
[19] Ermakova MA, Ermakov DY. Ni/SiO_2 and Fe/SiO_2 catalysts for production of hydrogen and filamentous carbon via methane decomposition. Catal Today 2002;77(3):225–35.
[20] Choudhary TV, Sivadinarayana C, Chusuei CC, Klinghoffer A, Goodman DW. Hydrogen production via catalytic decomposition of methane. J Catal 2001;199(1):9–18.
[21] Choudhary VR, Banerjee S, Rajput AM. Continuous production of H_2 at low temperature from methane decomposition over Ni-containing catalyst followed by gasification by steam of the carbon on the catalyst in two parallel reactors operated in cyclic manner. J Catal 2001;198(1):136–41.
[22] Li J, Lu G, Li K, Wang W. Active Nb_2O_5-supported nickel and nickel-copper catalysts for methane decomposition to hydrogen and filamentous carbon. J Mol Catal A: Chem 2004;221(1–2):105–12.
[23] Chen J, Li Y, Li Z, Zhang X. Production of CO_x-free hydrogen and nanocarbon by direct decomposition of undiluted methane on Ni-Cu-alumina catalysts. Appl Catal A: Gen 2004;269(1–2):179–86.
[24] Li D, Chen J, Li Y. Evidence of composition deviation of metal particles of a $Ni\text{-}Cu/Al_2O_3$ catalyst during methane decomposition to COx-free hydrogen. Int J Hydrogen Energy 2009;34(1):299–307.
[25] Ogihara H, Takenaka S, Yamanaka I, Tanabe E, Genseki A, Otsuka K. Formation of highly concentrated hydrogen through methane decomposition over Pd-based alloy catalysts. J Catal 2006;238(2):353–60.
[26] Avdeeva LB, Kochubey DI, Shaikhutdinov SK. Cobalt catalysts of methane decomposition: accumulation of the filamentous carbon. Appl Catal A: Gen 1999;177(1):43–51.
[27] Bai Z, Chen H, Li B, Li W. Methane decomposition over Ni loaded activated carbon for hydrogen production and the formation of filamentous carbon. Int J Hydrogen Energy 2007;32(1):32–7.
[28] Otsuka K, Ogihara H, Takenaka S. Decomposition of methane over Ni catalysts supported on carbon fibers formed from different hydrocarbons. Carbon 2003;41(2):223–33.
[29] Kim MH, Lee EK, Jun JH, Kong SJ, Han GY, Lee BK, et al. Hydrogen production by catalytic decomposition of methane over activated carbons: kinetic study. Int J Hydrogen Energy 2004;29(2):187–93.
[30] Moliner R, Suelves I, Lázaro MJ, Moreno O. Thermocatalytic decomposition of methane over activated carbons: influence of textural properties and surface chemistry. Int J Hydrogen Energy 2005;30(3):293–300.
[31] Bai Z, Chen H, Li B, Li W. Catalytic decomposition of methane over activated carbon. J Anal Appl Pyrolysis 2005;73(2):335–41.
[32] Abbas HF, Daud WMAW. Thermocatalytic decomposition of methane for hydrogen production using activated carbon catalyst: regeneration and characterization studies. Int J Hydrogen Energy 2009;34(19):8034–45.
[33] Muradov NZ. CO_2-free production of hydrogen by catalytic pyrolysis of hydrocarbon fuel. Energy Fuels 1998;12(1):41–8.
[34] Muradov N. Emission-free fuel reformers for mobile and portable fuel cell applications. J Power Sources 2003;118(1–2):320–4.
[35] Lee EK, Lee SY, Han GY, Lee BK, Lee T-J, Jun JH, et al. Catalytic decomposition of methane over carbon blacks for CO_2-free hydrogen production. Carbon 2004;42(12–13):2641–8.
[36] Muradov N. Catalysis of methane decomposition over elemental carbon. Catal Commun 2001;2(3–4):89–94.
[37] NIST Chemistry WebBook. 2009 [cited 2009 September 04]; Available from: http://webbook.nist.gov/chemistry/.
[38] Gadhe JB, Gupta RB. Hydrogen production by methanol reforming in supercritical water: suppression of methane formation. Indus Eng Chem Res 2005;44(13):4577–85.
[39] Gadhe JB, Gupta RB. Hydrogen production by methanol reforming in supercritical water: catalysis by in-situ-generated copper nanoparticles. Int J Hydrogen Energy 2007;32(13):2374–81.
[40] Vogel F, Blanchard JLD, Marrone PA, Rice SF, Webley PA, et al. Critical review of kinetic data for the oxidation of methanol in supercritical water. J Supercritical Fluids 2005;34(3):249–86.
[41] Byrd AJ, Pant KK, Gupta RB. Hydrogen production from ethanol by reforming in supercritical water

using Ru/Al_2O_3 catalyst. Energy Fuels 2007;21 (6):3541–7.
[42] Grol E, DiPietro J, Thijssen JHJS, Surdoval W, Quedenfeld H. The benefits of SOFC for coal-based power generation. U.S. Department of Energy; 2007.
[43] Watanabe M, Mochiduki M, Sawamoto S, Adschiri T, Arai K. Partial oxidation of n-hexadecane and polyethylene in supercritical water. J Supercritical Fluids 2001;20(3):257–66.
[44] Anitescu G, Zhang ZH, Tavlarides LL. A kinetic study of methanol oxidation in supercritical water. Ind Eng Chem Res 1999;38(6):2231–7.
[45] Brock EE, Savage PE, Barker JR. A reduced mechanism for methanol oxidation in supercritical water. Chem Eng Sci 1998;53(5):857–67.
[46] Brock EE, Oshima Y, Savage PE, Barker JR. Kinetics and mechanism of methanol oxidation in supercritical water. J Phys Chem 1996;100(39):15834–42.
[47] Dagaut P, Cathonnet M, Boettner JC. Chemical kinetic modeling of the supercritical-water oxidation of methanol. J Supercritical Fluids 1996;9(1):33–42.
[48] Hayashi R, Onishi M, Sugiyama M, Koda S, Oshima Y. Kinetic analysis on alcohol concentration and mixture effect in supercritical water oxidation of methanol and ethanol by elementary reaction model. J Supercritical Fluids 2007;40(1):74–83.
[49] Boukis N, Diem V, Habicht W, Dinjus E. Methanol reforming in supercritical water. Ind Eng Chem Res 2003;42(4):728–35.
[50] Boukis N, Diem V, Galla U, Dinjus E. Methanol reforming in supercritical water for hydrogen production. Combust Sci Technol 2006;178(1–3):467–85.
[51] Taylor JD, Herdman CM, Wu BC, Wally K, Rice SF. Hydrogen production in a compact supercritical water reformer. Int J Hydrogen Energy 2003;28(11):1171–8.
[52] Picou JW, Wenzel JE, Lanterman HB, Lee S. Hydrogen production by noncatalytic autothermal reformation of aviation fuel using supercritical water. Energy Fuels 2009;23:6089–94.
[53] Guo LJ, Lu YJ, Zhang XM, Ji CM, Guan Y, Pei AX. Hydrogen production by biomass gasification in supercritical water: A systematic experimental and analytical study. Catal Today 2007;129(3-4):275–86.
[54] Campbell TK, Falconer JL. Carbon dioxide hydrogenation on potassium-promoted nickel catalysts. Appl Catal 1989;50(1):189–97.
[55] Watanabe M, Inomata H, Osada M, Sato T, Adschiri T, Arai K. Catalytic effects of NaOH and ZrO_2 for partial oxidative gasification of n-hexadecane and lignin in supercritical water. Fuel 2003;82(5):545–52.
[56] Pinkwart K, Bayha T, Lutter W, Krausa M. Gasification of diesel oil in supercritical water for fuel cells. J Power Sources 2004;136(2):211–4.
[57] Pedersen-Mjaanes H, Chan L, Mastorakos E. Hydrogen production from rich combustion in porous media. Int J Hydrogen Energy 2005;30 (6):579–92.
[58] Drayton MK, Saveliev AV, Kennedy LA, Fridman AA, Li Y-E. Syngas production using superadiabatic combustion of ultra-rich methane-air mixtures. Proc Combust Inst 1998;27:1361–7.
[59] Dhamrat RS, Ellzey JL. Numerical and experimental study of the conversion of methane to hydrogen in a porous media reactor. Combust Flame 2006;144 (4):698–709.
[60] Fay M, Dhamrat R, Ellzey JL. Effect of porous reactor design on conversion of methane to hydrogen. Combust Science Technol 2005;177(11):2171–89.
[61] Toledo M, Bubnovich V, Saveliev A, Kennedy L. Hydrogen production in ultrarich combustion of hydrocarbon fuels in porous media. Int J Hydrogen Energy 2009;34(4):1818–27.
[62] Bingue JP, Saveliev A, Kennedy LA. Optimization of hydrogen production by filtration combustion of methane by oxygen enrichment and depletion. Int J Hydrogen Energy 2004;29(13):1365–70.
[63] Schoegl I, Ellzey JL. A mesoscale fuel reformer to produce syngas in portable power systems. Proc Combust Inst 2009;32:3223–30.
[64] Schoegl I, Newcomb SR, Ellzey JL. Ultra-rich combustion in parallel channels to produce hydrogen-rich syngas from propane. Int J Hydrogen Energy 2009;34(12):5152–63.
[65] Weinberg FJ, Bartleet TG, Carleton FB, Rimbotti P, Brophy JH, Manning RP. Partial oxidation of fuel-rich mixtures in a spouted bed combustor. Combust Flame 1988;72(3):235–9.
[66] Dixon MJ, Schoegl I, Hull CB, Ellzey JL. Experimental and numerical conversion of liquid heptane to syngas through combustion in porous media. Combust Flame 2008;154(1–2):217–31.
[67] Pastore A, Mastorakos E. Rich n-heptane and diesel combustion in porous media. Exp Thermal Fluid Sci 2010;34(3):359–65.
[68] Barra AJ, Diepvens G, Ellzey JL, Henneke MR. Numerical study of the effects of material properties on flame stabilization in a porous burner. Combust Flame 2003;134(4):369–79.
[69] Dobrego KV, Gnesdilov NN, Lee SH, Choi HK. Overall chemical kinetics model for partial oxidation of methane in inert porous media. Chem Eng J 2008;144(1):79–87.
[70] Dobrego KV, Gnezdilov NN, Lee SH, Choi HK. Partial oxidation of methane in a reverse flow porous media reactor. Water admixing optimization. Int J Hydrogen Energy 2008;33(20):5535–44.

[71] Dobrego KV, Gnezdilov NN, Lee SH, Choi HK. Methane partial oxidation reverse flow reactor scale up and optimization. Int J Hydrogen Energy 2008;33 (20):5501–9.
[72] Dieckmann G. Development of Ni-based sulfur-resistant catalyst for diesel reforming. Office of fossil Energy Fuel Cell Program, FY2006 Annual Report 2006:160–3.
[73] Ovenston A, Walls JR. Generation of heat in a single catalyst pellet placed in an electromagnetic-field for endothermic reforming of hydrocarbons. J Chem Soc-Faraday Trans I 1983;79:1073–84.
[74] Joensen F, Rostrup-Nielsen JR. Conversion of hydrocarbons and alcohols for fuel cells. J Power Sources 2002;105(2):195–201.
[75] Al-Mayman SI, Al-Zahrani SM. Catalytic cracking of gas oils in electromagnetic fields: reactor design and performance. Fuel Process Technol 2003;80(2): 169–82.
[76] Ovenston A, Walls JR. Generation of heat in composite catalytic materials in RF fields. Chem Eng Res Design 1990;68(6):530–6.
[77] Christensen TS. Adiabatic prereforming of hydrocarbons – an important step in syngas production. Appl Catal A: Gen 1996;138(2):285–309.
[78] Dybkjaer I. Tubular reforming and autothermal reforming of natural gas – an overview of available processes. Fuel Process Technol 1995;42(2–3): 85–107.
[79] Katikaneni S, Yuh C, Abens S, Farooque M. The direct carbonate fuel cell technology: advances in multi-fuel processing and internal reforming. Catal Today 2002;77(1–2):99–106.
[80] Minet RG, Warren D, Tomita T, Hirokawa K, Osaki K, Shinjo T. Assessment of fuel processing systems for dispersed fuel cell power plants. Electric Power Research Institute Report EM-1487; August 1980.
[81] Minet RG, Warren D, Bett J. Evaluation of hybrid THR-ATR fuel processor. Electric Power Research Institute Report EM-2096; October 1981.
[82] Pfefferle WC. Process for producing hydrogen. US Patent 3481722. 1969.
[83] Zheng J, Strohm JJ, Song C. Steam reforming of liquid hydrocarbon fuels for micro-fuel cells. Pre-reforming of model jet fuels over supported metal catalysts. Fuel Process Technol 2008;89(4):440–8.
[84] Aasberg-Petersen K, Christensen TS, Nielsen CS, Dybkjær I. Recent developments in autothermal reforming and pre-reforming for synthesis gas production in GTL applications. Fuel Process Technol 2003;83(1–3):253–61.
[85] Alphonse P, Ansart F. Catalytic coatings on steel for low-temperature propane prereforming to solid oxide fuel cell (SOFC) application. J Colloid Interface Sci 2009;336(2):658–66.
[86] Nagaoka K, Sato K, Nishiguchi H, Takita Y. Highly active Ni/MgO in oxidative steam pre-reforming of n-butane for fuel cell application. Catal Commun 2007;8(11):1807–10.
[87] Nagaoka K, Sato K, Nishiguchi H, Takita Y. Influence of support on catalytic behavior of nickel catalysts in oxidative steam prereforming of n-butane for fuel cell applications. Appl Catal A: Gen 2007;327 (2):139–46.
[88] Chen Y, Xu H, Jin X, Xiong G. Integration of gasoline prereforming into autothermal reforming for hydrogen production. Catal Today 2006;116 (3):334–40.
[89] Arena F, Trunfio G, Alongi E, Branca D, Parmaliana A. Modelling the activity-stability pattern of Ni/MgO catalysts in the pre-reforming of n-hexane. Appl Catal A: Gen 2004;266(2):155–62.
[90] Chen F, Zha S, Dong J, Liu M. Pre-reforming of propane for low-temperature SOFCs. Solid State Ionics 2004;166(3–4):269–73.
[91] Campbell TJ, Shaaban AH, Holcomb FH, Salavani R, Binder MJ. JP-8 catalytic cracking for compact fuel processors. J Power Sources 2004;129(1):81–9.
[92] Aicher T, Griesser L. Novel process to evaporate liquid fuels and its application to the catalytic partial oxidation of diesel. J Power Sources 2007;165 (1):210–6.
[93] Hartmann L, Lucka K, Köhne H. Mixture preparation by cool flames for diesel-reforming technologies. J Power Sources 2003;118(1–2):286–97.
[94] Kolaitis DI, Founti MA. On the assumption of using n-heptane as a "surrogate fuel" for the description of the cool flame oxidation of diesel oil. Proc Combust Inst 2009;32(2):3197–205.
[95] Edenhofer R, Lucka K, Köhne H. Low temperature oxidation of diesel-air mixtures at atmospheric pressure. Proc Combust Inst 2007;31(2):2947–54.
[96] Naidja A, Krishna CR, Butcher T, Mahajan D. Cool flame partial oxidation and its role in combustion and reforming of fuels for fuel cell systems. Prog Energy Combust Sci 2003;29(2):155–91.

CHAPTER

10

Deactivation of Reforming Catalysts

James J. Spivey

Louisiana State University, S. Stadium Dr., Baton Rouge, LA 70803, USA

OUTLINE

Fuel Cells **DOI: 10.1016/B978-0-444-53563-4.10011-2**

10.1. SCOPE OF THIS CHAPTER

This chapter focuses on the mechanisms of deactivation for catalysts used in the reformer step of the fuel processor, as shown in Fig. 10.1.[1]

The following terminology will be used to describe deactivation at conditions corresponding to the three modes of reformer operation, consistent with other chapters in this book:

- *Partial oxidation (POX)*: fuel + air/O_2
- *Oxy-steam reforming (OSR)*: fuel + H_2O/O_2
- *Steam reforming (SR)*: fuel + H_2O

$\rightarrow$ reformate

Autothermal reforming (ATR) is a special case of OSR, in which the ratios of oxygen and steam are such that the net heat of reaction is zero at the reformer temperature. The reformate consists primarily of CO, H_2, CO_2, and steam, with minor concentrations of olefins, methane, and contaminants such as H_2S.

10.2. INTRODUCTION – GENERAL MECHANISMS FOR FUEL REFORMING

Deactivation of catalysts used in fuel reforming can be caused by three general mechanisms [48–52]:

- Thermally induced changes to the catalyst structure or active metal;
- Poisoning by contaminants (primarily sulfur in the case of fuel processing);
- Coke/carbon deposition.[2]

[1] Here, we do not explicitly consider deactivation due solely to the dry reforming of fuels to produce syngas (CO_2 + fuel $\rightarrow$ CO + H_2), nor the water gas shift reaction (CO + $H_2O \rightarrow CO_2 + H_2O$) – even though these reactions undoubtedly take place within the reformer. Rather, any deactivation caused by these reactions is included implicitly in the results presented here for all reactions among the *primary* feed gases to the fuel processor – air/O_2 and/or steam, plus fuel. The reader is referred to recent studies published elsewhere on the deactivation of catalysts used in dry reforming [1–18] and water gas shift [19–47].

[2] Although the terms "coke" and "carbon" are used interchangeably in many studies, we will make an important distinction here. "Coke" will be used to define polynuclear aromatic compounds that are sufficiently high molecular weight to be retained on the catalyst at conditions present in fuel reforming, and typically have a H/C ratio of ~1:2. "Carbon" will be used to define coke *and* any other carbon-containing species on the catalyst that leads to deactivation – this includes graphitic deposits as well as elemental carbon. This terminology is consistent with that suggested by Bond [53].

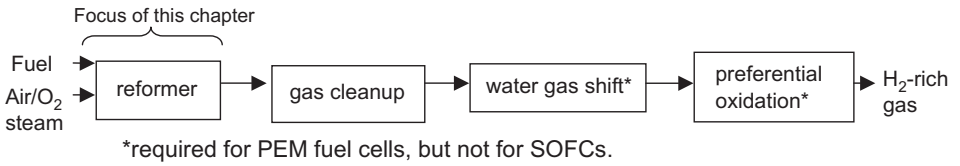

FIGURE 10.1 Schematic diagram of a fuel processor.

Other mechanisms of deactivation such as attrition or vaporization of the active metal are not generally found in fuel processing because these catalysts are not used in fluid beds, and because they have been designed to avoid gross metal loss by vaporization.[3]

These mechanisms are not generally independent: e.g., sulfur poisoning is almost always accompanied by carbon deposition. However, the following discussion is organized according to these three mechanisms to analyze the roles they play individually in the deactivation of fuel-reforming catalysts.

10.3. THERMALLY INDUCED DEACTIVATION

Thermal deactivation in fuel reforming is caused by

- *Structural transformations*: e.g., collapse of the pore structure, resulting in loss of active surface area.
- *Sintering of supported metal clusters*: thermally induced coalescence of active metal clusters, resulting in lower activity.
- *Solid–solid interactions* between the support and active metal(s), resulting in loss of the catalytic activity of the active metal(s).

Because fuel reforming is carried out at elevated temperatures (700–900 °C), thermal deactivation is typically a significant mechanism of deactivation. For catalysts consisting of metals supported on an oxide, sintering of the metal clusters can be extremely important at these temperatures [54,55]. For this reason, a great deal of effort is spent to develop catalysts with metal-support interactions strong enough to minimize sintering, but not so strong that the catalytic metal loses its activity by reacting with the support. This sort of reaction often leads to an inactive phase, such as a spinel, and is typically irreversible.

10.3.1. Minimizing Thermal Deactivation

10.3.1.1. Thermally Stable Supports

Attempts to minimize thermal deactivation include the intentional use of thermally stable oxides as supports for active metals – the logic being that the oxide will remain stable at reaction conditions and not react further with the active metal [17,54,56–58]. Examples of these types of catalysts, consisting of an active metal supported on a stable oxide, include Rh/$CaAl_{12}O_{19}$ hexaaluminate [54] and Ni/$MgAl_2O_4$ spinel [17]. However, depending on the strength of the interaction between the metal and the spinel support, sintering may still occur. An example is the use of a spinel as a support for nickel in a series of simulated SR tests [57]. Figure 10.2 shows sintering of a 14.8 wt% Ni/

[3] Though metal vaporization is possible for some metals (e.g., Ni or Rh) at the conditions present in the reformer, we are aware of no studies where this deactivation mechanism has been systematically examined for this application.

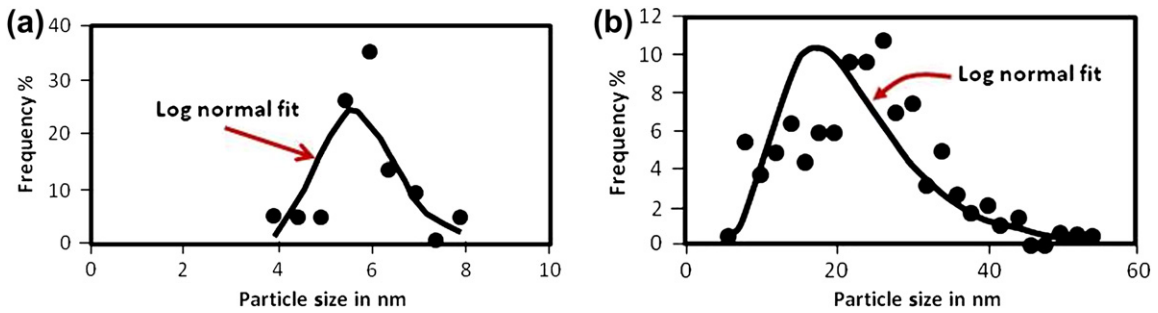

FIGURE 10.2 Particle size distributions in sintered Ni catalysts: (a) fresh 14.8 wt% Ni/spinel (20 particles counted), (b) 14.8 wt% Ni/spinel sintered for 770 h (187 particles counted) *Reprinted from Sehested et al. [57], Copyright (2001), with permission from Elsevier.*

$MgAl_2O_4$ catalyst exposed to a 10:1 steam:H_2 mixture[4] at 500 °C, 3 MPa. Comparison of the fresh and sintered catalyst shows a significant increase in the nickel particle size, due to coalescence of the nickel clusters.

10.3.1.2. Incorporating the Metal into a Stable Oxide

A related approach is to incorporate the active metal *into* the structure of a thermally stable oxide. In this case, the purpose is to prevent sintering by immobilizing the active metal, while retaining its catalytic activity. It is not immediately obvious whether an active metal would retain its activity when it is bound within an oxide structure. However, a number of studies show that the metal in such oxide structures is more active *and* stable than a directly comparable supported metal. For example, Bhattacharyya and Chang [59] compared a $NiAl_2O_4$ spinel, which had been synthesized by incorporating the nickel atoms into the cubic close pack spinel structure, with a physical mixture of NiO and alumina. Figure 10.3 shows that the $NiAl_2O_4$ spinel is not only more active but resists deactivation — probably because the larger clusters of Ni that lead to carbon deposition are not formed since the nickel atoms are bound within the spinel structure.

Substitution of active metals into other thermally stable oxides such as perovskites [12,13,60–62], hexaaluminates [63–65], and pyrochlores [66,67] has been reported — all with the objective of stabilizing the active metal within a thermally stable oxide structure.

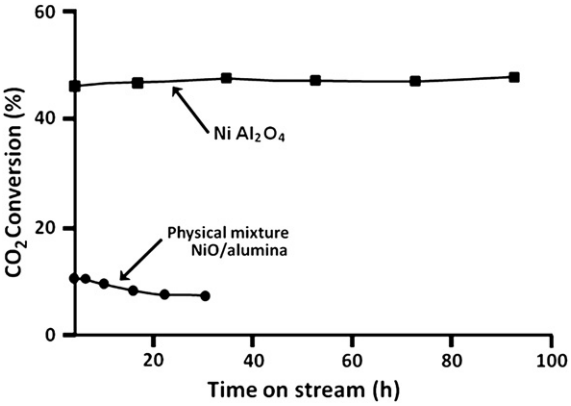

FIGURE 10.3 CO_2 conversion versus time for $NiAl_2O_4$ versus a physical mixture of NiO/alumina; $CO_2/CH_4/H_2O$ reforming, 816 °C, 2 MPa; $CO_2/CH_4/H_2O$ = 1.25/1/1; 7200 h^{-1}; *Reprinted from Bhattacharyya and Chang [59], Copyright (1994), with permission from Elsevier.*

[4] Although this steam/H_2 mixture was designed to simulate *pre*-reforming (rather than reforming) conditions, the observed sintering illustrates the effect of time and temperature on the particle size distribution of a spinel-supported Ni catalyst.

10.3.2. Effect of Reactor Temperature Gradients

Thermal deactivation may be significant even when the nominal temperatures reported for the reformer would not suggest temperatures sufficiently high to cause concern. This is because temperatures reported for most reforming studies are those at the inlet. Temperatures within the reformer may differ *significantly* from those at the inlet (or outlet), even for nominally autothermal reaction conditions – i.e., those with an inlet ratio of fuel/steam/oxygen yielding an overall heat of reaction to the desired products of near zero. For example, Fig. 10.4 shows the axial temperature profile for the ATR of a synthetic diesel fuel at an "inlet" temperature of 400 °C, which is measured in the uncatalyzed preheating section of the reactor [68]. Note that for this nominal inlet temperature, the bed temperature reaches 800 °C at the leading edge of the catalyst bed (located between $0.55 < x/L < 0.65$). Measurements of the "inlet" temperature in the preheating zone, or "outlet" temperatures near the exit of the catalyst bed, would *not* have detected this high temperature. This means that in the reforming of fuels, thermal deactivation may be important in reactions where it could be easily overlooked.

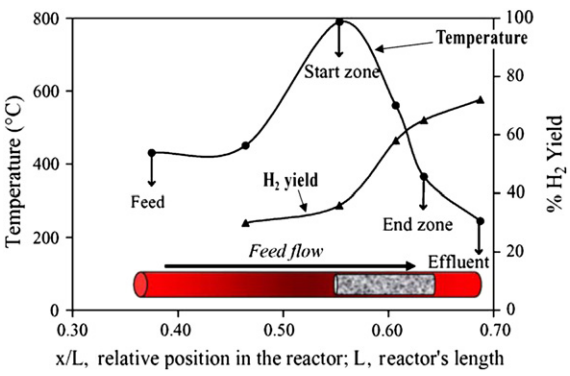

FIGURE 10.4 Temperature profile and hydrogen yield as a function of relative position inside the adiabatic autothermal reforming (ATR) reactor; *Reprinted from Cheekatamarla and Lane [68], Copyright (2005), with permission from Elsevier. The catalyst is located between 0.55 < x/L < 0.65. Preheating is provided between 0.35 < x/L < 0.55.*

10.3.2.1. Effect of Deactivation on Temperature Gradients

These reactor temperature gradients can change with time on-stream as the rates of the various reactions – oxidation, steam/CO_2 reforming, WGS – change as the catalyst deactivates. Figure 10.5 shows the change in temperature with time at various reactor positions as carbon forms on the catalyst during the ATR of a commercial diesel fuel [69]. It is not immediately obvious why the temperatures within the bed should *increase* as the catalyst deactivates. This unexpected behavior is due to the decrease in the rate of the endothermic SR reactions compared with the rate of the exothermic oxidation [69] (and perhaps methanation [70]) reactions. The magnitude of the temperature gradients within the reactor – from 650 °C at the inlet to 1050 °C at roughly the axial midpoint – is surprising. As discussed above, temperature measurements only at the inlet and exit of the reactor would not have identified these severe gradients.

10.3.2.2. Effect of Deactivation on Reformate Composition

These temperature gradients correspond to changes in reformate composition, which will generally change with both time and reactor position for a deactivating catalyst. Figure 10.6 shows the concentrations of H_2 and CO within a plate-type reactor coated with a Rh/alumina catalyst for OSR of a commercial gasoline containing 6 ppm sulfur [70]. The decreases in hydrogen and CO concentrations with time at any point are attributed to sulfur poisoning and the accompanying carbon deposition. Note that significant decreases in H_2 and CO yields due to deactivation are only observable at the outlet after ~2.5 h on-stream. In addition, concentration profiles (not shown here)

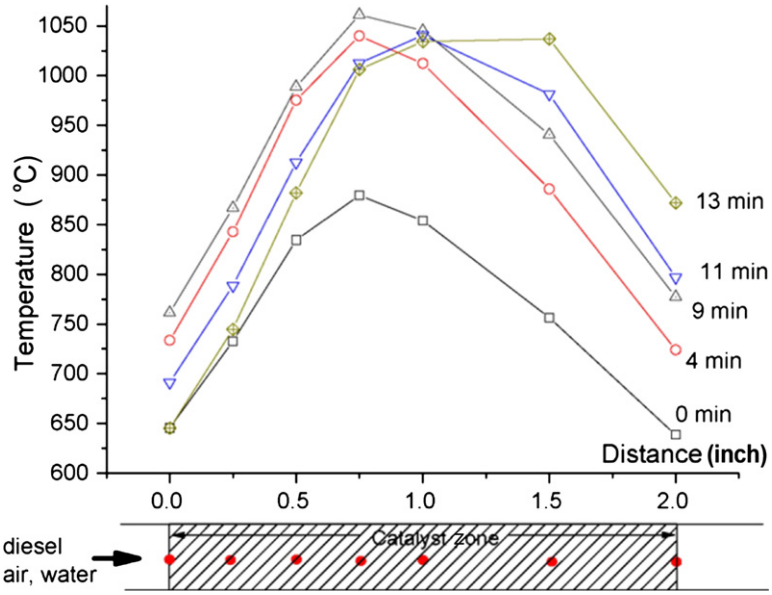

FIGURE 10.5 Temperature versus reactor position for the autothermal reforming of a commercial diesel for a Pt/Gd-CeO_2 catalyst; 5000 h^{-1}, 0.1 MPa; *Reprinted from Kang et al. [69], Copyright (2007), with permission from Elsevier. Temperatures within the reactor are measured as a function of time at the seven positions indicated in the diagram below the* x*-axis above.*

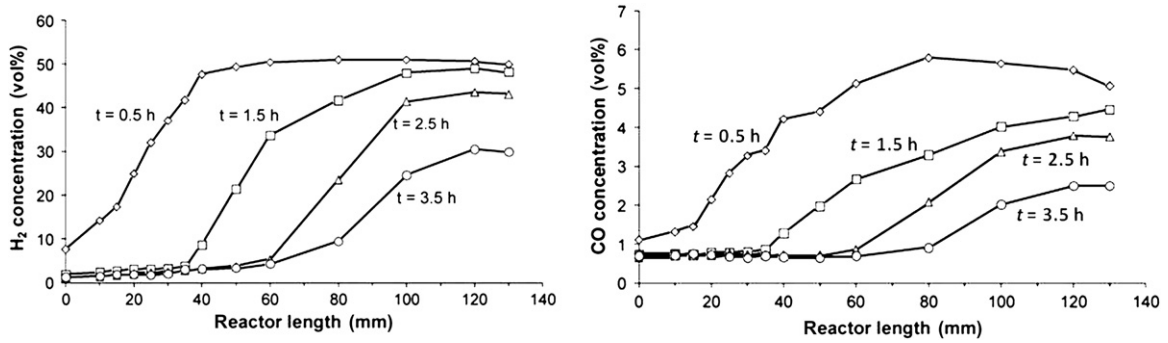

FIGURE 10.6 Concentration profiles for OSR of gasoline ($C_{7.3}H_{12.3}$, 6 ppm sulfur) over Rh/alumina supported on Fecralloy™ plates; 0.2 MPa, 650 °C. Temperatures within the catalyst bed were within 10 °C of the 650 °C set point. Front end of the catalyst is at 20 mm, outlet at 130 mm; *Reprinted from Rabe et al. [70], Copyright (2009), with permission from International Association for Hydrogen Energy.*

of CO_2, CH_4, H_2O, and hydrocarbons with time and position show that CO_2, H_2O, and hydrocarbons are formed as primary products near the reactor inlet, with CO and H_2 formed just downstream, presumably by steam and CO_2 reforming of the hydrocarbons. CH_4 is formed as a secondary product, most likely by the hydrogenation of CO.

10.4. SULFUR POISONING

The primary reason for poisoning in reforming of fuels used in fuel processing is the presence of sulfur compounds. Despite the low levels of sulfur in transportation fuels (e.g., 15 ppm in the United States), the effects of sulfur on the reforming catalyst tend to be cumulative,

so that even low levels of sulfur can eventually deactivate reforming catalysts. In addition, sulfur levels in non-transportation (e.g., military) fuels can be far greater, up to several 1000 ppm [71]. In these cases, the effects of sulfur must be taken into account in the initial design of the catalysts, and the catalysts themselves must be capable of extended operation at these levels of sulfur.

10.4.1. Thermodynamics

10.4.1.1. Metal Sulfide Formation

Sulfur-containing compounds contained in various fuels can be complex (e.g., dibenzothiophene, DBT). Although these complex compounds may not behave in the same way as H_2S [72], the thermodynamics of sulfur poisoning can be qualitatively examined by considering the reaction of H_2S with various reduced metals according to the following equation (Me^0 = reduced metal):

$$H_2S + Me^0 \rightarrow MeS + H_2 \qquad (10.1)$$

Figure 10.7 shows the equilibrium extent of this sulfidation reaction at 900 °C for various metals that are used in fuel reforming. All metals show less extent of sulfide formation at lower H_2S levels, as expected. Ni is the most sulfur-sensitive metal among those analyzed here, with cobalt the least sensitive.

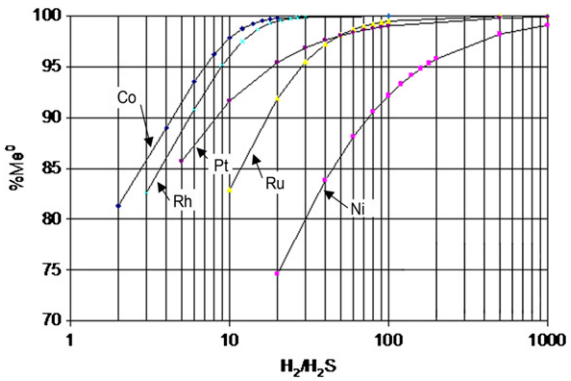

FIGURE 10.7 Equilibrium percent reduced metal (Me^0) versus H_2/H_2S ratio at 900 °C [see Eq. (1)]. *(Calculation using HSC Chemistry software).*

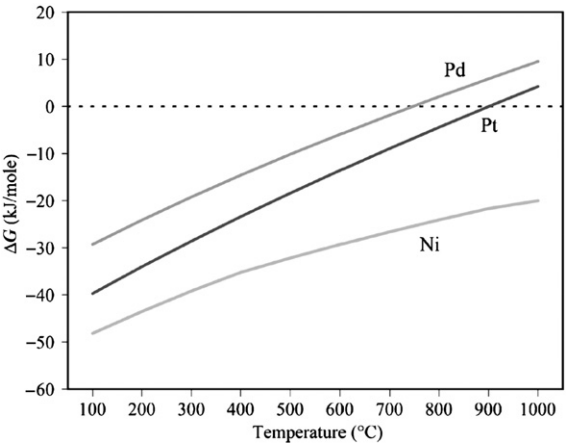

FIGURE 10.8 Effect of temperature on ΔG for sulfide formation for Ni, Pd, and Pt, according to Eq. (1) [52].

10.4.1.2. Effect of Temperature

Thermodynamically, sulfur tolerance is also a function of temperature. Figure 10.8 shows the equilibrium for Eq. (1) above for three of the metals shown in Fig. 10.7 [52]. Higher temperatures *decrease* sulfide formation, suggesting that higher temperatures would be expected to limit the thermodynamic driving force for deactivation due to sulfur poisoning, at least by bulk sulfide formation. However, sulfur poisoning is, of course, also a kinetic process so that the effect of temperature may differ in practice from the behavior predicted from thermodynamics.

10.4.2. Effect of Temperature and Sulfur Concentration

10.4.2.1. Effect of Temperature

The observed effect of temperature is generally consistent with thermodynamics. For

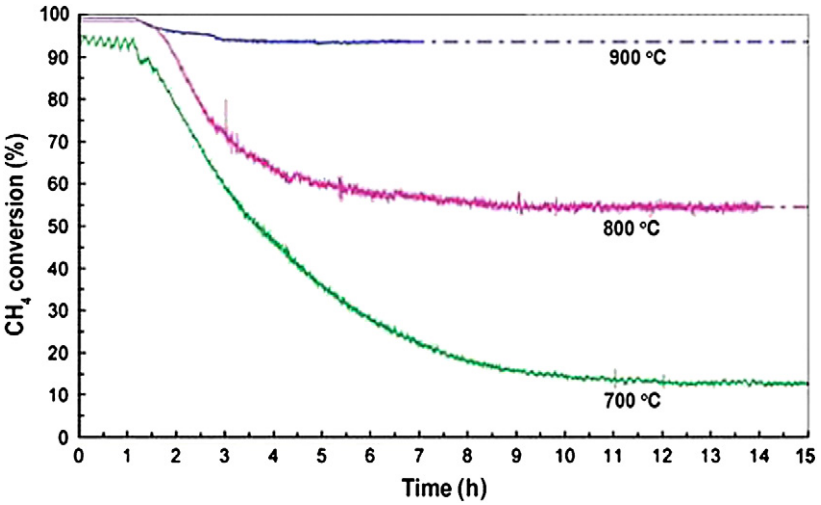

FIGURE 10.9 CH_4 conversion versus time on-stream for reforming of a CH_4/CO_2 biogas at different temperatures; CH_4/CO_2 mol ratio = 1.5, S/C = 2.91, SV = 17.7 $m^3\ kg^{-1}\ h^{-1}$, 30 ppmv H_2S, Ni catalyst (not fully described in; *Reprinted from Ashrafi et al. [73], Copyright (2008), with permission from American Chemical Society).*

example, Fig. 10.9 shows that deactivation due to sulfur poisoning by H_2S can be greatly reduced by increasing the temperature from 700 to 900 °C in the reforming of a bio-based fuel on a nickel catalyst [73]. At 900 °C, the rate of deactivation is insignificant after a small initial decrease in activity, at least over the time scale of this experiment.

10.4.2.2. Effect of Sulfur Concentration

Deactivation by sulfur poisoning is also a strong function of sulfur concentration. Representative results (Fig. 10.10) for the SR of a bio-derived mixture of CH_4 and CO_2 show a rapid decrease in methane conversion with increasing H_2S concentration at a given time on-stream [73]. Even concentrations as low as 15 ppmv decrease

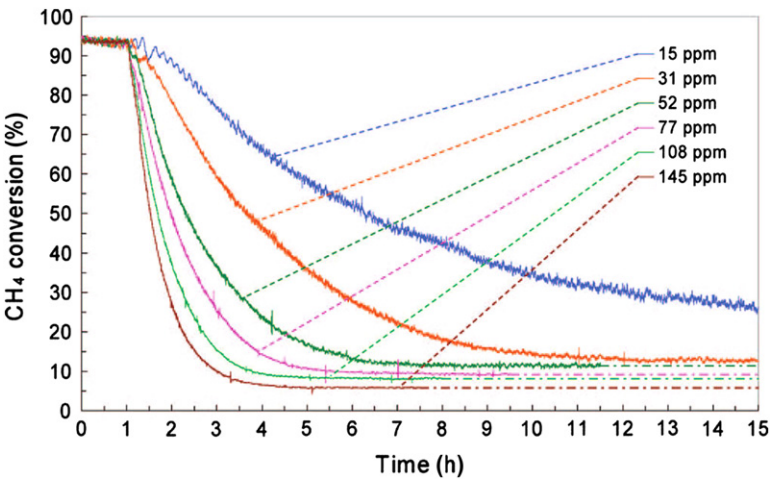

FIGURE 10.10 CH_4 conversion versus time on-stream; 700 °C, CH_4/CO_2 mol ratio = 1.5, S/C = 2.91, SV=17.7 $m^3\ kg^{-1}\ h^{-1}$, various concentrations of H_2S (in ppmv), Ni catalyst (not fully described in *Reprinted from Ashrafi et al. [73], Copyright (2008), with permission from American Chemical Society).*

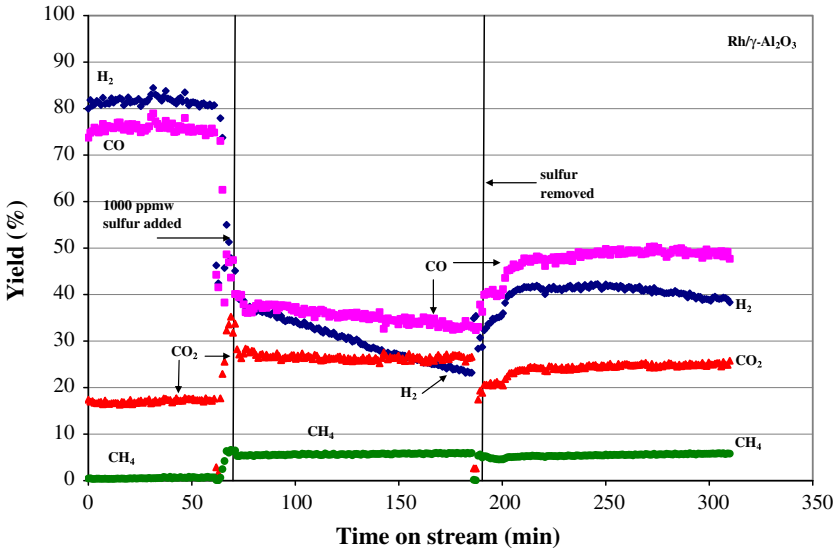

FIGURE 10.11 Step response plot for 0.5 wt% Rh/γ-Al_2O_3 after the addition of 1000 ppmw dibenzothiophene (DBT) at an O/C = 1.2, 0.23 MPa, 900 °C and 50,000 scc g_{cat}^{-1} h^{-1} [67].

the conversion to half its initial value within 8 h. Note, however, that the data in Fig. 10.10 are at 700 °C. At 900 °C (Fig. 10.9), this same catalyst shows negligible deactivation in the presence of 30 ppmv H_2S for 15 h.

10.4.3. Resistance to Sulfur Poisoning

10.4.3.1. Oxygen Mobility

The most widely reported approach to improve the resistance of various catalysts to deactivation by sulfur is to add oxygen mobility[5] to the catalyst. At least in part, this is because oxygen mobility helps limit carbon deposition that inevitably accompanies sulfur poisoning [67,72,74–76] and presumably helps avoid the formation of inactive metal sulfides. For example, Haynes et al. [67] compared a series of Rh- and Sr-substituted pyrochlores to a conventional 0.5 wt% Rh/Al_2O_3 catalyst. Introducing 1000 ppmw sulfur (as DBT) during the POX of *n*-tetradecane quickly and irreversibly deactivated the 0.5 wt% Rh/Al_2O_3 catalyst (Fig. 10.11), but the pyrochlore, with Rh substituted into the lattice and containing Zr and Sr, continued to produce H_2 and CO at relatively steady, but lower, levels compared with those before DBT was introduced (Fig. 10.12). They attribute the resistance to sulfur poisoning to the oxygen ion conductivity of the substituted pyrochlores [66,67], which also reduces the carbon formation that accompanies deactivation by sulfur. Although they did not report the effect of sulfur on carbon deposition, Choudhary et al. [77] also showed that the lattice oxygen mobility that accompanied the addition of ceria to $NiCoMgO_x$ greatly reduced the rate of sulfur deactivation in methane reforming.

Qualitatively identical results showing increased resistance to sulfur deactivation due to oxygen ion conductivity have been reported by others. For example, Xue et al. [75] used a GdO_2-doped Pt/CeO_2-Al_2O_3 catalyst to

[5] The general term "oxygen mobility" is frequently used in the literature to describe ability of various oxides to transport some form of oxygen within the material at the conditions of interest here. The more specific term "oxygen ion conductivity" refers to a specific mechanism in which oxygen ions are responsible for "oxygen mobility."

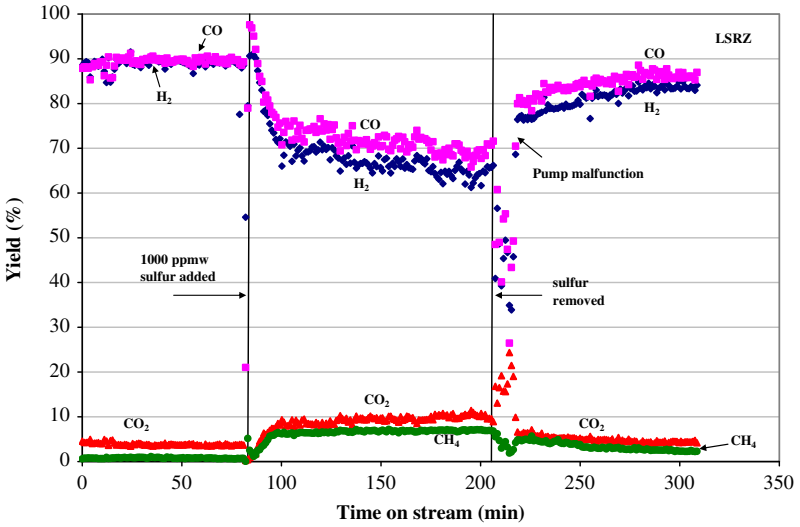

FIGURE 10.12 Step response plot for La-Sr-Rh-Zr pyrochlore (LSRZ) after the addition of 1000 ppmw dibenzothiophene (DBT) at an O/C = 1.2, 0.23 MPa, 900 °C, and 50,000 scc g_{cat}^{-1} h^{-1} [67].

reform commercial gasoline. The resistance to deactivation in the presence of 158 ppm sulfur in the gasoline, as well as lower carbon formation, was attributed to the oxygen ion conductivity of the ceria [75]. H_2 concentration in the product gas was stable at 67% over a 1000-h run, and fuel conversion remained at 95–97% over this same time. Similarly, Choudhary et al. [77] attributed lattice oxygen mobility due to ceria for the resistance of a $NiCoMgCeO_x$ to deactivation by 7400 ppm sulfur in an accelerated deactivation test.

10.4.4. Regeneration of Sulfur-Poisoned Catalysts

The regeneration of catalysts deactivated by sulfur is of great practical interest, especially if the regeneration can be done in situ. Although the methods of regeneration are highly catalyst-specific, there are several general methods described in the literature. One approach is to simply remove the sulfur from the feed for some period of time, which typically provides at least partial recovery of the initial activity [67,73,78,79]. As simple as this might be in the laboratory, it is impractical in an operational fuel processor since it requires essentially complete desulfurization of the liquid fuel.

10.4.4.1. Regeneration in Hydrogen

Regeneration can also be accomplished in some cases by heating in flowing hydrogen, as suggested by the thermodynamics shown in Fig. 10.7, essentially reversing the reaction that forms the metal sulfide. Complete regeneration of a molybdenum carbide catalyst deactivated in the reforming of hexadecane in the presence of 500 ppm benzothiophene was achieved by first treating the catalyst in flowing helium at 900 °C/1 h, then in hydrogen at the same conditions (Fig. 10.13) [78]. Heat treatment in helium may have removed less strongly bound sulfur from the surface, but hydrogen was needed to remove chemisorbed sulfur and, probably, to react with surface sulfides.

Temperature-programmed hydrogenation (TPH) can be used to characterize the nature of the sulfur on catalysts deactivated by sulfur. TPH is carried out by heating the sulfur-containing catalyst from near-ambient temperatures at a specific rate in a dilute

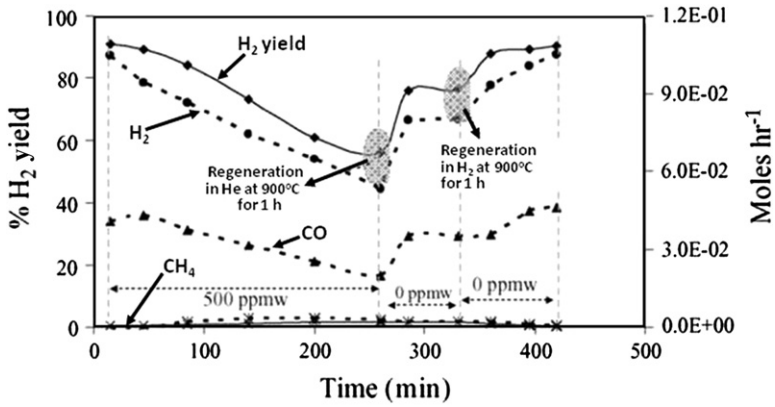

FIGURE 10.13 Hydrogen yield and product composition as a function of time during hexadecane oxidative-steam reforming experiments in presence of 500 ppmw of benzothiophene at the optimal conditions of S/C = 0.71, O_2/C = 0.36, GHSV= 4500 h^{-1}, 885 °C, and 0.1 MPa; *Reprinted from Cheekatamarla and Thomson [78], Copyright (2006), with permission from Elsevier.*

hydrogen-containing gas. In principle, sulfur compounds on the catalyst surface react to form H_2S, which is monitored continuously. The temperature at which the H_2S is formed, and the area under the H_2S–temperature curve, provides insight into the binding strength and amount of sulfur on the catalyst. An example is given in Fig. 10.14, which shows the TPH results for a "commercial" Ni-based catalyst deactivated by exposure to two levels of H_2S (500 and 2000 ppmv) at 900 °C, 2 MPa [79].

For the catalyst exposed to 500 ppmv H_2S, desorption starts at ~420 °C with a peak temperature at 610 °C. This is believed to be "chemisorbed" sulfur, perhaps having a layered morphology with less strongly bound sulfur in the layers furthest from the catalyst. If so, these outer layers would desorb (as H_2S) at the lower temperatures, with more strongly bound layers (closer to the surface) desorbing at higher temperatures. Note that there is a shoulder on this curve, which extends from 750 to 950 °C. This is attributed to the reduction of nickel sulfide ($NiS + H_2 \rightarrow Ni + H_2S$) [79]. For the catalyst exposed to 2000 ppmv H_2S, there is no observable H_2S until 650 °C, so that the sulfur on this catalyst consists almost entirely of nickel sulfide, which is not completely reduced to nickel even at 950 °C. This illustrates how TPH can be used to probe the form of sulfur on deactivated catalysts.

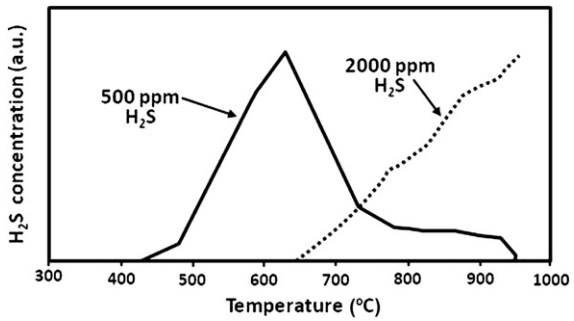

FIGURE 10.14 Temperature-programmed hydrogenation (70% Ar/30% H_2) of Ni-based catalysts after exposure to (a) 500 and (b) 2000 ppmv H_2S in N_2 at 2 MPa pressure, 900 °C, 4–6 h (catalyst not fully described); *Reprinted from Hepola and Simell [79], Copyright (1997), with permission from Elsevier.*

10.4.4.2. Regeneration in Oxygen

Regeneration can also be carried out in oxidizing conditions, e.g., with steam or oxygen. For example, exposure of a $NiCoMgCeO_x$ catalyst to 7400 ppm of thiophene in the POX of methane resulted in rapid deactivation. The reforming activity was completely restored by treatment in a 50/50 mixture of O_2/N_2 at 800 °C (Fig. 10.15) [77]. Though not stated in the original study, this oxidation presumably regenerates the active metal sites by oxidizing surface nickel sulfides, removing the sulfur as

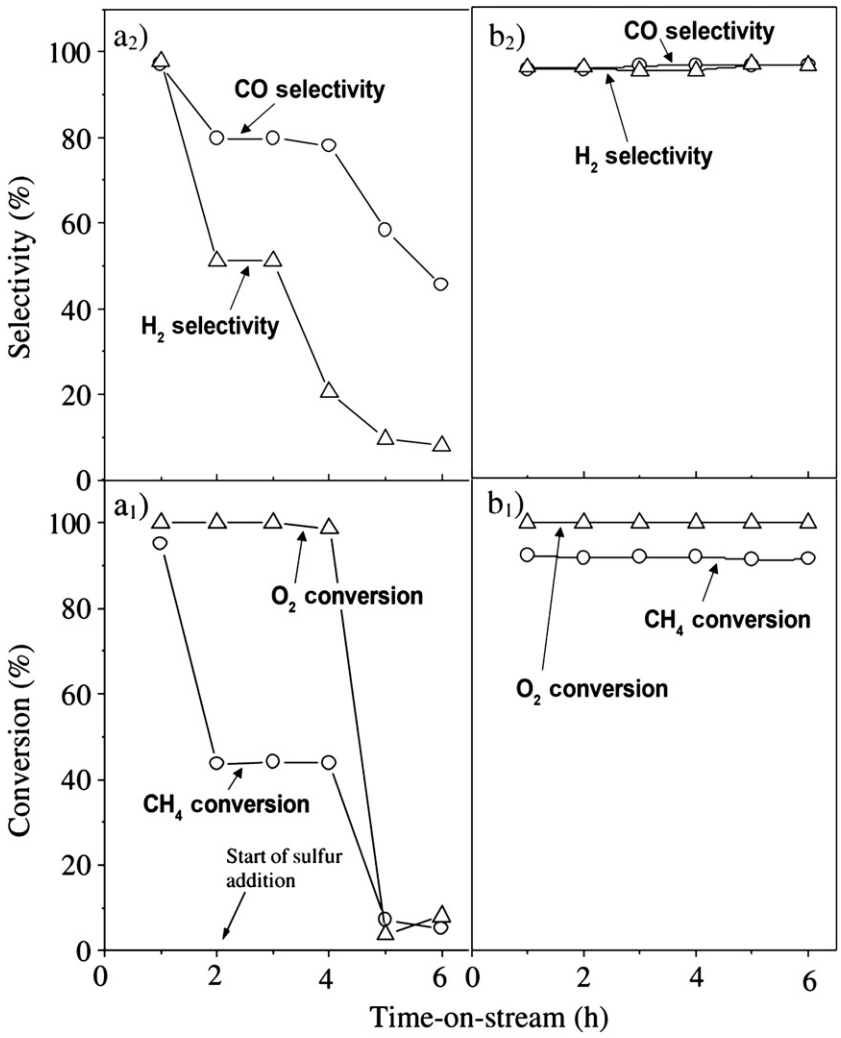

FIGURE 10.15 Time on-stream activity for the partial oxidation of methane at 850 °C over $NiCoMgCeO_x$ catalyst (calcined at 1400 °C) in the presence of thiophene (a1,a2) and after regeneration (b1,b2) of the catalyst in the presence of $O_2 + N_2$ in 50:50 at 800 °C (reaction conditions: GHSV = 62,000 $cm^3 g^{-1} h^{-1}$, CH_4/O_2 = 1.8); *Reprinted from Choudhary et al. [77], Copyright (2007), with permission from Elsevier.*

SO_2. Note that this oxidative process will also likely leave the nickel in an oxidized form, which must be reduced before it is active for reforming.

This sort of oxidative regeneration cannot be applied generally, even to all Ni-based catalysts. The exotherm associated with the oxidative regeneration reaction can irreversibly deactivate the catalyst by the type of thermal degradation that might be expected when supported catalysts of this type are exposed to high temperatures. For instance, repeated attempts to regenerate a completely deactivated Ni-based catalyst using a dilute air/N_2 mixture (3/100) that was exposed to a biogas containing 109 ppm sulfur were unsuccessful because of what the authors believe to be the irreversible formation of the inert $NiAl_2O_4$ spinel produced by the reaction of nickel with alumina at high temperatures [73]. The formation of this inactive nickel spinel is a widely reported reaction at these high temperatures [80,81].

10.4.4.3. *Regeneration in Steam*

Similar oxidative regeneration can be carried out using steam. Oudghiri-Hassini et al. [82] were able to restore the methane SR activity of a bulk nickel powder that had been exposed to *n*-decanethiol (H-$(CH_2)_{10}$-SH) by treating the deactivated catalyst in an Ar/steam gas mixture at 1050 °C (Fig. 10.16). The selectivity to the desired products (CO, H_2) of the deactivated catalyst is essentially zero − methane is the only product (Fig. 10.16a). Steam treatment restores the activity to essentially equilibrium levels of CO and H_2 (Fig. 10.16b). XPS and DRIFTS analyses show that the steam treatment removes all sulfur from the catalyst. Although some carbon remains on the surface, it does not affect the activity. DRIFTS also shows that the steam-treated catalyst has surface superoxo species (Ni=O), produced by the steam treatment.

Rostrup-Nielsen reports similar results for supported Ni-based catalysts deactivated by exposure to H_2S [83]. He found that steam can remove the sulfur as H_2S via:

$$\text{Ni-S} + H_2O \rightarrow \text{NiO} + H_2S \qquad (10.2)$$

While also oxidizing any reduced nickel:

$$\text{Ni} + H_2O \rightarrow \text{Ni-O} + H_2 \qquad (10.3)$$

Up to 90% of the sulfur in the catalyst can be removed at temperatures of 800−900 °C. He also found that certain alkali promoters (Ca, Mg) increased the rate of steam regeneration of the sulfided nickel. However, others (K, Na) did not − probably because the sulfur is converted into a form that is retained in the catalyst in the case of potassium and sodium.

10.4.5. Sulfur-Tolerant Catalysts

Considerable work has been directed to the development of catalysts that can maintain high levels of activity and selectivity in the presence of some level of sulfur. In a working fuel processor, however, even if such catalysts were to be developed, sulfur compounds would almost certainly need to be removed before the fuel cell [84]. Nevertheless, development of a sulfur-tolerant catalyst for the reformer gives the engineer an added option in designing an economically optimum fuel processor. Because gaseous sulfur

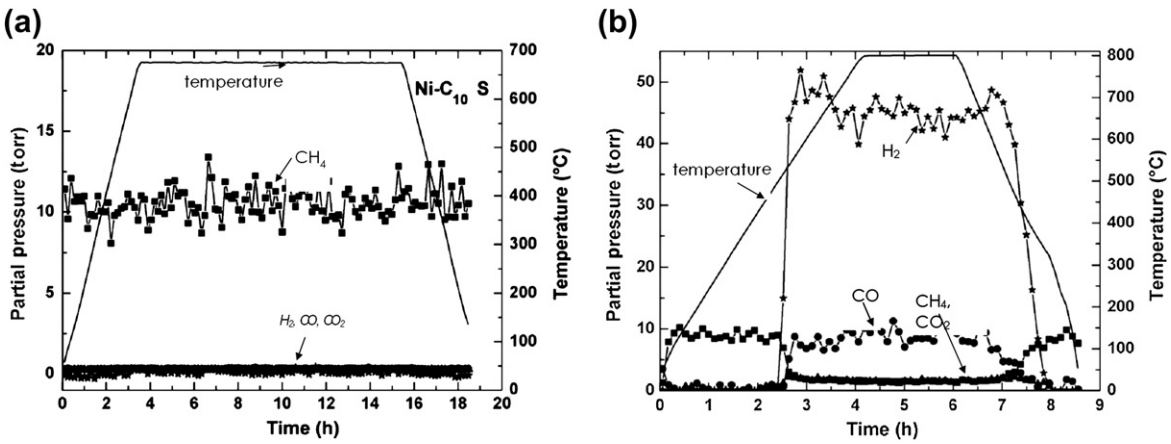

FIGURE 10.16 Effect of steam treatment on bulk Ni powder exposed to *n*-decanethiol (H-$(CH_2)_{10}$-SH) in the steam reforming of methane ($P(CH_4)$ = 10 torr, $P(H_2O)$ = 20 torr, P(Ar) = 730 torr); (a) product formation for the deactivated catalyst (exposed to thiol by immersion in 0.001 M thiol/methanol solution for 20 h), (b) same catalyst after treatment in Ar/steam at 1050 °C; *Reprinted from Oudghiri-Hassani et al. [82], Copyright (2007), with permission from Elsevier.*

compounds produced in the reformer (primarily H_2S [84]) are more easily removed than the liquid-phase compounds from which they are formed, a sulfur-tolerant catalyst would allow a more compact fuel reformer to be designed.

10.4.5.1. Sulfide-Forming Metals/Sorbents

Several approaches have been investigated to develop sulfur-tolerant catalysts. One of the most obvious is incorporating a sulfide-forming metal or an oxide sorbent into the catalyst that will preferentially react with the sulfur compounds [85,86]. Although such an approach has been shown to extend the life of catalysts in reforming reactions, a number of studies have shown unexpected effects of adding such compounds to supported noble metal catalysts. For instance, Azad and Duran actually found that on two Rh/ceria catalysts, one doped with Gd_2O_3 and one with ZrO_2, the presence of 50 ppmv H_2S *increased* H_2 yield in the SR of toluene with no deactivation over a 12-h run [71] (see Fig. 10.17).

They suggested this could be due to the formation of Ce_2O_2S, which presumably increases the reforming activity of the supported Rh. It might be expected that this positive effect of sulfur would eventually diminish as the catalyst retains ever greater levels of sulfur. This effect was not observed in directly comparable studies by these same authors on Rh + Pd or Pd-based catalysts prepared and tested in an identical way [71,87].

The addition of potassium to a 2 wt% Rh/Al_2O_3 catalyst in the SR of gasoline increased sulfur tolerance, but had several unanticipated effects as well [88]. Potassium addition limited the adsorption of sulfur on this Rh/alumina catalyst by site blockage. However, potassium addition also produced higher temperatures in the catalyst bed because it selectively inhibited the endothermic SR reactions more than the POX reactions. This, in turn, led to increased sulfur tolerance beyond what would be expected by potassium acting solely as a sorbent.

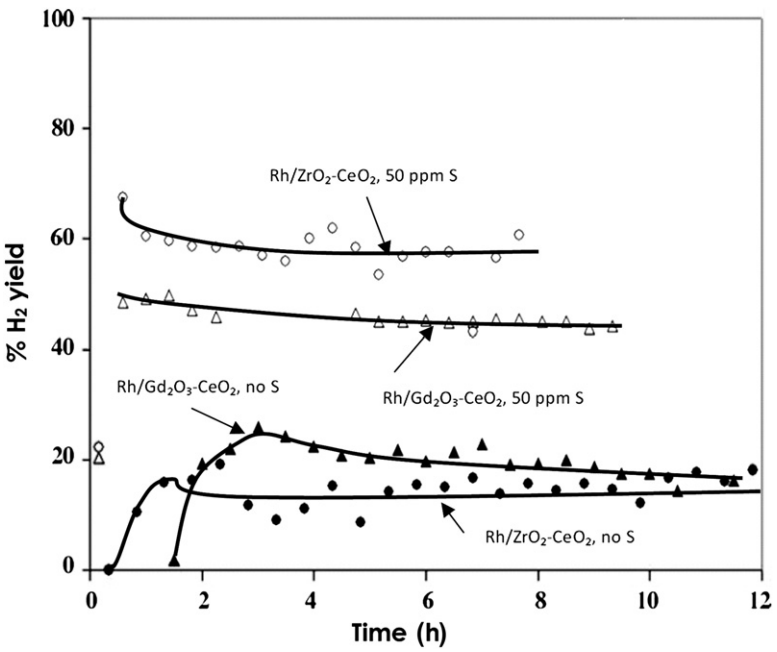

FIGURE 10.17 Comparison of the reforming performance of Rh-based catalysts in sulfur-free and 50 ppm sulfur-laden toluene feed at 825 °C; S/C = 3; *Reprinted from Azad and Duran [71], Copyright (2007), with permission from Elsevier.*

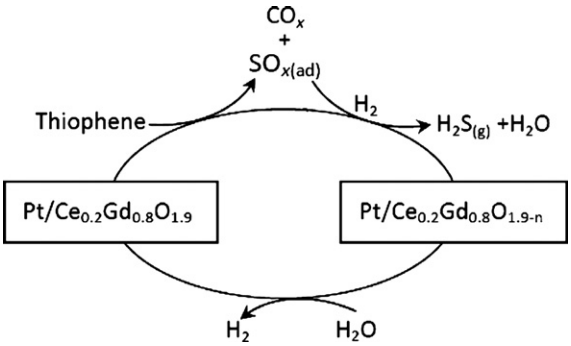

FIGURE 10.18 Redox mechanism illustration for thiophene sulfur conversion to H_2S; *Reprinted from Lu et al. [89], Copyright (2008), with permission from Elsevier.*

One possible mechanism for the conversion of sulfur compounds to gas-phase products is shown in Fig. 10.18. This is based on demonstrated results for a 1.5 wt% $Pt/Ce_{0.8}Gd_{0.2}O_{1.9}$ catalyst used in the SR of isooctane containing 300 μg/g thiophene [89].

There is a synergistic relationship between the CeGdO and Pt in this mechanism which centers on the redox behavior of the CeGdO oxide [90]. CeGdO alternately oxidizes thiophene and reduces H_2O, with this cycle apparently catalyzed by Pt. Preparation of the catalyst is critical. The sulfur tolerance depends on avoiding gross crystallization of CeGdO oxides by proper choice of the calcination temperature. Surprisingly, this synergistic effect is observed for catalysts calcined at 800 °C, but not at 600 °C − one might expect destructive crystalline growth at the higher temperatures.

10.5. COKE/CARBON DEPOSITION

Deposition of carbon-containing species on metal catalysts is virtually inevitable in any reaction involving hydrocarbons [53,91], including those involved in fuel processing. A number of general reviews on the subject of carbon deposition and coke formation are available [53,91−93] and will not be summarized here. Rather, the discussion below focuses on studies specifically for the deactivation of catalysts used for hydrocarbon reforming in fuel processors.

10.5.1. Thermodynamics of Elemental Carbon Formation

Although the deposition of carbon-containing species includes both elemental carbon and a range of other compounds such as polynuclear aromatics, the thermodynamics of elemental carbon formation[6] help illustrate the effect of temperature on the driving force for deactivation by carbon deposition.

For fuel reforming, the principal reactions leading to elemental carbon can be summarized as follows [94]:

$$\begin{aligned} &2CO_{(g)} \rightarrow C_{(s)} + CO_2(g); \\ &\Delta G_{900^\circ C} = +8.35 \text{ kcal/mol}; \\ &\Delta H_{900^\circ C} = -40.4 \text{ kcal/mol} \end{aligned} \tag{10.4}$$

$$\begin{aligned} &C_nH_{m,(g)} \rightarrow nC_{(s)} + m/2H_{2(g)}; \\ &\Delta G_{900^\circ C} = -369 \text{ kcal/mol}; \\ &\Delta H_{900^\circ C} = +109 \text{ kcal/mol} \end{aligned} \tag{10.5}$$[7]

$$\begin{aligned} &CO_{(g)} + H_{2(g)} \rightarrow C_{(s)} + H_2O_{(g)}; \\ &\Delta G_{900^\circ C} = +7.4 \text{ kcal/mol}; \\ &\Delta H_{900^\circ C} = -32.4 \text{ kcal/mol} \end{aligned} \tag{10.6}$$

Equations (10.4) and (10.6) are exothermic and are favored at low temperatures, while Eq. (10.5) is favored at high temperatures.

[6] Elemental carbon is calculated using the properties of graphite. Calculations made using HSC 6.0 (Outokumpu Technology; Espoo, Finland).

[7] Calculation made using $C_{16}H_{34}$ as a representative diesel fuel.

For the ATR of *n*-hexadecane at 900 °C:[8]

$$C_{16}H_{34(g)} + 4O_{2(g)} + 7H_2O_{(g)} \rightarrow 4C_{(s)} + 9CO_{(g)} + 24H_{2(g)} + 3CO_{2(g)} \quad (10.7)$$

$$\Delta G_{900°C} = -810 \text{ kcal/mol}; \Delta H_{900\,°C} \cong 0$$

The equilibrium composition as a function of temperature shows that elemental carbon formation decreases with increasing temperature, but carbon is still present at typical reforming temperatures (Fig. 10.19) [52].

A qualitatively similar result can be seen for a calculation of the equilibrium for OSR of this same hydrocarbon, in which chrysene (a coke-like compound) is allowed to form as the solid phase (Fig. 10.20):

$$2C_{16}H_{34(g)} + 5.5O_{2(g)} + 6H_2O_{(g)} = C_{18}H_{12(s)} + 34H_{2(g)} + 11CO_{(g)} + 3CO_{2(g)} \quad (10.8)$$

$$\Delta G_{900\,°C} = -1087 \text{ kcal/mol};$$
$$\Delta H_{900\,°C} = -16.7 \text{ kcal/mol}$$

Note in Fig. 10.20 that chrysene has a slight maximum at ~250 °C and a small but non-zero equilibrium level at higher temperatures. A comparison of Figs 10.19 and 10.20 shows that $C_{(s)}$ (Fig. 10.20) is present at far greater equilibrium levels at reforming temperatures than chrysene. Although this indicates a thermodynamic driving force for carbon formation (in preference to coke), the kinetics of the coke- and carbon-forming reactions will determine the form of carbon in any given case.

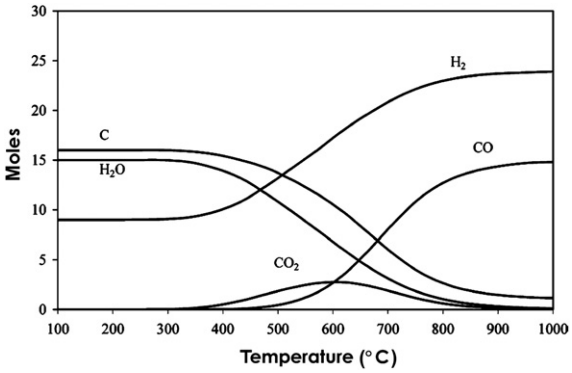

FIGURE 10.19 Equilibrium composition versus temperature; initial composition 1 mol *n*-$C_{16(g)}$, 4 mol $O_{2(g)}$, and 7 mol $H_2O_{(g)}$; 0.1 MPa; see Eq. (10.7) *(Calculations using HSC Chemistry 6.0)*.

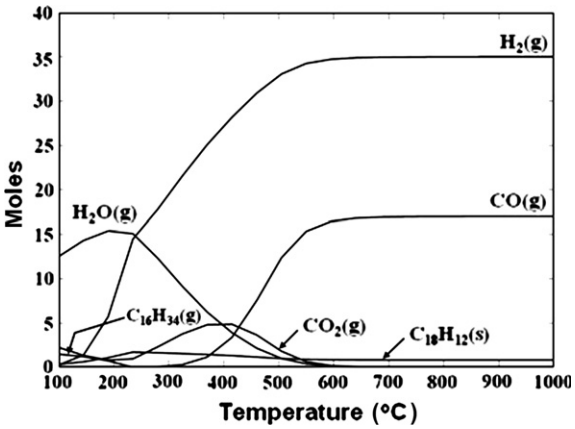

FIGURE 10.20 Equilibrium composition versus temperature; initial composition 2 mol *n*-$C_{16}H_{34(g)}$, 5.5 mol $O_{2(g)}$, and 6 mol $H_2O_{(g)}$; 0.1 MPa; see Eq. (10.8) *(Calculations using HSC Chemistry 6.0)*.

10.5.2. Effect of Aromatics

Carbon deposition is strongly affected by the presence of sulfur and aromatic compounds in the fuel. In virtually all studies of deactivation on reforming catalysts of interest here, carbon deposition accompanies deactivation by sulfur [69,70,72,74,75,78,95,96], though of course carbon can also be formed in the absence of sulfur [97]. The presence of aromatics in the fuel tends to increase carbon deposition far

[8] The stoichiometry of the reaction is adjusted so that ΔH_r, 900 °C ~ 0.

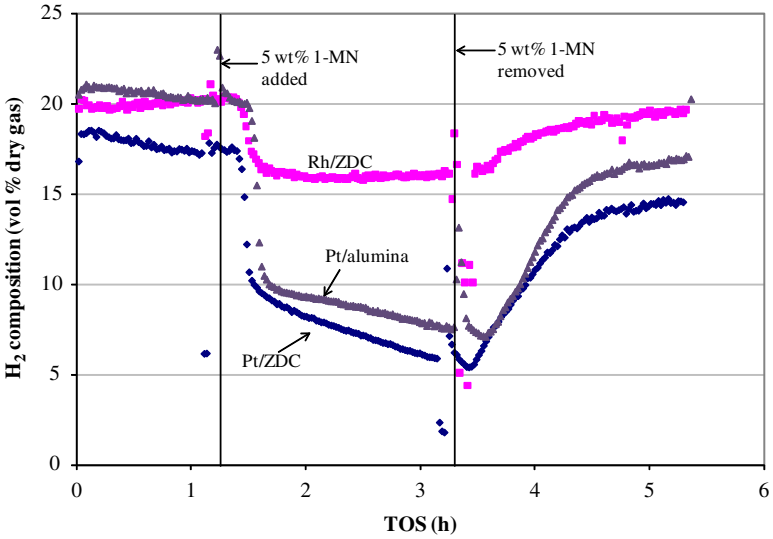

FIGURE 10.21 Step response plot for hydrogen production (concentration, dry gas vol%) from *n*-tetradecane with 5 wt% 1-methylnaphthalene for Pt/alumina, Pt/ZDC, and Rh/ZDC [97].

more than would be expected from their concentration in the fuel [97,98]. This is likely because carbon deposition is thought to proceed through a mechanism involving the formation of aromatics (e.g., dehydrogenation of alkanes) [53]. Once formed, these aromatics are less reactive than other compounds in the fuel and can serve as nucleation sites for the formation of polynuclear coke compounds.

Figure 10.21 shows the effect of adding 5 wt% 1-methylnaphthalene (MN) to a feed of pure tetradecane in the catalytic POX of this fuel over three catalysts [97]. Although the Rh/zirconia-doped ceria (Rh/ZDC) is less affected by the addition of MN, all catalysts show a decrease in H_2 yield when MN is added to the feed. An interesting result in this study is that although the presence of MN decreases the H_2 yield on Rh/ZDC compared with the yield in the absence of MN, the yield remains relatively constant after an initial drop. Shekhawat et al. [97] attribute this to both the oxygen conductivity of the support and the inherently greater resistance to carbon formation of Rh compared with Pt.

10.5.3. Minimizing Carbon Deposition

Carbon deposition is closely related to the proportion of oxygen in the feed gas, which is introduced as (a) diatomic oxygen (e.g., in air), (b) steam, or (c) both.[9] To a first approximation, carbon deposition is inversely related to the oxygen/carbon (O/C) and steam/carbon (S/C) ratios of the gas fed to the fuel processor. These quantities are often specified as reaction conditions in the fuel-processing literature because they correlate most closely with carbon deposition [99].

10.5.3.1. Effect of S/C Ratio

The effect of higher S/C ratio on carbon deposition is illustrated by the representative data in Table 10.1 for the SR of bio-oil having the empirical formula $CH_{2.70}O_{0.50}\cdot 0.79H_2O$ using a Mg-doped $12CaO\cdot 7Al_2O_3$ catalyst

[9] These modes of reforming correspond to (a) partial oxidation, POX (b) steam reforming, SR, and (c) oxy-steam reforming (OSR), as indicated earlier.

TABLE 10.1 Carbon Formation on the Surface of Mg-Doped $12CaO \cdot 7Al_2O_3$ at Different Temperatures and S/C Ratios (200 mg catalyst, N_2 carrier gas, and GHSV = 10,000 h^{-1}) [100].

Temperature (°C)	S/C ratio	Carbon formation mg C/(g_{cat} − h)
550	1.5	5.1
	4.0	2.8
	9.0	1.9
650	1.5	8.6
	4.0	4.2
	9.0	2.7
750	1.5	15.3
	4.0	8.1
	9.0	4.5

[100]. Post-run characterization of the catalyst showed that the deactivation was due solely to carbon formation, not, e.g., to structural changes in the catalyst. Note that carbon deposition *increases* significantly with temperature for all S/C ratios, which differs from what might be expected from the thermodynamics of carbon formation (Fig. 10.19). This is likely due to kinetically rapid carbon formation − note from Fig. 10.19 that even at 750 °C, the equilibrium amount of elemental carbon is much higher than the 15.3 mg C/g catalyst in Table 10.1.

Note further that carbon formation decreases with increasing S/C ratio. The authors attribute the lower carbon formation to higher rates of gasification of the surface carbon in the presence of steam:

$$C_{surface} + H_2O \rightarrow CO + H_2 \qquad (10.9)$$

In practice, the heat requirements for the endothermic SR reaction would almost certainly limit S/C ratios to levels well below the value of 9/1 as shown in this table, despite its effect on lowering carbon deposition.

Higher S/C and O/C ratios in the feed gas have been shown to have a similar effect on carbon deposition in the reforming of propane [98], LPG [99,101], hexadecane [102], and methane [103−105].

10.5.4. Regeneration of Catalysts Deactivated by Carbon Deposition

In general, catalysts deactivated by carbon deposition can be regenerated using oxygen or hydrogen [98,106];[10] (C_xH_y represents carbon on the catalyst; $1 \leq x/y \leq \sim 6$):

$$C_xH_y + O_2 \rightarrow CO_2 + H_2O \qquad (10.10)$$

$$C_xH_y + H_2 \rightarrow CH_4 + H_2O \qquad (10.11)$$

10.5.4.1. Types of Carbon

Different types of carbon deposits can be described by the x/y ratio: $x/y \sim 1$ corresponds to what may be termed "methynic" carbon (C_α) and $x/y \sim 6$ corresponds to "naphthenic" carbon (C_β) [98]. One study on the SR of propane on Co-Ni/alumina suggests that these two types of carbon are formed under different conditions: the more reactive C_α is formed initially from oxidative dehydrogenation of propane, and the more refractory, filamentous C_β in steam-lean conditions from the dehydropolymerization of surface methyne groups [98]. Regeneration of the catalyst containing both types of carbon using a H_2/O_2 treatment sequence resulted in a catalyst with essentially the same properties as the fresh catalyst by avoiding the higher

[10] Other gases have been reported for carbon removal as well, e.g., CO_2 and N_2 [107], but O_2 and H_2 are more widely studied. Unlike O_2 and H_2, CO_2 regeneration is endothermic, suggesting that mixing CO_2 and H_2 or O_2 may be an effective way to reduce exotherms during regeneration [107].

temperatures produced in an O_2/H_2 treatment sequence. These higher temperatures are caused by the higher rate of oxidation (versus reduction) of the C_α carbon [107],[11] which itself can lead to thermal deactivation of the catalyst [108].

Neither this particular type of carbon deposition nor the optimum regeneration sequence are universal – e.g., essentially irreversibly bound graphitic carbon can form at higher temperatures [109]. However, several studies report that these same two types of carbon are formed, e.g., in the SR, OSR, and POX of *n*-dodecane [109].

10.5.5. Characterization of Carbon Deposits

Characterization of coke deposits can be carried out using spectroscopic, chemical, and physical methods. These methods are too numerous to describe in detail here, and the reader is referred to representative studies on techniques used to characterize coke formed in reforming reactions, including X-ray adsorption spectroscopy [110,111], X-ray photoelectron spectroscopy [112–114], X-ray diffraction [112], Raman spectroscopy [114], transmission electron spectroscopy [112], scanning electron spectroscopy [109,115], laser desorption/mass spectrometry [116], and thermal gravimetric analysis [98,107,117].

These methods are complicated by the extremely complex nature of carbon on the surface of the deactivated catalyst, which can be graphitic (often in the form of filaments [16,109,118] or tubes [119]), aromatic [110], partially oxidized carbon [112], or amorphous. In addition, the carbon can have irregular three-dimensional morphologies that make complete chemical and physical characterization of the carbon virtually impossible, although techniques such as kinetic measurement of carbon oxidation can provide insight into the overall morphology [117,120].

10.5.5.1. Temperature-Programmed Oxidation

By far the most common method used to characterize catalysts deactivated by carbon deposition is temperature-programmed oxidation (TPO) [15,98,109,115,117,120–127]. This simple method involves heating the carbon-containing catalyst from near-ambient temperatures at a specific rate in an oxygen-containing gas.[12] Carbon deposits (represented by the empirical formula C_xH_y ($1 \leq x/y \leq \sim 6$) react to form CO_2,[13] which is continuously monitored in the exit gas:

$$C_xH_y + O_2 \rightarrow CO_2 + H_2O \qquad (10.12)$$

The resulting plot of CO_2 versus temperature provides an idea of the quantity and reactivity of the carbon deposits on the catalyst. TPO is similar in principle to the oxidative regeneration of carbon-containing catalysts (see Section 10.5.4 above) except that the CO_2 concentration in the exit gas is continuously monitored and can be directly assigned to carbon being oxidized at a specific temperature.

Figure 10.22 shows an example TPO result for a 0.61 wt% Pt/alumina catalyst that has been used for the POX of three fuels: 1-MN, tetradecane, and decalin [114]. This figure exemplifies the type of information a TPO experiment

[11] The oxygen or hydrogen can be diluted to a few percent to avoid excessive heat generation by either oxidation or reduction of the carbon deposits.

[12] Typically, the oxygen or hydrogen is diluted in an inert gas to a few percent to avoid excessive heat generation, which could irreversibly damage the catalyst. CO_2 can also be used as an oxidant in a TPO test, in which case the carbon on the surface can react to form CO ($CO_2 + C \rightarrow 2CO$) and H_2O ($CO_2 + C_xH_y \rightarrow CO + H_2O$) (see, e.g., [128]).

[13] Although in principle CO can also be formed, conditions are typically selected to eliminate the formation of CO, so that only CO_2 is usually reported.

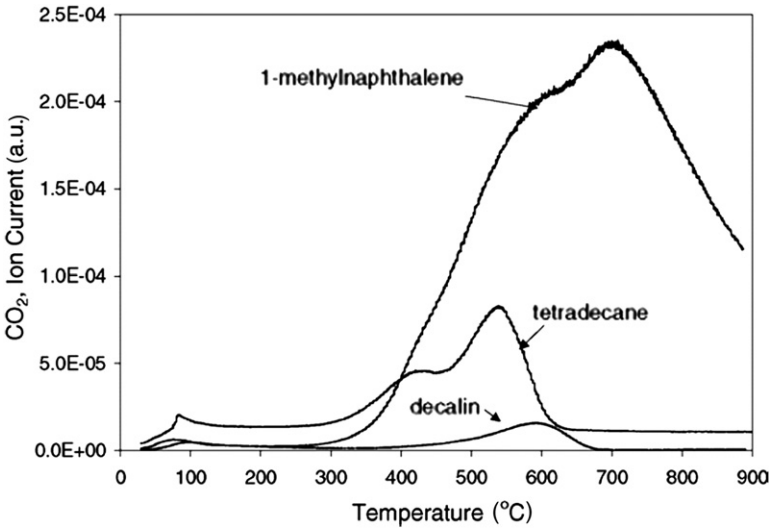

FIGURE 10.22 TPO of carbon deposited on a 0.61 wt% Pt/alumina during partial oxidation of diesel fuel compounds [114].

provides. For example, it is clear that 1-MN forms more carbon than tetradecane or decalin (as shown by a greater area under the TPO curve), and that the carbon is less reactive (as shown by the higher peak temperature). A less obvious result is shown by the identifiable shoulders on the 1-MN (~600 °C) and tetradecane (~420 °C) plots. A widely accepted interpretation of these shoulders is that they correspond to carbon that is either more reactive (e.g., less aromatic) or located closer to the Pt/support interface (and is therefore more readily oxidized than carbon on the support) [92,114].

10.5.5.2. Temperature-Programmed Hydrogenation

A directly analogous characterization of coke (C_xH_y) can be carried out using hydrogen instead of oxygen (TPH) [9,128–134]:

$$C_xH_y + H_2 \rightarrow CH_4 + H_2O \qquad (10.13)$$

in which case methane is monitored as a function of temperature instead of CO_2.

An example is shown in Fig. 10.23. Here, a series of Ni/MgO catalysts is first deactivated during a CH_4/CO_2 reaction, then the deposited carbon is characterized using TPH. Curves (a)–(d) are remarkably similar. Although there are slight differences in the areas (corresponding to the amount of carbon) and peak

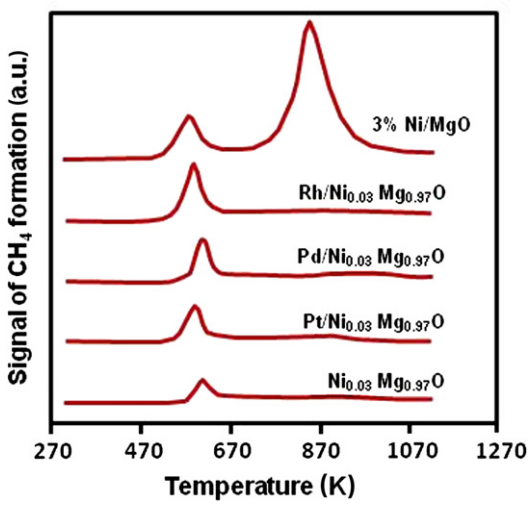

FIGURE 10.23 Temperature-programmed hydrogenation (TPH) profiles of (a) $NiO_{0.03}Mg_{0.97}O$ and this same catalyst promoted with 0.21 wt% of each of the following: (b) Pt, (c) Pd, (d) Rh, (e) 3 wt% Ni/MgO. Catalysts first tested for CH_4/CO_2 reforming at 0.1 MPa, 773K, $CH_4/CO_2 = 1$, $W/F = 0.1\ g_{cat}\,h\,mol^{-1}$. TPH at 20 K/min, pure H_2; *Reprinted from Chen et al. [129], Copyright (1997), with permission from Elsevier.*

heights (corresponding to the reactivity of the carbon) of the TPH peaks at ~600K, they are attributed to a common surface species: adsorbed CO_2 [129]. Curve (e), which contains much higher Ni loading and no noble metal, has a second peak at ~870K, which is attributed to "deposited carbon." An alternative interpretation of these two peaks is that the lower temperature peak corresponds to CH_x fragments from methane decomposition, while the higher temperature peak is due to relatively unreactive graphitic carbon [131].

10.5.5.3. *Comparison of TPO and TPH on the Same Catalyst*

Analysis of the same coked catalyst by TPO and TPH can provide insight into the nature of the coke deposit that may not be possible using one technique alone [112,132,133,135]. Wang and Lu [112] studied CH_4/CO_2 reforming on Ni/alumina catalysts and showed distinct differences in the reactivity of carbon deposits to hydrogen and oxygen. A direct comparison of TPO and TPH for the same catalyst at the same time on-stream can be made by comparing the 1 h TPO curve in Fig. 10.24 to the 5 wt% Ni/alumina catalyst in Fig. 10.25. The authors interpret the TPO result as two different curves, with the overall curve showing the sum of the two. A small portion of the curve (<600 °C) is attributed to the oxidation of a relatively reactive carbide, e.g., Ni_3C, formed by CH_4 decomposition. The larger, high-temperature peak (~670 °C) is believed to be Boudouard carbon ($2CO \rightarrow C + CO_2$) that encapsulated the nickel, requiring a higher temperature to oxidize this carbon since nickel is no longer available to active oxygen.

The TPH result for the same 5 wt% Ni/alumina catalyst in Fig. 10.25 shows three distinct types of carbon. First, two low-temperature peaks are attributed to amorphous carbon (peak <100 °C) and filamentous, graphitic carbon (peak at ~200 °C), where both are in contact with exposed metallic

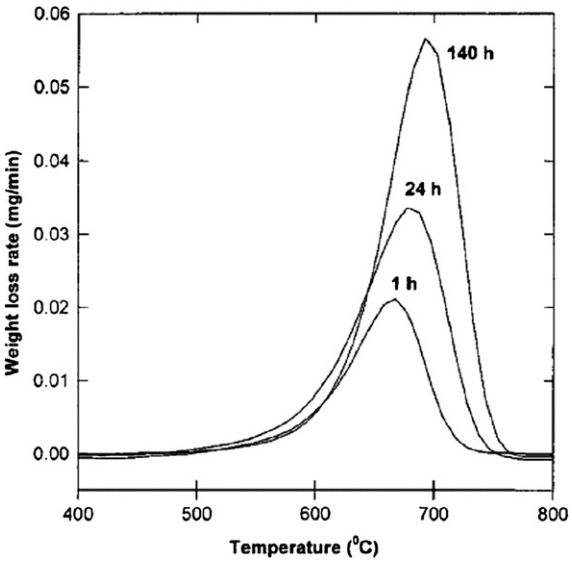

FIGURE 10.24 TPO profiles of carbonaceous species on 5 wt% Ni/γ-Al_2O_3 after reaction at 700 °C; *Reprinted from Wang and Lu [112], Copyright (1999), with permission from American Chemical Society.*

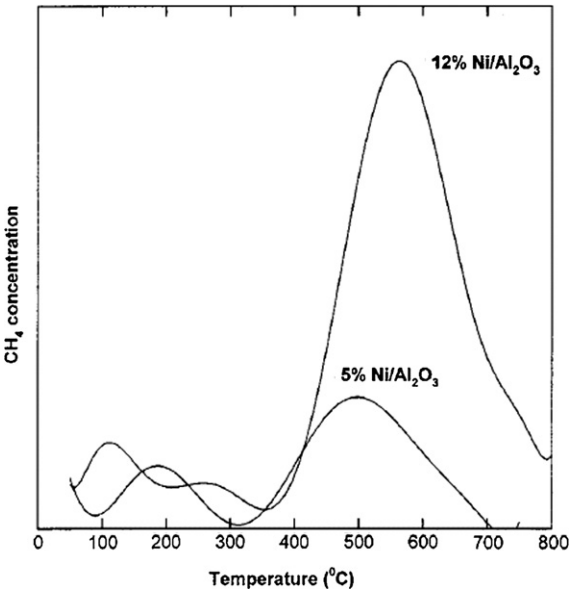

FIGURE 10.25 TPH profiles of carbonaceous species on 5 wt% Ni/γ-Al_2O_3 (and 12 wt% Ni/γ-Al_2O_3) after 1-h reaction at 700 °C; *Reprinted from Wang and Lu [112], Copyright (1999), with permission from American Chemical Society.*

nickel. The higher temperature peak (500 °C) corresponds to graphitic carbon in contact with the support, but not in contact with nickel. This distinction among carbon in contact with nickel, carbon in contact with the support, Boudouard carbon encapsulating the nickel, and presence of nickel carbide would not have been possible by TPH or TPO alone. Together, a much clearer picture of the carbon formation process is possible.

10.5.6. Computational Modeling of Carbon Deposition

Recently, advances in computational catalysis have been directed at understanding carbon deposition in fuel-reforming reactions. For example, several studies have shown computationally that alloying of Ni with Sn greatly reduces the energetics favoring the formation of extended carbon structures on these surfaces [136–138]. Figure 10.26 shows that the formation of carbon deposits (planar C_8 and graphene) is more favorable on Ni(211) than Sn/Ni(211) by 0.23 and 0.15 eV, respectively [136]. Furthermore, density functional theory (DFT) suggests that the Sn atoms break the connectivity of surface Ni sites, enhancing C atom oxidation versus the C–C bond formation that leads to carbon deposition. These results were confirmed experimentally in the SR of CH_4, propane, and isooctane [136].

10.6. KINETICS OF THE DEACTIVATION PROCESSES

Here, we consider simple models that can be used to describe the deactivation process. Kinetic models for the various reactions that take place in a fuel reformer (WGS, oxidation, CO_2 reforming, SR, etc.) are not considered here, but have been investigated, e.g., [70].

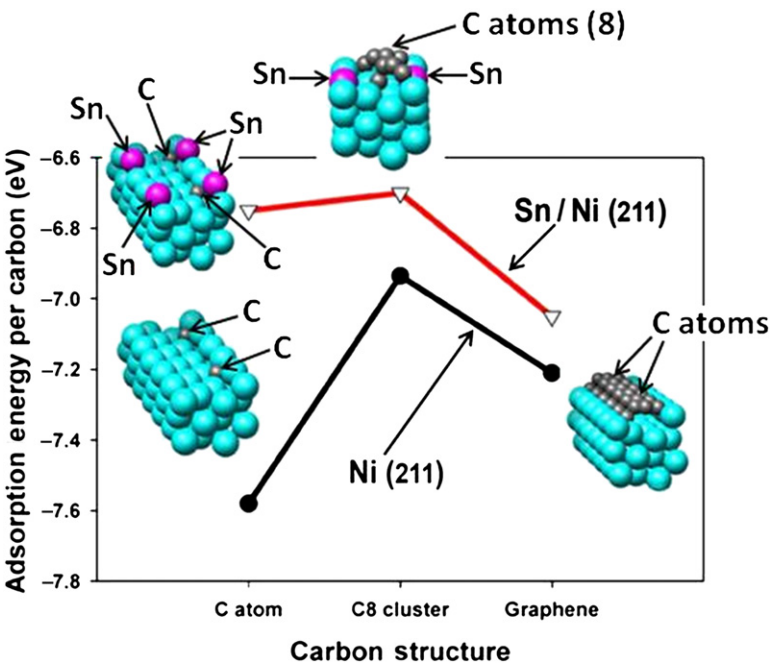

FIGURE 10.26 DFT-calculated adsorption energies per carbon atom for a C atom, C_8 cluster, and a graphene chain adsorbed on Ni(211) and Sn/Ni(211) (see text). Ni is depicted as a large blue (light), Sn as large magenta, and C as small black (dark) atom. The surface alloy is modeled by replacing every third Ni edge atom by Sn; *Reprinted from Nikolla et al. [136], Copyright (2007), with permission from Elsevier.*

The deactivation process introduces time as an independent variable in the equations describing the reactions taking place in the fuel reformer. The main reforming reaction can be described by a general equation of the form[14]

$$r = f_1(C_i)\cdot\exp(-E_a/RT)\cdot s \tag{10.14}$$

Where

f_1 = kinetic rate dependence on concentration of the reactants/products (e.g., a Langmuir–Hinshelwood or power law)

C_i = concentration(s) of the reactant(s)/product(s), mol/cm^3

E_a = apparent activation energy, kcal/mol

R = ideal gas constant, kcal/mol-K

s = activity function; r/r_o where r = reaction rate at time t, r_o = reaction rate at time t_0 (mol/min)[15]

A similar expression can be written for $s(t)$:

$$\begin{aligned} r_d &= -\frac{ds}{dt} = k_d f_2(C_i)s^m \\ &= k_o \exp(-E_d/RT) f_2(C_i)s^m \end{aligned} \tag{10.15}$$

Where

r_d = deactivation rate, h^{-1}

k_d = deactivation rate constant, appropriate units, depending on the dimensions of f_2.

k_o = pre-exponential factor for k_d

E_d= activation energy for deactivation, kcal/mol

C_i = concentration(s) of the reactant(s)/product(s), mol/cm^3

These two expressions are linked by $s(t)$ and the various concentrations (C_i). The simultaneous solution to these expressions gives an equation for the rate of the reforming reaction as a function of time.

For example, assume $m = 1$ in Eq. (10.15) and $f_2 = C_i^o$ for all i (i.e., r_d is independent of concentration), then

$$-\frac{ds}{dt} = k_d s \tag{10.16}$$

which gives $s(t)$:

$$s = \exp(-k_d t) \tag{10.17}$$

Showing that $s(0) = 1$ and $s(\infty) = 0$. Substituting Eq. (10.17) in Eq. (10.14) gives the relationship between the rate of the reforming reaction and time on-stream:

$$\begin{aligned} r &= f_1(C_i)\cdot\exp\left(-\frac{E_a}{RT} - k_d t\right) \\ &= f_1(C_i)\cdot\exp\left[-\frac{E_a}{RT} - k_o \exp(-E_d/RT)t\right] \end{aligned} \tag{10.18}$$

Though quite simple, this derivation illustrates the general approach to determining the dependence of the main reforming reaction on deactivation. There are several additional factors to consider. First, note that k_d is typically measured experimentally and may have no fundamental meaning. k_d depends on temperature, typically (but not always) in an Arrhenius relationship. Depending on the relative values of E_a and E_d, increasing temperature can either accelerate or slow down the rate at which the main reaction decreases with time.

10.6.1. Modeling of Poisoning

Consider deactivation due to the presence of sulfur, which can be modeled as the irreversible deposition of a poison (P) in parallel with the

[14] These equations do not account for the effect of a non-unity value of the effectiveness factors for the main or deactivation reactions (see [50]).

[15] s will generally decrease monotonically with time, starting at a value of unity. However, there are circumstances under which s can be greater than 1 (see [50] for a more detailed discussion).

main reaction in which the fuel (F) reacts to form products:

$$\mathrm{F} \xrightarrow{k} \text{products} \tag{10.19}$$

$$\mathrm{P} \rightarrow \mathrm{P}\downarrow \tag{10.20}$$

Assuming that s is first order in C_P, and that the main reaction is first order in C_F, the rates of the main and the deactivation reactions are given by

$$-\frac{dC_F}{dt} = r = kC_F \cdot s \tag{10.21}$$

$$-\frac{ds}{dt} = k_d C_P \cdot s^d \tag{10.22}$$

It can be shown that for a strongly adsorbed poison (like sulfur), $d \sim 0$ [94].[16] Assuming C_P is constant, solving Eq. (10.22) for $s(t)$:

$$s(t) = 1 - k_d C_P t \quad k_d C_P t \leq 1 \tag{10.23}$$

Note that Eq. (10.23) predicts that $s(t)$ decreases linearly with time and becomes negative for values of $k_d C_P t > 1$, which is physically impossible – meaning that Eq. (10.23) is only valid for values of $k_d C_P t \leq 1$. Substituting Eq. (10.23) in Eq. (10.21) gives the final expression for the main reaction as a function of the fuel concentration and time for this simple case:

$$r = kC_F(1 - k_d C_P t) \tag{10.24}$$

This result shows that the rate of the main reaction (r) decreases linearly with time at a rate equal to $kC_F k_d C_P$. Assuming k_d has an Arrhenius dependence on temperature with an activation energy E_d ($k_d = k_o \exp(-E_d/RT)$, then the observed *rate* of deactivation with time will increase with temperature when $E_d > E_a$, and will decrease less rapidly with temperature when $E_d < E_a$. Poisoning in an actual reformer is seldom as simple as this, but the procedure for modeling of poisoning is illustrated by the derivation above.

10.6.2. Modeling of Carbon Deposition

Carbon deposition can be taken into account by recognizing that the concentration of carbon (C_c) is inversely proportional to the activity, s. It then remains to determine the relationship between C_c and time for a given catalyst. Voorhies [139] described this relationship for catalytic cracking:[17]

$$C_c = At^n \tag{10.25}$$

Where A and n are determined empirically. Froment and Bischoff [140,141] show several different forms that the relationship between s and C_c can take, depending on the mechanism of coke formation (e.g., single or multilayer coke). Assuming monolayer coke formation, the following relationship can be shown [141,142]:[18]

$$s(C_c) = 1 - \gamma C_c / C_{c,max} \tag{10.26}$$

where γ is an empirical parameter and $C_{c,max}$ corresponds to the maximum monolayer coverage. Substituting Eqs (10.25) and (10.26) in Eq. (10.21):

$$r = kC_F(1 - \gamma A t^n / C_{c,max}) \tag{10.27}$$

For $n = 1$, this predicts a linear decrease in the rate with time, from an initial value ($t = 0$) of

[16] There is a further implicit assumption here – no diffusion resistance; i.e., the effectiveness factors for the main and deactivation rate expressions are 1. This is not always true. The derivations taking these factors into account can be found in [94].

[17] This relationship is somewhat empirical, but has been shown to apply to a wide range of coke-forming catalytic reactions.

[18] See Ostrovskii [143] for a discussion of the governing equations for other forms of this relationship.

kC_F, as expected.[19] Note that A depends on temperature, so that the relative rates of the main and carbon-forming reactions depend on the values of the activation energy of the main reaction and that of the carbon-forming reaction.

10.6.3. Modeling of Sintering

Thermal deactivation may be the result of sintering of a supported metal cluster. Sehested et al. [57] show that the dispersion of a series of Ni-based reforming catalysts used at simulated pre-reforming conditions (10/1 H_2O/H_2 mixture, 500 °C, 3 MPa) can be measured using the sulfur adsorption capacity. Their data on six different catalysts were fitted to a power-law expression relating the sulfur capacity for the fresh catalyst (S_o) to the capacity at time t (S) and the capacity at long times (S_{eq}):

$$\frac{d}{dt}\left(\frac{S}{S_o}\right) = k'\left(\frac{S - S_{eq}}{S_{eq}}\right)^2 \qquad (10.28)$$

Where k' is a temperature-dependent rate constant describing the rate of decrease in sulfur capacity with time. Because the sulfur capacity is directly related to dispersion, a corresponding relationship can be used to describe sintering — which is the loss of dispersion:

$$\frac{d}{dt}\left(\frac{D}{D_o}\right) = k_s\left(\frac{D - D_{eq}}{D_o}\right)^2 \qquad (10.29)$$

Where k_s is a sintering rate constant, D is dispersion at time t, D_o is the dispersion of the fresh catalyst, and D_{eq} is the dispersion at long times.[20] Assuming further that the activity, s, is directly related to dispersion at all times [145], then integration of Eq. (10.29) and substitution of s into the resulting equation gives $s(t)$:

$$s(t) = s_{eq} + \frac{1 - s_{eq}}{[1 - k_s t(1 - s_{eq})]} \qquad (10.30)$$

where s_{eq} is the activity at long times ($s_{eq} \neq 0$) and $s(0) = 1$. Substituting Eq. (10.30) in Eq. (10.21) gives the final expression for the main reaction as a function temperature, fuel concentration, and time:

$$r = kC_F\left[s_{eq} + \frac{1 - s_{eq}}{[1 - k_s t(1 - s_{eq})]}\right] \qquad (10.31)$$

As in the other models, the dependence of k_s on temperature is implicit in Eq. (10.31), and is often described using an Arrhenius model [144]:

$$k_s = k_o \exp(-E_d/RT) \qquad (10.32)$$

The specific dependence must be determined experimentally. Depending on the nature of this relationship, increasing temperature may decrease or increase the relative rates of sintering versus the desired reforming reaction.

10.7. CONCLUSIONS

Deactivation is inevitable in catalytic reforming for fuel cell applications. The principle mechanisms associated with the reformer are thermal degradation (e.g., sintering), poisoning (e.g., by sulfur), and coke deposition. Though these are discussed separately here, they are almost invariably linked in practice — coke deposition virtually always accompanies sulfur poisoning.

Strategies to minimize deactivation, and to regenerate spent catalysts, include oxidative or

[19] At present, we are aware of no literature in which the values of the fitting parameters required in this model have been evaluated at conditions corresponding to those in a fuel processor. In catalytic cracking, $n \sim 0.5$ [143].

[20] Bartholomew and Farrauto [94] and Fuentes [144] give a similar expression: $-dD/dt = k_d(D - D_{eq})^m$, where $1 < m < 2$ in most cases.

reductive regeneration to remove coke deposits, and developing sulfur-tolerant catalysts using an oxide sorbent in the catalyst formulation.

It is important to characterize the deactivated catalyst to identify the mechanism responsible for the deactivation. The complex nature of coke, sulfur poison, and sintered catalyst makes this especially difficult.

Finally, the future is likely to bring a new understanding of deactivation using first-principles modeling, which has already shown promise in characterizing Ni-based catalysts, among others.

References

[1] Althenayan FM, Foo SY, Kennedy EM, Dlugogorski BZ, Adesina AA. Bimetallic Co-Ni/Al_2O_3 catalyst for propane dry reforming: Estimation of reaction metrics from longevity runs. Chem Eng Sci 2010;65(1):66–73.

[2] Wu JCS, Chou HC. Bimetallic Rh-Ni/BN catalyst for methane reforming with CO_2. Chem Eng J 2009;148 (2–3):539–45.

[3] Bellido JDA, De Souza JE, M'Peko J-C, Assaf EM. Effect of adding CaO to ZrO_2 support on nickel catalyst activity in dry reforming of methane. Appl Catal A: Gen 2009;358(2):215–23.

[4] Zhang HG, Wang H, Dalai AK. Effects of metal content on activity and stability of Ni-Co bimetallic catalysts for CO_2 reforming of CH_4. Appl Catal A: Gen 2008;339(2):121–9.

[5] Wu QY, Chen JX, Zhang JY. Effect of yttrium and praseodymium on properties of $Ce_{0.75}Zr_{0.25}O_2$ solid solution for CH_4-CO_2 reforming. Fuel Process Technol 2008;89(11):993–9.

[6] Therdthianwong S, Therdthianwong A, Siangchin C, Yonprapat S. Synthesis gas production from dry reforming of methane over Ni/Al_2O_3 stabilized by ZrO_2. Int J Hydrogen Energy 2008;33(3): 991–9.

[7] Therdthianwong S, Siangchin C, Therdthianwong A. Improvement of coke resistance of Ni/Al_2O_3 catalyst in CH_4/CO_2 reforming by ZrO_2 addition. Fuel Process Technol 2008;89(2):160–8.

[8] Song QL, Xiao R, Li YB, Shen LH. Catalytic carbon dioxide reforming of methane to synthesis gas over activated carbon catalyst. Ind Eng Chem Res 2008;47 (13):4349–57.

[9] Rezaei M, Alavi SM, Sahebdelfar S, Yan ZF. Effects of CO_2 content on the activity and stability of nickel catalyst supported on mesoporous nanocrystalline zirconia. J Nat Gas Chem 2008;17(3): 278–82.

[10] Pan YX, Liu CJ, Cui L. Temperature-programmed studies of coke resistant Ni catalyst for carbon dioxide reforming of methane. Catal Lett 2008;123 (1–2):96–101.

[11] Khalesi A, Arandiyan HR, Parvari M. Production of syngas by CO_2 reforming on $M_xLa_{1-x}Ni_{0.3}Al_{0.7}O_{3-d}$ (M = Li, Na, K) catalysts. Ind Eng Chem Res 2008;47 (16):5892–8.

[12] de Lima SM, Pena MA, Fierro JLG, Assaf JM. $La_{1-x}Ca_xNiO_3$ perovskite oxides: Characterization and catalytic reactivity in dry reforming of methane. Catal Lett 2008;124(3–4):195–203.

[13] de Arauj GC, de Lima SM, Assaf JM, Pena MA, Fierro JL, Rangel MDC. Catalytic evaluation of perovskite-type oxide $LaNi_{1-x}Ru_xO_3$ in methane dry reforming. Catal Today 2008;133:129–35.

[14] Carrara C, Munera J, Lombardo EA, Cornaglia LM. Kinetic and stability studies of Ru/La_2O_3 used in the dry reforming of methane. Topics Catal 2008;51 (1–4):98–106.

[15] Wang R, Liu XB, Chen YX, Li WZ, Xu HY. Effect of metal-support interaction on coking resistance of Rh-based catalysts in CH_4/CO_2 reforming. Chinese J Catal 2007;28(10):865–9.

[16] Pechimuthu NA, Pant KK, Dhingra SC. Deactivation studies over Ni-K/CeO_2-Al_2O_3 catalyst for dry reforming of methane. Ind Eng Chem Res 2007;46 (6):1731–6.

[17] Guo J, Lou H, Zheng XM. The deposition of coke from methane on a Ni/$MgAl_2O_4$ catalyst. Carbon 2007;45(6):1314–21.

[18] Blanchard J, Nsungui AJ, Abatzoglou N, Gitzhofer F. Dry reforming of methane with a Ni/Al_2O_3-YSZ catalyst: the role of the catalyst preparation protocol. Can J Chem Eng 2007;85(6):889–99.

[19] Zhang L, Millet J-MM, Ozkan US. Effect of Cu loading on the catalytic performance of Fe-Al-Cu for water-gas shift reaction. Appl Catal A: Gen 2009;357 (1):66–72.

[20] Shishido T, Nishimura S, Yoshinaga Y, Ebitani K, Teramura K, Tanaka T. High sustainability of Cu-Al-Ox catalysts against daily start-up and shut-down (DSS)-like operation in the water-gas shift reaction. Catal Commun 2009;10(7):1057–61.

[21] Sekine Y, Takamatsu H, Aramaki S, Ichishima K, Takada M, Matsukata M, et al. Synergistic effect of Pt or Pd and perovskite oxide for water gas shift reaction. Appl Catal A: Gen 2009;352(1–2):214–22.

[22] Pirola C, Bianchi CL, Di Michele A, Vitali S, Ragaini V. Fischer Tropsch and water gas shift chemical regimes on supported iron-based catalysts at high metal loading. Catal Commun 2009;10 (6):823–7.

[23] Nishida K, Li D, Zhan Y, Shishido T, Oumi Y, Sano T, et al. Effective MgO surface doping of Cu/Zn/Al oxides as water-gas shift catalysts. Appl Clay Sci 2009;44(3–4):211–7.

[24] Mendes D, Garcia H, Silva VB, Mendes A, Madeira LM. Comparison of nanosized gold-based and copper-based catalysts for the low-temperature water-gas shift reaction. Ind Eng Chem Res 2009;48 (1):430–9.

[25] Liu P, Rodriguez JA, Takahashi Y, Nakamura K. Water-gas-shift reaction on a $Ni_2P(001)$ catalyst: formation of oxy-phosphides and highly active reaction sites. J Catal 2009;262(2):294–303.

[26] Kim YT, Park ED, Lee HC, Lee D, Lee KH. Water-gas shift reaction over supported Pt-CeO_x catalysts. Appl Catal B: Env 2009;90(1–2):45–54.

[27] Inoglu N, Kitchin JR. Atomistic thermodynamics study of the adsorption and the effects of water-gas shift reactants on Cu catalysts under reaction conditions. J Catal 2009;261(2):188–94.

[28] Guo P-J, Chen L-F, Yu G-B, Zhu Y, Qiao M-H, Xu H-L, et al. Cu/ZnO-based water-gas shift catalysts in shut-down/start-up operation. Catal Commun 2009;10(8):1252–6.

[29] Guo P, Chen L, Yang Q, Qiao M, Li H, Li H, et al. Cu/ZnO/Al_2O_3 water-gas shift catalysts for practical fuel cell applications: the performance in shut-down/start-up operation. Int J Hydrogen Energy 2009;34 (5):2361–8.

[30] Gunawardana PVDS, Lee HC, Kim DH. Performance of copper-ceria catalysts for water gas shift reaction in medium temperature range. Int J Hydrogen Energy 2009;34(3):1336–41.

[31] Carbo MC, Jansen D, Boon J, Dijkstra JW, van den Brink RW, Verkooijen AHM. Staged water-gas shift configuration: key to efficiency penalty reduction during pre-combustion decarbonisation in IGCC. Energy Procedia 2009;1(1):661–8.

[32] Andreeva D, Ivanov I, Ilieva L, Abrashev MV, Zanella R, Sobczak JW, et al. Gold catalysts supported on ceria doped by rare earth metals for water gas shift reaction: influence of the preparation method. Appl Catal A: Gen 2009;357(2):159–69.

[33] Abd El-Moemen A, Karpenko A, Denkwitz Y, Behm RJ. Activity, stability and deactivation behavior of Au/CeO_2 catalysts in the water gas shift reaction at increased reaction temperature (300 C). J Power Sources 2009;190(1):64–75.

[34] Zhang L, Wang X, Millet J-MM, Matter PH, Ozkan US. Investigation of highly active Fe-Al-Cu catalysts for water-gas shift reaction. Appl Catal A: Gen 2008;351(1):1–8.

[35] Ruettinger W, Liu XS, Xu XM, Farrauto RJ. Effect of Mo and Re promoters on the activity and stability of a Pt/ZrO_2 water-gas shift catalyst (Part 1). Topics Catal 2008;51(1–4):60–7.

[36] Fox EB, Velu S, Engelhard MH, Chin Y-H, Miller JT, Kropf J, et al. Characterization of CeO_2-supported Cu-Pd bimetallic catalyst for the oxygen-assisted water-gas shift reaction. J Catal 2008;260(2):358–70.

[37] Ilinich O, Ruettinger W, Liu XS, Farrauto R. Cu-Al_2O_3-$CuAl_2O_4$ water-gas shift catalyst for hydrogen production in fuel cell applications: mechanism of deactivation under start-stop operating conditions. J Catalysis 2007;247(1):112–8.

[38] Azzam KG, Babich IV, Seshan K, Lefferts L. A bifunctional catalyst for the single-stage water-gas shift reaction in fuel cell applications. Part 2. Roles of the support and promoter on catalyst activity and stability. J Catal 2007;251(1):163–71.

[39] Liu BS, Li L, Au CT, Cheung ASC. Investigation on reverse water-gas shift over La_2NiO_4 catalyst by cw-cavity enhanced absorption spectroscopy during CH_4/CO_2 reforming. Catal. Lett. 2006;108(1–2):37–44.

[40] Pasel J, Samsun RC, Schmitt D, Peters R, Stolten D. Test of a water-gas-shift reactor on a 3kW(e)-scale – design points for high- and low-temperature shift reaction. J Power Sources 2005;152(1):189–95.

[41] Liu XS, Ruettinger W, Xu XM, Farrauto R. Deactivation of Pt/CeO_2 water-gas shift catalysts due to shutdown/startup modes for fuel cell applications. Appl Catal B: Env 2005;56(1–2):69–75.

[42] Kolb G, Pennemann H, Zapf R. Water-gas shift reaction in micro-channels – results from catalyst screening and optimization. Catal Today 2005;110 (1–2):121–31.

[43] King DL, Brooks K, Fischer C, Pederson L, Rawlings G, Stenkamp VS, et al. Fuel reformation: catalyst requirements in microchannel architectures. In: Wang Y, Holladay JD, editors. Microreactor technology and process intensification, vol. 914. Washington, DC: American Chemical Society; 2005. p. 119–28.

[44] Dhar R, Pedrow PD, Liddell KC, Moeller TM, Osman MA. Synthesis of Pt/ZrO_2 catalyst on fecralloy substrates using composite plasma-polymerized films. IEEE Trans Plasma Sci 2005;33 (6):2035–45.

[45] Loffler DG, McDermott SD, Renn CN. Activity and durability of water-gas shift catalysts used for the steam reforming of methanol. J Power Sources 2003;114(1):15–20.

[46] Zalc JM, Sokolovskii V, Loffler DG. Are noble metal-based water-gas shift catalysts practical for automotive fuel processing? J Catal 2002;206(1):169–71.
[47] Vinas J, Barreto GF, Gonzalez MG, Laborde MA, Moreno NE. Water-gas shift reaction at high temperature. Study of kinetics and catalyst deactivation on a Fe_2O_3-Cr_2O_3 catalyst. Latin Am Appl Res 1999;29(2):91–8.
[48] Bartholomew CH. Mechanisms of catalyst deactivation. Appl Catal A: Gen 2001;212(1–2):17–60.
[49] Denny PJ, Twigg MV. Factors determining the life of industrial heterogeneous catalysis; catalyst deactivation. In: Delmon B, Froment GF, editors. Stud. Surf Sci Catal, vol. 6. Elsevier; 1980. p. 577–99.
[50] Bartholomew CH. Catalyst deactivation. Chem Eng 1984;91(23):96–112.
[51] Butt JB. Catalyst deactivation and regeneration. In: Anderson JR, Boudart M, editors. Catalysis, science and technology. New York: Springer-Verlag; 1984.
[52] Shekhawat D, Berry DA, Gardner TH, Spivey JJ. Catalytic reforming of liquid hydrocarbon fuels for fuel cell applications. In: Spivey JJ, Dooley KM, editors. Catalysis, vol. 19. Royal Society of Chemistry, Cambridge, UK; 2006. p. 184–253.
[53] Bond GC. The role of carbon deposits in metal-catalysed reactions of hydrocarbons. Appl Catal A: Gen 1997;149(1):3–25.
[54] Ferrandon M, Krause T. Role of the oxide support on the performance of Rh catalysts for the autothermal reforming of gasoline and gasoline surrogates to hydrogen. Appl Catal A: Gen 2006;311:135–45.
[55] Rasmussen FB, Sehested J, Teunissen HT, Molenbroek AM, Clausen BS. Sintering of Ni/Al_2O_3 catalysts studied by anomalous small angle X-ray scattering. Appl Catal A: Gen 2004;267(1–2):165–73.
[56] Pelletier L, Liu DDS. Stable nickel catalysts with alumina-aluminum phosphate supports for partial oxidation and carbon dioxide reforming of methane. Appl Catal A: Gen 2007;317(2):293–8.
[57] Sehested J, Carlsson A, Janssens TVW, Hansen PL, Datye AK. Sintering of nickel steam-reforming catalysts on $MgAl_2O_4$ spinel supports. J Catal 2001;197 (1):200–9.
[58] Xu Z, Li YM, Zhang JY, Chang L, Zhou RQ, Duan ZT. Bound-state Ni species – a superior form in Ni-based catalyst for CH_4/CO_2 reforming. Appl Catal A: Gen 2001;210(1–2):45–53.
[59] Bhattacharyya A, Chang VW. CO_2 reforming of methane to syngas – deactivation behavior of nickel aluminate spinel catalysts. In: Delmon B, Froment GF, editors. Catalyst deactivation; Stud Surf Sci Catal, vol. 88. Amsterdam: Elsevier; 1994. p. 207–13.
[60] Choi SO, Moon SH. Performance of $La_{1-x}Ce_xFe_{0.7}Ni_{0.3}O_3$ perovskite catalysts for methane steam reforming. Catal Today 2009;146(1–2):148–53.
[61] Goldwasser MR, Rivas ME, Lugo ML, Pietri E, Perez-Zurita J, Cubeiro ML, et al. Combined methane reforming in presence of CO_2 and O_2 over $LaFe_{1-x}CO_xO_3$ mixed-oxide perovskites as catalysts precursors. Catal Today 2005;107–8:106–13.
[62] Lim S-S, Lee H-J, Moon D-J, Kim J-H, Park N-C, Shin J-S, et al. Autothermal reforming of propane over Ce modified $Ni/LaAlO_3$ perovskite-type catalysts. Chem Eng J 2009;152(1):220–6.
[63] Gardner TH, Shekhawat D, Berry DA, Smith MW, Salazar M, Kugler EL. Effect of nickel hexaaluminate mirror cation on structure-sensitive reactions during n-tetradecane partial oxidation. Appl Catalysis A: Gen 2007;323:1–8.
[64] Liu Y, Cheng TX, Li DM, Jiang PB, Wang JX, Li WX, et al. Studies on the stability of a $La_{0.8}Pr_{0.2}NiAl_{11}O_{19}$ catalyst for syngas production by CO_2 reforming of methane. Catal Lett 2003;85(1–2):101–7.
[65] Xu ZL, Zhen M, Bi YL, Zhen KJ. Carbon dioxide reforming of methane to synthesis gas over hexaaluminate $ANiAl_{11}O_{19-\delta}$ (A=Ca, Sr, Ba and La) catalysts. Catal Lett 2000;64(2–4):157–61.
[66] Haynes DJ, Berry DA, Shekhawat D, Spivey JJ. Catalytic partial oxidation of n-tetradecane using pyrochlores: effect of Rh and Sr substitution. Catal Today 2008;136(3–4):206–13.
[67] Haynes DJ, Berry DA, Shekhawat D, Spivey JJ. Catalytic partial oxidation of n-tetradecane using Rh and Sr substituted pyrochlores: effects of sulfur. Catal Today 2009;145(1–2):121–6.
[68] Cheekatamarla PK, Lane AM. Catalytic autothermal reforming of diesel fuel for hydrogen generation in fuel cells – I. Activity tests and sulfur poisoning. J Power Sources 2005;152(1):256–63.
[69] Kang I, Bae J, Yoon S, Yoo Y. Performance improvement of diesel autothermal reformer by applying ultrasonic injector for effective fuel delivery. J Power Sources 2007;172(2):845–52.
[70] Rabe S, Vogel F, Truong T-B, Shimazu T, Wakasugi T, Aoki H, et al. Catalytic reforming of gasoline to hydrogen: Kinetic investigation of deactivation processes. Int J Hydrogen Energy 2009;34(19):8023–33.
[71] Azad AM, Duran MJ. Development of ceria-supported sulfur tolerant nanocatalysts: Rh-based formulations. Appl Catal A: Gen 2007;330:77–88.
[72] Kaila RK, Gutierrez A, Krause AOI. Autothermal reforming of simulated and commercial diesel: the performance of zirconia-supported RhPt catalyst in the presence of sulfur. Appl Catal B: Env 2008;84 (1–2):324–31.

[73] Ashrafi M, Pfeifer C, Proll T, Hofbauer H. Experimental study of model biogas catalytic steam reforming: 2. Impact of sulfur on the deactivation and regeneration of Ni-based catalysts. Energy Fuels 2008;22(6):4190–5.

[74] Lakhapatri SL, Abraham MA. Deactivation due to sulfur poisoning and carbon deposition on Rh-Ni/Al_2O_3 catalyst during steam reforming of sulfur-doped n-hexadecane. Appl Catal A: Gen 2009;364 (1–2):113–21.

[75] Xue Q, Gao L, Lu Y. Sulfur-tolerant Pt/Gd_2O_3-CeO_2-Al_2O_3 catalyst for high efficiency H_2 production from autothermal reforming of retail gasoline. Catal Today 2009;146(1–2):103–9.

[76] Menad S, Ferreira-Aparicio P, Cherifi O, Guerrero-Ruiz A, Rodriguez-Ramos I. Designing new high oxygen mobility supports to improve the stability of RU catalysts under dry reforming of methane. Catal Lett 2003;89(1–2):63–7.

[77] Choudhary VR, Mondal KC, Chouldhary TV. Oxy-methane reforming over high temperature stable NiCoMgCeOx and NiCoMgOx supported on zirconia-haffnia catalysts: accelerated sulfur deactivation and regeneration. Catal Commun 2007;8(3):561–4.

[78] Cheekatamarla PK, Thomson WJ. Catalytic activity of molybdenum carbide for hydrogen generation via diesel reforming. J Power Sources 2006;158 (1):477–84.

[79] Hepola J, Simell P. Sulphur poisoning of nickel-based hot gas cleaning catalysts in synthetic gasification gas II. Chemisorption of hydrogen sulphide. Appl Catal B: Env 1997;14:305–21.

[80] Han Y-S, Li J-B, Ning X-S, Chi B. Preparation of nickel aluminate spinel by solid state reaction. J Adv Mater 2006;1:23–5.

[81] Oh Y-S, Roh H-S, Jun K-W, Baek Y- S. A highly active catalyst, Ni/Ce-ZrO_2/θ-Al_2O_3, for on-site H_2 generation by steam methane reforming: pretreatment effect. Int J Hydrogen Energy 2003;28(12):1387–92.

[82] Oudghiri-Hassani H, Abatzoglou N, Rakass S, Rowntree P. Regeneration of an n-decanethiol-poisoned nickel catalyst. J Power Sources 2007;171 (2):811–7.

[83] Rostrup-Nielsen JR. Some principles relating to the regeneration of sulfur-poisoned nickel catalyst. J Catal 1971;21(2):171–8.

[84] Song CS. Fuel processing for low-temperature and high-temperature fuel cells – challenges, and opportunities for sustainable development in the 21st century. Catal Today 2002;77(1–2):17–49.

[85] Murata S, Hatanaka N, Kidena K, Nomura M. Improvement of lifetime of Ni/mordenite catalysts for CO_2 reforming of methane by support modification with alumina and Co-K loading. J Jpn Pet Inst 2006;49(5):240–5.

[86] Murata K, Saito M, Inaba M, Takahara I. Hydrogen production by autothermal reforming of sulfur-containing hydrocarbons over re-modified Ni/Sr/ZrO_2 catalysts. Appl Catal B: Env 2007;70 (1–4):509–14.

[87] Azad AM, Duran MJ, Mccoy AK, Abraham MA. Development of ceria-supported sulfur tolerant nanocatalysts: Pd-based formulations. Appl Catal A: Gen 2007;332(2):225–36.

[88] Ferrandon M, Mawdsley J, Krause T. Effect of temperature, steam-to-carbon ratio, and alkali metal additives on improving the sulfur tolerance of a Rh/La-Al_2O_3 catalyst reforming gasoline for fuel cell applications. Appl Catal A: Gen 2008;342 (1–2):69–77.

[89] Lu Y, Chen JC, Liu Y, Xue QS, He MY. Highly sulfur-tolerant Pt/$Ce_{0.8}Gd_{0.2}O_{1.9}$ catalyst for steam reforming of liquid hydrocarbons in fuel cell applications. J Catal 2008;254(1):39–48.

[90] Hennings U, Reimert R. Noble metal catalysts supported on gadolinium doped ceria used for natural gas reforming in fuel cell applications. Appl Catal B: Env 2007;70(1–4):498–508.

[91] RostrupNielsen JR. Industrial relevance of coking. Catal Today 1997;37(3):225–32.

[92] Barbier J. Deactivation of reforming catalysts by coking – a review. Appl Catal 1986;23(2):225–43.

[93] Guisnet M, Magnoux P. Organic chemistry of coke formation. Appl Catal A: Gen 2001;212(1–2):83–96.

[94] Bartholomew CH, Farrauto RJ. Fundamentals of industrial catalytic processes. 2nd ed. Wiley; 2006. p. 966.

[95] Cheekatamarla PK, Lane AM. Catalytic autothermal reforming of diesel fuel for hydrogen generation in fuel cells II. Catalyst poisoning and characterization studies. J Power Sources 2006;154(1):223–31.

[96] Gonzalez MG, Ponzi EN, Ferretti OA, Quincoces CE, Marecot P, Barbier J. Studies on H_2S adsorption and carbon deposition over Mo-Ni/Al_2O_3 catalysts. Adsorp Sci Technol 2000;18(6):541–50.

[97] Shekhawat D, Gardner TH, Berry DA, Salazar M, Haynes DJ, Spivey JJ. Catalytic partial oxidation of n-tetradecane in the presence of sulfur or poly-nuclear aromatics: effects of support and metal. Appl Catal A: Gen 2006;311:8–16.

[98] Hardiman KM, Cooper CG, Adesina AA, Lange R. Post-mortem characterization of coke-induced deactivated alumina-supported Co-Ni catalysts. Chem Eng Sci 2006;61(8):2565–73.

[99] Wang W, Turn SQ, Keffer V, Douette A. Study of process data in autothermal reforming of LPG using multivariate data analysis. Chem Eng J 2007;129(1–3):11–9.

[100] Wang ZX, Pan Y, Dong T, Zhu XF, Kan T, Yuan LX, et al. Production of hydrogen from catalytic steam reforming of bio-oil using $C_{12}A_7$-O^- based catalysts. Appl Catal A: Gen 2007;320:24–34.

[101] Goekaliler F, Selen Caglayan B, Ilsen Oensan Z, Erhan Aksoylu A. Hydrogen production by autothermal reforming of LPG for PEM fuel cell applications. Int J Hydrogen Energy 2008;33(4):1383–91.

[102] Goud SK, Whittenberger WA, Chattopadhyay S, Abraham MA. Steam reforming of n-hexadecane using a Pd/ZrO_2 catalyst: kinetics of catalyst deactivation. Int J Hydrogen Energy 2007;32 (14):2868–74.

[103] Furusawa T, Tsutsumi A. Comparison of Co/MgO and Ni/MgO catalysts for the steam reforming of naphthalene as a model compound of tar derived from biomass gasification. Appl Catal A: Gen 2005;278:207–12.

[104] Gardner DC, Bartholomew CH. Kinetics of carbon deposition during methanation of CO. Ind Eng Chem Prod Res Dev 1981;20:80–7.

[105] Dias JAC, Assaf JM. The advantages of air addition on the methane steam reforming over Ni/γ-Al_2O_3. J Power Sources 2004;137:264–8.

[106] Fung SC, Querini CA, Liu K, Rumschitzki DS, Ho TC. In-situ coking kinetics obtained from a new flow microbalance and reaction-kinetics monitored by Gc. Catalyst Deact 1994;88:305–12.

[107] Alenazey F, Cooper CG, Dave CB, Elnashaie SSEH, Susu AA, Adesina AA. Coke removal from deactivated Co-Ni steam reforming catalyst using different gasifying agents: an analysis of the gas-solid reaction kinetics. Catal Commun 2009;10(4): 406–11.

[108] Faungnawakij K, Fukunaga T, Kikuchi R, Eguchi K. Deactivation and regeneration behaviors of copper spinel-alumina composite catalysts in steam reforming of dimethyl ether. J Catal 2008;256 (1):37–44.

[109] Gould BD, Chen XY, Schwank JW. n-Dodecane reforming over nickel-based monolith catalysts: Deactivation and carbon deposition. Appl Catal A: Gen 2008;334(1–2):277–90.

[110] Shimada H, Imamura M, Matsubayashi N, Saito T, Tanaka T, Hayakawa T, et al. Characterization of coke deposited on catalysts by carbon K-edge near edge X-ray absorption fine structure (NEXAFS) spectroscopy. Topics Catal 2000;10(3–4): 265–71.

[111] Oudghiri-Hassani H, Rakass S, Abatzoglou N, Rowntree P. Inhibition of carbon formation during steam reforming of methane using thiol-coated nickel catalysts. J Power Sources 2007;171(2):850–5.

[112] Wang SB, Lu GQ. A comprehensive study on carbon dioxide reforming of methane over Ni/γ-Al_2O_3 catalysts. Ind Eng Chem Res 1999;38(7):2615–25.

[113] Li XC, Li SG, Yang YF, Min W, Fei H. Studies on coke formation and coke species of nickel-based catalysts in CO_2 reforming of CH_4. Catal Lett 2007;118(1–2):59–63.

[114] Shamsi A, Baltrus JP, Spivey JJ. Characterization of coke deposited on Pt/alumina catalyst during reforming of liquid hydrocarbons. Appl Catal A: Gen 2005;293:145–52.

[115] Altin O, Eser S. Analysis of carboneceous deposits from thermal stressing of a JP-8 fuel on superalloy foils in a flow reactor. Ind Eng Chem Res 2001;40 (2):589–95.

[116] Guell BM, Babich I, Nichols KP, Gardeniers JGE, Lefferts L, Seshan K. Design of a stable steam reforming catalyst-A promising route to sustainable hydrogen from biomass oxygenates. Appl Catal B: Env 2009;90(1–2):38–44.

[117] Querini CA, Fung SC. Temperature-programmed oxidation technique – kinetics of Coke O_2 reaction on supported metal-catalysts. Appl Catal A: Gen 1994;117(1):53–74.

[118] Bernardo CA, Alstrup I, Rostrup-Nielsen JR, Tavares MT. Behavior of bimetallic supported catalysts in the steam reforming of methane. I. Coke deposition. Actas Simp Iberoam Catal 9th 1984;2:1523–4.

[119] Pompeo F, Nichio NN, Ferretti OA, Resasco D. Study of Ni catalysts on different supports to obtain synthesis gas. Int J Hydrogen Energy 2005;30 (13–14):1399–405.

[120] Querini CA, Fung SC. Coke characterization by temperature programmed techniques. Catal Today 1997;37(3):277–83.

[121] Sanchez B, Gross MS, Dalla Costa B, Querini CA. Coke analysis by temperature-programmed oxidation: morphology characterization. Appl Catal A: Gen 2009;364(1–2):35–41.

[122] Rass-Hansen J, Christensen CH, Sehested J, Helveg S, Rostrup-Nielsen JR, Dahl S. Renewable hydrogen: carbon formation on Ni and Ru catalysts during ethanol steam-reforming. Green Chem 2007;9 (9):1016–21.

[123] Laosiripojana N, Assabumrungrat S. Methane steam reforming over Ni/Ce-ZrO_2 catalyst: influences of Ce-ZrO_2 support on reactivity, resistance toward carbon formation, and intrinsic reaction kinetics. Appl Catal A: Gen 2005;290(1–2):200–11.

[124] Shamsi A, Johnson CD. Effect of pressure on the carbon deposition route in CO_2 reforming of $^{13}CH_4$. Catal Today 2003;84(1–2):17–25.

[125] Liu BS, Au CT. Carbon deposition and catalyst stability over La_2NiO_4/γ-Al_2O_3 during CO_2 reforming of methane to syngas. Appl Catal A: Gen 2003;244(1):181–95.

[126] Lee JH, Joo OS, Baek YS, Yu YH, Jung KD. Accumulation of the carbonaceous species on the Ni/Al_2O_3 catalyst during CO_2 reforming of methane. Bull Korean Chem Soc 2003;24(11):1623–6.

[127] Effendi A, Hellgardt K, Zhang ZG, Yoshida T. Characterisation of carbon deposits on Ni/SiO_2 in the reforming of CH_4-CO_2 using fixed- and fluidised-bed reactors. Catal Commun 2003;4(4):203–7.

[128] Nagaoka K, Seshan K, Lercher JA, Aika K. Activation mechanism of methane-derived coke (CHx) by CO_2 during dry reforming of methane – comparison for Pt/Al_2O_3 and Pt/ZrO_2. Catal Lett 2000;70(3–4):109–16.

[129] Chen YG, Tomishige K, Yokoyama K, Fujimoto K. Promoting effect of Pt, Pd and Rh noble metals to the $Ni_{0.03}Mg_{0.97}O$ solid solution catalysts for the reforming of CH_4 with CO_2. Appl Catal A: Gen 1997;165(1–2):335–47.

[130] Irusta S, Cornaglia LM, Lombardo EA. Hydrogen production using Ni-Rh on ZrO_2 as potential low-temperature catalysts for membrane reactors. J Catal 2002;210(2):263–72.

[131] Li CL, Fu YL. Effect on the carbon deposit in CO_2 reforming of CH_4 over Ni/Ce-Zr-Al-Ox catalyst by adding steam. Acta Physico-Chimica Sinica 2004;20:906–10.

[132] Verykios XE. Mechanistic aspects of the reaction of CO_2 reforming of methane over Rh/Al_2O_3 catalyst. Appl Catal A: Gen 2003;255(1):101–11.

[133] Wang YH, Xu BQ. Comparative study of atmospheric and high pressure CO_2 reforming of methane over Ni/MgO-AN catalyst. Catal Lett 2005;99(1–2):89–96.

[134] Wang YH, Wang H, Li Y, Zhu QM, Xu BQ. Performance of Ni/MgO-AN catalyst in high pressure CO_2 reforming of methane. Topics Catal 2005;32(3–4):109–16.

[135] Quincoces CE, Basaldella EI, De Vargas SP, Gonzalez MG. Ni/γ-Al_2O_3 catalyst from kaolinite for the dry reforming of methane. Mater Lett 2004;58(3–4):272–5.

[136] Nikolla E, Schwank J, Linic S. Promotion of the long-term stability of reforming Ni catalysts by surface alloying. J Catal 2007;250(1):85–93.

[137] Saadi S, Hinnemann B, Helveg S, Appel CC, Abild-Pedersen F, Nørskov JK. First-principles investigations of the Ni_3Sn alloy at steam reforming conditions. Surf Sci 2009;603(5):762–70.

[138] Nikolla E, Schwank JW, Linic S. Hydrocarbon steam reforming on Ni alloys at solid oxide fuel cell operating conditions. Catal Today 2008;136(3–4):243–8.

[139] Voorhies A. Carbon formation on catalytic cracking. Ind Eng Chem Prod Res Dev 1945;37:318–22.

[140] Froment GF, Bischoff KB. Non steady state behavior of. Fixed bed catalytic reactors due to catalyst fouling. Chem Eng Sci 1961;16(3–4):189–201.

[141] Froment GF, Bischoff KB. Kinetic data and product distributions from fixed bed catalytic reactors subject to catalyst fouling. Chem Eng Sci 1962;17(1):105–14.

[142] Masamune S, Smith JM. Performance of fouled catalyst pellets. AICHE J 1966;12:384–94.

[143] Ostrovskii NM. New models of catalyst deactivation by coke: I. Multilayer coke formation via the consecutive mechanism. Kinet Catal 2001;42(3):317–25.

[144] Fuentes GA. Catalyst deactivation and steady-state activity: a generalized power-law equation model. Appl Catal 1985;15:33–40.

[145] Gudlavalleti S, Ros T, Lieftink D. Thermal sintering studies of an autothermal reforming catalyst. Appl Catal B: Env 2007;74(3–4):251–60.

CHAPTER

11

Desulfurization for Fuel Cells

Santosh K. Gangwal

Southern Research Institute, 5201 International Drive, Durham, NC 27712, USA

OUTLINE

Fuel Cells **DOI: 10.1016/B978-0-444-53563-4.10011-2**

11.1. INTRODUCTION

Over 60% of the precious fuel energy input to conventional power plants and transportation vehicles ends up as low-grade waste heat. Not only are these conventional energy systems undesirable due to their low efficiencies, they also result in a larger impact to the environment compared to higher efficiency energy systems. Fuel cell systems are significantly more energy efficient and cleaner than conventional energy systems [1–4]. Thus their development and deployment has attracted worldwide attention over the past two decades. Due to environmental regulations and/or to protect catalyst or equipment, desulfurization is an integral step in nearly all conventional and advanced power systems that use carbonaceous fuels, including fuel cells. This chapter discusses desulfurization methods that can be used for fuel processors for fuel cells with a particular emphasis on desulfurization using solid sorbents for compact fuel processors.

Pure hydrogen would be the fuel of choice for most types of stationary and mobile fuel cells other than those operating at high temperatures such as solid oxide fuel cells. Unfortunately, little or no infrastructure exists for widespread storage and distribution of large quantities of H_2. This necessitates that bulk quantities of H_2 be produced as well as consumed at or near the point of use, such as a petroleum refinery or an ammonia plant. Presently, natural gas is the primary source for producing bulk quantities of H_2 [4]. Other potential sources of H_2 for use in fuel cell systems include coal, biomass, alcohols and petroleum derivatives such as liquefied petroleum gas (LPG), gasoline and diesel. H_2 production first involves gasification, reforming, or partial oxidation of these fuels to produce a reformate gas or synthetic gas (syngas) consisting of CO and H_2 as fuel constituents [1]. For the purpose of this chapter reformate gas and syngas have the same meaning and are used interchangeably. Syngas can be directly fed to high temperature fuel cells such as molten carbonate fuel cells (MCFC) and solid oxide fuel cells (SOFC) that are capable of internally reforming CO. For fuel cells that cannot tolerate CO such as proton exchange membrane fuel cell (PEMFC), the syngas is subjected to water-gas shift to convert most of the CO to H_2 and additional CO removal steps such as selective oxidation or methanation that reduce the CO to single digit ppmv levels [1,5].

Natural gas and petroleum derivatives are the desirable fuels for fuel cells because they are easy to obtain through a wide distribution network. Environmental regulations have driven the sulfur levels in many of these fuels down to very low levels. Based on these factors, these fuels are the primary candidates that can lead to the development of compact fuel processors employing fuel cells. Even after meeting environmental regulations, these fuels still contain sulfur compounds such as mercaptans, sulfides, and thiophenes which are poisons for the catalysts used in the process steps (steam reforming, water-gas shift, preferential oxidation, methanation) for converting these fuels to H_2 [3,5–12]. It is thus necessary to remove most of these sulfur compounds prior to the catalytic reforming step unless an expensive sulfur-tolerant catalyst is used. During reforming of these fuels to syngas, the remaining small quantities of sulfur compounds, if any, are mostly converted to hydrogen sulfide (H_2S) and a smaller portion to carbonyl sulfide (COS). However, since H_2S even at a concentration of 0.1–1 ppmv is a strong poison for the fuel cell anode catalysts [5,12], the syngas may need to undergo a polishing desulfurization step [11,13] and a guard bed may be needed to prevent accidental H_2S slip. This would necessitate nearly complete desulfurization of these fuels before the reforming step followed by polishing after the reforming step before supplying H_2 or syngas to fuel cells.

Solid fuels such as coal and biomass have also received significant attention for providing syngas or H_2 to fuel cells particularly in conjunction with research and development of integrated gasification combined cycle (IGCC) and integrated gasification fuel cell (IGFC) power systems, and co-production plants that produce electricity, hydrogen, and liquid transportation fuels [11,14–21]. Unlike natural gas and petroleum derivatives, it is inconvenient and impractical to desulfurize these solid fuels before reforming. Desulfurization before the reforming step is not actually necessary because these solid fuels are thermally rather than catalytically reformed (gasified) using steam and/or oxygen at elevated temperatures to produce syngas. During gasification, the sulfur in these fuels is converted mostly to H_2S and some to COS.

Unlike the low H_2S levels in syngas from catalytic reforming of pre-desulfurized natural gas and petroleum derivatives, the H_2S levels in syngas from these solid fuels could be as high as several thousand ppmv depending directly on the original sulfur content of the solid fuel. To completely desulfurize this syngas, a bulk H_2S removal step, a polishing H_2S removal step, and a guard bed may be needed. Clean, sulfur free, syngas can be used to produce both electricity from turbines or fuel cells and liquid transportation fuels using established processes like Fischer–Tropsch synthesis [22]. The nearly complete desulfurization of syngas is not only necessary for protecting the fuel cell anode catalyst, but it is also a necessity to prevent synthesis catalyst poisoning.

One obvious way to get around the need for desulfurization prior to the fuel cell would be to use sulfur-free fuels such as methanol, ethanol, or Fischer–Tropsch-based transportation fuels. Not only are alcohol fuels sulfur-free, they are also generally easier to reform. However, alcohol fuels have relatively lower energy density and they do not enjoy a wide distribution network. As the focus is desulfurization, these sulfur-free fuels will not be discussed further in this chapter.

11.2. SCOPE

The focus of this chapter will be on the desulfurization of natural gas and petroleum derivatives prior to the reformer and/or the removal of H_2S from syngas after the reformer for the development of compact fuel processors. Desulfurization of syngas from solid fuel gasification is included in the scope due to significant current interest although solid fuels will not lead to compact fuel processors. A general schematic of a fuel cell system showing the positions of the desulfurizers is shown in Fig. 11.1. As stated in the introduction, nearly complete desulfurization of fuels down to 0.1 to 1 ppmv or lower H_2S levels in syngas or H_2 is the requirement for fuel cells. Development of fuel cell systems is benefiting not only due to their high energy efficiency and environmental friendliness, but also from the potential availability of deep desulfurized liquid fuels. This results from environmental regulations that now require less than 15 ppmw sulfur in diesel and 30–80 ppmw sulfur in gasoline [23,24]. This chapter focuses on newer methods that are being developed for the desulfurization of natural gas and petroleum derivatives prior to reforming, and desulfurization of raw syngas following gasification or reforming. The discussion of these methods will be in context with various types of fuel cells and tightening environmental regulations

Mature desulfurization methods such as amine scrubbing of natural gas [25,26], Merox mercaptan removal process [26,27], hydrodesulfurization (HDS) of petroleum derivatives [11,28], or desulfurization of syngas using gas-liquid absorption processes such as Rectisol and Selexol [25] are commercially practiced

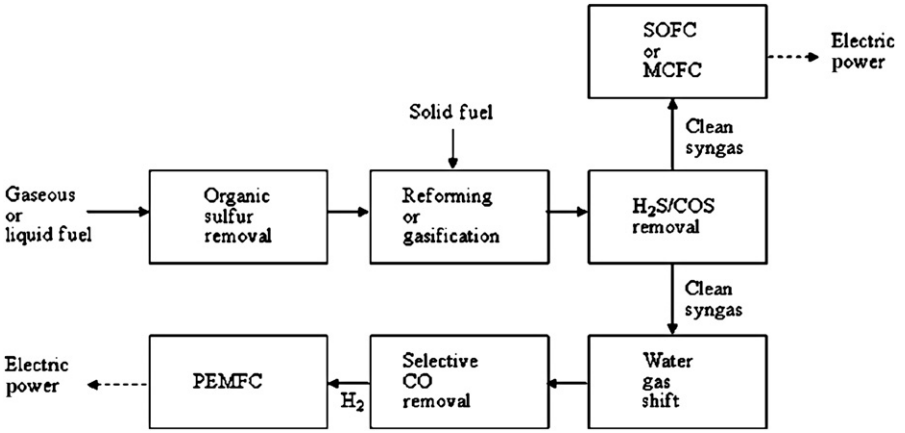

FIGURE 11.1 Generalized fuel to electric power scheme for fuel cells.

and are excluded from the scope except for comparison to newer developmental methods. HDS catalysts in particular are undergoing significant development for deep desulfurization [11] to enable HDS to meet the new sulfur standards for gasoline (30–80 ppmw) and diesel (15 ppmw). However, the deeply desulfurized fuels meeting these new standards still cannot be used in fuel cell systems without further desulfurization.

Among the newer methods being developed, the focus is on gas-phase and liquid-phase desulfurization using solid sulfur sorbents before the reformer and syngas desulfurization after the reformer or gasifier. Sorbent-based desulfurization processes are the most likely candidates for compact fuel processors employing fuel cells and they have the potential to reduce the H_2S in syngas to less than 0.1 ppmv. A discussion is also provided on selective oxidation-assisted adsorption that has received significant attention over the past decade. Other developmental methods for desulfurization of liquid petroleum derivatives such as bio-desulfurization [29–31] and selective extraction using ionic liquids [32–34] are in their infancy at present. Thus they are considered to be outside the scope of this chapter and will not be discussed further. Gas separation membrane-based processes [35–38] are also excluded from the chapter as they are unlikely to lead to compact fuel processors.

11.3. GAS PHASE DESULFURIZATION UPSTREAM OF REFORMER

11.3.1. Natural Gas and Liquefied Petroleum Gas (LPG)

11.3.1.1. Background

Pipeline natural gas, as opposed to wellhead natural gas, is an ideal fuel for large and small fuel cells because of its very low regulated sulfur content and its ready availability for industrial and residential use through an extensive production and distribution infrastructure. The primary fuel constituent of natural gas is methane. As received from the wellhead, it also contains smaller quantities of C_2-C_4 alkanes and impurities including H_2S, methyl mercaptan, mercury, and inerts (CO_2, nitrogen and water vapor). Wellhead natural gas undergoes extensive processing to meet pipeline specifications including operations such as CO_2 and H_2S absorption, pressure-swing or glycol-based dehydration, mercury adsorption, cryogenic or adsorption-based

nitrogen separation, and fractionation of natural gas liquids (C_2-C_4 alkanes) [25,26]. The amine absorption-based acid gas removal process for nearly complete desulfurization of sour natural gas at the wellhead to the pipeline specification of <4 ppmv is well established.

Liquefied Petroleum Gas (LPG), like pipeline natural gas, enjoys a large distribution network, and is a desirable low sulfur fuel for the development of a fuel cell system with a potential to serve a niche market. It is a versatile fuel that is used widely in decentralized residential and industrial applications requiring heat. It consists of predominantly propane and butane in various combinations. They are byproducts of both pipeline natural gas production plants as well as petroleum refineries. Unlike pipeline natural gas (CH_4), LPG becomes a liquid under modest pressure. This property of LPG makes it easier than natural gas to store and transport in vessels and cylinders.

As required by law for safety reasons, sulfur bearing odorants are intentionally added to both cleaned natural gas and LPG prior to their distribution and sale. Typical sulfur containing compounds present naturally and added as odorants are listed in Table 11.1. The typical odorants used are mercaptans, sulfides, and tetrahydrothiophene (THT) [39]. THT is commonly used to odorize natural gas in

TABLE 11.1 Typical Sulfur Compounds and Odorants in Natural Gas and LPG

Name	Formula	Structure	Boiling point (°C)
Hydrogen sulfide	H_2S	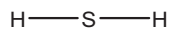	−60
Carbonyl sulfide	COS		−50
Methyl mercaptan	CH_3SH	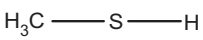	6
Ethyl mercaptan	C_2H_5SH	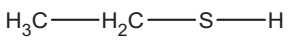	36
Dimethyl sulfide	C_2H_6S	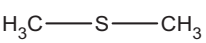	38
t-Butyl mercaptan	$C_4H_{10}SH$	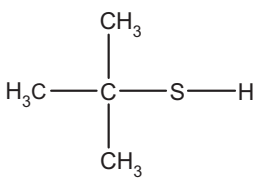	64
Tetrahydrothiophene	C_4H_8S	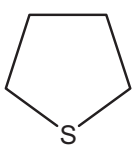	120

Europe while tert-butyl mercaptan (TBM) and sulfides, such as dimethyl sulfide (CH_3SCH_3) are commonly used in the USA. [40]. LPG is most often odorized with ethyl mercaptan (C_2H_5SH). The total sulfur in pipeline natural gas including odorants is typically in the 2–20 ppmv range [39] while it could be as high as 120 ppmv in LPG [40]. In addition to a widely available supply infrastructure, the low sulfur concentrations also make these fuels highly desirable for compact fuel cell systems.

11.3.1.2. Adsorption

Adsorption at or close to ambient temperatures could be a cost-effective desulfurization approach in comparison to HDS followed by H_2S removal which needs hydrogen and high temperature. However, the presence of H_2S and potential presence of COS, methyl mercaptan (CH_3SH), as well as a host of other sulfur-containing organic compounds (odorants) makes desulfurization of pipeline natural gas or LPG using adsorption a complex problem. Desulfurization using sorbents is a bigger challenge with LPG, not only because of its higher sulfur content but also because C_3-C_4 hydrocarbons are likely to provide greater competition to sulfur compounds for adsorption sites than methane. It is not surprising to see continued intense research to develop better, more universal, sorbent systems [3,39–48] even though major catalyst companies such as BASF offer commercial products like their Selectra Series D adsorbents for this purpose. A number of commercial companies such as FuelCell Energy, Hyradix, Engelhard, Siemens-Westinghouse, Idemitsu Kosan, Samsung, TDA Research, UOP, and Tokyo Gas have been involved in this research [39,41–44,46,49–54].

11.3.1.2.1. DESIRABLE SORBENT CHARACTERISTICS

Generally desirable characteristics of a sorbent for cleaning low sulfur concentration fuels such as natural gas and LPG for fuel cell applications are listed below:

- High activity – removal of all sulfur compounds down to <0.1 ppmv before breakthrough above 0.1 ppmv of the first compound(s) that breakthrough.
- High sulfur capacity (at least 1 g S/100 g sorbent, preferably 2.5–3 g S per 100 g sorbent) prior to breakthrough as defined above.
- No external heating of sorbent or fuel required for operation.
- Low exothermicity.
- Color change due to sulfur compound adsorption to provide a continuous visual indication of the impending breakthrough.
- Non-pyrophoric.
- Involves simple preparation which can be easily scaled up using commercially available equipment.
- Fully and simply regenerable, if designed for reuse, in an environmentally acceptable manner.
- Very low cost if non-reusable (disposable).
- Disposable as non-hazardous waste upon being spent.

These characteristics are generally also desirable in sorbents for desulfurization of other fuels such as gasoline, diesel, and jet fuel.

11.3.1.2.2. CONVENTIONAL SORBENTS

Sorbent materials based on activated carbon, zeolite, activated alumina, and base metal oxides such as CuO and ZnO are commercially available. Activated carbons and activated alumina operate via physisorption or chemisorption at room temperature but typically have low capacity. ZnO requires the presence of H_2 due to the presence of organic sulfur compounds. It operates via chemical reaction (reactive adsorption) to form ZnS but requires high temperature (>200 °C) as a C-S and/or H-S bond needs to be broken. The mechanism involves HDS followed by immediate reaction

of H_2S with ZnO. Activated carbons are generally considered non-regenerable and have low capacity. Capacity of these sorbents can be increased by impregnation of copper or potassium hydroxide and they apparently can be regenerated using a multiple-bed arrangement for continuous operation to reduce the sulfur in natural gas to <0.1 ppmv [51]. Zeolites operate via physisorption at room temperature but lose capacity due to competitive adsorption if higher hydrocarbons and polar compounds such as water and/or CO_2 are present in the fuel.

11.3.1.2.3. RECENT SORBENT DEVELOPMENT RESEARCH

Siemens-Westinghouse [49] tested several commercial and developmental sorbent materials obtained from various suppliers for pipeline gas desulfurization using natural gas containing 4.1–8.4 ppmv sulfur at 0.44 MPa and room temperature. These sorbents included ZnO, plain activated carbon, activated carbons with copper and chromium, nickel oxide, molecular sieve 13X, copper impregnated zeolite, CuO-ZnO, and some proprietary materials. Their results showed that dimethyl sulfide (DMS) broke through first irrespective of the sorbent used or irrespective of the other sulfur compounds present. The breakthrough capacity was provided in terms of a DMS performance index. From this index and the known average concentrations of DMS and total sulfur in the feed natural gas, the present author has calculated an approximate sulfur breakthrough capacity at 0.1 ppmv S in the effluent. The calculated results are shown in Fig. 11.2. As seen, the capacity ranged from 0.15 to 20 mg S/cm^3 sorbent. The two best sorbents from the study were a copper-impregnated zeolite-Y from Pacific Northwest National Laboratory (PNNL) [47] and a proprietary sorbent T from an unknown supplier. These sorbents had >20 fold capacity versus the third best sorbent, a molecular sieve 13X. Plain activated carbon as well as impregnated activated carbons had relatively low capacities. The material T was stated to operate via physisorption and was shown to be non-pyrophoric.

TDA Research [39,41,42] has developed a proprietary Sulfa Trap™ series of sorbents for natural gas and LPG which operates at

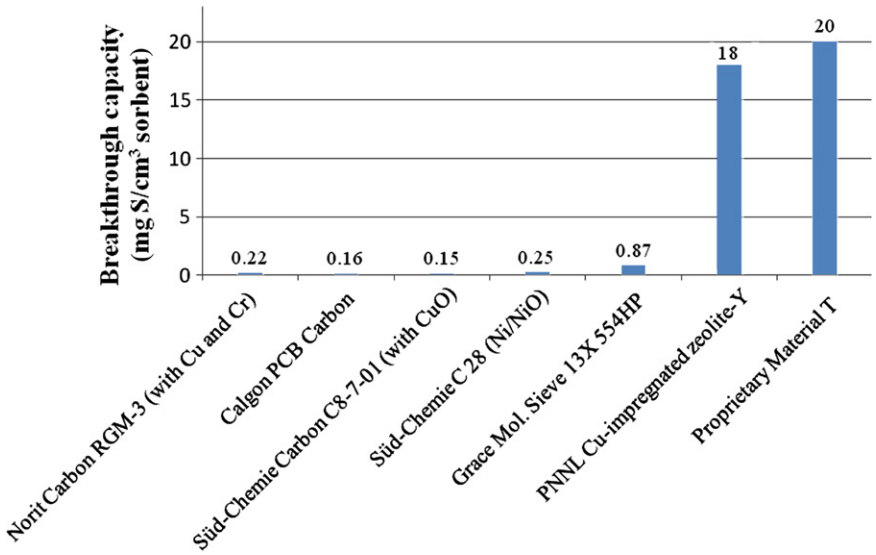

FIGURE 11.2 Sorbent breakthrough capacity for natural gas (4–8 ppmv S) at room temperature [49].

ambient temperature, has 25–30 fold greater capacity than activated carbon, is regenerable and non-pyrophoric, and has built in indication (probably color) of the movement of the sulfur adsorption wave through the bed. The sorbents could be regenerated by heating to 300 °C in the presence of H_2 or natural gas. The sorbents were also claimed to be minimally affected by the presence of moisture. Breakthrough capacity for DMS in natural gas was about 3 g/100 g sorbent. The sulfur capacity for LPG was stated to be 2.35 wt%. The sorbent cost was estimated to be \$10–25/lb depending on batch size manufactured and the cost for desulfurizing natural gas was estimated to be \$4.71/1000 m^3.

Energy Research Centre of Netherlands (ECN) [40] has concentrated on the development of sorbents for removing THT from natural gas and ethyl mercaptan from LPG. They have tested transition metal impregnated carbon, non-impregnated carbon, CuO-ZnO-Al_2O_3, activated alumina, Tokyo Gas zeolite TOSPIX94 (presumably, silver exchanged Y zeolite [50]), molecular sieve-13X, supported NiO, and their own proprietary NGDM (Natural Gas Desulfurization Material) series of sorbents. A latter patent application by ECN [48] indicates that these proprietary sorbents are sepiolite and metal-promoted sepiolite. Sepiolite is stated to be an inexpensive and environmentally friendly naturally occurring material.

The natural gas tested by ECN contained 4.5 ppmv THT and the LPG tested contained 30 ppmv ethylmercaptan (EM). They also tested a synthetically prepared natural gas with 1.4 ppmv DMS and 4 ppmv TBM. The sorbents tested were in the form of 1–2 mm extrudates or pellets and their test conditions were 0.11 MPa and 10–40 °C. The BET surface areas and capacities of various sorbents at 0.1 ppmv sulfur breakthrough are shown in Table 11.2.

As seen, the BET surface area appears to have no correlation with capacity. The promoted alumina had the best performance for removing THT from natural gas. However, it was not tested for the other odorants. The Tokyo Gas zeolite and the proprietary promoted NGDM1 sorbents (probably Cu- and $FeCl_3$-impregnated sepiolite based on ECN′s patent application [48]) had the best overall performance at all conditions among the sorbents tested. The

TABLE 11.2 Sulfur Capacity of Sorbents Tested at ECN [40]

	Fuel	**Natural gas**	**LPG**	**Simulated natural gas**
	Odorant	**THT**	**EM**	**DMS + TBM**
	Conc. (ppmv)	**4.5**	**30**	**1.4 + 4.0**
	Temp (°C)	**Ambient**	**40**	**40**
Sorbent	**BET surface area (m^2/g)**	**Sulfur capacity at 0.1 ppmv breakthrough (mg S/cm^3 sorbent)**		
Promoted alumina Alcoa SAS-6	200	4.9	NM	NM
Tokyo gas zeolite TOSPIX94	700	4.0	7.3	> 4.0
Molecular Sieve 13X Aldrich	540	3.6	0.2	NM
Norit Carbon RGMI	1300	0.7	NM	1.1
Unpromoted NGDM1	275	3.6	< 0.1	0.3
X-Promoted NGDM1	NM	3.2	1.5	2.9
Y-Promoted NGDM1	NM	4.5	1.8	4.3

NM = Not measured.

unpromoted NGDM1 and molecular sieve 13X had good performance for removing THT from natural gas at ambient temperature. However, they gave poor performance for the other odorants at 40 °C. The zeolite showed a strong exotherm upon initial exposure and required a special pretreatment to prevent it. For a 1KW_e PEMFC, ECN has estimated a ~2 liter annual requirement of their best NGDM sorbent. The capacities ECN reported for all materials are actually four- to sevenfold lower than those reported by Siemens-Westinghouse and TDA Research for their best materials. In contrast to ECN's sorbents, TDA Research did not see any THT breakthrough for any of the sorbents they tested for the 1400 min duration of their tests. The reason for this discrepancy among the results is unclear.

Satokawa et al. [50,55] from Tokyo Gas have studied Ag exchanged zeolites with Ag content ranging from 0% to 18 wt% for simultaneous room temperature removal of DMS and TBM from pipeline natural gas in the presence of up to 0.1 vol% moisture. The sorbents were prepared from a commercial Na-Y zeolite with a SiO_2/Al_2O_3 ratio of 5.7 by ion exchange using an aqueous $AgNO_3$ solution. As silver content increased from 0% to 18 wt%, the overall capacity increased from 0 g to 4.1 g sulfur per 100 g sorbent. The breakthrough curve of DMS was much sharper than TBM indicating that TBM was more strongly bound than DMS, even though the breakthrough capacity (at 0.1 ppmv) of TBM was much lower than DMS. Lee et al. [44] showed that THT was even more strongly adsorbed than TBM on these sorbents. Based on these results, they suggested using two beds in series consisting of the cheaper Na-Y zeolite followed by the expensive Ag exchanged zeolite to achieve higher capacity and reduce overall cost of desulfurization.

Temperature-programmed desorption of a DMS sulfided sorbent eluted DMS as pure compound indicating coordination of the DMS molecules on Ag cations without dissociation [50]. Sorbents could be partially or fully regenerated by heating in air at 500 °C. Full regeneration was achieved for the sorbents with Ag contents of 5 wt% or less. The color of the sorbent with 15 wt% Ag changed progressively from white to yellow to orange to brown with adsorption. This is a desirable property for indicating when replacement is needed and for protecting the downstream catalysts in a fuel cell system.

Lee et al. [44] are developing alkali metal-containing titanosilicate (ETS-10) and alumina-modified titanosilicate (ETAS-10) for simultaneous THT and TBM removal from natural gas. These were prepared by gel formation at a pH of 11.5 from precursor compounds followed by hydrothermal treatment at 200 °C. These sorbents had a saturation capacity of TBM of about 2 g S/100 g sorbent but breakthrough capacity has not been reported. The sorbents could be fully regenerated by heating to <500 °C in air, methane or inert gas. Over five cycles, no degradation in capacity was observed.

Yang and coworkers [3,45] have developed Cu(I)-exchanged Y zeolite and CuCl on mesoporous (MCM-41 and SBA-15) supports as sorbents for removing DMS from natural gas. The Cu(I)Y zeolite sorbent preparation involved passing CuCl vapor over HY zeolite at up to 430 °C followed by oxygen treatment at 200 °C to first yield Cu(II)Y zeolite. Auto-reduction in helium at 450 °C yielded the Cu(I)Y zeolite. Monolayer CuCl/MCM-41 and CuCl/SBA-15 were prepared by heating the appropriate solid mixtures in air to 380 °C to yield about 5–6 mmoles Cu per g sorbent. These Cu sorbents prepared by Yang and coworkers were shown to have similar activity and breakthrough capacity but superior regenerability compared to fully exchanged Ag-Y zeolite sorbents developed by Satokawa et al. [50,55]. The Cu sorbents were also found to be fully regenerable at 350 °C, and diffusion resistances were found

to be lower for the Cu sorbents prepared using mesoporous supports.

Idemitsu Kosan Company has recently patented CeO_2, 50/50 CeO_2-ZrO_2, 20/80 CeO_2-Al_2O_3, and 10 wt% metal-impregnated CeO_2 sorbents for desulfurizing gaseous fuels, particularly LPG [46]. The CeO_2 and CeO_2-ZrO_2 were prepared by coprecipitation of precursor nitrates with a base (NaOH or NH_4OH) at a pH of about 13 followed by washing, drying, and calcination. The CeO_2-Al_2O_3 was prepared by adding alumina to a cerium nitrate solution followed by drying and calcinations. The BET surface areas of these oxides were in the 120−200 m^2/g range and the mean crystallite size of CeO_2 was reported to be 3−5 nm. The adsorption breakthrough tests of the oxides and mixed oxides with 10 ppmv each of COS, DMS, TBM, and dimethyl disulfide in propane at room temperature showed a capacity prior to reaching 0.1 ppmv sulfur in the outlet gas of about 1 g S/100 ml sorbent based on calculations by the author from the data provided. The breakthrough capacity increased by 75% for COS by using Ni-, Ag-, or Mn-impregnated CeO_2 sorbents and that for DMS increased by a factor of about 2.5 by using Ag-impregnated CeO_2 sorbent. No regeneration data were presented so it is not clear whether these sorbents are regenerable.

Cui et al. [56] have recently attempted to optimize the use of modified activated carbons for adsorption of all sulfur compounds present in pipeline gas in Honolulu containing 5−10 ppmv total sulfur. Oxidation using HNO_3 and H_2O_2 and impregnation using Cu, Zn, Fe, Na, and K precursors were the methods used to modify a commercial coconut shell-derived carbon. Through mathematical modeling of experimental data, they found that a combination of about 11.9 kg of a $FeCl_3$ impregnated carbon and about 0.85 kg of a $Zn(NO_3)_2$ impregnated carbon gave the best composite sorbent amount that had the potential for completely desulfurizing natural gas for a 1 KW fuel cell for 1 year without replacement. These sorbents were not shown to be regenerable; also the amounts required were much higher than those reported by others.

11.3.1.2.4. APPLICATION TO FUEL CELL SYSTEMS

The most likely natural gas and LPG sulfur sorbents that could find application in a compact fuel cell system are those that operate without having to heat them or the fuel and have most of the desirable characteristics as mentioned above. Since the sulfur content of natural gas or LPG is low, the sorbent bed could be placed upstream of the reformer for nearly complete desulfurization or the fuel could be fed as is to a reformer that is using a sulfur tolerant reforming catalyst. In this later scenario, the sulfur in the fuel will appear as H_2S in the syngas and desulfurization would take place downstream of the reformer, which is discussed in a later section.

11.3.1.3. Selective Oxidation Followed by Adsorption

Engelhard [57,58] has developed and patented an alternative approach to passive adsorption based on selective oxidation. The approach was developed to circumvent the low capacity of passive adsorbents at room temperature for desulfurizing a fuel containing a complex mixture of sulfur compounds and odorants. In their process, a small amount of air is mixed with the hydrocarbon gas to achieve an O_2 to C mol ratio of about 0.02. The gas is then heated to 275−300 °C and passed over a monolithic platinum-based sulfur-tolerant catalyst to selectively oxidize all sulfur compounds to SO_x. The SO_x is then adsorbed on an inexpensive alkali metal-based adsorbent at the outlet temperature. The process was shown to achieve [57] essentially complete sulfur removal down to ppb levels from a synthetic natural gas containing 5.25 ppmv each of COS, DMS, THT, and ethyl mercaptan until SO_2 breakthrough from the

sorbent. The desulfurization was found to be very efficient for natural gas but not for LPG, potentially due to reactions of some of the higher hydrocarbons. Although the process is attractive for natural gas desulfurization, the added hardware required for heating, the oxidation reactor, and the additional safety requirements associated with introducing O_2 in the fuel probably does not justify the cost for its application to fuel cells.

Researchers at Oak Ridge National Laboratory [59,60] and National Energy Technology Laboratory [61,62] have evaluated specially prepared as well as commercial activated carbons for selective oxidation of H_2S, via $H_2S + (1/2)\ O_2 \rightarrow (1/n)\ S_n + H_2O$, and other odorants to elemental S at 135–175 °C. Note that this temperature range is significantly lower than the one used by Engelhard [57,58] for complete oxidation to SO_x. The process concept involves highly selective oxidation to S and adsorption of liquid S within the pores of the carbon. The process worked well for H_2S but poorly for most of the other odorants in natural gas. It is thus considered applicable primarily for H_2S removal downstream of the reformer or gasifier and will be discussed in a later section.

11.3.2. Gasoline, Jet Fuel, and Diesel

This section describes research and process development efforts for gas-phase desulfurization of these liquid fuels prior to the reformer whereas liquid-phase desulfurization of these liquid fuels prior to the reformer is covered in Section 11.4.

11.3.2.1. Background

Gasoline, jet fuel, and diesel are a highly complex mixture of hydrocarbons and heteroatom compounds containing sulfur, nitrogen, and oxygen. The sulfur contents of gasoline and diesel are currently being regulated down to 30–80 ppmw and 15 ppmw sulfur, respectively. The low sulfur content of these regulated fuels along with their widely available supply infrastructure and high energy density make them highly desirable as candidates for use in fuel cells. Sulfur in jet fuels per specifications, for example, in JP-8, however, is allowed to be as high as 3000 ppmw. Even so, the US military is highly interested in using jet fuels for fuel cells to generate electricity readily in remote locations.

The approximate boiling point ranges are as follows: gasoline: 38–204 °C, jet fuel (JP-8): 175–300 °C, and diesel: 149–371 °C. In addition to mercaptans and sulfides (see Table 11.1), a few of the numerous thiophenic sulfur compounds present in these fuels are shown in Table 11.3. In the order of boiling points, the sulfur compounds in these fuels include mercaptans, sulfides, disulfides, thiophene, benzothiophene (BT), and dibenzothiophene (DBT). They also contain several alkyl-substituted thiophenes, benzothiophenes, and dibenzothiophenes.

11.3.2.2. Hydrodesulfurization (HDS)

HDS, the primary sulfur removal technology used in refineries, uses very high pressure hydrogen at 330–370 °C to remove sulfur from these fuels as H_2S. The H_2S/H_2 stream is then sent to an amine scrubber to absorb the H_2S. The H_2S is then desorbed and sent to a Claus plant for sulfur recovery. HDS is highly unlikely to be used in tandem with a fuel cell system but is briefly mentioned here as a benchmark technology in comparison to newer processes being developed and that could be used in a fuel cell system. Conventional HDS is very efficient at removing mercaptans, sulfides, and disulfides but less efficient at removing thiophenes.

The ultra-low sulfur regulations for gasoline and diesel announced around the turn of the century sparked the development and commercialization of significantly improved HDS catalysts such as STARS, SMART, and NEBULA with up to four times the activity of conventional Co-Mo-Al_2O_3 HDS catalysts as described in recent reviews [63,64]. Based on these new catalysts that are aggressively promoted by

TABLE 11.3 Thiophenic Compounds in Petroleum-Derived Fuels

Name	Formula	Structure	Boiling point (°C)
Thiophene	C_4H_4S	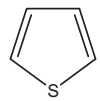	84
2-Methyl thiophene	C_5H_6S	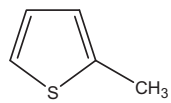	112–113
Benzothiophene	C_8H_6S	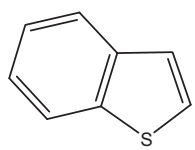	222
Dibenzothiophene	$C_{12}H_8S$	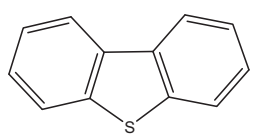	332–333
4-Methyl dibenzothiophene	$C_{13}H_{10}S$	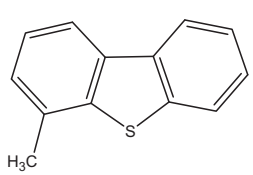	–
4,6 Dimethyl dibenzothiophene	$C_{14}H_{12}S$	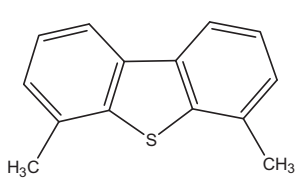	–

manufacturers, HDS maintains its dominant position as sulfur removal technology in the petroleum industry, even though it has the following limitations for deep desulfurization of gasoline and diesel [8,65]:

- High cost due to higher pressure hydrogen requirement, increased reactor size, and/or expensive catalysts.
- Low efficiency in removing sterically hindered dibenzothiophenes from diesel such as 4-methyldibenzo thiophene (4-MDBT) and 4,6-dimethydibenzothiophene (4,6-DMDBT).
- Olefin saturation resulting in octane loss for gasoline requiring selective multi-stage naphtha hydrotreating and/or octane enhancement using selective hydroconversion of the saturated naphtha.
- H_2S recombination with olefins during selective naphtha hydrotreating to form heavier mercaptans.

Recent process development efforts by PNNL to incorporate HDS using recycled reformate gas, rather than hydrogen, in to fuel cell systems is noteworthy [66].

11.3.2.3. Reactive Adsorption

11.3.2.3.1. PROCESS DEVELOPMENT

The sulfur regulations for gasoline and diesel and the high cost and limitations of HDS encouraged the development of reactive sorbent-based gas-phase bulk desulfurization processes in parallel to the development of improved HDS catalysts [67–72]. Although denoted as reactive adsorption by the scientific community because of the simplicity of the term, these processes are actually not at all based on adsorption; rather they potentially involve both gas-phase catalytic as well as gas-solid non-catalytic chemical reactions to getter sulfur from the fuel into a solid sulfur compound. The most notable developments are the Conoco-Phillips S Zorb gasoline and S Zorb diesel processes for deep desulfurization of full-range naphtha and diesel, respectively [67–69]. The S Zorb gasoline process has been commercialized. The first commercial S Zorb gasoline plant with a capacity of 6000 barrels per day came on line in 2001 at Conoco-Phillips Borger refinery in Texas to produce gasoline with 10 ppmw sulfur. Minimal saturation of olefin and octane loss in gasoline is claimed by the process. Although a number of licenses appear to have been sold, no additional S Zorb gasoline plants appear to have been built. The S Zorb diesel process has been scaled up to a 2–4 barrel/day pilot plant but has not acquired commercial status.

The process has been discussed in detail elsewhere [63,64,67,68]. Briefly, a mixture of H_2 and the fuel are fed into a fluidized bed of a proprietary pre-reduced sorbent containing base metals at conditions shown in Table 11.4.

The base metals react with the sulfur in the sulfur containing compounds such as mercaptans and thiophenes and get sulfided. The hydrocarbon portion of the sulfur compound remains in the fuel stream. The sulfided sorbent is sent to a fluidized-bed air regenerator to burn off sulfur from the sorbent as SO_2. The regenerated sorbent is then sent to a reducer that uses H_2 and the reduced sorbent is circulated back to the sulfider, closing the sorbent loop. The process operates continuously by circulating the necessary amount of sorbent.

11.3.2.3.2. SORBENT PREPARATION AND PERFORMANCE

Although the composition of the S Zorb sorbent is proprietary, zinc oxide may be a major

TABLE 11.4 Fluidized-Bed Desulfurization Operating Conditions for S Zorb Processes

	S Zorb gasoline	S Zorb diesel
Pressure, MPa	0.8–2.2	2.5–3.5
Temperature, °C	343–413	385–413
WHSV, h^{-1}	4–10	1–6

component based on Phillips Petroleum Company patents [73]. Research at Cosmos Research Institute and Cosmos Oil Company reveals the development of a process, that is essentially similar to the S Zorb process, using well-defined Ni/ZnO 'catalysts' [70,72]. The catalyst candidates were prepared by both co-precipitation of precursor Zn and Ni nitrates as well as impregnation of Ni nitrate on to granulated or extruded ZnO powder with alumina and silica binders. The optimum nickel content of the co-precipitated catalyst for desulfurization was found to be 13 wt% [72]. This catalyst reduced the sulfur content of kerosene from 51 ppmw to under 0.1 ppmw for more than 4000 h at a hydrogen partial pressure of 0.45 MPa, temperature of 270–290 °C, and a liquid hourly space velocity of 0.5 h^{-1}. Using catalysts prepared by impregnation, the results showed that no desulfurization occurred from gasoline in the absence of H_2 [70]. However, in the presence of a low H_2 partial pressure (~0.09 MPa), the sulfur content in gasoline was reduced from 310 ppmw to 5–30 ppmw. It was also shown that a poorer desulfurization from 310 ppmw to 200 ppmw occurred if the catalyst was not pre-reduced after air regeneration. Furthermore, it was shown that sulfur removal from diesel not only required higher temperatures (450 °C), but was also not as efficient as that from gasoline. This was probably because of the presence of sterically hindered sulfur compounds such as 4-MDBT and 4,6-DMDBT.

11.3.2.3.3. MECHANISM

A complex multi-step mechanism of desulfurization using these types of bimetallic reactive sorbents (or so called catalysts) has been tentatively proposed with auto-regeneration of Ni [64]. The proposed mechanism involves the formation of a surface NiS_{surf} species followed by transfer of the sulfur to ZnO to form ZnS. In the author's opinion, this transfer of sulfur from NiS_{surf} to ZnO to autoregenerate Ni is highly unlikely. This opinion is supported by recent research at the University of Bourgogne, France [74–76]. The more likely scenario based on this research is that zero-valent Ni and perhaps carbon-modified Ni are good HDS catalysts that promote desulfurization via the HDS route. The reaction of thiophenes with H_2 to probably form H_2S or other sulfur species and a hydrocarbon is shown below using thiophene as an example. ZnO then rapidly reacts with H_2S or other sulfur species to form ZnS and perhaps steam:

$$C_4H_4S + 4H_2 \rightarrow C_4H_{10} + H_2S$$

(Catalyzed by Ni or carbon-modified Ni)

$$ZnO + H_2S \rightarrow ZnS + H_2O$$

The absence of H_2S in the outlet gas suggests that the H_2S–ZnO reaction is faster than the thiophene desulfurization reaction which makes the latter the rate limiting step [74–76]. This suggests that the kinetics of the process can be improved by increasing the activity of the Ni catalyst, which might be achieved by finer dispersion or promotion of Ni using another metal.

11.3.2.3.4. APPLICATION TO FUEL CELL SYSTEMS

The reactive adsorption process is most likely limited in application to being a bulk desulfurization process (that is as a substitute for HDS) for gasoline and naphtha range hydrocarbons. It is improbable that the process would be applied to compact fuel cell systems employing gasoline or diesel because they are already regulated to 30–80 ppmw and 15 ppmw sulfur, respectively, and because of the heating requirements to vaporize the fuel. These regulated fuels would most likely undergo passive sorbent desulfurization in the gas phase as described in Section 11.3.2.4, passive sorbent desulfurization in the liquid phase upstream of the reformer as described in Section 11.4, or syngas desulfurization downstream of the reformer as discussed in Section 11.5 when a sulfur tolerant

reforming catalyst is being used. Jet fuels such as JP-8 on the other hand can have sulfur content as high as 3000 ppmw. Thus the reactive adsorption process could perhaps be used to bring down the sulfur content of JP-8 to around 50–100 ppmw in a stand-alone centralized facility. The partially desulfurized jet fuel could then be transported for use with compact fuel cell systems in which the rest of the desulfurization would be done upstream of the reformer using a passive sorbent in the liquid phase or downstream of the reformer when a sulfur tolerant reforming catalyst is used.

11.3.2.4. Adsorption

Adsorption-based gas-phase processes unlike reactive adsorption-based gas-phase processes imply passive and selective adsorption of sulfur compounds in the absence of hydrogen. Adsorption in the gas or vapor phase from gasoline, jet fuel, and diesel would involve nearly fully vaporizing these liquid fuels using external heat before passing them through a hot sorbent bed. The desirable sorbent characteristics as listed in Section 11.3.1.2.1 for gaseous fuels also generally apply for these liquid fuels. The adsorption rate increases with temperature, but since adsorption is exothermic, the equilibrium capacity decreases. Adsorption of sulfur compounds at or above the final boiling points of jet fuel and diesel that are 300 °C or higher may not be a feasible approach. Indeed, no studies were found in the literature for developing such sorbents.

On the other hand, there have been various attempts, as reviewed by Yang [8], to develop vapor-phase adsorbents for sulfur compounds such as mercaptans and thiophene typically present in gasoline with a final boiling point of about 200 °C. The sorbents that have been studied include activated alumina, activated carbon, zeolite 5A and 13X, ZSM-5, and silicalite, and ion-exchanged zeolites such as AgY. The gas phase thiophene adsorption capacity was found to be generally quite low (<< 1 wt%) on most of these sorbents. However, at 50 °C, with 1800 ppmv thiophene in the gas phase, the capacities of ZSM-5 and silicalite were 1.6 and 2.2 wt% respectively. However, these model compound adsorption studies are generally not representative of the sulfur capacity of these sorbents for desulfurizing commercial gasoline. In general, the sulfur capacity of sorbents is significantly lower due to competitive adsorption of the various compounds present in these complex real-world samples.

11.3.2.4.1. NICKEL-BASED SORBENTS

Ni-based adsorbents have been evaluated for gas-phase adsorption of sulfur compounds from commercial gasoline samples containing 210–305 ppmw sulfur and a low boiling fraction (below 230 °C) of JP-8 jet fuel containing 380 ppmw sulfur by researchers at Pennsylvania State University (PSU) [77–79]. The reduced nickel based sorbent, prepared by wet impregnation, contained 55 wt% Ni on silica-alumina with a BET surface area of 157 m^2/g. At an adsorption temperature of 220 °C, the sulfur capacity of this sorbent, upon reaching 30 ppmw sulfur in the treated JP-8 fraction, ranged from a low of 0.26 wt% to a high of 1.35 wt% depending on the adsorber column aspect ratio and the sorbent particle diameter.

For gasoline, the PSU researchers found vapor-phase adsorption at 200 °C to be more effective than liquid-phase adsorption at room temperature. The pre-breakthrough sulfur capacities for gasoline were however rather low at around 0.03 wt% at room temperature and at around 0.06 wt% at 200 °C. Following breakthrough, the sulfur content in the treated gasoline increased much more slowly at 200 °C than at room temperature. The capacity corresponding to 10 ppmw sulfur in the treated gasoline was as high as 0.73 wt% at 200 °C. This was attributed to significant reduction in competitive olefin adsorption at 200 °C versus room temperature. It was also attributed to increase in the rates of C-S bond cleavage and surface reaction of the

adsorbed sulfur compound with nickel. These steps were irreversible whereas olefin adsorption was deemed to be reversible, and this resulted in a reduced competition by olefins at higher temperature. Based on model compound desulfurization studies that showed the formation of ethyl benzene from benzothiophene at room temperature, it was concluded that in addition to chemisorption, C-S bond hydrogenolysis accompanied with the formation of nickel sulfides occurred even in the absence of hydrogen. The source of hydrogen was hypothesized to be surface hydrogen on the reduced nickel sorbent.

The important role of hydrogen in passive vapor-phase gasoline desulfurization over reduced nickel sorbents further comes to light in the work by Exxon researchers [80,81]. They evaluated deep vapor-phase desulfurization of pre-desulfurized gasoline containing 22 ppmw sulfur over a $Ni/Al\text{-}SiO_2$ sorbent in the absence and presence of 3 wt% ethanol in the gasoline. The sorbent was prepared by grafting of a silica gel with alumina using aluminum sec-butoxide followed by deposition-precipitation of nickel nitrate on the alumina grafted silica gel by urea hydrolysis. This preparation technique yielded a sorbent containing 59.5 wt% Ni with a BET surface area of 288 m^2/g, pore volume of 0.43 cm^3/g and average pore diameter of 5.8 nm. Reduction in hydrogen at 450 °C yielded a reduced nickel sorbent with an active nickel surface area of 29 m^2/g and Ni^0 crystallite size of 4 nm.

The sulfur capacity of the sorbent was measured at 230 °C. It was seen that the sulfur capacity prior to reaching a level of 2 ppmw sulfur in the desulfurized gasoline increased from about 0.5 wt% in the absence of ethanol to >2 wt% in the presence of 3 wt% ethanol. Based on extensive sorbent characterization, it was concluded that the beneficial effect of ethanol is due to reduction in carbon fouling and the change of the mode of sulfur uptake from chemisorption to reactive adsorption facilitated by hydrogen produced from the catalytic dehydrogenation of ethanol.

11.3.2.4.2. APPLICATION TO FUEL CELL SYSTEMS

Passive gas-phase desulfurization of gasoline (but not jet fuel or diesel which boil at higher temperatures) using adsorption at about 200 °C prior to the reformer of a fuel cell system appears to be a feasible approach. Gasoline is now readily available with <30 ppmw sulfur. Since sorbent capacities on the order of 2 wt% have been demonstrated, particularly using nickel-based sorbents, deep desulfurized gasoline could be delivered to the reformer for an extended time using a once-through sorbent. Recycle streams such as hydrogen as needed in HDS or reactive adsorption would not be necessary. The system, however, would require a gasoline vaporizer prior to the heated adsorber bed, which is not as desirable as operation at room temperature. It would be best to use a single use replaceable sorbent cartridge that is replaced periodically. The cartridge containing the activated reduced nickel sorbent would have to be kept sealed to avoid air exposure until ready to use. Periodic cartridge replacement without air exposure may present a challenge, particularly because the bed is operating at an elevated temperature. Disposal of the potentially pyrophoric spent sorbent after some sort of passivation, recycle of the sorbent to recover the nickel, or its offsite regeneration for immediate reuse (unlikely) are some of the issues that would also need to be addressed.

11.4. LIQUID PHASE DESULFURIZATION UPSTREAM OF REFORMER

11.4.1. Adsorption

As opposed to liquid fuel desulfurization by adsorption in the gas phase that requires

vaporizing the fuel and using a sorbent at about the fuel's final boiling point, desulfurization in the liquid phase by adsorption can be conducted at temperatures as low as ambient temperature. The search for a suitable sorbent for desulfurization of gasoline, jet fuel, and diesel by selective adsorption in the liquid phase has been a subject of intense research and development over the past 15 years [7,64,77,78,82–113],[114–129]. This research has been spurred by the environmental regulations for gasoline and diesel, the need for a deeply desulfurized fuel for fuel cells, and the apparent simplicity of the passive low temperature desulfurization concept.

11.4.1.1. Activated Carbon and Polarity-Based Sorbents

Babich and Moulijn [64] have reviewed the research and development of common sulfur adsorbents for liquid fuels during the 1990s. Briefly, a number of adsorbents including activated carbon, zeolite 5A, zeolite 13X, silica-alumina, and alumina were evaluated during this period. Besides activated carbon, which may carry out the adsorption based on more than one mechanism, these common adsorbents generally carry out the separation based on the principle of polarity. The metallic impurities on activated carbon, the content of which depends on the precursor employed to prepare the activated carbon, and the surface functional groups on the carbon which depend on the activation process employed to prepare the carbon can lead to multiple and/or complex adsorption mechanisms. Since the sulfur compounds are more polar than hydrocarbons, they can presumably be separated from each other using the principle of polarity. However, the sulfur capacity of the adsorbents that work purely on the principle of polarity prior to breakthrough is generally expected to be very low, on the order of less than 0.2 wt%.

Activated carbon was found to have the highest capacity among several adsorbents tested by Salem and coworkers [82,83]. However, it had low cleanup efficiency whereas zeolite 13X had low capacity but high efficiency. In other words, activated carbon could potentially be used for bulk sulfur removal and zeolite-13X could be used for final polishing of the effluent from the activated carbon bed. Based on their data, the authors proposed a series fixed-bed combination of activated carbon at 80 °C followed by zeolite 13X at room temperature for the deep desulfurization of naphtha.

Activated carbon was also found to be effective in removing sterically hindered sulfur compounds such as 4,6 DMDBT from hydrotreated middle distillate at 100 °C [84]. In contrast, a copper-exchanged Y-zeolite, which was effective in separating thiophene from benzene, could not remove any 4,6 DMDBT from hydrotreated middle distillate. The carbon tested in this study was Filtrasorb 400 from Calgon Carbon, which was also found to be regenerable by flushing with toluene. Breakthrough data for a two-cycle test with an interim toluene flush for hydrotreated middle distillate containing 1200 ppmw sulfur are shown in Fig. 11.3. Sulfur capacity before breakthrough to 25 ppmw was about 2 mg/cm^3 of the Filtrasorb 400 activated carbon. As seen from the figure, the sorbent was fully regenerable upon flushing with toluene.

Before the turn of the century, as the new diesel and gasoline sulfur regulations were proposed, the Irvad moving-bed process that used a proprietary promoted alumina sorbent from Alcoa and targeted primarily gasoline range hydrocarbons was developed [63,64,85,86] as a potential alternative to HDS. The process using alumina as the sorbent also appears to be based on the principle of polarity and thus the sulfur capacity of the sorbent is expected to be quite low. The process continuously removed sulfur compounds by counter-currently contacting the alumina with a sulfur-rich hydrocarbon stream at atmospheric pressure and mild temperatures and the spent alumina then moved to

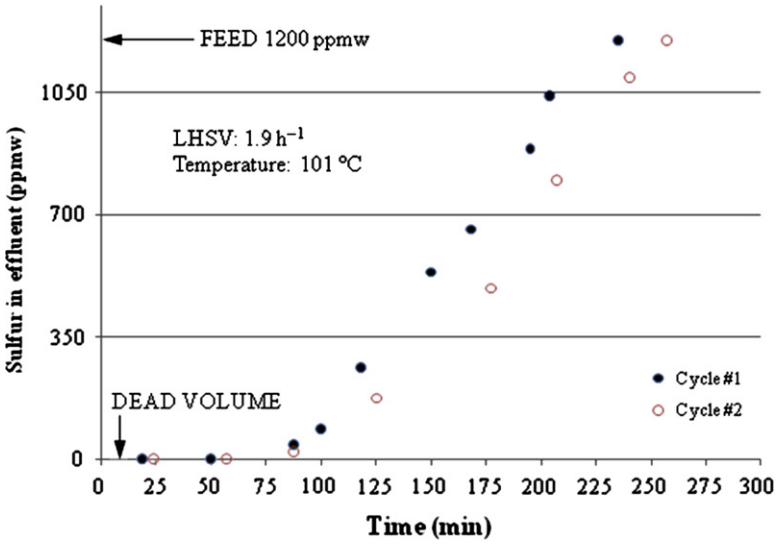

FIGURE 11.3 Sulfur breakthrough curve for hydrotreated middle distillate on Filtrasorb 400 carbon adsorbent [84].

a regenerator operating at a slightly higher temperature than the adsorber to desorb the sulfur compounds into a regeneration gas stream. The limitation associated with low capacity could be overcome by increasing the circulation rate of the alumina sorbent. Over 90% sulfur removal was demonstrated in pilot plant experiments with FCC feed and coker naphtha containing high levels of sulfur in the 1000–3000 ppmw range. Olefin saturation was not an issue since hydrogen was not used in the process. However, further development of the Irvad process was discontinued because it was not possible to fully develop the technology before the gasoline regulations were to go into effect.

During recent years, research has continued on both activated carbon as well as polarity-based sorbents [96–98,115,116,122,126]. Also, these sorbents have been used as metal supports as well as in tandem-bed combination with metal sorbents as discussed further in Sections 11.4.1.2 and 11.4.1.3. Activated carbons have been shown to exhibit high adsorption selectivities for 4-MDBT and 4,6-DMDBT [96,97]. The chemistry on the carbon surface appears to play an important role in sulfur compound adsorption. An increase in oxygen containing functional groups on the surface enhances the sulfur capacity.

Song and coworkers [98] have recently carried out a detailed investigation of the properties and sulfur compound adsorption performance of two commercially available activated carbons modified by oxidation using nitric acid at 60 °C for 3 h and using 5% O_2/N_2 at 350–400 °C for 3 h. One of the carbons was a microporous carbon from Calgon Carbon (PCB-G) and had a surface area of about 900 m^2/g, whereas the other carbon was a mesoporous carbon from Westvaco (Nuchar SA 20) with a surface area of about 1800 m^2/g. A model diesel fuel (MDF) containing 400 ppmw S in a 50:50 mixture of decane and dodecane was used to evaluate adsorption performance at 25 °C and a liquid hourly space velocity (LHSV) of 4.8 h^{-1}. Sulfur breakthrough capacity was reported as the total mg of sulfur adsorbed per g of sorbent before reaching 0.5 ppmw total sulfur in the effluent. The sulfur was added to the MDF using BT, DBT, 4-MDBT, and 4,6-DMDBT with each compound contributing 100 ppmw.

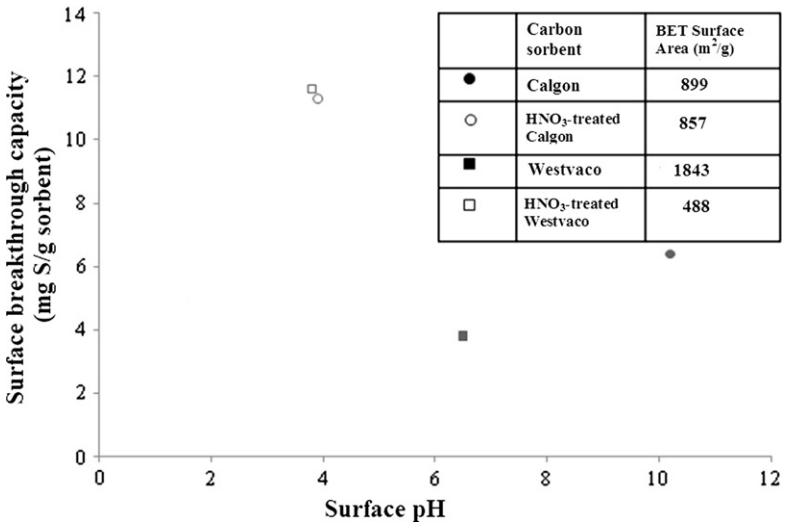

FIGURE 11.4 Effect of HNO_3 treatment on surface pH, BET surface area and breakthrough sulfur capacity of activated carbons [98].

Naphthalene, 2-methylnaphthalene, and tert-butylbenzene were also present in MDF to represent the aromatic portion of a commercial diesel. The breakthrough sulfur capacities of unmodified and HNO_3-treated carbons measured at 1 ppmw breakthrough are correlated with surface pH and BET surface area in Fig. 11.4.

Some important observations from this study are as follows:

- The order of elution of the sulfur compounds was BT followed by DBT and 4-MDBT followed by 4,6-DMDBT, which is consistent with their boiling points.
- The breakthrough sulfur capacity of the unmodified Calgon carbon was 6.4 mg/g which was about 68% higher than that of the unmodified Westvaco carbon (3.8 mg/g) even though the surface area of the latter was twice as high. The capacities appear to correlate with surface pH for unmodified carbons, with higher pH (a more alkaline surface) contributing to higher capacity.
- Oxygen treatment did not have a significant effect on capacity but with mild HNO_3 treatment, the capacities of both carbons increased significantly to >11 mg/g, even though their surface areas and surface pH reduced. The Westvaco carbon suffered a drastic decrease in surface area from 1843 m^2/g to 488 m^2/g but its sulfur breakthrough capacity increased over 200% from 3.6 mg/g to 11.6 mg/g.
- The increase in capacity of the nitric-acid treated carbons correlated almost linearly with increase in surface oxygen concentration as measured by X-ray photoelectron spectroscopy.

Based on these results, in the author's opinion, mild HNO_3 treatment to increase the oxygen-containing functional groups on the surface could be a reasonable approach for increasing the sulfur adsorption capacity of commercially available activated carbons. This appears to be consistent with the oxidation-assisted adsorption approach described in Section 11.4.2. However, the performance of HNO_3-treated carbons needs to be confirmed with tests using commercial diesel in addition to MDF. Also, the regenerability of these activated carbon sorbents needs to be addressed due to their low sulfur capacities of <1.2 wt%.

11.4.1.2. Sorbents Based on Sulfur–Metal (S–M) Interaction

Prior to the current regulations for gasoline (30–80 ppmw) and diesel (15 ppmw), gasoline and diesel were regulated to 350 and 500 ppmw, respectively, around the turn of the century. To reduce the sulfur levels in these fuels to meet fuel cell requirements of 0.1–1.0 ppmw sulfur, researchers at PSU proposed the SARS (selective adsorption for removing sulfur) process [87,88] consisting of two sorbent beds operating in cycles of adsorption and regeneration. Five wt% of an undisclosed transition metal supported on silica gel was used as the sulfur sorbent and the adsorption was conducted at room temperature. The sorbent was regenerated using a polar organic solvent.

The SARS process claims to separate the sulfur compound through selective sulfur–metal (S–M) interaction rather than π-complexation, which is covered in the next section. The pre-breakthrough capacity of the sorbent for a synthetically blended model diesel fuel containing 576 ppmw was rather low at the conditions used. For example, breakthrough occurred after 0.9 ml of the model diesel fuel was passed over 1 g of the sorbent. This translates into a breakthrough sulfur capacity of less than 0.4 mg/g sorbent.

Although the transition metal used in the SARS process was not disclosed, a number of bulk and supported transition metal sorbents, with major emphasis on Ni, were later evaluated by PSU researchers and others in an attempt to increase the breakthrough capacity and optimize the operating temperature with respect to gasoline, jet fuel and diesel [79,89–96,117,123,129]. The sorbents evaluated included ion exchanged Y zeolites (with Cu, Ni, Zn, Pd, and Ce), unsupported Ni, Ni/Al_2O_3, Ni/SiO_2-Al_2O_3, K-exchanged NiY zeolite, Zn-Fe-Ce/Al_2O_3, and Ni/mesoporous silica. In general, the breakthrough sulfur capacities were much less than 1.0 wt%, especially at room temperature. Competition from olefins in gasoline and aromatics in diesel and jet fuel appears to be a major cause of the low breakthrough capacities. Some specific examples follow.

Ma et al. [89] evaluated the desulfurization of a JP-8 jet fuel (736 ppmw S) and a lighter 70% fraction of the JP-8 (380 ppmw S) boiling at 230 °C that was obtained by distillation. The sorbents used included an unsupported Ni (90 m^2/g) and an alumina-supported Ni (150 m^2/g), and were evaluated at 27 °C and 200 °C in an LHSV range of 2.4–6.3 h^{-1}. Breakthrough to 1 ppmw occurred at less than 0.8 mg S/g sorbent in all experiments irrespective of the temperature. In fact, for the whole JP-8 breakthrough to 1 ppmw occurred at less than 0.2 mg S/g sorbent. Breakthrough to 30 ppmw was used to compare the sorbents and run conditions. Operation at the higher temperature significantly flattened the breakthrough curve indicating the influence of gas-phase adsorption (see Sections 11.3.2.3 and 11.3.2.4). Since at 200 °C, a substantial portion of the JP-8 could be in the gas phase, this work cannot be considered as adsorption in the liquid phase. The best breakthrough capacity at 30 ppmw sulfur breakthrough among all experiments was 16 mg S/g sorbent using the light JP-8 fraction for the unsupported nickel sorbent at 200 °C and 4.8 h^{-1}.

Using the same experimental setup as Ma et al. [89], Velu et al. [79,95] have evaluated Ni/SiO_2- Al_2O_3 and Ni/K-Y zeolite sorbents. The work using the Ni/SiO_2-Al_2O_3 was carried out at 220 °C for the light JP-8 fraction where most of the fuel was in the gas phase. This work is discussed in Section 11.3.2.4. The work with Ni/K-Y zeolite was carried out at 80 °C. The Ni/K-Y zeolite sorbent contained 8 wt% Ni loaded by ion exchange on to a K-Y zeolite prepared by calcination and ion exchange of a NH_4Y zeolite with a SiO_2/Al_2O_3 ratio of 5. Breakthrough experiments using the light JP-8 were carried out using both pre-reduced and unreduced sorbent. The breakthrough sulfur capacities were around 1.2 mg S/g sorbent at

1 ppmw breakthrough and 1.8 mg/g at 30 ppmw breakthrough for the unreduced sorbent. For the reduced sorbent, the capacities were better; 4.5 mg/g at 1 ppmw breakthrough and 5 mg/g at 30 ppmw breakthrough. However, all of these breakthrough capacities are considered to be rather low.

Katsuno et al. [121] evaluated polishing sulfur removal from a pre-desulfurized kerosene (65 ppmw S) using a Ni/SiO_2-Al_2O_3 sorbent. The sorbent contained 63 wt% Ni and was prepared by a special coprecipitation method followed by calcinations and reduction. The BET surface area was 345 m^2/g with pores 3 nm or less accounting for 141 m^2/g. At a liquid hourly space velocity of 3 h^{-1} and 150 °C, all of the sulfur compounds were reduced to less than 0.2 ppmw for 50 h, which was the duration of the test. Based on this data, the breakthrough capacity of this sorbents at 0.2 ppmw sulfur was $>$ 8 mg/ ml of sorbent. The experiment was not conducted till breakthrough so the absolute breakthrough capacity cannot be determined from the data. Katsuno et al. [121] prepared a number of additional such sorbents and demonstrated that it was necessary to have a surface area of $>$100 m^2/g in the pores 3nm or smaller to have good desulfurization performance.

Kim et al. [96] evaluated a commercial activated alumina (155 m^2/g), a commercial activated carbon (1800 m^2/g), and the Ni/SiO_2-Al_2O_3 sorbent of Velu et al. [79] with a surface area of 157 m^2/g for desulfurization of a model diesel fuel containing 687 ppmw sulfur at 25 °C. Among the three sorbents, it was actually the activated carbon that showed the best adsorption performance of about 6.3 mg S/g sorbent prior to breakthrough at around 1 ppmw. The other two sorbents had less than half the capacity of the activated carbon. Park et al. [123] prepared a nickel sorbent containing 30 wt% Ni on a mesoporous support, SBA-15 by pore volume impregnation of nickel nitrate dissolved in tetra hydro furan followed by calcination and reduction in H_2 at 600 °C. The sorbent was evaluated for removing sulfur from a diesel containing 240 ppmw S and a diesel containing 11.7 ppmw S. At room temperature, the sorbent had essentially no capacity since breakthrough occurred almost immediately. However, at 200 °C, the breakthrough sulfur capacity at 0.1 ppmw S in the cleaned fuel was 1.7 mg/g for the high sulfur diesel and 0.47 mg/g for the low sulfur diesel.

Zhang et al. [117] evaluated sulfur removal from gasoline containing 200 ppmw S at 35–90 °C using a series of sorbents containing ZnO, Fe_2O_3, and CeO_2 supported on alumina. The sorbents were prepared by wet impregnation of high surface area alumina using nitrates followed by filtration and air calcination at 730 °C. The best sorbent was found to be one designated AZFC0.52 containing 4.54 wt% ZnO, 2.25 wt% Fe_2O_3, and 2.5 wt% CeO_2. The Zn:Fe:Ce mole ratio was 2:1:0.52. In the 35–90 °C range, the best adsorption temperature was found to be 60 °C. Ce addition was shown to have a positive effect on sorbent performance. Following adsorption, the sorbent was regenerated using 6% O_2/H_2O at 250 °C. The sulfur capacity at 10 ppmw breakthrough was 26 mg S/g sorbent and the sorbent was found to be fully regenerable over 10 cycles of adsorption and regeneration. This result is significant considering that the sorbent is fully regenerable and nickel-based sorbents had breakthrough capacities for gasoline that were no better than 0.8 wt% even at temperatures as high as 200 °C (see Section 11.3.2.4.1).

11.4.1.3. Sorbents Based on π-Complexation

Another class of metal-based sulfur sorbents that were originally developed by Yang and coworkers [99–101] and also reported in a series of later papers [7,102–114] over the past 10 years, work on the basis of formation of a π complex between the sulfur compound and the metal rather than a direct S–M interaction as described above. The motivation behind this development,

which could possibly lead to more selective and higher capacity regenerable sulfur sorbents is that the adsorption based on π complexation is stronger than the van der Walls interaction yet weak enough to be reversible. A π-complex is said to be formed by donation of electron charges from the π-electrons of the sulfur compounds such as thiophenes to the empty s orbital of the metal along with back donation of electron charges from the d orbitals of the metal to the π^* orbital of the sulfur compound. Representative examples of the work by Yang and coworkers are described below.

The original π-complexation sulfur sorbents by Yang and coworkers were based on Ag-Y zeolite and Cu(I)-Y zeolite [99–101] prepared by conventional liquid-phase ion exchange using nitrates with a commercial Na-Y zeolite having a Si/Al ratio of 2.43. Cu(II)-Y zeolite resulting from ion exchange was auto-reduced in helium at 450 °C to yield the desired Cu(I)-Y zeolite sorbent. The Cu(I)-Y zeolite, by itself, and a series bed of a commercial Calgon PCB activated carbon with the Cu(I)-Y zeolite were used to desulfurize a commercial gasoline (335 ppmw S) and commercial diesel (430 ppmw S) at room temperature. The series bed consisted of 15 wt% carbon at the front. The breakthrough sulfur capacity at about 0.1 ppmw S in the effluent was about 11 mg S/g sorbent for diesel and 6 mg S/g sorbent for gasoline. The breakthrough capacity of Cu(I)-Y zeolite without the activated carbon present to remove the heavier molecules was about 20% lower.

Cu(I)-Y zeolite was also prepared using a vapor-phase ion exchange process that allows direct exchange of cuprous ions [108] and tested for sulfur removal at room temperature from a commercial jet fuel containing 364 ppmw S. The breakthrough sulfur capacity of this sorbent at about 0.1 ppmw S was 12.7 mg S/g sorbent. A series bed configuration of commercial alumina (Selexorb CDX from Alcoa) and the above sorbent was also tested with the alumina making up the front 25 wt% of the bed. This series sorbent configuration increased the breakthrough capacity at about 0.1 ppmw S to 16.7 mg S/g sorbent. The used sorbent bed was found to be nearly fully regenerable after treating with air at 350 °C for 6–12 h followed by 5% H_2/inert at 231 °C for 1 h.

The breakthrough capacities of Cu(I)-, Ni(II)-, and Zn(II)-zeolites prepared using various ion exchange techniques have been measured by Hernandez-Maldonado et al. [7]. Significant emphasis appears to have been given in this study to validate the analytical measurements of sulfur compounds using a gas chromatograph (GC)-flame photometric detector (FPD) which is very commonly used to selectively analyze and measure sulfur compounds. FPD can erroneously measure low values of sulfur compounds present in small quantities in a hydrocarbon matrix due to quenching of the flame of the FPD by the hydrocarbons [78]. A FPD that is free of quenching effects is claimed to have been used by Hernandez-Maldonado et al. [7]. As shown in Table 11.5, the breakthrough sulfur capacities at 1 ppmw in the effluent are in the range 1.4–5.4 mg S/g sorbent for sorbents prepared by liquid phase

TABLE 11.5 Breakthrough Sulfur Capacities* of π-Complexation Sorbents for Diesel (297 ppmw S) and Jet Fuel (364 ppmw S) Desulfurization [7]

Sorbent	Ion-exchanged method	Fuel	Breakthrough capacity (mg S/g sorbent)
Cu(I)-Y	Liquid-phase	Diesel	5.3
Cu(I)-Y	Vapor-phase, 700 °C	Diesel Jet Fuel	8.9 12.7
Ni(II)-X	Liquid-phase	Diesel	4.6
Ni(II)-Y	Solid-state, 500 °C	Diesel	5.1
Zn(II)-X	Liquid phase	Jet fuel	2.8
Zn(II)-Y	Liquid phase	Jet fuel	1.4

**At 1 ppmw sulfur breakthrough.*

and solid state ion exchange methods. For the sorbents prepared by vapor phase ion exchange, the capacities range from 9 mg S/g to 13 mg S/g sorbent. The Ni(II)- and Cu(I)-zeolites had similar capacities, which were significantly greater than Zn(II)-zeolite.

In more recent papers [109–114], Yang and coworkers have evaluated the effect of moisture and oxygenates and have prepared and evaluated π-complexation sorbents based on copper and palladium halides supported on alumina, activated carbon, and mesoporous supports (MCM-41 and SBA-15). The use of mesoporous supports is motivated by their potential for low pore diffusion resistances. $PdCl_2$/SBA-15 was found to have the highest capacity among these sorbents for desulfurizing a light fraction of a high sulfur JP-5 jet fuel (841 ppmw S) with a breakthrough capacity at 50 ppmw of 32 mg S/g sorbent. However, it is difficult to compare this sorbent with the others because of the high concentration of the breakthrough point chosen as compared to 1 ppmw or less for the others [7,99–101,108]. Regeneration of this sorbent using benzene extraction resulted in recovery of 44% of its original capacity.

Moisture and oxygenates were found to have a strong inhibiting effect on the desulfurization capability of Cu(I)-Y zeolite [110]. Most recently, Yang and coworkers have evaluated $AgNO_3$ supported on mesoporous silica (MCM-41), prepared by pore volume impregnation [114]. The breakthrough capacity of this sorbent at 10 ppmw S using a high sulfur JP-5 jet fuel (841 ppmw S) was 16 mg S/g sorbent. The sorbent was regenerated using air at 200 °C for 24 h. Only about 33% of the original breakthrough capacity was restored after the first regeneration. The capacity after the second regeneration, however, was the same as that after the first regeneration indicating that the sorbent may have stabilized.

Following the lead of Yang and coworkers, others have also prepared and evaluated π-complexation sorbents [118–120,124,128]. Bhandari et al. [118] demonstrated the strong negative influence of the presence of aromatics and moisture on the desulfurization capacity of these sorbents for diesel desulfurization. The breakthrough capacities for desulfurization of a commercial diesel (200ppmw S) using their Ni-Y zeolite and Cu-Y zeolite sorbents were less than 0.5 mg S/g sorbent. The poor performance was attributed to the non-retention of heavier sulfur compounds such as 4,6 DMDBT in the diesel. Dai et al. [119] evaluated CuCl/SBA-15 for thiophene adsorption and showed that this sorbent can be 90% regenerated by exposure to high temperature (350–450 °C) in an inert environment. King and Li [120] showed that the desulfurization performance of Cu-zeolites is strongly compromised in the presence of aromatics and olefins. They also showed the potential oxidation of thiols to disulfides by the Cu-Y zeolite. Zhang et al. [124] found CuZn/Y-zeolite and Ag/Y-zeolite to be promising deep desulfurization sorbents in their model compound studies. They found Ag/Y-zeolite to be fully regenerable by air calcination at 450 °C.

11.4.1.4. Application to Fuel Cell Systems

The concept of removal of sulfur compounds from gasoline, jet fuel, and diesel using sorbents in the liquid phase, especially at room temperature, is attractive because of its simplicity. Although there is significant research activity to develop such sorbents as detailed above, it is not clear if a viable liquid-phase desulfurization process can be developed for compact fuel processors.

Gasoline and diesel are now regulated to 30–80 ppmw and 15 ppmw, respectively, and are the most likely liquid fuels to be used for fuel cells. However, most of the research to date has been on fuels with much higher sulfur content and very little emphasis has been given to sorbent regeneration. Sorbents may have lower capacity when the sulfur content of the challenge fuel is lower. Thus, sorbents need to be tested using regulated sulfur concentration in the fuel to be desulfurized so that sulfur

capacity numbers can be established for fuels with sulfur contents in the 10–80 ppmw range.

For compact fuel processors, it is best for the regeneration to be carried out in a central location so that the spent adsorbent cartridge can be simply replaced by a new or regenerated one. For stationary fuel cells, sorbents beds should be designed with sufficient sulfur capacity to require annual replacement. For example, for a 1 KW_e residential fuel cell utilizing 15 ppmw diesel, the annual fuel requirement is about 650 gallons. For a sorbent with sulfur capacity prior to breakthrough of 5–10 mg S/g sorbent, a once-through sorbent bed containing 3–6 kg of sorbent would be required. These capacities are certainly in the realm based on the research to date, but they should definitely be improved further to about 20 mg/g to reduce bed size.

The sorbent performance should be confirmed with regulated diesel. Also, more research emphasis should be given to sorbent regeneration and/or safe disposal of spent sorbent. Finally, most of the sorbents to date have been in powder form for laboratory use. Sorbents need to be developed in the form of pellets or extrudates with minimal mass transfer resistances to use in packed beds without giving rise to excessive pressure drop.

11.4.2. Oxidation-Assisted Adsorption

11.4.2.1. Background

In parallel to the development of adsorption-based liquid-phase desulfurization sorbents, significant research and process development has also been carried out on liquid-phase oxidative desulfurization (ODS) processes [10,64,130–132] for producing ultra-low sulfur diesel. ODS has been proposed for use both as a replacement for HDS as well as in conjunction with HDS, either for HDS feed pretreatment or HDS effluent post-treatment. In the ODS process, the thiophenic sulfur compounds in diesel or other liquid hydrocarbon streams are converted by selective oxidation to their respective sulfones and sulfoxides at mild conditions (0.1 MPa, 25–90 °C) as shown in Fig. 11.5 for dibenzothiophene. Because of their higher polarity and boiling point, the sulfones and sulfoxides are then removed in a second step by liquid-liquid extraction, adsorption, or distillation. ODS is attractive compared to HDS because of the following reasons:

- It uses mild conditions that are more energy efficient.
- It does not use expensive hydrogen.
- It has the potential ability to remove sterically hindered thiophenes such as 4-MDBT and 4,6-DMDBT.

For compact fuel cell applications, liquid-liquid extraction or distillation would be considered impractical as the second step in the ODS process. Only the approach involving selective oxidation of sulfur compounds followed by selective adsorption of oxidized sulfur compounds would be of interest. Thus the approach is named oxidation-assisted adsorption.

11.4.2.2. Examples of the Use of Air (Oxygen) as Oxidant

A number of oxidants including hydrogen peroxide [133–136], organic hydroperoxides [137,138], and molecular oxygen (air)

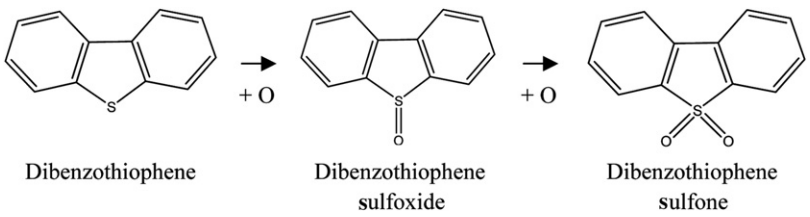

FIGURE 11.5 Selective oxidation of thiophenes to corresponding sulfones.

[139–144] and a variety of catalysts and sorbents have been used and/or proposed in the development of ODS processes. The peroxides provide high selectivity for thiophenic sulfur compound oxidation to their corresponding sulfones. All the relatively larger scale ODS process development and associated patents are based on the use of peroxide oxidants as reviewed by Skov and England [131]. However, because of the cost and inconvenience involved in the use of hydrogen peroxide and organic hydroperoxides, only the air oxidation based approaches that might be applicable in conjunction with compact fuel cell systems are discussed here.

Wismann and Gangwal [139] proposed using air as an oxidant to promote desulfurization of diesel by selective adsorption over commercially available activated carbons followed by toluene extraction to remove the sulfur compounds and regenerate the carbon for reuse. Berzutskiy [140] has proposed simultaneous oxidation (using air) and adsorption on a particulate catalyst-impregnated sorbent for desulfurization of petroleum-derived fuels. The adsorbed oxidized sulfur compounds are extracted from the sorbent using a polar solvent, thereby regenerating the sorbent. Murata et al. [141] investigated the oxidative desulfurization of diesel using oxygen in the presence of n-octanal and cobalt (II) acetate. Adsorption of the oxidized mixture using alumina resulted in >97% reduction from 193 ppmw to <5 ppmw. The mechanism proposed by Murata et al. [141] hypothesized the formation of octaneperoxic acid catalyzed by cobalt and oxidation of the thiophenic sulfur to corresponding sulfones that are selectively adsorbed on alumina.

Gatan et al. [142] are developing a process that uses a similar principle as Murata et al. [141] although the process details are proprietary. In this process an undisclosed hydrocarbon is first oxidized using oxygen to produce an organic hydroperoxide which selectively oxidizes the sulfur compounds in hydrotreated diesel to sulfones over an undisclosed heterogeneous catalyst at <95 °C and <0.8 MPa. After sulfone adsorption on an undisclosed adsorbent, the extent of diesel desulfurization >98% is claimed. The sulfones extracted from the adsorbent are blended directly into the heavy fuel oil pool in some locations or processed in a coker.

Ma et al. [143] have investigated iron impregnated activated carbon as a catalyst for direct oxidation of sulfur compounds in JP-8 using oxygen to sulfones. They showed that by adsorption alone on the activated carbon, only 16% removal of sulfur was achieved from JP-8. On the other hand, oxidation of JP-8 using oxygen over a Fe-impregnated activated carbon catalyst followed by adsorption on the activated carbon resulted in a removal of 82.4% of sulfur from 717 ppmw to 126 ppmw. This was attributed to the greater polarity of the sulfones formed during the oxidation step and subsequent enhancement in the selectivity of the adsorption step.

Sudararaman et al. [144] have investigated a multi-step oxidative process for diesel desulfurization. In the first step, a diesel containing 40 ppmw sulfur is catalytically or non-catalytically oxidized using molecular oxygen to produce about 0.06 wt% peroxides in the diesel as measured by ASTM D 3703-99. In this step the sulfur compounds in diesel were partially converted to sulfones. In the second step, the diesel fuel from the first step containing the peroxides, sulfones, and unconverted thiophenes was passed over a MoO_2/SiO_2 catalyst at 0.1 MPa and 80 °C to convert essentially all of the sulfur compounds to their corresponding sulfones. This step reduced the peroxide content of the fuel to 0.0145 wt% indicating that the oxidation was selectively carried out by the in situ generated peroxide. In the final step, adsorption is carried out to selectively remove the sulfur in diesel fuel down to less than 1 ppmw.

11.4.2.3. Application to Fuel Cell Systems

Although not as extensively studied as liquid-phase adsorption prior to the reformer for fuel cell applications, oxidation-assisted adsorption using air as the oxidant appears to be an approach worth further research and development, especially for jet fuel, diesel, and heavier petroleum products. The oxidation step needs to be developed to optimize it with respect to different fuels for the in situ formation of hydroperoxides and subsequent oxidation of the thiophenes. As mentioned earlier, most of the adsorbents studied in the liquid phase (Section 11.4.1) neither have sufficient capacity nor high selectivity compared to the hydrocarbons present in these fuels. Oxidation converts the thiophenic sulfur compounds to sulfones that are significantly more polar than the other hydrocarbons. This results in a significant increase in the pre-breakthrough capacity of the downstream adsorbent with potential capability to achieve the target 2–3 wt% sulfur capacity. The mild conditions, no hydrogen use, and no recycle requirements with the oxidation-assisted adsorption approach are attractive. The oxidation catalyst and adsorbent could possibly be placed in tandem in a single bed if the same conditions are used for the two steps. Also, the adsorbent for sulfones may be conventional, may not require pre-reduction, and may not need to be prepared using difficult to scale-up techniques. For a compact system, it would be best to use a single use replaceable cartridge.

11.5. SYNGAS DESULFURIZATION DOWNSTREAM OF REFORMER OR GASIFIER

Sulfur appears primarily as H_2S with some COS in the reformate gas (syngas) when a sulfur containing fuel is reformed or gasified. The H_2S concentration in the gas depends on the sulfur content of the fuel reformed or gasified and can range from less than 10 ppmv for regulated diesel or gasoline to >10,000 ppmv for a coal containing >3 wt% sulfur that is gasified using an oxygen-blown gasifier. Essentially, complete desulfurization of this gas down to <0.1–1 ppmv (H_2S + COS) is necessary before it can be used in a fuel cell. Complete desulfurization of syngas can be carried out using COS hydrolysis followed by conventional liquid-phase absorption methods such as amine scrubbing or Rectisol that operate at < 40 °C. However, these methods are not likely to lead to compact fuel cell systems, and as indicated in Section 11.2, are outside the scope of this chapter. This section focuses mainly on solid metal oxide sorbents for H_2S and COS removal that typically operate at >300 °C or thereabouts. Also an approach comprising selective catalytic oxidation of H_2S in a syngas environment is briefly described.

11.5.1. Metal Oxide Sorbents

11.5.1.1. Principle

Removal of H_2S using metal oxide sorbents involves a gas–solid reaction at elevated temperatures (~ >250 °C) between the metal oxide (MO) and H_2S that produces the corresponding metal sulfide (MS) and steam via the equilibrium-limited sulfidation reaction [145–150]

$$MO(s) + H_2S(g) \rightarrow MS(s) + H_2O(g) (\text{sulfidation})$$

Removal of COS is catalyzed by some sorbents and occurs simultaneously by H_2S formation primarily via hydrolysis and slightly via reduction:

$$COS(g) + H_2O(g) \rightarrow CO_2(g) + H_2S(g) (\text{hydrolysis})$$

$$COS(g) + H_2(g) \rightarrow CO(g) + H_2S(g) (\text{reduction})$$

The H_2S formed from the COS is removed by the metal oxide. However, removal of COS from

syngas containing significant amounts of CO and CO_2 is a challenge because of both rate inhibition as well as equilibrium hindrance of the above reactions.

Reducing gases (H_2, CO) present in syngas can reduce the metal oxide to a lower oxidation state depending on the temperature and the metal oxide's reduction potential. For example, CuO is quite easily reduced to Cu_2O and metallic Cu, whereas ZnO is quite stable in its oxide form in typical syngas at temperatures up to about 475 °C.

The maximum amount of H_2S removal in syngas is dictated by thermodynamic equilibrium of the reaction of H_2S with the reduced form of the metal oxide that is stable in the presence of bulk syngas constituents H_2, CO, H_2O, and CO_2 [149,150]. In other words, the metal oxide simultaneously reduces and sulfides, with the overall reaction being as follows rather than the simpler representation of the sulfidation reaction presented above:

$$M_xO_y(s) + zH_2S(g) + (y - z)H_2(g) \rightarrow M_xS_z(s) + yH_2O(g)$$

The thermodynamic H_2S removal efficiency of the metal oxides such as iron and copper oxides becomes worse as they are reduced to their metallic state, that is, the free energy change of the sulfidation reaction become**s** less negative. However, partial reduction to a desired reduced state for some metal oxides is essential for the sulfidation to proceed kinetically. For example, ZnO does not need to be reduced whereas Fe_2O_3 needs to be reduced to Fe_3O_4 and CeO_2 needs to be reduced to Ce_2O_3 to become effective desulfurization sorbents. Further reduction beyond the desired reduced state, for example, further reduction of Fe_3O_4 to FeO is generally detrimental to performance. Steam in the reformate gas helps to maintain a higher oxidation state for the metal oxide but since it is a product of the sulfidation reaction, high steam levels also reduce the thermodynamic H_2S removal efficiency.

Metal oxide sorbents can be either disposable (single use) or regenerable. The regeneration step can be carried out in a central location or it can be incorporated in to the desulfurization process by moving the sorbent from a sulfidation reactor to a regeneration reactor and vice versa. The regenerable sorbents need to be able to operate through numerous sulfidation-regeneration cycles with minimal loss in capacity, reactivity, and mechanical strength. For fuel cell systems, sorbent cartridges can contain a regenerable sorbent (with centralized regeneration) or a disposable sorbent for reformate gases containing low levels of H_2S ($\sim$ $<$20 ppmv or so). The spent sorbent cartridge can be simply replaced with a fresh sorbent cartridge which makes economic sense for the development of compact fuel cell systems that either employ a fuel desulfurization step prior to the reformer or reform a fuel with a small amount of sulfur ($\sim$ $<$100 ppmw). The decentralized or single use mode desulfurization step after the reformer is also called a sulfur polishing step.

Regeneration of metal sulfide (MS) can be carried out by oxidation using air (oxygen) in a manner similar to ore roasting. The regeneration step produces SO_2 as shown below that needs to be disposed in an environmentally acceptable manner:

$$MS(s) + {}^3/_2O_2(g) \rightarrow MO(s) + SO_2(g)(\text{regeneration})$$

The regeneration reaction is highly exothermic requiring the use of a dilute oxygen-containing gas and/or some other way such as fluidized-beds to control bed temperature to below the allowable temperature limit for the sorbent. The use of dilute oxidant produces a regeneration off-gas containing a low SO_2 concentration whose disposal could be both costly and complex. Another complication

associated with regeneration is a side reaction leading to formation of sulfate:

$$MO(s) + SO_2(g) + {}^1/_2O_2(g) \rightarrow MSO_4(s)(\text{sulfation})$$

Residual sulfate in the regenerated metal oxide sorbent can decompose in a reducing environment during subsequent sulfidation that could result in elution of gaseous sulfur compounds (H_2S, COS, SO_2) from the sorbent bed [151]. To minimize sulfate formation, the regeneration temperature needs to be controlled within a narrow window.

Theoretically, a "cleanly" regenerable sorbent can be used for numerous sulfidation-regeneration cycles, thereby essentially eliminating cost of the sorbent as a consideration. The complexities of regeneration as mentioned above, however, appear to rule out the use of an integrated dual-bed sulfidation-regeneration system for compact fuel cell systems. These compact systems thus need to incorporate either fuel desulfurization prior to the reforming step or use a regulated sulfur fuel such as natural gas, LPG, gasoline, or diesel with low sulfur content.

On the other hand, for relatively larger non-compact fuel cell systems using syngas with high H_2S concentration as formed from gasification of coal or black liquor, the use of a regenerable sorbent with centralized regeneration or a disposable sorbent is impractical. For these non-compact fuel cell systems, using syngas containing high levels of H_2S, a bulk sulfur removal step consisting of an integrated dual-bed sulfidation-regeneration system and a sulfur polishing step are both needed.

The bulk sulfur removal and regeneration steps transfer most of the sulfur from syngas to a regeneration off-gas in the form of SO_2 that needs to be disposed in an environmentally acceptable manner. Although there are various options for disposing the SO_2 such as conversion to elemental sulfur, sulfuric acid, or calcium sulfate, conversion to elemental sulfur is the most desirable and practical option [146,148,152].

11.5.1.2. *Metal Oxide Sorbents Employed in the Past*

Over the past 35 years or so, numerous metal oxides and mixed-metal oxides such as V_2O_5, MnO_2, ZnO, Fe_2O_3, CuO, CuO-ZnO, CuO-Al_2O_3, CuO-Cr_2O_3 , Fe_2O_3-SiO_2, ZnO-SiO_2, ZnO-Fe_2O_3, ZnO-TiO_2, ZnO-Al_2O_3, CeO_2-CuO, CeO_2-La_2O_3, CeO_2-ZrO_2, and others have been prepared and evaluated as regenerable sorbents for syngas desulfurization [13,151,153–185],[186–214]. Sorbent preparation techniques have included, among others, dry mixing followed by calcination to achieve solid state reaction and liquid phase techniques such as citrate complexation, impregnation, and co-precipitation. Most of this research and development has been targeted toward regenerable sorbents for bulk desulfurization of syngas in coal gasification-based IGCC systems. Although IGCC turbines have somewhat greater tolerance for H_2S ($\sim$20–50 ppmv) than fuel cells, this research is relevant to syngas desulfurization for fuel cells, particularly for non-compact fuel cells in IGFC systems, requiring both a bulk desulfurization step as well as a polishing step.

Fe_2O_3- and ZnO-based sorbents such as Fe_2O_3-SiO_2 and ZnO-SiO_2 were the initial sorbents to receive attention for low-BTU syngas desulfurization in IGCC systems. The IHI 200 ton/day hot-gas desulfurization demonstration plant was based on the use of a Fe_2O_3 sorbent [160]. Fe_2O_3 reduces to Fe_3O_4 in low BTU gas with Fe_3O_4 being the active desulfurization sorbent. Both Fe_3O_4 and ZnO sorbents have greater than 30 wt% theoretical sulfur capacity for H_2S. Fe_3O_4 has higher reactivity, but poor thermodynamic efficiency, whereas ZnO has lower reactivity and excellent H_2S removal efficiency. For example, ZnO can thermodynamically reduce the H_2S to $<$0.6 ppmv at 400 °C in the presence of even 20 vol% steam [210].

Although research continues on Fe_2O_3-based sorbents even to this date [211], recent large-scale development has been carried out only for ZnO-based sorbents because of their significantly higher thermodynamic efficiency. ZnO, by itself, is usable only up to about 475 °C above which ZnO reduction and zinc sublimation could occur. CuO can withstand higher temperatures and has even higher thermodynamic efficiency than ZnO but it readily reduces in a syngas environment to Cu metal that has very poor thermodynamic efficiency. CuO can be stabilized somewhat using Al_2O_3 as $CuAl_2O_4$ [162]. The CuO-Al_2O_3 sorbent showed significant promise in the first cycle bringing the H_2S and COS down to sub-ppm levels in low-BTU gas. However, its performance significantly deteriorated upon oxidative regeneration from the second cycle onward. Other CuO-based sorbents such as CuO-Cr_2O_3 have been developed [194,195,197] but CuO-based sorbents have never been scaled up beyond bench-scale.

Since higher temperature, more reactive, and more stable sorbents were of interest to reduce the cost of IGCC systems, ZnO-based mixed-metal oxide sorbents such as zinc ferrite, ZnO-Fe_2O_3 ($ZnFe_2O_4$), and zinc titanate, 2ZnO-TiO_2 (Zn_2TiO_4) were developed in the 1980s to increase the reactivity and high temperature stability of ZnO, respectively [155,161,163,166]. When using $ZnFe_2O_4$, Fe_2O_3 is thought to carry out the bulk desulfurization in a more kinetically efficient manner and ZnO carries out both bulk and polishing desulfurization. $ZnFe_2O_4$ extended the usable temperature range of ZnO and Fe_2O_3 to about 538 °C in low-BTU gases but was found to be mechanically unstable in reducing gases with low levels of steam. Also, low levels of steam led to significant carbon formation via the Boudouard reaction.

Zn_2TiO_4 was able to extend the usable temperature range of ZnO to 650−700 °C even in syngas with low levels of steam and did not catalyze carbon formation. Several zinc titanate phases can form including $ZnTiO_3$ and Zn_2TiO_4 depending on the sorbent preparation and calcination conditions [160,162,163,166]. The TiO_2 does not participate in the sulfidation reaction, but helps to prevent ZnO reduction to Zn.

Initially zinc titanate sorbents were developed as extrudates for fixed-bed application. However, severe sorbent spalling of extrudates under reducing conditions, and sulfate formation and difficulties of temperature control during regeneration in fixed beds motivated the development of attrition-resistant zinc titanate sorbents suitable for fluidized bed and transport reactor applications. Also the spalling of zinc titanate extrudates led to the development of more advanced, mechanically stable zinc-based fixed bed sorbents such as La_2O_3-doped zinc titanate and RVS-1 [183,190,196]. Fluidizable zinc oxide- and zinc titanate-based sorbents were the leading IGCC sorbent candidates in the 1990s [151,178,196]. An advanced version of a proprietary attrition-resistant zinc titanate sorbent, EX-SO_3, was scaled up to a 50,000 lb batch for the 100 MW_e Pinon-Pine IGCC plant for use in a dual-bed transport reactor sulfidation-regeneration system. Sorbent circulation was demonstrated but the plant was not able to operate due to technical problems related to the gasifier.

11.5.1.3. Recent Metal Oxide Sorbent Development Efforts

Although desulfurization at higher temperatures could lead to somewhat higher IGCC thermal efficiencies, problems of integration of the desulfurization system at temperatures above 450 °C using a control valve with a load following turbine required cooling the gas, thus defeating any efficiency advantages. Also, higher temperature operation was considered more stressful on the process equipment and sorbent. For these reasons, and since thermodynamically more efficient H_2S removal could be achieved at somewhat lower temperatures, along with potential capture of other coal-based

syngas contaminants such as heavy metals and chloride, attention has shifted in this decade to the so called "warm gas cleanup" temperature range of 300–400 °C [190,195,199,200]. Interest in co-production of liquid fuels, hydrogen, and electricity from coal-derived syngas has emphasized the need for sorbents and other methods for removal of sulfur and other contaminants such as chloride and heavy metals down to ppb levels to prevent poisoning the synthesis catalysts. Also, significant interest in fuel cells that require sulfur removal down to as low as <0.1–1 ppmv has contributed to recent research on sorbents specifically for syngas desulfurization for fuel cell applications [13,198,202–204,206,209,210]. This recent research, as described below, has primarily focused on zinc oxide- and cerium oxide-based sorbents.

11.5.1.3.1. ZINC OXIDE-BASED SORBENTS

Zinc oxide has historically maintained a leading role as the metal oxide desulfurization sorbent to be employed for H_2S removal from various gas streams [13], particularly natural gas, with recent emphasis on H_2S removal from syngas as described in Section 11.5.1.2. It has excellent thermodynamic efficiency, high theoretical sulfur capacity, and once sulfided, it is nonpyrophoric. For once-through applications, it has almost completely replaced hydrated iron oxide and is almost exclusively used as a low temperature sulfur guard in industry for protecting downstream catalysts from poisoning.

For application to IGCC systems, substantial effort as described in Section 11.5.1.2 has been expended for developing zinc oxide-based sorbents that can be regenerated for reuse. The warm gas cleanup temperature range of 300–400 °C, as stated earlier, is currently of particular interest for IGCC systems. This is also a temperature range in which zinc oxide does not suffer reduction to metallic zinc, has excellent thermodynamic removal efficiency down to less than 0.1 ppmv H_2S, and has reasonable kinetic activity. Gangwal et al. [205] prepared and scaled up an attrition-resistant ZnO-Al_2O_3 sorbent by precipitation and spray drying for application to fluidized-bed systems in this temperature range. A proprietary version of their sorbent, RTI-3, was able to reduce the H_2S and COS level to less than 5 ppmv with a breakthrough capacity of about 7 wt% S from a simulated syngas containing 10,000 ppmv H_2S [199,200]. Using a pilot-scale transport system consisting of circulating sulfidation and regeneration reactors, the sorbent's high efficiency, attrition resistance, and durability for H_2S and COS removal was demonstrated from an actual syngas slip-stream at Eastman Chemical Company's coal gasifier [212].

Zinc oxide in the temperature range of 300–400 °C has also been of recent interest for application to fuel cell systems as a polishing sulfur sorbent. For simplicity, a polishing sorbent should be in the form of extrudates or tablets for fixed-bed use rather than in fluidizable particulate form like the RTI-3 sorbent described above. Commercial efforts are under way for development of fuel processors using zinc oxide pellets as a polishing sorbent at 300–400 °C. One example is the development of a fuel processor for SOFC at Precision Combustion, Inc. [213]. Although no details were provided about the sorbent or its source, data is shown for H_2S removal at 350 °C and gas hourly space velocity of 4500 h^{-1} with a challenge gas containing 115 ppmv H2S, 20% steam and balance inert. At these conditions, the authors claim that H_2S is removed to around 0.5 ppmv or less for over 200 h prior to breakthrough. This corresponds to a breakthrough capacity of about 1.5 wt% sulfur for the sorbent.

Fundamental studies have been carried out at PSU and Auburn University to evaluate the performance of zinc oxide sorbents [13,202,209,210] for fuel cell applications. Researchers at Auburn University have carried out a systematic study of the effect of reformate constituents,

CO, CO_2, and steam on the performance and breakthrough capacity of a zinc oxide sorbent [209,210]. The zinc oxide sorbent was prepared as 17 wt% ZnO on silica particles by impregnation of zinc nitrate on to silica followed by drying and calcinations. The simulated reformate gas contained an artificially high 4000 ppmv H_2S to reduce the time for each experiment. Breakthrough experiments were carried out at atmospheric pressure and 400 °C with a gas hourly space velocity of about 14,000 h^{-1}. In the presence of H_2/H_2S as the challenge gas, the sorbent utilization at breakthrough was close to 90%. However, upon addition of CO, CO_2, and/or steam, the sorbent utilization decreased significantly due to formation of COS and/or inhibition of the desulfurization kinetics. For a typical simulated reformate gas containing 10% CO, 20% CO_2, 40% H_2, and 20% steam, the sorbent utilization was only 30%, which translates to a sulfur capacity prior to breakthrough of less than 2 wt%. Since these experiments were carried out using particles, the researchers further noted that the use of extrudates would result in an even greater reduction of sorbent utilization because of inhibition due to internal mass transfer resistances.

Researchers at PSU, in cooperation with Engelhard Corporation, carried out experiments with a zinc oxide sorbent in the form of particles, extrudates, and monolith [13,202] at 400 °C. Extrudates or pellets of sizes in the range from 3mm to 6 mm are the most likely sorbent form to be used commercially for fuel cell applications. Although the PSU experiments used a more realistic challenge gas H_2S concentration of 0.5−8 ppmv for a polishing mode, the reactive bulk constituents of the challenge gas generally contained only steam and hydrogen with neither CO nor CO_2. The particles exhibited a breakthrough sulfur capacity of 2.8 wt% whereas the extrudates had a much lower capacity of only about 0.4 wt%. In concurrence with results at Auburn University, in one experimental series, the inclusion of CO_2 by PSU researchers in the challenge gas was shown to reduce the breakthrough capacity, although not as significantly as that seen in the Auburn University work. This could be attributed to widely differing challenge gas H_2S concentrations used at the two universities. The use of ZnO washcoated monoliths significantly improved the performance. Sulfur cleanup down to 20 ppbv was achieved using the monolith and the breakthrough capacity increased to about 3.5 wt%. These results demonstrated the significant impact mass transfer resistance can have on the capacity. The PSU and the Auburn University works emphasize the need for the design of higher breakthrough capacity zinc oxide sorbents that have lower formation of COS in the presence of CO or CO_2, and can be prepared in extrudate form with low mass transfer resistances.

11.5.1.3.2. CERIUM OXIDE-BASED SORBENTS

Cerium oxide-based sorbents that operate in the 650−800 °C range are being developed as sorbent candidates [185,188,198,203,204,206,214] for removal of H_2S from syngas. Among the various cerium oxide-based sorbents that have been evaluated, a cerium-lanthanum (Ce-La) mixed-metal oxide sorbent, in particular, has been proposed by Tufts University researchers as a regenerable sorbent in the design of compact fuel processors for an SOFC [204,206]. The addition of La helps to stabilize the surface area of CeO_2. The CeO_2 sulfidation chemistry is as follows:

$$2CeO_2(s) + H_2(g) \rightarrow Ce_2O_3(s) + H_2O(g)$$

$$Ce_2O_3(s) + H_2S(g) \rightarrow Ce_2O_2S(s) + H_2O(g)$$

CeO_2 has very poor thermodynamic efficiency for H_2S removal. The chemistry thus involves the reduction of CeO_2 first to Ce_2O_3. Both Ce_2O_3 and La_2O_3 possess superior thermodynamic efficiency for H_2S removal down

to less than a few ppmv even at temperatures as high as 800 °C [200]. Oxidative regeneration of cerium oxysulfide results in the release of sulfur from the sorbent as elemental sulfur vapor:

$$Ce_2O_2S(s) + O_2(g) \rightarrow 2CeO_2(s) + (1/n)S_n(g)$$

The authors suggest that the Ce-La sorbent should be employed at high space velocity to only allow surface sulfidation. If bulk sulfidation is allowed to occur, significant degradation of the performance results due to structural changes during the sulfidation-regeneration cycles. The authors propose the use of anode off-gas for regeneration in an integrated SOFC system. They demonstrate that the sorbent can be efficiently regenerated over numerous cycles without loss of performance if only surface sulfidation is allowed to occur. Using zeolite supported Ce and Cu-Ce sorbents, similar results were demonstrated by researchers at the Army Research Laboratory [214].

With surface sulfidation, the reported breakthrough sulfur capacity of the Tufts University sorbent is only about 0.1–0.15 wt% which is low and necessitates the use of a dual reactor system for cycling between sulfidation and regeneration. Although, as a first thought, the 650–800 °C temperature range of operation is attractive for integration in SOFC that operates at very high temperatures, integration would involve the use of valves for cycling between sulfidation and regeneration that would also have to be durable at these conditions. Formation of COS from H_2S in the presence of CO and CO_2 and premature elution of COS could be problematic under surface sulfidation conditions. The authors have carried out a few experiments with simulated reformate gases containing 1% CO and 10% CO_2 in addition to H_2 and steam. However, no measurements have been reported for COS in the cleaned gas so it is not clear if COS formation presents a problem for the Ce-La sorbent system.

11.5.2. Selective Catalytic Oxidation of H_2S

As an alternative approach to desulfurization using metal oxide sorbents, selective catalytic oxidation of H_2S in reformate gas to elemental sulfur using air (O_2) is interesting, particularly for application to PEMFC [59,60,62]. The desired reaction chemistry is:

$$H_2S + {}^1/_2O_2 \rightarrow (1/n)S_n + H_2O$$

The idea is to condense the elemental sulfur that is formed in the pores of the catalyst used. However, side reactions between surface CO and O_2, and sulfur vapor could lead to formation of COS and SO_2, respectively:

$$CO + (1/n)S_n \rightarrow COS$$

$$(1/n)S_n + {}^1/_2O_2 \rightarrow SO_2$$

Gardner et al. [62] evaluated a well-characterized commercial activated carbon from Calgon Carbon Corporation (Centaur 4x6 granular) for selective catalytic oxidation of H_2S to elemental sulfur in a gasifier gas containing 36% CO, 27% H_2, and 1000 ppmv H_2S at 135–175 °C. The carbon prepared from bituminous coal had a BET surface area of 662 m^2/g and contained several metallic impurities presumed to have catalytic properties. The intent was bulk H_2S removal with direct formation of elemental sulfur that could be recovered by heating the carbon. The O_2/H_2S molar ratio in the feed was varied from 0.5 to 4. At a space velocity of 2500 h^{-1}, the authors demonstrated reduction of H_2S to less than 1.2 ppmv for 6 h. However, up to 150 ppmv COS was formed. Although COS formation could be reduced to 30 ppmv by increasing the O_2/H_2S ratio to 4, it could not be eliminated. Also, SO_2 appeared in the effluent after about 1.5 h and increased to 8 ppmv after 6 h.

Wu et al. [59,60] evaluated several carbons prepared from a pure cellulosic precursor and

a cellulosic precursor full of natural impurities by carbonization of the precursors at 850 °C followed by CO_2 activation at 875–975 °C. These authors claim that two of the ten carbons they prepared and tested designated W3 and W4 with BET surface areas of 770 and 1400 m^2/g, respectively, showed excellent results. On both of these carbons, 100% conversion of H_2S to elemental sulfur was demonstrated over a 10 h test duration with no COS or SO_2 formation. The tests were conducted using a simulated reformate gas containing 50% H_2, 15% CO_2, 9% CO, 2% CH_4, 23% H_2O, and 0.1% H_2S at 150 °C with a feed O_2/H_2S ratio of 2. The other carbons did not fare as well suggesting that both the type of precursor as well the CO_2 activation process for development of the surface and pore structure was important for making a good carbon catalyst. Presumably, in experiments by Wu et al. [59,60], all of the sulfur is retained in the carbon as elemental sulfur, and eventually the carbon would need to be regenerated by heating to remove the sulfur. However, the authors did not test regenerability of their carbon catalysts.

11.5.3. Application to Fuel Cell Systems

Based on the above discussion, there are three potential ways, among others, for removing H_2S from reformate gas for compact fuel processors. These include the use of metal oxide-based sorbents at moderate temperatures (300–400 °C) for sulfur polishing in a once-through mode for all types of fuel cells, CeO_2-based sorbents at high temperatures (650–800 °C) with dual-bed sulfidation and regeneration for SOFC, and selective catalytic oxidation of H_2S over activated carbons at lower temperatures (~150 °C) for PEMFC.

The most likely approach to be used commercially is that based on sulfur polishing using ZnO-based sorbents. These sorbents can be employed at even lower temperatures than 300 °C but may not possess sufficient capacity at lower temperatures due to kinetic limitations. ZnO-based sorbents in extrudate or pellet form with a breakthrough capacity of around 2.5–3 wt% sulfur need to be developed for capturing sulfur (H_2S + COS) down to <0.1 ppmv from realistic syngas containing both CO and CO_2. Although these capacities can be readily achieved as discussed earlier using a fluidizable particulate sorbent like RTI-3, these particles cannot be used in a fixed bed due to high pressure drop.

Reducing the sulfur down to <0.1 ppmv with high breakthrough capacity depends on the kinetics and thermodynamics. Higher temperatures provide better kinetics but reduce the thermodynamic efficiency. Also, the breakthrough capacity of ZnO sorbents reduces due to mass transfer limitations when using extrudates. The alternative approach of using monoliths is attractive and can reduce the H_2S to less than 0.1 ppmv for extended periods of time, but it may be costly.

The other approaches mentioned above are much less likely to be employed commercially. Very low surface capacity of the Ce-based sorbents necessitates the use of a dual-bed sulfidation-regeneration system. However, integration of such a system in a fuel processor could be highly problematic due to the necessity of shut-off valves that can operate at 650–800 °C reliably for long periods of time to allow cycling between the sulfidation and regeneration reactors. The use of catalytic H_2S oxidation using activated carbon at a milder temperature (150 °C) for PEMFC could possibly be applied using a once-through bed or dual beds in a cyclic configuration. In the once-through mode, the capacities of these carbons before breakthrough need to be increased to about 2–3 wt%, which may be a challenging task. For the dual bed system, simple regeneration methods need to be developed to alternate between H_2S oxidation and catalyst regeneration by removal of condensed sulfur.

11.6. INTEGRATION OF SULFUR REMOVAL

Based on review of gas-phase and liquid-phase desulfurization methods, the most likely integration of sulfur removal in compact fuel processors would involve sulfur removal from natural gas, LPG, and petroleum-derived liquid fuels either upstream or downstream of an oxidative steam reformer (OSR). In OSR, the fuel is injected along with steam and air. This causes dilution and results in a lower volumetric concentration of sulfur in the feed. Sulfur appears mostly as H_2S along with some COS in the reformate gas. Further reduction in sulfur volumetric concentration occurs because the reforming reactions occur with a volumetric expansion. Table 11.6 shows the approximate sulfur concentrations in the fuel and an OSR reformate gas when reforming fuels with regulated sulfur contents.

Sulfur removal can be carried out before the reformer, after the reformer, or in both locations and can be integrated in a compact fuel system in many different ways depending on the sulfur tolerance of the reforming catalysts and fuel cells. Multi-step processes before the reformer have also been proposed. For example, a two-stage liquid fuel adsorptive desulfurization (liquid phase followed by gas phase) before the reformer has been proposed as a way to increase the efficiency of desulfurization [215]. This makes sense from the view point of kinetics when electricity is not needed continuously from the fuel cell. The liquid desulfurization being slower, passively continues to desulfurize when placed in an interim storage tank during the periods of reduced or non-operation of the fuel cell. This reduces the desulfurization load on the faster gas phase desulfurizer during periods of electricity demand.

TABLE 11.6 Approximate Sulfur Concentration in OSR Reformate Gas Without Fuel Desulfurization

Fuel	Sulfur (ppmw) Fuel	Sulfur (ppmv) Reformate
Natural gas	2–12 (ppmv)	0.4–2.4
LPG	20–100	2–13
Gasoline	30–80	3–10
Diesel	15	1.5–2.0
Jet fuel	500–1500	50–190

Another example of a two-step fuel desulfurization process before the reformer is based on a pervaporation membrane followed by a sorbent for sulfur removal from commercial high sulfur jet fuels [127]. Although the membranes and sorbents used in this work were not disclosed, the authors claim that using their optimized membrane plus sorbent system, a jet fuel with a sulfur content of 1675 ppmw can be desulfurized to a sulfur level of 10 ppmw.

Single step desulfurization processes are more likely to be used in compact fuel processors. For illustrative purposes, two potential integrations concepts involving fuel desulfurization and reformate desulfurization, respectively, are schematically shown in Fig. 11.6. As shown in Fig. 11.6(a), by employing a sulfur-tolerant reforming catalyst, such as those based on noble metals [216–218], one might possibly forego the sulfur removal step upstream of the reforming step for the low sulfur-regulated fuels (natural gas, LPG, gasoline, and diesel). For potentially high sulfur fuels such as JP-8, sulfur removal upstream of the reformer is generally desirable, and if nearly complete sulfur removal is carried out upstream using, for example, the two stage configuration described above [215], a conventional Ni reforming catalyst can be used as shown in Fig. 11.6(b).

For SOFC, the reformate gas in Fig. 11.6(a) can be sent directly to a sulfur polishing step using a ZnO-based sorbent. Alternatively, a shift step using either a high temperature shift (HTS) or sour gas shift (SGS) catalyst could be employed to reduce the steam content of the

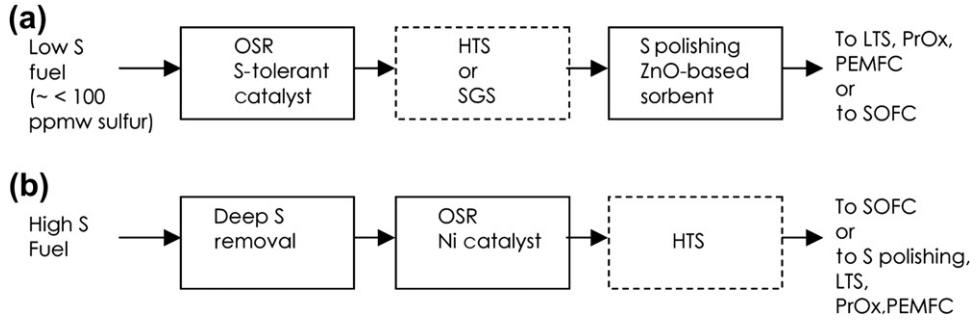

FIGURE 11.6 Integration of sulfur removal in a compact fuel cell system: (a) sulfur removal downstream of OSR; (b) sulfur removal upstream of OSR.

gas. Reduction in steam content of the gas might allow a greater degree of sulfur removal using the ZnO-based sorbent. For PEMFC, additional process steps to remove CO including a low temperature shift (LTS) and preferential oxidation (PrOx) are required. The reformate gas in Fig. 11.6(b) could be sent either directly or after HTS to an SOFC. For PEMFC, further sulfur polishing, LTS and PrOx are needed.

11.7. CONCLUSIONS AND FUTURE DIRECTIONS

Fuel cells can efficiently produce electricity using hydrogen and/or syngas obtained by reforming/gasification of conventional gaseous, liquid, and solid fuels. However, these fuels contain sulfur as impurity that must be nearly completely removed to prevent poisoning of the fuel cell anode catalyst with H_2S. Depending on the sulfur content of the fuel, deep desulfurization of gaseous and liquid fuels can be carried out either upstream of the catalytic reformer or syngas desulfurization can be carried out downstream of the reformer. The goal is to reduce the syngas sulfur content to about 1ppmv for SOFC or to reduce the sulfur content of the hydrogen produced from the syngas to <0.1 ppmv for PEMFC. Fuel desulfurization is impractical for solid fuels such as coal and biomass. These fuels can be gasified to produce a syngas that can then be desulfurized to meet the requirements of the fuel cell in a similar manner as above.

Among the gaseous and liquid fuels, natural gas, LPG, gasoline, diesel, and jet fuel are of most interest for fuel cells because of their ready availability. Use of these fuels can lead to the development of compact fuel processors for fuel cells which is of most commercial interest. Passive deep fuel desulfurization and/or polishing syngas desulfurization using solid sorbents are the methods of choice for compact fuel processors.

A number of promising sorbents continue to be developed for desulfurization of natural gas and LPG at room temperature and low pressure. It appears that adequate breakthrough capacity for one replacement per year has been achieved by many developers and researchers. Among the non-proprietary sorbents, the Ag-exchanged Y-zeolite [50] containing 5 wt% Ag appears to be promising. The sorbent is easy to prepare and is shown to be fully regenerable. The low Ag content would probably not result in an excessive exotherm as described to be problematic by de Wild [40] and the color change feature would be particularly attractive.

Desulfurization of gasoline can also be carried out in the gas phase by reactive adsorption or passive adsorption. Deep desulfurization of naphtha and gasoline by reactive adsorption in the gas phase has been demonstrated at

a commercial scale by Conoco-Phillips using a sorbent-circulated fluidized-bed process consisting of sulfidation (sulfur removal), air regeneration, and H_2 reduction. The process being a bulk desulfurization process with several unit operations appears unsuitable for fuel cell application. On the other hand, passive gas-phase desulfurization of gasoline using adsorption at about 200 °C prior to the reformer of a fuel cell system could be a feasible approach. Gasoline is now readily available with <30 ppmw sulfur. Since sorbent capacities on the order of 2 wt% have been demonstrated, particularly using reduced nickel-based sorbents, deep desulfurized gasoline could be delivered to the reformer for an extended time using a once-through sorbent. The disadvantages and challenges include the need for a gasoline vaporizer, the difficulty of handling and replacing the potentially pyrophoric reduced nickel-based sorbent cartridge, and the requirement of a centralized sorbent regeneration facility. Thus there is a low likelihood that this approach would ever be employed for a compact fuel cell system.

The concept of removal of sulfur compounds from gasoline, jet fuel, and diesel using sorbents in the liquid phase, especially at room temperature, is attractive because of its simplicity. Although there is significant research activity to develop such sorbents, it is not clear if a viable liquid-phase desulfurization process can be developed for compact fuel processors. A number of sorbents including activated carbons, polarity-based sorbents, sorbents based on sulfur−metal interaction, and π-complexation sorbents have been studied.

Activated carbon sorbents appear to be the most promising among the sorbents studied because they can fully remove sterically hindered sulfur compounds such as 4,6 DMDBT from diesel, and they can be regenerated by flushing with an organic solvent, which can be done off-site. Furthermore, it appears feasible to increase their breakthrough capacity to >1 wt % S by a mild HNO_3 treatment that increases the oxygen functional groups on their surface. Also, they do not require any activation, special handling, or heat for operation. Oxidation-assisted adsorption could also be employed upstream of the carbon bed to further increase their capacity.

Sorbents based on sulfur−metal interaction and π-complexation have been extensively studied. Although some of these sorbents achieved a breakthrough sulfur capacity of >1 wt %, the complex preparation, reduction /activation, and handling requirements associated with these sorbents make them somewhat unlikely candidates for application in compact fuel processors. The one exception appears to be the Zn-Fe-Ce sorbent for gasoline developed by Zhang et al. [117]. Since it is in oxide form, there appear to be no special handling requirements. The capacity of 26 mg/g is quite good, but it is reported at 10 ppmw breakthrough rather than 0.1−1 ppmw breakthrough. The operating temperature of 60 °C as opposed to room temperature is also not a desirable feature.

Bulk syngas desulfurization is required if a solid fuel such as coal is gasified for fuel cell use. Coal is of interest because of its abundant availability in the USA even though it will not lead to compact fuel processors for fuel cells. Commercial liquid-phase desulfurization processes such as amine-scrubbing or Rectisol can be used for bulk desulfurization of syngas from coal gasification containing several thousand ppmv sulfur. Also, there has been significant research activity over the past 30 years for development of regenerable metal oxide desulfurization sorbents for high sulfur syngas. Based on this research, regenerable fluidized-bed zinc oxide-based sorbents for bulk desulfurization are in an advanced stage of development.

Irrespective of whether a bulk syngas desulfurization step is required or not in a fuel cell system, a polishing syngas desulfurization step or a sulfur guard bed will generally always

be required to protect the expensive fuel cell. The most likely approach to be used commercially is that based on sulfur polishing using ZnO-based sorbents.

Sorbents that could find commercial application in a compact fuel cell system are those that have most of the desirable characteristics as mentioned in Section 11.3.1.2.1. Based on an extensive review of the literature, it appears that room temperature sorbents for natural gas and LPG are well developed and near commercial. However, room temperature liquid-phase sorbents for gasoline, diesel, and jet fuel desulfurization need to be further improved and developed. Further research and development is needed to measure and validate liquid phase sorbent capacities with fuels meeting current sulfur regulations, and to develop liquid phase sorbents that can be simply prepared and scaled up, easily regenerated offsite and/or onsite, and safely disposed. Further research and development is also needed for development of higher capacity polishing zinc oxide-based sorbents in a form suitable for use in a commercial packed bed for syngas desulfurization down to <0.1 ppmv H_2S. Thought should also be given to how the polishing sorbent is to be integrated with a SOFC and with a PEMFC.

References

[1] Song C. Fuel processing for low-temperature and high-temperature fuel cells: challenges, and opportunities for sustainable development in the 21st century. Catal Today 2002;77(1−2):17−49.

[2] Larminie J. Fuel cell systems explained. New York City, NY: Wiley; 2000.

[3] Crespo D, Qi G, Wang Y, Yang FH, Yang RT. Superior sorbent for natural gas desulfurization. Ind Eng Chem Res 2008;47(4):1238−44.

[4] Rand DAJ, Dell R. Hydrogen energy: challenges and prospects. Cambridge, UK: Royal Society of Chemistry; 2008.

[5] Haji S, Malinger K, Suib SL, Erkey C. Fuels and fuel processing. In: Sammes NM, editor. Fuel cell technology-reaching towards commercialization. London, UK: Springer-Verlag; 2006. p. 166−211.

[6] Bae Y-S, Kwon J-M, Lee C- H. Desulfurization of fuels by selective adsorption for ulrta-clean fuels. In: Zhou L, editor. Adsorption: progress in fundamental and application research. Singapore: World Scientific Publishing Company; 2007. p. 239−44.

[7] Hernandez-Maldonado AJ, Yang FH, Qi G, Yang RT. Desulfurization of transportation fuels by pi-complexation sorbents: Cu(I)-, Ni(II)-, and Zn(II)-zeolites. Appl Catal B: Env 2005;56(1−2):111−26.

[8] Yang YT. Sorbents for applications. In: Adsorbents: fundamentals and applications. Hoboken, NJ: Wiley; 2003. p. 280−382.

[9] Ruth L. Vision 21: energy plants for the 21st century. Prepr Am Chem Soc Div Fuel Chem 2002;47:659.

[10] Song C, Ma XL. New design approaches to ultra-clean diesel fuels by deep desulfurization and deep dearomatization. Appl Catal B: Env 2003;41 (1−2):207−38.

[11] Song C. Fuel processing for low- and high-temperature fuel cell: challenges and opportunities for sustainable development in the 21st century. In: Brandon NP, Thompsett D, editors. Fuel cell compendium. Amsterdam: Elsevier; 2005. p. 53−90.

[12] EG & G Technical Services, Inc., Fuel cell handbook 7th ed. DOE Contract No. DE-AM26-99FT40575, November 2004.

[13] Novochinskii II , Song CS, Ma XL, Liu XS, Shore L, Lampert J, et al. Low-temperature H_2S removal from steam-containing gas mixtures with ZnO for fuel cell application. 1. ZnO particles and extrudates. Energy Fuels 2004;18(2):576−83.

[14] Kharchenko NV. Clean coal power generation. In: Advanced energy systems, Chapter 9. Washington, DC: Taylor and Francis; 1998. p. 211−42.

[15] Rezaiyan J, Cheremisinoff NP. In: Integration of gasification technologies. Gasification technologies: a primer for engineers and scientists. Chapter 6. Washington, DC: Taylor and Francis; 2005. pp. 271−330.

[16] Grol E. Technical assessment of an integrated gasification fuel cell combined cycle with carbon capture. Energy Procedia 2009;1(1):4307−13.

[17] Craig KR, Mann MK. Cost and performance analysis of biomass-based integrated gasification combined cycle (BIGCC) power systems, NREL/TP-430−21657, October 1996.

[18] Iaquaniello G, Mangiapane A. Integration of biomass gasification with MCFC. Int J Hydrogen Energy 2006;31(3):399−404.

[19] Morita H, Yoshiba F, Woudstra N, Hemmes K, Spliethoff H. Feasibility study of wood biomass gasification/molten carbonate fuel cell power system − comparative characterization of fuel cell and gas turbine systems. J Power Sources 2004;138(1−2):31−40.

[20] National Energy Technology Laboratory. Proceedings of the 10th Annual SECA Workshop, Pittsburgh, PA, July 14–16, 2009.
[21] Lobachyov KV, Richter HJ. An advanced integrated biomass gasification and molten fuel cell power system. Energy Conv Manage 39(16-18):1931-43.
[22] Steynberg A, Dry M. Fischer-Tropsch technology. Amsterdam: Elsevier; 2004.
[23] EPA Office of Transportation and Air Quality, Regulatory Announcement, EPA420-F-06–027, EPA 420-F-06-040, 2006.
[24] Federal Register 40 CFR 80 Subpart H.
[25] Rojey A, Jaffret C, Cornot-Gondolpha S, Durand B, Julian S, Valais M. Natural gas processing. In: Natural gas production processing transport. Chapter 7. Paris: Editions Technip; 1997. p. 243–304.
[26] Kohl AL, Nielson R. Gas purification. 5th ed. Houston: Gulf Publishing Co.; 1997.
[27] Myers RA. Handbook of petroleum refining processes. Part XI. 3rd ed. New York: McGraw Hill; 2004.
[28] Whitehurst DD, Isoda T, Mochida I. Present state of the art and future challenges in the hydrodesulfurization of polyaromatic sulfur compounds. In: Eley DD, Haag WO, Bruce G, Helmut K, editors. Advances in catalysis. Academic Press; 1998. p. 345–471.
[29] Olson GJ. Microbial catalyst for desulfurization of liquid fuels. US Patent No. 6124130, 2000.
[30] Li FL, Xu P, Feng JH, Meng L, Zheng Y, Luo LL, et al. Microbial desulfurization of gasoline in a Mycobacterium goodii X7B immobilized-cell system. Appl Environ Microbiol 2005;71(1):276–81.
[31] Rhee SK, Chang JH, Chang YK, Chang HN. Desulfurization of dibenzothiophene and diesel oils by a newly isolated Gordona strain, CYKS1. Appl Environ Microbiol 1998;64(6):2327–31.
[32] Bosmann A, Datsevich L, Jess A, Lauter A, Schmitz C, Wasserscheid P. Deep desulfurization of diesel fuel by extraction with ionic liquids. Chem Comm 2001;23:2494–5.
[33] Sheldon R. Catalytic reactions in ionic liquids. Chem Comm 2001;23:2399–407.
[34] Welton T. Room-temperature ionic liquids. Solvents for synthesis and catalysis. Chem Rev 1999;99 (8):2071–83.
[35] Cussler EL. Facilitated and active transport. In: Paul DR, Yampol'skii YP, editors. Polymeric gas separation membranes. Boca Raton, FL: CRC Press; 1994. p. 273–300.
[36] Parrillo DJ, Thaeron C, Sircar S. Separation of bulk hydrogen sulfide hydrogen mixtures by selective surface flow membrane. AIChE J 1997;43(9):2239–45.
[37] Lin HQ, Van Wagner E, Freeman BD, Toy LG, Gupta RP. Plasticization-enhanced hydrogen purification using polymeric membranes. Science 2006;311(5761):639–42.
[38] Israelson G. Desulfurization for fuel cell systems using sulfur separating membranes. US Patent No. 6946209, 2005.
[39] Alptekin G, DeVoss S, Dubovik M, Monroe J, Amalfitano R, Israelson G. Regenerable sorbent for natural gas desulfurization. J Mat Eng Perform 2006;15(4):433–8.
[40] de Wild PJ, Nyqvist RG, de Bruijn FA, Stobbe ER. Removal of sulphur-containing odorants from fuel gases for fuel cell-based combined heat and power applications. J Power Sources 2006;159(2):995–1004.
[41] Alptekin GO. Sorbents for desulfurization of hydrocarbon fuels (Natural gas, LPG, and jet fuel) for fuel cell applications, 2006 SECA Workshop, Philadelphia, PA, September 2006.
[42] Alptekin GO, Jayaraman A, Dubovic M, Schaefer M, Amalfitano R., Ware M, et-al. Natural gas desulfurization for fuel cell applications, 2008 AIChE Spring National Meeting. New Orleans, LA, April, 2008.
[43] Kim S, Lee H, Woo H. Desulfurization adsorbent for fuel cell and desulfurizing method using the same. US Patent Application, 2007/0093385, 2007.
[44] Lee D, Kim S, Lee H, Park E, Ko E, Pak C, et-al. Desulfurizer for fuel gas for fuel cell and desulfurization method using the same. US Patent Application, 2007/0196258 A1, 2007.
[45] Yang RT, Wang Y, Amestica L. Natural gas desulfurization. US Patent Application No. 2009/0118528, 2009.
[46] Takatsu K, Takegoshi G. Adsorbent for removing sulfur compound, process for producing hydrogen, and fuel cell system. US Patent No. 7556872, 2009.
[47] King DL, Bimbaum JC, Singh P. Sulfur removal from pipeline natural gas. Proc Fuel Cell Seminar, Palm Springs, CA, 2002. p. 782.
[48] de Wild PJ. Method for desulphurisation of natural gas. US Patent Application No. 2006/0058565, 2006.
[49] Israelson G. Results of testing various natural gas desulfurization adsorbents. J Mat Eng Perform 2004;13(3):282–6.
[50] Satokawa S, Kobayashi Y, Fujiki H. Adsorptive removal of dimethylsulfide and t-butylmercaptan from pipeline natural gas fuel on Ag zeolites under ambient conditions. Appl Catal B: Env 2005;56 (1–2):51–6.
[51] Katikaneni S, Yuh C, Abens S, Farooque M. The direct carbonate fuel cell technology: advances in multi-fuel processing and internal reforming. Catal Today 2002;77(1–2):99–106.
[52] Engelhard develops fuel sulfur removal. Fuel Cells Bull 2003;2003(11):9.

[53] Texas LPG Fuel-Processor Development and Fuel Cell Demonstration, Final Report, DOE Contract Number DE-FC36−02GO12018.

[54] Russel B, Doshi KJ, Gorawara JK. Hydrogen generator having sulfur compound removal and processes for the same. International Patent Appliction No. WO 2004/033367, 2004.

[55] Satokawa S, Kobayashi Y, Fujiki H. Removal of sulfur compounds from natural gas by adsorption on Ag-exchanged zeolites for PEFC. In: Masakazu A, Makoto O, Hiromi Y, editors. Studies in surface science and catalysis. Amsterdam, The Netherlands: Elsevier B.V.; 2003. 145: p. 399−402.

[56] Cui H, Turn SQ, Reese MA. Removal of sulfur compounds from utility pipelined synthetic natural gas using modified activated carbons. Catal Today 2009;139(4):274−9.

[57] Lampert JK, Shore L, Farrauto RJ, Hwang S. Method of desulfurizing a hydrocarbon gas by selective partial oxidation and adsorption. US Patent No. 7074375, 2006.

[58] Lampert J. Selective catalytic oxidation: a new catalytic approach to the desulfurization of natural gas and liquid petroleum gas for fuel cell reformer applications. J Power Sources 2004;131 (1−2):27−34.

[59] Wu X, Kercher AK, Schwartz V, Overbury SH, Armstrong TR. Removing hydrogen sulfide from hydrogen rich gas streams by selective catalytic oxidation. Prep Pap-Am Chem Soc Div Fuel Chem 2004;49(2):893−4.

[60] Wu X, Kercher AK, Schwartz V, Overbury SH, Armstrong TR. Activated carbons for selective catalytic oxidation of hydrogen sulfide to sulfur. Carbon 2005;43(5):1087−90.

[61] Shekhawat D, Gardner TH, Berry DA. Natural gas odorant desulfurization. Poster presentation. Austin, TX: AIChE Ann. Mtg.; November 2004.

[62] Gardner TH, Berry DA, Lyons KD, Beer SK, Freed AD. Fuel processor integrated H_2S catalytic partial oxidation technology for sulfur removal in fuel cell power plants. Fuel 2002;81(17): 2157−66.

[63] Song C. An overview of new approaches to deep desulfurization for ultra-clean gasoline, diesel fuel and jet fuel. Catal Today 2003;86(1−4):211−63.

[64] Babich IV, Moulijn JA. Science and technology of novel processes for deep desulfurization of oil refinery streams: a review. Fuel 2003;82(6):607−31.

[65] Nafis DA, Houde EJ. Gasoline desulfurization. Chapter 11.6. In: Myers RA, editor. Handbook of petroleum refining processes. 3rd ed. New York: McGraw Hill; 2004.

[66] Huang X, King DA, Zheng F, Stenkamp VS, TeGrotenhuis WE, Roberts BQ, et al. Hydrodesulfurization of JP-8 fuel and its microchannel distillate using steam reformate. Catal Today 2008;136(3−4):291−300.

[67] Legg D, Gislason J, The S. Zorb sulfur removal technology applied to gasoline. Chapter 11.4. In: Myers RA, editor. Handbook of petroleum refining processes. 3rd ed. New York: McGraw Hill; 2004.

[68] Sughrue E, Parsons JS. ConocoPhillips S Zorb diesel process. Chapter 11.5. In: Myers RA, editor. Handbook of petroleum refining processes. 3rd ed. New York: McGraw Hill; 2004.

[69] Gislason J. Philips sulfur-removal process nears commercialization. Oil Gas J 2001;99:72−6.

[70] Tomoyuki Y, Suzuki T, Yoshinari T. Deep desulfurization catalyst, method of preparing the same, and method for desulfurization using the same. US Patent No. 6992041, 2006.

[71] Turk BS, Gupta RP, Arena BJ, 5th International conference refinery processing, AIChE Publication No. 158, 2002; p. 345−51.

[72] Tawara K, Nishimura T, Iwanami H, Nishimoto T, Hasuike T. New hydrodesulfurization catalyst for petroleum-fed fuel cell vehicles and cogenerations. Ind Eng Chem Res 2001;40(10):2367−70.

[73] Khare GP, Engelbart DR, Cass BW. Transport desulfurization process utilizing a sulfur sorbent that is both fluidizable and circulable and a method of making such sulfur sorbent. U.S. Patent Nos. 5914292, 1999 and 6056871, 2000.

[74] Bezverkhyy I, Ryzhikov A, Gadacz G, Bellat JP. Kinetics of thiophene reactive adsorption on Ni/SiO_2 and Ni/ZnO. Catal Today 2008;130(1):199−205.

[75] Ryzhikov A, Bezverkhyy I, Bellat JP. Reactive adsorption of thiophene on Ni/ZnO: role of hydrogen pretreatment and nature of the rate determining step. Appl Catal B: Environ 2008;84 (3−4):766−72.

[76] Bezverkhyy I, Safonova OV, Afanasiev P, Bellat JP. Reaction between thiophene and Ni nanoparticles supported on SiO_2 or ZnO: in situ synchrotron x-ray diffraction study. J Phys Chem C 2009;113 (39):17064−9.

[77] Ma XL, Sprague M, Song CS. Deep desulfurization of gasoline by selective adsorption over nickel-based adsorbent for fuel cell applications. Ind Eng Chem Res 2005;44(15):5768−75.

[78] Ma XL, Velu S, Kim JH, Song CS. Deep desulfurization of gasoline by selective adsorption over solid adsorbents and impact of analytical methods on ppm-level sulfur quantification for fuel cell applications. Appl Catal B: Env 2005;56(1−2):137−47.

[79] Velu S, Ma XL, Song CS, Namazian M, Sethuraman S, Venkataraman G. Desulfurization of JP-8 jet fuel by selective adsorption over a Ni-based adsorbent for micro solid oxide fuel cells. Energy Fuels 2005;19(3):1116–25.

[80] Landau M, Herskowitz M, Reizner I, Hou Z, Kegerrels JE. Process for removing sulfur compounds from hydrocarbon streams and adsorbent used in this process. US Patent Application No. 2005/0258077, 2005.

[81] Landau MV, Herskowitz M, Agnihotri R, Kegerreis JE. Ultradeep adsorption-desulfurization of gasoline with Ni/Al-SiO2 material catalytically facilitated by ethanol. Ind Eng Chem Res 2008;47 (18):6904–16.

[82] Salem ABSH. Naphtha desulfurization by adsorption. Ind Eng Chem Res 1994;33:336–40.

[83] Salem ABSH, Hamid HS. Removal of sulfur compounds from naphtha solutions using solid adsorbents. Chem Eng Tech 1997;20(5):342–7.

[84] Savage DW, Kaul BK, Dupre GD, O'Bara JT, Wales WE, Ho TC. Deep desulfurization of distillate fuels. US Patent No. 5454933, 1995.

[85] Irvine RL, Benson BA, Frye RA. IRVAD process-low cost breakthrough for low sulfur gasoline. NPRA Annual Meeting, San Antonio, Texas, March 21–23, 1999.

[86] Irvine RL. Process for desulfurizing gasoline and hydrocarbon feedstocks. US Patent No. 5730860, 1999.

[87] Ma XL, Sun L, Song CS. A new approach to deep desulfurization of gasoline, diesel fuel and jet fuel by selective adsorption for ultra-clean fuels and for fuel cell applications. Catal Today 2002;77(1–2):107–16.

[88] Ma X, Sprague M, Sun L, Song C. Deep desulfurizatin of gasoline by SARS process using adsorbent for fuel cells. Fuel Chem Div Preprints 2002;47 (2):452–3.

[89] Ma X, Velu S, Sun L, Song C, Namazian M, Sethuraman S. Adsorptive desulfurization of JP-8 jet fuel and its light fraction over nickel-based adsorbents for fuel cell applications. Prep Pap Am Chem Soc Div Fuel Chem 2003;48(2):688–9.

[90] Velu S, Ma XL, Song CS. Selective adsorption for removing sulfur from jet fuel over zeolite-based adsorbents. Ind Eng Chem Res 2003;42 (21):5293–304.

[91] Velu S, Ma X, Sun L, Song C. Fuel cell grade gasoline production by selective adsorption for removing sulfur. Prepr Am Chem Soc Div Pet Chem 2003;48:58–61.

[92] Velu S, Ma X, Song C. Mechanistic investigations on the adsorption of organic sulfur compounds over solid adsorbents in the adsorptive desulfurization of transportation fuels. Prep Pap Am Chem Soc Div Fuel Chem 2003;47(2):447–8.

[93] Watanabe S, Ma X, Song C. Selective sulfur removal from liquid hydrocarbons over regenerable CeO_2–TiO_2 adsorbents for fuel cell applications. Prepr Pap Am Chem Soc Div Pet Chem 2004;9 (2):511–4.

[94] Zhou A, Ma X, Song C. Deep desulfurization of diesel fuels by selective adsorption with activated carbons. Prep Pap Am Chem Soc Div Pet Chem 2004;49:329–32.

[95] Velu S, Song C, Engelhard MH, Chin Y- H. Adsorptive removal of organic sulfur compounds from jet fuel over K-exchanged NiY zeolites prepared by impregnation and ion exchange. Ind Eng Chem Res 2005;44(15):5740–9.

[96] Kim JH, Ma XL, Zhou AN, Song CS. Ultra-deep desulfurization and denitrogenation of diesel fuel by selective adsorption over three different adsorbents: a study on adsorptive selectivity and mechanism. Catal Today 2006;111(1–2):74–83.

[97] Zhou AN, Ma XL, Song CS. Liquid-phase adsorption of multi-ring thiophenic sulfur compounds on carbon materials with different surface properties. J Phys Chem B 2006;110(10):4699–707.

[98] Zhou A, Ma X, Song C. Effects of oxidative modification of carbon surface on the adsorption of sulfur compounds in diesel fuel. Appl Catal B: Env 2009;87 (3–4):190–9.

[99] Yang RT, Takahashi A, Yang FH. New sorbents for desulfurization of liquid fuels by pi-complexation. Ind Eng Chem Res 2001;40(26):6236–9.

[100] Hernandez-Maldonado AJ, Yang RT. Desulfurization of liquid fuels by adsorption via pi complexation with Cu(I)-Y and Ag-Y zeolites. Ind Eng Chem Res 2003;42(1):123–9.

[101] Yang RT, Hernandez-Maldonado AJ, Yang FH. Desulfurization of transportation fuels with zeolites under ambient conditions. Science 2003;301 (5629):79–81.

[102] Hernandez-Maldonado AJ, Yang RT. Desulfurization of commercial liquid fuels by selective adsorption via pi-complexation with Cu(I)-Y zeolite. Ind Eng Chem Res 2003;42(13):3103–10.

[103] Hernandez-Maldonado AJ, Yang RT. Desulfurization of diesel fuels by adsorption via pi-complexation with vapor-phase exchanged Cu(l)-Y zeolites. J Am Chem Soc 2004;126(4):992–3.

[104] Hernandez-Maldonado AJ, Yang RT. Desulfurization of diesel fuels via pi-complexation with nickel(II)-exchanged X- and Y-zeolites. Ind Eng Chem Res 2004;43(4):1081–9.

[105] Hernandez-Maldonado AJ, Yang RT. New sorbents for desulfurization of diesel fuels via pi-complexation. AIChE J 2004;50(4):791–801.
[106] Hernandez-Maldonado AJ, Stamatis SD, Yang RT, He AZ, Cannella W. New sorbents for desulfurization of diesel fuels via pi complexation: layered beds and regeneration. Ind Eng Chem Res 2004;43 (3):766–9.
[107] Hernandez-Maldonado AJ, Yang RT. Desulfurization of transportation fuels by adsorption. Catal Rev Sci Eng 2004;46(2):111–50.
[108] Hernandez-Maldonado AJ, Yang RT, Cannella W. Desulfurization of commercial jet fuels by adsorption via pi-complexation with vapor phase ion exchanged Cu(I)-Y zeolites. Ind Eng Chem Res 2004;43(19):6142–9.
[109] Hernandez-Maldonado AJ, Qi GS, Yang RT. Desulfurization of commercial fuels by pi-complexation: Monolayer CuCl/gamma-Al_2O_3. Appl Catal B: Env 2005;61(3–4):212–8.
[110] Wang YH, Yang FH, Yang RT, Heinzel JM, Nickens AD. Desulfurization of high-sulfur jet fuel by pi-complexation with copper and palladium halide sorbents. Ind Eng Chem Res 2006;45 (22):7649–55.
[111] Li YW, Yang FH, Qi GS, Yang RT. Effects of oxygenates and moisture on adsorptive desulfurization of liquid fuels with Cu(I)Y zeolite. Catal Today 2006;116(4):512–8.
[112] Wang YH, Yang RT. Desulfurization of liquid fuels by adsorption on carbon-based sorbents and ultrasound-assisted sorbent regeneration. Langmuir 2007;23(7):3825–31.
[113] Wang Y, Yang RT, Heinzel JM. Desulfurization of jet fuel by pi-complexation adsorption with metal halides supported on MCM-41 and SBA-15 mesoporous materials. Chem Eng Sci 2008;63(2):356–65.
[114] Chen H, Wang Y, Yang FH, Yang RT. Desulfurization of high-sulfur jet fuel by mesoporous [pi]-complexation adsorbents. Chem Eng Sci 2009;64(24):5240–6.
[115] Sano Y, Choi K-H, Korai Y, Mochida I. Adsorptive removal of sulfur and nitrogen species from a straight run gas oil over activated carbons for its deep hydrodesulfurization. Appl Catal B: Env 2004;49(4):219–25.
[116] Ng FTT, Rahman A, Ohasi T, Jiang M. A study of the adsorption of thiophenic sulfur compounds using flow calorimetry. Appl Catal B: Env 2005;56 (1–2):127–36.
[117] Zhang JC, Song LF, Hu JY, Ong SL, Ng WJ, Lee LY, et al. Investigation on gasoline deep desulfurization for fuel cell applications. Energy Conver Manage 2005;46(1):1–9.
[118] Bhandari VM, Hyun Ko C, Geun Park J, Han S-S, Cho S-H, Kim J- N. Desulfurization of diesel using ion-exchanged zeolites. Chem Eng Sci 2006;61 (8):2599–608.
[119] Dai W, Zhou YP, Li SN, Li W, Su W, Sun Y, et al. Thiophene capture with complex adsorbent SBA-15/Cu(I). Ind Eng Chem Res 2006;45(23):7892–6.
[120] King DL, Li L. Removal of sulfur components from low sulfur gasoline using copper exchanged zeolite Y at ambient temperature. Catal Today 2006;116 (4):526–9.
[121] Katsuno H, Matsuda S, Saito K, Yoshinaka M. Desulfurizing agent for hydrocarbon derived from petroleum, method for producing hydrogen for use in fuel cell and method for producing nickel-based desulfurizing agent. US Patent No. 7268097, 2007.
[122] Liu BS, Xu DF, Chu JX, Liu W, Au CT. Deep desulfurization by the adsorption process of fluidized catalytic cracking (FCC) diesel over mesoporous Al-MCM-41 materials. Energy Fuels 2007;21 (1):250–5.
[123] Park JG, Ko CH, Yi KB, Park J-H, Han S-S, Cho S-H, et al. Reactive adsorption of sulfur compounds in diesel on nickel supported on mesoporous silica. Appl Catal B: Env 2008;81(3–4):244–50.
[124] Zhang ZY, Shi TB, Jia CZ, Ji WJ, Chen Y, He MY. Adsorptive removal of aromatic organosulfur compounds over the modified Na-Y zeolites. Appl Catal B: Env 2008;82(1–2):1–10.
[125] van Rheinberg O, Lucka K, Köhne H, Schade T, Andersson JT. Selective removal of sulphur in liquid fuels for fuel cell applications. Fuel 2008;87 (13–14):2988–96.
[126] Linxue W, Chunhu L, Haiyan Y, Lijuan F, Yingmin Y, Yingfei H. Sulfur removal of FCC gasoline by selective adsorption over activated semi-coke. Chem Technol Fuels Oils 2009;45(2):85–91.
[127] Wang Y, Latz J, Dahl R, Pasel J, Peters R. Liquid phase desulfurization of jet fuel by a combined pervaporation and adsorption process. Fuel Proc Tech 2009;90(3):458–64.
[128] Meng CM, Fang YM, Jin LJ, Hu HQ. Deep desulfurization of model gasoline by selective adsorption on Ag^+/Al-MSU-S. Catal Today 2010;149 (1–2):138–42.
[129] Hernandez SP, Fino D, Russo N. High performance sorbents for diesel oil desulfurization. Chem Eng Sci 2010;65(1):603–9.
[130] Rang H, Kann J, Oja V. Advances in desulfurization research of liquid fuel. Oil Shale 2006;23(2):164–76.
[131] Skov ER, England DC. The ULSD oxidative desulfurization option. Hydrocarbon Eng 2007;12:33–8.

[132] Ito E, van Veen JAR. On novel processes for removing sulphur from refinery streams. Catal Today 2006;116(4):446–60.
[133] Mei H, Mei BW, Yen TF. A new method for obtaining ultra-low sulfur diesel fuel via ultrasound assisted oxidative desulfurization. Fuel 2003;82(4):405–14.
[134] Yu GX, Lu SX, Chen H, Zhu ZN. Oxidative desulfurization of diesel fuels with hydrogen peroxide in the presence of activated carbon and formic acid. Energy Fuels 2005;19(2):447–52.
[135] Kong LY, Li G, Wang XS, Wu B. Oxidative desulfurization of organic sulfur in gasoline over Ag/TS-1. Energy Fuels 2006;20(3):896–902.
[136] Etemadi O, Yen TF. Selective adsorption in ultrasound-assisted oxidative desulfurization process for fuel cell reformer applications. Energy Fuels 2007;21(4):2250–7.
[137] Karas L, Grey RA, Lynch MW. Desulfurization process. US Patent No. 7314545, 2008.
[138] Chica A, Corma A, Dómine ME. Catalytic oxidative desulfurization (ODS) of diesel fuel on a continuous fixed-bed reactor. J Catal 2006;242(2):299–308.
[139] Wismann W, Gangwal SK. Process for desulfurization of petroleum distillates. U.S. Patent No. 6565741, 2003.
[140] Berezutskiy VM. Method of purifying a liquid medium. US Patent Application 2006/0211906 A1, 2006.
[141] Murata S, Murata K, Kidena K, Nomura M. A novel oxidative desulfurization system for diesel fuels with molecular oxygen in the presence of cobalt catalysts and aldehydes. Energy Fuels 2004;18(1):116–21.
[142] Gatan R, Barger P, Gembicki V, Cavanna A, Molinari D. Oxidative desulfurization: a new technology for ULSD. Prepr Pap Am Chem Soc Div Fuel Chem 2004;49(2):577–9.
[143] Ma XL, Zhou AN, Song CS. A novel method for oxidative desulfurization of liquid hydrocarbon fuels based on catalytic oxidation using molecular oxygen coupled with selective adsorption. Catal Today 2007;123(1–4):276–84.
[144] Sundararaman R, Ma X, Song CS. Oxidative desulfurization of diesel fuels using air by in-situ hydroperoxide generation for fuel cell applications. Paper No. 2847, 21st NAM, San Francisco, 2009.
[145] Gangwal SK. Hot gas desulphurisation sorbent development for IGCC systems. IChemE Symposium Series 1991;123:159–70.
[146] Gangwal SK, Gupta R, McMichael WJ. Hot gas cleanup-sulfur recovery-technical, environmenetal, and economic issues. In: Heat recovery systems and combined heat and power, 15. New York: Elsevier; 1995. p. 205–14 (2).
[147] Gangwal SK. Sulfur removal from gas streams at high temperature. In: Schmidt E, Gang P, Pilz T, Dittler A, editors. High temperature gas cleaning. 1st ed. Karlsruhe, Germany: University of Karlsruhe; 1996. p. 489–501.
[148] Gangwal SK, Portzer JW, Gupta R, Turk BS. Sulfur recovery in advanced IGCC systems. Proceedings of the 12th Korea-US joint workshop on energy and environment. Taejon, Korea, October 1997, pp. 186.
[149] Westmoreland PR, Harrison DP. Evaluation of candidate solids for high-temperature desulfurization of low-BTU gases. Environ Sci Tech 1976;10(7):659–61.
[150] Hepworth MT, Benslimane R, Zhong S. Thermodynamic comparison of several sorbent systems for hot coal-derived fuel-gas desulfurization. Energy Fuels 1993;7(5):602–9.
[151] Gupta R, Gangwal SK. Enhanced durability of desulfurization sorbents for fluidized-bed applications. Final Report, Contract DOE/MC/25006–3271 (DE93000247), 1992.
[152] Gangwal SK, McMichael WJ, Dorchak TP. The direct sulfur recovery process. Environ Prog 1991;10(3):186–91.
[153] Schrodt JT, Hilton GB, Rogge CA. High-temperature desulphurization of low-CV fuel gas. Fuel 1975;54(4):269–72.
[154] Westmoreland PR, Gibson JB, Harrison DP. Comparative kinetics of high-temperature reaction between h2s and selected metal-oxides. Environ Sci Tech 1977;11(5):488–91.
[155] Grindley T, Steinfeld G. Development and testing of regenerable hot coal-gas desulfurization sorbents. Final Report, DOE Contract No. DOE/MC/16545–1125, 1981.
[156] Tamhankar SS, Bagajewicz M, Gavalas GR, Sharma PK, Flytzani-Stephanopoulos M. Mixed-oxide sorbents for high-temperature removal of hydrogen-sulfide. Ind Eng Chem Proc Des Dev 1986;25(2):429–37.
[157] Van der Wal JJW. Desulfurization of process gas by means of iron oxide on silica sorbents. PhD Thesis. University Utrecht; 1987.
[158] Hasatani M, Mastuda H, Kataoka A. Desulfurization of low-calorie gas produced by the gasification of a solid fuel in a packed bed of iron oxide pellets. Int Chem Eng 1988;28(3):497–503.
[159] Kyotani T, Kawashima H, Tomita A, Palmer A, Furimsky E. Removal of H_2S from hot gas in the presence of Cu-containing sorbents. Fuel 1989;68(1):74–9.
[160] Gangwal SK, Stogner JM, Harkins SM, Bossart SJ. Testing of novel sorbents for H_2S removal from coal-gas. Environ Prog 1989;8(1):26–34.

[161] Patrick V, Gavalas GR, Flytzani-Stephanopoulos M, Jothimurugesan K. High-temperature sulfidation regeneration of CuO-Al_2O_3 sorbents. Ind Eng Chem Res 1989;28(7):931–40.

[162] Gangwal SK, Harkins SM, Woods MC, Jain SC, Bossart SJ. Bench-scale testing of high-temperature desulfurization sorbents. Environ Prog 1989;8 (4):265–9.

[163] Lew S, Jothimurugesan K, Flytzani-Stephanopoulos M. High-temperature H_2S removal from fuel gases by regenerable zinc-oxide titanium-dioxide sorbents. Ind Eng Chem Res 1989;28(5):535–41.

[164] Sugitani T. Development of hot-gas desulfurization process. J Fuel Society Jpn 1989;68(9):787.

[165] Woods MC, Gangwal SK, Jothimurugesan K, Harrison DP. Reaction between H_2S and zinc-oxide titanium-oxide sorbents. 1. single-pellet kinetic-studies. Ind Eng Chem Res 1990;29(7):1160–7.

[166] Woods MC, Gangwal SK, Harrison DP, Jothimurugesan K. Kinetics of the reactions of a zinc ferrite sorbent in high-temperature coal-gas desulfurization. Ind Eng Chem Res 1991;30(1):100–7.

[167] Ayala RE, Marsh DW. Characterization and long-range reactivity of zinc ferrite in high-temperature desulfurization processes. Ind Eng Chem Res 1991;30(1):55–60.

[168] Gupta R, Gangwal SK, Jain SC. Development of zinc ferrite sorbents for desulfurization of hot coal-gas in a fluid-bed reactor. Energy Fuels 1992;6(1):21–7.

[169] Sasaoka E, Ichio T, Kasaoka S. High-temperature H_2S removal from coal-derived gas by iron-ore. Energy Fuels 1992;6(5):603–8.

[170] Baird T, Denny PJ, Hoyle R, McMonagle F, Stirling D, Tweedy J. Modified zinc-oxide absorbents for low-temperature gas desulfurization. J Chem Soc Faraday Trans 1992;88(22):3375–82.

[171] Lew S, Sarofim AF, Flytzani-Stephanopoulos M. Sulfidation of zinc titanate and zinc-oxide solids. Ind Eng Chem Res 1992;31(8):1890–9.

[172] Kidd DR. Nickel-promoted absorbing compositions for selective removal of hydrogen sulfide. US Patent No. 5094996, 1992.

[173] Sasaoka E, Sakamoto M, Ichio T, Kasaoka S, Sakata Y. Reactivity and durability of iron-oxide high-temperature desulfurization sorbents. Energy Fuels 1993; 7(5):632–8.

[174] Patrick V, Gavalas GR, Sharma PK. Reduction, sulfidation, and regeneration of mixed iron aluminum-oxide sorbents. Ind Eng Chem Res 1993; 32(3):519–32.

[175] Mojtahedi W, Salo K, Abbasian J. Desulfurization of hot coal gas in fluidized bed with regenerable zinc titanate sorbents. Fuel Proc Tech 1994;37(1):53–65.

[176] Sasaoka E, Hirano S, Kasaoka S, Sakata Y. Characterization of reaction between zinc-oxide and hydrogen-sulfide. Energy Fuels 1994;8(5):1100–5.

[177] Ben-Slimane R, Hepworth MT. Desulfurization of hot coal-derived fuel gases with manganese-based regenerable sorbents. 1. Loading (sulfidation) tests. Energy Fuels 1994;8(6):1175–83.

[178] Khare GP, Delzer GA, Kubicek DH, Greenwood GJ. Hot gas desulfurization with Phillips Z-sorb sorbent in moving bed and fluidized bed reactors. Env Prog 1995;14(3):146–50.

[179] Mojtahedi W, Abbasian J. H_2S removal from coal-gas at elevated-temperature and pressure in fluidized-bed with zinc titanate sorbents. 2. Sorbent durability. Energy Fuels 1995;9(5):782–7.

[180] Sasaoka E, Taniguchi K, Hirano S, Uddin MA, Kasaoka S, Sakata Y. Catalytic activity of ZnS formed from desulfurization sorbent ZnO for conversion of COS to H_2S. Ind Eng Chem Res 1995;34(4):1102–6.

[181] Davidson JM, Lawrie CH, Sohail K. Kinetics of the absorption of hydrogen-sulfide by high-purity and doped high-surface-area zinc-oxide. Ind Eng Chem Res 1995;34(9):2981–9.

[182] Sasaoka E, Taniguchi K, Uddin A, Hirano S, Kasaoka S, Sakata Y. Characterization of reaction between ZnO and COS. Ind Eng Chem Res 1996;35 (7):2389–94.

[183] Poston JA. A reduction in the spalling of zinc titanate desulfurization sorbents through the addition of lanthanum oxide. Ind Eng Chem Res 1996;35 (3):875–82.

[184] Konttinen JT, Zevenhoven CAP, Hupa MM. Modeling of sulfided zinc titanate regeneration in a fluidized-bed reactor. 2. Scale-up of the solid conversion model. Ind Eng Chem Res 1997;36(12):5439–46.

[185] Li ZJ, Flytzani-Stephanopoulos M. Cu-Cr-O and Cu-Ce-O regenerable oxide sorbents for hot gas desulfurization. Ind Eng Chem Res 1997;36(1):187–96.

[186] Jothimurugesan K, Gangwal SK. Regeneration of zinc titanate H_2S sorbents. Ind Eng Chem Res 1998;37(5):1929–33.

[187] Jothimurugesan K, Gangwal SK. Titania-supported bimetallic catalysts combined with HZSM-5 for Fischer-Tropsch synthesis. Ind Eng Chem Res 1998;37(4):1181–8.

[188] Kundakovic L, Flytzani-Stephanopoulos M. Reduction characteristics of copper oxide in cerium and zirconium oxide systems. Appl Catal A: Gen 1998;171(1):13–29.

[189] Zeng Y, Zhang S, Groves FR, Harrison DP. High temperature gas desulfurization with elemental sulfur production. Chem Eng Sci 1999;54 (15–16):3007–17.

[190] Siriwardane R. Regenerable sorbent pellets for removal of hydrogen sulfide from coal gas. US Patent No. 5866503, 1999.
[191] Jothimurugesan K, Gangwal SK. Durable zinc titanate H_2S sorbents. Adv Env Res 1999;2(4):426–37.
[192] Zeng Y, Kaytakoglu S, Harrison DP. Reduced cerium oxide as an efficient and durable high temperature desulfurization sorbent. Chem Eng Sci 2000;55 (21):4893–900.
[193] Alonso L, Palacios JM, García E, Moliner R. Characterization of Mn and Cu oxides as regenerable sorbents for hot coal gas desulfurization. Fuel Proc Tech 2000;62(1):31–44.
[194] Slimane RB, Abbasian J. Regenerable mixed metal oxide sorbents for coal gas desulfurization at moderate temperatures. Adv Env Res 2000;4(2):147–62.
[195] Slimane RB, Abbasian J. Copper-based sorbents for coal gas desulfurization at moderate temperatures. Ind Eng Chem Res 2000;39(5):1338–44.
[196] Clean Coal Today. US Department of Energy, DOE/FE-0215P-45, 2001.
[197] Slimane RB, Abbasian J. Utilization of metal oxide-containing waste materials for hot coal gas desulfurization. Fuel Proc Tech 2001;70(2):97–113.
[198] Kobayashi M, Flytzani-Stephanopoulos M. Reduction and sulfidation kinetics of cerium oxide and Cu-modified cerium oxide. Ind Eng Chem Res 2002;41 (13):3115–23.
[199] Gangwal S, Turk B, Gupta R, Siriwardane R. Development of fluidized-bed sorbent for desulfurization of chevron texaco quench gasifier syngas. 19th Annual Pittsburgh Coal Conference, Pittsburgh, PA, 2002.
[200] Gangwal S, Turk B, Portzer J, Gupta R, Toy L, Steele R, et-al. Development of a gas cleanup process for Chevron Texaco quench gasifier syngas. 20th Annual Pittsburgh Coal Conference, Pittsburgh, PA, 2003.
[201] Zhang J, Wang Y, Ma R, Wu D. A study on regeneration of Mn-Fe-Zn-O supported upon [gamma]-Al_2O_3 sorbents for hot gas desulfurization. Fuel Proc Tech 2003;84(1–3):217–27.
[202] Novochinskii II , Song CS, Ma XL, Liu XS, Shore L, Lampert J, et al. Low-temperature H_2S removal from steam-containing gas mixtures with ZnO for fuel cell application. 2. Wash-coated monolith. Energy Fuels 2004;18(2):584–9.
[203] Yi KB. Ceria-zirconia oxide high temperature desulfurization sorbent. PhD Dissertation. Louisiana State university; 2004.
[204] Wang Z, Flytzani-Stephanopoulos M. Cerium oxide-based sorbents for regenerative hot reformate gas desulfurization. Energy Fuels 2005;19(5):2089–97.
[205] Gangwal SK, Turk BS, Gupta RP. Zinc oxide-based sorbents and processes for preparing and using same. US Patent No. 2006;6951635.
[206] Flytzani-Stephanopoulos M, Sakbodin M, Wang Z. Regenerative adsorption and removal of H_2S from hot fuel gas streams by rare earth oxides. Science 2006;312(5779):1508–10.
[207] Bu X, Ying Y, Ji X, Zhang C, Peng W. New development of zinc-based sorbents for hot gas desulfurization. Fuel Proc Tech 2007;88(2):143–7.
[208] Karvan O, Atakül H. Investigation of CuO/mesoporous SBA-15 sorbents for hot gas desulfurization. Fuel Proc Tech 2008;89(9):908–15.
[209] Yang H, Cahela DR, Tatarchuk BJ. A study of kinetic effects due to using microfibrous entrapped zinc oxide sorbents for hydrogen sulfide removal. Chem Eng Sci 2008;63(10):2707–16.
[210] Yang HY, Sothen R, Cahela DR, Tatarchuk BJ. Breakthrough characteristics of reformate desulfurization using zno sorbents for logistic fuel cell power systems. Ind Eng Chem Res 2008;47 (24):10064–70.
[211] Bao WR, Zhang ZY, Ren XR, Li F, Chang LP. Desulfurization behavior of iron-based sorbent with MgO and TiO_2 additive in hot coal gas. Energy Fuels 2009;23(7):3600–4.
[212] Schlather JN, Turk B. Field testing of a warm-gas desulfurization process using a pilot-scale transport reactor system with coal-based syngas. 22nd Annual Pittsburgh Coal Conference, Pittsburgh, PA, 2005.
[213] Roychoudhury S, Lyubovsky M, Walsh D, Chu D, Kallio E. Design and development of a diesel and JP-8 logistic fuel processor. J Power Sources 2006;160 (1):510–3.
[214] Chu D, Hopkins J, Rong C. Test and characterization of some zeolite supported gas phase desulfurization sorbents. Army Research Laboratory, Report No. ARL-TR-4859, June, 2009.
[215] England DM, Rajashekara K. Method and apparatus for desulfurization for desulfurization of fuels. US Patent Application 2007/0092766 A1, 2007.
[216] Setzer HJ, Karavolis S, Bett JAS. Steam reforming utilizing sulfur tolerant catalyst. US Patent No. 4693882, 1987.
[217] Song C, Strohm J, Zhang J, Hoehn M, Ma X. In: Eguchi K, Machida M, Yamanaka I, editors. Science and technology in catalysis. Amsterdam, The Netherlands: Elsevier; 2007. p. 67–72.
[218] Wang L, Murata K, Inaba M. Development of novel highly active and sulphur-tolerant catalysts for steam reforming of liquid hydrocarbons to produce hydrogen. Appl Catal A: Gen 2004;257(1):43–7.

CHAPTER

12

Syngas Conditioning

Robert A. Dagle, Ayman Karim, Guosheng Li, Yu Su, David L. King

Pacific Northwest National Laboratory, 902 Battelle Boulevard, Richland, WA 99352, USA

OUTLINE

12.1. INTRODUCTION

Final conditioning of the syngas is required in order to assure that maximum power output of the fuel cell is achieved. This operation is most stringent for polymer electrolyte membrane (PEM) fuel cells, which can only convert H_2 to electrical power. Moreover, PEM fuel cells are readily poisoned by CO, necessitating its removal to ppmv levels. The content of this chapter focuses on the processing technologies required to allow operation of PEM fuel cells fuelled by reformate, including the final clean-up steps (PrOX, SMET), which are uniquely required for PEM. It should be noted that in 2004 the US Department of Energy (DOE) reached a "no go" decision regarding onboard (automobile) fuel processing, thereby ceasing funding research in onboard fuel processing for hydrogen production. The DOE support had been a key driver for preferential oxidation (PrOX), and selective methanation (SMET) technologies. However, these technologies are still relevant for applications, where PEM fuel cells are powered by hydrocarbon fuels via reforming. Other fuel cells, such as solid oxide fuel cells (SOFCs), which have been investigated for powering auxiliary power units (APUs) on trucks via fuel reforming, can electrochemically convert both H_2 and CO, and therefore the syngas conditioning is not required. For all fuel cells, CO_2 and H_2O in the syngas are generally inert and act as diluents. CH_4 is inert in PEM and may be internally reformed with higher temperature fuel cells such as SOFC and molten carbonate. Any sulfur compounds such as H_2S are permanent poisons and must be scrupulously removed.

The first unit operation to be described is water gas shift (WGS), which has a primary goal of maximizing H_2 concentration in the syngas and minimizing CO. This is a well-established technology at the industrial and refinery scales. WGS includes both a high temperature (Fe−Cr based) and a low temperature (Cu−Zn based) shift, which generally can reduce CO levels to 1 vol% or lower when combined together. A more extended discussion is also given to precious metal and gold-based water gas shift catalysts, which were developed specifically for onboard reformers. These developments arose from concerns that Cu-based shift catalysts could be subject to degradation in such reformers, for example, as a result of exposure to liquid water (resulting from on−off cycling and cooling without adequate purging, resulting in condensation of water) or to air (as a result of inadvertent leakage into the system). Precious metal water gas shift catalysts have not been considered for other applications of water gas shift.

The second step in the conditioning process is required to further decrease CO to ppmv levels. Two processes have been researched in some detail and are reported in this chapter: PrOX and SMET. These can be considered competitive processes, in that only one would be required to

be implemented. Each process has positive and negative attributes, as will be described. CO PrOX converts CO to CO_2; this process must be selective to minimize H_2 lost by a parallel pathway to form H_2O. Selective methanation converts CO to CH_4; in this case with "selective" referring to the requirement to convert CO but not CO_2 to methane. Both processes have the goal of reducing CO to acceptable levels with minimal loss of H_2.

12.1. WATER GAS SHIFT

Fuel processing, including hydrogen generation, purification, and storage, is the key technology for the implementation of fuel cells. Fuel cell systems are being developed for several applications, including distributed and portable power generation and other consumer applications [1–7]. Reforming of hydrocarbons is typically conducted at high temperatures, and water gas shift (WGS) is normally required to reduce CO concentration in the reformate from as high as 15% down to 1–2% [8]. WGS technology for large-scale applications is well-established commercially. The WGS reaction is an equilibrium-controlled, mildly exothermic reaction:

$$\begin{aligned} CO + H_2O &= CO_2 + H_2 \\ \Delta H^0_{298\ K} &= -41.1\ \text{kJ/mol} \end{aligned} \tag{12.1}$$

The water gas shift reaction has been the subject of several excellent reviews. Details on the conventional WGS process, reaction mechanisms, and industrial catalysts can be found in a review by Newsome in 1980 [9] and in Twigg's *Catalyst Handbook* [10]. Ratnasamy and Wagner [11] have recently provided an outstanding and comprehensive review of WGS catalysis. A particular emphasis for that work is on catalyst surface structures, active sites, reaction intermediates, and mechanisms, particularly for noble metal-based catalysts. The summary provided here is a succinct review of WGS catalysis and reactors, with an emphasis on fuel processing applications for fuel cells, and is not intended to provide a comprehensive review of WGS technology.

An overview of the four general classes of WGS catalysts is presented, which include: (1) high-temperature shift (HTS), (2) low-temperature shift (LTS), (3) sulfur-tolerant shift, and (4) precious metal-based shift. A review of WGS utilizing monoliths or other reactor technologies that pertain to fuel cell applications, an area of increasing interest over the past several years, is also presented. Finally, we discuss the advantages and disadvantages of different catalysts and reactors for different applications and provide a perspective on WGS technology.

12.1.1. Thermodynamics

WGS is an exothermic reaction, and CO conversion is favored at lower temperatures. The effect of temperature, steam-to-carbon (S/C) ratio, and the amount of H_2 in the reformate on the equilibrium CO conversion will be illustrated using model gas compositions (i.e., not representing a specific H_2 production process). Figure 12.1 shows the equilibrium CO conversion as a function of temperature for three S/C ratios. A higher S/C ratio favors lower CO equilibrium concentration. Depending on the fuel type (e.g., CH_4, ethanol) and the reforming process (steam reforming, partial oxidation, oxidative steam reforming, or dry reforming) used for H_2 production, the H_2 content in the reactant stream can vary significantly. Higher H_2 content in the reformate (e.g., steam reforming) will decrease the equilibrium CO conversion, and lower temperatures and/or higher S/C will be required to achieve the same CO conversion, as shown in Fig. 12.2. However, the effect of S/C ratio is much more pronounced than the amount of H_2 in the reformate. For fuel cell applications, the pressure of operation of the fuel processor will depend on

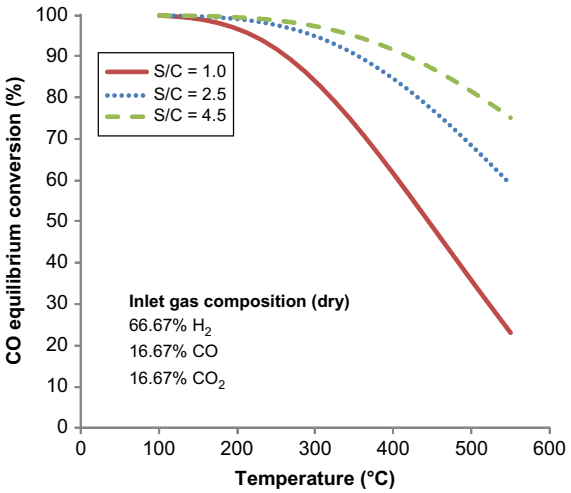

FIGURE 12.1 Effect of steam to carbon (S/C) ratio on the equilibrium conversion of CO at atmospheric pressure. (Calculations using HSC Chemistry 6.1.)

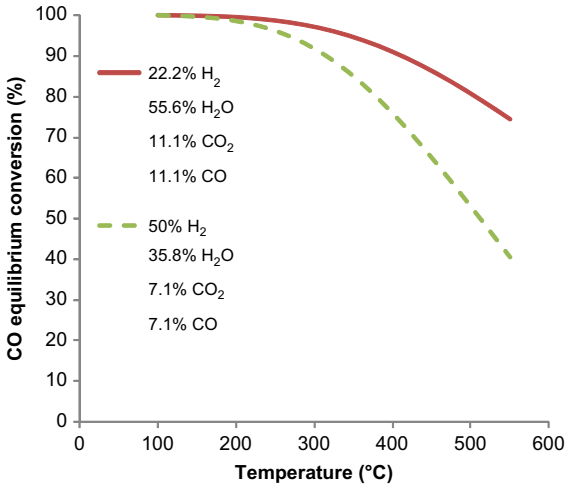

FIGURE 12.2 Effect of H_2 concentration on the equilibrium conversion of CO at atmospheric pressure and S/C = 2.5. (Calculations using HSC Chemistry 6.1.)

the feedstock. Liquid feedstocks that can be easily pumped may be reformed at elevated pressures, whereas gaseous feedstocks tend to be reformed at ambient pressure or slightly above to minimize the energy required to pressurize the reactants. The operating pressure has no effect on the WGS equilibrium conversion of CO, but it could affect the pore diffusion and reaction kinetics.

12.1.2. High-Temperature WGS Catalysts

High-temperature WGS (HTS) catalysts have been studied extensively and enjoy widespread industrial use due to their low cost, long lifetime (3–5 years), and resistance to poisoning. They are typically operated in the temperature range of about 320–450 °C. Due to the moderate activity of HTS catalysts, the CO conversion generally does not reach equilibrium. Reaching equilibrium CO conversion would require excessive catalyst bed volume. The amount of CO typically reduced from as high as 50% (on dry basis) in the inlet to 3–4% in the effluent. Most HTS catalysts are based on Fe_2O_3 (80–90 wt%) and Cr_2O_3 (8–10 wt%), with the balance being promoters/stabilizers (e.g., CuO_2, Al_2O_3, alkali, MgO, ZnO).

Cr_2O_3 and Al_2O_3 help minimize the sintering of Fe_2O_3, while Cr_2O_3 also increases the intrinsic activity of the iron oxide [11]. The active phase is Fe_3O_4, and the reduction from Fe_2O_3 needs to be performed carefully and the temperature controlled by sufficient heat removal to avoid further reduction to Fe [12,13]. Also, during the catalyst reduction, CrO_3 needs to be reduced to Cr_2O_3, which is highly exothermic. The catalyst activity and stability is highly dependent on the reduction procedure and on the reaction conditions, wherein the H_2O/H_2 and CO_2/CO ratios determine the stability of Fe_3O_4 and Cr_2O_3. Catalyst deactivation is mainly due to sintering [14], therefore reaction temperature should be limited to about 500 °C, or very fast deactivation will occur. Low sulfur amounts (50–100 ppmv H_2S) can be tolerated by Fe-based catalysts [15] due to the reversible formation of FeS [11,15].

Major limitations of Fe-based HTS catalysts for fuel cell applications include the following:

- Low volumetric activity (space velocities are typically 10,000−15,000 h^{-1}), which requires that the catalyst be operated in the kinetic rather than equilibrium regime in order to avoid excessive catalyst bed volume.
- A very controlled reduction procedure is required [12,13] to avoid over-reduction to Fe and the formation of iron carbides, which are active for methanation, the Boudouard reaction, and Fischer-Tropsch synthesis.
- High sensitivity to H_2O/gas ratio requires the use of excess water to keep $H_2O/H_2 > 1.4$ and $CO_2/CO > 1.2$ [11]. Low H_2O/gas ratios result in over-reduction of the catalyst from the active Fe_3O_4 phase to Fe leading to loss of activity, selectivity, and stability (due to volume shrinkage upon the formation of iron carbides and exotherms produced by the methanation and Boudouard reactions).
- The catalyst is pyrophoric in the reduced state, therefore accidental exposure to air could result in dangerously high and unsafe temperatures.
- Cr^{6+} is toxic (initially Cr is present as CrO_3), and being water soluble presents a safety hazard [16].

Studies on improving HTS catalysts have focused on replacing Cr and Fe by non-toxic metals or metal oxides (e.g., Cu, Ca, Ce, Zr, La) [16] and more active elements (e.g., noble metals) [5,17−19], respectively. Several promising chromium-free catalysts have been identified [13,16,20−26], however, Fe−Cr-based catalysts remain the standard used industrially.

12.1.3. Low-Temperature WGS Catalysts (LTS)

Low-temperature WGS is typically performed at 180−240 °C on Cu-based catalysts [4,11,27]. The most industrially employed LTS catalyst today is $Cu/ZnO/Al_2O_3$ [11]. The active phase is metallic Cu, while the ZnO and Al_2O_3 act as textural promoters and stabilizers to increase Cu dispersion and prevent it from sintering [11]. However, the Cu−ZnO interface has been reported to contribute to the high activity of $Cu/ZnO/Al_2O_3$ catalysts [28]. The CO amount is reduced from 3 to 4 vol% (on dry basis) to about 0.3−1 vol%. Due to high exothermicity of the copper oxide reduction, temperature control during reduction is crucial to avoid large temperature gradients causing irreversible catalyst sintering [5,11].

The $Cu/ZnO/Al_2O_3$ catalyst activity is highly dependent on the catalyst composition and preparation method [29,30]. The catalyst activity has been shown to correlate with the Cu surface area (which varies from 3 to 35 m^2/g) and Cu dispersion (which varies from 0.5% to 5% [31]). However, structure sensitivity was observed for similar Cu surface areas (3−35 m^2/g) [32], which could be due to a larger range of Cu dispersions (dispersion was not reported) and/or the different reaction conditions used for testing. Raney Cu−ZnO formulations have been reported to offer high durability (mechanical strength) and regenerability, while being as active as commercial co-precipitated catalysts [28]. Promoters (Mn, alkali) and other catalyst supports (CeO_2) have been investigated to increase the activity of Cu-based catalysts [27,33−36]. Cu supported on La-stabilized CeO_2 with low metal loading was as active as a commercial $Cu/ZnO/Al_2O_3$ at atmospheric pressure and it required no special activation [33]. It was also shown to retain its surface area after WGS tests up to 600 °C for 18 h. However, $Cu/ZnO/Al_2O_3$ remains the standard, industrially used catalyst for low-temperature WGS.

Major limitations of Cu-based low-temperature WGS catalysts for fuel cell applications are the following:

- Low volumetric activity (space velocities 5,000−15,000 h^{-1}), which requires large catalyst bed volumes to reach the equilibrium CO conversion.

- A very controlled, long reduction procedure (activation) is required.
- The catalyst is very sensitive at temperatures above ~280 °C, where fast sintering occurs [37]. However, Cu supported on La-modified ceria was reported to be stable up to 600 °C [38].
- The catalyst deactivates (irreversibly) easily when exposed to liquid water [4,5,11,37], which could occur during system shutdown or failure when water condenses on the catalyst surface.
- Pyrophoricity and therefore exposure to air could result in dangerously high temperature increases within the reactor [4–6,11,27,38]. However, non-pyrophoric alternative catalysts (base metal-based) have been reported by Ruettinger et al. [39] for low-temperature WGS.
- Sensitivity to low levels of poisons in the feed (e.g. sulfur, HCl), which results in fast catalyst deactivation [4,5,11]. Traces of chloride significantly accelerate the catalyst sintering [37].

Several non-Cu-based catalyst systems have been investigated for low-temperature WGS. Molybdenum carbide was reported to have higher activity at atmospheric pressure than a commercial $Cu/ZnO/Al_2O_3$ catalyst in the range of 220–290 °C [40]. Ni supported on La-stabilized CeO_2 was reported to be similar in activity (at atmospheric pressure) above 250 °C to Cu supported on the same support, however, catalyst stability was not investigated [33]. Tungsten carbide and nickel–molybdenum carbide have also been reported to be active for low-temperature WGS [41], with the Ni–Mo carbide catalyst showing a turnover frequency at 180 °C similar to a commercial Sud-Chemie Cu–Zn catalyst. However, both tungsten carbide and nickel–molybdenum carbide catalyst deactivation was observed with time on stream due to sintering. In view of the risks involved in changing substantially the catalyst formulation used in large-scale LTS reactors, such catalysts have not been viewed favorably to replace low temperature Cu catalysts [11].

12.1.4. Sulfur-Tolerant WGS Catalysts

In conventional hydrodesulfurization processes, Co (or Ni)–Mo–alumina catalysts are put in place upstream of sulfur-sensitive Ni-based reforming catalysts. The use of such Co–Mo-based catalysts has also been considered when syngas is generated by the gasification and partial oxidation of heavy fuel oil, tar sands, oil, or coal [11]. These sources typically contain high levels of both carbons, which result in high levels of CO, when reformed, and sulfur. Co–Mo-based catalysts remove sulfur from the process gas by absorption until an equilibrium sulfur composition is reached (sulfide form of the catalyst), subsequently excess sulfur may be released as H_2S. Additionally, these catalysts lower CO levels (via the WGS reaction), and thus serve as sulfur-tolerant, sour gas shift catalysts. They typically operate in a middle temperature range (250–350 °C) [11]. The main drawback is the low space velocity required to reach equilibrium conversions. Space velocities between 1700 and 3000 h^{-1} have been reported [11].

12.1.5. Precious Metal-Based WGS Catalysts

Where proton exchange membrane (PEM) fuel cells are considered for mobile applications, a WGS shift catalyst with activity much higher than the catalysts currently used in chemical plants is required. The WGS catalyst bed volume and weight affect the overall system efficiency, and therefore determine whether the process is economical. Fe-based HTS catalysts are far too inactive at temperatures below 350 °C and pose serious volume and weight restraints. Cu-based WGS catalysts are more active than Fe-based catalysts at lower temperatures, but their activity is still too low, making

the WGS reactor the largest among all the catalytic reactors in the different fuel processing steps [16,38]. In addition, as mentioned above, they become unstable at higher temperatures (>280 °C), and their pyrophoric nature makes them undesirable for safe and efficient operation [27].

12.1.5.1. Ceria and Titania-Supported Catalysts

Noble metal catalysts, specifically ceria and titania-supported platinum catalysts, have been seen as leading candidate water gas shift catalysts in fuel cell applications [11], and have been the most extensively studied [27,42–44]. Noble metal-based catalysts are not pyrophoric and do not need the very specific reduction/activation procedures required for Fe- and Cu-based catalysts [12]. Furthermore, the reaction rates are approximately zero order in CO [45], advantageous in driving the reaction to equilibrium with minimal volume as compared to the conventional Cu-based catalysts, which are approximately first order to CO [11,46–48]. For example, assuming the same reaction rate per gram of catalyst, the catalyst weight required to achieve 90% conversion for first-order reaction kinetics (on Cu) would be 2.5 times that for zero-order reaction kinetics (on Pt) and four times to achieve 98% conversion. However, while these precious metal-based catalysts are very active in the 250–400 °C range, they typically exhibit much lower activity compared to Cu-based catalysts at temperatures less than about 250 °C. Furthermore, instability of this catalyst under fuel processing conditions has been a recurring problem [43,44,49]. Research on ceria and titania-based platinum catalysts continues, with a particular emphasis on increasing catalytic activity at temperatures less than 250 °C, and enhancing stability.

It is widely argued that the ceria and titania-supported precious metal-based catalysts are bifunctional [42,50]. Both metal and support are involved in the reaction pathway. In fact, Pt/C was reported to be inactive for WGS [45]. Precious metals (e.g., Pt) offer CO adsorption sites. Partially reducible metal oxides (e.g., ceria, titania, iron oxides, and mixtures thereof) offer oxygen storage capacity, which is important in facilitating the CO oxidation [11]. It should be noted that the thermal stability of TiO_2 is reported to be better in the lower operating temperature range. Integration of ceria with titania was shown to enhance thermal stability [11]. Incorporation of Zr into ceria supports is also known to improve thermal stability, and increase oxygen storage capacity, which can increase WGS activity [11,51].

12.1.5.2. Mechanism

Debate exists in the literature regarding WGS mechanistic details. There are two primary mechanisms that are under consideration: the redox mechanism and the formate mechanism. Under the "redox mechanism," CO is adsorbed on the metal surface and is then oxidized by an oxide site on the support. The reduced support is then re-oxidized by steam [44], producing H_2 and completing the catalytic cycle. The "formate mechanism" proposes that the metal actually promotes ceria reduction, forming active sites on the ceria support. Partially reduced ceria adsorbs CO and forms surface formates. These formates subsequently decompose to CO_2 and H_2 [44,52].

Burch published a comprehensive study offering a "Universal Mechanism" for the WGS reaction that integrates aspects of both formate and redox mechanisms in a single model [53]. Ratnasamy and Wagner [11] outline these findings. It is suggested that no single mechanism can explain mechanistic details consistent with all experimental observations. Rather, different WGS mechanisms can prevail on the same catalyst under different reactant partial pressures and temperatures. This is especially likely considering the WGS reaction is equilibrium-limited at high temperatures and

kinetically limited at low temperatures [11,53]. Three general situations are envisoned [11]. At high temperatures, where conversion of formate and carbonate-like intermediates occur quickly, it is likely that the redox process would be expected to be important in determining the rate of the reaction. At low temperatures, the carbonate decomposition in the mechanism will be slower, thus, more likely to be rate limiting. At intermediate temperatures, mechanisms in operation would depend greatly on component concentrations. For example, the presence of large amounts of water would enhance the redox mechanism, making formate decompositions rate limiting [11,53].

12.1.5.3. Non-reducible Supports

On non-reducible supports such as alumina or silica, the redox mechanism, involving oxygen vacancies on the support, is excluded from consideration as a mechanistic explanation [11]. Studies indicate reaction intermediates consistent with a formate mechanism. Olympiou et al. [54] found that on alumina supports, the role of the noble metal was (a) to activate the CO molecule, and (b) to promote formate decomposition into CO_2 and H_2 products. It was suggested that adsorbed formate species residing on the alumina support and/or at the metal–support interface are important species in the WGS reaction [11,54]. In addition, a correlation between catalytic activity and the surface concentration and binding energy of CO on the noble metals was also reported [11]. Grenoble et al. [55] found that a volcano-type relation between the water gas shift activity of alumina-supported metal catalysts and the strength of interaction of molecular CO on the metal, with the optimum around Cu. Recently, Boisen et al. [56] systematically compared the WGS activity for 12 transition metals supported on magnesium aluminate ($MgAl_2O_4$) and ceria–zirconia-based supports. The magnesium aluminate-supported catalysts followed a volcano-type relation between activity and the adsorption energy of atomic oxygen (see Fig. 12.3). No clear correlation was found to exist with the adsorption energy of CO, in disagreement to Grenoble's earlier work [56], but there may be differences in catalyst surface chemistry arising between Al_2O_3 and $MgAl_2O_4$ supports. In contrast, for the ceria–zirconia supports it was found that activity was generally higher with these same metals (except for Cu and Au), with Pt being the most active. Activity is correlated with adsorption strength for CO. The relatively low activity of Cu was claimed to argue against oxygen adsorption as a key parameter on the Ce-based support [56]. Contributions due to water dissociation occurring on the redox-active ceria was rationalized as a possible explanation for differences between the two supports [56]. The higher rate of reaction for Pt on ceria-based supports, as compared to any of the metals supported on $MgAl_2O_4$, was shown in this work.

12.1.5.4. Deactivation Mechanisms

While ceria- and titania-supported Pt catalysts have shown good initial activity, catalyst deactivation under realistic conditions has been problematic. Moreover, there is some debate over what deactivation mechanisms are actually involved. Several studies have shown that CO causes irreversible deactivation through a metal sintering effect [11,43,44]. In a 2002 study by Zalc et al. [49], deactivation was found to be caused by over-reduction of the ceria. Some have since refuted this argument [11,57]. Other routes for deactivation could arise from undesirable hydrocarbon formation. It is known that precious metal catalysts have some Fischer-Tropsch activity (unlike Cu). Sometimes only small amounts of hydrocarbons are formed (e.g., methane), even at low pressures. However, once formed, a number of side reactions could occur, resulting in fouling of the catalyst by carbon formation [11].

Pt/TiO_2 promoted with Re or Sn showed highly enhanced stability [58]. The $Pt–Re/TiO_2$

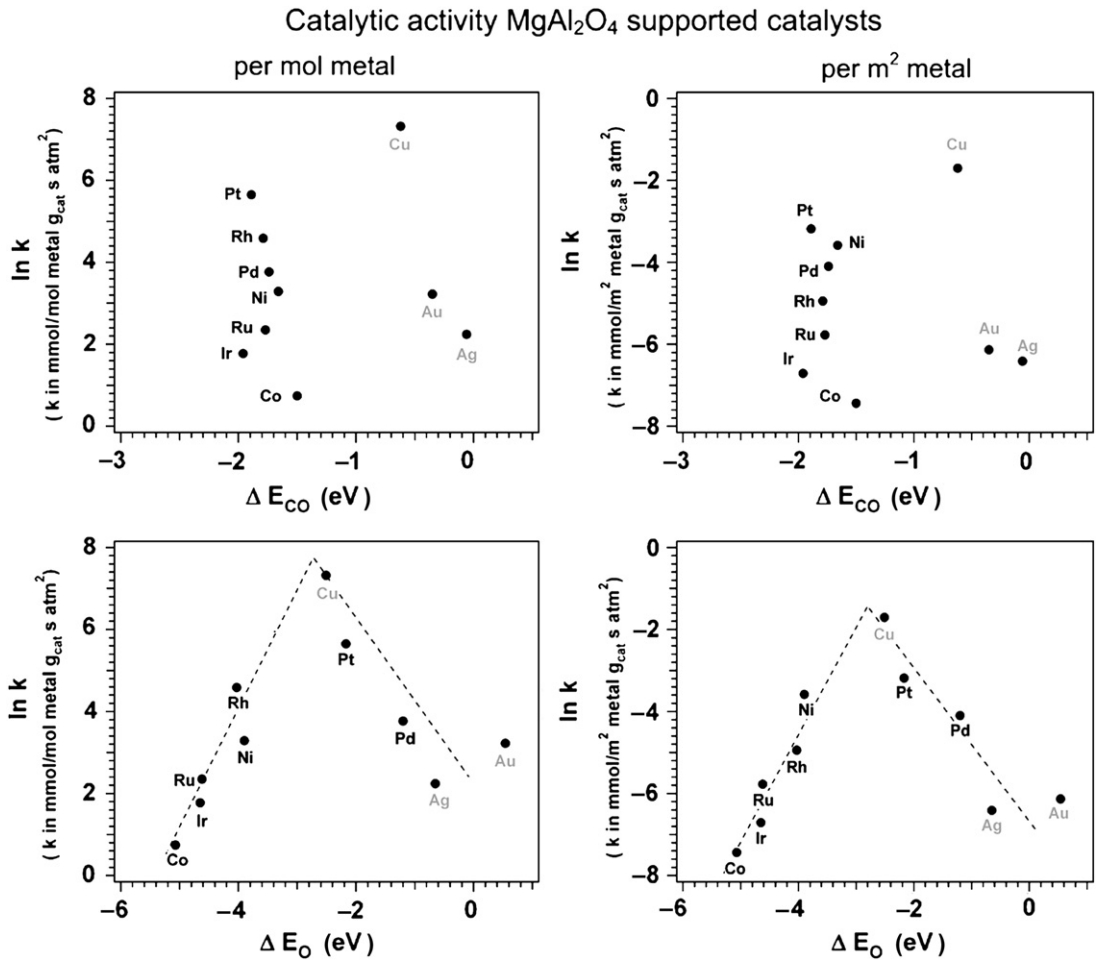

FIGURE 12.3 *Left panels*: Activity (ln *k*, *k* in mmol/(mol metal g_{cat}—s-atm^2)) of the $MgAl_2O_4$-supported catalysts at 270 °C as a function of the adsorption energy of carbon monoxide, E_{CO} (top) and atomic oxygen, E_O (bottom). A correction for dispersion (*right half*) largely results in the same trend. *Reprinted with permission from Boisen et al. [56], Copyright (2010) Elsevier.*

catalyst was more active than Pt/TiO_2 and showed no deactivation for 20 h on stream [58]. The role of Re in enhancing the activity was attributed to ReO_x species present under the WGS reaction conditions, providing an additional redox route for the WGS reaction, in which ReO_x is reduced by CO, generating CO_2 and is then re-oxidized by H_2O, forming H_2 [45]. On the other hand, Sato et al. [59] attributed the increase in activity to Pt—Re bimetallic formation, which resulted in stronger CO adsorption. The enhanced stability of $Pt—Re/TiO_2$ was attributed to Re stabilization of Pt against sintering [58]. An enhancement in activity and stability of Pt/ZrO_2 by Mo and Re promotion was reported by Ruettinger et al. [60]. Pt—Re, Pt—Mo, and Pt—Re—Mo alloy formation was shown to be responsible for the enhanced activity [60].

12.1.5.5. Palladium–Zinc-Based Catalysts

Although less studied, another class of catalyst has recently been considered for WGS. Arising from methanol steam reforming studies, catalysts based on a PdZn-ordered alloy (Pd/Zn = 1) were found to be active and selective for methanol steam reforming. Comparable in methanol reformation activity and selectivity to that of Cu-based catalysts under intermediate temperature conditions [61–63], the PdZn-ordered alloy offers a significantly different reaction pathway from that of metallic Pd [64–70]. A subsequent study by Dagle et al. [71] showed that, in the absence of methanol, the PdZn-ordered alloy supported on alumina was also active specifically for the WGS reaction. Between 250 and 300 °C equilibrium conditions were achieved, and initial activity for a PdZnAl-0.5 catalyst (Pd/Zn = 0.5, Pd content 11.1 wt.%) was comparable to a commercial Pt-based WGS catalyst (see Fig. 12.4) [71].

Tsai et al. [72] reported that an explanation for the similar catalytic function of PdZn and Cu is due to the fact that PdZn exhibits a similar valence electron density of states as pure Cu. These findings suggest that the PdZn-ordered alloy formulation is a possible alternative to the Cu-based and/or Pt-based ceria or titania-type of catalysts. However, much more investigation is required to assess the adequacy of the PdZn catalyst for fuel cell applications, and only limited stability data on this catalyst type have been reported [71].

12.1.6. Au-Based Catalysts

One of the disadvantages of the above-described metal-based catalysts is low activity below 250 °C. Au-based catalysts have been shown to be active at lower temperatures (<250 °C) [11]. Also, Au-based catalysts are non-pyrophoric [11]. A recent study showed that Au/CeO_2 was more active than a commercial $CuO/ZnO/Al_2O_3$ at 150 °C; however the Cu-based catalyst was more stable during long-term studies. It was found that high activity requires very good dispersion, with Au particle sizes in the range of 1–5 nm being required for high activity [11,73]. Maintaining an "ionic state" instead of forming an Au metallic phase has been reported to be a requirement for high activity, as well as enhancing thermal stability. Metallic Au formation becomes prevalent at temperatures above about 250 °C [11]. Two potential causes of catalytic deactivation have been reported: (1) Au particle

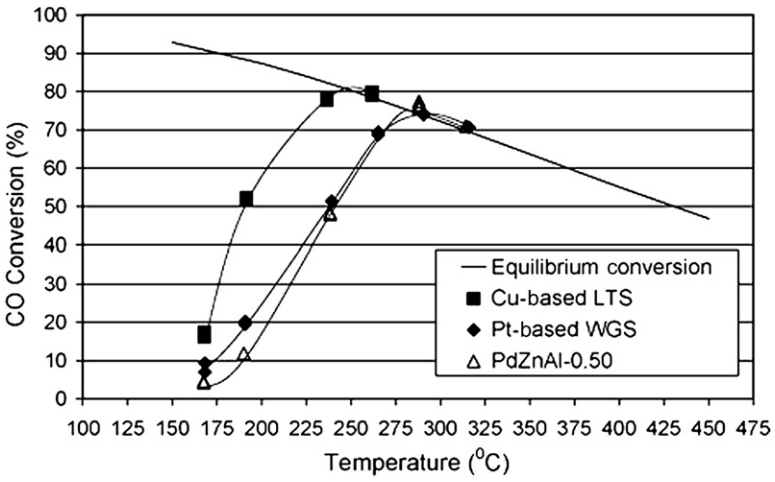

FIGURE 12.4 Activity comparison of PdZnAl-0.50 to commercial Cu-based low temperature shift (LTS) and Pt-based WGS catalysts (feed composition: $H_2 = 31.6\%$, $CO = 12.6\%$, $CO_2 = 3.2\%$, $H_2O = 12.6\%$, $N_2 = 40.0\%$; GHSV = 7660 h^{-1}). *Reprinted with permission from Dagle et al. [71], Copyright (2008) Elsevier.*

growth and (2) the formation of unreactive species, such as formates and carbonates, which serve to physically block active sites [11]. Performance enhancement of Au-based catalysts, with a particular emphasis on improving stability, has involved adding other metals (e.g., Pt) to the Au to form bimetallic catalysts [11]. Advancements in this area have been made. However, in view of ongoing stability issues surrounding the Au-based catalysts, the Pt-based catalysts are generally seen as superior for fuel processing systems [11].

12.1.7. Reactor Design

Compared to conventional industrial WGS plants for the generation of hydrogen, some estimates have suggested that a reduction in reformer and water gas shift catalytic reactor size by over two orders of magnitude is necessary before fuel cells can compete in automotive applications [11]. Thus, further WGS catalyst improvement is needed. Most of the reported results involving WGS have involved catalyst development utilizing powder catalysts. However, in many fuel cell applications, due to the requirement for high space velocity (to reduce reactor volume), low pressure drop, mechanical strength, and efficient heat integration, the use of monolith-type catalysts is indicated [11]. Monolithic WGS catalysts operating at temperatures as high as 300−350 °C can be employed to reduce the residual CO content to about 1% [11].

Monolith reactors are generally fabricated from ceramics or metal alloys coated by a washcoat containing the catalyst [5,39,74]. Other reactor types include the use of coating parallel plates [75] or direct washcoating on the reactor wall [76]. In addition to the above-mentioned advantages to using a monolith-based catalyst system, considerable advantages are to be gained by the use of such reactors in order to improve heat transfer. Many studies have integrated the WGS process with other conversion processes in order to more efficiently utilize heat exchange. For example, Palma et al. [74] reported integration of a precious metal-structured WGS reactor with a CH_4 oxidative steam reforming reactor. Mass transfer can also be enhanced with structured reactors due to lower diffusional limitations. This enables high conversions at high space velocities [11]. Modeling studies have also supported the notion that structured monolith reactors provide better results compared to adiabatic beds [77]. The main advantages observed typically include wider temperature windows, increased hydrogen yields, and smaller reactor volumes [77,78]. This is especially valid at very high throughput [77]. Giroux et al. [79] reviewed, in more detail, the use of monolith-supported precious metal catalysts for WGS. Ratnasamy and Wagner [11] also outlined preparation methods of monolith reactors and the catalytic properties thereof.

Microchannel reactor technology has been explored as a possible reactor configuration. Microchannel reactors have characteristic dimensions, such as channel gaps, which are on the microscale (typically <1000 μm) or mesoscale (1000 μm to a few centimeters). Example reactor microstructures are depicted in Fig. 12.5.

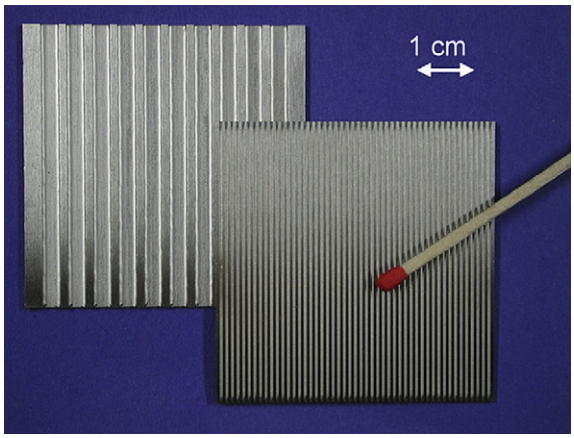

FIGURE 12.5 Different microchannel geometries utilized for water gas shift reactors developed at IMM. *Reprinted with permission from Kolb et al. [80], Copyright (2008) Elsevier.*

These dimensions are significantly smaller than many conventional reactors and can significantly enhance mass and heat transfer rates [1]. In addition, microchannel reactors offer uniform residence times and flow patterns. These unique advantages have led to the development of microchannel devices for numerous applications [81–83]. Fuel processing applications have specially been a major area of interest [81]. Holladay et al. [1] provided a review of microreactors developed for steam reforming, partial oxidation, and oxidative steam reforming reactions.

There are a few reported studies concerning microchannel reactors designed specifically for WGS. Researchers at the Institut für Mikrotechnik Mainz GmbH (IMM) studied washcoated alumina precious metal-based WGS catalysts applied to microchannels [84]. A Pt–ceria–alumina catalyst formulation was found to work well, particularly in the medium temperature range (between conventional HTS and LTS) [84]. However, consistent with many reports, some deactivation, likely due to CO poisoning, was reported [84]. Another study reported very short WGS residence times of less than 30 ms, at temperatures between 250 and 300 °C, using microchannel structures [85]. A microchannel WGS reactor with interleaved cooling channels, as part of a 50 kW_e automotive fuel processing application, was developed at Pacific Northwest National Laboratory [86]. The design incorporated an optimum thermal profile down the length of the reactor. Such a "temperature differential reactor" offers high conversion via enhanced kinetics at the hotter front end of the reactor, while favorable thermodynamics are allowed at the cooler reactor back end [86]. Kolb et al. [80] reported the design of an integrated microchannel WGS system as part of a 5 kW_e fuel processing system powered by isooctane.

Although promising, there are potential obstacles with microchannel reactors that need to be addressed, depending on the particular application. For example, cost of manufacturing and the complexity of design to achieve necessary performance are problematic. Unclean streams can cause clogging of the channels. Control of feed introduction through multiple parallel channels can be troublesome [81]. However, use of thermally integrated microchannel systems can result in highly efficient and compact WGS devices, meriting continued work to decrease costs and increase reliability of such systems.

12.1.8. Summary and Outlook

A brief review of WGS catalysts and reactor designs relevant to fuel cell applications has been provided. The major types of WGS catalysts, their characteristics, advantages and limitations have been discussed and a summary is provided in Table 12.1. The relatively small temperature operating window, gas composition requirements, and pyrophoric nature make the conventional high- and low-temperature WGS catalysts based on Fe and Cu less practical for mobile applications. The major advantages of precious metal catalysts appear to be their non-pyrophoricity, lack of special activation procedure, and low sensitivity to gas composition and water condensation on the catalyst surface. However, despite being actively promoted as the best WGS catalysts for fuel cell applications, noble metal catalysts (mainly Pt and Au) do not show good stability, and are less active than Cu-based catalysts below about 250 °C. Lower CO reaction order on Pt, compared to that on Cu, can result in a lower reactor volume, but only if the reaction rates are similar on both catalysts. Lower activity means higher residual CO levels, which would require larger methanation/PrOX clean-up reactors.

The temperature range for the WGS reactor is dependent on the reformer gas product temperature and the highest allowable concentration of CO for the downstream methanation and/or PrOX reactor. Therefore, depending on the

TABLE 12.1 Summary of the Different WGS Catalyst Types

Catalyst	Temperature (°C)	GHSV × 1000 h^{-1}	Stability	Advantages	Limitations
Fe-based	300–500	10–15	Acceptable for industrial use*	• Low cost	• Sensitive to gas composition • Pyrophoric • Special activation procedure
Cu-based	180–260	5–15	Good	• Low cost • Highest activity and stability among all catalysts below 240 °C	• Pyrophoric • Special activation procedure • Sensitive to high temperature and water condensation
Pt	220–350	10–25	Still an issue, however, Pt–Re showed promising stability [45,58]	• Non pyrophoric • Highly active above 250 °C. • Could replace HTS Fe catalysts. • No special activation procedure required.	• Deactivation • Low activity compared to Cu below 250 °C • High cost
Au	150–260	5–10	Still an issue	• Non pyrophoric • Highly active 150–240 °C • No special activation procedure required	• Deactivation • Sensitive to high temperatures • High cost

** The deactivation of Fe-based HTS catalysts is usually mitigated by increasing the catalyst bed temperature. However, this also would accelerate the sintering of the catalyst. Also, increasing the bed temperature might not be a feasible solution for portable applications.*

constraints imposed on the reformer (exit gas temperature and the CO level), one catalyst type might be sufficient or two WGS catalyst types might be necessary to drop the CO amount to the design level imposed by the downstream clean-up stage.

Monoliths and microchannel reactors are advantageous in terms of low pressure drop, better temperature control, and easier thermal integration with other parts of the fuel processor. For mobile applications where low pressure drop and efficient catalyst use are required, monoliths or microchannel reactors would be favored. However, packed-bed reactors remain the most compact reactor design. The volume of a packed-bed (for the same catalyst weight) is always smaller than monoliths or microchannel reactors. Therefore, for some applications (e.g., small size), packed-bed reactors could be favored due to their compact design.

In summary, the choice of catalyst type and reactor design is dependent on the fuel processor size and type of application. Non-pyrophoric WGS catalysts that are active and stable under a wide range of operating temperatures would be preferred; however, they are presently not available.

12.2. PREFERENTIAL OXIDATION (PrOX)

The PEM fuel cell has received much attention in the application to electric vehicles as

well as in stationary applications because of its high power density, rapid start-up capability, and high efficiency. Because PEM utilizes only hydrogen as fuel, a fuel processor has frequently been employed to convert hydrocarbons into hydrogen. Various options for hydrocarbon fuel reforming, including steam reforming, partial oxidation, or oxidative steam reforming to produce syngas are reviewed in Chapters 4-6. A water gas shift reactor typically follows the reformer, as described in Section 12.1.

The PEM fuel cell is unique in its intolerance toward CO in the syngas. This is a result of the platinum anode being readily poisoned by even small amounts of CO in the hydrogen stream. A generally accepted value for CO concentration in syngas fed to the conventional PEMFC anode is below 10 ppmv. Higher values of ~100 ppmv may be allowed over "CO-tolerant" alloy anodes [87–89]. Irrespective of the tolerable CO concentration handled by the PEM anode, the amount of CO from the water gas shift reactor is too high and the CO concentration must be reduced.

Figure 12.6 shows the calculated equilibrium CO concentration at the exit of the water gas shift reactor as a function of the inlet feed H_2O/CO ratio and the reaction temperature. The calculations assume a feed containing only H_2O and CO, without other reformate components present (CO_2, H_2). A CO concentration below 100 ppmv cannot be achieved solely by water gas shift even with high H_2O/CO ratios at practical reaction temperatures ($T \geq 200$ °C). Typically, about 1 vol% CO is contained in the hydrogen-rich stream after the water gas shift reactor.

The aim of preferential oxidation (PrOX) is to selectively oxidize CO, reducing its concentration to acceptable ppmv levels without simultaneous oxidation of the hydrogen present in the shifted reformate. The PrOX reaction is one approach to removal of CO to acceptable levels. Selective CO methanation is an alternative and will be described in the subsequent section. PrOX has been claimed by some researchers to be the simplest, most straightforward, and cost-effective approach to CO minimization [7,87,91,92], although that assertion appears to be open to debate. Attention is also called to two recent reviews of PrOX catalysis [7,92].

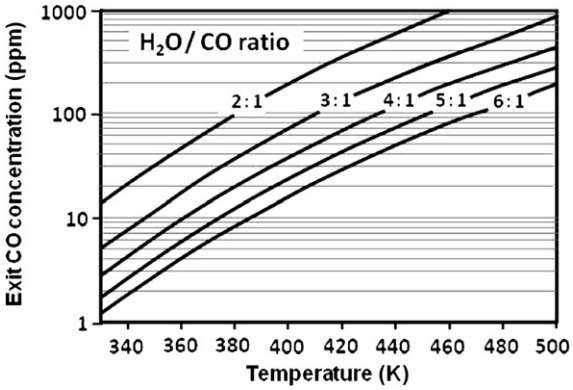

FIGURE 12.6 Calculated CO exit gas concentrations as a function of temperature and initial H_2O/CO feed ratio. *Reprinted with permission of Marschner et al. [90], Copyright (1983) Elsevier.*

12.2.1. Thermodynamics

Over the PrOX catalyst, the following reactions can occur:

$$\mathrm{CO} + \tfrac{1}{2}\mathrm{O_2} \rightarrow \mathrm{CO_2} \qquad \Delta H^0_{298\,\mathrm{K}} = -283.0\ \mathrm{kJ/mol} \tag{12.2}$$

$$\mathrm{H_2} + \tfrac{1}{2}\mathrm{O_2} \rightarrow \mathrm{H_2O(g)} \qquad \Delta H^0_{298\,\mathrm{K}} = -241.8\ \mathrm{kJ/mol} \tag{12.3}$$

$$\mathrm{CO} + \mathrm{H_2O} \rightarrow \mathrm{CO_2} + \mathrm{H_2} \qquad \Delta H^0_{298\,\mathrm{K}} = -41.2\,\mathrm{kJ/mol} \tag{12.4}$$

$$\mathrm{CO} + 3\mathrm{H_2} \rightarrow \mathrm{CH_4} + \mathrm{H_2O(g)} \qquad \Delta H^0_{298\,\mathrm{K}} = -206.2\ \mathrm{kJ/mol} \tag{12.5}$$

$$CO_2 + 4H_2 \rightarrow CH_4 + 2H_2O(g)$$
$$\Delta H^0{}_{298\,K} = -165.0\ \text{kJ/mol} \qquad (12.6)$$

The primary oxidation pathways are Eqs (12.2) and (12.3), with selective CO oxidation being the desirable outcome and H_2 oxidation to be avoided. The water gas shift reaction (Eq. (12.4)) can also reduce CO, although there are thermodynamic limitations as described above. On the other hand, the reverse water gas shift (RWGS) reaction can occur with some catalysts and must be considered in catalyst design, as reaching thermodynamic equilibrium via the reverse shift can counteract the effectiveness of the PrOX catalyst and reaction. Equations (12.5) and (12.6), CO and CO_2 methanation, respectively, may also occur. Although CO methanation is self-limiting, if it occurs, can lead to significant hydrogen loss. Because of the potential for both reverse shift and methanation to occur, it is important in PrOX catalyst development to test with feedstocks that contain realistic concentrations of CO_2.

12.2.2. General Considerations

In the early 1960s, the Engelhard Corporation developed and commercialized the Selectoxo™ catalyst and process for use in hydrogen plants to remove CO to levels acceptable for ammonia synthesis [93–96]. A promoted catalyst comprising 0.3–0.5 wt% Pt was employed, and was found capable of oxidizing up to 10,000 ppmv CO without significantly oxidizing the 70% H_2 (dry basis) present in the stream, with CO levels reduced to less than 5 ppmv under steady-state conditions (50 °C, 10,000 h^{-1} and 1.5–3 MPa). A key differentiating feature (compared to more recent PrOX application) was the scale of the operation, enabling employment of a CO_2 and H_2O scrubber prior to the PrOX reaction. For small-scale fuel processors dedicated for PEM fuel cell operation, both H_2O and CO_2 will generally be present in the feed in rather high concentrations. As a result, greater demands are placed on the catalyst.

PrOX is advantageous over other approaches to CO minimization, such as selective methanation, since by limiting the oxygen content in the feed there could be no danger of "reaction runaway." Although CO methanation is self-limiting in the absence of CO_2, the potential for CO_2 methanation, as described above, especially when large quantities are present in the reformate, is a significant concern. However, PrOX has its own challenges, a key one being (in practical application) to provide and maintain the appropriate level of O_2 (air) to the reactor. Too little air results in too high a concentration of residual CO and anode "poisoning"; too much air results in excess H_2 consumption, since all O_2 fed to the PrOX reactor is generally consumed. One of the challenges especially facing the transportation (automotive power) effort was the need to pay attention to the drive cycle and the non-steady-state nature of much of typical urban driving patterns. For proper operation, monitoring of the varying CO concentration would be required in order to continually provide the appropriate oxygen concentration to the PrOX unit.

For the discussions that follow, some definitions are necessary. The conversion and the selectivity toward CO oxidation are key parameters of catalyst performance. CO conversion (X_{CO}) is defined by:

$$X_{CO}(\%) = \frac{(n\text{CO}_{in} - n\text{CO}_{out})}{n\text{CO}_{in}} \times 100 \qquad (12.7)$$

Selectivity for CO conversion (S) is defined in terms of O_2 utilization:

$$S(\%) = \frac{n\text{CO}_{2,formed}}{2 \times (n\text{O}_{2,in} - n\text{O}_{2,out})} \times 100 \qquad (12.8)$$

An additional parameter lambda (λ) has been used to define the amount of available O_2

provided in the PrOX experiment relative to the CO concentration:

$$\lambda = \frac{2 \times nO_{2,in}}{nCO_{in}} \tag{12.9}$$

A value of $\lambda = 1$ indicates that the stoichiometric O_2 level has been provided, whereas $\lambda > 1$ indicates that excess O_2 is provided. How much of that excess O_2 ends up oxidizing H_2 to H_2O is a determining factor in catalyst design.

An important consideration in PrOX catalysis is thermal management and temperature control. Some catalysts are highly selective toward CO oxidation in the presence of H_2, but frequently only over a fairly narrow temperature range. In small fixed-bed tests typical of many laboratory studies, where gram or even sub-gram quantities of catalyst are used, thermal management is not a serious consideration. However, in larger catalyst beds, the potential for development of a significant exotherm with accompanying adiabatic temperature rise within the bed must be considered. Practical reactors typically comprise two or more stages with inter-stage cooling and supplemental air fed to each subsequent stage in order to provide necessary heat management.

Another consideration in testing is the importance of evaluating the catalyst with realistic feeds (i.e., all feed components and concentrations). Tests carried out with only CO, H_2, and O_2 present are insufficient to understand and characterize true performance of a PrOX catalyst, if the hydrogen source derives from hydrocarbon reforming. This is not to say that experiments employing only CO, H_2, and O_2 are not valid, since they may provide an important measure of scientific understanding of catalyst operation that could not be gained when H_2O and CO_2 are present. However, testing without H_2O can be misleading, since H_2O may interfere with (or in some cases enhance) CO oxidation activity. Testing without CO_2 in the feed may fail to disclose that the catalyst has important reverse water gas shift activity or CO_2 methanation activity, which could be a large consumer of H_2 as described above.

The temperature of operation of the PrOX unit is also of some significance. PrOX catalysts are located downstream of water gas shift units and directly upstream of the PEM fuel cell. This suggests an acceptable temperature of operation between ~80 and 225 °C. Although much attention has been focused on PrOX catalysts that can operate near 80 °C (notably Au-based catalysts), there appears to be no inherent advantage in energy efficiency with low temperature operation. The heat generated by the PrOX reaction in this temperature range has little value, whereas it might be possible to utilize the heat generated from a PrOX reactor operating in the higher temperatures ranges. This consideration, however, is secondary relative to the inherent activity and selectivity of the catalyst, which are the primary drivers determining operating temperature.

12.2.3. PrOX Catalysts

12.2.3.1. Pt Catalysts

Among the noble metals, Pt-based catalysts have been most extensively studied and applied practically. Early work by Cohn [97] with a Pt/Al_2O_3 catalyst demonstrated the selective CO oxidation in the presence of excess H_2. It was pointed out that maintaining selectivity highly depended on the precise control of reaction temperature and the oxygen injection rate. Kahlich et al. [98] studied PrOX over $Pt/\gamma\text{-}Al_2O_3$ in a "simulated" reformer gas (75% H_2; balance N_2) over a wide range of CO concentrations (0.02−1.5%) with relatively low stoichiometric O_2 excess ($\lambda = 1-3$). They reported an optimum temperature of ~200 °C for the PrOX reaction, and rates of CO methanation in this range were insignificant. Manasilp and Gulari [99] reported a significant positive order in water vapor and negative order in CO_2 and proposed

TABLE 12.2 Comparison of Promoted and Unpromoted Pt/Al_2O_3 for PrOX Reaction (Particle Size 40–60 μm, 1000 ppmv CO, 20 vol% H_2, 10 vol% H_2O, VHSV = 120,000 h^{-1}, WHSV = 150,000 l g^{-1} h^{-1})

Reaction conditions		Promoted Pt catalyst		Pt/Al_2O_3	
Temperature (°C)	O_2/CO ratio	X_{CO} (%)	Selectivity (%)	X_{CO} (%)	Selectivity (%)
90	0.5	68	78	13.2	82
90	0.75	90	65	12.7	66
150	0.5	62[a]	60[a]	26.8	57

[a]*Data were obtained with the monolith catalyst at VHSV at 80,000 h^{-1}; WHSV at 923,000 l g^{-1} h^{-1}.*
(Reprinted with permission from Korotkikh and Farrauto [96], Copyright (2000) Elsevier)

that the enhancement was due to the participation of hydroxyl groups formed by the dissociative adsorption of H_2O on Pt and the detrimental effect of CO_2 was attributed to the reverse water gas shift (RWGS) reaction.

Various zeolites have been used as supports for Pt-based PrOX catalysts. Igarashi et al. [100] reported a selectivity benefit with zeolite supports compared with a conventional Pt/γ-Al_2O_3 (with H_2O, CO_2 present). They reported the selectivity decreasing in the order zeolite A > mordenite > zeolite X > γ-Al_2O_3. Rosso et al. [101] reported a 1% Pt/3A zeolite catalyst that showed complete CO conversion over a wide temperature range, with minimal H_2 oxidation and reverse water gas shift. The best catalytic performance was observed at $\lambda = 3$, with "complete" CO conversion at 264 °C. Fukuoka et al. [102] found high PrOX activity and selectivity with a catalyst comprising Pt nanoparticles supported on mesoporous silica. CO conversion of 100% was obtained at temperature as low as 40 °C, and when operating at 60 °C no decrease in the CO conversion was observed when the feedstock included CO_2 (20%) and water vapor (2%). For comparison, a temperature of 423 °C was needed for Pt/SiO_2 or Pt/Al_2O_3 under their reaction conditions. Despite the interesting and intriguing results with zeolitic and mesoporous supports, the researchers have provided very little insight into why such supports should help to provide such unique activity and selectivity. Moreover, the long-term stability of such catalysts needs to be examined, especially with silica-based supports that would not be expected to strongly anchor the metal and keep it highly dispersed under long-term use.

Korotkikh and Farrauto [96] described studies with a Pt/Al_2O_3 catalyst with and without a promoter, generally thought to be iron oxide. Some comparative performance results are shown in Table 12.2 for powder-based catalysts. The benefit of adding a promoter was clear in terms of CO conversion activity, although selectivity appeared to be relatively unaffected. Employing a monolith-supported catalyst at $\lambda = 2$ and a VHSV = 20,000 h^{-1}, essentially all of the CO could be converted at a selectivity of about 50%. They reported a diminution in activity with the addition of water vapor, but no effect of CO_2 up to 180 °C. Above this temperature, they observed the presence of the reverse shift reaction, but no methanation up to 250 °C.

In addition to the practical nature of this work, another key concept emerges. A limitation of the Pt/Al_2O_3 catalyst is that the Pt sites must also provide for the dissociation of oxygen, which can be a problem if all sites are preferentially associated with CO. It has been proposed that a Langmuir-Hinshelwood model is operating, where the CO and O_2 compete for Pt sites [103]. It is because of this competition that elevated temperatures ($T > 150$ °C) must be

employed in order to maintain some site availability for O_2 dissociation. When the Fe-based promoter is added, the CO conversion is significantly increased, and increasing the concentration of CO does not inhibit the reaction (indicating approximately zero-order rate dependence of CO). This result is consistent with a dual site, non-competitive mechanism in which CO adsorbs onto the Pt sites and the O_2 dissociatively adsorbs on the metal oxide site. The surface reaction occurs between adsorbed CO and O on adjacent but different sites. This effect was further described in a subsequent report on PrOX activity over the Fe oxide-promoted Pt/alumina catalyst, in which a dual site, non-competitive mechanism for CO oxidation was proposed. In addition, it was suggested that the electronic states of the Pt metal particles could be changed by the Fe oxide [104].

Providing separate adsorption sites for O_2 dissociation is a theme that recurs with other catalytic metals, as will be seen. Following this mode of argument, several groups have reported that adding a second metal or metal oxide as promoter to Pt base catalysts can significantly enhance the PrOX reaction. Promoters include alkali metals [105–110], Ce [111–113], Co [114–118], Fe [96,104,119–128], Mn [129,130], Ni [131], and Nb [132] among others. It is not clear, however, that all these promoters operate through the activation of oxygen.

The favorable effect of ceria as a support for Pt for CO oxidation has also been studied widely due to the oxygen-storage properties of ceria [111,133–136]. Significant enhancement in CO conversion and selectivity on the ceria-promoted catalyst has been attributed to the ability of ceria to supply oxygen to Pt and suppress H_2 oxidation [111,136].

12.2.3.2. *Ru-, Rh-, Pd-, and Ir-Based Catalysts*

A study of CO oxidation using noble metal catalysts was conducted by Oh and Sinkevitch [137], who were looking for a catalyst more active and selective than the (at the time) leading candidate Pt/Al_2O_3. They also hoped that an improved catalyst operating at lower temperatures might enable use of a less complex PrOX reactor. They examined and compared Pt-, Rh-, Ru-, and Pd-supported Al_2O_3, along with several non-precious metal catalysts such as $Co–Cu/Al_2O_3$, $Ni–Co–Fe/Al_2O_3$, Fe/Al_2O_3, and Mn/SiO_2. All catalysts were obtained from commercial sources. Their work focused mainly on the effects of temperature and oxygen concentration. Unfortunately, the studies were limited to feeds containing non-representative low concentrations of H_2 (0.85 vol%), CO (900 ppmv), and O_2 (up to 2300 ppmv), and without the presence of either H_2O or CO_2. CO oxidation activity was tested in the presence of H_2 between 100 and 200 °C, and the activity was found to increase in the order Ru > Rh > Pt > Pd, with Pd showing quite low activity, as shown in Fig. 12.7. They also observed superior selectivity with the Ru and Rh catalysts compared with (unpromoted) Pt/Al_2O_3. All the noble metal catalysts showed a maximum

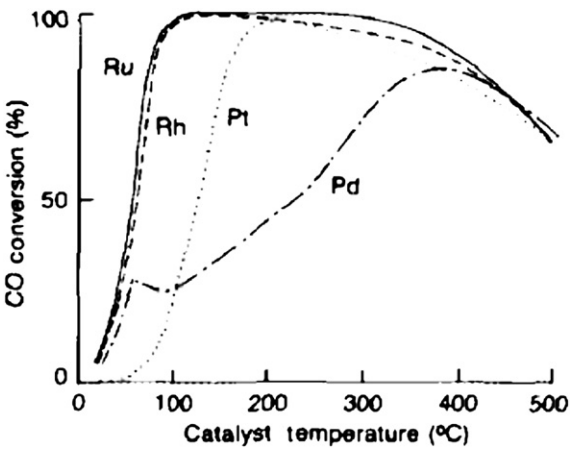

FIGURE 12.7 CO conversion over Al_2O_3-supported Ru, Rh, Pt, and Pd catalysts as a function of temperature. Feed: 0.85% H_2, 900 ppmv CO, 800 ppmv O_2, balance N_2. *Source: Reprinted with permission from Oh and Sinkevitch [137], Copyright (1993) Elsevier.*

activity with temperature, which they attributed to the onset of the (reverse) water gas shift reaction with increasing temperature. This reinforces the need to test the catalysts with both H_2O and CO_2 in the feed. The Co-containing catalyst was the most active of the non-precious metals, but deemed insufficiently active for further study.

Chin et al. [138] reported that Ru supported on either SiO_2 or Al_2O_3 provided an effective PrOX catalyst. They found that the preferred pre-treatment was to simply reduce the Ru precursor salts without an initial calcination, which provided a more highly dispersed catalyst. Deactivation by metal sintering was more pronounced with the SiO_2-supported catalysts compared to Al_2O_3-supported catalysts. Echigo et al. [139] reported that the outlet CO concentration could be reduced to 1 ppmv by using a novel Ru catalyst, and they reported durability for more than 16,000 h in a microreactor, and for more than 8000 h in a large-scale reactor. CO PrOX using a commercial 0.5% Rh/MgO catalyst was reported by Han et al. [140]. They claimed that low activity for both the reverse water gas shift reaction and methanation at temperatures below 300 °C made Rh/MgO an ideal PrOX catalyst for reaction at higher temperatures (250 °C), in particular for applications requiring highly dynamic operation under variable load conditions.

Galletti et al. [141] tested Rh-based catalysts supported on 3A zeolite, alumina, titania, and ceria. They reported a 1% Rh-3A zeolite catalyst with good performance at low temperature, and an exit CO concentration below 10 ppmv could be obtained within a temperature range of 80−120 °C without undesirable side reactions. Wörner et al. [142] employed a highly porous reticulated SiC foam support, with Ru added to a washcoat via impregnation. They operated at VHSV 2000−5000 h^{-1} (vol/vol foam) with $\lambda = 3$, so that there was no possibility of selectivity exceeding 33%. They claimed successful operation between 100 and 160 °C. However, the role of (reverse) water gas shift or methanation could not be assessed with their analytical system.

Mariño et al. [133] tested ceria-based supported Pt and Ir catalysts for the removal of CO in the presence of large quantities of hydrogen. The optimum performance was obtained at low temperatures ($T < 100$ °C). The best CO removal was obtained with Pt/$Ce_{0.15}Zr_{0.85}O_2$ at 225 °C and $\lambda = 4$. However, under such reaction conditions the CO concentration in the outlet feed was reduced to only approximately 700 ppmv, with simultaneous PrOX and WGS (and RWGS) reactions occurring. It was found that at $T > 175$ °C, the water gas shift reaction begins to participate even with the Ir-based catalyst. Although Ir does not demonstrate shift activity when supported on alumina, it does when supported on ceria−zirconia. This may be a limitation of the use of CeO_2-based supports at these operating temperatures. They also found that basic supports tend to make the precious metals more active for PrOX, even though dispersion is better on acidic supports. This was thought to be related to O_2 activation. They cite a non-competitive Langmuir-Hinshelwood mechanism when ceria is the support.

Jhalani and Schmidt [143] examined PrOX at short contact times of 10−15 ms with noble metals. The catalysts were prepared by multiple impregnations of metal onto alumina spheres. They obtained 90% CO conversion at 300 °C and stoichiometric O_2 ($\lambda = 1$) with Ru. They found that H_2O blocks H_2 competitive adsorption at elevated temperatures ($T > 200$ °C). They provided a reminder that in studies that are run without H_2O or CO_2, the water gas shift reaction (or its reverse) as well as CO_2 methanation propensity cannot be assessed. For Rh, Ru, and Pt−Ce catalysts, the WGS and CO methanation reactions were found to be significant in their system. Ru and Rh also demonstrated CO_2 methanation activity at 250−350 °C. Ru was found to be a good PrOX catalyst at

$T < 250$ °C, and Rh was found to be effective in the range of 250–400 °C. For Pt and Pt–Ce, they found that H_2O addition increased CO conversion significantly. This was found to be less with Rh and Ru, although water did suppress methanation. They did not see enhancement of CO oxidation with addition of Ce, unlike other researchers, but saw an increase in WGS activity, which had the effect of decreasing the CO concentration.

12.2.3.3. *Au Catalysts*

The use of gold catalysts for both CO oxidation and PrOX has received attention from many research groups. The preparation of a properly functioning Au-based catalyst has proven to be both a technical and intellectual challenge, as groups seeks to optimize the catalyst through obtaining the maximum size and shape of the particles, selecting the proper support, understanding the reaction pathways or mechanisms that are operative, and understanding the role of feed components on performance. It has become clear that there are many variables that must be controlled in order to obtain high activity gold-based catalysts. Of particular importance are the preparation method, the pre-treatment conditions, choice of support, presence of moisture in the feed, and the oxidation state of the Au in the particles [144].

12.2.3.3.1. CATALYST PREPARATION

Proper acknowledgment must of course go to the pathfinding work of Haruta and coworkers [145], who demonstrated the activity of small gold particles in hemispherical shape, stabilized on amorphous oxide supports, e.g., TiO_2, α-Fe_2O_3, Co_3O_4, for low temperature CO oxidation. The activity of gold catalysts for CO oxidation was attributed to the careful preparation process for achieving a highly dispersed distribution of gold species. It has been pointed out that it is particularly difficult to obtain gold in as high a dispersion as can be obtained with platinum and palladium [145,146].

The literature contains numerous examples of methods for preparing supported gold catalysts, with the general intention to produce catalysts having highly dispersed gold. Various gold catalyst preparation methods have been reported for achieving small Au particles, which is difficult to obtain using conventional impregnation methods [92]. For example, Bollinger and Vannice [147] showed that for a Au–TiO_2 catalyst prepared via impregnation, the greatest activity was obtained following a sequential pre-treatment consisting of high temperature reduction at 500 °C, calcination at 400 °C, and low temperature reduction at 200 °C. However, a catalyst prepared via co-precipitation was more active. Costello et al. [148] pointed out that the reported activity of Au/Al_2O_3 catalysts has varied from being inactive to significantly active, and pointed out the extreme sensitivity to the synthesis methods. Particularly important was the residual chloride content in the catalysts, the pre-treatment conditions, and the effect of water vapor on performance in activity tests.

In general, supporting gold catalysts with reducible metal oxides such as TiO_2, Fe_2O_3, Co_3O_4, MnO_x, CeO_2, and MnO_2–CeO_2 gives better results than with non-reducible oxide supports, and these catalysts are typically prepared via co-precipitation [92]. An aqueous co-precipitation method for making gold catalysts on various metal supports was described by Haruta et al. [145], in which an aqueous mixture of $HAuCl_4$ and a nitrate of the corresponding metal oxide support were poured into an aqueous solution of Na_2CO_3 to obtain a hydroxide or carbonate co-precipitate, which was subsequently washed, dried, and calcined at 400 °C. The particle sizes of Au catalysts on TiO_2 support obtained by deposition–precipitation method show a close relationship with the pH of the $HAuCl_4$ aqueous solution used in the synthesis procedure [146,149], as shown in Fig. 12.8. Additional co-precipitation methods for gold catalyst preparation have been described [150,151].

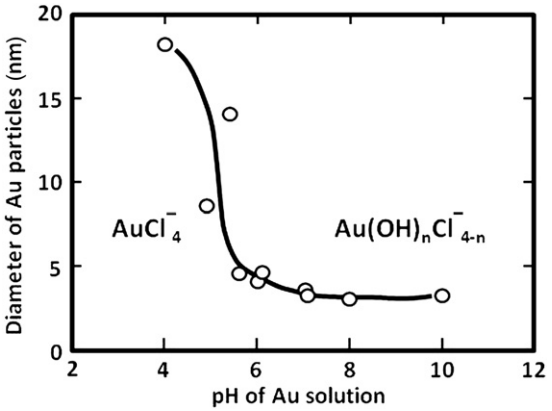

FIGURE 12.8 Mean diameter of Au particles as a function of pH of the $HAuCl_4$ solution employed in preparing Au/TiO_2 catalysts via the deposition–precipitation method. Au solution content 13 wt% relative to TiO_2, all catalysts calcined at 400 °C in air. *Reprinted with permission from Haruta [146], Copyright (1997) Elsevier.*

Ivanova and coworkers [152,153] adopted a direct anion exchange (DAE) method that differs from the deposition–precipitation method generally used, and suggested an advantage in that no gold was lost during the catalyst preparation. The gold particle size obtained by DAE is very sensitive to evolution and nature of the gold chloro-hydroxy species in the solution and on the surface of the support [152,153]. They also reported that when the catalysts were washed with water, the majority of the particles were in the range of 10–20 nm. The presence of less hydrolyzed complexes during the preparation, and especially during the calcination, led to the formation of Au–Cl–Au bridges and particle agglomeration, as shown by TEM photographs [152].

The poisoning effect of chloride on gold catalysts has been studied in detail by Oh et al. [154], who were able to quantitatively describe the complex manner in which chloride affects the Au catalyst. They employed a series of experiments where chloride was quantitatively removed and added. This investigation confirmed that deactivation during the oxidation reaction can result from the formation of Au–Cl bridges. In this same work, the authors also reported that residual chloride affects the activity in two different ways: it facilitates the agglomeration of Au particles during heat treatment, and it inhibits the catalytic activity by poisoning the active site.

Other methods, e.g., co-sputtering [155] and chemical vapor deposition [156], were also used to make gold particles on the metal supports; however, these are not practical methods for preparation of PrOX catalysts.

12.2.3.3.2. CATALYST PERFORMANCE

Au catalysts have excellent low temperature CO oxidation activity and selectivity, where they are mainly investigated. However, the selectivity toward CO oxidation in PrOX testing decreases dramatically with increasing reaction temperature. This can be a concern generally, and especially for larger-scale systems, where a significant adiabatic temperature rise in the catalyst bed could occur. Gold catalyst sintering during PrOX is an important issue. Moreover, deactivation of gold-based catalysts with time has been an issue. Few supported gold catalysts have been reported to show long-term stability under realistic PrOX conditions [7]. Trimm [5] has noted that the activity of gold-based catalysts is known to be sensitive to the preparation conditions, the nature of the support, the size of the gold particles, the performance at the gold–support interface, and the interaction between the gold and the support. This makes it a very complex catalyst system to study.

Bollinger and Vannice [147] described the performance of Au/TiO_2 for CO oxidation (not PrOX), and showed that initially very high activity below room temperature could be obtained. However, the catalyst activity declined substantially over a few hours on stream. They did not observe a correlation between Au particle size and activity, which they thought related to the difficulty to control migration and coverage over Au by the TiO_2.

They suggested CO adsorption onto Au sites, and invoked special interfacial Au−TiO_2 sites that can activate O_2, accounting for the high initial activity, thus a non-competitive Langmuir-Hinshelwood model. The CO_2 produced was thought to compete with CO for sites on the Au, serving to inhibit the reaction.

Raphulu et al. [157] point out that an Au/TiO_2 catalyst can deactivate simply during storage. They found that the catalyst deactivates under all variations in storage conditions over a 12-month period. Storage in vacuum significantly enhances the rate and extent of deactivation. The catalyst appears to deactivate through a combination of Au^{3+} reduction, Au nanoparticle agglomeration, loss of surface hydroxyl groups, loss of surface moisture, and accumulation of surface carbonates and formates. The rate and extent of catalyst deactivation can be limited by storing the catalyst in the dark at sub-ambient temperature (refrigerator) and under an inert atmosphere. These results simply point out the challenges of working with a gold catalyst for PrOX with the requirement for long-term stability.

Daniells et al. [158] describe an Au/Fe_2O_3 catalyst for CO oxidation. The catalyst was tested with CO, O_2, and H_2O but without H_2 or CO_2. The work focused primarily on the role of calcination temperature and the presence of water vapor in the feed. A catalyst calcined at 400 °C prior to use was found to give poorer performance than non-calcined samples; it was suggested that this might be due to the loss of hydroxyls from the Fe_2O_3 support. They propose that the CO is adsorbed on Au^0, while hydroxyl may be located on an adjacent Au^{3+} site, thus the catalyst is an ensemble of Au^{3+} and Au^0. The inclusion of water in the gas stream significantly enhanced the oxidation of CO at room temperature. This is consistent with a hydroxyl-facilitated decomposition of a carbonate intermediate, by transformation to less stable bicarbonate. They observed potential causes of catalyst deactivation, including depletion of OH groups on the catalyst surface, reduction of Au^{3+} to Au^0, and accumulation of carbonates at the active site.

Daté et al. [159], Costello et al. [148], and Bond and Thompson [144] have also described hydroxyl participation as a key factor in prolonging of CO oxidation activity, by aiding decomposition of inert deactivating carbonates. Thus, the presence of some minimal level of water in the feed seems to be essential for proper operation of the catalyst.

Navarro et al. [160], in a review of hydrogen production reactions point out that gold is active, but sensitive not only to water vapor, but also to CO_2. Therefore, PrOX testing without CO_2 does not reveal this limitation. They reiterated that reaction rates on gold particles, for both CO and H_2 oxidation, depend markedly on the choice of the support oxide. Although the variations in activity and stability are related to the tendency to form surface carbonates, the effect appears to be support dependent. They also noted complex particle size effects and support effects with Au, and observed that with Au/Al_2O_3 catalysts, deactivation with H_2 (PrOX) is slower than without H_2. This result suggests that the active sites contain hydroxyl groups, which may be maintained with the presence of hydrogen, but otherwise can be removed during CO oxidation. These weakly bonded hydroxyls are postulated to participate in the reaction, possibly by reaction with CO to form an active intermediate in the CO_2 formation pathway. Consistent with this interpretation is the high susceptibility of these catalysts to poisoning by chloride ions, because chloride may displace the OH groups.

Kahlich et al. [161] provided a detailed catalyst activity study for a 3.15 wt% Au/α-Fe_2O_3 PrOX catalyst. The catalyst was prepared via a co-precipitation route, and they pointed out the key importance of specific synthesis methodologies. They noted that catalysts prepared via impregnation onto an iron oxide support are one to two orders of magnitude less active.

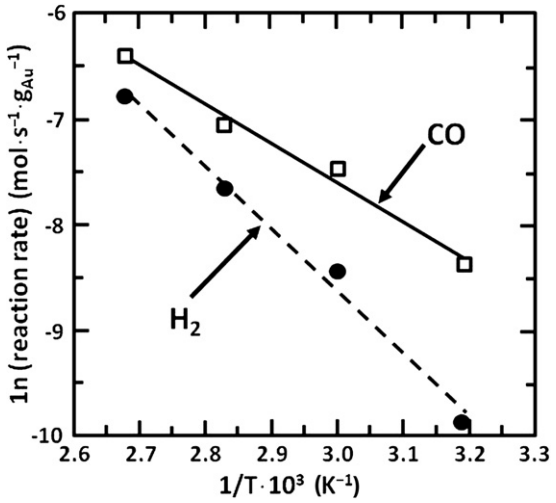

FIGURE 12.9 Arrhenius diagram of ln(rate) versus 1/T for CO (□) and H_2 (●) oxidation at $\lambda = 2$ employing a simulated reformer gas (1 kPa CO, 1 kPa O_2, 75 kPa H_2, balance N_2). *Reprinted with permission from Kahlich et al. [161], Copyright (1999) Elsevier.*

They tested their catalyst at relatively high space velocities (500,000−800,000 h^{-1}), with $\lambda = 2$, and kept O_2 conversion below 25% (in some cases <4%, O_2 partial pressure dependent) in order to assure an adiabatic temperature rise not greater than 20 °C in the catalyst bed. They reported a rapid initial deactivation of about 30% before the activity leveled out, and the activity only after 2 h was monitored. They measured CO oxidation rates over a broad range of CO and O_2 partial pressures. At 80 °C, reaction orders (power law kinetics) were determined to be 0.55 and 0.27, respectively, for CO and O_2. They found that the H_2 oxidation rate is independent of CO partial pressure, such that at higher CO partial pressures H_2 oxidation is relatively insignificant, whereas at low CO partial pressures H_2 oxidation is more important. The measured activation energy for H_2 oxidation was greater than for CO oxidation, as shown in Fig. 12.9, with values of 50 vs 31 kJ/mol, respectively, consistent with the loss of CO oxidation selectivity with increasing temperature. They claimed that a non-competitive Langmuir-Hinshelwood mechanism is operational with this catalyst, and referred to the work of Bollinger and Vannice [147] for a more rigorous kinetic discussion. They point out that the rate constant for CO oxidation with the Au/α-Fe_2O_3 catalyst is comparable to a Pt/γ-Al_2O_3 catalyst at 200 °C, as shown in Table 12.3 [161].

Tompos et al. [162] demonstrated that Au PrOX catalysts can be evaluated using a combinatorial method. The catalysts were prepared by homogenous precipitation. In their tests, a benchmark Au/MgO catalyst had only 62% CO conversion and 33% O_2 selectivity. Somewhat surprisingly, they found that the addition of Pb, Sm, and V improved performance, primarily by increasing the activity for both CO and H_2 oxidation. By allowing a lower reaction temperature with the promoters, improved CO selectivity could be obtained as well.

Bond and Thompson [163] provide a detailed exposition on possible reaction mechanisms in gold-catalyzed reactions. They note that the principal factors determining performance are known to include particle size and oxidation

TABLE 12.3 Power Law Rate Constants (k_{CO}), Reaction Orders (α_{CO}, α_{O_2}), and Activation Energies (E_a) for 3.15 wt% Au/α-Fe_2O_3 at 80 °C and for 0.5 wt% Pt/γ-Al_2O_3 at 200 °C

System	k_{co} ($mol_{co}/(g_{met}.s)$)	α_{CO}	α_{CO_2}	E_A (kJ/mol)
Au/α-Fe_2O_3 at 80 °C	9.81×10^{-4}	0.55 ± 0.03	0.27 ± 0.02	31
Pt/γ-Al_2O_3 at 200 °C	13.8×10^{-4}	-0.42 ± 0.05	0.82 ± 0.05	71

(Reprinted with Permission from Kahlich et al. [161], Copyright (1999) Elsevier).

state of the gold, the chemical and physical form of the support, and the presence or absence of poisons and accelerators. As a result, they point out the difficulty in arriving at definite conclusions concerning the importance of these parameters because of the variability under which the activities have been measured (reactant ratio, moisture content, time on-stream, etc.). However, the importance of particle size is very well established for CO oxidation over gold catalysts, and the evidence suggests that this holds for PrOX (and WGS) as well. Although it appears that CO can be bound stably only to Au sites of low coordination, if the adsorbed CO is too distant from the metal-support interface, then selective oxidation cannot occur. This helps to explain the effects of both particle size and particle thickness. It was pointed out that TEM methods can be ineffective in helping to assess the role of particle size if observations are made in only two dimensions. Gold particles can be modified by the support in ways that are either geometric (i.e., particle shape, degree of wetting of surface) or electronic. They note that H_2 is less effective than water in preventing deactivation over gold catalysts, as reported by others [164–166], and point out the important role of hydroxyl groups in maintaining activity [167]. Possible structures involving interaction between OH and Au are shown in Fig. 12.10, suggesting that different oxidation states of the metal may be present, depending upon coordination number. Very useful pictorial representations of CO oxidation mechanisms for Au on Al_2O_3 and reducible oxides are provided in [163].

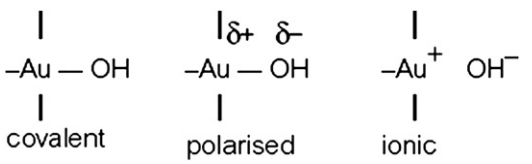

FIGURE 12.10 Possible representations of an OH group bonded to an Au atom. *Reprinted with permission from Bond and Thompson [163], Copyright (2008) Springer.*

Bion et al. [92] in their review of PrOX catalysts noted that the interface between the gold particle and vacancy sites on the support is important, i.e. CO oxidation over gold requires O atoms from the support, since O_2 cannot dissociatively adsorb on Au.

Debeila et al. [168] described an Au/TiO_2 catalyst promoted by In_2O_3. The $Au-TiO_2-In_2O_3$ was prepared by a deposition–precipitation method, using $HAuCl_4 \cdot H_2O$ as a source of gold. They showed that differences between the non-promoted and promoted catalyst are related to the relative ease by which the oxides become de-hydroxylated by thermal treatments. The $Au-TiO_2-In_2O_3$ catalyst exhibited lower CO oxidation activity than a benchmark $Au-TiO_2$ catalyst, but was highly resistant to irreversible deactivation due to sintering, even after reaction up to 500 °C. Excessive water vapor in the feed was found to reversibly deactivate the catalyst. They found no evidence that the addition of water vapor converted deactivating carbonates to less stable bicarbonates, unlike other reports on gold-based catalysts.

12.2.3.4. *Transition Metal Oxide Catalysts*

There is significant incentive to produce PrOX catalysts with components less expensive than gold or precious metals. The most active catalysts of this type are based on Co, Cu, or mixtures thereof. Avgouropoulos et al. [169] compared $Au/\alpha\text{-}Fe_2O_3$, $Cu\text{-}CeO_2$, and Pt/Al_2O_3 for PrOX catalysis. The $CuO-CeO_2$ catalyst was prepared by a sol gel peroxo method (1.9 wt% CuO, 19.5 m^2/g). Testing at $W/F = 0.03$ g-s/cm^3, the gold catalyst was found to be the most active, but the $Cu-CeO_2$ catalyst was the most selective, providing 100% selectivity over the temperature range 50–120 °C (with CO conversion varying from 3% to 84%). However, selectivity dropped to 66% at 200 °C, the temperature required for 99% CO conversion. At lower space velocities ($W/F = 0.144$ g-s/cm^3), the Cu catalyst reached 100% CO conversion with 94% selectivity at 120 °C. The

presence of CO_2 and H_2O in the feed increased the temperature required for the same level of CO conversion. Typically, λ values of 4 were required for good performance. The "light-off" of CO oxidation or of hydrogen oxidation was shown to be closely related to the respective peak temperatures observed by CO or H_2 temperature programmed reduction.

The significant activity of the Cu−CeO_2 catalysts was shown to result from the synergistic interaction of copper and CeO_2, as described by Liu and Flytzani-Stephanopoulos [170]. It has been shown that redox processes in ceria-supported copper materials during CO oxidation involve both copper and ceria species [171,172]. Investigations on mixed Cu−Ce oxide or CuO/CeO_2 catalysts reported that bulk copper oxides had negligible contribution to the catalytic activity of CO oxidation [170,173,174]. In further work with CuO−CeO_2, Avgouropoulos and coworkers [175,176] showed that a urea-nitrate combustion synthesis method gave superior catalytic performance, similar to but slightly better than a catalyst prepared via a citrate-hydrothermal method, while co-precipitated and impregnated samples exhibited poorer catalytic activity. Consistent with the other cited studies (above), they claimed that achieving high activity is related to the formation of well-dispersed copper oxide species in strong interaction with ceria particles.

A review by Bion et al. [92] includes a detailed discussion of Cu−CeO_2 catalyst performance from both their and others' work. The effects of synthesis approaches are reviewed in detail, and a table summarizing Cu−CeO_2 catalyst performance is provided. In contrast to the finding of Avgouropoulos and coworkers [175,177], it was claimed that preparation of CuO−CeO_2 catalysts by co-precipitation or impregnation of copper salt precursors on ceria can also give excellent results. However, they confirmed that CuO in bulk, segregated from the CeO_2, is essentially inactive, and that this can limit practical Cu loadings to about 5 wt%. In a test for the effect of calcination temperature on performance, they found very little difference in performance over the temperature range of 350−550 °C, as shown in Fig. 12.11. This was thought to be due to the fact that higher temperatures promote both sintering and Cu−CeO_2 interactions, the two effects operating in different directions and countering each other. The catalyst appears to operate by a Mars and van Krevelen redox mechanism, in which the redox changes occur in both copper oxide and ceria components.

In a study of supported base metal catalysts, the catalytic performances of ceria and ceria−zirconia-supported Co and Cu were compared [178]. It was concluded that only the ceria−copper and ceria−zirconia−copper catalysts appeared to be as active as the platinum group catalysts. In the same study, it was determined that among a series of supports − CeO_2, SiO_2−Al_2O_3, La_2O_3, and MgO − CeO_2 was the best, pointing to the importance of support redox properties over acidity or basicity. Effective catalyst performance was claimed to be based on synergistic redox properties produced by the

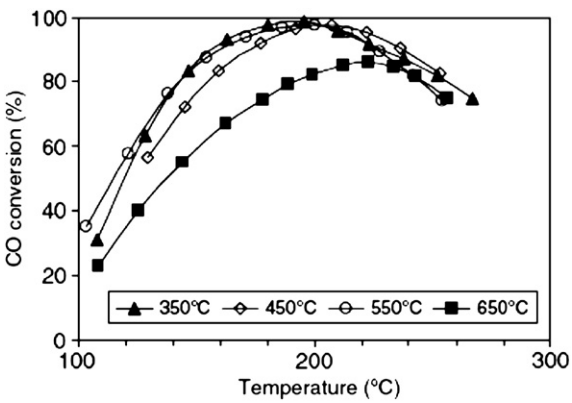

FIGURE 12.11 CO conversion versus temperature over a 1% CuO−CeO_2 catalyst, prepared using different calcination temperatures. Experimental conditions: 69% H_2, 2.76% CO, 1.78% O_2, 26.5% N_2, 200 mg catalyst, total gas inlet: 300 mL/min). *Reprinted with permission from Bion et al. [92], Copyright (2008) Springer.*

formation of copper oxide−ceria interfacial sites. H_2-TPR studies supported this conclusion [174,179]. The authors note that additional work is required to improve the stability of Cu−CeO_2 catalysts for industrial application, especially in terms of dealing with the effects of H_2O, which can deactivate the catalysts because of an accumulation of hydroxyl species on active interfacial sites [149], accumulation of carbonate species [180], copper redistribution [181], and the sintering of copper species [182].

Wang et al. [183] studied the PrOX reaction with a 5% CuO/samaria-doped ceria catalyst prepared via co-precipitation. Testing was carried out with a mixture comprising H_2/O_2/CO in a ratio of 97:2:1, without H_2O or CO_2. CO conversion of 90% was achieved at 140 °C, but O_2 selectivity declined below 100% starting at ~90 °C, and H_2 oxidation was pronounced at 130 °C. There was no evidence provided that CO conversion sufficient to reduce CO to <100 ppmv could be obtained. They suggested that there is interfacial oxygen associated with the vacancies in the support, and also oxygen associated with Cu^{2+}. At 140 °C and above, not only did they observe reduction of the interfacial support oxygen, but also onset of reduction of oxygen atoms associated with Cu^{2+}. Catalyst deactivation, via CuO reduction, would be a concern under long-term operation.

Zhou et al. [184] studied non-noble metal catalysts for carbon monoxide selective oxidation in excess hydrogen. They evaluated Ni, Co, and Ni−Co/activated carbon (AC) catalysts, and found Co and Ni−Co to be active. They claimed to achieve 99.5% CO conversion (1% CO, 0.5% O_2, 98.5% H_2), giving a product containing 50 ppmv CO, with a Co−Ni/AC catalyst over the range of 130−150 °C. They did not test with H_2O or CO_2 in the feed. No information was provided regarding H_2 consumption, as the only species measured was CO, using a methanizer and flame ionization detector. Although they claimed that no methane was produced, they could not measure it directly. Co_3O_4 was thought to be the active Co species. A higher activity of Co−Ni/AC in comparison with Co/AC was obtained and attributed to the higher dispersion of active Co_3O_4 species and the lower electronic cloud density of cobalt on the surface of Co−Ni/AC.

Park et al. [7] provided a review of hydrogen purification methods, with a primary focus on PrOX catalysis. Extensive tables are provided summarizing work with various catalytic metals from various groups. It must be pointed out that, with the recognized importance of catalyst preparation variables and test procedures, one must be careful in comparing catalyst performance provided in this summary. Among the base transition metal oxides, Co- and Cu-based catalysts are most promising. Cobalt catalysts have been described as the most active among the transition metal oxides [185], and several papers describe the use of supported Co catalysts for the reaction [186−188]. Zhao et al. [189] compared the performance of Co supported on CeO_2, Al_2O_3, ZrO_2, SiO_2, and TiO_2 and found the ZrO_2-supported Co to be the most active. They claimed that the active Co phase is Co_3O_4. Cobalt has also been employed to enhance the performance of Cu−CeO_2 catalysts. Park et al. [190] showed that when Cu−CeO_2 was promoted by 0.5% Co, 99% CO conversion could be achieved at 150−220 °C without H_2O or CO_2 in the feed and at 205 °C with H_2O and CO_2. However, in the presence of excess H_2 the Co catalyst under extended operation can undergo reduction and become a methanation catalyst at operational temperatures [191]. Seeking to take advantage of this, Kim et al. [192] coupled PrOX with subsequent methanation to achieve a wider effective temperature range of operation for CO removal.

Mn−Cu oxide (hopcalite) is known to be effective for CO oxidation [193−197] and such catalysts find commercial application for respiratory protection [198−200]. Not unexpectedly,

hopcalite-based catalysts have been examined for the PrOX reaction as well.

Hasegawa et al. [201] studied the PrOX reaction over a range of Cu/Mn ratios (1:8 to 1:1). Mesoporous manganese oxide without the additional metals, along with 0.5% Pt/Al_2O_3 and a commercially available hopcalite catalyst, were also tested for the PrOX reaction for comparison. The feed contained 1 vol% CO, 1 vol% O_2, 60 vol% H_2, and the remaining N_2, i.e., no H_2O or CO_2 was in the feed, with a W/F in the range of $1-4 \times 10^{-3}$ min-g_{cat}/mL. CH_4 formation was negligible in all cases. The copper-containing manganese oxide (Cu/Mn = $^1/_4$) prepared by the sol–gel method showed slightly improved low-temperature CO oxidation activity compared with the commercial hopcalite catalyst, but the difference was small, and maximum conversions of about 95% were achieved in both cases (at 125 °C and 150 °C, respectively). The mesoporous Mn catalyst was substantially less active, pointing to the importance of the copper component. It was claimed that the activity enhancement with Cu addition was the result of generating a highly active lattice oxygen that is not present with the Mn-based catalyst alone. The most important finding, however, was that the catalyst activity, as evidenced by CO conversion (but not O_2 selectivity), decreased with time, readily observable within only 1 h on stream. This effect was much more pronounced with H_2 present than when it was absent. The authors ruled out deactivation by H_2O or carbonate formation, and concluded that the deactivation was the result of slow reduction of the catalyst with time. The catalyst could be regenerated at 300 °C for 2 h in air, providing further evidence for the occurrence of catalyst reduction. CO adsorbs preferentially on the catalytically active sites. In the absence of CO, H_2 begins to react with lattice oxygen at temperature as low as 50 °C. Thus, it appears that hopcalite-based catalysts are not suitable for PrOX catalysis under extended operation.

12.2.4. Practical Application in Small Fuel Processors

Qi et al. [202] prepared a review of integrated fuel processors for fuel cell application. This review provides an excellent introduction to the issues involved in preparing a compact, integrated fuel processor for PEM. They claim that many studies discuss the application of reforming processes assisted by other technologies that do not necessarily integrate well, such as including pressure swing adsorption or membrane separation to provide pure hydrogen. For example, net efficiency may be compromised due to an imbalance of the mass/heat transfer rates as well as the reaction dynamics, either in the individual units or the complete system. They describe efforts at process intensification technologies, especially involving microscale components, which have much potential to improve this situation. Process intensification approaches include engineered catalysts and specific devices targeting heat management and product purification. The aim is to produce a device having the ability to improve overall efficiency, to mitigate requirements for materials and capital investments, and to reduce the overall footprint of the operation.

In the specific case of PrOX catalysis, for the basic classes of catalyst systems: Pt/Al_2O_3, Au/CeO_2 [203] or $Cu-Ce/\gamma\text{-}Al_2O_3$ [204], there is a modest allowable temperature range of approximately 40 °C where high CO selectivity is observed. Below this temperature range (which is catalyst dependent), activity is too low, and above this range, H_2 begins to compete favorably for O_2. As a result, thermal management is a major issue for a PrOX unit of any significant capacity. The Los Alamos National Laboratory developed a four-stage PrOX unit to minimize H_2 consumption, at the cost of size and a rather complex heat management. Brundage et al. [205] describe a PrOX reactor with a "plurality of sections," each individually

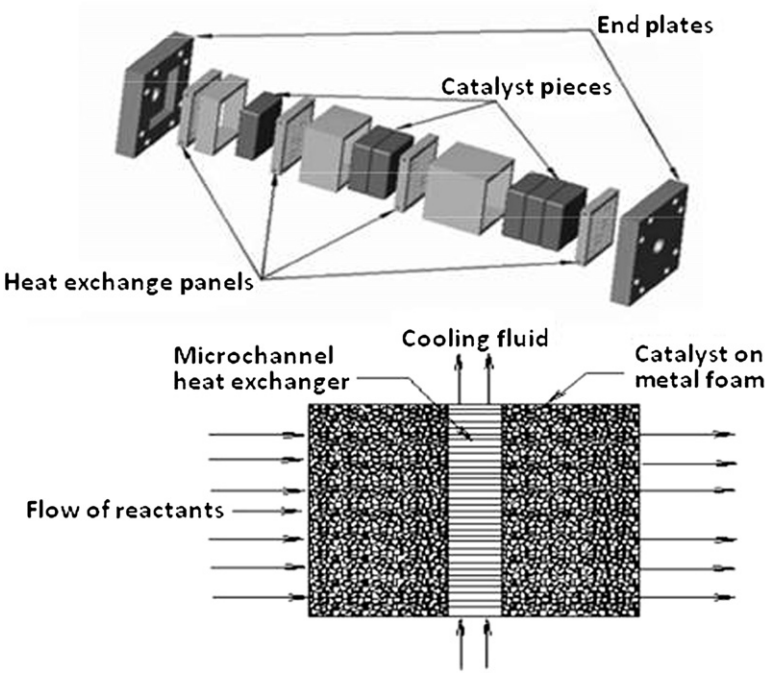

FIGURE 12.12 Design of the PrOX reactor (top). Catalyst foams are sandwiched between heat exchanger panels to maintain the reaction temperature nearly constant (bottom). *Reprinted with permission from Brooks et al. [206], Copyright (2005) American Chemical Society.*

optimized for operating at a preferred reaction temperature, different O_2/CO ratio, different cooling method, and even a different catalyst/promoter/support.

Brooks et al. [206] at the Pacific Northwest National Laboratory described a series of steam reforming, water gas shift, and PrOX reactors based on microchannel designs. The goal for the PrOX reactor was to convert 1% CO in reformate to <10 ppmv in the exit stream. The microchannel PrOX reactor comprised four stages of foam-supported catalyst with microchannel heat exchangers sandwiched in between (Fig. 12.12), so that the reaction temperature was held within ±20 °C and high selectivity could be achieved. Air was injected in small quantities in each reactor stage. The first stage catalyst operated at ~200 °C and employed a non-precious metal catalyst, and subsequent stages comprised a Pt-based precious metal catalyst also operating at ~200 °C. The selectivity and temperature profile could also be controlled by adjusting the amount and type of catalyst in each chamber. Overall, 10 ppmv CO was achieved at a GHSV of 93,000 h^{-1} and $\lambda = 2.4$ at a 2-kWe equivalent flow of hydrogen.

Castaldi et al. [207] describe the development of a proprietary "Microlith® substrate reactor, comprising a series of catalytically coated screens each with ultrashort channel lengths, high cell density, and low thermal mass, resulting in extremely high heat and mass transfer rates." Notable in this paper is the difficulty the authors had in selecting and preparing a suitable catalyst. It is worth emphasizing that an additional technological development is required in order to bind a PrOX catalyst to a substrate employed specifically for a device. Challenges include particle size, uniformity of coating, and compatibility of the binder with the catalyst. They operated optimally at $\lambda = 2.4$, 160 °C and a gas

hourly space velocity of 440,000 h^{-1}. They selected a supported Pt catalyst primarily because it provided a wide operating temperature range and had no methanation activity. They observed lower light-off but poorer selectivity with Rh, methanation activity with Ru, and virtually no activity with supported Pd. A gold catalyst of the composition Au/MnO_x/Al_2O_3 catalyst was also prepared but found to be virtually inactive. These results point to the difficulties in translating laboratory studies in well-controlled environments into a working device.

12.2.5. Summary

Preferential oxidation (PrOX) of CO in the presence of H_2 and other syngas components is a proven method to reduce CO concentrations to levels acceptable for operation of a PEM fuel cell, typically <10 ppmv, or <100 ppmv for CO "tolerant" PEM anode. A variety of catalysts have been demonstrated, capable of PrOX, including precious metals, gold-based catalysts, and transition cobalt and copper metal (oxides). Each catalyst has its own advantages and disadvantages.

Comparison of catalyst systems (both within and across metal types) is frequently challenging for reasons including different and complex methods of catalyst preparation (which may not always be scalable), different test conditions, and generally a lack of long-term testing to establish catalyst stability. Also, frequently tests only employ CO, H_2, and O_2 in the feed, thus other important syngas components such as H_2O, which could either increase or decrease activity (but in most cases the latter), and CO_2, which could participate in either reverse shift or methanation, as well as form deactivating carbonates, are not included. Any realistic test of PrOX catalysis must include H_2O and CO_2. Moreover, since the PrOX reaction is exothermic, awareness of actual temperatures within the catalyst bed, as well as temperature control in scale-up with the catalyst (hence its tolerance to temperature variation), must be considered in any PrOX development program.

Early work with catalysts such as Pt/Al_2O_3 demonstrated selective CO oxidation, but relatively high temperatures were required and relatively poor selectivity (reflecting H_2 instead of CO oxidation) was achieved. The high operating temperatures were required in order to free up metal sites (that were close to fully occupied by CO at lower temperatures) for O_2 dissociation, and these sites were also available for H_2 oxidation. It was found that promoters, such as iron oxide, provided separate sites for O_2 dissociation, thereby lowering the operating temperature and increasing selectivity relative to H_2 oxidation. A non-competitive Langmuir-Hinshelwood model was consistent with the experimental results. The same approach of providing separate CO and O_2 chemisorption sites appears to be operative in the design of gold and copper oxide-based PrOX catalysts.

In general, it appears that each of the catalyst types has an optimum operating temperature range, below which CO conversion is too low and above which selectivity decreases relative to undesired H_2 oxidation. Gold-based catalysts appear to be the most active at low temperatures (below 100 °C), and appear to benefit from the presence of water vapor as well as hydrogen, in order to maintain hydroxyl groups and avoid deactivation by carbonates. Copper-based catalysts appear to be highly selective at moderate temperatures, but lose selectivity at the higher temperatures required for full CO conversion. A strong interaction between CuO and the support (preferably CeO_2) appears to be required for good performance, bulk CuO apparently being inactive. Promoted Pt-based catalysts operate well at moderate to elevated temperatures, and appear to have a somewhat broader operating range, which has led to their preference in larger scale systems, despite catalyst cost.

12.3. SELECTIVE CATALYTIC METHANATION OF CO (SMET)

12.3.1. General Considerations

As with preferential oxidation (PrOX) of CO discussed in the previous section, selective methanation of CO is technology developed primarily to accommodate the low tolerance of PEM fuel cell anodes toward CO. The performance of current PEM fuel cells generally requires CO concentrations below 100 ppmv in a hydrogen-rich stream [89,208], while the pure Pt anode CO tolerance is even lower at <10 ppmv [209,210]. Therefore, selectively reducing the CO concentration in a hydrogen-rich reformate stream without substantial hydrogen consumption is the goal of selective methanation (SMET). This process is thermodynamically favorable and strongly exothermic (Eq. (12.10)). A benefit of this approach is that no additional gas component is required. Moreover, the methane produced does not affect the fuel cell performance.

$$\begin{aligned} &CO + 3H_2 \rightarrow CH_4 + H_2O \\ &\Delta H^0{}_{298\ K} = -206.2\ \text{kJ/mol} \end{aligned} \tag{12.10}$$

Furthermore, this process is less exothermic than that of PrOX on a per-CO converted basis, as shown in Eq. (12.11):

$$CO + \tfrac{1}{2}O_2 \rightarrow CO_2 \quad \Delta H^0{}_{298\ K} = -283\ \text{kJ/mol} \tag{12.11}$$

Three moles of H_2 are consumed with each mole of CO during methanation. This is not a significant concern as long as CO levels are low. A concern with this approach, however, is the hydrogen consumption by the competitive methanation of CO_2 present in the reformate, where 4 mol of hydrogen will be consumed by 1 mol of CO_2 (Eq. 12.12) and the CO_2 concentration is generally significantly higher than the CO concentration. Thus, CO_2 methanation must be avoided at the temperatures where CO methanation occurs.

$$\begin{aligned} &CO_2 + 4H_2 \rightarrow CH_4 + 2H_2O \\ &\Delta H^0_{298\ K} = -165\ \text{kJ/mol} \end{aligned} \tag{12.12}$$

Although the reaction rate of CO_2 methanation can be higher than that of CO methanation, especially at elevated temperatures, preferential methanation of CO in a typical hydrogen-rich reformate (containing about 1 vol% CO and considerable amounts of CO_2) always dominates at lower temperatures. This is due to the stronger adsorption strength of CO, thus successful competition for active sites compared with CO_2. At higher temperatures, however, CO adsorption becomes weaker and its competitive adsorption over CO_2 decreases, thus, the undesired CO_2 methanation becomes more pronounced. Therefore, a precondition of SMET is the selection of a reasonable temperature range (i.e., operating window) to remove the unwanted CO while keeping CO_2 unconverted as much as possible.

In addition, under certain conditions the undesired reverse water gas shift reaction is also possible (Eq. 12.13). It is endothermic and normally takes place at higher temperatures than that of CO methanation. However, if this reaction occurs to any significant extent, it limits the amount by which the CO concentration can be reduced through the methanation of CO.

$$\begin{aligned} &CO_2 + H_2 \rightarrow CO + H_2O \\ &\Delta H^0{}_{298\ K} = 41.1\ \text{kJ/mol} \end{aligned} \tag{12.13}$$

12.3.2. Catalysts for Selective Methanation (SMET)

A variety of catalytic metals, including Ru, noble metals, Ni, Au, and various alloys, have been investigated for the selective methanation

of CO. Most of the published literature has focused on Ru- and Ni-based catalysts.

12.3.2.1. Ru-Based Catalysts

Ru catalysts are well known for application in methanation as well as Fischer-Tropsch synthesis. It is therefore not uncommon that at the lower temperature operating ranges, Ru catalysts produce some lighter hydrocarbons along with methane. Generally, the high H_2/CO ratios found in reformate streams downstream of the water gas shift reactor favor methane production, so that production of higher hydrocarbons is not a serious concern for SMET applications.

Ru-based catalysts are reported to have high methanation activity, and thus have been extensively investigated for selective methanation. Vannice [211] measured the CO methanation activity of several alumina-supported group VIII metals, and found that Ru was by far the most active on a turnover frequency basis. Pioneering work by Baker et al. [212] on selective CO methanation showed that the CO concentration levels could be reduced from 0.29% to as low as 10−20 ppmv over an Ru/Al_2O_3 catalyst over the temperature range of 150−180 °C at relatively low space velocities (i.e., 500−1000 h^{-1}), while keeping CO_2 unreacted. The subsequent work by Rehmat and Randhava [213] reported that CO methanation with a Ru/α-Al_2O_3 catalyst predominates over both CO_2 methanation and the reverse water gas shift reaction (RWGS) below 250 °C. In this case, higher space velocities (i.e., 9000−36,000 h^{-1}) and a broader temperature range (i.e., 125−300 °C) were investigated.

By adjusting the preparation method of a Ru/γ-Al_2O_3 catalyst (i.e., single vs multiple impregnation), and through the use of different reduction temperatures, Dagle et al. [209] found that higher metal loadings increased H_2 consumption (i.e., CO_2 methanation) and shifted CO conversion to lower temperatures. Catalysts with larger particle sizes had lower activity but better inhibition of CO_2 methanation. A 3% Ru/γ-Al_2O_3 catalyst was shown to reduce CO in reformate to below 100 ppmv over the temperature range of 240 to 280 °C, while keeping hydrogen consumption below 10% (Fig. 12.13).

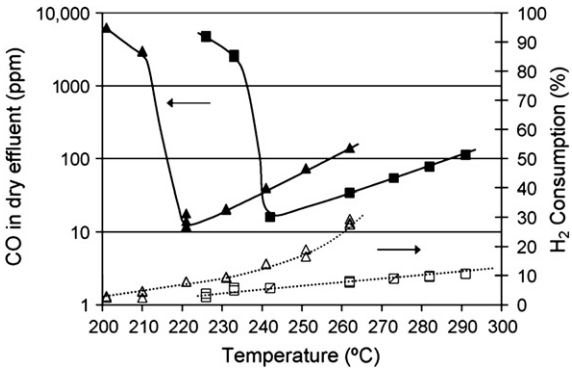

FIGURE 12.13 Effect of crystallite size for a 3% Ru/Al_2O_3 catalyst on CO exit concentration and H_2 consumption (feed composition: 0.9% CO, 24.5% CO_2, 68.9% H_2, 5.7% H_2O, SV = 13,500 h^{-1}). (■) Ru: 34.2 nm, (▲) Ru: 10.9 nm; CO dry exit concentration (filled symbols), H_2 consumption (open symbols). *Reprinted with permission from Dagle et al. [209], Copyright (2007) Elsevier.*

The effects of metal loading and particle size have also been described by others [214,215]. Kowalczyk et al. [214] found higher activity correlated with lower Ru dispersion, which they attributed to the dominant role of ensembles of contiguous surface planar Ru atoms. Panagiotopoulou et al. [215] concluded from kinetic measurements that both CO and CO_2 methanation reactions are structure sensitive, with larger particles being more active, when Ru was supported on either Al_2O_3 or TiO_2 (a wet impregnation method was used in the preparation). The highest CO turnover frequency, 13.3 μmol/g-s, was obtained with 5% Ru/TiO_2 at 215 °C, which corresponded to an average crystallite size of 4.5 nm (Fig. 12.14). The CO_2 turnover rate with this same catalyst at 330 °C was 64.8 μmol/g-s, corroborating the danger of higher temperatures (for example, adiabatic temperature rise) on loss of CO methanation

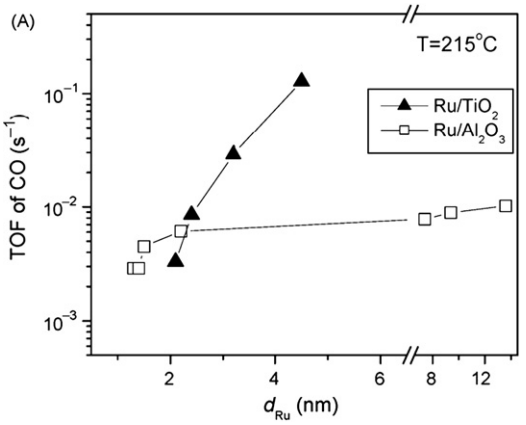

FIGURE 12.14 Effect of mean Ru crystallite size (d_{Ru}) on the turnover frequency of CO at 215 °C as a function of catalyst support. *Reprinted with permission from Panagiotopoulou et al. [215], Copyright (2009) Elsevier.*

selectivity with Ru catalysts. In the same work it was observed that CO_2 methanation would not initiate until the maximum CO methanation conversion was reached. Increasing temperature above this point resulted in more CO in the product, the result of the reverse water gas shift activity being greater than CO methanation activity. By increasing the loading and particle size, CO and CO_2 methanation activity increased faster than reverse WGS. It is notable in this work that a calcination treatment of a 5% Ru/Al_2O_3 catalyst to increase Ru crystallite size did not result in higher turnover rates. Moreover, it is not clear why increasing particle size, in which presumably many sites on the operating metal surface become available yet more distant from the support, should demonstrate such a notable support effect with TiO_2, especially since lower Ru loadings on TiO_2 showed low activity. It is possible that not only metal particle size, but also thickness (dimension of the particle normal to the surface of the support) may be important. The complexities of metal particle size and support effects are evident from this study, and more work would be helpful to resolve these issues.

Li et al. [216] studied 0.4 wt% and 0.8 wt% Ru/Al_2O_3 catalysts. They found that the former exhibited lower activity but higher selectivity compared with the 0.8 wt% Ru catalyst, and concluded that the catalyst with lower loading was preferable in that it could operate effectively over a wider temperature range. However, Galletti et al. [217] compared three Ru/Al_2O_3 catalysts (at the much higher Ru loadings of 3, 4, and 5 wt%), and found that the catalyst with 4 wt% Ru loading had the best overall performance between 300 and 340°C. The differences in operating ranges make comparison of the two studies difficult and point to the importance of catalyst preparation and activation, metal dispersion, and so on.

Support-dependent performance of Ru catalysts for selective methanation has been reported by several different groups [214,218–221], and explained in different ways. Kowalczyk et al. [214] postulated that the catalyst performance correlated with the Lewis acidity of the supports, thus rationalizing the highest activity of Al_2O_3 among MgO, $MgAl_2O_4$, carbon, and Al_2O_3. Panagiotopoulou et al. [215] reported an activity order of $TiO_2 > Al_2O_3 > CeO_2 > YSZ >> SiO_2$ (Fig. 12.15). Takenaka et al. [218] attributed the best performance of TiO_2 among the supports investigated (i.e., MgO, SiO_2, Al_2O_3, ZrO_2, and TiO_2) to the smaller particles (or higher dispersions) of Ru, thus more active sites exposed, in contradiction with the above-cited work by Panagiotopoulou et al. [215]. Kim et al. [220] found that the turnover frequency followed the order of $Ru/TiO_2 > Ru/YSZ \sim Ru/SiO_2 > Ru/ZrO_2 \sim Ru/\gamma\text{-}Al_2O_3$. Since turnover frequency is highly dependent on available metal sites (hence metal dispersion), the above order does not necessarily correlate with overall catalyst activity. Galletti et al. [222] found that ZrO_2 and CeO_2 supports were superior to TiO_2 for Ru-selective methanation. Again, the discrepancies among research reports are clear, suggesting that important variables in catalyst

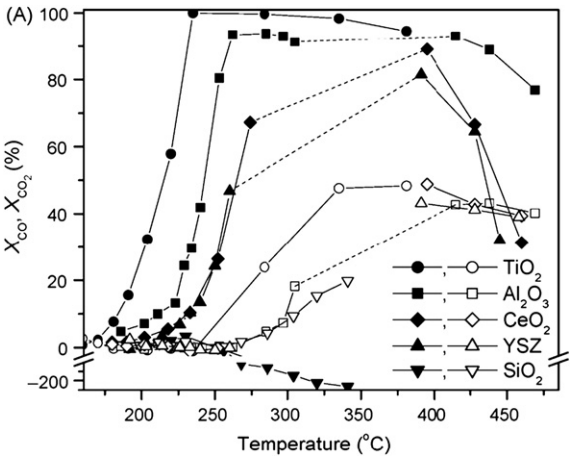

FIGURE 12.15 Catalytic performance of Ru (5 wt%) supported on the different commercial oxide carriers. Solid symbols: CO conversion: open symbols: CO_2 conversion. *Reprinted with permission from Panagiotopoulou et al. [215], Copyright (2009) Elsevier.*

preparation or activation may not yet be recognized in comparing catalyst performance on different supports.

Eckle et al. [223] compared the CO-selective methanation over commercially available Ru/zeolite and Ru/alumina catalysts. The zeolite was not identified, although zeolite Y seems likely. Several different feed gas compositions operating at atmospheric pressure were evaluated, the base case feed composition comprising only CO, N_2, and H_2 (0.6 kPa CO, 2.8 kPa N_2, balance H_2). Variations to this feedstock involved adding alternatively CH_4 (4.5 kPa), H_2O (5 kPa), or CO_2 (1.2 kPa), and as well a CO-free (CO_2 only) feed was evaluated. The zeolite-supported Ru catalyst showed the greater activity of the two catalysts, as evidenced by full conversion of CO at 200 vs 230 °C for the Ru/Al_2O_3 catalyst, respectively, with the base case feedstock. Especially notable was the distinct separation in temperature regimes for CO vs CO_2 methanation with Ru/zeolite when both gases were present, indicating that CO_2 methanation did not begin until CO was essentially completely converted. On the other hand, for the Ru/Al_2O_3 catalyst CO_2 conversion initiated before CO conversion was complete. With the Ru/zeolite catalyst when CO was not present, CO_2 methanation started at a significantly lower temperature than when CO was present, indicating that CO inhibits the methanation of CO_2 on this catalyst. Water vapor showed virtually no effect with the Ru/zeolite and showed only a modest inhibition effect with Ru/Al_2O_3. The Ru/zeolite catalyst showed a lower apparent activation energy and greater rate dependence on H_2 concentration. Although it is clear that the Ru/zeolite catalyst is the more active of the two catalysts both on an Ru mass-available basis and turnover frequency comparison, it also showed evidence of deactivation over time (for all the feed variations), whereas the Ru/Al_2O_3 catalyst showed more stable behavior. The authors had difficulty in rationalizing the difference in catalyst activity based on available metal dispersion or metal particle size, as limitations of the methods resulted in discrepancies between particle sizes estimated from H_2 chemisorption with those estimated from XRD and TEM. It is possible that small Ru particles could not be detected by these latter techniques. They proposed that methanation activity simply correlated with the available number of Ru^0 sites on the two catalysts. Finally, it is worth noting that the kinetic measurements obtained in this work agreed in some cases and disagreed in other cases with work reported by other researchers, perhaps not surprising but again pointing to the importance of preparation methods, metal loading, temperature ranges, etc. on results, making it difficult to compare results across laboratories.

Not unexpectedly, Ru catalyst performance has been reported to be dependent on the operating conditions used in the tests. Li et al. [216] found that the space velocity had a great effect on CO methanation over the $Ru/\gamma\text{-}Al_2O_3$ catalyst, where the increase of

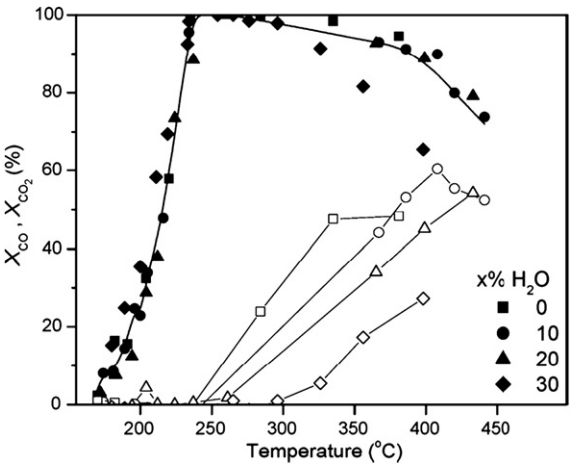

FIGURE 12.16 Effect of water vapor in the feed (0–30%) on the catalytic performance of 5% Ru/TiO_2 catalyst for the selective methanation of CO. Solid symbols: CO conversion; open symbols: CO_2 conversion. *Reprinted with permission from Panagiotopoulou et al. [215], Copyright (2009) Elsevier.*

the space velocity from 2500 to 5000 h^{-1} resulted in a narrower operating temperature window, which shifted the operating temperature range for CO to be below 10 ppmv from 150–210 °C to 175–195 °C.

Panagiotopoulou et al. [215,224] found that water vapor (up to 30%) was beneficial in offering a wider temperature window for selective CO methanation, because it shifted the CO_2 conversion curve toward higher temperatures but had no effect on CO methanation over the Ru/Al_2O_3 catalyst investigated (Fig. 12.16). On the other hand, an inhibition effect of H_2O on CO methanation was observed by Gorke et al. [219] and Men et al. [225], which was explained by its competition for the active sites.

By using microchannel reactors, Gorke et al. [219] found that Ru/SiO_2 had better activity and higher selectivity than a Ru/Al_2O_3 catalyst. However, competition between CO and CO_2 methanation existed while CO_2 methanation dominated above 250 °C. H_2O had some obvious inhibition effect on CO methanation, which was attributed to its competition for the active sites.

Despite the high activity and selectivity of the Ru catalysts, their deactivation under long-term operation remains a concern. During a stability test of selective CO conversion over a commercial 0.5% Ru/Al_2O_3 catalyst, Zhan et al. [226] observed a slight deactivation of the catalysts, which was explained by the deposition of the intermediate C species on the surface and the consequent blocking of the active sites. More studies are needed to establish long-term Ru stability and the required operating conditions to maintain this stability.

12.3.2.2. Ni-Based Catalysts

Ni-based catalysts have also been extensively studied because of their high methane selectivity and low metal cost compared with Ru. In general, it appears that Ni-based catalysts are less active than Ru catalysts, however, not all reports agree.

Herwijnen et al. [227] carried out systematic investigations of the reaction rate of methanation of CO and CO_2 over a $Ni/\gamma\text{-}Al_2O_3$ catalyst in the temperature ranges of 170–210 °C and 200–230 °C, respectively. Although the reaction rate of CO_2 methanation was much higher than that of CO, they demonstrated that in the mixture of CO and CO_2, the hydrogenation of CO_2 did not start until a very high conversion of CO was attained. Even in the presence of only 200 ppmv CO, the CO_2 methanation rate was not measurable. These results were explained by the stronger adsorption of CO during its competition against CO_2 for the active sites, and CO_2 adsorption proposed to be the rate-determining step of CO_2 methanation. Moreover, a definite catalyst surface heterogeneity was proposed, wherein only 8–10% of the catalyst surface was active for CO_2 adsorption and its subsequent conversion. Small concentrations of H_2O and methane were shown to have no significant effect on the methanation activity with this catalyst.

Liu et al. [228] investigated the Ni loading effect on Ni/ZrO_2 catalyst performance with a simulated reformate mixture. The optimum Ni loading was found to be 1.6%, and CO could be reduced from 1% to below 20 ppmv over the temperature range of 260–280 °C, with hydrogen consumption kept below 7%. Higher loadings of Ni (above 3%) provided poorer performance. On the other hand, Men et al. [225] reported that high Ni loadings (up to 43%) showed better activity in microchannel reactor studies, which was probably because the larger Ni particle size was more suitable for CO methanation. Moreover, they also found that the performance was strongly dependent on the catalyst promoters, where basic dopants (such as MgO and CaO) seemed to provide some activity enhancement for the Ni/Al_2O_3 catalyst.

As with Ru catalysts, the nature of the support is also reported to play a very important role on the performance of the Ni-based catalysts. In the work of Takenaka et al. [218], activity was found to increase in the order $MgO < Al_2O_3 < SiO_2 < TiO_2 < ZrO_2$ (Fig. 12.17). Larger Ni particles showed better activity, which was attributed to a higher capacity for CO decomposition into adsorbed carbon and oxygen atoms. Contrary to this, Men et al. [225] found that Al_2O_3-supported catalysts had better activity than those supported on TiO_2, and they concluded that an acidic support was more appropriate for CO methanation. An inhibition effect of H_2O was also shown in their work. A more recent study from this same group [229] reported that CeO_2- and Cr_2O_3- supported Ni catalysts were even more effective, and they could selectively decrease CO from 1.6 vol% to ppmv levels (<50 ppmv) in a microchannel reactor, with good stability (180 h on stream).

Ni-containing alloys such as $FeNi_3$ have been developed by Andersson et al. [230], which showed relatively low cost and good performance. In this work the possibility of catalyst development by computational screening was also discussed. Kramer et al. [231] reported novel catalysts comprising $Re_2Y_9Ni_{89}O_x$ and $Ti_8Hf_9Ni_{83}O_2$ with high activity, selectivity, and stability during CO-selective methanation. The improved performance was explained by the better dispersion and/or stabilization of Ni. Recently, the same group [232] showed that a $Re_2Zr_{10}Ni_{88}O_x$ catalyst had the same activity as the $Zr_{10}Ni_{90}O_x$ catalyst, with better selectivity toward CO removal. A thorough physicochemical study of the catalysts indicated that such improved selectivity was due to the modified surface properties by Re doping. They also found that ZrO_2 was a key component for the activation of the CO molecules.

Due to the much higher activity (several times to several hundred times) of an amorphous catalyst (i.e., Fe–Ni–P, Fe–Ni–B) compared with the corresponding crystalline

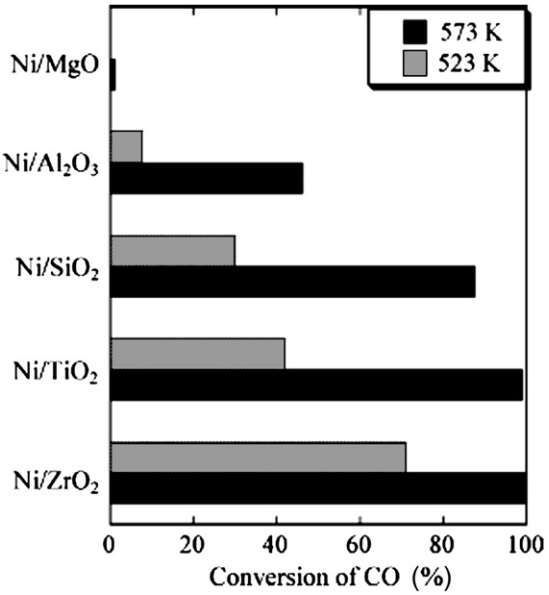

FIGURE 12.17 Methanation of CO over 10 wt% Ni catalysts on different supports. Catalyst charge, 0.120 g, $P(H_2)$ = 33.5 kPa, P(CO) = 0.8 kPa, P(He) = 67.0 kPa, flow rate = 61 ml/min. *Reprinted with permission from Takenaka et al. [218], Copyright (2004) International Association for Hydrogen Energy.*

sample during CO hydrogenation [233], Habazaki et al. [234] further investigated the CO hydrogenation over Co−Zr and Ni−Zr (−Sm) alloys in a mixed $CO/CO_2/H_2$ gas stream. They found that CO preferentially reacted with hydrogen, and CO_2 methanation occurred only after almost the entire CO was converted. Moreover, the presence of CO_2 suppressed carbon deposition by the disproportionation reaction of CO, thus preventing catalyst deactivation. In comparison, the Ni-based catalyst exhibited higher activity than Co samples. Along this line, Liu et al. [235] developed a novel Ni−B−ZrOx catalyst, and found that the catalyst performance was affected by the Ni/B molar ratio and was improved by the addition of zirconia. The $Ni_{29}B_{13}Zr_{58}Ox$ catalyst they developed could selectively reduce CO concentration to less than 40 ppmv between 230 °C and 250 °C, while CO_2 conversion was held below 8%. The same group [236] further developed an amorphous Ni−Ru−B/ZrO_2 catalyst with better activity, which could reduce CO concentrations below 10 ppmv at 210−230 °C, while keeping CO_2 conversion below 1.55% and H_2 consumption below 6.5%.

Men et al. [225] studied both Ru- and Ni-based catalysts in microchannel reactors. They found that methanation was strongly dependent on the metal type, loading, and promoters, where Ni/CaO/Al_2O_3 exhibited the best activity.

12.3.2.3. *Other Catalysts*

Different noble metal-based catalytic systems have been recently compared for SMET. Panagiotopoulou et al. [224] studied Al_2O_3-supported Ru, Rh, Pt, and Pd catalysts, with Ru and Rh exhibiting good reactivity toward both methanation and selective methanation, whereas Pt was less active and Pd virtually inactive (Fig. 12.18). For hydrogenation of CO in the absence of CO_2, methanation activity increased with temperature and, for the case of Ru, methane selectivity increased at the expense of higher hydrocarbons. Addition of water vapor had little effect on Ru performance, whereas it decreased activity of the Rh-based catalyst. With Pt, CO concentration decreased following addition of water vapor, but this was primarily the result of the water gas shift reaction rather than methanation. With Ru, CO_2 methanation (in the absence of CO) produced primarily CH_4 without higher hydrocarbons. For Ru and Rh, addition of H_2O increased the (onset) temperature of CO_2 methanation, effectively increasing the temperature window between CO and CO_2 methanation. However, with all metals some CO always remained from CO_2 hydrogenation, the result of the reverse water gas shift reaction competing with methanation (CO was being produced faster than it could be consumed). For "co-methanation" (both CO and CO_2 are present), hydrogenation of CO as a function of temperature only predominated until the onset of reverse water gas shift, at which point CO could be produced by this latter reaction and the CO derived in this fashion could consume substantial amounts of H_2. The importance of water vapor in helping to avoid this situation was emphasized.

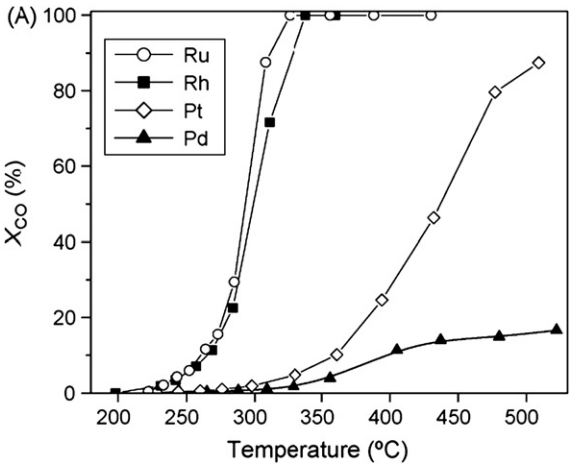

FIGURE 12.18 Conversions of CO as function of reaction temperature over Rh, Ru, Pt, and Pd catalysts (0.5 wt%) supported on Al_2O_3. *Reprinted with permission from Panagiotopoulou et al. [224], Copyright (2008) Elsevier.*

Vilchis-Nestor et al. [237] reported good performance for CO hydrogenation over an $Au/SiO_2{-}Al_2O_3$ catalyst, and showed that the catalyst activity was strongly dependent on the catalyst preparation method. A catalyst made by a novel bio-reduction method (i.e., using a renewable and low cost biological reducing agent − Camellia sinensis) showed better performance than that made by a conventional deposition−precipitation method. However, catalyst deactivation was observed with longer-term operation, which was mostly due to carbon deposition on the surface.

12.3.4. High-Throughput Synthesis and Testing of Selective Methanation Catalysts

High-throughput techniques have been used to prepare and test catalysts with a high degree of automation, which provides an ideal tool to facilitate the rapid discovery and optimization of solid-state catalysts for selective CO methanation.

Taking advantage of emissivity-corrected IR-thermographic images, Kramer et al. [231] obtained promising results with Y-, Hf-, Ho-, Cr-, Ce-, and Sm-doped Ni catalysts. In particular, $Hf_9Ni_{91}O_x$ and $Y_9Ni_{91}O_x$ catalysts exhibited much higher activity for CO hydrogenation (complete CO conversion occurred at 230 °C) and lower CO_2 hydrogenation activity (no observed CO_2 conversion below about 260 °C) in comparison with an industrial reference catalyst, 4 wt% Ru/TiO_2 (Fig. 12.19). They claimed that the unexpected increase in activity and selectivity was a result of addition of specific dopants, and found that in the absence of these dopants the Ni-based catalysts had poor performance. Moreover, the activity and selectivity of the catalyst could be further improved by adding some Ti to form a $Ti_8Hf_9Ni_{83}O_x$ catalyst. In the meantime, $Y_9Ni_{91}O_x$ catalyst showed a comparable activity, while further modification of these catalysts by doping a third metal

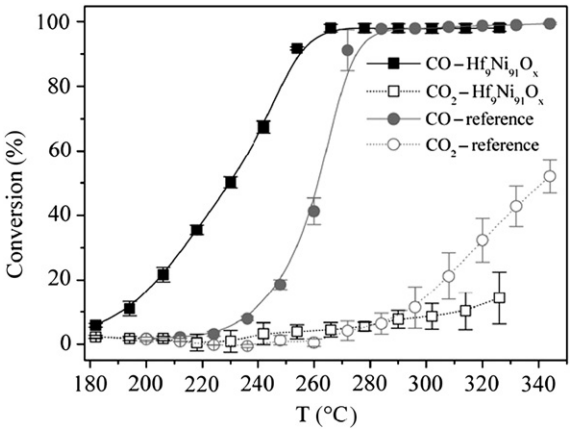

FIGURE 12.19 Comparison of CO and CO_2 methanation activities for $Hf_9Ni_{91}O_x$ and a 4% Ru/TiO_2 reference catalyst. Operating conditions: P = 0.1 MPa; $(CO/CO_2/N_2/H_2 = 2/14.9/19.8/63.3$, with feed saturated with water at room temperature. CO conversion (■) and CO_2 conversion (□) of $Hf_9Ni_{91}O_x$; CO conversion (●) and CO_2 conversion (○) of the 4% Ru/TiO_2 reference catalyst. *Reprinted with permission from Kramer et al. [231], Copyright (2007) Elsevier.*

such as Re (i.e., $Re_2Y_9Ni_{89}O_x$) led to a wider operating window from about 25 °C to about 60 °C.

With the help of a high-throughput scanning mass spectrometer and a scanning/sniffing sampling nozzle to locate the catalysts in the two-dimensional catalyst arrays (on wafers), Yaccato et al. [238] could screen more than 500 potential catalysts in a single day. Heat and mass transfer effects were negligible due to the small sample amount used (less than 1 mg per well). They found that Cu, Au, Co, and Ag were only slightly active, while Pd was only moderately more active. In comparison, Ru exhibited the highest methanation activity, with the activity following the order: Cu ~ Au ~ Co ~ Ag < Pd < Ir ~ NaCo ~ Re ~ KPt ~ PtCl < NaPt < Pt ~ Ni < Rh < KNaRu < Ru. Basic dopants (i.e., Na and K) resulted in a decrease of the methanation activity for all active metals (e.g., Pt, Ru, and Co), but an increase in the selectivity toward the water gas

shift reaction. The effect of precursor selection was observed to be particularly important with Pt, with $PtCl_4$ found to be inferior to chloride-free Pt precursors in terms of catalyst activity.

12.3.5. Engineering-Based Approaches to SMET

12.3.5.1. Thermally Differential Methanation

Based on the fact that methanation of CO always occurred earlier than CO_2 at lower temperatures, Xu et al. [208] firstly proposed the concept of temperature-staged methanation. This concept used at least one up-stream zone at higher temperature to methanate most of the CO with selectivity close to 100%, and at least one final zone at lower temperature to assure that the outlet CO concentration was below 100 ppmv. This latter reactor had relatively lower but still acceptable selectivity. They pointed out that the overall selectivity to CO methanation depended on the number of reaction stages adopted, and as high as 95% CO removal could be achieved through a three-stage system with simulated reformate consisting of 69% H_2, 30% CO_2, and 1.0% CO (dry composition) and up to 55% steam.

The same group [226] later reported a novel method of thermally differential methanation for deep removal of CO from H_2-rich reformates. In this method, a commercial 0.5 wt% Ru/Al_2O_3 catalyst was packed in a temperature-staged three-zone reactor, where the temperature was kept at 205 °C, 195 °C, and 185 °C for these zones. The feasibility and effectiveness of this method was further proved in a 820 h test, where CO in the outlet was successfully reduced and kept between 20−40 ppmv, with the CO methanation selectivity $(100 \bullet ([CO]_{inlet} - [CO]_{outlet})/[CH_4]_{outlet})$ maintained between 88% and 95%. However, some deactivation of the catalysts was observed, which was probably due to carbon deposition.

12.3.5.2. Two-Stage Methanation

Based on their testing results, Li et al. [216,239] found that it was technically difficult to reach the required CO removal while maintaining the CO_2 conversion below 5% by using only one catalyst. Therefore, they proposed a process of two-stage methanation by using a catalyst (i.e., 0.4 wt% Ru/Al_2O_3) with relatively low activity and high selectivity for the first stage at high temperatures, while another catalyst (i.e., 0.8 wt% Ru/Al_2O_3) with high activity and high selectivity for the second stage at low temperatures. This process successfully reduced CO content from 1% to 0.1% at 250−300 °C after the first stage, and further below 10 ppmv at 150−185 °C after the second stage, while keeping CO_2 conversion below 5%.

12.3.5.3. CO_2 Scrubbing in Combination with Methanation

Ledjeff-Hey et al. [240] proposed a CO purification system consisting of CO_2 scrubbing (with 10% mol MEA in H_2O) and CO methanation processes. Although this process was claimed to be viable, and could reduce the CO concentration below 10 ppmv, it is not in the spirit of other work described in this review, which seeks to selectively remove CO through improved catalyst formulations.

12.3.5.4. Membrane Reactor Combined with Methanation

Mori et al. [221] proposed a novel strategy of using a Pd/Ag membrane reactor with a selective CO methanation catalyst (i.e., 2% Ru/Al_2O_3) for the production of pure hydrogen. In this case, a Pd−Ag membrane with an inner diameter of 25 mm was installed in a reactor, with commercial 2 wt% Ru/Al_2O_3 catalyst packed upstream of and around the membrane for the hydrogen production from methane steam reforming (MSR temperature kept constant at 550 °C). On the shell side of the membrane, the same Ru catalyst was packed in order to remove trace amounts of CO in the

permeate and to achieve a CO-free hydrogen stream (CO methanation kept constant at 500 °C). The results indicated that such a system could obtain H_2 purity up to 99.8% with the CO concentration less than 10 ppmv, in which the presence of the methanation catalyst inside the membrane was believed to play a key role in reducing CO concentration to the low levels reported. By using different supported Ru catalysts, the operating temperature that could be employed to reduce the CO concentration to below 10 ppmv could be adjusted as needed.

12.3.6. Conclusions

Selective methanation (SMET) of CO is a viable approach for the removal of CO from hydrogen-rich gas streams to be used with PEM fuel cells. Ru- and Ni-based catalysts are among the most extensively investigated and have shown the most promising performance. The key criteria for good performance include high activity, which allows operation at lower temperatures, and high selectivity, reflecting low activity for CO_2 methanation and reverse water gas shift. It appears that Ru-based catalysts are more active than those derived using Ni, although there are some published results that argue against this. Catalysts based on these metals tend to be the most selective at the lower operating temperature ranges, generally because CO adsorption predominates and adsorption of CO_2 (hence reaction) is minimized. However, in order to obtain full CO conversion, higher temperatures may be required with subsequent loss of selectivity. Also, since the methanation reaction is strongly exothermic, adiabatic temperature rises in larger beds, to be expected in practical PEM fuel cell utilization, can also be a concern. Fortunately, it appears that when water vapor (up to 30%) is included in the feed (as would be anticipated for fuel cell applications with reformate), a wider temperature window for selective CO methanation results. This is primarily caused by a shift in the CO_2 conversion curve toward higher temperatures. Long-term stability of Ru-based catalysts has been raised as a concern.

The performance of these catalysts is strongly dependent on the support, preparation method, metal loading, metal particle size, promoter, and the operating conditions (T, space velocity). Some results indicate that larger metal particles result in greater turnover frequencies, especially in the case of Ru. TiO_2 and ZrO_2 appear to be the best supports for Ru and Ni, respectively. However, there are several studies that contradict these conclusions, pointing to the importance of preparation methods and test conditions in selective methanation catalyst performance. Finally, some promising SMET strategies have been proposed and demonstrated that show viability for both performances, with CO concentrations below 10 ppmv being achieved, and durability, in which stability has been demonstrated for as long as 800 h on stream.

References

[1] Holladay JD, Wang Y, Jones E. Review of developments in portable hydrogen production using microreactor technology. Chem Rev 2004;104 (10):4767–89.

[2] Palo D, Dagle R, Holladay J. Methanol steam reforming for hydrogen production. Chem Rev 2007;107:3992–4021.

[3] Palo DR, Holladay JD, Dagle RA, Chin Y-H. Integrated methanol fuel processors for poratable fuel cell systems. ACS Symp Ser 2005; 914:209.

[4] Onsan ZI. Catalytic processes for clean hydrogen production from hydrocarbons. Turkish J Chem 2007;31(5):531–50.

[5] Trimm DL. Minimisation of carbon monoxide in a hydrogen stream for fuel cell application. Appl Catal A: Gen 2005;296(1):1–11.

[6] Trimm D, Onsan Z. Onboard fuel conversion for hydrogen-fuel-cell driven vehicles. Catal Rev 2001;43 (1&2):39.

[7] Park ED, Lee D, Lee HC. Recent progress in selective CO removal in a H_2-rich stream. Catal Today 2009;130(4):280–90.

[8] Hoogers G. The fueling problem: fuel cell systems. In: Hoogers G, editor. Fuel cell technology handbook. Boca Raton: CRC Press; 2003. p. 5−1 to 5−23.
[9] Newsome DS. Water gas shift reaction. Catal Rev Sci Eng 1980;21:275.
[10] Twigg MW, editor. Catalyst handbook. 2nd ed. London: Wolfe Publishing Ltd; 1989.
[11] Ratnasamy C, Wagner JP. Water gas shift catalysis. Catal Rev 2009;51:325−440.
[12] Wang J, Musameh M, Laocharoensuk R, Gonzalez-Garcia O, Oni J, Gervasio D. Pt/Ru-functionalized magnetic spheres for a magnetic-field stimulated methanol and oxygen redox processes: towards on-demand activation of fuel cells. Electrochem Comm 2006;8(7):1106−10.
[13] Rethwisch DG, Phillips J, Chen Y, Hayden TF, Dumesic JA. Water gas shift over magnetite particles supported on graphite − effects of treatments in CO/CO_2 and H_2/H_2O gas-mixtures. J Catal 1985;91 (1):167−80.
[14] Keiski RL, Salmi T. Deactivation of the high-temperature water gas shift catalyst in non-isothermal conditions. Appl Catal A: Gen 1992;87 (2):185−203.
[15] Klein J, Stichert W, Strehlau W, Brenner A, Schunk SA, Demuth D. Process and apparatus for the combinatorial production and testing of material libraries by using at least two analytical methods. Germany: HTE A.-G.; 2001. Application: WO/2001/068236.
[16] Natesakhawat S, Wang XQ, Zhang LZ, Ozkan US. Development of chromium-free iron-based catalysts for high-temperature water-gas shift reaction. J Mol Catal A: Chem 2006;260(1−2):82−94.
[17] Lei Y, Cant NW, Trimm DL. Kinetics of the water-gas shift reaction over a rhodium-promoted iron-chromium oxide catalyst. Chem Eng J 2005;114(1−3):81−5.
[18] Lei Y, Cant NW, Trimm DL. Activity patterns for the water gas shift reaction over supported precious metal catalysts. Catal Lett 2005;103(1−2):133−6.
[19] Lei Y, Cant NW, Trimm DL. The origin of rhodium promotion of Fe_3O_4-Cr_2O_3 catalysts for the high-temperature water-gas shift reaction. J Catal 2006;239 (1):227−36.
[20] Andreev A, Idakiev V, Mihajlova D, Shopov D. Iron-based catalysts for the water-gas shift reaction promoted by 1st-row transition-metal oxides. Appl Catal 1986;22(2):385−7.
[21] de Araujo GC, Rangel MD. An environmental friendly dopant for the high-temperature shift catalysts. Catal Today 2000;62(2−3):201−7.
[22] Gottschalk FM, Hutchings GJ. Manganese oxide water gas shift catalysts − initial optimization studies. Appl Catal 1989;51(1):127−39.
[23] Hutchings GJ, Copperthwaite RG, Gottschalk FM, Hunter R, Mellor J, Orchard SW, et al. A comparative-evaluation of cobalt chromium-oxide, cobalt manganese oxide, and copper manganese oxide as catalysts for the water gas shift reaction. J Catal 1992;137(2):408−22.
[24] Hutchings GJ, Gottschalk F, Hunter R, Orchard SW. Cobalt-manganese oxide water-gas shift catalysts − a kinetic and mechanistic study. J Chem Soc Faraday Trans I 1989;85:363−71.
[25] Rethwisch DG, Dumesic JA. The effect of metal-oxygen bond strength on properties of oxides. 2. Water-gas shift over bulk oxides. Appl Catal 1986;21 (1):97−109.
[26] Junior IL, Millet JMM, Aouine M, do Carmo Rangel M. The role of vanadium on the properties of iron based catalysts for the water gas shift reaction. Appl Catal A: Gen 2005;283(1−2):91−8.
[27] Ghenciu AF. Review of fuel processing catalysts for hydrogen production in PEM fuel cell systems. Curr Opin Solid State Mater Sci 2002;6(5):389−99.
[28] Jiang C, Trimm DL, Wainwright MS. New technology for hydrogen production by the catalytic oxidation and steam reforming of methanol at low temperatures. Chem Eng Tech 1995;18(1):1−6.
[29] Uchida H, Isogai N, Oba M, Hasegawa T. Zinc oxide-copper catalyst for carbon monoxide-shift conversion. I. Dependency of catalytic activity on chemical composition of catalyst. Bull Chem Soc Jpn 1967;40 (8):1981.
[30] Uchida H, Oba M, Isogai N, Hasegawa T. Zinc oxide-copper catalyst for carbon monoxide-shift conversion. 2. Catalytic activity and catalyst structures. Bull Chem Soc Jpn 1968;41(2):479.
[31] Gines MJL, Amadeo N, Laborde M, Apesteguia CR. Activity and structure-sensitivity of the water-gas shift reaction over Cu-Zn-Al mixed-oxide catalysts. Appl Catal A: Gen 1995;131(2):283−96.
[32] Chinchen GC, Spencer MS. Sensitive and insensitive reactions on copper catalysts: the water-gas shift reaction and methanol synthesis from carbon dioxide. Catal Today 1991;10(3):293−301.
[33] Li K, Fu Q, Flytzani-Slephanopoulos M. Low-temperature water-gas shift reaction over Cu- and Ni-loaded cerium oxide catalysts. Appl Catal B: Env 2000;27(3):179−91.
[34] Tanaka Y, Takeguchi T, Kikuchi R, Eguchi K. Influence of preparation method and additive for Cu-Mn spinel oxide catalyst on water gas shift reaction of reformed fuels. Appl Catal A: Gen 2005;279 (1−2):59−66.
[35] Tanaka Y, Utaka T, Kikuchi R, Sasaki K, Eguchi K. Water gas shift reaction over Cu-based mixed oxides

for CO removal from the reformed fuels. Appl Catal A: Gen 2003;242(2):287–95.
[36] Tanaka Y, Utaka T, Kikuchi R, Takeguchi T, Sasaki K, Eguchi K. Water gas shift reaction for the reformed fuels over Cu/MnO catalysts prepared via spinel-type oxide. J Catal 2003;215(2):271–8.
[37] Twigg MV, Spencer MS. Deactivation of supported copper metal catalysts for hydrogenation reactions. Appl Catal A: Gen 2001;212(1–2):161–74.
[38] Song C. Fuel processing for low-temperature and high-temperature fuel cells: challenges, and opportunities for sustainable development in the 21st century. Catal Today 2002;77(1–2):17–49.
[39] Ruettinger W, Ilinich O, Farrauto RJ. A new generation of water gas shift catalysts for fuel cell applications. J Power Sources 2003;118(1–2):61–5.
[40] Patt J, Moon DJ, Phillips C, Thompson L. Molybdenum carbide catalysts for water-gas shift. Catal Lett 2000;65(4):193–5.
[41] Nagai H, Shinkawa T, Magari A, Makihara H. Method for wetting the hydrocarbon gas feeds in reformers. Japan: Mitsubishi Heavy Industries, Ltd; 1988. JP 87–88948.
[42] Panagiotopoulou P, Kondarides D. Effect of the nature of the support on the catalytic performance of noble metal catalysts for the water-gas shift reaction. Catal Today 2006;112:49–52.
[43] Wang X, Gorte RJ, Wagner JP. Deactivation mechanisms for Pd/Ceria during the water-gas shift reaction. J Catal 2002;212:225–30.
[44] Reuttinger W, Liu X, Farrauto RJ. Mechanism of aging for a Pt/CeO_2-ZrO_2 water gas shift catalyst. Appl Catal B: Env 2006;65(1–2):135.
[45] Azzam KG, Babich IV, Seshan K, Lefferts L. Role of Re in Pt-Re/TiO_2 catalyst for water gas shift reaction: a mechanistic and kinetic study. Appl Catal B: Env 2008;80(1–2):129–40.
[46] Keiski RL, Desponds O, Chang YF, Somorjai GA. Kinetics of the water-gas shift reaction over several alkane activation and water-gas shift catalysts. Appl Catal A: Gen 1993;101(2):317–38.
[47] Ayastuy JL, Gutierrez-Ortiz MA, Gonzalez-Marcos JA, Aranzabal A, Gonzalez-Velasco JR. Kinetics of the low-temperature WGS reaction over a CuO/ZnO/Al_2O_3 catalyst. Ind Eng Chem Res 2005;44(1):41–50.
[48] Ovesen CV, Clausen BS, Hammershoi BS, Steffensen G, Askgaard T, Chorkendorff I, et al. Microkinetic analysis of the water-gas shift reaction under industrial conditions. J Catal 1996;158(1):170–80.
[49] Zalc JM, Sokolovskii V, Loffler DG. Are noble metal-based water-gas shift catalysts practical for automotive fuel processing? J Catal 2002;206:169–71.
[50] Raman RK, Choudhury NA, Shukla AK. A high output voltage direct borohydride fuel cell. Electrochem Solid State Lett 2004;7(12):A488–91.
[51] Querino PS, Bispo JRC, Rangel M. The effect of cerium on the properties of Pt/ZrO_2 catalysts in the WGSR. Catal Today 2005;107–108:920–5.
[52] Shido T, Iwasawa J. Reactant-promoted reaction mechanism for water-gas shift reaction on Rh-doped CeO_2. J Catal 1993;141:71–81.
[53] Burch R. Gold catalysts for pure hydrogen production in the water-gas shift reaction: activity, structure and reaction mechanism. Phys Chem Chem Phys 2006;8:5483–500.
[54] Olympiou GG, Kalamara CM, Yazdi CDZ, Efstathiou AM. Mechanistic aspects of the water-gas shift reaction on alumina-supported noble metal catalysts: in-situ DRIFTS and SSITKA-mass spectrometry studies. Catal Today 2007;127: 304–18.
[55] Grenoble DC, Estadt MM, Ollis DF. The chemistry and catalysis of the water gas shift next term reaction: 1. The kinetics over supported metal catalysts. J Catal 1981;67:90.
[56] Boisen A, Janseens TVW, Schumacher N, Chorkendorff I, Dahl S. Support effects and catalytic trends for water gas shift activity. J Mol Catal A: Chem 2010;315:163–70.
[57] Hilaire S, Wang X, Luo T, Gorte RJ, Wagner J. A comparative study of water-gas-shift reaction over ceria-supported metallic catalysts. Appl Catal A: Gen 2004;258:271.
[58] Azzam KG, Babich IV, Seshan K, Lefferts L. A bifunctional catalyst for the single-stage water-gas shift reaction in fuel cell applications. Part 2. Roles of the support and promoter on catalyst activity and stability. J Catal 2007;251 (1):163–71.
[59] Sato Y, Terada K, Hasegawa S, Miyao T, Naito S. Mechanistic study of water-gas-shift reaction over TiO_2 supported Pt-Re and Pd-Re catalysts. Appl Catal A: Gen 2005;296(1):80–9.
[60] Ruettinger W, Liu XS, Xu XM, Farrauto RJ. Effect of Mo and Re promoters on the activity and stability of a Pt/ZrO_2 water-gas shift catalyst (Part 1). Top Catal 2008;51(1–4):60–7.
[61] Xia G, Holladay JD, Dagle RA, Jones EO, Wang Y. Development of highly active Pd-ZnO/Al_2O_3 catalysts for microscale fuel processor applications. Chem Eng Tech 2005;28(4):515–9.
[62] Takezawa N, Iwasa N. Steam reforming and dehydrogenation of methanol: difference in the catalytic functions of copper and group VIII metals. Catal Today 1997;36:45.

[63] Iwasa N, Takezawa N. New supported Pd and Pt alloy catalysts for steam reforming and dehydrogenation of methanol. Top Catal 2003;22(3–4):215.
[64] Iwasa N, Kudo S, Takahashi H, Masuda S, Takezawa N. Highly selective supported pd catalysts for steam reforming of methanol. Catal Lett 1993;19:211–6.
[65] Karim A, Conant T, Datye A. The role of PdZn alloy formation and particle size on the selectivity for steam reforming of methanol. J Catal 2006;243:420.
[66] Dagle RA, Chin Y-H, Wang Y. The effects of PdZn crystallite size on methanol steam reforming. Top Catal 2007;46:358–62.
[67] Chin Y-H, Dagle R, Hu J, Dohnalkova AC, Wang Y. Steam reforming of methanol over highly active Pd/ZnO catalyst. Catal Today 2002;77(1–2):79–88.
[68] Chin YH, Wang Y, Dagle RA, Li XS. Methanol steam reforming over Pd/ZnO catalyst preparation and pretreatment studies. Fuel Proc Tech 2003;83:193–201.
[69] Iwasa N, Masuda S, Ogawa N, Takezawa N. Steam reforming of methanol over Pd/ZnO: effect of PdZn alloys upon the reaction. Appl Catal A: Gen 1995;125:145–57.
[70] Iwasa N, Mayanagi T, Wataru N, Arai M, Takewasa T. Effect of Zn addition to supported Pd catalysts in the steam reforming of methanol. Appl Catal A: Gen 2003;248:153–60.
[71] Dagle RA, Platon A, Palo DR, Datye AK, Vohs JM, Wang Y. PdZnAl catalysts for the reactions of water-gas-shift, methanol steam reforming, and reverse-water-gas-shift. Appl Catal A: Gen 2008;342(1–2):63–8.
[72] Tsai A, Kameoka S, Ishii Y. PdZn=Cu: can an intermetallic compound replace an element? J Phy Soc Jpn 2004;73(12):3270–3.
[73] Haruta M, Tsubora S, Kobayashi T, Kageyama H, Genet MJ, Delmon B. Low temperature oxidation of hydrogen and of carbon monoxide. J Catal 1993;144:175–92.
[74] Palma V, Palo E, Ciambelli P. Structured catalytic substrates with radial configurations for the intensification of the WGS stage in H_2 production. Catal Today 2009;147S:S107–12.
[75] Robbins F, Huayang Z, Jackson G. Transient modeling of combined catalytic combustion/CH4 steam reforming. Catal Today 2003;83:141–56.
[76] Germani G, Alphonse P, Courty M, Schuurman Y, Mirodatos C. Platinum/ceria/alumina catalysts on microstructures for carbon monoxide conversion. Catal Today 2005;110:114–20.
[77] Marin P, Ordonez S, Fernando D. Performance of reverse flow monolithic reactor for water-gas shift reaction. Catal Today 2009;147S:S185–90.
[78] Francesconi J, Mussati M, Aguirre P. Analysis of design variables for water-gas-shift reactors by model-based optimization. J Power Sources 2007;173:467–77.
[79] Giroux T, Hwang S, Liu Y, Ruettinger W, Shore L. Monolithic structures as alternatives to particulate catalysts for the reforming of hydrocarbons for hydrogen generation. Appl Catal B: Env 2005;56:95–110.
[80] Kolb G, Baier T, Schurer J, Tiemann D, Ziogas A, Specchia S, et al. A micro-structured 5 kW complete fuel processor for iso-octane as hydrogen supply system for mobile auxiliary power units part II – development of water–gas shift and preferential oxidation catalysts reactors and assembly of the fuel processor. Chem Eng J 2008;138:474–89.
[81] Palo DR, Stenkamp VS, Dagle RA, Jovanovic GN. Industrial applications of microchannel process technology in the United States. In: Kockman N, editor. Advanced micro and nanosystems: micro process engineering. Weinheim: Wiley-VCH; 2006. p. 387–414.
[82] Wang Y, Holladay J. Preface. In: Wang Y, Holladay J, editors. Microreactor technology and process intensification. Washington, DC: American Chemical Society; 2005. p. xi–xii.
[83] Palo DR, Stenkamp VS, Dagle RA, Holladay JD, Brooks KP, Humble PH. Non-reactor micro-component development. In: Koch M, VandenBussche K, Chrisman R, editors. Micro-instrumentation for high throughput experimentation and process intensification, a tool for PAT. Weinheim: Wiley-VCH; 2007. p. 131–80.
[84] Kolb G, Pennemann H, Zapf R. Water-gas shift reaction in micro-channels – results from catalyst screening and optimization. Catal Today 2005;110:121–31.
[85] Goerke O, Pfeifer P, Schubert K. Water gas shift reaction and selective oxidation of CO in microstructures. Appl Catal A: Gen 2004;263:11–8.
[86] Brooks KP, Davis JM, Fischer CM, King DL, Pederson LR, Rawling GC, et al. Fuel reformation: microchannel reactor design. In: Wang Y, Holladay JD, editors. Microchannel technology process and intensification. Washington, D.C.: American Chemical Society; 2005. p. 246–51.
[87] Lemons RA. Fuel-cells for transportation. J Power Sources 1990;29(1–2):251–64.
[88] Igarashi H, Fujino T, Watanabe M. Hydrogen electrooxidation on platinum catalysts in the presence of trace carbon-monoxide. J Electroanalytical Chem 1995;391(1–2):119–23.

[89] Oetjen HF, Schmidt VM, Stimming U, Trila F. Performance data of a proton exchange membrane fuel cell using H_2/CO as fuel gas. J Electrochem Soc 1996;143(12):3838–42.

[90] Marschner F, Moeller FW. Methanol synthesis. In: Leach EL, editor. Applied industrial catalysis, vol. 2. New York: Academic Press; 1983. p. 215.

[91] Amphlett JC, Baumert RM, Mann RF, Peppley BA, Roberge PR, Rodrigues A. The effect of carbon-monoxide on PEM fuel-cells. Abstr Pap Am Chem Soc, Division of Fuel Chemistry 1993;206:95.

[92] Bion N, Epron F, Moreno M, Marino F, Duprez D. Preferential oxidation of carbon monoxide in the presence of hydrogen (PROX) over noble metals and transition metal oxides: advantages and drawbacks. Top Catal 2008;51(1–4):76–88.

[93] Brown M, Green A. Treatment of gases, U.S. Patent 3088919; 1963.

[94] Cohn JG. Process for selectively removing carbon monoxide from hydrogen-containing gases, U.S. Patent 3216782; 1965.

[95] Brown ML, Green AW, Cohn G, Andersen HC. Purifying hydrogen by selective oxidation of carbon monoxide. Ind Eng Chem 1960;52(10):841–4.

[96] Korotkikh O, Farrauto R. Selective catalytic oxidation of CO in H_2: fuel cell applications. Catal Today 2000;62(2–3):249–54.

[97] Cohn JG. Process for selectively removing carbon monoxide from hydrogen-containing gases, U.S. Patent 3216783; 1965.

[98] Kahlich MJ, Gasteiger HA, Behm RJ. Kinetics of the selective CO oxidation in H_2-rich gas on Pt/Al_2O_3. J Catal 1997;171(1):93–105.

[99] Manasilp A, Gulari E. Selective CO oxidation over Pt/alumina catalysts for fuel cell applications. Appl Catal B: Env 2002;37(1):17–25.

[100] Igarashi H, Uchida H, Suzuki M, Sasaki Y, Watanabe M. Removal of carbon monoxide from hydrogen-rich fuels by selective oxidation over platinum catalyst supported on zeolite. Appl Catal A: Gen 1997;159(1–2):159–69.

[101] Rosso L, Galletti C, Saracco G, Garrone E, Specchia V. Development of A zeolites-supported noble-metal catalysts for CO preferential oxidation: H_2 gas purification for fuel cell. Appl Catal B: Env 2004;48 (3):195–203.

[102] Fukuoka A, Kimura JI, Oshio T, Sakamoto Y, Ichikawa M. Preferential oxidation of carbon monoxide catalyzed by platinum nanoparticles in mesoporous silica. J Am Chem Soc 2007;129(33):10120–5.

[103] Farrauto RJ, Bartholomew CH. In: Fundamentals of industrial catalytic processes, vol. Chapter 1. Blackie Academic and Professional; 1997. p. 38–39.

[104] Liu XS, Korotkikh O, Farrauto R. Selective catalytic oxidation of CO in H_2: structural study of Fe oxide-promoted Pt/alumina catalyst. Appl Catal A: Gen 2002;226(1–2):293–303.

[105] Cho SH, Park JS, Choi SH, Kim SH. Effect of magnesium on preferential oxidation of carbon monoxide on platinum catalyst in hydrogen-rich stream. J Power Sources 2006;156(2):260–6.

[106] Kwak C, Park TJ, Suh DJ. Effects of sodium addition on the performance of $PtCo/Al_2O_3$ catalysts for preferential oxidation of carbon monoxide from hydrogen-rich fuels. Appl Catal A: Gen 2005;278 (2):181–6.

[107] Minemura Y, Ito S, Miyao T, Naito S, Tomishige K, Kunimori K. Preferential CO oxidation promoted by the presence of H_2 over K-Pt/Al_2O_3. Chem Comm 2005;11:1429–31.

[108] Pedrero C, Waku T, Iglesia E. Oxidation of CO in H_2-CO mixtures catalyzed by platinum: alkali effects on rates and selectivity. J Catal 2005;233(1):242–55.

[109] Minemura Y, Kuriyama M, Ito S, Tomishige K, Kunimori K. Additive effect of alkali metal ions on preferential CO oxidation over Pt/Al_2O_3. Catal Comm 2006;7(9):623–6.

[110] Kuriyama M, Tanaka H, Ito S, Kubota T, Miyao T, Naito S, et al. Promoting mechanism of potassium in preferential CO oxidation on Pt/Al_2O_3. J Catal 2007;252(1):39–48.

[111] Son IH, Lane AM. Promotion of Pt/γ-Al_2O_3 by Ce for preferential oxidation of CO in H_2. Catal Lett 2001;76(3–4):151–4.

[112] Son IH. Study of Ce-Pt/γ-Al_2O_3 for the selective oxidation of CO in H_2 for application to PEFCs: effect of gases. J Power Sources 2006;159(2):1266–73.

[113] Simsek E, Ozkara S, Aksoylu AE, Onsan ZI. Preferential CO oxidation over activated carbon supported catalysts in H-2-rich gas streams containing CO_2 and H_2O. Appl Catal A: Gen 2007;316(2): 169–74.

[114] Choi J, Shin CB, Suh DJ. Co-promoted Pt catalysts supported on silica aerogel for preferential oxidation of CO. Catal Comm 2008;9(5):880–5.

[115] Kwak C, Park TJ, Suh DJ. Preferential oxidation of carbon monoxide in hydrogen-rich gas over platinum-cobalt-alumina aerogel catalysts. Chem Eng Sci 2005;60(5):1211–7.

[116] Ko EY, Park ED, Lee HC, Lee D, Kim S. Supported Pt-Co catalysts for selective CO oxidation in a hydrogen-rich stream. Angew Chem Int Ed 2007;46 (5):734–7.

[117] Uysal G, Akin AN, Onsan ZI, Yildirim R. Hydrogen clean-up by preferential CO oxidation over Pt-Co-Ce/MgO. Catal Lett 2006;108(3–4):193–6.

[118] Epling WS, Cheekatamarla PK, Lane AM. Reaction and surface characterization studies of titania-supported Co, Pt and Co/Pt catalysts for the selective oxidation of CO in H_2-containing streams. Chem Eng J 2003;93(1):61–8.

[119] Watanabe M, Uchida H, Ohkubo K, Igarashi H. Hydrogen purification for fuel cells: selective oxidation of carbon monoxide on Pt-Fe/zeolite catalysts. Appl Catal B: Env 2003;46(3):595–600.

[120] Sirijaruphan A, Goodman JG, Rice RW. Effect of Fe promotion on the surface reaction parameters of Pt/γ-Al_2O_3 for the selective oxidation of CO. J Catal 2004;224(2):304–13.

[121] Kotobuki M, Watanabe A, Uchida H, Yamashita H, Watanabe M. Reaction mechanism of preferential oxidation of carbon monoxide on Pt, Fe, and Pt-Fe/mordenite catalysts. J Catal 2005;236(2):262–9.

[122] Kotobuki M, Shido T, Tada M, Uchida H, Yamashita H, Iwasawa Y, et al. XAFS characterization of Pt-Fe/zeolite catalysts for preferential oxidation of CO in hydrogen fuel gases. Catal Lett 2005;103(3–4):263–9.

[123] Tanaka K, Moro-oka Y, Ishigure K, Yajima T, Okabe Y, Kato Y, et al. A new catalyst for selective oxidation of CO in H_2: part 1, activation by depositing a large amount of FeO_x on Pt/Al_2O_3 and Pt/CeO_2 catalysts. Catal Lett 2004;92(3–4):115–21.

[124] Shou M, Tanaka KI, Yoshioka K, Moro-Oka Y, Nagano S. New catalyst for selective oxidation of CO in excess H_2 designing of the active catalyst having different optimum temperature. Catal Today 2004;90(3–4):255–61.

[125] Shou M, Tanaka K. Isotope effect of H_2/D_2 and H_2O/D_2O for the PROX reaction of CO on the FeOx/Pt/TiO_2 catalyst. Catal Lett 2006;111(3–4):115–8.

[126] Siani A, Captain B, Alexeev OS, Stafyla E, Hungria AB, Midgley PA, et al. Improved CO oxidation activity in the presence and absence of hydrogen over cluster-derived PtFe/SiO_2 catalysts. Langmuir 2006;22(11):5160–7.

[127] Kotobuki M, Watanabe A, Uchida H, Yamashita H, Watanabe M. High catalytic performance of Pt-Fe alloy nanoparticles supported in mordenite pores for preferential CO oxidation in H-2-rich gas. Appl Catal A: Gen 2006;307(2):275–83.

[128] Shi XY, Tanaka K, He H, Shou MSXu WQ, Zhang XL. The mechanism for the selective oxidation of CO enhanced by H_2O on a novel PROC catalyst. Catal Lett 2008;120(3–4):210–4.

[129] Ayastuy JL, Gonzalez-Marcos MP, Gonzalez-Velasco JR, Gutierrez-Ortiz MA. MnO_x/Pt/Al_2O_3 catalysts for CO oxidation in H_2-rich streams. Appl Catal B: Env 2007;70:532–41.

[130] Suh DJ, Kwak C, Kim JH, Kwon SM, Park TJ. Removal of carbon monoxide from hydrogen-rich fuels by selective low-temperature oxidation over base metal added platinum catalysts. J Power Sources 2005;142(1–2):70–4.

[131] Ko EY, Park ED, Seo KW, Lee HC, Lee D, Kim S. Pt-Ni/γ-Al_2O_3 catalyst for the preferential CO oxidation in the hydrogen stream. Catal Lett 2006;110(3–4):275–9.

[132] Guerrero S, Miller J, Wolf EE. Activity and selectivity control by niobium for the preferential oxidation of co on pt supported catalysts. Appl Catal A: Gen 2007;328(1):27–34.

[133] Marino F, Descorme C, Duprez D. Noble metal catalysts for the preferential oxidation of carbon monoxide in the presence of hydrogen (PROX). Appl Catal B: Env 2004;54(1):59–66.

[134] Tibiletti D, de Graaf EAB, Teh SP, Rothenberg G, Farrusseng D, Mirodatos C. Selective CO oxidation in the presence of hydrogen: fast parallel screening and mechanistic studies on ceria-based catalysts. J Catal 2004;225(2):489–97.

[135] Roh HS, Potdar HS, Jun KW, Han SY, Kim JW. Low temperature selective CO oxidation in excess of H-2 over Pt/Ce-ZrO_2 catalysts. Catal Lett 2004;93(3–4):203–7.

[136] Wootsch A, Descorme C, Duprez D. Preferential oxidation of carbon monoxide in the presence of hydrogen (PROX) over ceria-zirconia and alumina-supported Pt catalysts. J Catal 2004;225(2):259–66.

[137] Oh SH, Sinkevitch RM. Carbon-monoxide removal from hydrogen-rich fuel-cell feedstreams by selective catalytic-oxidation. J Catal 1993;142(1):254–62.

[138] Chin SY, Alexeev OS, Amiridis MD. Preferential oxidation of CO under excess H_2 conditions over Ru catalysts. Appl Catal A: Gen 2005;286(2):157–66.

[139] Echigo M, Shinke N, Takami S, Higashiguchi S, Hirai K, Tabata T. Development of residential PEFC cogeneration systems: Ru catalyst for CO preferential oxidation in reformed gas. Catal Today 2003;84(3–4):209–15.

[140] Han YF, Kahlich MJ, Kinne M, Behm RJ. CO removal from realistic methanol reformate via preferential oxidation – performance of a Rh/MgO catalyst and comparison to Ru/γ-Al_2O_3, and Pt/γ-Al_2O_3. Appl Catal B: Env 2004;50(4):209–18.

[141] Galletti C, Fiorot S, Specchia S, Saracco G, Specchia V. Activity of rhodium-based catalysts for CO preferential oxidation in H_2-rich gases. Topics Catal 2007;45(1–4):15–9.

[142] Worner A, Friedrich C, Tamme R. Development of a novel Ru-based catalyst system for the selective

oxidation of CO in hydrogen rich gas mixtures. Appl Catal A: Gen 2003;245(1):1–14.
[143] Jhalani A, Schmidt LD. Preferential CO oxidation in the presence of H_2, H_2O and CO_2 at short contact-times. Catal Lett 2005;104(3–4):103–10.
[144] Bond GC, Thompson DT. Gold-catalysed oxidation of carbon monoxide. Gold Bull 2000;33(2):41–51.
[145] Haruta M, Tsubota S, Kobayashi T, Kageyama H, Genet MJ, Delmon B. Low-temperature oxidation of CO over gold supported on TiO_2, α-Fe_2O_3, and Co_3O_4. J Catal 1993;144(1):175–92.
[146] Haruta M. Size- and support-dependency in the catalysis of gold. Catal Today 1997;36(1):153–66.
[147] Bollinger MA, Vannice MA. A kinetic and DRIFTS study of low-temperature carbon monoxide oxidation over Au-TiO_2 catalysts. Appl Catal B: Env 1996;8 (4):417–43.
[148] Costello CK, Yang JH, Law HY, Wang Y, Lin JN, Marks LD, et al. On the potential role of hydroxyl groups in CO oxidation over Au/Al_2O_3. Appl Catal A: Gen 2003;243(1):15–24.
[149] Moreau F, Bond GC, Taylor AO. Gold on titania catalysts for the oxidation of carbon monoxide: control of pH during preparation with various gold contents. J Catal 2005;231(1):105–14.
[150] Hodge NA, Kiely CJ, Whyman R, Siddiqui MRH, Hutchings GJ, Pankhurst QA, et al. Microstructural comparison of calcined and uncalcined gold/iron-oxide catalysts for low-temperature CO oxidation. Catal Today 2002;72(1–2):133–44.
[151] Finch RM, Hodge NA, Hutchings GJ, Meagher A, Pankhurst QA, Siddiqui MRH, et al. Identification of active phases in Au-Fe catalysts for low-temperature CO oxidation. Phy Chem Chem Phy 1999;1(3):485–9.
[152] Ivanova S, Petit C, Pitchon V. A new preparation method for the formation of gold nanoparticles on an oxide support. Appl Catal A: Gen 2004;267(1–2): 191–201.
[153] Ivanova S, Pitchon V, Petit C, Herschbach H, Van Dorsselaer A, Leize E. Preparation of alumina supported gold catalysts: gold complexes genesis, identification and speciation by mass spectrometry. Appl Catal A: Gen 2006;298:203–10.
[154] Oh HS, Yang JH, Costello CK, Wang YM, Bare SR, Kung HH, et al. Selective catalytic oxidation of CO: effect of chloride on supported Au catalysts. J Catal 2002;210(2):375–86.
[155] Kobayashi T, Haruta M, Tsubota S, Sano H, Delmon B. Thin-films of supported gold catalysts for co detection. Sens Actuators B: Chem 1990;1(1–6): 222–5.
[156] Okumura M, Tanaka K, Ueda A, Haruta M. The reactivities of dimethylgold(III)beta-diketone on the surface of TiO_2 – a novel preparation method for Au catalysts. Solid State Ionics 1997;95(1–2):143–9.
[157] Raphulu M, McPherson J, Pattrick G, Ntho T, Mokoena L, Moma J, et al. CO oxidation: deactivation of Au/TiO_2 catalysts during storage. Gold Bull 2009;42(4):9.
[158] Daniells ST, Makkee M, Moulijn JA. The effect of high-temperature pre-treatment and water on the low temperature CO oxidation with Au/Fe_2O_3 catalysts. Catal Lett 2005;100(1–2):39–47.
[159] Date M, Okumura M, Tsubota S, Haruta M. Vital role of moisture in the catalytic activity of supported gold nanoparticles. Angew Chem Int Ed 2004;43(16): 2129–32.
[160] Navarro RM, Pena MA, Fierro JLG. Hydrogen production reactions from carbon feedstocks: fossils fuels and biomass. Chem Rev 2007;107(10): 3952–91.
[161] Kahlich MJ, Gasteiger HA, Behm RJ. Kinetics of the selective low-temperature oxidation of CO in H_2-rich gas over Au/α-Fe_2O_3. J Catal 1999;182 (2):430–40.
[162] Tornpos A, Hegedus M, Margitfalvi JL, Szabo EG, Vegvari L. Multicomponent Au/MgO catalysts designed for selective oxidation of carbon monoxide – application of a combinatorial approach. Appl Catal A: Gen 2008;334(1–2):348–56.
[163] Bond G, Thompson D. Formulation of mechanisms for gold-catalysed reactions. Gold Bull 2009;42(4): 247–59.
[164] Calla JT, Davis RJ. Influence of dihydrogen and water vapor on the kinetics of CO oxidation over Au/Al_2O_3. Ind Eng Chem Res 2005;44(14):5403–10.
[165] Quinet E, Morfin F, Diehl F, Avenier P, Caps V, Rousset JL. Hydrogen effect on the preferential oxidation of carbon monoxide over alumina-supported gold nanoparticles. Appl Catal B: Env 2008;80 (3–4):195–201.
[166] Piccolo L, Daly H, Valcarcel A, Meunier FC. Promotional effect of H_2 on CO oxidation over Au/TiO_2 studied by operando infrared spectroscopy. Appl Catal B: Env 2009;86(3–4):190–5.
[167] Oh HS, Costello CK, Cheng C, Kung HH, Kung MC. Regeneration of Au/γ-Al_2O_3 deactivated by CO oxidation. Stud Surf Sci Catal 2001;139:375–81.
[168] Debeila MA, Wells RPK, Anderson JA. Influence of water and pretreatment conditions on CO oxidation over Au/TiO_2-In_2O_3 catalysts. J Catal 2006;239(1): 162–72.
[169] Avgouropoulos G, Ioannides T, Matralis HK, Batista J, Hocevar S. CuO-CeO_2 mixed oxide catalysts for the selective oxidation of carbon monoxide in excess hydrogen. Catal Lett 2001;73(1):33–40.

[170] Liu W, Flytzani-Stephanopoulos M. Total oxidation of carbon-monoxide and methane over transition metal-fluorite oxide composite catalysts. 1. Catalyst composition and activity. J Catal 1995;153(2):304–16.

[171] Martinez-Arias A, Fernandez-Garcia M, Soria J, Conesa JC. Spectroscopic study of a Cu/CeO_2 catalyst subjected to redox treatments in carbon monoxide and oxygen. J Catal 1999;182(2):367–77.

[172] Martinez-Arias A, Fernandez-Garcia M, Galvez O, Coronado JM, Anderson JA, Conesa JC, et al. Comparative study on redox properties and catalytic behavior for CO oxidation of CuO/CeO_2 and $CuO/ZrCeO_4$ catalysts. J Catal 2000;195(1):207–16.

[173] Liu W, Flytzani-Stephanopoulos M. Total oxidation of carbon-monoxide and methane over transition metal-fluorite oxide composite catalysts. 2. Catalyst characterization and reaction-kinetics. J Catal 1995;153(2):317–32.

[174] Luo MF, Zhong YJ, Yuan XX, Zheng XM. TPR and TPD studies of CuO/CeO_2 catalysts for low temperature CO oxidation. Appl Catal A: Gen 1997;162(1–2):121–31.

[175] Avgouropoulos G, Ioannides T, Matralis H. Influence of the preparation method on the performance of $CuO\text{-}CeO_2$ catalysts for the selective oxidation of CO. Appl Catal B: Env 2005;56(1–2):87–93.

[176] Avgouropoulos G, Ioannides T. Effect of synthesis parameters on catalytic properties of $CuO\text{-}CeO_2$. Appl Catal B: Env 2006;67(1–2):1–11.

[177] Avgouropoulos G, Papavasiliou J, Tabakova T, Idakiev V, Ioannides T. A comparative study of ceria-supported gold and copper oxide catalysts for preferential CO oxidation reaction. Chem Eng J 2006;124 (1–3):41–5.

[178] Marino F, Descorme C, Duprez D. Supported base metal catalysts for the preferential oxidation of carbon monoxide in the presence of excess hydrogen (PROX). Appl Catal B: Env 2005;58(3–4):175–83.

[179] Giordano F, Trovarelli A, de Leitenburg C, Giona M. A model for the temperature-programmed reduction of low and high surface area ceria. J Catal 2000;193 (2):273–82.

[180] Kim DH, Cha JE. A $CuO\text{-}CeO_2$ mixed-oxide catalyst for CO clean-up by selective oxidation in hydrogen-rich mixtures. Catal Lett 2003;86(1–3):107–12.

[181] Sedmak G, Hocevar S, Levec J. Kinetics of selective CO oxidation in excess of H_2 over the nanostructured $Cu_{0.1}Ce_{0.9}O_{2\text{-}(y)}$ catalyst. J Catal 2003;213 (2):135–50.

[182] Martinez-Arias A, Hungria AB, Munuera G, Gamarra D. Preferential oxidation of CO in rich H_2 over CuO/CeO_2: details of selectivity and deactivation under the reactant stream. Appl Catal B: Env 2006;65(3–4):207–16.

[183] Wang JB, Lin SC, Huang TJ. Selective CO oxidation in rich hydrogen over CuO/samaria-doped ceria. Appl Catal A: Gen 2002;232(1–2):107–20.

[184] Zhou GL, Jiang Y, Xie HM, Qiu FL. Non-noble metal catalyst for carbon monoxide selective oxidation in excess hydrogen. Chem Eng J 2005;109(1–3):141–5.

[185] Teng Y, Sakurai H, Ueda A, Kobayashi T. Oxidative removal of CO contained in hydrogen by using metal oxide catalysts. Int J Hydrogen Energy 1999;24 (4):355–8.

[186] Omata K, Kobayashi Y, Yamada M. Artificial neural network aided virtual screening of additives to a $Co/SrCO_3$ catalyst for preferential oxidation of CO in excess hydrogen. Catal Comm 2007;8(1):1–5.

[187] Omata K, Kobayashi Y, Yamada M. Artificial neural network-aided design of $Co/SrCO_3$ catalyst for preferential oxidation of CO in excess hydrogen. Catal Today 2006;117(1–3):311–5.

[188] Yung MM, Zhao ZK, Woods MP, Ozkan US. Preferential oxidation of carbon monoxide on CoO_x/ZrO_2. J Mol Catal A: Chem 2008;279(1):1–9.

[189] Zhao ZK, Yung MM, Ozkan US. Effect of support on the preferential oxidation of CO over cobalt catalysts. Catal Comm 2008;9(6):1465–71.

[190] Park JW, Jeong JH, Yoon WL, Jung H, Lee HT, Lee DK, et al. Activity and characterization of the Co-promoted $CuO\text{-}CeO_2/\gamma\text{-}Al_2O_3$ catalyst for the selective oxidation of CO in excess hydrogen. Appl Catal A: Gen 2004;274(1–2):25–32.

[191] Ko EY, Park ED, Seo KW, Lee HC, Lee D, Kim S. A comparative study of catalysts for the preferential CO oxidation in excess hydrogen. Catal Today 2006;116(3):377–83.

[192] Kim YH, Park ED, Lee HC, Lee KH, Kim S. Selective CO removal in the H_2-rich stream through a double-bed system composed of non-noble metal catalysts. Stud Surf Sci Catal 2007;167:171–6.

[193] Rogers TH, Piggot CS, Bahlke WH, Jennings JM. The catalytic oxidation of carbon monoxide. J Am Chem Soc 1921;43:1973–82.

[194] Jones HA, Taylor HS. The reduction of copper oxide by carbon monoxide and the catalytic oxidation of carbon monoxide in presence of copper and of copper oxide. J Phy Chem 1923;27(7):623–51.

[195] Puckhaber LS, Cheung HS, Cocke DL, Clearfield A. Reactivity of copper manganese oxides. Solid State Ionics 1989;32–3:206–13.

[196] Hasegawa Y, Fukumoto K, Ishima T, Yamamoto H, Sano M, Miyake T. Preparation of copper-containing mesoporous manganese oxides and their catalytic

performance for CO oxidation. Appl Catal B: Env 2009;89(3–4):420–4.

[197] Jones C, Cole KJ, Taylor SH, Crudace MJ, Hutchings GJ. Copper manganese oxide catalysts for ambient temperature carbon monoxide oxidation: effect of calcination on activity. J Mol Catal A: Chem 2009;305(1–2):121–4.

[198] Taylor SH, Hutchings GJ, Mirzaei AA. Copper zinc oxide catalysts for ambient temperature carbon monoxide oxidation. Chem Comm 1999;15:1373–4.

[199] Hutchings GJ, Mirzaei AA, Joyner RW, Siddiqui MRH, Taylor SH. Effect of preparation conditions on the catalytic performance of copper manganese oxide catalysts for CO oxidation. Appl Catal A: Gen 1998;166(1):143–52.

[200] Veprek S, Cocke DL, Kehl S, Oswald HR. Mechanism of the deactivation of hopcalite catalysts studied by Xps, Iss, and other techniques. J Catal 1986;100 (1):250–63.

[201] Hasegawa YI, Maki RU, Sano M, Miyake T. Preferential oxidation of CO on copper-containing manganese oxides. Appl Catal A: Gen 2009;371 (1–2):67–72.

[202] Qi AD, Peppley B, Karan K. Integrated fuel processors for fuel cell application: a review. Fuel Proc Tech 2007;88(1):3–22.

[203] Luengnaruemitchai A, Osuwan S, Gulari E. Selective catalytic oxidation of CO in the presence of H_2 over gold catalyst. Int J Hydrogen Energy 2004;29 (4):429–35.

[204] Park JW, Jeong JH, Yoon WL, Rhee YW. Selective oxidation of carbon monoxide in hydrogen-rich stream over Cu-Ce/γ-Al_2O_3 catalysts promoted with cobalt in a fuel processor for proton exchange membrane fuel cells. J Power Sources 2004;132(1–2):18–28.

[205] Brundage MA, Pettit WH, Borup RL. Reactor for preferential oxidation and method of use, U.S. Patent 6824904; 2004.

[206] Brooks KP, Davis JM, Fischer CM, King DL, Pederson LR, Rawlings GC, et al. Fuel reformation: microchannel reactor design. Microreactor Technol Process Intensification 2005;914:238–57.

[207] Castaldi MJ, LaPierre R, Lyubovski M, Pfefferle W, Roychoudhury S. Effect of water on performance and sizing of fuel-processing reactors. Catal Today 2005;99(3–4):339–46.

[208] Xu GW, Chen X, Zhang ZG. Temperature-staged methanation: an alternative method to purify hydrogen-rich fuel gas for PEFC. Chem Eng J 2006;121(2–3):97–107.

[209] Dagle RA, Wang Y, Xia GG, Strohm JJ, Holladay J, Palo DR. Selective CO methanation catalysts for fuel processing applications. Appl Catal A: Gen 2007;326 (2):213–8.

[210] Divisek J, Oetjen HF, Peinecke V, Schmidt VM, Stimming U. Components for PEM fuel cell systems using hydrogen and CO containing fuels. Electrochimica Acta 1998;43(24):3811–5.

[211] Vannice MA. Catalytic synthesis of hydrocarbons from H_2-CO mixtures over group-8 metals. 1. Specific activities and product distributions of supported metals. J Catal 1975;37(3):449–61.

[212] Baker BS, Huebler J, Linden HR, Meek J. Process for selective removal by methanation of carbon monoxide from a mixture of gases containing carbon dioxide, U.S. Patent 3615164; 1971.

[213] Rehmat A, Randhava SS. Selective methanation of carbon monoxide. Ind Eng Chem Prod Res Dev 1970;9(4):512.

[214] Kowalczyk Z, Stolecki K, Rarog-Pilecka W, Miskiewicz E, Wilczkowska E, Karpiniski Z. Supported ruthenium catalysts for selective methanation of carbon oxides at very low CO_x/H_2 ratios. Appl Catal A: Gen 2008;342(1–2):35–9.

[215] Panagiotopoulou P, Kondarides DI, Verykios XE. Selective methanation of CO over supported Ru catalysts. Appl Catal B: Env 2009;88(3–4):470–8.

[216] Li ZY, Mi WL, Gong J, Lu ZL, Xu LH, Su QQ. CO removal by two-stage methanation for polymer electrolyte fuel cell. J Natural Gas Chem 2008;17 (4):359–64.

[217] Galletti C, Specchia S, Saracco G, Specchia V. CO-selective methanationover Ru– γ-Al_2O_3 catalysts inH_2-rich gas for PEM FC applications. Chem Eng Sci 2010;65:590–6.

[218] Takenaka S, Shimizu T, Otsuka K. Complete removal of carbon monoxide in hydrogen-rich gas stream through methanation over supported metal catalysts. Int J Hydrogen Energy 2004;29(10):1065–73.

[219] Gorke O, Pfeifer P, Schubert K. Highly selective methanation by the use of a microchannel reactor. Catal Today 2005;110(1–2):132–9.

[220] Kim YH, Park ED, Lee HC, Lee D. Selective CO removal in a H_2-rich stream over supported Ru catalysts for the polymer electrolyte membrane fuel cell (PEMFC). Appl Catal A: Gen 2009;366(2):363–9.

[221] Mori N, Nakamura T, Sakai O, Iwamoto Y, Hattori T. CO-free hydrogen production by membrane reactor equipped with CO methanator. Ind Eng Chem Res 2008;47(5):1421–6.

[222] Galletti C, Specchia S, Saracco G, Specchia V. CO methanation as alternative refinement process for CO abatement in H_2-rich gas for PEM applications. Int J Chem Reactor Eng 2008;5. Article number A110.

[223] Eckle S, Denkwitz Y, Behm RJ. Activity, selectivity, and adsorbed reaction intermediates/reaction side products in the selective methanation of CO in reformate gases on supported Ru catalysts. J Catal 2010;269:255–68.

[224] Panagiotopoulou P, Kondarides DI, Verykios XE. Selective methanation of CO over supported noble metal catalysts: effects of the nature of the metallic phase on catalytic performance. Appl Catal A: Gen 2008;344(1–2):45–54.

[225] Men Y, Kolb G, Zapf R, Hessel V, Lowe H. Selective methanation of carbon oxides in a microchannel reactor – primary screening and impact of gas additives. Catal Today 2007;125(1–2):81–7.

[226] Zhan ZG, Xu GW. Thermally differential methanation – a novel method to realize highly selective removal of CO from H_2-rich reformates. Catal Comm 2007;8:1953–6.

[227] Herwijnen TV, Doesburg HV, Dejong WA. Kinetics of methanation of CO and CO_2 on a nickel-catalyst. J Catal 1973;28(3):391–402.

[228] Liu QH, Dong XF, Mo XM, Lin WM. Selective catalytic methanation of CO in hydrogen-rich gases over Ni/ZrO_2 catalyst. J Natural Gas Chem 2008;17 (3):268–72.

[229] Men Y, Kolb G, Zapf R, O'Connell M, Hessell V. Selective methanation of carbon monoxide in hydrogen-rich reformate using microstructured reactor. Chem Lett 2009;38(8):824–5.

[230] Andersson MP, Bligaard T, Kustov A, Larsen KE, Greeley J, Johannessen T, et al. Toward computational screening in heterogeneous catalysis: pareto-optimal methanation catalysts. J Catal 2006;239 (2):501–6.

[231] Kramer M, Duisberg M, Stowe K, Maier WF. Highly selective CO methanation catalysts for the purification of hydrogen-rich gas mixtures. J Catal 2007;251: 410–22.

[232] Kramer M, Stowe K, Duisberg M, Muller F, Reiser M, Sticher S, et al. The impact of dopants on the activity and selectivity of a Ni-based methanation catalyst. Appl Catal A: Gen 2009;369(1–2):42–52.

[233] Yokoyama A, Komiyama H, Inoue H, Masumoto T, Kimura HM. The hydrogenation of carbon-monoxide by amorphous ribbons. J Catal 1981;68(2): 355–61.

[234] Habazaki H, Yamasaki M, Zhang BP, Kawashima A, Kohno S, Takai T, et al. Co-methanation of carbon monoxide and carbon dioxide on supported nickel and cobalt catalysts prepared from amorphous alloys. Appl Catal A: Gen 1998; 172(1):131–40.

[235] Liu QH, Dong XF, Song YB, Lin WM. Removal of CO from reformed fuels by selective methanation over Ni-B-Zr-O-delta catalysts. J Natural Gas Chem 2009;18(2):173–8.

[236] Liu QH, Dong XF, Lin WM. Highly selective CO methanation over amorphous $Ni-Ru-B/ZrO_2$ catalyst. Chinese Chem Lett 2009;20(8):889–92.

[237] Vilchis-Nestor AR, Avalos-Borja M, Gomez SA, Hernandez JA, Olivas A, Zepeda TA. Alternative bio-reduction synthesis method for the preparation of $Au(AgAu)/SiO_2$-Al_2O_3 catalysts: oxidation and hydrogenation of CO. Appl Catal B: Env 2009;90 (1–2):64–73.

[238] Yaccato K, Carhart R, Hagemeyer A, Lesik A, Strasser P, Volpe AF, et al. Competitive CO and CO_2 methanation over supported noble metal catalysts in high throughput scanning mass spectrometer. Appl Catal A: Gen 2005;296(1):30–48.

[239] Li Z, Mi W, Liu S, Su Q. CO deep removal with a method of two-stage methanation. Int J Hydrogen Energy 2010;35:2820–3.

[240] Ledjeff-Hey K, Roes J, Wolters R. CO_2-scrubbing and methanation as purification system for PEFC. J Power Sources 2000;86(1–2):556–61.

CHAPTER

13

Direct Reforming Fuel Cells

John Bøgild Hansen

Haldor Topsøe, Nymøllevej 55, DK-2800 Kgs, Lyngby, Denmark

OUTLINE

Fuel Cells **DOI: 10.1016/B978-0-444-53563-4.10013-6**

13.1. INTRODUCTION

One of the major benefits of high temperature fuel cells is their ability to use other fuels than hydrogen. This simplifies system design, because a heated reformer and hydrogen clean-up is avoided, but it also increases the overall electrical efficiency. The presence of methane in the fuel cell feed enables waste heat from the fuel cell to be upgraded to chemical energy via endothermic reforming of the fuel.

The processing of the fuel can in principle be carried out in four different ways:

1. Externally in a heated or fired reformer (ER).
2. Directly in the anode chamber: direct internal reforming (DIR).
3. In a separate channel in thermal direct contact with the anode: indirect internal reforming (IIR).
4. Direct oxidation of the fuel in the anode or more correctly direct utilization (DU), meaning operation with a very small amount of steam or carbon dioxide added.

Already in early work on molten carbonate fuel cell (MCFC) [1,2], it was realized that DIR represented the most elegant and efficient way of utilizing hydrocarbons, oxygenated hydrocarbons, and fuels derived from biomass. Problems with poisoning of the reforming catalyst with alkali from electrolyte prevented early adoption of the principle. For the early solid oxide fuel cell (SOFC) applications, the high operating temperature of around 1000 °C would give rise to excessive temperature gradients if DIR was used due to the cooling effect of the reforming, so ER was the preferred fuel processing solution.

With the advent of better DIR catalysts for MCFC and intermediate temperature operation of SOFC the DIR is almost universally adopted in successful fuel cell systems. Direct utilization of fuels has been extensively studied as it an attractive principle due to system simplicity and the potentially highest electrical efficiency especially at high fuel utilization. It has, however, not been implemented so far outside the laboratory mainly due to problems with long-term stability of the anodes, remaining carbon formation problems, or low current densities.

13.1.1. Requirements for Internal Reforming Anodes

A SOFC stack operating on methane is a very interesting device both from a chemical

engineering, catalysis, and electrochemical perspective because it simultaneously performs a number of functions:

- It is obviously a fuel cell.
- Steam methane reforming is occurring within the anode chamber.
- Shift/reverse shift proceeds according to the inlet gas composition and fuel utilization.
- Planar, anode-supported cell-based stacks are very efficient plate heat exchangers.
- It is also a device separating oxygen from air.

An anode suitable for internal reforming has thus to fulfill a series of requirements simultaneously: it should obviously be very active for the electrochemical oxidation of hydrogen and it should be able to promote both the steam reforming and shift reaction. The mechanical strength should be high and the thermal expansion coefficient should match that of the electrolyte. A good resistance against carbon formation and sulfur poisoning is preferred and finally it should not be based on exotic and expensive materials and have to be amenable to industrial mass production.

13.1.2. Development Trends for SOFC Anodes

Nickel has so far been the preferred choice, most often in the form of ceramic-metal composites (cermets) where the electrolyte, typically yttria stabilized zirconia, is the other component. The trend has been toward lower operating temperatures and the progression in generations of cells [3] is shown in Fig. 13.1.

The first generation cells were electrolyte supported, with a relative thick (300 μm) electrolyte lending mechanical strength to the cells. The high area-specific resistance of the electrolyte made relatively high operating temperatures necessary. The anode consisted of only a thin functional layer but even that has such a high steam reforming activity that only small amounts of methane could be allowed in the feed in order not to generate excessive mechanical stresses due to the cooling effect of reforming.

The second generation cells use the anode (again typically Ni-YSZ (yttria-stabilized zirconia) or Ni-GDC (gadolinium-doped ceria)) as mechanical support for the structure and the

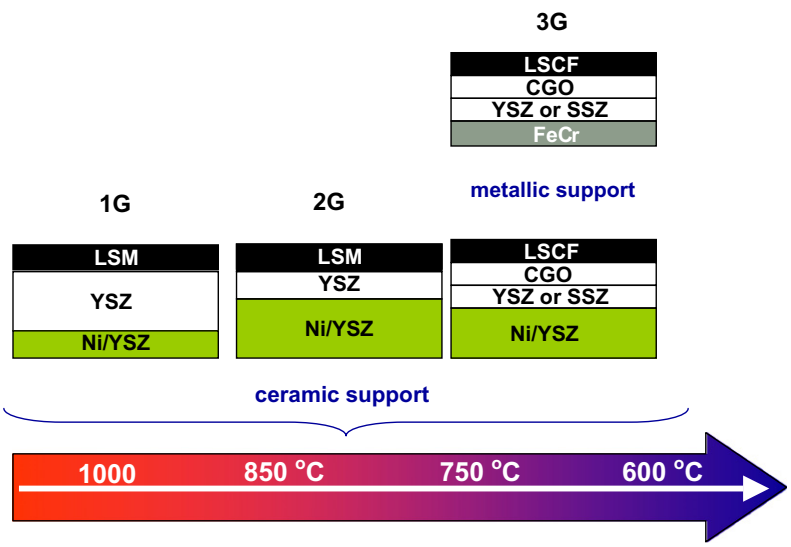

FIGURE 13.1 Development of SOFC cells.

anode normally consists of two layers: the electrochemically active anode and a support which, however, possesses catalytic activity for reforming (and shift). The temperature could be lowered to 750–800 °C making use of metallic interconnect and low-cost balance of plant components possible. More active cathodes like lanthanum strontium cobalt ferrite (LSCF) are used in generation 2.5, which are able to operate at even lower temperatures.

Recently a good deal of research has focused on developing metal-supported cells [4] as this could further reduce the costs of the cells and increase their mechanical reliability. Methods to impart these cells an optimum reforming activity still remain a challenge.

Despite the many desirable properties of nickel as an anode it has some drawbacks, namely a high propensity for carbon formation, high sensitivity toward sulfur poisoning, and is relatively easily damaged by unintended oxidation. For some cells the inherent internal reforming activity is also higher than optimum. This has led to attempts to develop alternative metals as active anode, all ceramic anodes or ingeniously modified nickel anodes.

The literature on the subject is vast and is expanding rapidly so this chapter does not intend to be comprehensive in any respect but will rather concentrate on the commercially used cells and focus on key challenges and endeavor to highlight some recent developments with respect to the catalysis and electrochemistry occurring on the anode side of the cells. The reader is referred to excellent reviews papers [5–12] for more in-depth, exhaustive treatment of the details.

13.2. THERMODYNAMICS

The most important gas phase reactions of interest for fuel processing and anode operation in an SOFC plant are:

TABLE 13.1 Equilibrium Constants (Standard State, 0.1 MPa, 298 K)

T(K)	13.1	13.2	13.3
773.15	5.00E + 00	9.94E − 03	6.99E + 13
823.15	3.53E + 00	8.15E − 02	6.81E + 12
873.15	2.61E + 00	5.29E − 01	8.64E + 11
923.15	2.00E + 00	2.82E + 00	1.37E + 11
973.15	1.58E + 00	1.27E + 01	2.61E + 10
1023.15	1.28E + 00	4.97E + 01	5.83E + 09
1073.15	1.06E + 00	1.71E + 02	1.50E + 09
1123.15	8.95E − 01	5.30E + 02	4.34E + 08
1173.15	7.69E − 01	1.49E + 03	1.39E + 08
1223.15	6.71E − 01	3.87E + 03	4.91E + 07
1273.15	5.92E − 01	9.30E + 03	1.87E + 07

$$CO + H_2O = CO_2 + H_2 \quad (13.1)$$

$$CH_4 + H_2O = CO + 3H_2 \quad (13.2)$$

$$H_2 + 0.5\,O_2 = H_2O \quad (13.3)$$

The thermodynamics have already been discussed in Chapter 4 but here the equilibrium constants for these three reactions (Eqs. 13.1–13.3) are given in Table 13.1.

13.3. BENEFITS OF INTERNAL REFORMING

13.3.1. Thermodynamic Considerations

The benefits of internal reforming can be illustrated by considering an SOFC plant as depicted in Fig. 4.9 in Chapter 4. The method employed to limit cooling requirements of the SOFC stack is to minimize the conversion of methane to hydrogen and carbon monoxide in the pre-reformer, and instead carry out methane steam reforming in the anode. Since the methane steam reforming is highly

endothermic, the heat needed to carry out the reaction can be supplied by the reversible and irreversible losses occurring in the fuel cell, thus removing part of the waste heat produced internally in the stack across a small temperature difference as the stack is a very efficient heat exchanger.

Unfortunately this elegant method is normally not able to remove all the heat produced by the fuel cells, but has to be combined with air-cooling by surplus cathode air.

There are three interrelated reactions proceeding in the anode chamber:

$$\mathrm{CH_4 + 2H_2O = CO_2 + 4H_2 - Q_{Reform}}$$
$$-\Delta H^{0,\mathrm{Reform}}_{923\mathrm{K}} = -189.2\ \mathrm{kJ/mole} \quad (13.4)$$

$$\mathrm{H_2 + 0.5O_2 = H_2O + E + Q_{Electro}}$$
$$-\Delta \mathrm{H}^{0,\mathrm{Water\ Form}}_{923\mathrm{K}} = 247.4\ \mathrm{kJ/mole} \quad (13.5)$$

$$\mathrm{H_2 + CO_2 = H_2O + CO - Q_{Rev\ Shift}}$$
$$-\Delta H^{0,\mathrm{Rev\ Shift}}_{923\mathrm{K}} = -35.5\ \mathrm{kJ/mole\ H_2} \quad (13.6)$$

E is the electric energy produced, Q_{Electro} is the electrochemically produced heat, Q_{Reform} is the heat of the reforming reaction, and $Q_{\mathrm{Rev\ Shift}}$ is the heat of the reverse shift reaction, which tends to proceed to the right, because the anode outlet temperature is higher than the anode inlet temperature and there is a net production of CO_2 in the anode chamber. The heat is given at a typical operating temperature of 923 K. E, Q_{Electro}, Q_{Reform}, and $Q_{\mathrm{Rev\ Shift}}$ are determined by:

$$-\Delta \mathrm{H}^{0,\mathrm{Water\ Form}} = E + Q_{\mathrm{Electro}} \quad (13.7)$$

$$E = 2FU \quad (13.8)$$

$$\Delta H^{0,\mathrm{Reform}} = Q_{\mathrm{Reform}} \quad (13.9)$$

$$\Delta H^{0,\mathrm{Rev\ Shift}} = Q_{\mathrm{Rev\ Shift}} \quad (13.10)$$

where F is Faraday's number, 96.486 kJ/mol/V, and U the cell voltage. The overall reaction and heat evolution are determined by the interplay between these three reactions.

13.3.2. Energy Balances Around the Stacks for a 250 kW SOFC Plant

The molar flows in the SOFC stack in the plant are shown in a schematic way in Fig. 13.2. The reforming Reaction (13.4) is providing hydrogen to the electrochemical reaction where oxygen from the air on the cathode is supplied through the electrolyte. Water is supplied from hydrogen oxidation (Reaction (13.5)) to drive the reforming toward completion. Simultaneously some CO_2 is reacting with hydrogen in the reverse shift reaction (Reaction (13.6)). H_2 is supplied from internal reforming and the balance from outside (pre-reformer). It is seen that for all practical purposes complete conversion of methane is achieved. There is some net production of CO, water, and CO_2 and a slight overall consumption of hydrogen in this particular case.

The net heat production is determined by the ratios of CH_4, CO, and H_2 entering the anode, the fuel utilization, α, and the cell voltage U.

If m mole of methane is converted according to Reaction (13.4), w mole H_2 according to Reaction (13.5), and r moles of H_2 in the reverse shift, the overall heat production, Q_{tot}, is

$$Q_{\mathrm{tot}} = w \cdot Q_{\mathrm{Electro}} - m \cdot Q_{\mathrm{Reform}} - r \cdot Q_{\mathrm{Rev\ Shift}} \quad (13.11)$$

The fuel utilization, α, is defined by:

$$\alpha = 1 - \frac{4 \cdot \mathrm{mole\ CH_4^{out}} + \mathrm{mole\ H_2^{out}} + \mathrm{mole\ CO^{out}}}{4 \cdot \mathrm{mole\ CH_4^{in}} + \mathrm{mole\ H_2^{in}} + \mathrm{mole\ CO^{in}}} \quad (13.12)$$

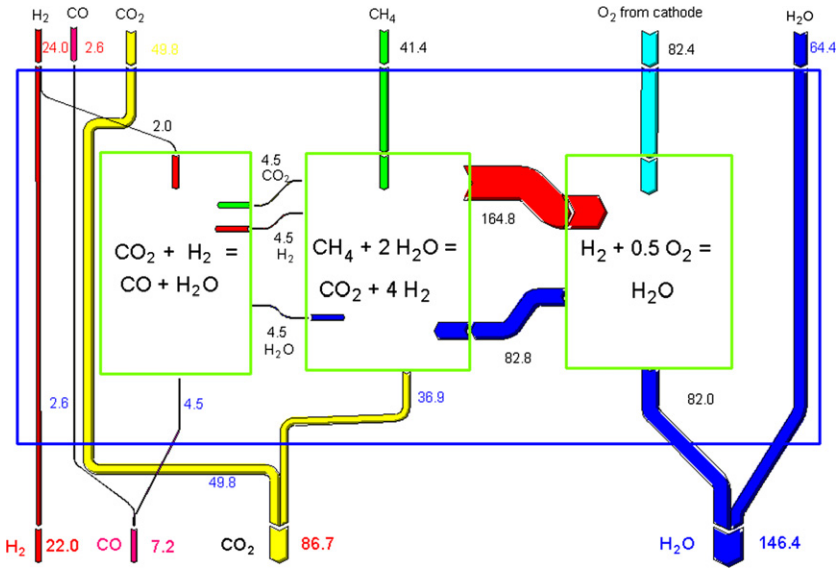

FIGURE 13.2 Flow of reactants (Nm^3/h) in the anode of a 250 kW SOFC plant.

As methane conversion is normally complete and reverse shift marginal one has that

$$Q_{\text{tot}} = -4\cdot\alpha\cdot(\Delta H^{0,\text{Water Form}} + 2\cdot F\cdot U) - \Delta H^{0,\text{Reform}} \tag{13.13}$$

One interesting corollary of Eq. (13.13) is that for cell voltages of 0.7 and 0.8 V the stack becomes thermoneutral at fuel utilizations of 42 and 51%, respectively. Below those fuel utilizations the stack will cool off. The energy and heat flows for the plant with a pre-reformer is shown in Fig. 13.3.

The heat generated in the electrochemical reaction, Q_{Electro}, which is not consumed by the reforming (and reverse shift) is heating the anode outlet flows and the rest has to be removed by the cathode air stream. It is also necessary to take the enthalpy value of the oxygen transferred across the electrolyte into account when calculating the balances. For the methane-based plant the balances are shown in Table 13.2.

It is then instructive to consider a situation where pure hydrogen is used as feed to the anode and no reforming thus takes place. The net power output from the plant is kept at 250 kW AC. This net power is after deduction of power used by the blowers and inverter losses. The heat balances around the stack are shown in Fig. 13.4.

It is seen that the duty of both the air compressor and air preheater, E3, is more than doubled and the necessary stack output increases by 33 kW or 11%.

As a rough guideline the heat which must be removed from an adiabatic SOFC stack in a plant with complete external reforming is Q_{Electro}, whereas with internal reforming it is only $Q_{\text{Electro}} - Q_{\text{Reform}}$. The amount of heat removed is approximately proportional to the cathode air flow and thus to the energy need for air compression and the cathode feed/effluent exchanger, E3, duty.

This ratio, υ, between power for the external reforming and internal reforming cases is accordingly calculated by

$$\upsilon \cong \frac{Q_{\text{Electro}}}{Q_{\text{Electro}} - Q_{\text{Reform}}} \cong \frac{4\cdot\alpha\cdot(\Delta H^{0,\text{Water Form}} + 2\cdot F\cdot U)}{4\cdot\alpha\cdot(\Delta H^{0,\text{Water Form}} + 2\cdot F\cdot U) + \Delta H^{0,\text{Reform}}} \tag{13.14}$$

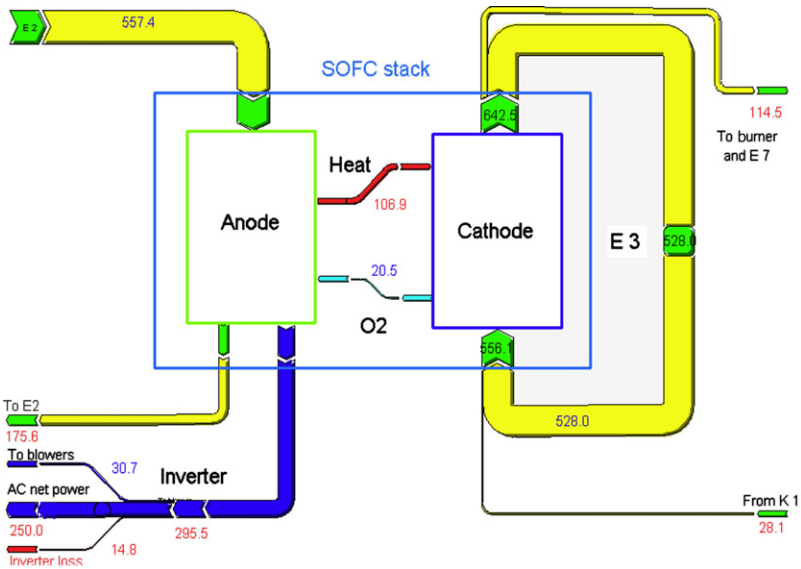

FIGURE 13.3 Energy flows in stack with pre-reformed natural gas.

TABLE 13.2 Energy Balance for SOFC Stack in a 250 kW Plant

Energy source or sink	kW	%
Energy generated by reaction	505.1	100.0
Heat consumed by reforming	97.1	19.2
Heat consumed by reverse shift	2.0	0.4
Heat used to heat anode stream	3.6	0.7
Heat used to heat cathode stream	106.9	21.2
Power output	295.5	58.5

13.3.3. Thermodynamics of Other Fuels than Methane

Many high temperature fuel cell anodes are in principle able to convert other fuels than methane by internal reforming, although carbon formation (see next section) will normally prevent this in practice except for the case of ammonia.

The endothermic heat of reforming (per mole of H_2 generated) for other fuels is, however, lower than for methane as shown in Fig. 13.5. The heat needed for reforming per mole hydrogen is almost constant around 91% of that of methane for the higher (C_{7+}) hydrocarbons, whereas it is roughly 50% for MeOH and dimethyl ether (DME) reforming, whereas ammonia is intermediate at 77% of the reforming heat compared to methane per mole of hydrogen generated. Both the shift and catalytic partial oxidation (CPOX) reaction are mildly exothermic.

13.4. CARBON FORMATION

Although this subject has already been dealt with in Chapter 4 of this book it is pertinent to focus again on this cumbersome phenomenon as it is to a large extent defining the choice of operating conditions, choice of fuels and anode materials, etc. and has prevented the practical use of internal reforming of other fuels than methane and ammonia.

Carbon formation may occur via

1. Pyrolysis of heavier hydrocarbons in the gas phase above 600–650 °C. Pyrolysis forms olefins or tars, which are strong coke

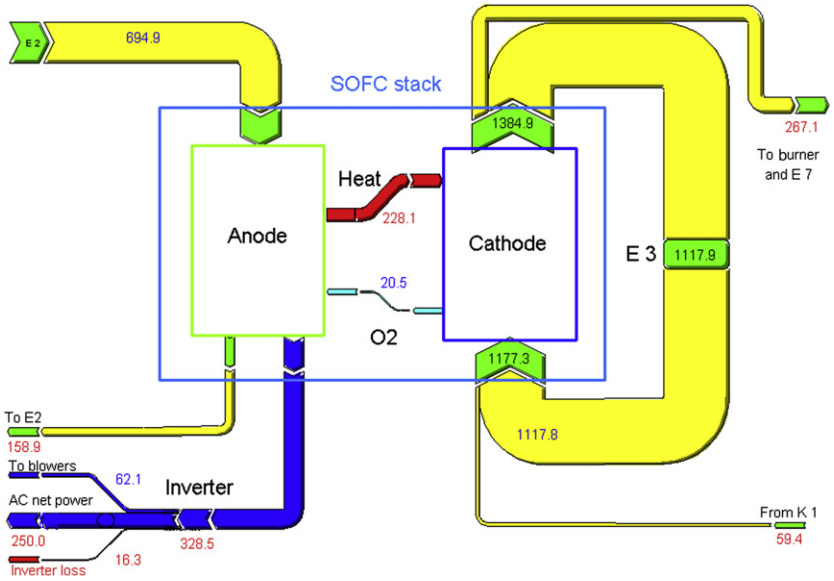

FIGURE 13.4 Energy flows in stack with pure hydrogen as feed.

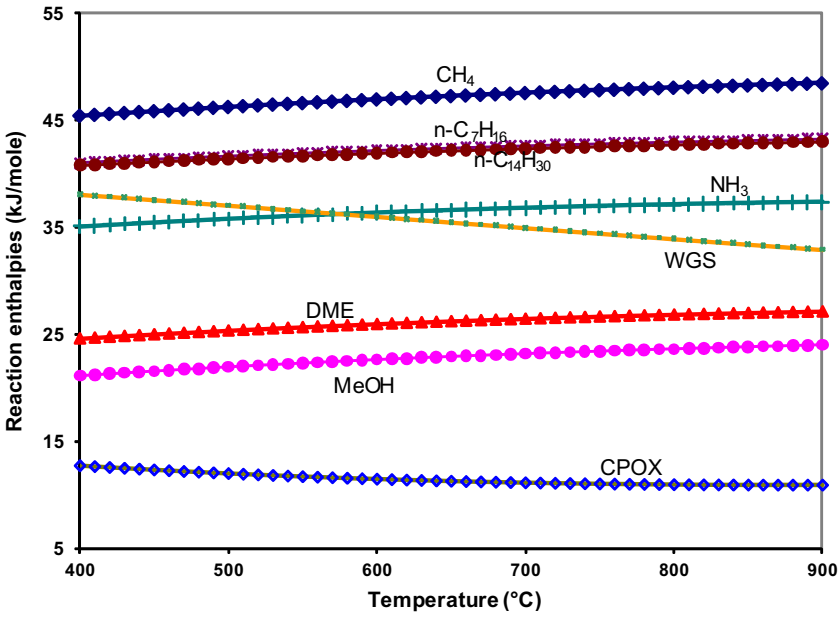

FIGURE 13.5 Reaction enthalpies (absolute value in kJ/mole of H_2 produced) for complete steam reforming of hydrocarbons (products CO_2 and H_2), methanol, DME, ammonia cracking, WGS, and CPOX (of methane) reaction.

precursors. An adiabatic pre-reformer quantitatively converts higher hydrocarbons and thus eliminates this risk.

2. Hydrocarbons may also form graphite.
3. Carbon nanotubes or whiskers may also form on notably Ni, Fe, or Co. The limit where carbon is formed is thus influenced by the choice of the reforming catalyst.

4. At lower temperatures encapsulating carbon (gum) formation can occur from heavier hydrocarbons (diesel or jet fuel). This is normally not a relevant concern for MCFC or SOFC with the present operating temperatures but may need revisiting if the operating temperature will be lowered due to improvement in stack performance.

Pyrolysis, gum, and graphite formation reduces the active area and blocks the pores, whereas whisker formation can lead to catastrophic destruction of anode because the carbon nanotubes are very strong.

13.4.1. Pyrolysis

Pyrolysis has to be taken into account when considering the total system as the fuel normally needs to be preheated in a heat exchanger and passed through manifolds before reaching the anode chamber. Empirical experience from olefin plants [13–15], which operates at conditions close to today's intermediate temperature SOFC, can provide some qualitative guidelines as the propensity to form carbon increased as: Methane < ethane < benzene < ethylene, paraffins, toluene < naphthalene < anthracenes < acetylene.

Recently it has been possible to model by free radical mechanistic reaction schemes [16–21] the extent of pyrolysis occurring in SOFC anodes (and preheaters) and furthermore obtain good correspondence with experimental observations.

13.4.2. Graphite Formation

Graphite formation can occur from the following reactions:

$$2\,CO = C + CO_2 \tag{13.15}$$

$$CH_4 = C + 2H_2 \tag{13.16}$$

$$CO + H_2 = C + H_2O \tag{13.17}$$

where Reaction (13.15) is the Boudouard reaction, Reaction (13.16) is methane decomposition, and Reaction (13.17) is the CO reduction reaction. When calculating the potential for carbon formation it is normally assumed that all steam reforming reactions, methanation as well as the shift reaction, are in equilibrium. The potential for carbon then depends only on the C/H/O ratios, the pressure, and the temperature. A convenient way of depicting the carbon limits is by way of triangle diagrams with C, H, and O on the axes. Such calculations have been carried out [22–24] using up to 300 possible species including hydrocarbons, alcohols, and ethers. It was found that at equilibrium only CH_4, CO, CO_2, H_2, and H_2O exist. All other species are below a few ppm. The carbon limits found are shown in Fig. 13.6. It is seen that the carbon deposition region expands at lower temperatures.

Another way of depicting the carbon limits is shown in Fig. 13.7, giving the limits for graphite formation (e.g., no catalyst present), and in Fig. 13.8 are shown the limits with a relatively low activity catalyst with Ni crystals around 250 nm. The conditions are $P = 0.15$ MPa and $H/C = 3$. The carbon limits can be moved even further toward lower O/C ratio by using a more active Ni catalyst or using noble metals.

It is seen from Fig. 13.7 that it is possible to operate without the risk of graphite formation in the anode with an O/C ratio above ~1.4 if the temperature is above 700 °C, which is typical for anode conditions.

13.4.3. Whisker (Carbon Nanotubes) Formation

As explained in the chapter on steam reforming the onset of carbon formation can be influenced by using nanocrystalline nickel crystals. In a pre-reformer an O/C of 1.4 is adequate to prevent carbon at all temperatures due to the small size of the nickel crystals as is evident from Fig. 13.8. Due to requirement of an electrical conducting network formed by percolated nickel, the crystals in nickel cermets are

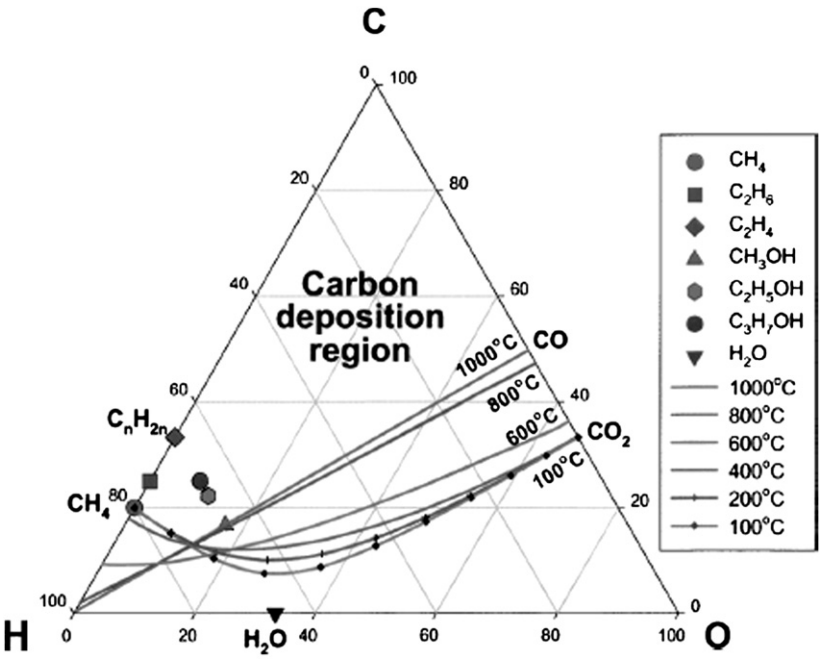

FIGURE 13.6 Carbon deposition limit lines in the C–H–O diagram *(Reprinted with permission from Sasaki and Teraoka [24], Copyright (2003) The Electrochemical Society).*

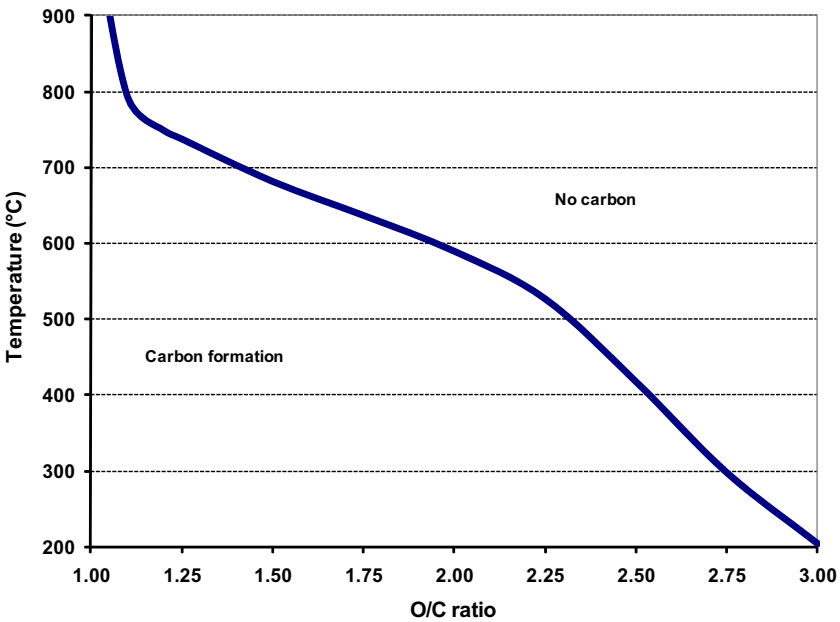

FIGURE 13.7 Carbon limits for graphite formation as function of temperature and O/C ratio.

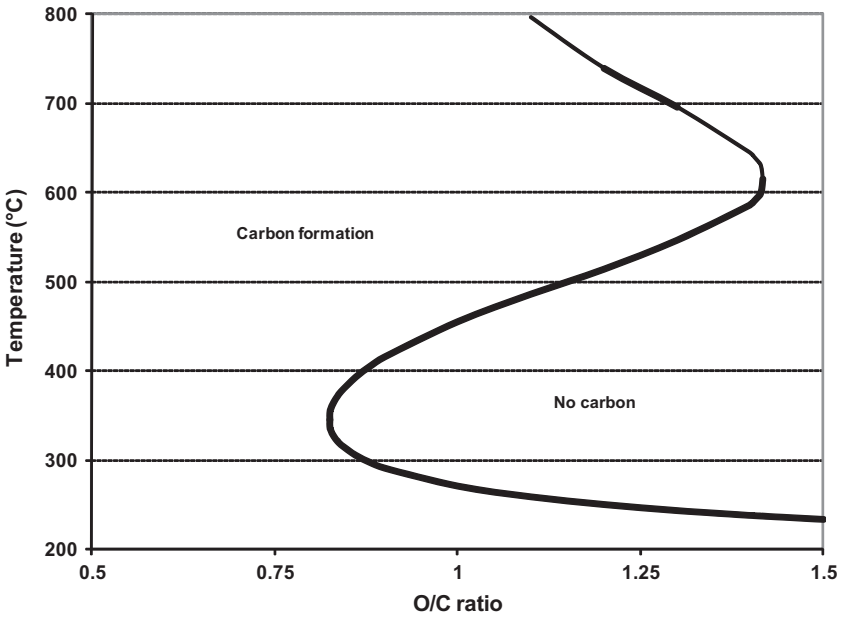

FIGURE 13.8 Carbon limits in a pre-reformer with Ni catalyst with a diameter of around 250 nm.

normally much larger, in the order of microns instead of nanometers as in optimized steam reforming catalysts. The carbons formed in the anode are normally more sphere like – although carbon tubes with diameters of several microns have been observed [25]. Whisker like carbon has also been observed by Mermelstein et al. [26] along with encapsulating and pyrolytric carbon causing severe disintegration of the nickel anodes when exposed to tar components.

In a series of interesting experiments, He and Hill [27] exposed Ni-YSZ pellets to methane with 3% water or a humidified mixture of 3:1 CO:H_2. They found that whisker formation took place up to 600 °C. At higher temperatures, significantly more carbon was formed but it was dissolved in the bulk of the large nickel particle (1–2 μm). The dimension of the pellet expanded substantially and the microstructure was destroyed by the carbon formation. Placing Zr-doped ceria catalyst pellets adjacent to the Ni-YSZ pellets reduced the amount of carbon formed on the Ni-YSZ and the cermet structure was not destroyed. The formed carbon was also easier to remove. The role of the ceria is more than just enhancing methane reforming because the same effects were seen with CO and H_2 mixtures.

13.5. EXPERIMENTAL STUDIES ON LOW O/C OPERATION

Lowering the amount of steam added to fuel for the anodes gives several benefits: the Nernst potential becomes higher and less steam generation/anode recycle becomes necessary. It is therefore not surprising that this research area has attracted a lot of attention. The literature is far too comprehensive to be completely reviewed in this chapter but some representative attempts to operate with different hydrocarbons inside the carbon formation area are summarized.

13.5.1. Carbon Formation with Methane as Fuel

Finnerty and coworkers [28–30] have studied Ni-YSZ with varying Ni content and preparation methods as well as Ni-YSZ containing small

amounts of Mo by temperature-programmed reduction (TPR), temperature-programmed oxidation (TPO), and electrochemical characterization in the same experimental set-up. Mo seems to impart better resistance against coking.

Marina and Mogensen [31] studied gadolinium-doped ceria with slightly humidified methane and found no carbon formation, but also insignificant steam reforming or electro catalytic activity. The performance of the cells was thus ascribed to thermal decomposition in the gas phase and on the alumina housing of the experimental set-up (formation of C_2 species was also detected). The ability of ceria to suppress coke formation was evident.

The effect of additives to suppress carbon formation on Ni-YSZ cermet anodes was studied by Takeguchi et al. [25]. Addition of CaO worked to decrease carbon formation by a factor of around 2 as did small amounts of CeO_2. SrO reduced the carbon formation rate by 50%. MgO had limited impact, but somewhat surprising large amounts of CeO_2 was observed to increase carbon formation.

Ni-scandia stabilized zirconia (SSZ) showed stable performance even with only 3% H_2O in CH_4 at 1000 °C with a current density of 1.0 A/cm^2 where Ni-YSZ performance deteriorated due to carbon formation as detected by Electron Spectroscopy for Chemical Analysis [32]. For the Ni-SSZ a maximum in over potential was noted around 2.0 A/cm^2. Above this value it actually decreased, which was ascribed to simultaneous partial oxidation of methane occurring. Ni-SSZ cermets are more resistant toward carbon lay down from methane (S/C = 0.9 at 700 °C) and propane when operated in the carbon deposition region than Ni-YSZ is and less carbon was deposited in the same time period on the SSZ cermets [33]. Both anode types did, however, suffer from carbon deposition.

When carbon deposition on these two cermet types (prepared as real anode) was studied as function of temperature at very low S/C = 0.03 with current drawn an interesting picture emerges [34]. The amount of carbon increased on the YSZ cermet with temperature from 800 to 900 °C after 10 h exposure, whereas it was significant at 800 °C but negligible at 900 and 1000 °C for SSZ. The fuel utilization was very low around 1% so the bulk gas phase composition was the same (97% CH_4 + 3% H_2O) but right at the triple phase boundaries (TPB) conditions may be different due to difference in concentration of the adsorbed species. An indication of this is also the generation of CO_2 as function of current density at 900 °C. Above a critical current density the evolution rises linearly on the SSZ cermet whereas there was no CO_2 evolution with the YSZ cermet.

It is a fact that SSZ is a better oxygen ion conductor than YSZ and it also interacts more strongly with the Ni as evidenced by TPR experiments. TPR experiments [33,34] show low temperature reduction peak at around 400 °C, indicating bulk NiO reduction is much larger for YSZ than for SSZ, e.g., there is more Ni strongly interacting with the YSZ support first being reduced above 500 °C. Leaching the cermets with HCl also indicates larger cavity after leaching in YSZ than in SSZ. There is also a smaller loss of BET area when a SSZ cermet is calcined at high temperature than for YSZ.

Weber et al. [35] tested single cells (5*5 cm^2) consisting of conventional Ni-YSZ anodes with dry hydrogen, CO, and CH_4. The best performance was observed with hydrogen but dry methane yielded almost the same power density. The use of pure CO caused unstable operation, extensive carbon deposition, and delamination. A single cell was operated stably on pure, dry methane for 1000 h at 0.4 A/cm^2, 950 °C with only very slight carbon formation. It is, however, noteworthy that a reference nickel electrode in the same set-up displayed significant carbon deposition and delamination.

Gunji et al. [36] investigated the influence of operating temperature and current density on the carbon deposition on Ni-Ce-SSZ anodes and found that the carbon formation decreased

with an increase in both parameters. At 900 °C and 0.5 A/cm^2 with 3% H_2O in CH_4 only very slight carbon deposits were observed but at 800 °C or open circuit voltage (OCV) massive carbon deposition occurred. The results are vividly illustrated by the photographs in Fig. 13.9.

Sumi et al. [37] carried out a comparison of Ni-Ce-SSZ and Ni-YSZ cells at 1000 °C. The two anodes gave almost identical performances with hydrogen as fuel, but the peak power using methane with 3% water was 15% higher for Ce-SSZ than for YSZ. The YSZ anodes degraded rapidly, whereas the Ce-SSZ was stable for 250 h.

Tabata et al. [38] used a scandia alumina stabilized zirconia (SASZ) as electrolyte and a thick Ni cermet component and could operate with methane at S/C of 0.5 at 800 °C without observing carbon.

Gavrielatos and coworkers [39,40] have prepared gold (1 at%) doped Ni-YSZ cermet anodes using in situ combustion synthesis. The addition of gold led to a remarkable increase in resistance toward carbon deposition in agreement with the theoretical predictions by Bengaard et al. [41] that Au would decorate the step sites, mainly prone to initial carbon

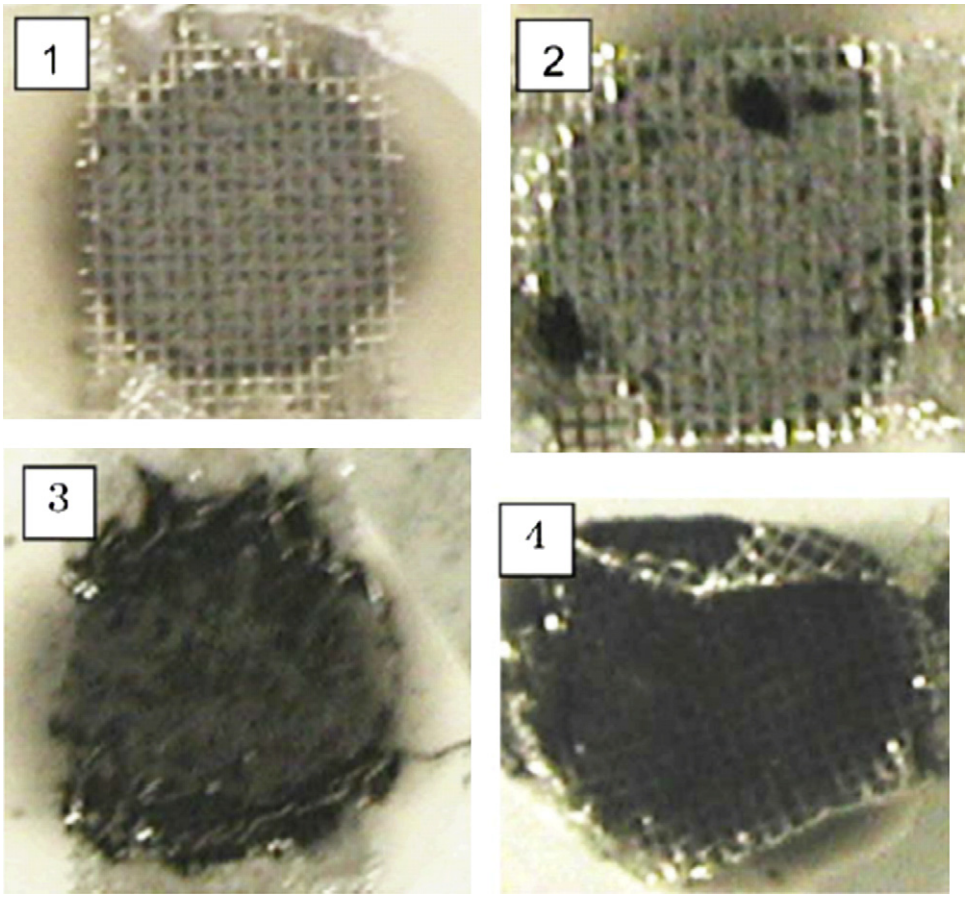

FIGURE 13.9 Images of anodes before or after stability tests: (1) before; (2) 900 °C, 0.5 A/cm^2; (3) 800 °C, 0.5 A/cm^2; (4) 900 °C, 0 A/cm^2. *Reprinted with permission from Gunji et al. [36], Copyright (2004) Elsevier.*

formation. Recently it has also been shown that small amounts of Sn can act in the same manner to suppress carbon formation both with methane [42] as well as with isooctane [43].

13.5.2. Carbon Formation with Biogas as Fuel or During CO_2 Reforming

Biogas from anaerobic fermentation of biomass contains 50–65% CH_4; the balance being mainly CO_2. The possibility of using such gases after some H_2S removal via the CO_2 (dry) reforming of methane has attracted increasing attention.

$$CH_4 + CO_2 = 2\,CO + H_2 \qquad (13.18)$$

There is, however, a potential to form carbon with the methane-rich gases (see Fig. 13.6).

Girona et al. [44] indeed saw degradation of the electrochemical performance and carbon formation using commercial Ni-YSZ anode supported cells at 800 °C with a CH_4:CO_2 ratio of 1.5 and 6% H_2O whereas with a CH_4:CO_2 ratio of 1.0 and 6% H_2O it yielded a stable performance and no carbon formation was observed. With the methane-rich gas carbon formation could be avoided at 120 mA/cm^2.

Yentekakis et al. [45] did experiments with Ni-YSZ at 875 °C as well as with Ni-GDC and Ni(Au)-GDC anodes at 700 °C and did not report any carbon formation problems but performance dropped especially for the Ni-YSZ anodes in the methane-rich region.

Lanzini and Leone [46] tested both Ni-YSZ anode supported and Ni-GDC electrolyte supported cells. With a CH_4:CO_2 ratio of 1.5 both cells showed carbon formation even under load. The anode supported cells failed catastrophically. Adding appropriate amounts of either steam, oxygen, or extra CO_2 to move into the region where carbon formation is not thermodynamically possible eliminated the carbon formation. The anode supported cells performed better for the CO_2 (dry) reforming probably due to the higher nickel content.

Xu et al. [47] used commercial Ni-YSZ anode supported cells in tests with CO_2 (dry) reforming of biogas and with additional steam or air added. They found coking even with equimolar amount of methane and carbon dioxide at 750–850 °C. Even with steam addition some coking was observed but not when a barrier layer of Ni-CeO_2 was coated on top of the anode. Adding both air and steam (30% CH_4, 30% air, 20% H_2O, and 20% CO_2) led to stable operation without coke formation for both coated and uncoated anodes.

Shiratori and coworkers [48–51] have used both Ni-SSZ and $Ni_{0.9}Mg_{0.1}O$-SSZ anodes for work on simulated and real biogases. No carbon was observed with simulated biogas containing no H_2S under a load of 200 mA/cm^2 at both 900 and 1000 °C. When the cells were run on real biogas with <0.5 ppm H_2S, massive carbon formation was, however, observed after 800 h operation. Carbon formation could be avoided if 10% O_2 was added to the anode feed gas. The authors did not comment on any temperature effect this addition of air must have had.

Laycock et al. [52] studied carbon formation in a CH_4:CO_2 = 2:1 gas on Ni-YSZ anodes as well as gold-, hafnia-, and ceria-doped Ni-YSZ anodes with and without sulfur addition. Carbon formation was quantified by post-reaction TPO. It increased dramatically with temperature from 750 to 1000 °C, but reduced very considerably when 5 ppm H_2S was added in accordance with the findings of Rostrup-Nielsen and Alstrup [53]. In the presence of sulfur, methane conversion was increased in the order Ce > Hf > Au, but carbon formation actually increased slightly compared to the undoped anodes.

13.5.3. Carbon Formation with Higher Hydrocarbons as Fuel

Higher hydrocarbons are much more prone to carbon formation than methane. Ethane and ethylene immediately started to form carbon at

1000 °C over Ni-YSZ as indicated by a drop in the electrochemical performance even when operated at S/C = 3.5 (e.g., outside the carbon formation region) [22].

Hibino et al. [54] achieved carbon-free operation on Ru containing Ni-GDC anodes at 600 °C with both methane, ethane, and propane only saturated with water at 24 °C. The results are somewhat uncertain for ethane and propane as the peak power density fell from 750 using methane and to 716 and 648 mW/cm^2 using ethane and propane respectively, which presumably would be easier to reform. It should also be noted that they used a GDC electrolyte which is an electron as well as a mixed oxide ion conductor, meaning that a certain short circuiting of the cells has occurred.

Yamaji et al. [55] managed to operate a Ni-SSZ anode with almost dry ethane for a week, but only at a very low temperature of 549 °C and only at high fuel utilization of above 46%. At lower fuel utilization of 20%, the anode was disintegrated at the fuel inlet. At the higher temperature of 700 °C, destruction of the anode occurred even at high fuel utilizations.

Iida et al. [56] investigated by thermo gravimetric analyses the propensity of different anode material to form carbon by exposing them to dry methane and found the order to be:

$$\text{Ni-SmDC} > \text{Ni-YSZ} > \text{Ni-SSZ} > \text{Ni-Ru-YSZ} > \text{Ru-YSZ}$$

Both Ni-SmDC (samaria-doped ceria) and Ni-SSZ could operate stably at 1000 °C at 300 mA/cm^2 with propane as fuel with an S/C ratio of 0.8.These electrodes could even withstand short-term exposure to OCV conditions without deterioration. With Ni-YSZ, carbon deposition and deterioration occurred even outside the region where carbon is not predicted thermodynamically (S/C = 3.0) at OCV. The fact that SmDC showed the highest carbon lay down rate but still was able to operate inside the carbon formation region with propane shows that the rate of carbon removal on this material was high enough to prevent accumulation and deterioration at least at S/C = 0.8.

Dekker et al. [57] operated cerium gadolinium oxide (CGO) anodes without any carbon formation or impact on cell voltage from a mixture of 1.4% ethylene and 0.1% acetylene at 850 °C with only 14% water in the gas.

Recently, Liu et al. [58] have shown excellent resistance against coking on cells using a mixed ion conductor: $BaZr_{0.1}Ce_{0.7}Y_{0.2-x}Yb_xO_{3-\delta}$ (BZCYYb). With a Ni-BZCYYb and an SmDC as electrolyte and a current density of 600 mA/cm^2 at 750 °C, dry propane gave stable performance for 24 h. It is interesting to note that large amounts of C_2H_4 and methane were observed at the outlet of the cell indicating a high activity for propane cracking. A cell comprising of Ni-BZCYYb and a YSZ electrolyte deactivated rapidly in dry propane at OCV but adding ~3.0% H_2O was enough to give stable performance for 24 h. A Ni-GDC/YSZ cell was observed to deactivate immediately under the same conditions due to carbon formation.

13.5.4. Carbon Formation in Tar Containing Gases

When biomass is gasified the product gas can contain significant amounts of tars. Incomplete reforming of diesel or jet fuels can also result in the presence of tar compounds in the feed to the SOFC unit [59]. With gadolinia-doped ceria Ni cermets in electrolyte-supported cells, quite significant amounts (up to 1000 ppm of tars) could be tolerated without any evidence of carbon formation in experiments lasting up to 900 h with only 14% water in the gas. Toluene, naphthalene, phenanthrene, and pyrene were used representing ring aromatics with 1–4 rings respectively [57]. Impedance spectroscopy also showed that there was no impact of 110 ppm naphthalene on Ni-GDC cells [60]. The steam reforming

rate was, however, affected (see Section 13.7.9.8).

Short-term (less than a few days) operation on gas from real gasifiers, with HCl and H_2S removed, also showed that operation without carbon formation could be realized with Ni-GDC anodes with gases containing >10 g/m^3 [61].

Mermelstein et al. [26] did, however, find significant carbon formation with dry operation with toluene, benzene, or mixtures of heavier tars also including naphthalene, phenol, and pyrene. The same group also observed carbon with both Ni-YSZ and Ni-CGO anodes when exposed to benzene (15 g/m^3) even at S/C > 1, e.g. in the thermodynamic region where carbon formation should not occur [62]. The anodes could be operated stably without carbon formation beyond the threshold current density above which carbon formation should not occur. Ni-CGO performed better than Ni-YSZ [63].

13.5.5. Carbon Formation with Alcohols as Fuel

Recently Huang et al. [64] have studied ethanol as fuel for Ni-SSZ cermets with a thin catalyst layer (8 μm) of LSCM (lanthanum strontium manganese chromite) − CeO_2, prepared by screen printing of the LSCM- CeO_2 slurry on the Ni-SSZ anode surface. Three different LSCM weight ratios were used: 1:0, 1:1, and 1:3. The anodes showed improved performance with increasing ceria content, in fact most pronouncedly with hydrogen at the low temperatures used. With ethanol the difference was less pronounced (28% improvement in peak power density compared to 90% improvement in H_2). It is remarkable that such big changes in performance can be brought about by just 8 μ catalyst layer on top of a 800 μm thick anode. A certain improvement in performance could be seen for the first three days by impedance spectroscopy. Thereafter, the performance decreased. The performance increase in the beginning could be explained by increased electronic conductance by a small amount of carbon deposited in the anode, although it could not be seen by scanning electron microscopy (SEM). The anode with the highest ceria ratio was very stable for at least 216 h. There was almost no carbon deposits observed after the experiment.

Cimenti and Hill [65,66] carried out thermodynamic as well as experimental work on the direct use of methanol for SOFC. The use of pure methanol will lead to carbon formation at OCV, but at 800 °C only 2.6 vol% of water or a fuel utilization of 2.1% is needed to avoid carbon deposition.

They found, however, that methanol will undergo different pyrolysis reaction above 700 °C mainly forming formaldehyde, H_2, and CO with traces of methane, water, ethylene, and acetylene. Carbon deposits were found on the quartz reactor used between 500 and 700 °C. YSZ did not have any catalytic effect with respect to methanol conversion. Different anodes consisting of Ni-YSZ, Ni-Ceria, Cu-Co/Ceria, and Cu-Ceria initially converted methanol to the equilibrium mixture of CO and H_2 but all completely lost their activity within a few hours. Carbon was found on all of them except the Cu-Ceria, which also deactivated, presumably due to thermal sintering.

The problems in using methanol as a fuel can be overcome by converting it to methane in a reactor with a special catalyst upstream the SOFC stack [67,68]. Pyrolysis of methanol as well as carbon lay down on the anode are avoided and the higher reaction heat for reforming methane instead of methanol leads to an overall higher system efficiency.

Cimenti and Hill [69] also tested the direct use of ethanol as fuel with three different anode types: Cu-ceria, Cu-ceria-zirconia, and finally Cu/Ru-ceria-zirconia. The addition of ruthenium delayed the onset of carbon formation but all the anodes eventually succumbed to this deactivation.

13.5.6. Carbon Formation on Copper-Based Anodes

A lot of research has been carried out at the University of Pennsylvania with copper ceria anodes, showing that these anodes can use a variety of hydrocarbons directly without problems with carbon lay down and good sulfur tolerance [10,70]. The durability of these anodes is, however, not quite satisfactory probably due to the relatively low melting point of copper. Due to these issues the group have used some ingenious new strategies to overcome these problems [8]. One approach has been to only use a thin, 12 μm, functional layer 40 wt% ceria impregnated YSZ with 1 wt% Pd or Ni combined with a current collection layer of lanthanum strontium titanate (LST). These anodes were stable even at OCV in dry methane (3% H_2O). The role of the metal is to enhance the electrochemical performance and the effect is indeed dramatic. Addition of Pd or Ni to the ceria increased the peak power from 110 to 520 and 420 mW/cm^2 for Pd and Ni respectively at 700 °C. In the dry methane addition of Pd increased the peak power from 9 to 335 mW/cm^2. The OCV value of 1.25 V was also higher than that obtained with reformate.

Another approach has been to use Co for conductivity and thermal stability (Co melts at even higher temperature than Ni) in the anode but to coat with Cu in order to prevent carbon formation in the form of whiskers. This can be achieved by electro-deposition of Co on Cu and then letting the Cu migrate through the Co by heating to 600 °C. The copper layer is only a few monolayers thick. This gave much stable and better performing cells than by co-impregnating the Cu and Co.

13.5.7. Ammonia as SOFC Fuel

The problems with carbon formation is obviously not an issue when using ammonia as a fuel and the benefit of internal reforming is possible albeit not to an extent offered when using methane. On the other hand there is no need to add water to the feed so operation can be performed at high voltages.

The first to demonstrate that ammonia could be used as an SOFC fuel were Farr and Vayenas in 1980 [71]. They operated the cells with a Pt electrode and found that NO_x was the predominant electrochemical oxidation product but significant complete conversion of the ammonia to nitrogen also took place. The aim of the study was thus to use SOFC with ammonia as a cogenerator of electricity and nitric acid. Perhaps this study has been the reason for the misconception that NO_x formation will take place in an SOFC with ammonia as fuel.

There was, however, almost no interest in the subject except for some analyses of use of ammonia decomposed outside the fuel cells by a group at Ecole de Mines in the 1990s [72,73]. These analyses indicated that ammonia was a better choice than methanol.

Researchers in Belarus did some thermodynamic analyses [74] on ammonia as SOFC fuel and later carried out experimental studies with different anodes on fuel mixtures of ammonia and alcohols [75].

Wojcik et al. [76] demonstrated that a combination of a silver anode and an iron catalyst worked as well with ammonia as fuel as with hydrogen. The current densities were, however, very limited. Platinum electrodes increased the performance by a factor of about 200 but the problem with respect to selectivity to NO is mentioned although no data was given.

The groups at both ECN [77,78] and Topsoe Fuel Cell/Risø [79] began reporting encouraging results with standard nickel cermet anodes in 2005 and the first flow sheet and system analyses were also presented [80]. Risø/Topsoe Fuel Cell found similar performance using ammonia and 3/1 mixtures of hydrogen and nitrogen (see Fig. 13.10).

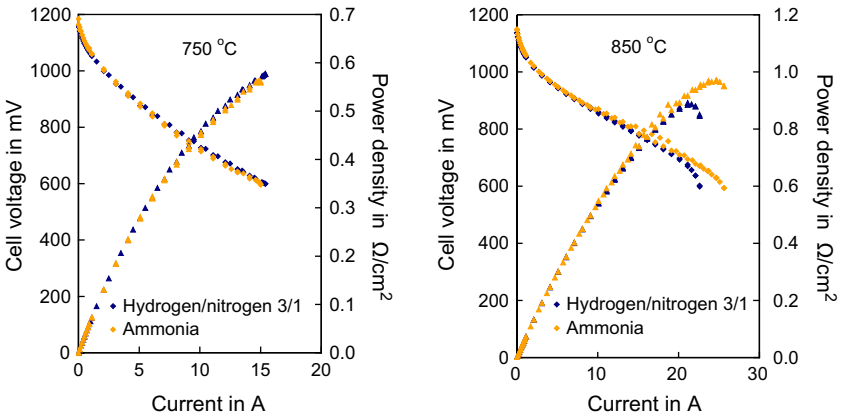

FIGURE 13.10 Comparison of cell performance of ammonia and 3/1 H_2/N_2 at 750 and 850 °C.

Dekker and coworkers [77,78] tested both electrolyte (ESC) as well as anode-supported cells (ASC) for more than 3000 h with a degradation rate less than 1% per 1000 h for both cell types similar to the ones obtained by using dry hydrogen. Performance was otherwise also similar to that of using dry hydrogen. The ESC cells converted ammonia to hydrogen and nitrogen to equilibrium at 1000 °C but had twice the equilibrium value at 900 °C. The ASC showed equilibrium conversion at 800 °C but not at 700 °C. The only NO_x formed in an ammonia-based system would be stemming from the catalytic afterburner. At exit temperatures below 950 °C, less than 0.5 ppm NO_x was measured.

Ammonia has become a popular fuel also for fuel cells with proton conducting electrolyte, perhaps also due to the absence of CO_2 in the anode chamber. Respectable power densities have been demonstrated considering the electrolyte thickness and low operating temperature using barium cerate doped with gadolinium, praseodymium, or europium. Even better results were later obtained by thinner electrolytes [81,82].

A Chinese research group has also lately been very active within this field [83–93] and the subject has very recently even had a review article [94].

13.6. KINETICS OF STEAM REFORMING ON NICKEL-YSZ ANODES

13.6.1. Importance of Kinetics and Comparison with Ordinary Steam Reforming

There is consensus that H_2 oxidizes electrochemically more readily than CO [22] but it can normally not be observed because the shift reaction is very fast. The rate with which the steam reforming occurs on the SOFC anode is of crucial importance for the performance of the stacks, because it determines to a large extent the temperature profile and availability of the hydrogen at the TPB. It is therefore somewhat surprising that the literature on the subject is rather limited considering the vast amounts of publications dealing with modeling of SOFC, which relies heavily on the accuracy of the employed kinetic models. It is, however, difficult to perform kinetic experiments on operating SOFC because the methane conversion normally is more or less complete. The studies have therefore mainly been carried out with anode in a separate catalytic reactor. It is important to obtain intrinsic kinetic data, free of mass transfer effects, and have good control of the

TABLE 13.3 Comparison of Parameters for Conventional Steam Reforming Catalysis and SOFC Anodes

	Conventional steam reforming	SOFC anode chamber
Ni particle size, nm	10–50	1000
Ni content, vol%	25	40
Support	α-Al_2O_3, MgO, $MgAlO_4$	YSZ, SSZ
Characteristic dimension, mm	5–20	0.2–1
Porosity, %	30	40–50
Temperature	>700	600–1000
Pressure, MPa	1–4	0.1–0.5
S/C	1.5–4	1.5–3
Conversion of methane, %	Limited by equilibrium	>99

temperatures. These conditions are far from satisfied in all studies. It is also difficult to compare the results because the activities very often have been reported on a geometric surface area basis instead of the more correct available metal surface or weight basis. It is also important to differentiate between the bulk anode and the electrochemically active part of the anode.

In principle it should be possible to transfer the kinetic information from ordinary steam reforming catalyst, but the operating conditions and catalyst composition differ to an extent that this cannot be done without careful validation of the results. Table 13.3 illustrates the difference in the used catalysts and typical operating conditions.

13.6.2. Experimentally Determined Kinetics

In Table 13.4, an overview of kinetic expressions reported in the literature is given.

The following comments can be added concerning the different experimental studies and the deviations from the simple first-order dependence on methane partial pressure found by Wei and Iglesia [107].

The very large retarding effect of water found by Lee et al. [95] is surprising. They did not fit the methane partial pressure dependency, but just assumed it to be 1.0. Lee et al. [95] used a CSTR which should ensure isothermal conditions but the pellets used were rather large and the S/C very high, indeed much higher than used in practice. No corrections for the distance from equilibrium were made although the conversion of methane was quite high (typically 0.25–0.75). The porosity and mean pore diameter were also low so mass transfer at the high temperatures used was probably significant. The observed conversion rates were also at least an order of magnitude lower than other reported rates on Ni-YSZ [98].

Ødegård et al. [98] also had very large methane conversion in their experiments (85–96%). No corrections were made for the distance to the equilibrium and isothermal conditions were probably not obtained. The fitting of the methane partial pressure dependency also gave very flat optimum for 1.15–1.2 and an order of 1.0 would not have made the fit much worse.

Achenbach [97] carefully corrected for mass transfer effect and approach to equilibrium. The methane conversion was kept differential (below 25%). Their experiments also included pressures up to 0.28 MPa. Their kinetics has been widely used for modeling purposes. It should be noted that it is based on anode geometric area.

Dicks et al. [100] developed a Langmuir-Hinshelwood type expression because they found a strong influence on the Arrhenius type activation energy with the steam content. They claim that the experiments were free of mass transfer effects as evidenced with no change in rates with change in dilution gas from He to Ar, but it should be noted that their study included some extreme S/C ratios up to 35.

TABLE 13.4 Overview of Kinetic Expressions Reported in the Literature

Expression	K	E_a kJ per mole	T (°C)	S/C	Support	Ni content (%)	Anode (u)	Reference
$kP_{CH_4}P_{H_2O}^{-1.28}$	490 4775	74.5 98.3	800–1000	2–8	YSZ	70 & 60 vol	2.4–4.8 mm	[95]
$kP_{CH_4}(1-\beta)$		135	600–1000	2	SmDC	2 wt	105–180 μ	[96]
$kP_{CH_4}(1-\beta)$	4274	82	700–940	2.6–8	YSZ	20 wt	1.4 mm	[97]
$kP_{CH_4}^{1.20}$	6300	58	900–1000	2.4	YSZ	60	39–44 μ	[98]
$k\,P_{CH_4}$		163	800–850	2–4	YSZ-CeO_2	5 wt	10 μ	[99]
$\frac{k\,P_{CH_4}}{(1+K_H(T)\sqrt{P_{H_2}}+K_S(T)P_{H_2O}/P_{H_2})}$			700–1000	1–35	YSZ	55 vol	40–60 μ	[100]
$kP_{CH_4}^{1.4}P_{H_2O}^{-0.8}$	$3.6*10^{8}$	208	838–922	1.4–3.0	YSZ + Basic additive		50 μ	[101]
$kP_{CH_4}^{0.85}P_{H_2O}^{-0.35}$	8542	95	854–907	1.53–2.5	YSZ		50 μ	[101]
$kP_{CH_4}^{1.00}P_{H_2}^{0.19}P_{H_2O}^{-0.31}$		142	650–750	2.5–9	Ce-ZrO_2	5 wt		[102]
$\frac{kP_{CH_4}}{(1+K_H(T)\sqrt{P_{H_2}}+K_S(T)P_{H_2O}/P_{H_2})}$		18	700–1000	2–7	YSZ − CeO_2	50	200 μ	[103]
$kP_{CH_4}^{1.19}$	$4.05*10^{-5}$	26.3	800–950	2–3	CGO	50	50 μ	[104]
kP_{CH_4}	$4.98*10^{-3}$	63.3	650–950	2	8YSZ	65 wt	40 μ	[105]
kP_{CH_4}	0.676	125	650–950	2	8YSZ + Cu Ni:Cu = 3:1	65 wt	40 μ	[105]
kP_{CH_4}		113–124	700–750	1–3	5YSZ	40	75–150 μ	[106]
kP_{CH_4}		102	550–750	0.5–2		7 and 15 wt %	250–425 μ	[107]
kP_{CH_4}	38	30	750–850	1–6	8YSZ		1000	[108]
kP_{CH_4}	1483	61	600–750	1–6	8YSZ		1000	[108]

Ahmed and Föger [101] used a proprietary basic additive and found much higher activation energy with this anode. With a normal Ni-YSZ, they found only a weak inhibiting effect of steam and a reaction order with respect to methane close to 1.

Matsuzaki et al. [109] experimentally determined the tortuosity of two different Ni anodes by studying limiting current and a current interruption technique and found values of 5.1−5.7.

Laosiripojana and Assabumrungrat [102] did a study on Ni/Ce-ZrO_2 with a low Ni loading and found the kinetics to be first order in methane, with a slight positive impact of hydrogen and a moderate negative influence of steam.

Hecht et al. [110] carried out studies in a specially designed experimental set up where a 0.75 mm thick anode material was sandwiched between two flow channels. One channel carried the fuel while the other had a gas simulating the composition at the TPB. They used a microkinetic model with 42 elementary steps. Mass transport restrictions were also incorporated in the model.

Peters et al. [111] found a retarding effect of CO_2, when simulating anode recycle in kinetic experiments with a 1.5 mm thick anode and attempted to use a Langmuir Hinshelwood expression first order in methane and water partial pressures with adsorption terms for methane, steam, and CO_2. They concluded that more investigations have to be carried out.

The very low activation energy (26 kJ/mole) found by Timmermann et al. [104] was ascribed to be due to pore diffusion limitations, but even if the activation energy would be doubled it still appears low. This is the only available study with a full kinetic expression for Ni on CGO. Clarke et al. [5] only indicated a first-order dependency on methane partial pressure.

Boder and Dittmeyer [105] conducted kinetic studies without load on standard Ni-YSZ anodes without and with copper impregnation. They only varied the temperature and residence time but found that a simple first-order rate law described the experimental findings well. The activation energy for the Ni:Cu 3:1 anode was almost double than that of the nickel anode.

Using several different characterization techniques used in catalyst research, two different kinds of nickel particles were observed by King et al. [106]. The larger (0.3−2.0 μm) originated from the NiO particles used to prepare the cermet, whereas the smaller (10−20 nm increasing to ~50 nm after >100 h) were evolved from the YSZ during reduction from solid solution. This evolution was retarded by high reduction temperature and steam contents. Both particles sintered considerably during the first 200 h of operation, the smaller more pronounced to around 50 nm in accordance with theory and observation in [112−114]. It would be interesting to investigate whether the dual particles could also play a role on the functional anode. The activity for steam reforming was observed to decrease by more than an order of magnitude during this initial deactivation period. After the activity had stabilized, there was no difference in turn over frequency for the two particles size indicating that the steam reforming activity was not structure sensitive on the small particles. The experiments were carried out with hydrogen in the methane plus steam feed. Without hydrogen in the inlet, the catalyst deactivated rapidly due to oxidation of nickel. This is an important fact that should be remembered when conducting kinetic studies. Some of the other reported results have relied on back diffusion of hydrogen. Interestingly enough, departures from shift equilibrium were observed on aged catalyst at relatively low temperatures (<750 °C) and high space velocities used in this study.

A Langmuir-Hinshelwood kinetics was proposed by Bebelis and Neophytides [115] but the experiments were carried deep into the carbon formation region (CH_4/H_2O ratios in most cases >>1) so that it is not really relevant

for internal reforming kinetics. The normal first-order dependence on methane partial pressure can, however, be observed for the experiments with $S/C > 1$.

Wei and Iglesia [107] have carried out a series of careful experiments free of mass transfer limitations and temperature gradients and found that the only rate-determining step was the breaking of the first C−H bond. This step is rate determining not only for steam reforming but also for CO_2 reforming and carbon formation. The theory was corroborated by isotopic tracer studies. It appears that there is now a general consensus about the following reaction scheme consisting of nine elementary steps [116]:

$$CH_4(g) + 2^* = CH_3^* + H^* \quad (13.19)$$

$$H_2O(g) + 2^* = OH^* + H^* \quad (13.20)$$

$$OH^* + {}^* = O^* + H^* \quad (13.21)$$

$$CH_3^* + {}^* = CH_2^* + H^* \quad (13.22)$$

$$CH_2^* + {}^* = CH^* + H^* \quad (13.23)$$

$$CH^* + {}^* = C^* + H^* \quad (13.24)$$

$$C^* + O^* = CO^* + {}^* \quad (13.25)$$

$$H^* = 0.5H_2(g) + {}^* \quad (13.26)$$

$$CO^* = CO(g) + {}^* \quad (13.27)$$

This mechanism is proposed by Jones et al. [116] based on first principles calculations (DFT) as well as experimental evidence. The latter, however, shows that CO formation is the rate-determining step at low temperatures ($\approx$500 °C), whereas close to 700 °C, methane dissociation is rate determining. In between, there is no single rate-determining step.

Mogensen et al. [117] have recently published a very thorough discussion of the kinetics in the literature up to 2009. They have also compared the measured reaction rates based on the geometric Ni areas and found surprisingly good agreement between the data at high temperature, despite the different rate equations proposed. The need for further detailed kinetic studies is also discussed in detail.

Timmermann et al. [108] studied both steam reforming of methane and methanation of gas simulating the product from a diesel catalytic partial oxidation reactor using a high performance anode supported cell. They found that a rate equation, which is first order in methane and corrected for the distance to equilibrium, could describe both reforming and methanation equally well assuming the shift reaction in equilibrium. No influence of the other gas constituents was observed. The activation energy found between 600 and 750 °C, 61 kJ/mole, decreased to half that value between 750 and 850 °C. Diffusion limitations were assumed to be the reason for this observation.

Some more qualitative observations on the effect of additives to Ni-YSZ cermets on steam reforming rate have also been reported by Takeguchi et al. [25]. CaO and small amounts of SrO increased the reforming rate. Addition of CaO did, however, decrease the electrochemical performance. Large amounts of SrO almost decimated the reforming activity. Small amounts of MgO decreased the reaction but larger MgO addition promoted the reaction. CeO_2 addition monotonously decreased the reforming rate.

The reforming activity of Ni-YSZ catalyst with 10−80 vol% is slightly better than Ni-SSZ for the same amount of Ni, but this is significantly lower than on a Ni on Al_2O_3 catalysts with 5 vol% Ni probably due to a much better Ni dispersion [33].

13.6.3. The Optimum Reforming Rate

The governing principle for design of SOFC plants will normally be to limit the maximum temperature in the stack so that degradation rate of the most sensitive elements, the metallic interconnects, and coatings do not become excessive. The area specific resistance of the cells will, however, decrease with temperature; so,

the designer will try to devise strategies including flow geometries which will keep the operating temperatures in the entire stack as close to the maximum allowable as possible.

As already pointed out by Hendriksen [118], the rate of methane steam reforming is very often much faster than the electrochemical oxidation of hydrogen. This will lead to steep temperature decreases at the fuel inlet. The average temperature will thus be considerably below the maximum allowable and large mechanical stresses can furthermore develop. The ideal situation would be one where the rate of heat removal by the reforming reaction matched that of the heat generation by hydrogen oxidation so that more or less isothermal conditions would result. By inspecting Eqs (13.4–13.8) at 923 K and 0.8 V, it is observed that the rate of hydrogen generation by Reaction (13.4) is roughly double that of the hydrogen oxidation by Reaction (13.5), e.g., the isothermal operation cannot be achieved throughout the entire fuel path. There is, however, a gross mismatch of the rates at the normal operating temperatures of anode supported cells of 700–800 °C as calculated by Mogensen et al. [117] for a 500 μm thick anode with a nickel content of 50% and a nickel particle size of 1 μm. For a 50/50 methane/steam mixture using the reaction rate expression of Wei and Iglesia [107], they observed that the steam reforming rate is one to two orders of magnitude faster than the electrochemical oxidation.

Various ways of achieving a better match between reforming and hydrogen oxidation rates without sacrificing electrochemical activity has been proposed. Boder and Dittmeyer [105] impregnated copper in their nickel anodes. The electrochemical performance remained almost constant and the reforming rate was reduced by a factor of 10 at 750 °C.

Another way to reduce the extent of the reforming is to operate with very low steam content in the inlet fuel and only let the reaction proceed by the formed water at the TPB. This obviously requires that the part of the anode where the reforming occurs is not prone to carbon formation. The principle, named as gradual internal reforming or GIR, has been studied by Klein et al. [119]. They applied a layer of Ir/CeO_2 on top of a Ni/YSZ cermet. Stable operation was observed for 30 h with dry methane. It should be noted, however, that they started with hydrogen operation before shifting to methane, so the steam reforming could be started with the steam available from that operation mode.

13.7. POISONS FOR SOFC ANODES

13.7.1. Sulfur

Sulfur can be present in gases stemming from gasification of coal or biomass as well as from fuel processing of diesel or jet fuel. The impact on SOFC performance has been gaining increasing attention and more quantitative assessments are emerging. Most of the work has been carried out on nickel-containing anodes, as they still are the optimum choice considering overall economics, performance, and ease of manufacturing.

13.7.2. Thermodynamics of Sulfur Poisoning

It is important to realize that the poisoning effect of sulfur is due to chemisorption and not bulk sulfidation, which would require higher concentrations, namely above 500–1000 ppm of H_2S, than normally occurring in an SOFC operation [120]. The trend toward lower operating temperatures will, however, make bulk sulfidation more likely as illustrated by the calculation for the Ni-O-S system carried out by Lohsoontorn et al. [121] shown in Fig. 13.11.

The discussion above also signifies that care should be exercised when the anode is exposed

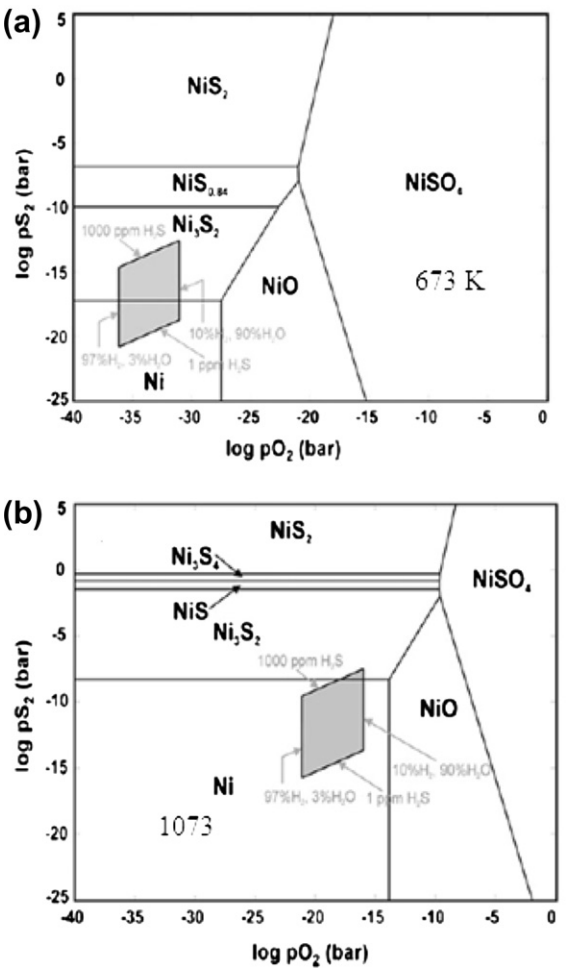

FIGURE 13.11 Phase diagrams for the Ni–O–S system at 673 K (a) and 1073 K (b). *Reprinted with permission from Lohsoontorn et al. [121], Copyright* (2008) Elsevier.

to sulfur containing fuel gas during heating up or cooling down.

The chemisorption of sulfur on nickel has already been described in Chapter 4 and a Temkin-like isotherm has been shown to provide excellent fit to experimental data:

$$\theta_s = 1.45 - 9.53\cdot10^{-5}\cdot T + 4.17\cdot10^{-5}\cdot T \ln\left(\frac{p_{H_2S}}{p_{H_2}}\right) \quad (13.28)$$

Density function theory (DFT) calculations with the appropriate thermodynamic corrections for the gas phase species both for the chemisorption equilibrium and the bulk reaction have also been carried out by Wang and Liu [122]. Galea et al. [123] have carried out similar calculations. A phase diagram (Fig. 13.12) for both the bulk and chemisorption equilibria between H_2S and Ni has been constructed based on these calculations.

The white region represents clean Ni, the blue region adsorbed S on Ni, and the yellow bulk Ni_3S_2. The black line represents the data of Rosenquist [124] that is still considered the most reliable for bulk thermodynamics. The red line is from the DFT calculations of Wang and Liu [122]. The black triangles are the chemisorption results at different surface coverages and finally the red dots are from the SOFC experiments of Matsuzaki and Yasuda [125].

Wang and Liu [122] calculated the variation of adsorption energy as function of surface coverage, which vary from −2.64 eV at 1/16 θ to −1.40 eV at 10/16 θ emphasizing the heterogeneous nature of the nickel surface, which is also shown by the Temkin isotherm.

Raman spectroscopy [126–131] has been used to characterize the surface Ni-S species. The studies should, however, be very carefully executed and preferably be done in situ as the Ni_3S_2 will undergo phase transformation if the sample is cooled down. Moreover, it can very easily be oxidized during handling [129].

13.7.3. Impact of Sulfur with Hydrogen as Fuel

With respect to the impact of sulfur on the electrochemical performance of SOFCs, there is, in general, a consensus in the literature that:

- The deactivation by H_2S increases by lowering temperature,

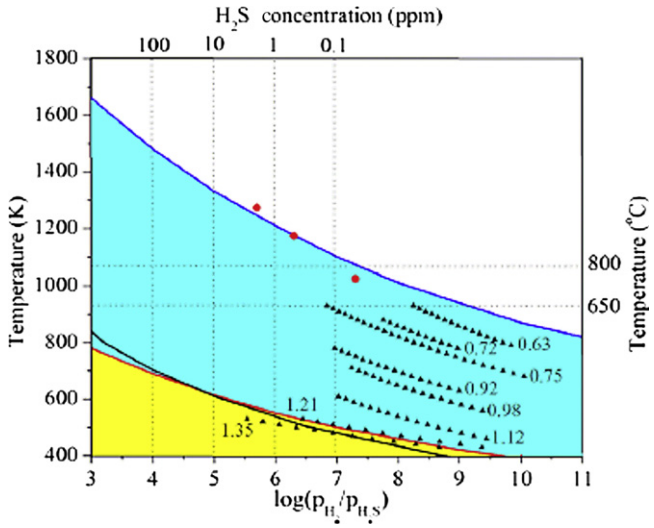

FIGURE 13.12 Phase diagram for H_2S and Ni. *Source: Reprinted with permission from Wand and Liu [122], Copyright (2007) The Electrochemical Society.*

- The effect levels off as the H_2S concentration increases, and
- The impact of sulfur is less at a high current density.

There is also a general agreement that sulfur has an immediate impact on the electrochemical performance of Ni anodes. The long-term effects and the degree of recovery achievable after sulfur is removed from the feed stream again remain, however, unclear. Some recent results have, however, shown [132] that H_2S leads to microstructure reconstruction seen as terracing which could be the initial step to nickel agglomeration. The effect was, however, also seen in the presence of steam. The impact of sulfur is limited to the anode, but its deactivating effects also changes the operating conditions of the cathode and for complete stacks, the temperature profile will be affected and will have to be taken into account. Impedance spectroscopy can unravel some of these issues.

Matsuzaki and Yasuda [125] varied the H_2S concentration from 0.02 to 15 ppm and used temperatures of 750, 900, and 1000 °C. The polarization resistance and the overvoltage started to increase when the H_2S concentration exceeded 0.05, 0.5, and 2 ppm at 750, 900, and 1000 °C, respectively. The time to attain steady state was found to be almost independent of the sulfur concentration but depend only on temperature. The anode recovered completely when pure fuel was used again.

Stolten et al. [133] carried out tests using nickel, zirconia, and some ceria anodes at 950 °C with H_2/H_2O mixtures and with synthetic coal gas plus water. The degradation rate at 150 mA/cm^2 in a 2600 h test was less than 1%/1000 h. The power output was reduced only by 2% for H_2S concentrations up to 10 ppm.

Zha et al. [134] studied the influence of H_2S concentration, cell voltage, time of exposure, and temperature on Ni-YSZ anodes. With 50 ppm H_2S at 800 °C and constant cell voltage of 0.6 V, a drop of 16.7% was observed within minutes of the introduction of sulfur followed by slow, continuous further drop up to 4% during the next 120 h. When clean H_2/N_2 was introduced, the performance improved

immediately followed by a gradual recovery, which was only 96% complete. With a clean fuel, it had been shown that the cells were completely stable at 800 °C after an initial conditioning at 900 °C. However, with 2 ppm H_2S, the degradation was only 12.7%. Recovery was quicker and more complete with only 1% permanent loss in performance. Short-term exposure of 6 min to 2 ppm H_2S could be completely recovered, thus a spike of low-level sulfur, due to upsets, should not cause permanent damage.

The immediate impact of H_2S as function of concentration and temperature is illustrated in Fig. 13.13. Even 0.18 ppm H_2S caused a drop in performance at all temperatures.

Hansen [135] have analyzed the data of Zha et al. [134] using the Temkin isotherm in Eq. (13.28). In Fig. 13.14, the cell performance drop in percent is plotted versus θ_s.

The performance loss in percent, *Pl*, of the cells can be very well described by Eq. (13.29):

$$Pl = k^*(\theta_s - \theta_{min}) = 53.8\theta_s - 32.2 \quad (13.29)$$

with $R^2 = 0.985$. Considering the wide span in temperatures and H_2S concentration,

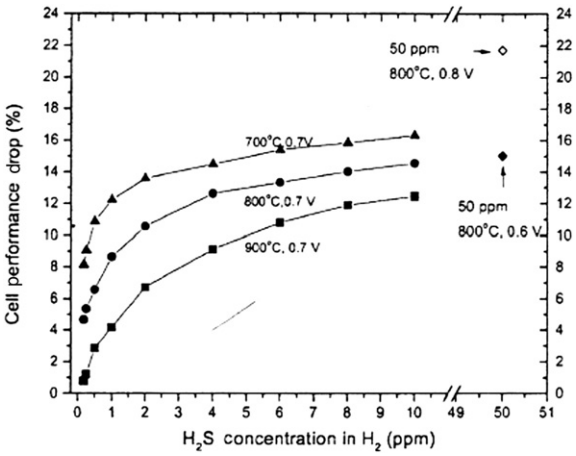

FIGURE 13.13 Percentage drop in current density as function of H_2S concentration and temperature. *Source: Reprinted with permission from Zha et al. [134], Copyright (2007) The Electrochemical Society.*

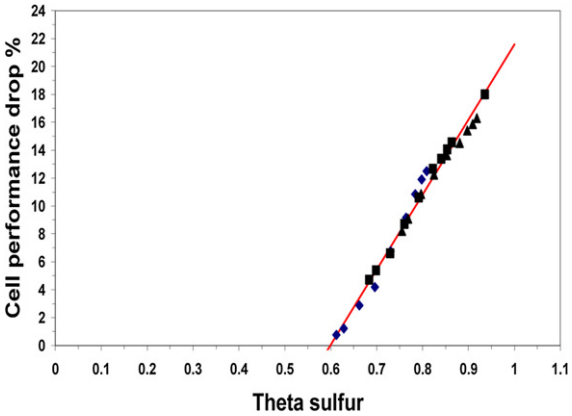

FIGURE 13.14 Cell performance drop versus sulfur coverage. *Source: Reprinted with permission from Hansen [135], Copyright (2008) The Electrochemical Society.*

this indicates that the performance drop is strongly related to sulfur chemisorption coverage of the nickel in the anode. Furthermore, it also shows that results from catalysis research can be used with good results on the electrochemistry.

Using Eqs (13.28) and (13.29) to correlate the data of Matsuzaki and Yasuda [125], it was calculated by Hansen [135] that the effect of sulfur was noticed at a θ_s of 0.645, 0.64, and 0.645 at 750, 900, and 1000 °C, respectively, which is in very good accordance with the findings shown in Fig. 13.14. Hansen [135] also found that Eq. (13.29) could correlate the findings of Stolten et al. [133] again showing that the important parameter is the ratio of H_2S to H_2, not the absolute H_2 pressure.

The influence of current density on sulfur sensitivity appears at first sight seems rather confusing. It depends on whether the measurements are carried out in the galvanostatic mode (constant cell current) or potentiostatic mode (constant cell voltage). If the stack is modeled as an equivalent circuit this can, however, be understood as described by Cheng et al. [136]. They carried out experiments both in the galvanostatic and potentiostatic mode at 800 °C. The relative increase in overall internal

cell resistance was calculated and it was demonstrated that the apparent contradiction concerning the sulfur impact as a function of current density is resolved if the influence of sulfur is correlated with the increase in cell resistance instead of power loss.

Hansen [135] also used the data of Cheng et al. [136] and correlated them using Eq. (13.28) and an equation similar to Eq. (13.20). The data were correlated very well by using these equations. The slopes of the curves are very similar, but the intercept with the abscissa, θ_{min}, increases with increasing current density. Rasmussen and Hagen [137] found by measuring in plane voltage changes that the sulfur poisoning of Ni anodes moved as a front through the cells.

Sasaki et al. [138,139] tested a range of Ni anodes containing either YSZ or SSZ. The effect of a number of additives was furthermore screened. The effect of H_2S was studied in both hydrogen and H_2/CO plus steam mixtures. The results are somewhat difficult to interpret. As an example, severe deactivation was observed at 850 °C already with 5 ppm H_2S in hydrogen-containing gas, which is not in line with other indications in the literature. An interesting observation is, however, that the cells almost completely ceased to function as the CO:H_2 ratio reached 9:1 in a gas with 5 ppm H_2S at 1000 °C. This could perhaps be explained by poisoning of the shift activity of the anode (as Kuhn et al. [140] observed with TPR studies on crushed anodes) and by a very low CO oxidation activity in the presence of H_2S. Of particular interest was the better sulfur tolerance of the anodes with SSZ. They survived 100 ppm H_2S exposure in hydrogen at 800 °C. In contrast, the YSZ-based anodes died completely with 20 ppm H_2S at the same conditions. This was ascribed to the better ionic conduction of SSZ compared to YSZ. Of the many additives to the anode (by impregnation) Ce, Y, La, and Mg turned out to be the best.

The carbon deposition resistant anodes based on ceria-copper have also been shown to be sulfur tolerant. He et al. [141] showed that the performance was stable in potentiostatic test in H_2 up to 450 ppm H_2S at 800 °C. Above that, the performance dropped dramatically at 900 ppm. This was ascribed to the formation of Ce_2O_2S which would be the stable form above 450 ppm.

Recently, Liu et al. [58] have also shown excellent resistance against sulfur poisoning using a barium zirconate codoped with Y and Yb: $BaZr_{0.1}Ce_{0.7}Y_{0.2-x}Yb_xO_{3-\delta}$ (BZCYYb). With a Ni-BZCYYb and an SmDC as electrolyte with a current density of 700 mA/cm^2 at 750 °C even 50 ppm H_2S did not affect the performance in hydrogen for 50 h.

13.7.4. Impact of Sulfur with Hydrogen and Carbon Monoxide as Fuel

The data of Sasaki et al. [138,139] and Kuhn et al. [140] indicate a stronger impact on the shift reaction than on the electrochemical hydrogen oxidation. This is also true in experiments conducted by He et al. [142] with CO as feed for Ni anodes. When hydrogen was used as a fuel, 1 ppm H_2S caused the normal moderate drop in performance but when CO, N_2, and steam mixtures (40:40:20 mole%) were used, the cells failed catastrophically when 1 ppm H_2S was introduced. The author evidently do not reflect upon the fact that there is a potential for bulk sulfidation of the nickel, but it is also a strong indication that the shift reaction is severely retarded by small amounts of sulfur. With the addition of sulfur tolerant shift functionality (metals plus ceria) to the Ni anodes, the impact of sulfur was modest.

13.7.5. Impact of Sulfur with Coal Gas as Fuel

Bayless and coworkers [143,144] used SOFCo cells with Ni-GDC anodes in synthetic coal gas

both in cell tests and in short stack tests at 850 °C. The cells did not show any degradation for a period of 290 h. If 200−240 ppm H_2S was added, there was an immediate 6−8% power loss followed by a slower degradation to 10−12.5% total loss.

13.7.6. Impact of Sulfur with Synthesis Gas from Biomass Gasification

Rietveld and coworkers [60,145,146] also used Ni/GDC in studies to study the influence of the gas composition including sulfur and other contaminants in simulated biogas. They could not observe any effect up to 9 ppm H_2S at 850 °C, but from the results obtained from methane-containing gases it could be seen that the reforming activity was severely affected and the fuel utilization had to be lowered from 80 to 30−40%.

Hofmann et al. [147] reported results using a real wood gasifier. These are the only data where the sulfur compound is COS. The small amount of COS − ~0.22 ppm − will, however, most probably be transformed to H_2S in the anode, which was of the Ni-GDC type. The gas contained a very low amount, 0.17 mg/Nm^3, of tars. During the 150 h of operation at 850 °C, neither the negative influence of the sulfur nor of tar could be detected.

Norheim et al. [148] used anode-supported cells from FZ Jülich to test the impact of sulfur in simulated biogas (Hydrogen with 33−40% CO_2). Short-term exposures of one day of sulfur levels up to 240 ppm at 800 °C caused a completely reversible increase in the cell ASR of up to 18%.

13.7.7. Impact of Sulfur with Methane-Containing Fuel

Sishtla et al. [149] carried out tests at 800 °C with a simulated gas from a plant with externally reformed natural gas: 76% H_2, 20% CO_2, and 4% CH_4 with a S/C of 2.2. When adding 2.6 ppm H_2S to the dry gas, the baseline of 675 mV at 300 mA/cm^2 dropped to 590 mV. The methane conversion decreased from 97 to 54%. After five days, H_2S was removed from the feed and the reforming activity recovered within 24 h. It took 172 h (including the last 72 h at OCV) to recover fully the electrochemical performance.

Silversand et al. [150] used a CPOX reactor with commercial diesel (1 ppm S) and jet fuel (65 ppm S as feed) to produce gas which was then desulfurized and hydrogenated and fed to a 10-cell stack. In a second series of tests, H_2S (0−50 ppm) was added to a synthetic CPOX gas containing 2% CH_4. The stack performed well with the desulfurized gases. Even at 700 °C, the electrochemistry seemed to be relatively unaffected by the sulfur with only a 10% drop in power output. The deactivating effect on the reforming activity could, however, be observed within minutes. It was also observed that when the current draw was increased, the exit of H_2S from the stack decreased. This was ascribed to electrochemical oxidation of H_2S to SO_2 which was not analyzed. The data was further analyzed especially concerning the reforming aspects in [151].

Noponen et al. [152,153] tested three different cell types from HTc, FZ Jülich, and ECN. Hydrogen and gas from an ATR was used. The natural gas contained 3−9 ppm tetrahydrothiophene. Fluctuations in S content caused the gas composition from the ATR and stack performance to fluctuate as well. Tests were performed with and without desulfurization by ZnO at 400 °C. The cells behaved quite differently. No degradation could be observed in hydrogen, but in reformate gas the ASR increased by 30−64%. The effect of sulfur seemed, however, to be rather small.

13.7.8. Impact of Sulfur with Biogas as Fuel

Xu et al. [47] observed catastrophic failure of their anode supported cells at 850 °C with

the combined CO_2 (dry) and steam reforming case (32% CH_4, 48% H_2O, 20% CO_2) 1.5 h after the introduction of 20 ppm H_2S. Post-mortem inspection revealed a completely delaminated anode and a green pattern indicating oxidized nickel. Coating the anode with 100 μm of Ni-CeO_2 prolonged the time to deactivate the cell completely but more significantly also made it possible to recover a considerable part of the performance after H_2S was removed from the synthesis gas. When air was added to the simulated biogas, performance could be recovered even with the uncoated anode. A second poisoning cycle leads, however, to irreversible loss of performance. The ceria-coated cells could withstand several poisoning cycles.

Shiratori et al. [50] observed a 9% drop in voltage and 40% lower internal reforming rate for their Ni-SSZ anodes at 1000 °C and current draw of 200 mA/cm^2 from the feed containing 1 ppm H_2S and CH_4 to CO_2 ratio of 1:5. Complete recovery of performance was observed after 4 h. At 800 °C, with 1 ppm H_2S initial voltage drop was 20% and reforming rate decreased by 80%. However, the performance continued to decrease further. It took 50 h for the performance to recover after H_2S addition was stopped. At 800 °C and a current density of 50 mA/cm^2, introduction of 790 ppm H_2S, like in raw biogas, caused complete loss of performance.

Laycock et al. [52] observed that methane conversion ceased completely within 4 h with addition of 5 ppm H_2S to simulated biogas. Above 900 °C, there was still a certain methane conversion and at 1000 °C the conversion was hardly affected by the 5 ppm H_2S. Addition of dopants could retard but not eliminate the effect of H_2S and ceria proved to be better than Au or Hf.

Recalling that the steam-reforming activity according to Rostrup-Nielsen [154] is proportional to the fraction of free sites not covered by sulfur to the 3rd power, the above findings can be rationalized. The impact of sulfur is much more severe in the case of biogas or other methane-containing gases because steam reforming is impaired much more severely than the hydrogen oxidation which only impacted linearly by the sulfur coverage at least at intermediate coverages according to Hansen [135]. If an SOFC cell is operated at constant current density, with predominantly methane as feed, introduction of sulfur can lead to fuel starvation due to lack of hydrogen provided by steam reforming. In severe cases, this can result in oxidation of the nickel in the anode as observed by Xu et al. [47]. The relatively mild impact of sulfur on the cells studied by Shiratori et al. [50] can probably be explained by the high operating temperatures and the presence of GDC which could result in oxidation of part of the hydrogen sulfide.

13.7.9. Other SOFC Anode Poisons

The development of SOFC technology for large coal based integrated gasification fuel cell (IGFC) gas turbine hybrids has been the focus area of the Solid state Energy Conversion Alliance (SECA) program of the U.S. Department of Energy. Coal can contain almost all the elements in the periodic table, some of them being potential, strong poisons for the SOFC anodes.

Trembly et al. [155] have, by thermodynamic calculations, narrowed down the number of potential harmful substances in the gas from a warm gas clean up unit by investigating the gas–solid partitioning as function of the likely operating temperatures and pressures (200–500 °C and 0.1–1.5 MPa). They found that traces of Cd, Pb, Hg, Se, Sb, As, and P could pass through the warm gas clean up but that only the last three would pose a risk for Ni-, ZrO_2-, and Y_2O_3-based anodes. The traces would not react with the ceramic components of the anodes, react only with Ni. Martinez et al. [156] extended the analysis to comprise 15

different gasifier types and found similar results. Cayan et al. [157] have reviewed the literature on coal impurity impacts up to 2008.

13.7.9.1. Chlorine

Although most of the chlorine in gasification synthesis gas can be removed by water scrubbing, substantial amounts can pass through. From a warm gas clean up around 1 ppm is estimated to be the concentration of the HCl slip [158]. Biogas from anaerobic digestion can also contain significant amounts of chlorine.

The literature on chlorine poisoning of Ni anodes is somewhat ambiguous. One of the most comprehensive studies done by Marina et al. [159] found that the poisoning by chlorine was completely reversible with a response time of only hours and the highest effect at lower temperatures in the range studied (650–850 °C). They found no impact of operating voltage or current density. There was no evidence of microstructural changes of the anode structure as studied using SEM, energy dispersive (EDS), or by Auger electron spectroscopy (AES). Their thermodynamic calculations also ruled out the possibility of formation of volatile $NiCl_2$ even if the highest HCl concentration of 800 ppm is used. The performance decline due to chlorine was almost linear with concentration up to 100 ppm, thereafter it became constant. Marina et al. [159] used anode-supported cells with Ni/YSZ anodes and 8 mol% YSZ electrolyte and LSM cathodes but found similar effects using electrolyte-supported cells [160]. In the latter study, they also found that small amounts of chlorine actually improved the electrochemical performance, which was ascribed to volatilization of Mn chloride species at the TPB. The manganese had diffused through the electrolyte during processing of the cells. Marina et al. [159] interpreted the impact of chlorine as a simple chemisorption phenomena in line with that of Trembly et al. [158]. Trembly et al. [158] used electrolyte-supported cells with an SSZ electrolyte and a Ni-GDC plus Ni-8YSZ anode and found with 130 ppm HCl, more substantial loss of performance (up to 13–51% at 800 and 900 °C) than Marina et al. [159] which only noted a 5–7% performance decline even with 800 ppm HCl at 700 °C. The performance of cells studied by Trembly et al. [158] also declined for around 100 h before they stabilized.

Haga et al. [161,162] not only used SSZ-based electrolyte-supported cells but also Ni-SSZ anodes. They used Cl_2 instead of HCl, although the stable form of chlorine in synthesis gas is HCl. Their thermodynamic calculations for the Ni-O-H-Cl system showed that $NiCl_2$ could be formed with chlorine concentration as low as 0.1 and 10 ppm at 800 and 1000 °C, respectively. This is in contrast to similar calculations made by all others [158,159,163,164]. Haga et al. [161,162] found significant degradation of performance: 1.7 and 13% per 100 h for 100 and 1000 ppm Cl_2, respectively as well as evidence of significant microstructural change by SEM showing considerable growth of nickel particles on the SSZ surfaces.

Bao et al. [163] tested the impact of both HCl and CH_3Cl on anode supported Ni-YSZ/YSZ/LSM cells. With 40 ppm, no degradation for 150 h was noticed with HCl both at 750 and 800 °C, but with methyl chloride 10% degradation could be observed after the performance had been stable for 100 h. At 800 °C, the performance was stable for 150 h. Tests with 2.5 ppm CH_3Cl at 750 °C showed no degradation for the first 100 h but then a steady degradation around 6.3% was observed for the next 400 h, but these results were later ascribed to a defect in the test cell [165].

A commercial Ni-YSZ/YSZ/LSM anode-supported cell with a relatively thick anode support of 0.8–0.9 mm was exposed by Xu et al. [164] to 100 ppm HCl at 800 and 850 °C for 300 and 150 h, respectively. Operating the cell galvanostatic at 0.5 A/cm^2, a cell voltage loss of 1.6 and 1.5% was observed in these two time periods. The SEM micrographs showed

the Ni surface to be rather scabrous after the HCl exposure, whereas the YSZ was unaffected.

The data reported in the literature seem somewhat conflicting but it seems safe to conclude that chlorine interacts with the anodes by chemisorption on the nickel and that the effect is much smaller than that of sulfur. The long-term effects at the presently used operating temperatures around 700–800 °C are not well documented or understood.

13.7.9.2. Phosphorus

Phosphorus is one of the most troublesome poisons for nickel-based SOFC anodes, because it causes not only both bulk transformations of nickel but also acts by chemisorption on nickel at the TPB. Kishimoto et al. [166] have calculated and discussed a generalized Ellingham diagram for the Ni-O-P-H system.

A symmetrical half cell with Ni-YSZ was exposed to 20 ppm of PH_3 in synthetic coal gas at 900 °C both at OCV and with a 0.7 V bias by Zhi et al. [167]. They observed a very dramatic and rapid increase in resistance due to the phosphorus exposure. Post-mortem analyses by X-ray photoelectron spectroscopy (XPS) and X-ray diffraction (XRD) revealed the formation of both $Ni_3(PO_4)_2$ and ZrP_2O_7 the amount of which increased when the electrical field was applied. These compounds have not been observed by later research but it should be noted that Zhi et al. [167] operated at a rather high operating temperature and with symmetrical cells.

Demircan et al. [168] found a degradation rate of around 2% per hour when exposing a commercial cell to 10 ppm PH_3 at 800 °C in synthetic coal gas. The XRD analyses revealed that Ni_5P_2 had been formed. A weak peak was attributed to P_2O_5 but no nickel or zirconia phosphates were observed. Demircan et al. [169] in a later paper varied the current densities and over potentials. They found formation of Ni_3P but no correlation between degradation rates, which were in the order of 0.2–0.7% per hour, and over potential or current density.

Bao et al. [163] observed an immediate 5–6% decrease in performance for the first 20 h when anode-supported Ni-YSZ cells were exposed to 35 ppm PH_3 at 750 °C after which the degradation rate became very slow. At 800 °C, they saw a steady degradation rate of around 0.1% per hour. With only 0.5 ppm PH_3 at 750 °C, the voltage dropped to around half after 800 h exposure [170].

Marina et al. [171] studied the impact of 0.5–10 ppm phosphorus as phosphine on both electrolyte- and anode-supported Ni-YSZ cells from 700 to 800 °C for up to 1700 h. Their findings are summarized in Fig. 13.15 for the anode-supported cells.

Several nickel phosphide species were found in post-mortem electron back scatter diffraction (EBSD) analyses: Ni_3P, Ni_5P_2, $Ni_{12}P_5$, and Ni_2P. Agglomeration and coalescence of the larger nickel phosphide particles were observed. This phosphide formation caused loss of percolation with consequent

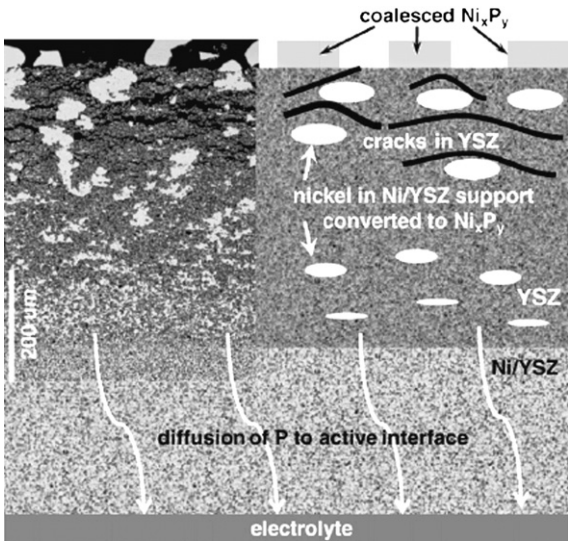

FIGURE 13.15 Diagram of reactions of phosphorus with Ni/YSZ anode. Ni phosphide phases forms in the outer portions. Surface diffusion to TPB occurs simultaneously. In the upper left corner is inserted a SEM image after 470 h operation at 800 °C with 5 ppm PH_3. *Reprinted with permission from Marina et al. [171], Copyright (2010) Elsevier.*

dramatic increases in ohmic resistance of the cells, although the phosphides are good electronic conductors. Surface adsorption of phosphorus in parts of the anode where bulk phosphides were not present was confirmed by both XPS and time of flight-secondary ion mass spectroscopy. This surface adsorption was also the explanation for the immediate drop in performance due to the increase in electrodic resistance when phosphines were introduced. The degradation rate due to the chemisorption was, however, lower than observed with sulfur. The fugacity of phosphorus in the anode chamber is controlled by the vapor pressure above Ni_3P according to the interpretation of the results by Marina et al. [171]. Phosphorus should be reduced to the ppb range to give acceptable lifetimes.

The thermodynamic calculations of Marina et al. [171] showed that the formation of bulk phosphide phases were possible in a wide temperature range even in the ppb range. The phase boundary calculation are, however, very sensitive to the choice of thermodynamic parameters, which are not sufficiently well known. Inclusion of parameters for HPO_2 and HPO_3 lead to the conclusion that HPO_2 should be the dominant gas phase species but also that formation of Ni_2P should not be possible in contradiction to the experimental findings. The nickel and zirconium phosphate reaction products found by others could not be detected by all the surface and bulk analysis techniques employed by Marina et al. [171].

Finite element stress analyses [172] showed that the volume expansion caused by the nickel phosphide formation could explain the observed local mechanical failures of the anodes.

Gong et al. [173] also observed irreversible degradation of nickel-free cells with a $LaSr_2Fe_2CrO_{9-\delta}$ anode when exposed to 5–20 ppm PH_3. An initial slow degradation was observed followed by a very rapid and complete degradation. The XRD showed formation of FeP_x and $LaPO_4$. The initial degradation was ascribed to chemisorptions, whereas the onset of rapid degradation was ascribed when most or all of Fe in the anode was converted to phosphide.

13.7.9.3. *Arsenic*

Arsenic, like phosphorus, reacts with nickel to form new solid phases, but do not apparently interact via chemisorption. The poisoning pattern is thus markedly different from that of phosphorus because little impact is seen before a considerable part of the nickel in the anodes is consumed in the reaction with arsenic, which will be in the form of AsH_3 at anode conditions.

Very little impact of arsine was thus noted by Trembly et al. [174] in tests with 1–2 ppm AsH_3 at both 750 and 800 °C. No nickel-arsenic bulk transformation was observed. There was no influence of the applied current density. With only 0.1 ppm AsH_3 in a 800 h experiment, a small amount of NiAs on the outmost surface was identified by XRD. A drop in cell voltage of around 9% per 1000 h was observed at 0.25 A/cm^2. The authors noted that the kinetics of arsine interaction with nickel appeared to be slow.

Bao et al. [163] observed complete loss of performance after 120 h exposure to 10 ppm AsH_3 at 800 °C which was ascribed to transformation and detachment of the nickel current collector. In addition, 64 wt% As was found on the top part of the anode. It is observed that 0.5 ppm AsH_3 at 750 °C showed no impact even after 1000 h, but 1 ppm caused the performance to start dropping after 700 h.

Coyle et al. [175] at Pacific Northwest National Laboratory have carried out a comprehensive study of the impact of arsine 0–10 ppm at 700–800 °C both on electrolyte- and anode-supported cells as well as Ni-YSZ coupons. They observed more or less “sudden death” of the cells depending on arsine concentration and temperature. There was no dependence on

either current density or fuel utilization. The arsine reacted rapidly with the Ni forming a sharp front moving through the anode creating Ni_5S_2 and $Ni_{11}As_8$, the latter only observed at lower temperatures. For the anode-supported cells, the degradation was due to loss of electronic conductivity as the nickel was converted to arsenide which migrated to the surface forming large grains. Their thermodynamic calculations indicated that nickel arsenides could form even at subppb concentrations and that a limit around 10 ppb would be needed to achieve 40,000 h of lifetime for the stacks.

13.7.9.4. Selenium

The effects of selenium resembles to a certain extent those of sulfur as the effect sets in immediately and appear to be almost completely reversible although less so than with sulfur [176]. A loss of 3–4% power density was observed with 0.5 ppm H_2Se, whereas 5 ppm caused a 20–25% loss at 800 °C. Interestingly, a clear effect of power density was observed by Marina et al. [171] with 0.5 ppm at 700 °C. In contrast to sulfur, the impact of selenium appears to be more severe at the higher current density. At 0.4 A/cm^2 and above, the performance became oscillatory and complete irreversible failure was observed. The SEM/EDX confirmed the presence of bulk nickel selenides at the TPB [177].

13.7.9.5. Antimony

At the 8 ppm level, antimony was reported to have a very limited impact on performance on anode supported at 750–850 °C up to 100 h [163]. There was some impact at high current densities. On the other hand, Marina et al. have observed rapid degradation of electrolyte-supported cells in the presence of 1 ppm at 800 °C [177] and surface transformation to Ni_3Sb was observed by SEM at 800 °C. So, perhaps, the exposure time for the anode supported cell experiments has been to short.

13.7.9.6. Cadmium

No effect of cadmium at the 5 ppm level was detected at 800 °C, but significant loss of performance was observed at 850 °C. More studies seem to be indicated [163].

13.7.9.7. Zinc and mercury

Neither zinc nor mercury seems to have any detrimental effects on SOFC anode performance at least at the 7–9 ppm level for a few hundred hours [163].

13.7.9.8. Tars

Tars can decrease the electrochemical performance in a subtle way as described by Dekker et al. [57]. The presence of naphthalene decreased the performance of CGO electrodes at 850 °C, because the methane steam reforming rate was decreased as illustrated in Fig. 13.16. The cell voltage dropped at the same time to around 5%. Pyrene had an even stronger impact, whereas toluene had no impact.

Naphthalene per se did not have any impact on the electrochemistry because there was no drop in cell performance if the naphthalene was tested in only hydrogen-containing gas. The tars probably act by strong adsorption to the nickel retarding methane reforming. The above discussion illustrates the benefits of analyzing the anode for gases, which is seldom done.

13.7.9.9. Synergistic Effects

As pointed out by Bao et al. [165], these different effects are not necessarily additive. They tested different combinations of poisons in the 0.5–2 ppm range on anode supported Ni-YSZ cells galvanostatically at 0.222 A/cm^2 at 750 °C. They observed that the presence of 1–1.3 ppm H_2S accelerated the permanent degradation caused by PH_3 and AsH_3. The explanation offered was that a lowering of the melting point of the phosphides or arsenides formed by the presence of sulfur. Nanowhiskers

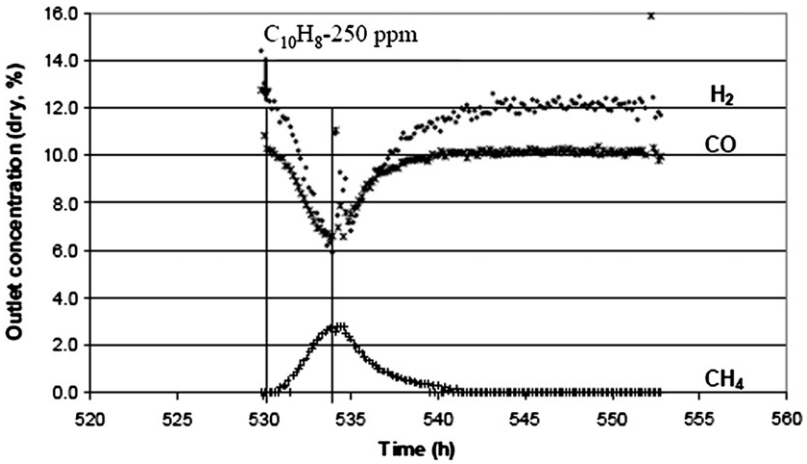

FIGURE 13.16 Influence of naphthalene on the anode off gas concentrations. The feed gas contained 4% methane. *Reprinted with permission of Dekker et al. [57], Copyright (2007) The Electrochemical Society.*

of nickel/phosphorus with rounded tips were observed when sulfur was present.

Addition of methyl chloride along with arsine or phosphine stabilized or even improved performance. The higher the phosphine concentration the more the chlorine was needed to counteract the degradation by phosphorus. The beneficial effect of chlorine was less pronounced when all four poisons were present simultaneously.

Xu et al. [178] also observed that the presence of 100 ppm Cl_2 could delay the impact of adding 20 ppm H_2S to biogas.

13.7.10. Summing Up: Impact of Poisons on Nickel-based SOFC Anodes

The impact of poisons on the nickel anodes can be divided into different classes depending on whether the interaction with nickel is primarily by chemisorption on the nickel or by bulk transformation forming new compounds or solid solutions. Furthermore, current density, over potential, or fuel utilization can have an influence on the impact of the poisoning. An attempt has been made to classify the poisons according to these criteria in the form of Table 13.5

Arsenic acts purely by transforming the nickel into arsenides, depleting the anode of metallic nickel eventually leading to complete cell failure due to loss of percolation. The arsenides/nickel front is extremely sharp. Phosphorus not only acts by bulk transformation but also by chemisorption of phosphorus vapor species defined by the vapor pressure above Ni_3P. Chlorine acts like sulfur by blocking the active sites on nickel by chemisorption. Sulfur is the only poison, where the impact is lower at higher current densities.

13.8. CONCLUDING REMARKS

From the above discussion, it is evident that a great deal of progress has been made, but some problem areas remain to be solved in order to make full use of the benefits of internal reforming. These are mainly the propensity to form carbon and the susceptibility to sulfur in the most commonly used anode materials. Although promising new solutions seem to evolve, long-term stability and ruggedness in real stack operation remain to be proven. There is also a lack of fundamental understanding of the mechanisms. The mechanisms of reactions in high temperature fuel cells' anodes are a complex interplay between catalysis and electrochemistry. Even

TABLE 13.5 Classification of Anode Poisons

Compound	Gas phase species	Bulk compounds	Chemisorption	Bulk Transformation	Reversible	Impact of Current Density
Sulfur	H_2S COS	Ni_3S_2	Yes	(No)	Yes	Yes
Chlorine	HCl CH_3Cl		Yes	No	Yes	No
Phosphorus	PH_3	Ni_3P, Ni_5P_2, $Ni_{12}P_5$, Ni_2P	Yes	Yes	No	No
Arsenic	AsH_3 As_2	Ni_5As_2 $Ni_{11}As_8$	No	Yes	No	No
Antimony	SbO	Ni_3Sb	?	?	?	Yes
Selenium	H_2Se AsSe, PbSe	NiSe	Yes	Yes	(Yes)	Yes

for the simplest reaction, the electrochemical oxidation of hydrogen at the three phase boundaries, the mechanism remains controversial [179]. The only thing agreed upon is: "Unfortunately, fundamental insight into these mechanisms is rather limited."

There is considerable controversy about, which elementary charge transfer steps are involved. The following principal pathways have been proposed: (1) Oxygen spill over from electrolyte to Ni. A variant is hydroxyl spill over. (2) Hydrogen spill over, where hydrogen either hops to an oxygen ion site on the YSZ or a hydroxyl site. (3) Interstitial hydrogen transfer, where hydrogen adsorbs on nickel and forms interstitial hydrogen in the metal and interstitial protons in the YSZ phase reacts with O^2 and forms water which desorbs from the YSZ, and finally (4) Oxygen evolution in the gas phase. This mechanistic scheme is a variant of the oxygen spill over mechanisms but assumes that molecular oxygen is formed in the gas phase in the anode space.

These proposals remain speculative. The mechanism(s) behind the crucial resistance to sulfur and carbon deposition is even more unclear, but it is interesting to note that the anodes tolerant to sulfur poisoning also possess resistance to carbon formation. It is also evident that operation at high current densities alleviates the problems with sulfur and carbon. It has been speculated [58,135,136] that the resistance is imparted by different abilities to oxidize the sulfur and carbon at the TPB. This ability is influenced by the choice of electrode material and operating conditions, but quantitative description is lacking.

If the full arsenal of characterization techniques, modeling tools, and fundamental understandings from electrochemistry and material sciences as well as those used in surface science and the heterogeneous catalysis fields are brought to bear on the anode (and total cell and stack), development breakthroughs are likely to increase the speed toward commercialization of high temperature fuel cells.

References

[1] Krumpelt M, Ackerman JP, Fee DC, Herceg JE, Slack C, Lwin Y. Advanced fuel cell concepts for the 0.1 to 100 MW range. Proc Am Power Conf 1983;45:470–3.

[2] Patel PS. Assessment of a 6500-btu/kwh heat rate dispersed generator final report, EPRI-EM-3307, project 1041–12, final report; 1983.

[3] Christiansen N, Hansen JB, Holm-Larsen H, Jørgensen MJ, Wandel M, Hendriksen PV, et al. Status of development and manufacture of solid oxide fuel cells at topsoe fuel cell A/S and Risø DTU. ECS trans 2009;25:133–42.
[4] Tucker MC. Progress in metal-supported solid oxide fuel cells: a review. J Power Sources 2010;195:4570–82.
[5] Clarke SH, Dicks AL, Pointon K, Smith TA, Swann A. Catalytic aspects of the steam reforming of hydrocarbons in internal reforming fuel cells. Catal Today 1997;38:411–23.
[6] Dicks AL. Advances in catalysts for internal reforming in high temperature fuel cells. J Power Sources 1998;71:111–22.
[7] Gorte RJ. Recent developments towards commercialization of solid oxide fuel cells. AIChE J 2005;51:2377–81.
[8] Gross MD, Vohs JM, Gorte RJ. Recent progress in SOFC anodes for direct utilization of hydrocarbons. J Mater Chem 2007;17:3071–7.
[9] Ivers-Tiffée E, Timmermann H, Leonide A, Menzler NH, Malzbender J. In: Vielstich W, Yokokawa H, Gasteiger HA, editors. Handbook of fuel cells; fundamentals, technology and applications. Chichester: Wiley; 2009. p. 933–57.
[10] McIntosh S, Gorte RJ. Direct hydrocarbon solid oxide fuel cells. Chem Rev 2004;104:4845–65.
[11] Zhu WZ, Deevi SC. A review on the status of anode materials for solid oxide fuel cells. Mater Sci Eng A 5-12-2003;362:228–39.
[12] Cimenti M, Hill JM. Direct utilization of liquid fuels in SOFC for portable applications: challenges for the selection of alternative anodes. Energies 2009;2: 377–410.
[13] Kopinke FD, Zimmermann G, Nowak S. On the mechanism of coke formation in steam cracking–conclusions from results obtained by tracer experiments. Carbon 1988;26:117–24.
[14] Kopinke FD, Zimmermann G, Reyniers GC, Froment GF. Relative rates of coke formation from hydrocarbons in steam cracking of naphtha. 2. Paraffins, naphthenes, mono-, di-, and cycloolefins, and acetylenes. Ind Eng Chem Res 1993;32:56–61.
[15] Kopinke FD, Zimmermann G, Reyniers GC, Froment GF. Relative rates of coke formation from hydrocarbons in steam cracking of naphtha. 3. Aromatic hydrocarbons. Ind Eng Chem Res 1993;32:2620–5.
[16] Gupta GK, Dean AM, Ahn K, Gorte RJ. Comparison of conversion and deposit formation of ethanol and butane under SOFC conditions. J Power Sources 2006;158:497–503.
[17] Gupta GK, Marda JR, Dean AM, Colclasure AM, Zhu H, Kee RJ. Performance predictions of a tubular SOFC operating on a partially reformed JP-8 surrogate. J Power Sources 2006;162:553–62.
[18] Pomfret MB, Marda J, Jackson GS, Eichhorn BW, Dean AM, Walker RA. Hydrocarbon fuels in solid oxide fuel cells: in situ Raman studies of graphite formation and oxidation. J Phys Chem C 2008; 112:5232–40.
[19] Randolph KL, Dean AM. Hydrocarbon fuel effects in solid-oxide fuel cell operation: an experimental and modeling study of n-hexane pyrolysis. Phys Chem Chem Phys 2007;9:4245–58.
[20] Sheng CY, Dean AM. Importance of gas-phase kinetics within the anode channel of a solid-oxide fuel cell. J Phys Chem A 2004;108:3772–83.
[21] Walters KM, Dean AM, Zhu H, Kee RJ. Homogeneous kinetics and equilibrium predictions of coking propensity in the anode channels of direct oxidation solid-oxide fuel cells using dry natural gas. J Power Sources 20-9-2003;123:182–9.
[22] Eguchi K, Kojo H, Takeguchi T, Kikuchi R, Sasaki K. Fuel flexibility in power generation by solid oxide fuel cells. Solid State Ionics 2002;152–153:411–6.
[23] Kikuchi R, Eguchi K. Solid oxide fuel cell as a multi-fuel applicable power generation device. J Jpn Pet Inst 2004;47:225–38.
[24] Sasaki K, Teraoka Y. Equilibria in fuel cell gases. J Electrochem Soc 2003;150:A885–8.
[25] Takeguchi T, Kani Y, Yano T, Kikuchi R, Eguchi K, Tsujimoto K, et al. Study on steam reforming of CH_4 and C_2 hydrocarbons and carbon deposition on Ni-YSZ cermets. J Power Sources 2002; 112:588–95.
[26] Mermelstein J, Millan M, Brandon NP. The impact of carbon formation on Ni-YSZ anodes from biomass gasification model tars operating in dry conditions. Chem Eng Sci 2009;64:492–500.
[27] He H, Hill JM. Carbon deposition on Ni/YSZ composites exposed to humidified methane. Appl Catal A: Gen 2007;317:284–92.
[28] Finnerty CM, Coe NJ, Cunningham RH, Ormerod RM. Carbon formation on and deactivation of nickel-based/zirconia anodes in solid oxide fuel cells running on methane. Catal Today 1998; 46:137–45.
[29] Finnerty CM, Cunningham RH, Ormerod RM. Development of a novel test system for in situ catalytic, electrocatalytic and electrochemical studies of internal fuel reforming in solid oxide fuel cells. Catal Lett 2000;66:221–6.

[30] Finnerty CM, Ormerod RM. Internal reforming over nickel/zirconia anodes in SOFCs operating on methane: influence of anode formulation, pre-treatment and operating conditions J. Power Sources 2000;86:390–4.

[31] Marina OA, Mogensen M. High-temperature conversion of methane on a composite gadolinia-doped ceria – gold electrode. Appl Catal A: Gen 1999;189:117–26.

[32] Ukai K, Mizutani Y, Kume Y. Current Status of SOFC development using Scandia Doped Zirconia. In: Yokokawa H, Singhal SC, editors. Proceedings – electrochemical society, solid oxide fuel cells VII. Electrochem Soc 2001;16:375–83.

[33] Eguchi K, Tanaka K, Matsui T, Kikuchi R. Reforming activity and carbon deposition on cermet catalysts for fuel electrodes of solid oxide fuel cells. Catal Today 2009;146:154–9.

[34] Ke K, Gunji A, Mori H, Tsuchida S, Takahashi H, Ukai K, et al. Effect of oxide on carbon deposition behavior of CH_4 fuel on Ni/ScSZ cermet anode in high temperature SOFCs. Solid State Ionics 2006; 177:541–7.

[35] Weber A, Sauer B, Muller AC, Herbstritt D, Ivers-Tiffee E. Oxidation of H_2, CO and methane in SOFCs with Ni/YSZ-cermet anodes. Solid State Ionics 2002;152–153:543–50.

[36] Gunji A, Wen C, Otomo J, Kobayashi T, Ukai K, Mizutani Y, et al. Carbon deposition behaviour on Ni-ScSZ anodes for internal reforming solid oxide fuel cells. J Power Sources 2004;131:285–8.

[37] Sumi H, Ukai K, Mizutani Y, Mori H, Wen CJ, Takahashi H, et al. Performance of nickel-scandia-stabilized zirconia cermet anodes for SOFCs in 3% H_2O-CH_4. Solid State Ionics 2004;174:151–6.

[38] Tabata Y, Orui H, Watanabe K, Chiba R, Arakawa M, Yamazaki Y. Direct internal reforming characteristics of SOFC with a thin SASZ electrolyte and a LNF cathode. J Electrochem Soc 2004;151:A418–21.

[39] Gavrielatos I, Neophytides S. High tolerant to carbon deposition Ni-based electrodes under internal steam reforming conditions. ECS Trans 2007;7:1483–90.

[40] Gavrielatos I, Drakopoulos V, Neophytides SG. Carbon tolerant Ni-Au SOFC electrodes operating under internal steam reforming conditions. J Catal 2008;259:75–84.

[41] Bengaard HS, Nørskov JK, Sehested J, Clausen BS, Nielsen LP, Molenbroek AM, et al. Steam reforming and graphite formation on Ni catalysts. J Catal 25-7-2002;209:365–84.

[42] Kan H, Lee H. Sn-doped Ni/YSZ anode catalysts with enhanced carbon deposition resistance for an intermediate temperature SOFC. Appl Catal B: Env 2010;97:108–14.

[43] Nikolla E, Schwank JW, Linic S. Hydrocarbon steam reforming on Ni alloys at solid oxide fuel cell operating conditions. Catal Today 31-7-2008; 136:243–8.

[44] Girona K, Laurencin J, Petitjean M, Fouletier J, Lefebvre-Joud F. SOFC running on biogas: identification and experimental validation of "safe" operating conditions. In: Singhal SC, Yokokawa H, editors. ECS Transactions. Electrochem Soc; 2009. p. 1041–50. 25.

[45] Yentekakis IV, Papadam T, Goula G. Electricity production from wastewater treatment via a novel biogas-SOFC aided process. Solid State Ionics 2008;179:1521–5.

[46] Lanzini A, Leone P. Experimental investigation of direct internal reforming of biogas in solid oxide fuel cells. Int J Hydrogen Energy 2010;35:2463–76.

[47] Xu C, Zondlo JW, Gong M, Elizalde-Blancas F, Liu X, Celik IB. Tolerance tests of H_2S-laden biogas fuel on solid oxide fuel cells. J Power Sources 2010;195:4583–92.

[48] Shiratori Y, Teraoka Y, Sasaki K. $Ni_{1-x-y}Mg_xAl_yO$-ScSZ anodes for solid oxide fuel cells. Solid State Ionics 2006;177:1371–80.

[49] Shiratori Y, Sasaki K. Microstructure and electrochemical properties of $Ni_{1-x}Mg_xO$-ScSZ cermet anodes for biogas fueled SOFCs. ECS Transactions. Electrochem Soc 2007;7:1701–10.

[50] Shiratori Y, Oshima T, Sasaki K. Feasibility of direct-biogas SOFC. Int J Hydrogen Energy 2008; 33:6316–21.

[51] Shiratori Y, Sasaki K. NiO-ScSZ and $Ni_{0.9}Mg_{0.1}O$-ScSZ-based anodes under internal dry reforming of simulated biogas mixtures. J Power Sources 2008;180:738–41.

[52] Laycock CJ, Staniforth JZ, Ormerod RM. Improving the sulphur tolerance of nickel catalysts for running solid oxide fuel cells on waste biogas. ECS transactions. Electrochem Soc 2008;16:177–88.

[53] Rostrup-Nielsen JR, Alstrup I. Innovation and science in the process industry steam reforming and hydrogenolysis. Catal Today 1999;53:311–6.

[54] Hibino T, Hashimoto A, Yano M, Suzuki M, Sano M. Ru-catalyzed anode materials for direct hydrocarbon SOFCs. Electrochim Acta 2003;48:2531–7.

[55] Yamaji K, Kishimoto H, Xiong Y, Horita T, Sakai N, Brito ME, et al. Feasibility of Ni-based cermet anode for direct HC SOFCs: fueling ethane at a low S/C condition to Ni-ScSZ anode-supported cell. J Power Sources 2006;159:885–90.

[56] Iida T, Kawano M, Matsui T, Kikuchi R, Eguchi K. Internal reforming of SOFCs: carbon deposition on fuel electrode and subsequent deterioration. J Electrochem Soc 2007;154:B234–41.

[57] Dekker NJJ, Ouweltjes JP, Rietveld G. Conversion of simulated biogas in a SOFC: the effect of organic compounds. ECS transactions. Electrochem Soc 2007;7:1465–73.

[58] Liu M, Yang L, Wang S, Blinn K, Liu M, Liu Z, et al. Enhanced sulfur and coking tolerance of a mixed ion conductor for SOFCs: $BaZr_{0.1}Ce_{0.7}Y_{0.2-x}Y_{bx}O_{3-delta}$. Science 2009;326:126–9.

[59] Shekhawat D, Berry DA, Haynes DJ, Spivey JJ. Fuel constituent effects on fuel reforming properties for fuel cell applications. Fuel 2009;88:817–25.

[60] Aravind PV, Ouweltjes JP, Woudstra N, Rietveld G. Impact of biomass-derived contaminants on SOFCs with Ni/gadolinia-doped ceria anodes. Electrochem Solid-State Lett 2008;11:B24–8.

[61] Hofmann P, Panopoulos KD, Aravind PV, Siedlecki M, Schweiger A, Karl J, et al. Operation of solid oxide fuel cell on biomass product gas with tar levels >10 g Nm^{-3}. Int J Hydrogen Energy 2009;34:9203–12.

[62] Mermelstein J, Brandon N, Millan M. Impact of steam on the interaction between biomass gasification tars and nickel-based solid oxide fuel cell anode materials. Energy Fuels 2009;23:5042–8.

[63] Mermelstein J, Millan M, Brandon N. The impact of steam and current density on carbon formation from biomass gasification tar on Ni/YSZ, and Ni/CGO solid oxide fuel cell anodes. J Power Sources 15-3-2010;195:1657–66.

[64] Huang B, Zhu X-j, Hu W-q, Wang Y-y, Yu Q-c. Characterization of the Ni-ScSZ anode with a LSCM-CeO2 catalyst layer in thin film solid oxide fuel cell running on ethanol fuel. J Power Sources 2010;195:3053–9.

[65] Cimenti M, Hill JM. Thermodynamic analysis of solid oxide fuel cells operated with methanol and ethanol under direct utilization, steam reforming, dry reforming or partial oxidation conditions. J Power Sources 2009;186:377–84.

[66] Cimenti M, Hill JM. Importance of pyrolysis and catalytic decomposition for the direct utilization of methanol in solid oxide fuel cells. J Power Sources 2010;195:54–61.

[67] Hansen JB, Pålsson J. Oxygenates and ammonia as SOFC fuels. Proceedings European Fuel Cell Technology Application Conference. Book of Abstracts, Rome; 2005.

[68] Rechberger J, Schauperl R, Hansen JB, Larsen PK. Development of a methanol SOFC APU demonstration system. In: Singhal SC, Yokokawa H, editors. ECS transactions. Electrochem Soc, 25; 2009. p. 1085–92.

[69] Cimenti M, Hill JM. Direct utilization of ethanol on ceria-based anodes for solid oxide fuel cells. Asia-Pac J Chem Eng 2009;4:45–54.

[70] Gorte RJ, Vohs JM. Novel SOFC anodes for the direct electrochemical oxidation of hydrocarbons. J Catal 2003;216:477–86.

[71] Farr RD, Vayenas CG. Ammonia high temperature solid electrolyte fuel cell. J Electrochem Soc 1980;127:1478–83.

[72] Metkemeijer R, Achard P. Comparison of ammonia and methanol applied indirectly in a hydrogen fuel cell. Int J Hydrogen Energy 1994;19:535–42.

[73] Metkemeijer R, Achard P. Ammonia as a feedstock for a hydrogen fuel cell; reformer and fuel cell behavior. J Power Sources 1994;49:271–82.

[74] Gamanovich NM, Novikov GI. Electrochemical oxidation of ammonia in high-temperature fuel cells. Russ J Appl Chem 1997;70:1136–7.

[75] Gamanovich NM, Gorbunova VA, Novikov GI. Oxidation of alcohol-ammonia mixtures in high-temperature fuel cell with various electrodes. Russ J Appl Chem 2001;74:746–9.

[76] Wojcik A, Middleton H, Damopoulos I, Van Herle J. Ammonia as a fuel in solid oxide fuel cells. J Power Sources 2003;118:342–8.

[77] Dekker N, Rietveld B. Highly efficient conversion of ammonia in electricity by solid oxide fuel cells. In: Rome: In Proc. Eur Fuel Cell Technol Appl Conf Book Abstr; 2005. p. 52–62.

[78] Dekker N, Rietveld G. Highly efficient conversion of ammonia in electricity by solid oxide fuel cells. J Fuel Cell Sci Tech 2006;3:499–502.

[79] Christiansen N, Hansen JB, Kristensen SH-LH, Linderoth S, Hendriksen PV, Larsen PH, et-al. SOFC development program at Haldor Topsøe/Risø national laboratory – progress, fuel cell seminar. FL: Palm Springs; 2005.

[80] Hansen JB, Pålsson J. Oxygenates and ammonia as SOFC fuels. In: Proc Eur Fuel Cell Technol Appl Conf Book Abstr. Rome; 2005. p. 49–51.

[81] Yoo Y, Tuck M, Lim N, McFarlan A, Maffei N. Fabrication of anode supported direct ammonia solid oxide fuel cells based on proton conducting Y-doped $BaCeO_3$ electrolyte. In: Eguchi K, Mizusaki J, Singhal S, Yokokawa H, editors. ECS Transactions, vol. 7; 2007. p. 2305–12.

[82] Yoo Y, Lim N, Phongaksorn M, McFarlan A, Maffei N. High performance direct ammonia fueled solid oxide fuel cells based on proton conducting solid electrolytes. In: Williams M, Krist K, Satyapal S,

Garland N, editors. ECS Transactions. Electrochem Soc, 12; 2008. p. 691–700.
[83] Liu M, Peng R, Dong D, Gao J, Liu X, Meng G. Direct liquid methanol-fueled solid oxide fuel cell. J Power Sources 2008;185:188–92.
[84] Ma Q, Peng R, Tian L, Meng G. Direct utilization of ammonia in intermediate-temperature solid oxide fuel cells. Electrochem Comm 2006;8:1791–5.
[85] Ma Q, Peng R, Lin Y, Gao J, Meng G. A high-performance ammonia-fueled solid oxide fuel cell. J Power Sources 2006;161:95–8.
[86] Ma Q, Ma J, Zhou S, Yan R, Gao J, Meng G. A high-performance ammonia-fueled SOFC based on a YSZ thin-film electrolyte. J Power Sources 2007; 164:86–9.
[87] Meng G, Jiang C, Ma J, Ma Q, Liu X. Comparative study on the performance of a SDC-based SOFC fueled by ammonia and hydrogen. J Power Sources 2007;173:189–93.
[88] Meng G, Ma G, Ma Q, Peng R, Liu X. Ceramic membrane fuel cells based on solid proton electrolytes. Solid State Ionics 2007;178:697–703.
[89] Meng G, Peng R, Xia C, Liu X. Research activities and progress on solid oxide fuel cells at USTC. In: Singh P, Bansal NP, Ohji T, Wereszczak A, editors. Advances in solid oxide fuel cells IV. New York: Wiley; 2009. p. 3–17.
[90] Xie K, Ma Q, Lin B, Jiang Y, Gao J, Liu X, et al. An ammonia fuelled SOFC with a $BaCe_{0.9}Nd_{0.1}O_{3\text{-delta}}$ thin electrolyte prepared with a suspension spray. J Power Sources 2007;170:38–41.
[91] Xie K, Yan R, Meng G, Liu X. Direct ammonia proton-conducting solid oxide fuel cells prepared by a modified suspension spray. Ionics 2009;15:115–9.
[92] Zhang L, Cong Y, Yang W, Lin L. A direct ammonia tubular solid oxide fuel cell. Chin J Catal 2007; 28:749–51.
[93] Zhang L, Yang W. Direct ammonia solid oxide fuel cell based on thin proton-conducting electrolyte. J Power Sources 2008;179:92–5.
[94] Ni M, Leung MKH, Leung DYC. Ammonia-fed solid oxide fuel cells for power generation-A review. Int J Energy Res 2009;33:943–59.
[95] Lee AL, Zabransky RF, Huber WJ. Internal reforming development for solid oxide fuel cells. Ind Eng Chem Res 1990;29:766–73.
[96] Saeki MJ, Uchida H, Watanabe M. Noble metal catalysts highly-dispersed on Sm-doped ceria for the application to internal reforming solid oxide fuel cells operated at medium temperature. Catal Lett 1994;26:149–57.
[97] Achenbach E. Three-dimensional and time-dependent simulation of a planar solid oxide fuel cell stack. J Power Sources 1994;49:333–48.
[98] Ødegård R, Johnsen E, Karoliussen H. Methane Reforming on Ni/Zirconia SOFC anodes. In: Dokiya M, Yamamoto O, Tagawa H, Singhal SC, editors. Proc Fourth Int Sym on Solid Oxide Fuel Cells (SOFC IV). The Electrochemical Society; 1995. p. 810–9.
[99] Belyaev VD, Politova TI, Marina OA, Sobyanin VA. Internal steam reforming of methane over Ni-based electrode in solid oxide fuel cells. Appl Catal A: Gen 1995;133:47–57.
[100] Dicks AL, Pointon KD, Siddle A. Intrinsic reaction kinetics of methane steam reforming on a nickel/zirconia anode. J Power Sources 2000;86:523–30.
[101] Ahmed K, Foger K. Kinetics of internal steam reforming of methane on Ni/YSZ-based anodes for solid oxide fuel cells. Catal Today 2000;63:479–87.
[102] Laosiripojana N, Assabumrungrat S. Methane steam reforming over $Ni/Ce\text{-}ZrO_2$ catalyst: influences of $Ce\text{-}ZrO_2$ support on reactivity, resistance toward carbon formation, and intrinsic reaction kinetics. Appl Catal A: Gen 2005;290:200–11.
[103] Nakagawa N, Sagara H, Kato K. Catalytic activity of $Ni\text{-}YSZ\text{-}CeO_2$ anode for the steam reforming of methane in a direct internal-reforming solid oxide fuel cell. J Power Sources 2001;92:88–94.
[104] Timmermann H, Fouquet D, Weber A, Ivers-Tiffée E, Hennings U, Reimert R. Internal reforming of methane at Ni/YSZ and Ni/CGO SOFC cermet anodes. Fuel Cells 2006;6:307–13.
[105] Boder M, Dittmeyer R. Catalytic modification of conventional SOFC anodes with a view to reducing their activity for direct internal reforming of natural gas. J Power Sources 2006;155:13–22.
[106] King DL, Strohm JJ, Wang X, Roh HS, Wang C, Chin YH, et al. Effect of nickel microstructure on methane steam-reforming activity of Ni-YSZ cermet anode catalyst. J Catal 2008;258:356–65.
[107] Wei J, Iglesia E. Isotopic and kinetic assessment of the mechanism of reactions of CH_4 with CO_2 or H_2O to form synthesis gas and carbon on nickel catalysts. J Catal 2004;224:370–83.
[108] Timmermann H, Sawady W, Reimert R, Ivers-Tiffee E. Kinetics of (reversible) internal reforming of methane in solid oxide fuel cells under stationary and APU conditions. J Power Sources 2010; 195:214–22.
[109] Matsuzaki Y, Baba Y, Sakurai T. Diffusion characteristics in anode-substrates for anode-supported SOFCs. Electrochemistry 2005;73:484–8.
[110] Hecht ES, Gupta GK, Zhu H, Dean AM, Kee RJ, Maier L, et al. Methane reforming kinetics within a Ni-YSZ SOFC anode support. Appl Catal A: Gen 2005;295:40–51.

[111] Peters R, Dahl R, Klüttgen U, Palm C, Stolten D. Internal reforming of methane in solid oxide fuel cell systems. J Power Sources 2002;106:238–44.
[112] Sehested J. Sintering of nickel steam-reforming catalysts. J Catal 2003;217:417–26.
[113] Sehested J, Gelten JAP, Remediakis IN, Bengaard H, Norskov JK. Sintering of nickel steam-reforming catalysts: effects of temperature and steam and hydrogen pressures. J Catal 2004;223:432–43.
[114] Sehested J, Gelten JAP, Helveg S. Sintering of nickel catalysts: effects of time, atmosphere, temperature, nickel-carrier interactions, and dopants. Appl Catal A: Gen 2006;309:237–46.
[115] Bebelis S, Neophytides S. AC impedance study of Ni-YSZ cermet anodes in methane-fuelled internal reforming YSZ fuel cells. Solid State Ionics 2002;152–153:447–53.
[116] Jones G, Jakobsen JG, Shim SS, Kleis J, Andersson MP, Rossmeisl J, et al. First principles calculations and experimental insight into methane steam reforming over transition metal catalysts. J Catal 2008;259:147–60.
[117] Mogensen D, Grunwaldt JD, Hendriksen PV, Dam-Johansen K, Nielsen JU. Internal steam reforming in solid oxide fuel cells: Status and opportunities of kinetic studies and their impact on modeling. J Power Sources 2010;196:25–38.
[118] Hendriksen PV. Model Studies of internal steam reforming in SOFC stacks. In: Stimming U, Singhal S, Tagawa H, Lehnert W, editors. In Proc. Fifth Int. Sym. Solid Oxide Fuel Cells (SOFC-V), 18. The Electrochemistry Society; 1997. p. 1319–28.
[119] Klein JM, Henault M, Gelin P, Bultel Y, Georges S. A solid oxide fuel cell operating in gradual internal reforming conditions under pure dry methane. Electrochem Solid-State Lett 2008;11.
[120] Zaza F, Paoletti C, Presti RL, Simoetti E, Pasquali M. Bioenergy from fuel cells: effects of hydrogen sulfide impurities on performance of MCFC fed with biogas, fundamentals and developments of fuel cells conference – FDFC2008, Nancy (France), Dec 10–12, 2008.
[121] Lohsoontorn P, Brett DJL, Brandon NP. Thermodynamic predictions of the impact of fuel composition on the propensity of sulphur to interact with Ni and ceria-based anodes for solid oxide fuel cells. J Power Sources 2008;175:60–7.
[122] Wang JH, Liu M. Computational study of sulfur-nickel interactions: a new S-Ni phase diagram. Electrochem Comm 2007;9:2212–7.
[123] Galea NM, Kadantsev ES, Ziegler T. Studying reduction in solid oxide fuel cell activity with density functional theory-effects of hydrogen sulfide adsorption on nickel anode surface. J Phys Chem C 2007;111:14457–68.
[124] Rosenquist T. A thermodynamic study of the iron, cobalt, and nickel sulfides. J Iron Steel Inst (London) 1954;176:37–57.
[125] Matsuzaki Y, Yasuda I. Poisoning effect of sulfur-containing impurity gas on a SOFC anode: part I. Dependence on temperature, time, and impurity concentration. Solid State Ionics 2000;132:261–9.
[126] Dong J, Zha S, Liu M. Study of sulfur-nickel interactions using Raman spectroscopy. In: Singhal SC, Mizusaki J, editors. In Proc Electrochem Soc. The Electrochemistry Society; 2005. p. 1284–93.
[127] Dong J, Cheng Z, Zha S, Liu M. Identification of nickel sulfides on Ni-YSZ cermet exposed to H_2 fuel containing H_2S using Raman spectroscopy. J Power Sources 2006;156:461–5.
[128] Cheng Z, Liu M. Characterization of sulfur poisoning of Ni-YSZ anodes for solid oxide fuel cells using in situ Raman microspectroscopy. Solid State Ionics 2007;178:925–35.
[129] Cheng Z, Abernathy H, Liu M. Raman spectroscopy of nickel sulfide Ni_3S_2. J Phys Chem C 2007; 111:17997–8000.
[130] Liu M, Abernathy H, Cheng Z, Lou X. The use of Raman spectroscopy in the analysis of SOFC anode reactions. Prepr Symp – Am Chem Soc Div Fuel Chem 2007;52:59–60.
[131] Maher RC, Cohen LF, Lohsoontorn P, Brett DJL, Brandon NP. Raman spectroscopy as a probe of temperature and oxidation state for gadolinium-doped ceria used in solid oxide fuel cells. J Phy Chem A 2008;112:1497–501.
[132] Ivey DG, Brightman E, Brandon N. Structural modifications to nickel cermet anodes in fuel cell environments. J Power Sources 2010;195:6301–11.
[133] Stolten D, Spah R, Schamm R. Status of SOFC development at Daimler-Benz/Dornier. In: Stimming U, Singhal S, Tagawa H, Lehnert W, editors. In Proc 5th Int Symp Solid Oxide Fuel Cells V. The Electrochemical Society; 1997. p. 88–93.
[134] Zha S, Cheng Z, Liu M. Sulfur poisoning and regeneration of ni-based anodes in solid oxide fuel cells. J Electrochem Soc 2007;154:B201–6.
[135] Hansen JB. Correlating sulfur poisoning of SOFC nickel anodes by a temkin isotherm. Electrochem Solid-State Lett 2008;11:B178–80.
[136] Cheng Z, Zha S, Liu M. Influence of cell voltage and current on sulfur poisoning behavior of solid oxide fuel cells. J Power Sources 2007;172:688–93.
[137] Rasmussen JFB, Hagen A. The effect of H_2S on the performance of Ni-YSZ anodes in solid oxide fuel cells. J Power Sources 2009;191:534–41.

[138] Sasaki K, Susuki K, Iyoshi A, Uchimura M, Imamura N, Kusaba H, et al. H_2S poisoning of solid oxide fuel cells. J Electrochem Soc 2006; 153:A2023–9.

[139] Sasaki K, Susuki K, Iyoshi A, Uchimura M, Imamura N, Kusaba H, et al. Sulfur tolerance of solid oxide fuel cells. In: Singhal SC, Mizusaki J, editors. In Proc of the 9th Int. Sym. Solid Oxide Fuel Cells, 7. The Electrochemical Society; 2005. p. 1267–74.

[140] Kuhn JN, Lakshminarayanan N, Ozkan US. Effect of hydrogen sulfide on the catalytic activity of Ni-YSZ cermets. J Mol Catal A: Chem 2008;282:9–21.

[141] He H, Gorte RJ, Vohs JM. Highly sulfur tolerant Cu-ceria anodes for SOFCs. Electrochem Solid-State Lett 2005;8:A279–80.

[142] He HP, Wood A, Steedman D, Tilleman M. Sulphur tolerant shift reaction catalysts for nickel-based SOFC anode. Solid State Ionics 2007;179:1478–82.

[143] Trembly JP, Marquez AI, Ohrn TR, Bayless DJ. Effects of coal syngas and H_2S on the performance of solid oxide fuel cells: single-cell tests. J Power Sources 2006;158:263–73.

[144] Marquez AI, Ohrn TR, Trembly JP, Ingram DC, Bayless DJ. Effects of coal syngas and H_2S on the performance of solid oxide fuel cells. Part 2. Stack tests. J Power Sources 2007;164:659–67.

[145] Ouweltjes JP, Aravind PV, Woudstra N, Rietveld G. Biosyngas utilization in solid oxide fuel cells with Ni/GDC anodes. J Fuel Cell Sci Technol 2006; 3:495–8.

[146] Aravind PV, Ouweltjes JP, De Heer E, Woudstra N, Rietveld G. Impact of biosyngas and its components on sofc anodes. In: Singhal SC, Mizusaki J, editors. In Proc.of the 9th Int Sym Solid Oxide Fuel Cells, 7. The Electrochemical Society; 2005. p. 1459–67.

[147] Hofmann P, Schweiger A, Fryda L, Panopoulos KD, Hohenwarter U, Bentzen JD, et al. High temperature electrolyte supported Ni-GDC/YSZ/LSM SOFC operation on two-stage Viking gasifier product gas. J Power Sources 2007;173:357–66.

[148] Norheim A, Wærnhus I, Brostrom M, Hustad JE, Vik A. Experimental studies on the influence of H_2S on solid oxide fuel cell performance at 800 °C. Energy Fuels 2007;21:1098–101.

[149] Sishtla CI, Krist K, Suchorabski DA, Pondo JM. Fuel cell seminar. Palm Springs, CA; 2005.

[150] Silversand F, Hansen JB, Jannasch AK, Pålsson J. Fuel cell seminar. Honolulu, HI; 2006.

[151] Rostrup-Nielsen JR, Hansen JB, Helveg S, Christiansen N, Jannasch AK. Sites for catalysis and electrochemistry in solid oxide fuel cell (SOFC) anode. Appl Phys A: Mater Sci Proc 2006;85:427–30.

[152] Noponen M, Kiviaho J, Halinen M, Saarinen J. Durability of anode supported solid oxide fuel cells on pre-reformed natural gas. In: Proc. Eur. Fuel Cell Technol. Applic. Conf. Book Abstr; 2005.

[153] Noponen M, Halinen M, Kiviaho J, Saarinen J. Feasibility of autothermally reformed natural gas on anode supported solid oxide fuel cells. J Fuel Cell Sci Technol 2006;3:438–44.

[154] Rostrup-Nielsen JR. Sulfur-passivated nickel catalysts for carbon-free steam reforming of methane. J Catal 1984;85:31–43.

[155] Trembly JP, Gemmen RS, Bayless DJ. The effect of IGFC warm gas cleanup system conditions on the gas-solid partitioning and form of trace species in coal syngas and their interactions with SOFC anodes. J Power Sources 2007;163:986–96.

[156] Martinez A, Gerdes K, Gemmen R, Poston J. Thermodynamic analysis of interactions between Ni-based solid oxide fuel cells (SOFC) anodes and trace species in a survey of coal syngas. J Power Sources 2010;195:5206–12.

[157] Cayan FN, Zhi M, Pakalapati SR, Celik I, Wu N, Gemmen R. Effects of coal syngas impurities on anodes of solid oxide fuel cells. J Power Sources 2008;185:595–602.

[158] Trembly JP, Gemmen RS, Bayless DJ. The effect of coal syngas containing HCl on the performance of solid oxide fuel cells: investigations into the effect of operational temperature and HCl concentration. J Power Sources 2007;169:347–54.

[159] Marina OA, Pederson LR, Thomsen EC, Coyle CA, Yoon KJ. Reversible poisoning of nickel/zirconia solid oxide fuel cell anodes by hydrogen chloride in coal gas. J Power Sources 2010;195:7033–7.

[160] Marina OA, Pederson LR, Thomsen EC, Edwards DJ, Coyle CA, Cramer CN. SOFC ohmic resistance reduction by HCl-induced removal of manganese at the anode/electrolyte interface. Electrochem Solid-State Lett 2010;13:B63–7.

[161] Haga K, Shiratori Y, Ito K, Sasaki K. Chlorine poisoning of SOFC Ni-cermet anodes. J Electrochem Soc 2008;155:B1233–9.

[162] Haga K, Adachi S, Shiratori Y, Itoh K, Sasaki K. Poisoning of SOFC anodes by various fuel impurities. Solid State Ionics 2008;179:1427–31.

[163] Bao J, Krishnan GN, Jayaweera P, Perez-Mariano J, Sanjurjo A. Effect of various coal contaminants on the performance of solid oxide fuel cells: Part I. accelerated testing. J Power Sources 2009;193:607–16.

[164] Xu C, Gong M, Zondlo JW, Liu X, Finklea HO. The effect of HCl in syngas on Ni-YSZ anode-supported solid oxide fuel cells. J Power Sources 2010; 195:2149–58.

[165] Bao J, Krishnan GN, Jayaweera P, Sanjurjo A. Effect of various coal gas contaminants on the performance of solid oxide fuel cells: Part III. synergistic effects. J Power Sources 2010;195:1316–24.

[166] Kishimoto H, Yamaji K, Brito ME, Horita T, Yokokawa H. Generalized ellingham diagrams for utilization in solid oxide fuel cells. J Mining Metall Sect B: Metall 2008;44:39–48.

[167] Zhi M, Chen X, Finklea H, Celik I, Wu NQ. Electrochemical and microstructural analysis of nickel-yttria-stabilized zirconia electrode operated in phosphorus-containing syngas. J Power Sources 2008;183:485–90.

[168] Demircan O, Xu C, Zondlo J, Finklea HO. In situ Van der Pauw measurements of the Ni/YSZ anode during exposure to syngas with phosphine contaminant. J. Power Sources 2009;194:214–9.

[169] Demircan O, Zhang W, Xu C, Zondlo J, Finklea HO. The effect of overpotential on performance degradation of the solid oxide fuel cell Ni/YSZ anode during exposure to syngas with phosphine contaminant. J Power Sources 2010;195:3091–6.

[170] Bao J Krishnan GN, Jayaweera P, Lau KH, Sanjurjo A. Effect of various coal contaminants on the performance of solid oxide fuel cells: Part II. ppm and sub-ppm level testing. J Power Sources 2009; 193:617–24.

[171] Marina OA, Coyle CA, Thomsen EC, Edwards DJ, Coffey GW, Pederson LR. Degradation mechanisms of SOFC anodes in coal gas containing phosphorus. Solid State Ionics 2010;181:430–40.

[172] Liu W, Sun X, Pederson LR, Marina OA, Khaleel MA. Effect of nickel-phosphorus interactions on structural integrity of anode-supported solid oxide fuel cells. J Power Sources 2010;195:7140–5.

[173] Gong M, Bierschenk D, Haag J, Poeppelmeier KR, Barnett SA, Xu C, et al. Degradation of $LaSr_2Fe_2CrO_{9-delta}$ solid oxide fuel cell anodes in phosphine-containing fuels. J Power Sources 2010;195:4013–21.

[174] Trembly JP, Gemmen RS, Bayless DJ. The effect of coal syngas containing AsH_3 on the performance of SOFCs: investigations into the effect of operational temperature, current density and AsH_3 concentration. J Power Sources 2007;171:818–25.

[175] Coyle CA, Marina OA, Thomsen EC, Edwards DJ, Cramer CD, Coffey GW, et al. Interactions of nickel/zirconia solid oxide fuel cell anodes with coal gas containing arsenic. J Power Sources 2009;193:730–8.

[176] Gerdes K, Trembly J, Gemmen R. Effect of H2Se exposure on performance of anode supported SOFC. In: Proceedings of the coal based fuel cell technology: status, needs and future applications. Morgantown, WV; 2007.

[177] Marina OA, Pederson LR, Coyle CA, Thomsen EC, Coffey GW. Ni/YSZ anode interactions with impurities in coal gas. ECS Trans 2009;25:2125–30.

[178] Xu C, Zondlo JW, Gong M, Liu X, Celik IB. Tolerance tests of co-feeding Cl_2 and H_2S impurities in biogas on a Ni-YSZ anode-supported solid oxide fuel cell. In: Eight Int.l Fuel Cell Sci. Brooklyn, New York: Eng. Tech. Conf; 2010.

[179] Atkinson A, Barnett S, Gorte RJ, Irvine JTS, McEvoy AJ, Mogensen M, et al. Advanced anodes for high-temperature fuel cells. Nature Mater 2004;3:17–27.

CHAPTER

14

Reactor Design for Fuel Processing

Z. Ilsen Önsan, Ahmet K. Avci

Department of Chemical Engineering, Boğaziçi University, Bebek 34342, Istanbul, Turkey

OUTLINE

14.1. DESIGN REQUIREMENTS OF THE FUEL PROCESSING UNIT

Fuel reforming reactor is the part of the fuel processing system in which catalytic conversion of hydrocarbon fuels (fossil or renewable) to a hydrogen-rich mixture takes place. Conversion can occur via different mechanisms, with the most well known ones being steam reforming (SR), partial oxidation (POX), and oxidative steam reforming (OSR) [1].

Steam reforming is the reaction of a hydrocarbon with steam to give a mixture of carbon monoxide and hydrogen:

$$C_mH_nO_k + (m-k)H_2O = mCO + \left(m-k+\frac{n}{2}\right)H_2, \quad (m>k);\ \Delta H^o > 0 \tag{14.1}$$

The reaction, which is reversible in the case of methane but almost irreversible in the case of higher hydrocarbons, is endothermic and requires elevated temperatures. In general, the type of catalyst and fuel dictate the reaction temperature, molar ratio of steam, and hydrocarbon in the feed and the product distribution. Note that the generalized reaction (14.1) is not valid for methanol, in which the number of carbon and oxygen atoms is equal; methanol is either decomposed into CO and H_2 according to (14.1) or steam reformed to give CO_2 and H_2. Steam reforming conditions favor water-gas shift (WGS) as an important side reaction which is fast and close to equilibrium [2]:

$$CO + H_2O = CO_2 + H_2 \qquad \Delta H^o = -41.2\,\text{kJ mol}^{-1} \tag{14.2}$$

Other side reactions that can affect the product composition include methanation and carbon dioxide reforming. The latter is reported to be slower than steam reforming [3] and is usually negligible when steam is present in the reaction medium [3,4]:

$$CO + 3H_2 = CH_4 + H_2O \qquad \Delta H^\circ = -206.2\,\text{kJ mol}^{-1} \tag{14.3}$$

$$C_mH_nO_k + (m-k)\,CO_2 = (2m-k)CO + \frac{n}{2}H_2, \quad (m>k);\ \Delta H^o > 0 \tag{14.4}$$

Hydrogen can also be produced by the catalytic partial oxidation of hydrocarbons:

$$C_mH_nO_k + \frac{(m-k)}{2}O_2 = mCO + \frac{n}{2}H_2 \quad (m>k);\ \Delta H^o < 0 \tag{14.5}$$

Once triggered, the reaction is fast and irreversible at temperatures in excess of ~1000 K and at short contact times in the order of milliseconds over precious metals supported on structured forms such as monoliths [5,6] and microchannels [7,8]. The reaction produces synthesis gas at a H_2:CO ratio between 1 and 2, depending on the hydrocarbon. Partial oxidation is faster than steam reforming which allows the use of smaller reactors and rapid dynamic responses against changes in power demands [4]. Although hydrogen can be produced without water, POX can only be used in fuel processing for PEMFC (proton exchange membrane fuel cell) if the reactor is coupled with a WGS converter to reduce the amount of CO by water injection to the limits acceptable by the catalytic CO clean-up unit (ca. 2 mole%) [9,10]; however POX is suitable for use in high-temperature fuel cells such as MCFC (molten carbonate fuel cell) and SOFC (solid oxide fuel cell).

When the fuel, oxidant (air, enriched air or oxygen), and steam are fed together to the same reactor to run the exothermic combustion and endothermic steam reforming simultaneously, the process is called oxidative steam (or autothermal) reforming (OSR). Autothermal

reforming (ATR) is an established scheme and has been used in industrial scale hydrogen/synthesis gas production for many years; it is currently the conventional method for synthesis gas production in medium-to-large scale gas-to-liquids (GTL) plants due to the possibility of obtaining H_2:CO ratios close to 2 by operating at low steam-to-carbon ratios between 0.6 and 1.0 [11]. Industrial reformers combine non-catalytic combustion with catalytic steam reforming and involve maximum temperatures higher than ~2500 K [11]. Since such temperatures are not practical in fuel cell applications, both combustion and reforming should run catalytically in fuel processors.

The major catalytic reactions involved in OSR are POX (Reaction 14.5) and steam reforming (Reaction 14.1). However, depending on the nature of the catalyst, the amount of oxidant in the feed and the residence time, the exothermic part of the OSR can also be characterized by total oxidation (Reaction 14.6) [4]. The onset of total oxidation (TOX) is followed immediately by a significant heat release through the irreversible stoichiometry given below:

$$C_mH_nO_k + \left(m + \frac{n}{4} - \frac{k}{2}\right) O_2 = mCO_2 + \frac{n}{2}H_2O, \quad \Delta H^o < 0 \tag{14.6}$$

In both definitions of OSR, WGS remains as an important side reaction. The combination of TOX, steam reforming, and WGS is also known as indirect partial oxidation (IPOX) [4,12].

The fuel conversion routes defined above can favor carbon formation, a phenomenon which has adverse effects on the reforming performance and must therefore be avoided. Carbon formation can occur via different mechanisms under specific combinations of operating conditions. The major reactions involving solid carbon as a product are given below [13]:

$$CO + H_2 = C + H_2O, \Delta H^o = -135.6\,\text{kJ mol}^{-1} \tag{14.7}$$

$$2CO = C + CO_2, \Delta H^o = -172.4\,\text{kJ mol}^{-1} \tag{14.8}$$

$$CH_4 = C + 2H_2, \Delta H^o = 74.9\,\text{kJ mol}^{-1} \tag{14.9}$$

$$C_mH_n = mC + \frac{n}{2}H_2, \quad \Delta H^o > 0 \tag{14.10}$$

The reactions, except the cracking of higher hydrocarbons (Reaction 14.10), are reversible, and Reaction (14.8) is known as Boudouard reaction. The methods used to minimize carbon formation, and their impacts on reformer design are described in the following sections.

Design of a reformer unit is mainly a function of the fuel conversion mode and the nature of the catalyst used. For example, if the conversion route is endothermic, such as in SR, structures providing improved heat input to the catalyst bed should be implemented. Similarly, exothermic reactions will require effective distribution of the generated heat to the catalyst bed. Details of such requirements are provided below for each fuel, as the nature of the hydrocarbon is as important as the conversion route and the catalyst in the reformer design.

14.1.1. Natural Gas and Liquefied Petroleum Gas

14.1.1.1. Steam Reforming

Natural Gas. Steam reforming of methane, model hydrocarbon for natural gas, gives the highest stoichiometric H_2:CO ratio, which is desirable in fuel processing. This advantage, however, comes at the expense of high temperature requirements; methane is the most stable hydrocarbon and requires energy input to react with steam. Methane steam reforming is thermodynamically favored at high temperatures and at high molar steam-to-fuel ratios in the feed. Thermodynamic predictions estimate 90% methane

conversion at ca. 923 K, 0.1 MPa, and at a steam-to-fuel ratio of 3, and complete conversions are estimated at temperatures in excess of 1073 K [14]. Although the industrial reformers operate at high pressures ($> \sim 2$ MPa) to save from the costs of post-reactor compression required for the pressure demanding hydroprocessing of Fischer-Tropsch operations [11,15], the reaction is not favored at elevated pressures. For example, 90% conversion is possible at ca. 1093 K when the pressure is increased to 1 MPa without changing the steam-to-fuel ratio [14]. Nevertheless, fuel processor reformers, except membrane-involving types, can be designed to operate at near-ambient pressures, as the unit sizes, and corresponding pressure drops, are significantly smaller than those of industrial counterparts [16].

The nature of the catalyst plays an important role in determining the operating temperature of the steam reformer. Typical catalysts are Ni-based, since they offer sufficient activity with low cost and high availability. Precious metal catalysts such as Rh and Ru can also be used in methane steam reforming, giving activities higher than that of Ni. However, high cost and low availability of Rh and Ru are major drawbacks. The activity of various catalysts for methane steam reforming is reported as follows [3]:

$$\mathrm{Ru, Rh} > \mathrm{Ir} > \mathrm{Pd, Ni, Pt} > \mathrm{Re} > \mathrm{Co}$$

A similar comparison with the turnover numbers relative to Ni is reported for ethane steam reforming when alumina is used as a support [2]:

$$\mathrm{Rh}(13) > \mathrm{Ru}(9.5) > \mathrm{Pd}(1.0), \mathrm{Ni}(1.0) > \mathrm{Pt}(0.9)$$

These findings indicate that, compared to a unit using Rh- or Ru-based catalyst, the presence of Ni will result in a steam reformer design with larger volumes, since the amount of catalyst required for an equivalent methane conversion level will be less in the case of precious metals due to their superior activity.

Carbon formation is a phenomenon that is favored under SR conditions and can occur via different mechanisms that lead to catalyst deactivation. The extent of this mechanism depends on the catalyst and on the operating conditions, with S/C ratio (moles steam/moles carbon) in the feed stream being the most important one. Presence of insufficient steam in the feed favors coke deposition over Ni. Therefore, S/C should be kept above stoichiometric values to minimize coking; for methane the recommended ratios lie between 2.5 and 3 [17]. In contrast with Ni-based catalysts, risk of carbon formation over precious metals, Rh and Ru, is low, allowing them to operate at S/C ratios as low as 1.0 [18]. Although addition of compounds such as MoO_3, SnO_2, WO_3 as well as oxides of K, Na, Mg, Ca, and Ba and use of Ce_2O_3 as support are found to reduce carbon formation over Ni [13,19,20], steam requirement will still be higher than those of precious metals. High S/C ratios, as in the case of Ni, will require large reformer volumes and water evaporation capacities at the reformer inlet. Moreover, the amount of heat to be transferred to the reformer should be high in order to overcome the high specific heat of steam and to raise the catalyst bed to the desired temperatures. Therefore, reformer design should involve configurations ensuring improved heat transfer coefficients between the heat source and the catalyst bed.

Liquefied Petroleum Gas (LPG). LPG can be converted to hydrogen by SR. Since studies involving the direct use of LPG as the hydrocarbon feed are scarce, the design requirements of an LPG reformer will be stated through its individual components, propane and *n*-butane.

Steam reforming of propane and *n*-butane can run at temperatures lower than those needed for methane and are almost irreversible. Comparable studies conducted on a $Ni/MgO-Al_2O_3$ catalyst showed that SR conversion of propane was almost complete at ca. 750 K, whereas only $\sim 30\%$ methane conversion was

obtained at the same temperature [21]. Near-complete SR conversions were reported also for *n*-butane at 678 K over a *δ*-alumina supported bimetallic Pt–Ni catalyst [22]. Both studies were conducted at a S/C (moles steam/moles carbon) ratio of 3, which is close to the values used in methane SR over Ni. However, the amount of steam needed for propane and *n*-butane will obviously be higher, since S/C is based on the number of carbon atoms. Therefore heat requirement for running the reaction is lower, but this advantage is counterbalanced by the extra energy needed to evaporate higher quantities of water. The need for keeping the S/C ratio at a minimum of 2.5 at the inlet is a condition peculiar to Ni-based catalysts and is set to minimize carbon formation via gasifying with steam [2,17]. However, the use of precious metal catalysts together with ceria offers the possibility of setting lower S/C ratios. Wang and Gorte [23] have reported carbon-free *n*-butane SR over a Pd/ceria catalyst at S/C ratios between 1.0 and 2.0, but have observed carbon formation over Ni/ceria, indicating the necessity of high S/C ratios for Ni-based catalysts. Similarly, propane SR run on a $Rh/Pt/CeO_2$ catalyst supported on alumina washcoated microchannels did not produce any coke at an inlet S/C ratio of 2.3 [24]. These results indicate that the choice of catalyst is important in determining the water needed to run the system and the associated evaporation load. Apart from being critical in the control of coking, addition of steam into the feed facilitates fuel conversion in the direction of hydrogen formation at different extents; changing S/C ratio between 1.0 and 2.0 shifted propane conversion by ca. 25%, while less than 5% change was observed when S/C ratio was increased from 2.0 to 3.0 at temperatures between 923 and 1023 K [24]. As a result, hydrogen producing and coke minimizing effect of steam addition comes at the expense of higher energy needs to evaporate the water, with the balance depending mainly on the catalyst type. Endothermic nature of SR also calls for reactor and/or catalyst combinations favoring efficient heat transport from the heat source to the reaction medium.

14.1.1.2. Partial Oxidation

Methane. In contrast with steam reforming, the stoichiometry of methane POX can yield a molar H_2/CO ratio of 2 without requiring steam in the feed. This fact simplifies reformer design, as it eliminates the complexities associated with water/steam management. However, running the reaction requires a set of extreme conditions such as very short contact times ranging between 10^{-4} and 10^{-2} s and high temperatures (1273–1373 K), mainly over Rh at C/O (moles C/moles O) ratios around 1.0 [5,25]. The use of other catalysts for methane POX is reported to show poor activity/selectivity performance (Pt, Ir), deactivation as a result of aluminate formation (Ni, Co), coking (Pd), and difficulty in sustaining autothermal operation (Re, Ru, Fe) [6]. Besides the type of active metal, the geometric form of the support material can affect the product spectrum of POX via heat and mass transport effects. Bodke et al. [26] reported that using monoliths with smaller pore sizes increased syngas selectivity by modifying the mass transfer rates. Hohn and Schmidt [27] compared spheres and monoliths as support shapes and observed that the former had better heat transfer characteristics in terms of ensuring uniform distribution of the generated heat throughout the catalyst bed, which eventually favored syngas selectivity. These observations show that a reformer involving methane POX should be compact as it leads to short contact times. Smaller volumes are also desirable in terms of uniform distribution of the heat generated during the reaction. Pressure drop can be important in the presence of high flow rates and may restrict the use of packed-bed structures. This can be resolved by using structured supports in which flow paths are well defined such as in monoliths and microchannels. Selection of the channel diameters,

however, requires an optimization between enhanced mixing, i.e., improved mass and heat transport rates versus pressure drop.

Partial oxidation is characterized by high temperatures. The upstream of the catalytic zone can be subject to very sharp temperature gradients (up to ca. 10^6 K/m) and adiabatic temperature elevations of ca. 2000 K due to the rapid oxygen consumption of the combustion reactions [28]. Therefore, the material of construction of the reformer and the catalyst support should have high thermal resistances and should be capable of handling temperature spikes by effective distribution of the local heat accumulation. Another feature of POX is related to the start-up period which requires pre-mixing of hydrocarbon-oxygen mixtures at high temperatures, which calls for careful selection of operating and design parameters to suppress the risk of possible explosions.

The residence time and C/O ratio can affect the mechanism of POX; instead of the "direct" route, the reaction can follow a mechanism which can be explained by sequential occurrence of TOX and SR reactions [29–33]. It was reported that the sequential route was significant at longer residence times, whereas the changes in mechanism toward direct formation of CO and H_2 were observed at higher flow rates (shorter residence times) in methane POX over a Ru/TiO_2 catalyst [30]. Apart from the operating conditions, the types of catalysts and supports can have impacts on the nature of POX. It was shown that the temperature increased sharply and then dropped during methane POX over Ir/TiO_2 and Rh/SiO_2 catalysts, while an initial decrease in temperature was followed by a small temperature elevation in the case of Rh/TiO_2 and Rh/Al_2O_3 catalysts. It was concluded that TOX followed by SR was dominant in the first case, and the initial temperature drop in the latter case was due to methane decomposition, which was the initial step of direct formation of synthesis gas [34]. Considering these facts, the use of reactors with well-defined flow paths will be important in POX, since structured configurations allow precise control of residence time via narrow distribution, which is difficult to achieve in random-flow path systems.

LPG. Partial oxidation of propane and *n*-butane over Rh-, Pt-, and Pd-coated alumina monoliths were studied at short contact times (10^{-3}–10^{-2} s) and at temperatures in excess of 1073 K by Huff et al. [35]. It was found that Rh gave the best syngas selectivity, while Pt and Pd favored olefin and carbon formation, respectively. Ethylene formation was also noted as a result of cracking. Use of Pt-based particulate catalysts for *n*-butane POX was recently demonstrated at considerably lower temperatures (ca. 700 K), which gave a maximum conversion of 58%, but satisfactory syngas selectivities due to decreased cracking of *n*-butane [36]. Higher syngas selectivity of Rh-based catalysts was confirmed by studies conducted later in microchannel geometries, which involved the use of propane as fuel; propane-to-syngas conversions were obtained at high temperatures around 1023–1073 K, at very low residence times varying between 7×10^{-3} and 1.3×10^{-2} s, and at C/O ratios between 0.8 and 1.0 [8,37–39]. These findings show that, as in the case of methane, direct production of syngas via POX of propane and *n*-butane are also favored at short contact times and at high temperatures. Similarly, reactor configurations that allow fast flow rates, low pressure drop, and resistance to sharp temperature gradients are required. The reactor material should be inert; for example, the presence of Ni in the plates of a microchannel reactor was reported to lead to carbon formation with subsequent reactor plugging and high pressure drop during Rh-catalyzed POX of propane [39].

14.1.1.3. *Oxidative Steam Reforming*

Methane. OSR has a sequential nature and starts with exothermic oxidation which releases the heat needed to sustain endothermic SR.

Start-up of the oxidation, however, does not occur at ambient conditions, except for fuels such as methanol and hydrogen, and requires some energy. This phase of OSR is called "light-off" and is characterized by the light-off temperature which corresponds to 10% TOX conversion of the fuel and is a function of the type of fuel, C/O ratio and the type of catalyst [40]. Compared to ethane and propane, methane is the most difficult alkane to activate and has the highest light-off temperature (Table 14.1). For all fuels, Pt gives activities higher than those of Ni leading to lower light-off temperatures [40]. Once the reactants and the catalyst bed are heated, oxidation occurs rapidly, and the temperature increases to a level dictated by the C/O ratio at the inlet. Since the feed stream in OSR is lean in oxygen, its complete consumption stops the oxidation, and the remaining fuel is steam reformed at high temperatures to produce hydrogen. SR then becomes significant and the temperature decreases at the downstream of the reformer with an almost flat profile. The product composition is generally characterized by the thermodynamic equilibria of SR and WGS reactions at the exit temperature [41].

Nature and sequence of these reactions facilitate formation of hot-spots, which may lead to local catalyst deactivation through thermally induced mechanisms such as sintering and carbon formation. The presence of hot-spots can also be considered as a deviation from ideal reactor behavior, since it prevents the use of catalyst bed effectively due to non-uniform temperature distribution in the axial direction. In such a case, catalyst bed at the downstream of the reformer may not be hot enough to drive SR at the required conversion levels. This is a critical issue for methane as it is the most energy demanding fuel to be steam reformed into hydrogen. Therefore, a major design target for an OSR unit is the minimization of hot-spot formation.

Hot-spots can be minimized by employing catalyst support structures or flow configurations which favor effective heat transfer and uniform axial temperature profiles. Since packed-bed configurations have relatively poor heat transfer properties, better performance can be obtained by using thermally conductive supports such as metallic monoliths, foams, and wire-gauzes, or microstructured reactors designed to operate like a heat exchanger [42,43]. The latter can be configured so that fuel/oxidant and fuel/steam streams are fed separately to run oxidation and reforming reactions in different zones allowing heat exchange between the reactions. Hot-spot formation depends also on the flow regime within the reformer. Turbulent flows enhance heat transfer coefficients at the gas–solid interface and therefore reduce the risk of local temperature spikes, but the high superficial fluid velocities involved increase the pressure drop. Therefore, reformer configurations that allow high fluid flow rates with minimal pressure drop constitute an important design target.

TABLE 14.1 Light-Off Temperatures of the Oxidation of Methane, Ethane, and Propane over Pt- and Ni-Based Catalysts (*Reprinted from Ma et al. [40], Copyright (1996), with permission from Elsevier*).

	$Pt/\delta-Al_2O_3$		$Ni/MgO-Al_2O_3$	
Hydrocarbon (HC)	**HC/O_2 (mol)**	**Light-off Temperature (K)**	**HC/O_2 (mol)**	**Light-off Temperature (K)**
CH_4	5.04	589	5.01	637
C_2H_6	0.89	515	0.85	588
C_3H_8	0.48	485	0.48	583

The feed composition, characterized by C/O and S/C ratios, has a significant impact on reformer operation and product distribution. C/O ratio is critical and has to be optimized for maximizing the amount of hydrogen produced. Higher quantities of oxygen in the feed will increase the extent of oxidation and the amount of energy released, leading to elevated temperatures. This is beneficial for SR, but less fuel will remain for hydrogen production. At the other extreme, there will be insufficient exothermal energy for running SR resulting in low quantities of hydrogen. S/C ratio is important in terms of controlling carbon formation during OSR. If the hydrogen production proceeds in the IPOX mode where TOX is much faster than and is followed by SR, then the water produced during TOX has to be taken into account. In this case, the steam-to-carbon ratio utilized by methane steam reforming, (S/C)*, can be expressed as follows:

$$(\mathrm{S/C})^{*} = \frac{\text{moles of } \mathrm{H_2O}(\text{fed} + \text{produced by TOX})}{\text{moles of } \mathrm{CH_4}(\text{fed} - \text{consumed by TOX})} \tag{14.11}$$

As in the case of SR, the $(\mathrm{S/C})^{*}$ ratio depends mainly on the type of catalyst; it should be higher than 2.5 on Ni-based catalysts, but can be lower if precious metals are employed. Apart from preventing carbon formation, steam may also act as a heat sink; it can absorb some of the exothermal energy due to its high specific heat and may help in dampening hot-spots. The maximum bed temperature was 888 K and 851 K at water-to-methane ratios of 1.17 and 2.34, respectively, when the methane-to-oxygen ratio was kept constant at 1.89 (corresponding to C/O of 0.94) in methane OSR over a physical mixture of Pt- and Ni-based catalysts [44]. Steam addition will also favor thermodynamics in the direction of hydrogen production with minimal carbon monoxide. The upper limit of steam addition is mainly dictated by the evaporation capacity of the water management system which must be incorporated into reformer design.

In addition to the specific design requirements stated above, a set of common processing elements should be implemented into the conversion routes. SR, POX, and OSR all require heating the catalyst bed and the feed stream to the necessary reaction temperatures; in the case of POX and OSR these are the light-off temperatures specific to the C/O ratio and catalyst combinations, whereas in SR it is the catalyst specific reaction temperature. It has been reported that the energy required for reformer start-up can be provided either by electrical heating or by combusting fuels such as hydrogen and methanol which can be catalytically oxidized at ambient conditions [4,45]. Continuous reformer operation can be ensured by heat integration within the fuel processing system involving reformate conditioning units, the fuel cell itself, and a catalytic afterburner. A generalized system that can be adapted to any reforming method is given in Fig. 14.1. In this system, sensible heats of the effluent from the catalytic afterburner (where unconverted hydrocarbons and hydrogen rejected by the fuel cell are completely oxidized) and of the hot reformate stream are utilized to condition the fuel–air–water mixture fed to the reformer according to the requirements of the reforming method used. Part of the recovered energy can be used in heating up the catalyst bed. The scheme also allows reduction of the high reformate temperatures down to the levels of low-temperature WGS (473–573 K) and preferential CO clean-up (373–423 K) units [10]. In the case of POX, however, the water needed to run the shift conversion can be injected (e.g., sprayed) after the reformer (e.g., into zone "*b*," Fig. 14.1), which will also be beneficial in terms of cooling the reformate and reducing the heat duty and exchanger size. This system was modeled and simulated to optimize hydrogen production from various fuels such as methane [12,46], isooctane [12], ethanol [47], methanol,

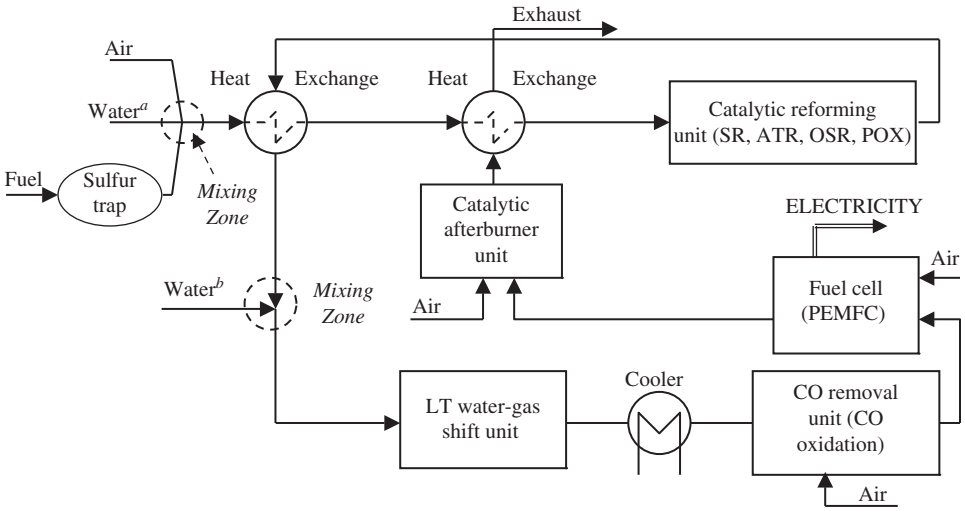

FIGURE 14.1 Flow diagram of the generalized fuel processing operation. *a*: Location of water injection in SR or OSR; *b*: location of water injection in POX. *(Reprinted from Avci et al. [46], Copyright (2002), with permission from Elsevier).*

and propane [12,48] and fuel conversion routes (IPOX and POX).

LPG. Hydrogen production via OSR of propane [37,49–52], *n*-butane [53], and their mixtures simulating LPG [54,55] has been investigated at various feed conditions, catalysts, and temperatures. In general, these studies report the mechanism of OSR by a combination of TOX, SR, WGS, and methanation. General characteristics of LPG conversion are similar to those of methane OSR; TOX is the fastest reaction and generates the heat needed to run SR. The onset of LPG conversion is easier than methane due to the lower light-off temperatures (Table 14.1). The temperature rise and the resulting maximum bed temperature are dictated by the C/O ratio in the feed. This phase of OSR is more critical for LPG than for methane since C_3–C_4 alkanes are less resistant to thermal cracking which may be followed by pyrolytic carbon formation favored at temperatures higher than ca. 920 K and is further facilitated at high residence times [56]. Nevertheless, the reformer can be designed to implement inherent resistance against pyrolytic coking via improved heat transfer and shorter residence times. For example, a dense-packed reformer with a small catalyst particle size range is more prone to coking than a wall-coated microstructured reformer with metallic supports.

Use of excess steam in the feed is an alternative method for minimizing carbon formation. The required amount of steam is determined by the particular active metal/support combination used. Inlet S/C and C/O ratios are reported to cluster around 3.0 and 1.0–1.35, respectively, in propane OSR at 600–700 K over alumina–supported, particulate monometallic Pt, Pd, Ru [51] and bimetallic Pt–Ni [55] catalysts at moderate residence times. The coke-free behavior of the same reaction was also demonstrated at a S/C ratio as low as 1.0 over a Rh/Al_2O_3/Fecralloy microchannel reactor at 1273 K, C/O ratio of 1.0, and a residence time of 12.6×10^{-3} s [37]. Propane–butane mixtures may call for steam inputs higher than those for propane only. An inlet S/C ratio of 3 was sufficient for propane conversion over a Pt–Ni/δ–Al_2O_3 catalyst without coking [49], whereas inlet S/C ratio of 5 and 7 were required for

the conversion of 75:25 [55] and 50:50 [54] C_3H_8/n-C_4H_{10} mixtures respectively, over the same catalyst with no carbon formation. These results indicate that an LPG reformer should include a water/steam management system capable of meeting the steam requirements of different LPG compositions and of evaporating water quantities much higher than in the case of methane, both of which will require an evaporation unit with extra volume and complexity and more efficient energy recovery from heat sources, such as the hot stream leaving the catalytic afterburner (Fig. 14.1). The use of a coke-resistant catalyst, such as Rh, together with short contact times can reduce the steam demands significantly and allow more compact evaporator systems.

A mixing zone/chamber is needed for ensuring well mixing of the reactants (Fig. 14.1). Mixing is less of an issue for gaseous fuels such as methane and LPG. In addition, a desulfurization unit should be implemented at the reformer upstream to strip the sulfur-containing compounds from hydrocarbon fuels and to protect expensive reformer catalysts from poisoning.

14.1.2. Gasoline and Diesel

Compared to the conversion of light alkanes to hydrogen, catalytic processing of gasoline and diesel require somewhat different conditions. Both fuels are in the liquid phase at ambient conditions and are complex mixtures of higher hydrocarbons ($>C_8$) with various types including linear and branched alkanes, alkenes, aromatics, and cycloalkanes and of sulfur-containing compounds. The average carbon number in gasoline is less than that of diesel and is modeled generally by isooctane or by isooctane + n-octane mixtures. Heavier alkanes such as n-decane, n-dodecane, and n-hexadecane and their mixtures are considered as diesel surrogates. Regardless of the type of conversion process (SR, POX, OSR), presence of a wide spectrum of hydrocarbons with diverse characteristics together with sulfur constitutes the major challenge in reforming of these fuels and poses the following issues − complete evaporation followed by fast and homogeneous mixing before the reformer and stable operation within the reformer.

14.1.2.1. Evaporation and Mixing

The design of the evaporation and mixing chamber has significant impacts on the operation of the reformer unit and calls for a set of critical requirements. First, evaporation of the fuel should be complete, as the contact of liquid fuel with the reformer catalyst will immediately lead to coke formation due to the presence of aromatics. Secondly, the evaporated fuel should be mixed with steam and/or the oxidant (usually air) and fed to the reformer homogeneously to ensure constant inlet S/C and C/O ratios required for sustainable and stable hydrogen throughput. To illustrate, coke formation and unexpected temperature spikes can be caused by local occurrence of insufficient steam (low S/C ratios) and excess oxidant (low C/O ratios), respectively [57]. The third requirement is related to operational safety for which rapid and uniform mixing is essential, because the auto-ignition temperatures for alkanes higher than n-decane are smaller than their boiling points. This is specific to oxygen-involving processes and becomes critical during evaporation of diesel due to the presence of linear alkanes up to C_{20}. The absence of fast mixing may lead to formation of local oxygen-rich zones where C/O ratios are lower than the critical values and may end up in auto-ignition followed by possible explosions. Therefore the fuel−air mixture should be rapidly mixed to homogenize the C/O ratio above the threshold limits throughout the evaporation chamber. Various designs of the evaporation-mixing unit have been addressed extensively by several research groups [57−63]. Pors et al. [58] have proposed a system in which diesel is sprayed together

with superheated steam into an evaporation chamber for turbulent mixing, and the resulting vapor stream is further mixed by subsequent air injection that homogenizes the composition at the reformer inlet. The system was designed by coupled use of computational fluid dynamics and flow visualization techniques and formed the basis for complete diesel conversions during 620 h time-on-stream tests without catalyst deactivation. Use of an automotive fuel injector to spray the fuel against the hot walls of the fuel-air mixing chamber for obtaining rapid evaporation and mixing has been demonstrated successfully during POX of various fuels used as surrogates of gasoline [63] and diesel [62,63].

Evaporation of gasoline and diesel requires high temperatures. The evaporation of gasoline starts at ca. 300 K and is complete at 600 K, with 90% of the fuel being vaporized around 473 K [64], while diesel, which contains heavier hydrocarbons, starts boiling at ~400 K which is almost complete around 700 K [64]. In addition to the fuels, water must also be evaporated in the cases of SR and OSR. Consequently, running the overall system will necessitate energy input, making heat integration an essential part of the fuel processing system. Heat integration can be established by several methods including recuperation of waste heat from the reformer and use of integrated catalytic afterburners [57,65], and remains as one of the challenges in gasoline and diesel reforming owing to the complexities of the evaporation phase.

14.1.2.2. *Steam Reforming*

Studies involving the catalytic conversion of gasoline and diesel to hydrogen have common features regardless of the conversion route. In general, Rh-based catalysts give the best conversion/selectivity performances with minimal/no coking, whereas the coking resistances of Ni-based catalysts are poor. Secondly, high temperatures are needed to minimize coking by overcoming the low reforming reactivity of aromatics and ensuring their complete conversion to synthesis gas, which necessitates materials of construction with high thermal resistance and tailoring of catalytic properties against sintering. In addition to these common features, individual processes can pose different requirements. As in the case of methane and LPG, steam reforming of gasoline and diesel gives the highest hydrogen concentration at the expense of high steam and energy requirements [66]. Typical inlet S/C ratios employed are between 3.6 and 4.0 to obtain near complete conversions of isooctane and hexadecane, surrogates of gasoline and diesel, respectively, at temperatures in excess of 973 K [67,68]. Effective heat recuperation is essential and should be implemented through the use of integrated, high-efficiency heat exchangers that can supply enough energy to evaporate the fuel and the excess water, and to drive endothermic SR reaction.

14.1.2.3. *Partial Oxidation*

Partial oxidation has been explored by several research groups for different fuel blends at various combinations of reaction conditions and catalysts [62,63,69–71]. For example, a series of studies on POX of surrogates of gasoline (isooctane, *n*-octane + isooctane) and diesel (*n*-decane, *n*-hexadecane, *n*-decane + *n*-hexadecane, *n*-decane + naphthalene) as well as commercial low sulfur diesel were conducted over Rh on alumina-coated monoliths at short contact times (5×10^{-3}–2.5×10^{-2} s) and C/O ratios of 0.6–2.5, which showed that lower C/O ratios lead to syngas selectivities and fuel conversions in excess of 80% and 99%, respectively, whereas higher C/O ratios favored olefin production. In addition to high syngas selectivity, oxygen-rich conditions also favor burning of the coke that may have formed during the reaction. Considering the maximum catalyst temperature (ca. 1473 K, where Rh starts to sublime) and auto-ignition limits of the process, a C/O ratio ca. 1.0 is recommended as an optimum value [71].

The absence of steam in POX reduces evaporation load and simplifies evaporator design. However, vigorous pre-mixing of evaporated fuel with air becomes more important for suppressing flame formation and possible explosions as steam absorbs some exotherms related to auto-ignition. Other disadvantages of steam-free operation are the risk of coking and formation of product mixtures with low hydrogen content, due to the absence of coke gasification and WGS, respectively.

The high conversion and selectivity levels achieved at high temperatures and millisecond contact times call for reactor structures and catalyst supports, such as ceramic monoliths, that can withstand excessive temperatures and allow high flow rates. Channel diameters in monoliths constitute an important design parameter owing to their impact on product distribution. To illustrate, H_2 and CO selectivities increased by 14% and 8%, respectively, when an 80 pores per square inch (ppi) monolith was used instead of a 20 ppi monolith in POX of cyclohexane, *n*-hexane, isooctane, and toluene over Rh-alumina monoliths. Similarly, introduction of a tortuous texture by γ-Al_2O_3 washcoating led to 9% and 7% higher H_2 and CO selectivities, respectively [71]. These observations clearly show the effect of fluid-to-washcoat transport processes which must be reduced by minimizing the boundary-layer. Effective mixing at the fluid−solid interface can be achieved by selection of suitable channel diameters and/or geometries characterized by high Sherwood and Nusselt numbers allowing high mass and heat transfer coefficients, respectively, as long as the pressure drop remains within acceptable limits.

14.1.2.4. Oxidative Steam Reforming

Oxidative steam reforming of gasoline and diesel is less energy intensive compared to SR, since catalytic oxidation of part of the fuel can supply energy to the reformer. Moreover, the co-existence of steam in the feed helps to minimize the risk of carbon formation; OSR produces less coke compared to SR and POX [72]. Studies addressing the gasoline and diesel OSR usually involve inlet S/C and C/O ratios between 1.5−3.0 and 1.0−2.5, respectively [57,58,60,61,72−77], but feed compositions outside these ranges have also been reported [65,78−80]. Reaction temperatures are in the range of ca. 800−1100 K. There is a general agreement that the mechanism of OSR can be described by the sequential occurrence of TOX/POX and SR reactions, which is supported by the observation of hot-spots along the reformer [65,80,81]. Moon et al. [78] observed that decreasing the C/O ratio reduced H_2 and CO yields, while increasing CO_2 yield, indicating TOX stoichiometry. In the cases of methane and LPG, the actual C/O ratio at reactor inlet is nearly the same as set in the feed due to almost perfect mixing, which is difficult to achieve for gasoline and diesel. In addition to careful design of the evaporator/mixing unit, reformer design must be robust enough to absorb local temperature spikes, which can be introduced by using structures with improved heat transfer characteristics and structured flow paths. The former will favor the distribution of high temperatures to the other parts of the reformer, while structured flow paths will have an indirect effect via allowing high flow rates with minimal pressure drop that will sweep hot-spots. Metallic microchannels and monoliths are examples of inherently robust reactor forms [57,60,61,65,80]. Despite their beneficial properties, the narrow flow paths may be problematic due to clogging in the case of coking initiated by aromatics. A second problem is irreversible sulfur poisoning which will necessitate the replacement of the entire catalytic structure, as the removal of the washcoat matrix from the support is not practical.

14.1.3. Oxygenated Hydrocarbons

Methanol and ethanol are the main oxygenated hydrocarbons that have received attention as potential hydrogen sources for PEM fuel cell systems since they are renewable.

Thermodynamic calculations show that methanol and ethanol SR require less energy per mol of H_2 formed (ca. 20 kJ mol^{-1} and 30 kJ mol^{-1}, respectively) than the SR of saturated hydrocarbons (ca. 70 kJ mol^{-1} for methane and propane) [82]; besides, methanol and ethanol SR produces mostly CO_2, some of which is converted to CO via reverse WGS (RWGS) at high temperatures [83].

14.1.3.1. Methanol

Methanol SR is mildly endothermic and at lower reaction temperatures of 500–673 K produce high H_2 yield at low S/C ≈ 1. Cu-based catalysts are highly selective for H_2 generation while base metals like Ni, Co, Fe, Mn, Mo, Cr, and some noble metals promote synthesis gas production [4]. Pd-containing catalysts (Pd/ZnO, Pd/CeO_2) also have high activity and H_2 production selectivity; apart from their cost, the main drawbacks are their tendency for coke formation and higher CO yield typical of noble metal catalysts [84,85]. The most widely used catalyst is $Cu–ZnO/Al_2O_3$, giving 100% methanol conversion at 553 K with exit reformate containing ca. 70% H_2 on a dry basis [86], which corresponds to an exit CO content of 5% at a S/C ratio of 1. S/C ratios $\geq$ 1.5 are generally preferred to reduce the CO level to $\leq$1% at the expense of decreasing the H_2 yield to ca. 65% [14,87] in order to avoid an external WGS converter and to complete CO clean-up only by preferential CO oxidation. Addition of sufficient water is also important for minimization of coking. The merit of Cu–ZnO catalysts is high activity and H_2 selectivity at temperatures as low as 523–573 K; their disadvantage is the sintering observed around 600 K, which necessitates careful temperature control for sustaining the active phase of $Cu–ZnO/Al_2O_3$ [88,89]. Cu–ZnO catalysts are pyrophoric [86], they need pre-treatment under hydrogen before start-up and are prone to sulfur and chlorine poisoning [90]. Catalyst deactivation models indicate a slow decline in activity starting at reactor inlet under typical operation conditions [87,91]. The use of coated catalysts was proposed for circumventing intraparticle mass transfer resistances that promote CO formation over $Cu–ZnO/Al_2O_3$ particles [92]. Methanol SR was also studied at 523 K, S/C = 1.1 and relatively low space times in microchannels coated with $Cu–CeO_2/Al_2O_3$ and, at about 50% methanol conversion, an exit CO level of 2% was observed [93–95].

Although thermodynamic considerations show that methanol SR can produce a reformate stream with ca. 70–75% H_2 on a dry basis, it requires external energy and is not compatible with operation under transient or cyclic conditions. OSR, on the other hand, combines catalytic total oxidation (TOX) and SR accompanied by WGS for better heat management and is the most promising technology enabling the design of compact adiabatic reactors with low pressure drop [96]. Methanol OSR is also feasible over Cu-based catalysts provided that the maximum reaction temperature is kept under 600 K. Since the light-out temperature for methanol SR is 510 K [45], the OSR reactor needs to be carefully controlled within this temperature bracket. The SR catalyst $Cu–ZnO/Al_2O_3$ loses its activity when it comes in contact with oxygen, unless the distribution of oxygen in the OSR reactor is properly designed. Quaternary catalyst formulations including particulate $CuO–ZnO/ZrO_2–Al_2O_3$ and ceramic monoliths washcoated with Al_2O_3 were designed to improve activity and stability in methanol OSR [90,97,98]. Among noble metal containing catalysts, Pd/ZnO was reported to be stable above 600 K with nearly 80% hydrogen selectivity at ca. 80% methanol conversion [99,100].

The independent variables of the OSR reactor are inlet temperature, inlet S/C and C/O ratios, and reactor pressure, while the dependent variables are exit temperature and methanol conversion; the parameter to be maximized is H_2 selectivity (mol H_2

produced/mol methanol converted). Lower OSR reactor pressures are critical for maximizing H_2 selectivity. High S/C ratios and high temperatures at reactor inlet favor methanol conversion, but undesirable CO yield also increases with temperature. These conditions also favor H_2 production in the sense that less methanol is oxidized for maintaining the SR reaction and hence higher C/O ratios can be used [10,101,102]. The reformate contains H_2, CO, and CO_2, and relative concentrations are determined by WGS occurring in the OSR reactor if thermodynamic equilibrium is attained [79]. The optimal inlet S/C ratio for achieving maximum H_2 yield in OSR is reported as 1.5 [82]. Although C/O ratios between 0.8 and 2.0 can be used on Cu−ZnO catalysts, important design issues are the distribution of the air feed in actual OSR reactors and temperature control for sustaining catalyst activity and stability, since methanol oxidation leads to temporary temperature fluctuations which eventually deactivate the catalyst [45,89,103].

14.1.3.2. *Ethanol*

The major reasons for consideration of ethanol as a hydrogen source are that it can be produced by fermentation from renewable resources, is less toxic, and safer to handle. Ethanol SR is more endothermic (173 kJ mol^{-1}) than methanol SR (49.5 kJ mol^{-1}), occurs at atmospheric pressure but requires higher temperatures on account of its C−C bond. Reaction temperatures of 600−1200 K and inlet S/C ratios higher than 2 produce high H_2 yield. However, both ethanol conversion and H_2 yield differ significantly depending on catalyst composition, method of catalyst preparation, and the process conditions used [104,105]. Ni, Co, Ni−Cu, and noble metals such as Pt, Pd, and Rh over suitable supports such as ZnO, CeO_2, Al_2O_3, and La_2O_3−Al_2O_3 were studied, and the major drawbacks listed are byproduct formation and coke deposition [106]. Side products of Ni-based catalysts are mainly CH_4, CO, and CO_2 [107]; ethylene is produced on Al_2O_3-supported noble metals, whereas acetaldehyde is also formed on CeO_2-supported catalysts [108]. Cobalt is another attractive base metal as it can cleave the C−C bond of ethanol; cobalt-based catalysts give complete ethanol conversion at 623 K with high H_2 selectivity around 70% [109−112]. Among Al_2O_3-supported noble metals tested between 873 and 1123 K at a S/C ratio of 1.5, Rh/Al_2O_3 proved to have the highest activity and lowest byproduct selectivity [113,114]; similarly, Rh/CeO_2 showed rather low CH_4 selectivity [115]. Deactivation patterns of Rh-based catalysts were consistent with coke deposition but total regeneration was possible at low temperatures [116]. At high temperatures (923 K) and metal loadings (5 wt%), Ru/Al_2O_3 showed similar performance to Rh catalysts, with 95% H_2 selectivity [114,117]. Ethanol SR performance of bimetallic Pt−Ni/δ−Al_2O_3 was studied at 623−823 K using inlet S/C ratios of 1.5−3.0, and ethanol conversions above 95% were reached at 823 K with an inlet S/C ratio of 2.5; 773 K was the optimum temperature at which high hydrogen selectivity was accompanied by low CO and CH_4 selectivity. The bimetallic catalyst was resistant to coking at inlet S/C ratios as low as 1.5 [118,119]. In Pt−Ni catalysts, Ni is functional in breaking the C−C bond of ethanol [120], while Pt promotes the simultaneous high-temperature WGS reaction which is essential for lowering the CO level in an SR or OSR reactor [104].

Although ethanol SR has the highest efficiency for hydrogen production, it requires external energy to initiate and sustain the reaction and can produce significant amounts of CO and coke depending on the catalyst. POX of ethanol in air at 773 K can generate H_2 and CO mixtures with high CO selectivity [121]. Ethanol OSR combines the features of oxidation and steam reforming to maximize H_2 production; coke formation which is

significant under SR conditions at 573–923 K and CO formation are both diminished under OSR conditions at C/O ratios < 1 along with S/C > 4 [122,123].

The number of reports in the literature is limited since studies on ethanol OSR are fairly new [104]. Ni-based catalysts on various supports and promoted with Cu, Cr, Zn, Na, or K were tested for ethanol SR and OSR in the 523–873 K range [120,124,125]. The performances of noble metals for ethanol OSR at 873–1123 K depended on the nature of the metallic phase, the metal loading (0–5 wt%), and the nature of the support material (Al_2O_3, MgO, CeO_2, and TiO_2) [126]. It was shown that the order of activity for Al_2O_3-supported metals is Rh ≥ Ru > Pd > Pt = Ni and that Rh is also more selective toward H_2 generation [127]. On the other hand, with CeO_2/ZrO_2-supported catalysts, the order of activity of metals at higher temperatures is Pt ≥ Rh > Pd [115]. Comparison of experimental conditions and results shows that ethanol conversion and H_2 selectivity change considerably with catalyst, support material, reaction temperature, inlet S/C, and C/O ratios; therefore, process engineering aspects determine economic feasibility of ethanol SR and OSR. In both cases H_2 selectivity is maximized by supplying sufficient steam to repress ethanol decomposition and dehydration reactions [104]. Since the first step in OSR is to initiate catalytic TOX, which is central to the heat management of the fuel processor, the light-off temperatures of ethanol over different catalysts need to be known.

14.2. DESIGN REQUIREMENTS OF WGS UNIT

The exit stream from a steam reformer may contain up to 12% CO, depending on the hydrocarbon fuel, while that of an OSR unit has about 6–8% CO [96]. The majority of this CO must be converted into CO_2 by the equilibrium-limited and mildly exothermic WGS reaction thermodynamically favored at temperatures where reaction kinetics is sluggish. Therefore, external high-temperature (573–723 K) and low-temperature (473–573 K) WGS converters downstream from the reformer are used in a row with in-between cooling for reducing the CO level first to 3–4% and then to 0.5–1%, as well as producing additional H_2 by steam injection into the reformate [128]. If the reformate has ~4% CO, as in methanol SR and OSR, only low-temperature WGS conversion is adequate for achieving 1–2% CO at the WGS exit [12,48].

Industrial high-temperature WGS catalysts are based on Fe–Cr oxides because of their low cost, longevity, and sulfur tolerance. Cr_2O_3 is used to stabilize the active phase consisting of FeO, Fe_2O_3, and Fe_3O_4. Since iron oxides function by means of a regenerative oxidation-reduction mechanism, the reaction temperature as well as the H_2O/H_2 and CO_2/CO ratios have to be strictly controlled to avoid methanation (caused by reduction of Fe oxides) and water condensation which harms chromium oxides; both events cause difficulties in sustaining the interchange between Fe oxides occurring above 623 K. The pyrophoric nature of Fe–Cr oxides also creates a risk, since exposure to air after activation leads to spontaneous heat generation resulting in excessive temperature upsurge causing loss of activity [86,128]. The low activity of Fe–Cr oxides requires high temperatures (> 573 K) and large adiabatic reactor volumes. Possibilities for increasing their activity include base metal or noble metal promoters among which Rh is the most active [129]. In the commercial Fe–Cr–Cu catalyst, Cr can be replaced by Al [130] or Mo [131] with similar activity levels. Cobalt catalysts also show high activity above 573 K and are sulfur resistant [96].

The low-temperature WGS reaction is catalyzed industrially by $Cu–ZnO/Al_2O_3$ at 453–523 K to reduce CO from 3–4% to 0.5–1%

[132]. Commercial Cu−ZnO/Al_2O_3 catalyst designed for large-scale steady-state adiabatic operation has much higher activity than all other catalysts, but it requires *in situ* reductive pretreatment with careful temperature control because of the highly exothermic nature of the process; similarly, exposure to oxygen induces an exothermic reaction over 900 K; temperatures above 553 K deactivate the catalyst due to sintering of copper crystallites; moreover, it is deactivated by steam condensation and poisoned by traces of sulfur and chlorine present in the fuel or water [96]. As a result, Cu−ZnO/Al_2O_3 is not suitable for fuel processors generating H_2 for mobile or small-scale fuel cell power systems having duty cycles with recurrent start-ups and shut-downs. Cu−Al_2O_3−$CuAl_2O_4$ catalysts with improved features are also prone to deactivation but can be regenerated by air calcination with full recovery [133]. Most WGS catalysts are affected by the reversibility of the reaction and strong product inhibition [10]. Among catalysts explored as alternatives, Cu−CeO_2 has high activity, low cost, and better thermal stability but is not resistant to sulfur poisoning [134]. A base metal non-pyrophoric proprietary alternative for Cu−ZnO was reported to maintain its activity upon exposure to liquid water and its stability up to 623 K [132].

Typical temperature at the high-temperature WGS exit is not less than 623 K, which must be cooled down to ca. 453 K at the inlet of the low-temperature WGS converter with the Cu−ZnO catalyst whose activity is proportional to the specific surface area of Cu. Both particulate Fe−Cr and Cu−ZnO catalysts require sizeable volumes with large heat capacity, which slows down their response to transients and constitutes another disadvantage for small-scale applications of fuel cell systems [135].

Noble metal catalysts such as Pd, Pt, Rh, and Ru are costly but thermally stable and insensitive to contact with air or liquid water; they also have the advantage of operating under both high and low temperature WGS conditions. These catalysts are not too active below 523 K which restricts their CO removal capacity, are inhibited by H_2 and CO_2 in the low temperature range, and have a tendency for CH_4 formation above 623 K. Mechanisms for WGS over Pt−CeO_2 and Pd−CeO_2, deactivation patterns, methods for enhancing activity by promoters and better pretreatment conditions have been reviewed [136]. A very important feature of these catalysts is that they can easily be deposited onto the walls of ceramic and metallic monoliths which are more appropriate for mobile applications and are stable up to 723 K. Monolithic catalysts present the possibility of increased activity and hence smaller reactor size, faster response to transients, and higher stability during start-up and shut-down [137]. Promoted Pt and Pt−Re catalysts supported on monoliths commercialized for low and high temperature WGS operation, respectively, showed high WGS and low methanation activity, good hydro-thermal stability with resistance to air and liquid water exposure, but low sulfur tolerance requiring a desulfurization unit; both catalysts permitted operation at high space velocities resulting in smaller reactor volumes, lower pressure drop, and faster response to transients involved in fuel processing in integrated fuel cell systems [135].

14.3. DESIGN REQUIREMENTS OF CARBON MONOXIDE REMOVAL UNIT

The CO content of gases exiting the low-temperature WGS reactor is determined by reaction equilibrium at 453−473 K and corresponds to 0.5−1.0% CO. However, considering the effluent of a methanol reformer that does not need WGS conversion or of a WGS unit downstream from a hydrocarbon OSR unit, it is necessary to design a CO cleaning process

suitable for handling 1−3% CO to achieve the final CO level of ca. 10−50 ppm before H_2-rich gases enter the PEM fuel cell [4]. CO removal is achieved by employing physical or chemical methods. Chemical processes are based on solid-catalyzed reactions like selective CO methanation and preferential CO oxidation (PrOX); the latter is mostly used in fuel processors integrated with low-temperature PEM fuel cells operating below 373 K. High-temperature PEMFCs with membranes operating above 453 K do not require PrOX since CO adsorption on the Pt anode catalyst is not inhibitory at this temperature. Physical processes used for CO clean-up include pressure swing adsorption (PSA), for operation at near-ambient temperatures and sufficiently high pressures, as in service stations for H_2 fueling [135], and membrane separation with selective H_2 membranes, applicable in cases where the pressure is high enough for reaching practical H_2 permeation rates [138].

14.3.1. Preferential CO Oxidation (PrOX)

The most effective method of CO clean-up is low-temperature PrOX at 373−423 K, and the purpose is to achieve almost 100% CO conversion with minimum hydrogen oxidation. Low-temperature PrOX catalysts generally contain a precious metal component such as Pt. Since noble metals on inert supports lack the selectivity required for PrOX, various promoters are added to facilitate CO oxidation via a dual-site mechanism with different adsorption sites for CO and oxygen. Studies on PrOX in the presence of ca.70% H_2 indicate Pt and Ir as the most active and selective noble metals, and CeO_2 with its high oxygen mobility as the best support material [139]. Pt/CeO_2 is an excellent PrOX catalyst while Pd/CeO_2 is inactive because of its affinity for hydrogen chemisorption [140]. Pt promoted by Co or K appears to be the best PrOX catalyst on oxide supports like Al_2O_3 [141], $CeO_2-Al_2O_3$ [142], CeO_2-MgO [143], and $MgO-Al_2O_3$ [144]. Recent reports on other Pt-based PrOX catalysts include $Pt/MnO_x-Al_2O_3$ [145], $Pt/SnO_2-Al_2O_3$ [146], $Pt/Fe_2O_3-Al_2O_3$ [147], Pt/mordenite [148], and activated carbon supported $Pt-CeO_x$ and $Pt-SnO_x$ [149,150]. Experiments carried out with mixed feed containing CO_2 and H_2O in actual WGS exit proportions indicate that promoted Pt/Al_2O_3 and Cu/CeO_2 catalysts retain their activity [151].

Key constraint of PrOX is to reduce the CO content of the reformate stream leaving the WGS converter down to $<$ 10−50 ppm with negligible loss of H_2. Other constraints are minimization of RWGS and CO/CO_2 methanation reactions, all of which consume H_2 and increase the CO level [128]. The PrOX unit should fit into fuel processor design with a minimum number of additional utilities; more explicitly, the PrOX catalyst must tolerate the CO_2 and H_2O levels in the WGS effluent as well as the entire range of space velocities related to the start-up and shut-down cycles of PEMFC operation, its structure must be suitable for operation at all space velocities with low pressure drop since PEMFCs operate over a series of output requirements, and finally, its operating temperatures must conform to the exit WGS ($>$473 K) and inlet PEM fuel cell (ca. 353 K) temperatures for more efficient heat management [135].

The performance of PrOX catalysts in actual reformate streams are, therefore, affected by the O_2/CO ratio, reactor temperature, and space velocity. Stoichiometric O_2/CO requirement for complete CO oxidation is 0.5, but excess O_2 is used since catalysts are not 100% selective in H_2-rich streams, and maximum 50% selectivity is attained over most PrOX catalysts at a molar O_2/CO ratio of 1, which means that higher O_2/CO ratios facilitate both CO and H_2 oxidation resulting in heat generation and temperature rise, which, in turn, promote RWGS and methanation of CO and CO_2. PrOX catalysts are designed to ensure sufficient

activity for coping with the CO in the reformate stream at its maximum flow, thus PrOX dominates at high space velocities whereas RWGS, which is much slower, is negligible. Pt-based catalysts produce CO by RWGS at low space velocities, due to extended reaction times and depletion of the O_2 near the reactor exit. Hence, successful PrOX catalysts must be able to selectively and almost completely convert CO in the presence of CO_2 and H_2O, in the space velocity range of the fuel processor and within a temperature bracket where the lower limit does not allow condensation of the steam in the reformate and the upper limit does not encourage RWGS and methanation [10]. Other issues related to the duty cycle of fuel cell operation are the effects of water condensation and presence of CO_2 on the catalyst at shut-down (water oxidizes base metal catalysts like Cu and CO_2 leads to surface carbonate formation on CeO_2-supported Au catalysts), and evaporation of water during start-up causing mechanical stresses in particulate catalysts. These are related to process design and may be minimized by proper choice of catalyst composition, support structure, and process conditions [96].

Particulate supports such as Al_2O_3, SiO_2, TiO_2, and Fe_2O_3 may be suitable for some stationary applications where duty cycles, reactor sizes, and response to transients are not exacting. The low values of the internal effectiveness factors of catalysts packed in granular or pellet form, poor heat transfer as well as pressure drop along packed-beds have forced the development of engineered catalysts using monolithic or foam substrates [137,152–154], wall-coated catalysts [155], and microstructured catalysts with new geometries [156], which allow higher space velocities resulting in reduction of catalyst volumes and improved heat transfer. Monolithic PrOX catalysts are structurally stable, respond faster to temperature transients, and withstand much higher gas space velocities (>50,000 h^{-1}) as opposed to particulate catalysts operating at lower space velocities (<10,000 h^{-1}) [135].

Depending on the amount of CO to be removed and the resultant heat dissipated, the PrOX reactor may be split into two or more stages. A system where the greater part of CO from the upstream WGS converter is oxidized over Pt/Al_2O_3 at a high temperature ca. 473 K followed by cooling and PrOX over $Au/\alpha-Fe_2O_3$ at 353 K was reported to decrease the CO level in the exit to $\leq$ 20 ppm [157]. Since O_2 consumption increases with decreasing space velocity and increasing temperature, two-stage monolithic precious metal catalysts operated adiabatically at ca. 40,000 h^{-1} gas space velocity with inter-stage cooling and two air injections can reduce the inlet 1% CO down to 10 ppm [135]. Another multi-step arrangement that can operate with 2–3% CO for achieving CO levels <10 ppm makes use of a series of monolithic PrOX stages followed by selective methanation for final polishing [158].

14.3.2. Selective CO Methanation

An alternative solid-catalyzed chemical method of CO clean-up is methanation of CO, which is highly exothermic and uses three moles of H_2 per mole of CO. An unwanted side reaction is CO_2 hydrogenation consuming four moles of H_2 per mole of CO_2. The RWGS reaction favored at high temperatures may also hinder CO removal by shifting CO_2 to CO [64].

The advantages of CO hydrogenation are that the reactants are already present in the feed, the CH_4 produced is an inert diluent and does not react with O_2 or H_2O at PEMFC temperatures, and moreover, it can be combusted in the afterburner together with the H_2 rejected by the cell and contribute to thermal efficiency. Major disadvantage is its H_2 consumption which can be tolerated considering that 0.5–1% CO is normally present in WGS exit stream.

Studies on complete CO removal from H_2-rich streams by methanation have focused on noble metal and Ni catalysts. Ni/ZrO_2 and Ru/TiO_2 were effective in decreasing CO from 0.5 wt% to 20 ppm in the presence of 25% CO_2 at 493–553 K, with very low CO_2 methanation [159]. Studies on 3% Ru/Al_2O_3 at 513–553 K reduced CO output to less than 100 ppm and kept H_2 consumption under 10% at high gas space velocity [160]. Al_2O_3-supported noble metals were used for methanation of CO, CO_2, and their mixtures at 473–620 K to find the effect of metal (Ru, Rh, Pt, and Pd) in the absence and presence of water [161]. Ru and Rh were significantly more active than Pt and Pd, and catalytic activity of Ru was unaltered in the presence of water. In the hydrogenation of CO/CO_2 mixtures over Ru, CO_2 conversion was suppressed until CO conversion reached its maximum, and addition of 30% H_2O did not affect CO but hindered CO_2 hydrogenation and expanded the temperature interval for operation. Further work at 443–743 K on Ru catalysts for CO methanation under excess CO_2 confirmed that CO methanation dominates that of CO_2 until CO concentration is reduced to 200–300 ppm [162].

The design challenge is to achieve complete CO removal in the presence of large amounts of CO_2 and steam coming from the WGS converter. Central issues are the development of CO methanation catalysts that are active at low temperatures where CO_2 hydrogenation and RWGS are held back, and temperature control for sustaining high CO methanation selectivity. Complete CO removal by methanation is not feasible for small-scale stationary, portable, and mobile fuel cell systems with very low CO concentrations in WGS exit [128,160,163], but may be applied in service station CO conversions. Multi-stage CO removal designs that can handle up to 2–3% CO in the upstream reformate for reducing CO levels to $<$10 ppm use two or more monolithic PrOX reactors followed by a monolithic selective CO methanation reactor (after all O_2 is consumed) for removing final traces of CO [158].

14.4. DESIGN REQUIREMENTS OF DESULFURIZATION UNIT

Various sulfur compounds are present in most hydrocarbon fuels used for H_2 generation, and fuel pre-processing is necessary for sulfur removal for catalyst protection. Base metals (Ni, Co, Fe, and Cu) are poisoned at sulfur contents below 100 ppbv, while noble metals can withstand sulfur levels of 1–10 ppmv [64]. Since sulfur is removed at an earlier industrial stage, commercial methanol has almost no sulfur. Ethanol excludes sulfur compounds [82]. Natural gas composition changes depending on source and process conditions, so that it may contain significant levels of sulfur as H_2S and sulfur-bearing odorants [135]. Sulfur content of pipeline natural gas in the US is 4–8 ppmw plus 5–20 ppmw of odorants [96]. LPG normally contains ca. 30 ppmw of sulfur compounds, but sulfur contents as high as 100 ppmw may be encountered [164]. Sulfur levels in clean transportation fuels for internal combustion engines (30 ppmw in gasoline, 15 ppmw in diesel) are too high for fuel cell applications; hence, gasoline, diesel, and jet fuels require further treatment for ultra-deep removal of sulfur before or after reforming. Reformate from OSR of these fuels may carry H_2S at ppmv levels, which can deactivate catalysts of subsequent processes such as WGS and PrOX, and also poison the anode catalyst of the PEMFC [165,166].

Different methods may be used for removing sulfur as a part of the fuel processor system. The industrial conditions used for sulfur removal from natural gas are not suitable for small-scale fuel processors [96,165]. In fuel cell systems, desulfurization of organic sulfur compounds can be achieved using packed beds of adsorbents operating at ambient

conditions; however, a single adsorbent may not remove all sulfur compounds under such mild conditions. Activated carbons impregnated with alkaline earth or transition metals can adsorb H_2S and mercaptans, while zeolites and metal-impregnated zeolites can remove *t*-butyl mercaptan (TBM) and dimethylsulfide (DMS); removal of carbonyl sulfide (COS) is a taxing problem [96,167]. Ni-based reforming catalysts are very sensitive to sulfur; hence it must be trapped at the front end of the reformer. Noble metal catalysts used in OSR are more resistant, so sulfur compounds may be converted to H_2S during reforming and then trapped in a bed of ZnO at reactor exit; however, the steam present in the reformate greatly reduces the scrubbing capacity of ZnO compared to pre-reformer adsorption with almost no steam present [96].

Use of LPG for hydrogen production also entails lowering its sulfur content to ppb levels. $CuO/ZnO/Al_2O_3$, Ag-exchanged beta zeolite, and Ag/CeO_2 were used for sulfur removal from propane at room temperature [168]. Performance of $CuO/ZnO/Al_2O_3$ in eliminating TBM and that of Ag-exchanged zeolite in removing TBM, DMS, and DMDS were excellent, while Ag/CeO_2 removed all sulfur compounds including COS.

A new approach, called selective adsorption for removing sulfur (SARS) from gasoline, diesel, and jet fuels at room temperature without using H_2 or other reactive gases, is commended for on-site removal of organic sulfur compounds in fuel cell systems [166]. Key issue is to find an adsorbent that selectively adsorbs sulfur compounds without adsorbing aromatics and alkenes. A silica gel-supported transition metal compound was used to remove organic sulfur compounds in gasoline by SARS but had limited adsorption capacity [169]. A Ni-based adsorbent was reported to reduce sulfur content in kerosene to 1 ppm at ambient temperature and pressure with no H_2 addition [170]. Some commercial activated carbons were tested for adsorptive desulfurization of liquid hydrocarbons [171]. Adsorbents for deep desulfurization include zeolites, activated alumina, and carbon aero gels [172].

The desulfurization unit must be designed to remove efficiently the most difficult molecules to adsorb and, considering fuel variability, its capacity must be sized to strip the highest sulfur levels likely to be in the fuel used [82]. In mobile applications, multi-stage adsorption units lead to sizeable systems, and desulfurization of feedstock with medium to high sulfur content is better conducted in the liquid phase at low liquid space velocities [64].

14.5. TYPES OF REACTORS USED IN FUEL PROCESSING

In this section, various catalytic reactor types — fixed beds, monoliths, microchannels, foams, and wire gauzes — that can be used in the specific steps of fuel processing — reforming, WGS, carbon monoxide removal, and desulfurization — will be outlined. Each reactor type will be described in terms of their particular geometric configurations, fluid flow properties, and mass-heat transfer characteristics. The compatibility of reactors for use in the units of fuel processing system will also be discussed. However, it should be remembered that the final selection of the reactor type will require a holistic analysis of the capital and operational expenses, which is out of the scope of this text. Integrated reactors, in which catalytic reactions are coupled either with heat exchange or with separation (membrane reactors), will be described separately. Since the reactions of the fuel processing operations involve the gas phase composed of reactants, products, and inerts and the solid phase representing the catalyst, description of the reactor types will be limited to two-phase (gas-solid) operation.

14.5.1. Fixed-Bed Reactors

The configuration of fixed-bed reactors is quite straightforward and involves a tube or a vessel packed with a definite amount of catalyst (Fig. 14.2). Depending on the heat of reaction, the reactor can be operated either in adiabatic or in isothermal mode. Adiabatic mode is suitable for reactions with low heats of reaction and can be established by implementing an insulating jacket around the reactor. In the case of high exotherms or endotherms giving excessive adiabatic temperature changes, however, reactor temperature should be kept constant to prevent uncontrolled deviations in activity, selectivity, and stability of the catalyst. Constant temperature or isothermal operation requires heat exchange between the catalyst and a heat source/sink, which is basically a heating/cooling fluid flowing within a volume — a jacket or a coil — surrounding the reactor. Heat transfer can also be achieved by coupling endothermic and exothermic reactions such as SR and TOX within the same geometry, in a so-called heat-exchanger reactor concept (see Section 14.5.5.1).

Flow in the fixed-bed reactors can be described by the motion of the gaseous bulk fluid through the gaps between the catalyst particles that constitute the solid phase. In fixed-bed operation, inlet flow rates of the reactants and the catalyst particle sizes should be arranged to facilitate turbulence due to a number of reasons. Heat and mass transfer resistances can occur within the catalyst particle or between the catalyst and the bulk-fluid. The former, i.e., intraparticle resistances, is proportional to the pore size and can be controlled by the dimensions of the catalyst particles: smaller particles will have pores with short diffusion paths that will make the inflow/outflow of the gas molecules to/from the active centers of the catalyst easier. However, transport resistances between the solid and gas phases, called interfacial resistances, are proportional to the thickness of the boundary layer at the gas—solid interface. The temperature gradients in the boundary layer become more pronounced when the heats of reaction are high, causing rapid changes in surface temperatures and concentrations. Boundary layer effect can be dampened by inducing vigorous mixing, i.e., turbulence at the interface. This is possible by the use of high gas flow rates and/or by the selection of small packing sizes that allows dense-packing with small void fractions. These arrangements will also ensure effective heat transfer between the external heat source/sink and the catalyst bed (in the case of non-adiabatic operation) and will facilitate the approach to isothermal behavior. Moreover, the magnitude of the hot-spots will be reduced as a result of vigorous convective heat transfer that will tend to distribute the high temperature zones along the catalyst bed.

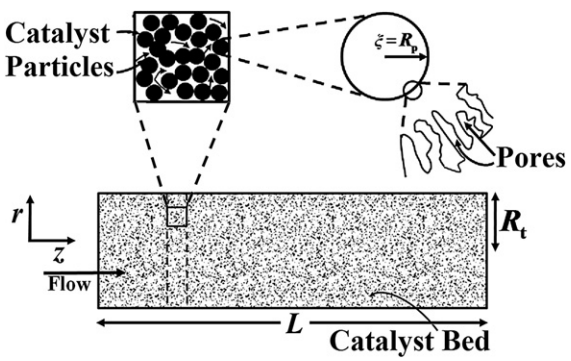

FIGURE 14.2 Schematic presentation of a fixed-bed reactor.

In general it can be assumed that the impact of intraparticle mass transfer resistance is more significant compared to heat transfer resistance, owing to the high thermal conductivity of the solid catalysts. However, intraparticle temperature gradients may become important in highly exothermic reactions of catalysts with large pore volumes. The significance of other effects can be quantified via a set of criteria given in Table 14.2. Note that these criteria are developed for a single reaction case described by n^{th} order power-law

TABLE 14.2 Transport Criteria for Heat and Mass Transfer in Fixed-Bed Operation

Resistance	Criterion (Single reaction case)	Criterion (Multiple reaction case)
Mears' criterion for interfacial mass transfer	$\frac{r_j \rho_b d_p n}{2 k_g c_i} < 0.15$	$\frac{R_i \rho_b d_p n}{2 k_g c_i} < 0.15$
Mears' criterion for interfacial heat transfer	$\left\lvert \frac{(-\Delta H_j) r_j \rho_b d_p E_A}{2 h_f T^2 R} \right\rvert < 0.15$	$\left\lvert \frac{\sum_j (-\Delta H_j)(r_j) \rho_b d_p E_A}{2 h_f T^2 R} \right\rvert < 0.15$
Weisz-Prater criterion for intraparticle diffusion	$\frac{r_j(c_i^s, T_s) \rho_p d_p^2}{4 D_{AB,eff} c_i^s} << 1$	$\frac{R_i(c_i^s, T_s) \rho_p d_p^2}{4 D_{AB,eff} c_i^s} << 1$

kinetics with respect to species *i*. Due to the multi-reaction character of the processes such as reforming, it may be more realistic to use the criteria in their "multi-reaction" versions which are obtained via an approximate approach and are outlined in Table 14.2 [173–175].

The geometric and operational measures of minimizing transport resistances generates conflict with pressure drop, the mechanical energy loss due to the friction between the gas and solid phases. As a result, the critical parameters such as feed flow rates, size, and type of packing need to be optimized. Fortunately, the presence of alternatives packing geometries widens the operating window of fixed-bed reactors without significant compromise from pressure drop. For example, packings such as Raschig rings and hollow cylinders have void fractions (ca. 0.6–0.8) higher than those of spheres and solid cylinders, with void fractions around 0.4 and 0.35, respectively. Fluid flow and heat transfer characteristics of various packings have been addressed extensively in [176]. Pressure drop in a packed bed of spherical particles can be described as functions of radius of packing (catalyst particle), void fraction of the packed-bed, superficial mass velocity, and gas density through the well-known Ergun equation [177]:

$$\Delta p = -L \frac{G}{d_p \rho_f} \left(\frac{1 - \varepsilon_p}{\varepsilon_p^3} \right) \left[\frac{150(1 - \varepsilon_p)\mu}{d_p} + 1.75G \right] \tag{14.12}$$

Regardless of the packing type, fluid motion in fixed-bed operation is unstructured due to the random nature of the packings. Regularity of the fluid streamlines is somewhat important in reactor operation and dictates the average time that the fluid molecules spend in the reactor which is quantified by the concept of residence time distribution (RTD). Reactors that allow narrow RTD of the fluid molecules tend to exhibit near-ideal operations. The opposite case with a wider RTD can, however, lead to deviations in product spectra and in temperature distribution with the magnitudes depending on the nature of the specific reaction. The end effects can be as serious as thermal runaways which may occur in the cases of uncontrolled, longer residence of reactants of highly exothermic reactions. In general, fixed-bed reactors exhibit non-ideal responses with wide RTDs due to their inherent randomness in fluid flow, e.g., increased channeling/bypassing at the packing zones close to the reactor wall vs. longer residence at the interior parts, and, therefore, subject to the undesired end effects stated above.

Considering their characteristics above, the use of fixed-bed reactors in fuel processing applications has some drawbacks. Fixed-bed operation is not suitable to run fast reactions with high heats of reaction as the mass and heat transport limitations will be dominant. As stated before, catalytic oxidations of hydrocarbons via TOX or POX can lead to the formation of hot-spots evolving at the active centers of the catalyst particles localized generally in the front zones of the catalyst bed. Since the particles do not constitute a continuum, i.e., separated by the voids, it will be inherently difficult to ensure uniform distribution of the high-temperature zone along the catalyst bed. Depending on the design of fixed-bed, this may cause local catalyst deactivation via sintering of the metals and support and ineffective use of the catalyst bed at the downstream. Inadequacy of the heat transport is critical also for the PrOX unit which should operate in a narrow temperature window (373−423 K) close to that of the PEM fuel cells and, therefore, calls for effective heat removal due to the exothermic nature of CO (and H_2) oxidation. The wide RTD of fixed-beds is another operational drawback and will become significant for reactions requiring short contact times throughout the reactor such as POX that will likely transform into TOX in case of longer residence times. Consequently, the product composition will deviate from the POX stoichiometry and local temperature spikes will be observed due to the higher exothermal heat of total oxidation.

It is possible to reduce the detrimental effects of transport limitations and non-uniform residence times by coupling the use of high flow rates with careful combination of the size, geometry, and packing uniformity of the catalyst support. The use of structured packings instead of random ones can further improve the operation in terms of residence time by regulating the flow paths to a certain extent. Nevertheless the applicability of these measures should always be crosschecked with the resulting pressure drop to figure out the boundaries of the optimum operating region.

Despite their inherent weaknesses pronounced at certain classes of reactions and conditions, fixed-bed reactors have the clear advantages of simple construction and practical operation. For example, ensuring the uniform distribution of reactants into a packed bed of catalysts is much easier than dividing and delivering flow equivalently into every cell of structured, multi-channel reactors (monoliths and microchannels); the structured configuration will require advanced diffuser components, meaning extra cost and complexity for the overall fuel processing system. Perhaps the most beneficial feature of the fixed-beds is the ease of removal and replacement of the catalyst bed in cases of irreversible deactivation due to, e.g., severe coking, thermal sintering, and sulfur poisoning, all of which are likely to occur in the reforming step. In this respect, fixed-bed scheme outperforms the other reactor types and offers significant downtime reductions in fuel processing. Another difference of fixed-beds is associated with the mechanism of radial heat transport (perpendicular to the axial flow along the bed); in addition to the conduction, radial heat transfer also runs via convection due to the presence of a flow component in that direction which can be further increased by customizing the geometry of the catalyst support. Shapes such as hollow or full cylinders with a length-to-diameter ratio of 1 to 3 are preferred over spheres for faster radial transport [176]. Co-existence of convection and conduction will enhance heat transport between the external heat source/sink and the catalyst bed and will make fixed-bed configuration suitable for use in non-adiabatic reactions.

14.5.2. Monolithic Reactors

These reactors are described by the use of monolithic catalysts to overcome the drawbacks

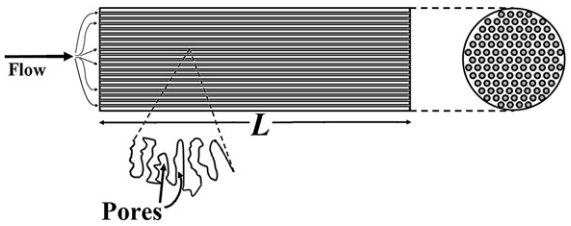

FIGURE 14.3 Schematic presentation of a monolithic reactor.

of the fixed-bed configuration. Monoliths are continuous structures with well-defined geometries involving numerous parallel, identical channels with small diameters and are used as catalyst supports. Depending on the porosity of the monolithic structure, the active metals can either be integrated directly with the channels of the monolithic support or be dispersed onto a washcoat, a porous layer which is deposited on the walls of individual channels. Monoliths can be made of metals or ceramics such as cordierite; the latter are more suitable for use as catalyst support structures in fuel processing mainly due to their high stability and integrity at elevated temperatures. A schematic presentation of a monolithic reactor and monoliths with various channel shapes are shown in Figs 14.3 and 14.4, respectively.

Monolithic catalysts are superior in terms of allowing access to high surface areas without compromising from pressure drop, which is up to two to three orders of magnitude smaller than observed in fixed-beds. The void fraction, i.e., ratio of the sum of the channel volumes to the overall volume can be as high as 75%. A detailed comparison of pressure drop in various configurations of monoliths and packing structures are given in Fig. 14.5 [178]. Transport phenomena at the micro and macro scales in monoliths are somewhat different from those in fixed beds. The thickness of the porous catalyst layer, and the pore dimensions, are usually small enough to prevent the formation of mass and heat transfer resistances within the washcoat phase. However, the resistances between the fluid−washcoat interface can become important when the reactions are fast. The flow regime in the monolithic channels is laminar. Assuming that the channels are smooth and non-porous, and that the entrance zone effect can be neglected, increasing the flow rate in laminar flow regime will not facilitate the interfacial transport; fluid-to-washcoat (or interfacial) mass and heat transfer coefficients will be dictated by the asymptotic Sherwood (*Sh*) and Nusselt (*Nu*) numbers which relate these coefficients to the hydraulic channel diameter, molecular diffusivity, and thermal conductivity of the fluid:

$$Sh = k_g d_h / D_{AB} \tag{14.13}$$

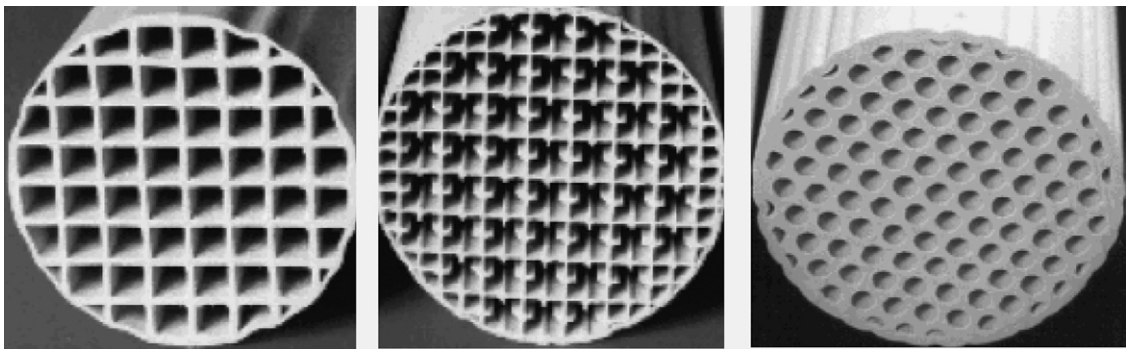

FIGURE 14.4 Monoliths with various channel shapes *(Reprinted from Boger et al. [178], Copyright (2004), with permission from American Chemical Society).*

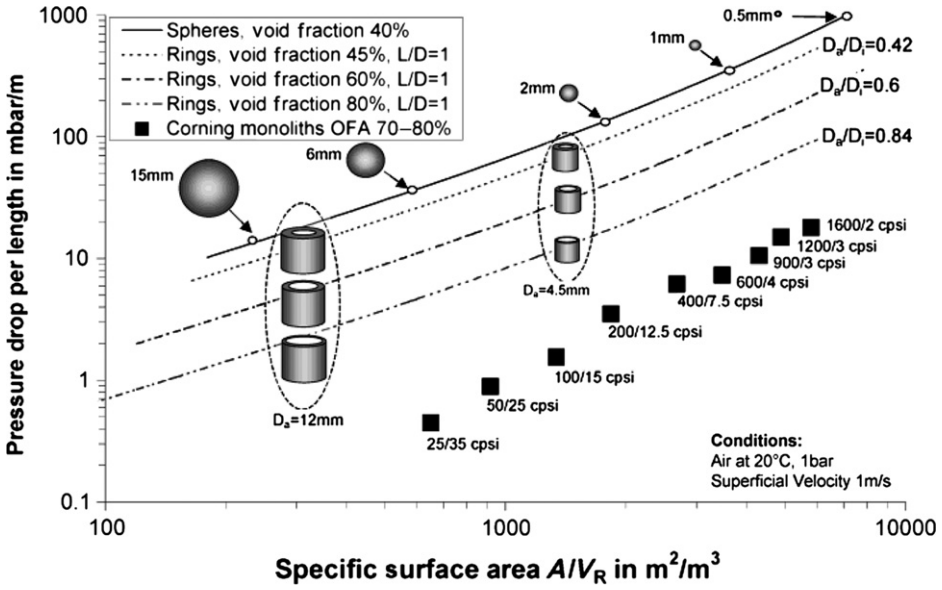

FIGURE 14.5 Benchmarking of pressure drop in various configurations of monoliths and packing structures *(Reprinted from Boger et al. [178], Copyright (2004), with permission from American Chemical Society).*

$$Nu = h_f d_h / \lambda_f \tag{14.14}$$

Sh and *Nu* numbers will have constant values for channels with fixed diameter and shape involving fully developed flow. However, the values will differ with the cross-sectional shape of the channel. For example, at constant surface concentration and temperature, channel shapes with equivalent cross-sectional areas have *Sh* and *Nu* numbers (given in parenthesis) in the decreasing order of circle (3.66) > square (2.98) > equilateral triangle (2.47) [179,180]. The structures of the extruded, straight channel monoliths are close to those of non-porous surfaces and, therefore, channel shape and diameter will be the only degrees of freedom for having higher transport coefficients. In this respect, the use of foam monoliths is more beneficial; the tortuous texture of the channel surfaces induce mixing at the fluid−wall interface and leads to the reduction of the thickness of the boundary layer, which − in contrast with non-porous surfaces − becomes more pronounced at higher flow rates. In addition to the interfacial mixing, the irregular texture of the foam monoliths also favors mixing along the channel length and will provide better axial heat transport characteristics. Needless to say, this will be most desirable in reactions leading to hot-spot formation. Nevertheless, the advantages of foam monoliths will partly be hindered by elevated pressure drop caused by the irregular surface.

The distinct advantages of the monolithic reactors should be considered together with the challenges and drawbacks in their operation. One of the challenges is related to the distribution of the incoming bulk flow equivalently to the channels, as uniform distribution is essential for ensuring a narrow RTD. This necessitates the use of flow distribution manifolds with designs becoming more complicated at higher number of channels. The use of monolithic reactors becomes questionable in the case of non-adiabatic reactions requiring external heat transfer. Rate of heat flow between the

external heating/cooling medium and the monoliths will be only via conduction and, as a result, will be less than those of fixed-beds due to the missing convective flow in the (radial) direction perpendicular to the axial flow. Moreover, the relatively low thermal conductivities of the ceramics will further reduce the radial heat transport rates. The variations in the process of reactor construction will lead to the presence of gaps between the monolithic bed and the reactor housing. Such gaps will obviously act as heat transfer resistances undesired in non-adiabatic operations. An additional challenge involved in the monoliths is the replacement of the catalysts that will become necessary when they deactivate permanently. Replacement is theoretically possible by the disintegration of the washcoat from the monolithic support but the whole matrix needs to be scraped if the active metals are directly coated onto the channels. Obviously, both scenarios are capital intensive and call for the combined use of catalyst and operating conditions tolerant to the deactivation mechanisms.

The benefits of monolithic reactors become notable in high temperature reactions running at near-adiabatic conditions. In this respect, it will be preferable to use this reactor type in the reforming step of fuel processing such as in POX or in OSR. Besides high temperatures, monoliths offer the possibility of handling high flow rates at acceptable levels of mechanical energy loss with narrow RTD patterns, and, therefore, demonstrate excellent fit with the POX route which is sensitive to temperature and residence time. The availability of numerous shape/size combinations with irregular surface textures allows control over micro and macro scale mass and heat transport effects which are important for POX and OSR. These facts have led to the use of ceramic monoliths in most of the experimental studies addressing POX of hydrocarbon fuels (see Section 14.1). It should however be remembered that high and sustainable performance of monoliths will require precise flow distribution and deactivation-tolerant catalysts.

14.5.3. Microchannel Reactors

Microchannel and monolithic reactors are similar in the sense that both of them can be described by the presence of parallel catalytic channels. However, when compared on the basis of a set of features, some notable differences can be observed. The most important distinction comes with the channel diameters; the average values are mostly limited to the sub-millimeter range ($\sim 10^{-6}$–10^{-3} m) for microchannels, whereas they are somewhat higher, and close to $\sim 10^{-3}$ m in the case of monoliths with a much broader range between ca. 3×10^{-4} m and 6×10^{-3} m [181]. The reactors also differ in terms of several design aspects. Monoliths are characterized mostly by straight channels, but microchannels can be constructed with a variety of regular non-standard shapes, such as wavy patterns along the channel length. In contrast with monoliths, materials of construction of microchannels are not limited to ceramics and metals; they can also be made of polymers, silicon, and glass. Nevertheless, the use of metals and ceramics will be considered here due to their compatibility with the conditions of fuel processing. Further discussion and review of the microchannel reactors are available in the literature [42,43].

A typical sketch of microchannel reactors is given in Fig. 14.6. In general, construction of these units cover the steps of micromachining of the metal plates to generate the flow paths, their coating with a porous layer followed by the deposition of active ingredients and bonding of the individual plates to form the catalytic fluid passages [182–185]. Sometimes the reactors can be manufactured from the catalytic material itself eliminating the need for the deposition of the catalytic layer [7,186,187]. Fluid mechanical properties of the microchannel units are similar to those of monoliths in

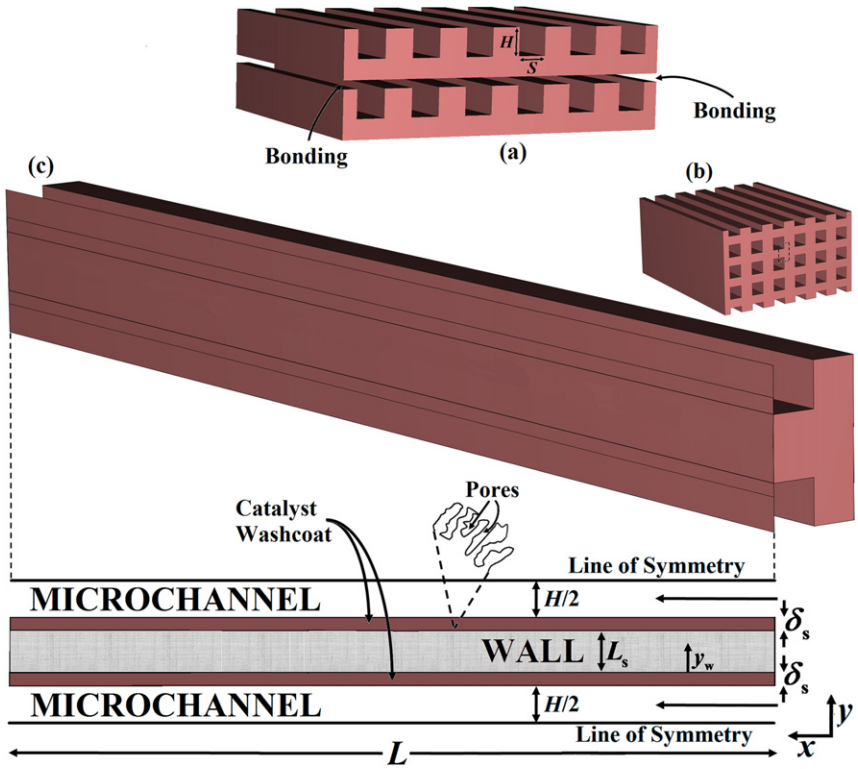

FIGURE 14.6 Schematic presentation of a microchannel reactor.

terms of low pressure drop and narrow RTD, and outperform the fixed-bed behavior.

The small channel dimensions in the sub-millimeter range shape the transport characteristics of the micro-size reactors. Compared to monoliths, microchannel units offer much better control over RTD, but this is partly hindered by increased pressure drops. The flow regime is well in the range of laminar flow and pressure drop along the channel length can be described by the following correlation [180]:

$$\Delta p = 2f\frac{\mu L}{d_h^2}U \tag{14.15}$$

Note that the same equation can be used to estimate pressure drop in monoliths. For channel shapes of equivalent cross-sectional areas, Fanning friction factor in Eq. (14.15) is equal to 16.00, 15.05, 14.23, and 13.33 for circular, hexagonal, square, and triangular geometries, respectively [180]. However, microchannels are mostly fabricated in rectangular shapes due to their ease of construction. Assuming that a rectangular shape is described by its height-to-width ratio (H/S) (Fig. 14.6), pressure drop in rectangular channels can be estimated using the following correlation [179]:

$$\Delta p = 32[0.8735 + 0.6265\cdot\exp(-3.636(H/S))]\frac{\mu L}{d_h^2}U \tag{14.16}$$

Laminar flow conditions favor the presence of external (fluid-to-catalytic washcoat) heat

and mass transport, which may become the rate-controlling step in fast reactions. However, assuming that the flow is fully developed, the transport coefficients will be high due to their inverse proportionality with the micro-sized hydraulic diameter (Eqs 14.13 and 14.14). This phenomenon is valid for the whole channel except the entrance zone in which the flow is not fully developed yet. The length of this zone can be predicted by the following relationship [188]:

$$L_e \leq 0.06 \cdot Re \cdot d_t \tag{14.17}$$

Comparison of fixed-bed and microchannel reactors involving a first order reaction with fast kinetics (i.e., limited by mass transfer) at equivalent geometric parameters and operating conditions in a fully developed laminar flow regime has shown that external mass transfer coefficients are higher in the case of microchannels [179]. The transport coefficients can further be increased by the use of channels with non-linear patterns or with well-defined wall corrugations along the channel both of which can be constructed by high-precision techniques such as μ-electrodischarge machining (μ-EDM), laser micro machining, and wet chemical etching [182]. Such patterns force mixing at the interface upon increasing the flow rate and reduce the external transport resistances. Hardt et al. [189] have reported that in straight channels Nu number remained constant whereas it increased more than three folds in sinusoidal channels upon changing the Re number from 0 to 800. Recently, Karakaya and Avci [190] has found that use of static mixing elements in the walls of 5.6×10^{-4} m^2 channels have increased the hydrogen yield in steam reforming of ethanol and propane heated by the combustion of these fuels in successive parallel channels. The increase was attributed to the improved mixing conditions at the interface. Non-linearity in the channel walls may increase the pressure drop, but this was shown to be minimal [190]. Compared to external effects, heat and mass transfer resistances within the washcoat layer are generally much less of an issue and are mostly negligible. Nevertheless, thickness of the porous catalytic layer is important; it should be in accordance with the following criterion to ensure a quasi-isothermal behavior in the washcoat layer [179]:

$$\delta_s \leq 0.3\sqrt{\frac{R}{E_A}\frac{\lambda_{eff,s}T_s^2}{|-\Delta H|r_j\rho_b}} \tag{14.18}$$

Similarly, the maximum washcoat thickness should meet the following criterion to ensure an effectiveness factor greater than 0.95 in an isothermal catalyst [179]:

$$\delta_s \leq b\sqrt{\frac{D_{AB,eff}c^s}{r_j}} \tag{14.19}$$

In Eq. (14.19), b is equal to 0.8, 0.3, and 0.18 for a zero, first, and second order reaction respectively, and concentration term represents the reactant concentration on the external catalyst surface. Both criteria are given in terms of the observed reaction rate.

Microchannel reactors are characterized by high surface area-to-volume ratios up to 5×10^{-4} m^2 m^{-3} [42]. When this is combined with the metallic construction of the units, local temperature elevations can be immediately dampened by the fast heat transport rates at the macro scale. This offers the possibility of a true isothermal operation and effective use of the catalyst bed. Although the flow is only in the axial direction, the compact, metallic structure of the units will provide high thermal conduction rates between the channels and external heat sources to drive the non-adiabatic reactions.

The challenges in operating monolithic units are also valid for the microchannel counterparts. The biggest issue lies in ensuring uniform flow at the inlet of each channel,

which has to be precise as it directly affects the RTD, and, in turn, temperature evolution and product selectivity patterns. Considering the diameters at the micro-scale, novel designs will be needed for the flow partition units [191]. The second issue arises in various scenarios of catalyst deactivation. Coke formation, a mechanism very likely to run at high carbon number fuels like diesel, can easily plug the small channels and lead to significant reductions in total pressure, wider RTDs, and even thermal runaways due to extended catalytic contact of explosive mixtures of fuel and oxidant. Although coke may be burned at oxygen-rich conditions, higher temperatures may lead to sintering of the catalyst. Sulfur components in the fuel can permanently occupy the active sites to reduce the catalytic activity. Occurrence of one of these mechanisms will necessitate the replacement of the whole unit, as the removal of deactivated catalyst will be practically infeasible. Replacements will be expensive due to the resulting downtimes and complex and time intensive nature of the construction techniques. Thirdly, the metallic construction of the units limits running high temperature reactions such as partial oxidations which are thermodynamically favored in excess of 1200 K. For example, the integrity of the 316-grade stainless steel, a highly available metal, starts to fail above ca. 873 K. High-temperature alloys such as Inconels offer sufficient temperature resistance but they are difficult to machine. Ceramics can be used instead of metals, but then the thermal responsiveness, an important benefit of microchannel reactors, will be sacrificed. Moreover, the number of options in micro machining of ceramics is less than those of metals. Finally, the level of precision in the steps of machining and catalyst coating are very important to give a uniform channel diameter along the length of the unit. Poor centerlining in any of these steps will lead to high standard deviations and elevated pressure drops [192].

The high degrees of freedom involved in their design and construction allow microchannel reactors to be customized for a wide range of combinations of fuels and reactions. In this respect, this reactor type can be used in fuel processing reactions such as steam and oxidative steam reforming, WGS, and selective CO oxidation [42,43,156,193]. These reactions can be run at the desired temperature range and with optimal use of catalyst by the help of inherently advanced temperature control features. Moreover, with the possibility of using high thermal conductivity metals such as copper and aluminum, micro-sized units can also be used as heat exchangers that can be integrated into the fuel processing system for heat recovery purposes. However, reactions favored at high temperatures such as POX may not be compatible, mainly due to the thermal stability issues of the metal substrates. As in the case of monoliths, operating conditions and catalysts should be selected to minimize the frequency of catalyst replacement, which is much more time and capital intensive than fixed-beds. It should also be remembered that compared to the well-known and established fixed-bed and monoliths, microchannel technology is quite new and requires advanced construction techniques which are not proven to operate economically at the commercial scale yet. Therefore, selection of microchannel reactors should be done holistically via comparing their technical benefits with the costs and complexities related to their construction.

14.5.4. Foam Reactors and Wire-Gauzes

14.5.4.1. Foam Reactors

Structured reactors are expected to play a major role in dynamic enhancement of processes. The most important feature of structured reactors is the multi-functional engineered catalysts that are used as reactor packing. Structured catalysts more frequently employed in various applications are ceramic

and metallic monoliths. More recently, solid foams are finding use as outstanding thermal management materials. Solid foam packings are made out of a range of materials such as metals, ceramics, silicon carbide, and graphite, and they represent a group of materials that bring together low density, high specific surface area, and low pressure drop owing to their open-celled structure with as high a void fraction as 97% in cellular metal foams [194].

Cellular metallic foams are used for flow control and heat transfer enhancement because of their complex interfacial geometry which creates a highly porous and isotropic structure with tortuous flow paths. Methods for manufacturing and characterizing metallic foams [195], modeling of pressure drop in aluminum foams [196], heat and mass transfer characterization in copper and FeCr-alloy foams [197,198] have been reported for single fluid phase systems. Various methods are used for coating foam supports with catalyst layers having thicknesses in the range of micrometers [199]. Experimental studies on the influence of metal foams on activity, selectivity and stability of metal-based catalysts were investigated for POX of methane over Ni−MgO catalyst supported on a ferrous alloy foam [200], and for methanol steam reforming over Cu-based catalysts supported on various metal and alloy foam materials [201]; both studies showed that catalytic properties of metal-based catalysts are modified by the foam support, possibly due to penetration of metal atoms from the foam to the catalyst layer. The foam-supported Ni−MgO catalysts used in methane POX had much lower carbon deposition rates than the corresponding unsupported powder catalyst. In methanol SR, on the other hand, external mass transfer resistances were insignificant due to the high mass transfer coefficients of metal foams, while internal diffusion resistances depended on the pore structure introduced by the calcination temperature as well as the Al_2O_3 washcoat ratio of the catalyst layer [202].

The properties of reticulated ceramic foams having open-cell structure make them suitable for use as catalyst support materials. The open-cell structure is sponge-like and composed of solid ceramic braces called struts supporting nearly spherical void spaces called cells which are also interconnected by openings called windows (Fig. 14.7a) [203]. Open-cell ceramic foams have high porosities (75−90%) formed

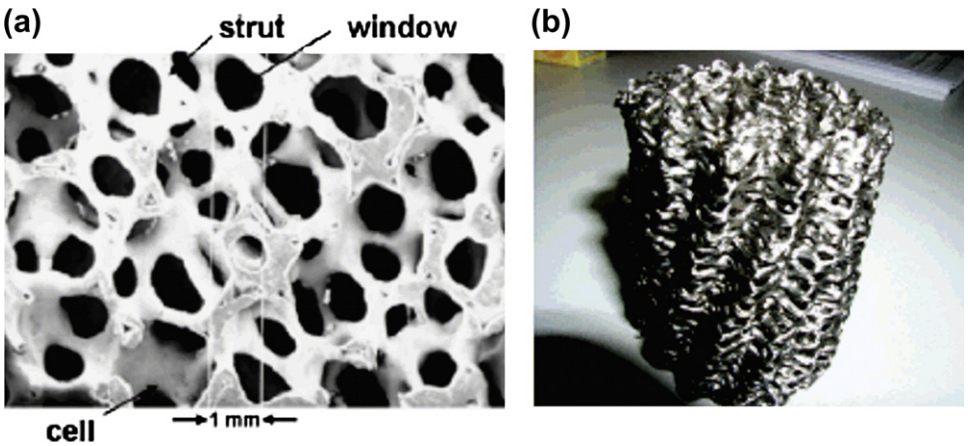

FIGURE 14.7 (a) SEM image of 30 ppi α-alumina ceramic foam (*Reprinted from Richardson et al. [203], Copyright (2000), with permission from Elsevier*); (b) Image of a Knitted wire gauze *(Reprinted from Pangarkar et al. [194], Copyright (2008), with permission from American Chemical Society).*

by 0.02–1.5 mm diameter mega pores, with pore densities of typically 10–100 ppi (pores per inch) and, as a result, low resistance to fluid flow and substantial turbulence caused by tortuous flow paths [204]. It is reported that pre-shaped "cartridges" of ceramic foam can simplify reactor loading by replacing the packed bed of particles; lead to lower pressure drop (since porosities are almost twice as large as packed beds) and to high geometric surface areas that improve external mass transfer rates as well as internal effectiveness factors; increase convective heat transfer because of turbulence and radial convection [205].

Properties describing ceramic foams are pore density (ppi), pore size ($d_{p,m}$, mean pore diameter between each cell), bulk density (ρ_b, mass of ceramic foam divided by its geometric volume), porosity (ε_s, the fraction of pore volume between solid struts), solid density (ρ_s, mass of ceramic foam divided by volume of helium displaced), external surface area (a_v, geometric surface area per unit volume of solid), and equivalent spherical diameter (d_p, the diameter of solid spheres with an external surface area of a_v). Only the parameters $d_{p,m}$, ρ_b, and ρ_s are measured, with ε_s and a_v being calculated from the densities and the hydraulic diameter model generally used for packed beds, respectively [204]:

$$\varepsilon_s = 1 - \rho_b/\rho_s \tag{14.20}$$

$$a_v = \frac{4\varepsilon_s}{d_{p,m}(1-\varepsilon_s)} \tag{14.21}$$

The transport properties of foams are described in terms of dimensionless parameters such as the Reynolds number, *Re*; there is disagreement on the characteristic length parameter to be used (d_p or $d_{p,m}$) for calculating *Re* and heat or mass transfer coefficients. It was suggested to base Re_s on the external surface area, a_v, although it is dependent on $d_{p,m}$, ε_s and the defining hydraulic diameter model, because of its simplicity and because it gives basically the same results as those from more complex models:

$$Re_s = U\rho_f/a_v\mu \tag{14.22}$$

where ρ_f is fluid density, μ is fluid viscosity, and U is the superficial velocity. The pressure drop which is an important design parameter was found to follow the Forchheimer equation as adapted by the Ergun model to packed beds where α and β are usually assumed to be constant [194,203]:

$$\frac{dP}{L} = \frac{\alpha a_v^2 \mu(1-\varepsilon_s)^2}{\varepsilon_s^3}U + \frac{\beta a_v \rho_f(1-\varepsilon_s)}{\varepsilon_s^3}U^2 \tag{14.23}$$

However, cellular materials like ceramic foams do not display similar geometry with packed beds of particles; both α and β depend on the properties (ε_s and $d_{p,m}$) of the foam, and empirical expressions were developed by fitting experimental data (with $d_{p,m}$ in meters) for 10–65 ppi of α-alumina foams in the range of 1–7 m s^{-1} superficial velocities [203]:

$$\alpha = 9.73 \times 10^2 d_{p,m}^{0.743}(1-\varepsilon_s)^{-0.0982} \tag{14.24}$$

$$\beta = 3.68 \times 10^2 d_{p,m}^{-0.7523}(1-\varepsilon_s)^{0.07158} \tag{14.25}$$

The second important foam property which makes the use of solid foams attractive is increased heat transfer as a result of convection due to turbulence induced by the tortuosity. Instead of the volumetric heat-transfer coefficients usually employed, empirical expressions providing suitable radial heat transfer correlations useful for one-dimensional reactor modeling were developed for 30 ppi α-alumina foams [204–206]:

$$\frac{U_{foam}}{\lambda_f a_v} = (3.43 \times 10^{-11})\varepsilon_s T^3 + 0.034 Re_s \tag{14.26}$$

where U_{foam} is the overall heat-transfer coefficient and λ_f is the thermal conductivity of the

fluid. The first term represents the combined solid thermal conductivity and the radiation between struts and the second term is the convective heat transfer. This correlation is appropriate for one-dimensional modeling of endothermic processes in ceramic foams; two-dimensional pseudo-homogeneous models can describe the severe radial temperature profiles in highly exothermic processes, in which case two additional parameters, effective radial conductivity of the bed and the heat-transfer coefficient at the wall, will be necessary [204].

Ceramic foams made of α-alumina with 20 and 45 ppi were compared with cordierite square-channel honeycomb monoliths with 400 cpsi (cells per square inch) on the basis of similar pore/channel count or surface area, and with α-alumina beads of 3.3 and 1.5 mm, respectively. These supports were coated with SnO_2-sol to obtain a uniform coat with 5–10 wt% loading and were tested for their performance in exothermic CO oxidation under the external diffusion control regime [207]. Catalytic foam packing was found to be highly permeable to gas flow with good heat and mass transfer properties; their pressure drop and mass transfer coefficients were between those of particles and honeycomb monoliths, whereas heat transfer within foams was very efficient and comparable with small particle beds.

14.5.4.2. Wire-Gauzes

Ceramic monoliths have become a worldwide standard for vehicle emission control mainly because of their low flow resistance and high specific surface area compared to packed beds. One drawback becomes evident in case of highly exothermic reactions and, as in the case of CO oxidation, honeycomb monoliths exhibit large temperature gradients due to suppressed radial mixing [207]. Currently, catalytic wire gauze internals (woven or knitted) seem very promising for short contact time operations like partial oxidations, and also for catalytic combustions with fast kinetics requiring improved interphase mass transfer and moderate flow resistance. Catalytic gauzes were formerly manufactured by weaving; recent reports indicate that the geometry of knitted gauzes (Fig. 14.7b) improves process selectivity and extends reactor lifetime [208]. Stacked wire gauze internals have a highly ordered structure providing high interphase heat/mass transfer rates with reasonable flow resistance; and several catalyst coating and deposition techniques having great potential are under development. An experimental program designed to study pressure drop for air flow through stacked wire gauzes (three woven gauzes and one knitted) showed that each type of wire gauze required its own correlation equation and that the previously reported models were not successful in describing all types of gauze [209]. A new model was proposed by adjusting the assumptions of the Ergun model to meet the geometry of stacked wire gauzes used as reactor internals [210]:

$$\frac{\Delta p}{L} = 4(f + f_{\text{app}})\frac{\rho_f U^2}{2d_w}\frac{(1-\varepsilon_s)}{\varepsilon_s^3}\frac{\tau^3}{\cos^3(\theta)} \quad (14.27)$$

where f is the Fanning friction factor, f_{app} is the Fanning friction factor for developing laminar flow, U is superficial velocity, d_w is the wire diameter, θ is the angle of flow direction slope to the bed axis, and τ is the bed tortuosity factor. In another study, interphase mass transfer coefficients in wire-mesh honeycomb reactors and the Pt/TiO_2-catalyzed intrinsic reaction kinetics of ethyl acetate oxidation were successfully extracted from experimental data using a one-dimensional reactor model [211]; it was also stated that the packed-bed Sherwood number best describes the mass transfer principles of wire-mesh honeycombs. In commercial applications, wire-mesh honeycombs are becoming an appealing alternative to the common honeycomb reactors and wire-mesh gauze reactors.

14.5.5. Integrated Reactors

Integrated reactors are based on the principle of coupling catalytic reactions with unit operations such as heat exchange or separation. The major benefit of integrated operation is intensification which is essential for space-limited applications such as fuel processing in mobile and in portable applications. Integration also offers cost savings in terms of minimizing the need for separate downstream operations. These beneficial features have paved the way for the development of various types of integrated units. Some of the basic designs, proposed for fuel processing applications, will be described below. More extensive reviews about this topic can be found in the open literature [212].

14.5.5.1. Heat-Exchanger Reactors

Heat-exchanger reactors, the units coupling reactions with heat exchange, generally involve the co-existence of exothermic oxidation and endothermic steam reforming and favor heat transfer in between. The resulting operation is adiabatic and can run without external heat exchange requirements. However, depending on the specific design, the reactions can run either together to achieve heat transfer within the same volume or can be decoupled to proceed in different catalytic zones. The former principle has set the basis for a set of specific design concepts. One of the concepts is based on guiding the reactive flow such that it contacts first with the oxidation zone/catalyst and then with the steam reforming zone/catalyst, as in the cases of coaxial cylindrical reactors [213] and wall reactors [214]. Both units are described by the existence of an inner and an outer tube, but differ with the physical form of the catalysts. In the coaxial cylindrical reactors, the oxidation and steam reforming catalysts are packed into the inner tube and the annular space between the tubes, respectively [213]. The flow is arranged such that it enters first to the combustion (inner) tube and then directed to leave the unit from the reforming (annular) zone, resulting in a countercurrent flow, as shown in Fig. 14.8a. Wall reactors involve the same concept of flow and contacting, but, rather than being packed, combustion and reforming catalysts are wash-coated onto the interior and exterior walls of the inner channel, respectively [214] (Fig. 14.8b). The particular flow mode in both reactor types allows the generation of combustion heat which is transferred via the wall of the inner tube to the reforming catalyst to drive the endothermic reaction. Part of the heat can also be transferred with the bulk flow via convection. Provided that the initial contact is with the

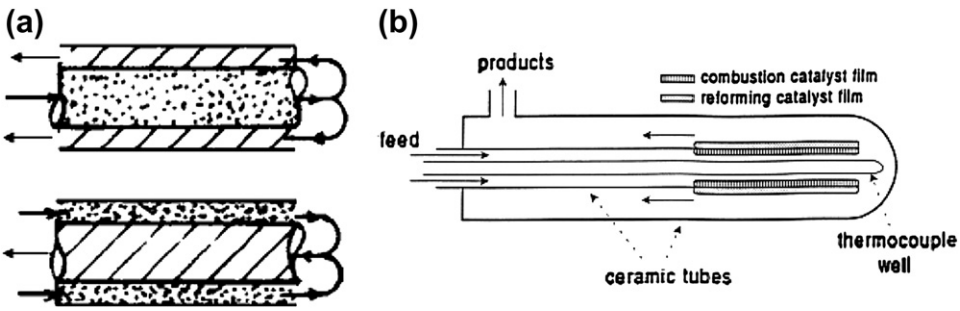

FIGURE 14.8 Integrated reactor concepts (a) coaxial cylindrical reactors *(Reprinted from Ma et al. [213], Copyright (1996), with permission from Elsevier)*, (b) catalytic wall reactor *(Reprinted from Piga and Verykios [214], Copyright (2000), with permission from Elsevier).*

oxidation catalyst, the catalysts can be placed opposite to the configuration described above. Although the operating concepts are the same, wall reactors exhibit much better control over hot-spot formation via the improved heat transfer characteristics of the washcoated catalysts, as demonstrated in the POX of methane to syngas [214].

The combustion and reforming catalysts can be placed differently from the configurations above. It has been shown that $Pt/\delta{-}Al_2O_3$ and $Ni{-}MgO/Al_2O_3$ catalysts specific for total oxidation and steam reforming of methane, respectively, can be packed either separately, in a consecutive fashion, or in the form of a physical mixture into a tubular reactor [44]. The results indicate that the second configuration is better in terms of lower hot-spot values, higher methane conversions, and improved hydrogen yields. The difference has been attributed to the heat exchange between the catalysts, which is much more enhanced in the mixture form due to the closeness of heat sources and sinks. Based on this idea, Ma and Trimm [44] have studied a third configuration involving a single type, bimetallic Pt–Ni catalyst. Under the same feed conditions, they have observed further reductions in maximum bed temperatures and improvements in methane conversion/hydrogen yield figures and speculated that the bimetallic catalyst particles worked as "micro heat-exchangers" by catalyzing oxidation and reforming over the Pt and Ni sites, respectively. The beneficial effects of the Pt–Ni catalysts have further been verified in a series of studies addressing the conversions of propane, *n*-butane, and their mixtures (LPG) [22,49,54,55,215].

Integration of reactions and heat exchange within the same reactor volume can also be established by the so-called reverse flow operation [216]. This mode is based on the principle of periodic reversal of the hot reaction front back to the inlet zone of a fixed-bed reactor to heat the feed. The operation is controlled by two valves set to switch flow directions periodically and allows heat transfer at the inlet and exit sections of the reactor together with the formation of a hot zone in the middle section of the fixed-bed. Reverse flow reactors are beneficial in the sense that they suppress the poor heat transfer characteristics of simple fixed-bed operation by favoring regenerative heat exchange at the reactor inlet and outlet. However the cyclic nature of flow reversal will not allow a steady, time-independent throughput, which may not be preferable in the fuel processing applications. Reverse flow operation has been demonstrated in the catalytic combustion and steam reforming of methane [217–219] and in oxidative steam reforming of methanol [220].

Heat-exchanger reactors can also be designed such that exothermic and endothermic reactions can be decoupled to run in separate, parallel flow paths and heat can be transferred across the separating medium. The most important success criterion in such a configuration is to establish effective heat transfer between the flow paths for eliminating the formation of hot-spots or thermal runaways that may result from the exothermic side. The extent of heat transfer is a function of a set of parameters such as the feeding strategies (co-current, countercurrent, cross-current, and split feeding configurations), heat capacity flux in the flow paths, physical form of the catalysts (fixed-bed and wall-coated configurations), and thermal conductivity of the reactor material. Kolios et al. [221,222] have studied impacts of these parameters by a series of computer simulations. They have reported that the countercurrent feeding of the reactants is not a robust operating strategy as it can lead to hot-spot formation or thermal runaways, and the heat capacity flux of the reactive streams should be close to each other for efficient heat transfer. Feeding strategies involving co-current or counter-current flow with the combustion

stream split and fed from multiple points along the channel length, and the use of wall-coated catalysts instead of fixed-bed configurations are stated to be measures for implementing robustness in terms of a well-controlled, stable, and safe operation [221,222].

Various reactor configurations involving heat exchange between the decoupled reactions have been demonstrated. Common feature of the reactors is that the catalysts are coated on the walls of the individual channels. One example of such units is the catalytic plate reactor (CPR) in which the washcoated plates are stacked and bonded such that exothermic and endothermic reactions run in successive flow paths (Fig. 14.9). The CPR concept has been proposed by Reay [223] and further demonstrated in coupling combustion and steam reforming reactions with near complete fuel conversions [224]. The performance of the CPRs depends on various geometric parameters such as channel height, thickness of the catalyst layer, thermal conductivity, and the thickness of the separating wall. Effects of these parameters on methane combustion-methane steam reforming and methane combustion-non-oxidative ethane dehydrogenation couplings in CPR geometry have been modeled and simulated by Zanfir and Gavriilidis [225,226]. In their simulations, they have used the operating conditions of a conventional reformer and reported that the temperature gradients estimated in CPR are much smaller than those of conventional reformers [226]. They have attributed this result to the minimized heat and mass transfer resistances of the CPR geometry characterized by small channel and catalyst thickness dimensions in the order of millimeters and micrometers, respectively. Similar concept but with smaller (micrometer range) channel dimensions can be realized by the implementation of microchannel technology. Due to their excellent heat transport properties related to their compact and metallic structures,

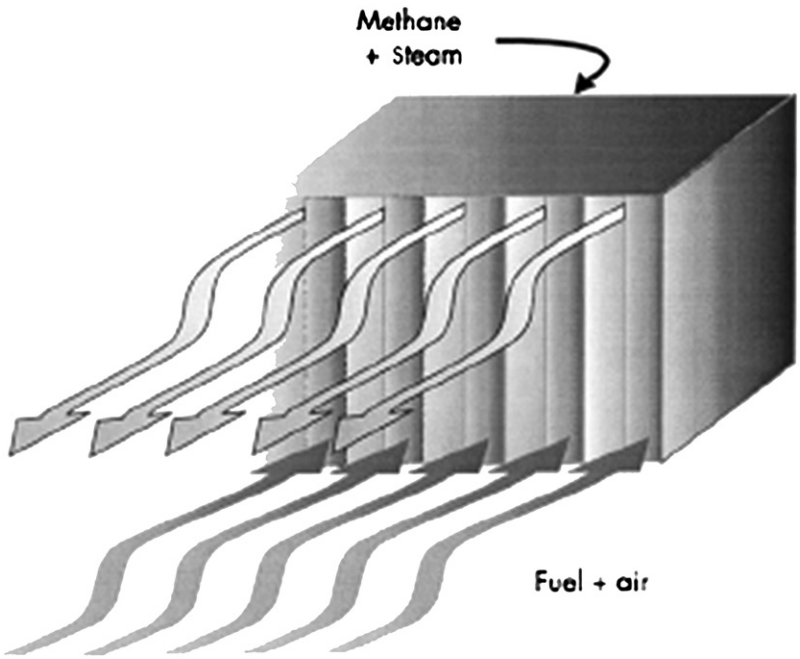

FIGURE 14.9 Catalytic plate reactor concept *(Reprinted from Polman et al. [224], Copyright (1999), with permission from Elsevier).*

microchannel heat-exchanger reactors offer rapid heat transfer between the exothermic and endothermic reactions and minimize the formation of hot/cold spots or thermal instabilities. The operation has been reported for coupled methane steam reforming and hydrogen combustion, and the possibility of obtaining near-equilibrium steam reforming conversions with approach values in excess of 98% at sub-millisecond contact times, as a result of very fast heat and mass transfer rates, has been demonstrated [227]. As mentioned in Section 14.5.3, microchannels are described by the laminar flow regime and, therefore, the fluid-to-washcoat transport resistances depend on the channel geometry. Tonkovich et al. [227] showed that optimizing the washcoat thickness and the channel opening allows obtaining near equilibrium conversions at even shorter contact times. The effects of geometric parameters have further been investigated in coupled catalytic combustion and steam reforming of methanol, ethanol, and propane to produce hydrogen for a 2 kW PEMFC powered Auxiliary Power Unit using computational fluid dynamics techniques [190]. Owing to the fact that heat transfer coefficients in microchannels can be improved by inducing mixing at the fluid–wall interface [189], they have compared the microchannel geometries with and without micro-baffles, as shown in Figs 14.10a and b, respectively. The results showed that hydrogen yields obtained in the presence of micro-baffles were notably higher than those of straight channels; micro-baffles functioned as static mixers at the fluid–washcoat interface and increased the interfacial mass and heat transfer coefficients [190].

Use of narrow catalytic passages for heat integration offers significant benefits, but it may also have some drawbacks. The most important disadvantage is associated with catalyst removal which becomes necessary in the cases of catalyst deactivation and plugging of the channels. However, some of these difficulties may be overcome by the use of an alternative microchannel configuration, the cascade reactor system, shown in Fig. 14.11. The configuration is based on the decoupling of reaction and heat exchange operations; catalyst, particulate or monolithic type, is placed in slots present within a heat exchange block of parallel microchannels. The slots, i.e., catalytic beds are arranged to run in adiabatic mode. The configuration is arranged such that inlet and exit of a group of microchannels are connected to the outlet and inlet of the preceding and succeeding endothermic beds, and, similarly, the remaining group of microchannels are linked

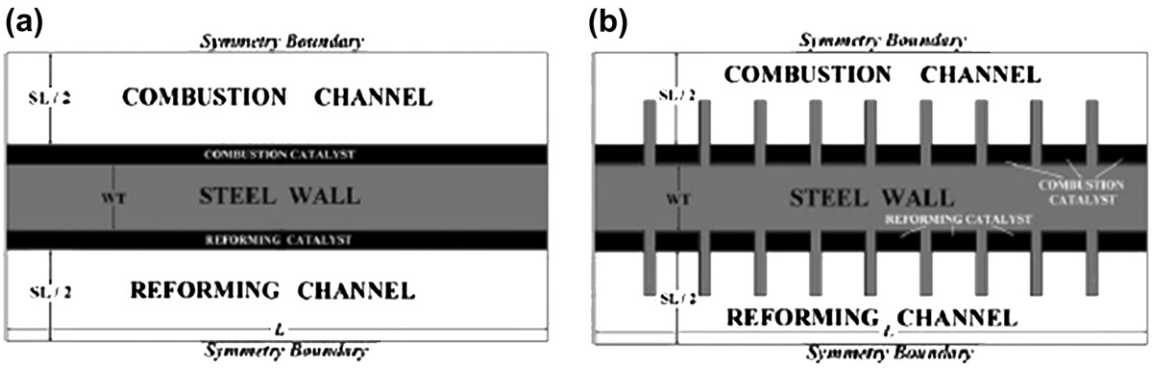

FIGURE 14.10 Description of the parallel microchannel geometries (a) without and (b) with micro-baffles *(Reprinted from Karakaya and Avci [190], Copyright (2009), with permission from Springer).*

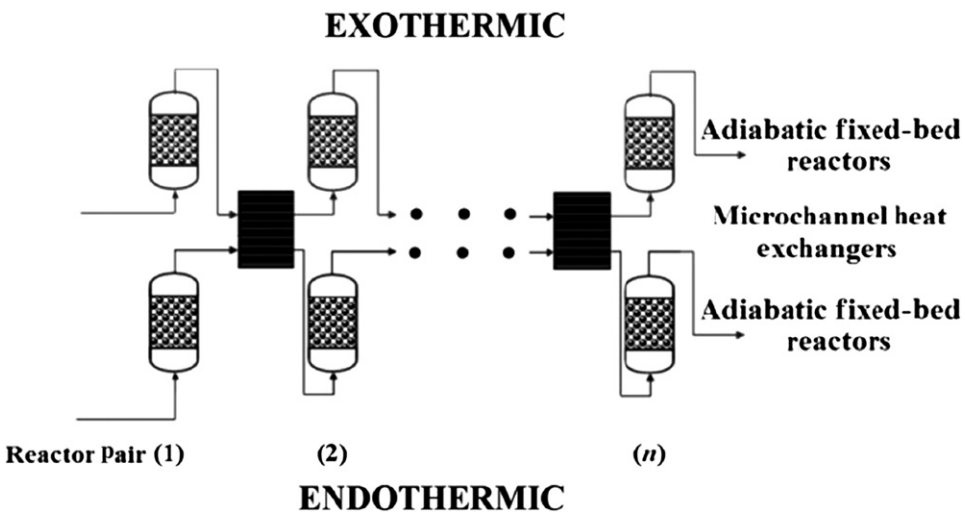

FIGURE 14.11 Cascade reactor configuration with co-current operation *(Reprinted from Karakaya and Avci [231], Copyright (2010), with permission from International Association for Hydrogen Energy).*

with the exothermic beds. With such an arrangement the need for redistributing the reactants is avoided and the catalyst bed can easily be replaced upon deactivation without sacrificing from the benefits of heat exchange at the micro-scale. Moreover, it is possible to arrange the number of beds, to split the feed into the beds and to set the heat exchanger flow modes (co-current, countercurrent, or cross-current) for achieving desired conversion levels. The concept correlates with the classical approach of using of catalytic reactors with interstage heating/cooling, but is a novel and an intensified version of the conventional applications due to the use of microchannel heat exchangers. The design and operation of the cascade reactor system that couples combustion and steam reforming of methane for hydrogen production has been demonstrated by Seris et al. [228,229].

The cascade system is also beneficial for reactions demanding strict temperature control such as steam reforming of methane and non-oxidative dehydrogenation of ethane. Both of these reactions are coupled with total oxidation of methane and the resulting cascade operations have been investigated by a series of computer simulations [230]. The results presented in Figs 14.12a and b indicate the formation of saw-tooth temperature profiles. The vertical lines in the profiles represent temperature changes at the inter-stage heat exchange zones whereas the rest show temperature elevations and reductions evolved in each catalytic bed. In cascade system, the combustion conversions can be regulated by bed sizes and flow rates such that they do not exceed the light-off limit, and, therefore, exothermal heat can be transferred to the endothermic reactions in a controlled scheme, as shown in Figs 14.12a and b. Consequently, steam reforming conversions as high as 90% are simulated with a maximum temperature of only 1032 K, and ethane conversion was obtained as 63.6%, which is close to the thermodynamic conversion of 72%, without disturbing the temperature limits of ethane cracking to form coke. For both reactions, the overall size requirement of the cascade system was shown to be smaller than that of a microchannel reactor-heat exchanger unit simulated under identical operating conditions [230]. A similar comparison of both systems was reported for

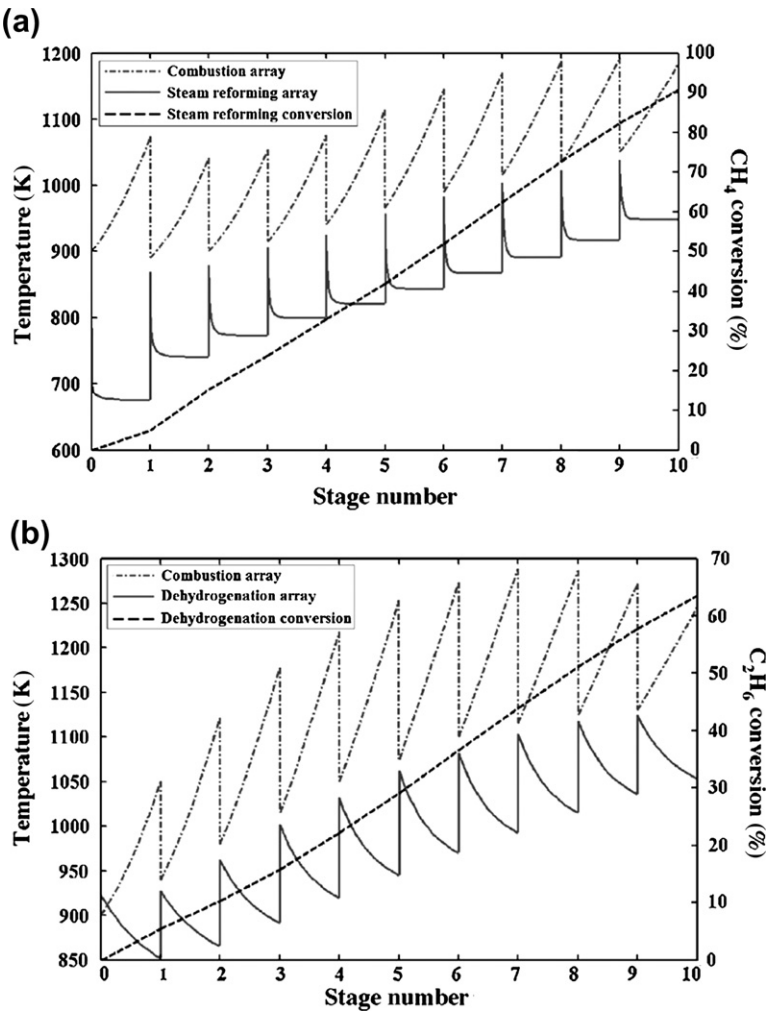

FIGURE 14.12 Temperature profiles obtained in the cascade reactor configuration for coupled methane oxidation/methane steam reforming (a), and methane oxidation/non-oxidative dehydrogenation of ethane (b) *(Reprinted from Avci et al. [230], Copyright (2010), with permission from Elsevier).*

coupled methane oxidation/*n*-heptane steam reforming to produce hydrogen for PEM fuel cell–based auxiliary power units in the 2–3 kW range, which showed that the cascade system was better in terms of higher efficiency and improved temperature control [231].

14.5.5.2. Membrane Reactors

Membranes are physical barriers that allow selective transport of mass species as the result of a driving force which is either a pressure or a concentration gradient. Membrane reactors are used to increase conversion in equilibrium-limited reactions as well as to increase selectivity in systems with multiple reactions. In equilibrium-limited exothermic reactions, such as the WGS reaction, increasing the temperature drives the reaction further to the reactant side while decreasing the temperature slows down the reaction to lower conversion levels which affects process feasibility. If the reaction

is endothermic, as in steam reforming of hydrocarbons, higher temperatures favor product formation but may also bring about catalyst deactivation. Selectivity of multiple reactions, as in POX of hydrocarbons, can be increased by feeding one of the key reactants (the oxidant) through the sides of a membrane along the reactor length, thus separating it from other reactants to control its concentration in the reaction zone.

Inorganic membranes of interest in fuel processing applications are metallic (dense phase) and ceramic (porous/non-porous) membranes, and the foremost objective is hydrogen separation. Hydrogen permselective inorganic membranes are further classified into three groups, namely microporous ceramic or molecular sieves, dense-phase metal or metal alloys, and dense ceramic perovskites; the former follows the activated diffusion mechanism while the latter (dense-phase) keeps to the solution-diffusion mechanism [232]. As a technical requirement for solution-diffusion or metallic membranes, it is critical to have a perfect crack-free selective layer that has a long working life in the presence of long-term pressurization and duty cycles. Similarly, for hydrogen, molecular sieve membranes should not have continuous pores with size greater than the pore size limit of 0.3–0.4 nm. Both types of membrane should provide sufficiently high diffusion fluxes for a feasible process. For hydrogen, the number of effective metallic membranes is quite limited; these are mostly Pd-based alloys having unique perm selectivity to hydrogen and fairly good mechanical stability. The thick (50–100 μm) dense self-supporting Pd-based membranes initially used have been replaced by membranes having a thin layer (<20 μm) of Pd or Pd alloy deposited onto a ceramic or metal substrate to increase permeability and/or solubility. An example is the Pd–Ag alloy most frequently used for hydrogen separation; the presence of Ag decreases hydrogen diffusivity, which is balanced by an increase in hydrogen solubility [232].

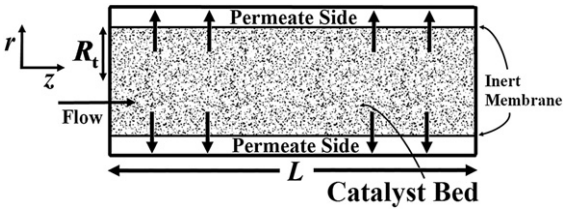

FIGURE 14.13 Schematic presentation of a packed-bed membrane reactor.

The two major types of reactor configurations using inorganic membranes are (a) the inert packed-bed membrane reactor (PBMR) with a packed-bed of catalyst particles on the feed side, where the membrane only provides a semi-permeable barrier from which one of the products (e.g., H_2) can diffuse out, thus hindering the reverse reaction and shifting the equilibrium to the product side (Fig. 14.13), and (b) the catalytic membrane reactor (CMR) where the catalyst is deposited on the membrane itself and only certain reaction products can diffuse to the permeate side of the membrane (Fig. 14.14) [174].

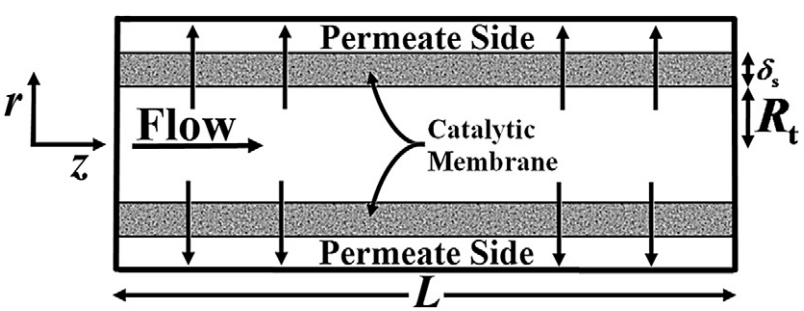

FIGURE 14.14 Schematic presentation of a catalytic membrane reactor.

The steam reforming of methane in packed-bed membrane reactors was modeled for two types of membranes, a dense Pd/Ag composite membrane and a series of microporous membranes [233,234]. Pd/Ag membranes were found to give better performance than silica membranes for all parameters studied (temperature, pressure, sweep gas ratio, and membrane thickness) while silica membranes worked much better when steam was used as sweep gas [234]. A new type of silica membrane prepared by CVD (chemical vapor deposition) was reported to give methane conversion above the equilibrium value because of 100% selectivity for H_2 with respect to CO, CO_2, CH_4 in the mixture; it was, however, emphasized that the use of membrane reactors on an industrial scale still depended on the cost of the membrane [233]. The mathematical model developed assumed isothermal operation and co-current flow, negligible pressure drop along the reactor length as well as negligible radial and axial dispersion; the permeation of hydrogen through the Pd/Ag membrane was assumed to follow Sievert's law while the only mode of transport through microporous silica was Knudsen flow. The mathematical model of the membrane reactor includes conservation equations for each component on the feed and permeate sides of the membrane, written for differential reactor length and consisting of convection, reaction, and permeation terms.

The WGS reaction is a good example of an equilibrium-limited exothermic reaction of great industrial importance and, if H_2 is removed from the reaction mixture through a membrane, the reaction shifts toward the product side and CO conversions rise above the equilibrium limit. This is very important for maximization of both hydrogen production and CO removal in fuel processors, since equilibrium conversion levels determine WGS reactor volumes. The effect of pressure on the performance of a membrane reactor (MR) for the WGS converter upstream of a 10 kW PEM fuel cell was analyzed with special emphasis on thermal effects [235]. Both convective and diffusive heat transfer mechanisms were used for computing energy transport through the membrane in an adiabatic environment. The membrane consisted of a dense Pd layer (selective only to H_2) deposited on a porous ceramic support. A one-dimensional pseudo-homogeneous mathematical model was used to simulate the operation of the multi-tubular MR (with catalyst in the shell and co-current flow of permeated hydrogen inside the tubes) and of an equivalent conventional packed-bed reactor with no H_2 permeation modeled for comparison.

14.6. MODELING AND DESIGN OF FUEL PROCESSING REACTORS

In this section, model equations that describe the operation of basic reactor types such as fixed-beds, wall-coated structured reactors (microchannel, monolithic, plate type reactors), and membrane reactors, that can be used in fuel reforming, WGS, CO removal and desulfurization stages of the fuel processing operation will be outlined. These equations combine the transport and reaction phenomena in the particular catalytic flow geometry and are used in sizing (designing) the reactors and in simulating their behavior. The most realistic simulations can be obtained by solving the momentum, energy, and mass transfer equations in three dimensions. Despite the fact that the computing capacities are much higher than in the past, solving 3D models are still expensive. Therefore, from an engineering point of view, it is common practice to simplify the models into two-dimensions, which lead to significant savings in computational demand with tolerable deviations from the 3D outputs. Based on this fact, the model equations below will be presented in their two-dimensional forms. Since fuel processing reactors do not involve high pressures or significant pressure

gradients, the model equations will be given under the assumptions of incompressible fluid flow and ideal gas equation of state. Under certain operating conditions, models can further be simplified and reactor operations can be simulated at sufficient accuracy by the use of low cost one-dimensional models. Such conditions and their simplifying effects on model equations will also be described below. Finally, computer-based techniques used to solve specific types of equation sets will be covered briefly.

14.6.1. Fixed-Bed Reactors

Fixed-bed reactors involve the presence of gaseous bulk fluid phase and the solid catalytic phase in a simple tubular geometry with cylindrical coordinates (Fig. 14.2). The conservation equations for the fluid phase can be written as follows:

Equation of species continuity:

$$\varepsilon_p \frac{\partial c_i}{\partial t} + v_z \frac{\partial c_i}{\partial z} = D_{AB,r}\left[\frac{1}{r}\frac{\partial}{\partial r}\left(r\frac{\partial c_i}{\partial r}\right)\right] + D_{AB,a}\frac{\partial^2 c_i}{\partial z^2} - k_g a_v (c_i - c_i^s|_{\xi=R_p}) \tag{14.28}$$

Equation of energy:

$$\varepsilon_p \rho_f C_{pf}\frac{\partial T}{\partial t} + \rho_f C_{pf} v_z \frac{\partial T}{\partial z} = \lambda_{f,r}\left[\frac{1}{r}\frac{\partial}{\partial r}\left(r\frac{\partial T}{\partial r}\right)\right] + \lambda_{f,a}\frac{\partial^2 T}{\partial z^2} + h_f a_v (T_s|_{\xi=R_p} - T) - \frac{2U_w}{R_t}(T - T_r) \tag{14.29}$$

The equations below describe the concentration and temperature changes in the catalyst particle that is assumed to be spherical in shape.

Equation of species continuity:

$$\varepsilon_s \frac{\partial c_i^s}{\partial t} = \frac{D_{AB,eff}}{\xi^2}\frac{\partial}{\partial \xi}\left(\xi^2 \frac{\partial c_i^s}{\partial \xi}\right) - \rho_s R_i(c_i^s, T_s) \tag{14.30}$$

Equation of energy:

$$\varepsilon_s \rho_s C_{ps}\frac{\partial T_s}{\partial t} = \frac{\lambda_{eff,s}}{\xi^2}\frac{\partial}{\partial \xi}\left(\xi^2 \frac{\partial T_s}{\partial \xi}\right) + \rho_s \sum_{j=1}^{N}(-\Delta H_j) r_j(c_j^s, T_s) \tag{14.31}$$

The initial and the boundary conditions accompanying the equations above are listed in Table 14.3. The model describes unsteady-

TABLE 14.3 Initial and Boundary Conditions for the Generalized Fixed-Bed Reactor Model

Initial Conditions

$t = 0; \forall z, r$
$c = c_{i0}$
$T = T_0$
$c_i^s = 0$
$T_s = T_{s0}$

Boundary Conditions

Fluid phase

1. *Reactor entrance*: $z = 0; \forall r$
   $c_i = c_i^{in}$
   $T = T^{in}$
2. *Symmetry at the center*: $\forall z;\ r = 0$
   $\partial c_i/\partial r = 0$
   $\partial T/\partial r = 0$
3. *Along the fluid–wall interface*: $\forall z;\ r = R_t$
   $\partial c_i/\partial r = 0$
   $h_w(T_w - T) = \lambda_{f,r}\dfrac{\partial T}{\partial r}$
4. *Reactor exit*: $z = L; \forall r$
   $\partial c_i/\partial z = 0$
   $\partial T/\partial z = 0$

Solid phase

5. *Symmetry at the center*: $\xi = 0; \forall r, z$
   $\partial c_i^s/\partial \xi = 0$
   $\partial T_s/\partial \xi = 0$
6. *On the fluid–solid interface*: $\xi = R_p; \forall r, z$
   $k_g\left(c_i^s|_{\xi=R_p} - c_i\right) = -D_{AB,eff}\dfrac{dc_i^s}{d\xi}$
   $h_f\left(T_s|_{\xi=R_p} - T\right) = -\lambda_{eff,s}\dfrac{dT_s}{d\xi}$

state, two dimensional operation and is of heterogeneous type as it accounts for the concentration and temperature changes in both phases. In this model, plug-flow assumption is made and, therefore, the radial variation of velocity is not considered. In general, this condition is favored to give reasonably flat velocity profiles if the following criterion is satisfied [173]:

$$d_t/d_p \geq 30 \tag{14.32}$$

The equations above can be coupled with the Ergun correlation (14.12) to estimate the pressure drop along the fixed-bed of catalyst particles. For spherical particles, heat and mass transfer coefficients at the fluid−solid interface, h_f and k_g, respectively, can be estimated by the following correlations [236]:

$$\frac{h_f d_p}{\lambda_f} = 2 + 1.1\left(\frac{\mu C_{pf}}{\lambda_f}\right)^{1/3}\left(\frac{U\rho_f d_p}{\mu}\right)^{0.6} \tag{14.33}$$

$$\frac{k_g d_p}{D_{AB}} = 2 + 1.1\left(\frac{\mu}{\rho_f D_{AB}}\right)^{1/3}\left(\frac{U\rho_f d_p}{\mu}\right)^{0.6} \tag{14.34}$$

The presence of transport resistances prevents the effective use of the active sites of the catalyst and is undesired in a reactor operation. In fixed-bed reactors, significance of these resistances can be quantified by the use of criteria outlined in Table 14.2. The expressions indicate the importance of reaction rate and heat of reaction and show that transport effects are favored in the case of fast reactions with high heats of reaction, such as oxidations. Nevertheless, these effects can be minimized by the careful selection of various design and operating parameters; fixed-bed reactors are designed to operate at the turbulent flow regime for reducing external transport effects (between the fluid and catalytic (solid) phases). In addition, transport resistances within the catalysts can be minimized by the use of smaller particle dimensions with short diffusive paths. Therefore it is desirable to operate a fixed-bed reactor at high superficial fluid velocities and with small catalyst dimensions to maximize the effective use of the catalysts. At these conditions, the temperature and concentration differences between the phases become small and the reactor operates in a "pseudo" homogeneous phase. This leads to important simplifications in the reactor model, and eliminates the equations (14.30 and 14.31) and terms including the surface quantities, c_i^s and T_s. The collection of resulting, simplified equations is known as the pseudo-homogeneous model. It is worth noting that elevated pressure drop can limit the applicability of the conditions above to a certain extent, but, as mentioned in Section 14.5.1, the availability of various packing shapes will widen the operating window in terms of pressure loss.

The pseudo-homogeneous model can further be simplified under certain operating states. The time-dependent terms (first terms in the left-hand sides of Eqs 14.28 and 14.29) will cancel out at the steady-state mode, which governs the whole operating span except the start-up and shut-down phases and periods involving changes in the feed properties. External heating or cooling will not be needed in the presence of adiabatic conditions, such as in the cases of OSR and POX, and the last term on the right-hand side of Eq. (14.29) will cancel out. The adiabatic conditions will also dampen the importance of radial transport and, therefore, the radial mass and thermal diffusivity terms will be negligible. Finally, provided that the following condition is satisfied, the diffusion terms, i.e., second order derivatives in z-direction, can be ignored:

$$L/d_p > 50 \tag{14.35}$$

After the simplifications explained above, fixed-bed reactors can be simulated and

designed using the one-dimensional steady-state pseudohomogeneous model:

$$\frac{dF_i}{dz} = A_c \rho_b R_i \tag{14.36}$$

$$\frac{dT}{dz} = \frac{A_c \rho_b \sum_{j=1}^{N} (-\Delta H_j) r_j}{\sum_{i=1}^{M} F_i C_{pi}} \tag{14.37}$$

$$F_i = F_i^{in}; T = T^{in} (\text{at } z = 0) \tag{14.38}$$

Instead of concentration of the species, the equations are written in terms of their molar flow rates, as the latter form is more suitable to incorporate multiple reactions into the reactor model. The transition between the two forms is achieved by the use following relationships:

$$F_i = c_i \upsilon \tag{14.39}$$

$$\upsilon = \upsilon^{in} \left(\frac{F_T}{F_T^{in}} \right) \frac{p^{in}}{p} \left(\frac{T}{T^{in}} \right) \tag{14.40}$$

Equation (14.40) is based on the ideal gas equation of state [174]. The change in the total pressure, p, can be found by the Ergun correlation, which can be re-written in differential form according to the format above for being coupled with the one-dimensional model:

$$\frac{dp}{dz} = -\frac{G}{d_p \rho_f^{in}} \left(\frac{1-\varepsilon_p}{\varepsilon_p^3} \right) \left[\frac{150(1-\varepsilon_p)\mu}{d_p} + 1.75G \right] \times \left(\frac{F_T}{F_T^{in}} \right) \frac{p^{in}}{p} \left(\frac{T}{T^{in}} \right) \tag{14.41}$$

$$p = p^{in} (\text{at } z = 0) \tag{14.42}$$

The one-dimensional pseudohomogeneous model can be used in approximate sizing of fixed-bed reactors with minimal computational demand. The model is satisfactory in most cases, but becomes questionable in the presence of fast reactions such as catalytic oxidations involved in the OSR or POX routes. In such reactions that operate under adiabatic conditions it may be preferable to use the one-dimensional heterogeneous model which takes the effects of transport resistances into account. The model equations − mole and energy balances at the bulk fluid and at the fluid−solid interface − adapted to simulate the multiple reaction cases are given below:

$$\frac{dF_i}{dz} = A_c k_g a_v \left(c_i^s|_{\xi=R_p} - c_i \right) \tag{14.43}$$

$$\frac{dT}{dz} = \frac{A_c h_f a_v (T_s|_{\xi=R_p} - T)}{\sum_{i=1}^{M} F_i C_{pi}} \tag{14.44}$$

$$k_g a_v \left(c_i^s|_{\xi=R_p} - c_i \right) = \sum_{j=1}^{N} \eta_j \alpha_{ji} r_{ji} (c_i^s, T_s)|_{\xi=R_p} \tag{14.45}$$

$$h_f a_v \left(T_s|_{\xi=R_p} - T \right) = \sum_{j=1}^{N} \eta_j (-\Delta H_j) r_j (c_i^s, T_s)|_{\xi=R_p} \tag{14.46}$$

It is worth noting that the intraparticle transport effects, which are normally described by the solution of concentration and temperature profiles within the catalyst particle via Eqs (14.30) and (14.31), respectively, are simply lumped into the effectiveness factors, η_j, given for each reaction j. Once the approximate values of effectiveness factors are known, they can be simply plugged into Eqs (14.45 and 14.46). These values are available for the reactions involved in the POX of methane to synthesis gas [237].

Solution of the equations above requires the use of rate laws for the particular reaction/catalyst combinations. A collection of rate laws for

steam reforming, total oxidation of hydrocarbons, and high- and low-temperature WGS reactions are given in Tables 14.4, 14.5, and 14.6, respectively [21,22,40,118,238–244]. Constants appearing in the kinetic expressions can be found from the references provided in Tables 14.4–4.6. Kinetic expressions for describing CO oxidation are available in the related literature [4,10]. Correlations that give estimates of parameters such as wall heat transfer coefficient, effective radial thermal conductivity, and diffusivity in fixed-bed operation are outlined in Table 14.7. These correlations are used in cases where non-adiabatic conditions and diffusive transport mechanisms are accounted in the model equations and in the pertinent boundary conditions.

Various forms of the fixed-bed models outlined above require specific numerical solution techniques. One-dimensional pseudo-homogeneous model (Eqs 14.36 and 14.37) is the least costly in terms of ease of solution. The model is described by a set of ordinary differential equations (ODEs) which can be solved by fourth order Runge-Kutta (RK) technique. However, RK technique may fail to converge in stiff problems in which one or more dependent variables (e.g., temperature or concentration) change sharply in a small spatial scale. A descriptive example of stiffness in fuel processing reactions is the partial/total oxidations which are described by rapid temperature elevations following light-off. Convergence in such problems is possible

TABLE 14.4 Rate Expressions for Catalytic Steam Reforming of Hydrocarbons

Reaction no.	Reaction	Rate (mol kg_{cat}^{-1} s^{-1})	Catalyst	Reference
1a	$CH_4 + H_2O = CO + 3H_2$	$r_{1a} = \frac{k_{1a}}{p_{H_2}^{2.5}} \frac{p_{C_1}p_{H_2O} - p_{H_2}^3 p_{CO}/K_{eq}^{I}}{1 + K_{CO}p_{CO} + K_{H_2}p_{H_2} + K_{C_1}p_{C_1} + K_{H_2O}p_{H_2O}/p_{H_2}}$	$Ni/MgAl_2O_4$	[238]
1b	$CH_4 + 2H_2O = CO_2 + 4H_2$	$r_{1b} = \frac{k_{1b}}{p_{H_2}^{3.5}} \frac{p_{C_1}p_{H_2O}^2 - p_{H_2}^4 p_{CO_2}/K_{eq}^{II}}{1 + K_{CO}p_{CO} + K_{H_2}p_{H_2} + K_{C_1}p_{C_1} + K_{H_2O}p_{H_2O}/p_{H_2}}$		
1c	$CO + H_2O = CO_2 + H_2$	$r_{1c} = \frac{k_{1c}}{p_{H_2}} \frac{p_{CO}p_{H_2O} - p_{H_2}p_{CO_2}/K_{eq}^{III}}{1 + K_{CO}p_{CO} + K_{H_2}p_{H_2} + K_{C_1}p_{C_1} + K_{H_2O}p_{H_2O}/p_{H_2}}$		
2	$C_3H_8 + 3H_2O = 3CO + 7H_2$	$r_2 = \frac{1.352 \times 10^{14}\exp(-22,798/T)p_{C_3}^{0.93}p_{H_2O}^{-0.53}}{1 + 52.481p_{H_2}^{0.86}}$	$Ni/MgO\text{-}Al_2O_3$	[21]
3	$n\text{-}C_4H_{10} + 4H_2O = 4CO + 9H_2$	$r_3 = k_3 p_{C_4}^{1.20} p_{H_2O}^{-0.18}$	$Pt–Ni/\delta–Al_2O_3$	[22]
4	$n\text{-}C_7H_{16} + 7H_2O = 7CO + 15H_2$	$r_4 = \frac{k_4 p_{C_7}}{[1 + K_{C_7}p_{C_7}(p_{H_2}/p_{H_2O}) + K_{H_2O}(p_{H_2O}/p_{H_2})]^2}$	$Ni/MgAl_2O_4$	[240]
5	$i\text{-}C_8H_{18} + 8H_2O = 8CO + 17H_2$	$r_5 = \frac{k_5 p_{C_8}^{1/2} p_{H_2O}^{1/2}}{(1 + \sqrt{K_{C_8}p_{C_8}})(1 + \sqrt{K_{H_2O}p_{H_2O}})}$	Ni/Al_2O_3	[241]
6	$CH_3OH + H_2O = CO_2 + 3H_2$	$r_6 = k_6 p_{MeOH}^{0.564}/(\theta + p_{H_2O})^{0.647}$	$Cu/ZnO–Al_2O_3$	[239]
7	$C_2H_5OH + H_2O = 2CO + 4H_2$	$r_7 = k_7 p_{EtOH}^{1.01} p_{H_2O}^{-0.09}$	$Pt–Ni/\ \delta–Al_2O_3$	[118]

TABLE 14.5 Rate Expressions for Catalytic Total Oxidation of Hydrocarbons

Reaction no.	Reaction	Rate (mol kg_{cat}^{-1} s^{-1})	Catalyst	Reference
8	$CH_4 + 2O_2 = CO_2 + 2H_2O$	$r_8 = \frac{k_8 K_{CH_4} K_{O_2}^{1/2} p_{CH_4} p_{O_2}}{[1 + K_{CH_4} p_{CH_4} + \sqrt{K_{O_2} p_{O_2}}]^2}$	$Pt/\delta{-}Al_2O_3$	[40]
9	$C_3H_8 + 5O_2 = 3CO_2 + 4H_2O$	$r_9 = k_9 p_{C_3}^{1.1} p_{O_2}^{-0.6}$	$Pt/\delta{-}Al_2O_3$	[40]
10	$CH_3OH + 1.5O_2 = CO_2 + 2H_2O$	$r_{10} = k_{10} p_{MeOH}$	Pt/Al_2O_3	[239]
11a	$C_2H_5OH + 0.5O_2 = CH_3CHO + H_2O$	$r_{11a} = k_{11a} p_{EtOH} p_{O_2}^{0.5}$	$Cu{-}CrO/Al_2O_3$	[242]
11b	$CH_3CHO + 2.5O_2 = 2CO_2 + 2H_2O$	$r_{11b} = k_{11b} p_{CH_3CHO} p_{O_2}$		

TABLE 14.6 Rate Expressions for Low-Temperature and High-Temperature WGS Reactions

Reaction no.	Reaction	Rate (mol kg_{cat}^{-1} s^{-1})	Catalyst	Reference
12	$CO + H_2O = CO_2 + H_2$ (LTS)	$r_{12} = k_{12}\left(p_{CO} p_{H_2O} - \frac{p_{CO_2} p_{H_2}}{K_e}\right)$	$Cu{-}ZnO/Al_2O_3$	[244]
13	$CO + H_2O = CO_2 + H_2$ (HTS)	$r_{13} = k_{13} p_{CO}^{0.9} p_{H_2O}^{0.31} p_{CO_2}^{-0.156} p_{H_2}^{-0.05}\left(1 - \frac{1}{K_e}\frac{p_{CO_2} p_{H_2}}{p_{CO} p_{H_2O}}\right)$	$Fe_2O_3{-}Cr_2O_3{-}CuO$	[243]

either by dividing the integration steps to very small increments or by using robust solvers that can automatically modify the dimension of the integration step. The former allows the use of RK technique in stiff problems, but stiff ODE solvers offer much faster convergence. These solvers are available in the database of commercial software; the "ode15s" routine in MATLAB has been demonstrated to provide converge in such problems [175,245].

One-dimensional heterogeneous model (Eqs 14.43–14.46), however, involves the co-existence of differential and algebraic equations. The resulting collection is known as a differential-algebraic equation (DAE) set. The algebraic group (Eqs 14.45 and 14.46) is non-linear, and can be solved by least-squares technique running Gauss-Newton method together with a mixed quadratic and cubic line search procedure. This technique, however, needs to be coupled with an ODE solver due to the interdependence of gas and solid phases. Consequently, the model will give more realistic results, especially in the case of fast reactions, but coupled use of differential and algebraic solvers will make it more expensive than the pseudohomogeneous model. One-dimensional heterogeneous reactor model problems can also be solved conveniently using packages such as DAEPACK and DASSL.

Two-dimensional or one-dimensional unsteady-state models are different from the ones above in the sense that they account for the presence of more than one independent variable, and, therefore, are described by partial differentials. Assuming that the pseudohomogeneous conditions prevail, the partial differential equations (PDEs) can be solved by several numerical techniques, including finite difference method (FDM) and the method of orthogonal collocation. FDM involves discretization, which is defined as the selection of grid points, i.e., division of the solution domain into structured grids and approximation of the partial derivatives by the

TABLE 14.7 Various Correlations Recommended for Fixed-Bed Operation (Adapted from Rase [173])

	Correlation	Deviation
Wall Heat Transfer Coefficient, h_w (1-D models)	Spherical Particle $\frac{h_w d_t}{\lambda_f} = 2.26 Re^{0.8} Pr^{0.33} \exp\left(-\frac{6 d_p}{d_t}\right)$ $20 \le Re \le 7600$ and $0.05 \le d_p/d_t \le 0.3$	21%
	Cylindrical Particle $\frac{h_w d_t}{\lambda_f} = 1.40 Re^{0.95} Pr^{0.33} \exp\left(-\frac{6 d_p}{d_t}\right)$ $20 \le Re \le 800$ and $0.03 \le d_p/d_t \le 0.2$	27%
Wall Heat Transfer Coefficient, h_w (2-D models)	Spherical Particle $\frac{h_w d_p}{\lambda_f} = 0.19 Re^{0.79} Pr^{0.33}$ $20 \le Re \le 7600$ and $0.05 \le d_p/d_t \le 0.3$	14%
	Cylindrical Particle $\frac{h_w d_p}{\lambda_f} = 0.18 Re^{0.93} Pr^{0.33}$ $20 \le Re \le 800$ and $0.03 \le d_p/d_t \le 0.2$	33%
Effective Radial Thermal Conductivity, $\lambda_{eff,s}$	$\frac{h_w d_p}{\lambda_{eff,s}} \frac{\varepsilon_p}{1-\varepsilon_p} = 0.27$ Use value of h_w to calculate $\lambda_{eff,s}$ Applies : $500 < \frac{d_p G}{\mu(1-\varepsilon_p)} < 6000$ $0.05 < d_p/d_t < 0.15$	Approximate
Effective Radial Diffusivity, $D_{AB,eff}$	Typical commercial reactors with $Sc \approx 0.7$ $\frac{\varepsilon_p D_{AB,eff}}{U d_p} = \frac{1}{m} + \frac{0.38}{Re}$ for $d_p/d_t > 0.1$ $m = 11$ for $Re > 400$, $m = 57.85 - 35.36 \log Re + 6.68(\log Re)^2$ for $20 < Re < 400$ for $d_p/d_t < 0.1$ divide $D_{AB,eff}$ calculated from above by $[1 + 19.4(d_p/d_t)^2]$	Very Approximate

Note: $Re = \frac{U \rho_f d_p}{\mu}$

finite difference expressions based on Taylor series expansions. The derivative of a function at a nodal point is written in terms of the values of the function at the neighboring nodal points. Such a configuration leads to a set of linear algebraic equations with the unknowns being the values of the dependent variables at each grid point. Differencing can be formulated to give implicit or explicit solution schemes. In the former, algebraic equations have to be solved simultaneously, whereas, in the explicit scheme, values at the $n + 1$ grid point can be solved directly as individual algebraic equations for each dependent variable if the values at nth and lower grid points are known. Although implicit scheme is more tedious in terms of computational effort, the chances of stability and convergence are higher than those of the explicit one. However, in general, FDM is not a robust technique and becomes highly questionable under stiff

conditions. An alternative method for solving the sets of PDEs is orthogonal collocation. This method is based on the discretization of the partial derivatives at the internal collocation points in the spatial direction and, depending on the technique, at the boundaries to reduce the PDEs into set of ODEs which can be solved by a suitable technique (RK or use of stiff solvers). The number of collocation points can be increased for more intense discretization to obtain more reliable solutions, but the computational effort will be higher. In-depth explanations of the numerical techniques above can be found in [246,247].

Informative examples about the use of fixed-bed reactor models can be found in various references [16,175,237]. Avci et al. [175] compares the steady-state 1D-pseudo-homogeneous and heterogeneous models in oxidative steam reforming of methane to hydrogen in various configurations of two types of particulate catalysts, Pt and Ni−MgO, used to drive TOX and SR, respectively. The effects of catalyst-bed configurations − sequential placement of the catalysts and their physical mixture − on heat transfer between the reactions are investigated. The results show that the mixed-bed configuration leads to higher hydrogen yields as a result of the closeness of the heat sources (Pt particles) and heat sinks (Ni−MgO particles) yielding better heat transport characteristics. Model comparisons in the light of criteria listed in Table 14.2 indicate that the 1D model may be inadequate in the presence of sharp temperature gradients caused by TOX after the light-off [175]. Reference [16] describes the use of 1D-pseudohomogeneous model in the sizing and design of fuel processing reactors − IPOX, low-temperature WGS, and CO-cleanup (PrOX) − for various PEM fuel cell power requirements ranging between 10 and 1500 W.

Mathematical modeling and simulation of foam reactors involves continuity equations and boundary conditions same as those of fixed-bed reactors. The characteristic physical properties of the foam structure are used in the various coefficients of the model equations. The methane dry reforming performance of an integral tubular reactor packed with metal-loaded (Rh or Pt-Re) ceramic foam catalyst was simulated at steady-state using a 1D-pseudo-homogeneous reactor model which assumed axial mass and heat flow into a differential element of catalyst with external heat entering in the radial direction through the tube wall [205]. The terms on the right hand side of the energy equation represented the heat consumed by the dry reforming and RWGS reactions as well as the heat supplied from the reactor wall; the latter was given by an overall heat transfer coefficient, U_{foam} (Eq. 14.26), that includes the thermal conductivity of the tube, the wall film coefficient, and the effective thermal conductivity of the catalyst bed in series.

14.6.2. Wall-Coated Structured Reactors

These reactors are different from fixed-beds in the sense that the catalyst is in the form of a porous layer which is washcoated onto the walls of the structured fluid passages. This fundamental configuration, shown for a micro-channel reactor in Fig. 14.6, also forms the basis of monolithic and plate type reactors. There are some other differences that need to be considered in the modeling of structured reactors; the flow is laminar and heat transport in the solid walls, which has a bigger share in the overall volume, is significant. The turbulent nature of the fixed-bed operation allows the simplification of fluid flow into simple plug-flow behavior, whereas laminar conditions require a more comprehensive interpretation, especially in the cases of fluid passages with non-standard shapes, via the inclusion of Navier-Stokes equations counting for the equations of continuity and motion. Based on these conditions, the model equations used to simulate wall-coated reactors according to the representative unit

geometry in Cartesian coordinates shown in Fig. 14.6 are given below:

Fluid phase:

Equation of continuity:

$$\frac{\partial v_x}{\partial x}+\frac{\partial v_y}{\partial y}=0 \tag{14.47}$$

Equations of motion:

$$\rho_f\left(\frac{\partial v_x}{\partial t}+v_x\frac{\partial v_x}{\partial x}+v_y\frac{\partial v_x}{\partial y}\right) = -\frac{\partial p}{\partial x}+\mu\left[\frac{\partial^2 v_x}{\partial x^2}+\frac{\partial^2 v_x}{\partial y^2}\right] \tag{14.48}$$

$$\rho_f\left(\frac{\partial v_y}{\partial t}+v_x\frac{\partial v_y}{\partial x}+v_y\frac{\partial v_y}{\partial y}\right) = -\frac{\partial p}{\partial y}+\mu\left[\frac{\partial^2 v_y}{\partial x^2}+\frac{\partial^2 v_y}{\partial y^2}\right] \tag{14.49}$$

Equation of species continuity:

$$\frac{\partial c_i}{\partial t}+v_x\frac{\partial c_i}{\partial x}+v_y\frac{\partial c_i}{\partial y}=D_{AB}\left[\frac{\partial^2 c_i}{\partial x^2}+\frac{\partial^2 c_i}{\partial y^2}\right] \tag{14.50}$$

Equation of energy:

$$\rho_f C_{pf}\left(\frac{\partial T}{\partial t}+v_x\frac{\partial T}{\partial x}+v_y\frac{\partial T}{\partial y}\right)=\lambda_f\left[\frac{\partial^2 T}{\partial x^2}+\frac{\partial^2 T}{\partial y^2}\right] \tag{14.51}$$

Washcoat phase:

Equation of continuity:

$$\frac{\partial v_x}{\partial x}+\frac{\partial v_y}{\partial y}=0 \tag{14.52}$$

Equations of motion:

$$\left(\frac{\rho_f}{\varepsilon_p}\right)\frac{\partial v_y}{\partial t}+\left(\frac{\mu}{\kappa}\right)v_y=-\frac{\partial p}{\partial y}+\left(\frac{\mu}{\varepsilon_p}\right)\left[\frac{\partial^2 v_y}{\partial x^2}+\frac{\partial^2 v_y}{\partial y^2}\right] \tag{14.53}$$

$$\left(\frac{\rho_f}{\varepsilon_p}\right)\frac{\partial v_y}{\partial t}+\left(\frac{\mu}{\kappa}\right)v_y=-\frac{\partial p}{\partial y}+\left(\frac{\mu}{\varepsilon_p}\right)\left[\frac{\partial^2 v_y}{\partial x^2}+\frac{\partial^2 v_y}{\partial y^2}\right] \tag{14.54}$$

Equation of species continuity:

$$\varepsilon_p\frac{\partial c_i}{\partial t}+v_x\frac{\partial c_i}{\partial x}+v_y\frac{\partial c_i}{\partial y}=D_{AB,eff}\left[\frac{\partial^2 c_i}{\partial x^2}+\frac{\partial^2 c_i}{\partial y^2}\right]-\rho_s R_i(c_i,T) \tag{14.55}$$

Equation of energy:

$$\rho_s C_{ps}\left(\varepsilon_p\frac{\partial T}{\partial t}+v_x\frac{\partial T}{\partial x}+v_y\frac{\partial T}{\partial y}\right)=\lambda_{eff,s}\left[\frac{\partial^2 T}{\partial x^2}+\frac{\partial^2 T}{\partial y^2}\right]+\rho_s\sum_{j=1}^{N}(-\Delta H_j)r_j(c_i,T) \tag{14.56}$$

Solid (wall) phase:

Equation of energy:

$$\rho_w C_{pw}\frac{\partial T}{\partial t}=\lambda_w\left[\frac{\partial^2 T}{\partial x^2}+\frac{\partial^2 T}{\partial y_w^2}\right] \tag{14.57}$$

The set of initial and boundary conditions to close the above equation set are given in Table 14.8. The model equations inherently possess the assumption of continuum flow meaning that the momentum or energy transport is dominated by the collisions of molecules between each other which is much more significant than collisions with the channel wall. This situation is quantified by the Knudsen number, *Kn*, which is the ratio of the mean free path of a gas molecule, λ', to the channel diameter, d_h:

$$Kn=\lambda'/d_h \tag{14.58}$$

$$\lambda'=\frac{k_B^* T}{\sqrt{2}\pi d_{mol}^2 p} \tag{14.59}$$

TABLE 14.8 Initial and Boundary Conditions for the Wall-Coated Structured Reactor Model

Initial Conditions

$t = 0; \forall x, y, y_w$
$p = p_0$
$v = v_0$
$c = c_{i0}$
$T = T_0$

Boundary Conditions

1. *Channel entrance*: $x = 0; \forall y$
   $U = U^{in}$
   $c_i = c_i^{in}$
   $T = T^{in}$
2. *Symmetry at the centerline*: $\forall x; y = 0$
   $n \cdot v = 0$
   $n \cdot (-D_{AB} \nabla c_i + v c_i) = 0$
   $n \cdot (-\lambda_f \nabla T + v \rho_f C_{pf} T) = 0$
3. Along the fluid–solid wall interface: $\forall x; y = H/2 + \delta_s$
   $n \cdot v = 0$
   $n \cdot (-D_{AB} \nabla c_i + v c_i) = 0$
   $n \cdot (-\lambda_w \nabla T) = n \cdot (-\lambda_f \nabla T + v \rho_f C_{pf} T)$
4. *Channel exit*: $x = L; \forall y$
   $p = p^{out}$
   $n \cdot (-D_{AB} \nabla c_i) = 0$
   $n \cdot (-\lambda_f \nabla T) = 0$
5. *Solid boundaries*: $x = 0$ and $x = L; \forall y_w$
   $n \cdot (-k_w \nabla T) = 0$

The assumption of continuum flow with no-slip boundary conditions, forming the basis of Navier-Stokes equations, holds if the Knudsen number is less than or equal to 10^{-2}. For microchannel reactors having the smallest range of channel diameters compared to monoliths and plate-type units, values of *Kn* are reported to be generally below 10^{-1}, which is still within the bounds of continuum flow but with slip boundary conditions ($10^{-2} \leq Kn \leq 10^{-1}$) [248]. Consequently, the *Kn* number for the system under consideration has to be calculated for checking the validity of the model equations above.

Despite the fact that hydraulic diameters are small, concentration and temperature gradients in the lateral (y) direction should be considered, as the reactions run in the catalyst coated walls of the channels. The lateral gradients become more pronounced if the reactors are operated in the integrated mode, i.e., with reaction and heat exchange between the parallel channels. Such cases necessitate the solution of Eqs (14.47–14.57) without any reduction in the number of spatial variables, x and y. The only simplification can be done at steady-state operation via the elimination of terms including time (t). However, if the channels operate at adiabatic conditions, which may be possible with identical reactions in all channels separated by a low-thermal conductivity material (e.g., ceramic monoliths), then the one-dimensional model can be used. It has been demonstrated that, in such conditions, simulation results of indirect POX of methane obtained from one- and two-dimensional models were comparable [245].

Mathematical solution of the wall-coated reactor model is more tedious compared to those of fixed-beds and necessitates the use of the method of computational fluid dynamics (CFD). The method involves the parsing of the solution domain by the grid points, transformation of the PDEs into sets of algebraic equations and their numerical solution. This process, known as discretization, can be done via finite difference, finite volume, and finite element methods. Finite difference method (FDM), explained in Section 14.6.1, is known to be suitable for structured grids such as quadrilateral cells. In general, structured grids are known for their deficiencies in complex geometries and in the presence of steep gradients. These drawbacks can be minimized by the selection of unstructured grids (e.g., triangular cells) which allows higher density of grid points in the regions with steep gradients. Unstructured grids are less compatible with FDM but much more suitable for use in finite volume method (FVM). This second technique calculates the field quantities (e.g., temperature, species concentration) by taking the reaction and flux terms within and across a unit cell (volume), respectively, into

account, and therefore involves a much more realistic discretization scheme than FDM which calculates only point values of field quantities. Based on this fact, FVM has some built-in error minimization routines and becomes a robust technique. FVM and FDM can be considered as special cases of the Finite Element Method (FEM), the third technique. FEM is based on shape functions and has the advantage of being highly adaptive in forming mesh structures for complex geometries. Extension of the set of shape functions is known to improve the convergence performance. However these advantages of FEM will come at the expense of longer computational times. Further information about these techniques are available in the literature [249,250].

The FVM and FEM techniques form the basis of the commercial CFD suites such as Fluent, Star-Cd, CFD-ACE+, CFX, and Comsol Multiphysics. Use of such packages in the design and optimization of reactive systems is becoming popular due to the fact that the interaction between transport phenomena and chemical reactions can be described efficiently by the CFD techniques. However, implementation of heterogeneous kinetics into these techniques is not straightforward. One approach is the integration of software tools such as CHEMKIN, used to solve chemical kinetics problems, into the commercial CFD packages. Alternatively, kinetic information can be fed into user-defined functions which can then be integrated as subroutines into the CFD codes. Some of the suites, such as Comsol Multiphysics, are more practical to use in the sense that they allow the direct input of the kinetic expressions as in the forms given in Tables 14.4–14.6.

A descriptive example that covers the contents of this section is available in [190] which involves the modeling and simulation of heat exchange between the co-current combustion (TOX) and steam reforming of methanol, ethanol, and propane in parallel, wall-separated catalytic microchannel geometries shown in Fig. 14.10. In this study, fluid flow is considered to occur in the parallel channels modeled by Eqs (14.47–14.51), and the catalytic washcoat phase, involving heat and mass transport plus catalytic reactions in porous media is described by Eqs (14.52–14.56). Conductive heat transfer within the stainless-steel wall is modeled by Eq. (14.57). The solution domain in Fig. 14.10 is selected to be the repeating unit of a multi-channel reactor (Fig. 14.6) where exothermic and endothermic reactions run consecutively in microchannels grouped in horizontal layers. As a result, heat transfer is assumed to be negligible in the intra-layer channels and to occur only in the inter-layer channels in the y-direction (Fig. 14.6). Rate expressions outlined in Tables 14.4 and 14.5 are utilized in integrating steam reforming and total oxidation reactions, respectively, into the model equations. Further details needed for modeling such as physical parameters of the overall system and feed conditions are provided in [190]. The equations above and the accompanying boundary conditions listed in Table 14.8 are solved at steady-state conditions, for both straight and micro-baffled channel configurations (Figs 14.10a and b, respectively), using FEM-based CFD technique with unstructured meshing under the Comsol Multiphysics environment. Selected results for ethanol conversions are presented in Fig. 14.15 in terms of surface plots of temperature. It can be observed that in both geometric configurations heat transfer between the reactions is very rapid; temperature gradients between the two channels are minimized just after the first couple of millimeters, showing the improved heat transfer characteristics of the microchannel units. The results also demonstrate the impact of using micro-baffles, which elongate the residence time of combustion stream and improve heat-transfer coefficient by functioning as static-mixers. The combination of these effects leads to higher temperatures in the micro-baffled steam reforming channel accompanied by increased

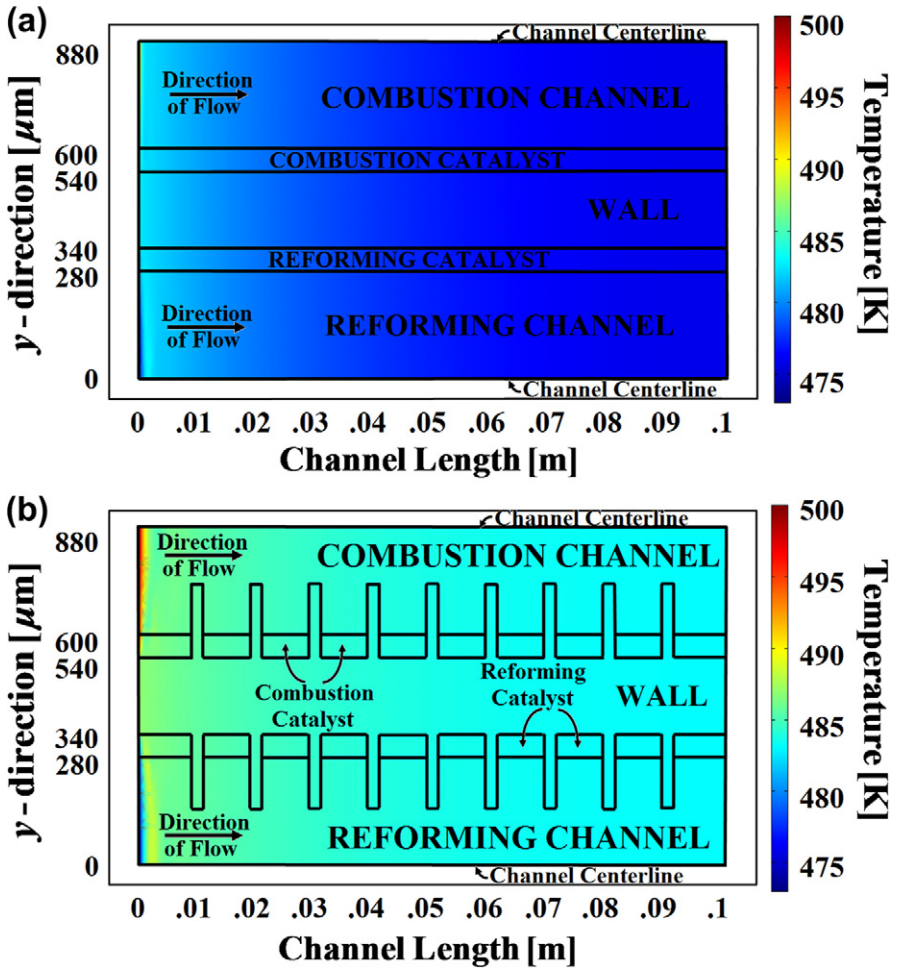

FIGURE 14.15 Surface temperature plots obtained in parallel microchannel geometries (a) without and (b) with microbaffles *(Courtesy of Ahmet K. Avci).*

hydrogen yields by ca. 21% [190]. The same study also includes the dynamic (time dependent) CFD simulations of the cases above.

Another recent example involves the steady-state modeling and simulation of the cascade reactor system (Section 14.5.5.1) for coupled methane TOX/SR and methane TOX/ethane dehydrogenation reactions [230]. The adiabatic reactors, assumed to be of fixed-bed type, are simulated using the 1D-pseudohomogeneous model with pressure drop (Eqs 14.36–14.38 and 14.41), whereas the interconnecting microchannel heat exchangers are simulated by Eqs (14.47–14.51 and 14.57). A stiff ODE solver and FEM-based CFD technique (in Comsol Multiphysics) are used to solve the ODE set of the 1D model and the PDE set describing the microchannel unit. The results are shown in Fig. 14.12 and discussed in Section 14.5.5.1. This study is descriptive as it combines the modeling of fixed-bed and structured-flow operations.

14.6.3. Membrane Reactors

Membrane reactors involve coupling of reaction and separation steps and can be designed in two major forms: (i) packed-bed membrane reactors (Fig. 14.13), where the membrane only provides a physical barrier through which one product (e.g., H_2) can diffuse out and (ii) catalytic membrane reactors (Fig. 14.14), where the catalyst is deposited on the membrane itself and one of the products (e.g., H_2) diffuses to the permeate side as it is formed on the catalyst (see Section 14.5.5.2). The model equations describing the operation of these reactor types are given in the following sections.

14.6.3.1. Packed-Bed Membrane Reactors

The general forms of the PBMR model equations below and initial and boundary conditions in Table 14.9 are based on cylindrical coordinates and given in line with Fig. 14.13:

Fluid phase:

Equation of species continuity:

$$\varepsilon_p\frac{\partial c_i}{\partial t}+v_z\frac{\partial c_i}{\partial z}=D_{AB,r}\left[\frac{1}{r}\frac{\partial}{\partial r}\left(r\frac{\partial c_i}{\partial r}\right)\right]+D_{AB,a}\frac{\partial^2 c_i}{\partial z^2}-k_g a_v\left(c_i-c_i^s|_{\xi=R_p}\right)+a_v J_i|_{r=R_t} \tag{14.60}$$

Equation of energy:

$$\varepsilon_p\rho_f C_{pf}\frac{\partial T}{\partial t}+\rho_f C_{pf}v_z\frac{\partial T}{\partial z}=\lambda_{f,r}\left[\frac{1}{r}\frac{\partial}{\partial r}\left(r\frac{\partial T}{\partial r}\right)\right]+\lambda_{f,a}\frac{\partial^2 T}{\partial z^2}+h_f a_v\left(T_s|_{\xi=R_p}-T\right)-\frac{2U_w}{R_t}(T-T_r)+a_v J_i|_{r=R_t}\overline{H}_i \tag{14.61}$$

Solid (catalyst) phase:

Equation of species continuity:

$$\varepsilon_s\frac{\partial c_i^s}{\partial t}=\frac{D_{AB,eff}}{\xi^2}\frac{\partial}{\partial\xi}\left(\xi^2\frac{\partial c_i^s}{\partial\xi}\right)-\rho_s R_i(c_i^s,T_s) \tag{14.62}$$

TABLE 14.9 Initial and Boundary Conditions for the Fixed-Bed Membrane Reactor Model

Initial Conditions

$t=0;\ \forall r,z,\xi$
$c_i=c_{i0}$
$T=T_0$
$c_i^s=0$
$T_s=T_0$

Boundary Conditions

Fluid phase

1. *Reactor entrance*: $z=0;\ \forall r$
   $c_i=c_i^{in}$
   $T=T^{in}$
2. *Symmetry at the center*: $\forall z;\ r=0$
   $\partial c_i/\partial r=0$
   $\partial T/\partial r=0$
3. Along the fluid–wall interface: $\forall z;\ r=R_t$
   $J_i=D_{AB,r}\dfrac{\partial c_i}{\partial r}$
   $h_w(T_w-T)+J_i\Delta H_i=\lambda_{f,r}\dfrac{\partial T}{\partial r}$
4. *Reactor exit*: $z=L;\ \forall r$
   $\partial c_i/\partial z=0$
   $\partial T/\partial z=0$

Solid (catalyst) phase

5. *Symmetry at the center*: $\xi=0;\ \forall r,z$
   $\partial c_i^s/\partial\xi=0$
   $\partial T_s/\partial\xi=0$
6. On the fluid–solid interface: $\xi=R_p;\ \forall r,z$
   $k_g\left(c_i^s|_{\xi=R_p}-c_i\right)=-D_{AB,eff}\dfrac{dc_i^s}{d\xi}$
   $h_f\left(T_s|_{\xi=R_p}-T\right)=-\lambda_{eff,s}\dfrac{dT_s}{d\xi}$

Equation of energy:

$$\varepsilon_s\rho_s C_{ps}\frac{\partial T_s}{\partial t}=\frac{\lambda_{eff,s}}{\xi^2}\frac{\partial}{\partial\xi}\left(\xi^2\frac{\partial T_s}{\partial\xi}\right)+\rho_s\sum_{j=1}^{N}(-\Delta H_j)r_j(c_i^s,T_s) \tag{14.63}$$

The equations above are comparable to those given for the fixed-bed operation since they describe the fluid and solid phases in the packed

bed of particles on the feed side of the membrane reactor (Eqs 14.28 and 14.29). The only difference is based on the separation stage, which is represented by a flux term on the right-hand side of the fluid phase continuity equation (14.60) for the product diffusing to the permeate side (e.g., J_{H_2}); for all other components in the mixture, the permeation flux term is equal to zero. Solution techniques outlined in Section 14.6.1 also hold for the packed-bed membrane reactor model, using the boundary conditions given in Table 14.9.

Examples of mathematical modeling studies reported for methane steam reforming and dry reforming in PBMR using dense and microporous membranes have assumed isothermal operation and co-current flow as well as negligible radial and axial dispersion. The pressure drop along reactor length was either taken to be negligible or was expressed by the Ergun equation in the packed section and by the standard equation for flow through a pipe on the permeate side. Permeation of H_2 through dense membranes (e.g., Pd/Ag) was assumed to follow Sievert's law while the only mode of transport through microporous silica or glass membranes was Knudsen flow [233,234].

A one-dimensional pseudo-homogeneous mathematical model was also used for simulating the operation of a multi-tubular MR (with catalyst packed in the shell side and co-current flow of permeated hydrogen in the tubes) and compared with an equivalent packed-bed reactor (PBR) with no H_2 permeation. The influence of pressure on MR performance was considered under adiabatic conditions using convective and diffusive heat transfer mechanisms for energy transport through the H_2-selective membrane consisting of a dense Pd layer deposited onto a porous ceramic support [235].

14.6.3.2. *Catalytic Membrane Reactors*

The general forms of the CMR model equations below and initial and boundary conditions in Table 14.10 are based on cylindrical coordinates and given in accordance with Fig. 14.14:

Fluid phase:

Equation of continuity:

$$\frac{1}{r}\frac{\partial}{\partial r}(rv_r) + \frac{\partial v_z}{\partial z} = 0 \tag{14.64}$$

Equations of motion:

$$\rho_f\left(\frac{\partial v_r}{\partial t} + v_r\frac{\partial v_r}{\partial r} + v_z\frac{\partial v_r}{\partial z}\right) = -\frac{\partial p}{\partial r} + \mu\left[\frac{\partial}{\partial r}\left(\frac{1}{r}\frac{\partial}{\partial r}(rv_r)\right) + \frac{\partial^2 v_r}{\partial z^2}\right] \tag{14.65}$$

TABLE 14.10 Initial and Boundary Conditions for the Catalytic Membrane Reactor Model

Initial Conditions

$t = 0; \forall z, r$
$p = p_0$
$\mathrm{v} = \mathrm{v}_0$
$c = c_{i0}$
$T = T_0$

Boundary Conditions

1. *Channel entrance*: $z = 0; \forall r$
   $U = U^{in}$
   $c_i = c_i^{in}$
   $T = T^{in}$

2. *Symmetry at the centerline*: $\forall z;\ r = 0$
   $\mathrm{n}\cdot\mathrm{v} = 0$
   $\mathrm{n}\cdot(-D_{AB}\nabla c_i + \mathrm{v}c_i) = 0$
   $\mathrm{n}\cdot(-\lambda_f\nabla T + \mathrm{v}\rho_f C_{pf}T) = 0$

3. *Along the membrane surface on the permeate side:*
   $\forall z; r = R_t + \delta_s$
   $\mathrm{n}\cdot\mathrm{v} = 0$
   $\mathrm{n}\cdot(-D_{AB}\nabla c_i + \mathrm{v}c_i) = J_i$
   $\mathrm{n}\cdot(-\lambda_f\nabla T + \mathrm{v}\rho_f C_{pf}T) = J_i\Delta H_i$
   For $i = H_2$, $J_i = J_{H_2}$; for $i \neq H_2$, $J_i = 0$

4. *Channel exit*: $z = L; \forall r$
   $p = p^{out}$
   $\mathrm{n}\cdot(-D_{AB}\nabla c_i) = 0$
   $\mathrm{n}\cdot(-\lambda_f\nabla T) = 0$

$$\rho_f\left(\frac{\partial v_z}{\partial t}+v_r\frac{\partial v_z}{\partial r}+v_z\frac{\partial v_z}{\partial z}\right) = -\frac{\partial p}{\partial z}+\mu\left[\frac{1}{r}\frac{\partial}{\partial r}\left(r\frac{\partial v_z}{\partial r}\right)+\frac{\partial^2 v_z}{\partial z^2}\right] \quad (14.66)$$

Equation of species continuity:

$$\frac{\partial c_i}{\partial t}+v_r\frac{\partial c_i}{\partial r}+v_z\frac{\partial c_i}{\partial z} = D_{AB}\left[\frac{1}{r}\frac{\partial}{\partial r}\left(r\frac{\partial c_i}{\partial r}\right)+\frac{\partial^2 c_i}{\partial z^2}\right] \quad (14.67)$$

Equation of energy:

$$\rho_f C_{pf}\left(\frac{\partial T}{\partial t}+v_r\frac{\partial T}{\partial r}+v_z\frac{\partial T}{\partial z}\right) = \lambda_f\left[\frac{1}{r}\frac{\partial}{\partial r}\left(r\frac{\partial T}{\partial r}\right)+\frac{\partial^2 T}{\partial z^2}\right] \quad (14.68)$$

$$\left(\frac{\rho_f}{\varepsilon_p}\right)\frac{\partial v_z}{\partial t}+\left(\frac{\mu}{\kappa}\right)v_z = -\frac{\partial p}{\partial z}+\left(\frac{\mu}{\varepsilon_p}\right)\left[\frac{1}{r}\frac{\partial}{\partial r}\left(r\frac{\partial v_z}{\partial r}\right)+\frac{\partial^2 v_z}{\partial z^2}\right] \quad (14.71)$$

Equation of species continuity:

$$\varepsilon_p\frac{\partial c_i}{\partial t}+v_r\frac{\partial c_i}{\partial r}+v_z\frac{\partial c_i}{\partial z} = D_{AB,eff}\left[\frac{1}{r}\frac{\partial}{\partial r}\left(r\frac{\partial c_i}{\partial r}\right)+\frac{\partial^2 c_i}{\partial z^2}\right]-\rho_s R_i(c_i,T) \quad (14.72)$$

Equation of energy:

$$\rho_f C_{\rho f}\left(\varepsilon_p\frac{\partial T}{\partial t}+\nu_r\frac{\partial T}{\partial r}+\nu_z\frac{\partial T}{\partial z}\right) = \lambda_{eff,s}\left[\frac{1}{r}\frac{\partial}{\partial r}\left(r\frac{\partial T}{\partial r}\right)+\frac{\partial^2 T}{\partial z^2}\right]+\rho_s\sum_{j=1}^{N}\left(-\Delta H_j\right)r_j\left(c_i,T\right) \quad (14.73)$$

Catalytic membrane phase:

Equation of continuity:

$$\frac{1}{r}\frac{\partial}{\partial r}(rv_r)+\frac{\partial v_z}{\partial z} = 0 \quad (14.69)$$

Equations of motion:

$$\left(\frac{\rho_f}{\varepsilon_p}\right)\frac{\partial v_r}{\partial t}+\left(\frac{\mu}{\kappa}\right)v_r = -\frac{\partial p}{\partial r}+\left(\frac{\mu}{\varepsilon_p}\right)\left[\frac{\partial}{\partial r}\left(\frac{1}{r}\frac{\partial}{\partial r}(rv_r)\right)+\frac{\partial^2 v_r}{\partial z^2}\right] \quad (14.70)$$

The model equations for the catalytic membrane reactor describe the fluid phase on the feed side of the reactor and the solid phase which is the catalytic membrane itself where reaction occurs and one product (e.g., H_2) selectively diffuses out to the permeate side; the permeation flux of the diffusing product is included in the boundary conditions listed in Table 14.10. CFD-based solution techniques outlined in Section 14.6.2 can be used to solve the CMR model.

It is difficult to find examples in the literature reporting the modeling and simulation of CMR operation. The closest example reported is a multi-scale modeling approach that was proposed as a scheme for modeling catalytic flow reactors including monolith and membrane reactors which couples continuum descriptions

of the fluid phase with kinetic Monte Carlo simulations of the catalyst domain using the concept of patch dynamics to handle concentration variations [251].

NOMENCLATURE

Symbol	Definition	Unit
a_v	Geometric surface area-to-volume ratio of a particle	$m^2\ m^{-3}$
A_c	Cross-sectional area of the reactor tube/channel	m^2
c_i	Concentration of species i in the fluid phase	$mol\ m^{-3}$
c_i^s	Concentration of species i inside the catalyst particle	$mol\ m^{-3}$
C_{pf}, C_{pi}	Specific heat of fluid/species i	$J\ kg^{-1}\ K^{-1}$
C_{ps}	Specific heat of catalytic washcoat/bed	$J\ kg^{-1}\ K^{-1}$
C_{pw}	Specific heat of microchannel wall	$J\ kg^{-1}\ K^{-1}$
d_h	Hydraulic diameter (4 × cross-sectional area/wetted perimeter)	m
d_{mol}	Diameter of the gas particle	m
d_p	Diameter of spherical catalyst particle ($6/a_v$ for equivalent sphere)	m
$d_{p,m}$	Mean pore diameter between each cell in foam structures	m
d_t	Diameter of reactor tube	m
d_w	Wire diameter	m
D_{AB}	Species diffusivity (A into stagnant B)	$m^2\ s^{-1}$
$D_{AB,a}$	Axial species diffusivity	$m^2\ s^{-1}$
$D_{AB,r}$	Radial species diffusivity	$m^2\ s^{-1}$
$D_{AB,eff}$	Effective species diffusivity in the washcoat layer or catalyst bed	$m^2\ s^{-1}$
E_A	Activation energy	$J\ mol^{-1}$
f	Fanning friction factor	–
f_{app}	Fanning friction factor for developing laminar flow	–
F_i	Molar flow rate of species i	$mol\ s^{-1}$
G	Superficial mass velocity ($\rho_f U$)	$kg\ m^2\ s^{-1}$
H	Height of microchannel	m
h_f	Film heat transfer coefficient	$W\ m^{-2}\ K^{-1}$
h_w	Convective heat transfer coefficient between the wall and the fluid	$W\ m^{-2}\ K^{-1}$
$\overline{H}_i$	Partial molar enthalpy of species i	$J\ mol^{-1}$
ΔH_j	Heat of reaction j at the specific reaction temperature	$J\ mol^{-1}$
i	Species index	–
j	Reaction index	–
J_i	Molar flux of species *i* through the membrane	$mol\ m^{-2}\ s^{-1}$
k_B^*	Boltzmann constant	$J\ K^{-1}$
k_j	Specific reaction rate of reaction j (unit depends on the rate law)	
k_g	Gas-phase mass transfer coefficient	$m\ s^{-1}$
K_{eq}^j	Equilibrium constant for reaction j (unit depends on the reaction)	
K_i	Adsorption/desorption constant for species i	MPa^{-1}
L	Microchannel/reactor tube length	m
L_e	Length of the entry zone in microchannels	m
M	Number of species	–
n	Normal unit vector	–
n	Reaction order	–
N	Number of reactions	–
Nu	Nusselt number ($h_f d_h/\lambda_f$)	–

(Continued)

Symbol	Definition	Unit
p	Total pressure	MPa
p_i	Partial pressure of species i	MPa
Pr	Prandtl number ($\mu C_{pf}/\lambda_f$)	–
r	Radial coordinate in reactor tube	m
r_j	Rate of reaction j	mol kg_{cat}^{-1} s^{-1}
$r_j(c_i^s, T_s)$	Rate of reaction j evaluated at c_i^s and T_s	mol kg_{cat}^{-1} s^{-1}
R	Ideal gas constant (8.314 J mol^{-1} K^{-1})	J mol^{-1} K^{-1}
R_i	Total rate of generation/depletion of species i	mol kg_{cat}^{-1} s^{-1}
$R_i(c_i^s, T_s)$	Total rate of generation/depletion of species i evaluated at c_i^s and T_s	mol kg_{cat}^{-1} s^{-1}
R_p	Radius of spherical catalyst particle	m
R_t	Radius of reactor tube	m
Re	Reynolds number ($U\rho_f d_p/\mu$) for single spherical pellet, ($U\rho_f d_h/\mu$) for tubes/channels, ($U\rho_f d_p/(1-\varepsilon_p)\mu$) for packed-beds, ($U\rho_f/a_v\mu$) for foams	–
S	Width of microchannel	m
Sc	Schmidt number ($\mu/\rho_f D_{AB}$)	–
Sh	Sherwood number ($k_g d_h/D_{AB}$)	–
t	Time	s
T	Temperature	K
T_s	Temperature inside the catalyst particle	K
T_w	Wall temperature	K
U	Superficial fluid velocity	m s^{-1}
U_{foam}	Overall heat transfer coefficient for foams	W m^{-2} K^{-1}
U_w	Overall heat transfer coefficient between the fluid and the wall	W m^{-2} K^{-1}
v_x, v_y	x- and y-components of fluid velocity (Cartesian coordinates)	m s^{-1}
v_r, v_z	Radial and axial components of fluid velocity (cylindrical coordinates)	m s^{-1}
v	Fluid velocity vector in microchannel	m s^{-1}
x	Axial coordinate in microchannel	m
y	Direction normal to the x-axis	m
y_w	Direction normal to the x-axis (inside the microchannel wall)	m
z	Axial coordinate in reactor tube	m
Greek letters		
α, β	Constants of the Ergun equation	–
α_{ji}	Stoichiometric coefficient of species i in reaction j	–
δ_s	Thickness of catalytic washcoat/membrane	m
ε_p	Void fraction of washcoat layer/catalyst bed	–
ε_s	Porosity of catalyst particle	–
η_j	Effectiveness factor for reaction j	–
κ	Permeability of washcoat layer	m^2
λ'	Mean free path of a gas molecule	m
λ_f	Fluid thermal conductivity	W m^{-1} K^{-1}
$\lambda_{f,a}$	Axial thermal conductivity	W m^{-1} K^{-1}
$\lambda_{f,r}$	Radial thermal conductivity	W m^{-1} K^{-1}
$\lambda_{eff,s}$	Effective thermal conductivity of the catalytic washcoat/bed	W m^{-1} K^{-1}
θ	Angle of flow direction slope to the bed axis	degrees

Symbol	Definition	Unit
ρ_b	Bulk density of the catalyst bed (mass of solid per unit volume of bed)	kg m^{-3}
ρ_f	Fluid density	kg m^{-3}
ρ_p	Catalytic washcoat/bed/ ceramic foam density (mass of solid per unit volume of solid (including pores))	kg m^{-3}
ρ_s	Catalytic washcoat/bed/ ceramic foam solid density (mass of solid per unit volume of solid (excluding pores))	kg m^{-3}
ρ_w	Density of microchannel wall	kg m^{-3}
μ	Viscosity	kg m^{-1} s^{-1}
τ	Bed tortuosity factor	−
υ	Total volumetric flow rate in the reactor tube	m^3 s^{-1}
ξ	Radial coordinate in spherical catalyst particle	m
∇	Gradient operator	m^{-1}
Subscripts and Superscripts		
0	Initial value of the variable	
a	Diffusivity or thermal conductivity in the axial direction	
eff	Effective diffusivity or conductivity	
f	Fluid	
in	Inlet value of the variable	
out	Outlet value of the variable	
r	Diffusivity or thermal conductivity in the radial direction	
s	Washcoat/membrane/ particle	
T	Total quantity	
w	Wall	

Acknowledgments

The authors are thankful to Mustafa Karakaya, PhD candidate, for his assistance in the formulation of model equations and in the unification of nomenclature.

References

[1] Ahmed S, Krumpelt M. Hydrogen from hydrocarbon fuels for fuel cells. Int J Hydrogen Energy 2001;26:291−301.

[2] Rostrup-Nielsen JR. Catalytic steam reforming. In: Anderson JR, Boudart M, editors. Catalysis, science & technology. Berlin: Springer-Verlag; 1984. p. 1−117.

[3] Rostrup-Nielsen JR, Hansen JHB. CO_2-reforming of methane over transition metals. J Catal 1993;144: 38−49.

[4] Trimm DL, Onsan ZI. Onboard fuel conversion for hydrogen-fuel-cell-driven vehicles. Cat Rev Sci Eng 2001;43:31−84.

[5] Hickman DA, Schmidt LD. Production of syngas by direct catalytic oxidation of methane. Science 1993; 259:343−6.

[6] Torniainen PM, Chu X, Schmidt LD. Comparison of monolith-supported metals for the direct oxidation of methane to syngas. J Catal 1994;176:1−10.

[7] Fichtner M, Mayer J, Wolf D, Schubert K. Microstructured rhodium catalysts for the partial oxidation of methane to syngas under pressure. Ind Eng Chem Res 2001;40:3475−83.

[8] Enger BC, Walmsley J, Bjørgum E, Lødeng R, Pfeifer P, Schubert K, et al. Performance and SEM characterization of Rh impregnated microchannel reactors in the catalytic partial oxidation of methane and propane. Chem Eng J 2008;144:489−501.

[9] Golunski S. Hotspot fuel processor. Platinum Metals Rev 1998;42:2−7.

[10] Onsan ZI. Catalytic processes for clean hydrogen production from hydrocarbon. Turk J Chem 2007;31: 531−50.

[11] Aasberg-Petersen K, Christensen TS, Dybkjaer I, Sehested J, Ostberg M, Coertzen RM, et al. Synthesis gas production for FT synthesis. In: Steynberg AP, Dry ME, editors. Fischer-Tropsch technology. Amsterdam: Elsevier; 2004. p. 258−405.

[12] Avci AK, Onsan ZI, Trimm DL. On-board fuel conversion for hydrogen fuel cells: comparison of different fuels by computer simulations. Appl Catal A: Gen 2001;216:243−56.

[13] Trimm DL. Catalysts for the control of coking during steam reforming. Catal Today 1999;49:3−10.

[14] Joensen F, Rostrup-Nielsen JR. Conversion of hydrocarbons and alcohols for fuel cells. J Power Sources 2002;105:195−201.

[15] Remans TJ, Jenzer G, Hoek A. In: Ertl G, Knözinger H, Schüth F, Weitkamp J, editors. Handbook of heterogeneous catalysis. Weinheim: Wiley-VCH; 2008. p. 2994–3010.
[16] Tan O, Masalaci E, Onsan ZI, Avci AK. Design of a methane processing system producing high-purity hydrogen. Int J Hydrogen Energy 2008;33:5516–26.
[17] Rostrup-Nielsen JR. Syngas for C_1-chemistry: limits of the steam reforming process. In: Bibby DM, Chang CD, Howe RF, Yurchak S, editors. Methane conversion. Amsterdam: Elsevier; 1998. p. 73–8.
[18] Wang Y, Chin YH, Rozmiarek RT, Johnson BR, Gao Y, Watson J, et al. Highly active and stable Rh/MgO-Al_2O_3 catalysts for methane steam reforming. Catal Today 2004;98:575–81.
[19] Borowiecki T, Golebiowski A, Stasinska B. Effects of small MoO_3 additions on the properties of nickel catalysts for the steam reforming of hydrocarbons. Appl Catal A: Gen 1997;153:141–56.
[20] Horiuchi T, Sakuma K, Fukui T, Kubo Y, Osaki T, Mori T. Suppression of carbon deposition in the CO_2-reforming of CH_4 by adding basic metal oxides to a Ni/Al_2O_3 catalyst. Appl Catal A: Gen 1996;144:111–20.
[21] Ma L. Ph.D. Thesis, University of New South Wales, 1995.
[22] Avci AK, Trimm DL, Aksoylu AE, Onsan ZI. Hydrogen production by steam reforming of n-butane over supported Ni and Pt-Ni catalysts. Appl Catal A: Gen 2004;258:235–40.
[23] Wang X, Gorte RJ. Steam reforming of n-butane on Pd/ceria. Catal Lett 2001;73:15–9.
[24] Kolb G, Zapf R, Hessel V, Löwe H. Propane steam reforming in micro-channels – results from catalyst screening and optimisation. Appl Catal A: Gen 2004;277:155–66.
[25] Hickman DA, Schmidt LD. Synthesis gas formation by direct oxidation of methane over Pt monoliths. J Catal 1992;138:267–82.
[26] Bodke AS, Bharadwaj SS, Schmidt LD. The effect of ceramic supports on partial oxidation of hydrocarbons over noble metal coated monoliths. J Catal 1998;179:138–49.
[27] Hohn KL, Schmidt LD. Partial oxidation of methane to syngas at high space velocities over Rh-coated spheres. Appl Catal A: Gen 2001;211:53–68.
[28] Veser G. Short contact-time reactors. In: Ertl G, Knözinger H, Schüth F, Weitkamp J, editors. Handbook of heterogeneous catalysis. Weinheim: Wiley-VCH; 2008. p. 2174–88.
[29] Basile F, Fornasari G, Trifiro F, Vaccari A. Partial oxidation of methane: effect of reaction parameters and catalyst composition on the thermal profile and heat distribution. Catal Today 2001;64:21–30.
[30] Boucouvalas Y, Zhang ZL, Verykios XE. Partial oxidation of methane to synthesis gas via the direct reaction scheme over Ru/TiO_2 catalyst. Catal Lett 1996;40:189–95.
[31] Dissanayake D, Rosynek MP, Kharas KCC, Lunsford JH. Partial oxidation of methane to carbon monoxide and hydrogen over a Ni/Al_2O_3 catalyst. J Catal 1991;132:117–27.
[32] Tsipouriari VA, Zhang Z, Verykios XE. Catalytic partial oxidation of methane to synthesis gas over Ni-based catalysts. J Catal 1998;179:283–91.
[33] van Looij F, Geus JW. Nature of the active phase of a nickel catalyst during the partial oxidation of methane to synthesis gas. J Catal 1997;168:154–63.
[34] Nakagawa K, Ikenaga N, Teng Y, Kobayashi T, Suzuki T. Transient response of catalyst bed temperature in pulsed reaction of partial oxidation of methane to synthesis gas over supported rhodium and iridium catalysts. J Catal 1999;186:405–13.
[35] Huff M, Torniainen PM, Schmidt LD. Partial oxidation of alkanes over noble metal coated monoliths. Catal Today 1994;21:113–28.
[36] Bass RJ, Dunn TM, Lin YC, Hohn KL. Syngas production from catalytic partial oxidation of n-butane: comparison between incipient wetness and sol-gel prepared Pt/Al_2O_3. Ind Eng Chem Res 2008; 47:7184–9.
[37] Aartun I, Gjervan T, Venvik H, Görke O, Pfeifer O, Fathi M, et al. Catalytic conversion of propane to hydrogen in microstructured reactors. Chem Eng J 2004;101:93–9.
[38] Aartun I, Venvik HJ, Holmen A, Pfeifer P, Görke O, Schubert K. Temperature profiles and residence time effects during catalytic partial oxidation and oxidative steam reforming of propane in metallic microchannel reactors. Catal Today 2005;110:98–107.
[39] Pennemann H, Hessel V, Kolb G, Löwe H, Zapf R. Partial oxidation of propane using micro structured reactors. Chem Eng J 2008;135S:S66–73.
[40] Ma L, Trimm DL, Jiang C. The design and testing of an autothermal reactor for the conversion of the light hydrocarbons to hydrogen I. The kinetics of the catalytic oxidation of light hydrocarbons. Appl Catal A: Gen 1996;138:275–83.
[41] Twigg MV. Catalyst handbook. 2nd ed. London: Wolfe Publishing Ltd; 1989.
[42] Kiwi-Minsker L, Renken A. Microstructured reactors for catalytic reactions. Catal Today 2005;110:2–14.
[43] Kolb G, Hessel V. Micro-structured reactors for gas phase reactions. Chem Eng J 2004;98:1–38.
[44] Ma L, Trimm DL. Alternative catalyst bed configurations for the autothermic conversion of methane to hydrogen. Appl Catal A: Gen 1996;138:265–73.

[45] Jiang C, Trimm DL, Wainwright MS. New technology for hydrogen production by the catalytic oxidation and steam reforming of methanol at low temperatures. Chem Eng Technol 1995;18:1–6.
[46] Avci AK, Trimm DL, Onsan ZI. Quantitative investigation of catalytic natural gas conversion for hydrogen fuel cell applications. Chem Eng J 2002;90:77–87.
[47] Orücü E, Karakaya M, Avci AK, Onsan ZI. Investigation of ethanol conversion for hydrogen fuel cells using computer simulations. J Chem Technol Biotechnol 2005;80:1103–10.
[48] Avci AK, Onsan ZI, Trimm DL. On-board hydrogen generation for fuel cell-powered vehicles: the use of methanol and propane. Top Catal 2003;22:359–67.
[49] Caglayan BS, Avci AK, Onsan ZI, Aksoylu AE. Production of hydrogen over bimetallic Pt–Ni/δ-Al_2O_3 I. Indirect partial oxidation of propane. Appl Catal A: Gen 2005;280:181–8.
[50] Pino L, Vita A, Cipiti F, Lagana M, Recupero V. Performance of Pt/CeO_2 catalyst for propane oxidative steam reforming. Appl Catal A: Gen 2006; 306:68–77.
[51] Lee HJ, Lim YS, Park NC, Kim YC. Catalytic autothermal reforming of propane over the noble metal-doped hydrotalcite-type catalysts. Chem Eng J 2009;146:295–301.
[52] Silberova B, Venvik HJ, Holmen A. Production of hydrogen by short contact time partial oxidation and oxidative steam reforming of propane. Catal Today 2005;99:69–76.
[53] Sato K, Nagaoka K, Nishiguchi H, Takita Y. n-C_4H_{10} autothermal reforming over MgO-supported base metal catalysts. Int J Hydrogen Energy 2009;34: 333–42.
[54] Gokaliler F, Caglayan BS, Onsan ZI, Aksoylu AE. Hydrogen production by autothermal reforming of LPG for PEM fuel cell applications. Int J Hydrogen Energy 2008;33:1383–91.
[55] Caglayan BS, Onsan ZI, Aksoylu AE. Production of hydrogen over bimetallic Pt-Ni/δ-Al_2O_3: II. Indirect partial oxidation of LPG. Catal Lett 2005;102:63–7.
[56] Rostrup-Nielsen JR. Industrial relevance of coking. Catal Today 1997;37:225–32.
[57] Pasel J, Meissner J, Pors Z, Palm C, Cremer P, Peters R, et al. Hydrogen production via autothermal reforming of diesel fuel. Fuel Cells 2004;4:225–30.
[58] Pors Z, Pasel J, Tschauder A, Dahl R, Peters R, Stolten D. Optimised mixture formation for diesel fuel processing. Fuel Cells 2008;2:129–37.
[59] Lindström B, Karlsson JAJ, Ekdunge P, De Verdier L, Häggendal B, Dawody J, et al. Diesel fuel reformer for automotive fuel cell applications. Int J Hydrogen Energy 2009;34:3367–81.
[60] Kopasz JP, Applegate D, Miller L, Liao HK, Ahmed S. Unraveling the maze: understanding of diesel reforming through the use of simplified fuel blends. Int J Hydrogen Energy 2005;30:1243–50.
[61] Nilsson M, Karatzas X, Lindström B, Pettersson LJ. Assessing the adaptability to varying fuel supply of an autothermal reformer. Chem Eng J 2008;142:309–17.
[62] Krummenacher JJ, West KN, Schmidt LD. Catalytic partial oxidation of higher hydrocarbons at millisecond contact times: decane, hexadecane, and diesel fuel. J Catal 2003;215:332–43.
[63] Subramanian R, Panuccio GJ, Krummenacher JJ, Lee IC, Schmidt LD. Catalytic partial oxidation of higher hdrocarbons: reactivities and selectivities of mixtures. Chem Eng Sci 2004;59:5501–7.
[64] Peters R. Fuel processors. In: Ertl G, Knözinger H, Schüth F, Weitkamp J, editors. Handbook of heterogeneous catalysis. Weinheim: Wiley-VCH; 2008. p. 3045–80.
[65] O'Connell M, Kolb G, Schelhaas KP, Schuerer J, Tiemann D, Ziogas A, et al. Development and evaluation of a microreactor for the reforming of diesel fuel in the kW range. Int J Hydrogen Energy 2009;34:6290–303.
[66] Cutillo A, Specchia S, Antonini M, Saracco G, Specchia V. Diesel fuel processor for PEM fuel cells: two possible alternatives (ATR versus SR). J Power Sources 2006;154:379–85.
[67] Thormann J, Pfeifer P, Schubert K, Kunz U. Reforming of diesel fuel in a micro reactor for APU systems. Chem Eng J 2008;135S:S74–81.
[68] Ming Q, Healey T, Allen L, Irving P. Steam reforming of hydrocarbon fuels. Catal Today 2002;77:51–64.
[69] Haynes DJ, Berry DA, Shekhawat D, Spivey JJ. Catalytic partial oxidation of n-tetradecane using pyrochlores: effect of Rh and Sr substitution. Catal Today 2008;136:206–13.
[70] Shekhawat D, Berry DA, Haynes DJ, Spivey JJ. Fuel constituent effects on fuel reforming properties for fuel cell applications. Fuel 2009;88:817–25.
[71] O'Connor RP, Klein EJ, Schmidt LD. High yields of synthesis gas by millisecond partial oxidation of higher hydrocarbons. Catal Lett 2000;70:99–107.
[72] Shamsi A, Baltrus JP, Spivey JJ. Characterization of coke deposited on Pt/alumina catalyst during reforming of liquid hydrocarbons. Appl Catal A: Gen 2005;293:145–52.
[73] Cheekatamarla PK, Lane AM. Efficient bimetallic catalysts for hydrogen generation from diesel fuel. Int J Hydrogen Energy 2005;30:1277–85.
[74] Chen X, Gould BD, Schwank JW. n-Dodecane reforming over monolith-based Ni catalysts: SEM study of axial carbon distribution profile. Appl Catal A: Gen 2009;356:137–47.

[75] Palm C, Cremer P, Peters R, Stolten D. Small-scale testing of a precious metal catalyst in the autothermal reforming of various hydrocarbon feeds. J Power Sources 2002;106:231–7.
[76] Chen X, Tadd AR, Schwank JW. Carbon deposited on Ni/Ce-Zr-O isooctane autothermal reforming catalysts. J Catal 2007;251:374–87.
[77] Qi A, Wang S, Fu G, Wu D. Autothermal reforming of n-octane on Ru-based catalysts. Appl Catal A: Gen 2005;293:71–82.
[78] Moon DJ, Sreekumar K, Lee SD, Lee BG, Kim HS. Studies on gasoline fuel processor system for fuel-cell powered vehicles application. Appl Catal A: Gen 2001;215:1–9.
[79] Krumpelt M, Krause TR, Carter JD, Kopasz JP, Ahmed S. Fuel processing for fuel cell systems in transportation and portable power applications. Catal Today 2002;77:3–16.
[80] Kolb G, Baier T, Schürer J, Tiemann D, Ziogas A, Ehwald H, et al. A micro-structured 5 kW complete fuel processor for iso-octane as hydrogen supply system for mobile auxiliary power units: Part I. Development of autothermal reforming catalyst and reactor. Chem Eng J 2008;137:653–63.
[81] Tadd AR, Gould BD, Schwank JW. Packed bed versus microreactor performance in autothermal reforming of isooctane. Catal Today 2005;110:68–75.
[82] Brown LF. A comparative study of fuels for on-board hydrogen production for fuel-cell-powered automobiles. Int J Hydrogen Energy 2001;26:381–97.
[83] Semelsberger TA, Brown LF, Borup RL, Inbody MA. Equilibrium products from autothermal processing for generating hydrogen-rich fuel-cell feeds. Int J Hydrogen Energy 2004;29:1047–64.
[84] Ranganathan ES, Bej SK, Thompson LT. Methanol steam reforming over Pd/ZnO and Pd/CeO_2 catalysts. Appl Catal A: Gen 2005;289:153–62.
[85] Cubeiro ML, Fierro JL. Selective production of hydrogen by partial oxidation of methanol over Zn-supported palladium catalysts. J Catal 1998;179:150–62.
[86] Ghenciu AF. Review of fuel processing catalysts for hydrogen production in PEM fuel cell systems. Curr Opin Solid St M 2002;6:389–99.
[87] Agrell J, Birgersson H, Boutonnet M. Steam reforming of methanol over a Cu/ZnO/Al_2O_3 catalyst: a kinetic analysis and strategies for suppression of CO formation. J Power Sources 2002;106:249–57.
[88] Wiese W, Emonts B, Peters R. Methanol steam reforming in a fuel cell drive system. J Power Sources 1999;84:187–93.
[89] Jiang CJ, Trimm DL, Wainwright MS, Cant NW. Kinetic study of steam reforming of methanol over copper-based catalysts. Appl Catal A: Gen 1993;93:245–55.
[90] Lindström B, Petterson LJ. Deactivation of copper-based catalysts for fuel cell applications. Catal Lett 2001;74:27–30.
[91] Amphlett JC, Mann RF, Peppley BA, Thurgood CP. A deactivation model for methanol-steam reformation on Cu/ZnO/Al_2O_3 catalyst for optimizing the production of fuel-cell hydrogen. Stud Surf Sci Catal 2001;139:205–12.
[92] Purnama H, Ressler T, Jentoft RE, Soerijanto H, Schlögl R, Schomaecker R. CO formation-selectivity for steam reforming of methanol with a commercial CuO/ZnO/Al_2O_3 catalyst. Appl Catal A: Gen 2004; 259:83–94.
[93] Men Y, Kolb G, Zapf R, Tiemann D, Wichert M, Hessel V, et al. A complete miniaturized micro-structured methanol fuel processor/fuel cell system for low power applications. Int J Hydrogen Energy 2008;33:1374–82.
[94] Men Y, Gnaser H, Zapf R, Kolb G, Ziegler C. Steam reforming of methanol over a Cu/CeO_2/Al_2O_3 catalysts in a microchannel reactor. Appl Catal A: Gen 2004;277:83–90.
[95] Men Y, Gnaser H, Zapf R, Kolb G, Hessel V, Ziegler C. Parallel screening of Cu/CeO_2/Al_2O_3 thin film catalysts for steam reforming of methanol in a 10-channel micro-structured reactor. Catal Commun 2004;5:671–5.
[96] Farrauto R, Hwang S, Shore L, Ruettinger W, Lampert J, Giroux T, et al. New material needs for hydrocarbon fuel processing: Generating hydrogen for the PEM fuel cell. Annu Rev Mater Res 2003;33: 1–27.
[97] Lattner JR, Harold MP. Autothermal reforming of methanol: Experiments and modeling. Catal Today 2007;120:78–89.
[98] Lindström B, Agrell J, Petterson LJ. Combined methanol reforming for hydrogen production over monolithic catalysts. Chem Eng J 2003;93:91–101.
[99] Liu S, Takahashi K, Ayabe M. Hydrogen production by oxidative methanol reforming on Pd/ZnO catalyst: effects of Pd loading. Catal Today 2003;87: 247–53.
[100] Liu S, Takahashi K, Uematsu K, Ayabe M. Hydrogen production by methanol reforming on Pd/ZnO catalyst: effect of the addition of a third metal component. Appl Catal A: Gen 2004;277: 265–70.
[101] Hagh BF. Stoichiometric analysis of autothermal fuel processing. J Power Sources 2004;130:85–94.
[102] Doss ED, Kumar R, Ahluwalia RK, Krumpelt M. Fuel processors for automotive fuel cell systems: a parametric analysis. J Power Sources 2001;102: 1–15.

[103] Reitz TL, Ahmed S, Krumpelt M, Kumar R, Kung HH. Characterization of CuO/ZnO under oxidizing conditions for the oxidative methanol reforming reaction. J Mol Catal A: Chem 2000;162:275–85.

[104] Ni M, Leung DYC, Leung MKH. A review on bio-ethanol reforming for hydrogen production. Int J Hydrogen Energy 2007;32:3238–47.

[105] Haryanto A, Fernando S, Murali N, Adhikari S. Current status of hydrogen production techniques by steam reforming of ethanol: a review. Energy Fuel 2005;19:2098–106.

[106] Vaidya PD, Rodrigues AE. Insight into steam reforming of ethanol to produce hydrogen for fuel cells. Chem Eng J 2006;117:39–49.

[107] Comas J, Marino F, Laborde M, Amadeo N. Bio-ethanol steam reforming on Ni/Al_2O_3 catalyst. Chem Eng J 2004;98:61–8.

[108] Erdohelyi A, Rasko J, Kecskes T, Toth M, Domok M, Baan K. Hydrogen formation in ethanol reforming on supported noble metal catalysts. Catal Today 2006;116:367–76.

[109] Llorca J, de la Piscina PR, Dalmon JA, Sales J, Homs N. CO-free hydrogen from steam-reforming of bioethanol over ZnO-supported cobalt catalysts: effect of the metallic precursor. Appl Catal B: Env 2003;43:355–69.

[110] Sahoo DR, Vajpai S, Patel S, Pant KK. Kinetic modeling of steam reforming of ethanol for the production of hydrogen over Co/Al_2O_3 catalyst. Chem Eng J 2007;125:139–47.

[111] Batista MS, Santos RKS, Assaf EM, Assaf JM, Ticianelli EA. Characterization of the activity and stability of supported cobalt catalysts for the steam reforming of ethanol. J Power Sources 2003;124:99–103.

[112] Batista MS, Santos RKS, Assaf EM, Assaf JM, Ticianelli EA. High efficiency steam reforming of ethanol by cobalt-based catalysts. J Power Sources 2004;134:27–32.

[113] Men Y, Kolb G, Zapf R, Hessel V, Löwe H. Ethanol steam reforming in a microchannel reactor. Process Saf Environ 2007;85:413–8.

[114] Liguras DK, Kondarides DI, Verykios XE. Production of hydrogen for fuel cells by steam reforming of ethanol over supported noble metal catalysts. Appl Catal B: Env 2003;43:345–54.

[115] Wanat EC, Venkataraman K, Schmidt LD. Steam reforming and water-gas shift of ethanol on Rh and Rh-ce catalysts in a catalytic wall reactor. Appl Catal A: Gen 2004;276:155–62.

[116] Roh HS, Platon A, Wang Y, King DL. Catalyst deactivation and regeneration in low temperature ethanol steam reforming with Rh/CeO_2-ZrO_2 catalysts. Catal Lett 2006;110(1–2):1–6.

[117] Vaidya PD, Rodrigues AE. Kinetics of steam reforming of ethanol over a Ru/Al_2O_3 catalyst. Ind Eng Chem Res 2006;45:6614–8.

[118] Soyal-Baltacioglu F, Aksoylu AE, Onsan ZI. Steam reforming of ethanol over Pt-Ni catalysts. Catal Today 2008;138:183–6.

[119] Orücü E, Gökaliler F, Aksoylu AE, Onsan ZI. Ethanol steam reforming for hydrogen production over bimetallic $Pt\text{-}Ni/\delta\text{-}Al_2O_3$. Catal Lett 2008;120: 198–203.

[120] Sun J, Qiu XP, Wu F, Zhu WT. Hydrogen from steam reforming of ethanol at low temperature over Ni/Y_2O_3, Ni/La_2O_3 and Ni/Al_2O_3 catalysts for fuel cell application. Int J Hydrogen Energy 2005;30: 437–45.

[121] Wanat EC, Suman B, Schmidt LD. Partial oxidation of alcohols to produce hydrogen and chemicals in millisecond-contact time reactors. J Catal 2005;235: 18–27.

[122] Frusteri F, Freni S, Chiodo V, Donato S, Bonura G, Cavallaro S. Steam and autoreforming of bio-ethanol over MgO and CeO_2 supported Ni catalysts. Int J Hydrogen Energy 2006;31:2193–9.

[123] Klouz V, Fierro V, Denton P, Katz H, Lisse JP, Bouvot-Maudit JP, et al. Ethanol reforming for hydrogen production in a hybrid electric vehicle: Process optimization. J Power Sources 2002;105: 26–34.

[124] Sun J, Qiu XP, Wu F, Zhu WT, Wang WD, Hao SJ. Hydrogen from steam reforming of ethanol in low and middle temperature range for fuel cell application. Int J Hydrogen Energy 2004;29:1075–81.

[125] Fatsikostas AN, Kondarides DI, Verykios XE. Production of hydrogen for fuel cells by reformation of biomass-derived ethanol. Catal Today 2002;75: 145–55.

[126] Goula MA, Kontou SK, Tsiakaras PE. Hydrogen production by ethanol steam reforming over a commercial $Pd/\gamma\text{–}Al_2O_3$ catalyst. Appl Catal B: Env 2004;49:135–44.

[127] Cheekatamarla PK, Finnerty JM. Reforming catalysts for hydrogen generation in fuel cell applications. J Power Sources 2006;160:490–9.

[128] Trimm DL. Minimisation of carbon monoxide in a hydrogen stream for fuel cell application. Appl Catal A: Gen 2005;296:1–11.

[129] Lei Y, Cant NW, Trimm DL. Activity patterns for the water gas shift reaction over supported precious metal catalysts. Catal Lett 2005;103:133–6.

[130] Natesakhawat S, Wang XQ, Zhang LZ, Ozkan US. Development of chromium-free iron-based catalysts for high-temperature water-gas shift reaction. J Mol Catal A: Chem 2006;260:82–94.

[131] Martos C, Dufour J, Ruiz A. Synthesis of Fe_3O_4-based catalysts for the high-temperature water gas shift reaction. Int J Hydrogen Energy 2009;34: 4475–81.

[132] Ruettinger W, Ilinich O, Farrauto RJ. A new generation of water gas shift catalysts for fuel cell applications. J Power Sources 2003;118:61–5.

[133] Ilinich O, Ruettinger W, Liu XS, Farrauto R. Cu-Al_2O_3-$CuAl_2O_4$ water-gas shift catalyst for hydrogen production in fuel cell applications: mechanism of deactivation under start-stop operating conditions. J Catal 2007;247:112–8.

[134] Tabakova T, Idakiev V, Papavasiliou J, Avgouropoulos G, Ioannides T. Effect of additives on the WGS activity of combustion synthesized CuO/CeO_2 catalysts. Catal Commun 2007;8:101–6.

[135] Farrauto RJ, Liu Y, Ruettinger W, Ilinich O, Shore L, Giroux T. Precious metal catalysts supported on ceramic and metal monolithic structures for the hydrogen economy. Cat Rev Sci Eng 2007; 49:141–96.

[136] Gorte RJ, Zhao S. Studies of the water-gas-shift reaction with ceria-supported precious metals. Catal Today 2005;104:18–24.

[137] Giroux T, Hwang S, Liu Y, Ruettinger W, Shore L. Monolithic structures as alternatives to particulate catalysts for the reforming of hydrocarbons for hydrogen generation. Appl Catal B: Env 2005;56: 95–110.

[138] Uemiya S. State-of-the-art of supported metal membranes for gas separation. Sep Purif Methods 1999;28:51–85.

[139] Marino F, Descorme C, Duprez D. Noble metal catalysts for the preferential oxidation of carbon monoxide in the presence of hydrogen. Appl Catal B: Env 2004;54:59–66.

[140] Pozdnyakova O, Teschner D, Wootsch A, Krohnert J, Steinhauer B, Sauer H, et al. Preferential CO oxidation in hydrogen (PrOX) on ceria-supported catalysts, part II: Oxidation states and surface species on Pd/CeO_2 under reaction conditions, suggested reaction mechanism. J Catal 2006;237:17–28.

[141] Ko EY, Park ED, Seo KW, Lee HC, Lee D, Kim S. A comparative study of catalysts for the preferential CO oxidation in excess hydrogen. Catal Today 2006;116:377–83.

[142] Ince T, Uysal G, Akin AN, Yildirim R. Selective low-temperature CO oxidation over Pt-Co-Ce/Al_2O_3 in hydrogen-rich streams. Appl Catal A: Gen 2005;292: 171–6.

[143] Uysal G, Akin AN, Onsan ZI, Yildirim R. Design of a Pt-Co-Ce/MgO catalyst for preferential CO oxidation. Catal Lett 2006;108:193–6.

[144] Cho SH, Park JS, Choi SH, Kim SH. Effect of magnesium on preferential oxidation of carbon monoxide on platinum catalyst in hydrogen-rich stream. J Power Sources 2006;156:914–20.

[145] Ayastuy JL, Gonzales-Marcos MP, Gonzales-Velasco JR, Gutierrez-Ortiz MA. MnO_x/Pt/Al_2O_3 catalysts for CO oxidation in H_2-rich streams. Appl Catal B: Env 2007;70:532–41.

[146] Uysal G, Akin AN, Onsan ZI, Yildirim R. Preferential CO oxidation over Pt-SnO_2/Al_2O_3 in hydrogen-rich streams containing CO_2 and H_2O (CO removal from H_2 with PROX). Catal Lett 2006;111:173–6.

[147] Liu X, Korotkikh O, Farrauto RJ. Selective catalytic oxidation of CO in H_2: structural study of Fe oxide-promoted Pt/alumina catalyst. Appl Catal A: Gen 2002;226:293–303.

[148] Ren SH, Hong XL. CO selective oxidation in hydrogen-rich gas over platinum catalysts. Fuel Process Technol 2007;88:383–6.

[149] Simsek E, Ozkara S, Aksoylu AE, Onsan ZI. Preferential CO oxidation over activated carbon supported catalysts in H_2-rich streams containing CO_2 and H_2O. Appl Catal A: Gen 2007;316:169–74.

[150] Ozkara S, Aksoylu AE. Selective low temperature carbon monoxide oxidation in H_2-rich gas streams over activated carbon supported catalysts. Appl Catal A: Gen 2003;251:75–83.

[151] Avgouropoulos G, Ioannides T, Matralis HK, Batista J, Hocevar S. CuO-CeO_2 mixed oxide catalysts for selective oxidation of carbon monoxide in excess hydrogen. Catal Lett 2001;73:33–40.

[152] Zhang Y, Zhao CY, Liang H, Liu Y. Macroporous monolithic Pt/γ-Al_2O_3 and K-Pt/γ-Al_2O_3 catalysts used for preferential oxidation of CO. Catal Lett 2009;127:339–47.

[153] Sirijaruphan A, Goodwin JG, Rice RW, Wei DG, Butcher KR, Roberts GW, et al. Effect of metal foam supports on the selective oxidation of CO on Fe-promoted Pt/γ-Al_2O_3. Appl Catal A: Gen 2005;281:11–8.

[154] Sirijaruphan A, Goodwin JG, Rice RW, Wei DG, Butcher KR, Roberts GW, et al. Metal foam supported Pt catalysts for the selective oxidation of CO in hydrogen. Appl Catal A: Gen 2005;281:1–9.

[155] Srinivas S, Dhingra A, Im H, Gulari E. A scalable silicon microreactor for preferential CO oxidation: performance comparison with a tubular packed-bed microreactor. Appl Catal A: Gen 2004;274: 285–93.

[156] Kolb G, Hessel V, Cominos V, Hofmann C, Löwe H, Nikolaidis G, et al. Selective oxidations in micro-structured catalytic reactors – for gas-phase reactions and specifically for fuel processing for fuel cells. Catal Today 2007;120:2–20.

[157] Kahlich MJ, Gasteiger HA, Behm RJ. Kinetics of the selective CO oxidation in H_2-rich gas on Pt/Al_2O_3. J Catal 1997;171:93–105.
[158] Gray P, Petch M. Advances with hotspot fuel processing. Platinum Metals Rev 2000;44:108–11.
[159] Takenaka S, Shimizu T, Otsuka K. Complete removal of carbon monoxide in hydrogen-rich gas stream through methanation over supported metal catalysts. Int J Hydrogen Energy 2004;29:1065–73.
[160] Dagle RA, Wang Y, Xia GG, Strohm JJ, Holladay J, Palo DR. Selective CO methanation catalysts for fuel processing applications. Appl Catal A: Gen 2007;326: 213–8.
[161] Panagiotopoulou P, Kondarides DI, Verykios XE. Selective methanation of CO over supported noble metal catalysts: effects of the nature of the metallic phase on catalytic performance. Appl Catal A: Gen 2008;344:45–54.
[162] Panagiotopoulou P, Kondarides DI, Verykios XE. Selective methanation of CO over supported Ru catalysts. Appl Catal B: Env 2008;88:470–8.
[163] Farrauto RJ. Introduction to solid polymer membrane fuel cells and reforming natural gas for production of hydrogen. Appl Catal B: Env 2005;56: 3–7.
[164] Löffler DG, Taylor K, Mason D. A light hydrocarbon fuel processor producing high-purity hydrogen. J Power Sources 2003;117:84–91.
[165] Song CS. An overview of new approaches to deep desulfurization for ultra-clean gasoline, diesel fuel and jet fuel. Catal Today 2003;86:211–63.
[166] Song C. Fuel processing for low-temperature and high-temperature fuel cells: Challenges, and opportunities for sustainable development in the 21st century. Catal Today 2002;77:17–49.
[167] Satokawa S, Kobayashi Y, Fujiki H. Adsorptive removal of dimethylsulfide and t-butyl mercaptan from pipeline natural gas on Ag zeolites under ambient conditions. Appl Catal B: Env 2005;56:51–6.
[168] Takatsu K, Takegoshi G, Katsuno H, Kawashima Y, Matsumoto H. Room temperature sulfur removal from LPG with adsorbent for fuel cell application: adsorption behavior of sulfur compounds. J Jap Pet Inst 2007;50:200–7.
[169] Ma XL, Sun L, Song CS. A new approach to deep desulfurization of gasoline, diesel fuel and jet fuel by selective adsorption for ultra-clean fuels and fuel cell applications. Catal Today 2002;77: 107–16.
[170] Fukunaga T, Katsuno H, Matsumoto H, Takahashi O, Akai Y. Development of kerosene fuel processing system for PEFC. Catal Today 2003;84:197–200.
[171] Zhou A, Ma XL, Song CS. Liquid phase adsorption of multi-ring thiophenic sulfur compounds on carbon materials with different surface properties. J Phys Chem B 2006;110:4699–707.
[172] Jayne D, Zhang Y, Haji S, Erkey C. Dynamics of removal of organosulfur compounds from diesel by adsorption on carbon aerogels for fuel cell applications. Int J Hydrogen Energy 2005;30:1287–93.
[173] Rase HF. Fixed-bed reactor design and diagnostics. London: Butterworths; 1990.
[174] Fogler HS. Elements of chemical reaction engineering. 4th ed. New Jersey: Pearson Education Inc.; 1999.
[175] Avci AK, Trimm DL, Onsan ZI. Heterogeneous reactor modeling for simulation of catalytic oxidation and steam reforming of methane. Chem Eng Sci 2001;56:641–9.
[176] Eigenberger G. Ullmann's processes and process engineering. Weinheim: Wiley-VCH; 2004. p. 1983–2023.
[177] Bird RB, Stewart WE, Lightfoot EN. Transport Phenomena. 2nd ed. New York: Wiley; 2002.
[178] Boger T, Heibel AK, Sorensen CM. Monolithic catalysts for the chemical industry. Ind Eng Chem Res 2004;43:4602–11.
[179] Kiwi-Minsker L, Renken A. Microstructured reactors. In: Ertl G, Knözinger H, Schüth F, Weitkamp J, editors. Handbook of heterogeneous catalysis. Weinheim: Wiley-VCH; 2008. p. 2248–64.
[180] Shah RK, London AL. Laminar flow forced convection in ducts. Advances in heat transfer, Supplement 1. New York: Academic Press; 1978.
[181] Cybulski A, Moulijn JA. The present and the future of structured catalysts: an overview. In: Cybulski A, Moulijn JA, editors. Structured catalysts and reactors. Boca Raton, FL: CRC Press; 2006. p. 1–17.
[182] Hessel V, Löwe H, Müller A, Kolb G. Chemical micro process engineering: processing and plants. Weinheim: Wiley-VCH; 2005.
[183] Zapf R, Becker-Willinger C, Berresheim K, Bolz H, Gnaser H, Hessel V, et al. Detailed characterization of various porous-alumina based catalyst coatings within microchannels and their testing for methanol steam reforming. Trans IChemE 2003;81A:721–9.
[184] Stefanescu A, van Veen AC, Mirodatos C, Beziat JC, Duval-Brunel E. Wall coating optimization for microchannel reactors. Catal Today 2007; 125:16–23.
[185] Conant T, Karim A, Datye A. Coating of steam reforming catalysts in non-porous multi-channeled microreactors. Catal Today 2007;125:11–5.
[186] Horny C, Kiwi-Minsker L, Renken A. Micro-structured string reactor for autothermal production of hydrogen. Chem Eng J 2004;101:3–9.

[187] Horny C, Renken A, Kiwi-Minsker L. Compact string reactor for autothermal hydrogen production. Catal Today 2007;120:45–53.
[188] Hoebink JHBJ, Harmsen JMA, Scholz CML, Marin GB, Schouten JC. Modeling of automotive exhaust gas converters. In: Cybulski A, Moulijn JA, editors. Structured catalysts and reactors. Boca Raton, FL: CRC Press; 2006. p. 311–54.
[189] Hardt S, Ehrfeld W, Hessel V, Vanden Bussche KM. Strategies for size reduction of microreactors by heat transfer enhancement effects. Chem Eng Commun 2003;190:540–59.
[190] Karakaya M, Avci AK. Simulation of on-board fuel conversion in catalytic microchannel reactor-heat exchanger systems. Top Catal 2009;52:2112–6.
[191] Commenge JM, Falk L, Corriou JP, Matlosz M. Optimal design for flow uniformity in microchannel reactors. AIChE J 2002;48:345–58.
[192] Delsman ER, De Croon MHJM, Elzinga GD, Cobden PD, Kramer GJ, Schouten JC. The influence of differences between microchannels on micro reactor performance. Chem Eng Technol 2005;28: 367–75.
[193] Goerke O, Pfeifer P, Schubert K. Water-gas shift reaction and selective oxidation of CO in microreactors. Appl Catal A: Gen 2004;263:11–8.
[194] Pangarkar K, Schildhauer TJ, Ommen JRV, Nijenhuis J, Kapteijn F, Moulijn JA. Structured packings for multiphase catalytic reactors. Ind Eng Chem Res 2008;47:3720–51.
[195] Banhart J. Manufacture, characterization and application of cellular metals and metal foams. Prog Mater Sci 2001;30:341–92.
[196] Fourie JG, Plessis JPD. Pressure drop modeling in cellular metallic foams. Chem Eng Sci 2002;57: 2781–9.
[197] Giani L, Groppi G, Tronconi E. Mass transfer characterization of metallic foams as supports for structured catalysts. Ind Eng Chem Res 2005;44: 4993–5002.
[198] Giani L, Groppi G, Tronconi E. Heat transfer characterization of metallic foams. Ind Eng Chem Res 2005;44:9078–85.
[199] Meille V. Review on methods to deposit catalysts on structured surfaces. Appl Catal A: Gen 2006; 315:1–17.
[200] Shamsi A, Spivey JJ. Partial oxidation of methane on Ni-MgO catalysts supported on metal foams. Ind Eng Chem Res 2005;44:7298–305.
[201] Yu H, Chen H, Pan M, Tang Y, Zeng K, Peng F, et al. Effect of foam materials on the performance of methanol steam micro-reformer for fuel cells. Appl Catal A: Gen 2007;327:106–13.
[202] Chen H, Yu H, Tang Y, Pan M, Peng F, Wang H, et al. Assessment and optimization of the mass transfer limitation in a metal foam methanol microreformer. Appl Catal A: Gen 2008;337:155–62.
[203] Richardson JT, Peng Y, Remue D. Properties of ceramic foam catalyst supports: pressure drop. Appl Catal A: Gen 2000;204:19–32.
[204] Twigg MV, Richardson JT. Fundamentals and applications of structured ceramic foam catalysts. Ind Eng Chem Res 2007;46:4166–77.
[205] Richardson JT, Remue D, Hung J-K. Properties of ceramic foam catalyst supports: mass and heat transfer. Appl Catal A: Gen 2003;250:319–29.
[206] Richardson JT, Garrait M, Hung J- K. Carbon dioxide reforming with Rh and Pt-Re catalysts dispersed on ceramic foam supports. Appl Catal A: Gen 2003;255: 69–82.
[207] Patcas FC, Garrido GI, Kraushaar-Czarnetzki B. CO oxidation over structured carriers: a comparison of ceramic foams, and beads. Chem Eng Sci 2007;62: 3984–90.
[208] Kolodziej A, Jaroszynski M, Janus B, Kleszcz T, Lojewska J, Lojewski T. An experimental study of the pressure drop in fluid flows through wire gauzes. Chem Eng Commun 2009;196:932–49.
[209] Kolodziej A, Lojewska J. Flow resistance of wire gauzes. AIChE J 2009;55:264–7.
[210] Kolodziej A, Lojewska J. Experimental and modeling study on flow resistance of wire gauzes. Chem Eng Process 2009;48:816–22.
[211] Jiang Z, Chung K-S, Kim G-R, Chung J-S. Mass transfer characteristics of wire-mesh honeycomb reactors. Chem Eng Sci 2003;58:1103–11.
[212] Qi A, Peppley B, Karan K. Integrated fuel processors for fuel cell applications: a review. Fuel Process Technol 2007;88:3–22.
[213] Ma L, Jiang C, Adesina AA, Trimm DL, Wainwright MS. Simulation studies of autothermal reactor system for H_2 production from methanol steam reforming. Chem Eng J 1996;62:103–11.
[214] Piga A, Verykios XE. An advanced reactor configuration for the partial oxidation of methane to synthesis gas. Catal Today 2000;60:63–71.
[215] Avci AK, Trimm DL, Aksoylu AE, Onsan ZI. Ignition characteristics of Pt, Ni and Pt–Ni catalysts used for autothermal fuel processing. Catal Lett 2003;88: 17–22.
[216] Matros YS, Bunimovich GA. Reverse-flow operation in fixed bed catalytic reactors. Cat Rev Sci Eng 1996;38:1–68.
[217] Blanks RF, Wittrig TS, Peterson DA. Bidirectional adiabatic synthesis gas generator. Chem Eng Sci 1990;45:2407–13.

[218] De Groote AM, Froment GF, Kobylinski T. Synthesis gas production from natural gas in a fixed bed reactor with reversed flow. Canad J Chem Eng 1996; 74:735–42.
[219] Kulkarni MS, Dudukovic MP. Periodic operation of asymmetric bidirectional fixed-bed reactors with temperature limitations. Ind Eng Chem Res 1998;37: 770–81.
[220] Kikas T, Bardenshteyn I, Williamson C, Ejimofor C, Puri P, Fedorov AG. Hydrogen production in the reverse-flow autothermal catalytic microreactor. Ind Eng Chem Res 2003;42:6273–9.
[221] Kolios G, Frauhammer J, Eigenberger G. A simplified procedure for the optimal design of autothermal reactors for endothermic high-temperature reactions. Chem Eng Sci 2001;56:351–7.
[222] Kolios G, Frauhammer J, Eigenberger G. Efficient reactor concepts for coupling of endothermic and exothermic reactions. Chem Eng Sci 2002;57: 1505–10.
[223] Reay DA. Catalytic combustion: current status and implications for energy efficiency in the process industries. Heat Recov Syst CHP 1993;13:383–90.
[224] Polman EA, Der Kinderen JM, Thuis FMA. Novel compact steam reformer for fuel cells with heat generation by catalytic combustion augmented by induction heating. Catal Today 1999;47: 347–51.
[225] Zanfir M, Gavriilidis A. Modeling of a catalytic plate reactor for dehydrogenation-combustion coupling. Chem Eng Sci 2001;56:2671–83.
[226] Zanfir M, Gavriilidis A. Catalytic combustion assisted methane steam reforming in a catalytic plate reactor. Chem Eng Sci 2003;58:3947–60.
[227] Tonkovich ALY, Yang B, Perry ST, Fitzgerald SP, Wang Y. From seconds to milliseconds to microseconds through tailored microchannel reactor design of a steam methane reformer. Catal Today 2007;120:21–9.
[228] Seris ELC, Abramowitz G, Johnston AM, Haynes BS. Scaleable, microstructured plant for steam reforming of methane. Chem Eng J 2008;135S:S9–16.
[229] Seris ELC, Abramowitz G, Johnston AM, Haynes BS. Demonstration plant for distributed production of hydrogen from steam reforming of methane. Trans IChemE 2005;83(A6):619–25.
[230] Avci AK, Trimm DL, Karakaya M. Microreactor catalytic combustion for chemicals processing. Catal Today 2010;155:66–74.
[231] Karakaya M, Avci AK. Comparison of compact reformer configurations for on-board fuel processing. Int J Hydrogen Energy 2010;35:2305–16.
[232] Lu GQ, Costa JCD, Duke M, Giessler S, Socolow R, Williams RH, et al. Inorganic memebranes for hydrogen production and purification: a critical review and perspective. J Colloid Interface Sci 2007;314:589–603.
[233] Prabhu AK, Liu A, Lovell LG, Oyama ST. Modeling of methane reforming reaction in hydrogen selective membrane reactors. J Membr Sci 2000;177: 83–95.
[234] Oklany JS, Hou K, Hughes R. A comparison of dense and microporous membrane reactors for the steam reforming of methane. Appl Catal A: Gen 1998;170: 13–22.
[235] Androver ME, Lopez E, Borio DO, Pedernera MN. Simulation of a membrane reactor for the water-gas shift reaction: pressure and thermal effects. Chem Eng J 2009;154:196–202.
[236] Wakao N, Kaguei S. Heat and mass transfer in packed beds. New York: Gordon and Breach Science Publishers; 1982.
[237] De Groote AM, Froment GF. Simulation of the catalytic partial oxidation of methane to synthesis gas. Appl Catal A: Gen 1996;138:245–64.
[238] Xu J, Froment GF. Methane steam reforming, methanation and water-gas shift: I. Intrinsic kinetics. AIChE J 1989;35:88–96.
[239] Varesano A, Guaglio I, Saracco G, Maffettone PL. Dynamics of a methanol reformer for automotive applications. Ind Eng Chem Res 2005;44:759–68.
[240] Tøttrup PB. Evaluation of intrinsic steam reforming kinetic parameters from rate measurements on full particle size. Appl Catal 1982;4:377–89.
[241] Praharso, Adesina AA, Trimm DL, Cant NW. Kinetic study of iso-octane steam reforming over a nickel-based catalyst. Chem Eng J 2004;99:131–6.
[242] Lee JK, Ko JB, Kim DH. Methanol steam reforming over $Cu/ZnO/Al_2O_3$ catalyst: kinetics and effectiveness factor. Appl Catal A: Gen 2004;278:25–35.
[243] Hla SS, Park D, Duffy GJ, Edwards JH, Roberts DG, Ilyushechkin A, et al. Kinetics of high-temperature water-gas shift reaction over two iron-based commercial catalysts using simulated coal-derived syngases. Chem Eng J 2009;146:148–54.
[244] Choi Y, Stenger HG. Water gas shift reaction kinetics and reactor modeling for fuel cell grade hydrogen. J Power Sources 2003;124:432–9.
[245] Karakaya M, Avci AK, Aksoylu AE, Onsan ZI. Steady-state and dynamic modeling of indirect partial oxidation of methane in a wall-coated microchannel. Catal Today 2009;139:312–21.
[246] Finlayson BA. Nonlinear analysis in chemical engineering. New York: Mc-Graw Hill; 1980.

[247] Rice RG, Do DD. Applied mathematics and modeling for chemical engineers. New York: Wiley; 1995.
[248] Schaaf S, Chambre P. Flow of rarified gases. Princeton, NJ: Princeton University Press; 1961.
[249] Rande VV. Computational flow modeling for chemical reactor engineering. San Diego, CA: Academic; 2002.
[250] Versteeg HK, Malalasekra M. An introduction to computational fluid dynamics. Harlow: Longman Scientific & Technical; 1995.
[251] Majumder D, Broadbelt LJ. A multi-scale scheme for modeling catalytic flow reactors. AIChE J 2006;52: 4214–28.

CHAPTER

15

Balance of Plant

Subir Roychoudhury, Rich Mastanduno

Precision Combustion, Inc., 410 Sackett Point Road, North Haven, CT 06473, USA

OUTLINE

15.1. INTRODUCTION

Components that constitute the balance of plant (BOP) for a fuel cell power generator can include sensors, controls, burners, heat exchangers, start-up power sources, power conditioners, sulfur cleanup, water recovery systems, steam generators, and fuel and air filters. Published articles vary in their representation of BOP components [1]. Although almost everything sans the fuel cell stack could be considered as BOP, in this chapter, however, the discussion of BOP is limited to an overview of fuel, air, water, and thermal management components. The power required for BOP components can have a significant effect on system efficiency, cost, and size, particularly in the lower output range (<10 kW_e).

15.2. FUEL, AIR, AND WATER MANAGEMENT

Feed delivery, control, and mixing are critical components for fuel reforming and vital for proper stack operation. Maintaining prescribed

steam to carbon (S/C) and oxygen to carbon (O/C) ratios are required. A high level of fuel/air/steam mixedness is also essential for proper reformer operation. Commercial off-the-shelf (COTS) components that can meet desired performance and parasitic criterion are desirable in order to achieve practical system-cost targets. The flow controls are particularly challenging for lower output ranges (<10 kW_e) in light of the narrow tolerances permissible for effective stack operation. For larger systems the flow control limits are more forgiving. The feed management effort can be reasonably parsed into flow pumping, control, and mixing. Aspects relating to water recycle and recovery are considered in a later section.

The two reforming systems suitable for fuel cell stacks considered here are autothermal reforming (ATR) (also known as oxidative steam reforming) and steam reforming (SR). In the ATR approach the fuel/air/steam are mixed together and reacted such that the endothermic reforming reactions and exothermic oxidation reactions occur homogeneously. In SR the oxidation and reforming reactions occur in separate chambers with heat generated on the oxidation side (fuel + air) used to supply the heat needed for the endothermic side (fuel + steam). Gaseous fuels are generally pressurized and can be readily mixed, e.g., with static mixers. However, liquid fuels require good atomization followed by vaporization and mixing. Liquid fuel atomization and mixing is significantly more challenging than that for gaseous fuels. In this chapter we will consider the options associated with liquid fuels.

Reforming reactions occur at high temperatures (e.g., 950 °C peak temperatures) and/or in the presence of H_2. At these temperatures there is little room for temperature excursions in order to keep within material limits. This consequently requires accurate flow control of the fuel and oxidant to maintain proper stoichiometry to avoid temperature excursions which may pose both safety and durability concerns.

Small systems are particularly difficult to design, as the low flow rates limit the choices of suitable technologies and vendors. Pumps and blowers need to be selected from COTS components. This limits the number of available options. Dedicated, low-cost, high efficiency, robust, and durable pumps and/or blowers are often developed for internal combustion engine applications that specifically conform to operational, manufacturing, and cost considerations. However, due to the low market entry volumes of fuel cell systems, COTS equipment have to be used, limiting available options. Flow rates can be controlled via direct control of the pumps and/or via closed-loop feedback control. Closed-loop control requires feedback from sensors. Often these consist of low cost flow measurement sensors. The automotive analogy is hot wire anemometer airflow sensors or electrochemical oxygen sensors.

Good atomization of the fuel/air/steam is required for efficient reforming without forming coke or coke precursors which can be fatal for fuel reforming catalysts and fuel cell stacks. Achieving good atomization requires a reasonable amount of energy that can be available in the form of fuel/air/steam pressures. Liquids can be readily pressurized with minimal pump power; however, pressurizing air can cause prohibitive parasitic losses. Utilizing fuel and water pressures and low air pressure is therefore key to designing efficient fuel cell power generators. In transitioning the reformer from the laboratory to the field it is imperative that it be operated on pumps and blowers with active feedback control in lieu of mass flow controllers. Candidate liquid pumps and air movers are discussed below.

15.2.1. Liquid Pumps

15.2.1.1. Fuel Pump

Fuel pumps can be of various types, including diaphragm, gear, piston, vane, and centrifugal. They must be controllable and compatible with

the target fuel. Seal materials such as Viton and PTFE (polytetrafluoroethylene) are commonly employed; seal-less pumps such as peristaltic or magnetic drive pumps must also have fluid-contacting surfaces made of materials compatible with the target fuel. They must also be capable of providing high fuel pressure needed for atomization. The automotive market has provided a baseline of low-cost, highly reliable fuel pumps for diesel.

COTS pumps capable of processing 5 kW_t fuel flow (at 30% overall fuel to electric efficiency this would be suitable for 1.6 kW_e power output) can be selected from pumps manufactured, for example, by KNF Neuberger. These pumps are capable of operating on distillate fuels and are robust. For higher flows (e.g., 30 kW_t or 10 kW_e output) suitable pumps may be available from Flight Works, Inc. These pumps are controllable and provide the required pressure at the fuel nozzle. Because of the low compressibility of liquids, parasitic power is very low for these pumps. A typical 5 kW_t pump may require <0.5 W_e, while a 30 kW_t pump may require <5 W_e.

Positive displacement liquid pumps are still subject to non-linearities due to leakages through seals and check valves, requiring knowledge of downstream pressure for accurate flow determination. A typical set of flow versus back pressure curves is shown in Fig. 15.1.

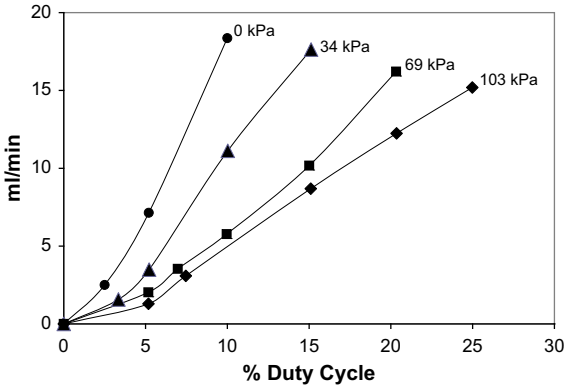

FIGURE 15.1 Liquid pump calibration showing effect of backpressure.

15.2.1.2. Water Pump

These pumps must also be controllable and compatible with water, which has minimal lubricity. Additionally, the water undergoes a phase change during the steam generation process which creates pressure pulses. These pulses can significantly impact the water flow rate. Some form of water treatment is usually done to prevent fouling of heat exchanger surfaces; if extremely pure deionized water is used in the system, there is a tendency to leach impurities from metals and plastics so that higher levels of corrosion resistance may be required. The pumps must also be designed to operate such as to be able withstand freezing conditions via hardware modifications or via a control strategy. COTS pumps for water, with the appropriate sealing materials, are available from several manufacturers, including KNF or FlightWorks. Most water pumps have low parasitic losses with good overall reliability.

15.2.2. Air Movers

Positive displacement of air can be done via pumps or blowers. Blowers (e.g., centrifugal or fan type) are desirable because they require lower power draw but are only capable of overcoming ~15″ of water pressure drop. This may not be sufficient for a complete system. In most cases air pumps or compressors (e.g., scroll, piston, or diaphragm) are necessary in order to meet the air flow and pressure requirements. This includes air pressure required for fuel/air/steam mixing. For low pressure drop applications, a centrifugal air blower such as Ametek's Microjammer® line of brushless DC motor blowers is shown in Fig. 15.2. Parasitic power is very low, 12 W at 2.5 kPa (10″ water column) at 28.3 SLPM (~1 CFM) for the device shown.

Air pumps and blowers are governed by Bernoulli's equation, which when applied to a pump can be expressed as

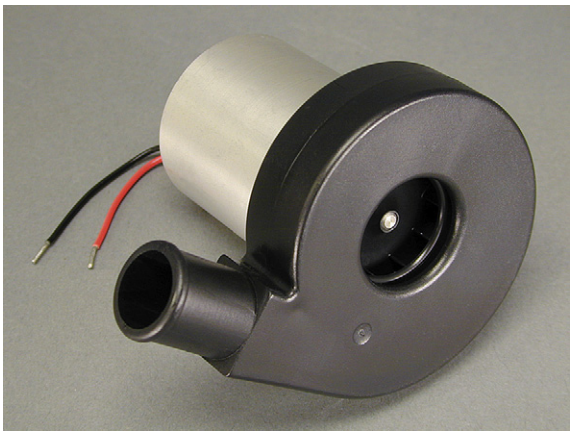

FIGURE 15.2 Microjammer® blower. *Source: Reprinted from [2], with permission from Ametek Corp.*

$$\frac{V_1^2}{2g}+\frac{P_1}{\rho_1 g}+h=\frac{V_2^2}{2g}+\frac{P_2}{\rho_2 g}$$

where V, P, and ρ are the velocity, pressure, and density of the air entering or leaving the pump, and h is a generic frictional loss. Since the density of the air changes with temperature entering the pump, even positive displacement pumps will have inconsistent mass flow versus speed curves, as either the pump heats up or conditions within the system enclosure change. Accurate knowledge of the mass flow entering the fuel cell system therefore requires measurement of pressure and temperature at the pump to translate the volumetric flow to a mass flow.

Even positive displacement pumps have pressure and temperature dependencies. A typical diaphragm pump is shown in Fig. 15.3. The pressure dependency of the flow rate on delivery pressure is shown in the graph (Fig. 15.3).

Also, second order effects such as seal leakage at check valves are pressure dependent, adding a pressure dependent, non-linear term to the volumetric flow versus pump speed equation. This non-linearity is shown in Fig. 15.4 for a diaphragm pump operating in pulse-width-modulation (PWM) mode.

In some applications, the fuel cell anode exhaust is recycled back to the reformer to provide water recovery and other system benefits. The anode exhaust temperature may be as high as 700 °C, which is beyond the reach of most blower materials. To avoid leakage within the fuel cell stack, the anode (as well as the cathode side) operates at near ambient pressures. In these applications it is necessary to repressurize the anode recycle fraction before entering the reformer. R&D Dynamics of Bloomfield, CT, is developing high temperature blowers with over 40% efficiency for this specialized application [4]. However, one of the key hurdles in implementing these blowers

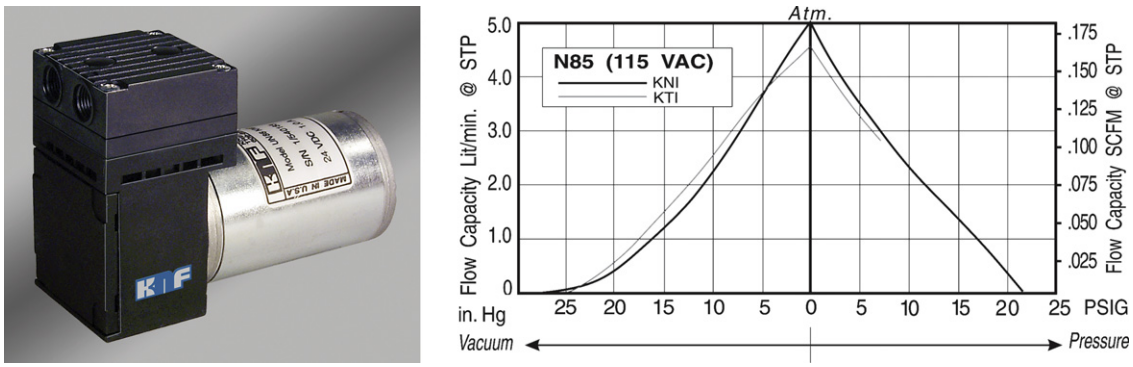

FIGURE 15.3 Small diaphragm pump and typical operation map. *Source: Reprinted from [3], with permission from KNF Neuberger.*

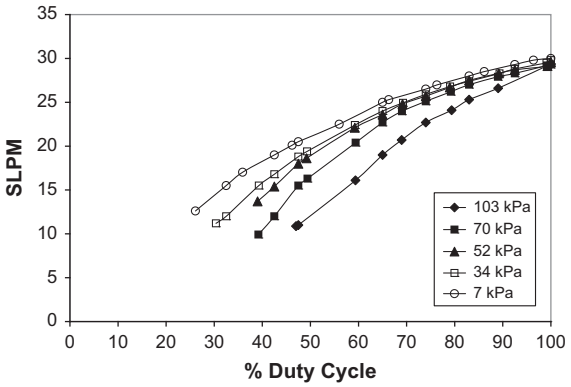

FIGURE 15.4 Operation of diaphragm pump at varying pressures.

is the low pressure rise (e.g., pressure ratio of 1.025). The use of high temperature materials can also negatively impact cost.

Air pumps or compressors are capable of providing high pressure ratios at desired flows. They, however, require more power than blowers and can be a significant source of parasitic losses. High system pressure drop necessitates high pressure air pumps, which are less efficient than lower pressure devices like blowers. The lower efficiency consequently compounds the effect of the higher system pressure. The strategy to address this problem is generally via a low pressure drop system (including mixer, piping, stack, reformer, sulfur trap, burner, heat exchangers, etc.). All these individual pressure drops contribute to the required overall system pressure. To provide the necessary air pressure scroll, piston, or diaphragm pumps may be used. They can range in efficiency from 25–40%. These may consume up to 200 W_e of power for a 5 kW_t/1.6 kW_e system. Although they use more power than blowers, they have better control characteristics, including turndown capability. Pumps are available from several vendors including Gast and KNF. In addition to its control characteristics, durability of air pump is an important consideration. Air pumps are very controllable but have many moving parts. Air blowers generally have fewer moving parts, primarily the impeller, so are expected to be more reliable. Controlling an air blower is more difficult, since it is not a positive displacement device. The need for turndown of practical fuel processors also complicates the choice of a prime air mover. Scroll compressors offer an option for medium pressure (generally below 550 kPa) applications as they are quiet, have fewer moving parts, and are durable, but their primary drawback is their cost.

15.3. FUEL INJECTION SYSTEM

As mentioned earlier the fuel/air/steam ratio within the reformer has a significant effect on the temperature and product distribution. Proper fuel atomization and mixing is critical to avoid local non-homogeneities which can cause hot/cold spots. These can cause failure due to excessive bed temperatures, carbon formation, or inadequate conversion. High air pressure is generally required in order to obtain good fuel atomization. The challenge is to develop atomizers/mixers that can operate at low air pressures to minimize parasitic loads. Pressure drop primarily arises from a combination of the atomizer and flow resistance created due to the reformer, sulfur trap, piping, fuel cell stack, and burner. It is important to obtain good atomization at a minimum of air pressure. COTS fuel injectors/atomizers are not available for these applications. Approaches consisting of vaporizers, piezoelectric and ultrasonic techniques have been examined. However, they can be problematic due to the complex composition of distillate fuels. This can result in fuel breakdown leading to formation of carbon deposits and acute sensitivity of the "exciting" techniques (acoustic or electrical) to operating conditions. Moreover, injectors that can be readily controlled are required in order to allow closed-loop feedback control.

One viable approach to obtain good atomization and mixing is to use high fuel and water

pressure since achieving high liquid pressures does not require significant parasitic power. Thereafter techniques to control the flow have to be implemented. Directly driving the pumps to the required flow rate using a DC or pulsed DC (PWM) is one technique. Another technique, common in automotive applications, is for the pump to provide a pressure source, and the flow metering be done by a separate device. This allows an inexpensive, reliable pump to be used, at the expense of an added component, but one which is an automotive standard part with known manufacturability, cost, and performance tolerance. This combination can permit controllable and reliable performance during transients and steady-state operation and the combined performance can be comparable to those obtained from using mass flow controllers, with the added advantage of faster control dynamics. (Note that mass flow controllers are impractical due to their high pressure drop, cost, and reliability.) These techniques can also be extended to the air side with some control development and proper selection of an air pump that can supply the needed pressure drop.

15.4. HEAT MANAGEMENT SYSTEMS

15.4.1. Heat Exchangers

A fuel cell power generator is a combination of multiple unit operations. Managing the interplay between these operations, both during steady-state and transient operations, is a vital aspect of viable fuel cell generator designs. Proper thermal management, consequently, becomes a key design characteristic. Heat exchangers can be bulky, costly, and slow in transient operation. Astute thermal management is required that balances effective unit operation conditions with dynamic loads as well as practical considerations (cost, size, and manufacturability). Heat exchange is required for preheating or cooling fuel cell feeds. This is a function of the specific fuel cell operating temperature. An example challenge for solid oxide fuel cell (SOFC) stacks is described here. The cathode air has to be maintained at a temperature so as to avoid thermal shock while also permitting heat removal from the stack. The anode feed also has to be maintained within a temperature range to avoid carbon formation and minimize thermal shock. This is a balancing act since anode and cathode flow rates also have an effect on fuel utilization in the stack. The anode exhaust has to be further processed for water recovery — via recycle or water condensation, and energy recovery — via tail gas combustion. The energy is often recovered by preheating the reformer inlet feeds, which may also include a steam generating heat exchanger. Care, however, has to be taken during system design when considering heat exchange between H_2-containing flows with flows containing oxygen. Since fixed geometry heat exchangers are used at high operating temperatures, each with individual thermal response characteristics, thermal management ultimately becomes an exercise in synchronization in order to maximize system efficiency while ensuring stable and safe operation.

Small and efficient heat exchangers are needed within the system to take advantage of waste heat and provide better system efficiency. For small fuel cell systems these devices cannot be easily purchased and often need to be custom designed for each application. The high heat flux in many parts of the system can be used to make them small and effective. A particularly challenging heat exchange task is the generation of steam for reformer operation. Steam generation involves a phase change and can cause pressure fluctuations, which can result in flow and reactor instabilities. This is especially critical for smaller systems. Various solutions that offset these fluctuations can be implemented. These can range from mechanical dampening systems to control adjustments via flow offsets. The materials and methods of construction of

the steam generator also have to be chosen such as to provide mechanical and thermal durability. Avoidance of braze or weld joints in hot areas is crucial to the mechanical integrity of these devices.

Water recovery through condensation of water from the tail gas is one way to achieve water neutral operation without the difficulties associated with anode blowers. This minimizes the need for makeup water. The challenges for achieving this range from the choice of materials tolerant of high temperatures in the presence of H_2 to having sufficient heat flux when cooled by ambient air (which may be as high as 50 °C). Figure 15.5 shows the theoretical maximum water recovery (i.e., the ratio of maximum water collected to the amount of water input) calculated at different ambient/cooling air temperatures. The water recovery required depends on the nature of the fuel cell system: for ATR systems used for SOFCs and operating at S/C of ~1, water recovery of 60–70% (depending upon stack fuel-utilization) is sufficient for water neutral operation. Figure 15.5 shows that this is theoretically achievable and can indeed be demonstrated with the proper choice of heat exchangers. These units have to be capable of condensing water from waste gas mixtures of up to ~800 °C, and depend on the maximum required water recovery. Additionally, a water separator has to be used. The purity of the recovered water is also an important concern. Any contamination found in the recovered water can eventually contaminate the reformer or stack. Special care has to be taken when dealing with inorganic contaminants. If needed, a water purification system may also have to be part of the water recovery system. These heat exchangers can be difficult to build by using off-the-shelf, commercially available condenser units and often have to be developed exclusively for the application. Nevertheless, utilizing COTS heat exchangers will be critical in developing practical, cost-effective systems.

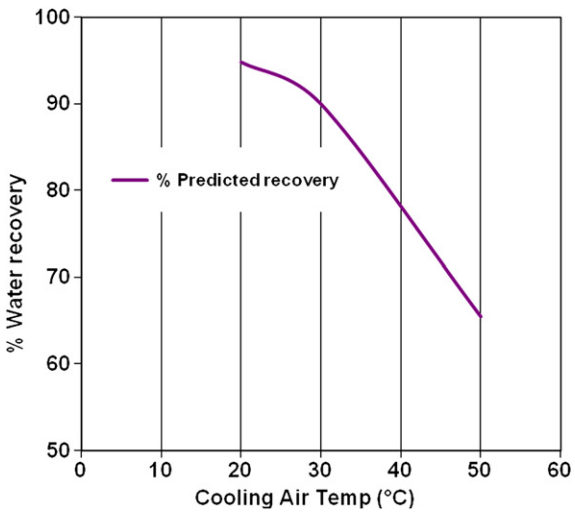

FIGURE 15.5 Maximum theoretical water recovery versus cooling air temperature.

15.4.2. Insulation

A variety of ceramic materials such as alumina, zirconia, and silica may be used for insulating materials within a fuel cell system. In small systems where size and weight are the major concern, high performance insulating materials such as aerogels may be considered, which act as good conductive insulators. Silica aerogel is especially good because silica is also a poor conductor of heat. For example, Aspen's Pyrogel® XT material has a thermal conductivity of 0.089 W/m-K at 600 °C [5], compared to over 0.200 W/m-K for standard mineral wool shapes. Above 650 °C, high purity alumina sheets, boards, and blankets are available from a number of vendors (e.g., Zircar, Cotronics, Unifrax, etc.).

15.5. OTHER COMPONENTS

15.5.1. Sensors

Since fuel cell systems are a combination of various unit operations, choreographing

the interaction among these components requires considerable feedback. Flow, pressure, temperature, and gas sensors are needed. Achieving accurate control with redundancy, while minimizing the number of sensors is a key aspect of practical system design. Pressure transducers, for instance, are needed for balancing the flows and sensing coke buildup; sulfur sensors are required for protecting the stack; temperature sensors are critical for safe operation of the reformer and stack. Automotive style, air mass flow sensors are not sufficiently accurate for fuel cell applications; however, in combination with pump performance curves reasonably accurate flow control is achievable. Considerable effort is being expended for sulfur sensor development. These include electrochemical as well as optical sensors. Although temperature measurement via thermocouples can be sufficient for control feedback, selecting the proper number of robust, accurate, fast response, and cost-effective thermocouples is critical for safely and accurately managing the multiple unit operations. A brief description of thermocouple use in these systems follows.

Type K or N thermocouples are generally used to measure reactor temperatures and may be used to measure temperatures up to 1000 °C. They are available in diameters from 0.01 to 0.125″ offering design flexibility suitable for most applications of interest here. The advantages of these sensors are easy installation and high temperature operation. The primary disadvantages are the fragility of small diameter devices and low output signals (<40 mV) making them susceptible to electromagnetic noise. At high temperatures within the reactor, failures due to oxidation or mechanical vibration of the thin thermocouple wires are possible. For lower temperatures, below about 600 °C, resistance temperature detectors (RTDs) may be used. These can function in a current measurement mode that is less susceptible to noise but require 3- or 4-wire measurements for high accuracy and the sensors themselves are often more physically robust. The most common RTD's are made of platinum, nickel, or nickel alloys. The economical nickel derivative wires may be used over a limited temperature range, but these are quite non-linear and tend to drift with time. Values of room temperature resistance vary from 10 ohms to a few thousand ohms; the single most common value is 100 ohms at 0 °C. The temperature coefficient (according to the DIN 43760/IEC 60751 standard) of platinum wire is $\alpha = 0.00385\ \Omega/\Omega/^{\circ}\mathrm{C}$ [6]. For a 100 Ω wire, this corresponds to 0.385 Ω/°C at 0 °C; thus, the value for α is actually the average slope from 0 to 100 °C. The temperature measured by an RTD is most commonly calculated using the Callendar–Van Dusen equation [7,8]:

$$R_T = R_o + R_o\alpha\left[T - \delta\left(\frac{T}{100} - 1\right)\left(\frac{T}{100}\right) - \beta\left(\frac{T}{100} - 1\right)\left(\frac{T}{100}\right)^3\right]$$

where R_T is the resistance at temperature T, R_o is the resistance at $T = 0$ °C, α is the temperature coefficient at $T = 0$ °C (typically + 0.00392Ω/Ω/°C), δ is 1.49 (typical value for 0.00392 platinum), and β is 0 for temperatures above 0 °C. The exact values for coefficients α, β, and δ are determined by calibrating the RTD. This familiar equation was replaced in 1968 by a 20th order polynomial so as to provide a more accurate curve fit [8].

15.5.2. Controls

The sensors discussed in the preceding section are used as inputs for the control system. Developmental control systems generally employ commercially available data control and acquisition hardware and software. For example, systems such as National Instruments Compact FieldPoint or Compact Rio hardware may be used. These have the capability for digital/analog data acquisition and control. The control

algorithm is based upon desired conditions for the various unit operations. The control hardware can be setup for stand-alone operation, or interfaced with a PC for real-time operational control. Dedicated control hardware, with boards and displays, can be developed for more advanced systems. A typical single-board controller is shown in Fig. 15.6, where the control algorithms are loaded onto a processor integrated into the control board. This hardware is inherently reliable and can readily be miniaturized within a small footprint. Fault tolerance in the system is generally built into control algorithms to predict hardware failures and to allow the system to take appropriate corrective action, or to compensate for disturbances in the system such as those caused by variances in fuel/air/steam flow.

15.5.3. Start-up Power

Start-up power accounts for only a small fraction of cost and volume. Battery technologies such as lithium ion or lithium polymer may be employed. Recharging systems need to be incorporated into power management electronics. Batteries can also be used in hybrid systems to improve transient response.

15.6. CONCLUSION AND FUTURE DIRECTIONS

Although the concept of fuel cells and fuel reforming have been around for over a 100 years, only recently have advances in materials, reactor design, and controls made small scale fuel cell power generators more practical. A key element for successful commercial implementation of these systems requires a well-conceived balance of plant integration of the various unit operations. These require use of dedicated pumps, blowers, sensors, and controls especially suited for fuel cell use. Investment in fuel cell technology has been primarily limited to government funding since commercial revenues are not imminent. This makes the development challenges particularly daunting. Nevertheless, by creatively using COTS hardware, despite its limitations, practical prototypes are being assembled. Increasing the opportunities for prototype system

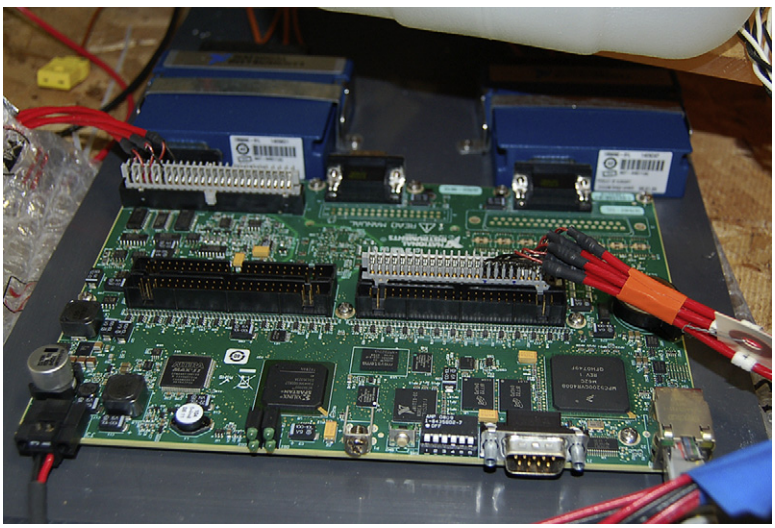

FIGURE 15.6 Dedicated, single-board hardware for data acquisition and control.

demonstrations will be needed to motivate and convince commercial acceptance of fuel cell power generators and will lead to additional development needed to develop practical, marketable systems.

References

[1] Conceptual Design of POX SOFC 5 kW Net System, Arthur D Little Inc. Final Report to U.S. Dept. of Energy. National Energy technology laboratory; Jan 2001.

[2] Microjammer® Brushless DC Blowers, AMETEK® Technical & Industrial Products. http://www.ametektip.com/index.php?option=com_content&view=article&id=95%3Amicrojammerr-brushless-dc-blowers&catid=16&lang=en, Website accessed on Oct 19; 2010.

[3] KNF Neuberger diaphragm pump. http://www.knf.com/pdfs/n85-86.pdf, Website accessed on Oct 20; 2010.

[4] Agrawal G. Advances in anode and cathode blowers. San Antonio, TX: 8th annual SECA workshop; Aug 2007.

[5] Pyrogel® XT Flexible industrial insulation for high-temperature applications. http://www.aerogel.com/products/pdf/Pyrogel_XT_DS.pdf, Website accessed on Oct 19; 2010.

[6] Platinum RTDs, reference and application data temperature sensors. http://content.honeywell.com/sensing/prodinfo/temperature/technical/c15_136.pdf, Website accessed on Oct 19; 2010.

[7] The Callendar–van Dusen coefficients. http://www.uniteksys.com/Graphics/CalVan.pdf, Website accessed on Oct 19; 2010.

[8] RTD measurement and theory. http://www.omega.com/temperature/z/thertd.html, Website accessed on Oct 19; 2010.

APPENDIX

A

Thermodynamic Data for Selected Chemicals

	Common name	Mol. wt	Lower heating value (kJ/mole)	Heat of formation, ΔH°_f (kJ/mole)	Gibbs energy ΔG°_f (kJ/mole)	Absolute entropy (J/mole/K)
H_2 (g)	Hydrogen	2.02	244	0	0	130.7
O_2 (g)	Oxygen	32.00	0	0	0	205.0
CO (g)	Carbon monoxide	28.01	305	−110.5	−137.1	197.6
CO_2 (g)	Carbon dioxide	44.01	0	−393.5	−394.4	213.8
H_2O (l)	Water	18.02	0	−285.8	−237.2	69.9
H_2O (g)	Steam	18.02	0	−241.8	−228.6	188.8
CH_4 (g)	Methane	16.04	803	−74.5	−50.5	186.3
CH_3OH (l)	Methanol	32.04	—	−238.7	−166.4	126.8
CH_3OH (g)	Methanol	32.04	638	−200.7	−162.0	239.7
C_2H_4 (g)	Ethylene	24.03	1323	52.3	68.1	219.8
C_2H_6 (g)	Ethane	30.07	1429	−84.7	−32.9	229.5
C_2H_5OH (l)	Ethanol	46.07	—	−277.7	−174.9	160.7
C_2H_5OH (g)	Ethanol	46.07	1235	−234.9	−167.8	280.6
C_2H_6O (g)	Dimethyl ether	46.07	1328	−184.1	−112.8	266.7
C_3H_8 (g)	Propane	44.10	2043	−103.8	−23.5	269.9
C_6H_6 (g)	Benzene	78.11	3136	82.9	129.7	269.2
C_6H_{12} (g)	Cyclohexane	84.16	3656	−123.3	31.9	297.3
C_6H_{14} (g)	n-Hexane	86.18	3855	−166.9	−0.1	388.7

(*Continued*)

	Common name	Mol. wt	Lower heating value (kJ/mole)	Heat of formation, ΔH°_{f} (kJ/mole)	Gibbs energy ΔG°_{f} (kJ/mole)	Absolute entropy (J/mole/K)
C_8H_{18} (g)	i-Octane	114.23	5065	−224.0	13.9	422.9
$C_{10}H_8$ (g)	Naphthalene	128.17	4981	150.1	224.1	333.2
$C_{10}H_{14}$ (g)	*cis*-Decalin	138.25	–	−169.6	–	–
$C_{10}H_{14}$ (g)	*trans*-Decalin	138.25	–	−180.2	–	–
$C_{10}H_{22}$ (g)	n-Decane	142.29	6294	−249.5	33.2	545.7
$C_{11}H_{10}$ (g)	1-Methylnaphthalene	142.20	–	116.9	–	–
$C_{14}H_{30}$ (g)	n-Tetradecane	198.39	8733	−332.4	66.0	702.6
$C_{16}H_{34}$ (g)	n-Cetane	226.45	9952	−374.2	82.2	781.0
$C_{16}H_{34}$ (g)	iso-Cetane	226.45	–	–	–	–

APPENDIX

B

Definitions

SPACE TIME

The space time (τ) (or contact time or residence time) is defined as the ratio of the reactor volume to the volumetric flow rate to the reactor at the reactor inlet conditions:

$$\tau(\text{h}) = \frac{\text{Reactor volume } (\text{m}^3)}{\text{Volumetric flow rate at the reactor inlet } (\text{m}^3/\text{h})}$$

SPACE VELOCITY

The space velocity (SV) is the reciprocal of the space time and can be defined as

$$\text{SV}(\text{h}^{-1}) = \frac{1}{\tau(\text{h})} = \frac{\text{Volumetric flow rate at reactor inlet } (\text{m}^3/\text{h})}{\text{Reactor volume } (\text{m}^3)}$$

However, for the heterogeneous reactor systems, different versions of space velocities are being used (see definitions of WHSV, GHSV, and VHSV).

WEIGHT HOURLY SPACE VELOCITY

The weight hourly space velocity (WHSV) is defined as the ratio of the mass flow rate of the reactor feed to the mass of the catalyst in the reactor:

$$\text{WHSV}\left(\frac{\text{kg/h}}{\text{kg of cat}}\right) = \frac{\text{Density of the feed } (\text{kg}/\text{m}^3) \times \text{Volumetric flow rate of the feed } (\text{m}^3/\text{h})}{\text{Mass of the catalyst taken (kg)}}$$

GAS HOURLY SPACE VELOCITY (GHSV)

The gas hourly space velocity (GHSV) is defined as total volumetric flow rate to the reactor at standard temperature and pressure divided by the catalyst bed volume or the reactor volume:

$$\mathrm{GHSV}\left(\frac{\mathrm{m^3(STP)/h}}{\mathrm{m^3}}\right) = \frac{\text{Volumetric flow rate of the feed at STP } (\mathrm{m^3/h})}{\text{Reactor or catalyst volume } (\mathrm{m^3})}$$

VOLUME HOURLY SPACE VELOCITY (VHSV)

The volume hourly space velocity (VHSV) is defined as total volumetric flow rate to the reactor at standard temperature and pressure divided by the mass of the catalyst taken in the reactor:

$$\mathrm{VHSV}\left(\frac{\mathrm{m^3(STP)/h}}{\text{kg of cat}}\right) = \frac{\text{Volumetric flow rate of the feed at STP } (\mathrm{m^3/h})}{\text{Mass of the catalyst taken (kg)}}$$

FUEL CONVERSION

The conversion of hydrocarbons (X_{HC}) can be defined as

$$X_{HC}(\%) = \frac{\text{Moles of hydrocarbons reacted}}{\text{Moles of hydrocarbon fed to the reactor}} \times 100$$

or

$$X_{HC}(\%) = \frac{(\text{Moles of hydrocarbon fed to the reactor} - \text{Moles of hydrocarbon in reactor effluent})}{\text{Moles of hydrocarbon fed to the reactor}} \times 100$$

However, it becomes challenging to quantify the moles of hydrocarbon in the reactor effluent if the higher hydrocarbons such as diesel are used as a fuel. For these fuels, the conversion is defined differently in the literature. Some authors define it as total conversion to the gaseous carbon species such as CO, CO_2, and C_1–C_6 hydrocarbons as a more practical calculation because these compounds can be analyzed using a gas chromatograph or mass spectrometer:

$$X_{HC}(\%) = \frac{\left([\mathrm{CO}] + [\mathrm{CO_2}] + \sum_{i}^{i=1-6} [\mathrm{iC_iH_r}]\right)}{n \times \text{Moles of hydrocarbon fed to the reactor}} \times 100$$

where [CO], [CO_2], and [C_iH_r] are moles of CO, CO_2, and hydrocarbon in the reactor effluent, respectively and n is the number of carbon atoms in hydrocarbon feed. Conversion to CO, CO_2, and CH_4 has also been reported in the literature since some laboratories may not be equipped to

quantify C_2–C_6 hydrocarbons. Consequently, the actual conversion may be higher than the calculated using Equation below:

$$X_{HC}(\%) = \frac{([CO] + [CO_2] + [CH_4])}{n \times \text{Moles of hydrocarbon fed to the reactor}} \times 100$$

or

$$X_{HC}(\%) = \frac{\text{Total reactor effluent in moles} \times (y_{CO} + y_{CO_2} + y_{CH_4})}{n \times \text{Moles of hydrocarbon fed to the reactor}} \times 100$$

where y_i is the mole fraction of i^{th} species in the reactor effluent. The reactor effluent compositions are generally measured by a GC or mass spectrometer. The known inlet flow rate of an inert gas (generally N_2) is used as an internal standard to calculate the total reactor effluent as follows:

$$\text{Total reactor effluent in moles} = \frac{\text{Moles of } N_2 \text{ fed to the reactor}}{\text{Mole fraction of } N_2 \text{ in the reactor effluent}}$$

Water conversion (X_{H_2O}) can be calculated:

$$X_{H_2O}(\%) = \frac{([CO] + 2[CO_2] - 2[O_2]\text{inlet})}{\text{Moles of water fed to the reactor}} \times 100$$

PRODUCT YIELD

The yield of product A (Y_A; A = H_2, CO, and CO_2) is defined as:

$$Y_A(\%) = \frac{\text{Moles of A in reactor effluent}}{n \times \text{Moles of hydrocarbon fed to the reactor}} \times 100$$

where n is the number of moles of hydrogen per mole of hydrocarbon for hydrogen yields and is the number of carbon atoms in hydrocarbon fuel for yields of CO and CO_2. In some cases, hydrogen yields may be higher than 100% in SR and ATR since SR and WGS reaction also contribute in H_2 production apart from hydrocarbons. Similarly, CO yields maybe higher than 100% in dry (CO_2) reforming due to contribution from dry reforming or Boudouard reaction.

Sometimes, yield of syngas (H_2 + CO) is also calculated to represent the total moles of H_2 produced to include both the H_2 production from reforming and the additional H_2 generated during WGS reaction in the downstream:

$$Y_{H_2 + CO}(\%) = \frac{(\text{Moles of } H_2 \text{ produced} + \text{Moles of CO produced})}{n \times \text{Moles of hydrocarbon fed to the reactor}} \times 100$$

If a recycle stream from the fuel cell to the reformer is used then the moles of A in the recycle stream should be accounted for in the yield calculation:

$$Y_A(\%) = \frac{(\text{Moles of A in reactor effluent} - \text{Moles of A in feed})}{n \times \text{Moles of hydrocarbon fed to the reactor}} \times 100$$

The yield of H_2 can also be defined by factoring in the water fed to the reactor for OSR and SR:

$$Y_{H_2}(\%) = \frac{\text{Moles of } H_2 \text{ in reactor effluent}}{(n \times \text{Moles of hydrocarbon fed to the reactor} + \text{Moles of water fed to the reactor})} \times 100$$

The yield of hydrocarbons (olefins, paraffins, and benzene) is defined as:

$$Y_{HC}(\%) = \frac{m \times \text{Moles of hydrocarbon produced}}{n \times \text{Moles of hydrocarbon fed to the reactor}} \times 100$$

where m is the number of moles of carbon in the hydrocarbon product.

PRODUCT SELECTIVITY

The H_2 selectivity (S_{H_2}) can be defined as:

$$S_{H_2}(\%) = \frac{\text{Moles of } H_2 \text{ in reactor effluent}}{\frac{m}{2} \times (\text{Moles of } C_nH_m \text{ fed to the reactor} - \text{Moles of } C_nH_m \text{ in reactor effluent})} \times 100$$

However, contribution of steam in OSR and SR to H_2 selectivity is not obvious from the above definition. The selectivity to CO and CO_2 (S_{COx}) is defined as:

$$S_{CO_x}(\%) = \frac{\text{Moles of } CO_x \text{ in reactor effluent}}{n \times (\text{Moles of } C_nH_m \text{ fed to the reactor} - \text{Moles of } C_nH_m \text{ in reactor effluent})} \times 100$$

For higher hydrocarbons such as gasoline, diesel, and jet fuels, the fuel conversion is almost complete to the gaseous products and therefore the yield becomes identical to selectivity of the products.

TURNOVER FREQUENCY

The catalyst performance can also be described by the turnover frequency (TOF) which can be defined as the number of molecules converted per catalytic active site per time:

$$\text{TOF}\left(\frac{\text{molecules/h}}{\text{number of active sites}}\right) = \frac{\text{Conversion } (\%) \times \text{Moles of hydrocarbon fed}}{\text{Metal dispersion } (\%) \times \text{Moles of active metal in the catalyst}}$$

The TOF can also be defined in terms of the moles of product formed per active catalytic site. For H_2 production, it can be written as

$$\text{TOF}\left(\frac{\text{molecules/h}}{\text{number of active sites}}\right) = \frac{\text{Moles of } H_2 \text{ produced}}{\text{Metal dispersion } (\%) \times \text{Moles of active metal in the catalyst}} \times 100$$

CARBON FORMATION

Carbon formation can be defined as

$$\text{Carbon selectivity (\% of C fed)} = \frac{\text{Moles of carbon formed on the catalyst}}{\text{Moles of total carbon fed to the reactor}} \times 100$$

Carbon formation can also be normalized by the mass of catalyst:

$$\text{Carbon formation}\left(\frac{\text{g of C formed}}{\text{g of cat}}\right) = \frac{\text{Mass of carbon formed on the catalyst}}{\text{Mass of catalyst}}$$

OXYGEN-TO-CARBON RATIO

The oxygen-to-carbon (O/C) ratio is generally calculated based on atomic oxygen in the inlet gas and carbon from hydrocarbons:

$$\frac{\text{O}}{\text{C}} = \frac{2 \times \text{Moles of } O_2 \text{ fed to the reactor}}{n \times \text{Moles of hydrocarbon fed to the reactor}}$$

Generally, the oxygen from the steam is not included in the O/C ratio for autothermal reforming. This ratio is also reported as diatomic oxygen to carbon as well as diatomic oxygen to fuel ratio in the literature. For oxygenated hydrocarbons, the O/C ratio can be defined in two different ways: (1) not including oxygen from within the fuel, which leads to a higher overall O/C ratio and (2) including oxygen from the fuel. For ethanol as a fuel, the O/C ratio by including oxygen from ethanol becomes

$$\frac{\text{O}}{\text{C}} = \frac{2 \times \text{Moles of } O_2 \text{ fed to the reactor} + \text{Moles of ethanol fed to the reactor}}{2 \times \text{Moles of ethanol fed to the reactor}}$$

EQUIVALENCE RATIO

The equivalence ratio (φ) can be defined as the ratio of the actual fuel-to-oxygen ratio to the stoichiometric fuel-to-oxygen ratio:

$$\phi. = \left(\frac{\text{Moles of fuel fed to the reactor}}{\text{Moles of } O_2 \text{ fed to reactor}}\right) \Big/ \left(\frac{\text{Moles of fuel fed to the reactor}}{\text{Moles of } O_2 \text{ required for a complete combustion}}\right)$$

Simply, the equivalence ratio is:

$$\phi = \left(\frac{\text{Moles of } O_2 \text{ required for a complete combustion}}{\text{Moles of } O_2 \text{ fed to reactor}}\right)$$

STEAM-TO-CARBON RATIO

The steam-to-carbon ratios (S/C) can be defined as:

$$\frac{S}{C} = \frac{\text{Moles of steam fed to the reactor}}{n \times \text{Moles of hydrocarbon fed to the reactor}}$$

RECYCLE RATIO

The recycle ratio (RR) is defined as the ratio of the exhaust gas flow from the reformer or anode recycled to the total exhaust flow from the reformer or anode.

$$\text{RR} = \frac{\text{Moles of the exhaust gas from the reformer or anode recycled}}{\text{Total moles of exhaust from the reformer or anode}}$$

REFORMER EFFICIENCY

Thermal efficiency (η) of fuel processor can be defined as

$$\eta(\%) = \frac{n_{H_2}\text{LHV}_{H_2}}{\text{LHV}_F}$$

where n_{H_2} is the number of moles of hydrogen produced per mole of fuel and LHV_k is the lower heating value per mole of species k. However, this definition ignores the heat added to the system to run the process. The above thermal efficiency definition can be modified to include that supplied heat as,

$$\eta(\%) = \frac{n_{H_2}\text{LHV}_{H_2}}{\text{LHV}_F + Q_{in}} \quad \text{(A)}$$

$$\eta(\%) = \frac{n_{H_2}\text{LHV}_{H_2} - Q_{in}}{\text{LHV}_F} \quad \text{(B)}$$

In the Definition (A), the heat is provided externally to the system. Whereas, the product hydrogen supplies the heat to the system in the Definition (B). Since CO can be completely converted to H_2 through WGS for the PEMFC, alternatively efficiency can also be defined as:

$$\eta(\%) = \frac{n_{H_2}\text{LHV}_{H_2} + n_{CO}\text{LHV}_{CO} - Q_{in}}{\text{LHV}_F} \times 100$$

Furthermore, used in conjunction with a high temperature fuel such as SOFC, efficiency can be defined as:

$$\eta(\%) = \frac{n_{H_2}\text{LHV}_{H_2} + n_{CO}\text{LHV}_{CO} + n_{CH_4}\text{LHV}_{CH_4} - Q_{in}}{\text{LHV}_F} \times 100$$

FUEL CELL EFFICIENCY

The fraction of the total electric and thermal energy generated in the fuel cell stack is often referred to as the cell or stack efficiency. The gross efficiency of a fuel cell system is defined as

$$\eta_{\text{gross}}(\%) = \eta_{\text{fuelprocessor}}(\%)\eta_{\text{powerconditioner}}(\%)\eta_{\text{fuelcell}}(\%)$$

The net system efficiency is defined as the total power extracted from the fuel cell to the lower heating value of the fuel to the reformer:

$$\eta(\%) = \frac{(\text{AC power from the fuel cell} - \text{parasitic load})}{\text{Lower heating value of fuel}} \times 100$$

Parasitic load includes the power required by the air compressors, pumps, etc.

START-UP TIME

The start-up time for a reformer can be defined as the time required to produce H_2 and/or CO at the steady-state levels.

APPENDIX

C

Acronyms

AC: Alternating Current
AFC: Alkaline Fuel Cell
ANN: Artificial Neural Network
APU: Auxiliary Power Unit
ASR: Area Specific Resistance
ASTM: American Society for Testing and Materials
ATR: Autothermal Reforming
BET: Brunauer, Emmet, and Teller
BNHA: Ni-substituted Ba-hexaalumina
BOP: Balance of Plant
BV: Bivalent
CFD: Computational Fluid Dynamics
CGO: Cerium Gadolinium Oxide
CHP: Combined Heat and Power
CNF: Carbon Nanofilament or Carbon Nanofiber
CNT: Carbon Nanotube
COTS: Commercial Off-the-Shelf
CPOX: Catalytic Partial Oxidation
CSTR: Continuous Stirring-tank Reactor
DBD: Dielectric Barrier Discharge
DBT: Dibenzothiophene
DC: Direct Current
DCFC: Direct Carbon Fuel Cell
DFT: Density Functional Theory
DIR: Direct Internal Reforming
DMDBT: Dimethydibenzo Thiophene
DME: Dimethyl Ether
DMFC: Direct Methanol Fuel Cell
DMS: Dimethyl Sulfide
DU: Direct Utilization
ECN: Energy Research Centre of Netherlands
EDX: Energy Dispersive using X-ray
EGR: Exhaust Gas Recycle
ER: External Reforming
FDM: Finite Difference Method
FEM: Finite Element Method
FPD: Flame Photometric Detector
FVF: Forward Vortex Flow
FVM: Finite Volume Method
GA: Gliding Arc
GDC: Gadolinium-doped Ceria
GHSV: Gas Hourly Space Velocity (h^{-1})
GTL: Gas-to-liquids
HDS: Hydrodesulfurization
HHV: Higher Heating Value
HSA: High Surface Area
HRTEM: High Resolution Transmission Electron Microscopy
HTS: High Temperature Shift
IGCC: Integrated Gasification Combined Cycle
IGFC: Integrated Gasification Fuel Cell
IIR: Indirect Internal Reforming
IPOX: Indirect Partial Oxidation
IR: Internal Reforming
LDC: Lanthanum-doped Ceria
LHC: Light Hydrocarbon
LHHW: Langmuir−Hinshelwood−Hougen−Watson
LHV: Lower Heating Value
LPG: Liquefied Petroleum Gas
LSA: Low Surface Area

LSCF: Lanthanum Strontium Cobalt Ferrite
LSZN: $La_{2-x}Sr_xZr_{2-y}Ni_yO_{7-\delta}$ pyrochlore
LTS: Low Temperature Shift
MCFC: Molten Carbonate Fuel Cell
MDBT: Methyldibenzo Thiophene
MDF: Model Diesel Fuel
MN: 1-Methylnaphthalene
NGDM: Natural Gas Desulfurization Material
NETL: National Energy Technology Laboratory
NSA: Near-surface Alloy
O/C: Oxygen-to-carbon (atomic) Ratio
OCV: Open Circuit Voltage
ODE: Ordinary Differential Equation
ODS: Oxidative Desulfurization
OSR: Oxidative Steam Reforming
PAFC: Phosphoric Acid Fuel Cell
PBMR: Packed-bed Membrane Reactor
PDE: Partial Differential Equation
PEFC: Polymer Electrolyte Fuel Cell
PEMFC: Proton Exchange Membrane Fuel Cell
PNNL: Pacific Northwest National Laboratory
POX: Partial Oxidation
PrOX: Preferential Oxidation
PTFE: Polytetrafluoroethylene
PWM: Pulse-width-modulation
RF: Radio Frequency
RK: Runge–Kutta
RTD: Residence Time Distribution
RTD: Resistance Temperature Detector
RVF: Reverse Vortex Flow
RWGS: Reverse Water Gas Shift
SARS: Selective Adsorption for Removing Sulfur
SASZ: Scandia Alumina-stabilized Zirconia
S/C: Steam-to-carbon Ratio
SEM: Scanning Electron Microscopy
SmDC: Samaria doped ceria
SMET: Selective Methanation
SNG: Synthetic Natural Gas
SOFC: Solid Oxide Fuel Cell
SR: Steam Reforming
SSZ: Scandia-stabilized Zirconia
STP: Standard Temperature and Pressure
SV: Space Velocity
TAP: Temporal Analysis of Products
TARDEC: Tank Automotive Research, Development and Engineering Center
TBM: tert-Butyl Mercaptan
TD: *n*-Tetradecane
TEM: Transmission Electron Microscope
THT: Tetrahydro Thiophene
TPH: Temperature Programmed Hydrogenation
TOF: Turnover Frequency (molecules/h/active sites)
TOX: Total Oxidation
TPB: Triple Phase Boundaries
TPO: Temperature Programmed Oxidation
TPR: Temperature Programmed Reduction
VDR: Varying Degree of Reduction
VHSV: Volumetric Hourly Space Velocity
WGS: Water Gas Shift
WHSV: Weight Hourly Space Velocity (g/g/h)
XANES: X-ray Absorption Near-edge Structure
XPS: X-ray Photoelectron Spectroscopy
XRD: X-ray Diffraction
YSZ: Yttria-stabilized Zirconia
ZDC: Zirconia-doped Ceria

Index

C

D

E

F

G

H

I

J

O

P